VESPA

Behaviour of Long-Lived Fission and Activation Products in the Nearfield of a Nuclear Waste Repository and the Possibilities of their Retention

Conducted by:

GRS - 374

Gesellschaft für Anlagen-
und Reaktorsicherheit
(GRS) gGmbH

VESPA

Behaviour of Long-Lived Fission and Activation Products in the Nearfield of a Nuclear Waste Repository and the Possibilities of their Retention

Barbara Bischofer (GRS),
Sven Hagemann (GRS),
Marcus Altmaier, Nidhu Banik (KIT),
Dirk Bosbach (FZJ),
Guido Bracke (GRS),
Vinzenz Brendler (HZDR),
Hildegard Curtius (FZJ),
Nicolas Finck (KIT),
Carola Franzen (HZDR),
Xavier Gaona, Horst Geckeis (KIT),
Frank Heberling, Michel Herm (KIT),
Jonathan Kindlein (GRS),
Remi Marsac, Volker Metz (KIT),
Andrés Muñoz (GRS),
Konstantin Rozov (FZJ),
Thorsten Schäfer (KIT),
Tina Scharge (GRS),
Yuri Totskiy, Martin Wiedemann (KIT),
Ezgi Yalcintas (KIT)

June 2016

Remark:

The underlying work of this report was supported under contract No. 02E10770, 02E10780, 02E10790 and 02E10800 by the German Federal Ministry of Economics and Energy (BMWi).

The work was conducted by the Gesellschaft für Anlagen- und Reaktorsicherheit (GRS) gGmbH, Forschungszentrum Jülich GmbH (FZJ), Helmholtz-Zentrum Dresden-Rossendorf e.V. (HZDR) and Karlsruher Institut für Technologie (KIT).

The authors are responsible for the content of this report.

GRS - 374
ISBN 978-3-944161-55-6

Keywords:

repository, radionuclides, modelling, sorption, solubility

Foreword

The present document is the final report of the Joint Research Project VESPA (Behaviour of Long-lived Fission and Activation Products in the Near Field of a Nuclear Waste Repository and the Possibilities of Their Retention), started in July 2010 with a duration of four years. The following four institutions were collaborative Partners in VESPA:

- Gesellschaft für Anlagen- und Reaktorsicherheit (GRS) gGmbH
- Institut für Energie- und Klimaforschung, IEK-6: Nukleare Entsorgung und Reaktorsicherheit, Forschungszentrum Jülich (FZJ)
- Institut für Ressourcenökologie (IRE), Helmholtz-Zentrum Dresden-Rossendorf (HZDR)
- Institut für Nukleare Entsorgung (INE), Karlsruher Institut für Technologie (KIT)

VESPA was funded by the German Federal Ministry of Economics and Energy (BMWi) under the contract numbers 02 E 10770 (GRS), 02 E 10780 (FZJ-IEF-6), 02 E 10790 (HZDR-IRE), 02 E 10800 (KIT-INE).

The chapters within this report have been prepared by the following authors and institutions:

- Chapter 4: HZDR-IRE: Carola Franzen, Norbert Jordan, Vinzenz Brendler
- Chapter 5: KIT-INE: Marcus Altmaier, Nidhu Banik, Nicolas Finck, Xavier Gaona, Frank Heberling, Michel Herm, Remi Marsac, Volker Metz, Thorsten Schäfer, Yuri Totskiy, Martin Wiedemann, Ezgi Yalcintas, Horst Geckeis
- Chapter 6: FZJ-IEK-6: Hildegard Curtius, Konstantin Rozov, Dirk Bosbach
- Chapter 7: GRS: Barbara Bischofer, Sven Hagemann, Guido Bracke, Jonathan Kindlein, Andrés Muñoz, Tina Scharge

Table of Contents

1 Einleitung

Die Bewertung der Langzeitsicherheit von Endlagersystemen erfolgt anhand verschiedener denkbarer Ereignisabläufe, die je nach Ausprägung zur Mobilisierung von Radionukliden in das Nahfeld führen können. In allen derzeit in Deutschland diskutierten Wirtsgesteinsformationen für wärmeentwickelnde Abfälle (Ton, Salz, Granit) ist ein Lösungszutritt Teil aller oder einiger Ereignisabläufe. Sollte es zu einem Zutritt von Lösung zu den Abfallbehältern kommen, ist mit einer Korrosion der Abfallbehälter und anderer metallischer Komponenten im Nahfeld zu rechnen. Diese kann in der Folge zu einem Ausfall der Behälter führen, so dass der sichere Einschluss der Radionuklide im einschlusswirksamen Gebirgsbereich in Frage gestellt sein kann. Derartige Entwicklungsmöglichkeiten des Endlagersystems können nach heutigem Kenntnisstand selbst bei konsequenter Umsetzung des Sicherheitskonzeptes bei einem Endlager in einer Tonformation oder Kristallinformation sowie mit einer geringeren Wahrscheinlichkeit auch bei einem Endlager in einer Salzformation auftreten. Zur Bewertung dieser Ereignisabläufe sind dann Langzeitsicherheitsanalysen durchzuführen, die in Modellform die Mobilisierung, die Ausbreitung und Rückhaltung von Radionukliden simulieren.

Diese Analysen basieren auf Modellen und Daten, mit denen sich die ablaufenden Prozesse beschreiben lassen, die in den zu betrachtenden Entwicklungen des Endlagersystems auftreten. Mobilitätsprozesse im Nahfeld werden in den Codes der Langzeitsicherheitsanalyse im Wesentlichen durch die Größen Radionuklid-Inventar, Mobilisierungsrate (Quellterm), Löslichkeitsgrenze, Diffusionskoeffizienten und Sorptionskoeffizienten abgebildet. Die zuverlässige und robuste Ableitung dieser Parameter stellen zentrale Arbeitsgebiete aktueller geochemischer Forschungen im Kontext der Endlagersicherheitsforschung dar. Eine besondere Rolle bei Freisetzungsszenarien spielen Spalt- und Aktivierungsprodukte, da sie im Gegensatz zu den Hauptkomponenten wärmeentwickelnder Abfälle den größten Teil der resultierenden Zusatzdosis in der Biosphäre ausmachen können ([KEE/NOS2005]: Salz/Ton, [GRA2008, NAG2002, AND2005]:Ton, [SKB2011]: Granit). Von hoher Relevanz sind dabei die mobilen Radionuklide ^{135}Cs, ^{129}I, ^{99}Tc, ^{79}Se, ^{36}Cl, ^{14}C, für die bislang keine oder nur eine sehr geringe Rückhaltung durch die im Endlager vorhandenen natürlichen und technischen Materialien angenommen wurde. Eine Verbesserung des Kenntnisstandes zu ihrer Löslichkeit und Rückhaltung kann bei Berücksichtigung in der Langzeitsicherheitsanalyse zu einer deutlichen Reduzierung berechneter Aktivitätsfreisetzungen führen.

Es bestand daher der Bedarf, die Rückhalteprozesse für die genannten Nuklide näher zu betrachten und somit ein realistischeres Gesamtbild bezüglich ihrer Mobilität zu erhalten. Hierzu war es nötig Information und Daten zu gewinnen, die für eine quantitative Beschreibung der Mobilisierung und des Transports dieser Stoffe auf dem Wasserpfad relevant sind.

Dies umfasst Untersuchungen zu

- Redoxverhalten und physikalisch-chemischen Eigenschaften der Bindungsformen in wässrigen Lösungen (Technetium, Selen, Iod, Cäsium)

- Identifizierung und Charakterisierung von Rückhaltungsprozessen an endlagerrelevanten Festphasen (Technetium, Selen, Iod an Eisenoxiden, magnesiumhaltigen Hydroxidphasen, Eisensulfiden und Calcit)

- Vorherrschenden Bindungsformen in den radioaktiven Abfällen (^{14}C)

Zur Beschreibung des chemischen Verhaltens von Radionukliden in wässrigen Systemen, also der Rückhaltung durch Festphasenbildung und der Bildung von Oberflächenkomplexen, ist eine genaue Kenntnis ihrer thermodynamischen Eigenschaften unerlässlich. Während der Informationsstand für die Hauptkomponenten potentieller Zuflusslösungen (Na+, K^+, Mg^{2+}, Ca^{2+}, H^+, Cl^-, SO_4^{2-}, OH^-, HCO_3^-, CO_3^{2-}, H_2O) auch bei erwarteten erhöhten Nahfeldtemperaturen > 25 °C als sehr gut bezeichnet werden darf, stehen Daten und Modelle für gelöste Selen-, Technetium, Cäsium und Iod-Spezies nur eingeschränkt zur Verfügung. Das trifft besonders auf die reduzierten Spezies von Selen und Technetium zu.

Im Rahmen des Vorhabens sollten daher relevante thermodynamische Daten für die genannten chemischen Elemente zusammengestellt und durch experimentelle Untersuchungen bei 25 °C und teilweise auch bei höheren Temperaturen (bis 90 °C) ergänzt werden. Die aus diesen Arbeiten abgeleiteten thermodynamischen Modelle sollten für alle diskutierten Wirts-gesteinsformationen und relevanten Ionenstärkebereiche gleichermaßen anwendbar sein. Dabei galt es einerseits die Redoxchemie der Elemente Selen und Technetium weiter aufzuklären als auch die Grundlage für Modelle zu schaffen, die Berechnung von Aktivitätskoeffizienten erlauben. Für das vierwertige Technetium sollten im Rahmen von VESPA konsistente Datensätze zur vollständigen thermodynamischen Beschreibung von Tc(IV) Löslichkeiten in verschiedenen Lösungssystemen gewonnen werden, die Eingang in die thermodynamische Referenzdatenbasis THEREDA finden sollen.

Um die Untersuchungen von Redoxgleichgewichten in salinaren Lösungen besser interpretieren zu können, sind Ansätze nötig, die die Umrechnung von gemessenen Redoxpotentialen in thermodynamisch eindeutig interpretierbare Größen erlaubt. Hierzu sollten ergänzende Arbeiten vorgenommen werden, um die Anwendung auf einen breiteren pH-Bereich zu erlauben. Der für die Untersuchungen vorgesehene Temperaturbereich umfasste 25 °C – 90 °C. Die an- gestrebten thermodynamischen Modelle sollten für alle diskutierten Wirtsgesteinsformationen und relevanten Ionenstärkebereiche gleichermaßen anwendbar sein.

Ein weiterer Schwerpunkt der Arbeiten war die Rückhaltung anionischer Spezies des Selens, des Technetiums und des Iods. Hier war insbesondere die Frage zu klären, ob und in welcher Weise eine Sorption an oder ein Einbau in endlagerrelevanten Festphasen erfolgt. Hierzu gehören Eisenoxide (aus der Korrosion von Behältermaterialien), Sorelphasen (aus technischen Barrieren), geschichtete Doppelhydroxide (*layered double hydroxides* – LDH, als Sekundärprodukt der Reaktion von aluminiumhaltigen Behälterbestandteilen), Calcit und Eisensulfide (Bestandteile von Tongesteinen) und Minerale aus Granitgesteinen. Wichtig war auch zu klären, welcher Mechanismus jeweils zur Rückhaltung beiträgt (z. B. Sorption, Mitfällung, Einbau). Bei redoxsensitiven Elementen wie Selen und Technetium kann die Rückhaltung gleichzeitig mit einer Reduktion einhergehen. Solche Prozesse sind nur durch Anwendung spektroskopischer Verfahren auf molekularer Ebene zweifelsfrei aufzuklären.

Eine direkte Einbindung der Projektergebnisse in die Modelle und Rechencodes der Langzeitsicherheitsanalyse sollte ein wesentlicher Bestandteil des Vorhabens werden. Diese Kopplung von Grundlagenforschung und Anwendung erfolgt durch Abstraktion der Forschungsergebnisse in diskrete Eingangsdaten (Sorptionskoeffizienten und Löslichkeitsgrenzen) für die notwendigerweise vereinfachenden Rechencodes. Mit den Rechnungen sollte gezeigt werden, wie sich die veränderten Eingangsparameter auf die Freisetzungsdosis von Radionukliden auswirkt.

Im Einzelnen war geplant, für ^{14}C den derzeitigen Wissenstand zu den vorherrschenden Bindungsformen in wärmeentwickelnden Abfällen zu dokumentieren. Die Bindungsform im Abfall bestimmt die primäre chemische Freisetzungsform des Kohlenstoffs und hat ganz erheblichen Einfluss auf seine Mobilität. Zudem sollten grundlegende Arbeiten zur ^{14}C Analytik in hochradioaktiven Lösungen durchgeführt werden.

Im Rahmen des Verbundprojektes haben die Partner folgende Aufgaben bearbeitet:

- GRS: Bestimmung thermodynamischer Daten für Iod, Selen und Cäsium in salinaren Lösungen bei Temperaturen von 25 – 90 °C, Bestimmung von Löslichkeitskonstanten aus Experimenten zur Löslichkeit von synthetisierten LDH-Verbindungen sowie Darstellung des aktuellen Wissensstandes zur Speziation von ^{14}C unter den Bedingungen von HAW-Endlagern. Arbeiten zu Methoden zur Umrechnung von Redoxpotentialen in salinaren Lösungen. Einbindung von Projektergebnissen zur Löslichkeit und Rückhaltung in Rechencodes der Langzeitsicherheitsanalyse.

- HZDR-IRE: Komplexbildung von Selen mit kationischen Liganden bei höheren Temperaturen. Sorptionsversuche mit Selen und Analyse von Sorbentien und Oberflächenspezies. Modellierung und Datenbewertung (und Bereitstellung für Einbindung in Datenbanken THEREDA und RES^{3}T)

- FZJ-IEF-6: Ermittlung experimenteller Daten zur Rückhaltung der in anionischer Form vorliegenden Radioisotope ^{129}I, ^{99}Tc, ^{75}Se an gezielt synthetisierten teilsubstituierten LDH-Verbindungen. Langzeitstabilität von Mischkristall-LDH-Verbindungen.

- KIT-INE: Aquatische Chemie und Thermodynamik von Tc(IV). Reduktionschemie von Tc(VII) / Tc(IV) in verschiedenen Medien. Einfluss der Reduktionskinetik auf die Technetium-Migration in natürlichen Systemen. Struktureller Einbau von Selen in Mineralphasen (Calcit, Pyrit). Analytische Arbeiten zur Bestimmung der Speziation von ^{14}C. Synthese von Sorelphasen für die Untersuchung der ^{129}I Rückhaltung.

2 Zusammenfassung

2.1 Chemische Bindungsform und Freisetzung von ^{14}C in radioaktiven Abfällen

Im Rahmen einer Literaturstudie der GRS wurde der Wissenstand zur chemischen Bindungsform und Freisetzung von ^{14}C in radioaktiven Abfällen dokumentiert. Dieser ist aufgrund spärlicher analytischer Daten weiterhin lückenhaft. Dies gilt sowohl hinsichtlich vernachlässigbar wärmeentwickelnder Abfälle als auch für abgebrannte Brennelemente. Angesichts unzureichender Informationen wird in Langzeitsicherheitsbetrachtungen langfristig eine vollständige Umsetzung des ^{14}C-Inventars zu CO_2, CH_4 und niedrigen Kohlenwasserstoffen erwartet.

Es wird davon ausgegangen, dass der ^{14}C-Bestand bei der Wiederaufbereitung von Brennelementen, gasförmig entweicht. Ebenso verhält sich ^{14}C bei der Aufbereitung von Kühlmitteln, wo es je nach Reaktortyp vornehmlich als Carbonate oder Kohlenwasserstoff auftritt. Für Brennelemente wird angenommen, dass ^{14}C negativ geladen als Carbid oder als neutraler Kohlenstoff vorliegt, entsprechend der vorherrschenden chemischen Speziation der Mutterelemente Sauerstoff und Stickstoff. Diese Annahmen sind aber weiterhin experimentell nicht belegt. Dementsprechend ist auch unklar, ob die Freisetzung konsequenterweise v. a. als Kohlenwasserstoff erfolgt.

Die Berücksichtigung der Unsicherheiten und der Unkenntnisse über das Verhalten von ^{14}C-haltigen Abfällen unterschiedlicher Art im Endlager führt letztlich zu erheblichen Konservativitäten in den Annahmen von Langzeitsicherheitsanalysen und daher vermutlich zu einer Überschätzung der errechneten potentiellen Strahlenexposition. Aufgrund der Datenlage erscheinen daher zur Verringerung der Unsicherheiten in der Abschätzung der potenziellen Strahlenexposition weitere Untersuchungen zur Speziation des ^{14}C in abgebrannten Brennstoffen, dessen Umsetzung und Freisetzungsverhalten erforderlich. Mit dieser Zielrichtung wurde Ende 2013 das EU-Forschungsprojekt CAST (Carbon-14 Source Term) gestartet. Das Projekt soll sowohl die chemische Form als auch das Freisetzungsverhalten von ^{14}C aus den Abfallarten Stahl, Zircaloy, Ionenaustauscherharz und Graphit zu untersuchen.

2.2 Analytische Arbeiten zur Bestimmung der Speziation von ^{14}C

Die vom KIT-INE konzipierten Arbeiten für den Aufbau einer Anlage zur Analyse der ^{14}C Speziation in wässrigen und gasförmigen Proben wurden erfolgreich abgeschlossen. Die Arbeiten zur ^{14}C Analytik erfolgen im Kontext der Arbeiten des KIT-INE im Rahmen des EU Projekts CAST. Zum Umgang mit den Proben, die neben ^{14}C weitere Aktivierungsprodukte wie ^{60}Co und Spaltprodukte wie ^{137}Cs in beachtlichen Aktivitätskonzentrationen enthalten, wurde ein spezieller Handschuhkasten angefertigt und im Kontrollbereich des INE aufgebaut. Die eigentliche Anlage zur Extraktion und Trennung von organischen und anorganischen ^{14}C Spezies wurde zunächst mit niedrig-dotierten Referenzproben in einem Abzug getestet. Nach diesen Testmessungen wurde die Anlage im Handschuhkasten installiert. Kalibrierungsarbeiten mit anorganischen und organischen Referenzproben (^{14}C dotiertes Na_2CO_3, CH_3CO_2Na, Mischungen aus Na_2CO_3 und CH_3CO_2Na) wurden im Handschuhkasten erfolgreich durchgeführt. Bei den mit 10 bis 1000 Bq ^{14}C dotierten Proben wurde ein Wiedererhalt von ≥ 90 % gemessen. Zur Optimierung der Genauigkeit der ^{14}C Analyse mittels Flüssigszintillationsanalyse (LSC) wurden verschiedene LSC-cocktails und Materialien für Probengefäße getestet.

2.3 Chemische Thermodynamik der Spaltprodukte Selen, Iod und Cäsium

Die wässrige Speziation des Selens hat einen signifikanten Einfluss auf Grenzflächenreaktionen. Daher wurde vom HZDR die Selen-Speziation als Funktion von Selen-Konzentration, pH, Redoxpotential, Ionenstärke und Temperatur, sowie in Wechselwirkung mit den Metallionen Na^+, Ca^{2+} und Mg^{2+} mittels NMR, FT-IR und RAMAN untersucht. Es konnten Stabilitätsbereiche der verschiedenen Se-Komplexe, Dimerisierungsreaktionen und strukturelle Parameter aufgeklärt werden.

Im Mittelpunkt der thermodynamischen Arbeiten der GRS stand die chemische Thermodynamik der Elemente Selen in den Oxidationsstufen +IV und +VI, Iod in der Oxidationsstufe –I und Cäsium in der Oxidationsstufe +I im Temperaturbereich 0 bis 90 °C. Für diese Elemente konnte ein polythermes physikalisch-chemisches Modell erstellt werden, das die Prognose der Aktivitätskoeffizienten für wichtige Lösungssysteme erlaubt.

Für 25 °C gab es für Lösungssysteme mit Cäsium, Selen und Iod kaum Datenlücken, so dass sich die Laboruntersuchungen auf Gleichgewichtseigenschaften bei höheren

Temperaturen konzentrierten. Der Schwerpunkt lag dabei auf Messungen binärer Systeme von 40 ° bis 90 °C. Für isopiestische Messungen wurde eine Schaukelapparatur entwickelt, die die Gleichgewichtseinstellung bei höheren Temperaturen beschleunigt.

Selenate und Selenite des Natriums, des Kaliums und Magnesiums wurden mit Hilfe von isopiestischen Messungen bei 40 ° – 90 °C untersucht. Für die weniger löslichen analogen Verbindungen des Calciums kamen Löslichkeitsversuche zum Einsatz. Vorläufig nicht zum Erfolg führten potentiometrische Messungen an Hydrogenselenit-Lösungen. Die neu entwickelte Methodik erlaubt zwar grundsätzlich die Ableitung von Aktivitätskoeffizienten, muss aber zur Ausschaltung von chemischen Störeffekten weiter entwickelt werden. Auf Basis der durchgeführten Laborversuche und weiterer Literaturdaten konnte ein polythermes Modell entwickelt werden, das die Aktivitätskoeffizienten des Selenits und des Selenats in binären Lösungen richtig beschreibt. Außerdem wurden neue Löslichkeitskonstanten für Calciumselenit und Calciumselenat abgeleitet. Besonders Calciumselenit könnte unter leicht reduzierenden Bedingungen die für Selen löslichkeitsbestimmende Phase darstellen.

Auf isopiestischem Wege wurden auch Lösungen des Natriumiodids und des Kaliumiodids untersucht. Die Messungen an Magnesiumiodid-Lösungen erwiesen sich als sehr anspruchsvoll, da die benötigten reinen MgI_2-Stammlösungen nur unter großem Aufwand herzustellen sind und sich bei geringstem Luftkontakt zersetzen. Die Probleme konnten letztlich überwunden werden, die Anzahl der erhaltenen Messpunkte ist aber beschränkt. Das entwickelte polytherme Modell erlaubt die Berechnung der Aktivitätskoeffizienten von Iodid in den besprochenen binären Lösungen bei 25 ° – 90 °C. Auf Basis von Annahmen zu gemischten Lösungen lässt sich das Modell auch auf komplexer zusammengesetzte Lösungen übertragen.

Die Untersuchungen zu Cäsium ergänzten frühere Modellentwicklungen, die im Rahmen von Vorgängerprojekten erstellt worden sind. Sie umfassten isopiestische Messungen bei calcium- und magnesiumhaltigen Mischsystemen bei 25 °C sowie Untersuchungen binärer Systeme bei 40-90 °C. Auf Basis der Versuchsergebnisse konnte das Modell bei 25 °C vervollständigt werden. Es ist nun weiterhin möglich, die Aktivitätskoeffizienten von Cäsium in binären Lösungen bis 90 °C zu prognostizieren.

Auf Grundlage dieser Modelle konnte die Löslichkeitsgrenze für Selen für einige angenommene Lösungstypen für Endlager in Steinsalz- und Tongesteinsformationen berechnet werden. Wenn Selenit die vorherrschende Spezies ist, so wird die Löslichkeit durch die Bildung von Calciumselenit begrenzt. Für Selenat, für Iodid und Cäsium konnten keine löslichkeitsbegrenzenden Phasen identifiziert werden.

2.4 Aquatische Chemie und Thermodynamik von Tc(IV)

Im Rahmen der Arbeiten von KIT-INE wurde die Redoxchemie von Technetium in endlagerrelevanten Lösungen eingehend untersucht. Auf Basis einer umfangreichen und systematischen Untersuchung der Technetium-Redoxchemie in verdünnten bis hochsalinaren Lösungen, konnte das Stabilitätsfeld des i.A. schwerlöslichen Tc(IV) genauer abgegrenzt werden und Aussagen zur Redoxkinetik abgeleitet werden. Es wurden Arbeiten in verdünnten bis hochsalinaren Na und $MgCl_2$ Lösungen durchgeführt, wodurch erstmalig der Einfluss der Ionenstärke auf die Redoxgleichgewichte des Technetium eingeschätzt werden konnte. Die durchgeführten Arbeiten erlauben die Validierung verschiedener thermodynamischer Modelle zur Tc-Redoxchemie. Die hohe Relevanz der tetravalenten Oxidationsstufe von Technetium in endlagertypischen stark reduzierenden geochemischen Verhältnissen wurde herausgestellt.

In verschiedenen experimentellen Studien wurde die Löslichkeit der amorphen Tc(IV)-Oxid/Hydroxid-Phase $TcO_2xH_2O(s)$ in wässriger Lösung über einen großen pH- und Ionenstärkebereich (NaCl, $MgCl_2$ und $CaCl_2$) bei 25 °C untersucht. Die umfangreichen Arbeiten ermöglichten die Ableitung experimentell belastbar abgesicherter thermodynamischer Daten (Löslichkeitsprodukt und Hydrolysekonstanten) und Ionenwechselwirkungsparameter (SIT + Pitzer), die in die thermodynamische Datenbasis THEREDA integriert werden. Die abgeleiteten thermodynamischen Daten sind standortunspezifisch und stellen grundlegende physikalisch-chemische Größen dar, die im Rahmen von geochemischen Modellrechnungen die gezielte Analyse der Technetiumchemie in verschiedenen Endlagerkonzepten und Szenarien erlauben.

2.5 Reduktion, Sorption und Einbau von Tc(VII) in Magnetit

Basierend auf EXAFS Untersuchungen gibt es starke Hinweise, dass es nicht nur zur Reduktion von Tc(VII) und Ausbildung eines Tc(IV)-Magnetit-Oberflächenkomplexes kommt, sondern es findet darüber hinaus ein Einbau von Tc(IV) in die Magnetit-Struktur statt. Dieses stellt einen potentiellen Rückhaltemechanismus in niedrigsalinaren NaCl-Lösungen dar. Zudem wurden weiterführende EXAFS-Messungen zum Redoxverhalten von Tc(VII)/Tc(IV) bei Anwesenheit von Eisenphasen durchgeführt. Die Ergebnisse lassen sich so interpretieren, dass der Umfang und Mechanismus der

Rückhaltung von Technetium an Eisenoxid-Phasen sehr stark von der Oberflächenbeladung und dem pH- Wert abhängig ist. Ein signifikanter Teil des Tc(IV) ist bei niedriger Technetium-Konzentration in Magnetit eingebaut, während er bei höheren Konzentrationen ausfällt. Der Einbau wird zusätzlich von höheren Magnetit-Umkristallisationsraten begünstigt. Diese Ergebnisse liefern Schlüsselinformationen zum Verständnis der Tc-Retention an der relevanten sekundären Eisenphase Magnetit in einem Endlager.

2.6 Einfluss der Reduktionskinetik auf die Tc-Migration in natürlichen Systemen

Die Wechselwirkung von Tc(VII) mit potentiellen Wirtsgesteinsmaterialien wurde an kristallinen Gesteinsproben aus dem Äspö-HRL (Hard Rock Laboratory, Schweden) und an Proben eines potenziellen Standorts für die tiefengeologische Endlagerung von abgebranntem Kernbrennstoff und hochradioaktiven Abfällen in Russland (Nižnekanskij-Massiv (NK), Sibirien) untersucht, sowie an Magnetitproben unterschiedlicher Stöchiometrie. Die Bohrkerne aus Äspö wurden im Rahmen des EU- Projektes CP CROCK unter anoxischen Bedingungen gewonnen, transportiert und gelagert, um möglichst ungestörte, naturnahe geochemische Bedingungen speziell bzgl. der Redoxchemie zu erhalten. Teile des so gewonnenen Äspö-Diorit (ÄD) wurden künstlich aufoxidiert, um den Effekt oxidativer Störung auf die Tc- Rückhaltung zu dokumentieren.

Die durchgeführten Batch-Experimente zeigen, dass die Reduktion von Tc(VII) an Fe(II)-haltigen Mineralphasen (speziell Biotit) stattfinden. Spektroskopische Untersuchungen mittels XPS und XANES konnten ausschließlich Tc(IV) an der Granitoberfläche identifizieren. Zusätzliche Untersuchungen zur Tc Bindungsumgebung mittels EXAFS werden ausgewertet. Weitere Untersuchungen unter Variation der eingesetzten Tc- Konzentration im Bereich 10^{-5} – 10^{-10} mol/L zeigen eine von der Tc(VII) -Konzentration abhängige Reduktion und Kinetik im Einklang mit der Reduktionskapazität des nicht oxidierten Gesteins. Die Untersuchungen an auf-oxidierten Proben dokumentieren weiterhin den starken Einfluss der Probenlagerung auf die Tc(VII) -Rückhaltung in den untersuchten kristallinen Gesteinen. Sorptionsdaten an nicht oxidierten ÄD nach drei Monaten Kontaktzeit bei niedrigen Tc-Konzentrationen zeigen Retardationskoeffizienten log Kd > 2.5 Kd-Werte für oxidiertem ÄD- und NK-Materialien sind deutlich niedriger als für die unoxidierten Proben aber untereinander sehr vergleichbar. Eine kolloidale Tc-Phase konnte unter den eingestellten Grundwasserbedingungen (pH 8, I = 0.2 M für ÄD und pH 8, I = 0.005 M für NK) nicht nachgewiesen werden. Die Tc-Desorption ist insignifikant unter den natürlichen Grundwasserbedingungen, erreicht aber durch Oxidation der Proben durch Luftsauerstoff ~ 95 %.

Weitere Untersuchungen fokussierten auf Tc-Migrationsexperimenten an einer natürlichen zuvor mittels µCT (Computer Tomographie) charakterisierten Kluft unter anaeroben Bedingungen.

Experimentell gewonnene HTO (tritiertes Wasser) und ^{36}Cl Durchbruchskurven (sog. break-through curves – BTC) unter Variation der Fließgeschwindigkeit zeigen ein ausgeprägtes Tailing bedingt durch die Kluftgeometrie bzw. Matrixdiffusion, jedoch konnte kein Anionen-Ausschluss unter den gewählten Versuchsbedingungen beobachtet werden. Die Tc-Migrationsstudien wurden mit ^{95m}Tc im Konzentrationsbereich ~10^{-11} M – 10^{-9} M durchgeführt. Der Tc-Wiedererhalt in diesen Versuchen nimmt mit Erhöhung der Verweilzeit in der Kluft ab und dokumentiert deutlich den Einfluss kinetischer Effekte auf die Tc-Mobilität bzw. -Rückhaltung. Die in diesen Versuchen beobachteten Raten der Tc-Oberflächenrückhaltung bzw. -Reduktionskinetik liegen mit 0.45 – 0.61 d^{-1} um ca. eine Größenordnung höher als die über Batchexperimente ermittelten Daten von 0.036 d^{-1}.

Die Erkenntnisse aus diesen grundlegenden Studien wurden zur Bewertung der Tc-Rückhaltung an Eisenoxiden bzw. der Untersuchung der Tc(VII)-Reduktionskinetik in natürlichen Systemen herangezogen, welche sowohl im Rahmen von Batchexperimenten als auch Migrationsstudien analysiert wurden. Die gewonnenen Daten bezüglich des Einflusses von kinetischen Aspekten der Tc-Reduktion können weiterhin zur Sensitivitätsanalyse im Vergleich zu einem Gleichgewichtsansatz bzgl. der reaktiven Transportmodellierung dienen.

Die im Vorhaben VESPA durchgeführten Arbeiten führten zu einem deutlich verbesserten Verständnis und erlauben eine wesentlich genauere quantitative Beschreibung der Tc-Retention in endlagerrelevanten Systemen.

2.7 Struktureller Einbau von Selen in Mineralphasen (Calcit, Pyrit)

Die oxidierten Selenspezies Selenat ($Se(VI)O_4^{2-}$) und Selenit ($Se(IV)O_3^{2-}$) sind relativ leicht löslich und wechselwirken nur schwach mit gewöhnlichen Mineraloberflächen. Daher wurde ^{79}Se von verschiedenen Waste-Management-Organisationen (z. B. Ondraf/Niras (Belgien), Andra (Frankreich), Nagra (Schweiz)) als für die Langzeitsicherheit eines Endlagers potenziell kritisches Radionuklid identifiziert, das über lange Zeiträume die Radioaktivität in der Umgebung eines Endlagers erhöhen kann. Nach den Erkenntnissen aus der Literatur und den Untersuchungen im Rahmen von VESPA kann vierwertiges Selen (Selenit, $Se(IV)O_3^{2-}$) sowohl an Calcit-Oberflächen adsorbieren, als auch in das Calcit-Volumen strukturell eingebaut werden. Es lässt sich leicht zeigen, dass durch solche Prozesse die Selenkonzentration in endlagerrelevanten Aquifersystemen um mehrere Größenordnungen herabgesetzt werden kann. Nach bisherigen Erkenntnissen erfolgen Sorption und Einbau von $Se(IV)O_3^{2-}$ an/in Calcit über die Bildung einer Oberflächen-solid-solution mittels eines Ionenaustauschprozesses. Die Se-dotierte Oberflächenmonolage wird beim Calcit-Wachstum überwachsen. Das pyramidale $Se(IV)O_3^{2-}$ verursacht an der Oberfläche nur geringe Spannungen in der Kristallstruktur und wird daher relativ stark eingebaut ($K_D = 0.002 \pm 0.001$ L/g, Verteilungskoeffizient (einer Monolagen dicken Oberflächen-solid-solution), $D = 0.02 \pm 0.01$). Die Zusammensetzung der Oberfläche wird beim Kristallwachstum konserviert. Dadurch entsteht ein im Volumen mit $Se(IV)O_3^{2-}$ dotierter Calcit-Kristall in dem $Se(IV)O_3^{2-}$ - CO_3^{2-} strukturell substituiert. Im Bulk-Kristall verursacht $Se(IV)O_3^{2-}$ sehr große Spannungen, weshalb die Se-Dotierung dort einem Ungleichgewichtszustand entspricht. Eine Konsequenz dieses „Adsorption/Entrapment“ Modells [HEB/VIN2014] ist, dass unter Calcit-Gleichgewichtsbedingungen Selenit nur durch Oberflächeneinbau an Calcit gebunden wird. Nur bei erhöhter Calcit-Übersättigung (abhängig von der Selenkonzentration) kann Selenit in signifikanten Mengen mit Calcit mitgefällt werden (Verteilungskoeffizient der Bulk-solid-solution, $D = 0.02 \pm 0.01$).

2.8 Kopräzipitation und Adsorption von Selen an FeS/FeS_2

Unter reduzierenden Bedingungen, wie sie über lange Zeiträume in Endlagern, beispielsweise im Ton, erwartet werden, liegt Selen in niedrigen Oxidationsstufen (Selenid: Se_2^{2-}, Se^{2-}) vor. Selenid-Spezies weisen eine niedrige Löslichkeit auf und werden somit stark im Nahfeld zurückgehalten. Allerdings sind kaum Daten zur Selenid-Rückhaltung, und insbesondere zum Prozessverständnis der Rückhaltemechanismen, in der Literatur vorhanden. Im Rahmen des Vorhabens VESPA wurde seitens des KIT-INE die Rückhaltung von Selenid an/in Eisensulfid untersucht. In einem ersten Schritt wurde ein experimentelles Verfahren zur elektrochemischen Reduzierung von Selenit (Se(IV)) zu Selenid (Se(-II)) etabliert und optimiert. Danach wurde die Selenid-Rückhaltung durch Kopräzipitation mit und durch Adsorption an Eisensulfid untersucht. Ergebnisse zeigen ausschließlich die Bildung von Mackinawit (FeS) durch Synthese von FeS in Anwesenheit von Se(-II). Die Bildung einer separaten Se-Phase wurde nicht beobachtet. Informationen auf molekularer Ebene wurden mittels Röntgenabsorptionsspektroskopie gewonnen. Die Ergebnisse zeigen einen Austausch von S(-II) durch Se(-II) in der Struktur, was auf Grund der ähnlichen Ionengröße von Selenid und Sulfid auch zu erwarten ist. Die Wechselwirkung von Se(-II) mit vorhandenem FeS in Suspension (Adsorptionsexperimente) wurde ebenfalls untersucht. In einer FeS Suspension sind immer Kolloide vorhanden, die sehr stark mit gelösten Se(-II) wechselwirken. Untersuchungen zeigen die Bindung von Selen in Phasen die, hinsichtlich der chemischen Umgebung der Se-Atome, sehr ähnlich zu den in Kopräzipitationsexperimenten gefundenen Phasen sind. Eisenselenid (FeSe) ist ebenfalls schwach löslich und wurde synthetisch hergestellt. FeSe und FeS sind isostrukturell und Endglieder einer $FeSe_xS_{1-x}$ Mischkristallreihe. Die Bildung solcher Phasen in einem Endlager sollte zu einer sehr effektiven Rückhaltung von Selen führen. Pyrit (FeS_2) ist die unter Standarddruck und -temperatur und reduzierende Bedingungen thermodynamisch stabilste Fe(II)-Sulfid-Phase und in natürlichen Tonformationen weit verbreitet. FeS_2 kann durch Reaktion von FeS mit H_2S gebildet werden. Genauso wie Selen in Mackinawit strukturell eingebaut werden kann, kann es auch in Pyrit eingebaut werden. Beispielsweise enthalten natürlich vorkommende Pyrite oftmals signifikante Mengen an Selen. Das legt nahe, dass der Einbau von Selen in die Precursor-Phase FeS, auch zur Langzeitrückhaltung von Selen in Pyrit führen kann.

2.9 Sorption von Selenit und Selenat an endlagerrelevanten Mineralphasen

Die Sorption von Selenat (SeO_4^{2-}) und Selenit (SeO_3^{2-}) wurde durch das HZDR exemplarisch an endlagerrelevanten Mineralphasen untersucht. Hierzu zählen Korrosionsprodukte (Hämatit und Maghemit), Komponenten der geotechnischen und geologischen Barriere (δ-Al_2O_3 und Kaolinit) und in der Umwelt ubiquitär vorkommende Modelloxide (Anatas).

Für ausgewählte Systeme wurde der Einfluss von Temperatur und Salzgehalt der Lösung bestimmt und Parameter, die für thermodynamische Datenbanken wie THEREDA relevant sind, wurden ermittelt. Die Ergebnisse werden in die Sorptionsdatenbank RES^3T aufgenommen.

Generell kann die Aussage getroffen werden, dass die Retention von Selenit effektiver ist als die von Selenat. Für beide Se-Spezies ist die Sorption an Eisenphasen am höchsten, während die Sorption an Tonmineralen sehr gering ist. Die Retention von

Selenat und Selenit wird daher an der technischen Barriere des Endlagers als am stärksten angenommen. Mit steigender Temperatur und Ionenstärke wird die Sorption von Selenat und Selenit generell erniedrigt, wobei der Temperatureinfluss bei den Oxiden höher ist als beim Kaolinit.

Strukturelle Informationen zu den sorbierten Komplexen mittels ATR FT-IR und EXAFS Spektroskopie zeigten die Bildung von innersphärischen Komplexen für Selenit an verschiedenen Mineralphasen. Selenat hat vorwiegend außersphärische Oberflächenkomplexe gebildet. Jedoch konnte bei der Sorption von Selenat zwischen zwei bestimmten außersphärischen Komplexen unterschieden werden, wobei für die Komplexe an den Eisenphasen und an δ-Al_2O_3 zum ersten Mal gezeigt werden konnte, dass es zu einer Symmetriereduktion kommt. Die gefundenen Strukturen lassen für das Selenit eine geringere Reversibilität der Sorption (und damit bessere Möglichkeiten für langfristige Inkorporationen) als für das Selenat erwarten.

Die Bildung einer kristallinen Selenit-Phase in Gegenwart von Ca^{2+} Ionen wurde mittels XRD, DTA/TG und Festphasen-NMR analysiert. Von den Ergebnissen kann abgeleitet werden, dass die Calcium-Ionen, die im natürlichen System eines Endlagers in Konzentrationen weit über denen des Selens vorkommen, zur Ausfällung von Se(IV) und damit zu einer Immobilisierung des Selens führen können.

Aus den Batch-Sorptionsversuchen wurden quasi-thermodynamische Parameter für die Oberflächenkomplexierung abgeleitet (Protolysekonstanten und Oberflächenkonzentration der Bindungsstellen, Komplexbildungskonstanten). Dazu wurden die experimentell bestimmten konditionellen Verteilungskoeffizienten (K_D-Werte) mittels einer Kopplung der Codes FITEQL und UCODE ausgewertet. Diese wurden in die mineralspezifische Sorptionsdatenbank RES^3T eingepflegt und gestatten eine Modellierung sogenannter „smart-Kd"-Werte, wie sie z. B. im Verbundprojekt WEIMAR (FKZ 02 E 11072B) genutzt werden.

2.10 Synthese von Sorelphasen für die Untersuchung der ^{129}I Rückhaltung

Zur Vorbereitung von Sorptionsexperimenten mit ^{129}I wurden verschiedene Methoden zur Synthese von monomineralischen Sorelphase-Proben angewendet. Die synthetisierten Sorelphase-Proben wurden mit mehreren Analysenmethoden hinsichtlich der Phasenreinheit analysiert. Hinreichend reine Sorelphase-Proben wurden mit konzentrierten Salzlösungen zusammengegeben und die Äquilibrierung der Sorelphase-

Salzlösungssysteme über mehrere Wochen durch Analysen von Feststoff- und Lösungsproben verfolgt. Synthese, Charakterisierung und Äquilibrierung der Sorelphase-Proben sind im Abschlussbericht dokumentiert. Die geplanten Arbeiten zur Rückhaltung von ^{129}I an Sorelphasen in salinaren Lösungen konnten im Bearbeitungszeitraum nicht mehr erfolgen. Auf Grund der erforderlichen Voräquilibrierungszeiten konnten die synthetisierten Sorelphasen innerhalb der Projektlaufzeit nicht mehr mit ^{129}I kontaktiert werden. Sie stehen aber für weitere Arbeiten zur Verfügung.

2.11 Synthese, Charakterisierung und Langzeitstabilität von LDH-Mischkristallen

Radionuklide zurückzuhalten, die in anionischer Form vorliegen, ist für die sichere Endlagerung von besonderer Relevanz. Interessant erscheint dabei eine Verbindungsklasse anionischer Tonminerale (sogenannte LDH = Lamellare Doppelhydroxid-Verbindungen, engl.: Layered Double Hydroxides), die als Korrosionsprodukte im Nahfeld eines Endlagers, gebildet werden. In Gegenwart von zementhaltigen Abfallumgebungen zum Beispiel, entstehen die so genannten ‚Friedel-Salze' mit der allgemeinen Formel $[Ca_2Al(OH)_6(Cl,OH)\cdot 2H_2O]$. Ebenfalls wurden, in Gegenwart von Behältern aus Metall LDH's des Typs ‚Grüner Rost' gefunden, die Fe^{2+} und Fe^{3+} beinhalten. Bei der Korrosion von Forschungsreaktorbrennelementen konnten MgAl-LDH-Verbindungen mit Chlorid und Sulfat in der Zwischenschicht und Fe-LDH's des Typs Grüner Rost nachgewiesen werden. LDH-Verbindungen sind zurzeit Forschungsobjekte vieler Wissenschaftler, da sie weitreichende Eigenschaften als Anionenaustauscher haben.

Die im Forschungszentrum Jülich durchgeführten Arbeiten im Rahmen des Verbundprojektes VESPA konzentrierten sich auf LDH Phasen, insbesondere auf drei ausgewählte Mischkristall-Verbindungen und deren Fähigkeiten über Ionenaustausch die Migration von Iodid, Selenit und Pertechnetat durch Anionenaustausch zu verzögern bzw. zu verhindern. Im Vergleich zu einer „reinen" MgAl-LDH-Verbindung sollte erstmals die Effizienz von Mischkristallen (0,0333 Molanteil des Magnesiums der Mg_3Al_1-LDH Verbindung wurde durch Eisen, Kobalt bzw. Nickel substituiert) untersucht werden. In der Natur sind Mischkristall-Verbindungen allgegenwärtig (Mischkristallbildung wird bei metallischen Mehrfachsystemen, besonders auch bei Mineralen (z. B. Feldspat) beobachtet), sodass auch im Endlagerbereich davon auszugehen ist, dass die Bildung von Mischkristallen von Relevanz ist.

Die drei Mischkristallverbindungen konnten selektiv, d. h. ohne Bildung weiterer kristalliner Nebenphasen synthetisiert werden. Der strukturelle Einbau von Eisen, Cobalt und Nickel in die Metallhydroxidschicht (oktaedrische Koordination der Metallkationen durch Hydroxidgruppen) wurde mit XRD und EXAFS bestätigt.

Im Vorhaben VESPA konnten thermodynamische Daten generiert werden, um die Stabilität der LDH-Mischkristallverbindungen zu beschreiben. Mit Hilfe des thermodynamischen Software Codes GEMS (entwickelt am PSI) wurden unter der Annahme eines thermodynamischen Gleichgewichtes zwischen synthetisierten Feststoffen und korrespondierender Syntheselösung die freien Gibbs-Bildungsenergien bestimmt. Es zeigt sich, dass der strukturelle Einbau von Eisen, Cobalt und Nickel keinen signifikanten Einfluss auf die Löslichkeit ausübt. Die bestimmten freien Gibbs-Bildungsenergien differieren um maximal 26 kJ/mol. Dem gegenüber belegen Ergebnisse aus ersten Untersuchungen, dass die Ladungsdichte des Anions in der Zwischenschicht erheblich die Stabilität der LDH-Verbindung beeinflusst. Beispielsweise ist eine MgAl-LDH-Verbindung mit Carbonat als Anion in der Zwischenschicht deutlich stabiler (geringer löslich) als wenn Chlorid in der Zwischenschicht vorhanden ist. Die bestimmten freien Gibbs-Bildungsenergien differieren um 127 kJ/mol.

Zukünftig soll die spärliche thermodynamische Datenbasis für LDH-Verbindungen (vollständige Mischkristallreihe) in Abhängigkeit unterschiedlicher Zwischenschichtanionen durch thermodynamische Modellierung und kalorimetrische Messungen erweitert werden, um verlässliche Aussagen zur Langzeitstabilität dieser LDH-Phasen angeben zu können.

2.12 Bestimmung der Löslichkeitskonstanten von LDH-Mischkristallen

Für die experimentelle Bestimmung der Löslichkeitskonstanten wurden der GRS vom FZJ drei synthetisierte LDH-Verbindungen zur Verfügung gestellt. Hierbei handelte es sich um teilsubstituierte Hydrotalcite, in denen ein kleiner Teil des Magnesiums durch Kobalt bzw. Nickel oder zweiwertiges Eisen ersetzt wurde. Die Löslichkeiten der LDH-Verbindungen wurden in endlagerrelevanten Wässern (Opalinuston-Porenwasser; $MgCl_2$-Lösungen sowie IP21-Lösung) bestimmt. Nach Gleichgewichtseinstellung der CO_2- bzw. z. T. auch O_2-empfindlichen Versuchsansätze erfolgte eine chemische Analyse der Lösungen. Auf Basis der Versuche konnten die Löslichkeitskonstanten für die mit Kobalt bzw. Nickel teilsubstituierten LDH-Phasen abgeleitet werden. Sie ist für beide Typen gleich groß. Damit wurden die theoretisch abgeleiteten Prognosen (Arbeiten des FZ Jülich) bestätigt. Analoge Berechnungen für die eisenhaltige LDH-Phase waren aufgrund nicht messbarer Gleichgewichtskonzentration von Eisen nicht möglich, jedoch ist aufgrund der chemischen Ähnlichkeit von Co^{2+}, Ni^{2+} und Fe^{2+} davon auszugehen, dass die mit Eisen substituierte Phase die gleiche Löslichkeitskonstante aufweist.

2.13 Rückhaltung anionischer Radionuklidspezies an den modifizierten LDHs

Die Rückhaltung anionischer Radioisotope über Ionenaustausch wurde in reinem Wasser, zur Abbildung endlagerrelevanter Bedingungen zudem in Tonporenwasser und gesättigten Salzlösungen untersucht. Die Ergebnisse zeigen, dass die LDH-Verbindungen für die untersuchten Anionen ein Retentionspotential besitzen. Aus den ermittelten Verteilungskoeffizienten (Kd-Werte) kann abgeleitet werden, dass in reinem Wasser und Tonporenwasser beachtliche Mengen durch die Mischkristall-Verbindungen zurückgehalten werden können, hingegen eine Rückhaltung durch Anionen-Austausch an der reinen MgAl-LDH-Verbindung nur in Wasser verifiziert werden konnte. Die in Tonporenwasser ermittelten Kd-Werte lagen um bis zu drei Größenordnungen (250 ml/g) für Selenit) und um eine Größenordnung (2,24 ml/g für Iodid und 5,62 ml/g für Pertechnetat) höher als ein Kd-Wert von 0.1 ml/g. Obwohl der Kd-Wert von 0,1 ml/g sehr klein ist, konnte für diesen Wert eine erhebliche Auswirkung auf die Migrationszeit bestimmt werden. Legt man eine Diffusionsstrecke von 50 m zu Grunde und nimmt als Diffusionskonstante einen Wert von ca. 5 10 – 12 m^2/s an, so erhöht sich laut Berechnungen (ANDRA) in Ton die Migrationszeit von 140.000 Jahren auf 700.000 Jahren. In Salzlösungen konnte nur eine Rückhaltung für Selenit (höhere Ladungsdichte als Chlorid), nicht aber für Iodid und Pertechnetat (diese Anionen besitzen geringere Ladungsdichten als Chlorid) bestimmt werden.

Die Ergebnisse verdeutlichen, dass Rückhaltung durch Anionen-Austausch durch das Angebot an in der Lösung vorhandenen Anionen, aber auch durch die im LDH vorhandenen Metallkationen, bestimmt wird. In zukünftigen Arbeiten soll der Zusammenhang zwischen Stöchiometrie/Struktur und Rückhaltung detailliert untersucht werden, um ein grundlegendes Prozessverständnis zu entwickeln.

Zusammenfassend lässt sich festhalten, dass die bisherige Annahme, dass in anionischer Form vorliegende Radionuklide nicht im Endlagersystem zurückgehalten werden, modifiziert werden sollte. LDH-Verbindungen, insbesondere Mischkristalle, zeigen, dass anionische Radionuklide durch Ionenaustausch, effizient zurückgehalten werden können. Die bestimmten Verteilungskoeffizienten (Kd-Werte) können in entsprechende Berechnungen/Codes zur Radiomigrationen verwendet werden.

2.14 Methodische Weiterentwicklung von Redoxmessungen bei hohen Temperaturen und Salinitäten

Die potentiometrische Messung des Redoxpotentials in salinaren Lösungen wird durch das Auftreten eines konzentrationsabhängigen Diffusionspotentials an der grundsätzlich vorhandenen Referenzelektrode erschwert. Frühere Untersuchungen zeigten, dass es zumindest in stark sauren eisenhaltigen Lösungen möglich ist, die primär erhaltenen Zellpotentiale in Aktivitätsverhältnisse von Eisen(II)- und Eisen(III)-Verbindungen umzuwandeln. Über diesen Weg erhält man den Zugang zu einem thermodynamisch definierten eisenspezifischen Redoxniveau. Der Ansatz wurde durch potentiometrische Untersuchungen in pH-neutralen KCl-Lösungen überprüft, die sowohl Kaliumhexacyanoferrat(II) als auch Kaliumhexacyanoferrat(III) enthielten. Für die Auswertung dieser Messungen war es erforderlich ein thermodynamisches Modell zu entwickeln, mit der sich die Aktivitätskoeffizienten der Hexacyanoferrate in KCl-Lösungen beschreiben lassen.

Die Untersuchungen zeigten, dass es mit Hilfe des Versuchskonzeptes möglich ist, einen einfachen Zusammenhang zwischen dem Verhältnis der Aktivitäten der beiden Hexacyanoferrate und dem gemessenen Zellpotential herzustellen. Damit wäre es umgekehrt möglich, aus einem Zellpotential einen Aktivitätsquotient (ein Redoxniveau) in Abhängigkeit von Hintergrundsalzgehalt abzuleiten. Es zeigte sich jedoch, dass der numerische Zusammenhang nicht mit dem Modell in Übereinstimmung zu bringen war, das für saure gemischte Fe(II)- und Fe(III)-Lösungen abgeleitet worden war.

Nach näherer Auswertung wurde der Schluss gezogen, dass das eingesetzte Aktivitätsmodell für Fe^{3+} einer weiteren Verbesserung bedarf. Für neutrale Lösungen wurde ein zusätzlich ein etwas anderer, vereinfachter Ansatz vorgeschlagen, der das gemessene Potential mit dem Konzentrationsverhältnisse der Hexacyanoferrate verknüpft.

2.15 Berücksichtigung der Ergebnisse in Ausbreitungsmodellen der Langzeitsicherheitsanalyse

Das Verbundvorhaben VESPA hatte insbesondere zum Ziel, Annahmen, die für die Radionuklide ^{14}C, ^{79}Se, ^{129}I, ^{135}Cs und ^{99}Tc in Langzeitsicherheitsanalysen verwendet werden, zu überprüfen und ggf. Konservativitäten zu reduzieren. Um die Auswirkungen dieser Annahmen auf die Radionuklid-Migration zu demonstrieren, wurden drei Anwendungsfälle und chemische Randbedingungen definiert: Strecken- sowie eine Bohrlocheinlagerung im Salz sowie Bohrlochlagerung im Ton. Die Projektpartner leiteten daraufhin auf Basis ihrer Arbeiten im Vorhaben VESPA neue Löslichkeitsgrenzen und Sorptionskoeffizienten ab. Diese Daten wurden dann bei der Aufstellung numerischer Modelle für Radionuklid-Ausbreitungsprozessen in Ton (Programmcode CLAYPOS) und Salz (Programmcode LOPOS) berücksichtigt.

Im Salzgestein resultiert die Berücksichtigung der neu ermittelten Löslichkeitswerte in einem etwa drei (^{79}Se) bzw. fünf (^{99}Tc) Größenordnungen niedrigeren Austrag, im Tongestein in einem vier Größenordnungen geringeren Austrag in das Deckgebirge. Die Berücksichtigung der Sorption an Eisenkorrosionsphasen führt bei Salzgestein zu einer Senkung des Austrags in Höhe von circa einer Größenordnung. Bei Tongestein ist der Effekt der Sorption an Eisenkorrosionsphasen vernachlässigbar, da hier die bereits berücksichtigte Sorptionskapazität des Tons deutlich größer ist. Insgesamt zeigen die Vergleichsrechnungen, dass eine detailliertere Würdigung von geochemischen Prozessen im Langzeitsicherheitsnachweis sehr bedeutsam sein kann, da konservative Annahmen bezüglich der Mobilität von Radionukliden deutlich reduziert werden können.

2.16 Resümee

Die Arbeiten der Partner GRS, FZJ, HZDR und KIT-INE im Verbundvorhaben VESPA weisen auf die herausragende Bedeutung der Geochemie für die Einschätzung von Mobilisierungs- bzw. Rückhaltungsprozessen von Radionukliden in einem Endlager für radioaktive Abfälle hin. Durch gezielte experimentelle Studien konnte sowohl ein grundlegend verbessertes Prozessverständnis des Verhaltens der langlebigen Spalt- und Aktivierungsprodukte ^{14}C, ^{79}Se, ^{99}Tc, ^{129}I, und ^{135}Cs in endlagerrelevanten Systemen gewonnen werden, als auch grundlegende standortunabhängige thermodynamische Daten und Modelle abgeleitet werden, die im Rahmen integraler geochemischer Modellrechnungen in Zukunft die Analyse verschiedener Endlagerkonzepte und unterschiedlicher Szenarien auf wesentlich verbessertem Niveau erlauben.

Das Projekt leistet einen wichtigen Beitrag für geochemische Datenbasen, die für die Langzeitsicherheitsanalyse von Endlagern benötigt werden. Zusätzliche spektroskopische Befunde tragen zum grundlegenden Verständnis von Sorptionsprozessen anionischer Spezies im Nahfeld eines Endlagers bei. Die Daten und Erkenntnisse gestatten eine realistischere Festlegung von Konservativitäten, verringern die numerische Unsicherheit der Ergebnisse der Langzeitsicherheitsanalyse, und erhöhen durch ein tieferes Prozessverständnis das Vertrauen in entsprechende Modelle und deren Ergebnisse.

3 Introduction

The long-term safety assessment of repository systems is performed on the basis of several conceivable event sequences that can result in a mobilisation of radionuclides into the near field. Solution intrusion is an element of some or all event sequences in all host rock formations (clay, salt, granite) that are currently discussed in Germany for the storage of heat developing radioactive wastes. If intruding solutions get into contact with waste containers, corrosion of the waste containers and other metallic components in the near field have to be taken into account. This process can result in a failure of the waste containers, so that the safe confinement of radionuclides in the effective containment zone is challenged. According to the current state of knowledge, such potential evolutions of a repository system may take place even if the safety concept for a repository in clay or crystalline rock formation is consequently implemented. These developments may also occur in a repository in a salt rock formation, but with a significantly lower probability. In order to assess these event sequences, long-term safety analyses have to be performed that use models to simulate mobilisation, migration and retention of radionuclides.

The analyses are based on models and data that allow the description of processes that are part of the considered evolutions of the repository system. In long-term assessment codes the mobility of radionuclides is reflected by the factors radionuclide inventory, release rate (source term), solubility limits, diffusion coefficients and sorption coefficients. The reliable and robust deduction of these parameters represents central activity fields of current geochemical research in the context of repository safety research. Fission and activation products play an important role in release scenarios, because they may account for the largest share of the resulting additional dose in the biosphere ([KEE/NOS2005]: salt/clay, [GRA2008, NAG2002]: clay, [SKB2011]: granite) – in contrast to the main components of heat developing wastes. The mobile radionuclides ^{135}Cs, ^{129}I, ^{99}Tc, ^{79}Se, ^{36}Cl, ^{14}C are of high relevance because it was assumed so far that there is no or only a very little retention by natural and technical materials in a repository. An improvement of the state of knowledge regarding solubility and retention may lead to a significant reduction of the calculated activity release within long-term safety analyses.

Therefore, it was necessary to investigate the retention processes for the mentioned nuclides more closely and to obtain a more realistic overall picture of their mobility and retention mechanisms. Furthermore, it was necessary to derive new information and data relevant for a quantitative description of mobilisation and transport of these compounds on the water path. These included investigations of

- redox characteristics and physicochemical properties of relevant species in aqueous solutions (technetium, selenium, iodine, caesium)

- Identification and characterisation of retention processes on relevant solid phases (technetium, selenium, iodine on iron oxides, magnesium containing hydroxide phases, iron sulphides and calcite)

- predominant speciation in radioactive wastes (^{14}C)

A precise understanding of the thermodynamic properties of radionuclides is necessary to describe their chemical behaviour in aqueous solutions, notably the retention caused by the formation of solid phases and the formation of surface complexes. While the state of knowledge of the major components of potentially intruding solutions (Na^+, K^+, Mg^{2+}, Ca^{2+}, H^+, Cl^-, SO_4^{2-}, OH^-, HCO_3^-, CO_3^{2-}, H_2O) is often very good, even at the expected increased near field temperatures of more than 25 °C, data and models for aqueous selenium, technetium, caesium and iodine species are much less available and/or precise. Particularly, this situation applies to reduced species of selenium and technetium.

Within the framework of the project relevant thermodynamic data for the mentioned chemical elements should be compiled and complemented by new experimental investigations at 25 °C and partly at higher temperatures (up to 90 °C). The thermodynamic models that could be derived from this work should be applicable for all host rock formations under consideration and for all relevant ionic strengths. Part of these efforts was to further clarify the redox chemistry of selenium and technetium and to prepare the basis for models that allow the calculation of activity coefficients. For technetium(IV) it was planned to develop consistent data sets for a complete thermodynamic description of Tc(IV) solubilities in different solution systems, which should be implemented in the thermodynamic reference database THEREDA.

An interpretation of redox equilibria in saline solutions depends on approaches that allow the transformation of measured redox potentials into thermodynamically and unambiguously interpretable quantities. Complementing activities should be undertaken in order to allow the application of Eh measurements to solutions over a broad range of pH values.

Another key area of activities was the retention of anionic species of selenium, technetium and iodine. It should be clarified if and how sorption or incorporation takes place on solid phases that are relevant to repositories. Considered phases include iron oxides (from the corrosion of container materials), layered double hydroxides (LDH, a secondary product of reactions with aluminium containing container components), calcite and iron sulphides (constituents of clay rock) and minerals from granites. An important part of the investigations was also to resolve which mechanism contributes in each case to the retention (e. g. sorption, co-precipitation, incorporation). If redox sensitive elements as selenium or technetium are concerned, the retention process may be accompanied by reduction. Such processes can only be analysed properly if advanced spectroscopic methods giving molecular level information are employed.

An essential element of the project was the direct integration of the research results into the models and computer codes for long-term safety assessment. This coupling of basic research and application is achieved by an abstraction of the results into discrete input data (sorption coefficients and solubility limits) for the necessarily simplifying codes. Calculations should show the impact of altered/improved input parameters on the release dose of radionuclides.

In particular it was planned to document the current state of knowledge on the predominant speciation of ^{14}C in heat developing waste. The speciation in waste determines in which chemical form carbon is initially released. This has a strong impact on the mobility of carbon. In addition, fundamental studies on the analysis of ^{14}C in highly radioactive solutions should be conducted.

The partners within the project focussed their work on the following areas:

GRS: Determination of thermodynamic data for iodine, selenium and caesium in saline solutions at temperatures between 25 and 90 °C. Determination of solubility constants for LDH phases from solubility measurements. Documentation of the state of knowledge on speciation of ^{14}C under the condition of a repository for HAW. Activities on methods for the calculation of redox potentials in saline solutions. Integration of project results on solubility and retention of radionuclides in computer codes for long-term safety assessment.

HZDR-IRE: Complex formation of selenium with cationic ligands at higher temperatures. Sorption experiments with selenium and analysis of sorbents and surface complexes. Modelling and data evaluation (including preparation for the integration into the databases THEREDA and RES^{3}T).

FZJ-IEF-6: Determination of experimental data on the retention of the anionic radioisotopes ^{129}I, ^{99}Tc, ^{75}Se by synthesized partly substituted LDH compounds (LDH solid solutions) and determination of their long-term stability.

KIT-INE: aquatic chemistry and thermodynamics of Tc(IV). Reduction chemistry of Tc(VII)/ Tc(IV) in different media. Influence of reduction kinetics on technetium migration in natural systems. Structural incorporation of selenium in mineral phases (calcite, pyrite). Analytical work to determine the speciation of ^{14}C. Synthesis of Sorel phases for the investigation of ^{129}I retention.

3.1 References (chapters 1 – 3)

[AND2005] ANDRA, Synthèse Argile: Évaluation de la faisabilité du stockage géologique en formation argileuse – Dossier, 2005.

[GRA2008] Grambow, B., Mobile fission and activation products in nuclear waste disposal. J. Contaminant Hydrol. 102, (2008) 180–186.

[KEE/NOS2005] Keesmann, S.; Noseck, U.; Buhmann, D.; Fein, W.; Schneider, A., Modellrechnungen zur Langzeitsicherheit von Endlagern in Salz- und Granitformationen. GRS-Bericht 206, 2005.

[KIE/LOI2001] Kienzler, B.; Loida, A., Endlagerrelevante Eigenschaften von hochradioaktiven Abfallprodukten - Charakterisierung und Bewertung - Empfehlungen des Arbeitskreises HAW-Produkte, Wissenschaftliche Berichte FZKA (6651), 2001,114 S.

[SKB2011] SKB, Long-term safety for the final repository for spent nuclear fuel at Forsmark. Main report of the SR-Site project. Technical Report TR-11-01, Svensk Kärnbränslehantering AB, 2011.

[NAG2002] Nagra, Technical Report 02-05. Project Opalinus Clay. Safety Report. Demonstration of disposal feasibility for spent fuel, vitrified high-level waste and long-lived intermediate-level waste (Entsorgungsnachweis), 2002.

4 Aqueous speciation and sorption of selenium[1]

4.1 Relevance and context

Performance assessments (PA) are necessary to quantify the mobilization, behavior and retardation of radionuclides in nuclear waste repositories. Several calculations [ANDRA '05a; BRASSER '08; ONDRAF/NIRAS '01a] have shown fission and activation products like ^{14}C, ^{79}Se, ^{129}I, ^{36}Cl, and ^{99}Tc to contribute significantly to the radiation dose potentially reaching the biosphere. A detailed knowledge of the mobility and bioavailability of selenium, mainly concerned by HZDR-IRE within this joint research project, is therefore of great importance for a safe disposal of radioactive waste.

Selenium speciation depends on both the pH and the redox potential of the surrounding environment. Selenium can be found in four main oxidation states: selenium(−II) (selenide Se^{2-}), selenium(0) (elemental selenium Se^0), selenium(IV) (selenite SeO_3^{2-}) and selenium(VI) (selenate SeO_4^{2-}). In the Pourbaix diagram of selenium (**Fig. 4.1**) calculated based on the data (**Tab. 4.1**) of the Nuclear Energy Agency-Organization for Economic Co-operation and Development [OLIN '05]), red lines represent oxidation and reduction equilibrium of water according to the following semi-equations:

$$2\ H^+ + 2\ e^- \leftrightarrow H_2(g)$$

with $E = -\ 0.059\ pH$ (H_2 pressure of 1 bar)

$$\tfrac{1}{2}\ O_2(g) + 2\ H^+ + 2\ e^- \leftrightarrow H_2O$$

with $E = 1.229 - 0.059\ pH$ (O_2 pressure of 1 bar)

---

[1] This chapter was prepared by Institut für Ressourcenökologie (IRE), Helmholtz-Zentrum Dresden-Rossendorf (HZDR)

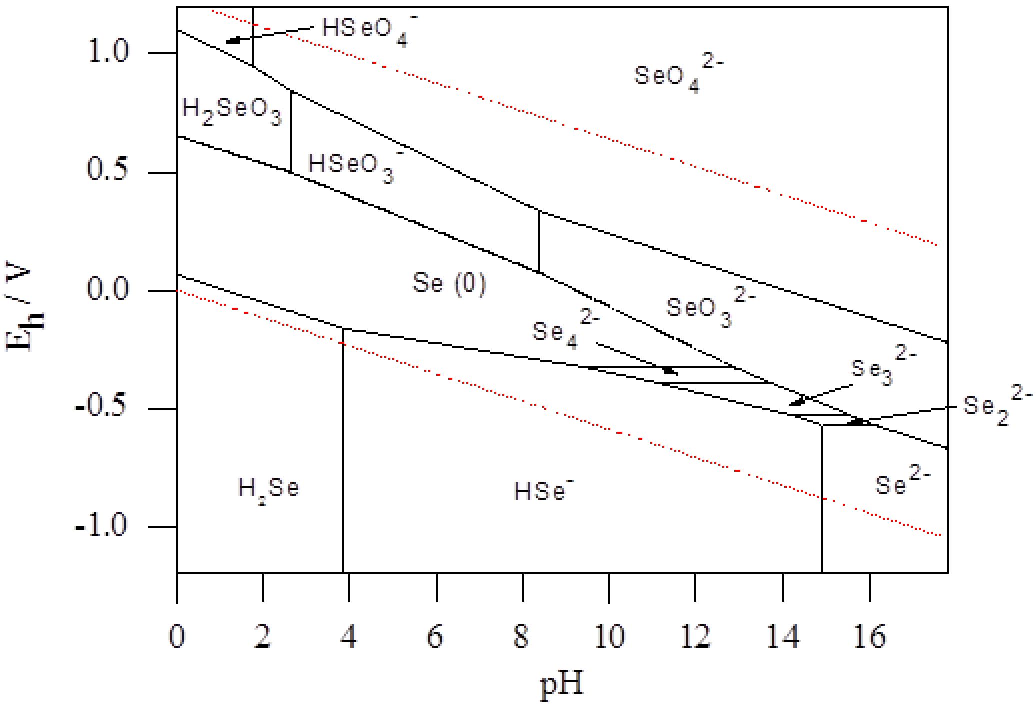

Fig. 4.1 E_h-pH diagram for Se at standard conditions and 298.15 K $[Se]_{tot} = 10^{-6}$ mol L^{-1}

Tab. 4.1 Equilibrium constants and standard potentials

Acido-basic couple		**Acido-basic equilibrium**	**log K°**
H_2Se (aq)/HSe^- (aq)		H_2Se (aq) ↔ HSe^- (aq) + H^+	−3.850
HSe^- (aq)/Se^{2-} (aq)		HSe^- (aq) ↔ Se^{2-} (aq) + H^+	−14.91
H_2SeO_3 (aq)/$HSeO_3^-$ (aq)		H_2SeO_3 (aq) ↔ $HSeO_3^-$ (aq) + H^+	−2.640
$HSeO_3^-$ (aq)/SeO_3^{2-} (aq)		$HSeO_3^-$ (aq) ↔ SeO_3^{2-} (aq) + H^+	−8.360
$HSeO_4^-$ (aq)/SeO_4^{2-} (aq)		$HSeO_4^-$ (aq) ↔ SeO_4^{2-} (aq) + H^+	−1.750
Redox couple		**Redox equilibrium**	**E° (V)**
Se_n^{2-}/Se(−II)	Se_2^{2-} (aq)/Se^{2-} (aq)	Se_2^{2-} (aq) + 2 e^- ↔ 2 Se^{2-} (aq)	−0.749
	Se_3^{2-} (aq)/Se^{2-} (aq)	Se_3^{2-} (aq) + 4 e^- ↔ 3 Se^{2-} (aq)	−0.739
	Se_4^{2-} (aq)/Se^{2-} (aq)	Se_4^{2-} (aq) + 6 e^- ↔ 4 Se^{2-} (aq)	−0.720
Se(0)/Se(−II)	Se(cr)/Se^{2-} (aq)	Se(cr) + 2 e^- ↔ Se^{2-} (aq)	−0.666
Se(IV)/Se(0)	H_2SeO_3 (aq)/Se(cr)	H_2SeO_3 (aq) + 4 H^+ + 4 e^- ↔ Se(cr) + 3 H_2O	0.742
Se(VI)/Se(IV)	$HSeO_4^-$(aq)/H_2SeO_3 (aq)	$HSeO_4^-$ (aq) + 3 H^+ + 2 e^- ↔ H_2SeO_3 (aq) + H_2O	1.103

Thermodynamic calculations with available data indicate that selenide and elemental Se should be found in reducing environments, selenite in mildly reducing environments, and selenate in oxidizing environments. As a function of pH, several protonated species are formed, according to the Pourbaix diagram (**Fig. 4.1**).

Selenium's mobility is depending on several parameters such as pH, ionic strength, temperature, and redox state. The question arises which oxidation state should be considered in performance assessments, in which the retention of selenium has so far been considered as negligible (K_d set to 0 for the +IV oxidation state).

The identification of the redox state of selenium in UO_2 spent fuel has been suffering the lack of reliable experimental data. By applying micro X-ray absorption near-edge structure (µ-XANES) spectroscopy, [CURTI '14] studied the pristine redox state and coordination environment of selenium in high-burnup UO_2 spent nuclear fuel. Results suggested that Se occurs as selenide, replacing oxygen atoms in a fairly disordered UO_2 lattice. Considering Se to be is tightly bound in the UO_2 lattice, it would be slowly released by matrix dissolution. This would explain why [JOHNSON '12] failed to detect Se during leaching experiments of high burnup UO_2 fuel. Though surface oxidation at the water-fuel interface cannot be excluded, such scenario would imply selenium to not be an Instant Released Fraction contributor and require a reinvestigation of its impact during Performance Safety assessments. In the far field, however, a re-oxidation could lead to the presence of Se oxyanions.

Therefore, it is of great importance to characterize at both the macroscopic and molecular level the different processes (sorption, reduction, surface precipitation, etc.) that can take place onto mineral surfaces and thus affect the availability and the mobility of selenium in the near field of nuclear waste repositories. Indeed, this data are necessary to improve the quality and accuracy of the different scenarios used in the performance of safety calculations. This information can be inserted in surface complexation models for the description and prediction of their interaction with several sorbent surfaces in a wide range of conditions.

A thorough understanding of the Se aqueous speciation is mandatory for the application of advanced spectroscopic techniques such as ATR FT-IR or EXAFS for the elucidation of sorption processes. The speciation of selenium(VI) and selenium(IV) can be accurately described at room temperature and dilute concentration by considering exclusively monomeric species [OLIN '05]. However, it has been established that the aqueous dimerization of selenium(IV) starts at concentrations above 1 mM [TORRES '10] and give rise to binuclear species linked by hydrogen bonding. This phenomenon, although reported in the past by conductometry and cryometry [JANICKIS '36; LEY '38; MIOLATI '01; ROSENHEIM '21], potentiometric [BARCZA '71; GANELINA '73; SABBAH '66], calorimetric [ARNEK '72] and kinetic [COOPER '76; DIKSHITULU '84; DIKSHITULU '81; NADIMPALLI '90] studies, was still controversial. [BAES JR. '76; GRENTHE '92] rejected the dimeric species postulating their inclusion in equilibrium models to arise from experimental artefacts. [OLIN '05], in their evaluation of Se experimental thermodynamic data available at the end of 2003, did not question the existence of these binuclear species, but highlighted that the published equilibrium constants were too large. As highlighted above, no spectroscopic evidence of the Se(IV) dimerization as well as no detailed knowledge of their vibrational spectral properties were so far available. This lack of knowledge severely hampers the elucidation of sorption processes by means of vibrational spectroscopy.

Most of the thermodynamic data for Se are available for standard temperature conditions at 25 °C, but only few focused on the changes that may occur at a higher temperature levels. Heat emitted by high level and long-lived radioactive waste is well-known to increase the temperature at the vicinity of the waste disposal site for at least 10,000 years. Such a thermal effect raises the question how the speciation of selenium is influenced at elevated temperatures. This point has so far never been addressed in the literature, to our knowledge. Same is true for influence of ubiquitous divalent cations such as Ca^{2+} and Mg^{2+} on the mobility of Se oxyanions.

Among the different processes (sorption, co-precipitation, surface precipitation, heterogeneous reduction, etc.) leading to retarding Se migration and transfer to the biosphere, sorption onto solid surfaces is of particular importance.

The affinity of selenate and selenite oxyanions towards mineral surfaces, e. g. iron oxides and oxyhydroxides, aluminum oxides and titanium oxides has already been evidenced. Compared to selenate, selenite adsorption onto iron oxides was always found to be greater and stronger in the same experimental conditions. The formation of the interface complexes was studied under specific and environmentally relevant conditions by variation of selective parameters, such as pH, ionic strength of the solvent, selenium concentration, etc. Reactions of selenium at the water/mineral interface, such as sorption via formation of inner- and outer-sphere complexes or surface precipitation were examined by application of vibrational (IR and Raman) and X-ray Absorption Spectroscopy (XAS), mainly. These techniques provided the structural identification of the metal atom coordination and the character of the chemical bonding of the sorbed surface species. These studies confirmed that selenium(VI) and selenium(IV) sorption mechanism is dependent on the nature of the sorbent surface, the pH and the ionic strength. A continuum in the adsorption mechanism with the presence of both outer and inner-sphere complexes, whose relative proportion is changing with pH and ionic strength, was observed [FERNANDEZ-MARTINEZ '09]. Nevertheless, the sorption processes of selenium oxyanions still showed major gaps of knowledge. Retention of Se(VI) and Se(IV) on anatase and transition alumina was only evidenced at the macroscopic scale, but no information on sorption mechanisms is available [SHI '09; ZHANG '09]. Although some EXAFS (Extended X-ray Absorption Fine Structure Spectroscopy) and FT-IR (Fourier transform Infrared spectroscopy) data were available for the Se(VI)/hematite binary system, they were limited to acidic pH conditions [PEAK '02]. The sorption capacity of maghemite, which was identified as a corrosion product of steel waste canisters [BEN LAGHA '07], was so far never investigated. The reversibility of sorption processes, if examined at all, was scarcely checked and only by means of desorption experiments [DUC '06; VAN DER HOEK '94]. Without this information, the interpretation of sorption mechanisms, for instance based on EXAFS data or IR applied to wet pastes, can be misleading.

So far, impact of ionic strength on Se sorption was mainly studied at moderate background electrolyte concentrations (up to 0.1 M). Sorption of selenium(IV) was mainly found to be independent of ionic strength variations [DUC '03; ELZINGA '09; HAYES '88; HAYES '87; SHI '09; SU '00], contrary to selenium(VI) sorption which was found to decrease upon increasing ionic strength [DUC '03; ELZINGA '09; HAYES '88; HAYES '87; JORDAN '11; SU '00]. However, high ionic strength conditions (up to 4 – 5 M) are to be expected at the vicinity of nuclear waste disposed in salt formations, in case of water intrusion. Therefore, the effect of high ionic strength with different electrolyte compositions (NaCl, $MgCl_2$, $CaCl_2$) on Se sorption needs to be investigated.

Almost all batch studies focused so far on the sorption selenium oxyanions (SeO_4^{2-} and SeO_3^{2-}) at room temperature. As mentioned before, the thermal effect coming from high level and long-lived radioactive waste raises the question how the sorption and mobility of selenium is influenced at elevated temperatures. Contradictory results have been obtained in the literature. Selenite (SeO_3^{2-}) sorption capacity onto iron oxides and oxyhydroxides (goethite and ferrihydrite) [BALISTRIERI '87; PARIDA '97b], ferromanganese nodules [PARIDA '97a], α and γ activated alumina [JEGADEESAN '03], alumina (α-Al_2O_3 and γ-Al_2O_3) [PARIDA '03], layered metal double hydroxides, e. g. Mg/Fe hydrotalcite [DAS '02] and TiO_2 nanoparticles [ZHANG '09] was found to decrease upon increasing the ambient temperature. In contrast, a hybrid adsorbent, i. e. anion-exchange resin impregnated with nano-hydrated iron oxides [PAN '10], a manganese nodule leached residue [DASH '07], a calcined Mg-Al-CO_3 LDHs [YANG '05], a calcined Mg–Fe–CO_3 layered double hydroxide (LDH) [DAS '07], a nano-magnetite [WEI '12] and FeOOH (probably goethite) [SHARRAD '12] showed increasing selenite sorption capacity with increasing temperature. Concerning Se(VI), data is even scarcer. Upon increasing temperature, [MISRA '00] showed increasing selenate sorption capacity onto activated γ-alumina, while [VLASOVA '04] and [HASAN '10] observed a decrease of selenium(VI) sorption onto goethite and agro-industrial waste. Furthermore, no information and insights about mechanisms involved at higher temperatures were provided. In addition, potential changes in surface properties of sorbent materials were not extensively studied. As far as we know, only [VLASOVA '04] related the decrease of selenium(VI) sorption with increasing temperature to a decrease of the pH_{PZC} (point of zero charge) of goethite.

The completion of thermodynamic and sorption data base at higher temperatures for safety assessments of water contamination is therefore strongly required. The thermodynamic parameters, i. e. $\Delta_R H$, $\Delta_R S$ and $\Delta_R G$ for Se sorption onto minerals phases have to be determined from the temperature dependence sorption data, and the exothermic/endothermic and spontaneous sorption characteristics has to be elucidated.

Surface complexation models (SCMs) are aiming at accurately and effectively descripting and predicting the migration of aqueous species through their interaction with sorbent surfaces in a wide range of experimental conditions (pH, ionic strength, temperature, etc.). They provide a molecular description of adsorption processes based on an equilibrium approach. The SCMs differ by the structural description of the solid-water interface, e. g. the electrical double layer, the number of sorbing sites, the surface configuration of adsorbed species as well as their charges, etc. An accurate description of chemical reactions occurring at the sorbent surface has to rely on a thorough understanding of sorption processes at a molecular level. This implies knowledge on the number of surface species, their nature (inner vs. outer-sphere complexes) and their dependency on geological parameters (pH, ionic strength, etc.). This information can only be gained by the application of advanced spectroscopic techniques such as EXAFS or ATR FT-IR, in order to obtain a realistic description of sorption processes. However, this rigorous approach was only applied in a few studies [FUKUSHI '07;

HIEMSTRA '07; HIEMSTRA '99]. Otherwise, SCM was performed on a pure speculative basis concerning the stoichiometries and nature of surface complexes at the interface [MARTINEZ '06; ROVIRA '08; SHI '09]. This gives poor confidence on the robustness and consistency of the derived surface complexation constants. In addition, surface complexation constants of Se(VI) and Se(IV) on anatase, maghemite and alumina are still lacking.

Contrary to selenium oxyanions species, literature concerning the retention of reduced species is extremely scarce. Significant sorption of selenium(–II) by pyrite (FeS_2) and chalcopyrite ($CuFeS_2$) was evidenced by [NAVEAU '07]. The presence of Se(–II) or Se(–I) onto both sulfide surfaces was evidenced by XPS. Selenium(–II) sorption onto pyrite was investigated by [LIU '08], under strictly anoxic and reducing conditions. By combining *in situ* XANES and XPS, [LIU '08] observed the presence of Se(0) on the pyrite surface, explaining the rapid disappearance of selenium during sorption experiments. [LIU '08] concluded that selenium(–II) immobilization by pyrite proceeds via surface redox reaction: Only [NAVEAU '07] compared the sorption behavior of Se(-II) and Se(IV) and found that pyrite and chalcopyrite have the same affinity towards these two species. A great effort must therefore be dedicated to the study of the sorption behavior of these reduced Se species.

As it was mentioned before, selenium mobility strongly depends on its redox state. Redox reactions of Se onto minerals like iron-bearing and sulfide-bearing compounds was evidenced and seemed to depend on the selenium reduction kinetics and local concentration of Se reduced species. Heterogeneous redox reactions of selenium oxyanions at iron-bearing and sulfide bearing compounds were evidenced by spectroscopic methods using X-ray techniques such as XANES, EXAFS or XPS. Elemental Se and/or Fe selenide phases reaction end products were observed. Whether the formation of iron selenides or elemental Se is favored depends on the selenium reduction kinetics. [SCHEINOST '08b] observed that the reaction products considering selenium(IV) reduction were Fe selenides for Fe(II) minerals with high specific surface area (magnetite, mackinawite, GR) and fast reduction kinetics, and elemental Se for siderite which had slower reduction kinetics. By comparing their spectroscopic results with thermodynamic equilibrium modeling, [SCHEINOST '08b] suggested that the nature of the reduction end product in these Fe^{II} systems is controlled by the concentration of HSe^{-}. Lower HSe^{-} concentrations due to a slower selenium(IV) reduction kinetics would explain the formation of elemental selenium Se(0). However, highly reactive surfaces would favor the rapid reduction of selenium(IV) and the presence of a high initial amount of reduced Se. This would consequently lead to the formation of iron selenide phases.

The question also arises how heterogeneous surface reduction leading to the immobilization and retardation of Se release to the biosphere is influenced by the increase of temperature. This point was so far never examined in details.

In this project, we studied in Chapter 2 the aqueous speciation of Se, focusing on the Se(IV) dimerization, the impact of elevated temperature (up to 333 K) and of divalent cations (Ca^{2+} and Mg^{2+}) by means of ^{77}Se NMR, FT-IR, DTA/TG (Differential Thermal Analysis (DTA)/Thermogravimetric analysis (TG)) and XRD. In Chapter 3, we thoroughly investigated the bulk and surface properties of the studied minerals, i. e. anatase, hematite, maghemite, δ-alumina, magnetite and kaolinite by a wide range of analytical and spectroscopic tools. Anatase was chosen as a model system for its chemical stability and well-known surface properties, while transition alumina was studied as a model mineral phase for more complex rock and backfill materials associated with a nuclear waste repository. Kaolinite was studied as model clay mineral. Hematite, maghemite and magnetite were chosen as representative corrosion products of stainless steel canisters and for their environmental ubiquity.

Sorption of Se(VI) and Se(IV) onto anatase, hematite, maghemite, alumina and kaolinite was studied by batch experiments, where the impact of pH, moderate and high ionic strength, as well as temperature were elucidated. Results are reported in chapter 4.4. Sorption mechanisms for the above-mentioned binary systems were elucidated by advanced spectroscopic techniques, namely EXAFS and *in situ* Attenuated Total Reflection Infrared Spectroscopy (ATR FT-IR) in chapter 4.5. The heterogeneous redox processes of Se(VI) and Se(IV) at the magnetite-water interface and the impact of elevated temperature were studied by means of X-ray Photoelectron Spectroscopy (XPS) and are also presented in chapter 4.5. Surface complexation modeling including potentiometric titration of minerals and determination of surface complexation constants is presented in chapter 4.6. Finally, chapter 4.7 deals with the synthesis of selenium(−II) as well as its sorption onto minerals.

4.2 Se aqueous chemistry

Se(IV) dimerization in aqueous solutions was studied by ^{77}Se NMR spectroscopy. The impact of elevated temperature (up to 333 K) on Se(VI) and Se(IV) speciation was investigated by FT-IR and NMR spectroscopy. Finally, the complexation of selenium oxyanions with divalent cations such as Ca^{2+} and Mg^{2+} was revealed by means of ^{77}Se solid state NMR, FT-IR, DTA/TG (Differential Thermal Analysis (DTA)/Thermogravimetric analysis (TG)) and XRD. All experimental details as well as supplementary information can be found in the Appendix (A.2).

4.2.1 Se(IV) dimerization

Considering the protonation state at moderate pH values, Se(IV) occurs as hydrogen selenite being able to form a homodimer $(HSeO_3)_2^{2-}$ via hydrogen bonding (**Fig. 4.2**).

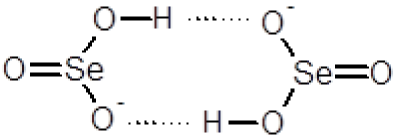

Fig. 4.2 Lewis structure of $H_2Se_2O_6^{2-}$ dimer resulting from intermolecular hydrogen bonding

As dimerization is equivalent to a lower degree of freedom, that is a lower flexibility and a reduced proton exchange rate between two monomers or the monomer and the solvent (water), the NMR line width may serve as a more sensitive probe for these molecular processes than the chemical shift of the selenium signal itself.

Fig. 4.3 shows the NMR spectra recorded at pH_c 5 and 13 at different Se(IV) concentrations as well as their graphical evaluation.

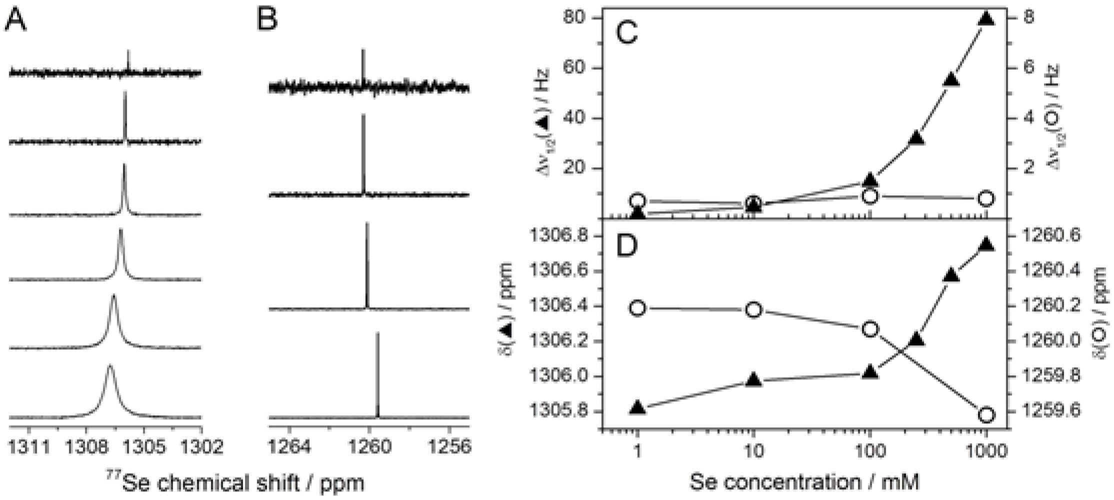

Fig. 4.3 ^{77}Se NMR of Se(IV) at pHc 5 (A) and 13 (B) with concentrations from 1 mmol L^{-1} through 1 mol L^{-1} and constant total ionic strength (3 mol L^{-1}). Dependence of selenite concentration on line width (C) and chemical shift (d) at pH$_c$ 5 (▲) and 13 (○)

The chemical shift is slightly selenium-concentration dependent (**Fig. 4.3**) with increasing values for pH$_c$ 5 and decreasing values for pH$_c$ 13, with overall changes of approximately 1 and 0.5 ppm, respectively. Considering a total Se chemical shift range of 2000 ppm, or at least the range for aqueous Se(IV) species of about 50 ppm, the changes are small, but, interestingly, the pH$_c$ 5 signal is clearly shifted to higher, that of pH$_c$ 13 to lower frequencies. Moreover, analysis of the line width, $\Delta\nu_{1/2}$, (i. e. the signal's width at half amplitude) clearly shows that the pH$_c$ 5 solution exhibits a strong line width dependence on concentration with line widths ranging over two orders of magnitude, whereas the line width of the pH$_c$ 13 solution is virtually constant. Since other concentration-dependent effects such as changes in susceptibility or viscosity would occur in both cases, these cannot be reasons for the broadening of the pH$_c$ 5 signal.

The apparent line width represents the sum of individual line width contributions from different effects: natural line width (resulting from energy uncertainty), magnetic field inhomogeneity (the line width of the reference sample is used as an indicator), and dynamics (including both proton and metal exchange reactions). The former two effects are assumed to be the same in all cases. Metal exchange reactions are considered to be negligible as it would have been indicated by line width changes upon increasing Na^+ (ionic strength) content. In order to exclude line broadening contributions by relaxation enhancement due to either dipolar interactions or chemical shift anisotropy (CSA), measurements with and without ^{1}H broadband decoupling or replacement of

H_2O by D_2O (data not shown) as well as measurements at different magnetic fields did not result in changes of the spectral behavior (

Fig. A.**1** in Appendix). Interestingly, the spin-lattice relaxation time, T_1, even increased from 1.72 ± 0.02 s to 4.54 ± 0.11 s at magnetic field strengths of 9.4 and 14.1 T, respectively.

Additionally, one also has to consider the ionic strength, resulting from the Se(IV) concentration itself and the pH adjustment. To obtain pH_c 5, this requires higher amounts of HCl at higher selenium concentrations and thus increases the ionic strength. The higher the ionic strength, the more downfield shifted is the signal as determined by 0.1 mol L^{-1} solutions at varying NaCl background concentrations (**Fig. A.2**). However, line broadening caused by increasing ionic strength can be ruled out.

Speciation calculation performed at $I = 0.3$ mol L^{-1} with the equilibrium constants of [TORRES '10] (derived from potentiometric titration) predict the $H_2Se_2O_6^{2-}$ dimer to become predominant at concentrations higher than 10 mmol L^{-1} (**Fig. A.3** and **Tab. A.1** in the Appendix).

Our NMR spectroscopic findings reflect exactly this threshold at which significant spectral changes were observed. However, one has to keep in mind that our NMR experiments were performed at $I = 3$ mol L^{-1}, at which the speciation (and hence the dimer/monomer ratio) might be different in comparison to lower ionic strength. Speciation calculations with and without consideration of dimerization also showing the concentration dependence, can be found in the Appendix (**Fig. A.3**). To perform these calculations at high ionic strength using the SIT or Pitzer model, one would need a consistent set of interaction coefficients, which are to our knowledge not available.

Consequently, the line broadening is, in general, attributed to dimerization. Proton exchange reactions between $HSeO_3^-$ and water (diluted solution) can be considered as rapid. With increasing $HSeO_3^-$ concentration (also referred to as lower water activity) the proton exchange rate is lowered because of hydrogen bonding between $HSeO_3^-$ molecules among one another instead of water, resulting in line broadening. Hence, the broadening is likely to be due to a reduced proton exchange rate in consequence of monomer association. The line broadening of 2 M Se(IV) signals in the pH range 4 – 7 was already observed by [KOLSHORN '77]. They suggested that additional species are involved in the equilibrium, which may be $H_2Se_2O_6^{2-}$ dimers, stabilized by hydrogen bridges.

4.2.2 Impact of temperature

4.2.2.1 IR spectroscopy

The impact of temperature on Se(IV) and Se(VI) speciation was first investigated by IR-spectroscopy within the range from 298 to 333 K at pH 4 and 10 (**Fig. 4.4**). A change of the speciation, for instance due to protonation, deprotonation or dissociation of dimers, implies changes of the molecule symmetry, thus, causing vibrational mode alterations with concomitant frequency shifts and/or band shapes.

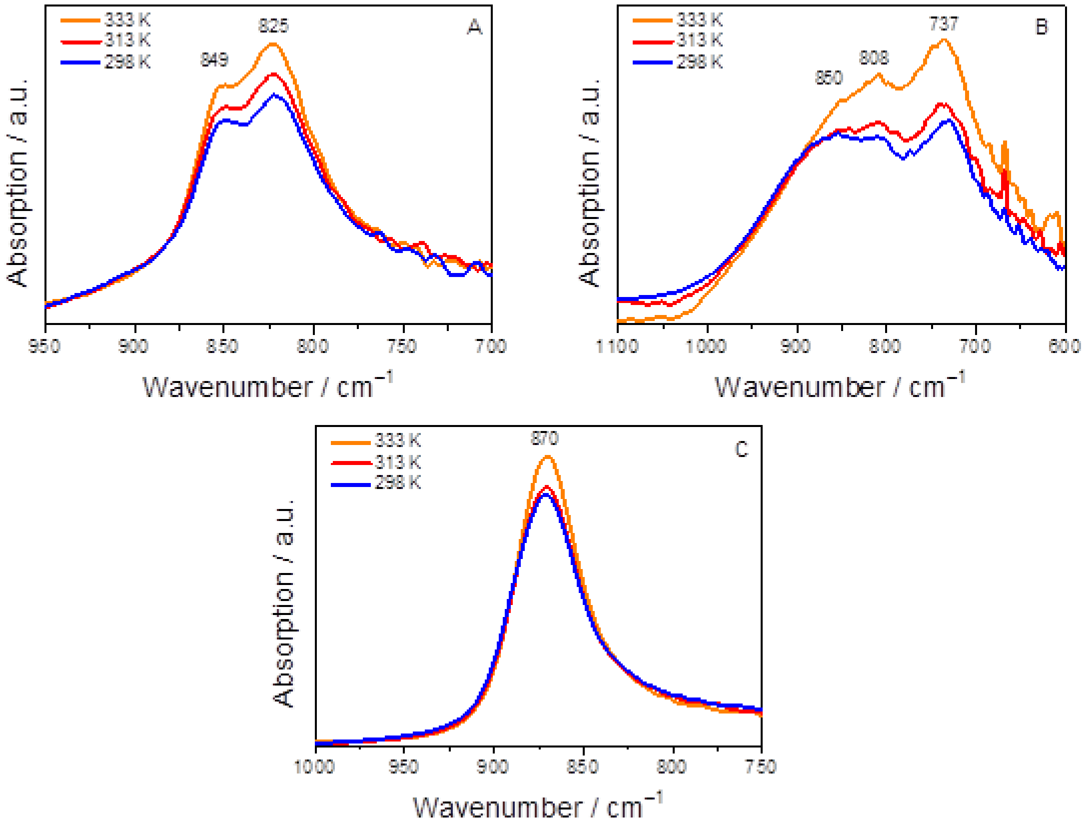

Fig. 4.4 FT-IR spectra of 0.1 mol L^{-1} solutions of Se(IV) at pH 4 (A) and pH 10 (B) and Se(VI) at pH 4 (C) at variable temperatures

The spectra of the Se(IV) solutions recorded at pH 4 do not significantly change with increasing temperature (**Fig. 4.4** a). As the bands at 849 and 823 cm^{-1} represent the symmetric and antisymmetric Se−O stretching modes of the $H_2Se_2O_6^{2-}$ dimer, respectively, it is obvious that a dissociation process does not occur in this temperature range. At pH 10, three main bands can be observed at 850, 808 and 737 cm^{-1} at ambient temperature (**Fig. 4.4** b), lower trace). These bands reflect a mixture of the $H_2Se_2O_6^{2-}$ dimer with maxima around 850 and 823 cm^{-1} and the SeO_3^{2-} monomer showing maxima around 808 and 737 cm^{-1}. Increasing the temperature does not significantly change the shape of the spectra apart from the slightly increased amplitude (**Fig. 4.4** b), upper trace). From the shape of the spectra, the predominance of the selenite monomer at pH 10 can be derived for all spectra recorded at pH 10 showing maxima at 808 and 737 cm^{-1}, whereas the characteristic maxima of the dimer around 850 and 820 cm^{-1} are hardly observed. These findings are also predicted by speciation calculations (**Fig. A.3**).

For the selenate ion (**Fig. 4.4** c), the band representing the asymmetric stretching vibration v_3(SeO) at 870 cm^{-1} remains unchanged upon temperature increase at pH 4. This is also valid for higher pH values as it is shown for pH 7.5 (**Fig. A.4**). To confirm the findings regarding temperature impact on selenium speciation, the samples were also investigated by NMR spectroscopy at different temperatures.

4.2.2.2 NMR spectroscopy

Chemical shifts are in principle temperature dependent. On the one hand, temperature changes affect the chemical shift by changing intrinsic molecular properties such as shielding tensors, bond lengths, excitation of rotational or vibrational inharmonic, etc. On the other hand, changes of the solvent’s physical properties such as viscosity, density or the solvation ability itself may also lead to chemical shift changes for the observed nucleus.

Temperature induced signal shifts are more or less linear and positive, *i. e.* higher temperatures correspond to larger chemical shifts, and depend strongly on the structure of the compounds [DUDDECK '95]. This behavior was used as a probe to monitor temperature induced changes in aqueous selenium speciation. The results obtained for Se(IV) can be found in **Fig. 4.5**.

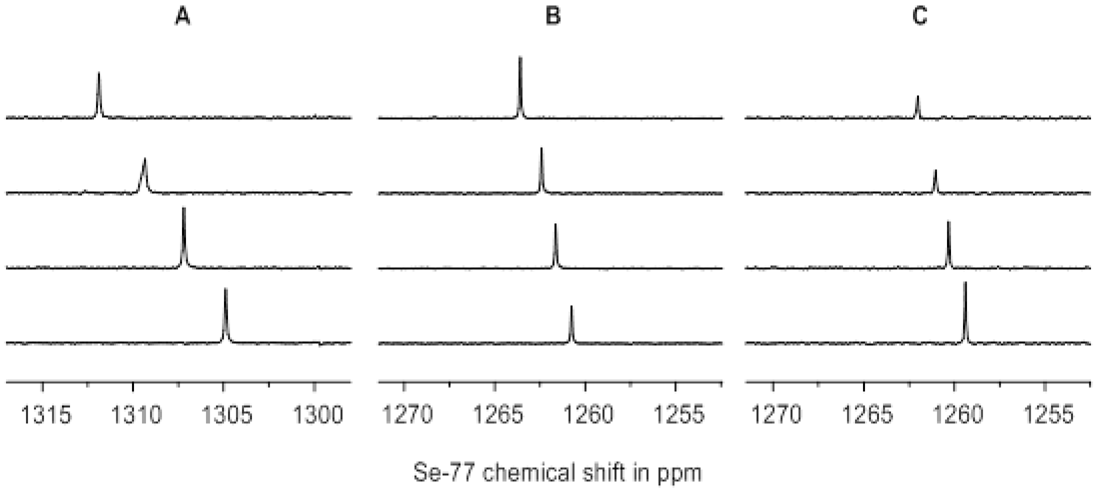

Fig. 4.5 ^{77}Se-NMR of 0.09 mol L^{-1} Se(IV) at pH 4 (A), pH 10 (B) and pH 13 (C) at variable temperatures (296, 308, 318 and 333 K from bottom to top)

At pH 10 and even more at pH 13, the fully deprotonated selenite ion, related to ≈ 1260 ppm, is the predominant species. At pH 4, the Se(IV) predominating species is the hydrogen selenite ion and, depending on Se concentration, its dimer (*vide supra*), corresponding to $\delta = 1305$ ppm. Obviously, the spectra show a temperature dependence of the chemical shift, also referred to as the slope of the fitted data, which can be considered as linear in all cases (**Fig. A.5** and **Tab. A.2** in Appendix).

Compared to a temperature-induced shift of 0.094 ppm K^{-1} attributed to H_2SeO_3 in H_2O [MILNE '93] , the determined values are reasonable (note that these experiments were performed with saturated H_2SeO_3 solution, which makes the exclusive presence of monomeric species highly questionable).

Although the investigated systems do not consist of one single species only, thereby allowing to address their individual δ–T correlation, it can be concluded that the value of $HSeO_3^-$ and SeO_3^{2-} must be close to 0.2 and 0.07 ppm K^{-1}, respectively. The considerable high δ–T value of the pH 4 solution signal – at least twice the value of the fully deprotonated monomeric selenite anion– is attributed to the predominating $H_2SeO_6^{2-}$ dimer at the chosen conditions (0.09 mol L^{-1}). The temperature dependence of the chemical shift at pH 10 and pH 13 are close to each other (**Tab. A.2** in Appendix). This was to be expected because the selenite ion is predominating at both pH values. The slightly higher value of δ–T correlation a pH 10 reflects the minor presence of a dimer species, as observed by IR spectroscopy (**Fig. 4.4** b).

Since the δ–T values of the $H_2SeO_6^{2-}$ dimer and selenite differ significantly, heat-induced changes in speciation, i. e. de/protonation, would result in different slopes between two adjacent points (temperature increments) in the above shown graphs, hence loosing linearity. Furthermore, the high sensitivity of the chemical shift to protonation changes itself would clearly indicate changes in speciation. As commonly known, chemical equilibrium constants, including acid–base equilibria, show logarithmic dependency (think of $\ln K$ vs. $1/T$ plots, or logarithmic titration curves). If the Se(IV) equilibria had been perturbed non-negligibly, the apparent temperature changes would not have shown linearity.

For Se(VI), the determined slopes of the δ vs. T plots are 0.068 ± 0.001 and 0.078 ± 0.002 ppm K^{-1}, corresponding to R^2 values of 0.9992 and 0.9990 for pH 4 and pH 7.5, respectively (spectra not shown). Again, the temperature-induced shifts can be considered as linear. Chemical shift differences at comparable temperatures as well as the different slopes (small difference compared to the Se(IV) case) indicate the presence of small amounts of hydrogen selenate at pH 4, but undergo fast exchange reactions with the coexisting and predominating selenate ion.

Consequently, both IR and NMR spectroscopy clearly showed the absence of significant changes in selenium aqueous speciation within the studied temperature range (296 to 333 K).

4.2.3 Complexation with Ca^{2+} and Mg^{2+}

In the presence of calcium or magnesium ions, the selenate and selenite NMR signals are shifted in comparison to the free aqueous oxy-anions. This highlights the interaction between selenium and these divalent metal ions (**Fig. 4.6**). The magnitude of the shift correlates with the selenium to metal ratio: the higher the ratio, the stronger the shift is. The observed shifts are significant, but weak. This agrees well with the high solubility as well as the low formation constants with $\log \beta \approx 2$ [OLIN '05] for selenate complexes of magnesium and calcium ions.

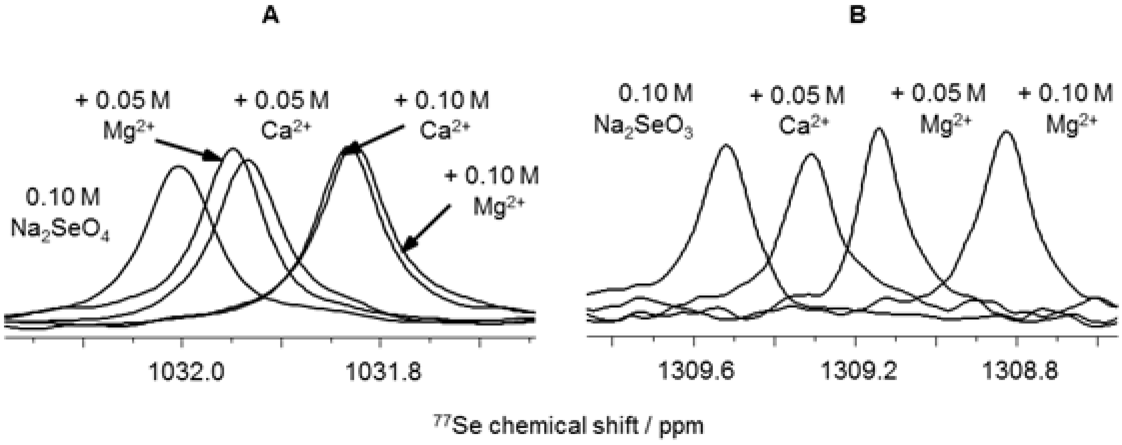

Fig. 4.6 Superimposed ^{77}Se NMR spectra of 0.1 mol L^{-1} sodium selenate (A) and 0.1 mol L^{-1} sodium selenite (B) solutions containing different amounts of Ca^{2+} or Mg^{2+}

In contrast, the selenite sample containing an equimolar calcium concentration showed precipitation. Evaluation of the solid state NMR spectra (**Fig. 4.7**) shows the occurrence of three selenium compounds, a major (96 %) and a minor (4 %) component with δ_{iso} at 1273.3 and 1315.3 ppm, respectively (**Tab. 4.2**).

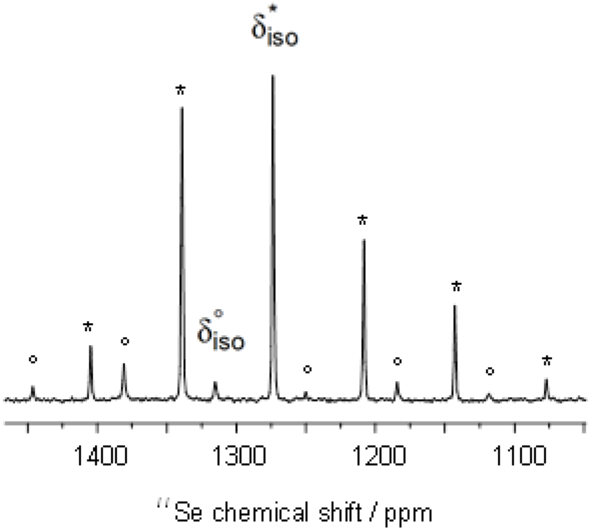

Fig. 4.7 ^{77}Se solid state CP/MAS NMR spectrum of the Se(IV)–calcium precipitate at a rotational frequency of 5 kHz; δ_{iso} and corresponding spinning sidebands (*,°)

Tab. 4.2 Analysis of CP/MAS spectra of the Se(IV)–calcium precipitate

δ_{iso}	δ_{11}	δ_{22}	δ_{33}	Ω	κ	% CP	% SP
1273.7	1396.4	1321.6	1103.1	293.3	0.49	86.5	96
1315.3	1443.7	1434.0	1068.1	375.6	0.95	13.3	4

δ in ppm | isotropic chemical shift $\delta_{iso} = {}^{1}/_{3}\,(\delta_{11} + \delta_{22} + \delta_{33})$, with δ_{11}, δ_{22}, δ_{33} as principal components of the chemical shift tensor, defined as $\delta_{11} > \delta_{22} > \delta_{33}$ | span $\Omega = \delta_{11} - \delta_{33}$ | skew $\kappa = 3(\delta_{22} - \delta_{iso})/\Omega$

With a content of 0.2 %, the third component (δ_{iso} = 1331.3 ppm) is disregarded. Though being precipitated from a pH_c 5 solution, with the Se(IV) predominating as hydrogen selenite ($HSeO_3^-$), the major component can clearly be assigned to a selenite species, as compared to the solution Na_2SeO_3 chemical shift value of ≈ 1260 ppm. The minor component, however, points to a hydrogen selenite species, as $NaHSeO_3$ resonates at 1305 ppm in solution.

Furthermore, comparing cross polarization (CP) and single pulse (SP) spectra, the latter allowing quantification, CP is more efficient for the minor component, suggesting hydrogen close to selenium (Se–O–H), whereas the major component is lacking of Se–OH groups. Moreover, solid state NMR line widths reveal the precipitate is crystalline, though being prepared as batch sample. Crystal water or surface sorbed water can neither be proven nor excluded by NMR, however, discounting the low amount of the minor solid hydrogen selenite species (containing OH) it is likely to assume crystal water due to both the morphology of the precipitate and the similarities between the selenium and the respective sulfur compounds.

The IR spectrum (**Fig. A.6**) of the Ca-Se(IV) precipitate clearly indicates the occurrence of OH as an important structural element as concluded from the asymmetric and symmetric stretching as well as the deformation vibration of OH, found at 3362, 3195 and 1672 cm^{-1}, respectively. None of the observed bands at 843, 777, 752, 704 and 633 cm^{-1} in the mid-IR region fit the bands of solid Na_2SeO_3 (790, 730 cm^{-1}) [TORRIE '73] or that of solid $NaHSeO_3$ (879, 848, 827, 790 cm^{-1}) [TORRIE '73]Thus, the band shifts are likely induced by complexation with calcium. Observed IR frequencies are in agreement with those formerly observed for $CaSeO_3{\cdot}H_2O$ [EBERT '81]. In order to determine the amount of crystal water, a thermogravimetric analysis (**Fig. A.7**) was performed and revealed the loss of one mole water.

As the precipitate is crystalline, X-ray diffraction is appropriate to finally confirm the obtained precipitate to be a calcium selenite monohydrate ($CaSeO_3{\cdot}H_2O$) (**Fig. A.8** in Appendix).

^{77}Se-NMR spectroscopy was shown to be a helpful tool in determining the aqueous speciation of selenium and its interactions with metal ions as well as to characterize the formed complexes in both the solution and the solid state. Our investigations confirmed that Se(IV) dimerization occurs in solution. We also observed that the aqueous speciation of Se(IV) as well as that of Se(VI) does not change within the investigated temperature range (296 – 333 K). Consequently, temperature dependent sorption behavior is not caused by changes in the aqueous selenium speciation. The results reveal the possibility of calcium ions to immobilize selenium in +IV oxidation state. However, neither calcium nor magnesium in the divalent state is able to precipitate and therefore immobilize selenium in its +VI oxidation state as it forms soluble complexes. These results will serve as reference data for further investigations addressing the mobility of selenium oxyanions in the environment.

4.3 Mineral phases characterization

An extended characterization of the bulk and surface properties of these solids was performed. The specific surface area (SSA) was determined. The potential presence of impurities in solids was checked by inductively coupled plasma-mass spectrometry (ICP-MS). For maghemite, potential contamination by Fe(II) was additionally checked by UV-VIS spectrophotometry.

Materials as delivered and heated up to 333 K were characterized by X-ray powder diffraction (XRD). Transmission Electron Microscopy (TEM) images/micrographs were obtained aiming at studying the shape, morphology and primary particle size of commercial samples. Mössbauer spectroscopy and X-ray Photoelectron Spectroscopy (XPS), which enable to distinguish the different Fe oxidation states [CHAMBERS '98; HUBER '12; MURAD '10; PRASAD '11; TUCEK '05; ZBORIL '02] was also applied for iron-bearing minerals.

The impact of pH and temperature (up to 333 K) on the isoelectric point (pH_{IEP}) and zeta potential of minerals was determined by electrophoretic mobility measurements. Possible changes in minerals' solubility and SSA at elevated temperature were also checked. More details about all these measurements are available in the Appendix C.

Anatase (TiO_2), hematite (α-Fe_2O_3), maghemite (γ-Fe_2O_3), alumina (δ-Al_2O_3) and kaolinite ($Al_2Si_2O_5(OH)_4$) were purchased. Due to the fact that the surface of magnetite (Fe_3O_4) corrodes very fast, this mineral has to be synthesized freshly prior to the sorption studies. A full description of the magnetite's synthesis is given in the Appendix C. The characteristics of the commercially samples, as given by the providers, are detailed in **Tab. 4.3**.

Tab. 4.3 Data from the provider for purchased solid samples

Mineral	Supplier	Purity	Average particle size (nm)	Specific surface area ($m^2\ g^{-1}$)
Anatase	MTI Corporation	99.99 %	5 - 10	210 ± 10
Hematite (α-Fe_2O_3)	US Research Nanomaterials	>99.5 %	30	20 - 60
Maghemite (γ-Fe_2O_3)	Alfa Aesar	>99 %	20 - 40	30 - 60
Alumina (δ-Al_2O_3)	Alfa Aesar	>99.5 %	40 - 50	32 - 40
Kaolinite (KGa-1b)	Clay Minerals Society	96 % [CHIPERA '01]	< 2000 (57.8 %) < 500 (32.0 %)	11.7 [PRUETT '93]

4.3.1 Specific surface area and presence of impurities

The determined specific surface area of anatase (234 $m^2\ g^{-1}$), hematite (41.1 $m^2\ g^{-1}$), maghemite (38.0 $m^2\ g^{-1}$), alumina (37 $m^2\ g^{-1}$) and kaolinite (11.8 $m^2\ g^{-1}$) [KŘEPELOVÁ '07] were in fair agreement with values provided by the suppliers. The synthesized magnetite showed a SSA of 89 $m^2\ g^{-1}$.

Minor contamination (in the range of 80 – 1000 $\mu g\ g^{-1}$) with Mg, Si, Zn, Nb, and Ta was evidenced by ICP-MS (ELAN 9000 Perkin Elmer) after digestion of anatase [MÜLLER '09]. For hematite, minor contamination (30 – 7050 $\mu g\ g^{-1}$) with Na, Mg, Al, Si, Ca, Cr, Mn, Ni and Zn was revealed. Small amounts of Na, Si, Mn, Ni, Cu, and Zn (below 40 $\mu g\ g^{-1}$) were found in the bulk of maghemite. For maghemite, less than 1.0 % (w/w) of total iron was found to be in the divalent state by UV-VIS spectrophotometry For δ−Al_2O_3, amounts of approx. 20 $\mu g\ g^{-1}$ were found for Mg, Cu, and W, 120 $\mu g\ g^{-1}$ for Fe and 550 $\mu g\ g^{-1}$ were found for Ca. Concerning kaolinite, Ca (5408 $\mu g\ g^{-1}$), Ti (8915 $\mu g\ g^{-1}$), Fe (1288 $\mu g\ g^{-1}$), Na (135 $\mu g\ g^{-1}$) and Cr(119 $\mu g\ g^{-1}$) impurities were found. Consequently, these solids were used as delivered without any pre-treatment.

4.3.2 X-ray diffraction

The X-ray diffraction patterns of the minerals are summarized in **Fig. 4.8**.

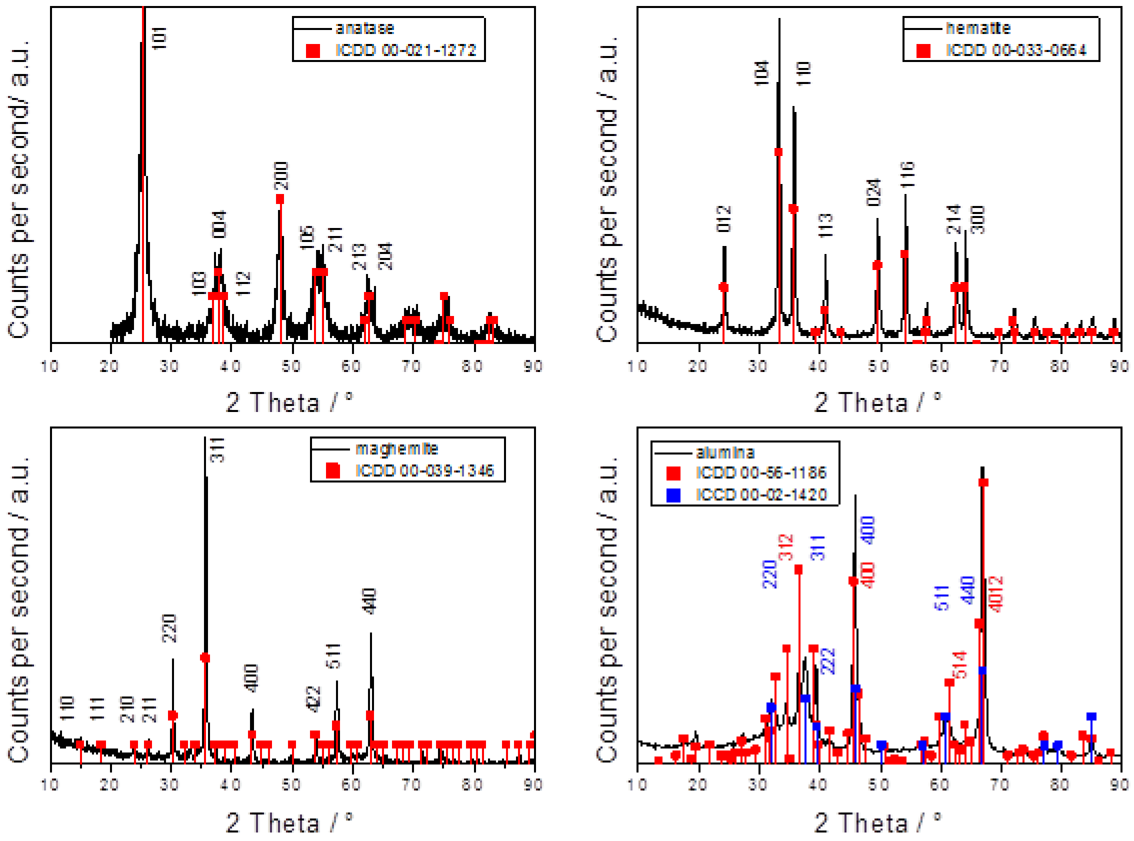

Fig. 4.8 X-ray diffraction pattern of anatase, hematite, maghemite and alumina samples compared to ICDD reference cards

By comparing the XRD patterns to the ICDD (International Centre for Diffraction Data) cards, the TiO_2 sample can be identified as a polycrystalline anatase phase (ICDD 00-021-1272), without any indications for the presence of rutile (ICDD 21-1276) or brookite (ICDD 29-1360). The XRD pattern of our α-Fe_2O_3 sample, with (012), (104), (110), (113), (024), (116), (214) and (300) diffraction lines, can be assigned to hematite according to the ICDD 033-0664 file.

The XRD pattern of the γ-Fe_2O_3 sample can be assigned to a maghemite phase with an ordered cubic structure. Indeed, the diffraction lines (110), (111), (210), (211), (220), (311), (400), (422), (511) and (440) matches well with the ICDD file 00-039-1346 (space group $P4_132$) or with the JCPDS file 89-5892 (space group $P4_332$). The XRD pattern indicates a partial ordering of vacancies on the octahedral sites. However, the presence of fully ordered maghemite cannot be excluded based on our X-ray diffractogram, since the extra lines showing up in the tetragonal symmetry are known to be very weak.

Based on the obtained X-ray diffractogram, the presence of magnetite in hematite or maghemite could be excluded. Indeed, the peaks positions of Fe_3O_4 are shifted to lower angle values [CHIN '06; SUN '04; ZENG '10; ZHU '07]. Based on the ICCD file 00-033-0664 and 00-029-0713, the presence of hematite or goethite as contaminant in iron-bearing minerals could also be excluded. If any of these phases are present, they are well below the detection limit of our device under the applied conditions.

The XRD pattern of alumina shows a mixture between $\delta-Al_2O_3$ (JCPDS/ICDD 00−056−1186) and $\gamma-Al_2O_3$ (JCPDS/ICDD 00−02−1420) with a ratio of approximately 70:30. However, no bayerite, gibbsite or boehmite were found. The XRD pattern of kaolinite confirmed a high purity mineral, together with traces of dickite, anatase and crandallite [CHIPERA '01].

All obtained XRD pattern show well-defined peaks and clearly indicate that all samples are crystalline.

The X-ray diffraction patterns of anatase, hematite and alumina heated up to 333 K are summarized in **Fig. 4.9**.

For anatase, hematite, and alumina, no changes in the diffractograms at elevated temperature were observed (**Fig. 4.9**) indicating the absence of any phase transformation or significant modification of crystallite size of anatase, hematite, and alumina at temperatures up to 333 K. Concerning anatase, this is in agreement with [HANAOR '11], who found transformations occurring between 673 K and 1473 K, with kinetics depending on several parameters (initial particle size/shape, synthesis way, heating rate, presence of impurities, etc.) [HANAOR '11]. Concerning hematite, it confirms the fact that this is one of the most thermodynamically stable iron oxide [CORNELL '03].

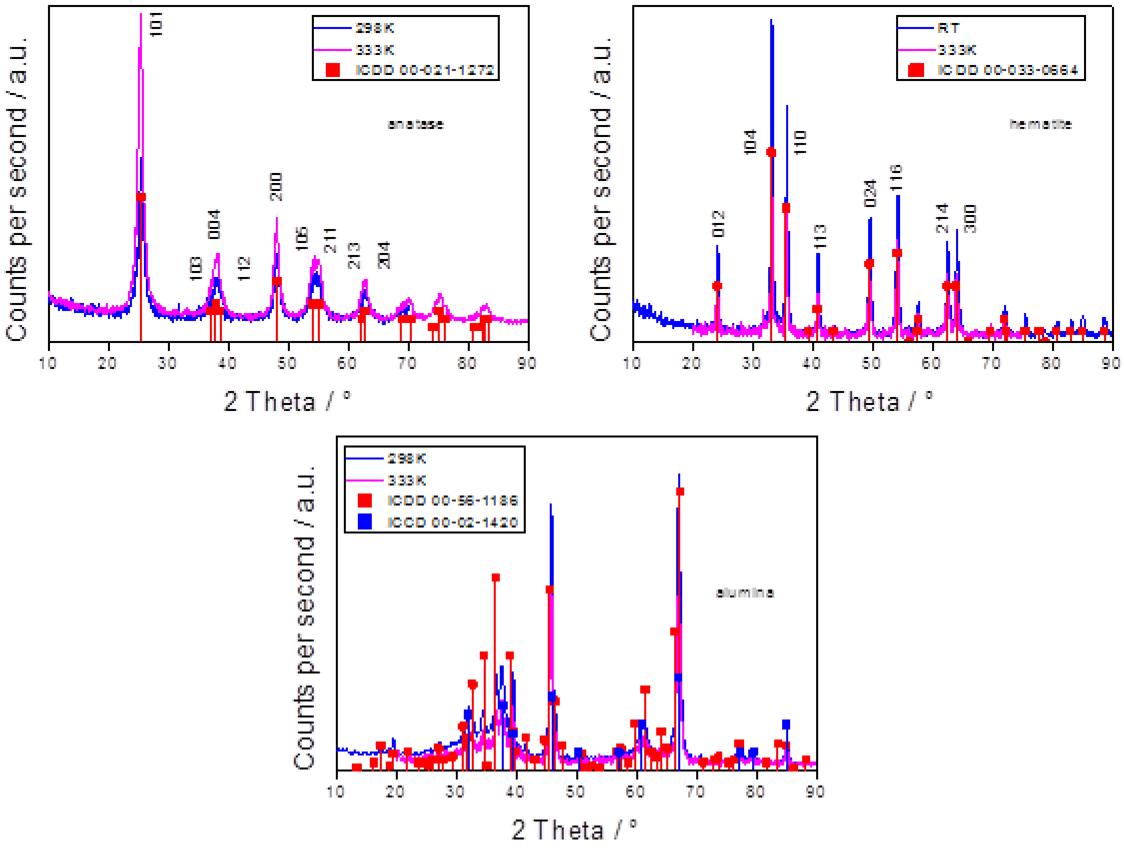

Fig. 4.9 X-ray diffraction pattern of anatase, hematite and alumina samples at room temperature and heated up to 333 K; ICDD cards are shown as references

4.3.3 TEM

The morphology of the four minerals was observed by TEM (**Fig. 4.10**). For anatase, TEM revealed slightly ellipsoidal shape, with a primary particle size between 5 to 10 nm. A high tendency to form agglomerates was also observed. Rounded particles with size ranging from 10 to 50 nm were found for hematite. Micrographs of nano-sized γ-Fe_2O_3 particles revealed particle sizes in the range of ~10 – 80 nm in diameter. Primary particle size observed by TEM was in agreement with supplier´s data.

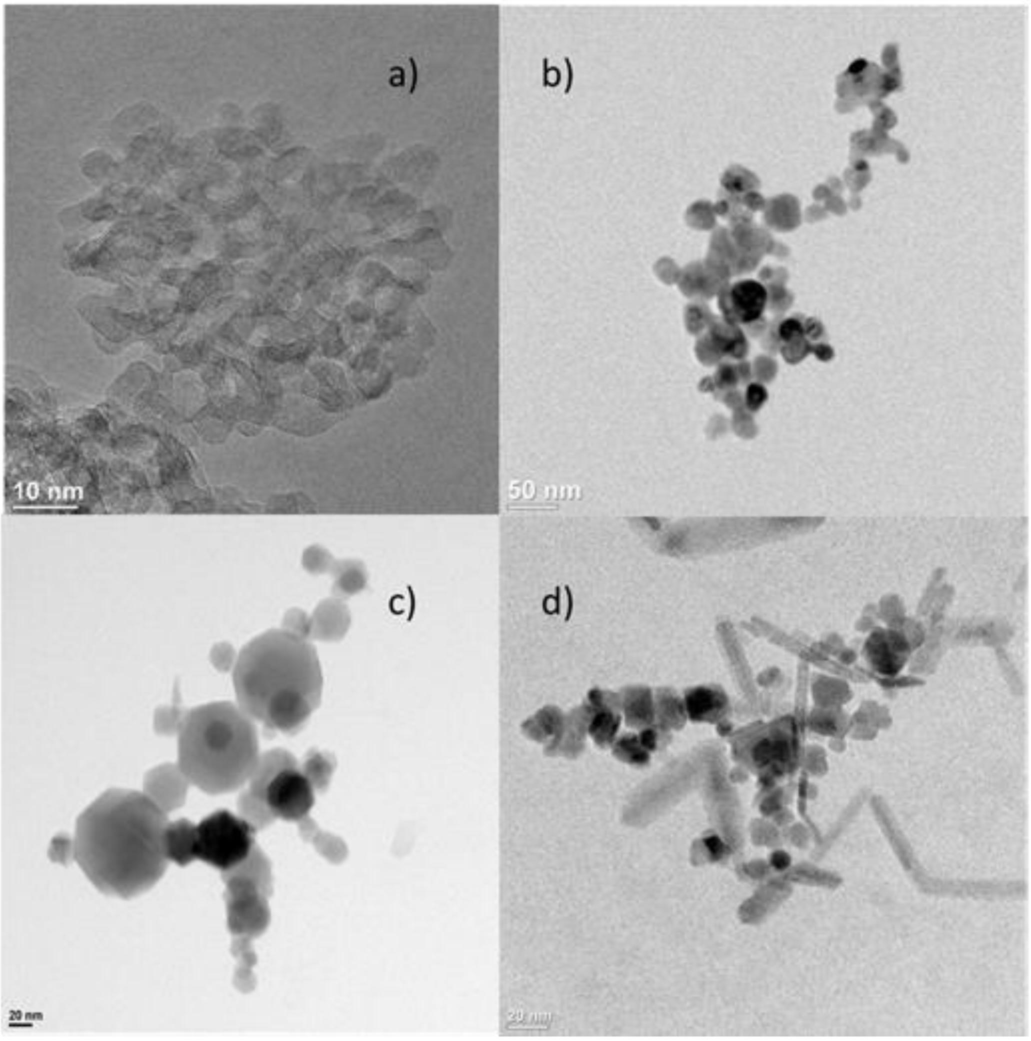

Fig. 4.10 Overview TEM images of (a) anatase (b) hematite (c) maghemite (d) magnetite nanoparticles

4.3.4 Mössbauer spectroscopy

Mössbauer spectroscopy enables to discriminate the different Fe oxidation states in iron-bearing minerals, allowing the distinction of hematite, magnetite and maghemite [MURAD '10; PRASAD '11; TUCEK '05; ZBORIL '02]. The Mössbauer spectrum of hematite fits well with one magnetic sextet (**Fig. 4.11** left).

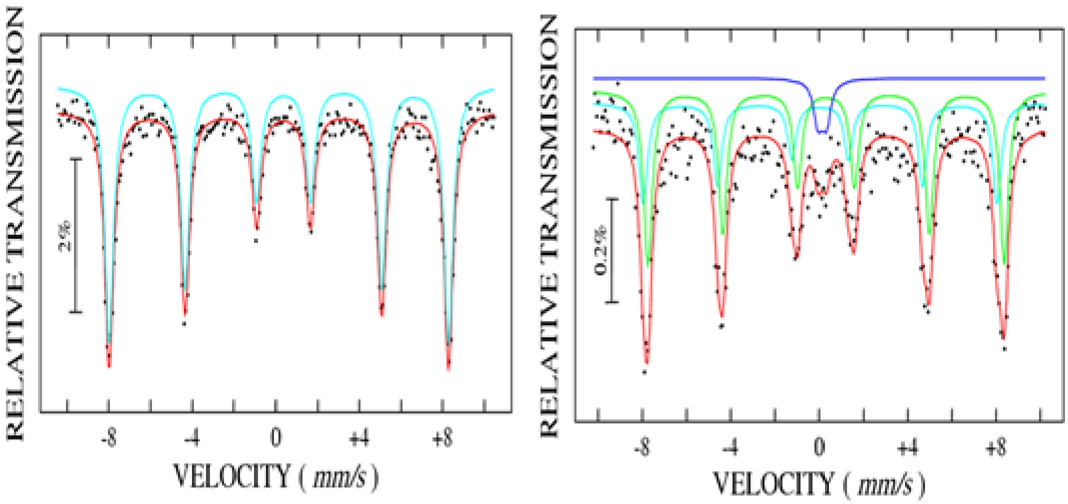

Fig. 4.11 Mössbauer spectrum recorded at room temperature of commercial hematite (US Research Nanomaterials, Inc.) (left) and commercial maghemite (Alfa Aesar) (right)

According to hyperfine parameters (isomer shifts, magnetic fields and quadrupole splitting) summarized in **Tab. 4.4**, the room temperature Mössbauer spectrum of this commercial sample shows that it only contains hematite [MURAD '10] and consequently only Fe^{3+} ions. In addition, typical magnetic fields of goethite, maghemite or magnetite were not identified, confirming the absence of these phases.

The Mössbauer spectrum of maghemite fits well with three subspectra, i. e. two magnetic sextets and one superparamagnetic quadrupole doublet (**Fig. 4.11** right). According to hyperfine parameters (isomer shifts, magnetic fields and quadrupole splitting) summarized in **Tab. 4.4**, the room temperature Mössbauer spectrum suggests that the commercial maghemite only contains Fe^{3+} ions.

Indeed, typical isomer shifts of Fe^{2+} ions in octahedral sites could not be detected. The small iron(II) traces determined by UV-VIS spectrophotometry are below the detection limit of our experiment. In addition, typical magnetic fields of hematite or goethite were also not identified, confirming the absence of these phases. The magnetic fields of the two sextets are close to those found in literature [MURAD '10]. The doublet might be due to the presence of nanometer-sized particles which exhibit superparamagnetism [CUVANOVA '07; DUTTA '10; PRASAD '11; SIDDIQUE '10; TUCEK '05].

Tab. 4.4 Mössbauer parameters of commercial hematite (US Research Nanomaterials, Inc.) and commercial maghemite (Alfa Aesar)

	Line Width (mm/s)	Isomer shifts (mm/s)	Quadrupole splitting (mm/s)	Inner magnetic field B_{hf} (T)	Relative spectrum area (%)
			Hematite		
Sextet	0.523	0.376	-0.222	50.4	100
	Maghemite				
Sextet 1	0.466	0.151		49.5	34.6
Sextet 2	0.466	0.414		49.9	59.4
Doublet	0.466	0.243	0.361		6.0

4.3.5 XPS

The survey XPS spectrum of maghemite evidenced the absence of major impurities at the surface (**Fig. 4.12**a).

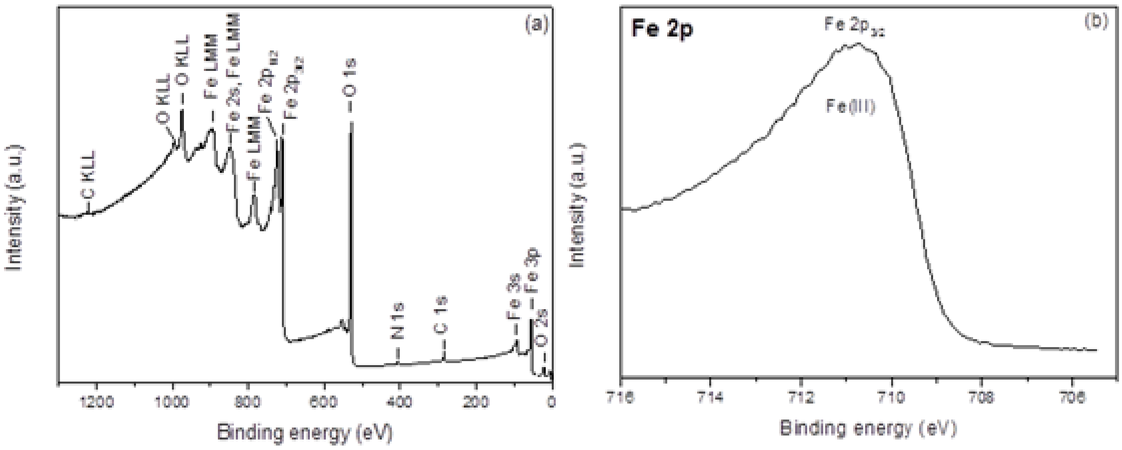

Fig. 4.12 (a) Survey XPS spectrum of maghemite (b) Narrow scan of Fe $2p_{3/2}$ spectrum

The minor contaminants of maghemite evidenced by ICP-MS (Na, Si, Mn, Ni, Cu and Zn) were not detected by XPS, indicating their presence in the bulk of the material.

The Fe $2p_{3/2}$ spectrum of maghemite (**Fig. 4.12**b) was measured to estimate the ratio between Fe(II) and Fe_{TOT} (Fe(II)+Fe(III)) [HUBER '12]. The maximum of the Fe $2p_{3/2}$ elemental line was located at 710.8 eV, in agreement with former studies [PARK '08; TEMESGHEN '02]. If Fe(II) was to be found in our maghemite sample, a shoulder at lower binding energy side of the Fe $2p_{3/2}$ spectrum, would have been expected

[CHAMBERS '98; HUBER '12]. The maghemite sample did not indicate presence of detectable amount of Fe(II). The Fe(II)/ Fe_{TOT} on the surface was well below 3 %, which is in the range of the analytical uncertainty.

The Fe $2p_{3/2}$ spectrum of magnetite (**Fig. 4.13**) was measured to estimate the ratio between Fe(II) and Fe_{TOT} [HUBER '12].

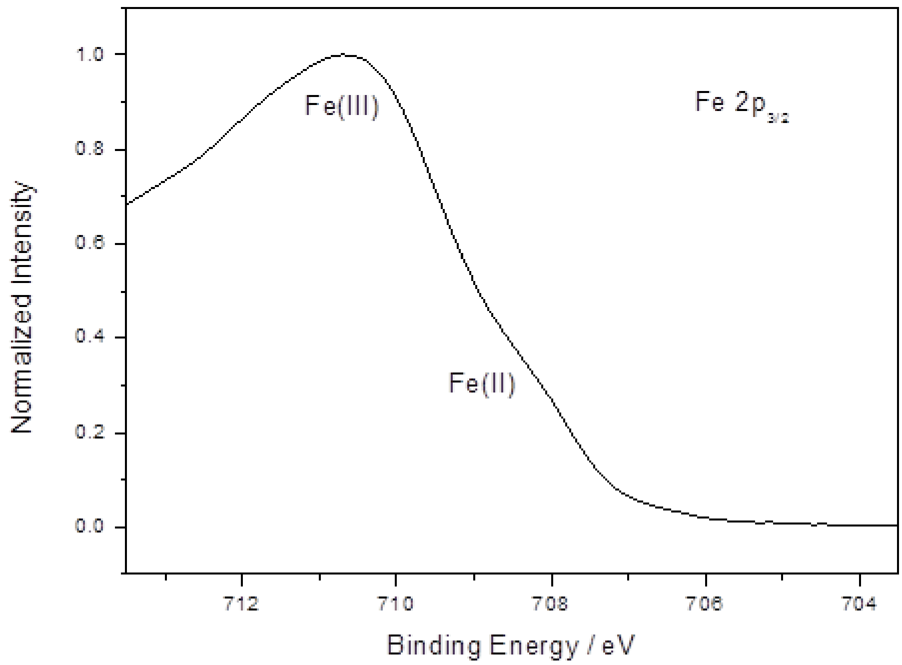

Fig. 4.13 Narrow XPS scan of Fe $2p_{3/2}$ spectrum of magnetite

The maximum of the Fe $2p_{3/2}$ elemental line was located at 710.8 eV, in agreement with former studies [PARK '08; TEMESGHEN '02]. A shoulder at lower binding energy side of the Fe $2p_{3/2}$ spectrum, shows the presence of Fe(II) [CHAMBERS '98; HUBER '12]. The intensity of the shoulder was determined and set into relation to spectra of a magnetite and a hematite reference by use of normalized spectra. The Fe(II)/ Fe_{TOT} on the surface of the magnetite was calculated to be between 22 and 23 %. This is below the expected Fe(II)/ Fe_{TOT} ratio of 33 % for a stoichiometric magnetite. Further improvements are therefore necessary.

4.3.6 Electrophoretic mobility measurements at room temperature and 333 K

The impact of pH (from 3.5 to 11) at room temperature on the zeta potential of the neat surfaces of the minerals is shown in **Fig. 4.14**.

At room temperature, the pH_{IEP} of anatase (**Fig. 4.14**) was found to be located at pH ~ 6.6, in close agreement with former studies [COMARMOND '11; GUSTAFSSON '00; KOSMULSKI '03].

For hematite, [CORNELL '03] reported pH_{IEP} values for hematite ranging from 7.0 to 9.5. The pH_{IEP} of our commercial hematite was found to be located at pH 9.5. This pH_{IEP} matches well with those reported in the past. Note that [SCHUDEL '97] who also performed their zeta potential measurement under CO_2-free conditions reported an pH_{IEP} of 9.2. This influence of CO_2 on the surfaces properties of minerals (e. g. hematite) was confirmed by [CARLSON '11]. This might explain lower reported values in the literature, in addition to different synthesis pathways, presence of impurities, etc. [COMARMOND '11].

The pH_{IEP} of maghemite was found to be located at pH 7.7 which fits well with recently reported values ranging from 6.8 to 8.3 [BOGUSLAVSKY '08; MORNET '05; PARK '09; TUUTIJÄRVI '10; YU '04].

For alumina, a pH_{IEP} of 9.6 was found. No literature data was found for $\delta{-}Al_2O_3$. However, the value is in good agreement with the literature concerning $\gamma{-}Al_2O_3$ (e. g. [JEGADEESAN '03]).

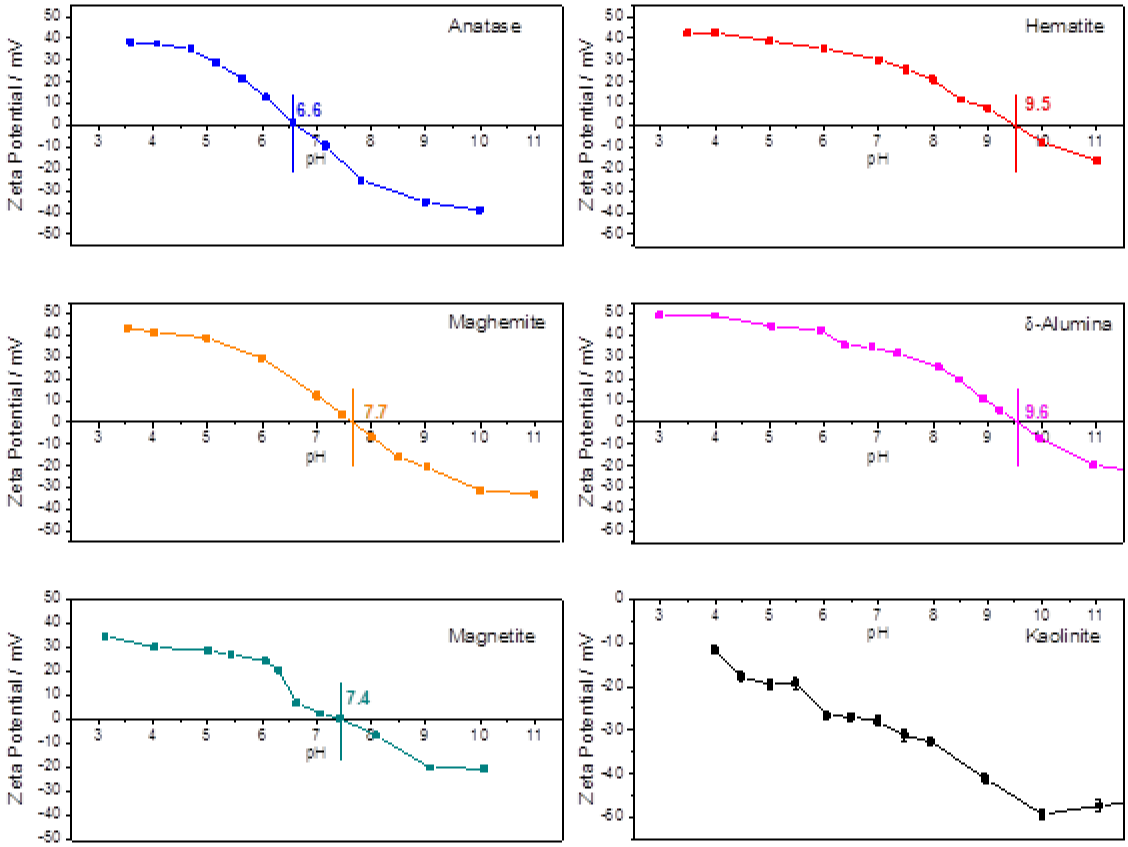

Fig. 4.14 Zeta potential of the neat surface of anatase, hematite, maghemite and alumina at room temperature

Anatase (0.01 mol L^{-1} NaCl, m/v = 0.25 g L^{-1}, 2 days of shaking). Hematite (0.1 mol L^{-1} NaCl, m/v = 0.25 g L^{-1}, 2 days of shaking). Maghemite (0.1 mol L^{-1} NaCl, m/v = 0.75 g L^{-1}, 2 days of shaking). Alumina (0.1 mol L^{-1} NaCl, m/v = 0.2 g L^{-1}, X days of shaking). Magnetite (0.1 mol L^{-1} NaCl, m/v = 0.2 g L^{-1}, X days of shaking). Kaolinite (0.1 mol L^{-1} NaCl, m/v = 0.1 g L^{-1}, 7 days of shaking)

For magnetite, the pH_{IEP} was found at pH 7.4 which is slightly higher than values reported in literature like e. g. [YANG '14a] who found values between 6.8 and 7.0. However, ageing tests of magnetite samples [CARLSON '13] showed that the pH_{IEP} of magnetite shifts to lower pH values due to ageing of the mineral. The pH_{IEP} of the magnetite of this study is in good agreement with the pH_{IEP} of magnetite which is not aged. For kaolinite, no isoelectric point was found and the surface charge was negative throughout the investigated pH range from pH 4 to pH 12.

With increasing temperature, the pH_{IEP} of anatase, hematite and alumina was shifted towards lower pH (**Fig. 4.15**). The observed decrease of the pH_{IEP} of anatase, hematite and alumina with increasing temperature is in good agreement with recent studies of

[VLASOVA '04], [VALDIVIESO '06] and [KULIK '00]. Based on both experimental observations and theoretical calculations, a decrease of the pH_{PZC} of different $(Al,Si,Fe,Ti,Zn)_xO_y$ oxides was found with increasing temperature [KULIK '00; VLASOVA '04].

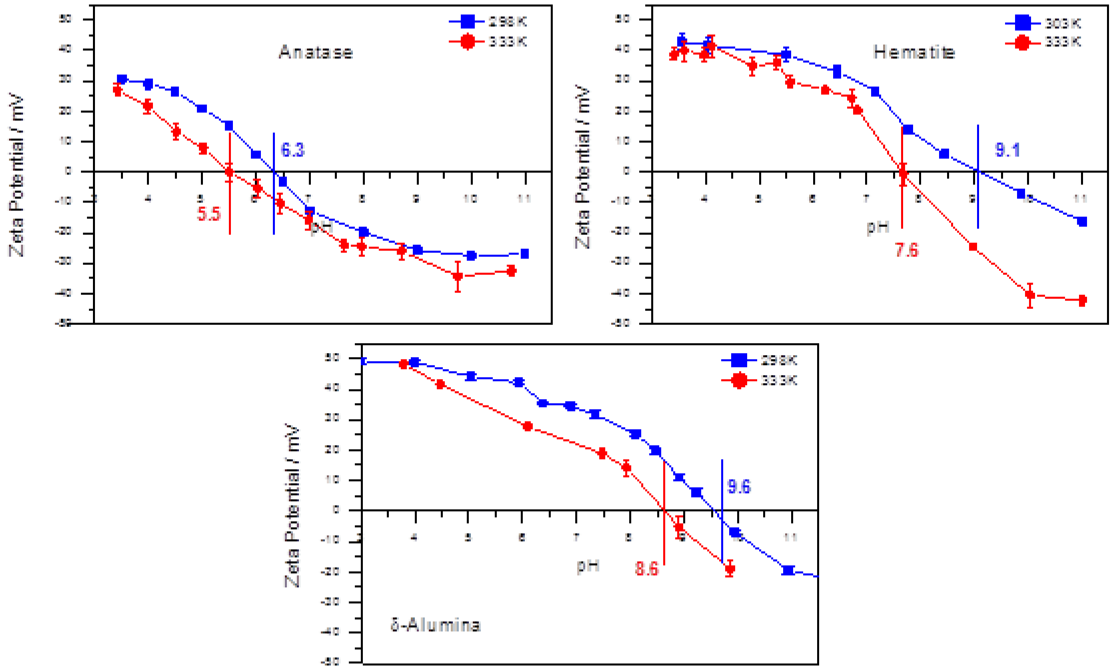

Fig. 4.15 Impact of temperature on the zeta potential of the neat surface of anatase, hematite and alumina at 0.1 mol L^{-1} NaCl

Anatase (m/v = 0.5 g L^{-1}, 2 days of shaking). Hematite (m/v = 0.75 g L^{-1}, 2 days of shaking). Alumina (m/v = 0.2 g L^{-1}, 2 days of shaking)

In addition, at constant pH lower than the pH_{IEP}, the total positive surface charge of anatase, hematite and alumina is decreased with increasing temperature up to 333 K. This could be due to a favored proton desorption from the oxides' surface upon increasing temperature, as suggested by [VALDIVIESO '06] for α-Al_2O_3.

Furthermore, no differences in the SSA and solubility of anatase, hematite and alumina were observed at 333 K. **Tab. 4.5** summarizes results obtained in this section.

Tab. 4.5 SSA, Impurities and pH_{IEP} of studied minerals

Mineral	**SSA ($m^2 g^{-1}$)**	**Impurities ($\mu g g^{-1}$)**	**pH_{IEP} @ [1]RT**	**pH_{IEP} @ 333 K**
Anatase	234	Mg, Si, Zn, Nb, Ta (80 – 1000)	6.6	5.5
Hematite	41.1	Na, Mg, Al, Si, Ca, Cr, Mn, Ni, Zn (30 – 7050)	9.5	7.6
Maghemite	38.0	Na, Si, Mn, Ni, Cu, Zn (< 40)	7.7	[2]N.D.
Alumina	37	Mg, Cu (20), Fe (120), Ca (550)	9.6	
Kaolinite	11.8	Ca, Ti, Fe, Na, Cr (119 – 8915)	<[3]4.0	[2]N.D.

[1] RT: Room Temperature

[2] N.D.: Not determined

[3] pH_{IEP} not detected under applied experimental conditions

4.4 Sorption of Se(VI) and Se(IV) onto mineral phases

Sorption of selenium(VI) and selenium(IV) onto anatase, hematite, maghemite, alumina and kaolinite was studied. Time dependent experiments were performed, and the influence of pH and ionic strength (moderate and high) was investigated. The impact of selenium oxyanions sorption on the zeta potential of the minerals was also checked. Finally, sorption experiments were also performed at elevated temperatures. Thermodynamic sorption parameters, namely Gibbs free energy of reaction ($\Delta_R G$), enthalpy of reaction ($\Delta_R H$), and entropy of reaction ($\Delta_R S$) were derived using the van’t Hoff plot. Experimental details can also be found in the Appendix D.

4.4.1 Impact of time, pH and moderate ionic strength

4.4.1.1 Impact of time

The sorption of selenium(VI) and selenium(IV) onto all minerals was extremely fast and already reached a plateau/saturation after 1 – 2 h to 24 h only. Examples for kinetic studies on anatase, hematite and maghemite are shown in **Fig. 4.16** and **Fig. 4.17**.

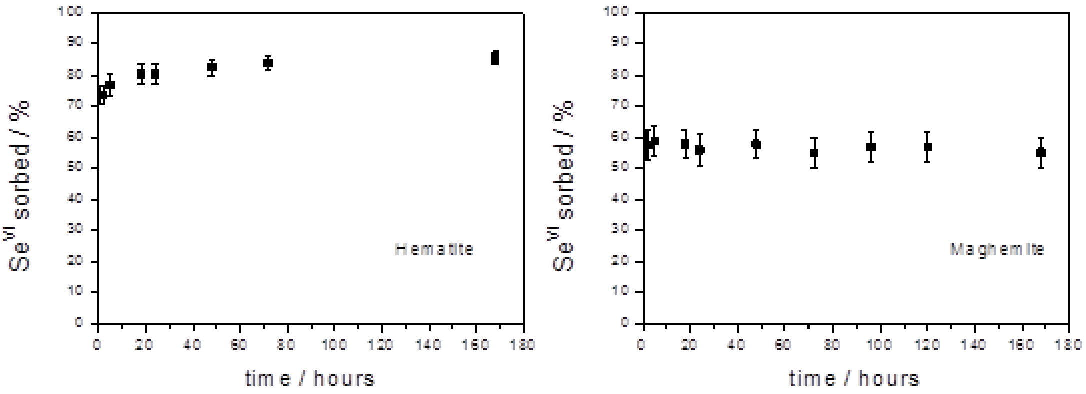

Fig. 4.16 Time-dependence sorption of selenium(VI) onto hematite and maghemite at pH 4.0. $[Se^{VI}]_{initial} = 1 \times 10^{-5}$ mol L^{-1}, 0.1 M mol L^{-1} NaCl; Hematite (m/v = 0.75 g L^{-1}); Maghemite (m/v = 1.0 g L^{-1})

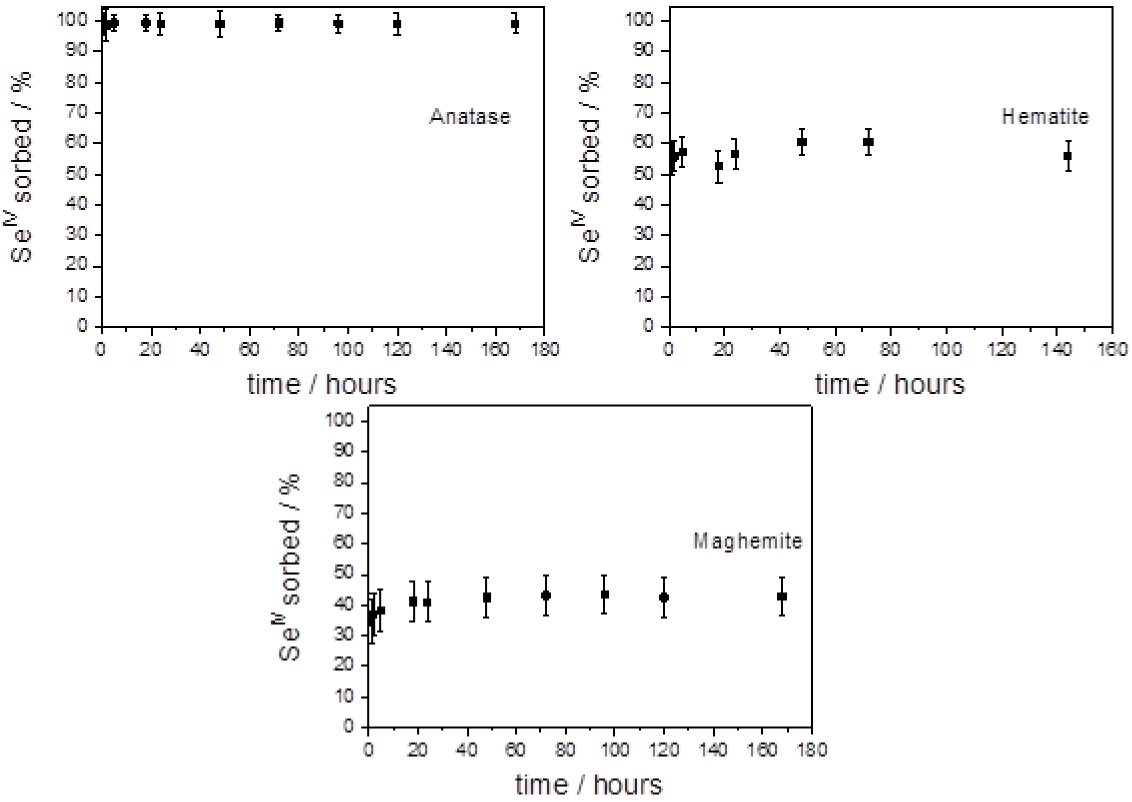

Fig. 4.17 Time-dependence sorption of selenium(IV) onto anatase, hematite and maghemite at pH 4.0. $[Se^{IV}]_{initial} = 5 \times 10^{-5}$ mol L^{-1}, 0.1 mol L^{-1} NaCl; Anatase (m/v = 0.75 g L^{-1}); Hematite (m/v = 0.1875 g L^{-1}); Maghemite (m/v = 0.25 g L^{-1})

The extent of sorption remained unchanged for longer contact times. Such a fast sorption equilibrium was already reported for selenium(VI) sorption onto nanosized jacobsite $MnFe_2O_4$ (GONZALES ‘10), nanosized anatase [JORDAN '11] and natural hematite [ROVIRA '08]. Same is true for the uptake of selenium(IV) by nano-anatase [DENG '12; LI '02; XU '12; YAMANI '14; YANG '14b] and natural [ROVIRA '08] or synthetic [JORDAN '09] hematite. The time needed to reach a plateau in terms of selenium(VI) or selenium(IV) sorption was assumed to be the period necessary to reach equilibrium. Adding a safety margin of 100 % and for convenient reasons, an equilibration time of 2, 3 or 4 days was chosen for all further sorption experiments. For the Se(VI)/anatase binary system, suspensions were shaken for 2 days, since a recent kinetic study showed that a plateau was reached after a contact time of 24 hours [JORDAN '11].

4.4.1.2 Impact of pH

The results of the batch experiments show selenium(VI) sorption onto all investigated minerals to be strongly pH-dependent, being at maximum in the acidic pH range and decreasing with increasing pH (**Fig. 4.18**), in agreement with former studies [DUC '03; JORDAN '11; ROVIRA '08; SANUKI '00; ZHANG '09].

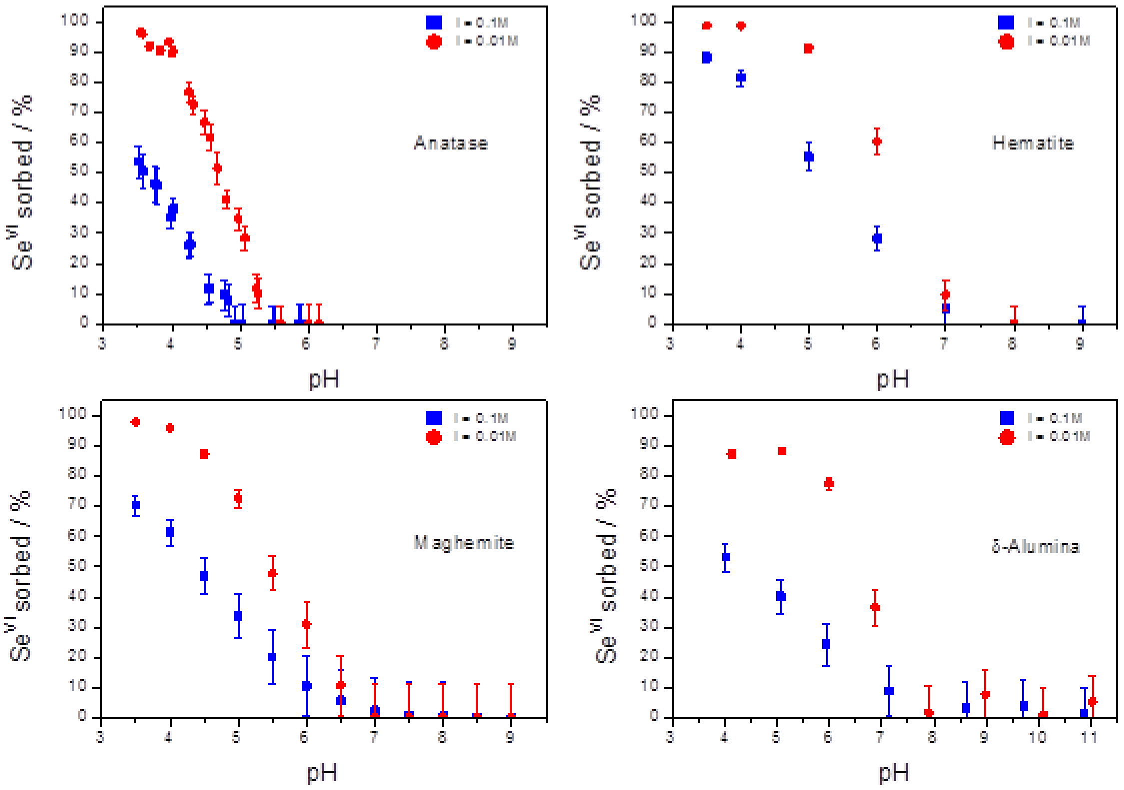

Fig. 4.18 Selenium(VI) sorption edges onto anatase, hematite, maghemite and alumina at two different ionic strengths in NaCl (0.1 and 0.01 mol L^{-1}); Anatase ($[Se^{VI}]_{initial} = 1 \times 10^{-5}$ mol L^{-1}, m/v = 0.5 g L^{-1}, 2 days of shaking); Hematite ($[Se^{VI}]_{initial} = 1 \times 10^{-5}$ mol L^{-1}, m/v = 0.75 g L^{-1}, 2 days of shaking); Maghemite ($[Se^{VI}]_{initial} = 1 \times 10^{-5}$ mol L^{-1}, m/v = 1 g L^{-1}, 2 days of shaking); Alumina ($[Se^{VI}]_{initial} = 2 \times 10^{-5}$ mol L^{-1}, m/v = 1 g L^{-1}, 2 days of shaking)

This behavior can be expected taking into account the surface charge of minerals and the speciation of selenium in solution. According to the Pourbaix diagram of selenium [OLIN '05], the selenate ion SeO_4^{2-} is the predominant aqueous species in solution between pH 3.5 and 11. Furthermore, at a pH lower than the isoelectric point (pH_{IEP}), the electrostatic attraction between the positively charged ($\equiv XOH_2^+$, X = Ti, Fe or Al)) surface groups of anatase, hematite, maghemite or alumina and negatively charged selenate oxyanions promotes sorption. At pH > pH_{IEP}, the neat surface of the minerals is then negatively charged. As the amount of ≡ XOH_2^+ (X =Ti, Fe or Al) and ≡ XOH (X = Ti, Fe or Al) surface groups decreases with progressing deprotonation, dominant negatively charged ≡XO^- (X = Ti, Al or Fe) surface groups are formed. Due to these unfavorable electrostatic conditions, the sorption of selenium(VI) decreases with increasing pH.

Selenium(IV) uptake onto anatase, hematite, maghemite and alumina strongly decreased with pH of the suspension (**Fig. 4.19**), as typically observed in the literature [BENEDICTO '13; DUC '06; DUC '03; JORDAN '09; ROVIRA '08; YANG '14b; ZHANG '09].

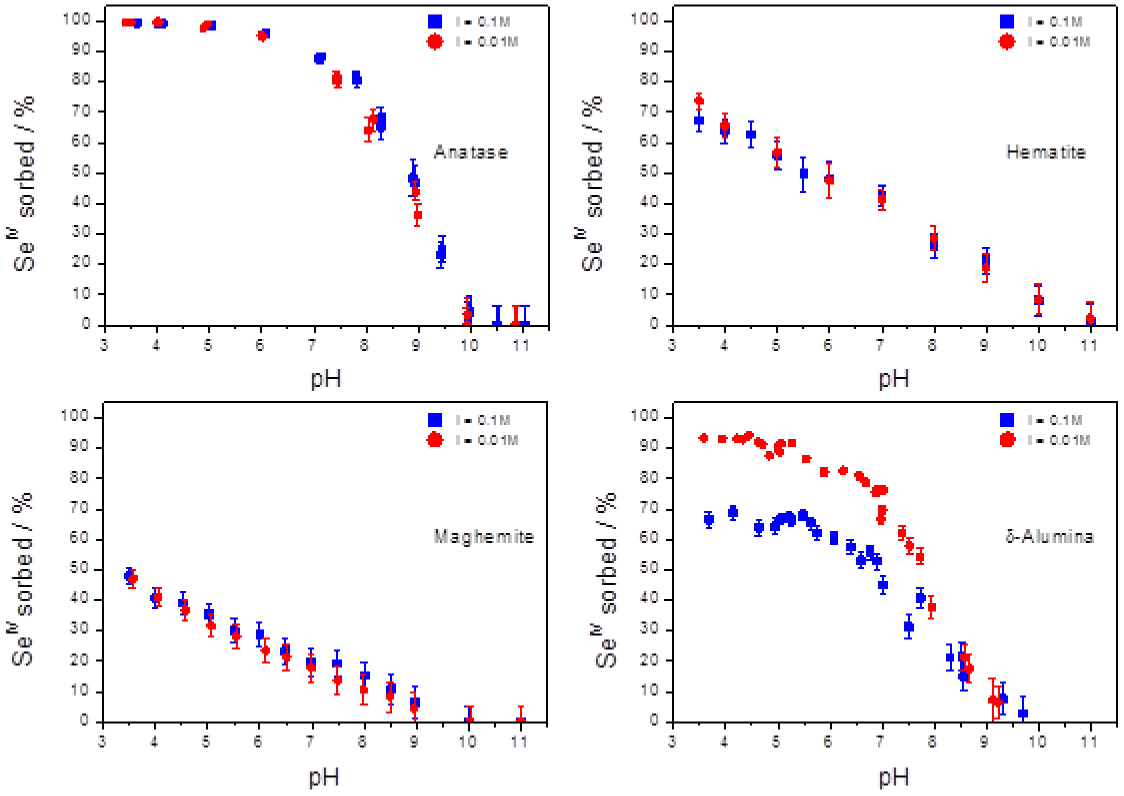

Fig. 4.19 Selenium(IV) sorption edges onto anatase, hematite, maghemite and alumina at two different ionic strengths in NaCl (0.1 mol L^{-1} and 0.01 mol L^{-1}); Anatase ($[Se^{IV}]_{initial} = 5 \times 10^{-5}$ mol L^{-1}, m/v = 0.75 g L^{-1}, 2 days of shaking); Hematite ($[Se^{IV}]_{initial} = 5 \times 10^{-5}$ mol L^{-1}, m/v = 0.25 g L^{-1}, 2 days of shaking); Maghemite ($[Se^{IV}]_{initial} = 5 \times 10^{-5}$ mol L^{-1}, m/v = 0.25 g L^{-1}, 2 days of shaking); Alumina ($[Se^{IV}]_{initial} = 10^{-5}$ mol L^{-1}, m/v = 0.5 g L^{-1}, 2 days of shaking)

For anatase, a high adsorption (> 90 %) was obtained in a wide pH range of 3.5 – 7, followed by a sharp decrease at higher pH values, as noticed by [DENG '12]. Sorption of selenium(IV) on hematite and maghemite was found to decrease linearly with the pH. The data presented in **Fig. 4.19** show that there is still a significant amount of selenium(IV) sorbed onto anatase, hematite and maghemite at pH values greater than the pH_{IEP}, where the surface is negatively charged. Similar observations were also reported for anatase [BENEDICTO '13], iron oxides [BALISTRIERI '87; PARIDA '97b] as well as for water-washed manganese nodule leached residues [DASH '07], where selenium(IV) sorption took place at pH values greater than the pH_{PZC} (point of zero charge) or pH_{IEP}. According to [STUMM '70] the free energy of adsorption is a combination of both chemical and electrostatic effects. This means that above pH_{IEP}, the chemical component dominates the electrostatic one [BALISTRIERI '87; PARIDA '97b].

For $\delta-Al_2O_3$ no sorption of Se(IV) was found above the pH_{IEP} of the neat mineral surface. This is in good agreement with recent studies about Se(IV) sorption onto gibbsite [GOLDBERG '14].

The results of the batch experiments of selenium(VI) and selenium(IV) sorption onto kaolinite are shown in **Fig. 4.20**.

Similarly to what was observed for single oxides, sorption of selenium(VI) and selenium(IV) onto kaolinite decreases with increasing pH. Sorption of selenium(VI) vanished at pH 5 already, whereas selenium(IV) sorption took place up to pH 8.

The sorption capacity of all minerals towards selenium(VI) ad selenium(IV) was compared by calculating coefficients distribution (K_d), at pH 4 and 0.1 mol L^{-1} NaCl
(**Tab. 4.6**).

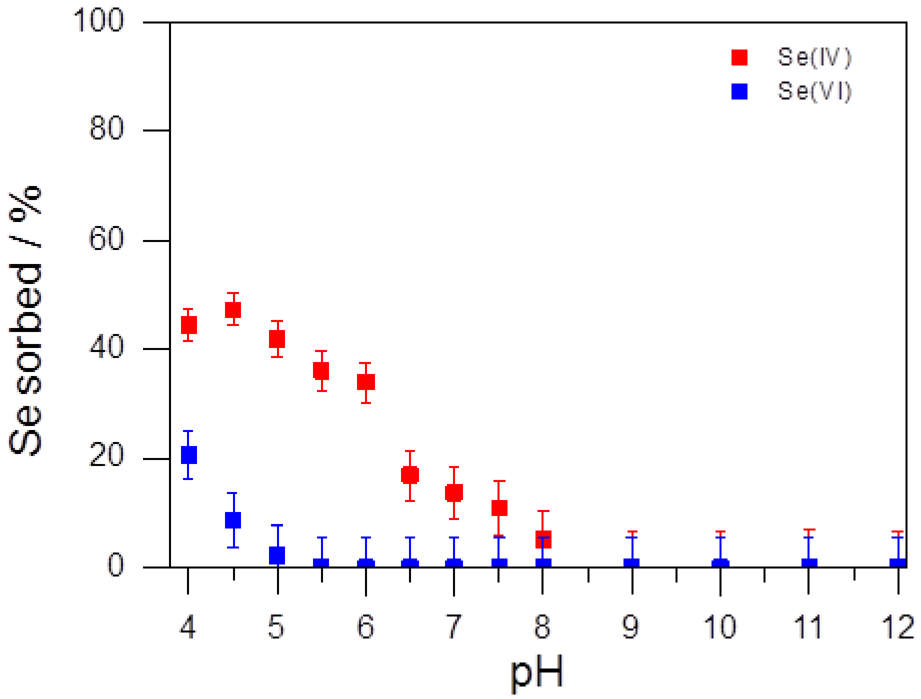

Fig. 4.20 Selenium(VI) and selenium(IV) sorption edges onto kaolinite (m/v = 30 g L^{-1}, 0.1 mol L^{-1} NaCl, 4 days of shaking, $[Se]_{initial} = 10^{-5}$ mol L^{-1}) (kaolinite was pre-equilibrated in 0.1 M NaCl during 4 weeks)

Tab. 4.6 Comparison of the K_d (m^3 kg^{-1}) of all minerals for Se(VI) and Se(IV) at pH 4 and 0.1 mol L^{-1} NaCl

Mineral	**Se(VI)**	**Se(IV)**
Anatase	1.22	525.33
Hematite	5.86	7.05
Maghemite	1.60	2.74
Alumina	1.57	4.35
Kaolinite	0.01	0.03

The sorption capacity of all studied minerals towards selenium(IV) is stronger than for selenium(VI), as expected [FERNANDEZ-MARTINEZ '09]. The sorption capacity of kaolinite is at least two orders of magnitude lower compared to single oxides (**Tab. 4.6**). This severely hampers the application of advanced spectroscopic techniques such as EXAFS and *in situ* ATR FT-IR. Consequently, kaolinite was not further considered during this study.

During all sorption experiments, HG-AAS evidenced the absence of homogenous reduction of selenium(VI) and selenium(IV) in the aqueous phase.

4.4.1.3 Impact of moderate ionic strength

Sorption of selenium(VI) onto anatase, hematite, maghemite and alumina was not only pH-dependent, but also ionic strength-dependent (**Fig. 4.18**). An increase of the ionic strength from 0.01 to 0.1 mol L^{-1} led to a significant decrease of the amount of selenium(VI) retained. This is in agreement with former studies investigating selenate sorption onto several mineral surfaces like goethite [DUC '03; HAYES '88; HAYES '87; SU '00], amorphous iron oxyhydroxide [HAYES '88; SU '00], hematite [DUC '03], cuprite Cu_2O [WALCARIUS '04], γ-Al_2O_3 [ELZINGA '09; WU '00], hydrous aluminum oxide [PEAK '06a] and nanosized-anatase [JORDAN '11]. This macroscopic observation is commonly considered as an indication for outer-sphere complexation.

Ionic strength variation between 0.1 and 0.01 M had no significant effect on Se(IV) sorption onto anatase, hematite and maghemite (**Fig. 4.19**), similar to previous studies on goethite [DUC '03; SU '00], amorphous iron oxyhydroxides [SU '00], hematite [DUC '06; DUC '03], anatase [SHI '09], and γ-Al_2O_3 [ELZINGA '09]. An indication for inner-sphere complexation is usually derived from such macroscopic observation.

For δ−Al_2O_3 an ionic strength dependency was observed – an increase of the ionic strength led a significant decrease. This is in good agreement with recent studies about Se(IV) sorption onto gibbsite [GOLDBERG '14] These macroscopic observations usually refer to outer-sphere complexation. While data from [ELZINGA '09] do not provide any direct indications for the presence of outer-sphere selenite complexes at the γ-Al_2O_3 surface, [PEAK '06a] proposed a mixture of inner-sphere and outer-sphere complexes on hydrous aluminum oxides at pH 4.5 – 8.0 based on the XANES data of adsorbed selenite.

4.4.2 Impact of high ionic strength

The influence of ionic strength on the sorption of selenium(VI) and selenium(IV) was studied exemplarily with δ-Al_2O_3 as mineral phase and NaCl and $MgCl_2$ as background electrolytes. An increase of the ionic strength from 0.01 to 1 M NaCl and 0.5 M $MgCl_2$, respectively led to a significant decrease of Se(VI) sorption. For example at pH 5 and at 0.01 M NaCl, 88 % of Se(VI) was sorbed whereas at an ionic strength of 1 M, Se(VI) sorption completely vanished (**Fig. 4.21**). Similar influences can be found for $MgCl_2$ as background electrolyte.

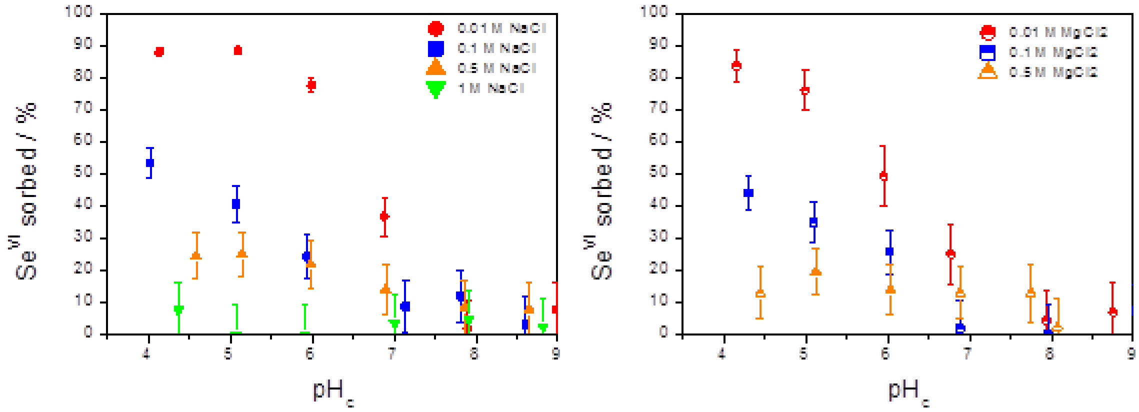

Fig. 4.21 Selenium(VI) sorption edges onto δ−alumina at different ionic strengths in NaCl and $MgCl_2$. ($[Se^{VI}]_{initial} = 1 \times 10^{-5}$ M, m/v = 0.5 g L^{-1}, 2 days of shaking)

The sorption of Se(IV) onto alumina also showed an ionic strength dependency (**Fig. 4.22**). However, the impact was not as high as for Se(VI). For example at pH 5, 90 % Se(IV) was sorbed at 0.01 M NaCl and 42 % Se(IV) was sorbed at 1 M NaCl.

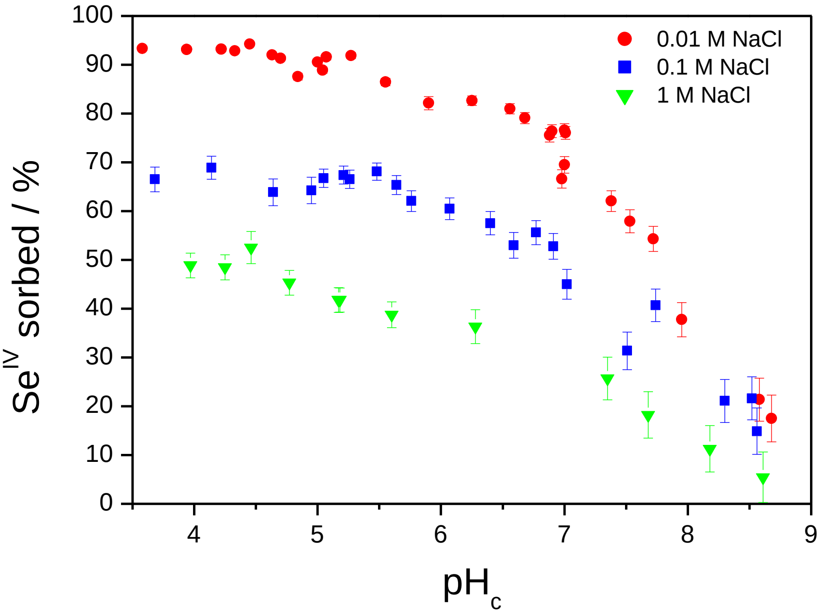

Fig. 4.22 Selenium(IV) sorption edges onto δ−alumina at different ionic strengths in NaCl. ($[Se^{IV}]_{initial} = 1 \times 10^{-5}$ M, m/v = 0.5 g L^{-1}, 2 days of shaking)

The decrease in sorption of Se(VI) and Se(IV) was consistent with changes in the variable surface charge of the neat mineral (**Fig. 4.23**). The isoelectric point (pH_{IEP}) of δ−Al_2O_3 was located at pH 9.6 for low NaCl concentration (I = 0.1 M). The increase of ionic strength (up to I = 1 M) resulted in a decrease of the zeta potential for both the acidic and alkaline pH range. However, in the alkaline range, the decrease of the zeta potential was more pronounced. Additionally, in the presence of $MgCl_2$, we observed that the pH_{IEP} was shifted to more alkaline values and at 0.1 M $MgCl_2$ no charge reversal was observed. Above pH 10, a sharp potential decrease occurs due to $Mg(OH)_2$ precipitation.

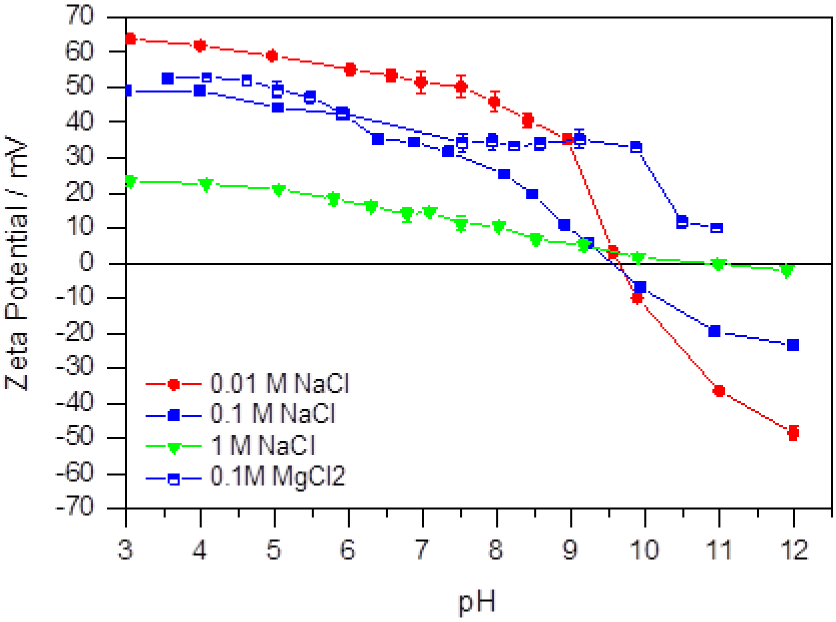

Fig. 4.23 Zeta potential of the neat surface of alumina at different background electrolyte concentrations (m/v = 0.2 g L^{-1}, 2 days of shaking)

4.4.3 Impact of sorption on the pH_{IEP} of minerals

The zeta potential of selenium(VI)-reacted anatase, hematite, maghemite, and alumina indicated that the isoelectric point of these minerals was not significantly impacted upon sorption (**Fig. 4.24**). Indeed, the differences between the pH_{IEP} of the neat surfaces (e. g. maghemite pH 7.7) and the pH_{IEP} of the selenium(VI)-reacted surfaces (e. g. maghemite pH 7.4) were within the experimental error and cannot be differentiated.

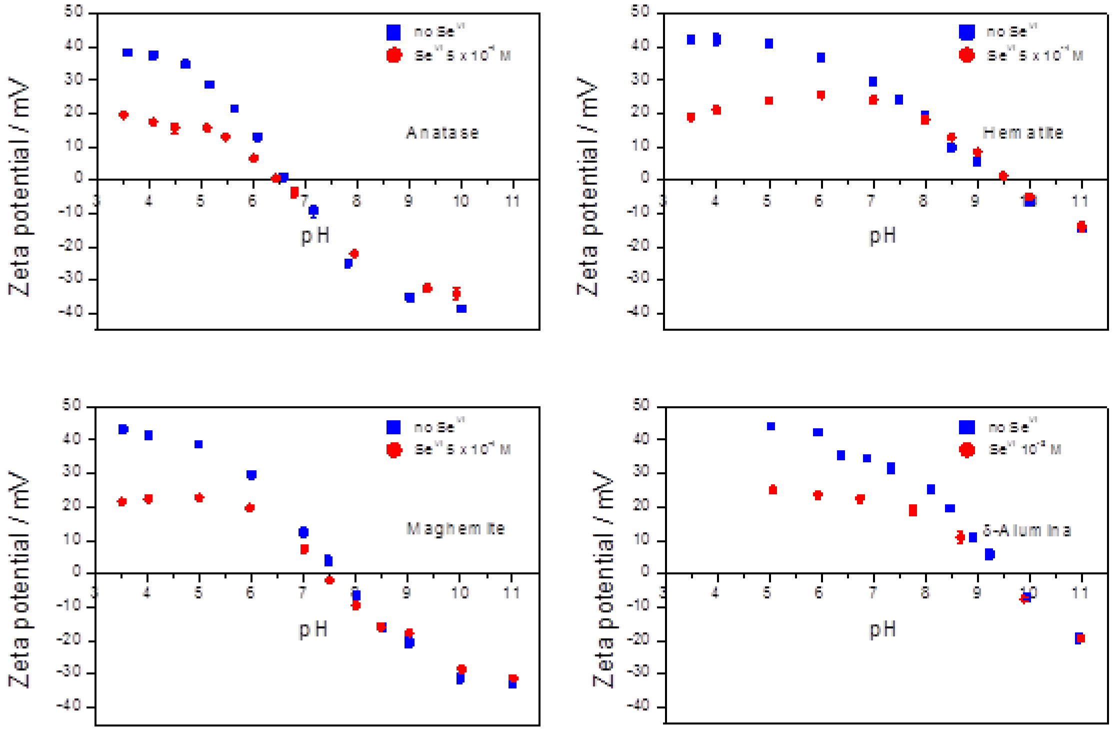

Fig. 4.24 Zeta potential of the neat and selenium(VI) reacted surface of anatase, hematite, maghemite and alumina. (■) $[Se^{VI}]_{initial} = 0$ mol L^{-1}, (●) $[Se^{VI}]_{initial} = 5 \times 10^{-4}$ mol L^{-1} or 1×10^{-3} mol L^{-1}

Anatase (0.01 mol L^{-1} NaCl, m/v = 0.5 g L^{-1}, 2 days of shaking); Hematite (0.1 mol L^{-1} NaCl, m/v = 0.75 g L^{-1}, 2 days of shaking); Maghemite (0.1 mol L^{-1} NaCl, m/v = 0.75 g L^{-1}, 2 days of shaking); Alumina (0.1 mol L^{-1} NaCl, m/v = 0.2 g L^{-1}, 2 days of shaking)

The zeta potential of minerals loaded with selenium(VI) correlates with those of the selenium-free surface, i. e. it decreased with increasing pH. The results suggest that the sorption of selenium(VI) still takes place at pH 6.0 and pH 7.5 for anatase and for maghemite, respectively. Sorption becomes then negligible at pH higher than 6.5 and 8.0 for anatase and for maghemite, respectively, since the zeta potentials of the solid phases are no longer affected (**Fig. 4.24**). However, sorption edges presented in **Fig. 4.18** clearly demonstrate that sorption of selenium(VI) is already completed at pH 5.5 for anatase, and 7.0 for maghemite. This discrepancy might be explained by the different mass/liquid ratio and initial selenium(VI) concentrations used in the different experiments.

A similar behavior of the pH_{IEP} upon sorption was also observed during selenate sorption onto $\gamma-Al_2O_3$ [ELZINGA '09] and anatase [JORDAN '11]. From these investigations, the formation of outer-sphere complexes was deduced from X-ray absorption

[ELZINGA '09] and vibrational spectroscopic measurements [JORDAN '11]. Thus, the absence of a shift of mineral's pH_{IEP} after selenium(VI) sorption gives a strong indication that selenium(VI) sorption onto solids leads to the formation of outer-sphere complexes.

The lowering of the surface charge of minerals at $pH < pH_{IEP}$ can generally be explained by the sorption of selenium(VI) anions creating negatively charged surface complexes possibly at the vicinity of the shear plane and, thus, indicating a close association to the surface. On the other hand, the reduction of the net positive charge during selenium(VI) sorption might be attributed to electrostatic H-bonding between the $\equiv XOH_2^+$ (X =Ti, Fe or Al) surface groups and the negatively charged selenate oxyanions. Again, this type of bonding requires a close association between the selenium(VI) ions and the investigated surfaces. This has also been suggested from investigations of selenate sorption onto $\gamma-Al_2O_3$ [ELZINGA '09].

After reaction with Se(IV), the pH_{IEP} of anatase, hematite, maghemite and alumina was significantly shifted toward lower pH (**Fig. 4.25**). At pH 10, the zeta potential of anatase and maghemite is no longer affected by Se sorption, whereas this happens for hematite and δ-alumina at pH 11. This suggests that sorption does not take place at these pH values. This is in agreement with batch sorption experiments (**Fig. 4.19**) for all minerals (although for anatase and δ-alumina, different initial selenium(IV) concentrations were used in the batch and zeta potential experiments).

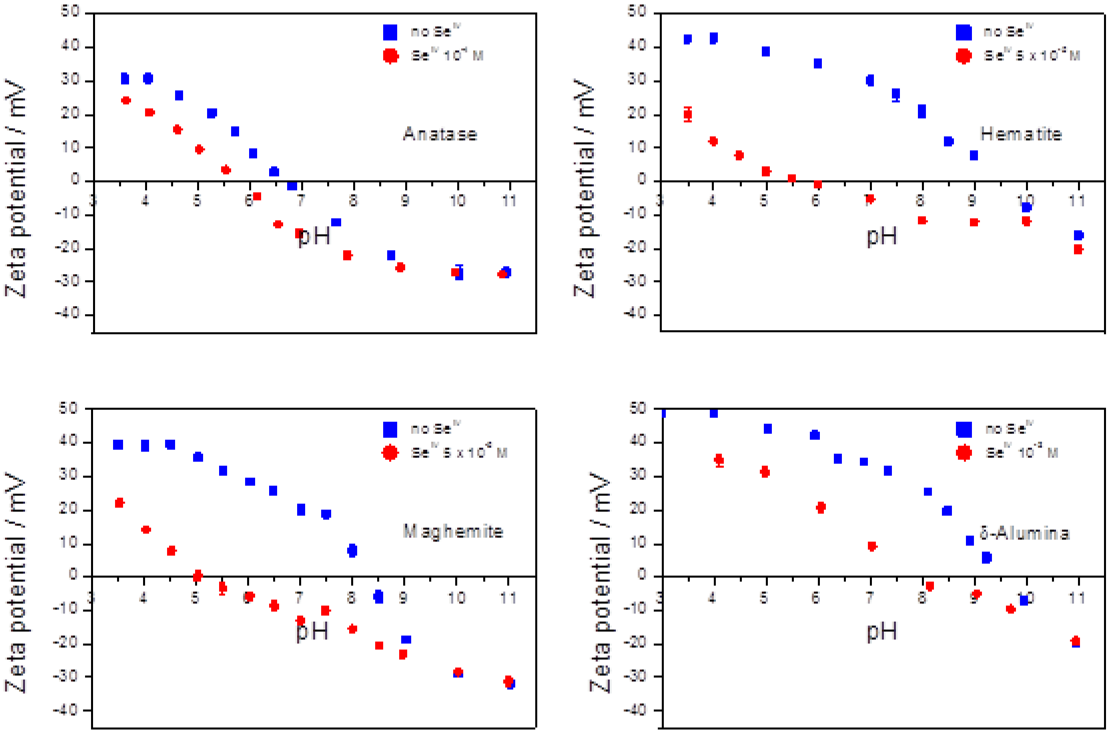

Fig. 4.25 Zeta potential of the neat and selenium(IV)-reacted surface of anatase, hematite, maghemite and alumina

(■) $[\mathrm{Se}^{IV}]_{\mathrm{initial}} = 0$ M, (●) $[\mathrm{Se}^{IV}]_{\mathrm{initial}} = 10^{-4}$ mol L^{-1}, 5 × 10^{-5} mol L^{-1} or 10^{-3} mol L^{-1}. NaCl 0.1 mol $L^{-1;}$ Anatase (m/v = 0.75 g L^{-1}, 2 days of shaking); Hematite (m/v = 0.25 g L^{-1}, 2 days of shaking); Maghemite (m/v = 0.25 g L^{-1}, 2 days of shaking); Alumina (m/v = X g L^{-1}, X days of shaking)

The shift of the $\mathrm{pH}_{\mathrm{IEP}}$ of mineral surfaces to lower values upon anion uptake, due to accumulation of negative charge within the shear plane, can be interpreted as inner-sphere coordination or surface precipitation. XAS showed no evidence for surface precipitates including iron(III) selenite phases for maghemite (see Chapter 4.5.5). Therefore, the formation of inner-sphere complexes is the most plausible explanation. Indeed, in parallel to spectroscopic investigations (EXAFS, FT-IR, Raman), the lowering of both $\mathrm{pH}_{\mathrm{IEP}}$ and zeta potential values of mineral surfaces after sorption was considered to be an indication of inner-sphere complexation, e. g., after sorption of As(V) onto maghemite [TUUTIJÄRVI '10] and $\mathrm{SeO_3}^{2-}$ onto am-$\mathrm{Fe(OH)_3}$ and γ-$\mathrm{Al_2O_3}$ [ELZINGA '09; SU '00].

4.4.4 Impact of temperature

4.4.4.1 Batch studies

The effect of temperature on the removal of selenium(VI) and selenium (IV) by anatase, hematite and alumina is comparatively shown in **Fig. 4.26** and **Fig. 4.27**.

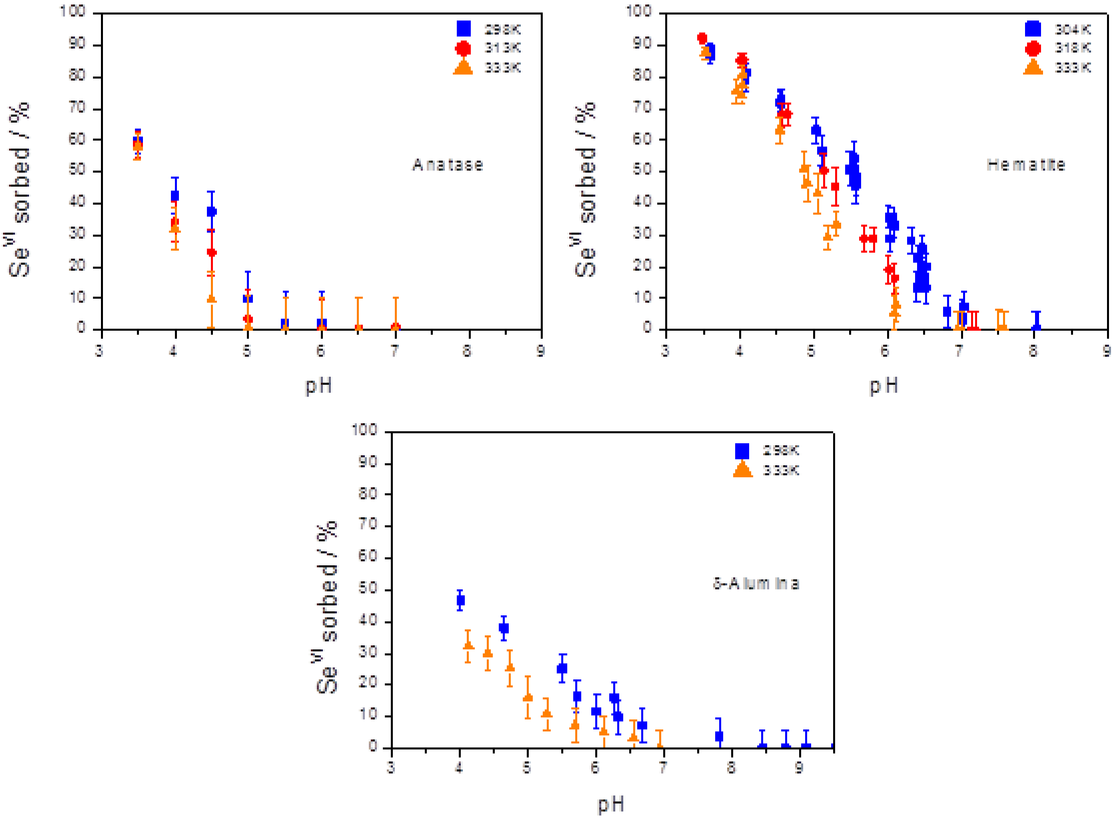

Fig. 4.26 Selenium(VI) sorption edges onto anatase, hematite and alumina at different temperatures

$[Se^{VI}]_{initial} = 1 \times 10^{-5}$ mol L^{-1}, NaCl 0.1 mol L^{-1}; Anatase (m/v = 0.5 g L^{-1}, 2 days of shaking); Hematite (m/v = 0.75 g L^{-1}, 2 days of shaking); Alumina (m/v = 0.5 g L^{-1}, 2 days of shaking)

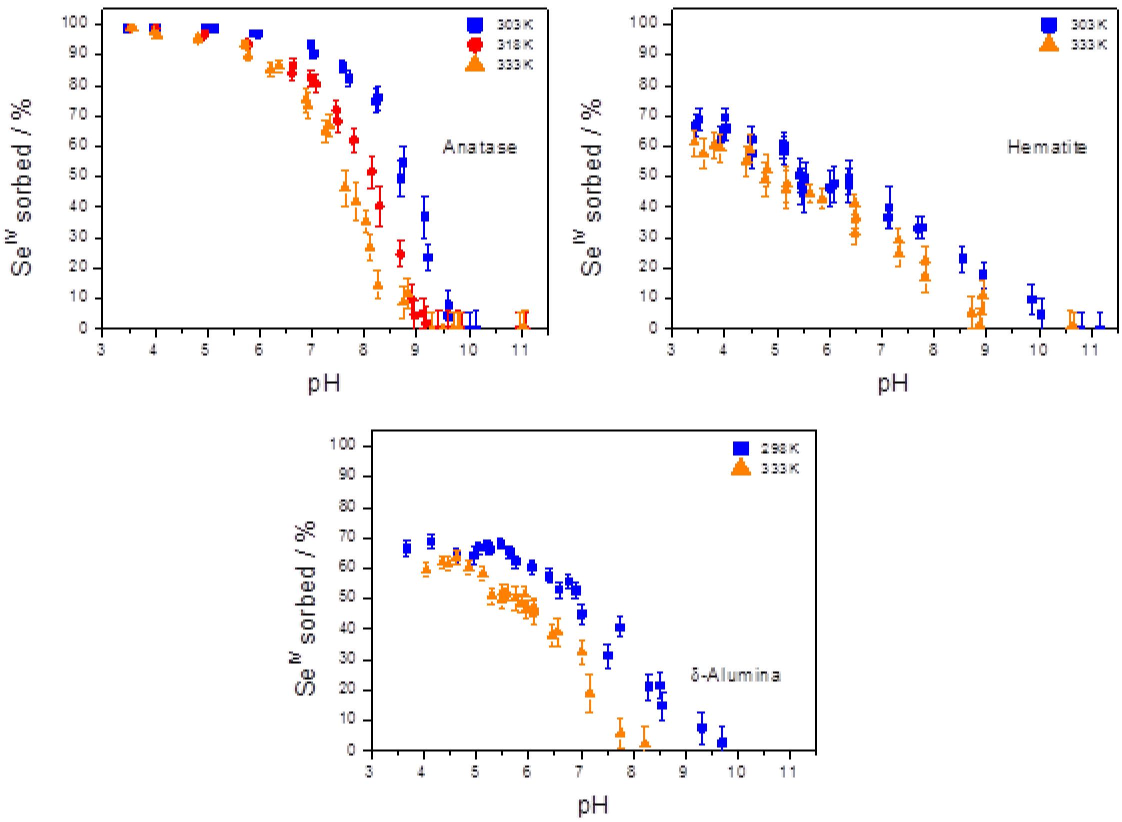

Fig. 4.27 Selenium(IV) sorption edges onto anatase, hematite and alumina at different temperatures

NaCl 0.1 mol L^{-1}; Anatase ([Se^{IV}]$_{initial}$ = 1 × 10^{-5} mol L^{-1}, m/v = 0.25 g L^{-1}, 2 days of shaking); Hematite ([Se^{IV}]$_{initial}$ = 5 × 10^{-5} mol L^{-1}, m/v = 0.25 g L^{-1}, 2 days of shaking); Alumina ([Se^{IV}]$_{initial}$ = 1 × 10^{-5} mol L^{-1}, m/v = 0.5 g L^{-1}, 2 days of shaking)

At elevated temperature, the influence of the pH on the sorption of selenium(VI) and selenium(IV) onto the investigated minerals shows a similar general tendency, that is, a decrease in the sorption with increasing pH. However, the sorption capacity of anatase, hematite and alumina towards selenium(VI) and anatase and alumina towards selenium(IV) is significantly lowered at higher temperatures. This is in agreement with the formerly observed decrease of selenium(VI) sorption onto goethite [KERSTEN '13; VLASOVA '04] and agro-industrial waste [HASAN '10] with increasing temperature, respectively. Impact of temperature on selenium(IV) sorption by anatase is also in agreement with recent studies, where selenite sorption capacity onto iron oxides and oxyhydroxides (goethite and ferrihydrite) [BALISTRIERI '87; PARIDA '97b], ferromanganese nodules [PARIDA '97a], α and γ activated alumina [JEGADEESAN '03], alumina ($\alpha\text{-A}_{l2}\text{O}_3$ and $\gamma\text{-Al}_2\text{O}_3$) [PARIDA '03], layered metal double hydroxides, e. g. Mg/Fe hydrotalcite [DAS '02], iron-coated fly ash [WASEWAR '09], TiO_2 nanoparticles [ZHANG '09], different biomaterials, e. g. a waste product from agro-industrial waste

[HASAN '10], dead green algae [TUZEN '10] was found to decrease upon increasing the ambient temperature. Note that the temperature impacts selenium(IV) sorption by hematite to a smaller extent in comparison to anatase. This might reflect surface precipitation of e. g. $Fe_2(SeO_3)_3$ phases, whose solubility would not be so significantly different at 333 K. Such phase precipitation upon Se(IV) sorption by hematite at room temperature was already suggested by [DUC '06]. Furthermore, the pH value at which Se(VI) and Se(IV) sorption is suppressed is shifted to lower pH values, reflecting modifications of the mineral surface properties with increasing temperature (see Chapter 4.4).

In addition to the change of the surface charge of the minerals, the decrease in selenium(VI) and selenium(IV) adsorption efficiency with increasing temperatures might involve other parameters: the exothermic nature of the sorption process or the instability of the selenium-mineral surface complex (which may result in the release of selenium ions from the solid phase to the solution). A phase transformation or an increasing dissolution of anatase and hematite leading to fewer available sorption sites can be discarded under our experimental conditions (see Chapter 4.3). The decrease of selenium(VI) and selenium(IV) sorption with increasing temperature, observed during the batch experiments, is also not related to a change in selenium aqueous speciation (see Chapter 4.2.2)

4.4.4.2 Thermodynamic evaluation of sorption process

Thermodynamic parameters were evaluated to assess the thermodynamic feasibility and to determine the exothermic/endothermic nature of the adsorption process. The changes in Gibbs free energy of reaction ($\Delta_R G$), enthalpy of reaction ($\Delta_R H$), and entropy of reaction ($\Delta_R S$) were determined at different temperatures and pH for the sorption of selenium(VI) by anatase, hematite and alumina and for the sorption of selenium(IV) by anatase and alumina. For this, the following equations were used:

$$K_d = C_{ads}/_{Ceq} \tag{4.1}$$

$$\Delta_R G = -\,RT \ln K_d \tag{4.2}$$

$$\Delta_R G = \Delta_R H - T\,\Delta_R S \tag{4.3}$$

where K_d expresses the distribution coefficient at equilibrium (L g^{-1}), while C_{ads} (µg g^{-1}) and C_{eq} (µg L^{-1}) are the equilibrium concentrations of selenium on the mineral surface and in the supernatant, respectively. R is the universal ideal gas constant (R = 8.314 J mol^{-1} K^{-1}) and T is the temperature (K) [DASH '07; HASAN '10; NEGREA '10; TUZEN '10].

The van't Hoff equation enables the calculation of $\Delta_R H$ and $\Delta_R S$:

$$\ln K_d = -\frac{\Delta_R H}{RT} + \frac{\Delta_R S}{R} \tag{4.4}$$

Hence, ln K_d was plotted as a function of 1/T (**Fig. 4.28** and **Fig. 4.29**), allowing the calculation of the $\Delta_R H$ (slope) and ΔRS (intercept) [DASH '07; HASAN '10; NEGREA '10; TUZEN '10]. It was assumed that enthalpy and entropy changes upon reaction were constant and therefore not temperature-dependent in the studied range.

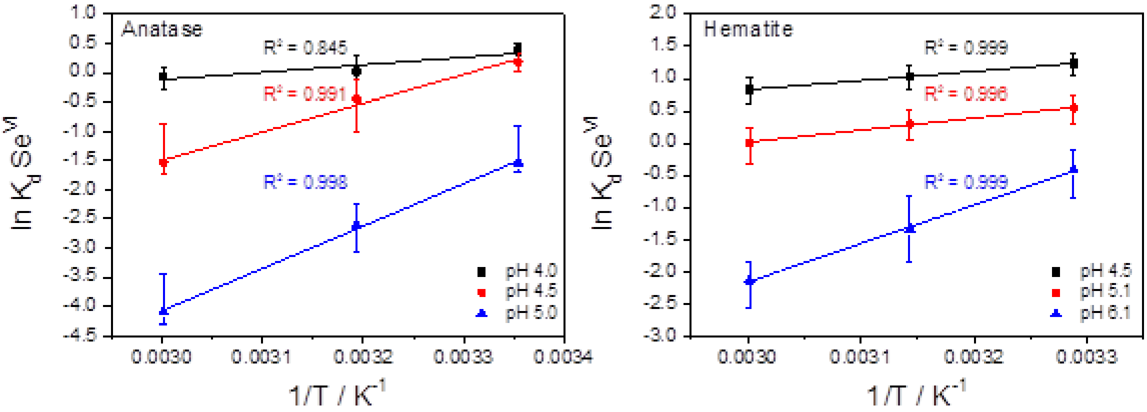

Fig. 4.28 van't Hoff plot for selenium(VI) sorption by anatase and hematite

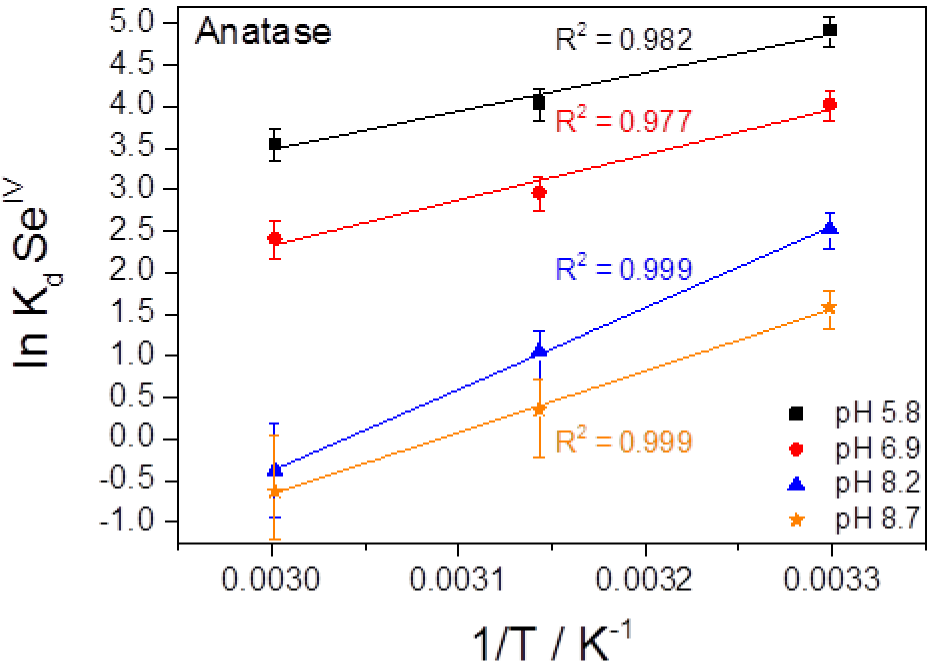

Fig. 4.29 van’t Hoff plot for selenium(IV) sorption by anatase

Except at pH 4.0 for the Se(VI)/anatase binary system, the van’t Hoff plot was found to be linear for all binary systems under investigations. The obtained correlation coefficients R^2 for the binary Se(VI)/anatase system are indicated in **Tab. 4.7**, as well as $\Delta_R G$, $\Delta_R H$ and $\Delta_R S$ values (Tables for Se(VI)/hematite and Se(IV)/anatase can be found in Appendix).

The negative values of the enthalpy of reaction $\Delta_R H$ indicate that the adsorption of Se(VI) onto anatase (**Tab. 4.7**) and hematite (**Tab. A.9** in Appendix) as well as the sorption of Se(IV) by anatase (**Tab. A.10**) is an exothermic process, in agreement with former studies [DAS '02; HASAN '10; JEGADEESAN '03; KERSTEN '13; TUZEN '10; ZHANG '09]. The negative values of $\Delta_R S$ might indicate a higher order, i. e. a reduced degree of freedom at the solid–solution interface due to the adsorption of selenium on the active surface sites of minerals, as already mentioned by Tuzen and Sari [TUZEN '10] and Hasan and Rajan [HASAN '10]. The increase in $\Delta_R G$ values with increasing pH and temperature indicates that the sorption process becomes unfavorable and less feasible [HASAN '10], in agreement with macroscopic results.

Tab. 4.7 Estimated values of $\Delta_R G$, $\Delta_R H$, $\Delta_R S$ and R^2 (correlation coefficient of the van't Hoff plot) for the adsorption of selenium(VI) onto anatase at different pH and temperatures

pH 4.0				
T (K)	**$\Delta_R G$ (kJ mol^{-1})**	**$\Delta_R H$ (kJ mol^{-1})**	**$\Delta_R S$ (J mol^{-1} K^{-1})**	**R^2**
298	-0.9 ± 0.3	-11.0 ± 5.0	-33.0 ± 15.0	0.845
313	-0.4 ± 0.1			
333	0.4 ± 0.3			
pH 4.5				
T (K)	**$\Delta_R G$ (kJ mol^{-1})**	**$\Delta_R H$ (kJ mol^{-1})**	**$\Delta_R S$ (J mol^{-1} K^{-1})**	**R^2**
298	-0.6 ± 0.2	-41.0 ± 4.0	-135.0 ± 13.0	0.991
313	1.5 ± 0.1			
333	4.2 ± 0.3			
pH 5.0				
T (K)	**$\Delta_R G$ (kJ mol^{-1})**	**$\Delta_R H$ (kJ mol^{-1})**	**$\Delta_R S$ (J mol^{-1} K^{-1})**	**R^2**
298	4.0 ± 0.2	-61.0 ± 3.0	-220.0 ± 10.0	0.998
313	7.0 ± 0.1			
333	12.0 ± 0.2			

In summary, anatase, hematite, maghemite and δ−alumina nanoparticles exhibited fast adsorption kinetics toward selenium(VI) and selenium(IV). Batch experiments showed a decreased sorption of both oxyanions with increasing pH (3.5 – 11) on studied minerals. Increase of ionic strength (0.01 to 0.1 M NaCl) led to a decrease of selenium(VI) sorption, while it had no significant influence on selenium(IV) sorption concerning anatase, hematite and maghemite. For the Se(IV) sorption, δ−alumina is an exception. Here, an increase of ionic strength led to a decrease in sorption. Electrophoretic mobility measurements showed that selenium(VI) sorption had no impact on the pH_{IEP} of minerals, while it was significant shifted toward lower values upon selenium(IV) sorption.

Results from sorption edges as well as electrophoretic mobility measurements strongly suggest that selenium(VI) forms outer-sphere complexes onto studied minerals, i. e. the interaction proceeds through electrostatic attraction. The occurrence of selenium(IV) inner-sphere complexes via the formation of chemical bonds between Se species and the anatase, hematite and maghemite surfaces, can be postulated. For δ−alumina, a mixture of inner- and outer-sphere complexes can be expected. However, a spectroscopic characterization is mandatory for a detailed knowledge of the sorbed species at the solid/liquid interface at a molecular scale. Upon increasing temperature up to 333 K, a decreased sorption was observed. Temperature-dependent studies revealed that selenium(VI) and selenium(IV) sorption is an exothermic process. The observed decrease of sorption upon increasing temperature leads to an increase mobility of selenium, which might have drastic consequences in the context of nuclear waste management. Hence, an increased mobility of selenium species must be taken into account in future safety assessments

4.5 Spectroscopic elucidation of Se(VI) and Se(IV) sorption and redox processes

A full understanding of adsorption mechanisms and identification of sorbed species at the molecular level can only be achieved by applying advanced spectroscopic techniques such as *in situ* ATR FT-IR and EXAFS. The identification of the sorption complexes of selenium onto minerals by *in situ* ATR FT-IR can be accomplished by a comparative analysis of vibrational data of structurally well-known selenium-complexes. Due to considerations of the molecule symmetry and valid selection rules of IR spectroscopy, the number of observed bands as well as their relative intensities potentially allows the derivation of structural characteristics of the surface species. Anatase, hematite, maghemite and alumina do not show any significant strong bands in their IR spectra between 1000 and 750 cm^{-1} (**Fig. A.9** in Appendix). Thus, the sorption processes of Se can be investigated without any spectral interferences of the mineral surfaces. By applying EXAFS spectroscopy, the distances between a central heavy metal atom and its neighbor atoms together with their coordination number can be determined. Different oxidation states of selenium can be observed at mineral surfaces down to a micromolar level using XANES. Experimental details about *in situ* ATR FT-IR and EXAFS, as well as additional information, can be found in the Appendix E. The redox reactions of Se(VI) and Se(IV) at the magnetite surface and the identification of the end-products were accomplished by applying XPS.

4.5.1 Se(VI) onto Anatase

The sorption process of selenium(VI) by anatase was elucidated by *in situ* ATR FT-IR and the impact of elevated temperature was on line monitored for the first time.

According to [OLIN '05], the uncoordinated tetrahedral SeO_4^{2-} molecule is the predominant aqueous species between pH 3.5 and 14. Due to the T_d symmetry, the selenate ion has only two IR active normal modes, i. e. the v_3 triply degenerate asymmetric Se–O stretching and the v_4 triply degenerate out of plane O–Se–O bending modes [NAKAMOTO '97; PERSSON '96; SU '00]. Because the v_4 mode is outside of the spectral range of our ATR device, it will be not considered in the following discussions.

[JORDAN '11] evidenced the sorption of selenium(VI) onto anatase to proceed via formation of outer-sphere complexes. Their study highlighted the absence of changes in the sorption mechanism of selenium(VI) onto anatase with increasing pH at room temperature. Hence, we performed our IR spectroscopic sorption experiments only at pH 3.5 where the highest sorption capacity was observed and at three different temperatures (298K, 313K and 333 K) (**Fig. 4.26**).

The course of an *in situ* sorption experiment is exemplarily shown for 313 K (**Fig. 4.30**). The prepared anatase film on the ATR crystal was sufficiently stable, reflected by IR spectra showing no relevant spectral changes after 60 min of equilibration (**Fig. 4.30**a). In addition, the absence of bands in the equilibration spectrum in the region between 1000 and 700 cm^{-1} enables the investigation of Se sorption processes without any spectral interferences of the anatase film.

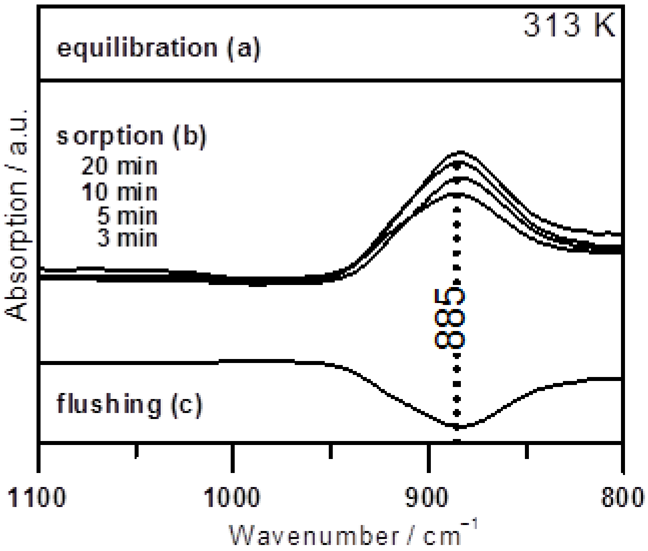

Fig. 4.30 Course of Se(VI) *in situ* IR spectroscopic sorption experiment at 313 K: (a) Equilibration of the anatase film with blank solution (0.1 mol L^{-1} NaCl, pH 3.5), (b) Se(VI) sorption onto anatase ($[\mathrm{Se}^{\mathrm{VI}}]_{\mathrm{initial}}$ = 5 × 10^{-4} mol L^{-1}, 0.1 mol L^{-1} NaCl, pH 3.5) recorded at different times after induced sorption as indicated and (c) Flushing of Se(VI) loaded anatase with blank solution. The indicated value is in cm^{-1}

Upon Se(VI) sorption, one distinct band at 885 cm^{-1} was detected (**Fig. 4.30**). The increasing intensity with contact time reflects the Se(VI) accumulation on the surface. No modification of the surface speciation during the sorption process was noticeable, since the shape of the band did not change throughout the complete contact time. The absence of intensity changes after 20 min of induced sorption indicates fast formation of equilibrium conditions (**Fig. 4.30**, black traces).

The nature of selenium(VI) sorbed species onto anatase can be identified by a comparative analysis of vibrational data of the free aqueous species as well as structurally well-known selenato-complexes. The slight blue shift of ν_3(Se-O) from 872 cm^{-1} to 885 cm^{-1} reflects a slightly disturbed local symmetry of the sorbed complex in comparison with the T_d symmetry of the aqueous species SeO_4^{2-} and can be explained by the formation of a predominantly outer-sphere complex. Such outer-sphere complexes with slightly disturbed T_d symmetry were recently observed for sulfate reacted onto γ-Al_2O_3 [MÜLLER '11] and SeO_4^{2-} surface species onto anatase [JORDAN '11] by *in situ* ATR FT-IR spectroscopy. Additionally, a slightly shifted frequency of the ν_3 (F_2) mode compared to the aqueous species was reported from selenate sorption experiments on goethite by Raman spectroscopy [WIJNJA '00].

Subsequent to sorption, the Se(VI) loaded film is flushed with the blank solution for another 30 min. The respective difference spectrum showed a negative band at nearly the same frequencies compared to those observed during the sorption process (**Fig. 4.30**c). The negative absorption is assigned to the release of sorbed selenate species from the anatase film. The fast and reversible sorption process of selenium(VI) onto anatase by *in situ* ATR FT-IR can be related to electrostatic interactions, in agreement with a recent study [JORDAN '11].

The courses of the sorption experiments at 298 and 333 K were found to be identical, and the calculated mid-IR difference spectra obtained at the end of the Se(VI) sorption process as a function of the temperature are compared in **Fig. 4.31**.

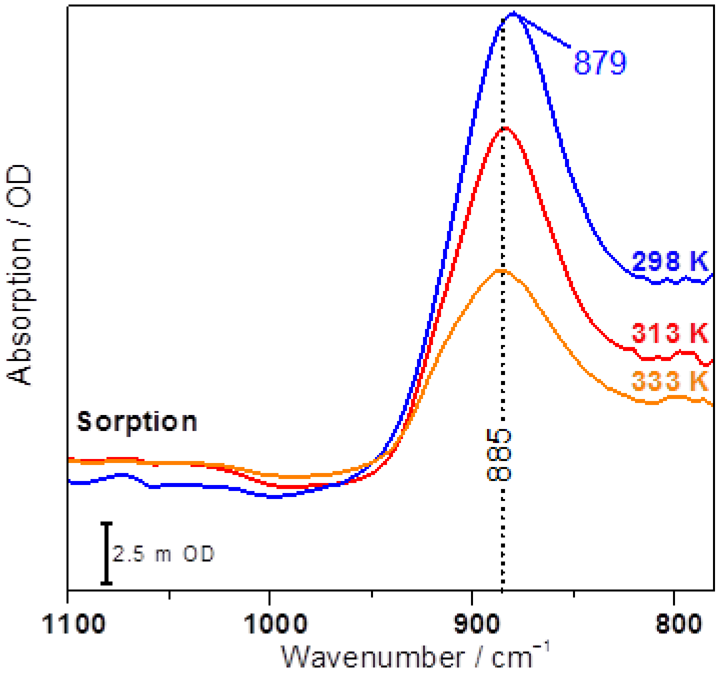

Fig. 4.31 *In situ* mid-IR spectra of selenium(VI) sorption complexes onto anatase ($[Se^{VI}]_{initial}$ = 5 × 10^{-4} mol L^{-1}, pH 3.5, 0.1 mol L^{-1} NaCl) recorded at different temperatures as given

Ordinate scaling is given by the bar in units of optical density. Other values indicated are in cm^{-1}

At all temperatures, the high congruence of the spectra suggests that the same Se(VI) surface species are formed on the anatase. With increasing temperature, a very small blue shift of 6 cm^{-1} of the asymmetric v_3(Se-O) stretching mode was observed, but no changes that would imply different sorption mechanisms. In agreement with the batch experiments, the decreasing amplitude of the band of v_3(Se-O) reflects that the sorption capacity of selenium(VI) was reduced at higher temperatures. This slightly disturbed symmetry can indicate some chemical contribution to the electrostatic attraction (shorter distance/reduced hydration shell), which would in turn induce a decreased entropy, in agreement with the negative entropy of reaction derived from the batch experiments.

In situ ATR FT-IR results evidenced the formation of outer-sphere surface complexes upon Se(VI) sorption onto anatase, with no significant structural changes within the investigated temperature range (298K to 333 K). The decreasing amplitude of the IR band was in agreement with batch studies (see Chapter 4.4.4).

4.5.2 Se(VI) onto Maghemite

4.5.2.1 In situ ATR FT-IR spectroscopy

The ν_3 mode of the SeO_4^{2-} molecule is observed at 867 cm^{-1} in the IR spectrum of a 0.1 mol L^{-1} aqueous solution at pD 4.0 **(Fig. 4.32**a). The slightly shifted frequency of this band compared to literature data [SU '00] is due to the isotopic effect of the solvent D_2O (**Tab. 4.8**).

The formation of a maghemite film with a sufficient stability during the preparation procedure was demonstrated by the IR spectra showing no relevant spectral changes after 45 minutes of equilibration (data not shown).

The sorption spectra (**Fig. 4.32**b) recorded after different times after induced sorption show a characteristic pattern of four partially overlapping bands in the spectral region between 1000 and 750 cm^{-1}. From second derivative spectra the maxima of these bands were determined to 911, 883, 855, and 830 cm^{-1}. The intensities of these bands are increasing within the first 20 minutes of sorption time. After this time, the band intensities did not change significantly, suggesting that the solid phase was saturated with SeO_4^{2-} and an equilibrium state was achieved. The shape of the band pattern does not change throughout the complete time of sorption (up to 120 min) indicating that there is no change of the surface speciation during the sorption process. Additionally, this precludes the formation of surface precipitates at extended sorption times.

Subsequently, the maghemite film was again flushed with a 0.1 mol L^{-1} NaCl blank electrolyte for another 45 min. The respective spectra (**Fig. 4.32**c) show negative bands at nearly the same frequencies compared to those observed during the sorption process. As mentioned before, there are no bands expected from maghemite between 1000 and 750 cm^{-1}, thus, these bands must be due to the release of sorbed selenate species from the maghemite film.

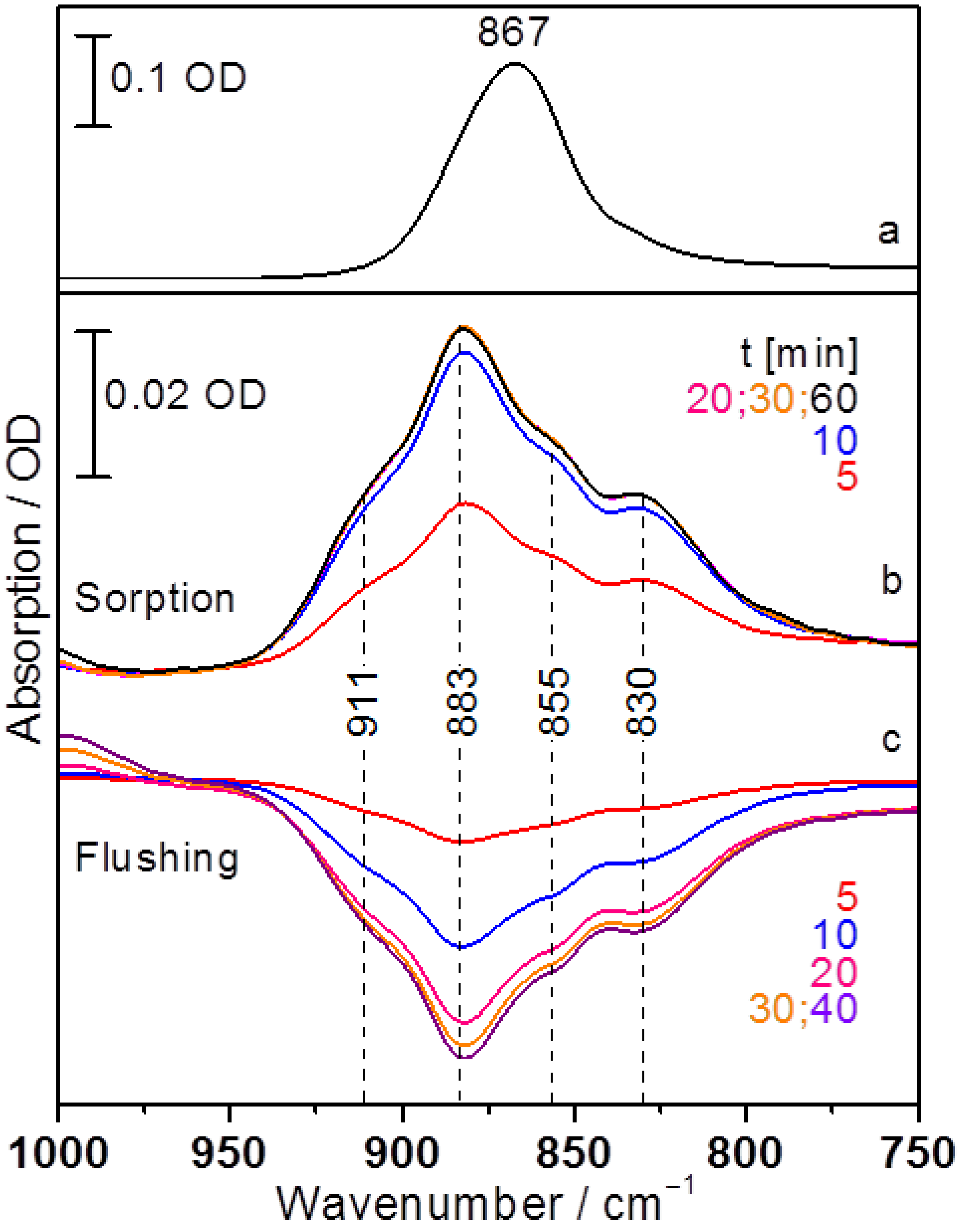

Fig. 4.32 IR spectra of selenium (IV)

(a) IR spectrum of 0.1 mol L^{-1} selenium(VI) in aqueous solution at 0.1 mol L^{-1} NaCl in D_2O. (b) *In situ* IR spectra of selenium(VI) sorption complexes onto maghemite ($[Se^{VI}]_{initial} = 5 \times 10^{-4}$ mol L^{-1}, D_2O, pD 3.5, 0.1 mol L^{-1} NaCl, N_2) recorded at different points of time after induced sorption. (c) *In situ* IR spectrum of released selenium(VI) sorption complex recorded at different points of time after subsequent flushing of the maghemite phase with blank solution (D_2O, pD 3.5, 0.1 mol L^{-1} NaCl, N_2)

Tab. 4.8 Observed frequencies of vibrational modes and assigned symmetry group of aqueous and complexed selenate ions observed by IR and Raman spectroscopic techniques

	Symmetry	**Mode and observed frequency (cm^{-1})**				**Technique**	**Coordination**	**Reference**
		ν_1	ν_3					
SeO_4^{2-} free aqueous species								
	T_d		872			IR		[SU '00]
	T_d		867			IR		[1]This study
	T_d	837	873			Raman		[WIJNJA '00]
Solid cobalt selenato(VI) complexes								
	C_{3v}	800	885	845		IR	Monodentate	[2][ROSS '70]
	C_{2v}	780	930	895	[3]830	IR	Bidentate mononuclear	[4][BENELLI '77]
	C_{2v}	801	908	872	822	IR	Bidentate bridging	[5][WIEGHARDT '71]
Selenium(VI) sorption complexes on iron oxides and oxyhydroxides								
Sorbent								
α-Fe_2O_3	C_{3v}	820	880	850		IR	Monodentate	[1][PEAK '02]
[6]hydrous Fe-oxide	C_{2v}		910	880	820	IR	Bidentate bridging	[HARRISON '82]
[6]α-FeOOH	C_{2v}		911	885	815	DRIFT	Bidentate bridging	[SU '00]
γ-Fe_2O_3	C_{2v}	829	904	879	859	IR	Bidentate	[1]This study
α-Fe_2O_3	C_{2v}	827	912	882	853	IR	Bidentate	[1]This study

[1] Measurements performed in D_2O;

[2] $[Co(NH_3)_5SeO_4]Cl$

[3] As highlighted by Wijnja and Schulthess (2000), this band was present in the IR spectrum, but not attributed to SeO_4 species;

[4] $Co(p_3)SeO_4$;

[5] $[Co_2(SeO_4)_2(OH)(NH_3)_6]Cl$;

[6] air-dried solids

The high congruence of the spectra in the sorption and flushing step strongly suggests that the same selenium(VI) species observed during the sorption process are released from the solid phase during the flushing step. With desorption time, the intensity of the observed bands increases with accumulation time during the first 20 minutes (with a constant width). At longer desorption times, no more selenium(VI) is desorbed. The fast and reversible sorption process of selenium(VI) onto maghemite observed by *in situ* ATR FT-IR can be related to an outer-sphere complexation mechanism, in agreement with batch sorption experiments and zeta potential measurements. In addition, the formation of similar outer-sphere complexes upon Se(VI) sorption onto γ-Al_2O_3 was recently derived from batch experiments, electrophoretic mobility measurements and EXAFS [ELZINGA '09]. However, since the amplitude of the desorption reaction spectra does not exceed 80 % of the sorption spectra, it can be assumed that the reversibility of the sorption reaction is not fully given under the prevailing conditions. This might be due to different kinetics of both reactions or even due to the formation of a small fraction of another not yet identified surface species.

The spectral features representing the selenate anions sorbed onto the solid phase (Fig. 4.32b,c) clearly reflect a different local symmetry in comparison to the T_d symmetry of the aqueous species (Fig. 4.32a). From the second derivative spectrum four spectral components were identified in the sorption spectra. The resulting fitting procedure provides a best fit as shown in Fig. 4.33 with four single peaks located at 904, 879, 859 and 829 cm^{-1} and a local residual root-mean-square error of 4.2×10^{-5}.

The first three former peaks are assigned to the v_3 mode which is split upon sorption to the solid phase. Such a splitting of this mode is observed for selenato groups showing a C_{2v} symmetry, either with a bidentate mononuclear configuration in compounds like $Co(p_3)SeO_4$ [BENELLI '77] or with a bidentate bridging configuration in compounds like $[Co_2(SeO_4)_2OH(NH_3)_6]Cl$ [WIEGHARDT '71] (**Tab. 4.8**). There, the lowering of the symmetry from T_d to C_{2v} led to the appearance of three bands, located at 908, 872 and 822 cm^{-1}. Moreover, the v_1 mode observed at 801 cm^{-1} becomes IR active and shows a lower frequency compared to the free selenate aqueous species.

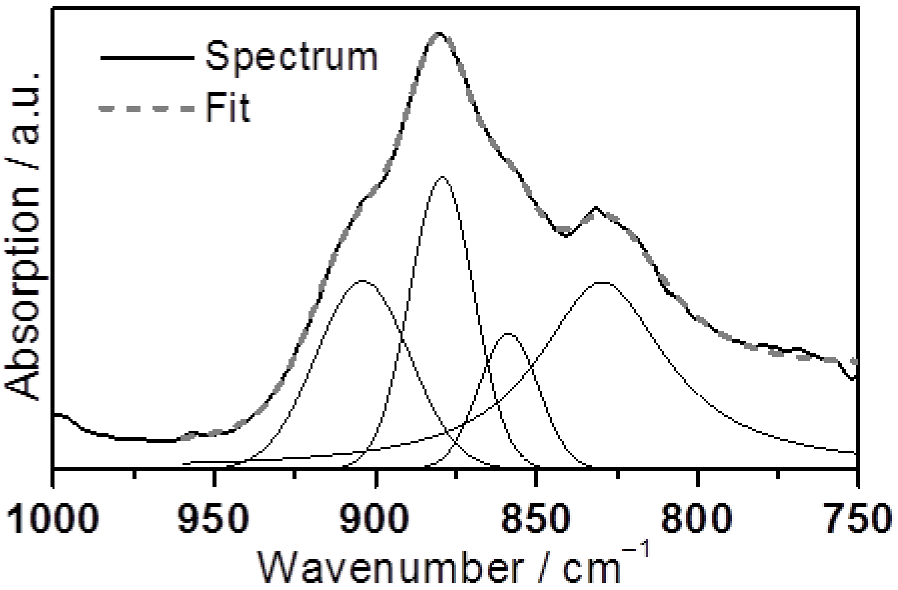

Fig. 4.33 Deconvolution of the IR spectrum of selenium(VI) sorption onto maghemite ($[Se^{VI}]_{initial} = 5 \times 10^{-4}$ mol L^{-1}, D_2O, pD 3.5, 0.1 mol L^{-1} NaCl, N_2). Dotted line indicates the overall fit

A similar split of the v_3 mode into three bands has been also observed for the isostructural sulfate anion in the $[Co_2(NH_3)_8(NH_2)SO_4](NO_3)_3$ complex by [NAKAMOTO '57] which has a bidentate bridging configuration and a C_{2v} symmetry. In this case, the v_1 mode becomes also IR active, but it is blue shifted compared to the free sulfate aqueous species.

From these findings, we conclude that the three bands observed at 904, 879, 859 cm^{-1} in Fig. 4.32 represent the split v_3 mode while the band at 829 cm^{-1} is attributed to the v_1 mode becoming IR active due to the lowered symmetry of the sorbed ions. Consequently, the spectra strongly suggest a bidentate coordination of the selenate ions to the maghemite surface.

In analogy to the batch experiments, the impact of the ionic strength on the sorption processes can be spectroscopically verified by the *in situ* IR measurements. Reducing the ionic strength by a factor of 10 (0.01 mol L^{-1}) led to the same spectral characteristics (**Fig. 4.34**a).

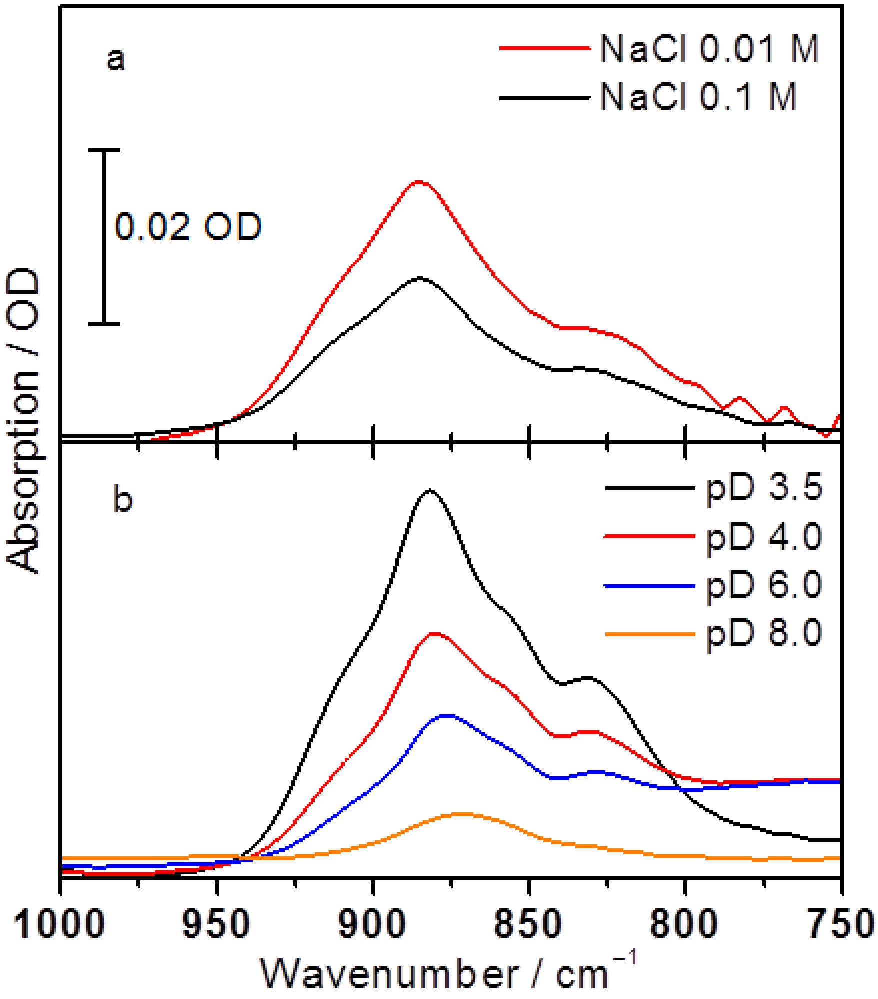

Fig. 4.34 *In situ* IR spectra of selenium(VI) sorption complexes

(a*) In situ* IR spectra of selenium(VI) sorption complexes onto maghemite ([Se^{VI}]$_{initial}$ = 5 × 10^{-4} mol L^{-1}, H_2O, pH 4, 10 min of sorption, N_2) recorded at different ionic strength. The amplitude is decreasing with increasing ionic strength, reflecting the reduced amount of sorbed selenate with increasing the background electrolyte concentration. (b) *In situ* IR spectra of selenium(VI) sorption complexes onto maghemite ([Se^{VI}]$_{initial}$ = 5 × 10^{-4} mol L^{-1}, D_2O, 0.1 mol L^{-1} NaCl, 10 min of sorption, N_2) recorded at different pD values. The amplitude is decreasing with increasing pD reflecting the reduced amount of sorbed selenate with increasing pH

Moreover, in agreement with batch sorption studies, it can be explicitly demonstrated that the sorption of selenium(VI) was higher at a lower ionic strength. These findings corroborate the postulated formation of outer-sphere complexes from the batch experiments.

Furthermore, at higher pD values the same spectral characteristics are observed (**Fig. 4.34**b). In accordance to observations made of the sorption edge, the band amplitudes correlate with the amount of sorbed selenium(VI), i. e. their amplitudes are decreasing with increasing pD. The formation of different surface complexes between pD 3.5 and pD 6.0 can be discarded, since no significant band shifts were observed. However, one can see that the spectra at pD 8.0 has no splitting anymore and its peak maximum is located at 871 cm^{-1}, i. e. close to the aqueous selenate species (867 cm^{-1}). This means that at pD 8.0, no sorption takes place, as suggested by the batch experiments presented in **Fig. 4.18**.

4.5.2.2 EXAFS

In this section, we discuss results obtained from samples adjusted to pH 3.5 and 4.0. At higher pH values, spectra were too noisy to be analyzed because of the low loading levels. The XANES edge energy of 12.663 keV as well as the strong white-line intensity (Fig. 4.35 left, Tab. 4.9) of the selenate-reacted maghemite samples is in line with Se(VI).

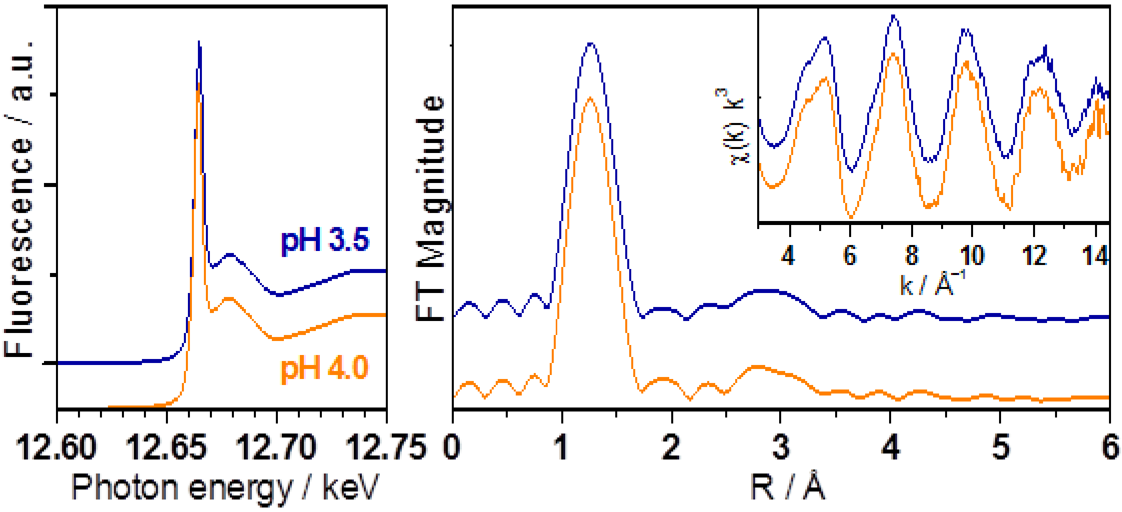

Fig. 4.35 XAS spectra of selenate sorbed onto maghemite at two different pH values; (Left: XANES; right: EXAFS Fourier transform (3-13 Å^{-1}) with k^3-weighted chi functions as insert)

Tab. 4.9 Se-K edge XAFS, fit results ($S_0^2 = 0.8$)
(The fits include all tri- and four-legged MS paths as described in the text)

	Oxygen shell			**Iron shells**			**ΔE_0 [eV]**	**$\chi^2_{res\ \%}$**
pH	**^{1}CN**	**^{2}R [Å]**	**$^3\sigma^2$ [Å^2]**	**CN**	**R [Å]**	**σ^2 [Å^2]**		
3.5	3.8	1.65	0.0004	0.3	3.38	0.0006	15.4	15.1
4.0	4.1	1.65	0.0004	0.3	3.38	0.0008	14.8	14.3

Since no additional shoulders at lower energy, i. e. 12.662 keV, characteristic of selenium(IV) and 12.656 – 12.657 keV characteristic of elemental selenium and selenium(−II) were observed, it can be deduced that sorption to maghemite did not change the Se oxidation state. Therefore, the presence of Fe(II) traces as verified by UV-VIS spectrophotometry did not lead to a significant amount (> 2.5 %) of reduced selenium. Hence, only sorption processes were responsible for the withdrawal of selenate oxyanions from the aqueous phase.

The Fourier transform magnitude (**Fig. 4.35** right) shows a strong peak at about 1.3 Å (not corrected for phase shift), which was fit with four Se-O paths at 1.65 Å, typical for the tetrahedral coordination of selenate. At around 3 Å, there is another broad FT peak visible. While its height may appear insignificant, it is consistently reproduced in both spectra. Furthermore, this peak arises from a beat pattern, which is already present at low k-range (see e. g. the shoulder at 4.5 Å^{-1}) and much higher than the noise level. Therefore, this small and broad peak has to be considered as significant backscattering contribution from atoms beyond the coordination sphere.

In earlier work, this region was fitted with about two Se-Fe paths between 3.29 and 3.38 Å distance and interpreted as binuclear bridging inner-sphere sorption complex [HAYES '87; MANCEAU '94]. When we fitted this region in the same way, i. e. with a Se-Fe path, we obtained a coordination number of 2 - 3 and distances of 3.33 – 3.35 Å, which would confirm the earlier interpretation. However, this result is in obvious contradiction to the results obtained by IR spectroscopy, the ionic strength dependence and the absence of the pH_{IEP} shift observed in zeta potential measurements, all suggesting formation of outer-sphere sorption complexes.

Wavelet analysis [FUNKE '05], which allows the discrimination of backscattering from Fe and from Se, showed for this FT peak a k-space maximum at 6 Å^{-1} in line with Fe backscattering, and lower than a maximum at 7 – 8 Å^{-1} expected for Se-Se backscattering [SCHEINOST '08b]. Therefore, we can exclude formation of Se ion pairs or surface polymerization of selenate at the surface of maghemite. This is consistent with the fact that as far as we know, the polymerization of the selenate ion in sodium selenate aqueous solutions has never been reported [MANCEAU '94; OLIN '05; SU '00].

In a next step, we considered multiple scattering (MS) contributions from the coordination sphere. In tetrahedral coordination all four Se-O distances have the same length (within the EXAFS resolution of about 0.13 Å at the given k-range of 2.0 – 14.5 $Å^{-1}$), giving rise to 16 tri-legged Se-O-O MS paths with distances around 3.0 Å, and to 16 four-legged Se-O-Se-O MS paths at twice the distance of the coordination shell (3.3 Å), as for instance in $Na_2(SeO_4)$ [FUKAMI '03]. When these MS paths were included into the fit (CN, distances and Debye-Waller factors linked to the single scattering path of the coordination shell), then the Se-Fe CN dropped to 0.3 and the fit improved significantly. Therefore, only these fit results are shown in **Tab. 4.9**.

The Se-Fe distance in both pH samples is 3.38 Å, in line with previous results of selenate sorption to Fe oxides. Assuming a straight corner-sharing arrangement between a selenate tetrahedron and a $Fe(O,OH)_6$ octahedron, the expected distance would be between 3.59 and 3.69 Å, assuming an Se-O distance of 1.64 Å and Fe-O/OH distances between 1.95 and 2.05 Å. The observed, much shorter distance of 3.38 Å indicates hence a bent angle along the Fe-O-Se unit, which has been previously interpreted – along with a Se-Fe coordination number of two – as a bidentate, binuclear corner-sharing complex.

Since maghemite contains also Fe(III) in tetrahedral coordination, the coordination to Fe-O tetrahedra (R(Fe-O) = 1.92 Å) has to be considered. To obtain the distance of 3.38 Å, an angle Se-O-Fe of 143º would be required, which is still unreasonable for a single corner-sharing arrangement. A binuclear corner-sharing arrangement between selenate and either two tetrahedral Fe centers, or one tetrahedral and one octahedral Fe center is more likely. However, previous studies elucidating the bonding structure of As(III), Sb(III) and Pu(III) on magnetite have demonstrated, that the octahedrally terminated {111} faces are the most reactive [KIRSCH '11; KIRSCH '08; MORIN '09; WANG '08]. This was also confirmed for As(III) sorption to maghemite [AUFFAN '08; MORIN '08]. Therefore, sorption of selenate to Fe octahedral centers in binuclear corner-sharing is the most likely explanation for the observed Se-Fe distance of 3.38 Å, although the coordination numbers far below 2 seem to contradict this interpretation.

Taking into account the outer-sphere complexes suggested by IR spectroscopy, however, allows deriving an explanation. Such outer-sphere complexes do not show Se-Fe interactions, because their distances would be too far and to disordered to be detectable by EXAFS spectroscopy, but show only the Se-O backscattering from the coordination shell. Since the signal from the coordination shell is expected to be similar (again within EXAFS resolution) for the inner-sphere and the outer-sphere complexes, and since EXAFS spectra represent the weighted statistical average of all excited Se atoms and hence Se species, the low coordination number may arise from a special mixture of these inner- and outer-sphere complexes. Since the Se-Fe coordination number is 0 for the outer-sphere complex, and 2 for the binuclear corner-sharing complex, the fraction of the binuclear complex is 0.3/2 = 0.15. The majority of Se, 85 %, can then be assumed to be present as outer-sphere complex, so the EXAFS results are largely in line with the conclusion from batch sorption experiments, zeta potential measurements and *in situ* ATR FT-IR studies, that selenate is sorbed to maghemite predominately as outer-sphere complex under the given conditions.

The IR spectra of the wet pastes prepared under identical conditions to the EXAFS samples (with similar surface loadings) are similar to those obtained during the *in situ* experiments (**Fig. 4.36**).

Therefore, it can be assumed that outer-sphere species are predominantly observed by IR spectroscopy, irrespective of the sample preparation. However, we do not completely rule out the presence of inner-sphere complexes also showing a bidentate coordination. A relatively small fraction of formed inner-sphere complexes might be present and cannot be resolved under the prevailing conditions by the IR technique applied. We can hypothesize that this small fraction could represent the unreleased fraction observed during the flushing step in the *in situ* IR experiments.

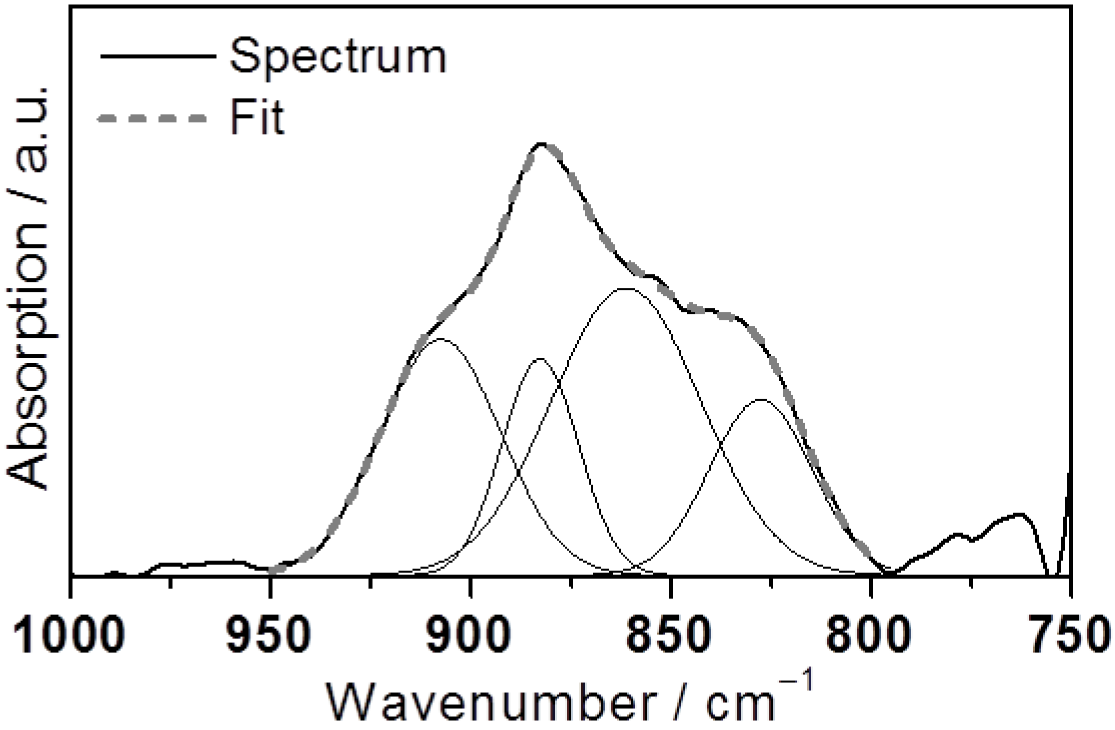

Fig. 4.36 Deconvolution of the IR spectrum of selenium(VI) sorption onto maghemite (wet paste). ($[Se^{VI}]_{initial} = 10^{-4}$ mol L^{-1}, m/v = 2 g L^{-1}, D_2O, pD 3.9, 0.1 mol L^{-1} NaCl, 3 days of shaking)

Gray dotted line indicates the overall fit. The resulting fitting procedure provides a best fit with four single peaks located at 907, 883, 861 and 828 cm^{-1} and a local residual root-mean-square error of 3.12×10^{-4}, in agreement with *in situ* ATR FT-IR measurements showed in Fig. 4.33. At higher pD (4.4), the amplitude is decreasing with increasing pD reflecting the reduced amount of sorbed selenate with increasing pH, and a similar shape spectra was obtained (results not shown)

4.5.2.3 Outer-sphere complexation classification

The appearance of inner-sphere complexes results from the formation of a chemical bonding between the sorbed species and a functional group located at the surface. This sorption mechanism is referred to specific adsorption. If the selenate oxyanions are coordinated to such a functional group via one or two of their oxygen atoms, their symmetry will be lowered compared to the free aqueous species. This change of the molecule symmetry is expected to be reflected by significant alterations in the vibrational spectra compared to those of the fully hydrated aqueous oxyanions. Generally, because of the symmetry change vibrational modes might become IR active which were previously IR inactive and/or a different splitting of multiple degenerate modes might be observed.

During outer-sphere complexation, water molecules separate the sorbed species and the functional surface groups. This is referred to non-specific adsorption. Indeed, during the formation of outer-sphere surface complexes, the oxyanions retain their hydration shell and do not form chemical (covalent) bonds with the surface sites. Rather, the attraction is done by electrostatic forces. Therefore, the symmetry of outer-sphere complexes is expected to be very similar to those of the free oxyanions in solution, i. e. T_d. However, a slight distortion could lead the v_1 mode to become IR active and the frequency of the v_3 mode should increase. For example, [NAKAMOTO '57] studied the complex $[Co(NH_3)_6]_2(SO_4)_3 \cdot 5H_2O$. In the IR spectra, the v_3 (F_2) mode of the SO_4^{2-} ion, which is isostructural to SeO_4^{2-}, was not split, but its frequency was shifted to higher wavenumbers. In addition, the authors observed a very weak v_1 mode, due to the presence of $[Co(NH_3)_6]^{3+}$. Despite the slight distortion, a tetrahedral T_d symmetry for such complexes was assumed. Such outer-sphere complexes with slightly disturbed T_d symmetry were recently observed for sulfate reacted onto γ-Al_2O_3 [MÜLLER '11] and SeO_4^{2-} surface species onto anatase [JORDAN '11] by *in situ* ATR FT-IR spectroscopy. Additionally, a slightly shifted frequency of the v_3 (F_2) mode compared to the aqueous species was reported from selenate sorption experiments on goethite by Raman spectroscopy [WIJNJA '00].

In this study, we observed the formation of bidentate outer-sphere complexes during selenium(VI) sorption onto maghemite showing a C_{2v} symmetry instead of T_d by IR spectroscopy. A close association of these outer-sphere complexes to the maghemite surface could take place via H-bonds, as it was recently suggested from sorption experiments of atmospherically derived carbonate onto ferrihydrite [HAUSNER '09]. From this study, an outer-sphere H-bonded surface species was derived showing a significantly different IR spectra compared to the aqueous species.

Such an intermediate complex would not be easily detectable by EXAFS spectroscopy because of two reasons. First, the specific geometry suggests that Se-Fe distances are longer than 4 Å, which are difficult to detect for non-solids. Second, the H-bond is most likely weak, leading to a disordered arrangement at the surface. The resulting length variation of the Se-Fe backscattering paths is then subject to substantial destructive interference, which annihilates the corresponding signal. Therefore, the absence of a Se-

Fe path at > 3.5 Å does not contradict the formation of such a specific type of outer-sphere complex.

For the first time, this study highlights the possibility to differentiate between different types of outer-sphere complexes of the selenate anion by IR spectroscopy. These findings are related to the work of [LEE '10], who investigated the hydrated cation speciation (Cu^{2+}, Zn^{2+}, Sr^{2+}, Hg^{2+}, and Pb^{2+}) at the muscovite (001)-water interface using resonant anomalous X-ray reflectivity. Among the formation of inner-sphere complexes, the existence of two types of outer-sphere complexes was proposed: the classical outer-sphere complex which retains its hydration shell, but is adsorbed at the surface by displacing the hydration layer of the surface, and an extended outer-sphere surface complex located farther from the surface than the “classical” outer-sphere complex, i. e. above the surface hydration layer.

In the context of our study, this implies that selenium(VI) forms a “classical” outer-sphere complex on the maghemite surface showing a symmetry reduction from T_d (**Fig. 4.37**a) to C_{2v} (**Fig. 4.37**b).

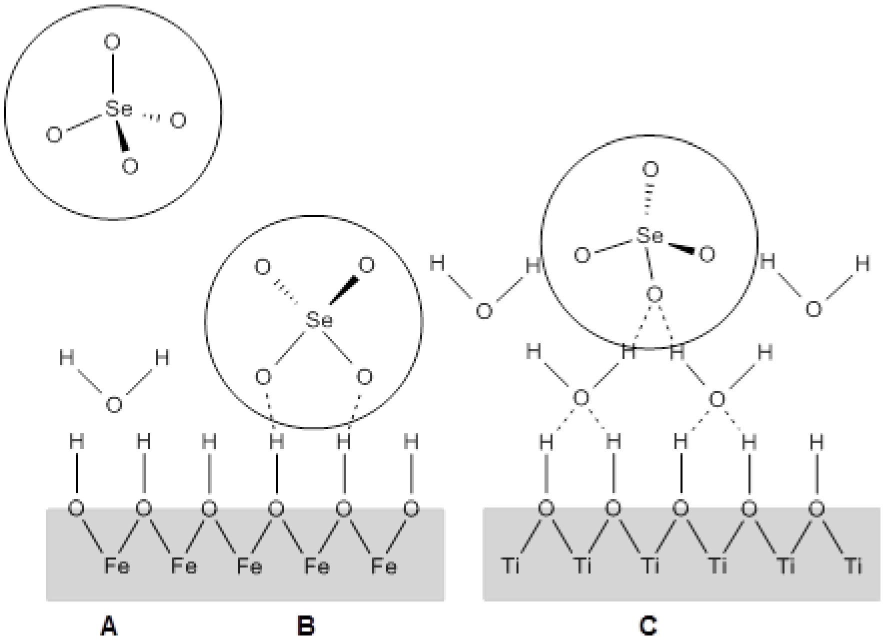

Fig. 4.37 Scheme of SeO_4^{2-} surface species.

Aqueous species (A), outer-sphere complex as derived for maghemite surfaces (B) and extended outer-sphere complex as derived for anatase surfaces (C). The circles around the selenate ions symbolize intact hydration shells of the anion.

This can only be explained by specific molecular interactions occurring due to the sorption process. It is conceivable that the SeO_4^{2-} ion is compelled into the predominant lowered symmetry at the hydration layer of maghemite surface by keeping the characteristics of an outer-sphere complex (**Fig. 4.37**b). However, the selenate ion must be located in a less specific molecular environment on the anatase surface, because its molecular symmetry was close to the T_d symmetry of the aqueous species. This can only be interpreted in terms of the formation of an extended outer-sphere surface complex (**Fig. 4.37**c) [JORDAN '11]. However, the spectroscopic results of this work do not provide any detailed information about the molecular properties of the water network at the mineral interface. In the end, we are inclined to conclude that the classification of inner- and outer-sphere coordination might not be accurate enough for the full interpretation of the spectroscopic results presented in this work.

Based on *in situ* ATR FT-IR studies, we concluded that selenium(VI) is sorbed onto maghemite as bidentate outer-sphere surface complexes over the whole pH range studied (3.5 – 8), i. e. the selenate oxyanions are sorbed onto the maghemite surface primarily via electrostatic interaction. However, EXAFS results revealed the presence of a small portion of inner-sphere complexes together with outer-sphere surface complexes, at acidic pH.

4.5.3 Se(VI) onto Hematite

4.5.3.1 In situ ATR FT-IR spectroscopy

The sorption spectra (**Fig. 4.38**) recorded at pD 4 after different times after induced sorption show a characteristic pattern of four partially overlapping bands in the spectral region between 1000 and 750 cm^{-1}. From second derivative spectra the maxima of these bands were determined to 912, 882, 853, and 827 cm^{-1} (**Tab. 4.8**).

The intensities of these bands are increasing within the first 20 minutes of sorption time (**Fig. 4.38**). After this time, the band intensities did not change significantly, suggesting that hematite was saturated with SeO_4^{2-} and an equilibrium state was achieved. The shape of the band pattern does not change throughout the complete time of sorption (up to 120 min) indicating that there is no change of the surface speciation during the sorption process, as observed for maghemite.

Subsequently, the hematite film was flushed with a 0.1 M NaCl blank electrolyte for another 45 min. The respective spectra (**Fig. 4.38**) show negative bands at nearly the same frequencies compared to those observed during the sorption process. The high congruence of the spectra in the sorption and flushing step strongly suggests that the same selenium(VI) species observed during the sorption process are released from the solid phase during the flushing step.

With desorption time, the intensity of the observed bands increases with accumulation time during the first 20 minutes (with a constant width). At longer desorption times, no more selenium(VI) is desorbed. The fast and reversible sorption process of selenium(VI) onto hematite observed by *in situ* ATR FT-IR can be related to an outer-sphere complexation mechanism, in agreement with batch sorption experiments and zeta potential measurements and with the findings for maghemite.

However, since the amplitude of the desorption reaction spectra does not exceed 70 % of the sorption spectra, it can be assumed that the reversibility of the sorption reaction is not fully given under the prevailing conditions. This might be due to different kinetics of both reactions or to the formation of a small fraction of an inner-sphere surface species like for maghemite.

From the second derivative spectrum four spectral components were identified in the sorption spectra. The resulting fitting procedure provides a best fit as shown in **Fig. 4.39** with four single peaks located at 912, 882, 854 and 828 cm^{-1} and a local residual root-mean-square error of 9×10^{-5}.

Based on the similarity with maghemite in terms of sorption pattern and high reversibility, it can be assumed that the formation of an outer-sphere complex with a reduce symmetry (C_{2v}) also takes place at the hematite surface.

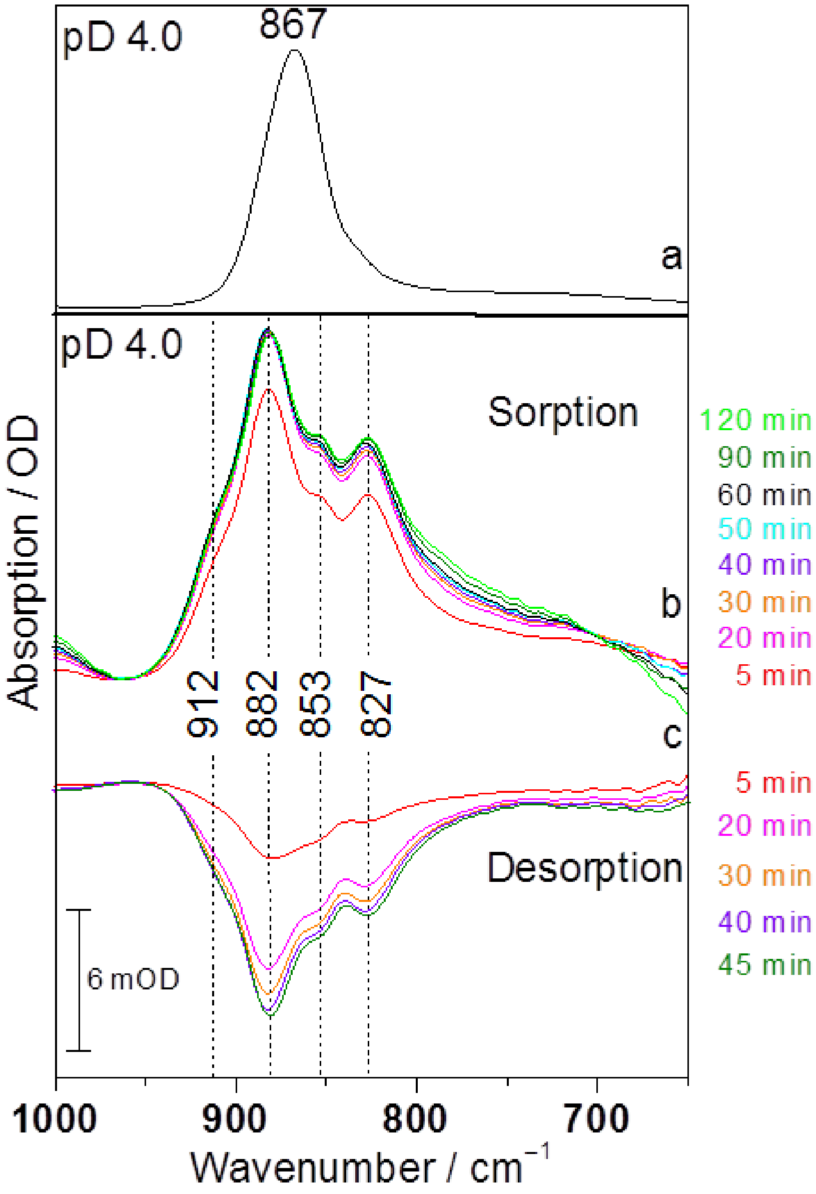

Fig. 4.38 IR spectra of selenium(VI)

(a) IR spectrum of 0.1 mol L^{-1} selenium(VI) in aqueous solution at 0.1 mol L^{-1} NaCl in D_2O. (b) *In situ* IR spectra of selenium(VI) sorption complexes onto hematite ($[Se^{VI}]_{initial} = 5 \times 10^{-4}$ mol L^{-1}, D_2O, pD 4.0, 0.1 mol L^{-1} NaCl, N_2) recorded at different points of time after induced sorption. (c) *In situ* IR spectrum of released selenium(VI) sorption complex recorded at different points of time after subsequent flushing of the hematite phase with blank solution (D_2O, pD 4.0, 0.1 mol L^{-1} NaCl, N_2)

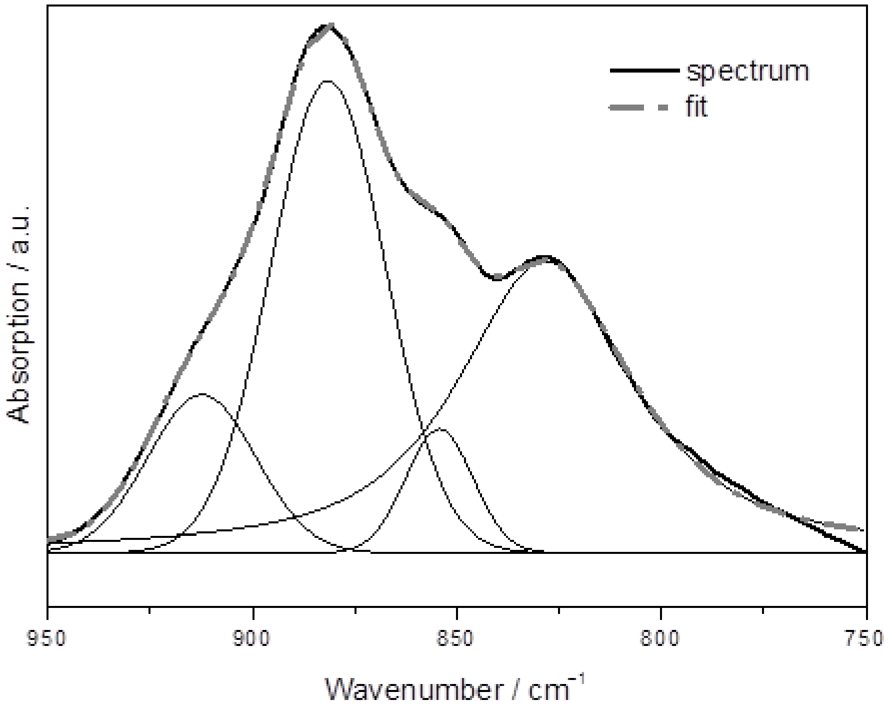

Fig. 4.39 Deconvolution of the IR spectrum of selenium(VI) sorption onto hematite ($[Se^{VI}]_{initial} = 5 \times 10^{-4}$ mol L^{-1}, D_2O, pD 4.0, 0.1 mol L^{-1} NaCl,120 min of sorption, N_2). Dotted line indicates the overall fit

At higher pD values, the band amplitudes correlate with the amount of sorbed selenium(VI), i. e. their amplitudes are decreasing with increasing pD (**Fig. 4.40**) in accordance with batch experiments (**Fig. 4.18**).

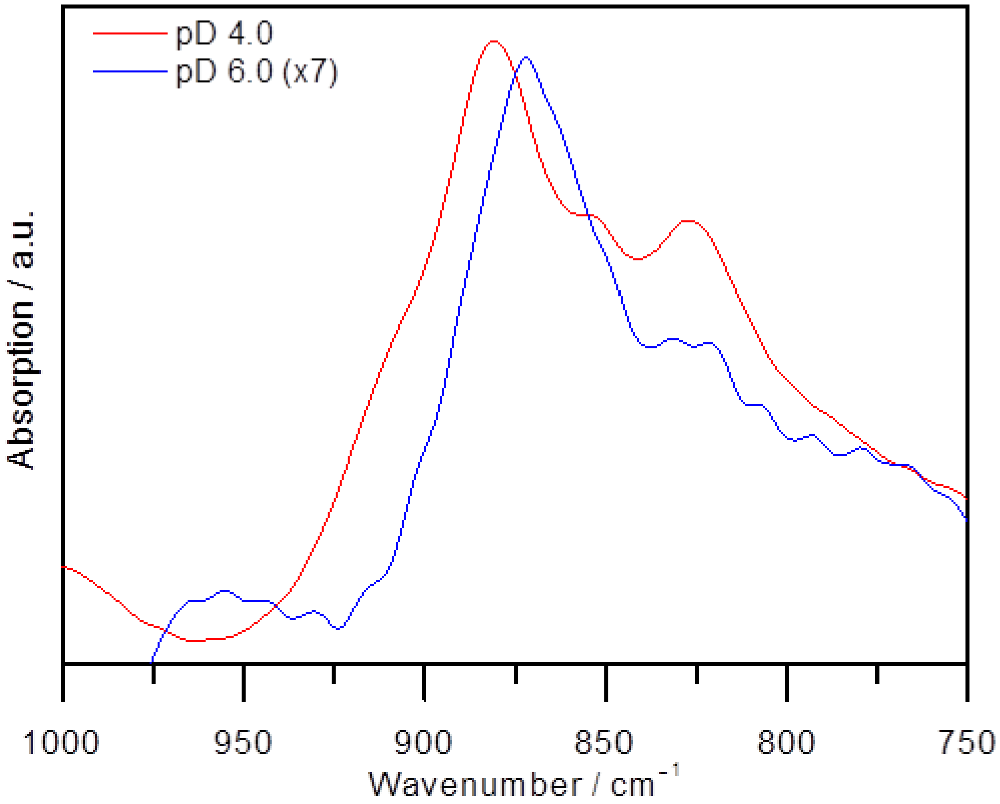

Fig. 4.40 *In situ* IR spectra of selenium(VI) sorption complexes onto hematite ($[Se^{VI}]_{initial} = 5 \times 10^{-4}$ mol L^{-1}, D_2O, 0.1 mol L^{-1} NaCl, 120 min of sorption, N_2) recorded at different pD values
(For clarity, the amplitude of the spectrum recorded at pH 6 is enlarged by a factor of ~7)

At pD 3.5 (**Fig. A.10** in Appendix) and pD 4.0 (**Fig. 4.38**), identical spectral characteristics can be observed. This indicates that a bidentate outer-sphere complex is predominantly formed at the hematite surface at acidic pD conditions. However, at pD 6.0 (**Fig. A.11** in Appendix) and pD 8.0 (**Fig. A.12** in Appendix), the band pattern is significantly changed and does not correspond any longer to a C_{2v} symmetry (**Tab. 4.8**).

Sorption spectra at pD 6.0 (**Fig. A.11** in Appendix) and pD 8.0 (**Fig. A.12** in Appendix) exhibit two main peaks around 870 and 820 cm^{-1}. The resulting fitting procedure provides a best fit at 824 and 871 cm^{-1} at pD 6 (**Fig. A.13** in Appendix) and at 822 and 870 cm^{-1} at pD 8 (**Fig. A.14** in Appendix). The local residual root-mean-square error was 2×10^{-5} and 1.1×10^{-4} at pD 6 and pD 8, respectively.

From these results, a change of the surface speciation with increasing pD values can be derived. However, the assignment of the spectral findings to a distinct surface species at higher pD values is still equivocal. Diverse interpretations of the predominant bands centered at 870 and 820 cm^{-1} observed at pD 6 and 8 can be given. On the one hand, the bands represent a species showing a C_{3v} symmetry where the splitting of the ν_3 mode is only of low extent. On the other hand, the spectrum might represent a mixture of surface species showing C_{2v} and T_D symmetry. The C_{3v} symmetry species would imply the formation of a monodentate complex whereas the mixed species reflect the formation of bidentate and tetrahedral surface species. In particular the latter species should represent an outer-spheric species according to the Se(VI)/anatase sorption system. However, this is in contradiction to the findings of the lower reversibility during the experiments performed at higher pD values, where the amplitude of the desorption reaction spectra did not exceed 60 — 70 % of the sorption spectra. This suggests a slight increase of inner-sphere complexation with increasing pD. Unfortunately, the spectra recorded at higher pD values are of reduced quality for a more detailed spectral deconvolution.

It can be concluded that selenium(VI) sorption onto hematite proceeds predominantly via the formation of outer-sphere complexes through the whole pH range. A transition in the symmetry of the outer-sphere complex upon increasing pD was noticed. An increasing fraction of inner-sphere complex at higher pD correlated with a lowered reversibility of the sorption process was also observed.

4.5.3.2 EXAFS

In this section, we discuss results obtained from the seven XAFS samples listed in **Tab. 4.10**. In tetrahedral coordination all four Se-O distances have the same length (within the EXAFS resolution of about 0.13 Å at the given k-range of 2.0 – 14.5 Å^{-1}), giving rise to 12 tri-legged Se-O-O MS paths with distances around 3.0 Å, and to 12 four-legged Se-O-Se-O MS paths at twice the distance of the coordination shell (3.3 Å), as for instance in $Na_2(SeO_4)$ [FUKAMI '03]. Considering these MS paths during the fitting (CN, distances and Debye-Waller factors linked to the single scattering path of the coordination shell), the Se-Fe CN dropped to 0.3 and the fit improved significantly. Therefore, only these fit results are shown in **Tab. 4.10**.

Tab. 4.10 List of EXAFS samples for the Se(VI)/hematite binary system

Sample	**pH**	**$[Se^{VI}]_{initial}$ (mol L^{-1})**	**Ionic strength (mol L^{-1})**	**%Se(VI) sorbed**	**Se loading [mg/kg]**
1	6.0	250	0.1	4.8	475
2	5.0	250	0.1	15.4	1525
3	3.5	50	0.1	85.9	1697
4	3.5	100	0.1	66.3	2620
5	4.0	250	0.1	30.6	3025
6	3.5	250	0.1	33.7	3325
7	3.5	250	0.01	43.8	4325

The XANES edge energy of 12.663 keV as well as the strong white-line intensity (**Fig. 4.** A) is in line with Se(VI). All XANES spectra are well reproduced by one single principal component, demonstrating the absence of redox processes at the hematite surface across the investigated pH and Se-loading range.

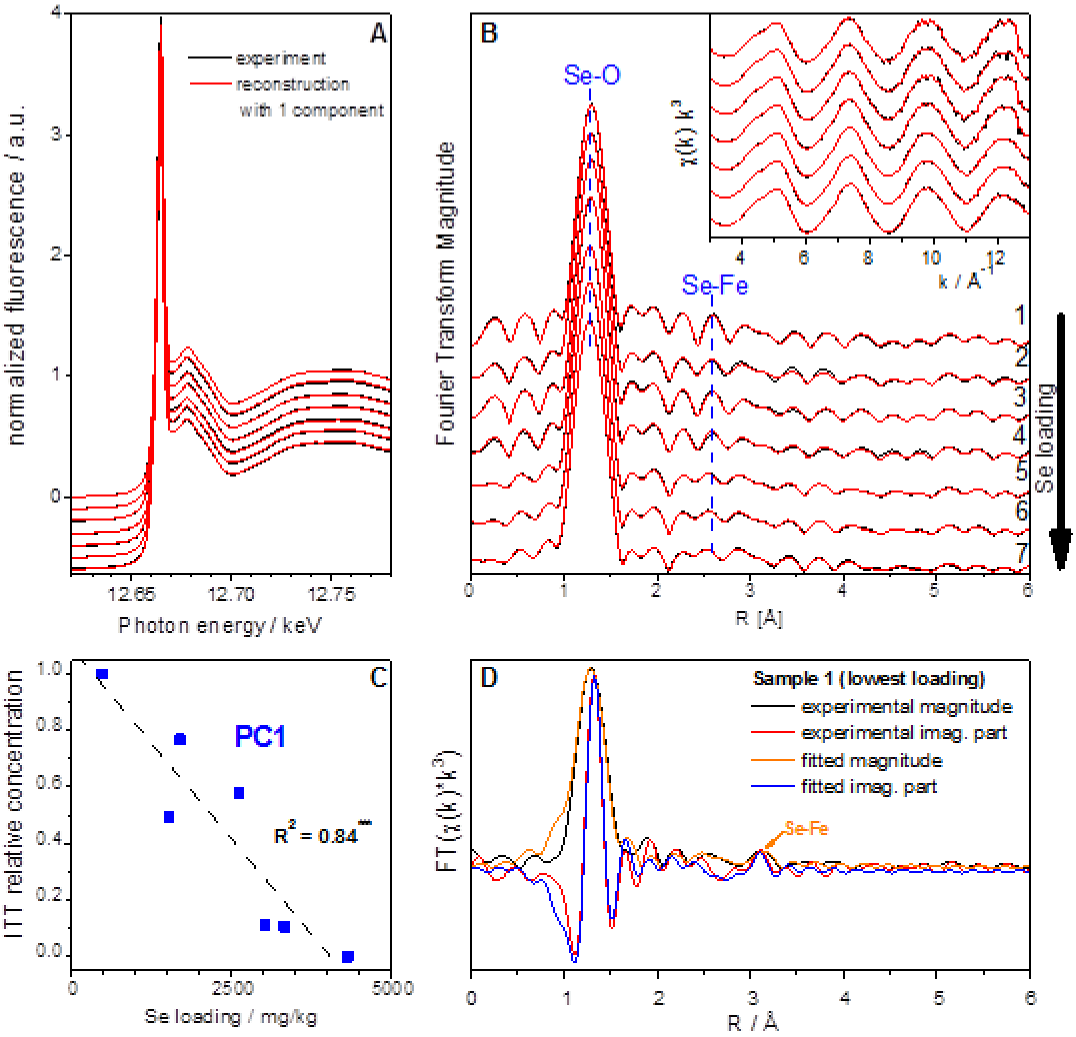

Fig. 4.41 Se K-edge XAS results of Se(VI) sorbed hematite

(A) XANES spectra and their reconstruction by 1 principal component (B) Fourier Transform EXAFS spectra and their reconstruction by 2 principal components, k3-weighted chi spectra as insert (C) ITT-derived relative concentration of principal component 1 as a function of Se loading (D) Fitted EXAFS spectrum of sample 1 with lowest Se loading

The Fourier transform magnitude (**Fig. 4.**b) is dominated by strong peak at about 1.3 Å (not corrected for phase shift), arising from the typically four O atoms in the coordination sphere of selenate [SCHEINOST '08b]. In our previous study on the selenate sorption complex on maghemite, we observed additional peaks out to about 3 Å clearly arising above the background noise at higher R-space. These were fitted with 3 and 4-legged multiple scattering contributions from the O coordination shell, and with one Se-Fe path at 3.38 Å indicative of formation of a small percentage of an edge-sharing, inner-sphere complex in addition to the prevalent outer-sphere complex (see Chapter 4.6.2). While the multiple scattering contributions are again visible, the existence of a statistically significant Se-Fe path is much less clear (**Fig. 4.**b). Furthermore, there seems to be small changes in this region, but hardly above the background noise level. Therefore, we performed a detailed factor analysis to investigate whether there are statistically significant trends within the data set [ROSSBERG '03]. The analysis revealed in fact that 2 principal components are required to reconstruct the spectra (see red lines in **Fig. 4.**b and insert) and based on a minimum of the Malinowski indicator value for 2 (not shown). Sorting the spectra along their Se loading showed that the relative contribution of principal component 1 (PC1) decreases systematically with increasing loading (**Fig. 4.**d). When fitting the two most extreme spectra, only spectrum 1 with the lowest Se loading could be fitted with an Se-Fe path at 3.41 Å, while this was not possible for spectrum 7 with the highest loading (**Fig. 4.**c). No attempt was made to fit the intermediate spectra, since they are simply composites of the two end-member spectra.

The Se-Fe distance observed for low loading is 3.41 Å and hence, although slightly longer than the one observed before for maghemite, in line with a bidentate, binuclear corner-sharing (CS) complex (**Tab. 4.11**) (see Chapter 4.6.2).

Tab. 4.11 Se-K edge XAFS, fit results ($S_0^2 = 0.8$). (The fits include all tri- and four-legged MS paths as described in the text.)

Sample	**Se loading [mg Se/kg]**	**Edge [eV]**	**[1]CN**	**[2]R [Å]**	**[3]σ^2 [$Å^2$]**	**ΔE_0 [eV]**	**χ_{res} %**
1	475	12,663.1	4.0 O	1.66	0.0011	13.8	20.0
			0.4 Fe	3.41	0.0011		
7	4325	12,662.8	4.0 O	1.64	0.0009	13.1	19.5

[1] CN: coordination number, error ± 25 %

[2] R: radial distance, error ± 0.01 Å

[3] σ^2: Debye-Waller factor, error ± 0.0005 $Å^2$

Likewise the maghemite case, the observed coordination number for the Se-Fe path of 0.4 arises from the sum signal of two different complexes, the outer-sphere complex with a coordination number of 0, and the binuclear corner-sharing complex with a coordination number of 2. The fraction of the binuclear complex is therefore 0.4/2 = 0.2, while the fraction of the outer-sphere complex is 0.8. Note that this surface speciation accounts only for the lowest loading of about 500 mg Se/kg. As suggested by **Fig. 4.**c, the fraction of the inner-sphere complex decreases linearly with increasing Se loading, and reaches 0 at a loading of about 4000 mg Se kg^{-1}.

The first two samples at pH 6 and 5 reflect the expected anion sorption behavior, i. e. a decrease of loading with increasing pH. Note, however, that sample 3 with a pH of 3.5 has a similar loading as sample 2, simply because of a 5-fold lower initial Se concentration (**Tab. 4.11**). Therefore, the fraction of the inner-sphere complex appears solely as a function of surface loading, and not of pH. The pH and IS act only indirectly on the inner-sphere complex fraction through loading (**Fig. 4.42**).

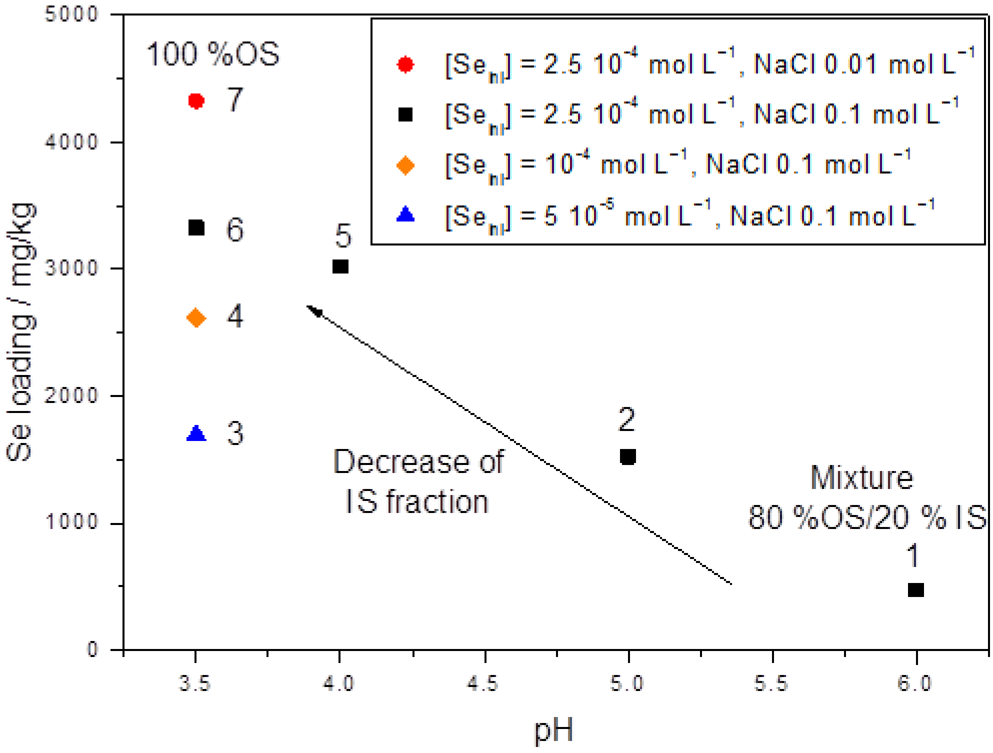

Fig. 4.42 Surface loading of EXAFS samples for the Se(VI)/hematite binary system.

Note, however, that the absolute amount of the IS complex may remain constant: Due to the about 9-fold increase in surface loading, its fractional contribution to the EXAFS sum signal would decrease to 0.02, which falls below the lower detection limit of about 0.05 to 0.10. Therefore, expected additional controls on the surface speciation like pH and ionic strength (i. e. competition by the background electrolyte) cannot be ascertained with the current data set and method.

From EXAFS data, Se(VI) sorbs prevalently as outer sphere complex. When the Se loading decreases by about one order of magnitude, also a small percentage of a CS inner sphere sorption complex becomes visible.

The increasing fraction of inner-sphere complex with increasing pH is in line with IR observations, where a decreased reversibility was noticed. The bidentate outer-sphere complexes detected by IR spectroscopy do not show Se-Fe interactions, because their distances would be too far and to disordered to be detectable by EXAFS spectroscopy. Same is true for the monodentate or tetrahedral (mixed with bidentate) outer-spheric species observed by IR at pD 6 and pD 8.

Based on *in situ* ATR FT-IR studies and EXAFS, we conclude that selenium(VI) is predominantly sorbed onto hematite as outer-sphere surface complexes over the whole pH range studied (3.5 – 8). A change in the symmetry of the outer-sphere complex is also observed upon increasing pH by *in situ* ATR FT-IR. Both IR and EXAFS data revealed an increasing fraction of inner-sphere complex at higher pH. EXAFS evidenced this inner-sphere complex to be a bidentate, binuclear corner-sharing (CS) one. This might represent the unreleased fraction observed during the desorption step in the *in situ* IR experiments at high pD.

4.5.4 Se(VI) onto Alumina

The sorption process of selenium(VI) by alumina was elucidated by *in situ* ATR FT-IR. The formation of an alumina film with a sufficient stability during the preparation procedure was demonstrated by the IR spectra showing no relevant spectral changes after 60 minutes of equilibration with 0.1 M NaCl blank solution (data not shown).

Upon Se(VI) sorption onto $\delta-Al_2O_3$, both band shifting and band splitting of the v_3 mode of the SeO_4^{2-} is observed **Fig. 4.43**a). The sorption spectrum recorded five minutes after induced sorption shows a broad band with two shoulders. The maxima or shoulders are approximately at 922, 898, and 874 cm^{-1}, respectively. The intensities of these bands are increasing for the first 60 minutes; after this time, a further increase is very slow; indicating the approach to an equilibrium state. Additionally, during the course of the sorption process, the band pattern changes and more shoulders are shaped out, indicating that there might be a change of the surface speciation or the formation of surface precipitates during the sorption process.

After the sorption process, the alumina film was flushed with a 0.1 M NaCl blank solution for another 60 min. The respective spectra (**Fig. 4.43**b) show negative bands at nearly the same frequencies compared to those observed during the sorption process. Here, it is interesting that the first spectra after 5 min is the inversion of the last spectra of sorption (90 min) and the spectra after 60 min is the inversion of the first spectra (5 min). This indicates that the secondly formed species is removed first and subsequently the firstly formed species is removed. However, in general it is observed, that desorption spectra intensities increase very fast at the beginning, indicating a fast reversibility of the sorption process. This can be related to an outer-sphere complexation mechanism, in agreement with batch sorption experiments and zeta potential measurements. Additionally, the formation of similar non-protonated outer-sphere complexes upon Se(VI) sorption onto γ−Al2O3 was recently derived from both macroscopic and spectroscopic investigations. [ELZINGA '09]

At longer flushing times (> 60 min), no more Se(VI) is desorbed and the amplitude of desorption reaction spectra does not achieve the level of the sorption spectra. Hence, it can be assumed that the reversibility of the sorption reaction is not fully given under the prevailing conditions. This might be due to different kinetics of both reactions or to the formation of a small fraction of an inner-sphere surface species like for maghemite and hematite.

In order to elucidate the exact sorption process and the formed species, further *in situ* ATR FT-IR and additionally EXAFS experiments will be performed.

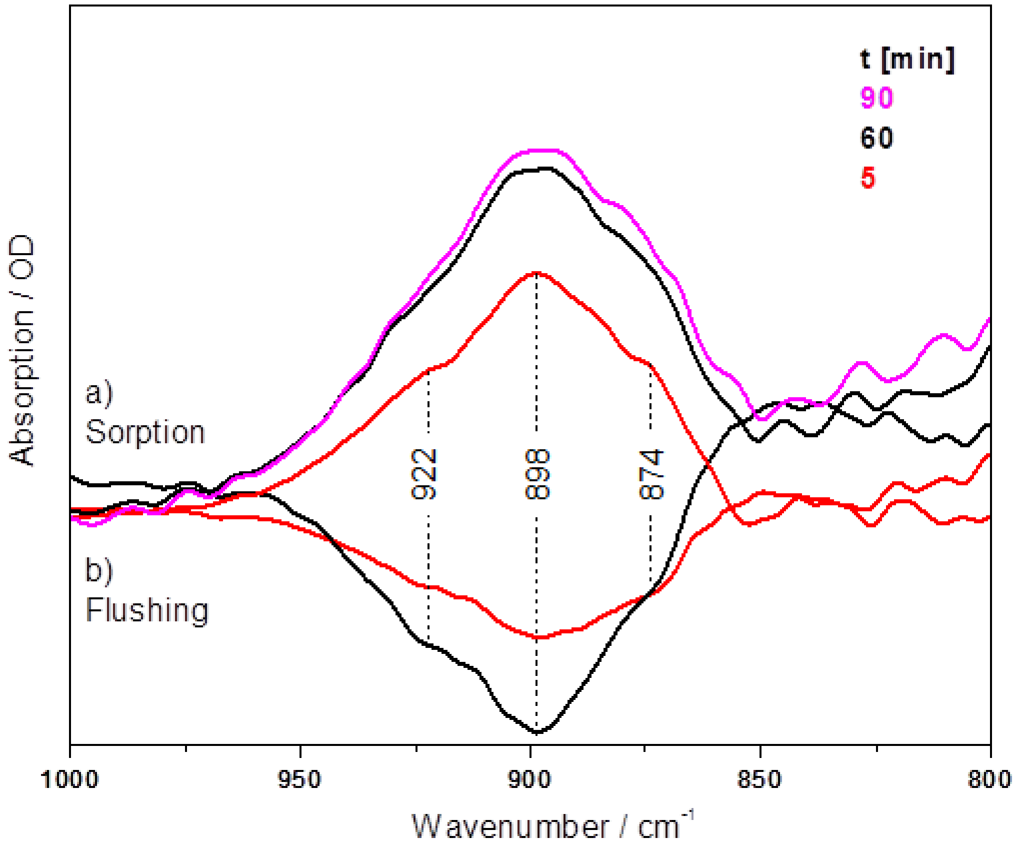

Fig. 4.43 *In situ* IR spectra of Se(VI)

(a) *In situ* IR spectra of Se(VI) sorption complexes onto δ-alumina ($[Se^{VI}]_{initial}$ = 5×10^{-4} mol L^{-1}, D_2O, pD 4.0, 0.1 mol L^{-1} NaCl, N_2) recorded at different times after induced sorption. (b) *In situ* IR spectra of released Se(VI) sorption complex recorded at different times after subsequent flushing of the alumina phase with blank solution (D_2O, pD 4.0, 0.1 mol L^{-1} NaCl, N_2).

4.5.5 Se(IV) onto Maghemite

4.5.5.1 in situ ATR FT-IR spectroscopy

A decrease of spectral intensity with increasing pD can be observed in **Fig. 4.44**, confirming the observed tendency in batch experiments (**Fig. 4.19**). A significant change of spectral bands at different pD is not observable. However, a shift of the bands at 845 and 770 cm^{-1} at pD > 6 can be seen, indicating a change in the sorption mechanism.

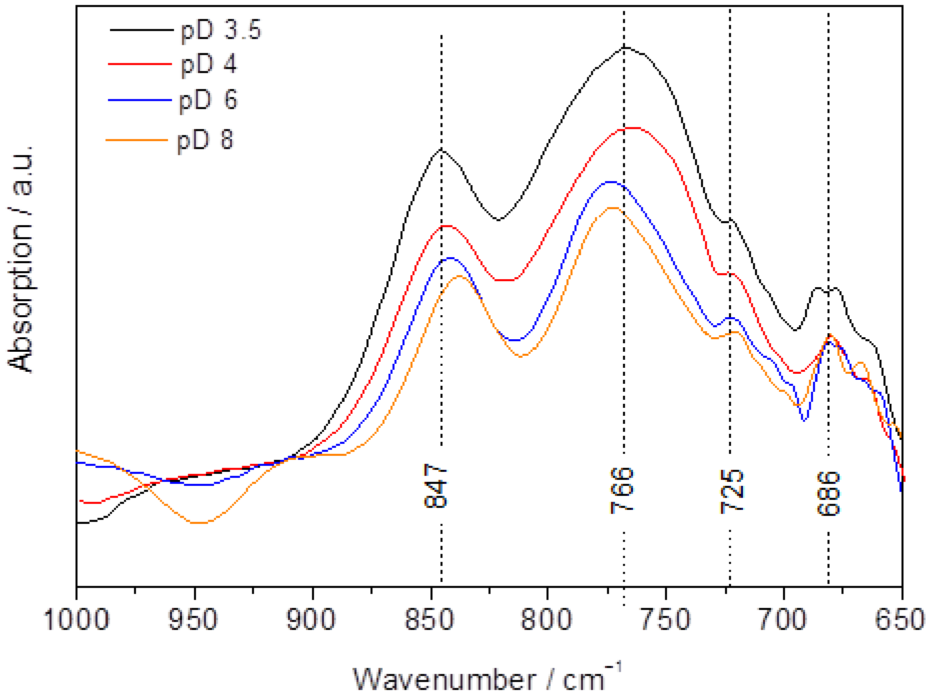

Fig. 4.44 *In situ* IR spectra of selenium(IV) sorption complexes onto maghemite ($[Se^{IV}]_{initial}$ = 5 × 10^{-4} mol L^{-1}, D_2O, 0.1 mol L^{-1} NaCl, 120 min of sorption, N_2, recorded at different pD

The spectra recorded at two different ionic strengths (**Fig. 4.45**) showed that at constant pD the sorption increased at lower ionic strength, which could not be verified by batch experiments (**Fig. 4.19**). This could originate from kinetic effects because during *in situ* IR experiments no thermodynamic equilibrium state is reached. In addition, in comparison to Se^{VI}, the relative change in intensity at different ionic strength was less significant for Se^{IV} which again implies kinetic effects.

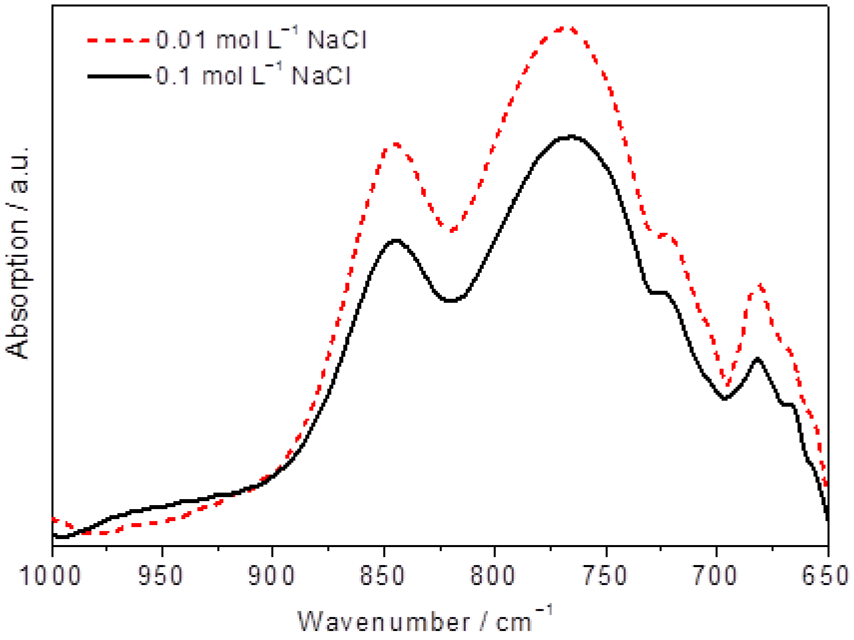

Fig. 4.45 *In situ* IR spectra of selenium(IV) sorption complexes onto maghemite ($[Se^{IV}]_{initial} = 5 \times 10^{-4}$, D_2O, pD 4.0, 120 min of sorption, N_2, recorded at different ionic strength

The time resolved IR spectra of Se^{IV} sorption by maghemite at pD 3.5 and pD 8.0 show that after 10 minutes sorption, a major amount of Se^{IV} is already sorbed (Fig. 4.46). After 20 – 30 minutes, a small increase of sorption is still to be observed. The saturation of the maghemite surface seems to occur later in comparison to Se^{VI} sorption (Fig. **4.32**).

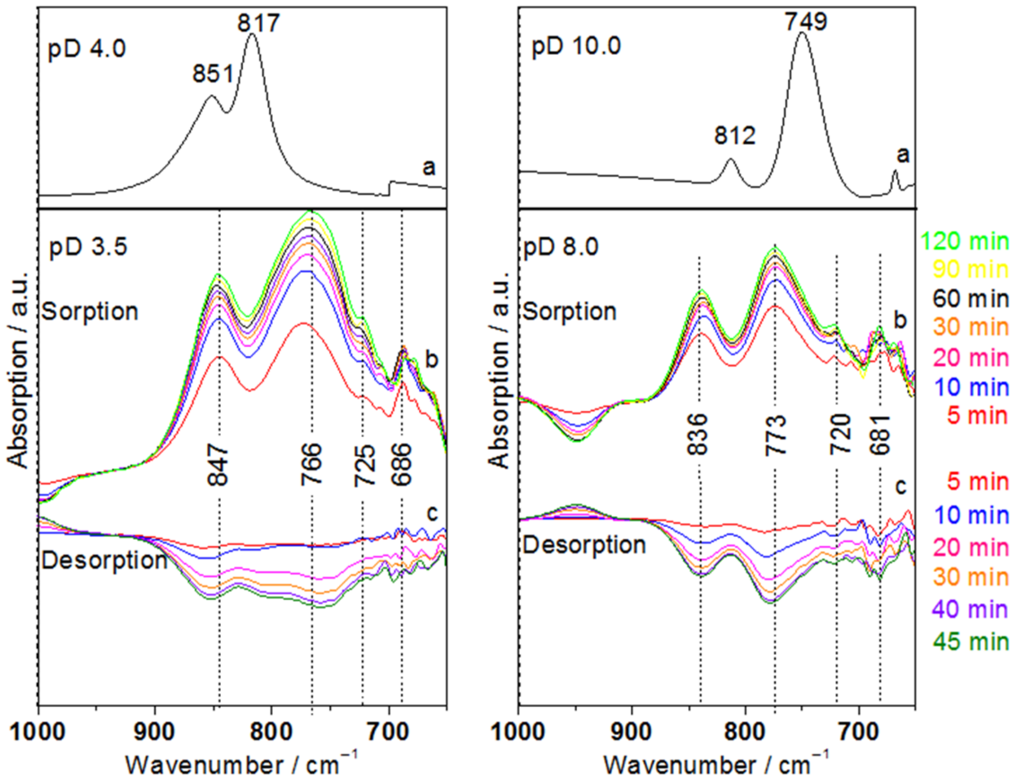

Fig. 4.46 IR-Spectra of selenium(IV)

(a) IR-Spectrum of 0.1 mol L^{-1} aqueous selenium(IV) in 0.1 mol L^{-1} NaCl in D_2O, pD 4.0 (left) and pD 10 (right)

(b) *In situ* IR-Spectra of selenium(IV) sorption complexes onto maghemite recorded at different points of time after induced sorption. ($[Se^{IV}]_{initial} = 5 \times 10^{-4}$ mol L^{-1}, D_2O, 0.1 mol L^{-1} NaCl, N_2), pD 3.5 (left) und pD 8.0 (right)

(c) *In situ* IR-Spectra of selenium(IV) sorption complexes onto maghemite recorded at different points of time after subsequent flushing of the maghemite phase with blank solution (I = 0.1 mol L^{-1} NaCl, N_2). pD 3.5 (left) und pD 8.0 (right)

The shape of the band pattern did not change throughout the complete time of sorption (up to 120 min) at pD 3.5 (**Fig. 4.46**, left). However, a slight shift of the most intensive band with increasing contact time was noticeable. After 5 minutes, this band exhibits a peak maximum at 773 cm^{-1} while it was located at 766 cm^{-1} after 120 minutes of sorption.

Subsequently, the maghemite film was again flushed with a 0.1 M NaCl blank electrolyte for another 45 min at pD 3.5.The respective spectra show negative bands at slightly shifted frequencies (853 and 755 cm^{-1}) compared to those observed during the sorption process (847 and 766 cm^{-1}) (**Fig. 4.46**, left).

Based on the shift observed during the desorption process, the formation of two different inner-sphere surface species upon sorption is indicated at pD 3.5. During the desorption step, the species which is the less attached to the surface and characterized by a bigger gap of the bands at 853 and 755 cm^{-1} is desorbed. The most stable surface species will therefore be created in an earlier sorption stage and exhibits frequencies at 847 and 773 cm^{-1} (**Fig. 4.46**, left).

Contrary to observations at pD 3.5, no change of the band pattern and no significant shift of the peak maxima throughout the complete time of sorption (up to 120 min) occurs at pD 8.0 (**Fig. 4.46**, right). Same is true for the desorption stage. The high congruence of the spectra in the sorption and flushing step strongly suggests that a single selenium(IV) species observed during the sorption process are released from the solid phase during the flushing step**.**

The amplitude of the desorption reaction spectra at pD 3.5 and pD 8.0 (**Fig. 4.46**) is significantly lowered in comparison to sorption spectra, indicating that the reversibility of the sorption reaction is far away from being fully given under the prevailing conditions, contrary to observations for Se(VI) (**Fig. 4.32**).

Based on the different band pattern observed during sorption as for the free Se(IV) species, it can be deduced that a change of the selenite ion symmetry (C_{3v}) takes place. The two bands at 720 and 680 cm^{-1} cannot be assigned to sorbed selenium(IV) species, since maghemite itself exhibits IR bands at the same frequencies (**Fig. A.9** in Appendix).

Considering the low reversibility of sorption process observed by ATR FT-IR as well as the macroscopic results (see Chapter **4.4.1**), it can be concluded that selenium(IV) sorption onto maghemite proceeds via the formation of inner-sphere complexes through the whole pH range. A mixture of two inner-sphere complexes occurs from pH 3.5 to 6.0. At pH 8.0, only one surface complex is formed.

4.5.5.2 EXAFS

The Se K-edge XANES spectra of selenium(IV)-reacted maghemite samples (data not shown) are dominated by a strong white line at 12.662 keV, characteristic of the +IV oxidation state of selenium [SCHEINOST '08a]. Since no additional shoulders at lower energy (12.656 – 12.657 keV) characteristic of elemental selenium and selenium(−II) were observed, it can be deduced that the presence of Fe(II) traces as verified by UV-VIS spectrophotometry did not lead to a significant amount (> 2.5 %) of reduced selenium. Therefore, sorption was not accompanied by a significant reduction of selenium(IV) in contrast to Fe(II)-bearing minerals [SCHEINOST '08a].

Sorption samples at four different pH values (3.4, 4.0, 6.0 and 8.0) were analyzed by Se K-edge XAFS spectroscopy (**Fig. 4.47**).

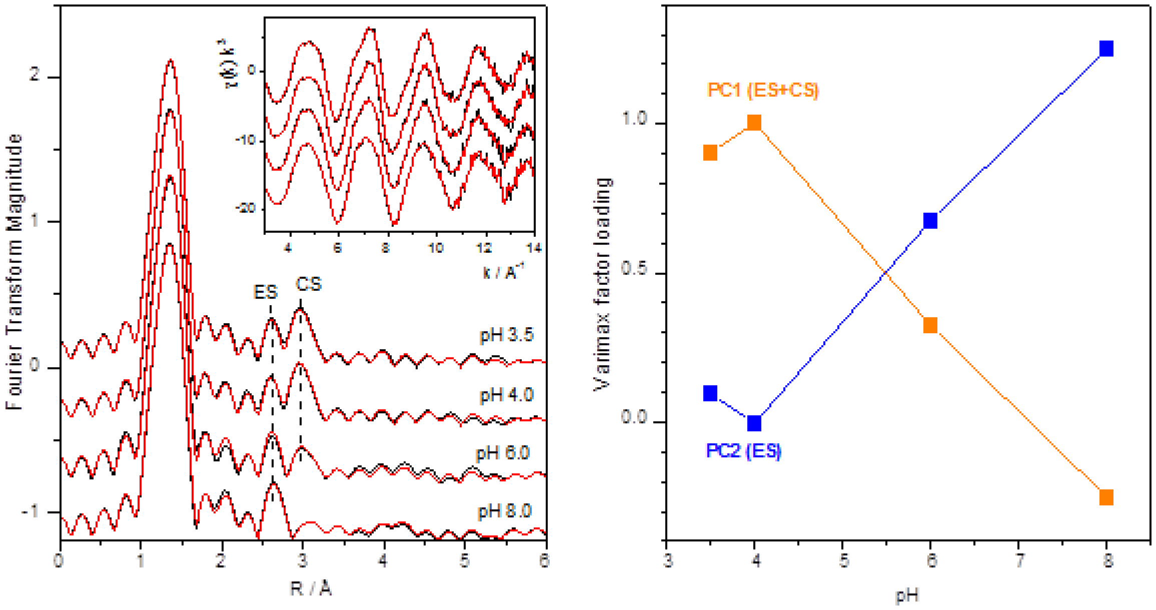

Fig. 4.47 Se K-edge EXAFS spectra of Se(IV) sorbed to maghemite

Left: Experimental spectra (black lines) and their reconstruction by two factors (red lines) shown as Fourier Transform and k^3-weighted chi spectra (insert). Right: Varimax loadings of the two factors, the first one predominating at low pH representing both edge- and corner-sharing complexes, the second one predominating at high pH representing only the edge-sharing complex

The Fourier transform magnitude is dominated by a strong peak at about 1.3 Å (uncorrected for phase shift), which arises from backscattering of the oxygen atoms in the coordination sphere. This peak was fitted with 3 Se-O paths with a length of 1.71 Å (**Tab.**

4.12), confirming the structure of the pyramidal selenite $Se^{IV}O_3$ unit [CHARLET '07; PEAK '06b].

Tab. 4.12 Se-K EXAFS fit results of Se(IV)-sorbed maghemite (amplitude reduction factor $S_0^2 = 0.9$)

	Oxygen shell			Iron shells			ΔE_0 [eV]	$\chi^2_{res\ \%}$
pH	**^{1}CN**	**^{2}R [Å]**	**$^3\sigma^2$ [Å^2]**	**CN**	**R [Å]**	**σ^2 [Å^2]**		
3.5	3.0	1.71	0.0020	0.5 1.3	2.91 3.38	0.0077 0.0065	17.0	13.0
4.0	2.9	1.71	0.0015	0.2 1.2	2.91 3.38	0.0024 0.0055	16.3	15.1
6.0	3.0	1.71	0.0018	0.2 0.5	2.89 3.36	0.0021 0.0040	16.2	14.9
8.0	2.9	1.71	0.0020	0.5	2.88	0.0046	16.7	14.1

[1] CN: coordination number, error ± 25 %

[2] R: radial distance, error ± 0.01 Å

[3] σ^2: Debye-Waller factor, error ± 0.0005 Å^2

Beyond this coordination sphere, the signal intensity becomes very weak, but two peaks (depending on pH) clearly rise above the background noise level in the region beyond 3.5 Å. The first one at about 2.6 Å (labeled ES) is present for all four pH values, while the second at 2.9 Å (labeled CS) is present for the three more acidic samples, and seems to be absent at pH 8.0. The ES peak was fitted with 0.2 to 0.5 Fe atoms at distances of 2.88 – 2.91 Å. The CS peak was fitted with up to 1.3 Fe atoms at distances of 3.36 – 3.38 Å (**Tab. 4.12**). While such small coordination numbers have a large error and may appear statistically insignificant, they were necessary to obtain a satisfying fit of the spectra. Furthermore, they are supported by the factor analysis as shown further down.

While the fit with two Se-Fe paths provided consistent results, two alternative scenarios have to be considered. (1) For the SeO_3^{2-} ion, the Se-O double bond is fully delocalized, resulting in C_{3v} symmetry and three equal Se-O distances, while the $HSeO_3^-$ and $H_2SeO_3^0$ species have lower symmetry and Se-O distances varying by up to 0.05 Å [PEAK '06b; VALKONEN '78]. In the case of the SeO_3^{2-} ion, a tri-legged multiple scattering path Se-O-O about 3.0 Å in length may become significant, resulting in a 6-fold degeneracy for the C_{3v} symmetry as has been also observed for other oxyanions such as arsenic(V) [SHERMAN '03]. (2) The ES peak could also arise from a Se-O single-scattering path about 2.9 Å in length, occurring in selenite solids. A wavelet analysis of the 2.5 to 3.5 Å region, however, did not reveal significant contributions of lighter atoms besides the heavier Fe [SCHEINOST '08b]. Furthermore, by considering these two additional paths during the shell fit, neither significant contribution to the “ES” FT peak, nor changes in the fit parameters of the Se-Fe shell appeared. They were consequently omitted. The absence of the tri-legged multiple scattering path points to a deviation from the C_{3v} symmetry, induced by the surface complexation.

The shorter Se-Fe distance of 2.9 Å is in line with a bidentate mononuclear edge-sharing (^1E) linkage between one SeO_3^{2-} pyramid and one FeO_6 octahedron, as e. g. in the structure of the solid $Fe_3(H_2O)(SeO_3)_3$ [XIAO '04]. The longer Se-Fe distance of 3.37 Å is in line with a bidentate binuclear corner-sharing (^2C) linkage between one SeO_3^{2-} pyramid and two FeO_6 octahedral [XIAO '04]. The even longer Se-Fe distances ≥ 3.5 Å of monodentate mononuclear corner-sharing complexes (^1V) could not be fitted, indicating that they occur only in negligible proportion if at all. The small coordination numbers exclude formation of precipitates.

Based on EXAFS studies, the co-existence of bidentate mononuclear edge-sharing (^1E) and bidentate binuclear corner-sharing (^2C) inner-sphere selenite surface complexes on Hydrous Ferric Oxide (HFO) was suggested [MANCEAU '94], while only the bidentate binuclear corner-sharing (^2C) complex was consistently observed on goethite [HAYES '87; MANCEAU '94; MISSANA '09]. According to Manceau and Charlet [MANCEAU '94], the presence of additional bidentate mononuclear edge sharing (^1E) surface complex onto HFO was due to structural differences between goethite and HFO (different proportion of edge termination on both solids). From IR studies on air-dried goethite and air-dried am-$Fe(OH)_3$, [SU '00] suggested that sorption of selenite leads to the formation of bidentate bridging surface complex.

Former studies highlighted the influence of surface loading on the coordination fashion of oxyanions onto iron oxides. [FENDORF '97] examined by XAS the sorption of AsO_4^{3-} onto goethite according to the surface loading (arising from different pH). The formation of monodentate complex was favored at low surface coverage, while formation of a bidentate-binuclear complex and bidentate-mononuclear complex was observed at higher surface coverage (the bidentate-binuclear complex was the predominant one for high surface loadings) [FENDORF '97]. [MISSANA '09], who studied selenite sorption onto magnetite by EXAFS, observed that the ^1E surface complex was favored at low surface loading (i. e. at pH 9.4), while a mixture of ^1E and ^2C complexes appeared at higher surface loading (i. e. pH 6.4).

In our study, we observe that the bidentate mononuclear edge-sharing ^1E complex prevails at pH 8, while at lower pH both complexes occur. Not surprising due to their relatively high uncertainty, the Se-Fe coordination numbers do not show a clear trend with pH. However, the FT peaks suggest that ^2C becomes more important for the samples at pH 3.5 and 4.0 in comparison to the sample at pH 6.0, where the ^1E peak height seems to be higher **Fig. 4.47**). To follow this trend more systematically, we applied factor analysis [ROSSBERG '03; SCHEINOST '08a]. The close match between the experimental spectra (black in **Fig. 4.47**) and their reconstruction by two factors (red) demonstrates that two structural entities or species are present in all four samples. The Varimax factor loading confirms that the samples at pH 3.5 – 4.0 and at pH 8.0 constitute extremes; however, only sample pH 8.0 with ^1E configuration represents a limiting species, while the samples at pH 3.5 and 4.0 contain a mixture of both species. The factor loadings further validate the visual impression that the sample at pH 6 represents an intermediate in speciation, with a higher ratio of ^1E over ^2C. These results match perfectly with the IR observations for this binary system. Reasons for such pH-dependent transition will be given in the following section.

While this is to the best of our knowledge the first molecular study of selenite sorption to maghemite, previous studies were conducted on selenite sorption to magnetite. Due to its Fe(II) content and low bandgap, magnetite reduced selenite to the −II oxidation state [SCHEINOST '08a; SCHEINOST '08b]. However, in the study of [MISSANA '09], no reduction occurred. In our study, we observed the transition from solely ^1E to a mixture of ^1E and ^2C complexes with increasing surface loading (decreasing pH), in agreement with [MISSANA '09] observations onto nano magnetite particles (nanocrystals (50 – 200 nm)), confirming the crystal similarity between both maghemite and magnetite surfaces.

According to literature, based on the Wulf theorem and morphology studies (TEM and SEM), the magnetite and maghemite nanoparticles with a cubic symmetry expose predominantly the {111}, {110} and {100} low-index and low energy crystallographic planes, which are the three densest lattice planes [AUFFAN '08; ZHAO '09]. The morphology of our commercial nano-sized γ-Fe_2O_3 particles was observed by TEM (**Fig. 4.48**).

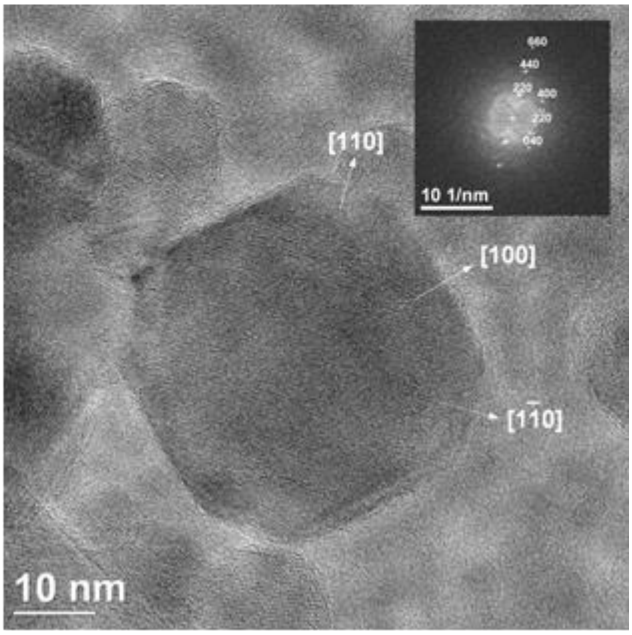

Fig. 4.48 HRTEM image of an γ-Fe_2O_3 nanoparticle along the [100] zone axis together with its Fourier transform indexed based on the cubic structure of maghemite

In particular, **Fig. 4.48** shows a HRTEM image of a maghemite nanoparticle. Fourier transformation of the corresponding part of the high-resolution electron micrograph indicates, that the nanoparticle is oriented along the [100] zone axis and exhibits {100} and {110} facets. {111} facets are not observed in **Fig. 4.48**. They would be inclined to the [100] zone axis by 54.7°.

Based on structural information [AUFFAN '08; WANG '11; WANG '08], a scheme representing the crystalline structure of maghemite (**Fig. 4.49**) containing the three main lattices was drawn.

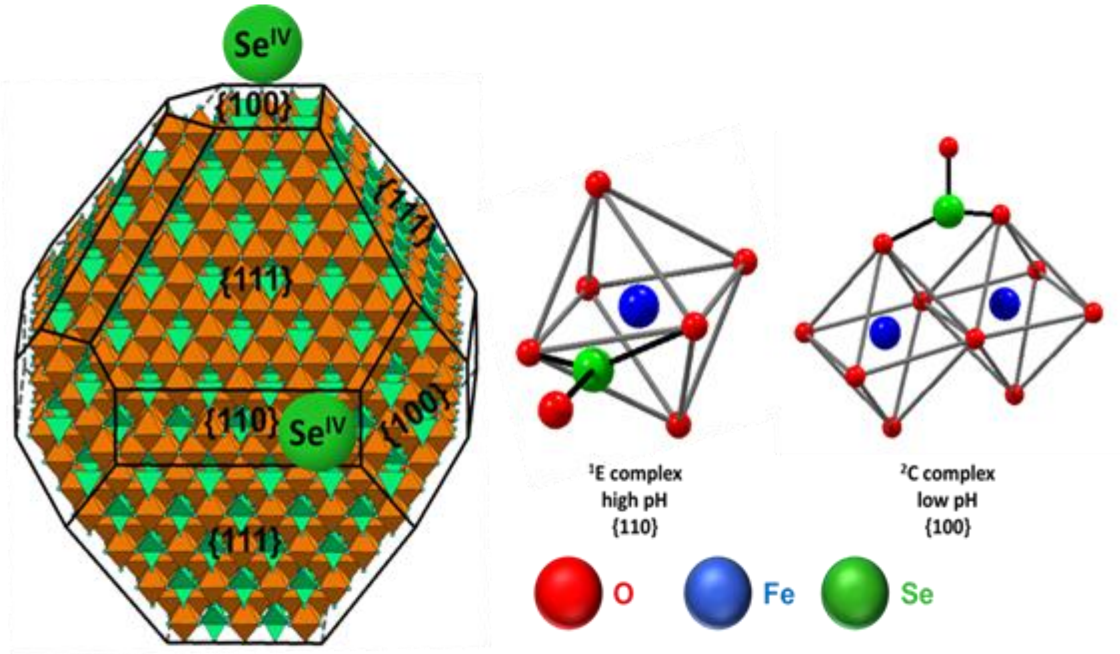

Fig. 4.49 Scheme representing the crystalline structure of maghemite containing the three main lattices {111}, {110} and {100} and the two observed ^{1}E and ^{2}C surface complexes

In agreement with Wang et al. [WANG '11; WANG '08], it becomes obvious that the formation of bidentate binuclear ^{2}C complex on the octahedral surface termination of the {111} facet of maghemite is not possible since adjacent iron octahedra do not show the required singly coordinated oxygens for such complexation pathway [WANG '11; WANG '08]. However, such complexes can be formed on the {100} facet, where rows of octahedra with singly coordinated oxygens are clearly visible [WANG '11]. The formation of the second kind of surface complex, namely the bidentate mononuclear edge-sharing complex, is likely to occur on the {110} facet of maghemite (**Fig. 4.49**). We hypothesize that edge sites, located e. g. at the {110} facet, are high energy sites and active at low surface loading, while the formation of ^{2}C takes place at {100} facets having rows of octahedra with singly coordinated oxygens (low energy sites). This seems to be a reasonable explanation of the presence of a mix of bidentate mononuclear edge-sharing (^{1}E) and bidentate binuclear corner-sharing (^{2}C) complexes whose proportion change upon surface loading. Note that the formation of ^{1}E complexes could also alternatively take place at the {111} facet or at edges between {111} and {100} or {110} facets [DULNEE '13]. Surface charge effects, which may be distinct for each facet, could be another possibility to explain the relative proportion of inner-sphere complexes. To get further information, Resonant Anomalous X-ray Reflectivity

[CATALANO '08] or Crystal truncation rod diffraction [PETITTO '10] on maghemite could be excellent methods, but require single crystals.

However, we cannot definitely rule out the presence of outer-sphere complexes during selenium(IV) sorption onto maghemite. Indeed, it is difficult by EXAFS to detect the occurrence of outer-sphere surface complexes in the simultaneous presence of inner-sphere surface complexes [CHARLET '11]. The ability of resonant anomalous X-ray reflectivity (RAXR) and Grazing-Incidence X-ray absorption fine structure (GI-XAFS) spectroscopy to observe outer-sphere complexes during sorption processes was evidenced by [CATALANO '08] and [BARGAR '96], as recently highlighted [CHARLET '11]. Indeed, [CATALANO '08] showed, for the first time, by using RAXR the presence of outer-sphere complexes (probably hydrogen-bonded species) in addition to inner-sphere ^{2}C complexes upon As(V) sorption onto corundum and hematite (012) surfaces. In addition, GI-XAFS was used by [BARGAR '96] to study the adsorption of Pb(II) onto α-Al_2O_3 (0001) single crystal surface (although data were not corrected for polarization effects, which may question the numbers of reported Al(III) neighbors and interatomic distances).

Our *in situ* ATR FT-IR and EXAFS spectroscopic results provide new detailed knowledge at the molecular level to improve surface complexation modeling and to predict the retention behavior of selenium(IV) by maghemite. They allow constraining without ambiguity the surface complexes denticity. A mixture of bidentate bridging and bidentate chelate inner-sphere complexes formed on two different facets of maghemite occurs from pH 3.5 to 6.0, whose proportion is pH-dependent. At pH 8.0, only the bidentate chelate complex is formed. These surface complexes observed for maghemite might also be the surface complexes forming on magnetite, before the interfacial reduction step to Se(−II).

4.5.6 Se(VI) and Se(IV) redox reactions with magnetite (Fe_3O_4)

The interaction of Se(VI) and Se(IV) with freshly synthesized magnetite nanoparticles ($Fe^{II}Fe^{III}{}_2O_4$) was examined. All experiments were conducted under anoxic conditions and exclusion of CO_2. The pH values of the solutions were set to pH 5.4, concentration of both Se(VI) and Se(IV) ranged from 1mM to 5mM. XPS was applied to probe the presence of reduced selenium species and to analyze the amount of oxidized Fe(II).

The Fe $2p_{3/2}$ spectrum of magnetite (**Fig. 4.50**) was measured to estimate the ratio between Fe(II) and Fe_{TOT} [HUBER '12]. Compared to the pure magnetite, the selenium-reacted magnetite samples showed a less pronounced shoulder at the lower binding energy side of the Fe $2p_{3/2}$ spectrum.

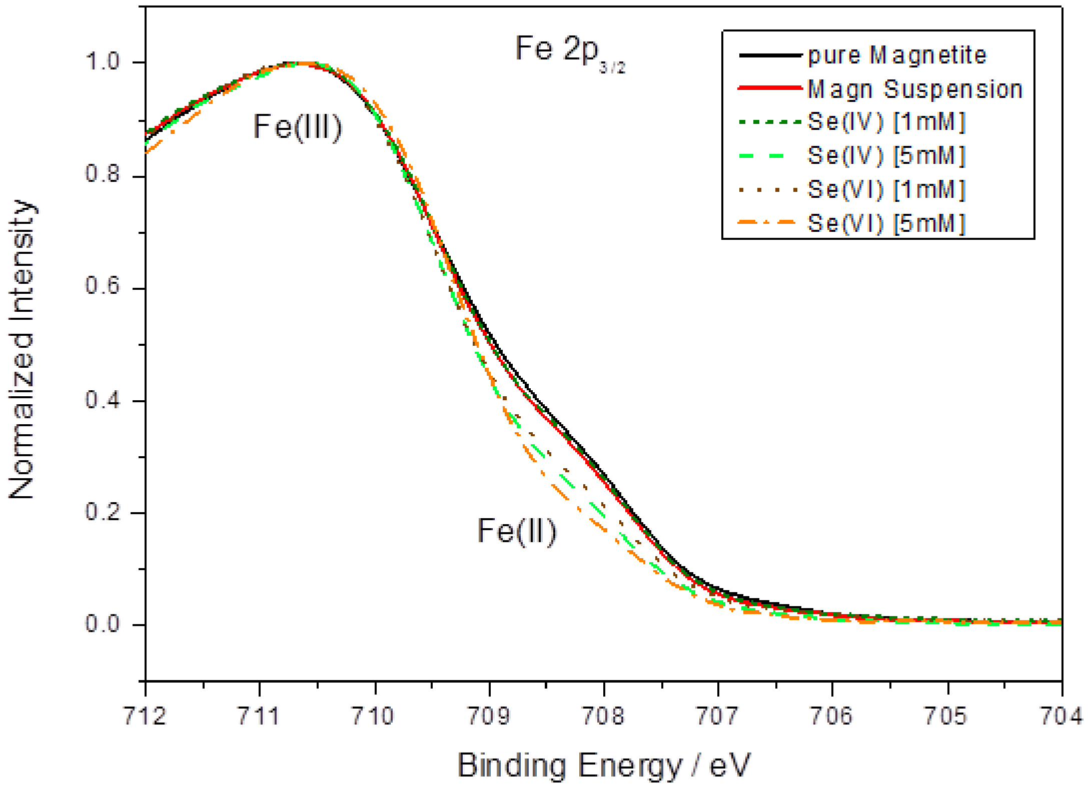

Fig. 4.50 Narrow XPS scan of Fe $2p_{3/2}$ spectrum of fresh magnetite and magnetite reacted with Se(VI) or Se(IV)

The calculated ratios between Fe(II) and Fe_{TOT} show that due to the reaction with selenium, part of the Fe(II) is always oxidized (**Tab. 4.13**). In general, the amount of oxidation of Fe(II) is higher for Se(VI) samples than for Se(IV) samples and higher for the sample with higher selenium concentrations.

Tab. 4.13 Ratio between Fe(II) and Fe_{TOT} for the pure magnetite and magnetite reacted with Se(VI) and Se(IV)

	Fe_3O_4	**Fe_3O_4 1mM Se(IV)**	**Fe_3O_4 1mM Se(VI)**	**Fe_3O_4 5mM Se(IV)**	**Fe_3O_4 5mM Se(VI)**
Fe(II)/Fe_{TOT}	22.6	21.9	18.4	17.5	15.9

Due to the fact that the most intensive Se line (Se 3d) interferes with the Fe 3p line, the Se 3p line was measured (**Fig. 4.51**). However, this line makes it difficult to distinguish between the selenium oxidation states. Samples with Se(VI) showed slightly higher binding energies compared to samples with Se(IV) indicating that a small amount of selenium was reduced.

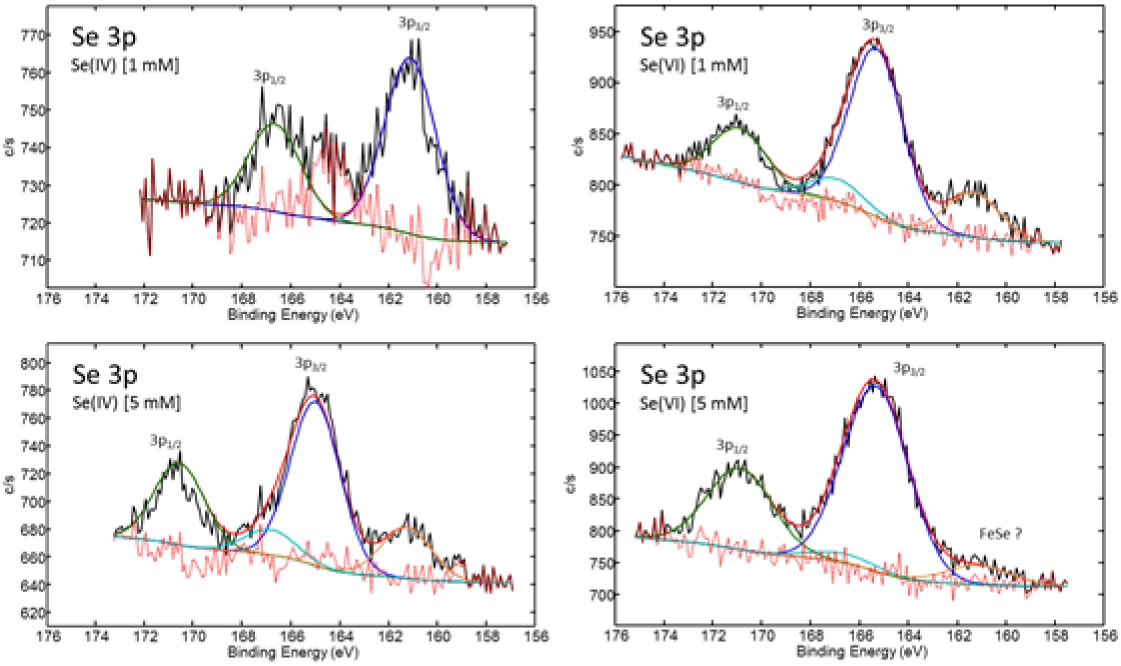

Fig. 4.51 Narrow XPS scan of Se 3p spectrum of magnetite reacted with Se(VI) or SeIV)

The combination of determining the Fe(II)/Fe_{TOT}–ratio and the Se 3p spectra show that for both systems, Se(VI) and Se(IV), Fe was oxidized while Se was reduced. For a better quantification of the redox reactions further experiments will have to be conducted.

4.6 Surface Complexation Modeling of Se(VI) and Se(IV) sorption processes

In this chapter, potentiometric titrations of anatase and maghemite were performed and were fitted using a Charge Distribution MUlti-SIte Complexation model (CD-MUSIC) with a basic Stern model to describe the electrical double layer. Surface complexation constants of two binary systems, i. e. Se(VI)/anatase and Se(IV)/maghemite were then determined. Experimental details about potentiometric titrations can be found in the Appendix F.

4.6.1 Minerals surface properties

Potentiometric titration data of anatase and maghemite were modeled using the CD-MUSIC model [HIEMSTRA '96]. For anatase, following the approach of [BOURIKAS '01] based on crystallographic studies, singly $\equiv TiOH^{-1/3}$ and doubly coordinated groups $\equiv Ti_2O^{-2/3}$, were considered, with a site density for both sites of 6 sites nm^{-2}. Since spectroscopic results clearly highlighted the formation of two different surface complexes on two different binding sites (belonging to two different surfaces), two sites, i. e. singly-coordinated hydroxyl groups with fractional charges $\equiv FeOH^{-1/2}$, were considered for maghemite. To reflect the proportion of each site available for sorption, a density of 4 and 8 sites.nm^{-2} for site 1 and site 2 were taken, respectively. Identical pK for the two sites of anatase and maghemite was taken. A basic Stern model with electrolyte binding was applied and the adjustable parameters were the pK value of the sites, the electrolyte association constants (Equation 1 and 2 exemplarily shown for $\equiv FeOH^{-1/2}$) and a capacitance value (C).

$$\equiv FeOH^{-1/2} + Na^+ \leftrightarrow \equiv FeOH^{-1/2 \cdots\cdots} Na^+$$

$$\equiv FeOH^{-1/2} + H^+ + Cl^- \leftrightarrow \equiv FeOH_2^{+1/2 \cdots\cdots} Cl^-$$

The shear-plane distance s was also fitted using the experimental zeta potential data. The obtained parameters are given in **Tab. 4.14**.

Tab. 4.14 Parameters of the surface complexation model to describe titration curves of anatase and maghemite

Solid/ Parameter	**pK (protonation)**	**log K (Cl- association)**	**log K (Na- association)**	**C (F m^{-2})**	**s (nm)**
Anatase	6.55	−0.565	−0.155	0.90	0.84
Maghemite	7.70	−0.209	−0.209	1.14	0.59

The models fit to the experimental data for the titration curves and for the zeta-potential are shown in **Fig. 4.52** and **Fig. 4.53** for anatase and in **Fig. 4.54** and **Fig. 4.55** for maghemite.

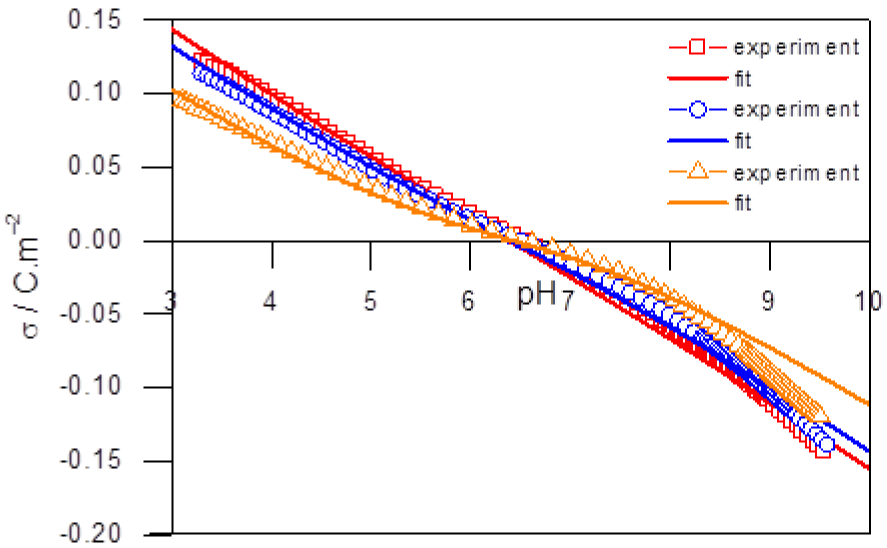

Fig. 4.52 Surface charge of the neat surface of anatase (m/v = 12 g L^{-1}). (□) experiment; —— fit: 0.1 mol L^{-1} NaCl; (○) experiment; —— fit: 0.05 mol L^{-1} NaCl; (Δ) experiment; —— fit: 0.01 mol L^{-1} NaCl

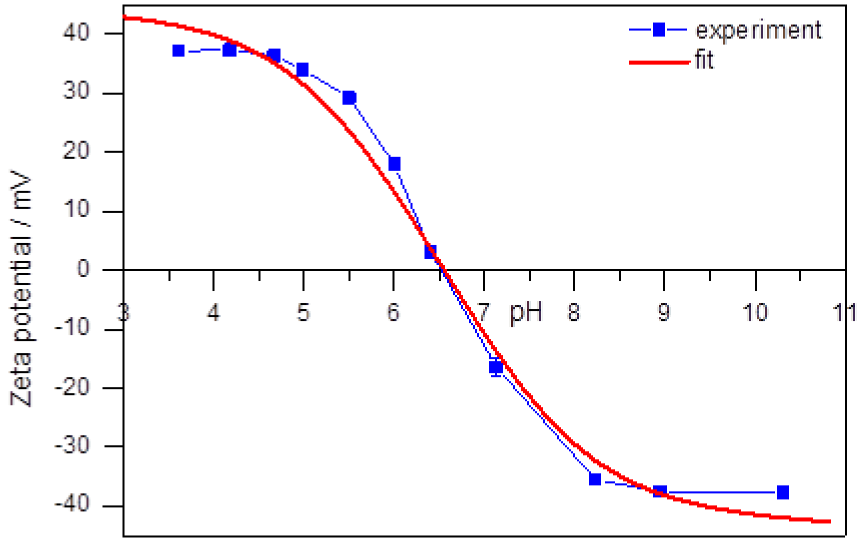

Fig. 4.53 Zeta potential of the neat surface of anatase (m/v = 0.25 g L^{-1}, 1 mmol L^{-1} NaCl). (■) experiment; —— fit.

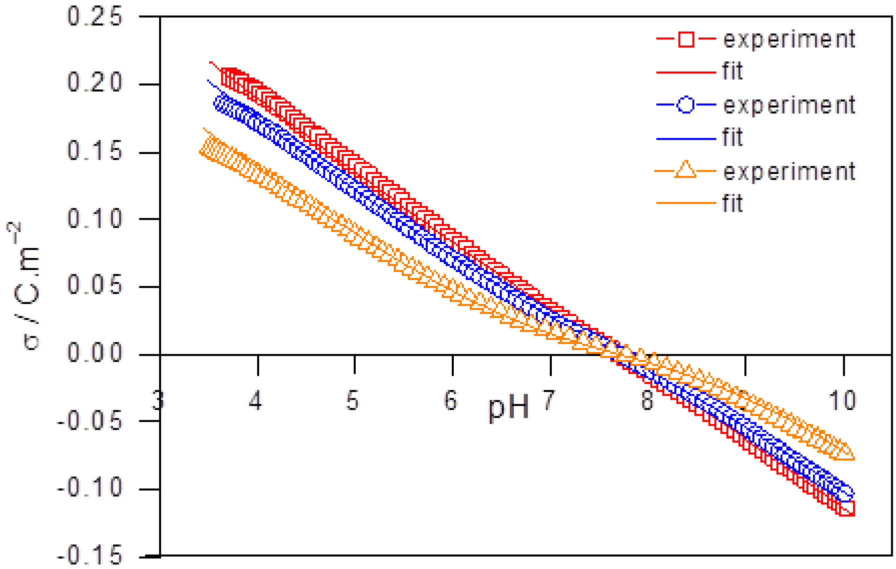

Fig. 4.54 Surface charge of the neat surface of maghemite (m/v = 30 g L^{-1}). (□) experiment; —— fit: 0.1 mol L^{-1} NaCl; (○) experiment; —— fit: 0.05 mol L^{-1} NaCl; (Δ) experiment; —— fit: 0.01 mol L^{-1} NaCl.

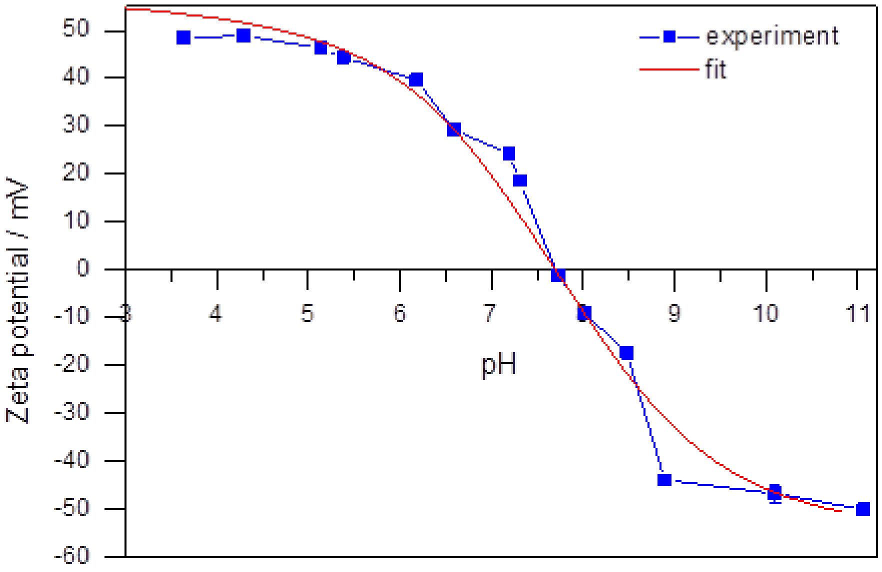

Fig. 4.55 Zeta potential of the neat surface of maghemite (m/v = 0.5 g L^{-1}, 1 mmol L^{-1} NaCl). (■) experiment; —— fit.

For anatase, the model fits perfectly the titration curves except in the pH range higher than 8.0, whereas the whole pH region can be described for maghemite. The zeta potential and isoelectric point of anatase and maghemite are perfectly matching with the experimental data.

The parameters from the acid-base model were kept constant during the parametrization of the adsorption model. We considered that the adsorption of selenium oxyanion does not change the inner layer capacitance.

4.6.2 Surface complexation modeling

The acidity constants of selenium(IV) and selenium(VI) were taken from the NEA-TDB review [OLIN '05].

H_2SeO_3 (aq) ⇌ $HSeO_3^-$ (aq) + H^+, log K = −2.64

H_2SeO_3 (aq) ⇌ SeO_3^{2-} (aq) + 2 H^+, log K = −11.00

$HSeO_4^-$ (aq) ⇌ SeO_4^{2-} (aq) + H^+, log K = −1.75

4.6.2.1 Se(VI) onto anatase

The spectroscopic data (see Chapter 4.5.1) suggest formation of outer-sphere surface complexes at the anatase surface. We assumed the interaction between the selenate ion and the surface to involve singly coordinated hydroxyl groups only. Two stoichiometries were needed to obtain a good fit. This results in 5 adjustable parameters, i. e. the two log K and the two charge distribution (CD) factors of the two stoichiometries, and the shear plane distance as well. The model is summarized in the following reaction equations and the model fit to the data is shown in **Fig. 4.56**.

$\equiv TiOH^{-1/3} + H^{+} + SeO_4^{2-} \rightleftharpoons \equiv TiOH_2^{0.56}SeO_4^{-1.9}$ (log K = 7.26)

$\equiv TiOH^{-1/3} + 2H^{+} + SeO_4^{2-} \rightleftharpoons \equiv TiOH_2^{0.56}HSeO_4^{-0.9}$ (log K = 11.5)

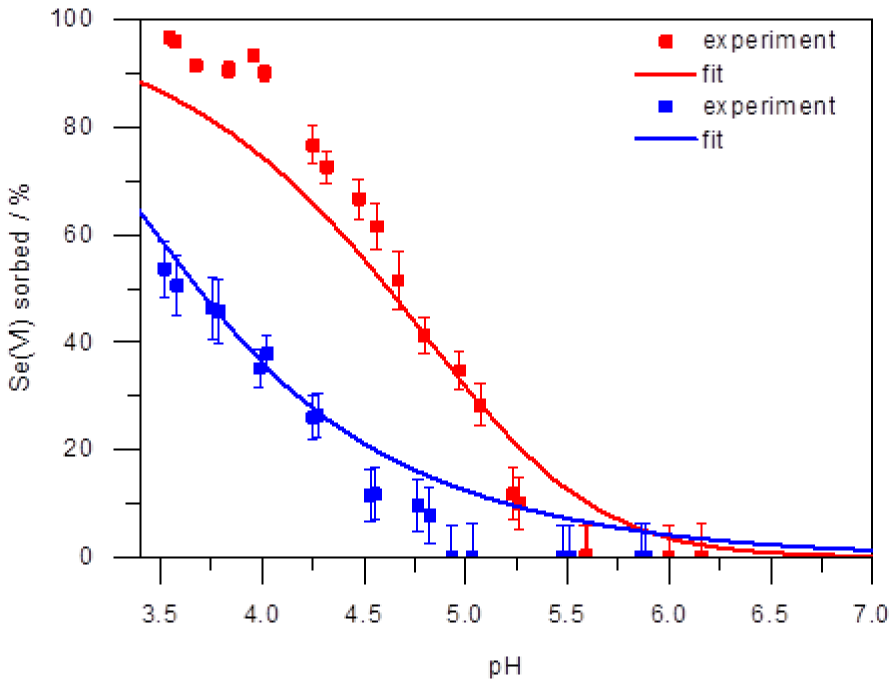

Fig. 4.56 Selenium(VI) sorption edges onto anatase ($[Se^{VI}]_{initial} = 1 \times 10^{-5}$ mol L^{-1}, m/v = 0.5 g L^{-1}, 2 days of shaking). (■) experiment; — fit: 0.01 mol L^{-1} NaCl; (■) experiment; — fit: 0.1 mol L^{-1} NaCl

At lower ionic strength, the adsorption of selenium(VI) is underestimated below pH 5, while the adsorption is overestimated at pH above 4.5 for the higher ionic strength. A better description of the anatase titration curves could be obtained by following the recent approach of [RIDLEY '13], who considered the formation of an inner-sphere Na-bidentate species, an outer-sphere Na-monodentate species, and outer-sphere Cl-monodentate species (with support of DFT calculations). The involvement of an additional site; i. e. $\equiv Ti_2O^{-2/3}$ could improve the adsorption model but this would lead to more adjustable parameters. A better knowledge of the interaction of Se(VI) at the anatase surface by application of Resonant Anomalous X-ray Reflectivity (RAXR) on single crystals of anatase would help to better define the stoichiometries and the involved sites. Such approaches will be followed in the future to improve the model.

4.6.2.2 Se(IV) onto maghemite

For this binary system, EXAFS results evidenced the formation of two inner-sphere complexes, one bidentate bridging and one bidentate chelate on two different facets (see Chapter 4.5.5). This helped to constrain the stoichiometries of the surface complexes. Again, we assumed the interaction between selenium(IV) and the surface of maghemite to involve singly coordinated hydroxyl groups only, resulting in two reaction equations. During the fitting procedure, again 5 parameters were adjusted (as for anatase). The model is summarized in the following reaction equations and the model fit to the data is shown in **Fig. 4.57**.

(Site 1) $(\equiv FeOH^{-1/2})_2 + H_2SeO_3 \rightleftharpoons (\equiv FeO)_2^{-0.8}SeO^{-0.2} + 2H_2O$ $\log K_1 = 5.86$

(Site 2) $\equiv FeOH^{-1/2} + H_2SeO_3 \rightleftharpoons \equiv FeO^{-0.4}\,SeO_2^{-1.1} + H^+ + H_2O$ $\log K_3 = 1.17$

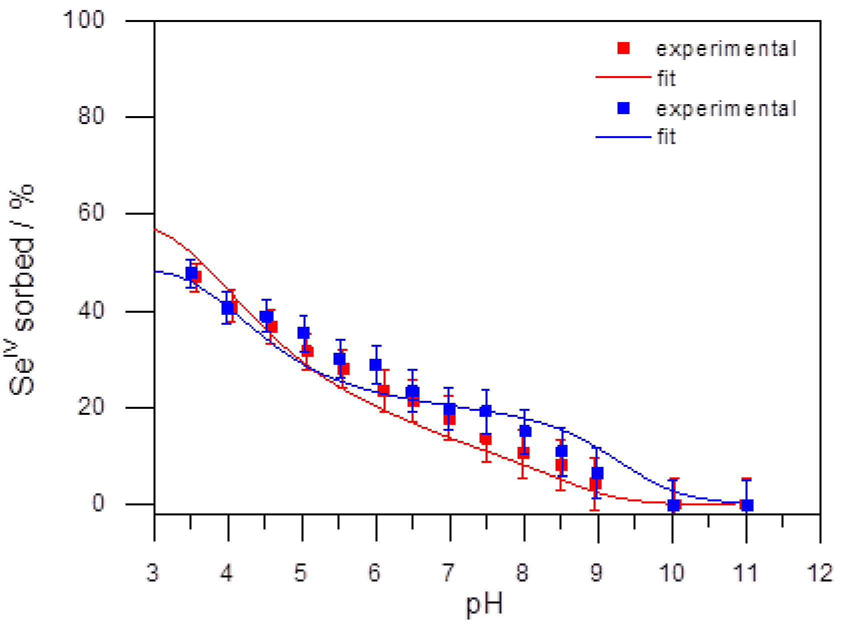

Fig. 4.57 Selenium(IV) sorption edges onto maghemite ($[Se^{IV}]_{initial} = 5 \times 10^{-5}$ mol L^{-1}, m/v = 0.25 g L^{-1}, 2 days of shaking). (🟥) experiment; — fit: 0.01 mol L^{-1} NaCl; (🟦) experiment; — fit: 0.1 mol L^{-1} NaCl

In this case, the sorption edges at two different ionic strengths are properly fitted along the whole pH range. As for anatase, a better comprehensive overview on the surface sites of maghemite involved during sorption would allow improving the model.

The Se(VI)/anatase and Se(IV)/maghemite sorption edges were fitted using a CD-MUSIC model. In each case, two stoichiometries were required, based on spectroscopic results. The results will be implemented into the sorption database RES^{3}T. This data will help to improve the description and prediction of selenium oxyanions reactive transport through the different retention barriers.

4.7 Sorption of Se(−II) onto mineral phases

In this chapter, we present the setup established to generate Se(−II) from the electrochemical reduction of Se(IV). The presence of Se(−II) was confirmed by UV-vis and ^{77}Se NMR spectroscopy. Experimental details about UV-vis and NMR spectroscopy can be found in the Appendix G.

4.7.1 Electrochemical synthesis of Se(−II)

As highlighted by [LIU '08b], three main ways were so far applied to produce selenide solutions:

- the chemical reduction of Se(0) by hydrazine (N_2H_4) [IIDA '11; IIDA '14]
- the hydrolysis of Al_2S under inert gas, which generated volatile hydrogen selenide which needs to be trapped [WAITKIN '46]
- the electrochemical reduction of Se(IV) or Se(0) in NH_4Cl or NaOH with a mercury pool electrode [DIENER '11; FINCK '12; LICHT '95; LINGANE '48; LIU '08b]

We opted for the last option since it is safer and allows more reproducible selenide concentration [LIU '08b]. The starting solution was made of 5 mmol L^{-1} of Se(IV) in 1 mol L^{-1} NH_4Cl at pH 8. A scheme representing the setup used for the electrochemical reduction of Se(IV) to Se(−II) is shown in **Fig. 4.58**. This experiment was performed in a glovebox under inert conditions (N_2). Prior to electrolysis, the solution was purged at least 30 minutes with argon. The applied potential was set at -1.55 V /AgCl (std NaCl).

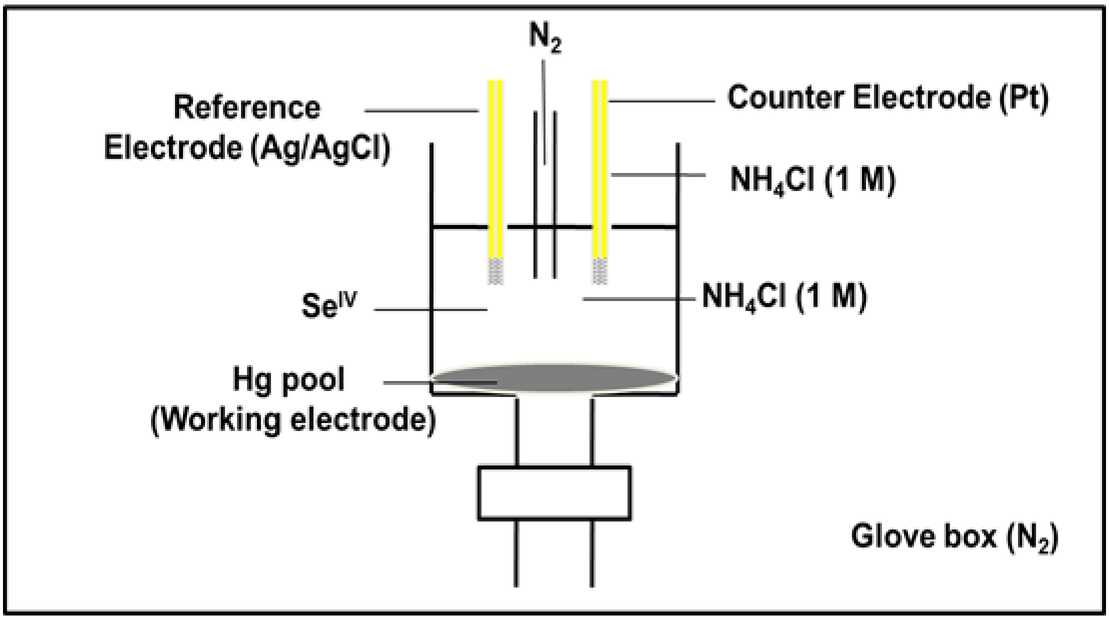

Fig. 4.58 Scheme of the electrochemical reduction of Se(IV) to Se(−II)

At the beginning, the selenite solution is colorless and turns rapidly red, due to the formation of amorphous red Se(0) colloids. After 3 – 4 hours, the solution is again colorless due to the generation of HSe$^-$ (**Fig. 4.59**).

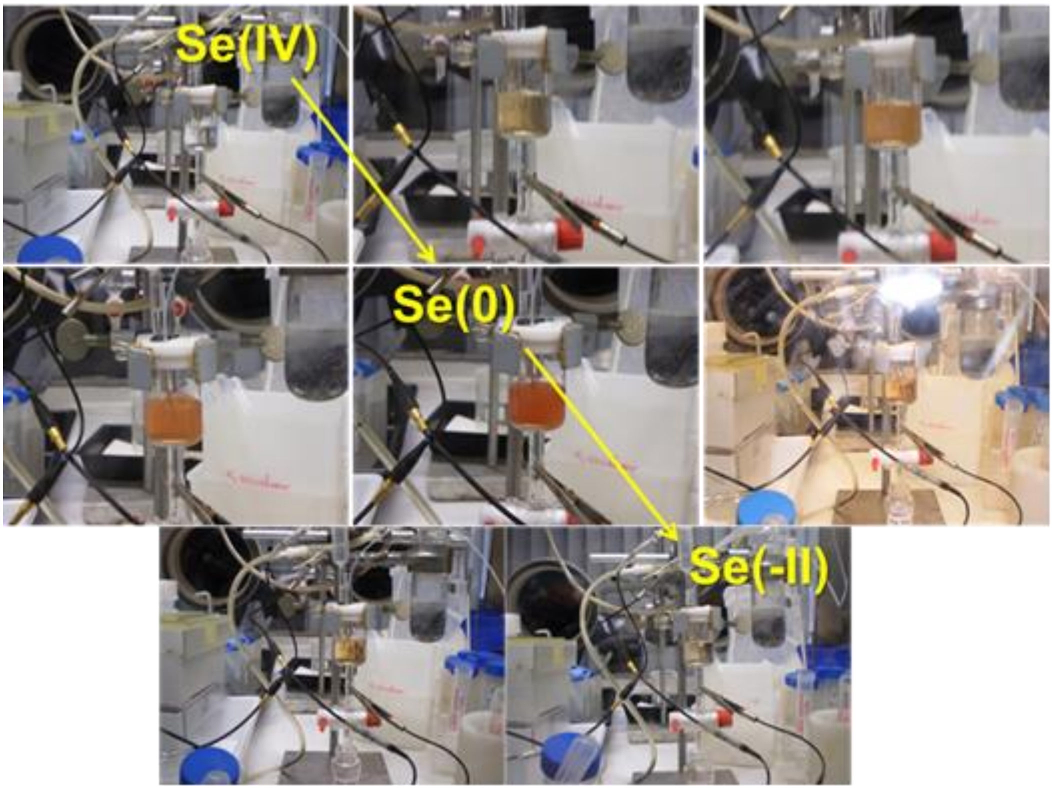

Fig. 4.59 Evolution of the selenium solution during the electrochemical reduction.

The obtained solution was characterized at first by UV-vis spectroscopy (**Fig. 4.60**). From the obtained 5 mmol L^{-1} Se(−II) solution, different concentrations ranging from 5 × 10^{-5} mol L^{-1} to 10^{-4} mol L^{-1}. All solutions were prepared in 1 mol L^{-1} NH_4Cl at pH 8. The UV-vis spectra exhibit one single peak at 247 nm, characteristic of the HSe^- species [IIDA '11; LICHT '95; LIU '08a].

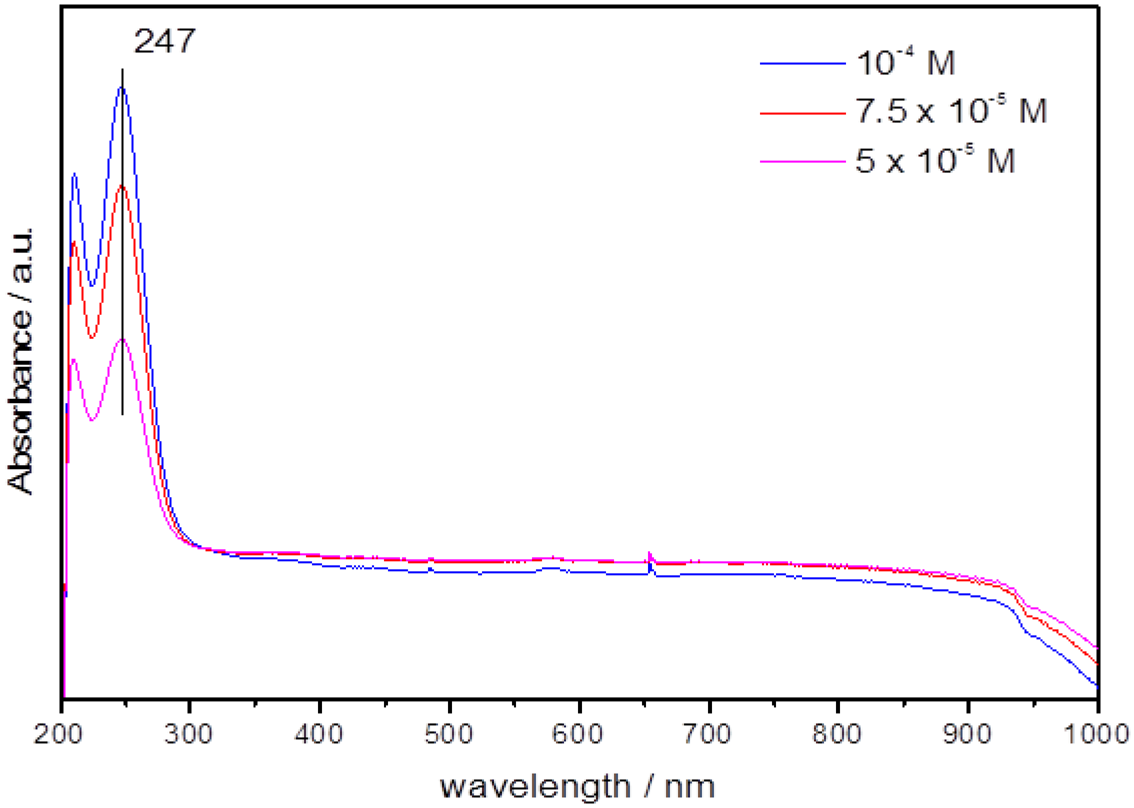

Fig. 4.60 UV-vis spectra of the Se(−II) solution at different concentrations.

Afterwards, 6 mL of the Se(−II) solution were mixed with 6 mL of hydrazine $N_2H_4.H_2O$ (98 %) in order to keep the Se(−II) stable for NMR spectroscopy. Indeed, Se(−II) solutions are extremely sensitive towards oxygen and can be extremely rapidly re-oxidized to Se(0) [LIU '08a]. NMR spectroscopy of solutions measured 1 day and 1 week after their preparation revealed a single signal at a chemical shift of −499 ppm (**Fig. 4.61**), in agreement with expected values for the HSe^- ion [DUDDECK '95]. In addition, no additional signals in other regions could be observed (data not shown), highlighted absence of re-oxidation of the HSe^- ion.

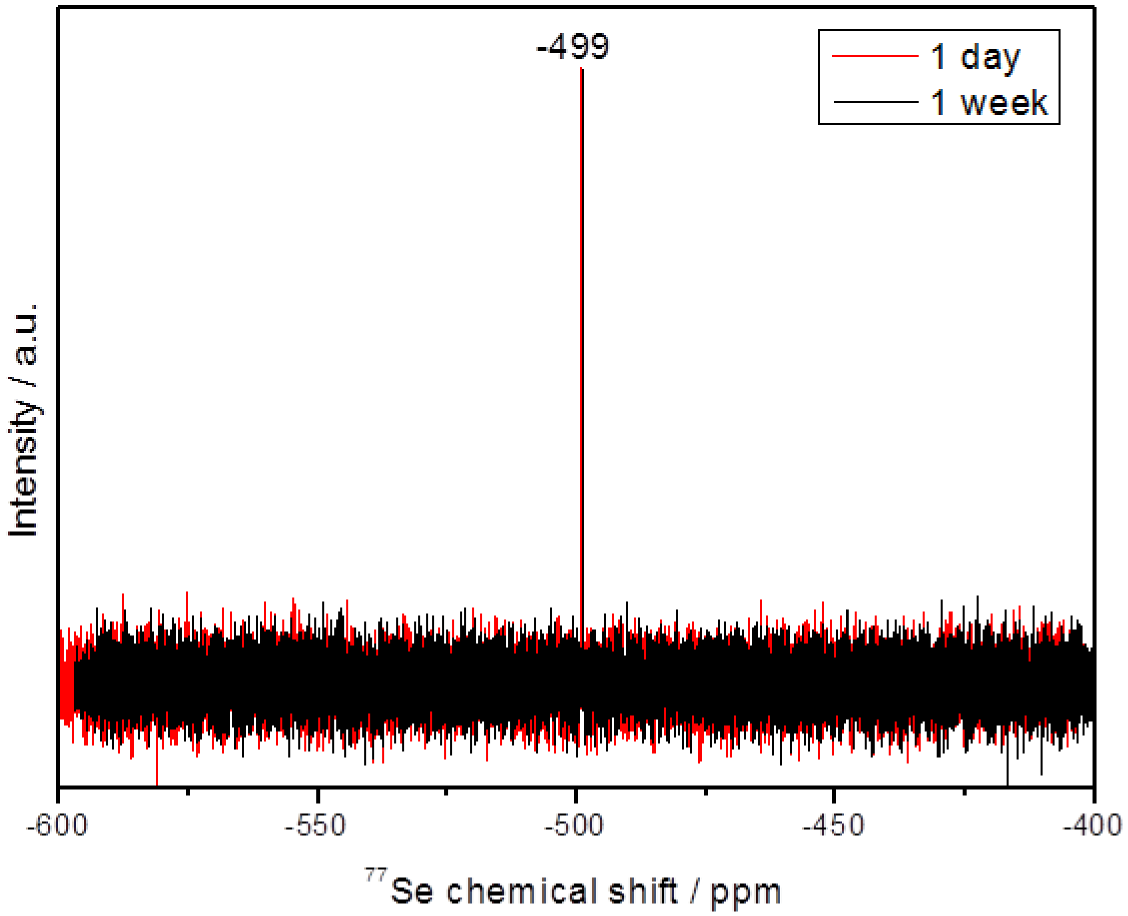

Fig. 4.61 ^{77}Se NMR of Se(−II) solution after 1 day and 1 week of storage.

4.7.2 Batch sorption experiments

Due to experimental difficulties in establishing the set-up for the electrochemical reduction of Se(IV) to Se(−II) and to keep the obtained solution stable, sorption experiments could not be started. They will be part of the VESPA II project, where the focus will be the study of sorption processes onto iron phases.

4.8 Implications on Se mobility in the context of nuclear waste disposals

Within the project VESPA, the aqueous selenium speciation has been thoroughly investigated. Impact of different oxidation states, concentration, pH, ionic strength and temperature as well as divalent cations such as Ca^{2+} and Mg^{2+} was studied by means of NMR, FT-IR and RAMAN.

The formation of Se(IV) oxoanion dimers occurs in aqueous solution as it was demonstrated by the combined spectroscopic and theoretical approach (data not shown) of this work. Hence, this data will serve as references for future spectroscopic investigations of the sorption processes of Se on mineral phases. The evaluation of these surface reactions requires a detailed knowledge of the spectral properties of the dominating aqueous species present at the interfaces under investigation. In particular, the occurrence of transient unknown species during the surface reactions is necessary to be identified spectroscopically. Thus, the spectral data presented in this work might be of invaluable help in future times.

During the last years the impact of elevated temperatures on the sorption processes attracts wide interest in the research field of deep ground repositories. The findings of this work evidenced that temperature dependent sorption behavior (at least up to 333 K) is not related to changes of the aqueous selenium speciation.

^{77}Se NMR spectroscopy was shown to be a helpful tool in determining the aqueous speciation of selenium and particularly its interactions with metal ions as well as to characterize the formed complexes in both the solution and the solid state. The results reveal the possibility of calcium ions to immobilize selenium in +IV oxidation state. However, neither calcium nor magnesium in the divalent state is able to precipitate and therefore immobilize selenium in its +VI oxidation state as it forms soluble complexes. These findings contribute to a deeper understanding for further investigations addressing the mobility of selenium oxyanions in the environment.

Sorption of selenate (SeO_4^{2-}) and selenite (SeO_3^{2-}) onto relevant phases such as iron corrosion products (hematite, maghemite), components of the geological barrier (δ-Al_2O_3 and kaolinite), and environmental ubiquitous model oxides (anatase) have been investigated. In general, it could be shown that the retention of selenite is much more effective than the one of selenate. For both Se-species the sorption is the highest on iron phases, whereas the sorption on clay minerals is very low. The retention of selenite and selenate is therefore supposed to be most efficient at the technical barrier of the repository.

For some selected systems, elevated temperature up to 333 K decreased the sorption of selenium oxyanions onto mineral phases. The impact of temperature was not due to changes in selenium aqueous speciation as explained above, but to modification of the surface properties of sorbing phases (i. e. the surface charge and the pH_{IEP}). Thermodynamic parameters relevant for thermodynamic databases like THEREDA, namely $\Delta_R G$, $\Delta_R H$ and $\Delta_R S$ have been calculated. The exothermic nature of the sorption processes was revealed. The reduction at elevated temperatures of the sorption capacity of mineral surfaces towards selenium(VI) and selenium(IV) might have drastic consequences in the context of nuclear waste management. Hence, an increased mobility of these species must be taken into account in future safety assessments.

For the first time, the impact of high ionic strength on selenium sorption was studied on δ-Al_2O_3. An increase of the ionic strength led to a significant decrease of both Se(IV) and Se(VI) sorption at which the decrease was more pronounced for the sorption of S(VI) than the one of Se(IV). Even at 1 M NaCl and within the pH range of pH 5 to 6, no more sorption of Se(VI) took place for Se(VI) concentrations, which resulted in an 80 to 90 % sorption at 0.01 M NaCl. Concerning Se(IV) at least around 40 % were sorbed at the same conditions. These results show, that especially in regard to repository-relevant ionic strengths, the speciation of selenium is essential in terms of retention.

Structural information on the sorbed complexes obtained by ATR FT-IR and EXAFS revealed the exclusive formation of inner-sphere complexes of selenium(IV) on the different mineral phases. Selenate mostly formed outer-sphere complexes, together with a small fraction of inner-sphere complexes on maghemite and hematite. On the surface of the iron phases and δ-Al_2O_3, a new type of outer-sphere complexes with a reduced symmetry could be identified for the first time. In summary, the spectroscopic results enabled to discriminate among two distinct types of outer-sphere complexes arising from selenate sorption on different mineral surfaces. Se retention through outer-sphere complexes was found to be highly reversible, giving rise to a high mobility for selenium(VI) in the near-field of nuclear waste repositories. However, selenium(IV) binding through inner-sphere complexes was more irreversible and thus can contribute to its long-term retardation.

Surface complexation modeling with FITEQL coupled to UCODE was performed for some systems for the first time. The parametrization of mechanistic sorption models, e. g. the number of sorbing sites, the number of surface species and their stoichiometry, was constrained by considering the information delivered by the applied spectroscopic techniques. The results will be implemented into the sorption database RES^{3}T. These new results will help to improve the description and prediction of selenium oxyanions reactive transport through the different retention barriers.

A setup could be established to generate Se(−II) from the electrochemical reduction of Se(IV). The formation of Se(−II) was confirmed by UV-vis and ^{77}Se NMR spectroscopy. This will serve as a basis for future investigations of the behavior of Se(−II) at the water/mineral interface.

4.9 Perspectives

The VESPA project could reach its goals to a very high degree. The results enabled a substantial improvement of the long-term safety assessment, namely the submodels concerning the selenium migration. This could be shown in a variety of before-after analyses comparing directly the effects of the newly derived Se sorption coefficients and solubility products onto the transport of Se through both salt rock and argillaceous rock. These computations were performed by the project partner GRS (see their final report) and showed a decrease in mobility of Se up to two orders of magnitude, i. e a substantial impact.

It is important to state here once again, that the pure numerical facts are only one outcome of the project. The newly gained process understanding on a molecular level, the identification and characterization of species and physico-chemical processes is to be put on an equal scale of relevance at least. The VESPA findings clearly increase confidence in the results of long-term safety assessments and reduce any associated uncertainties, also on a conceptual level. Here it is also worth mentioning that the combination of complementary spectroscopic and other tools (NMR, ATR FT-IR, EXAFS, quantum chemistry to name only the most prominent ones) was very efficacious and allowed the derivation of sensible chemical models for many Se systems. This multi-way approach certainly should be pushed forward with high intensity.

As usually is the outcome of such ambitious and large-scale projects, the number of answered questions is coupled to the identification of new challenges. The following paragraphs thus identify those research directions that are most essential for a further reduction in conservatism.

Any quantification of Se retention is strongly effected by sorption onto and incorporation into secondary iron phases. They are present either as corrosion products form the technical barrier or a natural component of the geotechnical backfill or the host rock itself. VESPA results combined with published studies form the literature showed that though nominally the same mineral phase was investigated sorption coefficients can vary significantly between solid samples differing in grain size, degree of crystallinity, specific surface area, topology, or preparation procedure. Thus a succeeding project should address these heterogeneities by investigating in parallel different specimens of, e. g., hematite, maghemite, goethite or magnetite simultaneously under identical experimental boundary conditions, thus reflecting their natural variability. These specimens could be either natural samples, commercially produced ones, or phases created in the laboratory following (several) reaction schemes. This would then allow for a separation of intrinsic physico-chemical properties of a single mineral and other effects imprinted by structural differences.

VESPA also signaled the high importance of lower oxidation states. In case of selenium this implies additional experiments with Se(0) and Se(-II). In a first step this involves the development of highly reproducible procedures to obtain (and keep) well-defined Se(0) and Se(-II) samples. In case of Se(0) biotechnology may prove as a very promising approach.

Eventually, a further development of the analytical and spectroscopic setups to increase sensitivity and reliability is necessary. The focus should be set on higher ionic strengths (as expected in salt rock and also northern German clay rocks) as well as higher temperatures. Various experiments could profit from the use of Se-75 as radioactive tracer with a half-life of about 120 days.

Acknowledgements

The authors would like to sincerely acknowledge all contributors to the project:

- Dipl.-Ing. Ursula Schaefer, Dipl.-Ing. Aline Ritter, Mrs. Sabrina Gurlit, Mrs. Ina Kapler and Mrs. Stefanie Schubert for ICP-MS and HG-AAS measurements.
- Mrs. Carola Eckardt for BET determination.
- Mrs. Andrea Scholz and Dr. Jörg Grenzer for XRD analysis.
- Dr. Arndt Mücklich and Dr. René Hübner for TEM measurements.
- Dr. Helfried Reuther for his support with Mössbauer spectroscopy.
- Dr. Dieter Schild (KIT-INE) for XPS measurements.
- Mrs. Heidrun Neubert, Mrs. Christa Müller, Mrs. Stephanie Schubert, Mrs. Birke Pfützner and Mr. Veit Zimmermann for their help during batch experiments.

- Mrs. Annegret Krzikalla and Mrs. Sandra Strehle for their assistance during samples preparation for NMR spectroscopy.

- Mrs. Christa Müller and Stephan Weiss for their technical assistance for electrophoretic mobility measurements.

- Dipl.-Ing. Aline Ritter, Mr. Steffen Domaschke and Mr. David Hering for their contribution through their training period of their Diploma and Bachelor degree.

- Dr. habil. Andreas Scheinost, Dr. Dipanjan Banerjee, Dr. Christoph Hennig, Dr. André Rossberg, Dr. Marisol Janeth Lozano Rodriguez and Dr. Butzbach Randolf for their kind assistance during XAS measurements.

- Dipl.-Ing. Karsten Heim, Dr. Katharina Müller and Dr. Harald Foerstendorf for their technical assistance for ATR FT-IR and helpful discussions.

- Dr. Erica Brendler (TUBAF) for her kind assistance with NMR spectroscopy.

- Dr. habil. Andreas Scheinost for the treatment and analysis of XAS data.

- Dr. Johannes Lützenkirchen (KIT-INE) for his support for surface complexation modeling.

4.10 Dissemination of results

4.10.1 International peer-reviewed publications

Jordan, N.; Scheinost, A.C.; Lützenkirchen J.; Franzen, C.; Weiss, S. Uptake of Se(IV) by anatase. *Environmental Science & Technology (submitted).*

Franzen, C.; Hering, D.; Jordan, N.; Grenzer, J.; Weiss, S. Retention of selenate onto transition alumina as a function of ionic strengths. *Chemical Geology (submitted).*

Jordan, N.; Domaschke, S.; Foerstendorf, H.; Scheinost, A.C.; Franzen, C.; Zimmermann, V.; Weiss, S.; Heim, K.; Hübner, R. Sorption of Se(VI) by hematite. *Geochimica et Cosmochimica Acta (submitted).*

Kretzschmar, J.; Jordan, N.; Brendler, E.; Tsushima, S.; Franzen, C.; Foerstendorf, H; Scheinost, A. C.; Heim, K; Brendler, V. The aqueous speciation of selenium oxyanions: impact of concentration, temperature and divalent cations. *Inorganic Chemistry (submitted)*.

Jordan, N.; Ritter, A.; Scheinost, A. C.; Weiß, S.; Schild, D.; Hübner, R. (2014). Selenium(IV) uptake by maghemite (γ-Fe_2O_3). *Environmental Science & Technology 48, 1665-1674*.

Jordan, N.; Müller, K.; Franzen, C.; Brendler, V. (2013): Temperature impact on the sorption of selenium(VI) onto anatase. *Journal of Colloid and Interface Science 390, 170-175.*

Jordan, N.; Ritter, A.; Foerstendorf, H.; Scheinost, A. C.; Weiß, S.; Heim, K.; Grenzer, J.; Mücklich, A.; Reuther, H. (2013). Adsorption mechanism of selenium(VI) onto maghemite. *Geochimica et Cosmochimica Acta 103, 63-75.*

Franzen, C.; Hering, D.; Jordan, N. (2013). Retention of selenate at the water-mineral interface in the context of salt dome repositories. Goldschmidt 2013, 25.-30.08.2013, Florence, Italy; *Mineralogical Magazine, Goldschmidt Abstracts 77(5), 1107*.

4.10.2 National and International Conferences

Franzen, C.; Hering, D.; Jordan, N.; Weiss, S.: Retention of selenium oxyanions at the water-mineral interface in the context of nuclear waste repositories. IMA 2014, 21st General Meeting of the International Mineralogical Association, 01.-05.09.2014, Gauteng province, South Africa (Oral).

Foerstendorf, H.; Jordan, N.; Heim, K.: Surface speciation of dissolved radionuclides on mineral phases derived from vibrational spectroscopic data. 248th ACS National Meeting & Exposition, 10.-14.08.2014, San Francisco, U.S.A. (Oral).

Jordan, N.; Domaschke, S.; Foerstendorf, H.; Scheinost, A. C.; Franzen, C.; Zimmermann, V.; Weiß, S.; Heim, K.: Uptake of selenium oxyanions by hematite. Goldschmidt 2014, 08.-13.06.2014, Sacramento, USA (Oral).

Foerstendorf, H.; Gückel, K.; Jordan, N.; Rossberg, A.; Brendler, V.: Surface speciation of dissolved radionuclides on mineral phases – A vibrational and X-ray absorption spectroscopic study. 5th Asia-Pacific Symposium on Radiochemistry (APSORC 13), 22.-27.09.2013, Kanazawa, Japan (Oral).

Jordan, N.; Domaschke, S.; Zimmermann, V.; Foerstendorf, H.; Scheinost, A. C.; Weiß, S.; Heim, K.: Sorption of selenium oxyanions onto hematite. 14th International Conference on the Chemistry and Migration Behaviour of Actinides and Fission Products in the Geosphere, 08.-13.09.2013, Brighton, United Kingdom (Poster).

Franzen, C.; Hering, D.; Jordan, N.: Retention of selenate at the water-mineral interface in the context of salt dome repositories. Goldschmidt 2013, 25.-30.08.2013, Florence, Italy (Poster).

Kretzschmar, J.; Jordan, N.; Brendler, E.: 77Se-NMR spectroscopic investigations on aqueous selenium speciation at higher temperatures and in the presence of divalent metal ions. EURACT-NMR Workshop, 17.-19.07.2013, Karlsruhe, Germany (Poster).

Jordan, N.; Ritter, A.; Foerstendorf, H.; Scheinost, A.C.; Heim, K.; Weiß, S.; Brendler, V.: Sorption of Se(VI) and Se(IV) oxyanions onto maghemite: a macroscopic and spectroscopic study. SELEN 2012- Selenium in geological, hydrological and biological systems. 08.-09.10.2012, Karlsruhe, Deutschland (Oral).

Franzen, C.; Hering, D.; Jordan, N.: The impact of salinity on the sorption of selenate onto aged γ−Al2O3 in the context of salt dome repositories. European Mineralogical Conference. 02.-06.09.2012. Frankfurt, Deutschland (Oral).

Franzen, C.; Jordan, N.; Müller, K.: Influence of Temperature on the Sorption of Selenate onto Anatase. Experimental Mineralogy, Petrology and Geochemistry. 04.-07.03.2012. Kiel, Deutschland (Oral).

Franzen, C.; Jordan, N.; Müller, K.; Meusel, T.; Brendler, V.: Temperature Impact on the Sorption of Selenate onto Anatase. HiTAC Workshop, 09.11.2011, Karlsruhe, Deutschland (Poster).

Jordan, N.; Foerstendorf, H.; Scheinost, A. C.; Lützenkirchen, J.; Schild, D.; Weiß, S.; Heim, K.; Brendler, V.: Uptake of selenium(VI) and selenium(IV) onto anatase. Geological Disposal of Radioactive Waste: Underpinning Science and Technology, 18.-20.10.2011, Loughborough, England (Poster).

Jordan, N.; Müller, K.; Franzen, C.; Foerstendorf, H.; Weiß, S.; Heim, K.; Brendler, V.: 13th International Conference on the Chemistry and Migration Behaviour of Actinides and Fission Products in the Geosphere, 18.-23.09.2011, Beijing, China (Poster).

4.11 References (chapter 4)

Abdullah, M. I., Shiyu, Z., and Mosgren, K. (1995): Arsenic and selenium species in the oxic and anoxic waters of Oslof jord, Norway. *Marine Pollution Bulletin* 31, 116-126.

Abrams, M. M., Burau, R. G., and Zasoski, R. J. (1990): Organic selenium distribution in selected California soils. *Soil Science Society of America Journal* 54, 979-982.

Allan, C. B., Lacourciere, G. M., and Stadtman, T. C. (1999): Responsiveness of selenoproteins to dietary selenium. *Annual Review of Nutrition* 19, 1-16.

Altmaier, M., Metz, V., Neck, V., Muller, R., and Fanghanel, T. (2003): Solid-liquid equilibria of $Mg(OH)_2$(cr) and $Mg_2(OH)_3Cl\cdot 4H_2O$(cr) in the system Mg-Na-H-OH-O-Cl-H_2O at 25 °C. *Geochimica Et Cosmochimica Acta* 67, 3595-3601.

Altmaier, M., Neck, V., and Fanghanel, T. (2008): Solubility of Zr(IV), Th(IV) and Pu(IV) hydrous oxides in $CaCl_2$ solutions and the formation of ternary Ca-M(IV)-OH complexes. *Radiochimica Acta* 96, 541-550.

Amrhein, C., Hunt, M. L., Roberson, M. J., Yannoff, J. A., Qiu, S. R., and Lai, H.-F. (1998): The use of XANES, STM, and XPS to identify the precipitation products formed during the reaction of U, Cr, and Se with zero-valent iron.*Goldschmidt Conference*, Toulouse, France.

ANDRA (2005a): Synthèse: Evaluation de la faisabilité du stockage géologique en formation argileuse. In: argileuse, S. E. d. l. f. d. s. g. e. f. (Ed.). Agence Nationale pour la gestion des Déchets RAdioactifs, Châtenay-Malabry.

ANDRA (2005b): Synthèse: Evaluation de la faisabilité du stockage géologique en formation argileuse.*Dossier 2005 Argile*.

Ankudinov, A. L. and Rehr, J. J. (1997): Relativistic calculations of spin-dependent x-ray-absorption spectra. *Physical Review B* 56, R1712-R1715.

Aretaki, I. N. I. and Kallithrakas-Kontos, N. G. (2009): Total reflection X-ray fluorescence selenium analysis after reduction and quartz reflector adsorption. *Journal of Analytical Atomic Spectrometry* 24, 979-982.

Arnek, R. and Barcza, L. (1972): Thermochemical studies of hydrolytic reactions .2. Polyselenite equilibria in various ionic media. *Acta Chemica Scandinavica* 26, 213-217.

Auffan, M., Rose, J., Proux, O., Borschneck, D., Masion, A., Chaurand, P., Hazemann, J. L., Chaneac, C., Jolivet, J. P., Wiesner, M. R., Van Geen, A., and Bottero, J. Y. (2008): Enhanced adsorption of arsenic onto maghemites nanoparticles: As(III) as a probe of the surface structure and heterogeneity. *Langmuir* 24, 3215-3222.

Bacon, M. and Ingledew, W. J. (1989): The reductive reactions of thiobacillus-ferrooxidans on sulfur and selenium. *Fems Microbiology Letters* 58, 189-194.

Baes Jr., C. F. and Mesmer, R. E. (1976): *The hydrolysis of cations*. Wiley & Sons New York.

Balistrieri, L. S. and Chao, T. T. (1987): Selenium adsorption by goethite. *Soil Science Society of America Journal* 51, 1145-1151.

Balistrieri, L. S. and Chao, T. T. (1990): Adsorption of selenium by amorphous iron oxyhydroxide and manganeses-dioxide. *Geochimica et Cosmochimica Acta* 54, 739-751.

Ball, S. and Milne, J. (1995): Studies on the interaction of selenite and selenium with sulfur donors. Part 3. Sulfite. *Canadian Journal of Chemistry-Revue Canadienne De Chimie* 73, 716-724.

Banuelos, G. S. and Lin, Z. Q. (2007): Acceleration of selenium volatilization in seleniferous agricultural drainage sediments amended with methionine and casein. *Environmental Pollution* 150, 306-312.

Barcza, L. and Sillen, L. G. (1971): Equilibrium studies of polyanions .19. Polyselenite equilibria in various ionic media. *Acta Chemica Scandinavica* 25, 1250-1260.

Bargar, J. R., Towle, S. N., Brown, G. E., and Parks, G. A. (1996): Outer-sphere Pb(II) adsorbed at specific surface sites on single crystal alpha-alumina. *Geochimica et Cosmochimica Acta* 60, 3541-3547.

Bataille, M. C. and Galley, R. (2011): Rapport de l'Office Parlementaire d'Evaluation des Choix Scientifiques et Technologiques No 612 (1997 / 1998) http://www.senat.fr/rap/o97-612/o97-612.html.

Beauwens, T., De Canniere, P., Moors, H., Wang, L., and Maes, N. (2005): Studying the migration behaviour of selenate in Boom Clay by electromigration. *Engineering Geology* 77, 285-293.

Ben Lagha, S., Crusset, D., Mabille, I., Tran, M., Bernard, M. C., and Sutter, E. (2007): Corrosion of iron: A study for radioactive waste canisters. *Journal of Nuclear Materials* 362, 485-492.

Benedicto, A., Missana, T., and Degueldre, C. (2013): Predictions of TiO_2-driven migration of Se(IV) based on an integrated study of TiO_2 colloid stability and Se(IV) surface adsorption. *Science of the Total Environment* 449, 214-222.

Benelli, C., Divaira, M., Noccioli, G., and Sacconi, L. (1977): Synthesis, Properties, and Characterization of Sulfato and Selenato Complexes of Cobalt(II) and Nickel(II) with 1,1,1-Tris(diphenylphosphinomethyl)ethane (p_3) - Crystal and Molecular Structures of $Co(p_3)SO_4$ and $Ni(p_3)SeO_4$. *Inorganic Chemistry* 16, 182-187.

Bienvenu, P., Cassette, P., Andreoletti, G., Be, M. M., Comte, J., and Lepy, M. C. (2007): A new determination of Se-79 half-life. *Applied Radiation and Isotopes* 65, 355-364.

Blaylock, M. J. and James, B. R. (1993): Selenite and Selenate quantification by hydride generation atomic-absorption spectrometry, ion chromatography, and colorimetry. *Journal of Environmental Quality* 22, 851-857.

Boguslavsky, Y. and Margel, S. (2008): Synthesis and characterization of poly (divinylbenzene)-coated magnetic iron oxide nanoparticles as precursor for the formation of air-stable carbon-coated iron crystalline nanoparticles. *Journal of Colloid and Interface Science* 317, 101-114.

Boult, K. A., Cowper, M. M., Heath, T. G., Sato, H., Shibutani, T., and Yui, M. (1998): Towards an understanding of the sorption of U(V) and Se(IV) on sodium bentonite. *Journal of Contaminant Hydrology* 35, 141-150.

Bourikas, K., Hiemstra, T., and Van Riemsdijk, W. H. (2001): Adsorption of Molybdate Monomers and Polymers on Titania with a Multisite Approach. *Journal of Physical Chemistry B* 105, 2393-2403.

Brand, R. A. (1987): Improving the validity of hyperfine fields distributions from magnetic-alloys .1. Unpolarized source. *Nucl. Instrum. Methods Phys. Res. Sect. B-Beam Interact. Mater. Atoms* 28, 398-416.

Brasser, T., Droste, J., Müller-Lyda, I., Neles, J., Sailer, M., Schmidt, G., and Steinhoff, M. (2008): Endlagerung wärmeentwickelnder radioaktiver Abfälle in Deutschland. GRS-247. Gesellschaft für Anlagen und Reaktorsicherheit (GRS) mbH and Öko-Institut e.V., Braunschweig / Darmstadt.

Breynaert, E., Bruggeman, C., and Maes, A. (2008): XANES-EXAFS analysis of se solid-phase reaction products formed upon contacting Se(IV) with FeS_2 and FeS. *Environmental Science & Technology* 42, 3595-3601.

Bruggeman, C., Maes, A., Vancluysen, J., and Vandenmussele, P. (2005): Selenite reduction in Boom clay: Effect of FeS_2, clay minerals and dissolved organic matter. *Environmental Pollution* 137, 209-221.

Bruggeman, C., Vancluysen, J., and Maes, A. (2002): New selenium solution speciation method by ion chromatography plus gamma counting and its application to FeS_2-controlled reducing conditions. *Radiochimica Acta* 90, 629-635.

Bueno, M. and Potin-Gautier, M. (2002): Solid-phase extraction for the simultaneous preconcentration of organic (selenocystine) and inorganic [Se(IV), Se(VI)] selenium in natural waters. *Journal of Chromatography A* 963, 185-193.

Carlson, J. J. and Kawatra, S. K. (2011): Effects of CO_2 on the zeta potential of hematite. *International Journal of Mineral Processing* 98 8-14.

Carlson, J. J. and Kawatra, S. K. (2013): Factors Affecting Zeta Potential of Iron Oxides. *Mineral Processing and Extractive Metallurgy Review: An International Journal* 34, 269-303.

Catalano, J. G., Park, C., Fenter, P., and Zhang, Z. (2008): Simultaneous inner- and outer-sphere arsenate adsorption on corundum and hematite. *Geochimica et Cosmochimica Acta* 72, 1986-2004.

Chambers, S. A., Kim, Y. J., and Gao, Y. (1998): Fe 2p Core-Level Spectra for Pure, Epitaxial a-Fe_2O_3(0001), g-Fe_2O_3(001), and Fe_3O_4(001). *Surface Science Spectra* 5, 219-228.

Charlet, L., Morin, G., Rose, J., Wang, Y. H., Auffan, M., Burnol, A., and Fernandez-Martinez, A. (2011): Reactivity at (nano)particle-water interfaces, redox processes, and arsenic transport in the environment. *Comptes Rendus Geoscience* 343, 123-139.

Charlet, L., Scheinost, A. C., Tournassat, C., Greneche, J. M., Gehin, A., Fernandez-Martinez, A., Coudert, S., Tisserand, D., and Brendle, J. (2007): Electron transfer at the mineral/water interface: Selenium reduction by ferrous iron sorbed on clay. *Geochimica et Cosmochimica Acta* 71, 5731-5749.

Chen, Y. W., Truong, H. Y. T., and Belzile, N. (2009): Abiotic formation of elemental selenium and role of iron oxide surfaces. *Chemosphere* 74, 1079-1084.

Chin, A. B. and Yaacob, I. I. (2006): Synthesis and characterization of iron oxides nanoparticles, *Fracture and Strength of Solids VI, Pts 1 and 2*. Trans Tech Publications Ltd, Stafa-Zurich.

Chipera, S. J. and Bish, D. L. (2001): Baseline Studies of the Clay Minerals Society Source Clays: Powder X-ray Diffraction Analyses. *Clays and Clay Minerals* 49, 398-409.

Comarmond, M. J., Payne, T. E., Harrison, J. J., Thiruvoth, S., Wong, H. K., Aughterson, R. D., Lumpkin, G. R., Müller, K., and Foerstendorf, H. (2011): Uranium sorption on various forms of titanium dioxide - Influence of surface area, surface charge, and impurities. *Environmental Science & Technology* 45, 5536-5542.

Comte, J., Bienvenu, P., Brochard, E., Fernandez, J. M., and Andreoletti, G. (2003): Determination of selenium-79 in solutions of fission products after pretreatment by ion exchange chromatography and ETV-ICP-MS. *Journal of Analytical Atomic Spectrometry* 18, 702-707.

Cooke, T. D. and Bruland, K. W. (1987): Aquatic chemistry of selenium - evidence of biomethylation. *Environmental Science & Technology* 21, 1214-1219.

Cooper, J. N., Woods, M., Sullivan, J. C., and Deutsch, E. (1976): Kinetics of the Oxidation of Selenium(IV) by Neptunium(VII) in Aqueous Acidic Perchlorate Media. *Inorganic Chemistry* 15, 2862-2864.

Cornell, R. M. and Schwertmann, U. (2003): The iron oxides: structure, properties, reactions, occurrences, and uses. *Wiley-VCH*.

Cui, D., Puranen, A., Devoy, J., Scheidegger, A., Leupin, O. X., Wersin, P., Gens, R., and Spahiu, K. (2009): Reductive immobilization of Se-79 by iron canister under simulated repository environment. *Journal of Radioanalytical and Nuclear Chemistry* 282, 349-354.

Curti, E., Froideval-Zumbiehl, A., Gunther-Leopold, I., Martin, M., Bullemer, A., Linder, H., Borca, C. N., and Grolimund, D. (2014): Selenium redox speciation and coordination in high-burnup UO_2 fuel: Consequences for the release of ^{79}Se in a deep underground repository. *Journal of Nuclear Materials* 453, 98-106.

Cutter, G. A. (1978): Species determination of selenium in natural-waters. *Analytica Chimica Acta* 98, 59-66.

Cuvanova, S., Lovas, M., Matik, M., and Vaclavikova, M. (2007): Microwave hydrothermal synthesis of maghemite nanoparticles as a precursor of magnetic fluids. *Magnetohydrodynamics* 43, 453-457.

Das, J., Das, D., Dash, G. P., and Parida, K. M. (2002): Studies on Mg/Fe hydrotalcite-like-compound (HTlc) - I. Removal of inorganic selenite (SeO_3^{2-}) from aqueous medium. *Journal of Colloid and Interface Science* 251, 26-32.

Das, J., Patra, B. S., Baliarsingh, N., and Parida, K. M. (2007): Calcined Mg-Fe-CO_3 LDH as an adsorbent for the removal of selenite. *Journal of Colloid and Interface Science* 316, 216-223.

Dash, S. S. and Parida, K. M. (2007): Studies on selenite adsorption using manganese nodule leached residues. *Journal of Colloid and Interface Science* 307, 333-339.

Dauchy, X., Potingautier, M., Astruc, A., and Astruc, M. (1994): Analytical methods for the speciation of selenium-compounds - a review. *Fresenius Journal of Analytical Chemistry* 348, 792-805.

De Gregori, I., Lobos, M. G., and Pinochet, H. (2002): Selenium and its redox speciation in rainwater from sites of Valparaiso region in Chile, impacted by mining activities of copper ores. *Water Research* 36, 115-122.

Deng, D. Y., Zhou, J. R., Ai, X., Yang, L., Hou, X. D., and Zheng, C. B. (2012): Ultrasensitive determination of selenium by atomic fluorescence spectrometry using nano-TiO_2 pre-concentration and in situ hydride generation. *Journal of Analytical Atomic Spectrometry* 27, 270-275.

Dhillon, S. K. and Dhillon, K. S. (2000): Selenium adsorption in soils as influenced by different anions. *J. Plant Nutr. Soil Sci.* 163, 577-582.

Diener, A. and Neumann, T. (2011): Synthesis and incorporation of selenide in pyrite and mackinawite. *Radiochimica Acta* 99, 791-798.

Diener, A., Neumann, T., Kramar, U., and Schild, D. (2012): Structure of selenium incorporated in pyrite and mackinawite as determined by XAFS analyses. *Journal of Contaminant Hydrology* 133, 30-39.

Dikshitulu, L. S. A., Vani, P., and Kumar, B. V. (1984): Kinetics and mechanism of oxidation of selenium(IV) by n-bromosuccinimide. *Journal of the Indian Chemical Society* 61, 385-388.

Dikshitulu, L. S. A., Vani, P., and Rao, V. H. (1981): Kinetics and mechanism of oxidation of selenium(IV) by chloramine-T. *Indian journal of chemistry Section A* 20, 36-39.

Djogic, R., Pizeta, I., and Zelic, M. (2000): Voltammetric study of uranyl-selenium interactions. *Analytica Chimica Acta* 404, 159-166.

Duc, M., Lefevre, G., and Fedoroff, M. (2006): Sorption of selenite ions on hematite. *Journal of Colloid and Interface Science* 298, 556-563.

Duc, M., Lefevre, G., Fedoroff, M., Jeanjean, J., Rouchaud, J. C., Monteil-Rivera, F., Dumonceau, J., and Milonjic, S. (2003): Sorption of selenium anionic species on apatites and iron oxides from aqueous solutions. *Journal of Environmental Radioactivity* 70, 61-72.

Duddeck, H. (1995): Selenium-77 nuclear magnetic resonance spectroscopy. *Progress in Nuclear Magnetic Resonance Spectroscopy* 27, 1-323.

Dulnee, S., Banerjee, D., Merkel, B. J., and Scheinost, A. C. (2013): Surface Complexation and Oxidation of Sn^{II} by Nanomagnetite. *Environmental Science & Technology* 47, 12852−12859.

Dutta, B., Jana, S., Bhattacharjee, A., Gutlich, P., Iijima, S. I., and Koner, S. (2010): g-Fe_2O_3 nanoparticle in NaY-zeolite matrix: Preparation, characterization, and heterogeneous catalytic epoxidation of olefins. *Inorganica Chimica Acta* 363, 696-704.

Ebert, M. and Havlicek, D. (1981): Calcium selenites. *Collection of Czechoslovak Chemical Communications* 46, 1740-1747.

El-Shafey, E. I. (2007a): Removal of Se(IV) from aqueous solution using sulphuric acid-treated peanut shell. *Journal of Environmental Management* 84, 620-627.

El-Shafey, E. I. (2007b): Sorption of Cd(II) and Se(IV) from aqueous solution using modified rice husk. *Journal of Hazardous Materials* 147, 546-555.

Elrashidi, M. A., Adriano, D. C., Workman, S. M., and Lindsay, W. L. (1987): Chemical-equilibria of selenium in soils - a theoretical development. *Soil Science* 144, 141-152.

Elzinga, E. J., Tang, Y. Z., McDonald, J., DeSisto, S., and Reeder, R. J. (2009): Macroscopic and spectroscopic characterization of selenate, selenite, and chromate adsorption at the solid-water interface of g-Al_2O_3. *Journal of Colloid and Interface Science* 340, 153-159.

Fendorf, S., Eick, M. J., Grossl, P., and Sparks, D. L. (1997): Arsenate and chromate retention mechanisms on goethite .1. Surface structure. *Environmental Science & Technology* 31, 315-320.

Fernandez-Martinez, A. and Charlet, L. (2009): Selenium environmental cycling and bioavailability: a structural chemist point of view. *Rev. Environ. Sci. Biotechnol.* 8, 81-110.

Finck, N., Dardenne, K., Bosbach, D., and Geckeis, H. (2012): Selenide Retention by Mackinawite. *Environmental Science & Technology* 46, 10004-10011.

Floor, G. H., Margui, E., Hidalgo, M., Queralt, I., Kregsamer, P., Streli, C., and Roman-Ross, G. (2013): Study of selenium sorption processes in volcanic ash using Total Reflection X-ray Fluorescence (TXRF). *Chemical Geology* 352, 19-26.

Fukami, T. and Chen, R. H. (2003): Refinement of crystal structure of Na_2SeO_4 at room temperature. *Journal of the Physical Society of Japan* 72, 3299-3300.

Fukushi, K. and Sverjensky, D. A. (2007): A surface complexation model for sulfate and selenate on iron oxides consistent with spectroscopic and theoretical molecular evidence. *Geochimica et Cosmochimica Acta* 71, 1-24.

Funke, H., Scheinost, A. C., and Chukalina, M. (2005): Wavelet analysis of extended x-ray absorption fine structure data. *Physical Review B* 71, 94110-1-94110-7.

Ganelina, E. S., Kuz'micheva, V. P., and Krasnopol'skaya, M. B. (1973): State of the selenite ion in aqueous solution. *Russian Journal of Inorganic Chemistry* 18, 698-700.

Giester, G. and Miletich, R. (1995): Crystal structure and thermal decomposition of the coquimbite-type compound $Fe_2(SeO_4)_3.9H_2O$. *Neues Jahrbuch für Mineralogie - Monatshefte* 5, 211-223.

Gissel-Nielsen, G., Gupta, U. C., Lamand, M., and Westermarck, T. (1984): Selenium in soils and plants and its importance in livestock and human-nutrition. *Adv. Agron.* 37, 397-460.

Glasoe, P. K. and Long, F. A. (1960): Use of glass electrodes to measure acidities in deuterium oxide. *Journal of Physical Chemistry* 64, 188-190.

Glass, R. S., Singh, W. P., Jung, W., Veres, Z., Scholz, T. D., and Stadtman, T. C. (1993): Monoselenophosphate: synthesis, characterization, and identity with the prokaryotic biological selenium donor, compound SePX. *Biochemistry* 32, 12555-12559.

Goh, K. H. and Lim, T. T. (2004): Geochemistry of inorganic arsenic and selenium in a tropical soil: effect of reaction time, pH, and competitive anions on arsenic and selenium adsorption. *Chemosphere* 55, 849-859.

Goldberg, S. (2014): Macroscopic Experimental and Modeling Evaluation of Selenite and Selenate Adsorption Mechanisms on Gibbsite. *Soil Science Society of America Journal* 78, 473-479.

Gomez-Ariza, J. L., Sanchez-Rodas, D., Morales, E., Herrgott, O., and Marr, I. L. (1999): Inorganic and organic selenium compound speciation with coupled HPLC-MW-HG-AFS. *Applied Organometallic Chemistry* 13, 783-787.

Greiver, T. N. and Zaitseva, I. G. (1967): Interaction of selenium with sulfide solutions and of sulfur with selenide solutions. *Russian Journal of Applied Chemistry* 40, 1623-1626.

Greiver, T. N., Zaitseva, I. G., and Saldau, E. P. (1971): Sodium sulfoselenides. *Zhurnal Prikladnoi Khimii* 44, 1689-&.

Grenthe, I., Fuger, J., Konings, R. J. M., Lemire, R. J., Muller, A. B., Nguyen-Trung, C., and Wanner, H. (1992): *Chemical Thermodynamics of Uranium*. North Holland Elsevier Science Publishers B. V., Amsterdam, The Netherlands.

Gu, B. H., Schmitt, J., Chen, Z. H., Liang, L. Y., and McCarthy, J. F. (1994): Adsorption and desorption of natural organic-matter on iron-oxide - mechanisms and models. *Environmental Science & Technology* 28, 38-46.

Gustafsson, J., Mikkola, P., Jokinen, M., and Rosenholm, J. B. (2000): The influence of pH and NaCl on the zeta potential and rheology of anatase dispersions. *Colloids and Surfaces a-Physicochemical and Engineering Aspects* 175, 349-359.

Gustafsson, J. P. and Johnsson, L. (1994): The association between selenium and humic substances in forested ecosystems - laboratory evidence. *Applied Organometallic Chemistry* 8, 141-147.

Hanaor, D. A. H. and Sorrell, C. C. (2011): Review of the anatase to rutile phase transformation. *Journal of Materials Science* 46, 855-874.

Harrison, J. B. and Berkheiser, V. E. (1982): Anion interactions with freshly prepared hydrous iron-oxides. *Clays and Clay Minerals* 30, 97-102.

Hasan, S. H. and Ranjan, D. (2010): Agro-Industrial Waste: A Low-Cost Option for the Biosorptive Remediation of Selenium Anions. *Industrial & Engineering Chemistry Research* 49, 8927-8934.

Hausner, D. B., Bhandari, N., Pierre-Louis, A. M., Kubicki, J. D., and Strongin, D. R. (2009): Ferrihydrite reactivity toward carbon dioxide. *Journal of Colloid and Interface Science* 337, 492-500.

Hayashi, H., Kanie, K., Shinoda, K., Muramatsu, A., Suzuki, S., and Sasaki, H. (2009): pH-dependence of selenate removal from liquid phase by reductive Fe(II)-Fe(III) hydroxysulfate compound, green rust. *Chemosphere* 76, 638-643.

Hayes, K. F., Papelis, C., and Leckie, J. O. (1988): Modeling ionic-strength effects on anion adsorption at hydrous oxide solution interfaces. *Journal of Colloid and Interface Science* 125, 717-726.

Hayes, K. F., Roe, A. L., Brown, G. E., Hodgson, K. O., Leckie, J. O., and Parks, G. A. (1987): In situ X-ray absorption study of surface complexes: Selenium oxyanions on a-FeOOH. *Science* 238, 783-786.

He, M., Jiang, S., Jiang, S., Diao, L., Wu, S., and Li, C. (2002): Measurement of the half-life of ^{79}Se with PX-AMS. *Nuclear Instruments and Methods in Physics Research Section B: Beam Interactions with Materials and Atoms* 194, 393-398.

Hiemstra, T., Rietra, R., and Van Riemsdijk, W. H. (2007): Surface complexation of selenite on goethite: MO/DFT geometry and charge distribution. *Croatica Chemica Acta* 80, 313-324.

Hiemstra, T. and Van Riemsdijk, W. H. (1996): A Surface Structural Approach to Ion Adsorption: The Charge Distribution (CD) Model. *Journal of Colloid and Interface Science* 179, 488-508.

Hiemstra, T. and Van Riemsdijk, W. H. (1999): Surface structural ion adsorption modeling of competitive binding of oxyanions by metal (hydr)oxides. Journal of Colloid and Interface Science 210, 182-193.

Huang, T. (2013): Kinetic and Thermodynamic Studies on Removal of Selenium from Aqueous Solution by Using Nano-TiO2. Asian Journal of Chemistry 25, 2125-2128.

Huber, F., Schild, D., Vitova, T., Rothe, J., Kirsch, R., and Schäfer, T. (2012): U(VI) removal kinetics in presence of synthetic magnetite nanoparticles. Geochimica et Cosmochimica Acta 96, 154-173.

Hurel, C. and Marmier, N. (2006): Sorption of selenium(IV) on mineral mixtures: role of minor phases in the modelling part. Mat. Res. Soc. Symp. Proc. 932, 967-974.

Iida, Y., Tanaka, T., Yamaguchi, T., and Nakayama, S. (2011): Sorption Behavior of Selenium(-II) on Rocks under Reducing Conditions. Journal of Nuclear Science and Technology 48, 279-291.

Iida, Y., Yamaguchi, T., and Tanaka, T. (2014): Sorption behavior of hydroselenide (HSe-) onto iron-containing minerals. Journal of Nuclear Science and Technology 51, 305-322.

Ike, M., Takahashi, K., Fujita, T., Kashiwa, M., and Fujita, M. (2000): Selenate reduction by bacteria isolated from aquatic environment free from selenium contamination. Water Research 34, 3019-3025.

Jackson, B. P. and Miller, W. P. (1999): Soluble arsenic and selenium species in fly ash organic waste-amended soils using ion chromatography inductively coupled plasma mass spectrometry. Environmental Science & Technology 33, 270-275.

Jadhav, R. A., Agnihotri, R., Gupta, H., and Fan, L. S. (2000): Mechanism of selenium sorption by activated carbon. Canadian Journal of Chemical Engineering 78, 168-174.

Janickis, J. and Gutmanaite, H. (1936): The condition of selinium acid salts of sodium, potassium, and ammonium in aqueous solution. Zeitschrift für anorganische und allgemeine Chemie 227 1-16.

Jayaweera, G. R. and Biggar, J. W. (1996): Role of redox potential in chemical transformations of selenium in soils. Soil Science Society of America Journal 60, 1056-1063.

Jegadeesan, G., Mondal, K., and Lalvani, S. B. (2003): Comparative study of selenite adsorption on carbon based adsorbents and activated alumina. Environmental Technology 24, 1049-1059.

Jiang, S., Guo, J., Jiang, S., Li, C., Cui, A., He, M., Wu, S., and Li, S. (1997): Determination of the half-life of 79Se with the accelerator mass spectrometry technique. Nuclear Instruments and Methods in Physics Research Section B: Beam Interactions with Materials and Atoms 123, 405-409.

Jiang, S., He, M., Diao, L., Li, C., Gou, J., and Wu, S. (2002): Re-measurement of the half-life of 79Se. Nuclear Instruments and Methods in Physics Research Section A: Accelerators, Spectrometers, Detectors and Associated Equipment 489, 195-201.

Jiang, S. S., He, M., Diao, L. J., Guo, J. R., and Wu, S. Y. (2001): Remeasurement of the half-life of 79Se with the projectile x-ray detection method. Chinese Physics Letters 18, 746-749.

Johnson, L., Günther-Leopold, I., Kobler Waldis, J., Linder, H. P., Low, J., Cui, D., Ekeroth, E., Spahiu, K., and Evins, L. Z. (2012): Rapid aqueous release of fission products from high burn-up LWR fuel: Experimental results and correlations with fission gas release. Journal of Nuclear Materials 420, 54–62.

Johnson, T. M. and Bullen, T. D. (2003): Selenium isotope fractionation during reduction by Fe(II)-Fe(III) hydroxide-sulfate (green rust). Geochim. Cosmochim. Acta 67, 413-419.

Jordan, N., Foerstendorf, H., Weiss, S., Heim, K., Schild, D., and Brendler, V. (2011): Sorption of selenium(VI) onto anatase: Macroscopic and microscopic characterization. Geochimica et Cosmochimica Acta 75, 1519-1530.

Jordan, N., Marmier, N., Lomenech, C., Giffaut, E., and Ehrhardt, J. J. (2009): Competition between selenium (IV) and silicic acid on the hematite surface. Chemosphere 75, 129-134.

Jörg, G., Buhnemann, R., Hollas, S., Kivel, N., Kossert, K., Van Winckel, S., and Gostomski, C. L. V. (2010): Preparation of radiochemically pure Se-79 and highly precise determination of its half-life. Applied Radiation and Isotopes 68, 2339-2351.

Kaminski, R., Glass, R. S., Schroeder, T. B., Michalski, J., and Skowronska, A. (1997): Monoselenophosphate: Its hydrolysis and its ability to phosphorylate alcohols and amines. Bioorganic Chemistry 25, 247-259.

Kang, Y., Yamada, H., Kyuma, K., Hattori, T., and Kigasawa, S. (1991): Selenium in soil humic-acid. Soil Science and Plant Nutrition 37, 241-248.

Kersten, M. and Vlasova, N. (2013): The influence of temperature on selenate adsorption by goethite. Radiochimica Acta 101, 413-419.

Kirsch, R., Fellhauer, D., Altmaier, M., Neck, V., Rossberg, A., Fanghanel, T., Charlet, L., and Scheinost, A. C. (2011): Oxidation State and Local Structure of Plutonium Reacted with Magnetite, Mackinawite, and Chukanovite. Environmental Science & Technology 45, 7267-7274.

Kirsch, R., Scheinost, A. C., Rossberg, A., Banerjee, D., and Charlet, L. (2008): Reduction of antimony by nano-particulate magnetite and mackinawite. Mineralogical Magazine 72, 185-189.

Kolshorn, H. and Meier, H. (1977): Selenium-77 Magnetic Resonance. pH Dependence of the Chemical Shift of 77Se in Aqueous Selenious Acid. Journal of Chemical Research 338-339.

Kosmulski, M., Dukhin, A. S., Priester, T., and Rosenholm, J. B. (2003): Multilaboratory study of the shifts in the IEP of anatase at high ionic strengths. Journal of Colloid and Interface Science 263, 152-155.

Křepelová, A., Brendler, V., Sachs, S., Baumann, N., and Bernhard, G. (2007): U(VI)-Kaolinite Surface Complexation in Absence and Presence of Humic Acid Studied by TRLFS. Environmental Science & Technology 41, 6142–6147.

Krumhansl, J. L., Pless, J. D., Chwirka, J. B., and Holt, K. C. (2006): Yucca Mountain Project Getter Program Results (Year 1): I-129 and Other Anions of Concern, SAND2006-3869, Albuquerque and Livermore, USA.

Kulik, D. A. (2000): Thermodynamic properties of surface species at the mineral-water interface under hydrothermal conditions: A Gibbs energy minimization single-site 2pK(A) triple-layer model of rutile in NaCl electrolyte to 250 degrees C. Geochimica et Cosmochimica Acta 64, 3161-3179.

Kvashnina, K. O., Butorin, S. M., Cui, D., Vegelius, J., Puranen, A., Gens, R., and Glatzel, P. (2009): Electron transfer during selenium reduction by iron surfaces in aqueous solution: high resolution X-ray absorption study. 14th International Conference on X-Ray Absorption Fine Structure (Xafs14), Proceedings 190, 4.

Lantenois, S., Prelot, B., Douillard, J. M., Szczodrowski, K., and Charbonnel, M. C. (2007): Flow microcalorimetry: Experimental development and application to adsorption of heavy metal cations on silica. Applied Surface Science 253, 5807-5813.

Lee, S. S., Fenter, P., Park, C., Sturchio, N. C., and Nagy, K. L. (2010): Hydrated Cation Speciation at the Muscovite (001)-Water Interface. Langmuir 26, 16647-16651.

Lemos, V. A. and Maciel, M. V. (2013): An on-line preconcentration system for the determination of selenium in seawater samples. Analytical Methods 5, 4501-4505.

Ley, H. and König, E. (1938): Die Lösungsspektren von wichtigeren Säuren der Elemente der Schwefelgruppe. Zeitschrift für Physikalische Chemie-Abteilung B-Chemie der Elementarprozesse Aufbau der Materie 41, 365-387.

Li, C. S., Guo, J. R., and Li, D. M. (1997): A procedure for the separation of 79Se from fission products and application to the determination of the 79Se half-life. Journal of Radioanalytical and Nuclear Chemistry 220, 69-71.

Li, S. X. and Deng, N. S. (2002): Separation and preconcentration of Se(IV)/Se(VI) species by selective adsorption onto nanometer-sized titanium dioxide and determination by graphite furnace atomic absorption spectrometry. Analytical and Bioanalytical Chemistry 374, 1341-1345.

Licht, S. and Forouzan, F. (1995): Speciation analysis of aqueous polyselenide solutions. Journal of the Electrochemical Society 142, 1546-1551.

Lingane, J. J. and Niedrach, L. W. (1948): Polarography of selenium and tellurium .1. The -2 states. Journal of the American Chemical Society 70, 4115-4120.

Liu, X. (2008a): Adsorption du séléniure sur la pyrite sous conditions redox, Université de Nantes.

Liu, X., Fattahi, M., Montavon, G., and Grambow, B. (2008b): Selenide retention onto pyrite under reducing conditions. Radiochimica Acta 96, 473-479.

Lubal, P. and Havel, J. (1997): The study of complex equilibria of uranium(VI) with selenate. Talanta 44, 457-466.

Magnuson, M. L., Creed, J. T., and Brockhoff, C. A. (1997): Speciation of selenium and arsenic compounds by capillary electrophoresis with hydrodynamically modified electroosmotic flow and on-line reduction of selenium(VI) to selenium(IV) with hydride generation inductively coupled plasma mass spectrometric detection. Analyst 122, 1057-1061.

Manceau, A. and Charlet, L. (1994): The mechanism of selenate adsorption on goethite and hydrous ferric-oxide. Journal of Colloid and Interface Science 168, 87-93.

Martinez, M., Gimenez, J., de Pablo, J., Rovira, M., and Duro, L. (2006): Sorption of selenium(IV) and selenium(VI) onto magnetite. Applied Surface Science 252, 3767-3773.

Masscheleyn, P. H., Delaune, R. D., and Patrick, W. H. (1990): Transformations of selenium as affected by sediment oxidation reduction potential and pH. Environmental Science & Technology 24, 91-96.

Milne, J. (1987): Haloselenate(IV) formation and selenous acid dissociation equilibria in hydrochloric and hydrofluoric acids. Canadian Journal of Chemistry-Revue Canadienne De Chimie 65, 316-321.

Milne, J. (1993): Chemical Shift References for 77Se NMR Spectroscopy. Selenous Acid. Magnetic Resonance in Chemistry 31, 652-655.

Milne, J. and Lahaie, P. (1979): Chloroselenate(IV) Equilibria in Aqueous Hydrochloric Acid. Inorganic Chemistry 18, 3180-3183.

Milne, J. and Lahaie, P. (1985): Bromoselenate(IV) Equilibria in Aqueous Hydrobromic Acid. Inorganic Chemistry 24, 840-844.

Miolati, A. and Mascetti, E. (1901): Contribute alia conoscenza di alcuni acidi inorganici. Gazzetta Chimica Italiana 31, 93-139

Misra, M. and Adutwum, K. O. (2000): Adsorption of oxyanions of selenium onto lanthanum oxide and alumina. In: Young, C. (Ed.), Minor Elements 2000: Processing and Environmental Aspects of As, Sb, Se, Te, and Bi. Soc Min Engineers Aime, Littleton.

Missana, T., Alonso, U., Scheinost, A. C., Granizo, N., and Garcia-Gutierrez, M. (2009): Selenite retention by nanocrystalline magnetite: Role of adsorption, reduction and dissolution/co-precipitation processes. Geochimica et Cosmochimica Acta 73, 6205-6217.

Monteil-Rivera, F., Fedoroff, M., Jeanjean, J., Minel, L., Barthes, M. G., and Dumonceau, J. (2000): Sorption of selenite (SeO32-) on hydroxyapatite: An exchange process. Journal of Colloid and Interface Science 221, 291-300.

Morin, G., Ona-Nguema, G., Wang, Y. H., Menguy, N., Juillot, F., Proux, O., Guyot, F., Calas, G., and Brown, G. E. (2008): Extended X-ray absorption fine structure analysis of arsenite and arsenate adsorption on maghemite. Environmental Science & Technology 42, 2361-2366.

Morin, G., Wang, Y. H., Ona-Nguema, G., Juillot, F., Calas, G., Menguy, N., Aubry, E., Bargar, J. R., and Brown, G. E. (2009): EXAFS and HRTEM Evidence for As(III)-Containing Surface Precipitates on Nanocrystalline Magnetite: Implications for As Sequestration. Langmuir 25, 9119-9128.

Mornet, S., Portier, J., and Duguet, E. (2005): A method for synthesis and functionalization of ultrasmall superparamagnetic covalent carriers based on maghemite and dextran. Journal of Magnetism and Magnetic Materials 293, 127-134.

Müller, K., Foerstendorf, H., Brendler, V., and Bernhard, G. (2009): Sorption of Np(V) onto TiO2, SiO2, and ZnO: An in Situ ATR FT-IR Spectroscopic Study. Environmental Science & Technology 43, 7665-7670.

Müller, K. and Lefevre, G. (2011): Vibrational Characteristics of Outer-Sphere Surface Complexes: Example of Sulfate Ions Adsorbed onto Metal (Hydr)oxides. Langmuir 27, 6830-6835.

Murad, E. (2010): Mossbauer spectroscopy of clays, soils and their mineral constituents. Clay Minerals 45, 413-430.

Murphy, A. P. (1988): Removal of selenate from water by chemical-reduction. Industrial & Engineering Chemistry Research 27, 187-191.

Myneni, S. C. B., Tokunaga, T. K., and Brown, G. E. (1997): Abiotic selenium redox transformations in the presence of Fe(II,III) oxides. Science 278, 1106-1109.

Nadimpalli, S., Rallabandi, R., and Lanka, D. S. A. (1990): Mechanism of oxidation of selenium(IV) by cobalt(III) in perchloric acid- a kinetic study. Transition Metal Chemistry 15, 191-196.

Nakamoto, K. (1997): Infrared and Raman Spectra of Inorganic and Coordination Compounds. Part A: Theory and Applications in Inorganic Chemistry. Wiley-Interscience, New York.

Nakamoto, K., Fujita, J., Tanaka, S., and Kobayashi, M. (1957): Infrared spectra of metallic complexes .4. Comparison of the infrared spectra of unidentate and bidentate metallic complexes. Journal of the American Chemical Society 79, 4904-4908.

Naveau, A., Monteil-Rivera, F., Guillon, E., and Dumonceau, J. (2007): Interactions of aqueous selenium(-II) and (IV) with metallic sulfide surfaces. Environmental Science & Technology 41, 5376-5382.

Nishimura, T., Hata, R., and Hasegawa, F. (2009): Chemistry of the M (M=Fe, Ca, Ba)-Se-H2O Systems at 25 °C. Molecules 14, 3567-3588.

Olegario, J. T., Yee, N., Miller, M., Sczepaniak, J., and Manning, B. (2010): Reduction of Se(VI) to Se(-II) by zerovalent iron nanoparticle suspensions. Journal of Nanoparticle Research 12, 2057-2068.

Olin, A., Noläng, B., Osadchii, E. G., Öhman, L.-O., and Rosén, E. (2005): Chemical thermodynamics of selenium. Elsevier, Amsterdam.

ONDRAF/NIRAS (2001a): Technical overview of the SAFIR 2 report - Safety assessment and feasibility interim report 2 (NIROND 2001–05 E). In: E), T. o. o. t. S. r.-S. a. a. f. i. r. N. (Ed.). Belgian Agency for Radioactive Waste and Enriched Fissile Materials, Brussels.

ONDRAF/NIRAS (2001b): Technical overview of the SAFIR 2 report. Safety Assessment and Feasibility Interim Report 2. NIROND 2001-05E.

Pan, B. J., Xiao, L. L., Nie, G. Z., Pan, B. C., Wu, J., Lv, L., Zhang, W. M., and Zheng, S. R. (2010): Adsorptive selenite removal from water using a nano-hydrated ferric oxides (HFOs)/polymer hybrid adsorbent. Journal of Environmental Monitoring 12, 305-310.

Parida, K. M. and Gorai, B. (2003): Removal of aqueous selenite using alumina International Journal of Environmental Studies 60, 75-86.

Parida, K. M., Gorai, B., and Das, N. N. (1997a): Studies on Indian ocean manganese nodules .3. Adsorption of aqueous selenite on ferromanganese nodules. Journal of Colloid and Interface Science 187, 375-380.

Parida, K. M., Gorai, B., Das, N. N., and Rao, S. B. (1997b): Studies on ferric oxide hydroxides .3. Adsorption of selenite (SeO32-) on different forms of iron oxyhydroxides. Journal of Colloid and Interface Science 185, 355-362.

Park, H., Ayala, P., Deshusses, M. A., Mulchandani, A., Choi, H., and Myunga, N. V. (2008): Electrodeposition of maghemite (g-Fe2O3) nanoparticles. Chemical Engineering Journal 139, 208-212.

Park, H., Myung, N. V., Jung, H., and Choi, H. (2009): As(V) remediation using electrochemically synthesized maghemite nanoparticles. Journal of Nanoparticle Research 11, 1981-1989.

Parker, D. R., Tice, K. R., and Thomason, D. N. (1997): Effects of ion pairing with calcium and magnesium on selenate availability to higher plants. Environmental Toxicology and Chemistry 16, 565-571.

Parker, G. W., Creek, G. E., Hebert, G. M., Lantz, P. M., and Martin, W. J. (1949): Oak Ridge National Laboratory Classified Report ORNL-499, December 1949 (unpublished). Cited as reference “ParkG49a”. In: Lederer C.M., Hollander J.M., and Perlman I. (1967) Table of Isotopes, sixth edition, p. 30, p. 210, p. 212, p. 214, and p. 527. John Wiley & Sons, Inc., New York • London • Sydney.

Parkhurst, D. L. and Apello, C. A. J. (1999): User's guide to PHREEQC (version 2) – A computer program for speciation, batch-reaction, one dimensional transport, and inverse geochemcal calculations. U.S. Geological Survey.

Peak, D. (2006a): Adsorption mechanisms of selenium oxyanions at the aluminum oxide/water interface. Journal of Colloid and Interface Science 303, 337-345.

Peak, D., Saha, U. K., and Huang, P. M. (2006b): Selenite adsorption mechanisms on pure and coated montmorillonite: An EXAFS and XANES spectroscopic study. Soil Science Society of America Journal 70, 192-203.

Peak, D. and Sparks, D. L. (2002): Mechanisms of selenate adsorption on iron oxides and hydroxides. Environmental Science & Technology 36, 1460-1466.

Persson, P. and Lövgren, L. (1996): Potentiometric and spectroscopic studies of sulfate complexation at the goethite-water interface. Geochimica et Cosmochimica Acta 60, 2789-2799.

Petitto, S. C., Tanwar, K. S., Ghose, S. K., Eng, P. J., and Trainor, T. P. (2010): Surface structure of magnetite (111) under hydrated conditions by crystal truncation rod diffraction. Surface Science 604, 1082-1093.

Philippini, V., Aupiais, J., and Vercouter, T. (2013): Formation of MSeO4(aq) complexes (M2+=Mg2+, Co2+, Ni2+, Cu2+, Cd2+) studied as a function of temperature by affinity capillary electrophoresis. Electrophoresis 34, 541-551.

Philippini, V., Aupiais, J., Vercouter, T., and Moulin, C. (2009): Formation of CaSO4(aq) and CaSeO4(aq) studied as a function of ionic strength and temperature by CE. Electrophoresis 30, 3582-3590.

Pitts, L., Fisher, A., Worsfold, P., and Hill, S. J. (1995): Selenium speciation using high-performance liquid-chromatography hydride generation atomic fluorescence with online microwave reduction. Journal of Analytical Atomic Spectrometry 10, 519-520.

Prasad, N. K., Gohri, V., and Bahadur, D. (2011): Nanoparticles of Pure and Substituted Maghemites (g-MxFe2-xO3 Where M = Al, Cr, Mn, Zn and 0 ≤ x ≤ 1.3): A Comparative Study. Journal of Nanoscience and Nanotechnology 11, 2710-2716.

Pruett, R. J. and Webb, H. L. (1993): Sampling and Analysis of KGa-1B Well-Crystallized Kaolin Source Clay. Clays and Clay Minerals 41, 514-519.

Puranen, A., Jonsson, M., Dahn, R., and Cui, D. Q. (2009): Immobilization of selenate by iron in aqueous solution under anoxic conditions and the influence of uranyl. Journal of Nuclear Materials 392, 519-524.

Puranen, A., Jonsson, M., Dahn, R., and Cui, D. Q. (2010): Reduction of selenite and selenate on anoxically corroded iron and the synergistic effect of uranyl reduction. Journal of Nuclear Materials 406, 230-237.

Qiu, S. R., Lai, H. F., Roberson, M. J., Hunt, M. L., Amrhein, C., Giancarlo, L. C., Flynn, G. W., and Yarmoff, J. A. (2000): Removal of contaminants from aqueous solution by reaction with iron surfaces. Langmuir 16, 2230-2236.

Rai, D., Felmy, A. R., and Moore, D. A. (1995): The Solubility Product of Crystalline Ferric Selenite Hexahydrate and the Complexation Constant of $FeSeO^{3+}$. Journal of Solution Chemistry 24, 735-752.

Reddy, K. J., Zhang, Z. H., Blaylock, M. J., and Vance, G. F. (1995): Method for detecting selenium speciation in groundwater. Environmental Science & Technology 29, 1754-1759.

Refait, P., Simon, L., and Genin, J. M. R. (2000): Reduction of SeO_4^{2-} anions and anoxic formation of iron(II)-iron(III) hydroxy selenate green rust. Environmental Science & Technology 34, 819-825.

Ressler, T. (1998): WinXAS: a program for X-ray absorption spectroscopy data analysis under MS-Windows. Journal of Synchrotron Radiation 5, 118-122.

Ridley, M. K., Machesky, M. L., and Kubicki, J. D. (2013): Anatase Nanoparticle Surface Reactivity in NaCl Media: A CD−MUSIC Model Interpretation of Combined Experimental and Density Functional Theory Studies. Langmuir 29, 8572−8583.

Rosenheim, A. and Krause, L. (1921): Selenic acids and hetero-polyselenites. Zeitschrift für anorganische und allgemeine Chemie 118, 177-192

Ross, S. D. and Thomas, N. A. (1970): Forbidden transitions in infra-red spectra of tetrahedral anions .9. Monodentate selenato complexes. Spectrochim. Acta A A 26, 971-975.

Rossberg, A., Reich, T., and Bernhard, G. (2003): Complexation of uranium(VI) with protocatechuic acid - application of iterative transformation factor analysis to EXAFS spectroscopy. Analytical and Bioanalytical Chemistry 376, 631-638.

Rovira, M., Gimenez, J., Martinez, M., Martinez-Llado, X., de Pablo, J., Marti, V., and Duro, L. (2008): Sorption of selenium(IV) and selenium(VI) onto natural iron oxides: Goethite and hematite. Journal of Hazardous Materials 150, 279-284.

Sabbah, R. and Carpeni, G. (1966): Etude électrométrique des systèmes H2SeO3 - Na2SeO3 (ou K2SeO3) en milieux Cl-(Na+ ou K+)=3 M à 25 °C. Journal De Chimie Physique 63, 1549-1554.

Sanuki, S., Shako, K., Nagaoka, S., and Majima, H. (2000): Photocatalytic reduction of Se ions using suspended anatase powders. Materials Transactions Jim 41, 799-805.

Sato, H. and Miyamoto, S. (2004): Diffusion behaviour of selenite and hydroselenide in compacted bentonite. Applied Clay Science 26, 47-55.

Scheidegger, A. M., Grolimund, D., Cui, D., Devoy, J., Spahiu, K., Wersin, P., Bonhoure, I., and Janousch, M. (2003): Reduction of selenite on iron surfaces: A micro-spectroscopic study. Journal De Physique Iv 104, 417-420.

Scheinost, A. C. and Charlet, L. (2008a): Selenite reduction by mackinawite, magnetite and siderite: XAS characterization of nanosized redox products. Environmental Science & Technology 42, 1984-1989.

Scheinost, A. C., Kirsch, R., Banerjee, D., Fernandez-Martinez, A., Zaenker, H., Funke, H., and Charlet, L. (2008b): X-ray absorption and photoelectron spectroscopy investigation of selenite reduction by Fe-II-bearing minerals. Journal of Contaminant Hydrology 102, 228-245.

Schellenger, A. E. P. and Larese-Casanova, P. (2013): Oxygen Isotope Indicators of Selenate Reaction with Fe(II) and Fe(III) Hydroxides. Environmental Science & Technology 47, 6254-6262.

Schudel, M., Behrens, S. H., Holthoff, H., Kretzschmar, R., and Borkovec, M. (1997): Absolute Aggregation Rate Constants of Hematite Particles in Aqueous Suspensions: A Comparison of Two Different Surface Morphologies. Journal of Colloid and Interface Science 196, 241–253.

Seah, M. P., Gilmore, L. S., and Beamson, G. (1998): XPS: Binding energy calibration of electron spectrometers 5 - Re-evaluation of the reference energies. Surface and Interface Analysis 26, 642-649.

Sharrad, M. O. M., Liu, H. J., and Fan, M. H. (2012): Evaluation of FeOOH performance on selenium reduction. Separation and Purification Technology 84, 29-34.

Sherman, D. M. and Randall, S. R. (2003): Surface complexation of arsenic(V) to iron(III) (hydr)oxides: Structural mechanism from ab initio molecular geometries and EXAFS spectroscopy. Geochimica et Cosmochimica Acta 67, 4223-4230.

Shi, K. L., Wang, X. F., Guo, Z. J., Wang, S. G., and Wu, W. S. (2009): Se(IV) sorption on TiO2: Sorption kinetics and surface complexation modeling. Colloids and Surfaces a-Physicochemical and Engineering Aspects 349, 90-95.

Siddique, M., Ahmed, E., and Butt, N. M. (2010): Particle size effect on Mossbauer parameters in g-Fe2O3 nanoparticles. Physica B-Condensed Matter 405, 3964-3967.

Singh, B. and Hermann, O. W. (1993): A- chains 79 update. Nucl. Data Sheets 70, 452.

Skovbjerg, L. L., Christiansen, B. C., Nedel, S., Dideriksen, K., and Stipp, S. L. S. (2010): The role of green rust in the migration of radionuclides: An overview of processes that can control mobility of radioactive elements in the environment using as examples Np, Se and Cr. Radiochimica Acta 98, 607-612.

Sladkov, V. (2010): Interaction of uranyl with Se(IV) and Se(VI) in aqueous acid solutions by means of capillary electrophoresis. Electrophoresis 31, 3482-3491.

Sladkov, V. (2013): Uranyl complexation with selenate at variable temperatures studied by affinity capillary electrophoresis. Journal of Chromatography A 1276, 120-125.

Sladkov, V., Fourest, B., and Mercier, F. (2009): Uranyl-Se(IV) interaction in aqueous acid solutions studied by time-resolved laser-induced fluorescence spectroscopy (TRLFS) and UV-Vis spectrophotometry. Dalton Transactions, 7734-7740.

Stolz, J. F. and Oremland, R. S. (1999): Bacterial respiration of arsenic and selenium. Fems Microbiology Reviews 23, 615-627.

Stumm, W., Huang, C. P., and Jenkins, S. R. (1970): Specific chemical interaction affecting stability of dispersed systems. Croatica Chemica Acta 42, 223-6.

Su, C. M. and Suarez, D. L. (2000): Selenate and selenite sorption on iron oxides: An infrared and electrophoretic study. Soil Science Society of America Journal 64, 101-111.

Sun, Y. K., Ma, M., Zhang, Y., and Gu, N. (2004): Synthesis of nanometer-size maghemite particles from magnetite. Colloids and Surfaces a-Physicochemical and Engineering Aspects 245, 15-19.

Tachi, Y., Shibutani, T., Sato, H., and Yui, M. (1998): Sorption and diffusion behavior of selenium in tuff. Journal of Contaminant Hydrology 35, 77-89.

Temesghen, W. and Sherwood, P. M. A. (2002): Analytical utility of valence band X-ray photoelectron spectroscopy of iron and its oxides, with spectral interpretation by cluster and band structure calculations. Analytical and Bioanalytical Chemistry 373, 601-608.

Torres, J., Pintos, V., Dominguez, S., Kremer, C., and Kremer, E. (2010): Selenite and Selenate Speciation in Natural Waters: Interaction with Divalent Metal Ions. Journal of Solution Chemistry 39, 1-10.

Torres, J., Pintos, V., Gonzatto, L., Domínguez, S., Kremer, C., and Kremer, E. (2011): Selenium chemical speciation in natural waters: Protonation and complexation behavior of selenite and selenate in the presence of environmentally relevant cations. Chemical Geology 288, 32-38.

Torrie, B. H. (1973): Raman and Infrared Spectra of Na2SeO3, NaHSeO3, H2SeO3, and NaH3(SeO3)2. Canadian Journal of Physics 51, 610-615.

Tucek, J. and Zboril, R. (2005): Zero-field and in-field Mossbauer spectroscopy as a tool for structural and magnetic characterization of maghemite (g-Fe2O3) nanoparticles. Czech. J. Phys. 55, 893-911.

Tuutijärvi, T., Lu, J., Sillanpaa, M., and Chen, G. (2010): Adsorption Mechanism of Arsenate on Crystal g-Fe_2O_3 Nanoparticles. Journal of Environmental Engineering 136, 897-905.

Tuzen, M. and Sari, A. (2010): Biosorption of selenium from aqueous solution by green algae (Cladophora hutchinsiae) biomass: Equilibrium, thermodynamic and kinetic studies. Chemical Engineering Journal 158, 200-206.

Valdivieso, A. L., Bahena, J. L. R., Song, S., and Urbina, R. H. (2006): Temperature effect on the zeta potential and fluoride adsorption at the a-Al2O3/aqueous solution interface. Journal of Colloid and Interface Science 298, 1-5.

Valkonen, J. and Koskenlinna, M. (1978): The crystal structure of iron(III) hydrogen biselenite, $FeH(SeO_3)_2$. Acta Chemica Scandinavica A 32, 603-606.

Van Der Hoek, E. E., Bonouvrie, P. A., and Comans, R. N. J. (1994): Sorption of As and Se on mineral components of fly ash: relevance for leaching processes. Applied Geochemistry 9, 403-412.

Vassileva, E., Becker, A., and Broekaert, J. A. C. (2001): Determination of arsenic and selenium species in groundwater and soil extracts by ion chromatography coupled to inductively coupled plasma mass spectrometry. Analytica Chimica Acta 441, 135-146.

Vlasova, N. N., Kersten, M., and Kulik, D. A. (2004): Effect of temperature on selenate adsorption by goethite. In: Wanty, B. and Seal, R. R. Eds.), Water-Rock Interaction. Balkema Publ., Leiden.

Waitkin, G. R. and Schutt, R. (1946): 55. Aluminum selenide and hydrogen selenide. Inorganic syntheses 183, 183-186.

Walcarius, A., Devoy, J., and Bessiere, J. (2004): Interactions of selenate with copper(I) oxide particles. Langmuir 20, 6335-6343.

Wallschläger, D. and Bloom, N. S. (2001): Determination of selenite, selenate and selenocyanate in waters by ion chromatography-hydride generation-atomic fluorescence spectrometry (IC-HG-AFS). Journal of Analytical Atomic Spectrometry 16, 1322-1328.

Wang, Y. H., Morin, G., Ona-Nguema, G., Juillot, F., Calas, G., and Brown, G. E. (2011): Distinctive Arsenic(V) Trapping Modes by Magnetite Nanoparticles Induced by Different Sorption Processes. Environmental Science & Technology 45, 7258-7266.

Wang, Y. H., Morin, G., Ona-Nguema, G., Menguy, N., Juillot, F., Aubry, E., Guyot, F., Calas, G., and Brown, G. E. (2008): Arsenite sorption at the magnetite-water interface during aqueous precipitation of magnetite: EXAFS evidence for a new arsenite surface complex. Geochimica et Cosmochimica Acta 72, 2573-2586.

Wasewar, K. L., Prasad, B., and Gulipalli, S. (2009): Adsorption of Selenium Using Bagasse Fly Ash. Clean-Soil Air Water 37, 534-543.

Webb, S. M. (2005): SIXpack: a graphical user interface for XAS analysis using IFEFFIT. Physica Scripta T115, 1011-1014.

Wei, X. C., Bhojappa, S., Lin, L. S., and Viadero, R. C. (2012): Performance of Nano-Magnetite for Removal of Selenium from Aqueous Solutions. Environmental Engineering Science 29, 526-532.

Wells, C. F. and Salam, M. A. (1968): Complex Formation between Iron(II) and Inorganic Anions. Part II. The Effect of Oxyanions on the Reaction of Iron(II) with Hydrogen Peroxide. Journal of the Chemical Society A -Inorganic Physical Theoretical, 308-315.

Wieghardt, K. and Eckert, J. (1971): Di- m-sulfato-m-hydroxo-bis(triamminecobalt(III)) and di-m-selenato-m-hydroxo-bis(triamminecobalt(III)) complexes. Zeitschrift Fur Anorganische Und Allgemeine Chemie 383, 240-248.

Wijnja, H. and Schulthess, C. P. (2000): Vibrational spectroscopy study of selenate and sulfate adsorption mechanisms on Fe and Al (hydr)oxide surfaces. Journal of Colloid and Interface Science 229, 286-297.

Wu, C. H., Lo, S. L., and Lin, C. F. (2000): Competitive adsorption of molybdate, chromate, sulfate, selenate, and selenite on g-Al2O3. Colloids and Surfaces a-Physicochemical and Engineering Aspects 166, 251-259.

Xiao, D. R., Hou, Y., Wang, E. B., An, H. Y., Lu, H., Li, Y. G., Xu, L., and Hu, C. W. (2004): Hydrothermal synthesis and crystal structure of a three-dimensional metal selenite containing double helical chains: Fe3(H2O)(SeO3)3. Journal of Solid State Chemistry 177, 2699-2704.

Xu, S. X., Zheng, M. L., Zhang, X. F., Zhang, J. L., and Lee, Y. I. (2012): Nano TiO2-based preconcentration for the speciation analysis of inorganic selenium by using ion chromatography with conductivity detection. Microchemical Journal 101, 70-74.

Yamani, J. S., Lounsbury, A. W., and Zimmerman, J. B. (2014): Adsorption of selenite and selenate by nanocrystalline aluminum oxide, neat and impregnated in chitosan beads. Water Research 50, 373-381.

Yang, L., Shahrivari, Z., Liu, P. K. T., Sahimi, M., and Tsotsis, T. T. (2005): Removal of trace levels of arsenic and selenium from aqueous solutions by calcined and uncalcined layered double hydroxides (LDH). Industrial & Engineering Chemistry Research 44, 6804-6815.

Yang, Q., Wang, J., Zhou, L. Y., Zeng, H. X., and Wei, S. Y. (2014a): Preparation of two magnetites and application for the removal of fluoride from waters. In: Sung, W. P. and Chen, R. Eds.), Biotechnology, Chemical and Materials Engineering Iii, Pts 1 and 2. Trans Tech Publications Ltd, Stafa-Zurich.

Yang, W. L., Gao, Y., Wu, L., Hou, X. D., Zheng, C. B., and Zhu, X. F. (2014b): Pre-concentration and in-situ photoreduction of trace selenium using TiO2 nanoparticles, followed by its determination by slurry photochemical vapor generation atomic fluorescence spectrometry. Microchimica Acta 181, 197-204.

Yoon, I. H., Kim, K. W., Bang, S., and Kim, M. G. (2011): Reduction and adsorption mechanisms of selenate by zero-valent iron and related iron corrosion. Applied Catalysis B-Environmental 104, 185-192.

Yu, S. and Chow, G. M. (2004): Carboxyl group (-CO2H) functionalized ferrimagnetic iron oxide nanoparticles for potential bio-applications. Journal of Materials Chemistry 14, 2781-2786.

Zboril, R., Mashlan, M., and Petridis, D. (2002): Iron(III) oxides from thermal processes-synthesis, structural and magnetic properties, Mossbauer spectroscopy characterization, and applications. Chemistry of Materials 14, 969-982.

Zelic, M., Pizeta, I., and Djogic, R. (2013): Voltammetric Study of Uranyl-Selenium Interactions. Part 2. Uranyl(V) Selenate Complex. Croatica Chemica Acta 86, 21-26.

Zeng, Y., Hao, R., Xing, B. G., Hou, Y. L., and Xu, Z. C. (2010): One-pot synthesis of Fe3O4 nanoprisms with controlled electrochemical properties. Chemical Communications 46, 3920-3922.

Zhang, L., Liu, N., Yang, L. J., and Lin, Q. (2009): Sorption behavior of nano-TiO2 for the removal of selenium ions from aqueous solution. Journal of Hazardous Materials 170, 1197-1203.

Zhang, N., Lin, L. S., and Gang, D. C. (2008): Adsorptive selenite removal from water using iron-coated GAC adsorbents. Water Research 42, 3809-3816.

Zhang, Y. Q. and Moore, J. N. (1996): Selenium fractionation and speciation in a wetland system. Environmental Science & Technology 30, 2613-2619.

Zhang, Y. Q., Wang, J. F., Amrhein, C., and Frankenberger, W. T. (2005): Removal of selenate from water by zerovalent iron. Journal of Environmental Quality 34, 487-495.

Zhao, N., Ma, W., Cui, Z. M., Song, W. G., Xu, C. L., and Gao, M. Y. (2009): Polyhedral Maghemite Nanocrystals Prepared by a Flame Synthetic Method, Preparations, Characterizations, and Catalytic Properties. Acs Nano 3, 1775-1780.

Zhu, H., Yang, D., Zhu, L., Yang, H., Jin, D., and Yao, K. (2007): A facile two-step hydrothermal route for the synthesis of g-Fe2O3 nanocrystals and their magnetic properties. *Journal of Materials Science* 42, 9205-9209.

Zingaro, R. A., Dufner, D. C., Murphy, A. P., and Moody, C. D. (1997): Reduction of oxoselenium anions by iron(II) hydroxide. Environment International 23, 299-304.

5 Redox behaviour, solubility, speciation and incorporation of Tc, Se and ^{14}C[2]

5.1 Introduction

The studies of KIT-INE within VESPA highlight the key relevance of geochemistry for assessing radionuclide retention and mobilization processes in a repository for radioactive waste. Based upon detailed and systematic experimental studies, a significantly improved process understanding of the chemical behavior of long-lived fission and activation products in repository relevant systems was achieved. Fundamental site-independent thermodynamic data and models were derived which are required for comprehensive geochemical model calculations. As a consequence of the research performed by KIT-INE within VESPA, different repository concepts and scenarios can be analyzed on a significantly improved level.

---

[2] This chapter was prepared by Institut für Nukleare Entsorgung (INE), Karlsruher Institut für Technologie (KIT)

5.2 Redox behaviour of Tc(VII)/Tc(IV) in dilute to concentrated saline systems

5.2.1 Studies on Tc(VII)-(IV) redox processes in dilute 0.1 NaCl solution

5.2.1.1 Introduction

The studies performed by KIT-INE within VESPA on Tc(VII) redox chemistry in dilute NaCl solutions are summarized in the following. Dilute 0.1 M NaCl solutions were analysed in a first part of the studies performed in VESPA in order to derive fundamental understanding, validate general concepts and establish experimental protocols which were later applied to for medium to high ionic strength conditions. The redox behaviour of the Tc(VII)/Tc(IV) couple over a wide range of pH conditions in 0.1 M NaCl/NaOH solution was investigated in various homogenous and heterogeneous reducing systems. Stock solution of Tc(VII) was added to each reducing system, and after given periods, the Tc concentration was measured and compared to the initial Tc(VII) concentration ($1 \cdot 10^{-5}$ $mol \cdot dm^{-3}$). The results can be systematized according to E_h-pH conditions in solution and a general borderline for the reduction of Tc(VII) to Tc(IV) independent of the reducing systems is obtained. The experimental borderline is slightly lower than the calculated equilibrium line between TcO_4^- and $TcO_2(s) \cdot xH_2O(s)$. This may suggest that more soluble solid phase such as small Tc(IV) oxyhydroxide particles are formed under the given conditions. Reaction kinetics are also discussed and correlated to the measured redox potentials and the reduction borderline.

5.2.1.2 Experimental

In the experiments described in this chapter, aliquots of $NaTcO_4$ stock solution was added to 0.1 mol/dm^3 (M) NaCl/NaOH pre-equilibrated with the following reducing agents (p. a. grade chemicals); 3 mM anthraquinone disulfonate (AQDS) (ratio of oxidized form (ox.) to reduced form (red.) = 1:3), 3 mM hydroquinone solutions, Fe(II)/Fe(III) mixed solutions and precipitates (Fe(II):Fe(III) = 1 mM:0.1 mM), 1 mM $Na_2S_2O_4$ solutions, Fe powder suspensions (1 mg/15 ml), 2-hydroxy-1,4-naphthoquinone (Lawsone) solutions (ox.:red. = 1:3), and 1 mM Sn(II) solutions and precipitates. A list of the chemicals and conditions used in the study is given in **Tab. 5.1**. The initial Tc(VII) concentration was set to 10^{-5} M. The hydrogen ion concentration

(pH_c) of the sample solutions were adjusted by adding HCl (Merck) and carbonate-free NaOH (Baker), using a combination glass electrode (type ROSS, Orion) calibrated against standard buffers (pH_c 2 – 12, Merck). The redox potential was measured with a combined Pt and Ag/AgCl reference electrode (Metrohm). The measured redox potentials were converted to redox potential (E_h) versus the standard hydrogen electrode (S.H.E.) by the correction for the potential of the Ag/AgCl reference electrode (+208 mV for 3 M KCl junction electrolyte). The apparent electron activity (pe = $-\log a_{e-}$) was calculated from $E_h = -(RT/F) \ln a_{e-}$ according to the relation: pe = 16.9 E_h (V) at 25 °C. The Tc concentrations after ultrafiltration were investigated over a wide pH_c range as a function of time.

Tab. 5.1 Reducing aqueous systems investigated in dilute 0.1 M NaCl solutions

Reducing chemical system	State[1)]	Concentration of reducing chemicals	Initial TcO_4^- concentration
Hydroquinone	Sol	3 mM, 10 mM	$1 \cdot 10^{-5}$ M
AQDS/AH2QDS (ox/red)	Sol	3 mM (2.25 mM / 0.75 mM)[2)]	$1 \cdot 10^{-5}$ M
Lawsone (ox/red)	Sol	1.6 mM (1.2 mM / 0.4 mM)[2)]	$1 \cdot 10^{-5}$ M
Methylene blue (ox/red)	Sol	0.4 mM (0.3 mM / 0.1 mM)[2)]	$1 \cdot 10^{-5}$ M
Sn(II)	Sol/prep	1 mM[3)]	$1 \cdot 10^{-5}$ M
$Na_2S_2O_4$	Sol	1 mM	$1 \cdot 10^{-5}$ M
Fe(II)/Fe(III)	Sol/prep	1 mM / 0.1 mM[4)]	$1 \cdot 10^{-5}$ M
Fe powder	Sus	1 mg / 15 ml	$1 \cdot 10^{-5}$ M

1) State of reducing chemicals in the system. sol, prep, sus represent solution, precipitate, and suspension.

2) Oxidized form partly reduced by $Na_2S_2O_4$ to obtain ox : red = 1:3 ratio.

3) Sn(II)Cl_2 dissolved at acidic pH region. After pH adjustment, white precipitate observed at neutral pH (6 < pH < 10).

4) Fe(II)Cl_2 and Fe(III)Cl_3 were mixed to Fe(II) : Fe(III) = 10:1 ratio in the acidic pH region. At pH > 6, Fe precipitate formed.

After given time intervals of up to several months, pH_c and E_h values were measured and the supernatants of the solutions filtrated through 10 kDa (2 – 3 nm) ultrafiltration membranes (Pall Life Sciences). The Tc concentration was determined by Liquid Scintillation Counting (TriCarb 2500 Tr/AB instrument, Canberra-Packard) with a detection limit of $\sim 10^{-8}$ M. The Tc oxidation state of the soluble species was investigated by solvent extraction technique, where TcO_4^- was extracted into chloroform using 1 mM tetraphosphonylchloride (TPPC). All samples were prepared and stored in an Ar glove box under inert gas atmosphere.

5.2.1.3 Results and discussions

5.2.1.3.1 Redox behaviour of Tc(VII)/Tc(IV) observed in the individual series

The systems studied within VESPA are discussed and E_h, pH_c conditions and Tc concentrations in solution for the investigated aqueous systems given: (1) Hydroquinone, (2) AQDS/AH_2QDS, (3) Lawsone, (4) Methylene blue, (5) Sn(II), (6) Na-dithionite, (7) Fe(II)/Fe(III), (8) corroding Fe powder systems. In Na-dithionite, Fe(II)/Fe(III) and corroding Fe powder systems the pH_c range is limited to neutral and alkaline pH_c (Na-dithionite, corroding Fe powder) and acidic and neutral pH_c (Fe(II)/Fe(III)) because of chemical instability of the solutions.

The graphs to the left side show the measured E_h values for each individual sample plotted against the corresponding pH_c as a function of equilibration time. The broken lines in (A) represent the calculated equilibrium line between TcO_4^- and $TcO_2 \cdot 1.6H_2O(s)$ [RAR/RAN1999]. The upper and lower decomposition lines of water (at 1 bar $O_2(g)$ and 1 bar $H_2(g)$) and a “redox neutral” line at pe + pH_c = 13.8 are included for comparison.

In graphs to the right side the Tc concentrations measured in solution after 10 kDa (2 – 3 nm) ultrafiltration are plotted for each of the samples shown at the left side versus pH_c.

In all Figures below, blue colour indicates no reduction of initial Tc(VII), red colour indicates reduction to Tc(IV) species with lower solubility.

In **hydroquinone solutions**, Tc concentration was constant at the initial TcO_4^- concentration level from pH_c 2.2 to 12.3 for up to 8 months (**Fig. 5.1**). The E_h values are slightly higher than the equilibrium line between TcO_4^- and $TcO_2 \cdot xH_2O(s)$ calculated from the literature [RAR/RAN1999]. In the oxidation state analysis for the samples at pH_c 3.9, 8.5, and 12.3, more than 99 % of total Tc in the solutions was extracted to the organic phase, indicating that dominant species is TcO_4^- and no reduction of Tc(VII) had occurred.

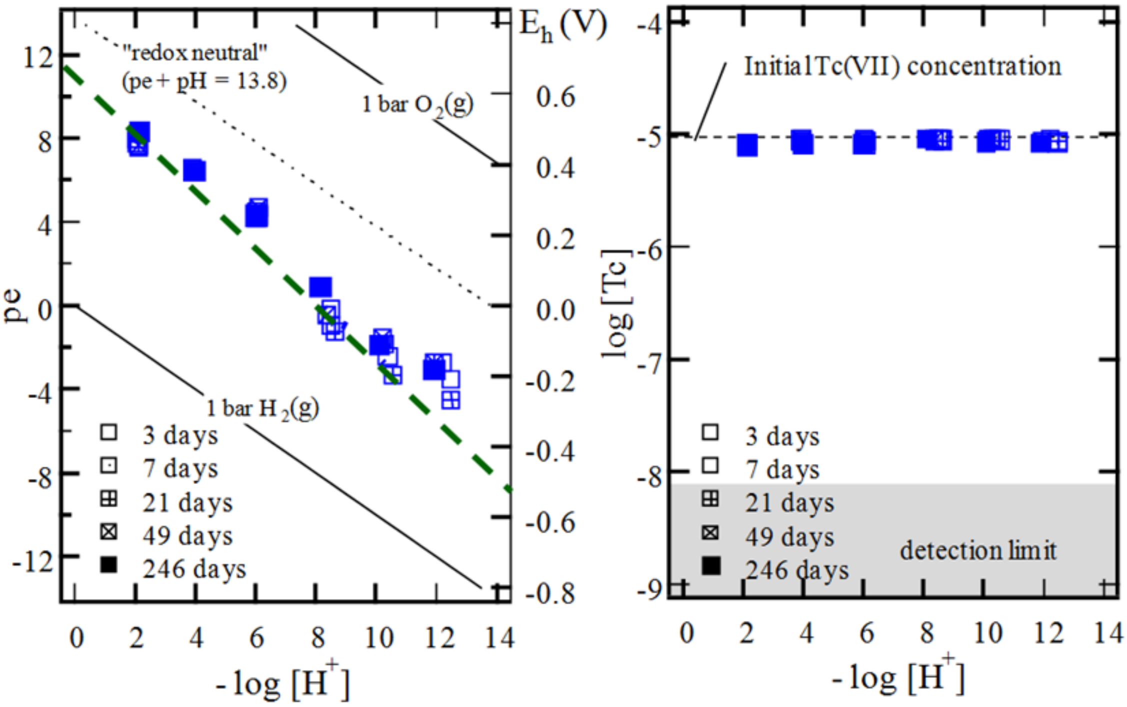

Fig. 5.1 E_h and Tc concentrations (10 kDa filtration) in 3 mM hydroquinone (HQ) solutions as a function of time and pHc

The broken line represents the calculated equilibrium line between TcO_4^- and $TcO_2(s)\cdot xH_2O(s)$

In **AQDS redox buffer solutions** at pH_c 5.0 and 8.1, the initial Tc concentration (10^{-5} M) decreased rapidly to about 10^{-7} M, suggesting that TcO_4^- was reduced and sparingly soluble $TcO_2\cdot xH_2O(s)(s)$ had precipitated (see **Fig. 5.2**). In contrast, at pH_c 10.5, a considerably slower reduction was observed. Under alkaline condition at $pH_c > 11$, E_h values are higher than the calculated TcO_4^- / $TcO_2\cdot xH_2O(s)(s)$ equilibrium line and the Tc concentration is constant at initial TcO_4^- concentration level, indicating that no reduction of Tc(VII) occurred within the investigated time.

In **Lawsone redox buffer solutions**, the Tc concentration decreased from the initial Tc(VII) concentration level over the entire investigated pH_c range of 2 – 12 as shown in **Fig. 5.3**. In the alkaline pH region, extremely slow reduction was observed and not reached the equilibrium state up to 85 days. Experiments in **1 – 4 Methylene Blue buffer solution** , a similar behaviour is observed up to pH 5 (see **Fig. 5.4**), at higher pH conditions no reduction was observed.

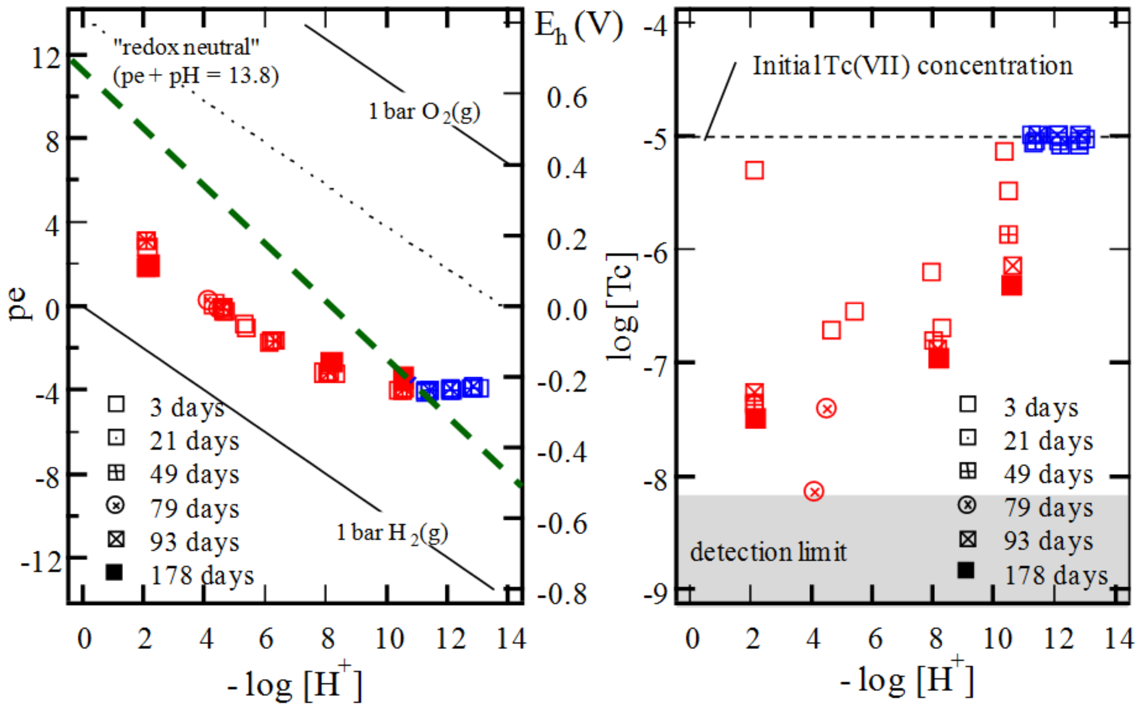

Fig. 5.2 E_h and Tc concentrations (10 kDa filtration) in AQDS buffer solutions as a function of time and pH_c

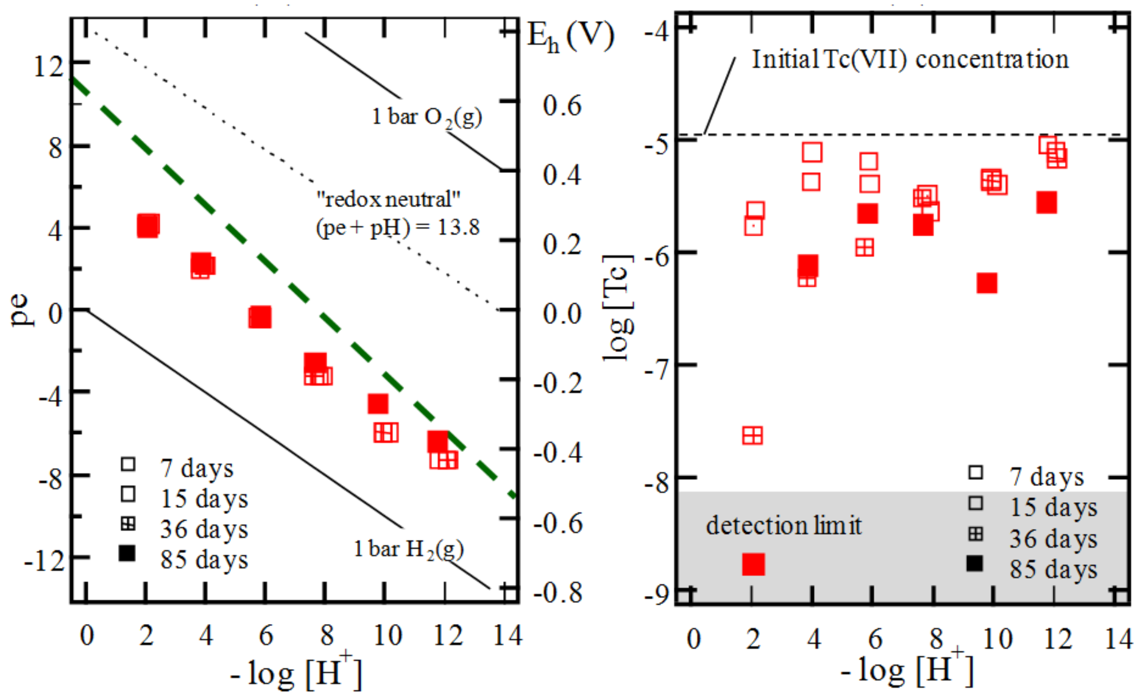

Fig. 5.3 E_h and Tc concentrations (10 kDa filtration) in Lawsone buffer solutions as a function of time and pH_c

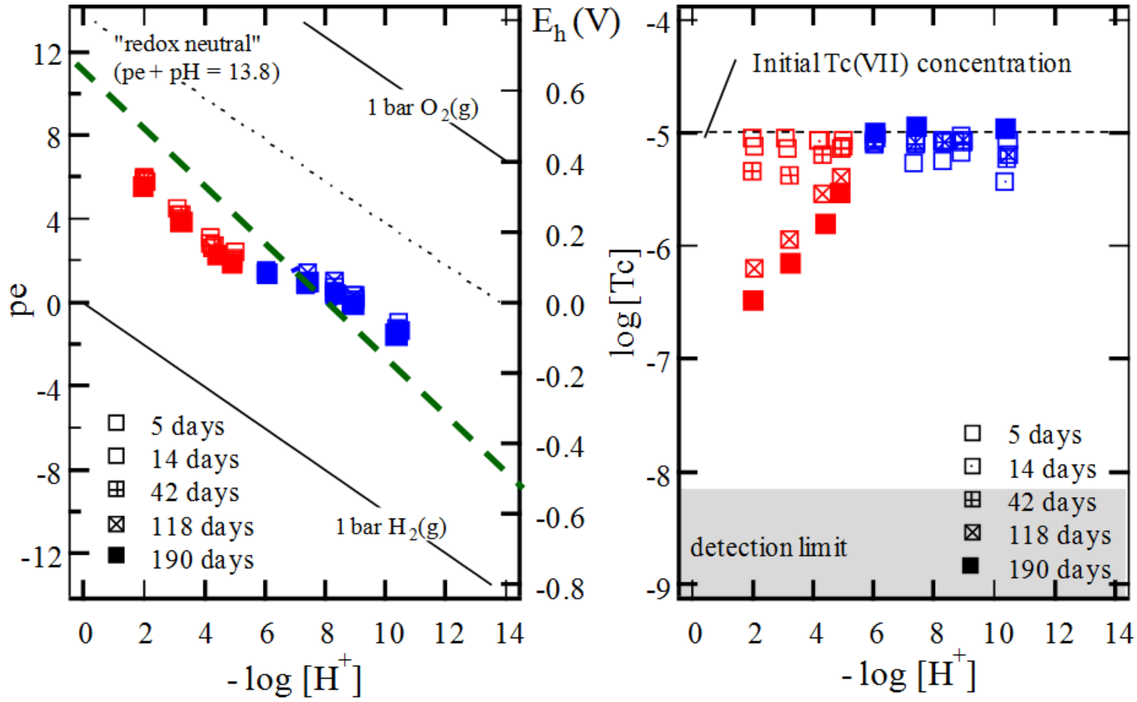

Fig. 5.4 E_h and Tc concentrations (10 kDa filtration) in 1-4 Methylene Blue solutions as a function of time and pH_c

In the systems with **Sn(II)**, the white Sn(II) hydroxide precipitate was observed in the range of pH_c 5 - 11 before adding Tc(VII) stock solution. At higher pH the precipitates disappear and anionic Sn(II) hydrolysis species ($Sn(OH)_3^-$) considered dominant [HOU/KEL1984]. The Tc concentration decreases rapidly over the pH_c range 2 - 11 and stable conditions are achieved within several days (**Fig. 5.5**). At pH_c > 11, the concentration of reduced Tc(IV) species increases with increasing pH_c. The results of the oxidation state analysis by solvent extraction under these pH conditions indicates negligible contribution of remaining Tc(VII), suggesting the formation of anionic Tc(IV) hydrolysis species such as anionic $TcO(OH)_3^-$ as proposed in the literature [ERI/NDA1992, WAR/ALD2007].

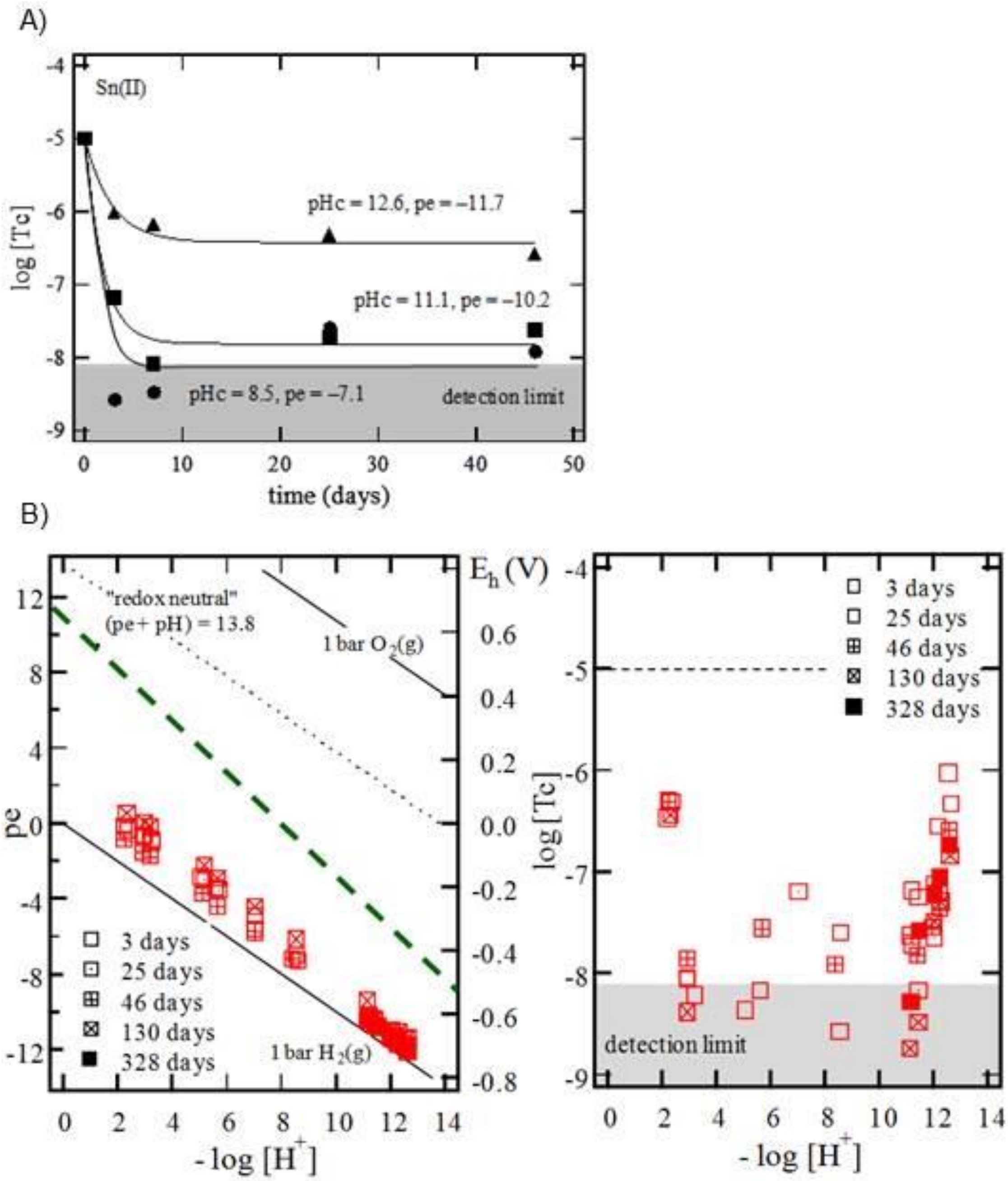

Fig. 5.5 (A) Tc concentrations (10 kDa filtration) in 1 mM Sn(II) solutions and precipitates as a function of time. (B) E_h and Tc concentrations (10 kDa filtration) in Sn(II) solutions as a function of time and pH_c

In **$Na_2S_2O_4$ solution** in the pH_c range 6.9 – 10.9, the Tc concentrations in the solutions decrease and stable state conditions (10^{-7} – 10^{-8} M) are achieved within a few weeks, indicating the reduction of Tc(VII) to a Tc(IV) solid as shown in **Fig. 5.6**. Similarly to the literature where $Na_2S_2O_4$ was used to reduce Tc(VII) for the preparation of Tc(IV) solid phase ($TcO_2 \cdot xH_2O$) [HES/XIA2004], a black-colored Tc(IV) solid phase was immediately precipitated, however, an aging time of a few weeks is needed to reach equilibrium state. At pH_c > 11, the Tc concentrations after reduction increases with an increase of pH_c, suggesting the formation of anionic Tc(IV) species similar to Sn(II) system. It should be noted that at pH 6.9, the amount of Tc(VII) in the solution was more than 30 %, as under neutral pH conditions $Na_2S_2O_4$, which is supposed to maintain reducing conditions, is not stable over prolonged periods of a few months.

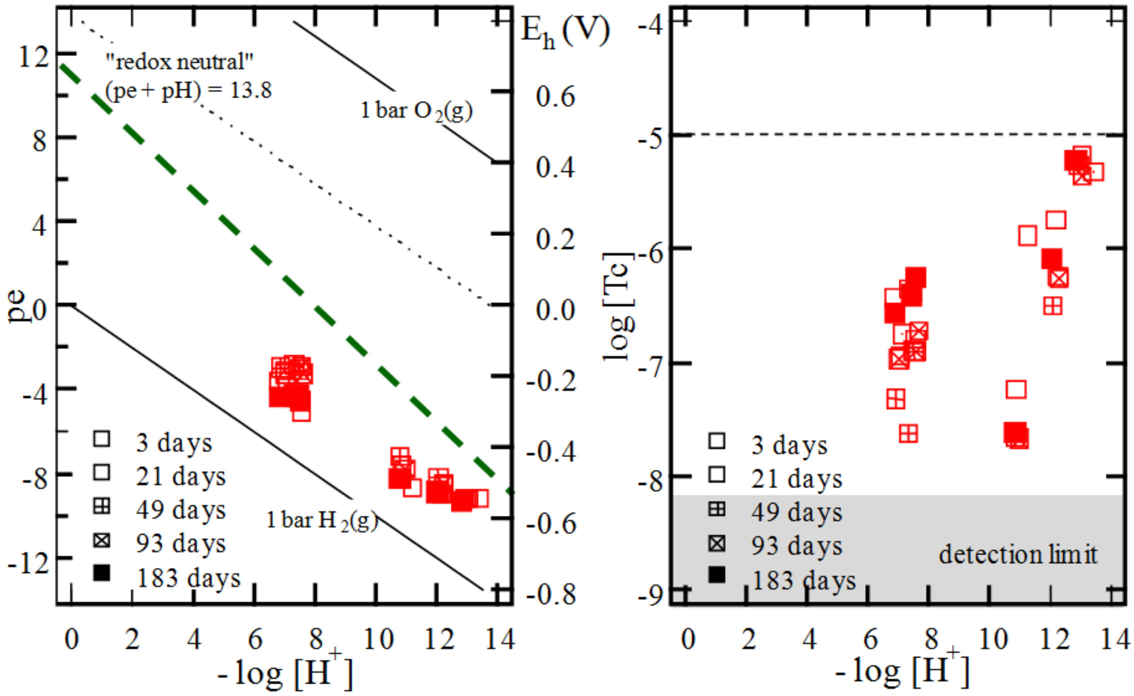

Fig. 5.6 *E*$_h$ and Tc concentrations (10 kDa filtration) in dithionite solutions as a function of pH_c

In the system of **Fe(II)/Fe(III) mixed solutions and precipitates**, at pH_c = 2.1 and pe = 11.3, no change in the Tc concentration was observed up to 49 days (see **Fig. 5.7**). On the other hand, at pH_c 6.0 (pe = -0.2) and pH_c 8.4 (pe = −0.2), Fe(II)/Fe(III) solid phase precipitates were observed before adding Tc(VII) stock solution and the Tc concentrations decreased to almost detection limit (10^{-8} M) within three days after Tc(VII) was added. The reduction of Tc(VII) with Fe(II)/Fe(III) redox buffers and suspensions of the precipitates has been reported in several studies. Cui *et al.* reported that the TcO_4^- concentration at pH < 7.5 was constant at initial concentration level over a few days in the presence of about 10^{-5} M aqueous Fe(II) [CUI/ERI1996a]. Ben Said *et al.* showed, reduction kinetics were also depending on the Fe(II) concentration, Fe(II)/Fe(III) ratio, and initial Tc(VII) concentration [BEN/FAT1998]. The difference between Cui *et al.* [CUI/ERI1996a], Ben Said *et al.* [BEN/FAT1998], and our results probably arise from the different experimental conditions such as Fe(II) concentration. Unfortunately, the redox potentials in these studies were not reported. Zachara *et al.* also investigated the reduction of Tc(VII) in Fe(II) systems in near neutral pH range and the redox behaviour was supported by measured redox potentials [ZAC/HEA2007]. The observed rapid reduction at pH > 6.8 generally agrees with the results in this study, although the reported E_h values were higher than those in this study.

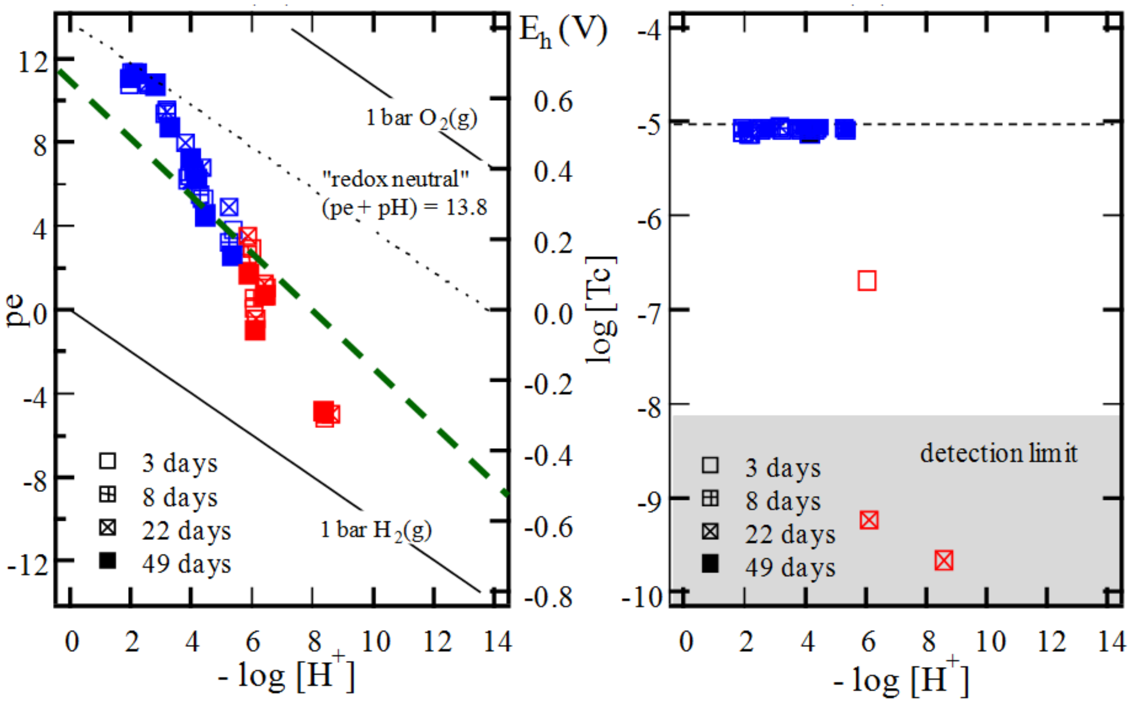

Fig. 5.7 E_h and Tc concentrations (10 kDa filtration) in systems of Fe(II)/Fe(III) mixed solutions and precipitates as a function of pH_c

In the samples containing corroding **Fe powder** in the pH_c range 6 – 10, the Tc concentration rapidly decreased to the detection limit (10^{-8} M) within three days (see **Fig. 5.8**a). In contrast, no reduction was observed in all samples at pH_c > 10 as shown in **Fig. 5.8**b.

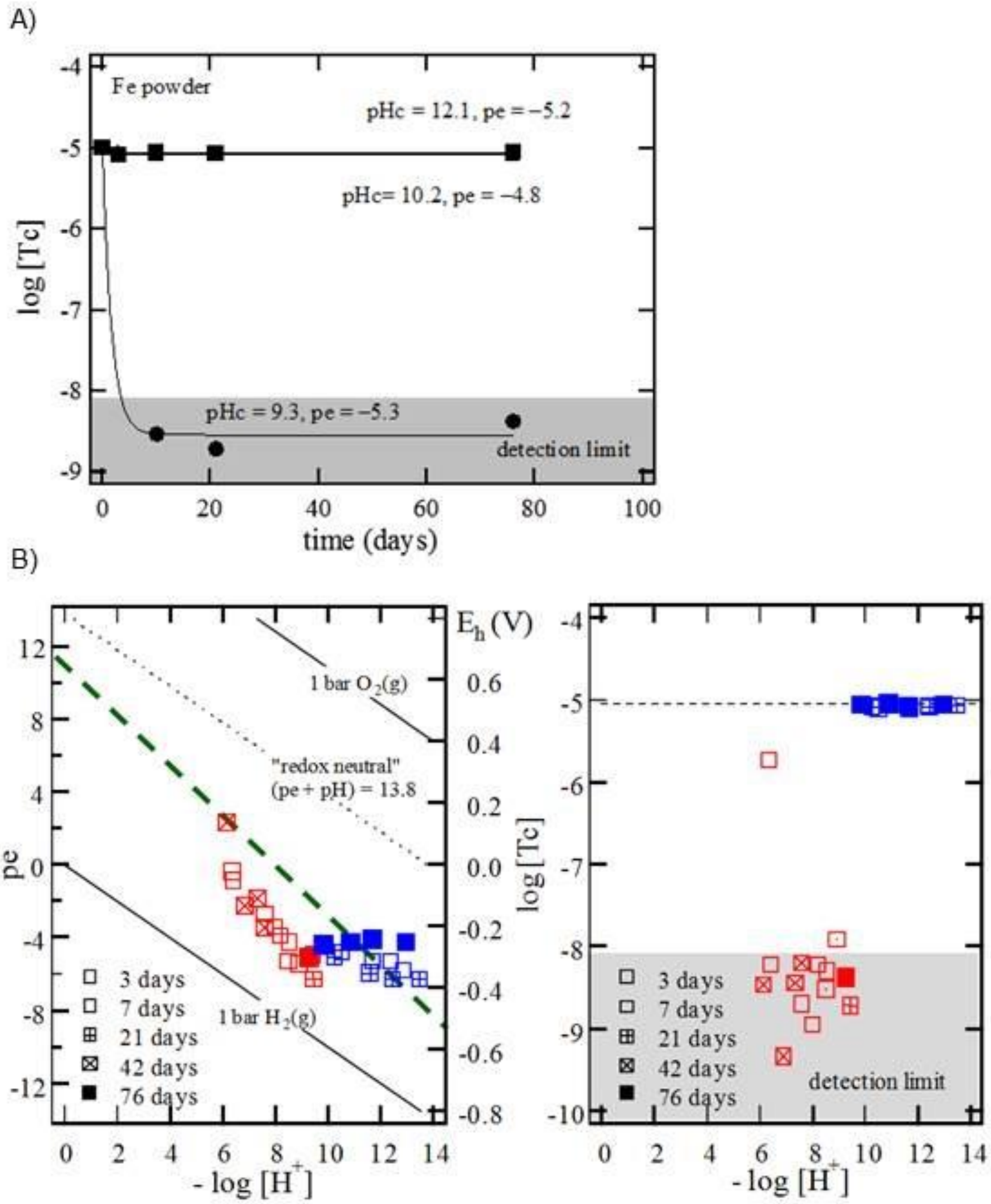

Fig. 5.8 A) Tc concentrations (10 kDa filtration) in 1 mg / 15 ml Fe powder suspensions as a function of time. B) E_h and Tc concentrations (10 kDa filtration) in solutions under presence of Fe powder as function of time and pH_c

5.2.1.3.2 Trends of Tc(VII)/Tc(IV) redox behaviour and kinetic effects in 0.1 M NaCl

The results discussed above are summarized in the E_h-pH diagram shown in **Fig. 5.9**. Samples in which no reduction was observed are plotted as filled symbols. Samples in which initial Tc(VII) was completely or partly reduced are plotted as open symbols. The bold dot line and broken line in the figure represent an experimental borderline for Tc(VII) reduction obtained in this study and the calculated equilibrium line between TcO_4^- and $TcO_2 \cdot xH_2O(s)$ [RAR/RAN1999], respectively. The reduction of Tc(VII) to Tc(IV) occurred in both homogeneous solutions and heterogeneous suspensions with redox potentials below the experimental borderline. In the systems with redox potentials above the borderline, Tc(VII) was not reduced. It should be noted that in Fe powder systems, no reduction was observed at $pH_c = 10.2$ and pe = -4.8 up to 49 days, on the other hand, Tc(VII) was slowly reduced at $pH_c = 10.5$ and pe = -4.0 in the AQDS/AH_2QDS solution. In Fe powder suspension, the deviation of measured E_h values are relatively large, compared to stable E_h values in the AQDS / AH_2QDS solution.

In the investigated systems, the reduction of Tc(VII) to Tc(IV) can be described with the equilibrium constant (K), and the equilibrium line (50 % Tc(VII), 50 % Tc(IV)) is calculated from the equation (shown as broken line in figures): $TcO_4^- + 3e^- + 4H^+ \Leftrightarrow TcO_2 \cdot xH_2O(s) + (2-x)H_2O$ and $\log K^o = \log [TcO_4^-] - 3\,pe + 4 \log [H^+]$ with $\log K^o = 37.8 \pm 0.6$ ($I = 0$) from the data selected by the Rard *et al.* [RAR/RAN1999]. For 0.1 M NaCl/NaOH solution, the K value was corrected using the SIT method and ion interaction coefficients of $\varepsilon\ (H^+, Cl^-) = 0.12\ kg \cdot mol^{-1}$ and $\varepsilon\ (ClO_4^-, Na^+) = 0.01\ kg \cdot mol^{-1}$ [GUI/FAN2003], which is taken as analogue for $\varepsilon\ (TcO_4^-, Na^+)$. Under the condition of initial Tc concentration ($[Tc]_{init}$) = 10^{-5} M, i. e., $\log [TcO_4^-] = \log ([[Tc]_{init} / 2]) = -5.30$, the calculated borderline was $pe = -1.3 \cdot (-\log [H^+]) + 11.0$. The results in **Fig. 5.9** indicate that the experimental borderline for the reduction of Tc(VII) (bold dot line) is about 2 pe-units (about 100 mV) lower than the calculated line (broken line). This may suggest that the reduction with slow kinetics by reducing chemicals lead to different solid phases, or at least different particle size distribution compared to more crystalline solid phases assumed for the thermodynamic calculation. The value of $\log K^o$ for the Tc(IV) solid phase selected by Rard *et al.* [RAR/RAN1999] was calculated from the standard redox potential (E^o), which was determined from the investigation of redox potential measurement data of the $TcO_4^-/TcO_2 \cdot xH_2O(s)$ couple [COB/SMI1953, MEY/ARN1991a]. In the literature, the solid phases were prepared by electrochemical reduction of macroscopic amounts of TcO_4^-. Under the experimental condition of lower initial Tc concentration in this study, Tc(VII) may be precipitated not as $TcO_2 \cdot xH_2O(s)$ but rather small colloidal particles, $TcO_2 \cdot xH_2O$(coll, hyd). This explanation would be similar to the Np(V) reduction processes and the role of colloidal Np(IV) phases described recently by Neck *et al.* [NEC/ALT2009]. In their study on the reduction of Np(V) to Np(IV), the experimental borderline was also observed to be lower than the calculated equilibrium line from the thermodynamic constant of NpO_2(am, hyd) and NpO_2(coll, hyd) considered as small solid phase particles was proposed. In **Fig. 5.9**, the experimental borderline was determined to be pe = -1.3·pH + 9.3, and log K for $TcO_2 \cdot xH_2O$(coll, hyd) was obtained to be 33.1 at I = 0.1.

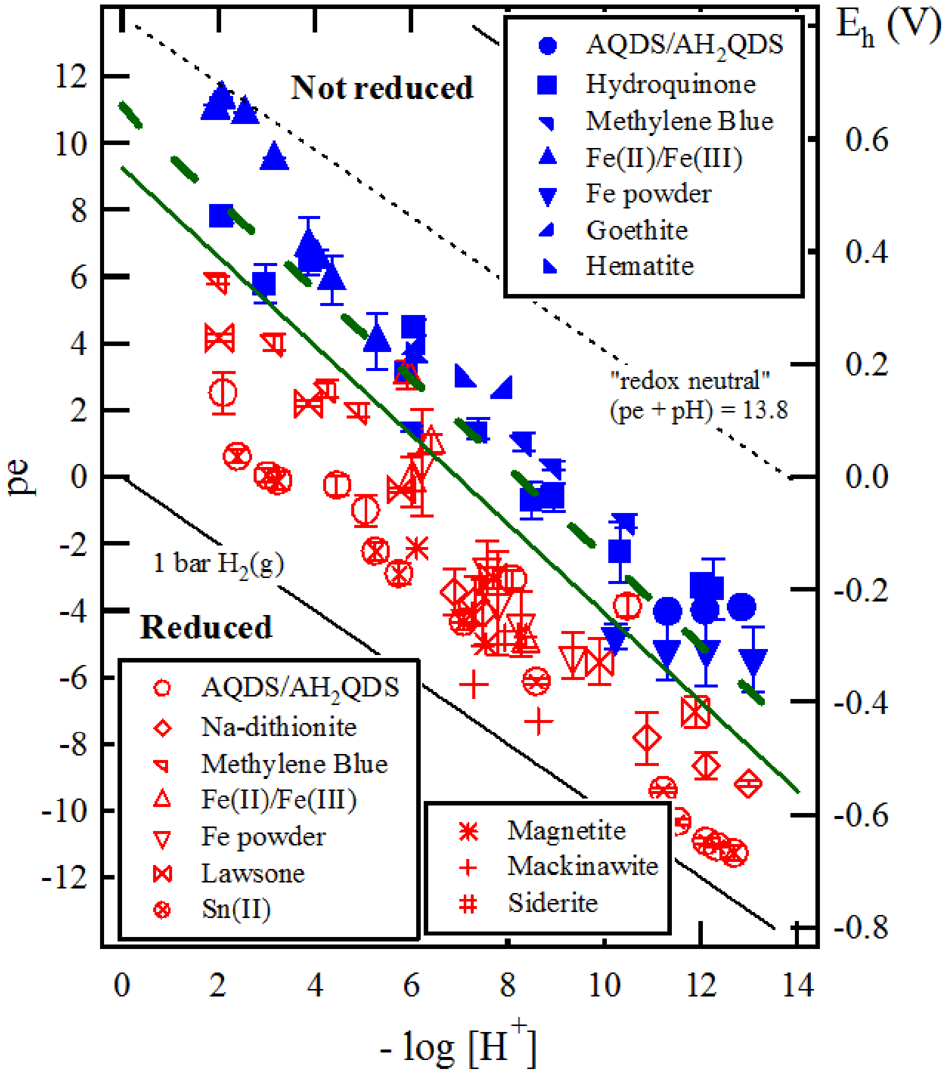

Fig. 5.9 Experimental plots on the reduction of Tc(VII) ($[TcO_4^-]_{init} = 10^{-5}$ M)

Samples reduced are shown as open symbols, samples not reduced as filled symbols

The kinetics for the reduction of Tc(VII) generally showed a significant dependence on E_h in homogeneous solutions systems (**Fig. 5.10**). The reduction rate decreased when E_h increased from strongly negative values, such as in Sn(II) system, to near the reduction borderline and in the systems such as Lawsone, the rate of reduction was extremely slow. On the other hand, a rapid decrease of the initial Tc concentration was observed in suspensions where the E_h values were lower than the borderline in **Fig. 5.9**. In Fe powder suspensions at pH_c < 10, the Tc concentration decreased to detection limit level (10^{-8} M) within 3 days, although the E_h values were closed to those in the Lawsone system, where slow kinetics were observed.

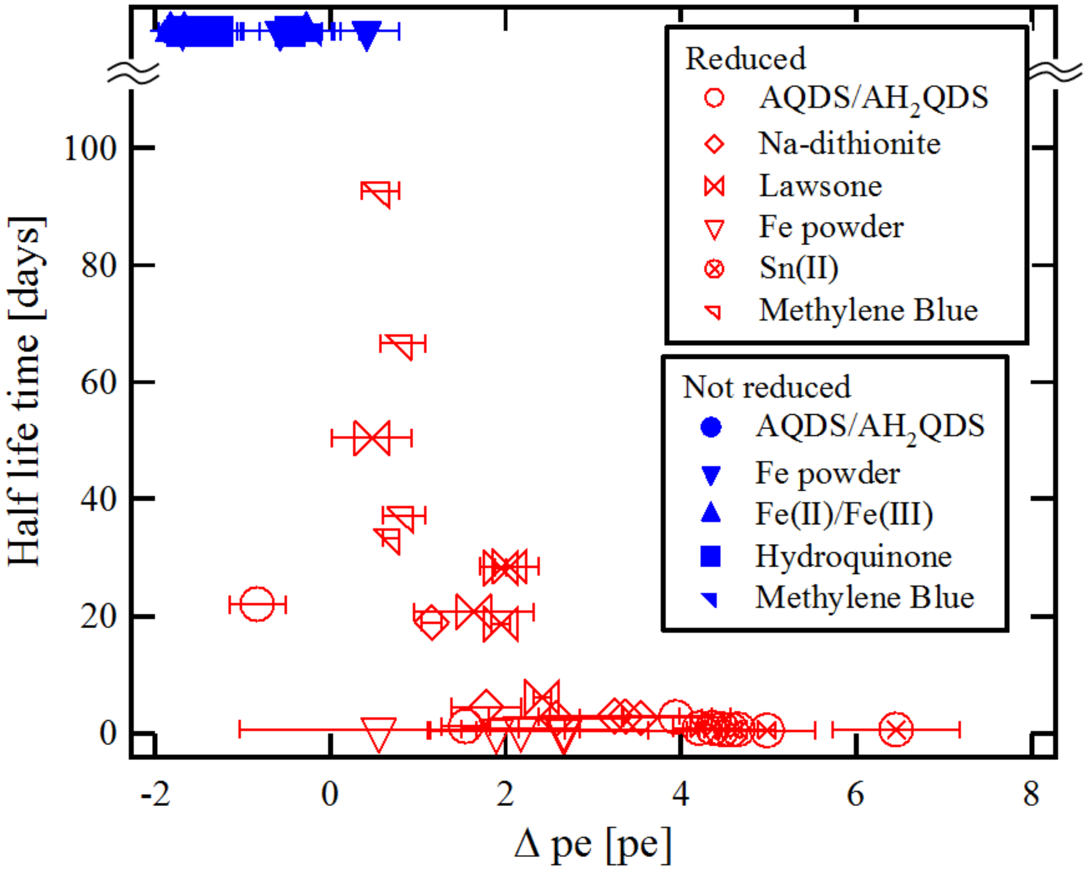

Fig. 5.10 Reduction rate half life time as a function of the difference of pe values between the measured value in each reducing system and experimental borderline in **Fig. 5.9** (Δ pe)

5.2.2 Studies on Tc(VII)-(IV) redox processes in medium and high ionic strength NaCl and $MgCl_2$ solution

5.2.2.1 Introduction

The mobility of Tc is strongly dependent on its oxidation state. Although several oxidation states of Tc are reported in the literature (+III, +IV, +V, +VI, +VII) [RUS/CAS1978, GRA/ROG1978,GRA/DEV1979_ENREF_13], Tc(VII) and Tc(IV) are the prevailing stable redox states in the absence of any complexing ligands under non reducing and reducing conditions, respectively. Heptavalent Tc exists as highly soluble and mobile TcO_4^- pertechnetate anion under environmental conditions, whereas Tc(IV) forms sparingly soluble hydrous oxide ($TcO_2 \cdot xH_2O$) under reducing conditions.

The redox behaviour of the Tc(VII)/Tc(IV) couple was investigated by several authors in different reducing systems. Owunwanne *et al.* [OWU/MAR1977] and Warwick *et al.* [WAR/ALD2007] used Sn(II) to reduce Tc(VII) under highly acidic (pH < 2) and highly alkaline (pH > 13.3) conditions, respectively. A fast and complete reduction of Tc(VII) was observed in both cases, although no solid phase characterization was performed in these studies. Cui *et al.* [CUI/ERI1996a] observed that the reduction of Tc(VII) to Tc(IV) by $Fe(II)_{(aq)}$ was kinetically hindered, whereas Fe(II) precipitated or sorbed on the vessel walls rapidly reduced Tc(VII). Zachara *et al.* [ZAC/HEA2007] also studied the reduction of Tc(VII) in presence of $Fe(II)_{(aq)}$ in the neutral pH region (6-8). The authors reported that reaction kinetics were strongly pH dependent and reduction of Tc(VII) was a combination of a homogenous and heterogeneous reaction. Ben Said *et al.* [BEN/FAT1998] investigated the reduction of Tc(VII) in acidic solutions as a function of [Tc], $[Fe(II)]_{(aq)}$ and Fe(II)/Fe(III) ratio. Several studies have also focussed on the reduction/sorption mechanisms of Tc on solid iron phases of special relevance for nuclear waste disposal [UM/CHA2011, WHA/ATK2000, LIU/TER2008, LIV/JON2004, MCB/LLO2011, LLO/DEN2008]. In spite of the large numbers of experimental studies, the understanding of Tc(VII)/Tc(IV) redox behaviour is currently rather restricted to dilute aqueous systems.

The present work builds upon studies in dilute 0.1 M NaCl solution and focusses on Tc redox and solubility chemistry in repository-relevant brine systems which are so far lacking in the case of waste disposal in rock salt formations. The redox behaviour of Tc(VII)/Tc(IV) couple was investigated in diluted to concentrated saline solutions. Redox experiments were performed in NaCl (0.5 M and 5.0 M) and $MgCl_2$ (0.25 M, 2.0 M and 4.5 M) solutions by using homogenous and heterogeneous reducing systems. The results are systematised according to the E_h-pH conditions in solution to assess Tc redox behaviour in high saline systems. The experimental data are compared to thermodynamic calculations after determination of technetium concentration and redox state. XANES analysis is used to characterize the redox state and molecular environment of Tc in the heterogeneous reducing systems evaluated.

5.2.2.2 Thermodynamic background

Thermodynamic data of Tc are reported in the NEA-TDB series [RAR/RAN1999], within a comprehensive evaluation of Tc literature including discussion of the redox potential of Tc(VII)/Tc(IV) couple in dilute systems [COB/SMI1953, CAR/SMI1955, MEY/ARN1991a]. Tc(VII) is the most stable oxidation state of Tc, and exists as pertechnetate anion (TcO_4^-) in non-reducing and oxidizing solutions. Under reducing conditions, Tc is predominantly found as Tc(IV), which forms sparingly soluble hydrous oxide ($TcO_2{\cdot}xH_2O$). The redox reaction between TcO_4^-/ $TcO_2{\cdot}xH_2O(s)$ is summarized in the NEA-TDB as:

$$TcO_4^- + 4H^+ + 3e^- \Leftrightarrow TcO_2{\cdot}xH_2O(s) + 0.4H_2O \qquad (5.1)$$

The standard potential selected in the NEA-TDB is E^o= 0.747 ± 0.004 V, which leads to $\log{}^*K^\circ = 37.8 \pm 0.6$ for reaction (5.1).

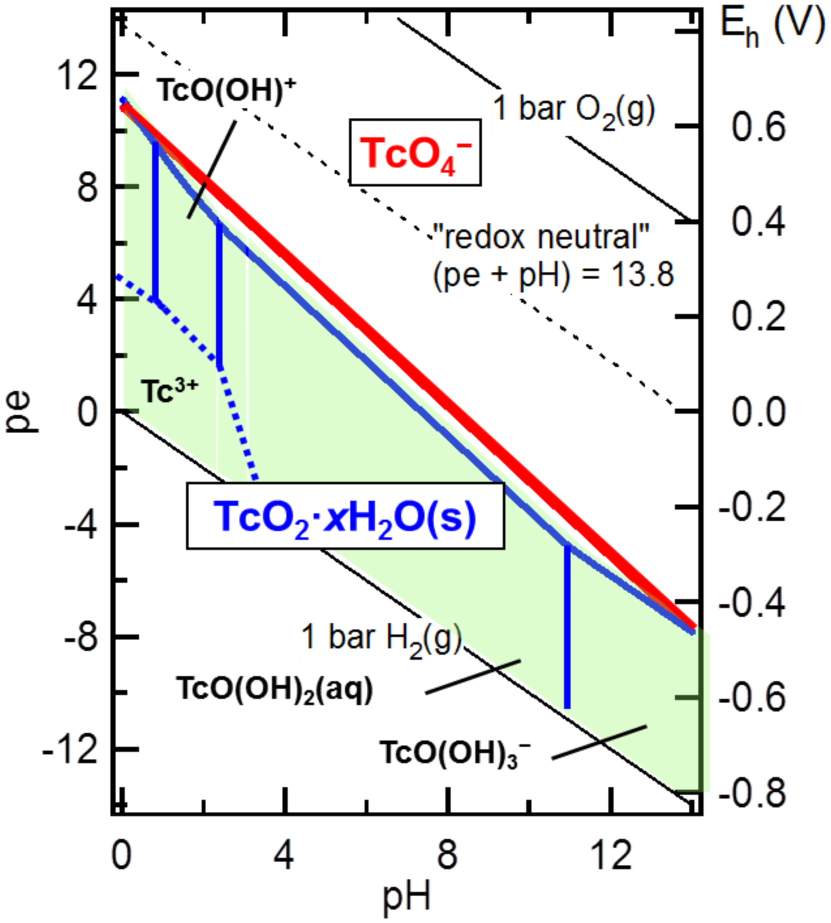

Fig. 5.11 *Pourbaix* diagram of Tc(VII)/Tc(IV) at I = 0, $[TcO_4^-]=10^{-5}$ M calculated based on NEA-TDB

Fig. 5.11 shows the *Pourbaix* diagram of Tc within 0 ≤ pH ≤ 14 and -14 ≤ pe ≤ 14. The red line in the figure corresponds to the thermodynamically calculated equilibrium line (at I = 0) based on the reaction (5.1). For the description of highly saline systems, ionic strength corrections for thermodynamic data at I = 0 are necessary.

The specific ion interaction theory (SIT approach) is the method for ionic strength corrections adopted in NEA-TDB. The basic formalisms used in SIT are summarized below.

Activity coefficient:

$$\log_{10} \gamma_j = -z_j^2\, D + \sum_k \varepsilon(j, k, I_m)\ m_k \qquad (5.2)$$

Debye-Hückel constant:

$$\mathrm{D} = \frac{\mathrm{A}\sqrt{\mathrm{I_m}}}{1 + \mathrm{Ba_j}\sqrt{\mathrm{I_m}}} \tag{5.3}$$

Ionic strength:

$$I_\mathrm{m} = \frac{1}{2}\sum_\mathrm{i} \mathrm{m_i z_i^2} \tag{5.4}$$

The summation in Eq (5.2) extends over all ions k present in solution. Their molality is denoted m_k, and $\varepsilon(j, k, I_m)$ is the specific ion interaction parameters. A and B in the Debye-Hückel term are constants which are temperature and pressure dependent, whereas a_j is an ion size parameter for the hydrated ion j.

In this study, the activity coefficients were corrected for each specific saline system (0.5 M and 5.0 M NaCl; 0.25 M, 2.0 M and 4.5 M $MgCl_2$) by SIT approach based on the chemical analogues of Tc (i. e. $\varepsilon(ClO_4^-, Na^+) = 0.01$) in NEA-TDB. Ionic strength corrections were applied on the Tc(VII)/Tc(IV) equilibrium line (dashed lines) on the *Pourbaix* diagram. The E_h and pH values measured in individual reducing systems are plotted on the diagrams to assess the redox behaviour of Tc. Tc concentrations were measured in the aqueous phase to confirm the reduction to Tc(IV), as the formation of $TcO_2 \cdot xH_2O(s)$ leads to decrease from the initial TcO_4^- concentration level (10^{-5} M) in solution (see Reaction (5.1).

5.2.2.3 Experimental techniques

5.2.2.3.1 Chemicals

Hydroquinone ($C_6H_4(OH)_2$), sodium dithionite ($Na_2S_2O_4$), and metallic iron powder (grain size 10 µm) were obtained from Merck, $FeCl_3 \cdot 6H_2O$, $SnCl_2$ and tetraphenylphosphonium chloride (TPPC) were purchased from Sigma-Aldrich, and $FeCl_2$ from Alfa Aesar. HCl and NaOH titrisol (Merck) were used for adjusting the pH of solutions. All solutions were prepared with purified water from a Milli-Q-academic apparatus (Millipore). Before its use, O_2 was removed by bubbling argon through the Milli-Q water.

All sample preparation and handling was performed in an Ar-glove box at the controlled area of KIT-INE.

5.2.2.3.2 Sample preparation

The samples were prepared at different ionic strength conditions in NaCl (0.5 M and 5.0 M) and in $MgCl_2$ (0.25 M, 2.0 M and 4.5 M) with additions of 1 mM $Na_2S_2O_4$, 1 mM $SnCl_2$, 3 mM hydroquinone (HQ), 1 mM/0.1 mM Fe(II)/Fe(III), 1 mg/15 ml Fe powder and in the presence of Fe(II) minerals (magnetite, mackinawite and siderite). The pH values were adjusted using HCl, NaOH or $Mg(OH)_2$ of same ionic strength. The initial Tc(VII) concentration was set to $[TcO_4^-] = 10^{-5}$ M by addition of 13 mM $NaTcO_4$ stock solutions to the pre-equilibrated solutions.

5.2.2.3.3 Measurements and analysis

After equilibration times of three days to several months, the hydrogen ion concentration (pH_c) and redox potential were measured using combination pH electrodes (type ROSS, Orion) calibrated against standard pH buffers (pH 1–11, Merck), and Pt combination electrodes with Ag/AgCl reference system (Metrohm). The values of $pH_c = pH_{exp} + A_c$ were obtained from the operational “measured” pH_{exp} values using empirical corrections factors [ALT/MET2003].

Redox potentials were measured with Pt combination electrodes with Ag/AgCl reference system (Metrohm) and converted to E_h versus the standard hydrogen electrode by correction for the potential of the Ag/AgCl reference electrode (+208 mV for 3 M KCl at 25 °C). Stable E_h readings were obtained within 10 minutes in most of the samples, although in some cases longer equilibration times (up to 30 minutes) were needed. The apparent electron activity ($pe = -\log a_{e^-}$) was calculated from $E_h = -(RT/F) \ln a_{e^-}$, according to the relation $pe = 16.9\ E_h$ (V). The performance of the redox electrode was tested with a standard redox buffer solution (Schott, +640 mV vs. Ag/AgCl) and provided readings within ± 10 mV of the certified value. Previous studies [BIS/HAG2009, SCH/BIS2010] have suggested the need of (experimentally determined) correction factors for E_h measured at high ionic strengths, which should mostly account for variations in the liquid junction potential. Liquid junction potentials below 50 mV are expected in the conditions of this study [BAR1994]. These values are well within the uncertainty considered for E_h measurements, and thus the use of such corrections has been disregarded in this work.

After 10 kDa (2 − 3 nm) ultrafiltration, the Tc concentration in the filtrate was determined by Liquid Scintillation Counting (Quantulus, Perkin Elmer). The detection limit for Tc–99 under the given conditions is ~10^{-9} M. The technetium oxidation state of the aqueous species was investigated by a solvent extraction technique [OMO/MUR1994, KOP/ABU1998], where TcO_4^- is extracted into chloroform using TPPC. The supernatant of the sample solution was contacted to chloroform containing 50 mM TPPC. After vigorous mixing for 1 minute and subsequent separation of the aqueous and organic phases by centrifugation, the Tc concentrations in both phases were determined by LSC.

5.2.2.4 Results and discussion

The Tc(VII)/Tc(IV) redox behaviour was investigated in various homogenous and heterogeneous reducing systems. Measured E_h and pH values are summarized on *Pourbaix* diagrams to assess Tc redox behaviour in highly saline systems. The broken lines on the E_h-pH diagrams represent equilibrium line between TcO_4^- and $TcO_2 \cdot 1.6H_2O(s)$ (50 % Tc(VII), 50 % Tc(IV)) thermodynamically calculated and corrected by SIT approach for each ionic strength conditions. The dotted line and solid lines on the E_h-pH diagrams correspond to the “redox neutral line” [NEC/ALT2007] and the border for the reduction of water, respectively. The measured Tc concentrations after different aging times from three days up to several months are shown besides the E_h-pH diagrams. The decrease of the Tc concentration in the aqueous phase from the initial Tc(VII) level (10^{-5} M) is interpreted as a reduction of Tc(VII) due to formation of $TcO_2 \cdot 1.6H_2O$ solid phase. This information was complemented for selected samples by solvent extraction technique (see **Tab. 5.2**).

Tab. 5.2 Tc(IV) ratios in selected samples by solvent extraction

Background Electrolyte	**Concentration of Background Electrolyte**	**Reducing System**	**pH_c**	**E_h (mV)**	**%Tc(IV)**
NaCl	0.5 M	$Na_2S_2O_4$	7.5	-269	98
	0.5 M	$Na_2S_2O_4$	6.6	-120	99
	0.5 M	$Na_2S_2O_4$	12	-437	92
	5.0 M	$Na_2S_2O_4$	12.7	-445	99
	0.5 M	Sn(II)	1.9	28	98
	0.5 M	Sn(II)	13.3	-760	99
	5.0 M	Sn(II)	2.9	80	92
	5.0 M	Sn(II)	14	-759	99
	0.5 M	HQ	1.8	396	1.4
	5.0 M	HQ	2.9	398	0.8
	0.5 M	Fe(II)/Fe(III)	2	643	0.4
	5.0 M	Fe(II)/Fe(III)	2.8	400	0.07
	5.0 M	Fe(II)/Fe(III)	4.5	634	0.36
$MgCl_2$	2.0 M	$Na_2S_2O_4$	7	28	99
	4.5 M	$Na_2S_2O_4$	9	-56	99
	2.0 M	Sn(II)	3.7	4	73
	4.5 M	Sn(II)	4	140	62
	4.5 M	Sn(II)	6.4	-10	85
	4.5 M	Sn(II)	9	-215	99
	0.25 M	Fe(II)/Fe(III)	3.4	203	0.1
	2.0 M	Fe(II)/Fe(III)	3.8	485	0.2
	4.5 M	Fe(II)/Fe(III)	4.2	608	0.3
	4.5 M	Fe(II)/Fe(III)	6.4	363	0.6
	4.5 M	Fe Powder	9	-196	99
	4.5 M	Fe Powder	8.9	-127	99

5.2.2.4.1 Tc(VII) reduction by $Na_2S_2O_4$ in medium and high ionic strength NaCl and $MgCl_2$ Solutions

Fig. 5.12 (left) shows the E_h-pH diagram of Tc(VII)/Tc(IV) redox couple in 1 mM $Na_2S_2O_4$ system in 0.5 M and 5.0 M NaCl solutions. In all samples, measured E_h values were found below the thermodynamically calculated Tc(VII)/Tc(IV) borderline. E_h values with large uncertainties (up to 100 mV) were observed in neutral pH region because of the degradation of $Na_2S_2O_4$ in H_2O [GAN/STU1992]. No changes were observed between the E_h values in dilute and concentrated NaCl solutions in this system. The Tc concentrations were measured after given contact times and are shown in **Fig. 5.12** (right). The decrease from the initial TcO_4^- concentration (10^{-5} M) was attributed to the reduction of Tc(VII). The predominance of Tc(IV) was further confirmed by solvent extraction (**Tab. 5.2**). Although Tc concentrations were found lower than the initial level at each pH_c, relatively high Tc concentrations such as 10^{-7} M and 10^{-6} M were observed in neutral (pH_c 6 - 8) and alkaline ($pH_c > 12$) conditions, respectively. In alkaline pH region, this increase can be explained by the formation of anionic Tc(IV) hydrolysis species such as $TcO(OH)_3^-$, which increase $TcO_2 \cdot 1.6H_2O(s)$ solubility [ERI/NDA1992]. In the neutral region, Tc concentrations were found above the solubility limit. Although the reported formation of Tc(IV) eigencolloid might explain our experimental observations, the known degradation of $Na_2S_2O_4$ in these conditions (see also increase in E_h) may lead to decomposition products interacting with the Tc species and thus hinders any definitive interpretation of Tc data in this region.

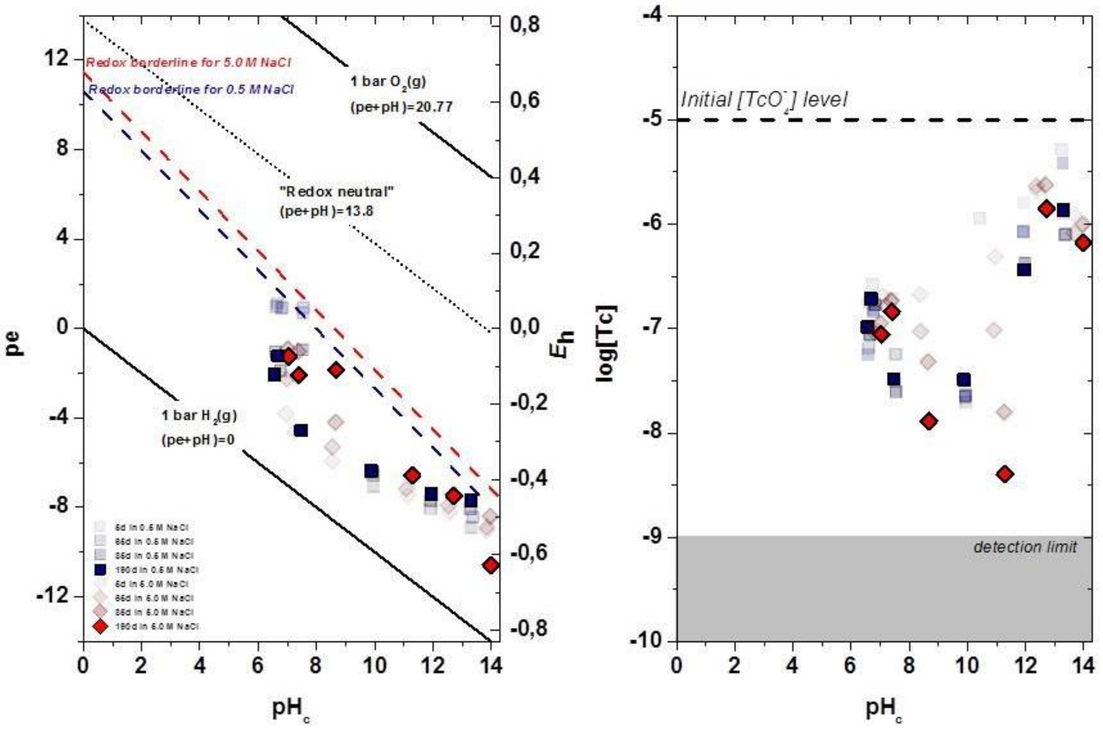

Fig. 5.12 E_h-pH diagram of Tc(VII)/Tc(IV) couple (left) and concentration of Tc (right) in 1 mM $Na_2S_2O_4$ systems in NaCl

The dashed line represents an equilibrium line calculated from NEA-TDB with ionic strength correction by SIT

Fig. 5.13 (left) shows the E_h-pH diagram of Tc(VII)/Tc(IV) redox couple in 1mM $Na_2S_2O_4$ system in 0.25 M, 2.0 M and 4.5 M $MgCl_2$ solutions. All the measured E_h values were found below the thermodynamically calculated Tc(VII)/Tc(IV) borderline. The strong ionic strength effect was observed on the E_h values in alkaline pH (pH_c 9) region up to 5-pe units, while there is no ionic strength effect in the near neutral pH region. The Tc concentrations were measured after equilibration times and are shown in **Fig. 5.13** (right). The decrease from the initial TcO_4^- level and solvent extraction results (**Tab. 5.2**) confirmed the complete reduction of Tc(VII). However, the Tc concentrations in the concentrated $MgCl_2$ solutions are higher than in the dilute $MgCl_2$ solutions.

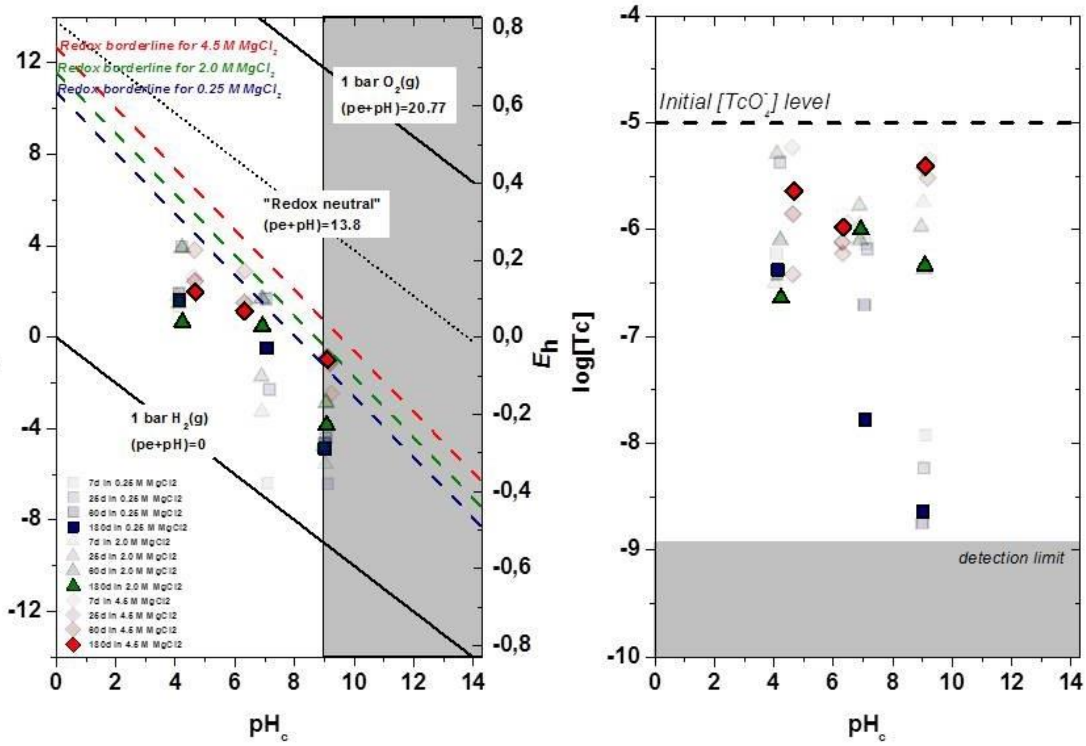

Fig. 5.13 E_h-pH diagram of Tc(VII)/Tc(IV) couple (left) and concentration of Tc (right) in 1 mM $Na_2S_2O_4$ system in $MgCl_2$

5.2.2.4.2 Tc(VII) reduction by Sn(II) in medium to high ionic strength NaCl and $MgCl_2$ Solutions

Fig. 5.14 (left) shows the E_h-pH diagram of Tc(VII)/Tc(IV) redox couple in 1mM Sn(II) system in 0.5 M and 5.0 M NaCl solutions. In all cases, Sn(II) leads to E_h values far below the thermodynamically calculated Tc(VII)/Tc(IV) borderline. Measured Tc concentrations indicate a fast and complete reduction of Tc(VII) (**Fig. 5.14** (right)). In addition, predominance (99 %) of Tc(IV) in all samples was confirmed by solvent extraction (**Tab. 5.2**). However, the Tc concentrations were found relatively high (10^{-5} M - 10^{-6} M) in acidic ($pH_c < 3$) and alkaline ($pH_c > 12$) pH range similar to the $Na_2S_2O_4$ system. Similar trends were observed in the studies of Meyer *et al*. and Eriksen *et al.* at $I \sim 0$.

Their studies proposed the formation of Tc hydrolysis species as TcO^{2+} [MEY/ARN1991a] and $TcO(OH)_3^-$ [ERI/NDA1992] in acidic and alkaline pH range, respectively. A wide range of ionic strength (up to 5.0 M NaCl) was assessed by Hess *et al.* in their Tc(IV) solubility experiments under acidic conditions. Experimental data obtained in this work are in a qualitatively good agreement with the solubility data of Hess *et al.* which are also shown in **Fig. 5.14** (right).

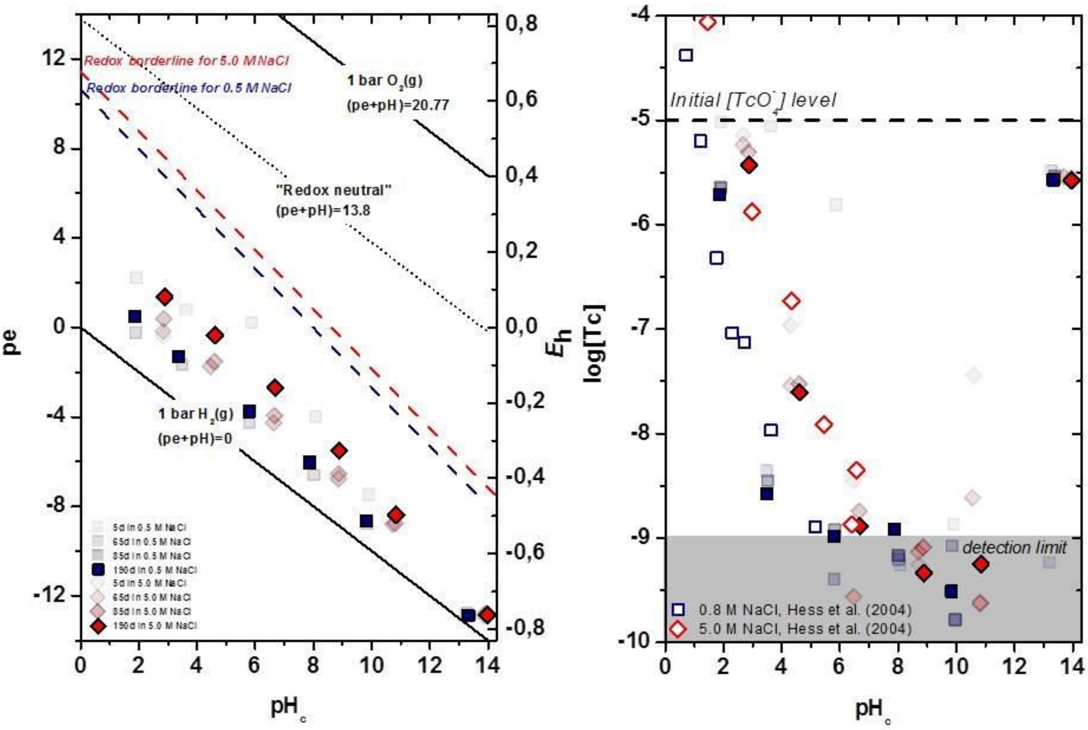

Fig. 5.14 E_h-pH diagram of Tc(VII)/Tc(IV) couple (left) and concentration of Tc (right) in 1 mM Sn(II) system in NaCl

Fig. 5.15 (left) shows the E_h-pH diagram of the Tc(VII)/Tc(IV) couple in the 1mM Sn(II) system in 0.25 M, 2.0 M and 4.5 M $MgCl_2$ solutions. In this system, a strong and linear effect of ionic strength was observed on the measured E_h values. Tc concentrations also indicate a strong ionic strength effect and are shown in **Fig. 5.15** (right). Similarly to the $Na_2S_2O_4$ system, the Tc concentrations increase with increasing the ionic strength in $MgCl_2$ solution. The solvent extraction results show that the content of Tc(IV) in the samples lays between 60 % — 99 % depending on the pH and ionic strength (**Tab. 5.2**). Hess *et al.* also reported similar solvent extraction results in concentrated NaCl solutions, although confirming the predominance of Tc(IV) in aqueous phase by UV-Vis. analysis. The solvent extraction method which extract anionic species in a solution, might give a high uncertainty in case the formation of anionic Tc(IV)-Cl complexes in highly concentrated $MgCl_2$ solutions.

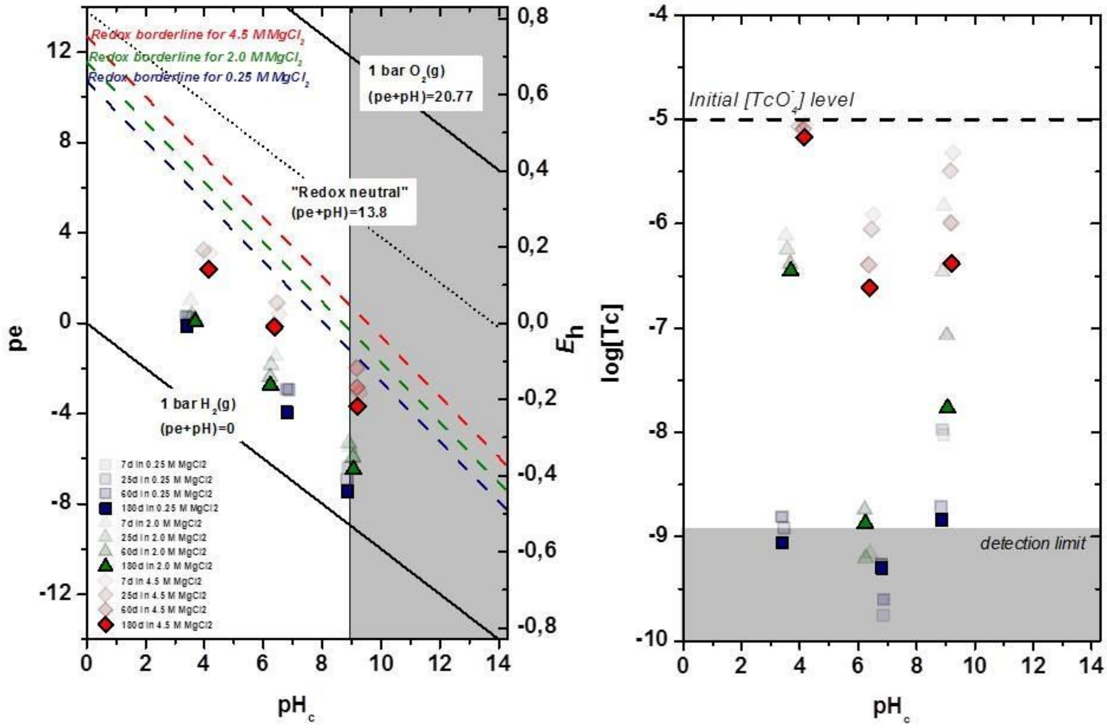

Fig. 5.15 E_h-pH diagram of Tc(VII)/Tc(IV) couple (left) and concentration of Tc (right) in 1 mM Sn(II) system in $MgCl_2$

5.2.2.4.3 Tc reduction by hydroquinone in medium to high ionic strength NaCl and $MgCl_2$ solutions

The measured E_h values in 3 mM HQ system are above the borderline in 0.5 M - 5.0 M NaCl and in 0.25 M - 2.0 M $MgCl_2$ solution over the entire pH region (**Fig. 5.16** (left) and **Fig. 5.17** (left)). However, the E_h values in 4.5 M $MgCl_2$ media are below the thermodynamically calculated Tc(VII)/Tc(IV) borderline. In both cases, it is seen that Tc concentrations remained at initial level (10^{-5} M) in all samples. No change was observed in the Tc concentrations over up to one year equilibration. Predominance of (99 %) Tc(VII) by solvent extraction confirmed that no reduction occurred in this system so far (**Tab. 5.2**). On the other hand, the HQ system confirms that reduction of Tc(VII) does not occur where the E_h values are above the borderline, except one system in 4.5 M $MgCl_2$.

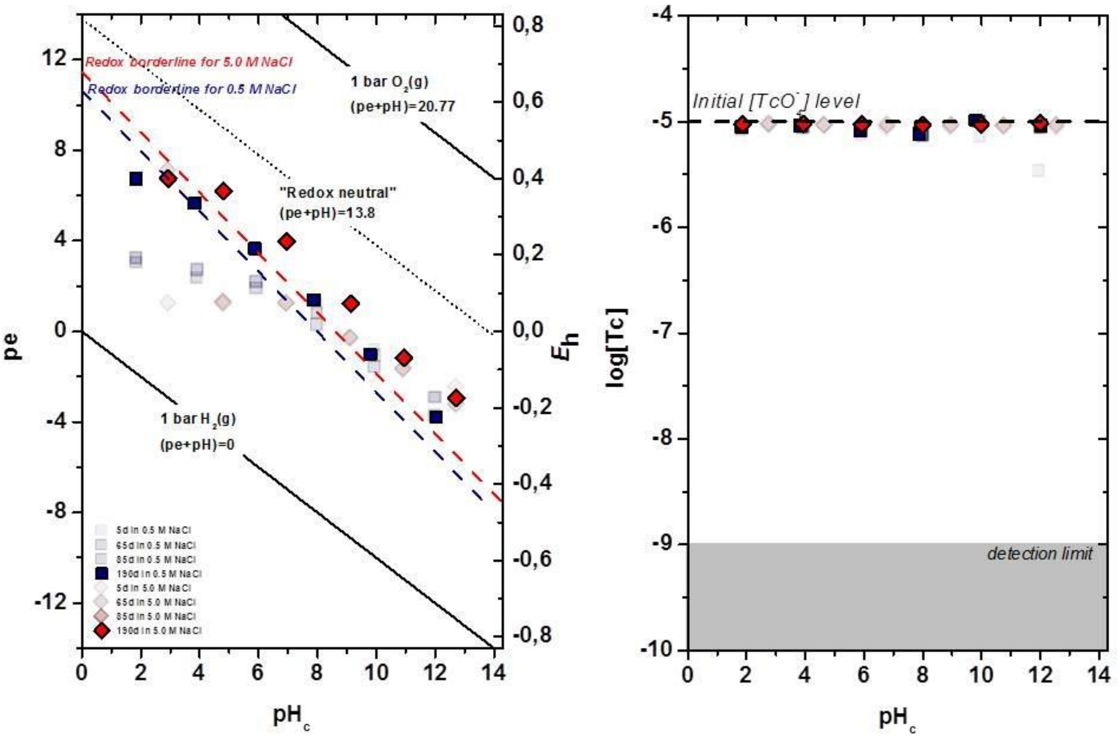

Fig. 5.16 E_h-pH diagram of Tc(VII)/Tc(IV) couple (left) and concentration of Tc (right) in 3 mM HQ systems in NaCl

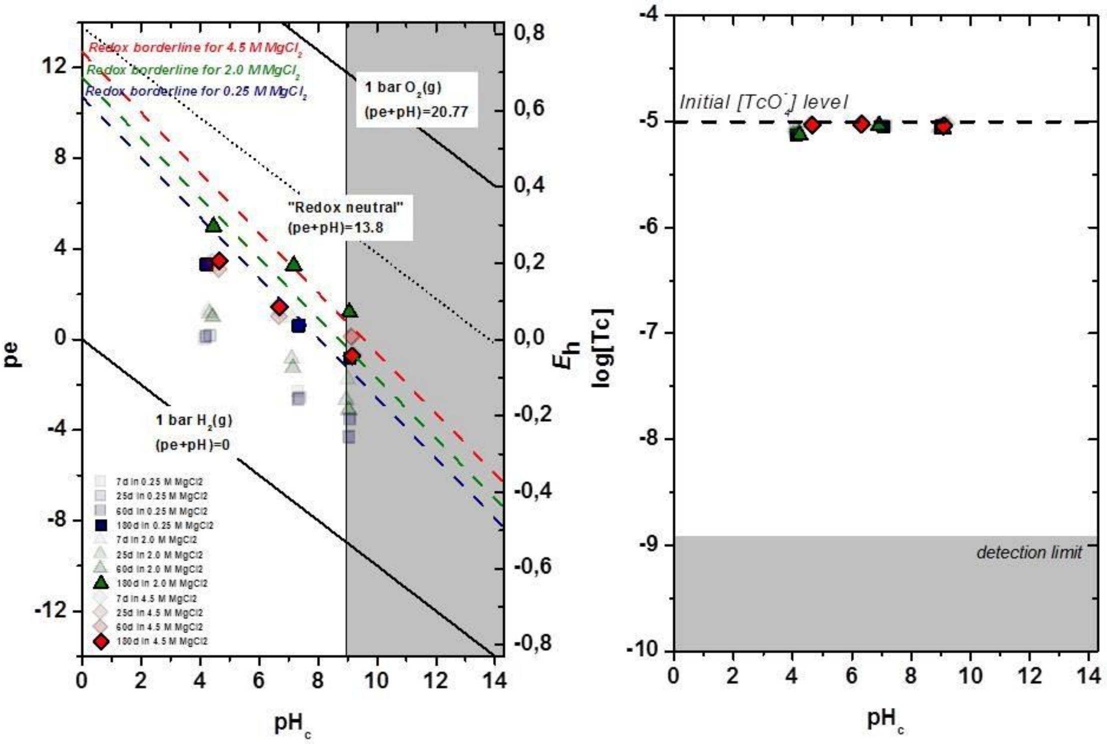

Fig. 5.17 E_h-pH diagram of Tc(VII)/Tc(IV) couple (left) and concentration of Tc (right) in 3 mM HQ systems in $MgCl_2$

5.2.2.4.4 Tc(VII) reduction by Fe(II)/Fe(III) systems in medium to high ionic strength NaCl and MgCl$_2$ solutions

Fig. 5.18 (left) shows the E_h-pH diagram of Tc(VII)/Tc(IV) redox couple in 1 mM/0.1 mM Fe(II)/Fe(III) system in 0.5 M and 5.0 M NaCl solutions. In the acidic pH region, the E_h values are above the calculated Tc(VII)/Tc(IV) borderline, whereas they are below the line in the near neutral and alkaline pH region. Tc concentrations at each pH$_c$ are completely consistent with the measured E_h values. The reduction is only observed in the neutral and alkaline region, while no change of Tc concentration is observed in the acidic pH region (**Fig. 5.18** (right)). Solvent extraction results indicate the predominance of Tc(VII) in the acidic pH region (**Tab. 5.2**). The data observed at neutral pH agrees with the results of Zachara *et al.*, who observed rapid reduction of Tc(VII) in presence of Fe(II) at pH > 6.8 [ZAC/HEA2007] whereas Cui *et al.* reported that no reduction of Tc(VII) occurs by Fe(II) system up to pH 7.5 [CUI/ERI1996a]. Tc concentrations in the aqueous phase do not increase in the alkaline pH range, in contrast to $Na_2S_2O_4$ and Sn(II) systems. This could be attributed to Fe(III) precipitation as a solid phase and sorption or incorporation of Tc(IV) on the precipitated Fe-phases.

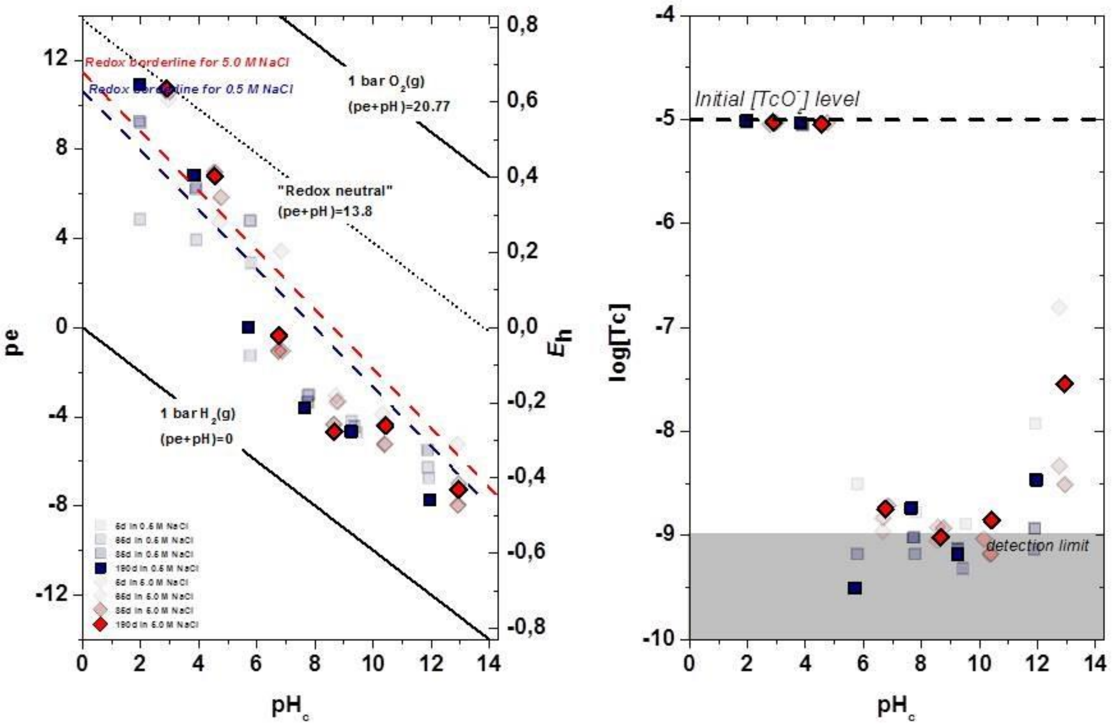

Fig. 5.18 E_h-pH diagram of Tc(VII)/Tc(IV) couple (left) and concentration of Tc (right) in 1 mM/0.1 mM Fe(II)/Fe(III) systems in MgCl$_2$

Fig. 5.19 (left) shows the E_h-pH diagram of Tc(VII)/Tc(IV) redox couple in 1 mM/0.1 mM Fe(II)/Fe(III) system in 0.25 M, 2.0 M and 4.5 M $MgCl_2$ solutions. The strong ionic strength effect was observed on the E_h values at each pH_c in this system. The measured Tc concentrations confirmed the complete reduction of Tc(VII) in the samples which have the E_h values below the borderline (except for one point under acidic conditions) (**Fig. 5.19** (right)). In the neutral pH_c region, the measured E_h values in $MgCl_2$ (up to 2.0 M) were found below the borderline at pH 6 – 7 and reduction was confirmed by the rapid decrease of Tc concentrations. However, the E_h value of the sample in 4.5 M $MgCl_2$ solution is above the calculated borderline. No reduction (stable Tc concentration (10^{-5} M) and 99 % Tc(VII) by solvent extraction) was observed for this sample. It can be concluded that the experimental data is in a very good agreement with thermodynamically calculated Tc(VII)/Tc(IV) redox borderline and ionic strength effects on Tc(VII)/Tc(IV) redox process reasonably assessed within the SIT approach as well.

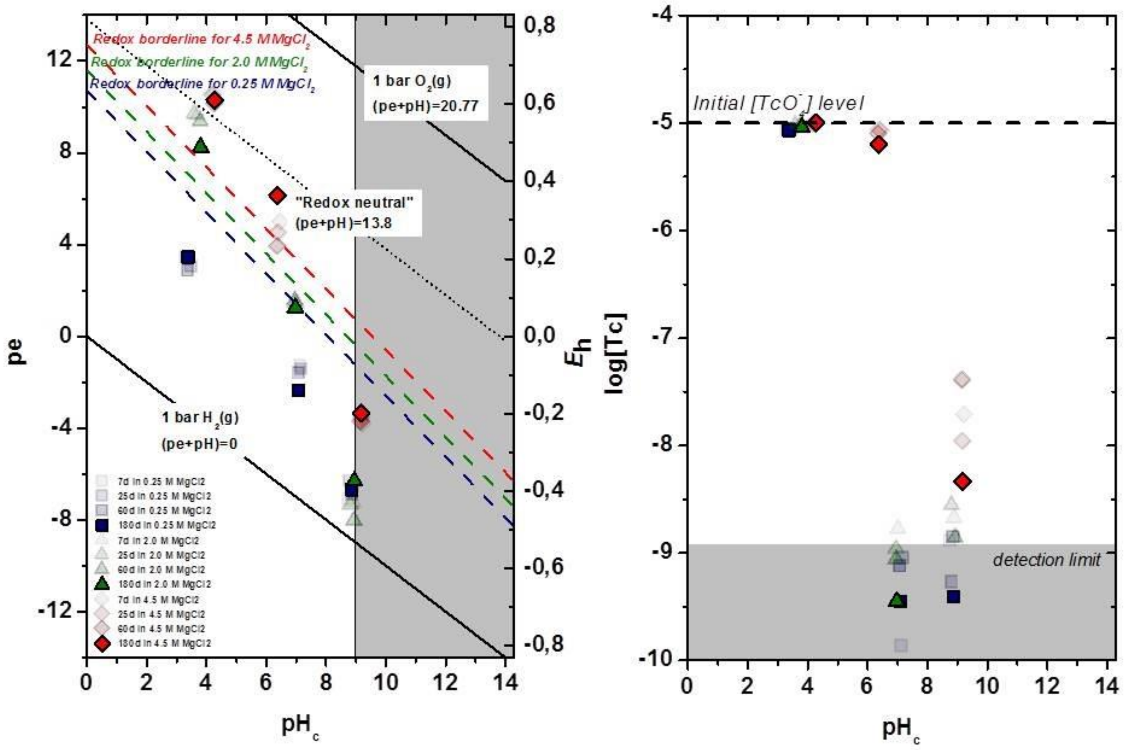

Fig. 5.19 E_h-pH diagram of Tc(VII)/Tc(IV) couple (left) and concentration of Tc (right) in 1 mM/0.1 mM Fe(II)/Fe(III) systems in $MgCl_2$

5.2.2.4.5 Tc(VII) reduction by Fe Powder systems in medium to high ionic strength NaCl and $MgCl_2$ solutions

Fig. 5.20 (left) and **Fig. 5.21** (left) show the E_h-pH diagram of the Tc(VII)/Tc(IV) redox couple in Fe Powder (1 mg Fe in 15 ml solution) in NaCl (0.5 M and 5.0 M) and $MgCl_2$ (0.25 M, 2.0 M and 4.5 M) solutions, respectively. Tc concentrations in NaCl solutions (**Fig. 5.20** (right)) rapidly decreased to detection limit (10^{-9} M) at pH_c 6 - 8. However, no reduction was observed in all samples at $pH_c > 10$ where E_h values are above the calculated Tc(VII)/Tc(IV) redox borderline. In $MgCl_2$ media, all samples shifted to pH_c 9 (**Fig. 5.21** (right)). The results give similar conclusions as observed for the previous reducing systems: a generally good agreement with thermodynamic data and model calculations and strong ionic strength effects both on the experimental E_h values and the Tc concentrations.

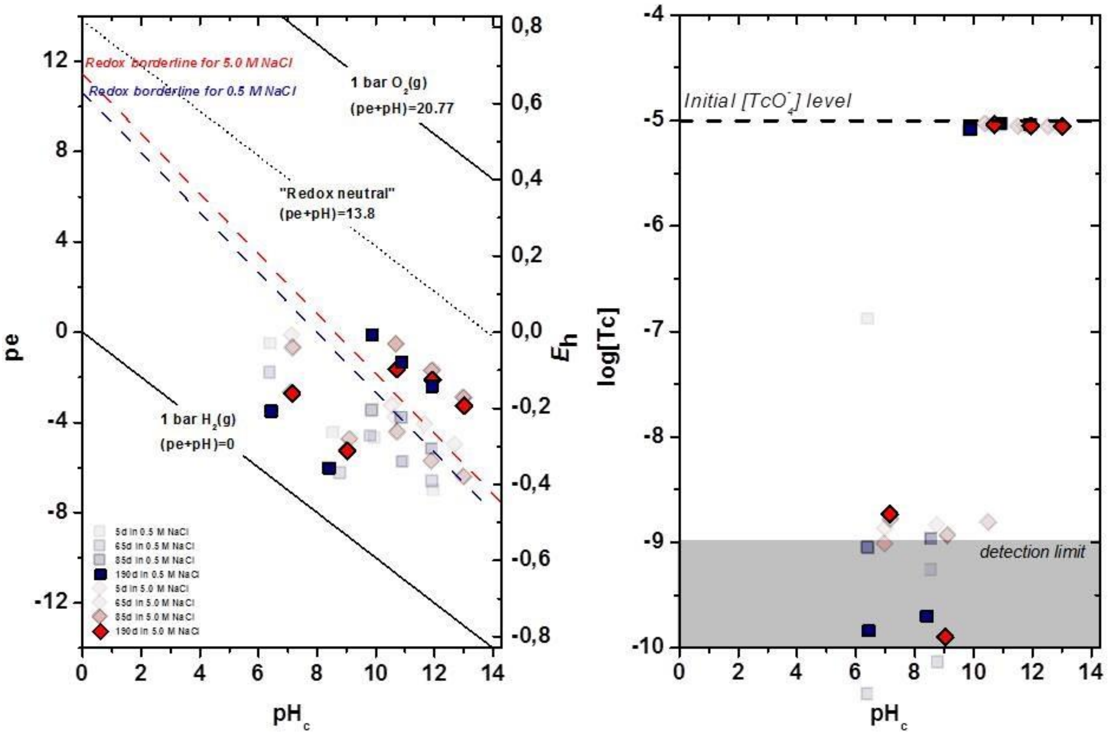

Fig. 5.20 E_h-pH diagram of Tc(VII)/Tc(IV) couple (left) and concentration of Tc (right) in 1 mg Fe Powder systems in NaCl.

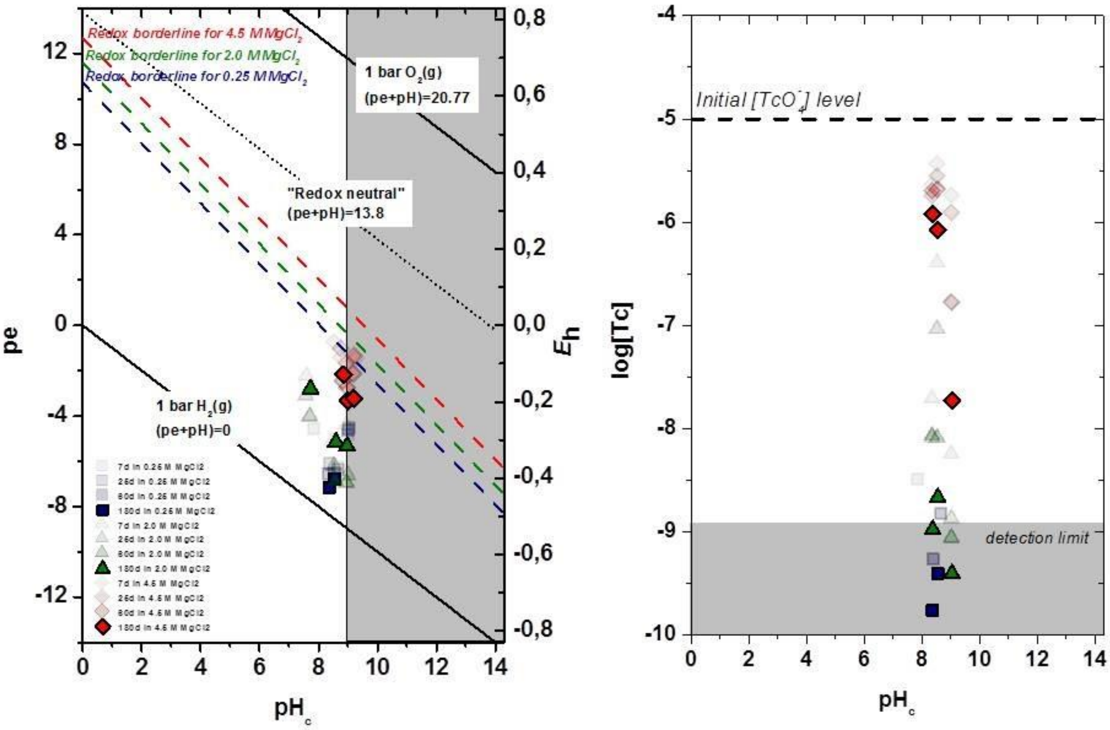

Fig. 5.21 E_h-pH diagram of Tc(VII)/Tc(IV) couple (left) and concentration of Tc (right) in 1 mg Fe Powder systems in $MgCl_2$

5.2.2.4.6 Tc(VII) reduction by Fe(II) minerals in concentrated NaCl and $MgCl_2$ solutions

E_h and pH_c values measured in the Fe mineral suspensions (magnetite, mackinawite and siderite) with Tc after 4 weeks equilibration time are summarized in **Tab. 5.3**. In all cases, experimental E_h values are below the observed Tc(VII)/Tc(IV) reduction borderline. In analogy to previous observations for other reducing systems reported in this work, E_h values in 4.5 M $MgCl_2$ media are significantly higher than in 5.0 M NaCl (~2 pe-units) at the same pH_c. As discussed previously, this observation can be attributed to the impact of high $[Cl^-]$ and/or $[Mg^{2+}]$ on the redox couple controlling the redox conditions of the system.

R_d values[3] for the uptake of Tc by Fe phases in 5.0 M NaCl and 4.5 M $MgCl_2$ are summarized in **Tab. 5.3**. A stronger uptake is observed in 5.0 M NaCl ($4.6 \leq \log R_d$ ($L \cdot kg^{-1}$) ≤ 7.2) compared to sorption samples in 4.5 M $MgCl_2$ ($3.0 \leq \log R_d$ ($L \cdot kg^{-1}$) ≤ 4.1). This

---

[3] calculated as $R_d = \frac{[Tc]_s}{[Tc]_{aq}} \cdot \frac{V}{m}\ (L \cdot kg^{-1})$

is consistent with the expected shift of the sorption edge of Tc(IV) towards higher pH_c values with increasing ionic strength, analogously to observations made for hydrolysis ([HES/XIA2004], p.w.). A similar effect of ionic strength on sorption was recently reported by Schnurr *et al.* for the uptake of Eu(III) by illite [SCH/MAR2013], where a much stronger decrease of sorption in the presence of divalent cations (Ca^{2+} and Mg^{2+}) was observed.

Tab. 5.3 pH_c, E_h and log R_d values determined for the uptake of Tc by Fe minerals (after 4 weeks of equilibration time)

Fe mineral	Background Electrolyte	pH_c[a]	E_h (mV)[b]	log R_d ($L \cdot kg^{-1}$)[c]
Magnetite	5.0 M NaCl	9.6	-140	4.7
Magnetite	4.5 M $MgCl_2$	8.7	10	3.0
Mackinawite	5.0 M NaCl	8.7	-290	7.2
Mackinawite	4.5 M $MgCl_2$	8.3	-150	4.1
Siderite	5.0 M NaCl	8.7	-175	6.0
Siderite	4.5 M $MgCl_2$	8.3	-25	3.8

a: ± 0.05; b: ± 50 mV; c: ± 10 % for log $R_d \leq 3$; ± 50 % for log $R_d \geq 3$

Fig. 5.22 shows the Tc *K*-edge XANES spectra collected for Tc(VII) reacted with Fe(II) minerals. Note that the spectra were collected at a sample temperature of 10 — 15 K in He atmosphere to prevent changes of Tc oxidation state induced by atmospheric O_2 or by O-radicals produced by the high X-ray photon flux. All mineral samples have an edge position near 21058 eV and a white line position at 21065 to 21070 eV in line with Tc(IV), while the distinct pre-edge peak of Tc(VII) at 21050 eV is absent in these samples. Accordingly, Tc(VII) has been reduced to Tc(IV) in all the samples. The edge and white line positions as well as the fine structure are furthermore suggesting coordination to O atoms; therefore, we find no evidence for the (partial) coordination of Tc(IV) by S atoms in the high-salt mackinawite systems. This is in contrast to previous findings at lower ionic strengths in this work and in the literature, where formation of a TcS_2-like phase was found after precipitating mackinawite in the presence of pertechnetate [WHA/ATK2000]. Tc(IV) coordinated to S was also found after sorption of pertechnetate to mackinawite at an ionic strength of 0.1 M [LIV/JON2004, KOB/SCH2013], pointing to a decisive role of ionic strength on the reaction product, but this needs confirmation by more detailed investigations.

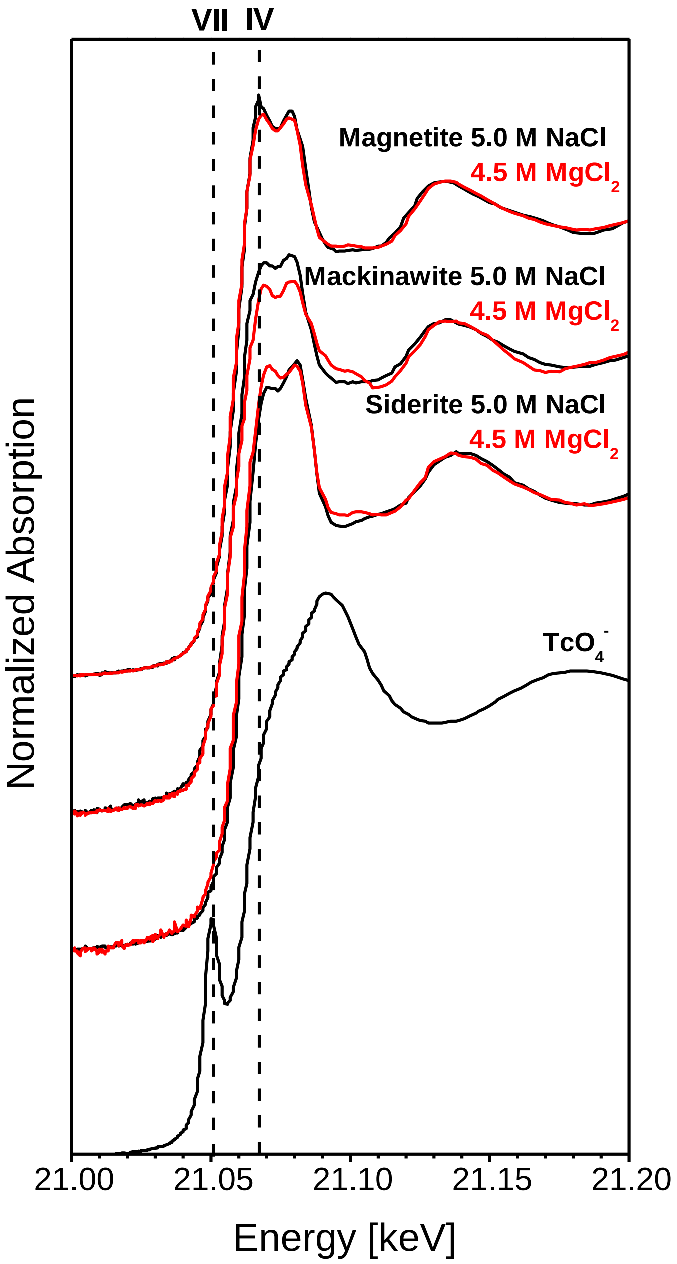

Fig. 5.22 Tc *K*-edge XANES spectra of Tc(VII) reacted with magnetite, mackinawite and siderite

5.2.3 Conclusions on Tc(VII)-Tc(IV) redox processes

The Tc(VII)/Tc(IV) redox behaviour was investigated in dilute to concentrated NaCl and $MgCl_2$ solutions to assess the effect of homogeneous and heterogeneous reducing systems and ionic strength on Tc redox behaviour. It is seen that the redox behaviour of Tc strongly depends on the E_h values measured in these solutions. The thermodynamically calculated borderline of the Tc(VII)/Tc(IV) couple corrected by SIT agrees well with experimental data. The borderline is found to be independent of the reducing systems. Reduction of Tc(VII) to Tc(IV) is observed with redox potentials below this borderline in any conditions, while no Tc(VII) reduction occurs in the systems with redox potentials above the borderline. For a given reducing system, the concentration of Tc(IV) increased with increase of ionic strength (and high Cl concentration).

5.3 The solubility of Tc(IV) in dilute to concentrated NaCl, $MgCl_2$ and $CaCl_2$ systems

5.3.1 Introduction

Previous redox studies showed that $TcO_2{\cdot}xH_2O$ is the predominant solid phase which forms under reducing conditions. There is small number of studies on the solubility of Tc(IV). Meyer *et al.* [MEY/ARN1991a] investigated the solubility of Tc(IV) in the pH range 1 to 10. They used electrodeposited oxide solid phase and oxide precipitated onto sand particles from reduction of Tc(VII) by hydrazine. The authors suggested the solubility limit of $TcO_2{\cdot}xH_2O$ as 10^{-8} to 10^{-9} M in basic solutions. On the other hand, the solubility increases in the acidic pH range due to the formation of hydrolysis species like TcO^{2+} and $TcO(OH)^+$. The authors proposed the number of hydration waters in $TcO_2{\cdot}xH_2O$ to be 1.63 ± 0.28. Eriksen *et al.* [ERI/NDA1992] performed solubility experiments with electrodeposited Tc(IV) oxide as a function of pH and P_{CO2}. They reported pH independent solubility limit as $7{\cdot}10^{-9}$ M over the pH range 6 to 9.5. The increase of the solubility was observed above pH 9.5 with a linear slope of 1. This was interpreted as formation of anionic $TcO(OH)_3^-$ species with $\log{}^*K^{o} = -19.3 \pm 0.3$ at high pH. These two studies were reviewed in NEA Thermochemical Database Project (NEA-TDB) series and considered for the final thermodynamic data selection of Tc [RAR/RAN1999]. Recently, Warwick *et al.* investigated the solubility of Tc(IV) reduced by Sn(II) and Fe(II) within pH range 11.8 to 14.4. In contrast to NEA-TDB, these authors observed two orders of magnitude lower solubility in highly alkaline conditions above pH 13.5. The formation constant of $TcO(OH)_3^-$ was reported as $\log{}^*K^{o} = -21.6 \pm 0.3$ [WAR/ALD2007]. Hess *et al.* conducted solubility experiments in highly saline (up to 5.0 M NaCl) and highly acidic (up to 6.0 M HCl) solutions. Solubility data reported in this study at low ionic strength agrees well with NEA-TDB, whereas higher solubility of Tc(IV) was observed with increasing ionic strength. Comprehensive thermodynamic and activity models for Tc(IV) under acidic conditions were derived by the authors based on their experimental results and speciation analysis [HES/XIA2004]. Although the solubility of Tc(IV) has been extensively investigated in acidic pH conditions in dilute to concentrated saline solutions, significant discrepancies arise under alkaline conditions, where available studies are also limited to dilute systems.

This work focuses on Tc(IV) solubility chemistry in repository-relevant brine systems which are so far lacking in the case of waste disposal in rock salt formations. The redox studies completed in the first part of this work (see Chapter 5.2 of this report) served a starting point for the comprehensive Tc(IV) solubility studies in brine solutions. Solubility experiments are performed in NaCl (0.1 – 5.0 M), $MgCl_2$ (0.25 – 4.5 M) and $CaCl_2$ (0.25 – 4.5 M) solutions. Solubility data of Tc(IV) are generated in dilute to concentrated saline systems to develop a complete thermodynamic description (SIT, Pitzer) for the system Tc^{4+}-H^+-Na^{+-}-Mg^{2+}-Ca^{2+}-$OH^–$-$Cl^–$ valid over the pH range 2 – 14.

5.3.2 Experimental

5.3.2.1 Chemicals

All solutions were prepared with purified water (Milli–Q academic, Millipore) and purged with Ar before use. All sample preparation and handling was performed in an Ar-glove box at 22 ± 2 °C. NaCl (p. a.), $MgCl_2·6H_2O$ (p. a.), $Mg(OH)_2$(cr), $CaCl_2·2H_2O$ (p. a.), $Ca(OH)_2$ (p. a.), sodium dithionite ($Na_2S_2O_4$) and metallic iron powder (grain size 10 µm) were purchased from Merck; $SnCl_2$, pH buffers MES (pH 5 – 7) and PIPES (pH 7 – 9) were obtained from Sigma-Aldrich. HCl and NaOH Titrisol© (Merck) were used for adjusting the pH of solutions.

5.3.2.2 pH and E_h measurements

The hydrogen ion concentration ($pH_m = -\log(m_{H^+})$) was measured using combination pH electrodes (type ROSS, Orion) calibrated against standard pH buffers (pH 1 – 12, Merck). The values of $pH_m = pH_{exp} + A_m$ were calculated from the operational "measured" pH_{exp} using empirical corrections factors (A_m), which entail both the liquid junction potential and the activity coefficient of H^+. A_m values determined as a function of NaCl, $MgCl_2$ and $CaCl_2$ concentration are available in the literature [ALT/MET2003]. In NaCl–NaOH solutions with $[OH^–] > 0.03$ M, the H^+ concentration was calculated from the given $[OH^–]$ and the conditional ion product of water. In $MgCl_2$ and $CaCl_2$ solutions, the highest pH_m (pH_{max}) is fixed by the precipitation of $Mg(OH)_2$ and $Ca(OH)_2$ (or corresponding hydroxochlorides at Ca/Mg concentrations above ~2 m), which buffer pH_m at ~9 and ~12, respectively [ALT/MET2003].

Redox potentials were measured with Pt combination electrodes with Ag/AgCl reference system (Metrohm) and converted to E_h versus the standard hydrogen electrode by correction for the potential of the Ag/AgCl reference electrode (+208 mV for 3 M KCl at 25 °C).

5.3.2.3 Solid phase preparation and characterization: Solubility measurements

The Tc(VII) stock solution was electrochemically reduced in 1.0 M HCl solution at E_h ~ -50 mV *vs*. S.H.E.. The resulting Tc(IV) suspension was quantitatively precipitated as $TcO_2 \cdot 1.6H_2O$ (s) in a 5 mM $Na_2S_2O_4$ solution at pH_m ~12, and was aged for two months before further use. About 5 mg of Tc from the resulting solid phase were added to several experimental series in (0.1 M – 5.0 M) NaCl with $2 \leq pH_m \leq 14.5$, (0.25 M – 4.5 M) $MgCl_2$ with $2 \leq pH_m \leq 9$ and (0.25 M – 4.5 M) $CaCl_2$ with $7 \leq pH_m \leq 12$. $Na_2S_2O_4$, $SnCl_2$ or Fe powder (depending upon target pH_m) were used to maintain reducing conditions.

The Tc concentration in solution was monitored at regular time intervals by Liquid Scintillation Counting (LSC, Quantulus, Perkin Elmer) after 10 kDa ultrafiltration (2 – 3 nm, Pall Life Sciences). Samples for LSC analysis were mixed with 10 mL of LSC–cocktail Ultima Gold XR (Perkin–Elmer), resulting in a limit of confidence ~10^{-9} M. The oxidation state of Tc in the aqueous phase was determined by solvent extraction as reported elsewhere [OMO/MUR1994, KOP/ABU1998]. Briefly, the supernatant of the sample was contacted with 50 mM TPPC in chloroform. After vigorous mixing for 1 minute and subsequent separation of the aqueous and organic phases by centrifugation, Tc concentration in the aqueous phase was determined by LSC.

For solid phase analysis, an aliquot of each solid (~1 mg) was washed under Ar-atmosphere in triplicate with ethanol to remove the matrix solution. A first fraction of the resulting solid was dissolved in 2 % HNO3, and technetium and Na/Mg/Ca concentrations were quantified by LSC and ICP-OES, respectively. A second fraction of the washed solid was characterized by scanning electron microscope-energy disperse spectrometry (SEM-EDS), using a CamScan FE44 SEM equipped with a Noran EDS unit and by powder XRD (D8 Advance, Bruker).

Tc *K*-edge (21044 eV) XANES spectra of the supernatant solution in selected solubility samples were recorded in fluorescence mode at the INE–Beamline [ROT/BUT2012] at ANKA.

5.3.3 Results and discussion of Tc(IV) solubility data

5.3.3.1 Solubility of Tc(IV) in dilute to concentrated NaCl solutions

Tc(IV) solubility data measured within the timeframe 3-600 days in 0.1 M, 0.5 M, 3.0 M and 5.0 M NaCl solutions in comparison with the solubility data reported in the literature (MEY/ARN1991a, ERI/NDA1992, HES/XIA2004, WAR/ALD2007) are shown in **Fig. 5.23**. Except a sample at $pH_m = 2$ in 5.0 M NaCl, equilibrium conditions were attained within few months in all NaCl systems, as confirmed by the stable Tc concentration and pH_m readings. Experimental data obtained in dilute NaCl agree very well with previous solubility data reported by Meyer *et al.* [MEY/ARN1991a] and Eriksen *et al.* [ERI/NDA1992], as well as the current hydrolysis scheme reported in the NEA–TDB [GUI/FAN2003]. However, the newly generated solubility data is in disagreement with data reported in Warwick *et al.* [WAR/ALD2007], likely indicating significant differences in the crystallinity of the solid phase controlling the solubility of Tc(IV). In agreement with the Tc(IV) chemical model selected in the NEA–TDB, the increase in solubility observed at $pH_m \leq 4$ and $pH_m \geq 10$ might indicate the formation of TcO^{2+} (with a minor contribution of $TcOOH^{+}$) and $TcO(OH)_3^{-}$ hydrolysis species, respectively. Furthermore, the pH–independent solubility reaction $TcO_2 \cdot 1.6H_2O(s) \Leftrightarrow TcO(OH)_2(aq) + 0.4H_2O$ controls the solubility of Tc(IV) within $4 \leq pH_m \leq 10$.

The solubility behaviour of Tc(IV) significantly increases (up to 3 orders of magnitude) at $pH_m \leq 6$ with increasing ionic strength. This trend is qualitatively agreeing with previous experimental evidences reported by Hess *et al.* [HES/XIA2004]. However, it is in contradiction with the previous Tc(IV) chemical model proposed by Hess *et al.*, based upon solubility data (with slope of -1) obtained with significantly shorter equilibration times (t = 4 – 29 days). Note that the slope of -2 observed in all investigated NaCl systems in the present study, which might agree with the formation of TcO^{2+} selected in the NEA–TDB. On the other hand, later spectroscopic studies in the acidic pH-range reported the formation/predominance of polymeric $Tc_nO_p^{(4n-2p)+}$ hydrolysis species at pH ≤ 3 [VIC/OUV2002, VIC/FAT2003, POI/FAT2006]. Hence, the chemical models derived in this study are based on the spectroscopic evidences in the acidic pH region instead of NEA–TDB selection for this specific case. The pH–independent solubility behaviour is observed in the neutral pH region with low Tc concentration, regardless of ionic strength. This observation agrees very well with NEA–TDB and consequently, the solubility reaction selected. Under hyperalkaline conditions ($pH_m \leq 11$), the solubility of

Tc(IV) slightly decreases with increasing ionic strength. As for diluted systems, the slope of +1 determined in this pH region confirms the predominance of the species $TcO(OH)_3^-$ in the aqueous phase.

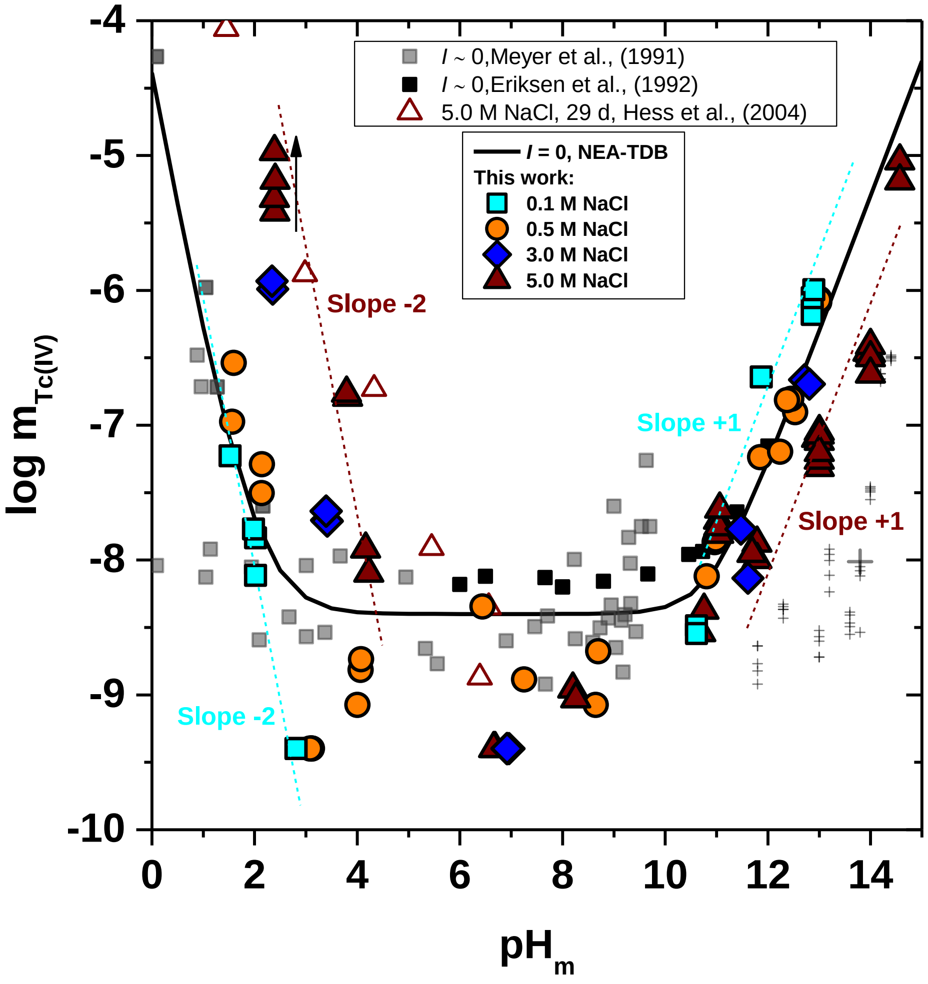

Fig. 5.23 Solubility of Tc(IV) in dilute to concentrated NaCl. Solid line corresponds to $TcO_2 \cdot xH_2O(s)$ solubility calculated with the current NEA–TDB selection at *I* = 0. Dashed lines indicate the defined slope in the present work

5.3.3.2 Solubility of Tc(IV) in dilute to concentrated $MgCl_2$ solutions

Tc(IV) solubility data obtained in 0.25 M – 4.5 M $MgCl_2$ solutions (t ≤ 500 days) are shown in **Fig. 5.24**. The experimental data at 2 ≤ pH_m ≤ 9 in 0.25 M $MgCl_2$ agree well with solubility data in dilute NaCl solutions and with thermodynamic calculations at *I* = 0 using the NEA–TDB selection. The increase in solubility observed at pH_m ≤ 6 is interpreted with the formation of the same hydrolysis species as in NaCl system, while the pH–independent solubility reaction $TcO_2 \cdot 1.6H_2O(s) \Leftrightarrow TcO(OH)_2(aq) + 0.4H_2O$ is responsible for the control of Tc(IV) solubility within $4 \leq pH_m \leq 9$.

A very significant increase in solubility (up to 4 orders of magnitude) is observed in 4.5 M $MgCl_2$ compared to dilute systems. This observation is consistent with the data previously reported from oversaturation conditions [YAL/GAO2014] and further confirms the higher solubility of Tc(IV) in concentrated brines in this pH-region. The increase of solubility stops at $pH_m = 3.5$ in 4.5 M $MgCl_2$ solutions. Under alkaline conditions, an earlier and steeper increase of the solubility with slope of +3 hints towards the formation of higher hydrolysis species which are not formed in NaCl and diluted $MgCl_2$ solutions. This observation likely indicates the participation of magnesium in the stabilization of a highly hydrolysed Tc environment. Note that analogous species were previously described for An(IV) and Zr(IV) in concentrated $CaCl_2$ solutions [ALT/NEC2008, FEL/NEC2010].

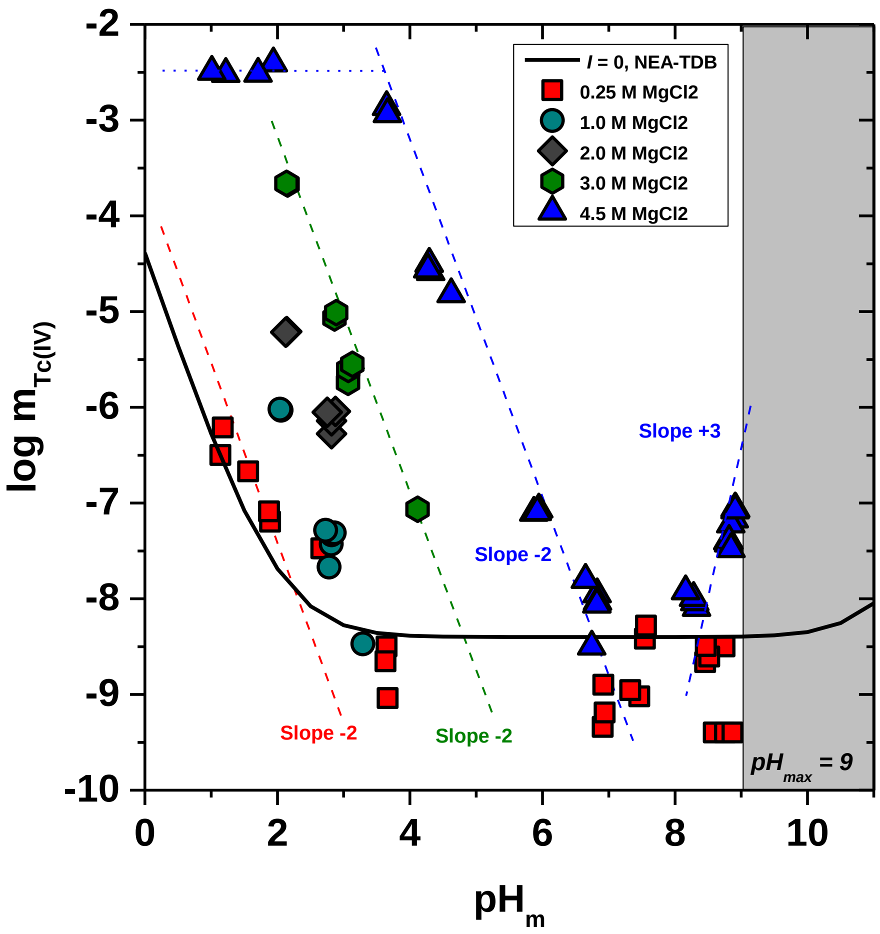

Fig. 5.24 Solubility of Tc(IV) in 0.25 M-4.5 M $MgCl_2$

Solid line corresponds to $TcO_2 \cdot xH_2O(s)$ solubility calculated with the current NEA–TDB selection at *I* = 0. Dashed lines indicate the defined slope in the present work

5.3.3.3 Solubility of Tc(IV) in dilute to concentrated $CaCl_2$ solutions

Tc(IV) solubility data obtained in 0.25 M – 4.5 M $CaCl_2$ solutions (*t* ≤ 500 days) are shown in **Fig. 5.25**. Solubility experiments with $CaCl_2$ as background electrolyte were performed within 7 ≤ pH$_m$ ≤ 12 (pH$_{max}$) with the aim of extending Tc(IV) solubility in $MgCl_2$ solutions to higher pH values. As in the case of concentrated $MgCl_2$ solutions, a very steep increase of solubility with a slope of +3 is obtained in 4.5 M $CaCl_2$ under alkaline conditions (9.5 ≤ pH$_m$ ≤ 10.5). Considering $TcO_2 \cdot 1.6H_2O(s)$ as the solid phase controlling the solubility of Tc(IV) in this conditions, the increase in solubility observed in concentrated $MgCl_2$ and $CaCl_2$ solutions is explained by the formation of the ternary species $Mg_x[TcO(OH)_5]^{2x-3}$ and $Ca_x[TcO(OH)_5]^{2x-3}$ according with the chemical reactions (5.5) and (5.6), respectively. Similar ternary species were previously reported by Altmaier, Neck and Fellhauer for An(IV) ($Ca_4[An(OH)_8]^{4+}$, with An = Th, Np, Pu) and Zr(IV) ($Ca_3[Zr(OH)_6]^{4+}$) [ALT/NEC2008, FEL/NEC2010].

$$TcO_2{\cdot}1.6H_2O + xMg^{2+} + 2.4H_2O \Leftrightarrow Mg_x[TcO(OH)_5]^{2x-3} + 3H^+ \quad (5.5)$$

$$TcO_2{\cdot}1.6H_2O + xCa^{2+} + 2.4H_2O \Leftrightarrow Ca_x[TcO(OH)_5]^{2x-3} + 3H^+ \quad (5.6)$$

Fig. 5.25 shows that thermodynamic equilibrium has not been reached at *t* = 500 days for samples in 2.0 M and 4.5 M $CaCl_2$ at $pH_m \geq 10.5$. Note that strong kinetics were also observed by Fellhauer *et al.* [FEL/NEC2010, FEL2013] for the solubility of Np(IV) and Np(V) in concentrated $CaCl_2$ system under analogous pH conditions. Longer equilibration time as well as accurate solid phase characterization after attaining equilibrium conditions is needed to properly assess the behavior of Tc(IV) in this system.

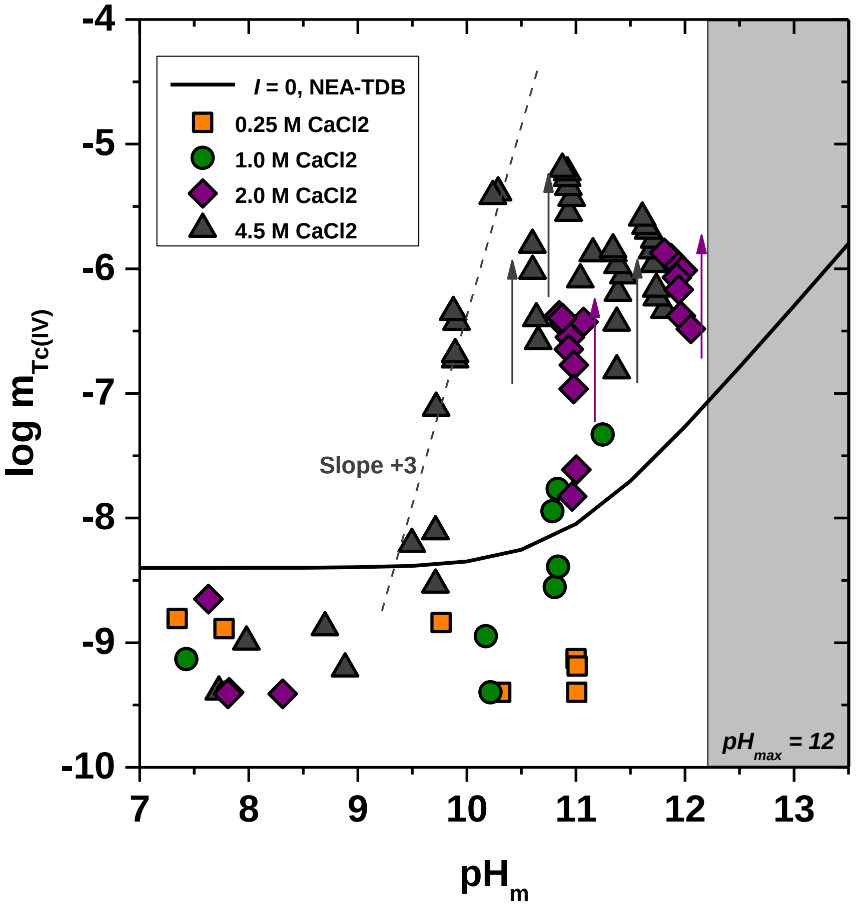

Fig. 5.25 Solubility of Tc(IV) in 0.25 M – 4.5 M $CaCl_2$

Solid line corresponds to $TcO_2{\cdot}xH_2O(s)$ solubility calculated with the current NEA–TDB selection at *I* = 0. Dashed lines indicate a slope of +3

5.3.3.4 Aqueous and solid phase characterisation

After attaining equilibrium conditions, solvent extraction, XAFS and solid phase characterization (XRD, SEM–EDS, chemical analysis) were conducted for selected samples. Solvent extraction results are shown in **Tab. 5.4**. The predominance of Tc(IV) in the aqueous phase of NaCl solutions is confirmed by solvent extraction, whereas it is seen that Tc(IV) ratio decreases in 4.5 M $MgCl_2$ towards acidic pH region (**Tab. 5.4**). Similar observations with solvent extraction were reported by Hess *et al.* [HES/XIA2004] for the solubility of Tc(IV) in concentrated NaCl and HCl solutions. In order to evaluate the possible oxidation of Tc(IV) to Tc(VII) under acidic concentrated brines, complementary XANES analysis were performed at ANKA for one sample at pH_m = 2 in 4.5 M $MgCl_2$ (data not shown). The outcome of these measurements demonstrates the predominance of Tc(IV) in aqueous phase, thus confirming the limitations of the solvent extraction technique under these experimental conditions.

Tab. 5.4 Tc(IV) content in the aqueous phase of selected samples as quantified by solvent extraction. Reducing chemicals and measured pH_m and E_h for each sample also provided

Background Electrolyte	Reducing system	pH_m[a]	E_h[b] (mV)	%Tc(IV)[c]
0.5 M NaCl	$Na_2S_2O_4$	12.4	-670	99
5.0 M NaCl	Sn(II)	2.5	80	99
5.0 M NaCl	$Na_2S_2O_4$	13.0	-540	98
5.0 M NaCl	$Na_2S_2O_4$	14.0	-580	98
4.5 M $MgCl_2$	Sn(II)	2.0	n.m.	13
4.5 M $MgCl_2$	Sn(II)	4.0	–50	52
4.5 M $MgCl_2$	Fe Powder	8.9	–170	91
4.5 M $MgCl_2$	Sn(II)	9.0	–175	94

a: ± 0.05; b: ± 50 mV; c: ± 10 %; n.m. = not measured

X-ray diffractograms show broad patterns attributed to amorphous $TcO_2{\cdot}xH_2O(s)$ in all investigated samples in NaCl, $MgCl_2$ systems (**Fig. 5.26**) and $CaCl_2$ systems at $pH_m \leq 10.5$ (**Fig. 5.27**). XRD patterns of the samples in 4.5 M $CaCl_2$ at $pH_m \leq 10.5$ show the presence of an unknown peak at $2\Theta = 11.6°$. This feature could not be assigned to any previously reported Tc compound, and may hint towards the transformation of $TcO_2{\cdot}xH_2O$ into a more stable Ca-Tc(IV)-OH phase. Longer equilibration time and a more detailed investigation of this particular system are needed.

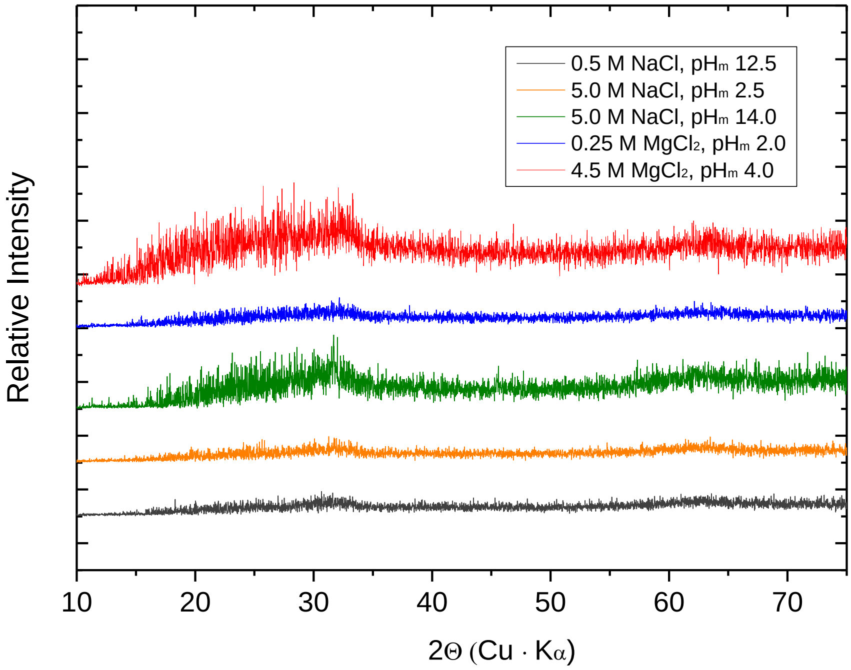

Fig. 5.26 XRD spectra of solid phases from selected solubility experiments in NaCl and $MgCl_2$ systems

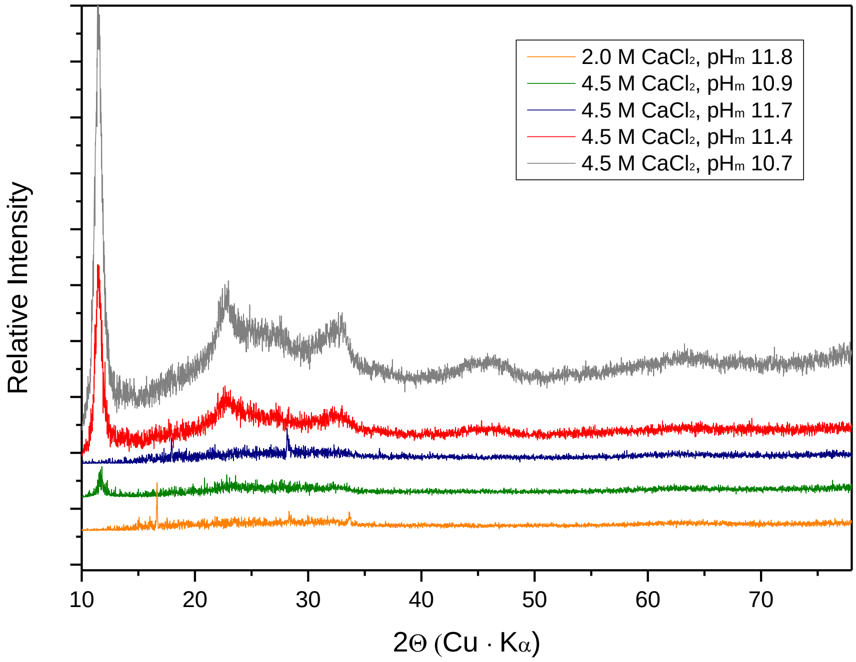

Fig. 5.27 XRD spectra of solid phases from selected solubility experiments in $CaCl_2$ systems

SEM images of the samples in all investigated NaCl and $MgCl_2$ systems show the Tc amorphous aggregates as main component, in good agreement with XRD observations

(**Fig. 5.28**). In alkaline $MgCl_2$ systems with $pH_m \approx pH_{max}$, the presence of Mg-OH-Cl(s) phase can be observed (spot A in **Fig. 5.28**, right) in good agreement with the high concentration of Mg determined by chemical analysis.

Elemental analysis of the solubility samples at $10.5 \leq pH_m < 11.7$ in 4.5 M $CaCl_2$ solutions show the precipitation of $CaCl_2$ and corresponding oxochloride as well as Sn and S compounds, which are coming from degradation/oxidation of reducing systems i. e. $SnCl_2$ and $Na_2S_2O_4$, respectively. Despite of that, Ca:Tc ≈1:1 is observed on the amorphous Tc-like phases (**Fig. 5.28**, bottom) by subtracting any other elements. This observation may hint towards solid phase transformation to Ca-Tc(IV)-OH in that region.

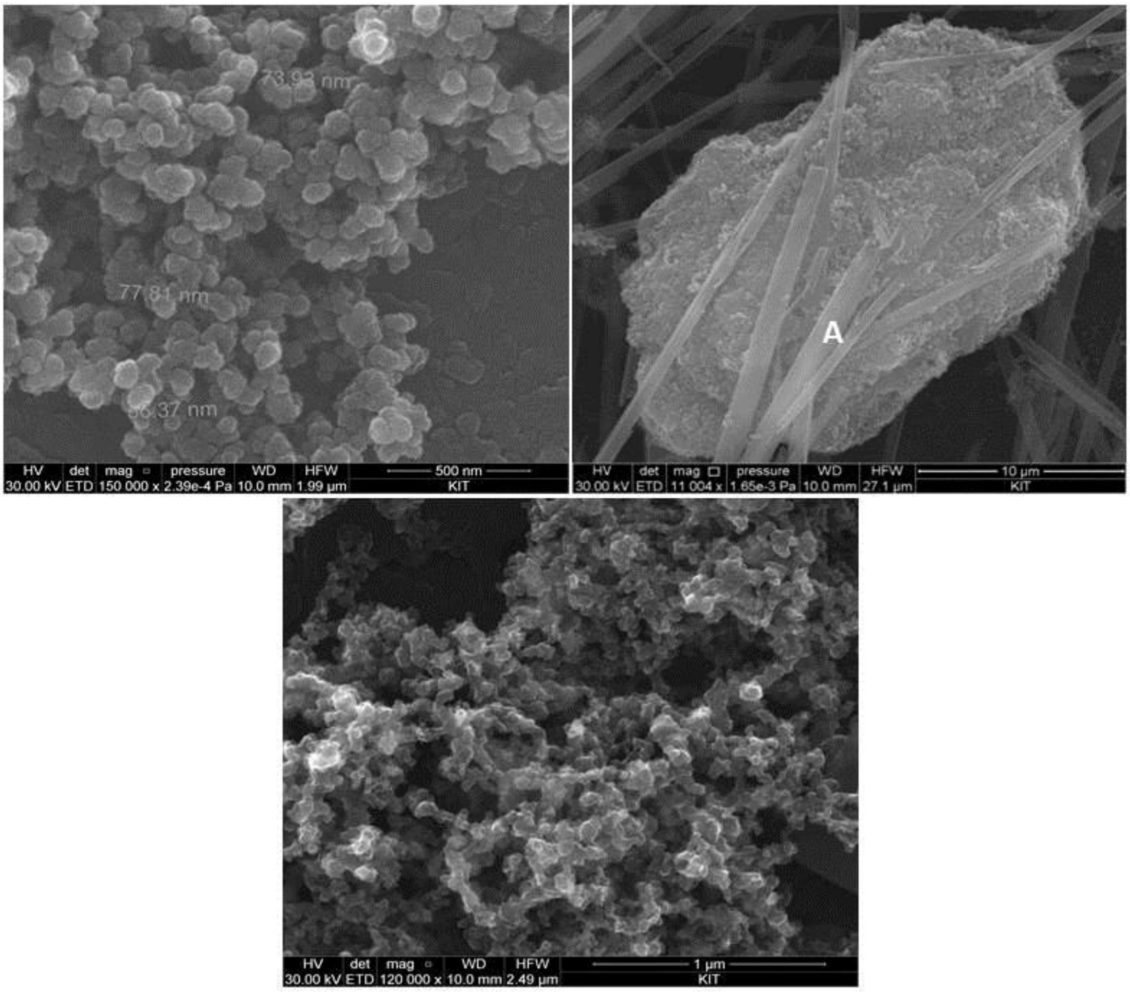

Fig. 5.28 SEM images of the solubility samples at $pH_m = 14.0$ in 5.0 M NaCl (left), at $pH_m = 9.0$ in 4.5 M $MgCl_2$ (right) and at $pH_m = 11.4$ in 4.5 M $CaCl_2$ (bottom)

Quantitative chemical analyses show the absence of Na in the Tc solid phases controlling the solubility in NaCl system, even for those phases equilibrated in 5.0 M NaCl solutions. Similarly, no Mg is detected in solid phases controlling the solubility under acidic conditions in 4.5 M $MgCl_2$, whereas very high Mg concentration are observed in alkaline samples where pH = pH_{max}. In these samples, precipitated hydroxochlorides are very clearly seen on SEM images (**Fig. 5.28**, right). These observations clearly hint to the absence of Na and Mg as component of the Tc(IV) solid phase controlling the solubility in NaCl and $MgCl_2$ systems, respectively. The measured samples indicate the presence of a significant amount of Ca in the solid in $CaCl_2$ systems. Although precipitation of $CaCl_2$ and/or calcium hydroxochlorides is observed on SEM pictures, EDS analysis of amorphous Tc spots (**Fig. 5.28**, bottom) gives a clear correlation between Ca and Tc (with Ca:Tc ≈ 1:1) suggesting the possible formation of ternary Ca-Tc(IV)-OH solid phase.

All these results hint towards $TcO_2 \cdot xH_2O(am)$ as solid phase controlling the solubility of Tc(IV) in all evaluated NaCl and $MgCl_2$ systems within the entire pH region and in $CaCl_2$ system up to $pH_m = 10.5$. Provided the very good agreement between experimental solubility data measured in this work in dilute systems and thermodynamic calculations using NEA–TDB selection, it can be postulated that the same number of hydration waters ($x = 1.6$ in $TcO_2 \cdot xH_2O$) applies also to the solid phase synthesized in this work.

5.3.3.5 Chemical, thermodynamic and activity models

In the present study, chemical, thermodynamic and activity model of Tc(IV) solubility in NaCl, $MgCl_2$ and $CaCl_2$ systems in entire pH region were developed using SIT and Pitzer approaches. First of all, available thermodynamic and activity models reported in literature are used to explain the experimental solubility data. It was seen that none of these models could explain the experimental observations gained in dilute to concentrated saline systems in the present work. The new chemical model was developed for the solubility of Tc(IV) in NaCl, $MgCl_2$ and $CaCl_2$ systems based on the slope analysis, solid and aqueous phase characterisation performed in the present work as well as the spectroscopic evidences reported in the literature. The thermodynamic and activity models were later developed based on the experimental solubility data using SIT and Pitzer approaches.

Determined standard stability constants together with the developed chemical models are summarized in Tab. 5.5. The chemical model developed for Tc(IV) solubility in the present work differs from NEA–TDB data selection in the acidic pH region where the new spectroscopic evidences are available since the publication of last update book of NEA–TDB. Also, new complexes have been derived in alkaline $MgCl_2$ and $CaCl_2$ systems based on the very different solubility behaviour observed under these conditions. The ion interaction coefficients derived for newly generated Tc(IV) species are shown in. Fig. 5.29, Fig. 5.30 and Fig. 5.31 show all the experimental solubility data determined in the present work, together with the thermodynamic calculations performed using the SIT and Pitzer activity model. Determined thermodynamic models for Tc(IV) solubility in dilute to concentrated saline solutions can properly explain the experimental solubility data in the present work, as well as the experimental solubility data at *I* = 0 considered in NEA–TDB selection for the selection of Tc(IV) thermodynamic data.

Tab. 5.5 Stability constants determined by SIT and Pitzer models for the formation of Tc(IV) aqueous species in NaCl, $MgCl_2$ and $CaCl_2$ solutions

Chemical reactions	**SIT**	**Pitzer**
	log*K^o	**log*K^o**
$TcO_2 \cdot 1.6H_2O(s) + 2/3H^+ \Leftrightarrow 1/3Tc_3O_5^{2+} + 1.93H_2O$	–1.53 ± 0.16	–1.56 ± 0.10
$TcO_2 \cdot 1.6H_2O(s) \Leftrightarrow TcO(OH)_2 + 0.6H_2O$	–8.80 ± 0.50	–8.80 ± 0.50
$TcO_2 \cdot 1.6H_2O(s) + 0.4H2O \Leftrightarrow TcO(OH)_3^- + H^+$	–19.27 ± 0.10	–19.32 ± 0.10
$TcO_2 \cdot 1.6H_2O(s) + 3Mg^{2+} + 2.4H_2O \Leftrightarrow$ $Mg_3[TcO(OH)_5]^{3+} + 3H^+$	–40.06 ± 0.50	–40.34 ± 0.50
$TcO_2 \cdot 1.6H2O(s) +3Ca^{2+} + 2.4H_2O \Leftrightarrow$ $Ca_3[TcO(OH)_5]^{3+} + 3H^+$	–41.47 ± 0.20	–41.48± 0.10

Tab. 5.6 Ion interaction coefficients for Tc hydrolysis species in NaCl, $MgCl_2$ and $CaCl_2$ media at 25 °C

SIT ion interaction coefficients: ε_{ij} [kg·mol^{-1}] and Pitzer parameters: $\beta^{(0)}_{ij}$, $\beta^{(1)}_{ij}$, λ_{ij}, $\Theta_{ii'}$ in [kg·mol^{-1}], $C^{(\phi)}$ and $\Psi_{iji'}$ in [kg$_2$·mol^{-2}]

Species		**SIT**	**Pitzer**				
i	**j**	$\boldsymbol{\varepsilon_{ij}}$	**Binary parameters**			**Mixing parameters**	
			$\boldsymbol{\beta^{(0)}}$	$\boldsymbol{\beta^{(1)}}$	$\boldsymbol{C^{(\phi)}}$	$\boldsymbol{\Theta_{ii'}}$	$\boldsymbol{\Psi_{iji'}}$
$Tc_3O_5^{2+}$	Cl^-	–0.34 ± 0.1	0.20	1.3	0	0	0
$TcO(OH)_3^-$	Na^+	0.10 ± 0.02	0.01	0.3	0.04	0	0
$Ca_3[TcO(OH)_5]^{3+}$	Cl^-	–0.28 ± 0.04	0.08	4.3*	0	0	0
$Mg_3[TcO(OH)_5]^{3+}$	Cl^-	–0.28 ± 0.04	0.08	4.3*	0	0	0
$TcO(OH)_2$	$NaCl//MgCl_2$	0	0	0	0	0	0

a *Fixed value for the corresponding charge type, according to [GRE/PUI1997]

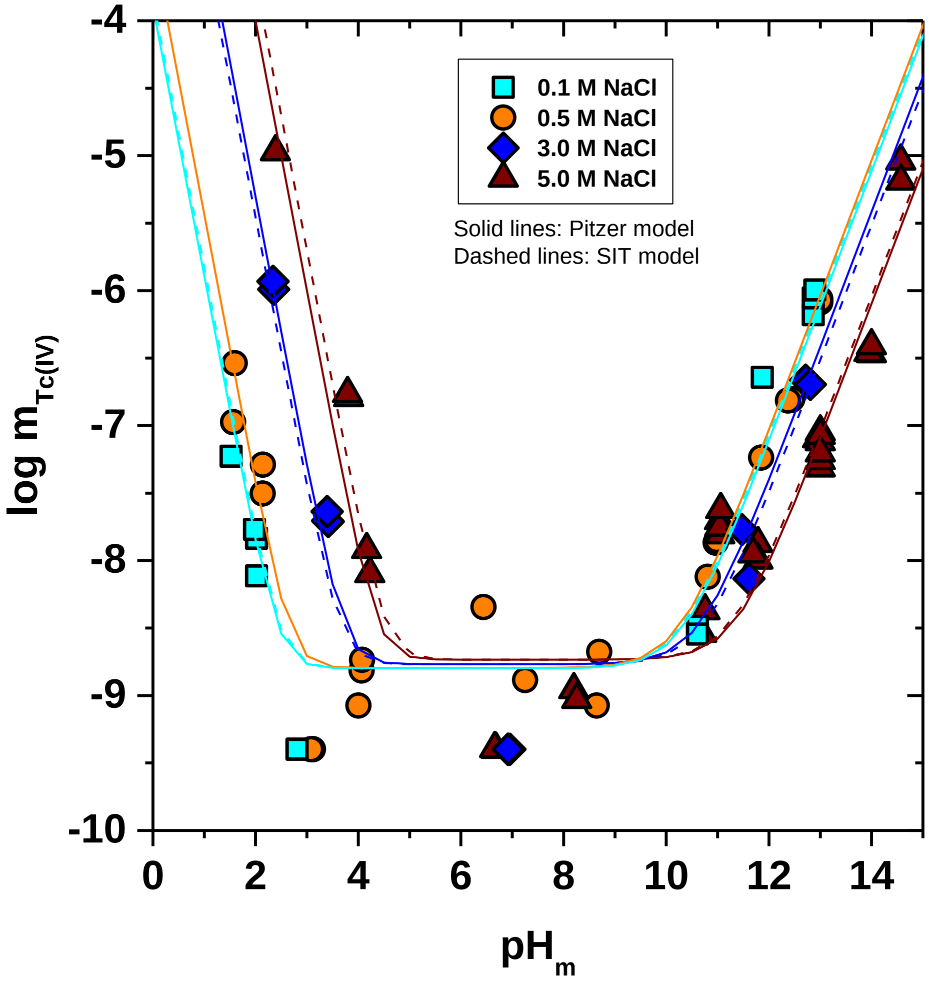

Fig. 5.29 Thermodynamic model obtained for solubility of Tc(IV) in dilute to concentrated NaCl systems

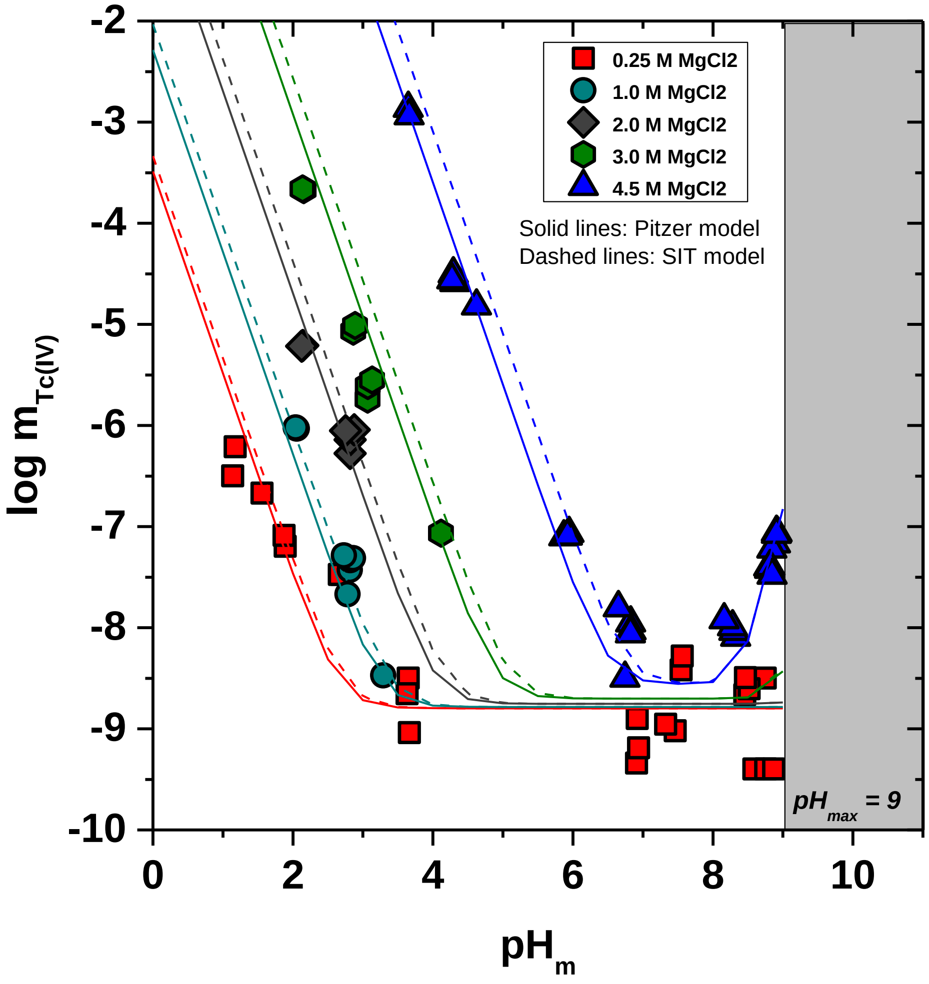

Fig. 5.30 Thermodynamic model obtained for solubility of Tc(IV) in dilute to concentrated $MgCl_2$ systems

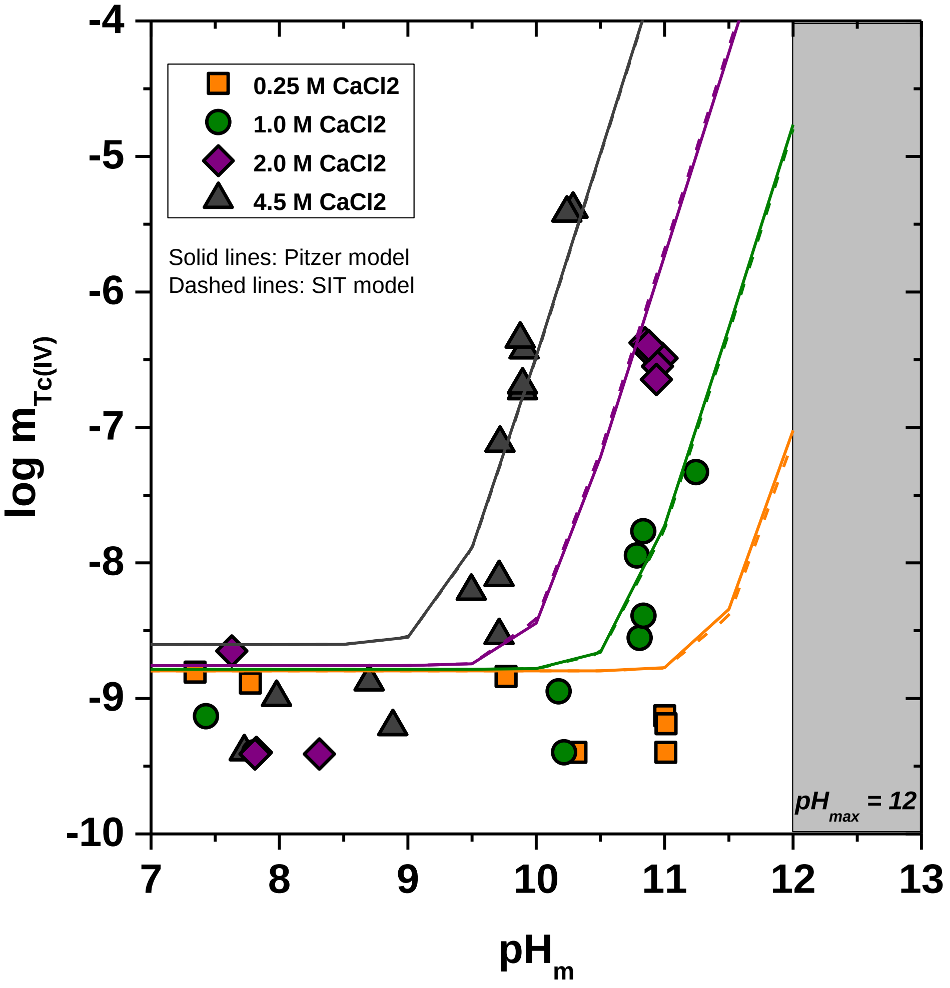

Fig. 5.31 Thermodynamic model obtained for solubility of Tc(IV) in dilute to concentrated $CaCl_2$ systems

5.3.4 Conclusion for Tc(IV) solubility

The solubility of Tc(IV) was investigated in dilute to concentrated NaCl, $MgCl_2$ and $CaCl_2$ solutions in the presence of different reducing agents ($Na_2S_2O_4$, $SnCl_2$, Fe powder). In the acidic pH range, a very significant increase in the solubility (up to 4 orders of magnitude) is observed with increasing ionic strength for all considered salt systems. This increase was explained with the formation of polynuclear $Tc_3O_5^{2+}$ species based on newly generated solubility data as well as the spectroscopic evidences. In concentrated alkaline NaCl solutions, the same speciation as for diluted systems is retained (e. g. predominance of $TcO(OH)_3^-$), although a decrease in solubility compared to dilute systems takes place due to ion interaction processes. Changes in the aqueous speciation are observed in concentrated alkaline $MgCl_2$ and $CaCl_2$ brines, where the formation of $Mg_3[TcO(OH)_5]^{3+}$ and $Ca_3[TcO(OH)_5]^{3+}$ ternary species is proposed based on the slope analysis of the corresponding solubility curves. XRD, SEM–EDS and chemical analysis confirm that $TcO_2 \cdot 1.6H_2O(s)$ is the solid phase controlling the solubility of Tc(IV) in all the saline systems evaluated, except the systems at $pH_m \leq 10.5$ in $CaCl_2$. Complete chemical, thermodynamic and activity models (SIT, Pitzer) were derived for the system Tc^{4+}–H^+–Na^+–Mg^{2+}–Ca^{2+}–OH^-–Cl^-–H_2O based upon the newly generated experimental solubility data.

5.4 Influence of the reduction kinetics on the Tc migration in natural systems

5.4.1 Tc(VII) sorption/migration studies on crystalline rocks from Äspö (Sweden) and Nizhnekansky massif (Russia)

5.4.1.1 Introduction

The main challenge during the deep geological disposal of SNF and high level waste (HLW) is safety assessment, which includes the estimation of the radionuclides migration from the repository. Due to long half-life (2.14×10^5 years) and high fission yield (*ca.* 6.14 %) the fate of ^{99}Tc is of great importance for safety assessment. Technetium mobility in natural systems depends on the redox conditions. The most stable Tc form under aerobic atmosphere is pertechnetate (TcO_4^-), which is very soluble under oxidizing conditions. Under anoxic conditions it is reduced to Tc(IV) and the solubility is limited by oxyhydroxide solid phase $TcO_2\cdot1.6H_2O(s)$ [MEY/ARN1991a]. Therefore, distribution coefficients and apparent diffusion coefficients of technetium on natural minerals found in literature are very scattered. Moreover, they are rarely published together with the pe/pH conditions studied. Tc redox kinetics strongly depend on the availability of reactive Fe(II) in host rock and the mineral association/speciation (surface complexed, precipitated, ion exchangeable) [FRE/ZAC2009, HEA/ZAC2007, JAI/DON2009, PER/ZAC2008A, PER/ZAC2008B, ZAC/HEA2007]. The generally accepted concept of spent nuclear fuel and high-level waste long-term storage is its disposal in deep- geological formations at a depth of more than 300 – 500 meters. The repository host rock as part of the multi-barrier system plays an important role as retention barrier to retard the radionuclide migration. Thus, the selection of the host rock formation with appropriate geochemical and hydro-geological properties is a key challenge in the task of nuclear waste disposal siting. Geochemical parameters of host rock formations for deep geological disposal of radioactive waste and spent nuclear fuel (SNF) under discussion in Europe (Opalinus Clay, Callovo-Oxfordian, crystalline host rocks in Sweden, Russia) are investigated now [MAR/HOR2005, PET/VLA2012, SCH/STA2012] to develop radionuclides (RN) transport models. However, mobility and migration studies in anoxic preserved natural host rock formations are scarce. Therefore, the main motivation of this work is to investigate technetium mobility on crystalline rock materials from prospective sites of generic underground research laboratories (URL) with similar host rock formations favored for SNF and HLW deep geological disposal.

Crystalline host rocks contain fractures, which are potential migration pathways in cases of radionuclide releases from a repository. Radionuclide transport depends strongly on the hydrogeological and geochemical conditions (pH, E_h, ionic strength) of bedrock and may include different immobilization-remobilization processes [GRA2008]. Beside advective transport in water conduction features, matrix diffusion may contribute significantly to radionuclide retention. Redox conditions have a tremendous impact on technetium mobility in natural systems. Both batch type sorption and column experiments with Hanford sediments [UM/SER2005, ZAC/HEA2007] have revealed that ^{99}Tc is highly mobile and shows virtually no retardation under fully oxidizing conditions. Consequently, it can be used to trace tank waste migration through a vadose zone [HU/ZAV2008).

In the case of Tc(VII), Äspö *in situ* and laboratory migration studies (CHEMLAB-2) done prior to the CROCK project (http://www.crockproject.eu/) using Äspö derived natural groundwater (GW) ~ 1 % Tc recovery (after 254 days) of the quantity injected could be revealed [KIE/VEJ2003, KIE/VEJ2009]. Batch type studies, done in parallel, derived K_s values of ~2.1×10^{-3} m for ^{99}Tc ($t_{contact}$ = 14 d), whereas altered material showed significantly lower values. These results show contact time/residence time dependency on retardation and/or reduction processes. Significant DOC concentration (42.3 mg/L) in natural GW probably can be attributed to the microbial activity. Distribution coefficient for Tc sorption is strongly dependent on the experimental environment. Under aerobic conditions reported K_d values are negligible (< 1 mL/g in [ALL/KIG1979] on granitic rocks and 0.2 mL/g in [ALB/CHR1991] on bentonite), whereas under anaerobic conditions the values are much higher (50 mL/g in [ALL/KIG1979] and 10^3 mL/g in [ALB/CHR1991]).

Two types of crystalline rock materials were used within this work. The first is from Äspö Hard Rock Laboratory, Sweden. It is a generic URL for *inter alia in situ* studies of radionuclides retention processes in crystalline formations concerning deep geological disposal of spent nuclear fuel. It is not planned to dispose radioactive waste on this site. The Swedish deep geological disposal site will be located at Forsmark, about 350 km to the northeast. The second material was obtained from Nizhnekansky massif, Russia. According the modern concept the development of the atomic energy industry in Russia, the final geological disposal site for the SNF and HLW will be located in

Krasnoyarsky Krai, near the city of Zheleznogorsk (about 6 km from the industrial area of the city). The construction of the URL there is planned to start in 2016. The decision on transformation of the URL into the final disposal repository is expected by 2025 after investigation of the site geochemical suitability.

5.4.1.2 Materials and methods

5.4.1.2.1 Äspö diorite

Crystalline rock cores were retrieved from CROCK drilling site of Äspö HRL (Sweden). Details of the sampling procedure and material characterization are presented in the CROCK S&T contribution of [SCH/STA2012]. The bore cores (#1.32 and #1.33) of Äspö diorite were chosen for investigations. They were transferred into an Ar glovebox, equipped with a circular saw, and cut into small discs (0.5 – 1 cm in width). The discs obtained were crushed by hammer and separated by sieves into several size fractions. For the sorption experiments documented here the 1 – 2 mm size fraction was chosen. Part of crushed diorite material was exposed to air for 1 week for surface oxidation to investigate the influence of sample preservation and preparation. Unoxidized material was stored permanently under Ar atmosphere in the glovebox (≤ 1 ppm O_2). General composition of the material used is presented in **Tab. 5.7**.

Tab. 5.7 XRF data on Äspö diorite composition
Material used in this study (taken from [SCH/STA2012]) is compared with data presented in [HUB/KUN2011]

Element	Äspö diorite [SCH/STA2012] concentration, wt. %	Äspö diorite [HUB/KUN2011] concentration, wt. %
SiO_2	62.71	66.06
Al_2O_3	17.27	16.89
Fe_2O_3	4.39	2.6
FeO	2.51	0.87
MnO	0.08	0.05
MgO	1.76	0.8
CaO	3.75	2.41
Na_2O	4.55	4.91
K_2O	3.05	4.38
TiO_2	0.66	0.35
P_2O_5	0.24	0.12
Loss on ignition (LOI)	0.67	1.37
Sum	*99.1*	*98.6*

5.4.1.2.2 Nizhnekansky massif rock material

Granitic drill core material from Nizhnekansky (NK) massif was available from Kamenny (depth of sampling down to 700 m) and Itatsky (depth of sampling down to 500 m) sites. Cores were transferred to the Institute of Geology of Ore Deposits, Petrography, Mineralogy and Geochemistry RAS (IGEM RAS, Russia) under oxidized conditions, cut by circular saw, then part of the material was transferred to the KIT-INE. At KIT-INE, the material was broken up by jaw crusher into small grains and sieved to obtain the 1-2 mm grain size fraction. Thereafter, material was used for sorption experiments. Tc(VII) sorption kinetics was investigated using material only from a core from Itatsky site (core from approx. depth of 92 m). A detailed description of the NK material used in this study can be also found in [PET/VLA2012]. The petrographic characteristics of the mock material used for batch sorption studies are shown in **Tab. 5.8**.

Tab. 5.8 Petrographic characterization of rock material from Nizhnekansky massif [PET/VLA2012]

Rock type	Mineralogical composition, %	Textural characteristic	Structural characteristic
Quartz diorite – monzodiorite	Plagioclase, 45-50 Hornblende, 25 Quartz, 15 Potash feldspar (microcline, orthoclase), 5-10 Non-transparent minerals (magnetite, leucoxene, hematite), 2-3 Biotite Grothite Zircon	Massive, weakly gneissic	Gipidyomorpho-granular, monzonitic; evenly granular

5.4.1.2.3 Groundwater

Äspö groundwater simulant (ÄGWS) for batch-type sorption experiments was prepared in accordance with the CP-CROCK drilling site outflow groundwater composition (sample CROCK-2) (see [SCH/STA2012]). All chemicals used were of analytical grade; Milli-Q water was used for dilution. GWS has comparable composition to the groundwater KA3600-F-2 sampled in a 50 L barrel at the CP-CROCK site [HEC/SCH2012]. Contents of the used ÄGWS and natural groundwater samples are shown in **Tab. 5.9** together with natural Grimsel groundwater used for desorption studies.

Synthetic groundwater for NK material (NKGWS) was prepared in accordance with [PET/VLA2012] by dissolution of 62.5 mg/L $NaHCO_3$ and 187.5 mg/L $Ca(HCO_3)_2$ in Milli-Q water. The total amount of dissolved salts is 250 mg/L and pH = 8. Sustainability of the chemical mixture under argon atmosphere was tested by classical HCl titration of a reference sample during a sorption experiment.

Tab. 5.9 Overview of the chemical compositions of the synthetic Äspö groundwater simulant (ÄGWS), Äspö groundwater and Grimsel groundwater, respectively

	synth. Äspö GWS	**Synth. Äspö GWS after 122 h contact time**	**Äspö GW (KA-3600-F-2)**	**Grimsel GW (MI-shear zone)**
pH	8.0		7.8	9.67
[Mg^{2+}]	103.64 ± 0.84 mg/L	104.6 mg/L	69.4 mg/L	12.6 µg/L
[Ca^{2+}]	1109.36 ± 94.46 mg/L	1134 mg/L	1135 mg/L	5.3 µg/L
[K^{+}]	19.346 ± 3.855 mg/L	21.56 mg/L	10.5 mg/L	
[Li^{+}]	2.526 ± 0.04 mg/L	2.50 mg/L	6.0 mg/L	
[$Fe^{2+, 3+}$]	n.m.	n.m.	0.2 mg/L	< D.L.
[Mn^{-}]	2.32 ± 3.02µg/L	23.8 µg/L	0.338 mg/L	< D.L.
[Sr^{2+}]	19.678 ± 0.294 mg/L	20.14 mg/L	19.9 mg/L	182 µg/L
[Cs^{+}]	<D.L	< D.L		0.79 µg/L
[La^{3+}]	n.m.	n.m.		< D.L.
[U]	0.05 ± 0.01 µg/L	1.70 µg/L	0.105 µg/L	0.028 µg/L
[Th]	0.024 ± 0.005 µg/L	0.07 µg/L	0.001 µg/L	0.00136 µg/L
[Al^{3+}]	182.75 ± 56.29 µg/L	439.6 µg/L	13.3 µg/L	42.9 µg/L
[Na^{+}]	1929.25 ± 28.58 mg/L	1905 mg/L	1894 mg/L	14.7 mg/L
[Cl^{-}]	4749.408 ± 145.046 mg/L	4895.10 mg/L	4999 mg/L	6.7 mg/L
[Si]	n.m.	n.m.	4.7 mg/L	5.6 mg/L
[SO_4^{2-}]	408.682 ± 4.967 mg/L	411.88 mg/L	394.4 mg/L	5.8 mg/L
[F^{-}]	1.974 ± 0.093 mg/L	1.98 mg/L	1.41 mg/L	6.3 mg/L
[Br^{-}]	21.17 ± 0.37 mg/L	20.96 mg/L	23.2 mg/L	
[NO_3^{-}]	n.m.	n.m.	n.m.	< D.L.
[HCO_3]	n.m.	n.m.	n.m.	3.0 mg/L
[B]	306.54 ± 212.54 µg/L	146.1 µg/L	885 µg/L	

5.4.1.2.4 Radionuclides

Batch-type sorption studies were performed using ^{99}Tc isotope in form of $NaTcO_4$. Stock solution of 13 mM $NaTcO_4$ was diluted down to required concentrations. For experiments with Tc concentrations lower than 10^{-9} M ^{95m}Tc isotope with shorter half-life (61 day) and strong gamma lines in the spectrum was applied. Detection limit of gamma spectrometry under 10 mL geometry for this radionuclide (RN) using high-purity germanium (HPGe) semiconductor detector is about 10^{-14}-10^{-15} M (three hours measurement time). The isotope was produced by proton irradiation of natural Mo foil (50 µm thickness) at ZAG Zyklotron AG (Karlsruhe, Germany). After cooling the foil was transported to Karlsruhe Institute of Technology, Institute for Nuclear Waste Disposal (KIT-INE) and processed to separate technetium according the technique of [BOY/LAR1960]. The foil was dissolved in mixture of concentrated H_2SO_4 and 30 % H_2O_2, and then the solution was slowly neutralized with saturated NaOH (up to alkaline pH). The obtained alkaline solution was passed through a column of anion exchanger Dowex 1x8 (100 - 200 mesh particle size) with total volume ca. 3 mL. The column was washed first with 20 mL 1 M $K_2C_2O_4$ to remove residues of molybdate and after rinsing with 20 mL of Milli-Q water pertechnetate was eluted with 30 mL 1 M $HClO_4$. The last fraction was collected in 2 mL vials, which were measured with γ-spectrometry and samples with ca. 90 % of ^{95m}Tc were merged and neutralized with concentrated NaOH. The purification level was monitored with ICP-MS.

Processing of the first Mo foil shows that the material was highly contaminated with rubidium isotopes ^{83}Rb and ^{84}Rb with total activity comparable to ^{95m}Tc. After the first separation step on Dowex resin rubidium was fully isolated (see **Fig. 5.32**), but Tc fraction contained substantial amount of Mo (350 ppm, natural ÄGW contains 10-25 ppm [HEC/SCH2012]). Therefore, Tc-contained samples were merged, pH was adjusted to the alkaline range and the separation was performed again. The final ^{95m}Tc fraction was mixed with ÄGWS with further pH and salts concentration adjustment. ^{95m}Tc-ÄGWS obtained was used for first core migration experiments.

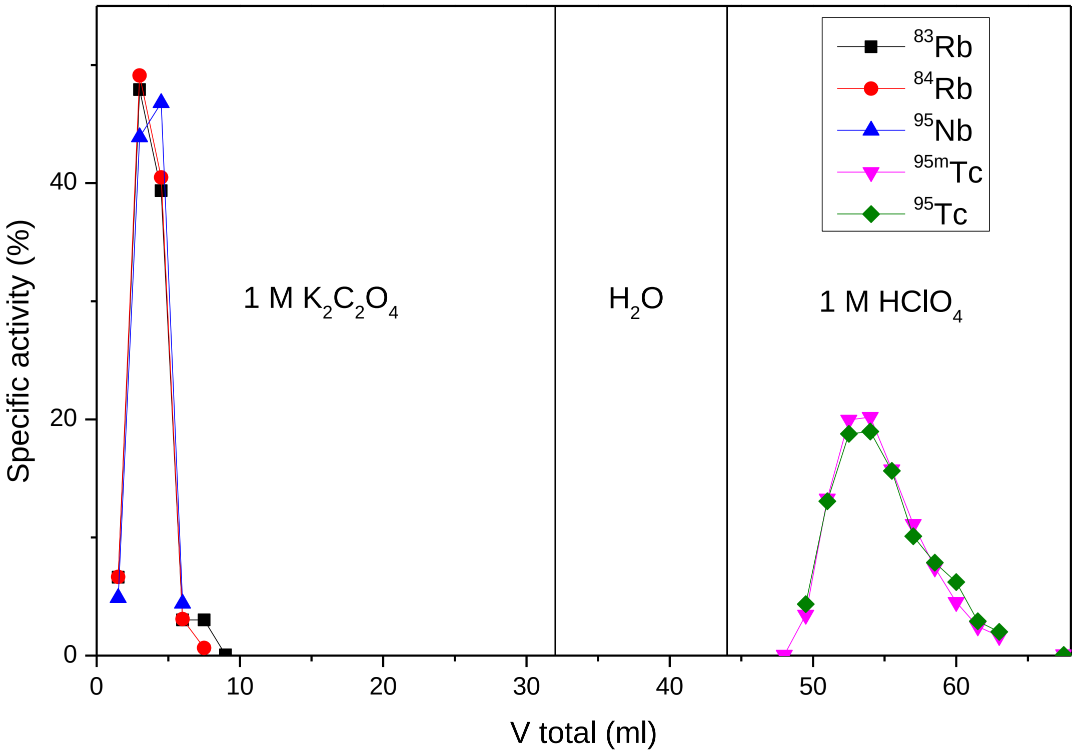

Fig. 5.32 Separation of the irradiated Mo target on Dowex 1×8 resin column (100-200 mesh, 3 mL column volume)

For the second set of experiments with ^{95m}Tc another Mo foil was dissolved in 30 % H_2O_2 with further addition of concentrated H_2SO_4. Alkaline media was reached by slow dropwise addition of saturated NaOH. Then Tc was isolated on Teva® Resin (Eichrom Technologies, LLC) column **Fig. 5.33**) according the technique from [TAG/UCH1999]. Separation was performed from ~1.5 M HNO_3 media with further washing of the column with 2 M HNO_3. ^{95m}Tc was eluted with 8 M HNO_3 and then was purified from NO_3^- by separation on DOWEX resin column (**Fig. 5.34**). Filled area represents the ^{95m}Tc fraction merged for further application. NO_3^- content in samples was estimated using nitrate test strips (Merck). Then NO_3^- concentration was measured using ion chromatography (IC), the results were the same.

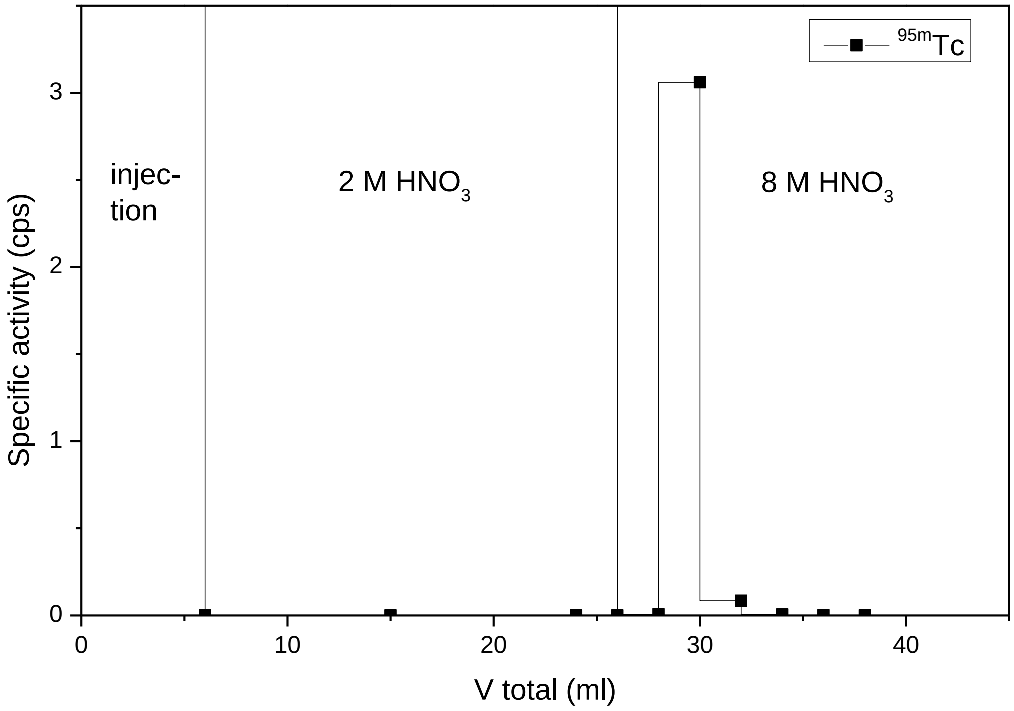

Fig. 5.33 Separation of the irradiated Mo target on TEVA resin column (50 – 100 µm, 3 mL column volume)

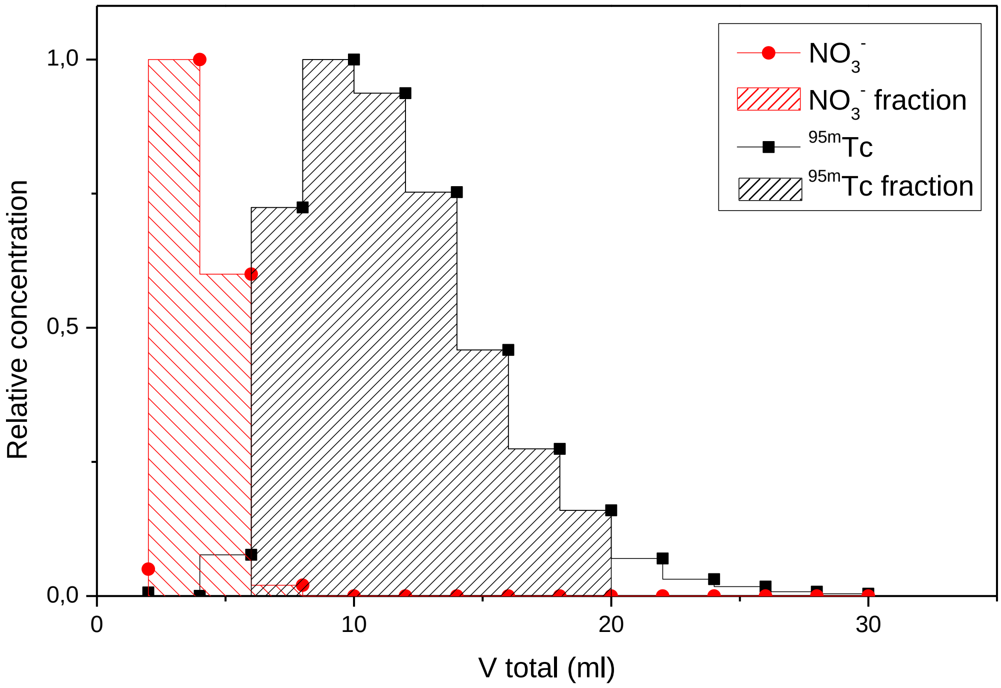

Fig. 5.34 Separation of ^{95m}Tc from NO_3^- on DOWEX 1×8 resin column (100 – 200 mesh, 3 mL column volume)

For core migration study HTO was used as a conservative tracer. Anion exclusion effect was investigated using ^{36}Cl isotope.

5.4.1.2.5 Batch-type studies

Batch-type sorption experiments were carried out in 20 mL liquid scintillation counter (LSC) vials (HDPE, type Zinsser) inside the Ar glovebox with O_2 concentrations ≤ 1 ppm at room temperature (20 ± 2 °C). Solid-liquid ratio was 2 g of granitic rock and 8 mL of GWS in case of natural materials or 2 g/L of iron oxide for magnetite batches. For each condition and kinetics point, two separate samples were prepared and closed during the equilibration to prevent oxidation of Fe(II) species at mineral surfaces. All sorption experiments were conducted at pH equal to 8.1 ± 0.1. Tc(VII) solutions in GWS with final concentrations of 10^{-5} M, 10^{-8} M and 10^{-9} M were used for experiments. For measurement of ^{99}Tc content in supernatants after sorption 1 mL aliquots were taken, added to 10 mL of LSC cocktail Ultima Gold and analyzed with LSC (PerkinElmer Quantulus). To differentiate between colloidal phases and true solution species a phase separation by ultracentrifugation (Beckman Optima XL-90, 90,000 rpm, 694,000 × g) for 1 h was applied.

Redox potential was measured in the Ar glovebox by using a Metrohm (Ag/AgCl, KCl (3 M)) electrode. The measurements were performed directly in the sample without separation of the supernatant. The potential values were recorded every hour and then corrected for the standard hydrogen potential (against the standard hydrogen electrode (S.H.E.)).

Samples of sorption experiments were taken to desorption experiments after three month contact time. The Tc containing supernatant was removed and 8 mL of fresh liquid phase added. For NK rock material only NKGWS was used, whereas in case of ÄD besides ÄGW also natural Grimsel GW were used as a glacial melt water simulant. For each kinetics point liquid phase was removed, analyzed with LSC and substituted with new portion of groundwater. Some samples after sorption experiments were oxidized on air for one month and the same desorption study was performed under oxidizing conditions. NKGWS and ÄGWS were used for NK and ÄD materials, respectively. Desorption experiments cover time range between few seconds and 1 month contact time.

5.4.1.2.6 XANES and XPS

For surface sensitive analytics small diorite fragments with unpolished faces after cutting by circular saw were equilibrated with 10^{-5} M Tc(VII) in GWS for 2 months, washed by Milli-Q water for a few seconds to prevent salt precipitation and then investigated with X-ray photoelectron spectroscopy (XPS) system PHI 5600-CI (Physical Electronics Inc.) to determine Tc redox speciation.

XANES measurements were performed at the INE-Beamline [ROT/BUT2012] at the ANKA synchrotron light source at KIT, Karlsruhe, Germany. Tc samples were collected in fluorescence mode using a KETEK detector. Uranium compound meta-schoepite was used as a reference. The set of technetium samples on magnetite and crystalline rock materials with Tc concentrations of ~10^{-3} M was prepared and handled under argon atmosphere (**Tab. 5.10**). During the measurement argon was pumped through the cell (**Fig. 5.35**). Spectra were processed in ATHENA software [RAV/NEW2005].

Tab. 5.10 List of measured XANES samples

Sample	[Tc], M	Description
Tc(VII) reference	0.01	TcO_4^- solution
Tc(IV) reference	-	Solid TcO_4 covered with supernatant
Tc on magnetite	0.002	Centrifuged suspension
Tc on ÄD	0.001	Centrifuged suspension
Tc on NK	0.001	Centrifuged suspension

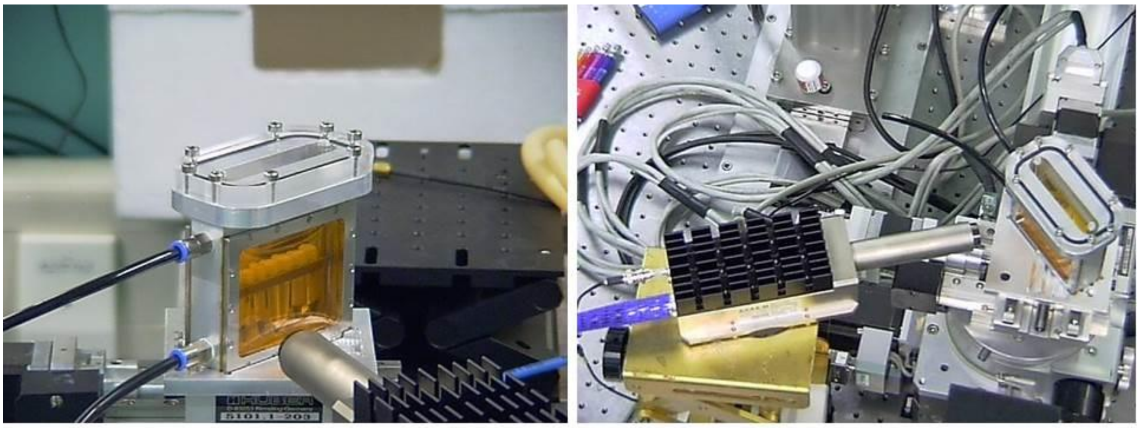

Fig. 5.35 XANES measurement device and cell with Tc samples

5.4.1.2.7 Migration

An unoxidized Äspö diorite core #2.2 (0.53-0.97 m, borehole KA2370A-01) was used for a migration experiment. The sample contains a natural fracture at ~0.70 m that was opened during on-site handling at the Äspö HRL. The original drill core was sealed into a plastic bag (**Fig. 5.36**) and transferred into an Ar glovebox. The core segment containing the natural fracture was cut, both parts have been assembled together to obtain the original position as much as possible and fixed with tape and a bar clamp without applying excessive pressure. Afterwards, the suture (outer rim) of the fracture was glued using high viscous Plexiglas resin. The glue process was done stepwise applying only small amounts of resin in each step to avoid potential intrusion of the organic material into the fracture itself. Several layers of resin have been applied to guaranty that the fracture rim is fully sealed. After finalization of the glue process the core was placed in a Plexiglas cylinder and the remaining void space between core and inner wall of the cylinder was filled up using the same resin as mentioned above. After drying of the resin, the upper and lower bottom of the core was sawed again and carefully polished by hand. The last step in sealing of the core fragment (final length ~4.2 cm) was gluing of top and bottom caps with connectors to the fracture in- and outlet.

Fig. 5.36 Drill core #2.2 (0.53 – 0.97 m, borehole KA2370A-01) with a natural fracture

The core fragment was sealed in an Ar filled plastic bag as second confinement, transferred to the Federal Institute for Materials Research and Testing (BAM, Berlin) and characterized by 3D micro-computed tomography (µCT) with a voxel resolution of 16 µm. The fracture volume after segmentation was estimated to be 0.415 mL and the total fracture surface area is 4.235×10^{-3} m^2. The main steps of the core #2.2 preparation together with µCT picture are shown in **Fig. 5.37**. More detailed information on core #2.2 characterization can be found in [KIT/INE2012].

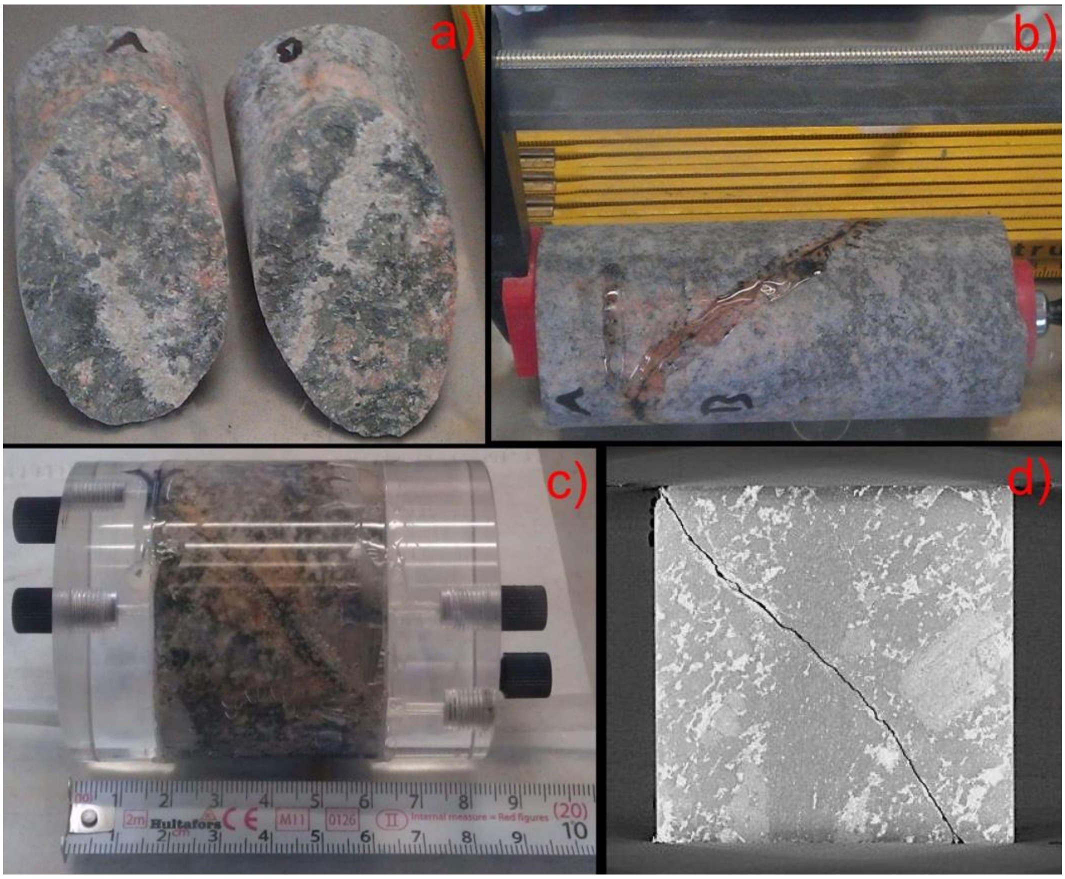

Fig. 5.37 Äspö core #2.2

a) Details on both fracture surfaces. b) Core as prepared before gluing into the Plexiglas cylinder. c) Core after preparation fitted with tubing ready for µCT measurements and the migration experiments. d) µCT slice of the core showing the fracture

The core was handled at KIT-INE solely inside the Ar glovebox with oxygen concentration < 1 ppm to avoid oxidation. For tracer migration experiments ÄGWS containing HTO and ^{36}Cl admixtures with specific activity of each RN of ~3 kBq were applied. Injection loop were filled with 1 mL of solution, which then was eluted through the core by ~50 mL of ÄGWS using a syringe pump under different flow rates (10 mL/h, 1.5 mL/h and 0.2 mL/h). The eluate was gathered with a fraction collector (Gilson FC 203b) and measured with LSC. The general set-up of the core migration experiment is presented in **Fig. 5.38**. For a reactive transport investigation, the same experiment was performed with injection of Tc containing ÄGWS. Experiments under low Tc concentrations (~10^{-11} M) were possible due to the availability of ^{95m}Tc, detected by γ-spectrometry. To achieve residence time comparable to the batch sorption studies the stop-flow experiments were performed, when the injection of ~10 pore volumes of ^{95m}Tc-containing ÄGWS was followed by the pump stop and then its restart after a defined time interval.

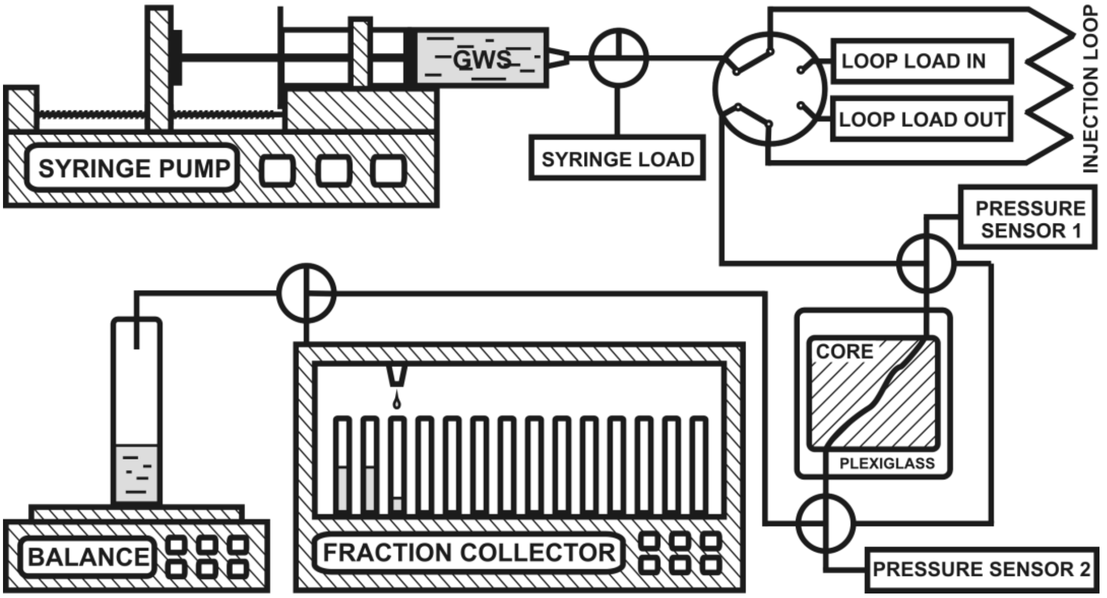

Fig. 5.38 Schematic illustration of core migration setup

5.4.1.3 Results and discussion

5.4.1.3.1 Redox potential measurements

Redox measurements were carried out after about 2 weeks and 1 month contact time in the sorption experiments. Every sample was measured over a period of one day in an open vial in the Ar glovebox (< 1 ppm O_2) to obtain the E_h evolution. A typical time dependent E_h evolution is shown in **Fig. 5.39**. The initial drop of the E_h is interpreted as the influence/readout of the sample, whereas the continuous increase in the later period is explained to be a result of oxidation due to traces of oxygen in the Ar glovebox (< 1 ppm O_2) that seems to be enough to compensate the redox capacity of the sample over 24 hours.

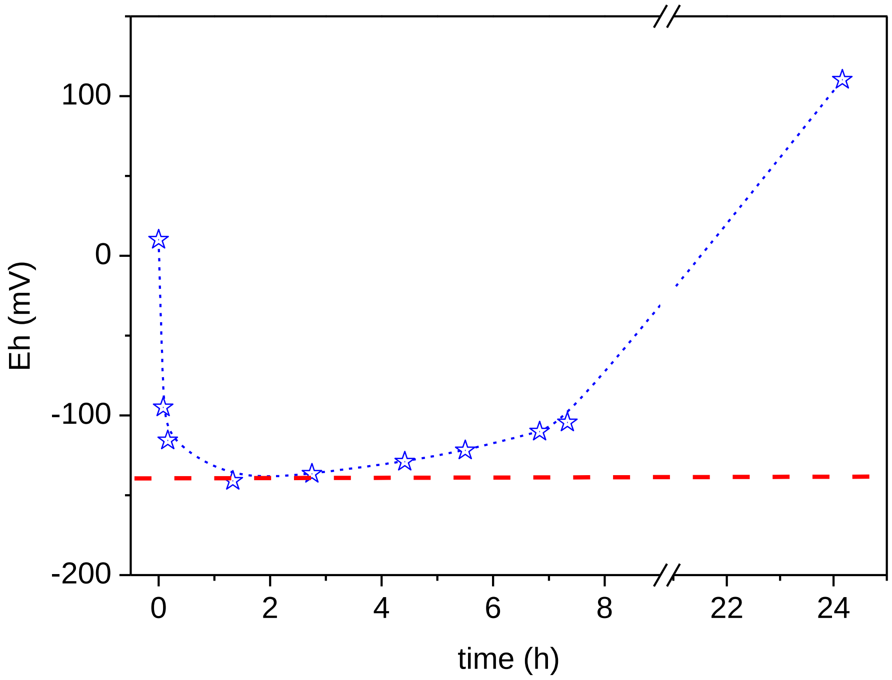

Fig. 5.39 Typical E_h evolution for synthetic Äspö GWS with [Tc] = 10^{-10} mol/L equilibrated with unoxidized ÄD

Fig. 5.40 shows the E_h measurements for synthetic groundwater containing different ^{99}Tc concentrations equilibrated with oxidized and un-oxidized ÄD. *Pourbaix* diagram is plotted using HYDRA/MEDUSA code. For oxidized ÄD material the redox potential as a function of Tc concentration does not change significantly and is within the range of +250 to +300 mV. However, for un-oxidized ÄD material two trends can be observed: (a) for low Tc concentration (up to 10^{-8} M) the E_h value decreases with time from 14 days to one month and (b) for the highest Tc concentration used (10^{-5} M) the redox potential value reaches after one month the E_h range of oxidized ÄD material. Our current explanation for the E_h trend observed at 10^{-5} M is that this Tc concentration is already sufficient to exceed the redox capacity of the contacted diorite material with the solid to liquid ratio 2 g/8 mL used. Furthermore, the established E_h values for the lower Tc concentrations make Tc(VII) reduction thermodynamically feasible.

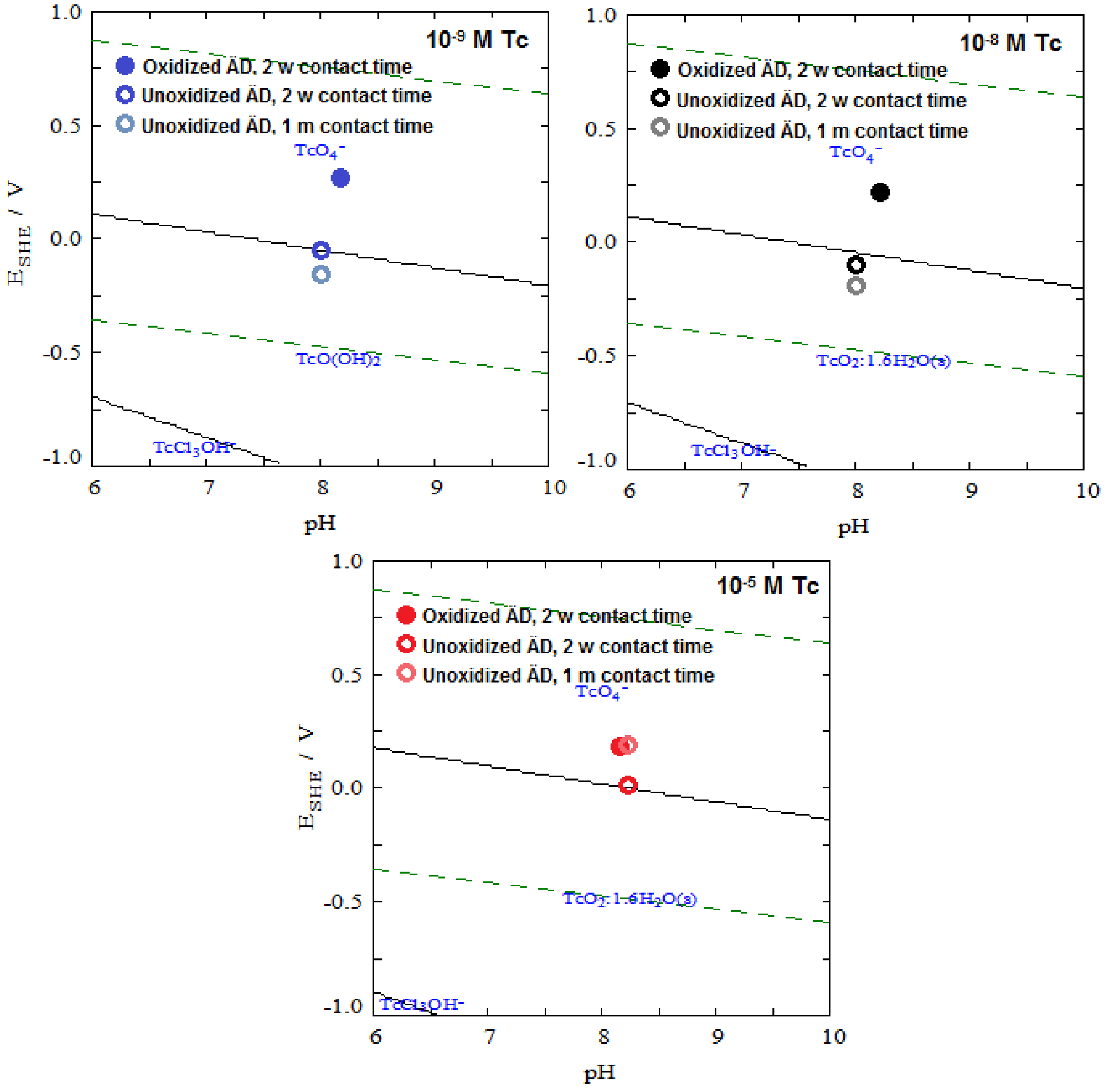

Fig. 5.40 *Pourbaix* diagram for Tc-ÄGWS system with experimental redox potential values for synthetic groundwater containg 10^{-9} M, 10^{-8} M and 10 and 10^{-5} M Tc equilibrated with unoxidized and oxidized ÄD

Redox potential values of the NK systems during the sorption studies were similar to the oxidized ÄD samples with deviations ≤ 40 mV. Thus, both oxidized materials are establishing the same redox conditions after equilibration.

5.4.1.3.2 Batch-type sorption studies

Sorption kinetics of different Tc concentrations on oxidized and unoxidized ÄD are given in **Fig. 5.41**. Here the term “sorption” implies the total amount of Tc associated with the solid phase (crushed fraction of ÄD with diameter of particles 1 – 2 mm) after ultracentrifugation. It can be sorption/surface complexation itself, but also a precipitation of $TcO_2 \cdot xH_2O$ due to Tc(VII) reduction by e. g. Fe(II) species is a potential process. Especially in case of the highest Tc concentration this process might occur, as the Tc(IV) solubility is significantly exceeded.

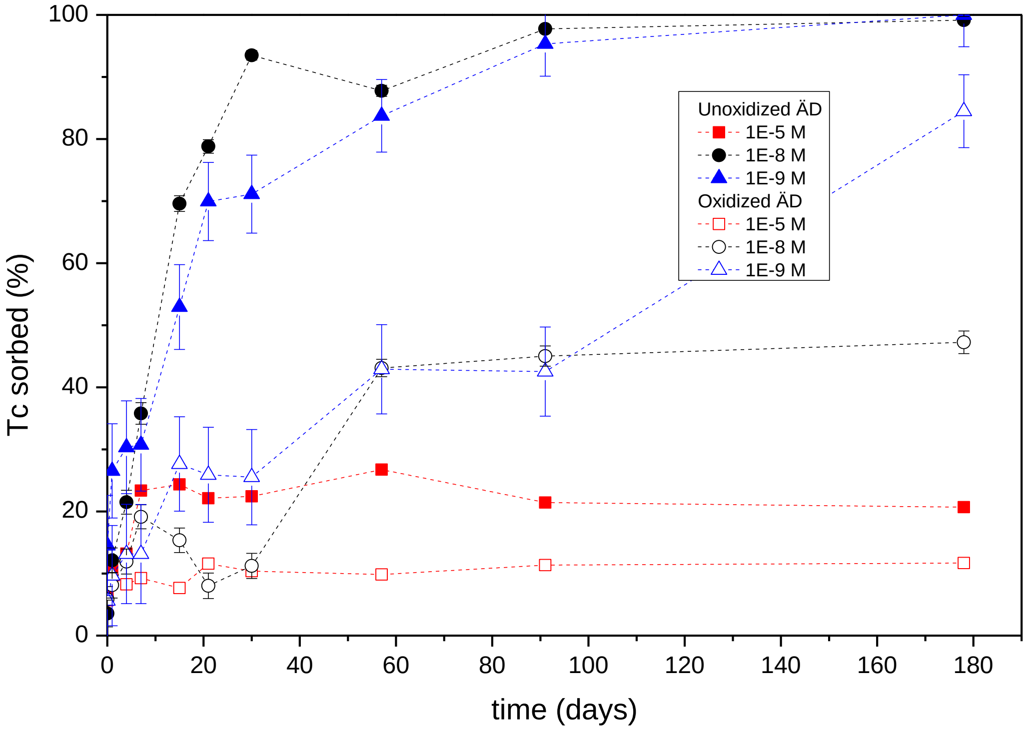

Fig. 5.41 Sorption kinetics of different Tc(VII) concentrations on oxidized and unoxidized ÄD

The formation of colloidal Tc phases (eigencolloids) in ÄD/NK GW by comparison of ultracentrifuged to non-centrifuged samples was not detectable within the uncertainty limits (± 5 – 10 %). Either these colloidal phases are not formed or are not stable under the GWS conditions chosen (ionic strength ~ 0.2 M, pH 8 for ÄGWS, ionic strength ~ 4 mM, pH 8 for NKGWS).

From the Tc sorption kinetic experiments it is evident, that sorption on unoxidized material is much higher compared to the artificially oxidized samples. For the 10^{-8} M and 10^{-9} M Tc on unoxidized material plateau values close to 100 % sorption are obtained (after 90 days), whereas during the same observation period on oxidized ÄD only ~40 % are sorbed, showing the tendency to reach equilibrium within this range. Based on the E_h/pH conditions established Tc(VII) reduction on the unoxidized ÄD crushed material or in solution seems to be feasible from a thermodynamic point of view. General scheme of the processes involved into Tc(VII) immobilization is shown in **Fig. 5.42**. Here, only Fe(II) is considered as a potential reducing agent for Tc(VII)/Tc(IV) transformation according the equation (5.7):

$$Tc(VII)O_4^- + 3Fe^{2+} + (n+7)H_2O \rightarrow Tc(IV)O_2 \cdot nH_2O_{(s)} + 3Fe(OH)_{3(s)} + 5H^+ \tag{5.7}$$

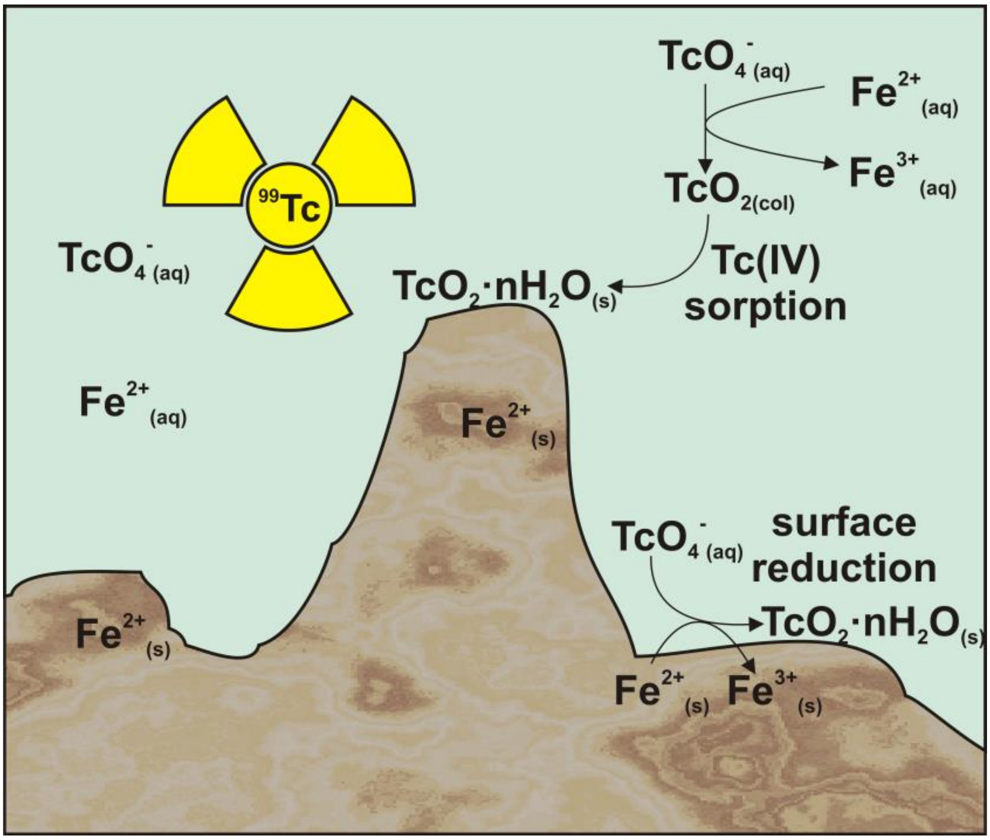

Fig. 5.42 General scheme of Tc(VII) sorption/reduction processes

In order to estimate the amount of the ferrous iron buffer available in the oxidized and unoxidized ÄD material we used here the quantification of the ion exchangeable Fe(II) fraction. Furthermore, data on oxidized and non-oxidized ÄD material by XRF are given in [SCH/STA2012], showing that the overall Fe(II) redox buffer is drastically reduced for the oxidized samples. The ion-exchangeable Fe(II) fraction determined after [HER/CRO1994] for the oxidized ÄD was quantified with approx. 1 – 3 µg/g, whereas for the unoxidized samples higher values around 4 – 6 µg/g are obtained. The rather high uncertainty in the measurements is attributed to the natural heterogeneity of the ÄD material. It has to be mentioned here, that ultracentrifugation (90,000 rpm) of the supernatant after 1 M $CaCl_2$ extraction before UV/VIS measurement for Fe(II) quantification using the ferrozine method leads to values around the detection limit (0.1 – 0.5 µg/g) for both types of diorite samples. This can be explained by an initial exchange of Fe(II) from the ÄD surface with calcium cations and subsequent Fe(II) oxidation in the solution to form colloidal ferric iron oxyhydroxides that was separated by centrifugation. However, ultracentrifugation step is not present in the technique of Heron *et al.*, therefore the non-centrifuged data are taken as the final results. Again, the samples with Tc concentrations of 10^{-5} mol/L are outlying this trend and show a sorption plateau already reached after seven days around 20 – 25 % for the un-oxidized samples and ~10 % for the oxidized sample.

Taking the quantified ion-exchangeable ferrous iron buffer in the sorption samples to be from $3.6 \cdot 10^{-8}$ mol/vial (oxidized ÄD) to $2.1 \cdot 10^{-7}$ mol/vial (un-oxidized ÄD) with respect to the total amount of Tc contacted, $8 \cdot 10^{-7}$ mol/vial (10^{-5} mol/L Tc), $8 \cdot 10^{-11}$ mol/vial (10^{-8} mol/L Tc) and $8 \cdot 10^{-12}$ mol/vial (10^{-9} mol/L Tc), the sorption kinetics observed can be expected and underpin the need of well-preserved un-oxidized rock material for sorption studies on redox sensitive radionuclides to estimate reliably the *in situ* retention. Batch-type sorption study on NK material was performed under conditions comparable to the ÄD experiments. Tc sorption evolution with different Tc concentrations is shown in **Fig. 5.43**.

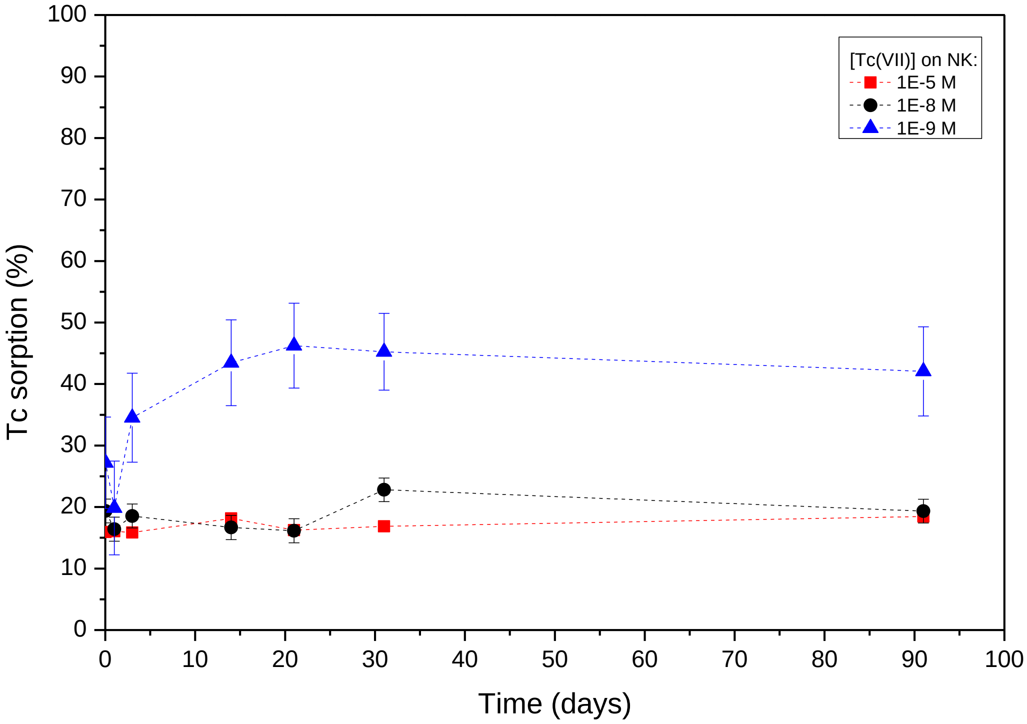

Fig. 5.43 Sorption kinetics with different Tc(VII) concentrations on NK granitic rocks

After three weeks of equilibration time, plateau values of sorption within the analytical uncertainty were reached for all tested Tc concentrations. In the case of the lowest concentration (10^{-9} M) the final Tc retention was ~45 %, and for the highest concentration used (10^{-5} M) ~18 %. These values are quite similar to the results found for the sorption onto oxidized ÄD, performed under similar conditions – ~40 % for the initial Tc concentration of 10^{-9} M and ~10 % for 10^{-5} M, respectively. Only for the intermediate Tc concentration (10^{-8} M) sorption values differ considerably – ~20 % for NK and ~40 % for ÄD. Observed sorption decreases towards the last kinetic points (195 days contact time) for 10^{-9} M Tc samples, which can be explained by oxygen intrusion into the glovebox and partial re-oxidation of a Tc(IV) species. Data on ion-exchangeable Fe(II) extraction (0.1 – 1 µg/g of Fe(II) for NK granite, and 1 – 3 µg/g for oxidized ÄD) indicate that the investigated NK cores were stronger oxidized by air than ÄD or the cores had a lower overall redox buffer capacity. The difference in sorption of the intermediate Tc concentration used, might serve as reasoning for the assumptions made above. According to N_2-BET analyses NK granite has higher surface area with 0.32 m^2/g than ÄD with 0.16 m^2/g, respectively. However, since mineral surfaces are not saturated with Tc, surface area does not limit Tc sorption and Fe(II) content is considered to be the more important factor in the immobilization process.

Technetium concentration change during sorption experiment can be described with exponential decay equation (5.8):

$$C_t = \left(C_0 - C_{eq}\right)e^{-kt} + C_{eq} \tag{5.8}$$

Where $\mathrm{C_0}$ and $\mathrm{C_{eq}}$ are the initial and equilibrium Tc concentrations, respectively, and k – sorption rate coefficient. Hence, sorption kinetics can be fitted with a first order rate constant:

$$S_t = \mathrm{A}e^{-kt} + S_{eq} \tag{5.9}$$

where S_t and S_{eq} are the sorption values at the moment t and at equilibrium, respectively, A is the pre-exponential factor. Sorption rate coefficients for both ÄD and NK materials obtained from this fitting are presented in **Tab. 5.11**.

Tab. 5.11 Main parameters obtained within Tc(VII) sorption experiments onto ÄD and NK materials

Material	**Fe(II) ion-exchangeable, mg/g**	**Initial Tc concentration, mol/L**	***E*$_h$, 1-2 months, mV**	***k*, d^{-1}**	**K$_d$, L/kg**	**Tc sorbed after 6 months, %**
ÄD unoxidized	4-6	1.07×10^{-5}	76	0.24 ± 0.10	1.1 ± 0.2	21 ± 2
		$(1.05 \pm 0.05)\times10^{-8}$	-187	0.075 ± 0.009	500 ± 200*	99.2 ± 0.6
		$(1.1 \pm 0.1)\times10^{-9}$	-142	0.036 ± 0.004	900 ± 800*	99.5 ± 6
ÄD oxidized	1-3	1.07×10^{-5}	238	0.15 ± 0.04	0.53 ± 0.05	12 ± 1
		$(1.05 \pm 0.05)\times10^{-8}$	280	0.017 ± 0.01	3.6 ± 1.0	47 ± 8
		$(1.1 \pm 0.1)\times10^{-9}$	264	0.0071 ± 0.0008	22 ± 8*	84 ± 6
NK oxidized	0.1-1	1.09×10^{-5}	235	N/A	0.9 ± 0.2	19 ± 3
		$(1.07 \pm 0.03)\times10^{-8}$	205	N/A	2 ± 0.2	34 ± 2
		$(1.1 \pm 0.1)\times10^{-9}$	230	0.19 ± 0.13	3.4 ± 0.9	46 ± 7**

* absolute errors represent the lower limit N/A – not applicable.
** after 21 day contact time.

Sorption rate increase for the higher Tc concentrations might due to competition of two processes of Tc immobilization – fast bulk precipitation and slow sorption of Tc(IV) species from the solution. Fitting of the kinetics curves for the highest Tc concentrations experiments is giving much better correlation using the sum of two exponential functions (rate constants). For instance, kinetics curve of 10^{-5} M Tc on oxidized ÄD can be fitted with two exponential functions with k values of 0.017 ± 0.008 and 0.265 ± 0.056 d^{-1}, which could correspond to the sorption and precipitation processes, respectively. Exponential fitting of the kinetics curve of the Tc sorption studies from [BON/FRA1979] gives a k value around 1.1 ± 0.4 d^{-1} for an initial Tc concentration of 0.11 µM with Westerly granite as a solid material. pH/E_h values for this material was also comparable (pH 8, -0.1 V) to the conditions used in present work.

Distribution coefficient K_d obtained for Tc sorption onto Äspö and Nizhnekansky massif rock materials were calculated using equation (5.10):

$$K_d = \frac{C_0 - C_l}{C_l} \times \frac{V}{m_{solid}} \qquad (5.10)$$

Typical values are presented in **Tab. 5.11** together with measured initial Tc concentrations, amount of ion-exchangeable Fe(II) and redox potentials.

From the thermodynamical point of view the K_d approach deals with reversible processes, but in most papers it is used even when irreversible reduction/precipitation processes are involved [ALB/CHR1991, ALL/KIG1979, KAP/SER1998]. In the report of [UNI/STA1999] authors describe “conditional” K_d for interpretation of experimental data in cases when the rigorous application of the K_d approach is prohibited (non-equilibrium or irreversible systems). In the present work K_d values are considered as conditional distribution coefficients. Use of alternative approaches (R_f, R_s, etc.) was rejected due to lack of appropriate literature references.

5.4.1.3.3 Tc desorption from rock materials

Desorption experiments, which covered one month of equilibration time on initially three months contacted sorption samples, show very low desorption in all studied cases for both ÄD and NK materials, regardless of oxidized or unoxidized material used. For the case of ÄD samples two types of natural groundwater – Äspö and Grimsel GWs (representing glacial melt water composition with low ionic strength) were used.

Desorption was found only for samples after equilibration with 10^{-5} M Tc ÄGWS, for lower concentrations Tc was not detected in liquid phase. After one day contact time desorption achieved values of up to 7 %. This level remained relatively stable up to 30 days of equilibration. The current interpretation of this observation is the initial washing out of Tc(VII) present in retained water through water exchange without further contribution from surface associated Tc(IV).

Pre-oxidation of the ÄD samples on air for one month before addition of ÄGWS changed the Tc desorption behavior drastically (**Fig. 5.45**, left). Both sorption experiments, with originally oxidized and unoxidized materials were treated by air revealed the same desorption behavior possibly indicating a comparable Tc surface species. Desorption process shows fast kinetics, the main part of technetium is released after few seconds contact time and after one day already a plateau value was reached. The strong dependence on initial Tc concentration can be explained with a hypothesis of matrix diffusion. However, the uncertainty in initial Tc amount on mineral surface after sorption experiment may also affect this difference. Visualization of the desorption process is shown in **Fig. 5.44**.

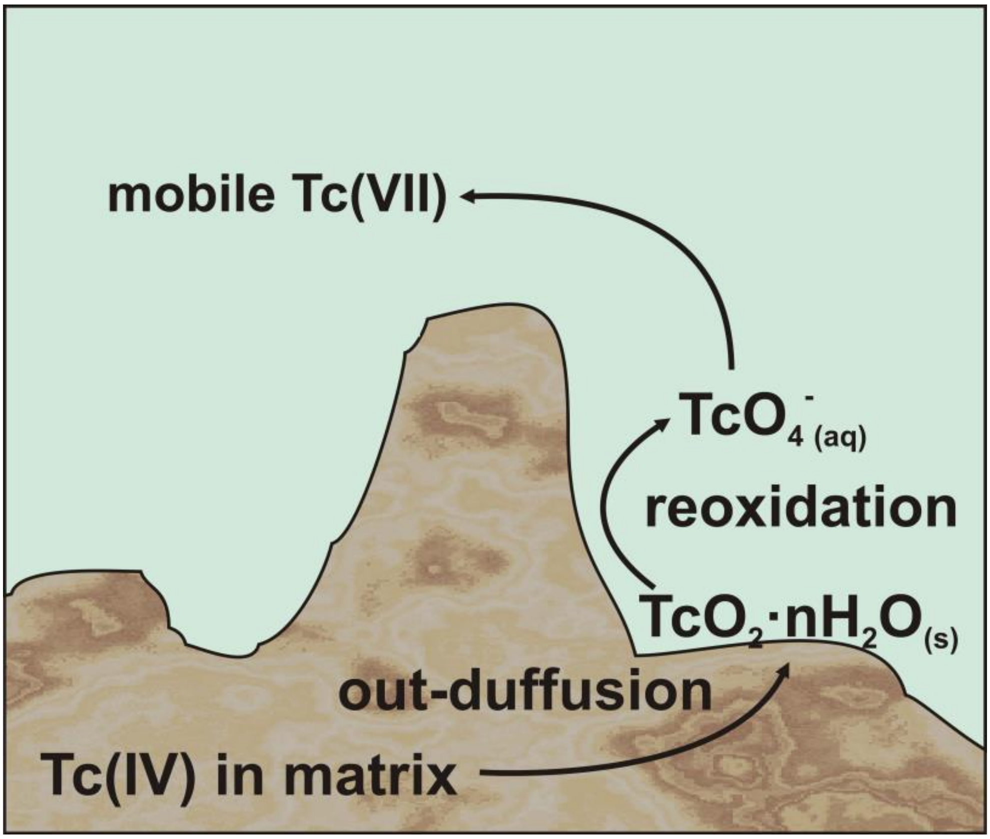

Fig. 5.44 General scheme of Tc desorption processes

Similar studies were also performed for the NK material. After pre-oxidation of the rocks the same desorption kinetics was found for 10^{-5} M and 10^{-8} M Tc samples (**Fig. 5.45**, right), however in 10^{-9} M Tc samples radionuclide was not detected in aqueous phase within experimental time-scale. Furthermore, desorption values of ~65 % are almost identical for both ÄD and NK materials in case of 10^{-8} M Tc samples, whereas 10^{-5} M ones show decrease of desorption for NK granite in comparison with ÄD. Absolute values of Tc concentration in the liquid phase after desorption is shown in **Tab. 5.12**.

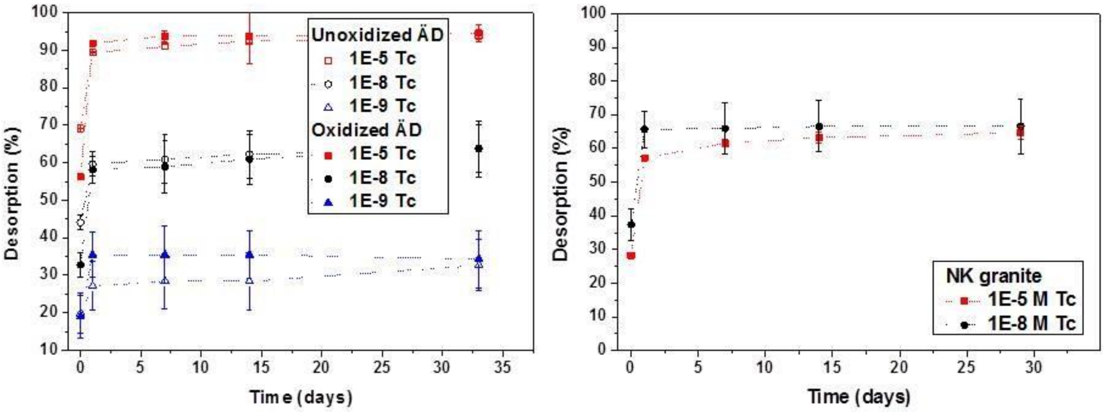

Fig. 5.45 Desorption kinetics of Tc sorption experiments performed with oxidized and unoxidized ÄD material by ÄGWS (left) and oxidized NK granite by NKGWS (right) after one month pre-oxidation under atmospheric conditions

Tab. 5.12 Tc concentration after each change of the GW during desorption studies

Material	**Unoxidized ÄD**			**Oxidized ÄD**			**NK**		
pTc, M	**5**	**8**	**9**	**5**	**8**	**9**	**5**	**8**	**9**
Time, d	**Desorbed Tc concentration, M**			**Desorbed Tc concentration, M**			**Desorbed Tc concentration, M**		
0	1.6×10^{-6}	5×10^{-9}	3.6×10^{-10}	6.7×10^{-7}	1.7×10^{-9}	2.8×10^{-10}	4.9×10^{-7}	1.2×10^{-9}	2.5×10^{-11}
1	4.7×10^{-7}	1.8×10^{-9}	1.3×10^{-10}	4.3×10^{-7}	1.4×10^{-9}	2.4×10^{-10}	5.1×10^{-7}	8.8×10^{-10}	3.2×10^{-11}
7	3.8×10^{-8}	1.4×10^{-9}	2.3×10^{-11}	2.2×10^{-8}	4.3×10^{-11}	n.d.	7.4×10^{-8}	6.8×10^{-12}	n.d.
14	3.4×10^{-8}	1.5×10^{-10}	n.d.	4.1×10^{-10}	1.1×10^{-10}	n.d.	3.0×10^{-8}	2.0×10^{-11}	n.d.
29	-	-	-	-	-	-	2.5×10^{-8}	n.d.	n.d.
33	3.1×10^{-8}	1.8×10^{-10}	7.7×10^{-11}	9.0×10^{-9}	n.d.	n.d.	-	-	-

n.d. – not detected.

5.4.1.3.5 Surface analysis

XPS analysis of ÄD disc fragments after exposing to 10^{-5} M Tc(VII) in GWS for 2 months revealed that Tc is located on dark regions of rock material (**Fig. 5.46**), whereas on light minerals it was not observed. According the binding energy data of XPS spectrum (**Fig. 5.47**) technetium is reduced most probably on mica-type mineral surface (biotite) from +7 to +4 oxidation state and present in TcO_2 form. Tc(VII) was not detected on the material after sorption. XANES measurements results are presented in **Fig. 5.48**.

Fig. 5.46 ÄD sample for XPS. Red circle indicates region where Tc(IV) was found

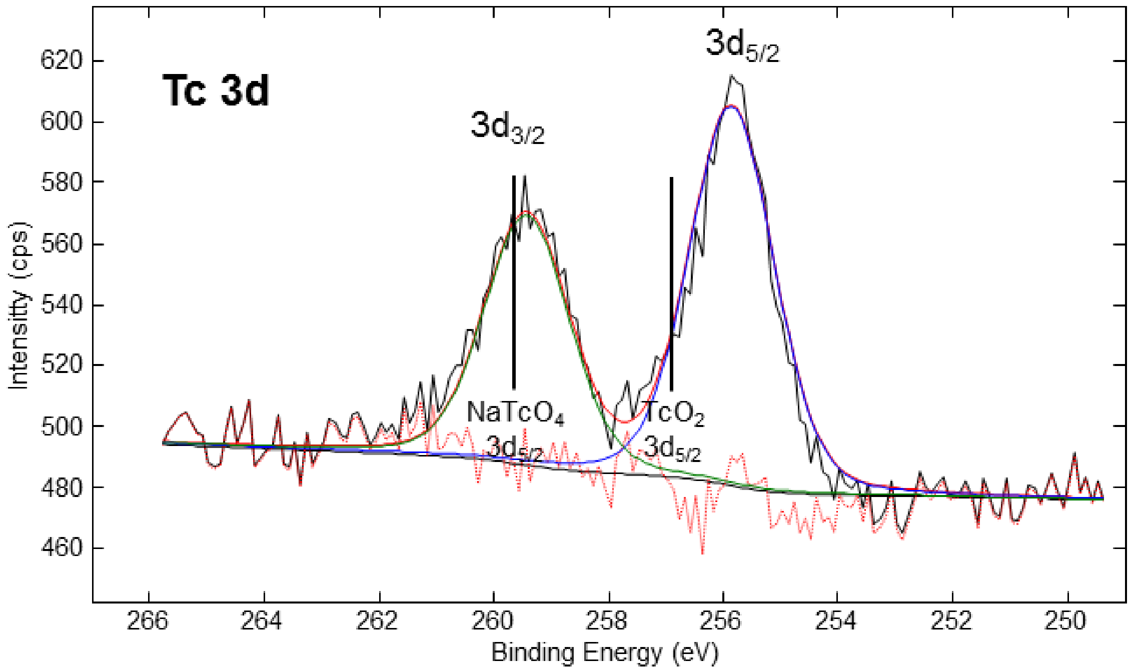

Fig. 5.47 XPS narrow scan of Tc 3*d* spectrum after sorption onto ÄD surface

According to the spectra obtained, Tc on magnetite and Äspö diorite only in tetravalent oxidation state could be identified, while NK sample contains mainly Tc(VII). The ratio of oxidation states was received from linear combination fitting (ATHENA software): 12 ± 5 % Tc(IV) and 88 ± 5 % Tc(VII). Based on the batch sorption studies, Tc(IV) oxide concentration on the mineral surface is low for both ÄD and NK materials. Even small amount of original Tc(VII) solution in the rock pores is enough to damp the signal of Tc(IV) species.

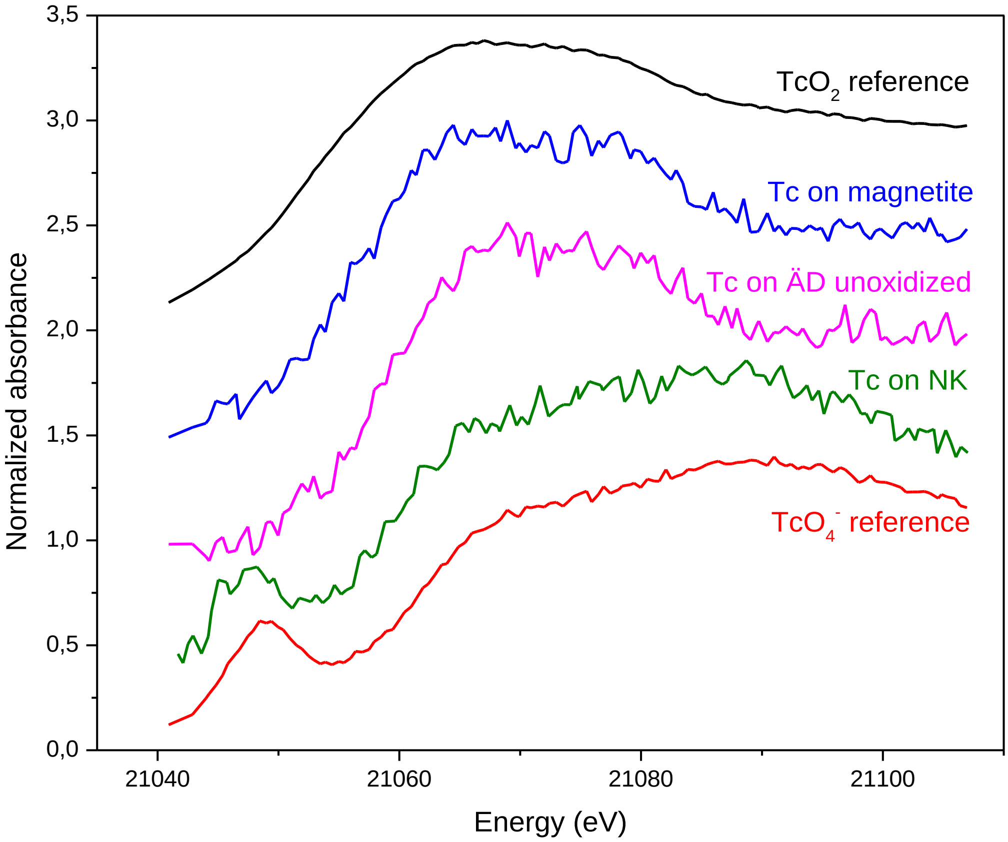

Fig. 5.48 Normalized Tc *K*-edge XANES spectra of samples after sorption of Tc onto magnetite, ÄD and NK rock materials

5.4.1.3.7 Core migration studies

The schematic illustration of the main processes involved into the radionuclides migration through the porous media is presented in **Fig. 5.49**. The marked rectangular area is dedicated to Tc sorption/reduction processes shown above in **Fig. 5.42**.

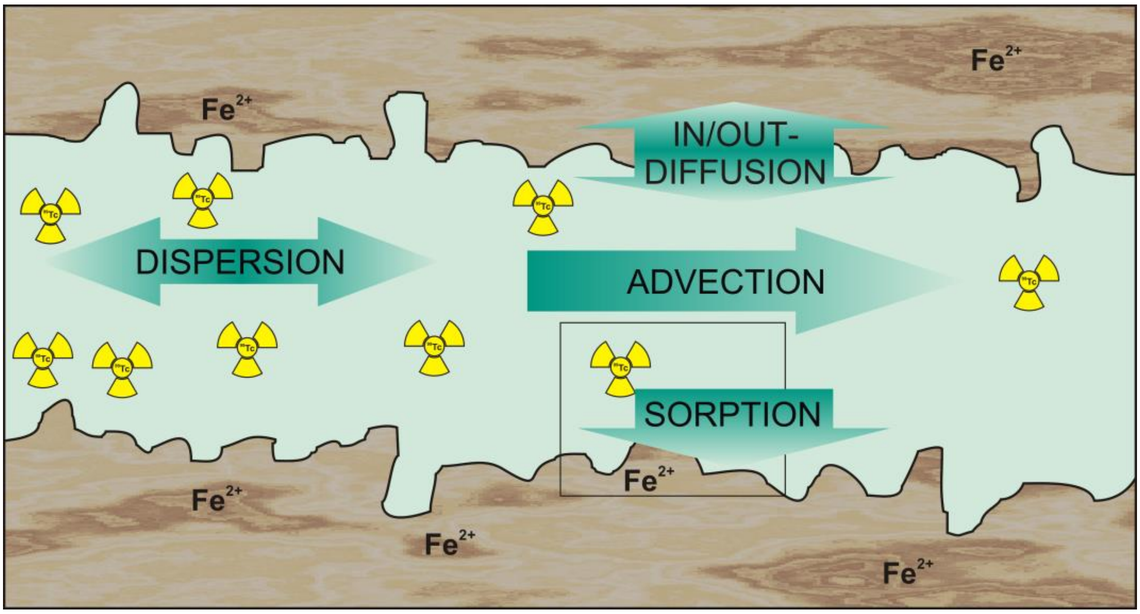

Fig. 5.49 General scheme of Tc migration through the core fracture

Conservative tracer tests for hydraulic characterization of a natural fracture were performed by HTO and the effect of potential anion exclusion was monitored in parallel through addition of ^{36}Cl. Typical breakthrough curves (BTC) for both radionuclides at different flow rates are shown in **Fig. 5.50**. The long tailing of the BTC is most likely due to channeling through the fracture with different flow rates as identified by µCT measurements. A significant contribution of the experimental set-up to the observed tailing was excluded by additional tests bypassing the core. Injection function for 10 mL/h test is also presented in **Fig. 5.50**.

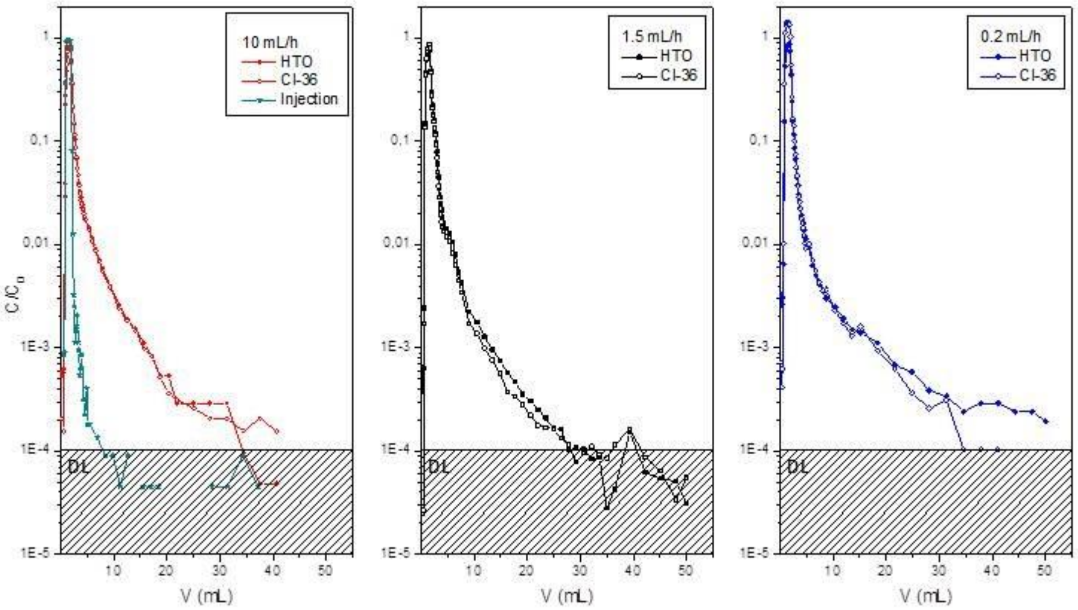

Fig. 5.50 HTO and ^{36}Cl breakthrough curves for natural fracture in Äspö core #2.2

Based on the differential pressure of the core measured during the experiments under three different flow rates (10, 1.5 and 0.2 mL/h), permeability $(3.7 \pm 0.3)\times10^{-14}$ m^2 and hydraulic conductivity $(3.6 \pm 0.3)\times10^{-7}$ m/s were calculated. The comparison of HTO and ^{36}Cl BTC for different flow velocities clearly shows an influence of fracture residence time on breakthrough tailing. As far as HTO and ^{36}Cl show similar behavior, anion exclusion effect was not observed in the fracture investigated under the hydraulic conditions established.

Results of Tc migration studies using ^{95m}Tc(VII) at trace concentrations below the Tc(IV) solubility (~10^{-11} M ^{99}Tc(VII) was taken) are presented in **Fig. 5.51**. Shoulders on the curve are disappearing with decrease of flux probably due to preferential flow through the largest channels in the fracture. Another effect, that may influence the decrease of BTC tailing is kinetically controlled Tc(VII) reduction followed by sorption of Tc(IV) species, which might be indicated by the decreasing recovery. Injections of high Tc concentrations will help to reveal its speciation using surface analysis. Residence time and recovery for ^{95m}Tc is given in **Tab. 5.13**. Sorption rates obtained from batch-type experiments (see **Tab. 5.11**) allow to predict recovery in core migration study using equation (5.8). Longer contact times (1 day and more) were achieved by stop-flow experiments. Typical stop-flow breakthrough curve is shown in **Fig. 5.52**, where the small peak after pumping restart corresponds to the mobile Tc amount recovered form the core fracture. This peak also includes Tc solution inside the small tubing fragments on the both sides the core, but this correction was calculated and taken into account for the total recovery estimation (see **Tab. 5.13**). A gradual decrease of Tc concentration is caused by the radioactive decay of ^{95m}Tc isotope.

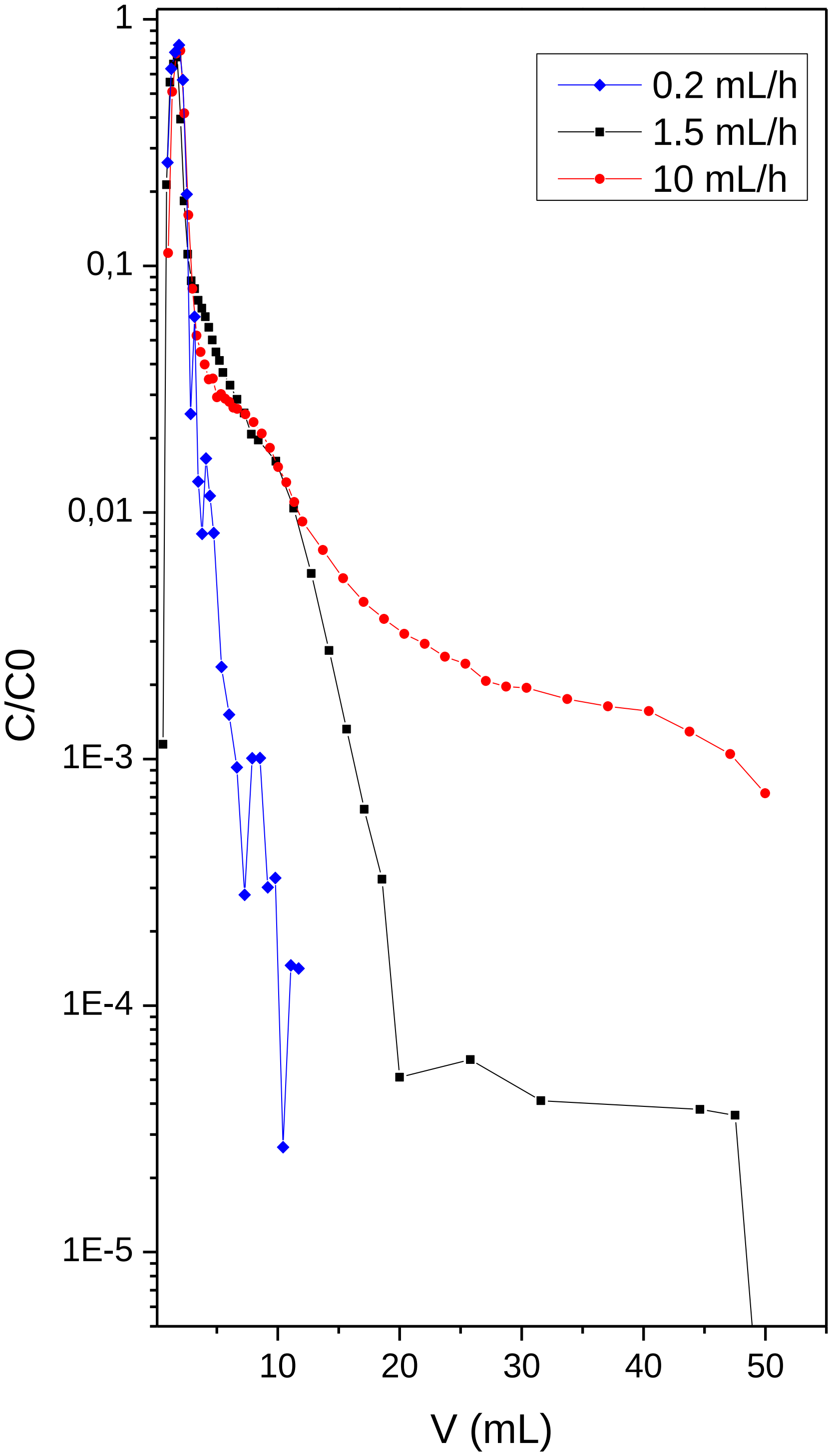

Fig. 5.51 ^{95m}Tc(VII) breakthrough curves in Äspö core #2.2

Tab. 5.13 Migration results for the lowest ^{95m}Tc concentration used

Flow rate, mL/h	C_0 (^{95m}Tc), mol/L	Residence time	Recovery, %
10	2.1×10^{-11}	10 min	100
1.5	1.4×10^{-11}	59 min	92
0.2	9.3×10^{-12}	490 min	87
10; stop-flow	3.7×10^{-12}	1 day	71
10; stop-flow	3.5×10^{-12}	2 days	37
10; stop-flow	2.8×10^{-12}	4 days	16
10; stop-flow	2.8×10^{-12}	8 days	0

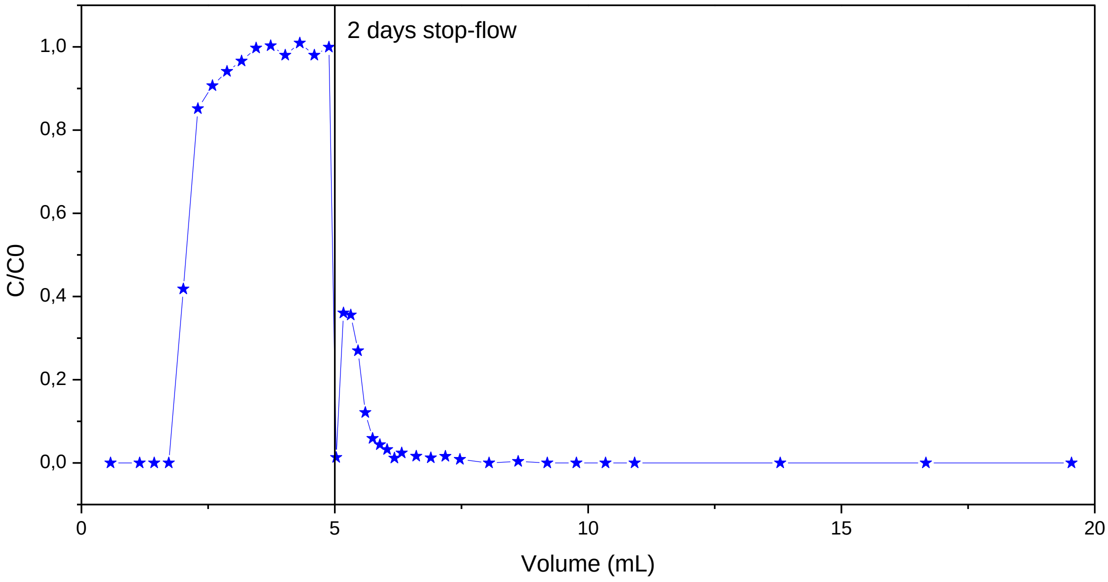

Fig. 5.52 Breakthrough curve for 2 days stop-flow injection of ^{95m}Tc(VII)-containing ÄGWS into Äspö core #2.2 (10 mL/h)

Comparison between recoveries after 10^{-11} and 10^{-9} M Tc injections is given in **Fig. 5.53**. As for the batch sorption studies, kinetics curves can be divided into two parts. Initial retention rate (the first 1 – 2 days) is higher for the elevated Tc concentrations, but after 2 days contact time recovery curve bends and further recovery rate is higher for the 10^{-11} M Tc concentration. **Fig. 5.53** also illustrates the comparison between migration and batch-type studies retention rates. For the first kinetics points (up to 1 day) the sorption values for both batch and migration studies are almost similar, but further kinetics is much faster for the migration experiments.

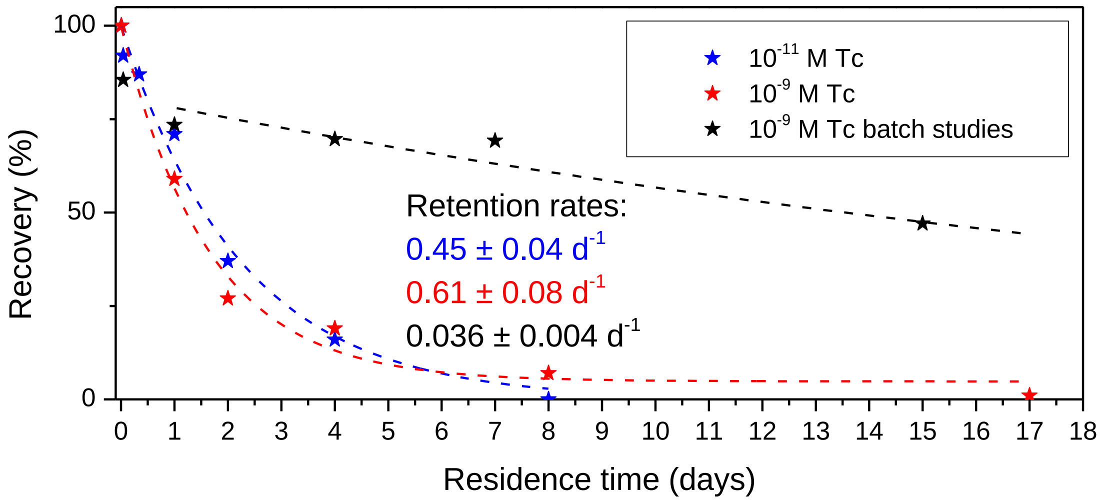

Fig. 5.53 Retention kinetics during the migration studies for 10^{-11} M and 10^{-9} M Tc compared with the 10^{-9} M Tc batch studies results

A general trend of faster retention kinetics for the higher initial Tc concentration was also found in batch sorption studies (see **Tab. 5.11**). As far as two retention processes (sorption and precipitation) are taking place simultaneously in the same system, fast initial retention for the high Tc concentrations can be attributed to the bulk $TcO_2 \cdot 1.6H_2O$ precipitation. According to the work done by [ZAC/HEA2007], Tc(VII) reduction by Fe(II) aqueous solution at pH 8 is very fast (complete reduction within 1 hour). Based on the E_h measurements, in case of high Tc concentration available Fe(II) content in the solution is not enough for complete Tc reduction. Taking into account also the surface analysis data, where Tc(IV) hotspots were found only on Fe(II)-containing mica minerals, the surface reduction can be a limiting process with a lack of reducing agent in the solution.

5.4.1.4 Conclusions

According the experimental data, during the equilibration with Fe(II)-containing minerals Tc(VII) is reducing to +4 oxidation state with precipitation in $TcO_2 \cdot nH_2O$ form. Apparently, the Tc(VII) concentration is directly influencing the sorbed Tc amount on unoxidized and oxidized material, which can be correlated with the ion-exchangeable Fe(II) buffer available. Tc behavior on both ÄD and NK oxidized materials is quite similar, but it differs dramatically with non-oxidized ÄD samples. Oxidized rocks can sorb up to 40 % – 50 % of Tc trace concentrations (10^{-9} M) and up to 10 % – 20 % of Tc at a relatively high (10^{-5} M) concentration under GW conditions. Varying values between ÄD and NK samples at an intermediate (10^{-8} M) concentration indicates that NK samples contain less available Fe(II), than ÄD. Distribution coefficients obtained within this work are in a good agreement with available published data. The Tc(VII) reduction by ferrous iron resulting in insoluble Tc(IV) species was proved by XPS analysis.

Colloidal phase formation was not detected during the batch studies under the GW conditions established. This observation is very important for safety assessment of the nuclear waste repository, because colloidal particles formation could significantly increase the Tc mobility.

Technetium desorption from crystalline rock materials under natural conditions is insignificant for all investigated cases, but after artificial oxidation of samples technetium mobility is increased.

Core migration experiments show much faster retention kinetics than batch sorption studies (0.61 ± 0.08 d^{-1} and 0.036 ± 0.004 d^{-1} for 10^{-9} M Tc, respectively), which is very promising concerning the deep geological disposal. Anion exclusion was not observed for the core material in use. The experimental data should be implemented into the reliable reactive transport model for further upscaling of technetium migration for safety assessment.

5.4.2 Sorption and redox behaviour of technetium in natural clay rocks

5.4.2.1 Introduction

^{99}Technetium is mainly considered as a fission product with long half time (2.1×10^5 years) and plays an important role for the long-term radiotoxicity of the inventory of nuclear waste repositories [KUB1993]. In aqueous solutions, the chemical form of Tc depends mainly on the redox potential [BON/FRA1979]. Under typical oxidizing environmental conditions, technetium forms the pertechnetate ion $Tc(VII)O_4^-$, whose salts are very soluble, which shows only weak interaction with inorganic solids and clay minerals and is, therefore, considered as a rather mobile species in the environment [PAL/MEY1981, RAR/RAN1999, LIE/BAU1987]. Under reducing conditions, as found in a deep bedrock repository for high-level nuclear wastes, Tc(IV) is expected to form, which is sparingly soluble [CUI/ERI1996b).

In order to perform the long-term safety assessments of high-level nuclear waste repositories in clay formation, a detailed knowledge of redox behaviour, solubility, complexation, sorption, and diffusion of Tc in natural clay rocks are essential. Two natural clay rocks are in the focus of sorption studies related to safety analysis of nuclear repositories. Opalinus Clay (OPA, Mont-Terri, Switzerland) [BRA/BAE2003] is considered as potential host rocks for deep geological disposal of radioactive waste due to their low permeability and high surface area. However, only few studies have been dedicated to the uptake and redox behaviour of Tc in natural clay rocks like OPA. TcO_4^- is only slightly sorbed on most rocks and minerals under oxidic conditions, probably by surface ion exchange, and it is excluded from sorption in some negatively charged sediments by repulsion within the charged double layer thereby leading to an enhanced geochemical mobility [PAL/MEY1981, ELW/GER1992, KAP2003]. Therefore, the understanding of redox behaviour, retention, and mobilization of Tc in natural clay rocks are required for evaluation of safety assessments of the nuclear waste repository.

The aim of this study was to characterize the uptake of Tc on OPA. Batch experiments were carried out to investigate the interaction of Tc with crushed OPA material at different S/L ratios, Tc concentrations and oxidizing and reducing condition, effect of contact time, effect of ionic strength. Because Tc(VII) is redox sensitive in reducing conditions and its sorbing behaviour strongly depends on the oxidation state ─ Tc(VII) or (IV) ─ the experiments also focused on the redox speciation of technetium. The Tc oxidation state distribution in OPA suspension was investigated by X-ray absorption near edge spectroscopy and liquid-liquid extraction combined with liquid scintillation counting (LSC).

5.4.2.2 Materials and methods

All chemicals were of p. a. quality or better and are obtained from Merck (Darmstadt, Germany) or Riedel de Haen (Seelze, Germany). All experiments were conducted using de-ionized, “Milli-Q” water (specific resistivity, $\rho = 18.2$ MΩ·m). The activity of ^{99}Tc in solution was measured by liquid scintillation counting (LSC; Tri-Carb 3500 TR/AB, Canberra, Packard, Meriden) using the scintillation cocktail Ultima Gold XR (Packard).

5.4.2.2.1 Artificial Pore Water

The artificial pore water was prepared according to the recipe of [VAN/SOL2003, PEA/ARC2003]. The pH was adjusted to 7.8 using NaOH and HCl. The composition of the synthetic pore water is given in **Tab. 5.14**. One set of experiments was dedicated to the effect of the ionic strength on Tc uptake on OPA. Another artificial pore water was prepared, where the ionic strength was increased to 3.4 M by using NaCl.

Tab. 5.14 Composition of the artificial pore water [VAN/SOL2003]

The additional, highly saline, pore water investigated has the same composition except that [NaCl] was increased to reach I = 3.4 M

Ion	**mmol/L**
Na^+	240.5
K^+	1.6
Ca^{2+}	25.8
Mg^{2+}	17.0
Sr^{2+}	0.5
Cl^-	300.1
SO_4^{2-}	14.1
Inorganic carbon	0.5
Ionic strength (*I*)	386.2

5.4.2.2.2 Measurements of pH and E_h

The pH of the solutions was measured by using an Orion 525A device equipped with a Ross electrode calibrated with 4 standard buffers (pH 3, 5, 7 and 9, Merck). For pH measurements at I = 3.4 M, where the major background electrolyte is NaCl, an empirical correction term was applied for the measured operational pH-values (pH_{exp}) to obtain thermodynamically well-defined quantities. An empirical correction coefficient (A) that depends on background electrolyte composition and concentration and that has been accurately determined in our laboratories for aqueous NaCl systems and at room temperature was used to correct the operational pH_{exp} values according to equations (5.11) and (5.12).

$$pH_C = pH_{exp} + A_{NaCl} \tag{5.11}$$

$$A_{NaCl} = 0.0013 * (m_{NaCl})^2 + 0.1715 * m_{NaCl} - 0.09 \qquad (5.12)$$

The redox potentials in the clay suspensions were measured using an Orion 525A (E_h meter) and a Pt combined electrode with Ag/AgCl reference system (Metrohm) and converted into E_h vs. standard hydrogen electrode (S.H.E.) by correcting for the potential of the reference electrode. A commercial redox-buffer (220 mV, Schott instruments) was used for calibration. An equilibration time of 15 min was applied for all E_h measurements. The suspension was stirred prior to the E_h measurement.

5.4.2.2.3 Technetium

For all batch experiments, the isotope ^{99}Tc was used and the stock solution contained 100 % heptavalent technetium (Tc(VII) = TcO_4^-, pertechnetate). The Tc concentration was determined by liquid scintillation counting (LSC).

5.4.2.2.4 Opalinus Clay mineral (OPA)

The OPA was already well characterized and reported in the literature [NAG2002]. For the batch type studies Opalinus Clay mineral (OPA) was crushed, sieved (< 500 µm), freeze dried, and stored under Ar- glove box. The anaerobic OPA crushed powder is prepared in under Ar atmosphere (inert glove box) from the OPA bore core BHE-24-2 (Mont Terri, 3.3 – 3.56 m). OPA from Mont Terri consists mainly (> 65 %) of different sheet silicates (kaolinite, illite, illite/smectite mixed layers, and chlorite) but also > 10 % quartz and calcite. In addition to these main fractions, OPA contains ≈ 4 % Fe(II) containing minerals (pyrite and siderite) as well as traces of albite, feldspars, and organic carbon.

5.4.2.2.5 Batch experiments

Three series of batch experiments were conducted. The first series has been performed under 100 % argon atmosphere (anaerobic conditions). The second one has been performed under ambient air conditions. For both series, Tc uptake was studied after 7 days contact time for S/L = 20 g/L and various $[Tc]_{tot}$ (10^{-8} – 10^{-6} M) in the two synthetic pore waters (i. e. with I = 0.38 and 3.4 M). The third series of experiments has been performed under argon atmosphere with 1 % $CO_{2(g).}$ Tc uptake was studied after 42 and 120 days contact time for S/L = 10, 20, 50 and 200 g/L and $[Tc]_{tot} = 3\times10^{-7}$ M, in the synthetic pore water with $I = 0.38$ M.

The batch experiments were carried out in Zinsser vials (20 mL HDPE) at room temperature and in presence of light. For the experiments the clay powder was preconditioned in artificial pore water and the solution mixture was shaken continuously for 10 – 15 days. Then Tc(VII) was added on this preconditioned suspension. After adding Tc(VII), the pH was readjusted to 7.8 by adding 0.1 M HCl or 0.1 M NaOH. The pH of the suspension solutions was controlled regularly. The E_h of the suspension was only controlled for the third series (argon atmosphere with 1 % $CO_{2(g)}$). For determination of the distribution coefficient R_d, the solid and liquid phases were separated by ultrafiltration with 10 kDa ultrafilter (5000 rpm for 1 h) or ultracentrifugation (90,000 rpm) for 1 h. After ultrafiltration/ultracentrifugation, the supernatants were analysed in order to determine the content of free Tc in the liquid phase by liquid scintillation counting (LSC). The fraction of Tc sorbed and the distribution coefficient were calculated by using the following equations:

$$Sorption = 1 - \frac{[Tc]_{eq}}{[Tc]_0} \times 100\ (\%) \tag{5.13}$$

$$R_d = \frac{x}{m} \times \frac{1}{[Tc]_{eq}} \tag{5.14}$$

where $[Tc]_{eq}$ and $[Tc]_0$ (moL/L) are the equilibrium concentration in solution and initial total concentrations of Tc, respectively; *x* (mol) is the amount of sorbate; *m* (kg) is the mass of sorbent.

5.4.2.2.6 X-ray absorption fine structure (XAFS) spectroscopy

One sample was prepared for XAFS analysis (S/L = 50 g/L, $[Tc]_{tot} = 3\times10^{-4}$ M, I = 0.38 M, Ar atmosphere with 1 % CO_2, 120 days contact time). For the XAFS measurements, filtrate solution or paste-like filter cake of Tc-OPA were filled into 400 µL capped PE vials and mounted in a special air tight sample holder. The holder was connected to an Ar supply line at the experimental station to keep the samples under near oxygen-free conditions during XAFS measurements. The measurements were performed at the

INE-Beamline by using this type of inert gas sample cell design [BRE/BAN2009] for redox sensitive radionuclides. The spectra were calibrated against the first derivative X-ray absorption near edge structure (XANES) spectrum of a Zr foil, defining the energy of the first inflection point as E(Zr 1s) = 17998.0 eV. All Tc K-edge XAFS spectra were measured in standard fluorescence yield detection mode.

5.4.2.2.7 Liquid-liquid extraction

The oxidation state of technetium in solution at low concentration after ultrafiltration (10 kDa filter) under anaerobic conditions was analyzed by liquid-liquid extraction. Two protocols were applied: 1-phenyl-3-methyl-4-benzoylpyrazolone-5 (PMBP) or 2-thenoyltrifluoroacetone (TTA) was used to extract Tc(IV) into the organic phase [NIT/ROB1994]. Tc(VII) remains in solution. To 0.6 mL portion of the filtrate solution 0.2 mL 2 M HCl and either 0.8 mL 0.025 M PMBP in Xylene and 0.5 M TTA in Toluene was added and then vigorously shaken for 10 min. The aqueous and organic phases were separated by centrifugation for 30 min (5000 rpm) and aliquots of each phase were taken for LSC analysis. To prove the Tc oxidation state on the surface of the clay, the filter cake of clay (i. e. OPA) was re-suspended in 1 M HCl for 2 days under argon atmosphere. We assumed that the Tc, (IV) and (VII), was released into the solution. The two phases were separated by ultrafiltration with10 kDa filters and the solution (1 M HCl) was probed by the same extraction procedure as before described.

5.4.2.2.8 Geochemical speciation modeling

pH-E_h diagrams for Tc were obtained using PhreePlot [KIN/COO2009], which contains an embedded version of the geochemical speciation program PHREEQC [PAR/APP1999]. The SIT database provided with PHREEQC is used, in which the thermodynamic constants for Tc correspond to the ones selected by the NEA [GUI/FAN2003]. For the calculations, carbonate concentrations are assumed to be in equilibrium with calcite. Nevertheless, preliminary calculations showed that carbonate have a minor impact on Tc speciation in the presently investigated conditions (i. e. with or without 1 % $CO_{2(g)}$ or calcite), according to the available thermodynamic database. The reduction of sulfate and CO_2 is not considered in the calculations.

5.4.2.3 Results and discussions

5.4.2.3.1 Technetium uptake on Opalinus Clay

5.4.2.3.1.1 Effect of O_2 and total Tc concentration

Tc uptake on OPA in the synthetic pore water (I = 0.38 M, pH = 7.8) was investigated in the presence (ambient air atmosphere) and in the absence (Ar glovebox, no CO_2) of O_2 for S/L = 20 g/L and various Tc concentrations ($[Tc]_{tot} = 10^{-8}$-10^{-6} M), after 7 days contact time. The results are shown in **Fig. 5.54**. No Tc uptake is observed under air atmosphere while ~25 % of Tc is sorbed to OPA under Ar atmosphere for $10^{-7} < [Tc]_{tot} < 10^{-6}$ M. This result points to the reduction of Tc(VII) to Tc(IV), as anionic Tc(VII) sorbs weakly to minerals with negative surface charge. The uptake of Tc does not evolve with $[Tc]_{tot}$ under Ar atmosphere.

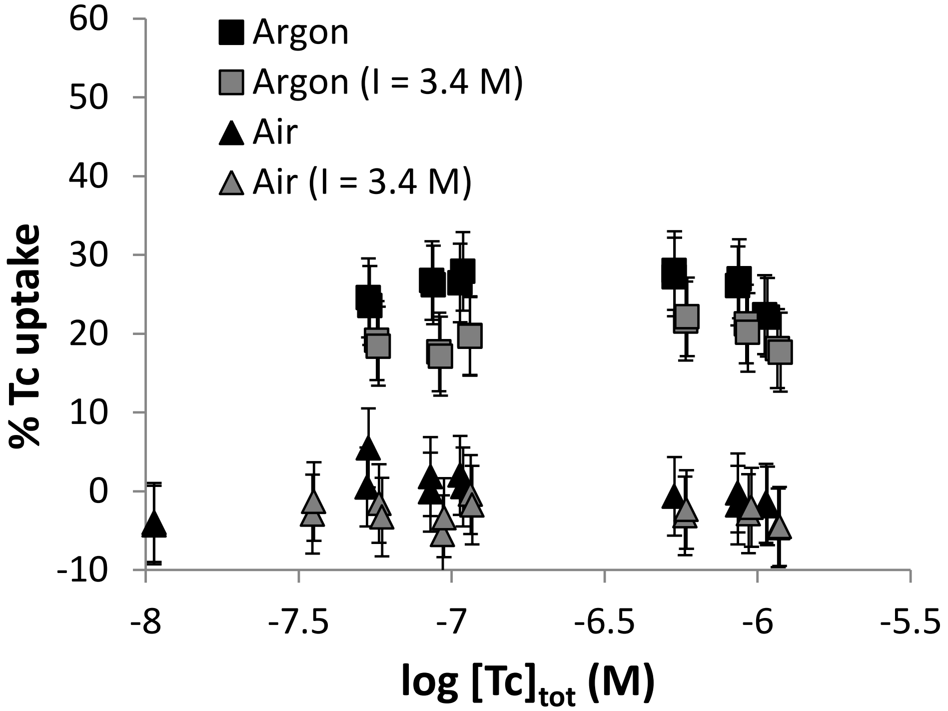

Fig. 5.54 Uptake of Tc on OPA (Mont Terri) as a function of Tc concentration for S/L= 20 g/L, pH=7.8 and 7 days contact time

Experiments are performed under argon (no CO_2; squares) or ambient air atmosphere (triangles). Experiments are performed in synthetic pore water (I = 0.38 M), as used in previous studies (black symbols), or in a synthetic pore water with I = 3.4 M (grey symbols)

5.4.2.3.1.2 Ionic strength effect

Tc uptake on OPA after 7 days contact time is investigated in the presence (ambient air atmosphere) and the absence (Ar-glovebox, no CO_2) of O_2 for S/L = 20 g/L and various Tc concentrations ($[Tc]_{tot} = 10^{-8}$-10^{-6} M) in the synthetic pore water with high ionic strength (I = 3.4 M, pH_C = 7.8). The results are compared with the results obtained in the original synthetic pore water in **Fig. 5.54**. No significant influence of NaCl is found either in presence or in absence of O_2. This shows that, in presence of O_2, Tc(VII) sorption is not promoted by the high background electrolyte concentration, which might induce an increased (i. e. less negative) charge of the mineral surfaces. In absence of O_2, the uptake of Tc is not significantly impacted by the ionic strength. It shows that if reduced to the tetravalent oxidation state, Tc(IV) uptake is not controlled by an ion exchange process. Schnurr *et al.* [SCH/MAR2014] showed that surface complexation of trivalent Eu/Cm to illite and smectite is weakly impacted by the ionic strength for 0.1 < [NaCl] < 4 M. Our results suggest that it is also the case for Tc(IV) surface complexation to OPA clay minerals, assuming that no Tc(IV) surface precipitate is formed.

5.4.2.3.1.3 Effect of the contact time and the solid to liquid ratio (anaerobic conditions)

The influence of contact time on Tc uptake on OPA is investigated for $[Tc]_{tot} = 3\times10^{-7}$ M, in the synthetic pore water, under argon atmosphere with 1 % CO_2 and 10 < S/L < 200 g/L. The percentage of Tc sorbed versus S/L is shown in **Fig. 5.55**a after 42 and 120 days contact time. A marginal difference on Tc uptake is observed between both reaction times: Tc uptake is ~5 – 10 % higher after 120 days for all S/L ratios, which is close to the experimental uncertainty on the percentage uptake (± 5 %).

Additionally, Tc uptake data discussed in the previous section for S/L = 20 g/L, $[Tc]_{tot} = 3 \times 10^{-7}$ M, in absence of CO_2 (argon) after 7 days contact time is also plotted in **Fig. 5.55**a with the data obtained after 42 and 120 days (argon with 1 % CO_2). This highlights the almost insignificant time dependence on Tc uptake previously discussed. In addition, it suggests that the partial pressure of CO_2 has an insignificant influence on Tc uptake on OPA in the presently investigated conditions. Even if the partial pressure of CO_2 controlled the carbonate concentration in our experiments, according to the thermodynamic constants provided by the NEA [GUI/FAN2003], Tc(VII) and Tc(IV) complexation by carbonate is insignificant in the presently investigated conditions.

At constant pH (7.8) and 3×10^{-7} M Tc, the percentage of Tc sorbed increases proportionally to the solid-to-liquid ratio (**Fig. 5.55**a), i. e. to the amount of sorption site available for Tc. Tc uptake data after 120 days contact time are converted to log R_d (L/kg) and plotted versus S/L in **Fig. 5.55**b. The log R_d values for all S/L are not significantly different. The average log R_d is 1.22 ± 0.56 L/kg (2σ). From comparison with log R_d values of other tetravalent like Th(IV) this value is low. At the moment we cannot decide whether this is not a real sorption coefficient because the process of surface precipitation of hydrolysed Tc(IV) is not considered. Nevertheless, the constant Tc uptake with $[Tc]_{tot}$ (**Fig. 5.54**) and the constant R_d with S/L point to ideal uptake behaviour, suggesting that surface complexation is the dominant uptake process. On the other side, because we do not know the quantitative amount of tetravalent technetium in relation to the total Tc concentration, this value mirrors also the marginal sorption strength of Tc(VII) (see also section 5.4.2.3.2.3).

5.4.2.3.2 Tc redox speciation

5.4.2.3.2.1 Redox state analysis by liquid-liquid extraction ($[Tc]_{tot} < 10^{-6}$ M)

In order to shed light on the redox behaviour of Tc, the oxidation state of the remaining Tc in the liquid phase contacted with OPA is determined by liquid-liquid extraction. PMBP [NIT/ROB1994] and TTA are used as extractants for Tc(IV) in the organic phase. Tc redox speciation is determined in solution on contact with OPA with $[Tc]_{tot} = 3\times10^{-7}$ M, in the synthetic pore water, under 1 % CO_2 (Ar) and 10 < S/L < 200 g/L after 120 days contact time. On average for all S/L, 50 ± 6 % of Tc(VII) and 50 ± 6 % of Tc(IV) are found in solutions contacted with OPA. This confirms the partial reduction of Tc(VII) to Tc(IV) in the in the OPA-artificial pore water system. This redox state analysis provides two important information. First, on a *Pourbaix* diagram, a Tc(VII):Tc(IV) ratio of 50:50 is located at the Tc(VII)/Tc(IV) borderline. This result will be compared with the redox potential measurements in section 5.4.2.3.2.3. Second, the final Tc(IV) aqueous concentration in the OPA pore water can be determined. Log $[Tc(IV)]_{eq}$ ranges between -7 (S/L = 10 g/L) and -7.3 (S/L = 200 g/L). These values are 1 to 2 orders of magnitude higher than the solubility of $TcO_2{\cdot}1.6H_2O_{(s)}$ (-8.4 ± 0.5; [GUI/FAN2003]). Therefore, one cannot exclude Tc(IV) precipitation as an uptake process. Nevertheless, the higher apparent Tc(IV) solubility might suggest the formation of a dissolved complex in the synthetic pore water contacted with OPA, as also further discussed in section 5.4.2.3.2.3.

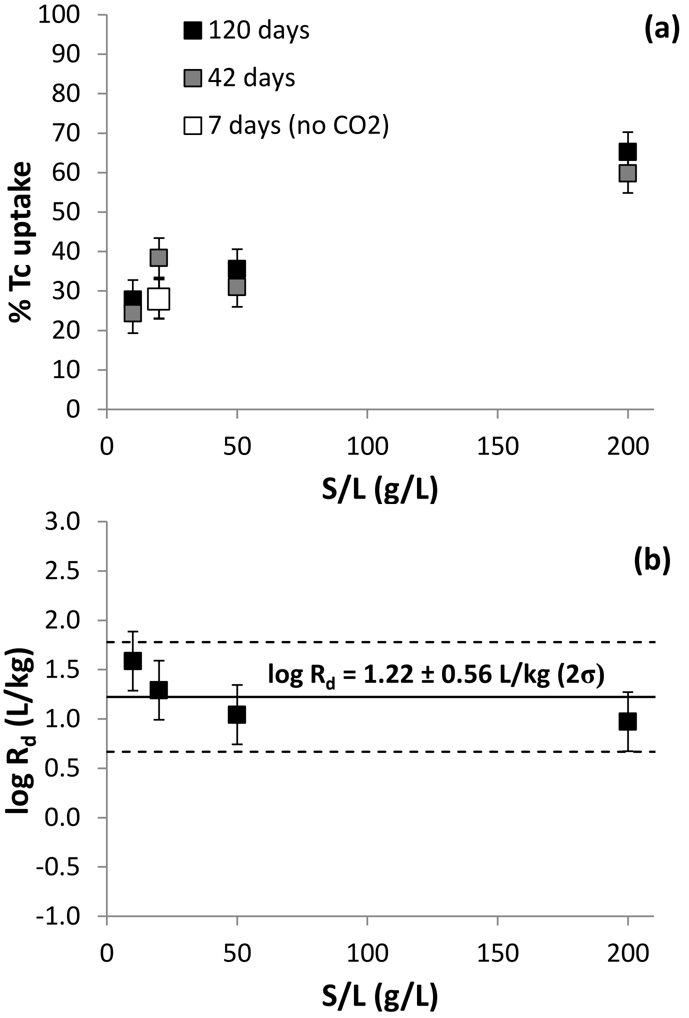

Fig. 5.55 (a) Influence of contact time on the uptake of Tc on OPA (1 % CO_2; argon) in synthetic pore water (*I* = 0.38 M) as a function of solid to liquid ratio ($[Tc]_{tot} = 3\times10^{-7}$ M)
Data obtained in the absence of CO_2 under argon atmosphere ($[Tc]_{tot}$ = 3×10^{-7} M; S/L = 20 g/L; see Fig. 5.54) after 7 days contact time are also shown.
(b) Distribution coefficient (R_d in L/kg) for the uptake of Tc on OPA after 120 days contact time (1 % CO_2; argon) versus S/L.

Additionally a test experiment is performed to determine the redox state of Tc on the solid phase. After one week contact time, a sample prepared for $[Tc]_{tot} = 10^{-6}$ M, 20 g/L of OPA under argon atmosphere (no CO_2) is filtrated at 10 kDa. The wet solid is re-suspend in 1 M HCl and shaken for 2 days. After that, the sample is filtrated again at

10 kDa and the solution is analysed by both PMBP and TTA extraction to determine the oxidation states. The results are summarized in **Tab. 5.15**. Around 27 % of the initial $[Tc]_{tot}$ sorbed to OPA. Only 28 % of the adsorbed Tc can be leached with HCl. The low desorbed amount of Tc in HCl points to the relatively strong interaction of Tc with OPA minerals. In the HCl solution, Tc(IV) was detected by extraction into the organic phase, although the amount appears rather low (~10 %). However, solvent extraction is an invasive method and we cannot exclude that it might change the genuine Tc-redox state. Nevertheless, this test experiments hints qualitatively to partial reduction of Tc(VII) to Tc(IV) in the OPA-artificial pore water system.

Tab. 5.15 Tc speciation in re-suspended Tc-OPA solid in 1 M HCl (S/L= 20 g /L, contact time 7 days, pH = 7.8, artificial pore water, 0 % CO_2 and Argon atmosphere).

Tc(VII) initial concentration, M	**Uptake (in % of the total amount)**	**Leaching (in % of the sorbed amount)**	**Extraction of Tc(IV) from the 1 M HCl into the organic phase (in % of the total desorbed amount)**	
			0.025 M PMBP	**0.5 M TTA**
1.10^{-6} M	27 ± 5	28 ± 5	12 ± 5	9 ± 5

5.4.2.3.2.2 Tc redox speciation on clay solid phases by XANES

One OPA sample was also analysed by XANES after 120 days contact time. The Tc *K*-edge X-ray absorption spectroscopy on Tc element is performed at the INE-Beamline [ROT/BUT2012]. As a reference sample, $Tc(VII)_{ref}$ and $Tc(IV)_{ref}$ are prepared and measured. Tc-OPA sample was measured as a solid and filtrate solution. The XANES spectra of $Tc(IV)_{ref}$, $Tc(VII)_{ref}$ in 1 M $HClO_4$ and Tc-OPA are show in **Fig. 5.56**. The Tc *K*-edge XANES of the $Tc(VII)O_4^-$ 'pertechnetate' moiety, where Tc is surrounded by 4 oxygen atoms in tetrahedral conformation, exhibits a strong pre-edge resonance at 21050 eV, reflecting a Tc $1s \rightarrow 5p/4d$ transition allowed due to *p-d* mixing in the final state. Tc(IV) is generally octahedrally coordinated (inversion symmetry), where this transition is forbidden, so no pre-peak can be seen. A pre-peak is clearly visible on the XANES spectra recorded for OPA, which evidence the prevalence of Tc(VII). Tc(VII) was also found by XANES measurements in the filtrate solutions even after 120 days contact time (not shown).

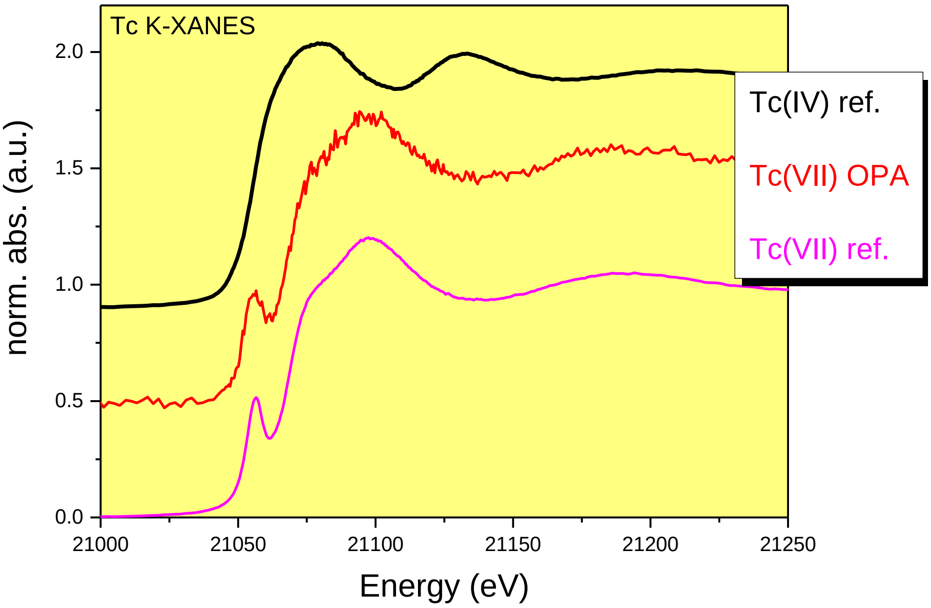

Fig. 5.56 Tc *K*-edge XANES spectra of Tc speciation in OPA

[Tc] =3E-04 M, 0.1 M NaCl, S/L = 50 g/L , 1 % CO_2 and Argon atmosphere, contact time = 120 days, solid sample = filtrate suspension

The prevalence of Tc(VII) appears contrasting with the results in the batch experiments. However, the E_h of the suspension (+200 mV) is much higher than in the batch experiments (see also section 5.4.2.3.2.3). The high E_h value is very likely due to the high $[Tc]_{tot}$ investigated. Higher E_h are recorded for high concentrations of Tc(VII) in presence of granite (see section 5.4.1 of this report) as well as a high $[Np(V)]_{tot}$ in the presence of illite [MAR/BAN2014]. Assuming pyrite as the predominant Fe(II) source responsible Tc(VII) reduction to Tc(IV) in our samples, the Fe(II) quantity in our experiments with S/L = 50 g/L amounts to 4×10^{-3} mol/L in the solid, which is in excess over 9×10^{-4} mol/L of electrons required for the complete Tc(VII) reduction to Tc(IV). The absence of Tc reduction might be explained by the limited accessibility of its redox partner. Therefore, the presence of Tc(IV) on OPA cannot be evidenced by XANES analysis in the present study.

Tc uptake by OPA for $[Tc]_{tot} = 3\times10^{-4}$ M is relatively small after 120 days contact time (6 — 8 %). Although Tc(VII) sorbs very weakly to minerals, we cannot exclude that the XANES signal is partially due to adsorbed Tc(VII) (i. e. below 5 %). In addition, a wet solid phase is analysed and small amounts of dissolved Tc(VII) might also be present in the remaining pore water.

5.4.2.3.2.3 Redox potential measurements after 120 days contact time

For the series of experiments where Tc uptake on OPA was determined after 120 days ($[Tc]_{tot}$ = 3×10^{-7} M, S/L = 10 – 200 g/L, Ar atmosphere with 1 % CO_2), the redox potential of the suspension was measured. The values are plotted in a pH-E_h predominance diagram for Tc in **Fig. 5.57**. The redox speciation of Tc was investigated by liquid-liquid extraction in the filtrate solution, i. e. all solid phases (including potentially precipitated Tc-phases) were discarded. Therefore, only the speciation of Tc in the aqueous solution is shown on the pH-E_h diagram (i. e. no precipitation is considered), which allows the comparison with the experimental redox state analysis of Tc. E_h values are close or within the stability field of Tc(IV), consistent with the redox state analysis of Tc in the aqueous phase, although some of the E_h values appear rather low (≈ -200 mV). These measurements are consistent with the observed Tc uptake as Tc(IV) by OPA in these conditions. The measured E_h are comparable with literature data for OPA [LAU/BAE2000].

From the redox state analysis in solution by liquid-liquid extraction and the E_h measurements, it appears that the average log R_d of 1.22 ± 0.56 L/kg (2σ) obtained after 120 days contact time in batch experiments is highly conditional. Indeed, it is valid only at the Tc(VII)/Tc(IV) borderline ($[Tc(IV)]_{eq} \approx [Tc(VII)]_{eq}$). Since Tc(VII) weakly sorbs to minerals by contrast with Tc(IV), the overall R_d is expected to vary with the E_h. The experimental $R_{d,exp}$ can be expressed as follow:

$$R_{d,exp} = \frac{[Tc(IV)]_{sorbed}}{[Tc(IV)]_{eq} + [Tc(VII)]_{eq}} \times \frac{V}{m} \tag{5.15}$$

The independent R_d of Tc(IV) (R_d(IV)), i. e. the one that would be measured in more reducing conditions where $[Tc(VII)]_{eq} = 0$, can be determined knowing the fraction of Tc(IV) in solution (F_{IV}):

$$R_d(IV) = \frac{[Tc(IV)]_{sorbed}}{[Tc(IV)]_{eq}} \times \frac{V}{m} = R_{d,exp}/F_{IV} \tag{5.16}$$

After 120 days contact time, the extraction experiments showed $[Tc(IV)]_{eq} = [Tc(VII)]_{eq}$, which leads to $R_d(IV) = 2\times R_{d,exp}$. Therefore, log R_d(IV) is calculated equal to 1.52 ± 0.56 L/kg, the uncertainty associated to the redox state analysis of Tc in solution (± 6 %) having a minor impact on these calculations. Eqn. WIL/FAR2001 allows the calculation of Tc uptake on OPA in synthetic pore water as a function of F_{IV}, which is related to the E_h.

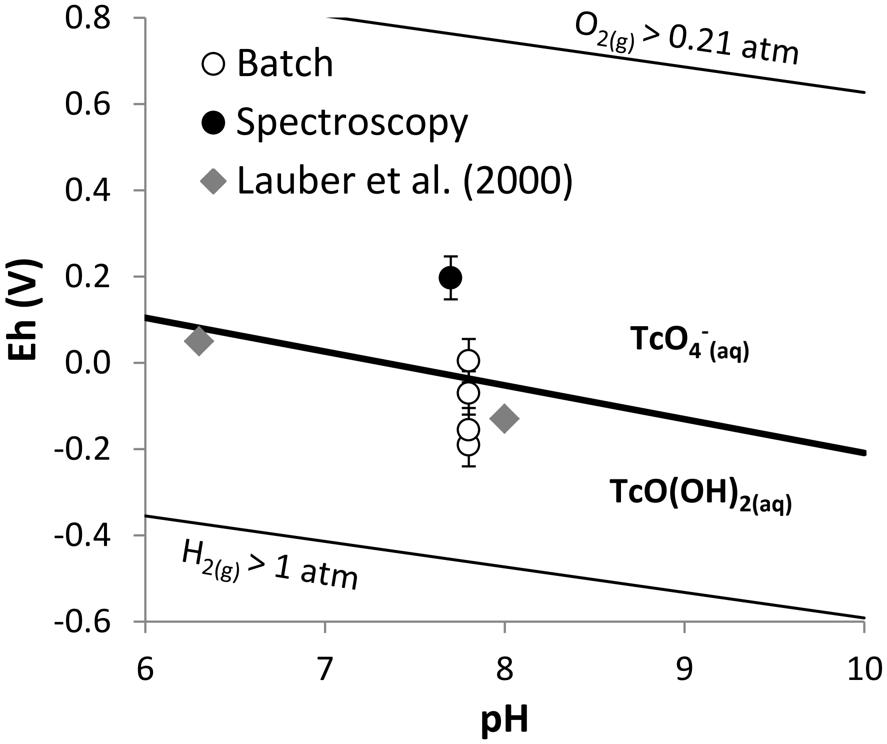

Fig. 5.57 pH-E_h diagram for technetium ($[Tc]_{tot} = 3×10^{-7}$ M; no precipitation considered) in the synthetic pore water (1 % CO_2)

Experimental E_h recorded in the OPA suspensions after 120 days contact time during the batch experiments (S/L = 10-200 g/L; $[Tc]_{tot} = 3×10^{-7}$ M) and in the sample prepared for spectroscopic measurements (S/L = 50 g/L; $[Tc]_{tot} = 3×10^{-4}$ M) are also shown and compared with E_h measurements obtained by Lauber *et al.* [LAU/BAE2000]

The calculated R_d(IV) value appears very low, when comparable to literature values. For instance, Baston *et al.* [BAS/BER1995] reported under reducing conditions R_d values of 4200 to 10000 L/kg for Tc uptake on bentonite (log R_d = 3.6 – 4 L/kg) at an ionic strength of 0.68 mol/L and pH 8.2, i. e. around 2 orders of magnitude higher than in the present study. Because $[Tc(IV)]_{eq}$ is also found between 1 and 2 orders of magnitude higher than the solubility of $TcO_2·1.6H_2O_{(s)}$, the formation of an aqueous Tc(IV) complex with a ligand either present in the synthetic pore water or released from OPA is suspected. For instance, OPA contains organic matter that can be released in synthetic pore water [COU/CHR2008] and Tc(IV) was shown to strongly interact with natural organic matter [BOG/DON2010, EVA/HAL2012]. Therefore, the exact mechanism of Tc uptake on OPA-synthetic pore water system is not fully elucidated yet. Further investigations are required.

5.4.2.4 Summary

In the present study, we investigated the interaction of Tc with OPA at different S/L ratios, Tc concentrations, redox condition (i. e. air or argon atmosphere), effect of contact time, effect of ionic strength. Under air atmosphere, at low Tc concentrations ($<10^{-6}$ M) the heptavalent (anion) state remains predominant and almost no uptake is observed. Under anaerobic conditions (argon) with, at low Tc concentrations ($<10^{-6}$ M), Tc uptake on OPA is significant and is attributed to the partial reduction of Tc(VII) to Tc(IV). Tc uptake is not affected in highly saline conditions ($I > 3$ M). Given the reducing conditions and the relatively high redox capacity of OPA, reduction of Tc(VII) to Tc(IV) is relatively fast, as suggested by the small increase in the uptake between 42 and 120 days contact time. Tc uptake on OPA does not depend neither on $[Tc]_{tot}$ (between 10^{-8} and 10^{-6} M for S/L = 20 g/L) or S/L (between 10 and 200 g/L for $[Tc]_{tot} = 3\times10^{-7}$ M).

Tc redox state analysis in the solution contacted with OPA shows that the final Tc(VII) and Tc(IV) concentration are equal in solution after 120 days contact time with OPA. E_h measurements are relatively close to the Tc(VII)/Tc(IV) borderline on a pH-E_h diagram, in agreement with Tc redox state analysis in solution. We could not confirm the reduction of Tc(VII) to Tc(IV) on OPA by XANES. Even after 120 days contact time Tc remains heptavalent in solution and in the wet solid phase. This is consistent with the high E_h value measured for the sample. This high E_h is very likely due to high Tc(VII) concentration required for such analysis ($>10^{-4}$ M), which acts as an oxidant and affects the redox potential of the system, as observed in previous studies (chapter above and [MAR/BAN2014]). In a real nuclear waste repository environment, because of the very reducing conditions - high redox capacity of clay - and the high S/L ratio, Tc will very likely occur as Tc(IV).

The experimental R_d value measured after 120 days is extrapolated to more reducing conditions where no Tc(VII) is present. The log R_d value for Tc(IV) taken independently is found equal to 1.52 ± 0.56 L/kg, which allows the prediction of Tc uptake as a function of the E_h in OPA-synthetic pore water systems. This low R_d value, in combination with the higher $[Tc(IV)]_{eq}$ than the solubility of $TcO_2{\cdot}1.6H_2O_{(s)}$, suggest the formation of a Tc(IV) complex with a ligand either present in the synthetic pore water or released from OPA. Further investigations are required to verify this observation.

Acknowledgements

We thank Dr. T. Kobyashi for the preparation of Tc(VII) stock solution.

5.5 Incorporation of selenium in iron sulfide and calcite

As for many elements, selenium is on the one hand an essential nutrient for animals and humans, while on the other hand above certain concentration limits it is toxic [FIN/DAR2012]. The critical issue in the case of selenium is that the acceptable range of selenium intake is relatively narrow (e. g. for humans the lower and upper bounds are 40 µg/day versus 400 µg/day, respectively). The bioavailability of selenium in natural systems depends to a large degree on its chemical speciation. Depending on the geochemical milieu (pH-E_h conditions) of natural systems selenium may be present in various oxidation states: -II, (-I), 0, +IV, and +VI [OLI/NOL2005]. Solid phases formed by reduced and elemental selenium are less soluble compared to phases formed by the oxidized species selenium (IV) and (VI). Oxidized selenium forms the oxyanions selenite, $Se(IV)O_3^{2-}$, and selenate, $Se(VI)O_4^{2-}$, in aqueous solution. Compared to the reduced species, the oxidized species need to be considered more mobile in subsurface environments [MAS/DEL1990] and show a higher chemical toxicity [FIN/DAR2012].

In the context of nuclear waste disposal, the radioisotope ^{79}Se is of special concern due to its long half-life ($3.27 \cdot 10^5$ years [JOR/BUH2010]) and expected high mobility. It is created in nuclear reactors by the fission of ^{235}U. The Belgian nuclear waste management organization ONDRAF/NIRAS for example, has concluded that ^{79}Se is a potentially critical radionuclide that might, within a relevant timeframe (10^4 – 10^5 years), diffuse through the geological barrier (Boom Clay) and increase the radiotoxicity in adjacent aquifers [OND/NIR2001].

Sorption reactions with surrounding mineral phases may have an essential impact on the mobility and bioavailability of the oxidized selenium species in soils and sediments. Numerous sorption mechanisms have been observed and characterized on a molecular scale within the past few decades. Besides pure surface reactions (outer-sphere and inner-sphere adsorption, or ion exchange) structural incorporation into mineral phases as a consequence of coprecipitation or recrystallization (dissolution/ reprecipitation) reactions has significant potential to immobilize toxic trace elements, such as selenium, in soils, aquifers, and host rocks of future nuclear waste disposal sites.

Here we present results for selenium incorporation into mineral phases for two different scenarios. Selenium incorporation into iron sulfides represents reducing conditions. Certainly the biggest potential to remove selenium from solution is by reduction to elemental selenium or reduced selenium species. Under these conditions, the incorporation of selenide (selenium(-II)) into iron sulfide phases may effectively retain selenium from migration through the geosphere. Results on selenium incorporation into iron sulfide phases are presented in section 5.5.1. More critical with respect to selenium mobility are oxidizing conditions. Under these conditions selenate and selenite are the relevant aqueous selenium species. Selenate shown only very limited interactions with calcite as well as with other common mineral phases. Results on selenite interactions with calcite at various conditions regarding selenium concentration and calcite supersaturation are presented in section 5.5.2.

5.5.1 Selenium(-II) in iron sulfide

The work on selenide retention by iron sulfide performed in the frame of the VESPA project has been published elsewhere [FIN/DAR2012]. The results presented here are largely taken from that publication.

5.5.1.1 Introduction

Selenium is a non−metal having properties resembling that of sulfur. The solubility of Se is largely controlled by its oxidation state, which depends on the redox conditions of the surrounding environment. Although selenium will be released as selenite oxyanions upon nuclear waste matrix corrosion, a conversion to lower oxidation states is likely to occur because the geochemical environment in a clay−based repository is expected to be reducing [GAU/BLA2006]. Under such conditions, $FeSe_2$ is the dominating phase forming upon Se(IV) interaction with iron canister [CUI/PUR2009]. A recent report also concluded that selenide, with HSe^- as the main aqueous species, is the predominant thermodynamically stable chemical form of Se under the reducing conditions prevailing in Boom Clay environment [CAN/MAE2010]. Finally, the presence of microorganisms needs to be considered because Se(IV) oxyanions can be microbially reduced [HE/YAO2010]. Obviously, various reasons support the fact that Se is expected to be present as reduced species in the waste repository. Consequently, the geochemical behavior of reduced Se species, and especially selenide, needs to be investigated in detail.

The geochemistry of selenium is largely controlled by that of iron, with which Se is closely affiliated in both oxidizing and reducing environments [HOW1977]. Nanoparticulate stoichiometric mackinawite ($Fe_{1.00 \pm 0.01}S$) is the primary precipitate formed from the reaction between Fe(II) and S(-II) in aqueous solutions at ambient temperature and pressure [RIC/GRI2006]. It is a highly reactive phase having a high adsorption capacity and was used as substrate in adsorption experiments of various radionuclides (RN) in their higher oxidation state [HUA/DEN2008, KIR/FEL2011, LIU/TER2008, MOY/JON2002]. In almost all cases, a reduction of the oxidation state is associated with the retention of the RN. In contrast, only very scarce studies report trace contaminant sequestration by incorporation in the bulk structure. The coprecipitation of Tc(IV) with FeS was shown to form a TcS_2−like phase but the data could not confirm an incorporation in the bulk phase [WHA/ATK2000]. Since mackinawite is stable only under reducing conditions, substitution for elements in the bulk structure may only be (meta)stable for reduced monoatomic species. For example, the ionic radius [SHA1976] of selenide (r^{VI}Se(-II) = 1.98 Å) is only slightly larger than that of sulfide (r^{VI}S(-II) = 1.84 Å) so that it is very likely that Se(-II) can substitute S(-II) in mackinawite. Actually, it was suggested that FeS can contain a FeSe component, given that Se(-II) substitutes for S(-II) [MAS/DEL1991]. The existence of a solid solution phase is also comforted by the similarities in the FeS and FeSe structures: both can crystallize in tetragonal crystal systems and only the unit cell parameters differ slightly. Recently, the synthesis of FeS in the presence of Se(-II) was reported [DIE/NEU2011, DIE/NEU2012]. In these studies, the syntheses implied an aging time of 4 days, yielding crystalline FeS. However, this compound presumably converted [CSA/ROD2012] from freshly precipitated FeS (FeS_{fresh}) and thus could a have different reactivity towards dissolved species than FeS_{fresh}. Finally, no data on Se(-II) adsorption on mackinawite can be found in the literature.

Mackinawite is often used as precursor phase in the synthesis of pyrite (FeS_2). Pyrite is the most stable and ubiquitous authigenic ferrous sulfide in Earth-surface reducing environment and is present in backfill material (e. g., bentonite) in HLW disposal sites. Furthermore, the structure of pyrite can accommodate various trace elements in its structure such Co, Ni or Cu substituting for Fe but also Se or As substituting for S (e. g., [MOR/LUT1999]). In this study we focused on the Se(-II) retention (adsorption and coprecipitation) by mackinawite.

The selenide retention upon coprecipitation with and adsorption on freshly precipitated mackinawite was investigated. The solid phases obtained in every experiment were first characterized by X−ray diffraction (XRD) and by scanning electron microscopy

(SEM). Information on the Se speciation and on its local chemical environment is obtained by X−ray absorption spectroscopy (XAS).

5.5.1.2 Experimental part

Samples preparation and characterization

All samples were prepared with deoxygenated ultra−pure water (Milli−Q system, 18.2 MΩ·cm) and reagents of ACS grade or higher. All experiments were conducted under anoxic conditions (glove−box filled with Ar). The samples were kept under Ar from the beginning of the synthesis until the end of the characterization (XRD, XAS), except for SEM where the samples were transferred in a closed vessel filled with Ar to reduce the exposure time to air. The selenide solution was prepared as described in [LIU/FAT2008]. After preparation in the fume cupboard, the solution was introduced in the glove−box. Solutions of S(-II) and Fe(II) were freshly prepared before every experiment by dissolving $Na_2S\cdot 9H_2O$ and Mohr's salt $[Fe(NH_4)_2(SO_4)_2\cdot 6H_2O]$, respectively.

Mackinawite (sample Mack) was prepared by mixing equimolar Fe(II) and S(-II) solutions (Tab. 5.16). In the coprecipitation experiment (sample SeCopMack), a sulfide solution was added to the selenide solution before addition of the Fe(II) solution under stirring. In the adsorption experiment (sample SeAdsMack), FeS was freshly precipitated, filtered and washed before addition to the selenide solution (m/V = 2 g/L). Separately, a Fe(II) solution was added to a selenide solution (sample FeSelenide) and used as reference compound. All suspensions were filtered (0.45 µm pore size diameter) before analysis of the solid phases.

Tab. 5.16 Experimental conditions (pH and E_h) and initial and final element concentrations (subscript i and f, respectively)

Sample	**pH**	**E_h mV *vs* S.H.E.**	**$[Fe]_i$ mol/L**	**$[S]_i$ mol/L**	**$[Se]_i$ µmol/L**	**$[Fe]_f$ mmol/L**	**$[Se]_f$ µmol/L**
Mack	7.11(5)	-240(20)	2.0(1) $\times 10^{-1}$	2.1(1) $\times 10^{-1}$	/	n.d.	/
SeCopMack	6.95(5)	-210(20)	10(1) $\times 10^{-3}$	11(1) $\times 10^{-3}$	200(5)	0.47(1)	9.7(1)
SeAdsMack	6.89(5)	-250(20)	/	/	220(5)	1.3(1)	9.4(1)
FeSelenide	6.95(5)	-190(20)	2.4(2) $\times 10^{-4}$	/	220(5)	d.l.	6.3(1)

All solid phases were characterized by X-ray diffraction (XRD) prior to further analysis. Powder diffractograms were collected under anoxic conditions with an airtight sample holder with a D8 Advance (Bruker) diffractometer (Cu K_α radiation) equipped with an energy dispersive detector (Sol-X). The phases were identified with the EVA 2 software (Bruker) by comparison with the PDF 2 database and the data fit was performed with the TOPAS 4.2 software (Bruker). The samples were further characterized by scanning electron microscopy (SEM) with a CamScan CS44FE microscope. Electron micrographs gave information on the shape and the atomic concentrations were determined by energy-dispersive X-ray (EDX) spectroscopy.

X-ray absorption spectroscopy

Sulfur, iron and selenium *K-edges* X-ray absorption near-edge structure (XANES) and extended X-ray absorption fine structure (EXAFS) spectroscopy data were collected at the INE−Beamline [ROT/BUT2012] (ANKA, Germany) with a storage ring energy of 2.5 GeV and a ring current of 90 − 170 mA. Energy calibration was done by setting the white line crest of Na_2SO_4 at 2482.0 eV, the *K*−edge of a Fe foil (α−Fe, first inflection point) at 7112.0 eV and the *K*−edge of a Se foil (trigonal Se) at 12658.0 eV. At the Fe and Se *K-edges*, the reference foils were measured along with the samples and at the S *K*-edge the reference was measured before and after each sample. The data for the samples were collected in fluorescence-yield detection mode using a five elements LEGe solid state detector (Canberra-Eurisis) or a silicon drift detector (Vortex, SII NanoTechnology). Reference XAS data were collected in transmission mode for commercial powders of methionine ($C_5H_{11}NO_2S$), Na_2SO_3, Na_2SO_4, Mohr's salt, Fe_2O_3, FeSe, Na_2SeO_3 and Na_2SeO_4. Analysis of the data was performed following standard procedures by using Athena and Artemis interfaces to the Ifeffit software [RAV/NEW2005].

The EXAFS spectra (χ(k)) were extracted from the raw data and Fourier transforms (FT) were obtained from the k^2×χ(k) functions. Data fit was performed in R-space using phase and amplitude functions calculated with feff8.4 [ANK/RAV1998]. The amplitude reduction factor (S_0^2) was set to 0.67 for the S *K*-edge data to correctly reproduce the number of S neighboring O atoms in Na_2SO_4 [HAW/FER1975], 0.66 for the Fe *K*-edge data to correctly model the data collected for α−Fe [HUL1917], and 0.98 for the Se *K*-edge data to correctly reproduce the number of Se atoms in the trigonal Se phase [CHE/UNG1967]. For a given sample, the fits were performed simultaneously for all probed elements and the interatomic distance for a given atomic pair was fit considering simultaneously the data from both probed atoms. The uncertainties on EXAFS distances are typically ± 0.02 Å for well−resolved atomic shells and ± 20 % on the number of neighboring atoms.

5.5.1.3 Results and discussion

Reference phases

The samples Mack, FeSelenide and FeSe were characterized and used as reference phases. Mack can be identified as tetragonal mackinawite from its diffractogram (**Fig. 5.58**). The modeling of the powder diffractogram of the FeSe reference indicates the presence of both tetragonal (~75 %) and hexagonal (~25 %) phases. FeSelenide could not be characterized by XRD because of the absence of diffraction peaks. SEM micrographs (**Fig. 5.59**) reveal no significant difference in the morphology between Mack and FeSelenide: both have small sizes and exhibit a layered structure. They are composed of aggregates consisting of subparticles of sizes ranging from ~50 to ~400 nm. Based on SEM−EDX analyses, Mack contains a slight excess of sulfur (molar ratio Fe:S = 1.0:1.1) and FeSelenide obviously contains an excess of selenium (molar ratio Fe:Se = 1.0:3.6), very likely as elemental Se which is not detected by XRD.

In XAS, the XANES region of the probed element can be used as a fingerprint, being dependent upon both the valence state and the coordination environment. For S and Se, the position of the edge is shifted toward higher energy with increasing oxidation state and the white line intensity increases [KEO/MUL2004, PIC/BRO1995] (**Fig. 5.60**). The S white line position of Mack (2470.2(1) eV (thereafter the number in parentheses indicates the uncertainty)) is located at 11.9 eV lower energy than for sulfate. This energy span from the sulfate group to Mack correlates with a -II oxidation state of S in

FeS. In FeSe, the position of the Se *K*-edge (12657.2(1) eV) is also indicative of Se(-II) compared to Se(0) (12658.0 eV). For iron, the position of the pre-edge (1*s*→3*d*/4*p* transition) is commonly used to determine the Fe oxidation state [WIL/FAR2001]. Compared to the pre−edge feature in Mohr's salt (7111.4(1) eV) and in hematite (7112.9(1) eV), Fe has a +II oxidation state in all samples, including FeSe (**Fig. 5.60**).

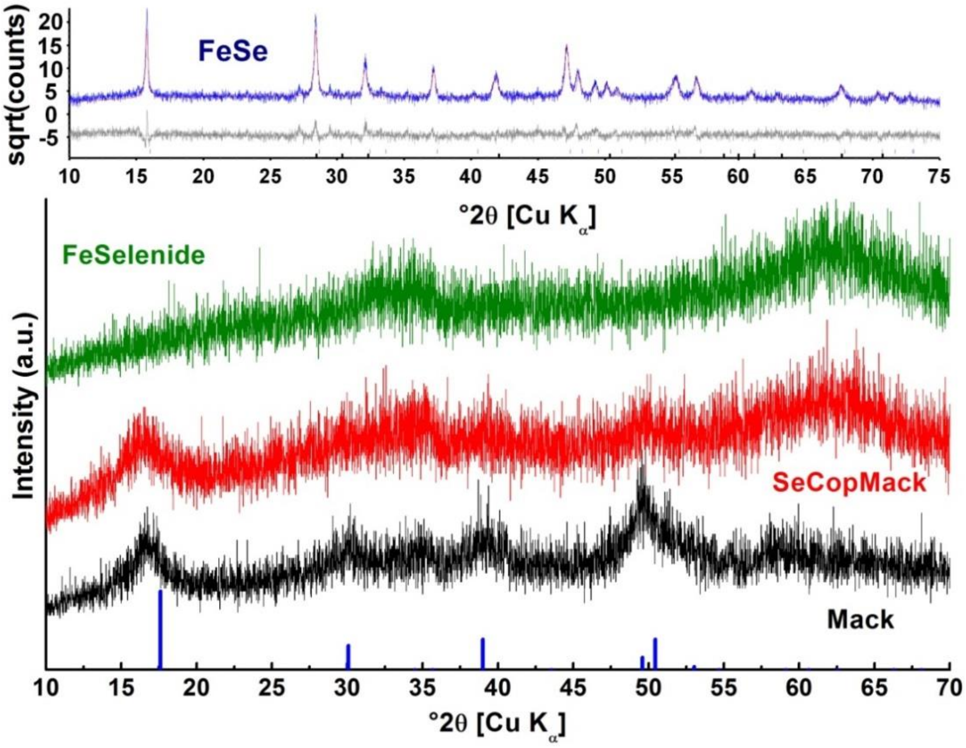

Fig. 5.58 X−ray diffractogram of the samples Mack, SeCopMack and FeSelenide
Mack is identified as tetragonal FeS by comparison with the JCPDS Card No 086-0389 (blue bars on plot)

Information on the crystallo-chemical environment is obtained from the EXAFS data modeling. The data of Mack are modeled considering only Fe and S backscatterers (**Tab. 5.17**, **Fig. 5.61**). The S and Fe *K*-edge data are fit simultaneously considering common interatomic distances *d*(Fe-S)) of 2.23(1), 4.08(4) and 4.29(3) Å, matching reported crystallographic values [LEN/RED1995]. At the Fe *K*-edge, Fe neighbors are also detected at *d*(Fe−Fe) = 2.60(1) and 3.68(1) Å, both belonging to FeS. Another Fe shell is detected at 3.16(1) Å, a distance reported for monoclinic pyrrhotite [TOK/NIS1972]. At the S *K*-edge, the S neighbors at *d*(S−S) = 3.66(4) Å match reported data for mackinawite, whereas the shells at 2.18(2) and 2.76(4) Å may best be explained by amorphous S(0). The coordination numbers for the Fe *K*-edge data are lower than the reported crystallographic values, whereas they are closer to what would be expected for the S *K*-edge data. The best explanation to account for that result is the presence of a mixture of two end-member phases having different long−range ordering [WOL/GAA2003]. The EXAFS oscillatory amplitudes are damped because of destructive interferences of oscillations having small differences in their frequencies due to variation in the bond distances.

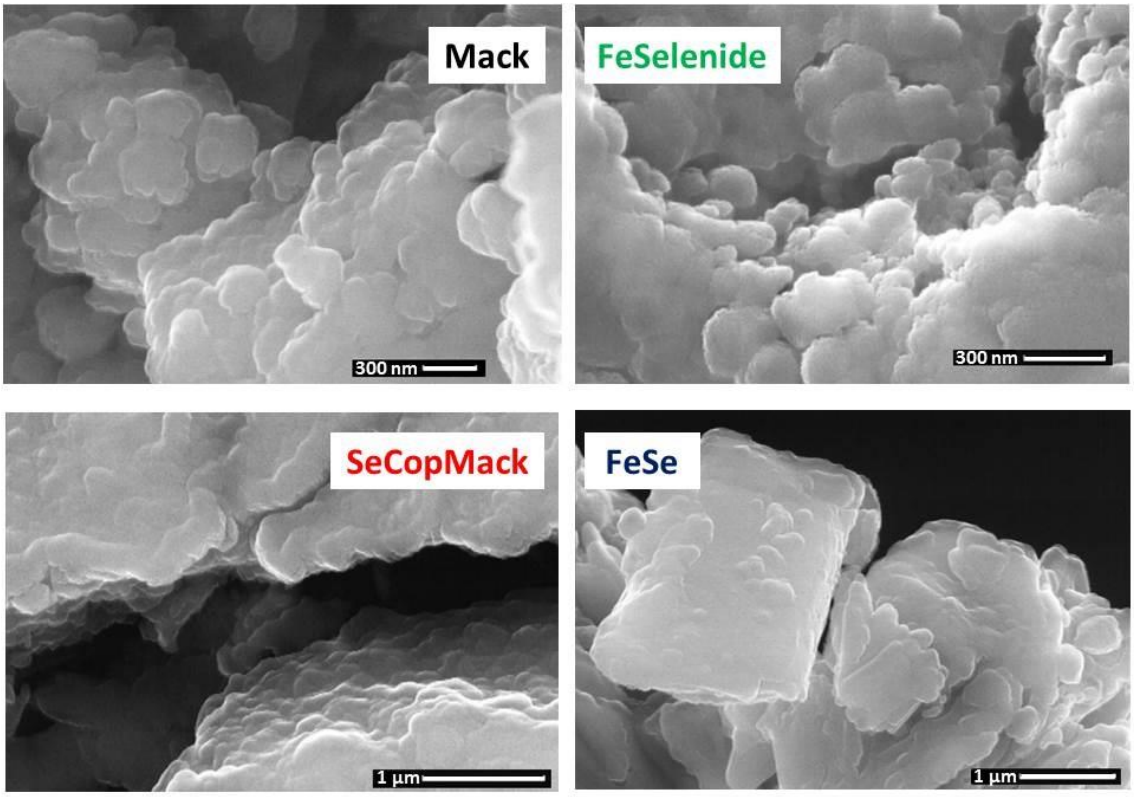

Fig. 5.59 SEM micrographs of Mack, FeSelenide, commercial SeCopMack and FeSe

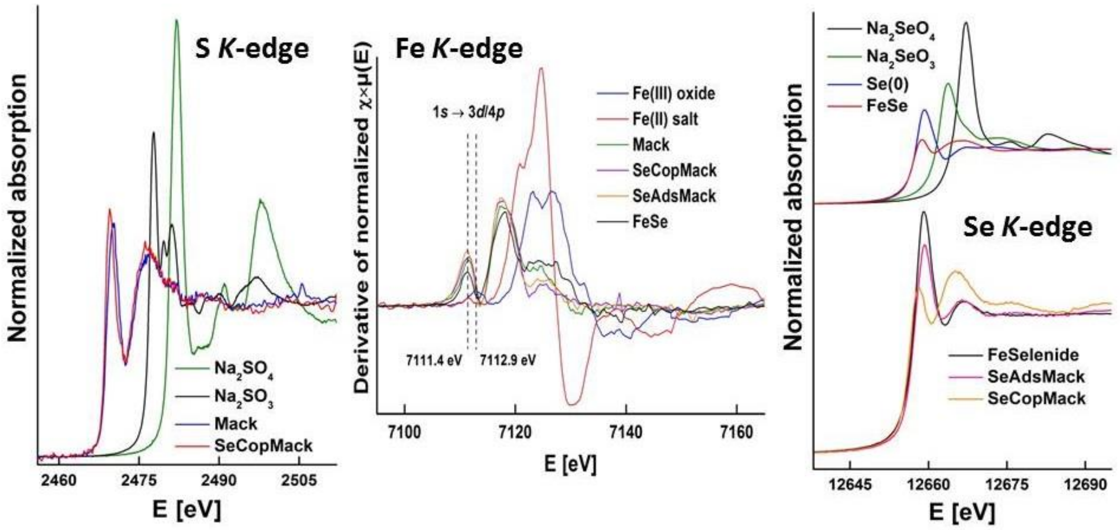

Fig. 5.60 XANES region of the S *K*-edge, Fe *K*-edge and Se *K*-edge data

Tab. 5.17 Quantitative EXAFS analysis of the reference samples (S_0^2 = 0.67 / 0.66 / 0.98 for the S / Fe / Se *K*−edge, respectively)

Mack							
S K-edge				***Fe K-edge***			
Shell	N	R [Å]	σ^2 [Å^2]	Shell	N	R [Å]	σ^2 [Å^2]
S	3.0[1]	2.18(2)	0.004	S	1.8[1]	2.23(1)	0.005
Fe	7.6[1]	2.23(1)	0.005	Fe	0.7[1]	2.60(1)	0.006
S	2.0[1]	2.76(4)	0.004	Fe	0.8[1]	3.16(1)	0.006
S	6.0(2.2)	3.66(4)	0.005	Fe	0.8[1]	3.68(1)	0.006
Fe	4.8[1]	4.08(4)	0.007	S	0.4(2)	4.08(4)	0.007
Fe	0.8[1]	4.29(3)	0.007	S	1.0[1]	4.29(3)	0.007
FeSe (Se *K*-edge)				**FeSelenide (Se *K*-edge)**			
Shell	N	R [Å]	σ^2 [Å^2]	Shell	N	R [Å]	σ^2 [Å^2]
Fe	1.5(1)	2.39(1)	0.003	Se	0.5[1]	2.32(1)	0.002
Se	0.2(1)	2.77(3)	0.003	Fe	0.9(2)	2.39[1]	0.002
Se	0.3(3)	3.54(6)	0.004	Se	0.2[1]	2.75(3)	0.005
Se	1.9(9)	3.72(4)	0.008	Se	0.3(2)	3.73[1]	0.002
Se	1.6(8)	3.96(2)	0.007	Se	0.2[1]	3.88(5)	0.002
Fe	1.9(4)	4.52(4)	0.007	Se	0.2[1]	3.96[1]	0.002
Fe	1.2[1]	4.71(9)	0.007	Fe	0.2(2)	4.34(9)	0.004

[1] Held fix during the fitting procedure

The EXAFS data collected at the Se *K*-edge for FeSe are adequately modeled considering only Fe and Se neighboring shells (**Tab. 5.17**, **Fig. 5.61**). Fe backscatterers are detected at 2.39(1) and 4.52(4) Å and Se neighbors at 3.72(4) and 3.96(2) Å: these shells are attributed to backscatterers from the tetragonal phase [HAE/KIN1933]. The other detected shells are assigned to hexagonal [ALS1925] FeSe (Se neighbor at 3.54(6) Å and Fe atoms at 4.71(9) Å) and possibly Se(0) (0.2(1) atom at 2.77(3) Å). The detection of backscatterers from both polymorphs agrees with the XRD characterization of FeSe.

The fit results of the FeSelenide Se *K*-edge data (**Tab. 5.17**, **Fig. 5.61**) indicate the presence of Fe neighbors at 2.39(2) and possibly at 4.34(9) Å, and Se backscatterers at 3.54(6), 3.72(4) and 3.96(2) Å. This result agrees with reported data for tetragonal FeSe [ALS1925]. Additional Se shells are detected at 2.32(1) Å, which is typical of monoclinic Se_8 [CHE/UNG1972], and at 2.75(3) Å which is also detected in FeSe. The presence of amorphous Se(0) in FeSelenide corroborates the excess selenium detected by SEM−EDX. The overall low coordination numbers are attributed to the small particle sizes: atoms located at the surface have less neighboring shells compared to atoms from the bulk solid [CAL/MIL2003].

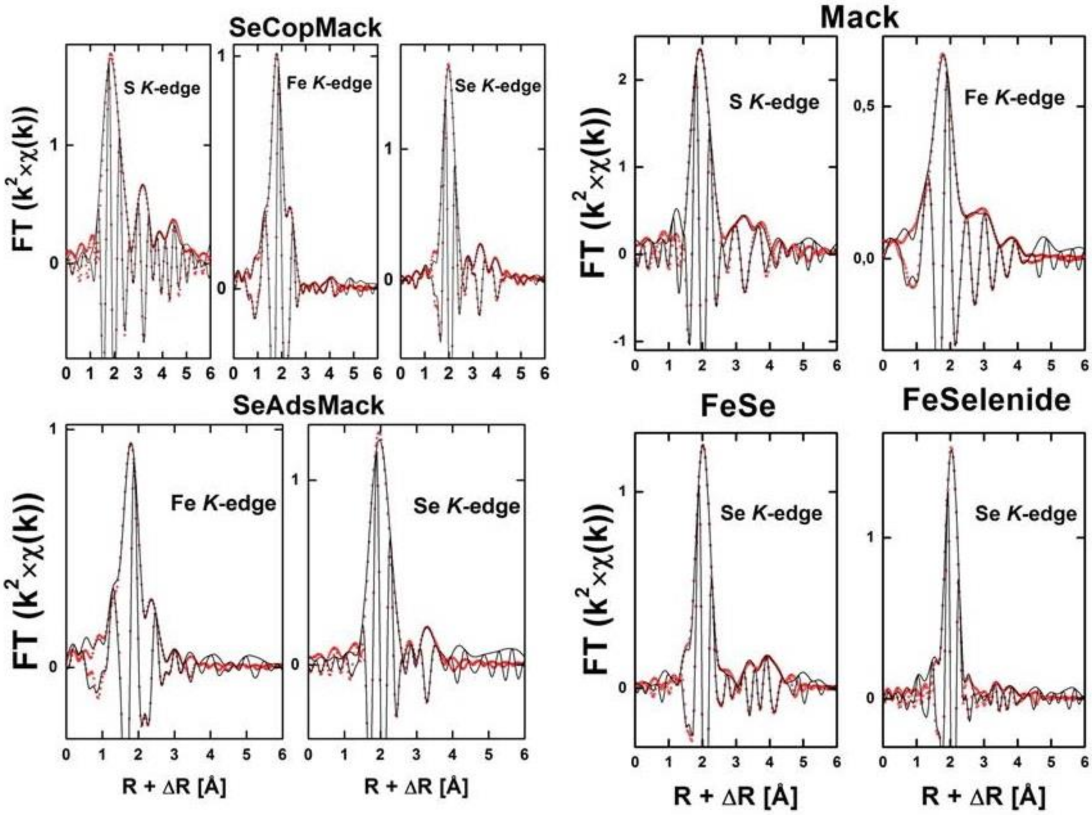

Fig. 5.61 Modelled (open symbols) and experimental (line) EXAFS data of the reference compounds (right) and of the coprecipitation and adsorption samples (left)

Selenide coprecipitation with mackinawite

SeCopMack was precipitated under almost identical pH and E_h conditions as Mack and FeSelenide (**Tab. 5.16**). Even though the diffraction peak corresponding to the (001) plane (~17.5° 2θ) is similar to that in Mack (**Fig. 5.58**), the structure of the sample cannot be identified by XRD. Yet, SEM micrographs suggest a layered structure consisting in aggregates of smaller particles (**Fig. 5.59**). This layered structure and particle aggregation is very similar to that of Mack, pointing to similarities in the structure. The SEM-EDX analysis gives molar ratios of Fe:S:Se = 0.99:1.00:0.01 and no presence of local high Se content can be detected. Consequently, selenium is present in trace levels and dispersed within the sample.

XAS data were collected at the S, Fe and Se *K*-edges for SeCopMack. In the XANES region (**Fig. 5.60**), the position and features of the S white line and the position of the Fe pre-edge are very similar to that in Mack. Thus S and Fe have identical oxidation state in both samples and very close electronic environment. The Se *K*−edge is located at slightly lower energy in SeCopMack (12656.6(1) eV) than in FeSe (12657.2(1) eV), unambiguously pointing to a Se(-II) species (**Fig. 5.60**). These XANES results show that all elements constitutive of the sample are in their lowest oxidation state (including selenium) and that no detectable oxidation occurred from the sample preparation up to the XAS measurements.

The EXAFS data collected at all three edges are modeled simultaneously (**Tab. 5.18**, **Fig. 5.61**). At the S and Fe *K*−edges, *d*(Fe−S) = 2.21(1) Å, *d*(S−S) = 3.70(6) and 4.21(2) Å, as well as *d*(Fe−Fe) = 2.60(1) and 4.37(2) Å are close to values obtained in Mack and match reported crystallographic data of mackinawite [LEN/RED1995]. Consequently, the bulk structure consists in tetragonal FeS. Additional S backscatterers are needed to correctly model the experimental data, suggesting the possible presence of amorphous S(0). At the Fe and Se *K*−edges, *d*(Fe−Se) = 2.37(1) Å is needed to model the data. The increase in interatomic distance from *d*(Fe−S) = 2.21(1) Å to *d*(Fe−Se) = 2.37(1) Å is within uncertainty identical to the increase in ionic size [SHA1976] from sulfide (1.84 Å) to selenide (1.98 Å). Furthermore, no Se is detected in the selenium first coordination sphere ruling out the presence of Se(0) but corroborating dispersion within the matrix. Consequently, Se can only be located in a Fe−bearing phase, either FeS and/or FeSe. At the S and Se *K*−edges, *d*(S−Se) = 3.82(2) Å is used to correctly model the data. Here again the increase in interatomic distance from *d*(S−S) = 3.70(6) Å to *d*(S−Se) = 3.82(2) Å is remarkably close to the increase in ionic size from S(-II) to Se(-II). Note that no higher distance Se backscatterer was needed to model the data at the Fe and Se *K*−edges, ruling out the presence of iron selenide by comparison with FeSe. These EXAFS data indicate a bulk mackinawite structure in SeCopMack and both interatomic distances *d*(Fe−Se) = 2.37(1) Å and *d*(S−Se) = 3.82(2) Å can only be explained by a random structural Se substitution for S in the mackinawite structure, indicating a possible structural incorporation of selenide in the host FeS structure upon coprecipitation. The present results provide experimental evidence that precipitated FeS can contain a FeSe component and that the fraction of the latter component is very low in the Fe(S,Se) solid solution.

Tab. 5.18 Quantitative EXAFS analysis of the coprecipitation (SeCopMack) and adsorption (SeAdsMack) samples. Z indicates the neighboring shell

SeCopMack											
S *K*−edge				**Fe *K*−edge**				**Se *K*−edge**			
Z	N	R [Å]	σ^2 [$Å^2$]	**Z**	N	R [Å]	σ^2 [$Å^2$]	**Z**	N	R [Å]	σ^2 [$Å^2$]
Fe	3.8(4)	2.21(1)	0.005	S	1.8(1)	2.21(1)	0.004	Fe	3.3(1)	2.37(1)	0.004
S	2.3(1.0)	2.85(4)	0.005	Se	0.4(1)	2.37(1)	0.004	Fe	0.5(3)	3.44(5)	0.005
S	1.9(1.3)	3.16(6)	0.005	Fe	1.0(2)	2.60(1)	0.005	S	4.1(8)	3.82(2)	0.005
S	2.8(1.6)	3.70(6)	0.005	S	1.0^1	2.85(2)	0.005	S	3.7(1.0)	4.07(3)	0.008
Se	4.81	3.82(2)	0.005	S	0.3(2)	3.98(8)	0.005				
Se	5.51	4.48(3)	0.005	S	0.8(3)	4.371	0.005				
Fe	1.5(2.7)	4.211	0.004								

SeAdsMack							
Fe *K*−edge				**Se *K*−edge**			
Z	N	R [Å]	σ^2 [$Å^2$]	**Z**	N	R [Å]	σ^2 [$Å^2$]
S	1.8(1)	2.22(2)	0.005	Se	1.3(3)	2.31(1)	0.004
Se	0.7^1	2.36(2)	0.005	Fe	0.8(3)	2.36(2)	0.004
Fe	1.0^1	2.62^1	0.005	S	0.6^1	2.94(4)	0.005
S	0.6(2)	2.89(3)	0.006	Fe	0.3^1	3.36^1	0.006
S	0.2(2)	3.36(7)	0.005	S	1.4^1	3.78(4)	0.004
S	0.2^1	4.00(12)	0.005	S	0.4(8)	3.97(16)	0.005

However, no conclusion on (thermodynamic) stability can be drawn from this study, but the very similar pH and E_h conditions in the Mack and SeCopMack syntheses (**Tab. 5.16**) point to a relative stability/solubility, at least similar to that of FeS. Furthermore, all elements constitutive of SeCopMack are in their lowest oxidation state so that no oxidation is expected to occur unless changing the environmental conditions. Consequently, the formation of such phases in the far field of a HLW repository site represents a very effective retention mechanism.

Selenide adsorption on mackinawite

Selenide was adsorbed on mackinawite (sample SeAdsMack) under conditions almost identical to that in the SeCopMack and FeSelenide precipitation resulting in very similar low final Se concentrations remaining in solution (**Tab. 5.16**). Consequently, similar solid phases can be expected to be present at equilibrium. XAS data were collected at the Fe *K*−edge to gain information on the substrate and at the Se *K*−edge to determine the selenium oxidation state and to probe its local chemical environment. In the Fe XANES region (**Fig. 5.60**), the pre−edge position indicates the presence of Fe(II), and thus excludes the (compelling) oxidation of mackinawite. Additionally, the Se white line position (**Fig. 5.60**) is located at an energy (12657.5(1) eV) between that of Se(0) (12658.0(1) eV) and FeSe (12657.2(1) eV) pointing to the presence of more than one Se species in SeAdsMack. These results indicate that the substrate undergoes no substantial change in the structure compared to the adsorbate for which some change in the oxidation state may have occurred.

The Fe *K*−edge EXAFS data indicate the presence of S (*d*(Fe−S) = 2.22(2) Å) and Fe (*d*(Fe−Fe) = 2.62(2) Å) shells surrounding Fe at distances typical of mackinawite and identical to that in SeCopMack (**Tab. 5.18**, **Fig. 5.61**). Thus, the bulk structure very likely remains FeS. Fit to the Fe and Se *K*−edges EXAFS data are conducted simultaneously by considering an interatomic distance of *d*(Fe−Se) = 2.36(2) Å. Additional S (*d*(Se−S) = 3.78(4) and 3.97(16) Å) and Fe (*d*(Se−Fe) = 3.36(2) Å) shells are detected at distances similar to that in SeCopMack. Consequently, at least part of Se is located in a FeS−like sulfide environment.

At the Se *K*−edge, selenium (1.3(3) atom at 2.31(1) Å) is also detected in the first coordination sphere. This interatomic distance is also found in FeSelenide and is typical of monoclinic Se_8 [CHE/UNG1972]. Additionally, sulfur (0.6 atom) is detected at *d*(Se−S) = 2.94(4) Å in SeAdsMack but not in SeCopMack. This shell can be attributed to the substrate where Se(0) binds the surface since this bond length is very close to the sum of the atomic radii of S(-II) (1.84 Å) and Se(0) of the monoclinic phase (2.32/2 = 1.16 Å). The simultaneous presence of two Se species corroborates the XANES data. Finally, at the Fe *K*−edge S backscatterers are detected at *d*(Fe−S) = 2.89(3), 3.36(7)

Å and possibly at 4.00(12) Å. The physical origin of these shells is unclear, but they can best be explained by the presence of S(0) at the surface of FeS.

S and Fe are in their lowest oxidation state in SeAdsMack. Consequently, the oxidation of Se(-II) suggested from the XANES data cannot be explained by an adsorption and concomitant reduction of elements constitutive of the substrate such as reported for pyrite [LIU/FAT2008] because S and Fe are already in their lowest oxidation state. Selenide is known to be extremely reactive towards atmospheric oxygen [NUT/ALL1984]. For example, solutions of concentration greater than 10^{-6} mol/L exposed to atmospheric levels of oxygen oxidize within minutes in colloidal Se(0). A possible explanation to the presence of Se(0) may be a partial oxidation of Se(-II) by residual traces of oxygen during the transfer from the preparation setup in the fume cupboard to the glove box. The same explanation may also possibly account for Se(0) present in FeSelenide.

The removal of Se(-II) from the solution can occur via different mechanisms. First, Se(- II) very likely adsorbs on FeS in SeAdsMack because of the positively charged surface [WOL/CHA2005]. Second, selenide and sulfide form very low soluble solids in the presence of low concentrations of Fe(II) (e. g., FeSe, FeS) and thus an iron selenide phase can have precipitated. Consequently both retention mechanisms (surface adsorption and precipitation) have to be considered. However, EXAFS data point to part of Se located in an environment very similar to that in SeCopMack being very likely entrapped in a solid phase rather than surface adsorbed. To account for that result, the first hypothesis is that the experimental conditions were similar to that in the precipitation of SeCopMack, i. e., dissolved S(-II) and Fe(II) were present in solution with Se(-II). Yet, the XAS data point to a FeS-like structure, suggesting that selenium was present as minor species compared to S and Fe. The second hypothesis to account for the result is that Se(-II) reacted with the pre-existing FeS and the resulting system evolved dynamically, through dissolution and re-precipitation, to form a compound similar to SeCopMack. In a suspension containing mackinawite, aqueous $FeS_{(aq)}$ cluster complexes form fast [WOL/CHA2005, RIC2006] (cluster ≤ 5 nm in size) and these clusters are more reactive than the bulk solid phase. Furthermore, these clusters are in equilibrium with Fe^{2+} (and HS^{-}) as demonstrated by voltammetry [RIC2006]. Consequently, the reaction of Se(-II) with FeS in suspension appears to be a rather complex system, where selenide can react with various dissolved species and with the solid mackinawite phase. This corresponds at least partly to the initial experimental conditions of the synthesis of SeCopMack. It is thus reasonable to assume that part of Se(-

II) was taken up during the re−precipitation of the dissolved constituents of FeS, and that part reacted with FeS as bulk solid. In that latter case, Se(-II) came in contact with FeS followed by a concomitant dissolution/precipitation reaction at the surface of mackinawite. This can be seen as a reorganization of the surface or as an overgrowth from the dissolved cluster complexes, leading to the release of sulfide being exchanged for selenide according to: $FeS + x\ Se^{2-} = FeSe_xS_{(1-x)} + x\ S^{2-}$. This investigation does not allow to differentiate between the possible mechanism(s) that account for the observed results. Nevertheless, the present study is the first to report experimental evidence on the formation of a selenide−containing iron monosulfide compound upon Se(-II) adsorption on FeS and which may undoubtly exist in nature.

5.5.1.4 Conclusion

In a nuclear wastes disposal site, sulfur and selenium may also occur as S(0) and Se(0) and have some influence on the stability of the various mineral phases in presence such as iron sulfide and iron selenide. Over time, iron monosulfides oxidize to pyrite [BER1970] in the presence of elemental sulfur ($FeS + 2\ S(0) \rightarrow FeS_2$) and convert to achavalite [HOW1977] in the presence of elemental selenium ($FeS + Se(0) \rightarrow FeSe + S(0)$). Furthermore, by analogy with the FeS oxidation to pyrite, it is very likely that iron monoselenide reacts with S(0) to form FeSeS ($FeSe + S(0) = FeSeS$), although the existence of such a compound has not been proven yet . Another mineral to consider under near−neutral to alkaline conditions is ferroselite ($FeSe_2$), the stable compound of iron and selenium occurring in deposits where iron sulfides have very high selenium content [HOW1977]. In the presence of an excess S(0), ferroselite is unstable with respect to pyrite and the released Se(0) is very likely incorporated in pyrite. Overall, this shows the close affiliation of the S, Fe and Se geochemistry and the complexity of this system.

Finally, both interaction mechanisms (interaction with pre−existing substrate and co-precipitation) with FeS represent an effective retention potential for selenide by forming a (meta)stable solid solution. This study does not exactly reflect the expected conditions of a nuclear waste repository, but provide important results that have implications with regard to the final disposal in deep geological repositories. The data show that Se will certainly be retained in the multi−barrier system and thus reduce the need for conservatism assumption in the safety case.

5.5.2 Selenium(IV) in calcite

Our work on selenium(IV) interactions with calcite, which has been performed in the frame of the VESPA project, has recently been accepted for publication in Geochimica et Cosmochimica Acta. Therefore, the report presented here is largely taken from this publication.

5.5.2.1 Introduction

Calcite is the most common polymorph of calcium carbonate and the thermodynamically most stable at standard conditions (room temperature and atmospheric pressure). It is abundant in many environmental settings and plays a key role in controlling the geochemical milieu (pH, alkalinity) of soils and ground water. In the surroundings of potential nuclear waste disposal sites calcite may be present, for example, as a mineral constituent in clay formations (up to 20 % in some cases), as a fracture filling material in granitic rocks, or as a corrosion product of concrete based materials in the technical barrier. Due to the high reactivity of its surface and its tendency to tolerate considerable variation in its chemical composition, calcite has often been considered as a mineral phase with considerable potential for the sequestration of toxic metals. Many studies have investigated the adsorption and incorporation of environmentally relevant elements onto/into calcite [BLA/BAE1992, CAR/BRU1992, ELZ/ROU2006, HEB/DEN2008, REE/NUG2000, ROU/ELZ2005, TES/PAN1996, ZHO/MUC1995]. Wang and Liu [WAN/LIU2005] were able to show that calcite has a significant impact on the mobility of selenium in soils.

Cowan *et al.* [COW/ZAC1990] published a systematic investigation of selenite adsorption on calcite. They found decreasing adsorption with increasing pH in the range from 7 to 9. Competing anionic ligands (SO_4^{2-}, PO_4^{3-}) cause decreased selenite adsorption, while Mg^{2+} has no significant influence on selenite adsorption. They proposed a thermodynamic model for selenite adsorption on calcite based on surface ion-exchange reactions. The surface ion-exchange mechanism for selenite sorption at calcite has been confirmed by X-ray standing wave measurements by Cheng *et al.* [CHE/LYM1997]. They found after 24 hours of adsorption, starting from undersaturated conditions, selenite incorporated into the surface monolayer of a calcite single crystal.

Recent studies have shown that upon coprecipitation with calcite from highly supersaturated solutions (0.5 mol/L Ca^{2+} and CO_3^{2-}) [AUR/FER2010] and at elevated temperatures and pressures (30 – 90 °C, 25 – 90 bar) [MON/SAR2011] selenite can be incorporated into calcite. EXAFS Se *K*-edge spectroscopy and neutron scattering experiments were used to characterize the structural environment of selenite in calcite and the influence of selenite incorporation on the calcite lattice. A density functional theory (DFT) based theoretical investigation of the structural environment of selenite in calcite was also presented. Based on these results the authors propose that selenite substitutes for carbonate in the calcite structure [AUR/FER2010]. Recently, Renard *et al.* [REN/MON2013] published an atomic force microscopy study, where they investigated the influence of selenium on calcite growth. Selenite is shown to influence the morphology of growth hillocks as well as the growth rates.

In the study presented here the structural incorporation of selenite into calcite is further investigated. Coprecipitation experiments at room temperature and surface controlled growth conditions are used to prepare selenite-doped calcite samples. The structural environment of selenite in calcite is characterized using on the one hand Se *K*-edge EXAFS spectroscopy measured on selenite-doped calcite powder, and on the other hand polarization dependent Se *K*-edge EXAFS measured on a selenite-doped calcite single crystal. Selenite incorporation into calcite is quantified at various selenite concentrations (10^{-13} M to 10^{-4} M) at surface controlled growth conditions for a range of calcite supersaturations (SI[4](calcite): 0.14 – 0.9). The experimental results are compared to DFT-based theoretical investigations of selenite incorporation into bulk calcite and into the calcite (104) surface. The statistical-thermodynamic properties are modeled here with a modified version of the recently introduced Single Defect Method, SDM [SLU/KAW2002, VIN/BRA2013]. The present version of the SDM is specially adapted for the thermodynamic description of a non-isostructural solid solution.

Besides the structural characterization of the selenite incorporation species in calcite, the main focus of this study is quantification and modeling of selenite incorporation into calcite at equilibrium and steady state experimental conditions. The model presented as a result of this study provides a framework to predict quantitatively at which conditions calcite supersaturation is sufficiently high to enable entrapment and coprecipitation of a certain amount of selenite with calcite, and at which conditions coprecipitation

---

[4] Saturation index, e. g. SI(calcite) = $\log_{10}(a(Ca^{2+})\cdot a(CO_3^{2-}) / K_{SP}(calcite))$.

is not possible and calcite growth is inhibited. To serve simplistic modelling approaches as envisaged in performance assessment calculations, the data and model presented here can be used to calculate a conditional K_D value for selenite adsorption at calcite.

5.5.2.2 Equilibrium states between aqueous- and solid solutions and consequences for SeO_3^{2-} incorporation into calcite

To describe the affinity of a foreign ion for incorporation into a mineral phase the empirical Henderson-Kracek partition coefficient [HEN/KRA1928], *D*, is often used. It relates the composition of the solid to the composition of the aqueous solution. The composition of the solid is described by the mole fractions, X_i, of the endmember chemical components. To describe the composition of the aqueous solution the ion concentration product (ICP) of the two endmembers is used. Selenite incorporation into calcite can be described with the aid of the host (calcite, $CaCO_3$) and the solute ($CaSeO_3$) endmembers, such that X(calcite) + $X(CaSeO_3) = 1$. The corresponding ICPs are:

$$\mathrm{ICP(CaSeO_3)} = c(\mathrm{Ca^{2+}}) \cdot c(\mathrm{SeO_3^{2-}}) \quad (5.17)$$

$$\mathrm{ICP(calcite)} = c(\mathrm{Ca^{2+}}) \cdot c(\mathrm{CO_3^{2-}}) \quad (5.18)$$

where c_i are the concentrations of the ions in solution. The partition coefficient, *D*, is given by:

$$D = \mathrm{X(CaSeO_3)/X(calcite) \cdot ICP(calcite) / ICP(CaSeO_3)} \quad (5.19)$$

At equilibrium conditions, the partition coefficient can be related to thermodynamic properties of the endmembers [GLY2000, SHT/PUN2006]. Equilibrium states between aqueous and solid solution are defined through the ion activity products (IAP) of the endmember constituents:

$$\mathrm{IAP(CaSeO_3)} = a(\mathrm{Ca^{2+}})\, a(\mathrm{SeO_3^{2-}}) \quad (5.20)$$

$$\mathrm{IAP(calcite)} = a(\mathrm{Ca^{2+}})\, a(\mathrm{CO_3^{2-}}) \quad (5.21)$$

where a_i are the activities of the ions in solution. γ_i are the corresponding products of all relevant aqueous solution activity coefficients. In such a system the IAPs would be linked to the solubility products (K_{SP}) of the endmember phases by:

$$\mathrm{IAP(CaSeO_3) = K_{SP}(CaSeO_3)\ X(CaSeO_3)\ f(CaSeO_3} \tag{5.22}$$

$$\mathrm{IAP(calcite) = K_{SP}(calcite)\ X(calcite)\ f(calcite)} \tag{5.23}$$

with the solid solution activity coefficients, f_i.

Combining equations (5.20) to (5.23) with equation (5.19), the partition coefficient, *D*, can be directly related to the solubility products of the endmember phases:

$$D = \frac{\mathrm{K_{SP}(calcite) f(calcite)}\ \gamma\ \mathrm{(CaSeO_3)}}{\mathrm{K_{SP}(CaSeO_3) f(CaSeO_3)}\ \gamma\ \mathrm{(calcite)}} \tag{5.24}$$

For binary solid solutions that do not involve coupled substitution mechanisms, as in the case considered here, charges of the ions involved in the substitution mechanism are equal. Furthermore, at low ionic strength no ion specific aqueous activity coefficients need to be considered. Therefore, $\gamma(\mathrm{CaSeO_3}) = \gamma(\mathrm{calcite})$ and equation (5.24) simplifies to:

$$D = \frac{\mathrm{K_{SP}(calcite) f(calcite)}}{\mathrm{K_{SP}(CaSeO_3) f(CaSeO_3)}} \tag{5.25}$$

Considering that concentrations of $CaSeO_3$ in the solid solution are relatively small (< 7 %) a further simplification is possible. At low concentrations of the solute phase Henry's law ($f(CaSeO_3)$ = constant; f(calcite) = 1) can be applied. As the solubility product of the $CaSeO_3$ endmember in the calcite structure and its activity coefficient are unknown, it is convenient to combine these two unknown variables by defining a hypothetical virtual $CaSeO_3$ endmember via the equation:

$$D = \frac{\mathrm{K_{SP}(calcite)}}{\mathrm{K_{SP}\left(CaSeO_{3\_virtual}\right)}} = \mathrm{const.} \tag{5.26}$$

This simplification is valid if the partition coefficient is constant over the range of solid solution compositions considered.

The Gibbs free energies of the endmember phases are related to their corresponding solubility products by:

$$G^0(CaSeO_{3\_virtual}) = RT\ \ln(K_{SP}(CaSeO_{3\_virtual})) + G(Ca^{2+}_{(aq)}) + G(SeO_3^{2-}{}_{(aq)}) \quad (5.27)$$

and:

$$G^0(calcite) = RT\ \ln(K_{SP}(calcite)) + G(Ca^{2+}_{(aq)}) + G(CO_3^{2-}{}_{(aq)}) \quad (5.28)$$

where G_i denotes the Gibbs free energies of formation (all relevant values used in this study are listed in **Tab. 5.21**), while R and T are the universal gas constant and the absolute temperature (= 298.15 K), respectively. Eqns. (5.26) to (5.28) can be used to relate the partition coefficient to the standard Gibbs free energies of $CaCO_3$ and $CaSeO_3$:

$$D = \exp[(G^0(calcite) – G^0(CaSeO_{3\ virtual}) - G^0(CO_3^{2-}{}_{(aq)}) + G^0(SeO_3^{2-}{}_{(aq)}))/(RT)] \quad (5.29)$$

The subscript “virtual” is used here to emphasize that the structure of this endmember cannot be crystallographically defined. The virtual endmember is a purely mathematical construction. Consequently, its solubility product cannot be directly measured. However, as we show below, the Gibbs free energy of the virtual endmember can be accurately computed by applying the single defect method.

Eqns. (5.22) to (5.29) are based on the condition of thermodynamic equilibrium. This implies that the aqueous solution is saturated with respect to the solid phase. However, the coprecipitation experiments used in this study to quantify the uptake of selenite by calcite were run at supersaturated steady state conditions. To be able to treat the steady state experiment within the equilibrium thermodynamic concept we assume that the supersaturated solution remains in true equilibrium with an infinitesimally thin layer of precipitated calcite. This assumption is consistent with the concept of Astilleros *et al.* [AST/PIN2003] that the aqueous solution is in thermodynamic equilibrium with an infinitely small precipitate, whose composition corresponds to the highest value of the supersaturation function. This thin layer of calcite is treated here as a phase, which is named hereafter the surface solid solution. The thermodynamic description of this phase requires definition and characterization of the standard thermodynamic properties of the surface endmember and the determination of its excess Gibbs free energy. The thermodynamic properties of the surface endmember differ from the properties of its bulk analogue due to the influence of surface tension and interfacial energy effects. Below we show that for the quantification of surface incorporation only the difference in the Gibbs free energies of the virtual surface endmembers is required and that this thermodynamic quantity can be computed both from experimental data and from first principles.

The concept developed here is similar to the model of surface enrichment and entrapment during calcite growth presented by Watson [WAT2004]. Here a value equivalent to Watson's surface enrichment factor is defined based on atomistic calculations and experimental data. However, our model avoids any kinetic variables and is fitted into the formalism of equilibrium thermodynamics. In essence, we assume that an apparent thermodynamic equilibrium exists between the aqueous solution and a thin surface layer of calcite. Layers that are entrapped under the surface layer are assumed to be out of equilibrium.

The Single Defect Method (SDM) for the "bulk" solid solution

The single defect method of Sluiter and Kawazoe (2002) [SLU/KAW2002] has recently been successfully applied to the modeling of isostructural solid solutions of barite and aragonite type crystal structures [VIN/BRA2013]. It has been shown that a dilute solid solution obeys the regular mixing model, while the slope of the enthalpy of mixing in an isostructural solid solution, measured at the trace composition limit, is equal to the Margules parameter. It has also been shown that the slope can be accurately predicted with the aid of first principles methods from the excess enthalpy of a supercell structure containing a single substitutional defect of the solute phase. Such a treatment is based on the assumption that the excess Gibbs free energy of a regular solid solution can be approximated by its excess enthalpy. The latter condition is particularly valid at low temperatures. In this section we develop a modified version of the SDM, which is specifically designed for non-isostructural solid solutions. Indeed, the solid solution between calcite and $CaSeO_3$ cannot exist in the calcite structure over the whole range of mole fractions. The existing stable phase of $CaSeO_3$ composition crystallizes in the space group $P2_1/n$ [WIL/GIE2007]. Thus the excess free energy of mixing of the non-isostructural solid solution should have an inflection at an intermediate composition due to the structural transformation. The thermodynamic modeling of mixing functions of such a solid solution over the whole composition range is a very complicated task. Fortunately, the modeling of the whole range of the compositions is not required as we are interested in the thermodynamic properties of the solid solution only in the vicinity of the composition of the host phase. This is consistent with the definition of the virtual endmember via eqn. (5.26), as a hypothetical phase, which forms an ideal solid solution with the host phase. The Gibbs free energy of this solid solution is defined to be indistinguishable from the free energy of the real solid solution in the Henry's law region.

The excess enthalpy of a solid solution in the dilute range can be modeled in an atomistic calculation as the excess enthalpy of a reasonably large supercell structure containing a single defect of the solute component. The excess enthalpy defines the slope of the excess mixing enthalpy relative to the mechanical mixture of calcite and the monoclinic $P2_1/n$ phase of $CaSeO_3$, here referred to as $CaSeO_3$ (monocl.). Consequently, the slope includes the excess enthalpy of a hypothetical isostructural solid solution with the calcite structure and the enthalpy of the structural transition in the endmember phase from the trigonal to the monoclinic structure. Conveniently, the latter two quantities do not have to be known separately. The slope to the excess enthalpy determined in the dilute limit and extrapolated to X=1 defines the excess enthalpy of the virtual endmember relative to the monoclinic phase.

Practically, the slope can be computed at the composition of $X = 1/n$, where n is the total number of anions (CO_3^{2-} and SeO_3^{2-}) in the supercell, which is equal to the number of calcium atoms. The excess enthalpy at the composition X can be computed with the equation;

$$\Delta H^E(1/n) = [H(Ca_n(CO_3)_{n-1}SeO_3) - (n-1)\ H(\text{calcite}) - H(CaSeO_3\ (\text{monocl.}))]/n \quad (5.30)$$

where H(calcite) and H($CaSeO_3$ (monocl.)) are the total enthalpies of calcite and $CaSeO_3$ (monocl.), respectively. A linear extrapolation of this difference from the mole fraction of $1/n$ to 1 is equivalent to multiplication of the excess value by n. Thus the excess enthalpy of the virtual $CaSeO_3$ (bulk) endmember relative to the enthalpy of the monoclinic phase can be calculated as:

$$\Delta H^E(1) = H(Ca_n(CO_3)_{n-1}SeO_3) - (n-1)\ H(\text{calcite}) - H(CaSeO_3\ (\text{monocl.})) \quad (5.31)$$

The last quantity is defined per one mole of $CaSeO_3$. If the excess vibrational free energy of the solid solution is small, this quantity is approximately equal to the excess Gibbs free energy of the virtual compound:

$$\Delta G^E = G(Ca_n(CO_3)_{n-1}SeO_3) - (n-1)\ G^0(\text{calcite}) - G^0(CaSeO_3\ (\text{monocl.})) \quad (5.32)$$

The evaluation of vibrational contributions to ΔG^E requires the calculation of the phonon density of states of the reference phases and of the supercell. The evaluation of these properties based on DFT is possible, but is computationally very demanding for the large supercells used to capture realistic defect concentrations. The vibrational density of states can be also computed with the aid of a force-field model. The results of such calculations, which are described in the Results section, show that the vibrational terms make only a small contribution to the excess Gibbs free energy under the conditions of interest. The dominant part of the ΔG^E is represented by the ΔH^E term. Thus in the following text the vibrational contributions will be ignored and the assumption of $\Delta G^E = \Delta H^E$ will always be made, except for the case of the bulk solid solution, for which the vibrational effects will be explicitly calculated via a force-field model.

The absolute standard Gibbs free energy of the virtual endmember can be computed by adding ΔG^E to the standard Gibbs free energy of the reference phase:

$$G^0(CaSeO_{3\ \mathrm{virtual}}) = G^0(CaSeO_3\ (\mathrm{monocl.})) + \Delta G^E \qquad (5.33)$$

The thermodynamic relation between the host phase (calcite), the virtual endmember ($CaSeO_3$ in calcite structure) and the reference phase ($CaSeO_3$ (monocl.)), and how the real solid solution fits into this picture is illustrated in **Fig. 5.62**.

The Single Defect Method for a "surface" solid solution

As we will show below, the Gibbs free energy of the virtual (bulk) $CaSeO_3$ estimated with the SDM appears to be so large that the bulk solid solution with the calcite structure cannot contain a measurable fraction of $CaSeO_3$. To be able to explain the rather high concentrations of SeO_3^{2-} in calcite, which are observed in mixed flow reactor (MFR) coprecipitation experiments, we develop here a more complex thermodynamic model, which assumes a significant enrichment of the $CaSeO_3$ in the surface layer of calcite and its continuous entrapment under stationary supersaturation conditions.

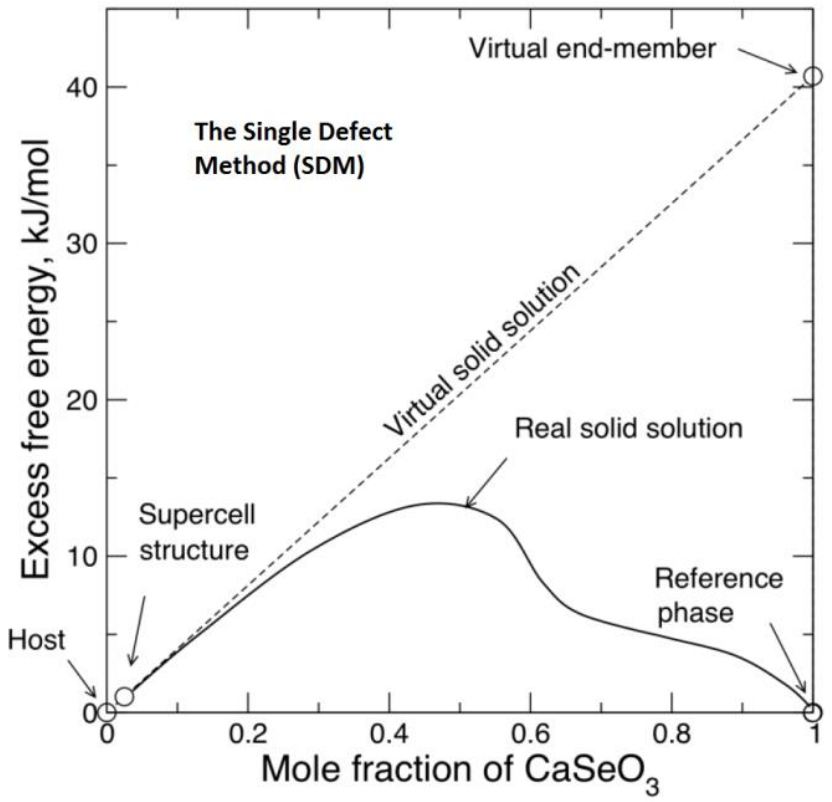

Fig. 5.62 The relation between the host phase calcite, the reference phase $CaSeO_3$ (monocl.) and the virtual $CaSeO_3$ endmember in terms of excess free energy as used in the Single Defect Method

Indicated is the hypothetical ideal (linear dashed) behavior of the virtual solid solution, as opposed to the behavior of the real solid solution (solid curve), which is equal to the virtual solid solution at low mole fractions of $CaSeO_3$ and then follows an arbitrary trend

The thermodynamic description of the surface phase requires the determination of the standard thermodynamic properties of its endmembers. The endmembers of the surface solid solution can be defined by analogy with the bulk solid solution. The $CaCO_3$ endmember can be associated with the surface layer of calcite. The atomistic modeling of this layer requires construction of a supercell of calcite, which contains a surface. This surface is implemented in DFT calculations by inserting a sufficiently thick vacuum layer into a 3D periodic supercell. The surface $CaSeO_3$ endmember can be defined as a virtual endmember by computing the enthalpy of a similar supercell with one CO_3^{2-} unit in the surface layer substituted with a SeO_3^{2-} unit. The obvious difficulty of such a model is that the surface layer can be simulated only with the substratum of bulk-like calcite layers below the surface. While one can compute the free energy of the whole supercell, this creates the difficulty of how this energy should be separated into the energy of the surface layer and the energy of the quasi-bulk region. For pure phases this difficulty is usually dealt with by the consideration of surface free energy. In our case this difficulty implies that the absolute energies of the surface endmembers cannot be computed. However, as the distribution coefficient depends just on the difference in the free energies of the $CaCO_3$ and $CaSeO_3$ surface endmembers, the absolute free energies of the surface endmembers are not required. Combining Eqns. (5.29) and (5.33) we obtain:

$$D_{bulk} = \exp[(G^0(\text{calcite}) - G^0(CaSeO_{3\ \text{monocl.}}) - \Delta G^E_{bulk} - G^0(CO_3^{2-}{}_{(aq)}) + G^0(SeO_3^{2-}{}_{(aq)}))/(RT)] \tag{5.34}$$

Eqn. (5.34) shows that, provided that the standard Gibbs free energies of calcite, $CaSeO_3$ (monocl.), $CO_3^{2-}{}_{(aq)}$, and $SeO_3^{2-}{}_{(aq)}$ are known, the distribution coefficient is determined by the single value of $\Delta G^E = \Delta G^E_{bulk}$. An analogous equation can be defined for the surface solid solution:

$$D_{surface} = \exp[(G^0(\text{calcite}) - G^0(CaSeO_{3\ \text{monocl.}}) - \Delta G^E_{surface} - G^0(CO_3^{2-}{}_{(aq)}) + G^0(SeO_3^{2-}{}_{(aq)}))/(RT)] \tag{5.35}$$

Here we note that ΔG^E_i in Eqns. (5.34) and (5.35) in fact defines the difference between the free energies of two $CaCO_3$ and $CaSeO_3$ endmembers in a given phase (i = surface or bulk), relative to the difference of the free energies of the $CaCO_3$ and $CaSeO_3$ reference compounds, calcite and $CaSeO_3$(monocl.). Thus the ΔG^E_{bulk} in Eqn. (5.34)can be understood as:

$$\Delta G^E_{bulk} = [G^0(CaSeO_3(\text{virt., bulk})) - G^0(CaCO_3(\text{bulk}))] - [G^0(CaSeO_3(\text{monocl.})) - G^0(CaCO_3(\text{calcite}))] \tag{5.36}$$

For the case of the bulk solid solution eqn. (5.36) is equivalent to eqn. (5.32) as $G^0(CaCO_3(\text{calcite})) = G^0(CaCO_3(\text{bulk}))$. Combining eqns. (5.32) and (5.34) we find that:

$$G^0(CaSeO_3(\text{virt., bulk})) - G^0(CaCO_3(\text{bulk})) = G^0(Ca_n(CO_3)_{n-1}SeO_3) - G^0(Ca_n(CO_3)_n) \tag{5.37}$$

where the right hand part of the equation is represented by a supercell of calcite in which one CO_3^{2-} unit is substituted with a SeO_3^{2-} unit and a supercell of pure calcite.

In the case of the surface solution an equation analogous to eqn. (5.36) takes the form:

$$\Delta G^{E}_{surface} = [G^{0}(CaSeO_3(virt., surface)) - G^{0}(CaCO_3(surface))] - [G^{0}(CaSeO_3(monocl.)) - G^{0}(CaCO_3(calcite))] \quad (5.38)$$

In the particular case of the bulk solid solution, the $CaCO_3$ (bulk) endmember coincides with $CaCO_3$ (calcite). Due to this simplifying circumstance we can, in fact, compute the absolute free energy of the virtual bulk $CaSeO_3$ endmember (eqn. (5.33). A similar simplification is not possible in the case of the surface solid solution. However, this is not a problem as the distribution coefficient depends only on the difference between the free energies of the surface endmembers, $CaCO_3$(surface) and $CaSeO_3$(virt., surface). Analogously to eqn. (5.37) it is possible to show that:

$$G^{0}(CaSeO_3(virt.,surface)) - G^{0}(CaCO_3(surface)) = G^{0}(Ca_n(CO_3)_{n-1}SeO_3)^{*} - G^{0}(Ca_n(CO_3)_n)^{*} \quad (5.39)$$

where * denotes supercells including a free surface. This leads to a rigorous definition of $\Delta G^{E}_{surface}$ as:

$$\Delta G^{E}_{surface} = [G^{0}(Ca_n(CO_3)_{n-1}SeO_3)^{*} - G^{0}(Ca_n(CO_3)_n)^{*}] - [G^{0}(CaSeO_3(monocl.)) - G^{0}(CaCO_3(calcite))] \quad (5.40)$$

In our study the $\Delta G^{E}_{surface}$ parameter is computed with the aid of a supercell composed of a slab of 5 calcite layers parallel to (104) and a vacuum layer (which may or may not additionally contain water molecules) of equivalent thickness (see the section on atomistic simulations for further details). Each calcite layer consists of 8 $CaCO_3$ units, such that the slab contains in total 40 $CaCO_3$ units, 16 of which are at the surface.

Estimation of the standard Gibbs free energy of the monoclinic $CaSeO_3$

The monoclinic $P2_1/n$ phase is the only compound of $CaSeO_3$ composition for which the crystal structure is available [WIL/GIE2007]. This phase serves perfectly as the reference compound. However, its thermodynamic properties are unknown. Here we estimate the standard Gibbs free energy of the $CaSeO_3$ (monocl.) from the total energy changes in the reactions:

$$BaSeO_3 + CaCO_3\ (aragonite) \rightarrow CaSeO_3 + BaCO_3 \quad (5.41)$$

$$SrSeO_3 + CaCO_3 \text{ (aragonite)} \rightarrow CaSeO_3 + SrCO_3 \qquad (5.42)$$

The standard free energies of all phases involved in eqns. (5.41) and (5.42), except for $CaSeO_3$, are known (**Tab. 5.21**). If we know the free energies of these reactions, we can compute the free energy of $CaSeO_3$ (monocl.). As the structures of the reactants and products are similar, and the temperature of interest (298.15 K) is small, we assume that entropy effects are negligible. Thus the changes in the total energy in these reactions are assumed to be equal to the free energy changes.

5.5.2.3 Experimental and computational methods

5.5.2.3.1 Synthesis of Selenite-doped calcite

Various crystal growth methods are applied here to synthesize selenite-doped calcite. Mixed flow reactor experiments are used to examine the incorporation at surface controlled growth conditions. In MFR experiments the selenite concentration is varied from $2 \cdot 10^{-13}$ mol/L to $2 \cdot 10^{-4}$ mol/L in order to measure the partition coefficient and growth rate as a function of selenite concentration. A batch type crystal growth experiment at 0.001 mol/L SeO_3^{2-} concentration is used to synthesize a SeO_3^{2-} doped calcite single crystal, which is used for the polarization dependent Se *K*-edge EXAFS measurements. In order to investigate crystal growth even closer to equilibrium than in MFR experiments, aragonite to calcite recrystallization experiments are applied. The recrystallization rate of aragonite in a pure system is compared to that in the presence of 10^{-4} mol/L selenite. In order to compare selenite coprecipitation at supersaturated conditions to selenite adsorption at equilibrium conditions batch type adsorption experiments are conducted. In the following sections the experiments will be described in detail.

MFR experiments

To grow calcite in an MFR experiment, the MFR is fed continuously with three independent input solutions: one containing 18 mmol/L Ca^{2+}, added as $CaCl_2 \cdot 2H_2O$ pa., the next containing 9 mmol/L inorganic carbon, added as $NaHCO_3$ pa., and the third containing the selenite. Solutions are prepared from purified water (18.2 MΩ·cm, < 2 ppb dissolved organic carbon). All input solutions contain 0.01 mol/L NaCl as a background electrolyte. Seed crystals are provided in the reactor. Merck calcium carbonate suprapure is used for seed crystals. Powder X-ray diffraction on a Bruker D8 Advance showed that the seed crystals consist of pure calcite to within the level of uncertainty (± 0.5 %). The specific surface area of the calcite seeds measured by N_2-BET is 0.51 ± 0.04 m^2/g. XPS C1*s* spectra confirmed that the contamination of the Merck calcium carbonate suprapure with adventitious carbon is relatively low compared to XPS data reported in literature [STI/HOC1991]; about 20 % of the C1*s* spectrum is related to organic carbon while the rest is attributed to carbonate. The diameters of the seed crystals are in the range of 5 to 20 µm. The solution in the MFR is permanently agitated by a magnetic stirring bar, which is suspended to avoid grinding effects. The stirrer is rotated at 850 rpm. The size of the seed crystals and the rotation speed of the magnetic stirrer are chosen to minimize any boundary layer effects [NIE/TOF1984, WAN/XU2001] and to ensure surface controlled crystal growth kinetics. MFR experiments were typically run for 14 days. After an initial period of elevated growth rate, steady state conditions establish in the MFR, and the selenite-doped calcite precipitates homogeneously onto the surface of the seed crystals. Perfect mixture is assumed inside the MFR; therefore the solution composition in the outlet is considered representative of the solution composition in the reactor. To monitor the progress of the reaction, samples of the outlet solution were taken on a daily basis. With each sampling the exact pump rate, F, was measured and the pH was checked. The sample was acidified and stored for further analysis of the Ca^{2+} and SeO_3^{2-} concentrations. Ca^{2+} concentrations were measured on a Perkin Elmer Optima 2000 DV inductively coupled plasma optical emission spectrometer (ICP-OES). A spike of 13 kBq/L of radioactive $^{75}SeO_3^{2-}$ was added to the solution reservoir containing the non-radioactive selenite. Carrier free $^{75}SeO_3^{2-}$ was purchased from Eckert & Ziegler Nuclitec GmbH. It has a half-life of 120 days and the concentration was analyzed by gamma-spectroscopy. Selenite concentration after the reactor was calculated assuming that the percentage reduction of the ^{75}Se concentration in the MFR is representative of the reduction in total selenite concentration. The decrease in calcium concentration is taken as a measure of calcite growth inside the MFR. It is assumed that the combined total inorganic carbon concentration and selenium concentration decreases by the same amount as the calcium concentration in the MFR due to calcite precipitation. The calcite growth rate, R_{ca}, in the MFR can be calculated according to:

$$R_{ca} = \frac{\Delta \mathrm{c}(\mathrm{Ca}^{2+}) \cdot \mathrm{F}}{\mathrm{A}} \qquad (5.43)$$

where ‘A’ is the reactive surface area of the calcite seeds in the MFR, which is assumed to remain constant during the MFR experiment. The mole fraction of $CaSeO_3$ in the precipitated solid can be calculated from:

$$X(CaSeO_3) = \frac{\Delta c(SeO_3{}^{2-})}{\Delta c(Ca^{2+})} \tag{5.44}$$

while X(calcite) = 1 - X($CaSeO_3$). Partition coefficients are then calculated according to eqn. (5.19), which simplifies to:

$$D = X(CaSeO_3)/X(\text{calcite}) \cdot c(CO_3{}^{2-}) \,/\, c(SeO_3{}^{2-}) \tag{5.45}$$

It is important to note that the composition of the solid, represented by X($CaSeO_3$)/X(calcite), is related to the molalities of the free $CO_3{}^{2-}$ and $SeO_3{}^{2-}$ species in solution and not the total element concentrations. Species distributions, as well as saturation indices, were calculated using PhreeqC [PAR/APP1999] and the Nagra/PSI thermodynamic database [HUM/BER2002]. During all MFR experiments the solutions were undersaturated with respect to $CaSeO_3 \cdot H_2O$ (SI < -0.4), the selenite phase most likely to precipitate from aqueous solution at standard conditions [OLI/NOL2005].

Ten MFR experiments were conducted for the present study; seven using $^{75}SeO_3{}^{2-}$, to quantify the selenite coprecipitation, one using only non-radioactive selenite, to produce an inactive selenite-doped calcite powder for EXAFS measurements, and two growing pure calcite in order to obtain reference growth rates in pure calcite systems.

Using $NaHCO_3$ as the carbonate source, the pH during the precipitation reaction was in the range 7.3 to 8.0. This pH region was chosen as it has been previously reported that selenite adsorption on calcite is preferred at lower pH [COW/ZAC1990]. In this pH region a high calcium concentration (0.006 mol/L) has to be used to achieve the desired calcite supersaturation. The combination of high calcium concentration and low growth rate resulted in a very low percentage difference in calcium concentration between input and output solutions. In many cases the interpretation of the MFR data is limited by the analytical uncertainty of the ICP-OES measurements of the calcium concentration. MFR experiments for which the difference between calcium input and output concentration is significant (larger than uncertainty) are labeled with (ΔCa) in **Tab. 5.19**.

For the other MFR experiments (labeled with (ΔpH) in **Tab. 5.19** the amount of precipitated calcite was calculated with PhreeqC based on the pH difference between a 1:1:1 mixture of the three input solutions and the average pH of the output solution.

Errors in the surface area were derived from the estimated analytical uncertainty for N_2-BET measurements, which is 9 %. Errors for the measured values of pH and F in **Tab. 5.19**, but also calcium and ^{75}Se concentrations, are standard deviations of the values measured during steady state conditions. For the calculated values, R_{ca}, c(Se), $\Delta c(Ca^{2+})$, $\Delta c(SeO_3^{2-})$, X($CaSeO_3$), X(calcite), and *D*, error propagation calculations were applied to estimate the standard deviations, based on all experimental uncertainties. For values calculated using PhreeqC, like SI(calcite), c(CO_3^{2-}), and c(SeO_3^{2-}), uncertainties were estimated by calculating a bandwidth of possible results. Therefore the input values were varied about their standard deviations and the highest and lowest results obtained are taken as the standard deviation of the resulting values. Uncertainties in the relevant equilibrium constants are not considered.

Preparation of a selenite doped calcite single crystal

For the preparation of a selenite-doped single crystal a batch type crystal growth experiment was performed. Initially a 0.1 mol/L NaCl solution in equilibrium with calcite and atmospheric CO_2 was prepared. Here calcite powder was added to a 0.1 mol/L NaCl solution that was continuously stirred and percolated with air until the calculated equilibrium pH value 8.2 was reached. Then the solution was filtered through a 0.45 µm Millipore membrane. As a single crystal substrate an Iceland spar crystal from Mexico Chihuahua was freshly cleaved along the crystallographic (104) plane to obtain an optically flat crystal surface. Directly after cleavage the crystal was immersed in the filtered equilibrium solution. Then NaOH and Na_2SeO_3 stock solutions were added to reach a concentration of 0.001 mol/L NaOH and 0.0001 mol/L Na_2SeO_3 in the reaction vessel. This caused an increase in pH to a value of 10, and, according to PhreeqC calculations, corresponds to an SI(calcite) of 1.2. After the addition of NaOH and Na_2SeO_3 the vessel was sealed to avoid further reaction with air. After six days the solution reached a pH of 9.8. This indicates that the SI(calcite) had decreased to a value of about 0.7 and about $4 \cdot 10^{-4}$ mol/L calcite precipitated. Taking into account the 20 mL solution volume and the reactive surface area of the single crystal of about 3 cm^2, this corresponds to roughly 0.03 mol/m^2, 3,000 monolayers, or 1 µm, of calcite precipitation onto the single crystal surface. The selenite-doped calcite single crystal was analyzed by polarization dependent EXAFS measurements.

Tab. 5.19 Reaction conditions during MFR experiments. Listed are the input concentration of selenium, $c_0(Se)$, the reactive calcite surface inside the MFR, A(calcite), the average pH after the MFR, pH_{out}, the average supersaturation after the MFR, which is meant to represent steady state conditions, SI_{out}, the pumping rate, F, the solid solution growth rate, R_{Ca}, and the partition coefficient, *D*

Label	**$c_0(Se)$** mol/L	**A(calcite)** m^2	**pH_{out}**	**SI_{out}**	**F** mL/min	**R_{ca}** 10^{-9} mol/(m^2s)	***D***
MFR-Se 1 (ΔCa)	$1.7 \cdot 10^{-13}$	0.082 ± 0.007	7.73 ± 0.08	0.7 ± 0.1	0.29 ± 0.02	16 ± 12	0.05 ± 0.04
MFR-Se 2 (ΔCa)	$2.5 \cdot 10^{-10}$	0.082 ± 0.007	7.72 ± 0.09	0.7 ± 0.1	0.286 ± 0.005	10 ± 6	0.07 ± 0.05
MFR-Se 3 (ΔCa)	$2.5 \cdot 10^{-7}$	0.15 ± 0.01	7.47 ± 0.05	0.43 ± 0.06	0.270 ± 0.007	6 ± 4	0.002 ± 0.001
MFR-Se 4 (ΔpH)	$6.7 \cdot 10^{-6}$	0.15 ± 0.01	7.56 ± 0.05	0.50 ± 0.06	0.267 ± 0.003	3 ± 2	0.02 ± 0.01
MFR-Se 5 (ΔpH)	$1.7 \cdot 10^{-5}$	0.15 ± 0.01	7.43 ± 0.04	0.39 ± 0.05	0.288 ± 0.002	7 ± 5	0.02 ± 0.01
MFR-Se 6 (ΔpH)	$3.3 \cdot 10^{-5}$	0.15 ± 0.01	7.60 ± 0.04	0.59 ± 0.05	0.297 ± 0.001	7 ± 5	0.02 ± 0.01
MFR-Se 7 (ΔCa)	$2.5 \cdot 10^{-4}$	0.082 ± 0.007	8.0 ± 0.1	0.9 ± 0.2	0.277 ± 0.001	7 ± 4	0.01 ± 0.01
MFR-Se EXAFS (ΔCa)	$1.1 \cdot 10^{-4}$	0.20 ± 0.02	10.33 ± 0.02	1.0 ± 0.1	0.59 ± 0.01	12 ± 1	-
MFR-Cc1	0	0.082 ± 0.006	7.31 ± 0.04	0.25 ± 0.05	0.57 ± 0.02	17 ± 14	-
MFR-Cc2	0	0.082 ± 0.006	7.36 ± 0.12	0.28 ± 0.1	0.28 ± 0.01	16 ± 3	-

Aragonite recrystallization experiments

For aragonite recrystallization experiments 1 g of aragonite was added to 50 mL of 0.1 mol/L NaCl solution. Recrystallization rates of a pure aragonite experiment were compared to an experiment where an additional 10^{-4} mol/L Na_2SeO_3 is added. The essential idea behind these experiments is that, due to the difference between the solubility products of aragonite ($\log_{10} K_{SP}$ = -8.34) and calcite ($\log_{10} K_{SP}$ = -8.48), an aragonite equilibrated solution intrinsically has SI(calcite) = 0.14. Therefore it is expected that aragonite dissolves slowly and calcite precipitates at a very low supersaturation. The reaction progress of the recrystallization experiment was monitored by pipetting a 5 mL aliquot of the suspension onto a 0.45 µm filter membrane, drying the obtained powder at 105 °C over-night, and analyzing it by powder XRD. Powder XRD measurements were performed on a Bruker D8 Advance diffractometer. Rietveld analysis of diffractograms was performed using the Bruker AXS DiffracPlus Topas 4.2 software.

A self-synthesized sample of aragonite was used for the experiments. Aragonite was synthesized according to a method after Ogino *et al.* [OGI/SUZ1987], by mixing equal amounts of 0.5 mol/L Na_2CO_3 and 0.5 mol/L $CaCl_2 \cdot 2H_2O$ solution at 90 °C. After two to three minutes the precipitated powder is separated from the solution by filtration, dried at 105 °C over-night, and analyzed by powder XRD, N_2-BET and SEM. According to the Rietveld analysis of powder diffractograms, the obtained powder consists of > 97 % aragonite, with some vaterite (< 3 %), and traces of halite and calcite (< 0.3 %). The specific surface area of the aragonite powder was 4.2 m^2/g, and consisted of 1 – 10 µm sized needle like aggregates.

Adsorption experiments

In order to compare selenite coprecipitation at supersaturated conditions to selenite adsorption at equilibrium conditions, adsorption experiments were conducted. Selenium adsorption was studied using batch-type experiments. Solutions were prepared from purified water (18.2 MΩ·cm, < 2 ppb TOC) equilibrated with calcite and air ($\log_{10}(p(CO_2))$ = -3.44). Reagent grade HCl, or NaOH, and NaCl were added to achieve an ionic strength of 0.1 mol/L and the desired equilibrium pH in a range from 7.5 to 9.6. 25 g/L Merck calcium carbonate suprapure, with a specific surface area of 0.51 m^2/g (N_2-BET), was used as the crystal substrate (as in MFR experiments). Experiments were performed using radioactive $^{75}SeO_3^{2-}$. The initial selenium(IV) concentration was 10^{-13} mol/L, and final Se-concentrations were analyzed by gamma-spectroscopy.

5.5.2.3.2 Extended X-ray absorption fine structure (EXAFS) spectroscopy

After the experiment, the selenite-doped calcite powder from MFR experiment, MFR Se EXAFS (see **Tab. 5.19**), was taken out of the MFR, dried and sealed between two layers of Kapton foil for fluorescence mode EXAFS measurements at the INE-beamline for actinide research at ANKA [ROT/BUT2012]. Eight Se *K*-edge X-ray absorption scans in an energy range from 12.508 keV to 13.358 keV (Se *K*-edge energy (Se 1*s* Se(0)) at 12.658 keV) were recorded. Se K_α fluorescence was measured with a five pixel LEGe solid state detector (Canberra-Eurisys). For energy calibration, a selenium foil was measured in parallel behind the second ionization chamber in transmission mode, where the first inflection point is assigned to the Se(0) Se 1*s* energy. Data treatment and analysis were performed using ATHENA and ARTEMIS from the IFEFFIT software package [RAV/NEW2005]. The k^3-weighted extracted XAFS signal was used in a k-range from 2.0 to 12.0 $Å^{-1}$. Hanning windows were applied in the Fourier Transformation. Data modeling was performed in R space in a range from 1.3 to 4.0 Å. Backscattering amplitude and phase shift functions, obtained from FEFF 6 [ANK/RAV1998] calculations, were used as theoretical standards for modeling the data.

As synchrotron radiation is linearly polarized, with the polarization vector, $\vec{\varepsilon}$, perpendicular to the beam and in the plane of the storage ring, it is perfectly suited for polarization dependent experiments. For polarization dependent EXAFS measurements the selenite-doped single crystal, prepared as described above, was dried and mounted onto the goniometer at the INE-Beamline. Beam-slits were used to obtain a rectangular shaped beam with 200 µm vertical diameter by ~500 µm horizontal diameter. The sample with the (104) face of calcite on top was positioned in the beam at an incidence angle of the beam relative to the surface just above the critical angle of total external reflection for calcite, which is 0.152° at 12.658 keV, the Se *K*-edge energy, to ensure a certain penetration depth of the beam into the sample. The experimental setup of the polarization dependent EXAFS measurements is shown in **Fig. 5.63**a. The sample was slightly rocked during the energy scans, to account for the variation of the critical angle with the photon energy. The intensity of the beam behind the single crystal sample and the second ionization chamber was not high enough for the measurement of a reference spectrum for energy calibration. The energy was calibrated before the measurements and no drift was observed during the measurements.

The sample was rotated around the surface normal to measure EXAFS spectra at three different orientations of the sample relative to the beam, or the polarization vector $\vec{\varepsilon}$, as shown in **Fig. 5.63**b. The orientation labeled “bpa” corresponds to measurements with the beam approximately parallel to the crystallographic [42-1] direction and $\vec{\varepsilon}$ parallel to the [010] direction. The orientation labeled “bpb” corresponds to measurements with the beam offset by approximately 12° from the [010] direction, which corresponds to $\vec{\varepsilon}$ being about parallel to the [43-1] direction. For the last orientation, labeled “bpk”, the beam was parallel to the edge of the crystal, which corresponds to the [-441] direction. Therefore, $\vec{\varepsilon}$ was approximately parallel to the [46-1] direction during the “bpk” measurement (parallel or antiparallel does not matter for this experiment as will be explained later). Angles were only adjusted approximately using a laser alignment method. At each orientation 7 to 11 scans were recorded in an energy range from 12.458 keV to 13.258 keV. For polarization dependent measurements the Se K_{α} fluorescence was recorded using a silicon drift detector (SIINT Vortex EX-60), mounted looking directly down on to the sample surface (cf. **Fig. 5.63**a).

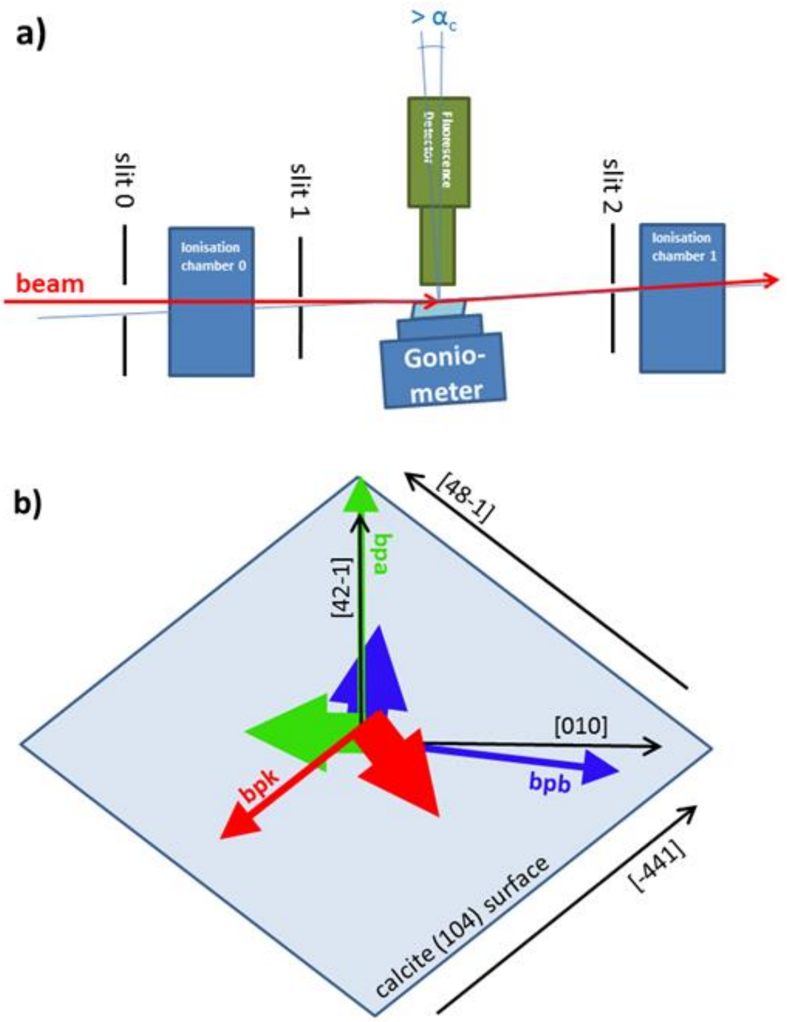

Fig. 5.63 a) Experimental setup used for the polarization dependent EXAFS measurements (grazing incidence setup)

Indicated are the beam, the ion chambers, the beam-slits, the goniometer, the fluorescence detector, and the angle between the sample surface and the incident beam (> α_c), which is equal to the angle between the surface normal and the vertical direction. The sample is depicted by the light blue rhomb on top of the goniometer

b) Orientation of the rhombic calcite single crystal sample relative to the beam in the polarization dependent EXAFS experiment (top view).

Black arrows indicate the directions of crystallographic direct space vectors, thin colored arrows indicate the direction of the beam, and thick colored arrows indicate the direction of the polarization vector during the measurements. Polarization dependent measurements are performed at three different orientations labeled: ”bpa” (green), “bpb” (blue), and ”bpk” (red)

EXAFS oscillations, χ, are interpreted as being caused by interference between photoelectron waves going out from the absorbing atom (i) and scattered back from neighboring atoms (u_j). Therefore they may be decomposed into contributions from successive atomic shells (j), composed of N_j^{real}, atoms. For the atomic scale interpretation of the polarization dependent EXAFS data we follow the approach by Schlegel *et al.* [SCH/MAN1999]. In EXAFS data measured on a powder sample, the amplitude of the EXAFS signal attributed to the j^th^ shell, χ_{ij}^{iso}, is proportional to the number of atoms in the j^th^ shell, N_j^{real}. In a polarization dependent experiment the amplitude depends additionally on the angle between the vectors, $\vec{R}_{iu_j}$, connecting the absorbing atom (i) with the u_j atoms in the j^{th} shell, and the polarization vector $\vec{\varepsilon}$. At *K-edges*, and in the plane wave approximation, the relationship between the isotropic EXAFS signal, χ_{ij}^{iso}, and the polarized EXAFS signal, χ_{ij}^{P}, can be expressed as [SCH/MAN1999]:

$$\chi_{\mathrm{ij}}^{\mathrm{P}} = 3\ \chi_{\mathrm{ij}}^{\mathrm{iso}} \sum_{\mathrm{u_j=1}}^{\mathrm{N_j^{real}}} \cos^2\theta_{\mathrm{iu_j}} \tag{5.46}$$

where θ_{iu_j} are the angles between the vectors $\vec{R}_{iu_j}$ and the polarization vector $\vec{\varepsilon}$. Only the amplitude of the EXAFS signal is modified by changes of the orientation of the sample relative to $\vec{\varepsilon}$. As the amplitude is proportional to N_j^{real}, we can use this relation and retrieve from polarization dependent EXAFS data not the real coordination number, N_j^{real}, but an effective coordination number, N_j^{eff}.

Deviating from the approach by Schlegel *et al.* we do not relate the polarization dependent amplitude variation to special angles relative to the crystal axes, but calculate the contribution of each neighboring atom to the polarization dependent EXAFS signal explicitly. In terms of an effective coordination number the contribution of one single atom in the j^{th} shell, u_j, to the EXAFS amplitude can be expressed as:

$$\mathrm{N_{u_j}^{eff}} = 1 \cdot 3\cos^2\theta_{\mathrm{iu_j}}. \tag{5.47}$$

The $\cos^2$ dependence between θ and N^{eff} explains why it does not matter if a vector is parallel or antiparallel to a certain crystallographic direction during the measurements. Taking the sum over all atoms in the j^{th} shell, we get the effective coordination number of the j^{th} shell as:

$$\mathrm{N_j^{eff}} = 3 \sum_{\mathrm{u_j}=1}^{\mathrm{N_j^{real}}} \cos^2 \theta_{\mathrm{iu_j}} = 3 \sum_{\mathrm{u_j}=1}^{\mathrm{N_j^{real}}} \left(\frac{\vec{\mathrm{R}}_{\mathrm{iu_j}} \cdot \mathrm{G} \cdot \vec{\varepsilon}}{|\vec{\mathrm{R}}_{\mathrm{iu_j}}| \, |\vec{\varepsilon}|} \right)^2 , \tag{5.48}$$

where G is the metric tensor of the calcite lattice. Equation (5.48) enables us to refine an atomic scale structure from the polarization dependent EXAFS data that considers not only distances, but also the angular relations between the atoms and the polarization vectors. Real coordination numbers are equal to three in all cases in the relevant structure. The analysis of the polarization dependent EXAFS data is performed as a multiple dataset fit in ARTEMIS [RAV/NEW2005], meaning that all polarization dependent EXAFS data are fitted simultaneously. The bond-distances and the Debye-Waller factors are treated as global parameters (equal for all orientations). Individual parameters are used for the coordination numbers, N^{eff}, for each shell and orientation. Modeling is performed on k^2-weighted EXAFS data. The limited signal to noise ratio, especially in the “bpk” data set, required the k-range to be limited to 2 $Å^{-1}$ to 9.4 $Å^{-1}$. Hanning windows are used for the Fourier transformation. Fitting is performed in R-space, in an R-range from 1.3 Å to 4.1 Å.

5.5.2.3.3 Atomistic calculations

In order to get an impression of the uncertainties involved in the single defect calculations, we have computed the enthalpy changes in eqns.(5.30 to(5.40) by applying different exchange-correlation functionals within Kohn-Sham DFT, and comparing the results. We have applied two functionals within the Generalized Gradient Approximation (Wu-Cohen [WU/COH2006] and Perdew-Burke-Ernzerhof [PER/BUR1996]) and two methods of describing the influence of core electrons (ultrasoft pseudopotentials and the projector augmented wave approach). A short description of the various theoretical methods is given in the following subsections. Images of the supercells used for the various DFT calculations are shown in **Fig. 5.64**.

DFT calculations using the Wu-Cohen functional and ultrasoft pseudopotentials (WC-USP)

This set of DFT calculations was performed with the CASTEP code. Here the electronic wave functions of the valence electrons are expanded in a plane-wave basis set, while the combined potentials of the nuclei and core electrons are modeled using pseudopotentials. The present calculations were performed with the "on-the-fly-generated" ultrasoft pseudopotentials supplied with Materials Studio 6.0[5]. The exchange and correlation potential was treated with the Wu-Cohen (WC) functional [WU/COH2006]. Brillouin zone sampling was performed according to the Monkhorst-Pack scheme [MON/PAC1976] with a separation between individual k-points of 0.03-0.035 $Å^{-1}$. The calculations were performed with a plane-wave cutoff energy of 810 eV. The conversion tests were performed in the range of 710-1210 eV. Our tests have shown that with this cutoff of 810 eV the differences in total energies, e. g. the energy effects of the reactions (5.41) and (5.42) are converged to within 0.001 eV.

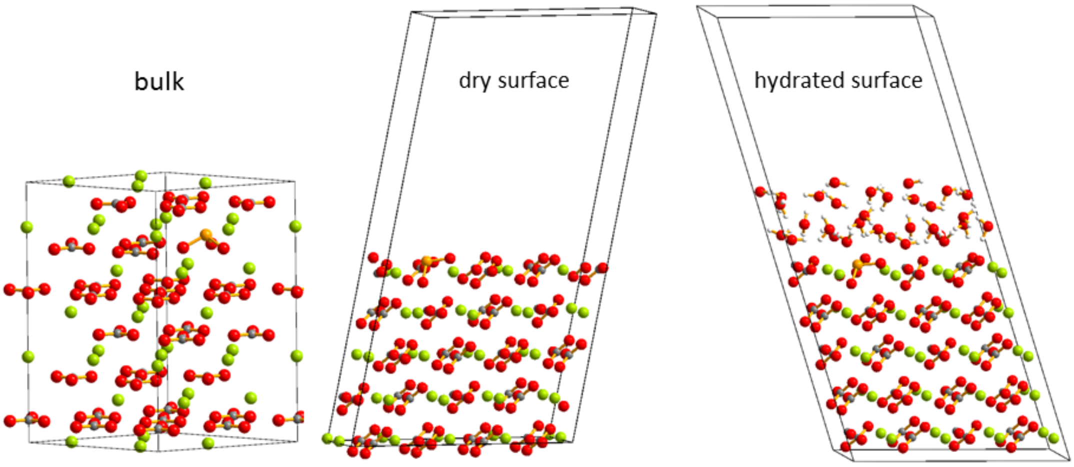

Fig. 5.64 Supercells used in DFT- and force-field calculations for the simulation of the SeO_3^{2-} substitution in bulk calcite (left), at the calcite-vacuum interface (middle), and the calcite-water interface (right) (Ca: green, C: grey, O: red, Se: yellow, H: white)

The WC-USP calculations were used to calculate the enthalpy differences in eqns. (5.30 to (5.42. The enthalpieatoms of the reactions, which involve supercells with water layers, were computed with different methods. The total energies of $CaSeO_3$ (monocl.), $CaCO_3$(calcite, aragonite), $SrCO_3$ and $BaCO_3$ were computed with symmetry constraints consistent with the reported space groups of these compounds. The lattice parameters and the atomic coordinates were fully relaxed. The single defect calculations were performed with two different supercells. The substitution of the SeO_3^{2-} in the bulk structure was studied with a 2x2x1 supercell prepared from the hexagonal unit cell of

---

[5] http://accelrys.com/products/materials-studio/

calcite. One of the 24 CO_3^{2-} groups was replaced with a SeO_3^{2-} group, such that the initial coordinates of the three oxygen atoms were the same as in the removed CO_3^{2-} group, while the Se atom is slightly displaced along the *c*-axis (**Fig. 5.64** (left)). The SeO_3^{2-} substitution at the surface was investigated with a supercell composed of 5 layers of $CaCO_3$ arranged parallel to the (104) direction and a vacuum layer with a thickness equivalent to 5 $CaCO_3$ layers. The SeO_3^{2-} unit was located in the boundary layer replacing a CO_3^{2-} unit such that the Se atom is shifted relative to the removed C atom away from the surface, as shown in **Fig. 5.64** in the middle. The supercell parameters and the coordinates of all atoms were relaxed in P1 symmetry. The geometries were optimized until the residual forces and stresses are less than 0.005 eV/Å and 0.1 GPa, respectively.

DFT calculations using the Perdew-Burke-Ernzerhof functional and the projector augmented wave method (PBE-PAW)

PBE-PAW calculations were carried out using the Vienna ab-initio simulation package, VASP [KRE/FUR1996, KRE/HAF1993, KRE/HAF1994], which similarly to CASTEP employs periodic boundary conditions and a plane-wave basis set. Electron exchange and correlation are described using the Perdew-Burke-Ernzerhof (PBE) functional [PER/BUR1996]. The nuclei and core states are modeled with the projector augmented wave (PAW) method [BLO1994] as described by Kresse and Joubert [KRE/JOU1999].

In contrast to the WC-USP setup, the bulk incorporation was modeled using a 2x2x2 calcite supercell of monoclinic shape, whose vectors were chosen such that one face of the cell is parallel to (104) as was also used by Heberling *et al.* [HEB/TRA2011]. The other termination plains of this cell correspond to (010) and (42-1) in hexagonal coordinates. The different cell geometry was chosen to assess the possible effect of the size and shape of the supercell on the predicted ΔG^E of the virtual bulk $CaSeO_3$ endmember.

The monoclinic $P2_1/n$ structure [WIL/GIE2007] of the $CaSeO_3$ reference phase has been optimized to determine the electronic energy of the unit cell. For more information on the unit cell parameters please refer to the supporting information that comes with the original article [HEB/VIN2014]. The energy cut-off of 650 eV for the kinetic energy of the plane-waves was used in all calculations. The modeling of the SeO_3^{2-} incorporation into the bulk of calcite employed complete optimization of the cell volume and the ionic positions.

The modeling of the SeO_3^{2-} incorporation into the surface layer was done using the optimized calcite supercell of monoclinic shape consisting of 5 $CaCO_3$ layers. The supercell is similar to that used in the WC-USP setup. Above the $CaCO_3$ layers a 15 Å thick layer of vacuum was added, which is sufficient to isolate the five layers from their periodic images. The total energy was calculated first for the supercell of pure calcite and subsequently for a supercell, in which one surface CO_3^{2-} unit is substituted with SeO_3^{2-}.

To explore the influence of partial hydration on the selenite surface substitution the surface calculations were repeated with supercells containing three layers of water molecules (**Fig. 5.64** (right)). These layers of water were inserted above the calcite vacuum interfaces. The water molecules of the first layer were located on top of the Ca^{2+} ions, while the molecules of the second layer were placed above the CO_3^{2-} ions, in agreement with previous experimental [HEB/TRA2011] and computational [RAI/GAL2010] studies. Initially the water molecules of the first two layers were arbitrarily oriented. The subsequent geometry optimization resulted in reorientation of the water molecules and in slight changes in the positions of the oxygen atoms. A well-ordered structure of the water layer is thus obtained. Then the third layer, consisting of 15 water molecules, was introduced on top of the second layer. This layer is intended to simulate the effect of bulk water on the first two layers, as motivated by our earlier work on corundum [JAN/NET2014]. The geometry of the whole structure was then optimized. The optimization of three layers of water at the surface resulted in a water structure showing a periodicity of the water molecules along the [42-1] direction of calcite. Due to this periodicity, only each second CO_3^{2-} group at the interface finds itself surrounded by an equivalent arrangement of water molecules (i. e. neighboring CO_3^{2-} groups are surrounded by slightly different configurations of water). To simulate CO_3^{2-} substitution by SeO_3^{2-} at the calcite water-interface we subsequently substituted the two non-equivalent carbonate sites and optimized the surface supercell. The corresponding configurations will be subsequently referred to as Se1 and Se2.

DFT calculations using the Perdew-Burke-Ernzerhof functional and ultrasoft pseudopotentials (PBE-USP and PBE+D-USP)

To assess whether any small differences between WC-USP and PBE-PAW calculations originate either from functionals or from pseudopotentials, the whole set of bulk and dry surface incorporation calculations was repeated with the PBE functional in combination with the “on-the-fly-generated” ultrasoft pseudopotentials supplied with Materials Studio 6.0 (http://accelrys.com/products/materials-studio/). These calculations were again performed using the CASTEP code [CLA/SEG2005]. Converged structures from WC-USP and PBE-PAW calculations are used as input configurations for these calculations. The plane-wave cutoff energy remained at 810 eV. As recent work has shown that the description of water in DFT calculations is improved by the inclusion of corrections for the long-range dispersion [WAN/ROM2011], the calculations of the SeO_3^{2-} incorporation at the calcite-water interface were additionally studied with the PBE+D-USP method, where dispersion corrections are included according to the method of Tkatchenko and Scheffler [TKA/SCH2009]. As our previous calculations revealed periodicity in the structure of the water layer, the water-interface incorporation was modeled using PBE+D for the two distinct sites, Se1 and Se2.

Force-field calculations

The entropy effects of the SeO_3^{2-} substitution in the bulk structure have been investigated with the aid of a force-field model. The present model is based on the recent flexible carbonate model derived to yield thermodynamically accurate properties for calcium carbonate [DEM/RAI2011]. Here this force field is extended to include the interactions within the SeO_3^{2-} unit and the interactions between this anion with the surrounding host material, calcite. Intramolecular bonded parameters for the selenite group were determined by fitting to the quantum mechanically (QM) determined structure and vibrational modes for the isolated ion. These QM calculations were performed at the M06/cc-pVDZ level of theory [ZHA/TRU2008] using the program NWChem [VAL/BYL2010]. While formally the selenite anion should lose an electron *in vacuo*, the finite basis set constrains the system to remain as SeO_3^{2-}. The parameterization of the intermolecular interactions within the model was performed by fitting to the experimental structure data of $CaSeO_3$ (monocl.) and to the elastic constants of the same phase, which have been computed with the aid of WC-USP by applying the strain-stress relationship. WC-USP based elastic constants are compared to the constants predicted with the optimized force-field model and DFT based and experimental cell parameters are compared in the supporting information to the original article [HEB/VIN2014]. The fitting and the geometry optimization were performed with the General Utility Lattice Program (GULP) [GAL/ROH2003]. The entropies of the supercell within a single defect supercell and the entropies of $CaCO_3$ and $CaSeO_3$ (monocl.) were computed at 298.15 K from the phonon densities of states. These calculations included the calculation of the heat capacity from the phonon density of states at the optimized volume. No correction for thermal expansion was included as this is an insignificant contribution at 298.15 K. The calculations were fully converged with respect to the k-point density within the Brillouin zone.

Given that it is not currently practical to extensively sample the configuration space of water molecules over the surface of calcite using DFT, further use of the force-field calculations can be made to assess the validity of the solvation contribution to the energetics of selenite incorporation. To do this, the COSMIC solvation model [GAL/ROH2007] has been employed to provide information on the solvation free energies of the calcite surface, with and without selenite present. In order to do this, there are several key parameters that go into determining the solvent accessible surface, including the radii of the ions. In a recent work the same solvation model has been used to estimate the interfacial energy between calcite and water [BRU/MAS2013]. However, here the radii were taken from standard tabulations without checking whether they yield the correct thermodynamics for the component ions in solution. In the present work we have fitted the radii of Ca, C, Se, and O against the free energies of hydration of Ca^{2+}, CO_3^{2-} and SeO_3^{2-}. Here the values adopted for Ca^{2+} (-1444 kJ/mol) and CO_3^{2-} (-1315 kJ/mol) [MAR1991] are taken from experiment, while in the case of SeO_3^{2-} the only estimates of the free energy of hydration come from quantum mechanical calculations [WIC/MEL2010] and we have taken the upper bound (-945 kJ/mol). The final solvation parameters are a water dielectric constant of 78.4, a radius shift of 1.2 Å during creation of the solvent accessible surface, which consists of 110 points per atom, and a smoothing range of 0.2 Å. The fitted van der Waals radii for the elements are 1.89, 1.32, 1.32 and 3.34 Å for Ca, C, O and Se, respectively. All force-field calculations for surfaces were run using 2-D periodic boundary conditions within the two region approach, in which the region nearest the surface is fully relaxed while the underlying region is held fixed at the bulk geometry to recreate the potential on the surface region. A thickness of 4 layers of calcite for each region was found to be sufficient to yield converged surface energies.

5.5.2.4 Results and discussion

5.5.2.4.1 Structure of the selenite incorporation species

EXAFS data measured on the powder sample and in a polarization dependent experiment on a single crystal are shown in **Fig. 5.65** (circles). Absorption edge raw data are not shown, but it should be mentioned that none of the spectra showed any indication of reduction or oxidation of selenium during the coprecipitation reactions. The edge energy (E^0) for the subtraction of the background is set to the first inflection point at the absorption edges, which is at 12.664 keV for the powder EXAFS data and at 12.663 keV for the single crystal data. The k-space EXAFS data in **Fig. 5.65**a shows that the orientation of the polarization vector relative to the sample had a clear effect on the amplitude of the signal. For the “bpa” orientation (green) increased amplitude of the EXAFS signal relative to the isotropic data (black) measured on the powder sample is especially obvious. This is expected because the data labeled “bpa” were measured with $\vec{\varepsilon}$ parallel to the [010] direction, which is in the plane of the carbonate ions. This already shows qualitatively that there must be a preferential orientation of the selenite molecule relative to the calcite structure, which is a clear indication for the structural incorporation of selenite into calcite. It is likely that this orientation is parallel to that of the carbonate ions. Quantitative interpretation of the EXAFS data is performed as described in the experimental section. All the spectra are modeled considering four shells of backscattering atoms.

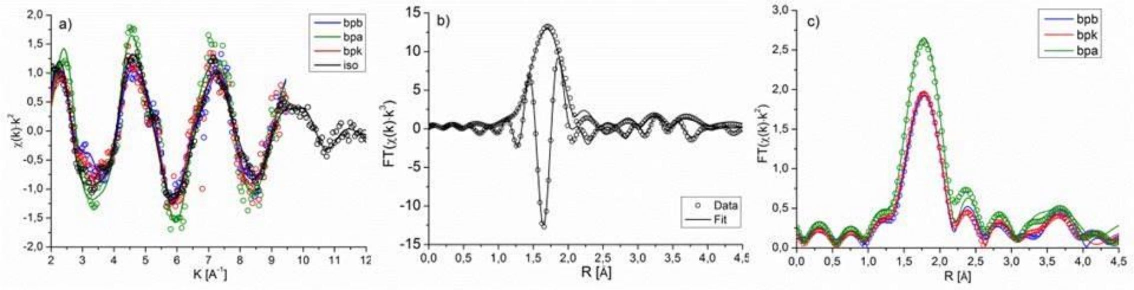

Fig. 5.65 EXAFS data.

a) shows the k^2-weighted EXAFS data (circles) and the corresponding model curves (lines) from isotropic (black, labeled: iso) and the polarization dependent measurements (blue, green, red, labeled: bpb, bpk, bpa (for explanation please see text)

Fourier transformed EXAFS data (circles) and modeling results (lines) are shown in Figures b) and c). b) shows the Fourier transform magnitude and imaginary part of the isotropic data, while c) shows the Fourier transform magnitudes of the polarization dependent data. For reasons of clarity the imaginary parts are not depicted

The first shell (O-SeO_3) contains the three oxygen atoms belonging to the SeO_3^{2-} ion. The second shell (O-CO_3) is also comprised of three oxygen atoms. It is assumed that these oxygen neighbors belong to three different carbonate ions located above the pyramidal selenite ion. The next two shells (Ca1 and Ca2) consist of three calcium atoms each. In the original calcite structure all of these six calcium atoms have the same distance to the central carbon atom of the carbonate ion, but on substituting the flat carbonate ion by a pyramidal selenite ion they become split into two shells with clearly distinct bond distances. The results from the EXAFS data modeling are listed in **Tab. 5.20**. The amplitude reduction factor S_0^2 is 0.85 ± 0.05 for all datasets. It is adjusted to make the coordination number of the O-SeO_3 shell, N_{iso}(O-SeO_3) = 3.0. The bond distances obtained from modeling the isotropic data are in excellent agreement with those reported by Aurelio *et al.* [AUR/FER2010]. They concluded from their structural study of selenium(IV) substitution in calcite, that selenite is structurally incorporated into calcite, where it substitutes for a carbonate ion in the crystal structure. This is the most likely substitution mechanism from a crystal chemical perspective, and is in excellent agreement with our data as well. The coordination numbers we obtain from modeling the isotropic dataset are in even better agreement than the previous work with the value of three, expected for all shells for a substitution of carbonate for selenite. This is probably due to the fact that Aurelio *et al.* kept the Debye-Waller factors, which are strongly correlated with the coordination numbers, at a very low value of 0.002 ± 0.001 for all shells. The adjustment of the Debye-Waller factors in this study, not only improves the agreement with the expected coordination numbers, but it also improves the quality of the fit. Considering the size of the selenite ion compared to a carbonate, we consider it likely that there is a certain degree of disorder in the structure surrounding the selenium atom, which is expressed in elevated Debye-Waller factors.

Tab. 5.20 Results from EXAFS data modeling:

Bond distances, R, Debye Waller factors, σ^2, coordination number obtained from modeling the isotropic data, N_{iso}, and effective coordination numbers obtained from the polarization dependent data, N_{eff}. DFT based bond distances calculated using the WC-USP and PBE-PAW methods (see text for explanation) are listed for comparison

	isotropic / powder			**polarization dependent / single crystal**					**WC-USP**	**PBE-PAW**
shell	R [Å]	σ^2 [Å^2]	N_{iso}	R [Å]	σ^2 [Å^2]	N_{eff} (bpa)	N_{eff} (bpb)	N_{eff} (bpk)	R [Å]	R [Å]
O-SeO_3	1.68 ± 0.01	0.001 ± 0.001	3.0 ± 0.1	1.68 ± 0.01	0.001 ± 0.001	3.8 ± 0.2	2.9 ± 0.2	3.1 ± 0.4	1.71	1.73
O-CO_3	2.88 ± 0.02	0.013 ± 0.006	3.1 ± 0.7	2.88 ± 0.02	0.008 ± 0.003	1.9 ± 0.6	3.2 ± 0.6	3.1 ± 1.1	2.87	2.93
Ca1	3.26 ± 0.02	0.010 ± 0.003	2.7 ± 0.7	3.26 ± 0.02	0.012 ± 0.002	3.6 ± 0.8	2.7 ± 0.7	3.3 ± 1.4	3.27	3.26
Ca2	3.50 ± 0.03	0.009 ± 0.003	2.6 ± 0.8	3.46 ± 0.05	0.008 ± 0.002	3.0 ± 0.7	2.8 ± 0.6	2.5 ± 1.3	3.52	3.59

Uncertainties are standard deviations calculated by ARTEMIS.

Besides the EXAFS investigation, Aurelio *et al.* present neutron diffraction data that indicates a significant variation of the unit cell parameters of calcite due to selenite coprecipitation. However, due to the limited amount of selenium in their precipitates, the change of the unit cell volume is not well correlated with the selenite content of the crystals. A second important point regarding the neutron diffraction data is that there is no indication for the formation of a separate $CaSeO_3$ phase. In the search for additional evidence for the structural incorporation of selenite in calcite we performed polarization dependent EXAFS experiments. Bond distances and Debye-Waller factors derived from modeling the polarization dependent data are in good agreement with those obtained from the isotropic data. The quantification of the polarization effect in terms of N_{eff} values is listed in **Tab. 5.20** and depicted in **Fig. 5.66**. The quantitative interpretation is limited by the uncertainty limits of the effective coordination numbers. For data measured in orientations “bpa” and “bpb” differences in effective coordination numbers are greater than the uncertainty limits for the first two shells. Data measured in orientation “bpk” have a worse signal to noise ratio than the other two datasets. This translates to uncertainties in the effective coordination numbers. Nevertheless, the effective coordination number measured for the first shell in the “bpk” orientation is significantly different from the one measured for orientation “bpa”. The number of degrees of freedom, that are in principle available when trying to find a structural model that fits EXAFS bond distances and effective coordination numbers, is very high. Therefore it has been decided to make some assumptions in regards to the structural model in order to keep it as simple as possible. The selenite ion is placed at the position of a carbonate ion in the calcite structure, with the selenium atom on a threefold symmetry axis, parallel to the *c* axis of the hexagonal calcite coordinate system. Atoms in one shell are only translated in planes perpendicular to the symmetry axis, or the planes are moved along the symmetry axis. Rotations of groups of atoms around the axis do not influence the result and are therefore not considered. Even though this might be more strictly constrained than necessary, this model is already able to reproduce all the effective coordination numbers within the uncertainty, while matching the bond distances determined from the polarization dependent data exactly. Effective coordination numbers obtained for the structural model (Neff_..._model), compared to the measured effective coordination numbers (Neff_..._exp) are displayed in **Fig. 5.66**, along with effective coordination numbers as calculated for the structure obtained from WC-USP calculations (Neff_..._WC). The model, as well as the theoretical structure, matches the experimentally derived effective coordination numbers very well. For a detailed description of the structure resulting from the quantitative interpretation of the polarization dependent EXAFS data and a comparison of this structure to theoretical results please refer to the Supplementary Information file which is available with the original publication [HEB/VIN2014].

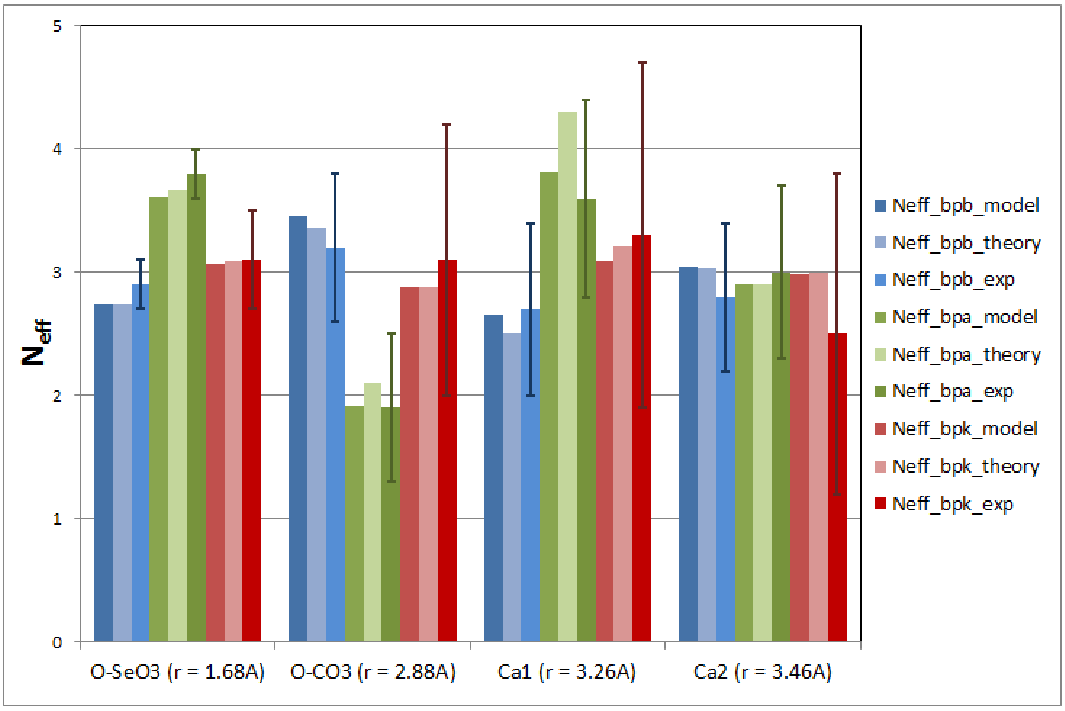

Fig. 5.66 Effective coordination numbers (N_{eff}) for the three different orientations bpa, bpb, and bpk, resulting from the polarization dependent EXAFS experiment (exp) compared to effective coordination numbers according to a simple structural model adjusted to fit the measurements using equation (5.48) (model) and according to the structure obtained from WC-USP calculations (theory). Error bars plotted for the experimental N_{eff} values are standard deviation calculated by the ARTEMIS software

A representation of the proposed best fit structure of the incorporated anion is displayed in **Fig. 5.67**. Indicated are the orientation of the calcite (104) plane and the directions of the polarization vectors corresponding to the three different orientations investigated. The same structure would, of course, be possible with the selenite pyramid pointing the other way around. Due to the $\cos^2$ relation between θ and N_{eff}, the polarization dependent EXAFS data cannot be used to distinguish between these two orientations. It is interesting to note that the effective coordination numbers for orientation “bpk” are all close to three, the value of the real coordination numbers. This is because during the “bpk” measurements $\vec{\varepsilon}$ was parallel to the [46-1] direction. This vector comprises an angle of 57.1 ° with the threefold symmetry axes, which is close to the “magic angle” for polarization dependent EXAFS measurements of 54.7° [SCH/MAN1999].

Based on the structural investigations presented here it is proposed that selenite is structurally incorporated into calcite upon coprecipitation under surface controlled growth conditions. In the calcite structure selenite substitutes a carbonate ion and forms a solid solution with the stoichiometry $Ca(SeO_3)_X(CO_3)_{(1-X)}$, where X denotes the mole fraction of selenite in the solid. This observation is in excellent agreement with the study by Aurelio *et al.* [AUR/FER2010]. In their study calcite is precipitated at very high initial supersaturations (SI(calcite) ~5). Therefore, results by Aurelio *et al.* indicate that the same substitution mechanism is active, even if calcite is precipitated at much higher supersaturations.

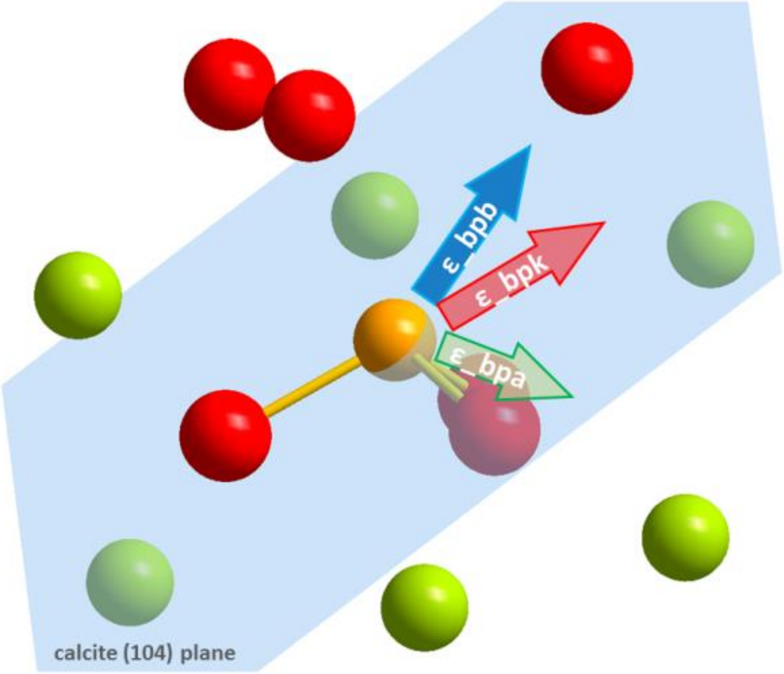

Fig. 5.67 Ball and stick representation of the proposed best-fit structure (Ca: green, O: red, Se: yellow)

Indicated are the orientation of the calcite (104) plane and the directions of the polarization vectors during the polarization dependent measurements. The selenite ion substitutes a carbonate ion in the calcite structure, the selenium atom is located 0.65 Å above the carbon position in calcite, the selenite oxygen atoms are 0.1 Å below the plane of the original carbonate ion and 1.51 Å away from the central axis to yield a trigonal pyramid, as expected for selenite. The calcite environment reacts mainly by upwards and lateral displacement of the calcium atoms, which are located above the selenium atom. ("up" implies the positive direction along the *c*-axis)

5.5.2.4.2 Thermodynamic interpretation of the experimental and theoretical results

Partition coefficients are constant over a large range of selenite content in the solid or liquid phase. This relation can be seen as the linear dependence between c(SeO_3^{2-}) /c(CO_3^{2-}) and X($CaSeO_3$)/X(calcite) in **Fig. 5.68**. From linear regression of the data in **Fig. 5.68** (y-intercept = 0) we obtain the apparent partition coefficient: D_{exp} = 0.02 ± 0.01 (R^2 = 0.99).

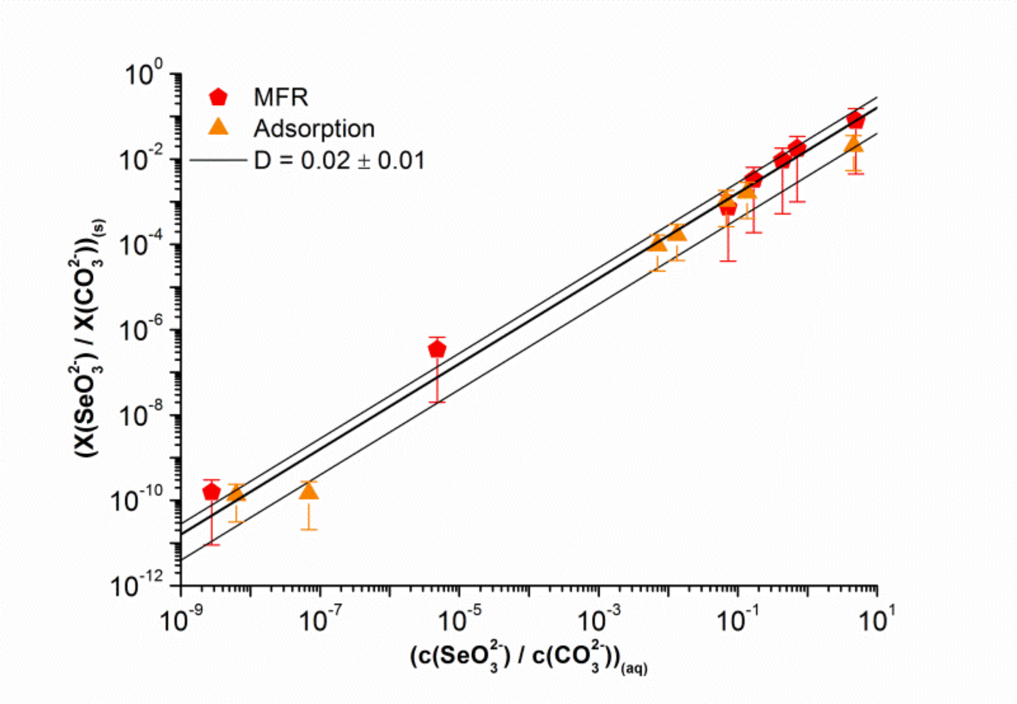

Fig. 5.68 Solid composition, X($CaSeO_3$)/X(calcite), of selenite doped calcite as a function of the composition of the growth (equilibrium) solution, c(SeO_3^{2-})/c(CO_3^{2-})

Over a large range of solid compositions a linear trend is observed, which indicates a constant partition coefficient, consistent with ideal or Henry's law mixing behavior. Results from MFR experiments (red diamonds) are compared to results from adsorption experiments (orange circles). Adsorption data at the highest Se concentration is taken from Cheng *et al.* [CHE/LYM1997], data at intermediate concentrations is adopted from *Cowan et al.* [COW/ZAC1990], adsorption data at the lowest Se concentration is from this study. Error bars show uncertainties estimated for a single measurement based on error propagation calculations

A constant partition coefficient over a large range of solid compositions suggests that it is possible to describe the system as an ideal solid solution (cf. equation (5.26)). If we apply eqns. (5.26), (5.29) and (5.34) to the apparent partition coefficient obtained from linear regression (D = 0.02 ± 0.01), we can calculate an apparent solubility product of the virtual $CaSeO_3$ endmember of $\log_{10}(K_{SP}(CaSeO_{3\_exp})) = -6.7 \pm 1.0$, and a Gibbs free energy of formation of -953 ± 6 kJ/mol, which corresponds to an ΔG^E_{exp} of 2 ± 2 kJ/mol (**Tab. 5.21** and **Tab. 5.22**).

Tab. 5.21 Compilation of thermodynamic data used and obtained in this study

Phase / Species	**ΔG^0 (kJ/mol, at 298.15 K)**	**$\log_{10} K_{SP}$**	**reference**
$CaCO_3$ (calcite)	-1129.08	-8.48	[HUM/BER2002]
$CaSeO_3 \cdot H_2O$	-1188.87	-6.40	[OLI/NOL2005]
$BaCO_3$	-1134.4		[HUM/BER2002]
$BaSeO_3$	-957.2		[OLI/NOL2005]
$CaCO_3$ (aragonite)	-1128.3	-8.34	[HUM/BER2002]
$SrCO_3$	-1144.7		[HUM/BER2002]]
$SrSeO_3$	-962.2		[OLI/NOL2005]
$CaSeO_3$ (monoclinic, reference phase)	-955.5 ± 4	-7.06 ± 0.7	this work
$Ca^{2+}_{(aq)}$	-552.81		[OLI/NOL2005]
$CO_3^{2-}{}_{(aq)}$	-527.90		[OLI/NOL2005]
$SeO_3^{2-}{}_{(aq)}$	-362.39		[OLI/NOL2005]
$H_2O_{(l)}$	-237.14		[OLI/NOL2005]
$CaSeO_{3\ bulk}$ (WC-USP)	-919		this work
$CaSeO_{3\ bulk}$ (PBE-PAW)	-907		this work
$CaSeO_{3\ bulk}$ (PBE-USP)	-912		this work
$CaSeO_{3\ bulk}$ (average)	-912 ± 10	0.5 ± 1.7	this work
$CaSeO_{3\ virtual}$ (experiment)	-953 ± 6	-6.7 ± 1.0	this work

Estimation of the thermodynamic stability of the monoclinic reference $CaSeO_3$ compound

The reaction enthalpy of the reaction $BaSeO_3 + CaCO_3$(aragonite) → $CaSeO_3 + BaCO_3$ (eqn. (5.41)) calculated by WC-USP is -3 kJ/mol. This value, together with the free energies of formation of all the relevant phases (**Tab. 5.21**), yields G($CaSeO_3$, monocl.) = -954 kJ/mol. The enthalpy of the reaction $SrSeO_3 + CaCO_3$(aragonite) → $CaSeO_3$ + $SrCO_3$ (eqn. (5.42)) is -11 kJ/mol. The corresponding free energy value of $CaSeO_3$ is -957 kJ/mol. The difference between these values of the free energy is assumed to characterize the lower limit of uncertainty in these calculations, as it doesn't include the uncertainty of the tabulated thermodynamic constants, which could easily add another 2 kJ/mol to the estimated uncertainty. In subsequent calculations we adopt the average value G($CaSeO_3$, monocl.) = -956 ± 4 kJ/mol. This value corresponds to a solubility product of $\log_{10}(K_{SP}(CaSeO_3$, monocl.)) = -7.06 ± 0.70. It is similar to the measured solubility product of $CaSeO_3 \cdot H_2O$, $\log_{10}(K_{SP}(CaSeO_3 \cdot H_2O))$ = -6.40 ± 0.25 [OLI/NOL2005], the phase that precipitates at elevated Ca^{2+} and SeO_3^{2-} concentrations from aqueous solution at room temperature. This might indicate that the hydrate, $CaSeO_3 \cdot H_2O$, is a metastable phase that persists at standard conditions during the time frame of solubility experiments, while $CaSeO_3$ (monocl.) is only observed in experiments at hydrothermal conditions [WIL/GIE2007]. Another possible explanation is that the stability of $CaSeO_3$ (monocl.) is slightly overestimated.

Tab. 5.22 ΔG^E values and corresponding partition coefficients, *D*

Structure	**Source**	**ΔG^E (kJ/mol)**	***D***
Bulk	average	43 ± 6	10^{-9} (± 1OM)*
Calcite-vacuum interface	PBE-PAW	-15	15
Calcite-vacuum interface	WC-USP	-7	1
Calcite-vacuum interface	PBE-USP	-12	5
Calcite-vacuum interface	average	-11 ± 4	7 (± 1OM)*
Calcite-water interface (Se1)	PBE-PAW	26	$1.2 \cdot 10^{-6}$
Calcite-water interface (Se2)	PBE-PAW	22	$5.7 \cdot 10^{-6}$
Calcite-water interface (Se1)	PBE+D-USP	23	$3.7 \cdot 10^{-6}$
Calcite-water interface (Se2)	PBE+D-USP	11	$4.3 \cdot 10^{-4}$
Calcite-water interface (Se2)	average (Se2)	16 (± 10-18)	$5.0 \cdot 10^{-5}$ (± 2-4 OM)*
Calcite-water interface	experimental	2 ± 2	0.02 ± 0.01

*) ± xOM = ± x order(s) of magnitude

Thermodynamics of the bulk calcite-$CaSeO_3$ solid solution

Using eqn. (5.31) and the calculated DFT enthalpies we obtain values for the excess enthalpy of the virtual bulk $CaSeO_3$ endmember, which are 41 kJ/mol, 53 kJ/mol, and 48 kJ/mol from WC-USP, PBE-PAW, and PBE-USP calculations, respectively. Our force-field calculations give a much smaller value of the excess enthalpy (17 kJ/mol) and an even smaller value of excess Helmholtz free energy (13 kJ/mol). We believe that the force-field model significantly underestimates the excess enthalpy, however, we take the difference between the last two values as the best estimate of the effect of the vibrational free energy. According to our force-field model the vibrational free energy decreases the total excess Gibbs free energy of the virtual bulk $CaSeO_3$ endmember by 4 kJ/mol. Thus our best estimate of the excess Gibbs free energy of the virtual bulk $CaSeO_3$ endmember is 43 ± 6 kJ/mol based on correcting the average DFT excess enthalpy. We conclude that the effect of the vibrational free energy makes a relatively small contribution to the excess Gibbs free energy of the virtual endmember. In subsequent calculations the vibrational contributions to the excess functions will therefore be ignored. The absolute standard Gibbs free energy of the virtual bulk $CaSeO_3$ endmember can be calculated by adding the excess effect of 43 kJ/mol to the standard Gibbs free energy of $CaSeO_3$(monocl.). Thus we obtain a value of $G^0(CaSeO_{3\ bulk}) = -912 \pm 10$ kJ/mol, corresponding to $\log_{10}(K_{SP}(CaSeO_{3\_bulk})) = 0.5 \pm 1.7$.

The computed $G^0(CaSeO_{3\ bulk})$ allows straightforward estimation of the maximum concentration of $CaSeO_3$ in calcite that can be in equilibrium with aqueous solution. In this estimation we assume that the equilibrium ion activity product $IAP(CaSeO_3)$ (cf. eqn. (5.20) and (5.21)) is limited by the solubility product of $CaSeO_3 \cdot H_2O$. Thus the maximum concentration (or mole fraction) can be computed from the equation:

$$G^0(CaSeO_{3\ virtual}) + RT\ln(X_{max}(CaSeO_3)) = G^0(CaSeO_3{*}H_2O) - G^0(H_2O) \qquad (5\text{-}37)$$

Using the values from **Tab. 5.21** we obtain $X_{max} = 10^{-7}$. This value is six orders of a magnitude lower than the highest concentration measured in MFR experiments (ca. 7 %). A more general way to see the striking difference between the experiment and the bulk solid solution theory is to compare the apparent and the theoretically predicted solubility constants of the $CaSeO_3$ endmember ($\log_{10}K = -6.7$ and $\log_{10}K = 0.5$, respectively), the corresponding partition coefficients (0.02 and 10^{-9}, respectively), and ΔG^E values (2 kJ/mol and 43 kJ/mol, respectively).

The small value of the maximum mole fraction of SeO_3^{2-} in calcite is the consequence of the predicted large excess Gibbs free energy of the virtual endmember. Apparently, this value reflects the large stress that the SeO_3^{2-} unit experiences in the calcite structure. This stress can be related to the geometry misfit between the planar CO_3^{2-} unit and the larger SeO_3^{2-} pyramid.

The surface solid solution concept and the thermodynamic entrapment model

Obviously a disagreement of several orders of magnitude between the experimental and computational results for SeO_3^{2-} incorporation into bulk calcite highlighted above requires an explanation. Although the DFT calculated bulk structures are in close agreement with the EXAFS results, the predicted partition coefficient and ΔG^E value differ greatly from those measured experimentally.

Our first assumption was that the high partition coefficient observed in the experiments could be explained within the kinetic model of Shtukenberg *et al.* [SHT/PUN2006]. However, our model calculations showed that if the theoretical partition coefficient, 10^{-9}, is assumed to reflect equilibrium partitioning and the partition coefficient is assumed to approach unity for infinitely high supersaturation, the experimentally observed partition coefficient of 0.02 would be expected at supersaturations exceeding those in MFR experiments by 7 orders of magnitude.

A solution to the problem can be found under the assumption that the experimental concentration of SeO_3^{2-} in calcite is controlled not by the thermodynamic properties of the bulk solid solution, but by the properties of the surface layer of calcite, which provide favorable conditions for the SeO_3^{2-} adsorption. It appears possible that this Se-enriched surface layer can be continuously entrapped and renewed if the supersaturation is sufficiently high.

Cowan *et al.* [COW/ZAC1990] suggested that the selenite adsorption on calcite occurs as an ion-exchange process. This assumption was later confirmed by X-ray standing wave measurements [CHE/LYM1997]. The results of these studies imply that the selenite incorporation into the calcite surface monolayer is more favorable than the incorporation into the bulk of calcite. Conceptually, ion-exchange at the surface is equivalent to the formation of a solid solution within the surface monolayer. Following this line of thought, we can assume that the partition coefficient measured in MFR experiments reflects the thermodynamics of selenite incorporation into the calcite surface monolayer.

SeO_3^{2-} incorporation into such a surface solid solution should be determined by the difference in the free energies of the surface endmembers of $CaCO_3$ and $CaSeO_3$ composition. The latter difference can in turn be defined relative to the free energy difference between calcite and monoclinic $CaSeO_3$ via the $\Delta G^E_{surface}$ parameter, as discussed above. Applying eqn. (5.35) to the experimentally derived partition coefficient, we obtain, $\Delta G^E_{exp} = \Delta G^E_{surface} = 2 \pm 2$ kJ/mol.

The surface solid solution entrapment concept is further developed in **Fig. 5.69**. In coprecipitation experiments, calcite grows with a composition that is determined by the stationary activities of CO_3^{2-} and SeO_3^{2-} in the reactor, and by the thermodynamic properties of the surface solid solution (reaction 1 in **Fig. 5.69**). As discussed above, the precipitation from a supersaturated solution can be fitted into the equilibrium thermodynamic concept under the assumption that the most highly supersaturated solid solution composition precipitates [PRI2009]. The observed high selenite content in MFR experiments can be explained under the assumption that upon crystal growth the surface solid solution is buried under newly formed mineral layers, without being able to change its composition. In other words, the surface solid solution is entrapped (reaction 2 in **Fig. 5.69**). It likely takes a couple of add layers (>4, [FEN/STU2012]) until a bulk-like situation is achieved. Once entrapped in the bulk, the selenite ion and the surrounding calcite host experiences a considerable strain, as reflected by the thermodynamic parameters derived from bulk DFT calculations ($\Delta G^E_{bulk} = 43 \pm 6$ kJ/mol). The amount of energy needed to transform the surface solid solution into a bulk solid solution (indicated in **Fig. 5.69** as $\Delta G_{entrapment}$) can be approximated as:

$$\Delta G_{entrapment} = X \cdot (\Delta G^E_{bulk} - \Delta G^E_{surface}) = X \cdot (41 \pm 8) \text{ kJ/mol.} \qquad (5.38)$$

For the lattice layer to be entrapped continuously, this energy needs to be balanced by the supersaturation. The entrapment model of Watson [WAT2004] includes the possibility of diffusion of the entrapped ions out of a near surface region. If such a process would take place, eqn. (5.38) would not be correct. However, later we'll show that the composition of the surface solid solution formed in the adsorption experiments at equilibrium conditions appears to be consistent with the composition of the solid phase formed via coprecipitation. Therefore we consider the backward diffusion process to be insignificant for selenite coprecipitation with calcite at room temperature. The negligible reverse diffusion is likely to be related to the large size of the SeO_3^{2-} ion.

High SeO_3^{2-} concentrations in bulk calcite resulting from entrapment reflect non-equilibrium. It is interesting to speculate on the fate of Se-calcites at close-to-equilibrium conditions. It is likely that the surface layer might easily change its composition and be equilibrated with an aqueous solution. However, ions in the non-equilibrium bulk cannot exchange with ions in solution except through the surface. The surface layer could thus effectively passivate the solid against the reverse reaction. Whether, over geological periods of time, calcite recrystallization and release of SeO_3^{2-} back into solution (reaction 3 in **Fig. 5.69**) or a metastable preservation of the non-equilibrium bulk is to be expected, remains an open question.

In order to corroborate this thermodynamic entrapment concept we attempt to derive the $\Delta G^E_{surface}$ values required to quantify surface incorporation according to eqn. (5.35) from DFT calculations. Based on equations (5.35) to (5.42) and the various surface DFT calculations, we obtain a range of $\Delta G^E_{surface}$ values. It is interesting to note that calcite-vacuum interface calculations consistently predict a relative stabilization ($\Delta G^E_{surface} < 0$) of the calcite surface upon substitution of surface CO_3^{2-} for SeO_3^{2-}. The corresponding partition coefficients are in the range from 0.6 to 15 and are higher than the experimental value, 0.02 (**Tab. 5.22**).

To simulate the influence of interfacial water on the selenite surface substitution, we have performed DFT calculations including 31 water molecules per supercell above one side of the calcite slab. The water molecules are arranged in three layers as described in the section on atomistic simulations. The predicted structuring of the interfacial water is in good agreement with previous experimental and computational results [FEN/KER2013, HEB/TRA2011, RAI/GAL2010]. The specific effect we were after is the difference in the total energies of the supercells with and without a substitutional defect of SeO_3^{2-} placed in the surface layer. We are aware that a model with only three layers of water in a single configuration represents a crude approximation to dynamical solvation effects. Nevertheless, the calculations with the interfacial water reveal some interesting effects. The $\Delta G^E_{surface}$ values obtained for selenite substitution at the calcite-water interface are drastically increased in the presence of water, compared to the calcite-vacuum interface calculations (**Tab. 5.22**). We observe a periodicity in the water structure, which results in (at least) two non-equivalent sites for the selenite substitution (labeled Se1 and Se2 in **Tab. 5.22**). The $\Delta G^E_{surface}$ values obtained are 26 kJ/mol and 22 kJ/mol for PBE-PAW calculations and 23 kJ/mol and 11 kJ/mol for PBE+D-USP calculations for Se1 and Se2, respectively. The Se1 configuration obviously represents a metastable local minimum in the structure optimization, and so the more stable Se2 configuration is considered the relevant structure for comparison with experimental data. The average $\Delta G^E_{surface}$ value for Se2, 17 kJ/mol, is in relatively good agreement with the experimental value $\Delta G^E_{exp} = 2 \pm 2$ kJ/mol considering the approximate nature of the model.

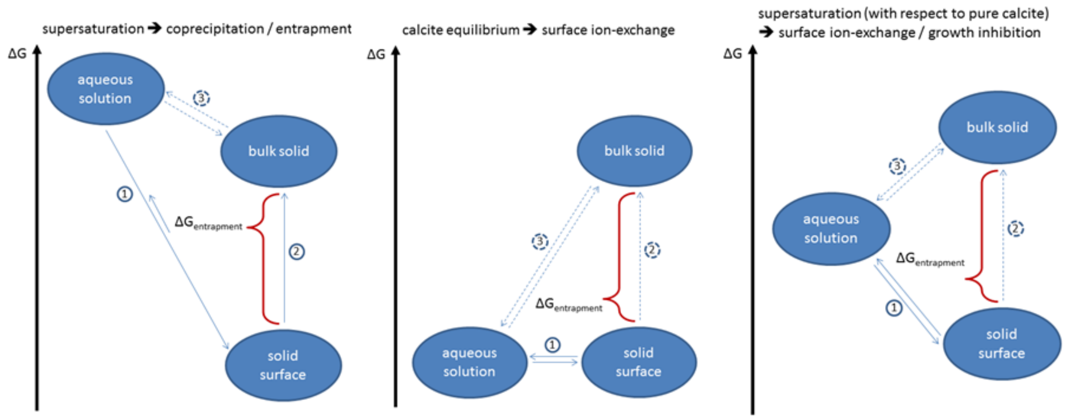

Fig. 5.69 Schematic representation of the entrapment concept

Left, coprecipitation scenario: 1) The composition of the solid surface (SeO_3^{2-}/CO_3^{2-} ratio) “equilibrates” with the aqueous solution according to $\Delta G^E_{surface} = 2 \pm 2$ kJ/mol, meaning the most highly supersaturated surface solid solution forms. 2) Upon growth, the surface solid solution is covered by subsequent crystal layers while keeping its composition. The final bulk solid solution, characterized by the thermodynamic properties of the bulk endmember, $CaSeO_{3\_bulk}$, is highly strained and out of equilibrium. 3) Ions in the bulk cannot exchange with ions in solution except through the surface. Therefore, the surface solid solution may passivate the bulk solid solution against equilibration with aqueous solution. Indicated is the amount of free energy, $\Delta G_{entrapment}$, required for the entrapment process, i. e. the transformation of the surface solid solution into a bulk solid solution of equal composition. Middle, calcite equilibrium conditions: 1) The solid surface equilibrates with the aqueous solution, a surface solid solution forms through a surface ion-exchange / recrystallization process. 2) As there is no driving force for entrapment, no bulk incorporation / recrystallization is expected. 3) If the bulk is pure calcite, no reaction is expected. If there is a non-equilibrium bulk solid solution underneath the surface the same passivation effect as for supersaturated conditions may apply. Right, growth inhibition scenario: 1) The solid surface equilibrates with the aqueous solution. Even though the aqueous solution is supersaturated with respect to pure calcite, the supersaturation is not sufficient to accomplish entrapment. Therefore solid solution growth is inhibited and only surface ion exchange occurs

Due to computational time limitations, we did not explore the convergence of the results with respect to the concentration of selenite in calcite (the size of the supercell) and we have ignored entropic effects. The limited size of the 2x2 supercell also does not allow us to exclude the effect of defect-image interactions. Indeed, due to periodic boundary conditions the SeO_3^{2-} defect will experience the presence of the defect images located in the neighboring periodically repeated images of the supercell. An estimate of the possible error due to defect-image interactions can be obtained from comparing the bulk DFT calculations using different unit cell shapes. Accordingly, we take the standard deviation of ΔG^E_{bulk} values, 6 kJ/mol, as an estimate of this uncertainty. A similar uncertainty is expected in the calculations for the supercells including a vacuum- or water-interface. The model of three layers of water certainly represents a crude approximation to the full dynamical picture of solvation. It is likely that in reality $\Delta G^E_{surface}$ is determined by the averaged effect of many different configurations of water. Our calculations probe just two slightly different configurations of water, Se1 and Se2. The differences between $\Delta G^E_{surface}$ values obtained for the different SeO_3^{2-} substitution sites in the calcite-water interface calculations of 4 – 12 kJ/mol plus the uncertainty due to the defect-image interactions of ca. 6 kJ/mol is used here to associate the likely error in the range of 10 – 18 kJ/mol with the estimated $\Delta G^E_{surface}$ values.

Despite the limitations of surface calculations discussed above, the $\Delta G^E_{surface}$ values derived from DFT closely approach the experimentally derived value, and confirm the assumption that the incorporation of SeO_3^{2-} into the calcite surface is energetically more favorable than the incorporation of SeO_3^{2-} into the bulk calcite structure. It appears that the specific orientation of the SeO_3^{2-} unit, with the Se atom pointing away from the surface, allows a reduction in the stress that exists in the bulk structure. This structural arrangement, obtained in all surface substitution calculations, is in qualitative agreement with the structure obtained by Cheng *et al.* from X-ray standing wave measurements [CHE/LYM1997].

Surface hydration stabilizes the pristine calcite (104) cleavage plane by reducing the surface energy. Therefore it makes the substitution reaction energetically less favorable by ~30 kJ/mol. In other words, the presence of interfacial selenite weakens the surface hydration. This effect is a consequence of the less exothermic free energy of solvation of the selenite anion relative to the carbonate anion. Thus it appears that the presence of the selenite defect reduces the stabilization of the calcite-water interface by decreasing the interfacial free energy.

Using the force-field approach with the COSMIC continuum solvation model this effect can be confirmed, in that hydration increases the $\Delta G^E_{surface}$ value for surface incorporation of selenite by 50 kJ/mol.

Although there is a quantitative discrepancy between the DFT and the force-field result, the key result is the validation of the trend (i. e. the effect of hydration of the surfaces is to increase $\Delta G^{E}_{surface}$ by 23 kJ/mol, 37 kJ/mol, and 50 kJ/mol, for PBE(+D)-USP, PBE-PAW, and Force-Field, respectively).

One significant result that emerges from the continuum solvation calculations is that the calcite (104) surface energy on hydration is reduced from 0.71 Jm^{-2} to 0.28 Jm^{-2}. This change of -0.43 Jm^{-2} is an order of magnitude larger than the equivalent value found by Bruno *et al.* [BRU/MAS2013] using the same approach. In their work Bruno *et al.* claim to have examined the sensitivity to the choice of solvation parameters to demonstrate that the answers they obtain are not especially influenced by these. However, for Ca^{2+} they only examined radii in the range of 2.75 to 2.90 Å, compared to a best fit value of 1.89 Å used here. (Note that the exact radius that should be used to reproduce our results is 1.8885 Å). This means that their free energies of hydration for Ca^{2+} were underestimated by between 453 and 504 kJ/mol, leading to strongly reduced solvation of the calcite surface.

Adsorption

The entrapment concept implies that equilibrium incorporation into the bulk crystal is practically impossible, while the spontaneous structural incorporation of SeO_3^{2-} into calcite at equilibrium conditions can occur within the surface monolayer (**Fig. 5.69**, middle). To test this hypothesis we compare the partition coefficients measured in MFR coprecipitation experiments to the partition coefficients that describe the surface incorporation (ion-exchange) measured in selenite adsorption experiments at equilibrium conditions (SI(calcite) = 0). Our experiments (**Fig. 5.70**) are consistent with $K_D \approx 2$ mL/g at pH < 9.

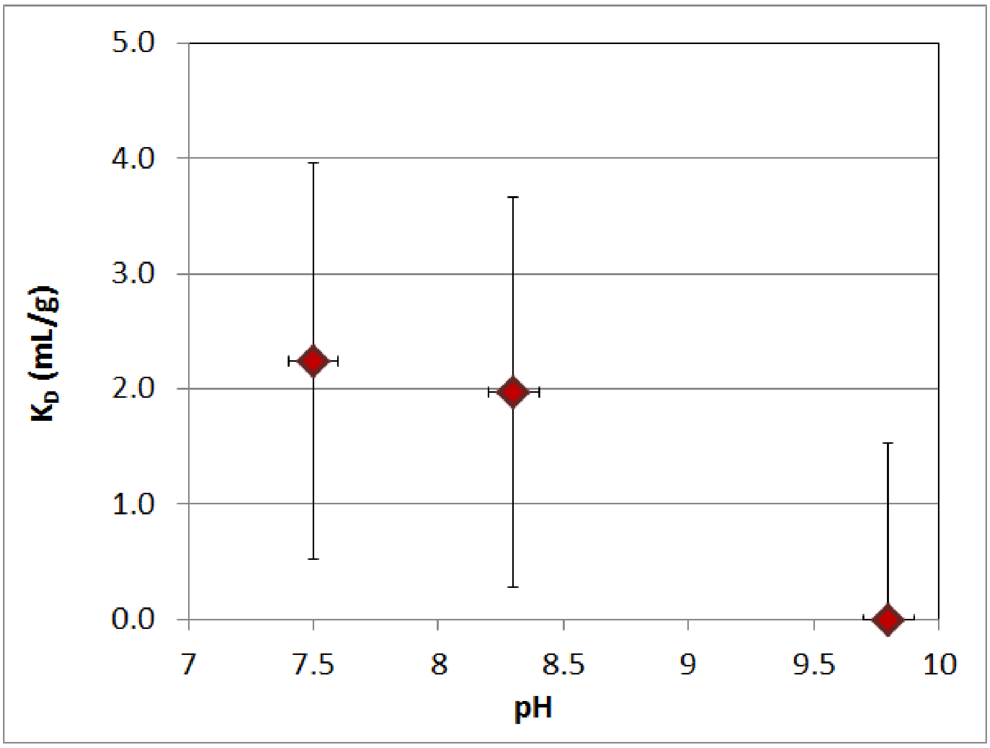

Fig. 5.70 K_D values for selenite adsorption on calcite as a function of solution pH, as derived from batch type adsorption experiments in this study

Error bars show uncertainties estimated for a single measurement based on error propagation calculations

Regarding the total adsorbed amount and the pH dependence of adsorption, our results are in good agreement with previous experiments by Cowan *et al.* [COW/ZAC1990]. Within the proposed entrapment concept the adsorption K_D can be translated into a partition coefficient related to a surface monolayer solid solution. The data for adsorption experiments in the pH range from 7.5 to 8.2 are plotted as orange circles in **Fig. 5.68**. This range covers the pH range of MFR experiments (except for the experiment MFR-Se EXAFS). The data in **Fig. 5.68** at low concentrations are taken from the adsorption experiments performed in the present study, while the data at intermediate concentrations are calculated from the adsorption isotherms by Cowan *et al.* [COW/ZAC1990]. The data point at the highest Se concentration is calculated from the surface coverage and the solution composition reported by Cheng *et al.* [CHE/LYM1997]. The agreement between the *D* values related to adsorption and coprecipitation is remarkable. It strongly supports the concept that coprecipitation is a series of surface ion-exchange reactions and subsequent entrapment events. The observed similarity of the *D* values supports the hypothesis that surface diffusion plays a negligible role during selenite coprecipitation. Furthermore, the agreement between partition coefficients obtained in equilibrium adsorption and coprecipitation experiments at supersaturated conditions justifies the approach to apply equilibrium thermodynamic expressions to coprecipitation experiments at supersaturated conditions.

The fact that the surface adsorption strongly decreases at high pH, and the similarity between surface adsorption and coprecipitation, suggests that similar pH dependence should be expected in coprecipitation experiments. However, the MFR experiment conducted to synthesize the non-radioactive Se-calcite, MFR-Se EXAFS, showed significant selenite incorporation at pH 10.33. The amount of selenite incorporation was, however, not quantified in this experiment. Further MFR experiments will be necessary to investigate selenite coprecipitation with calcite as a function of pH.

Entrapment energy and growth inhibition

For a crystal to grow a supersaturated contact solution is required. Our entrapment concept suggests that for a surface solid solution to grow, the driving force should be sufficient to compensate the free energy, which is required for transforming the surface solution into the bulk solid solution. This energy is indicated as $\Delta G_{entrapment}$ in **Fig. 5.69**. This driving force for solid solution growth is only sufficient if the aqueous solution is supersaturated with respect to the bulk solid solution. The composition of the bulk solid solution, for which the supersaturation condition has to be fulfilled, is determined by the thermodynamics of the surface solid solution.

According to Prieto [PRI2009], the stoichiometric supersaturation of an aqueous solution with respect to a solid solution is defined as;

$$\sigma = [a(Ca^{2+})\ (a(CO_3^{2-})^{(1-X)}\ a(SeO_3^{2-})^{X})\ ]\ /\ [K_{SP}(calcite)\ ^{(1-X)}\ K_{SP}(CaSeO_{3\_virtual\_bulk})^{X}\ ] \qquad (5.39)$$

where *X* is the mole fraction of $CaSeO_3$ in the solid solution. It can be calculated on the basis of the experimental value, $\Delta G^E_{surface} = 2 \pm 2$ kJ/mol, and eqns. (5.35) and (5.19). Eqn. (5.39) implies that the solid solution with the composition X can grow only when $\sigma > 1$.

The above concept provides a consistent explanation of our aragonite recrystallization experiments in the presence and absence of selenite. In these experiments the maximum supersaturation with respect to calcite is given by the solubility difference between aragonite and calcite, and is intrinsically very low (SI(calcite) = 0.14). The SeO_3^{2-} concentration in the selenite containing experiment is chosen to be relatively high: 10^{-4} mol/L. Based on the experimentally measured partition coefficient, at these conditions, the surface solid solution is predicted to contain 3 % (mol) $CaSeO_3$. In these calculations we assume that the aqueous speciation is controlled by the equilibrium with aragonite and atmospheric CO_2. Consequently, the aqueous solution is supersaturated with respect to pure calcite, but is undersaturated with respect to the bulk calcite-$CaSeO_3$ solid solution (σ = 0.79, right scheme in **Fig. 5.69**). **Fig. 5.71** illustrates our experimental results. These results show that in the selenite-free system (blue diamonds) aragonite dissolves over the experimental period of 420 days in favor of precipitation of the thermodynamically more stable calcite. In the selenite containing system (red squares) the formation of calcite is inhibited. In this system pure calcite cannot form, as all calcite surfaces would contain 3 % (mol) $CaSeO_3$, and the driving force is not high enough to entrap such a solid solution.

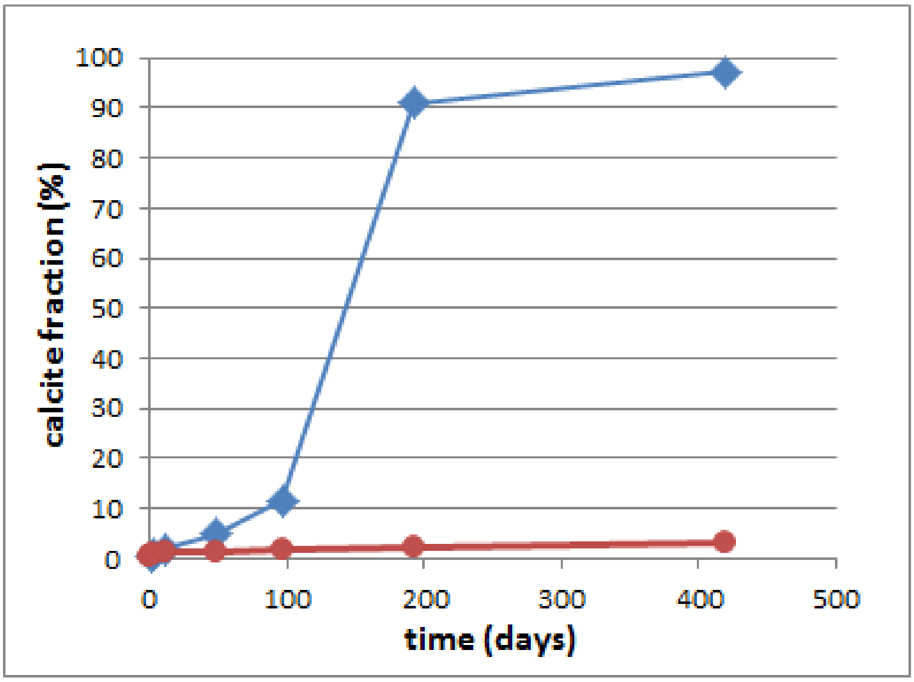

Fig. 5.71 Aragonite → calcite recrystallization experiments

In the selenite free system (blue diamonds) the calcite fraction increases during the run of the experiment due to recrystallization of aragonite to calcite. In the selenite containing system (red squares) the formation of calcite is inhibited

The observed inhibition could also be explained under the assumption that protruding step edges at the calcite surface are blocked by the impurities and are only able to proceed if the impurities are released back into the solution. It seems very likely that such a process would be extremely slow. At this stage we can only speculate on the exact mechanism of inhibition. Nevertheless, the absence of growth in the aragonite to calcite recrystallization experiment in the presence of Se(IV) is a strong experimental confirmation of the low stability of the virtual bulk $CaSeO_3$ endmember, because the high ΔG^E_{bulk} value is required to explain the undersaturation with respect to the bulk solid solution.

It should be mentioned that the aragonite used in the recrystallization experiments initially contains about 3 % of vaterite. Due to the lower stability of vaterite compared to aragonite this leads to an initial period where SI(calcite) = 0.6 and the bulk solid solution is supersaturated ($\sigma = 2.63$ at an expected mole fraction of: $X = 2$ % (mol)). Accordingly, solid solution growth is expected for an initial period until all vaterite is consumed. Indeed, the increase in the calcite fraction during the 420 day reaction period is not zero, but just enough (2.9 %) to account for the initial presence of vaterite.

5.5.2.5 Summary and conclusions

According to EXAFS investigations selenite is structurally incorporated into calcite upon coprecipitation at low supersaturation and slow growth rates. Upon coprecipitation a $Ca(SeO_3)_X(CO_3)_{(1-X)}$ solid solution is formed. The structural environment of selenite in calcite according to EXAFS is in good agreement with the corresponding structures derived from DFT calculations and with previous studies [AUR/FER2010].

From Mixed Flow Reactor experiments we derive an apparent partition coefficient for the selenite incorporation, $D = 0.02 \pm 0.01$, which corresponds to a solubility of a virtual $CaSeO_3$ endmember of: $\log_{10}(K_{SP}(CaSeO_{3\_exp})) = -6.7 \pm 1.0$.

To corroborate this result, density functional theory based SDM calculations are used to predict the thermodynamics of mixing in the diluted solid solution of $CaSeO_3$ in $CaCO_3$. The SDM as used here is seen as a generalization of the previously introduced Single Defect Method [SLU/KAW2002, VIN/BRA2013] to a non-isostructural solid solution. The application of SDM provides the possibility to compute the standard Gibbs free energy of a virtual endmember, which by definition makes an ideal solid solution with the host phase. In contrast to the experiment, our DFT result suggests a much lower stability of the virtual bulk endmember, $\log_{10}(K_{SP}(CaSeO_{3\_bulk})) = 0.5 \pm 1.7$. This low stability suggests a maximum concentration of SeO_3^{2-} in calcite of $X_{max} = 10^{-7}$ and a partition coefficient of $D = 10^{-9}$. This shows that incorporation of selenite into calcite under the conditions of true thermodynamic equilibrium is practically impossible.

To resolve the discrepancy between experiment and calculations, a surface entrapment model is proposed. The concept is based on the idea that substitution of carbonate by selenite in the calcite surface monolayer is energetically much less unfavorable compared to incorporation into the bulk crystal structure. The surface layer of calcite is therefore treated as a separate solid solution phase.

By treating the present batch type adsorption experiments and earlier results on selenite-adsorption [CHE/LYM1997, COW/ZAC1990] in a pH range between 7.5 and 8.2 as the thermodynamic equilibrium between the aqueous and the surface solid solutions, it is shown that the adsorption data can be described by the same partition coefficient as the results of the selenite uptake via coprecipitation in an equivalent pH range. The adsorption experiments thus differ from the analogous coprecipitation experiments only in the degree of supersaturation, which may or may not be sufficient to maintain the continuous entrapment process. In the close to equilibrium case the incorporation stops when the original surface is equilibrated, while in the latter case continuous adsorption, growth, and entrapment are expected. Aragonite recrystallization experiments confirm that continuous growth of the solid solution is only possible if the aqueous solution is supersaturated with respect to the bulk calcite-$CaSeO_3$ solid solution, i. e. if the driving force is high enough to accomplish entrapment. These observations strongly support the central argument of the proposed concept, that there is a relatively large energetic difference between the surface and the bulk calcite-$CaSeO_3$ solid solutions. It can be quantified by the entrapment energy, $\Delta G_{entrapment} = X \cdot (41 \pm 8)$ kJ/mol. This difference in the Gibbs free energies of the endmembers of this solid solution and consequently the relative ease of the SeO_3^{2-}/CO_3^{2-} substitution within the surface layer is confirmed with the SDM.

The practical consequence of the entrapment model for the interaction between aqueous selenite and calcite is that in equilibrium solutions interactions between selenite and calcite are restricted to the calcite surface monolayer. Thus, at near-equilibrium conditions calcite has only a limited potential to immobilize SeO_3^{2-}. However, depending on the system in consideration the retention can still be significant with the K_D for adsorption being 0.002 ± 0.002 L/g (= 0.004 ± 0.003 L/m^2) below pH 9 and going to zero above pH 9. Structural incorporation into bulk calcite only occurs if the aqueous solution is supersaturated with respect to the bulk calcite-$CaSeO_3$ solid solution. In such a case selenite coprecipitates with calcite with the partition coefficient of $D = 0.02 \pm 0.01$. As a consequence, high SeO_3^{2-} concentrations in bulk calcite reflect non-equilibrium. So far we can only speculate on the long-term behavior of Se-calcites at close-to-equilibrium conditions. It is likely that the surface layer can easily change its composition and be equilibrated with an aqueous solution. However, ions in the non-equilibrium bulk are not able to exchange with ions in solution except through the surface. The surface layer could thus effectively passivate the solid against recrystallization and release of SeO_3^{2-} into solution.

The model proposed here to describe selenite coprecipitation with calcite is not necessarily restricted to this system only. It might also apply to other pairs of host mineral and incorporated impurity. This will especially be true where the impurity ions experience a large stress upon incorporation into the bulk of the host mineral, while they are relatively well structurally compatible with the host mineral surface. Most obvious candidates for such systems are anionic substitutions where anions of the host mineral are substituted by complex anions that differ in size and geometry, like the case considered in this study. Similar effects might govern the incorporation of complex cations (e. g. actinyl cations) into host minerals of monatomic cations. Even simple cationic substitutions, particularly those characterized by large size mismatch between the host and the impurity cation, could to some extent be influenced by different thermodynamic properties of the surface and bulk solid solutions.

Acknowledgements

The synchrotron light source ANKA (Karlsruhe, Germany) is gratefully acknowledged for provision of synchrotron radiation beam time. The German Federal Ministry of Economics and Technology (BMWi) within the VESPA project (grant agreement n° 02 E 10800) is thanked for financial support. The authors would like to thank Eva Soballa and Dr. Dieter Schild for SEM and XPS. Tanja Kisely is acknowledged for performing BET analyses. The INE workshop is thanked for technical assistance.

5.6 Studies on ^{14}C speciation, Tc uptake by Fe(II) phases and synthesis of Mg-oxychloride phases

5.6.1 Synthesis and pretreatment of Mg-oxychloride for I-129 diffusion experiments

Mg-oxychloride phases (so-called Sorel phases) are binder phases of magnesia cement which is considered as geo-engineered in current concepts for the final disposal of radioactive waste in salt rock. In recent studies it was shown that Mg-oxychloride phases are capable to buffer pH conditions, sequester dissolved inorganic carbon species and influence favourably the geochemical conditions in the near field of radioactive waste products, which then in turn directly affect potential radionuclide migration processes (e. g. [ALT/MET2003, MET/VEJ2004, XIO/DEN2010]. In recrystallizing experiments a significant sorption of trivalent europium and curium onto Mg-oxychloride was found in concentrated $MgCl_2$ (± NaCl) solutions [WIE2012]. Experiments to determine the retention of ^{129}I by Mg-oxychloride are prepared to be performed within the VESPA-II project. In the framework of this work package of the VESPA-I project, various methods were applied to synthesize virtually monomineralic Mg-oxychloride samples. The Mg-oxychloride samples were characterized using a series of solid phase analyses. Finally, synthesized Mg-oxychloride was equilibrated in concentrated $MgCl_2$ (± NaCl) solutions, to be used in future ^{129}I diffusion experiments.

5.6.1.1 Synthesis of Mg-oxychloride samples

In the system $Mg(OH)_2$–$MgCl_2$–H_2O two Mg-oxychloride phases occur at ambient temperature, whereof the metastable $Mg_3(OH)_5Cl\cdot 4H_2O(s)$ phase transforms into the thermodynamically stable $Mg_2(OH)_3Cl\cdot 4H_2O(s)$ phase [FRE/VOI2010]. For application in future ^{129}I diffusion experiments the long-term stable phase $Mg_2(OH)_3Cl\cdot 4H_2O(s)$ was synthesized by reaction of brucite $Mg(OH)_2(s)$ (BioUltra, 99.0 %, Fluka) and $5\ mol\cdot(kg(H_2O))^{-1}$ $MgCl_2$ solution in a glove box with an argon atmosphere (≤ 5 ppm CO_2 / O_2) at room temperature. Other synthesis procedures, such as dissolution of periclase MgO(s) in $MgCl_2$ solution or precipitation of $Mg_2(OH)_3Cl\cdot 4H_2O(s)$ in oversaturated $MgCl_2$-NaOH solution resulted in polymineralic solids. In the following, solely the $Mg_2(OH)_3Cl\cdot 4H_2O(s)$ synthesis by means of brucite dissolution in $MgCl_2$ solution is described.

The $MgCl_2$ solution was prepared by dissolving $MgCl_2 \cdot 6H_2O(s)$ (p. a., Merck) in purified water from a Milli-Q$^{(+)}$ plus ultra-pure water system (with a resistivity of 18.2 MΩ·cm at 25 °C, Merck Millipore) and saturated with argon over 30 minutes to remove CO_2. The stoichiometric ratio of 3 $Mg(OH)_2$: 1 $MgCl_2$: 11 H_2O includes pore water ($MgCl_2$ solution) which speeds up the transformation of the metastable $Mg_3(OH)_5Cl \cdot 4H_2O(s)$ phase into the $Mg_2(OH)_3Cl \cdot 4H_2O(s)$ phase, as illustrated in reaction scheme (eqn. 5.40). After two weeks the setting of the Mg-oxychloride phase was finished. Thereafter the sample was purified with ultra-pure Milli-Q water and dried for one week at 60 °C.

$$\begin{aligned} & 15\ Mg(OH)_2(s) + \underbrace{5\ MgCl_2 + 55\ H_2O}_{5\ m\ MgCl_2\ \text{solution}} \\ & \xrightarrow{\text{RT, Ar}} \underbrace{6\ Mg_3(OH)_5Cl \cdot 4H_2O + 2\ MgCl_2 + 31\ H_2O}_{\text{metastable phase + pore water}} \\ & \xrightarrow{\text{RT, Ar}} 10\ Mg_2(OH)_3Cl \cdot 4H_2O(s) + 15\ H_2O \end{aligned} \tag{5.40}$$

5.6.1.2 Characterization of synthesized Mg-oxychloride samples

The synthesized Mg-oxychloride was characterized by means of X-ray diffraction (XRD), scanning electron microscopy with energy-dispersive X-ray analysis (SEM-EDX), thermal gravimetric analysis combined with difference scanning calorimetry (TGA-DSC), BET-N_2 surface area analysis, Raman spectroscopy and X-ray photoelectron spectroscopy. Results of the solid phase analyses indicate a virtually pure Mg-oxychloride sample; besides $Mg_2(OH)_3Cl \cdot 4H_2O(s)$ no additional phase was detected.

The Mg-oxychloride sample was grinded to fine powder and mounted on a crystal silicon wafer for XRD analysis. The data was collected within 5° $\leq 2\Theta \leq$ 80° with a step size of 0.01°, 8 seconds measuring time per step, rotation of 15 rpm and a divergent slit of 20 mm using an AXS D8 Advance diffractometer (Cu K_α radiation) equipped with an energy dispersive detector (Sol-X). The phase identification was performed with the *DIFFRAC.EVA* software (version 2.1, Bruker) by comparison to the *JCPDS 2* database. The diffractogram of the synthesized Mg-oxychloride sample shows a single phase with strong reflexes at 10.9°, 21.9°, 23.0°, 32.9° and 36.6° (**Fig. 5.72**). The observed reflexes are in good accordance with the $Mg_2(OH)_3Cl{\cdot}4H_2O(s)$ diffraction pattern (PDF 036-0338) recorded by de Wolff *et al.* [DEW/WAL1953].

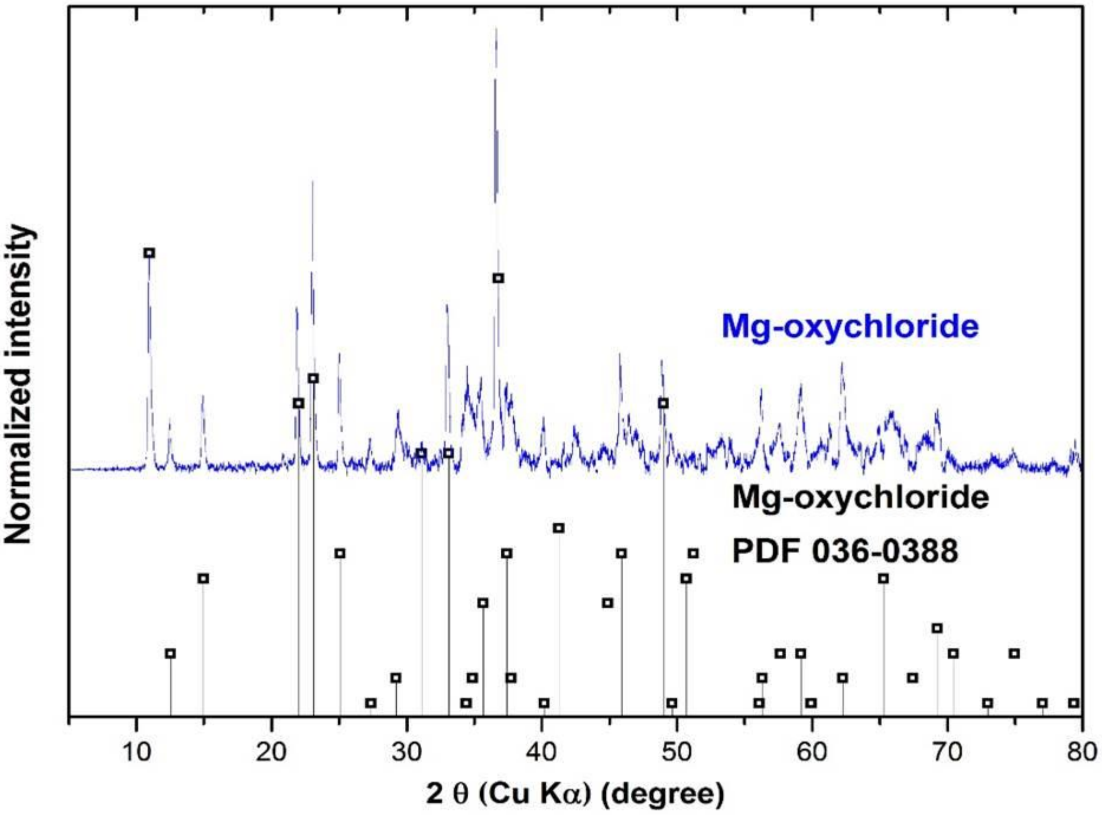

Fig. 5.72 XRD pattern of synthesized Mg-oxychloride

Reference spectrum of Mg-oxychloride ($Mg_2(OH)_3Cl{\cdot}4H_2O(s)$, PDF 36-0388) is included for comparison purposes

The thermal behaviour of the synthesized Mg-oxychloride sample was investigated by TGA-DSC. Five replicate measurements were performed with a STA409C/CD TG-DSC apparatus from NETZSCH. The sample was heated up to a temperature of 600 °C in steps of 10 $K{\cdot}min^{-1}$. The heat induced mass change of Mg-oxychloride proceeds via several steps to the final decomposition product MgO(s) [FEI/HEL1944, COL/DEM1955]. Equation (5.41) represents the thermal degradation of Mg-oxychloride by elimination of H_2O and HCl:

$$Mg_2(OH)_3Cl{\cdot}4H_2(s) \xrightarrow{\Delta T} 2\,MgO(s) + 5\,H_2O\uparrow + HCl\uparrow \qquad (5.41)$$

The thermal behaviour of Mg-oxychloride in the temperature range of 0 – 60 °C is displayed in **Fig. 5.73**. The thermal decomposition proceeds in two steps. From 60 –

300°C, the four chemically bound water molecules are released. From the intermediate phase $Mg(OH)_3Cl$, H_2O and HCl are eliminated by formation of MgO(s) at 400 – 550°C. The measured mass loss of the Mg-oxychloride sample (59.64 ± 0.15 %) is close to the calculated mass loss for $Mg_2(OH)_3Cl{\cdot}4H_2O(s)$ (61.09 %).

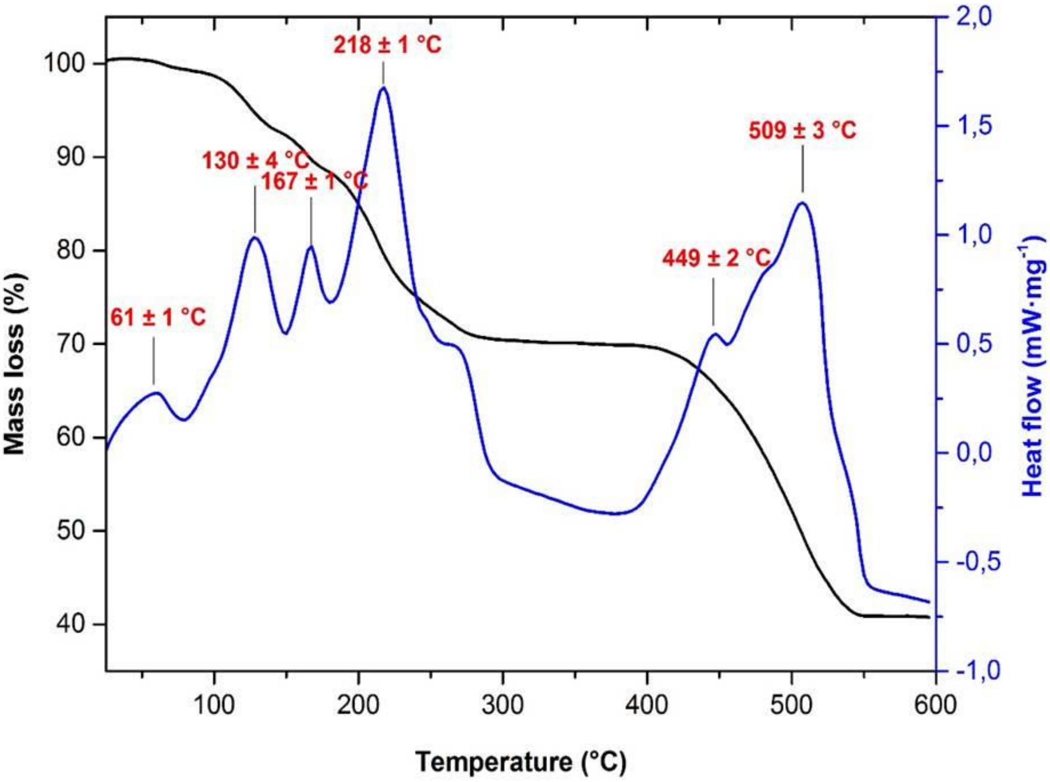

Fig. 5.73 Thermal gravimetric analysis of synthesized Mg-oxychloride

The morphology of the synthesized Mg-oxychloride was analysed using a scanning-electron microscopy with a Quanta 650 ESEM (FEI) microscope, and the elemental composition of the sample was determined using an EDX detector (Noran). The measurements were conducted with a cathode acceleration potential of 30 kV and a current of 1 µA. SEM micrographs of the Mg-oxychloride sample show several 100 micrometres large aggregates composed of rod shaped particles (**Fig. 5.74**). Individual Mg-oxychloride particles have a length of a few micrometres (≤ 10 µm). A Mg:Cl ratio of 1.5 ± 0.3 was determined by EDX and is in agreement with the chemical formula of $Mg_2(OH)_3Cl{\cdot}4H_2O(s)$.

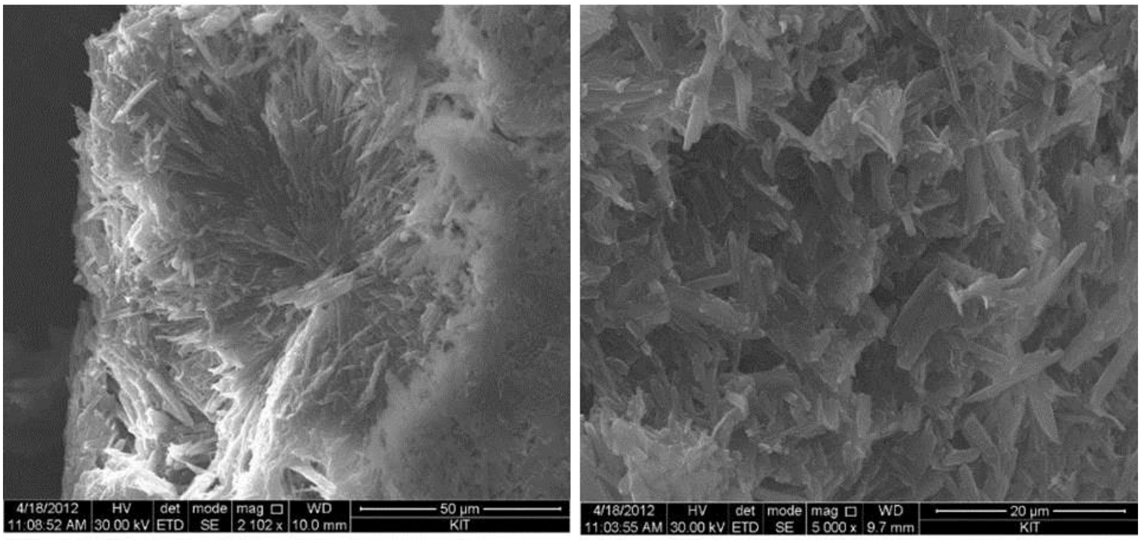

Fig. 5.74 Scanning-electron microscope images of synthesized Mg-oxychloride

The BET-N_2 adsorption method [BRU/EMM1938] was used to determine the surface area of the synthesized Mg-oxychloride. The sample was de-gassed *in vacuo* for 24 h at 60 °C and analysed five times using an Autosorb device (Quantachrome). A specific surface area of $10.5 \pm 0.3\ m^2 \cdot g^{-1}$ was found for the synthesized Mg-oxychloride sample.

Raman spectra of the sample were recorded using a Senterra spectrometer (Bruker) at excitation wavelengths of 532 and 785 nm. Signals at both wavelengths were identified as Raman bands. Before the measurement, Mg-oxychloride was prepared on an indium foil. The recorded Raman bands for Mg-oxychloride are shown in **Fig. 5.75**. Mg-O stretching vibration of the MgO_6 octahedra causing the Raman band in the region between 800 and 100 cm^{-1}, referring to the Raman spectrum of the precursor material $Mg(OH)_2$(s) (BioUltra 99.0 % Fluka brucite) with a sharp band of the Mg-O stretching vibration at 451 cm^{-1}. The Raman spectrum of Mg-oxychloride is in good accordance with $Mg_2(OH)_3Cl \cdot 4H_2O$(s) spectra of Dinnebier *et al.* [DIN/OES2012] and Kanesaka *et al.* [KAN/AOY2001].

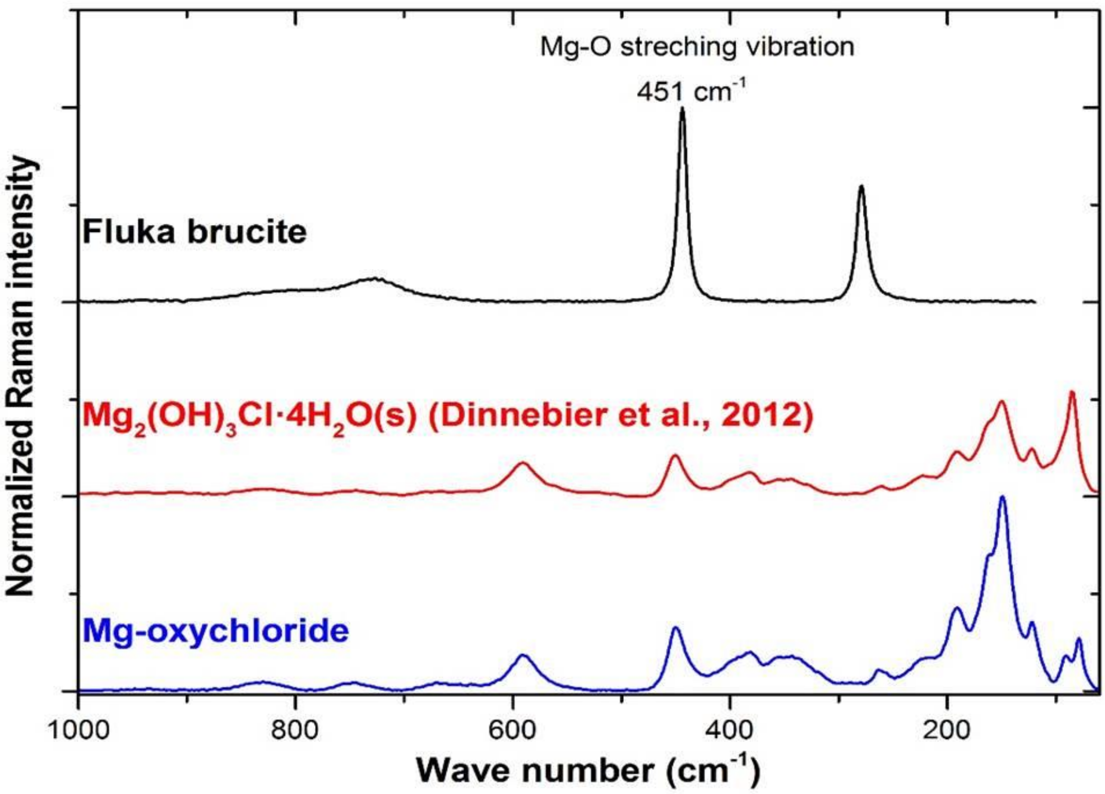

Fig. 5.75 Raman spectra of synthesized Mg-oxychloride and brucite (BioUltra, 99.0 %, Fluka). Reference spectrum of $Mg_2(OH)_3Cl\cdot 4H_2O(s)$ [DIN/OES2012] is included for comparison purposes

XPS analyses of the sample surface was performed using a VersaProbe spectrometer (ULVAS-PHI), equipped with a hemispherical analyser and a multichannel detector. Mg-2*s* signals are induced by excitation with Al-K_α X-rays at 1486.6 eV. The sample preparation was the same as applied for the Raman spectroscopy. The error of the method is ± 10 – 20 at. %. The wide-scan spectrum of Mg-oxychloride shows the elements Mg, Cl, O, F and C present on the few nanometres thin sample surface (**Fig. 5.76**a). The surface composition was rescaled without C and consists of 51 ± 10 At % O, 27 ± 5 At % Mg, 18 ± 4 At % Cl and an impurity of 4 ± 1 At % F. The Mg:Cl ratio of 1.5 ± 0.3 is in good accordance with the results from SEM-EDX and with the chemical composition of $Mg_2(OH)_3Cl\cdot 4H_2O(s)$. A narrow scan in the energy range of the C 1*s* signal is shown in **Fig. 5.76**b. Due to contact with the laboratory atmosphere during the preparation, about 23 % of the C 1*s* signal was related to carbonate. The rest of the C 1*s* signals are traces of organic hydrocarbons (C_xH_y). It is emphasized that flour and carbon contamination is restricted to the few nanometres thick surfaces of the Mg-oxychlorides.

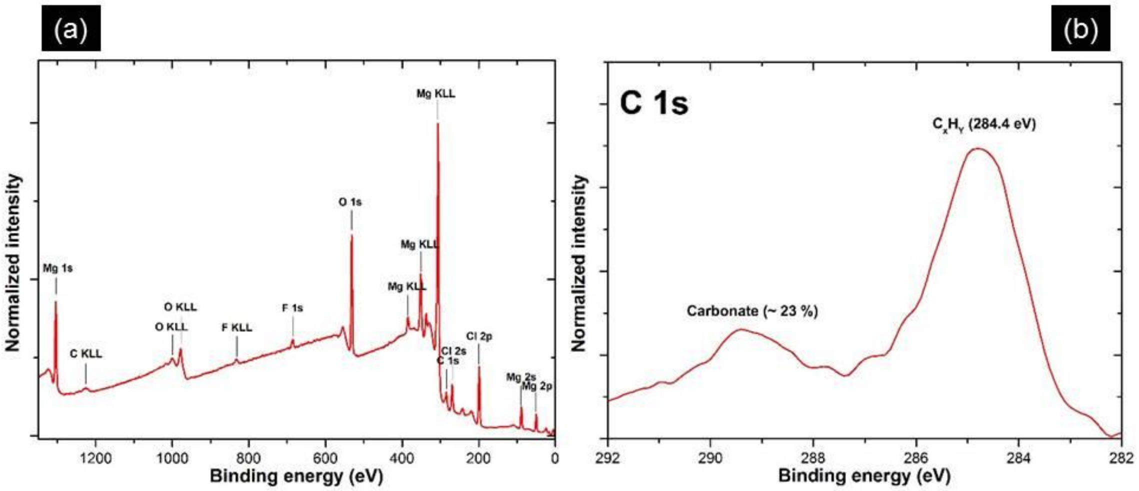

Fig. 5.76 XPS results of synthesized Mg-oxychloride: (a) shows the wide-scan XPS spectrum of the Mg-oxychloride sample and (b) a narrow scan in the energy range of C 1*s*

5.6.1.3 Equilibration of synthesized Mg-oxychloride in salt brines

Synthesized Mg-oxychloride samples were equilibrated for more than two months in 3.3 mol·$(kg(H_2O))^{-1}$ $MgCl_2$, 5.0 mol·$(kg(H_2O))^{-1}$ $MgCl_2$ and 3.0 mol·$(kg(H_2O))^{-1}$ $MgCl_2$ + 1.0 mol·$(kg(H_2O))^{-1}$ NaCl solutions with ionic strengths ≥ 9.9 mol·$(kg(H_2O))^{-1}$ (**Tab. 5.23**). Solution compositions in equilibrium with Mg-oxychloride were calculated using the PHREEQC geochemical code [PAR/APP1999] and the Harvie *et al.* [HAR/MOL1984] thermodynamic database. **Fig. 5.77** presents the studied Mg-oxychloride / $MgCl_2$ (± NaCl) solution systems together with the stability fields of brucite $Mg(OH)_2(s)$ and Mg-oxychloride $Mg_2(OH)_3Cl{\cdot}4H_2O(s)$ at 25 °C (system Mg^{2+}—Na^+—Cl^-—OH^-—H_2O). Calculated equilibrium pH_m values are given in **Tab. 5.23**.

Tab. 5.23 Studied Mg-oxychloride/$MgCl_2$ (± NaCl) solution systems, calculated equilibrium pH_m values, corresponding ionic strengths and parameters for conversion of measured pH values into pH_m values, A_m

Solution	**Solid**	**equilibrium pH_m (calc.)**	***I* (molal)**	**A_m (molal)**
3.0 m $MgCl_2$ + 1.0 m NaCl	Mg-oxychloride	8.77	10	1.64
3.3 m $MgCl_2$	Mg-oxychloride	8.72	9.9	1.6
5.0 m $MgCl_2$	Mg-oxychloride	8.66	15	2.62

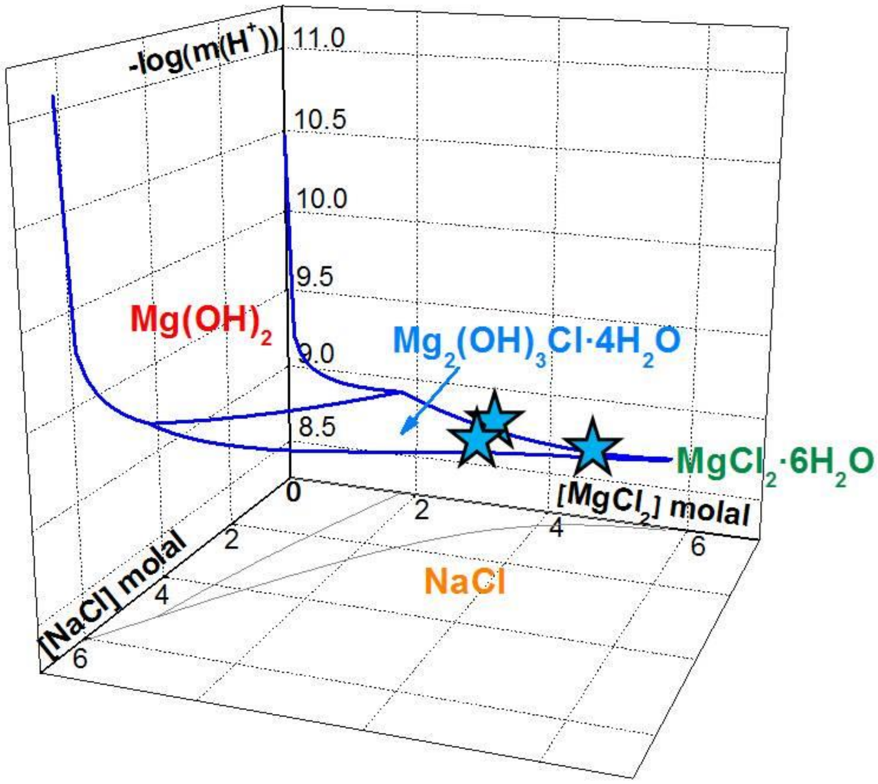

Fig. 5.77 Mg-oxychloride / $MgCl_2$ (± NaCl) solution systems, indicated by stars, in the phase diagram for Mg^{2+}-Na^+-Cl^--OH^--H_2O at 25 °C

Equilibration experiments with these three Mg-oxychloride / salt brine suspensions were conducted in a glove box with an argon atmosphere (≤ 5 ppm CO_2 / O_2) at room temperature. The salt solutions were prepared by dissolving $MgCl_2 \cdot 6H_2O(s)$ (p. a., Merck) and NaCl(s) (p. a., Merck) in ultra-pure Milli-Q water and saturated with argon over 30 minutes to remove CO_2. Equilibration of the Mg-oxychloride / $MgCl_2$ (± NaCl) solution systems was monitored by pH measurements following the procedure of Altmaier *et al.* [ALT/MET2003].

The molal H^+ concentration ($pH_m = -\log[m(H^+)]$) was determined with combination pH electrodes (Orion Ross, Thermo Scientific). In general, calibration against pH standard buffers (pH 3 – 12, Merck) achieves operational measured "pH_{exp}" values in salt solutions of ionic strength $I > 0.1$ mol·(kg(H$_2$O))$^{-1}$, with $pH_m = pH_{exp} + A_m$. The parameter A_m includes the individual activity coefficient $\gamma_H{}^+$ and a contribution ΔE_j entailing the difference in liquid junction potential E_j between dilute pH buffer solutions (calibration) and samples with high concentration of background electrolyte. Altmaier *et al.* previously reported empirical A_m values for $MgCl_2$ and NaCl systems [ALT/MET2003, ALT/NEC2008]. The analytical uncertainty of the pH measurement is ± 0.03 pH_m units

Fig. 5.78 shows the variation of pH_m with time in the three Mg-oxychloride / salt brine suspensions over a monitoring period of two months. After suspending brucite powder in the $MgCl_2$ (± NaCl) solutions, the pH_m of the initially weakly acidic solutions increased to some extent due to dissolution of the brucite. In each of the experiments, pH_m values of the first measurements were about 0.1 pH_m units higher than the calculated equilibrium pH_m values. Thereafter pH_m values decreased until achieving their specific equilibrium pH_m values after three weeks. Within the analytical uncertainty, pH values are constant during three consecutive measurements between 20 and 60 days, and these measurements agree with calculated equilibrium pH_m values.

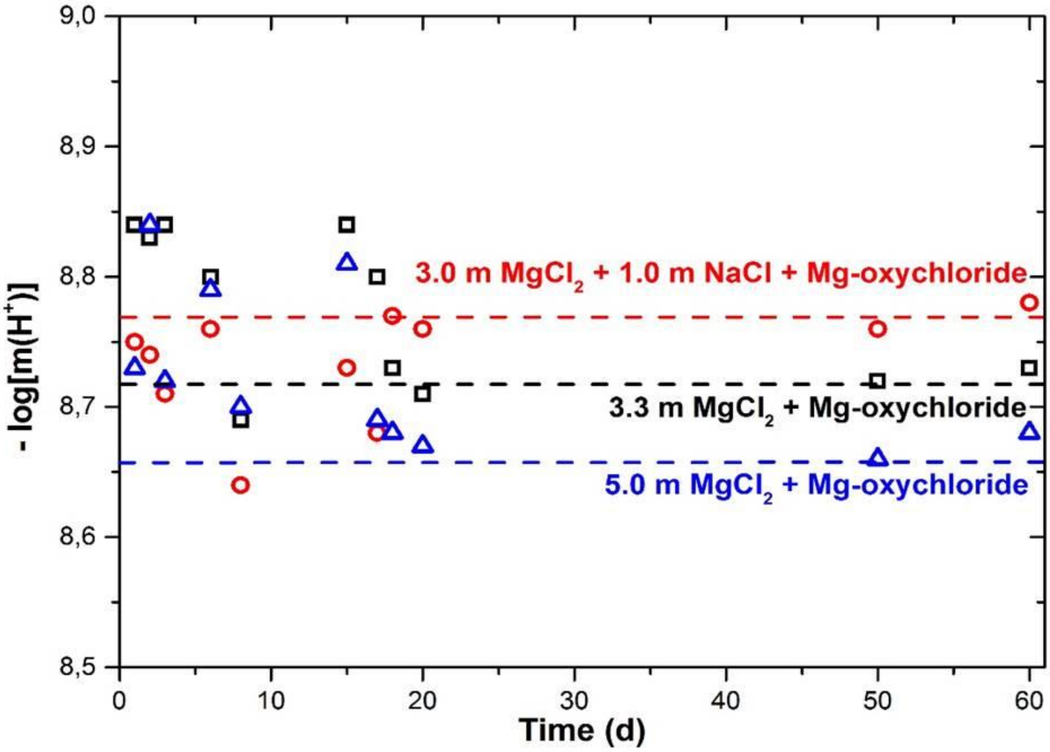

Fig. 5.78 Variation of pH_m during equilibration of Mg-oxychloride with $MgCl_2$ ± NaCl solutions ($I \geq 9.9$ mol·$(kg(H_2O))^{-1}$)

Dashed lines show the equilibrium pH_m values calculated with the PHREEQC geochemical code and the Harvie *et al.* [HAR/MOL1984] database. Size of error bars for pH measurements is smaller than symbols

The characterization of the solid by means of XRD, TGA-DSC, SEM-EDX, Raman spectroscopy and XPS indicated that the synthesized material is a pure $Mg_2(OH)_3Cl \cdot 4H_2O(s)$ phase. Moreover, the equilibration of the synthesized Mg-oxychloride in $MgCl_2$ (± NaCl) solutions achieved equilibrium within 20 to 60 days demonstrated the suitability of the synthesized Mg-oxychloride for future ^{129}I diffusion experiments.

5.6.2 Experimental set-up for quantification and speciation of ^{14}C from spent nuclear fuel elements

^{14}C is one of the radionuclides important in safety assessments of spent nuclear fuel (SNF) disposal facilities due to its assumed mobility and half-life of about 5730 a. Upon contact with water, ^{14}C-bearing species may be released from the fuel rods into aqueous solution and to some extent to the gas phase as inorganic and/or organic compounds. Solubility, sorption behaviour and distribution of ^{14}C in solution and gas depend strongly on the chemical form of ^{14}C.

Experimental studies to determine the inventory and speciation of ^{14}C in parts of an irradiated UO_2 fuel rod segment are prepared to be performed within the 7th FP CAST (CArbon-14 Source Term) project. In the framework of this work package of the VESPA-I project, a method was set up in a specifically manufactured glove box in the KIT-INE hot laboratories that allows the separation, quantification and speciation of ^{14}C species in gaseous and aqueous samples derived from future SNF dissolution experiments. The activities within VESPA-I comprise planning and manufacturing of the glove box and testing of the ^{14}C extraction line and the analytical set-up.

5.6.2.1 Physical formation of ^{14}C in spent nuclear fuel elements

^{14}C is an activation product formed in parts of fuel assemblies by neutron capture reactions of ^{14}N, ^{17}O and ^{13}C (**Tab. 5.24**). ^{14}N is the main naturally occurring nitrogen isotope (99.63 %), whereas ^{13}C (1.10 %) and ^{17}O (0.038 %) are low abundance naturally occurring carbon and oxygen isotopes, respectively [MAG/PFE2006]. A very small amount of ^{14}C is also formed by ternary fission in the fuel (**Tab. 5.24**). Nitrogen and carbon are present as impurities in fuel, Zircaloy cladding and structural parts of light water reactor (LWR) fuel assemblies.

Tab. 5.24 Relevant neutron capture mechanisms for the ^{14}C formation

Mechanism	$\sigma_{thermal}$ **[barn]**	$\sigma_{resonance}$ **[barn]**
$^{14}N(n,p)^{14}C$	1.821	0.818
$^{17}O(n,\alpha)^{14}C$	0.235	0.106
$^{13}C(n,\gamma)^{14}C$	1.4×10^{-3}	5.9×10^{-4}
ternary fission in LWR fuel	1.7×10^{-6} per thermal ^{235}U fission 1.8×10^{-6} per thermal ^{239}Pu fission	

Since ^{14}C is mainly formed by a $^{14}N(n,p)^{14}C$ reaction, estimations of ^{14}C inventories in parts of SNF assemblies are calculated based on published nitrogen impurities. Exemplary N impurities and calculated ^{14}C inventories in spent pressurized water reactor (PWR) fuel, Zircaloy-4 and stainless steel of spent PWR fuel assemblies with an average burn-up (BU) of ~50 GWd/t_{HM} are given in **Tab. 5.25**.

Tab. 5.25 Typical N impurities and calculated inventory of ^{14}C

Material	**Burn-up [GWd/t_{HM}]**	**N impurity [ppm]**	**calculated ^{14}C inventory [Bq/g]**	**Data reference**
PWR fuel	50	~10	~27200	[KIE/BOH2014]
Zircaloy-4	48	~40	~30000	[SAK/TAN2013]
stainless steel	48	~500	~80000	[SAK/TAN2013]

Possible reaction partners of ^{14}C, after formation, are among others, U, O, Zr, Fe, Cr and Ni and it is potentially present in the fuel or structural parts of the fuel assemblies as oxide or carbide. Corrosion of these materials leads to formation of volatile and/or dissolved compounds like carbonates and hydrocarbons.

5.6.2.2 Experimental procedure and analytical methods

A method that allows the separation and quantification of inorganic and organic ^{14}C species in gaseous and aqueous samples derived from dissolution experiments with various parts of a nuclear fuel element, such as irradiated UO_2 fuel, irradiated stainless steel or cladding material, was set-up in the specifically manufactured glove box based on a method developed for determining ^{14}C in spent ion exchange resins and process water from nuclear reactors [MAG2007, MAG/STE2005, MAG/STE2008]. The analytical separation procedure, shown in **Fig. 5.79**, involves several steps (i. e. acid stripping and wet oxidation) during which the inorganic and organic carbon fractions are extracted and converted into CO_2 which is then absorbed in washing bottles containing 2 M NaOH. A catalytic furnace between the two sets of washing bottles (bottle numbers 2/3 and 4/5, **Fig. 5.80**) ensures oxidation of reduced compounds like CO or CH_4. The content of ^{14}C (weak β^- emitter) in the NaOH solutions is finally determined by liquid scintillation counting (LSC).

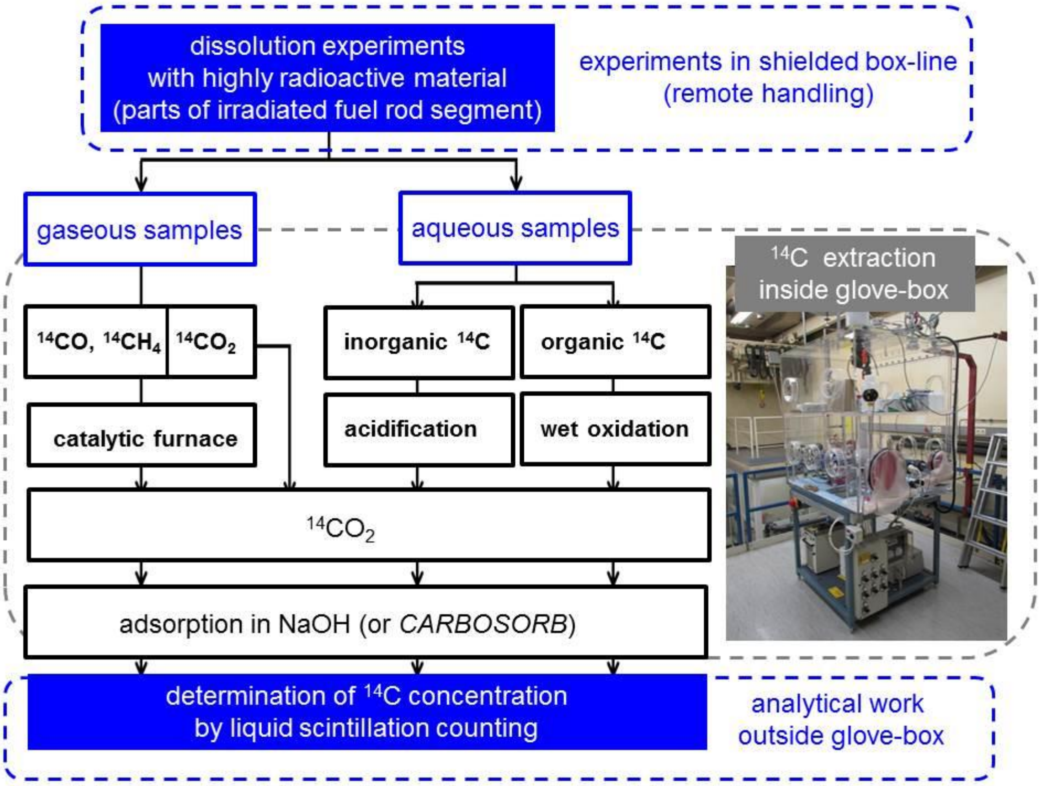

Fig. 5.79 Scheme of ^{14}C extraction and analysis procedure for aqueous and gaseous samples of experiments with highly radioactive material

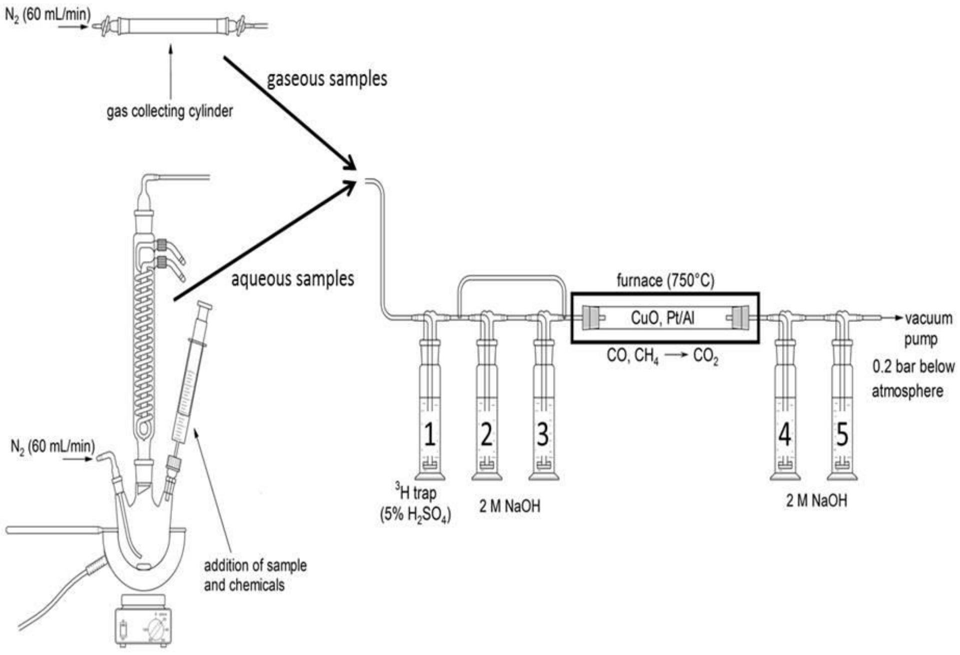

Fig. 5.80 Experimental design for ^{14}C extraction of gaseous and aqueous samples

The experimental design outlined in **Fig. 5.80** consists either of a 500 mL three-neck flask with connections (Rodaviss, Duran) for gas-inlet, cooler and septum for aqueous samples or a gas collecting cylinder with two valves (**Fig. 5.81**; Swagelok) for gaseous samples, connected to the CO_2 gas absorption system.

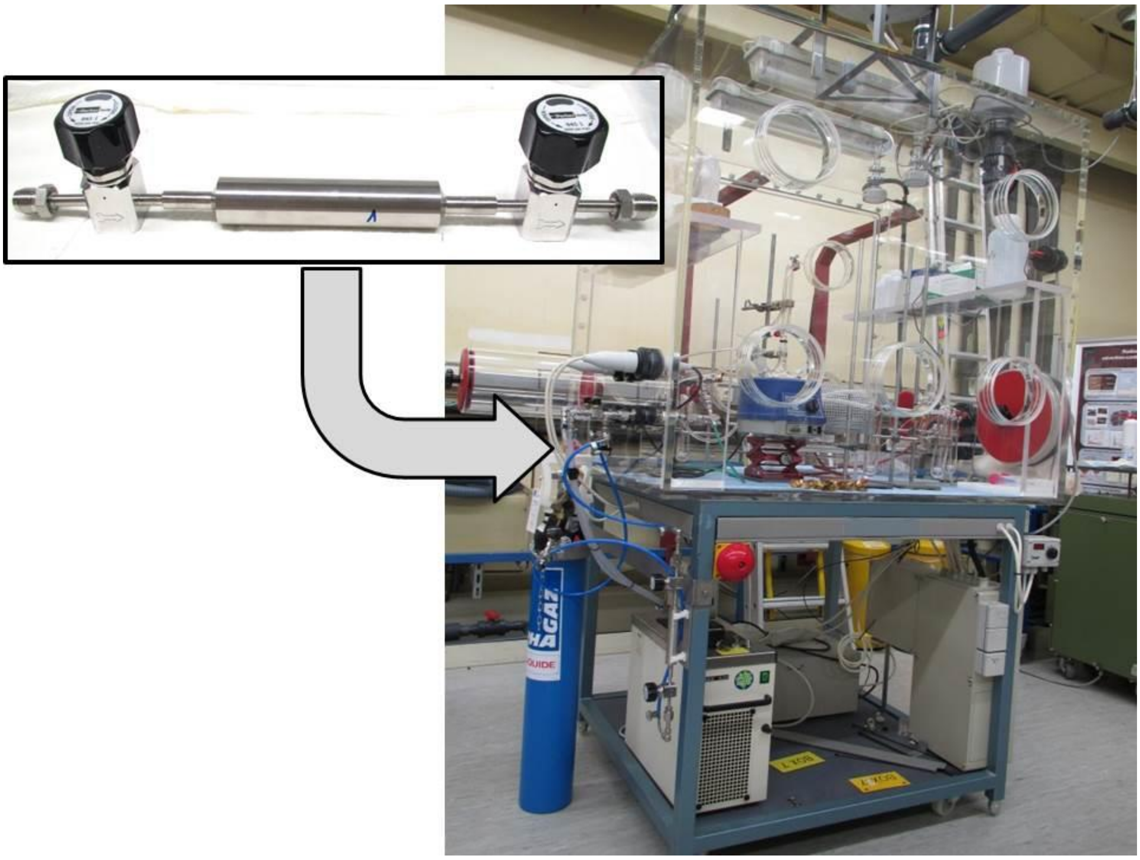

Fig. 5.81 Two valves gas collecting cylinder for gaseous samples and connection of cylinder to ^{14}C extraction set-up within the glove-box

The CO_2 gas absorption system consists of in total five customized washing bottles equipped with a fritted glass tip of porosity 1 (see **Fig. 5.82**) filled with 100 mL 2 M NaOH respectively (TitriPUR, Merck), except bottle no. 1, which is the ^3H trap and contains 100 mL 5 % H_2SO_4 (p. a., Merck). The washing bottles nos. 3 and 5 are used as safety bottles.

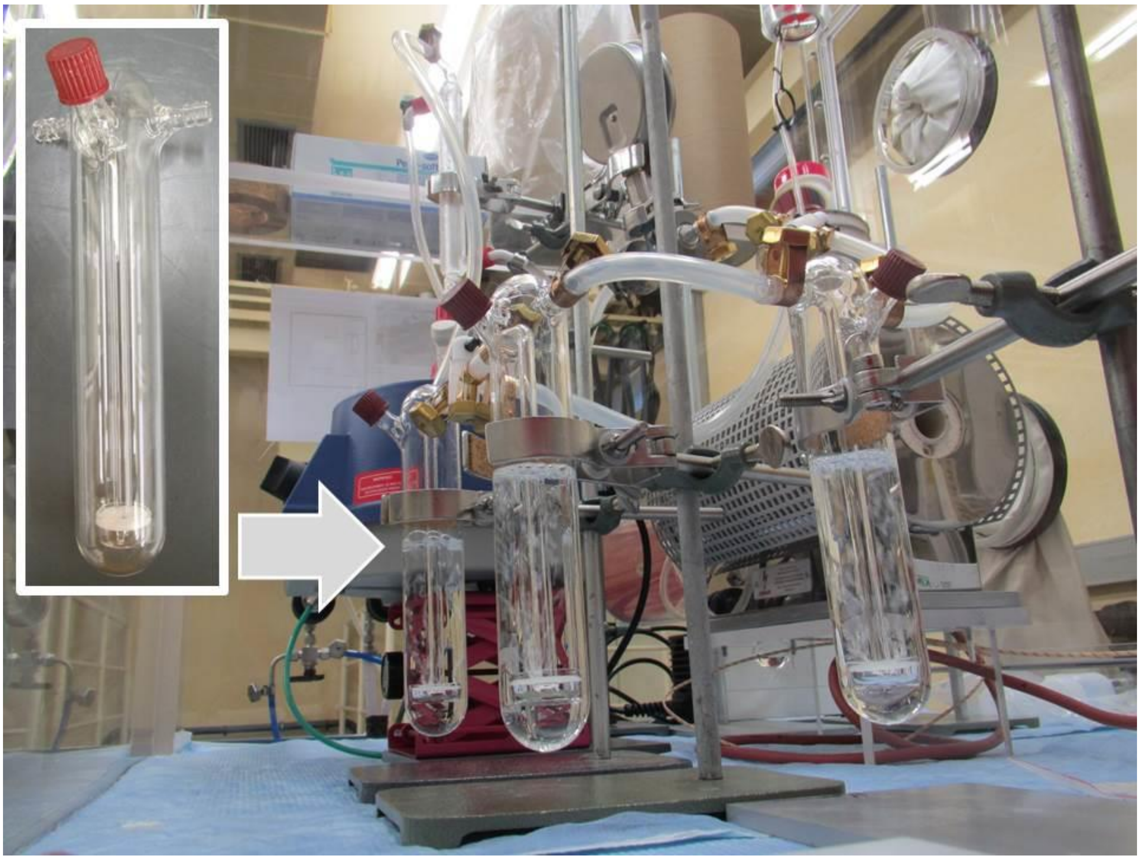

Fig. 5.82 Customized washing bottles equipped with a fritted glass tip of porosity 1 within the ^{14}C extraction set-up

The catalytic furnace consist of a tube furnace (MTF 12/25/250, Carbolite) operated at 750 °C, holding a quartz glass tube of ~50 cm length with an outer diameter (OD) of around 2.5 cm. The glass tube is filled with the catalyst mixture over the length of about 20 cm. The mixture is composed of 1 wt. % platinum on alumina pellets (3.2 mm, Sigma-Aldrich) and CuO/Cu_2O wire (0.65 mm×6 mm, p. a., Merck). The mixing ratio is about 30 wt. % Pt on Al and 70 wt. % copper oxide wire. The mixture is held in place inside the quartz glass tube by quartz glass wool.

The system is interconnected by silicon tubing (8.5 mm ID, 11.5 mm OD) with two PP/PTFE three-way stopcocks (Nalgene) placed before and after washing bottles nos. 2 and 3. Nitrogen (99.9999 %, Alphagaz 2, Air Liquide), supplied by a gas bottle, is used as carrier gas. Flow rate (~60 mL/min) through the system is controlled by a flow meter (Model P, Aalborg Instruments & Controls). In order to prevent the loss of CO_2 gas in the case of a leakage, the system is operated under subatmospheric pressure (0.2 – 0.3 bar below atmosphere) by means of a diaphragm vacuum pump with fine-adjustment valve and manometer (max. 16 L/min, N816.3 KT.18, KNF).

5.6.2.2.1 Treatment of aqueous samples

From the dissolution experiments obtained aqueous samples are placed in the three-neck flask (100 mL) and the nitrogen carrier gas flow rate is set to 60 mL/min. Subsequently the system is evacuated to 0.3 bar below atmosphere. A volume of 50 mL 8 M H_2SO_4 is added to the flask through the septum using a glass syringe. The solution is purged and stirred for one hour, during which the inorganic fraction is released as CO_2 and absorbed in the washing bottle no. 2 (**Fig. 5.80**). Reduced carbon compounds like CO, released during the acid stripping are oxidized in the catalytic furnace and absorbed in washing bottle no. 4. Prior to the wet oxidation step, washing bottles nos. 2 and 3 are disconnected from the system using the three-way stopcocks. The remaining carbon compounds in the sample solution (organic fraction) is oxidized by a strong oxidant ($K_2S_2O_8$, p. a., Merck), catalyst ($AgNO_3$, VWR Chemicals), heat and magnetic stirring. Consecutively 5 mL 4 % $AgNO_3$ solution and 50 mL 5 % potassium peroxodisulfate solution are added to the sample container through the septum using glass syringes under simultaneous heating (~95 °C). After one hour the same amounts of silver nitrate and potassium peroxodisulfate are added to the flask and the mixture is purged, heated and stirred for another hour. After in total three hours 3 mL samples are collected from the washing bottles and mixed with 18 mL scintillation cocktail (Hionic Fluor, Perkin-Elmer) for LSC measurements (30 min per sample after allowing to stand for 24 hours, Quantulus 1220, Wallac Oy, PerkinElmer).

5.6.2.2.2 Treatment of gaseous samples

The gas collecting cylinder with two valves (**Fig. 5.81**) is connected to the first washing bottle of the CO_2 gas absorption system and the nitrogen gas bottle as shown in **Fig. 5.85**. The pressure in the system is lowered to about 0.3 bar below atmosphere and the N_2 gas flow rate is set to 60 mL/min. The content of the gas collecting cylinder is flushed into the CO_2 gas absorption system, where carbon dioxide released from inorganic carbon compounds during the dissolution experiments is absorbed in washing bottle no. 2. Reduced carbon compounds like CH_4 will be oxidized in the catalytic furnace to CO_2 and absorbed in washing bottle no. 4 after passing through bottles nos. 2 and 3 unaffectedly. After in total one hour 3 mL samples are collected from the washing bottles for LSC measurements as described above.

5.6.2.3 Set-up of a specifically manufactured glove box for the ^{14}C analytical separation procedure

A specifically designed glove box was manufactured, which meets the requirements to operate the ^{14}C extraction and analyses system outlined in **Fig. 5.83** and allows us to handle hot samples derived from dissolution experiments from the KIT-INE shielded box line (ABL). Technical drawings and photographs of the glove box with the dimensions (L×W×H) 1200 mm×1000 mm×1200 mm are shown in **Fig. 5.83** and **Fig. 5.84**. The box is equipped with feedthroughs for ten gloves, two small locks (208 mm diameter) one with antechamber, a big lock (300 mm diameter), electrical power, BNC connectors (for pH, E_h measurements), flow and return for the cooling water (water cooling is established by a refrigerated circulating bath, K20, Haake), water and temperature sensors and gas feedthroughs as well as a manometer and security valve (Jacomex).

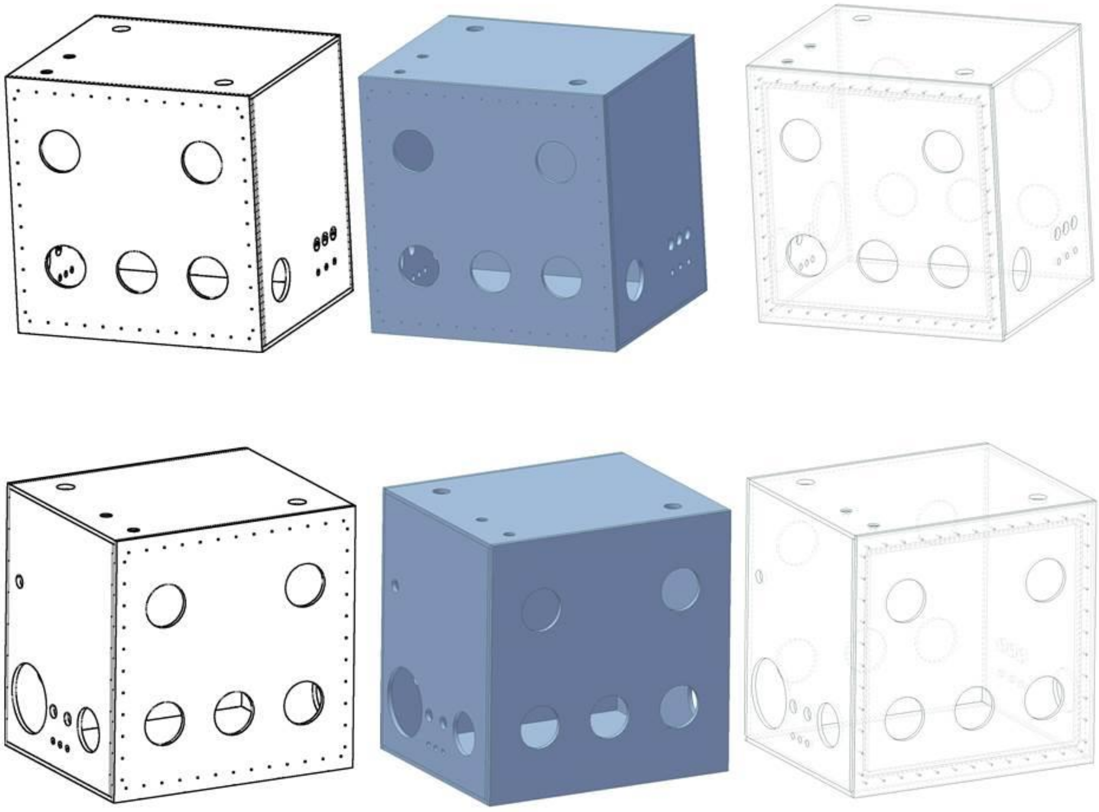

Fig. 5.83 Technical drawings of the specifically designed glove box for the ^{14}C analytical separation procedure

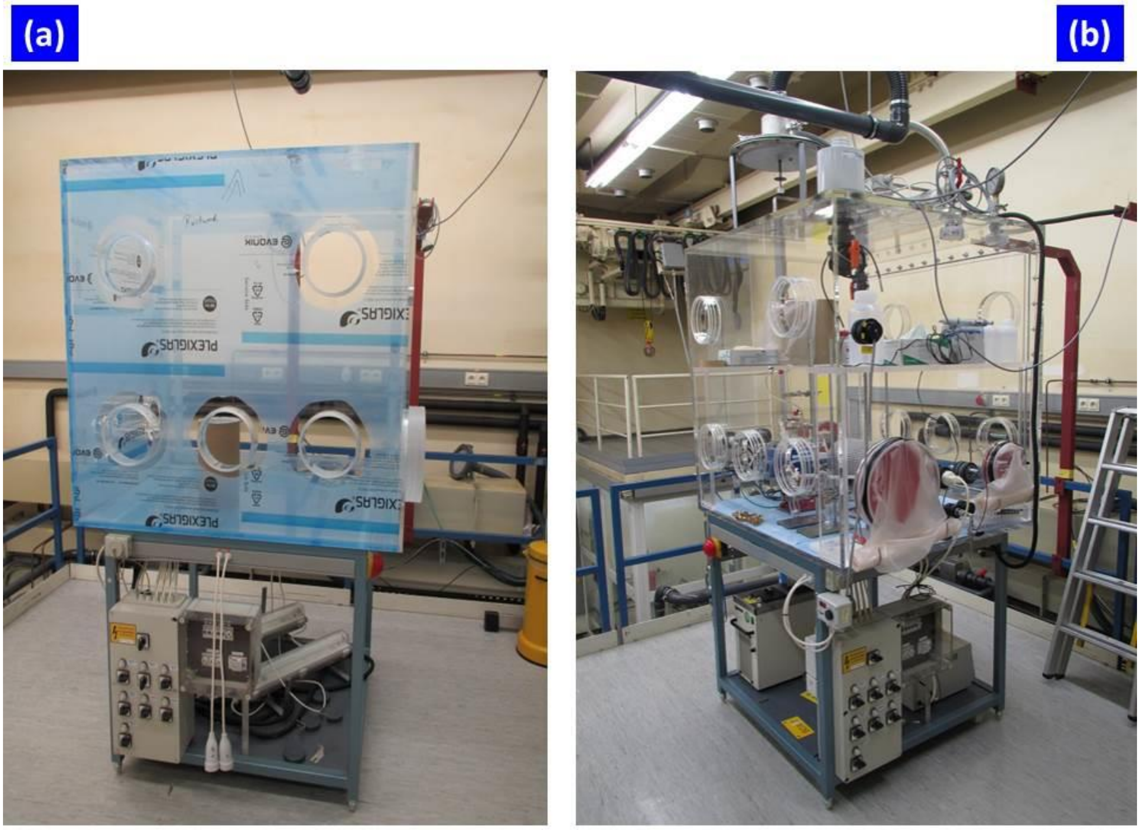

Fig. 5.84 Photographs of the glove box for the ^{14}C analytical separation procedure
(a) shows the box, when it was delivered in December 2013, and (b) shows the glove box when most installations were finished in March 2014

In order to handle aqueous and gaseous samples a N_2 gas flow set-up as shown in **Fig. 5.85** was elaborated. For purging aqueous samples in the flask, the “green” line is used. The gas collecting cylinder is integrated in the system by connecting one end to the N_2 gas supply with flow meter and the other to the gas feedthrough of the glove box as schematically shown in **Fig. 5.85**. Three 3-way stopvalves (Swagelok) are used to switch between aqueous and gaseous samples purge.

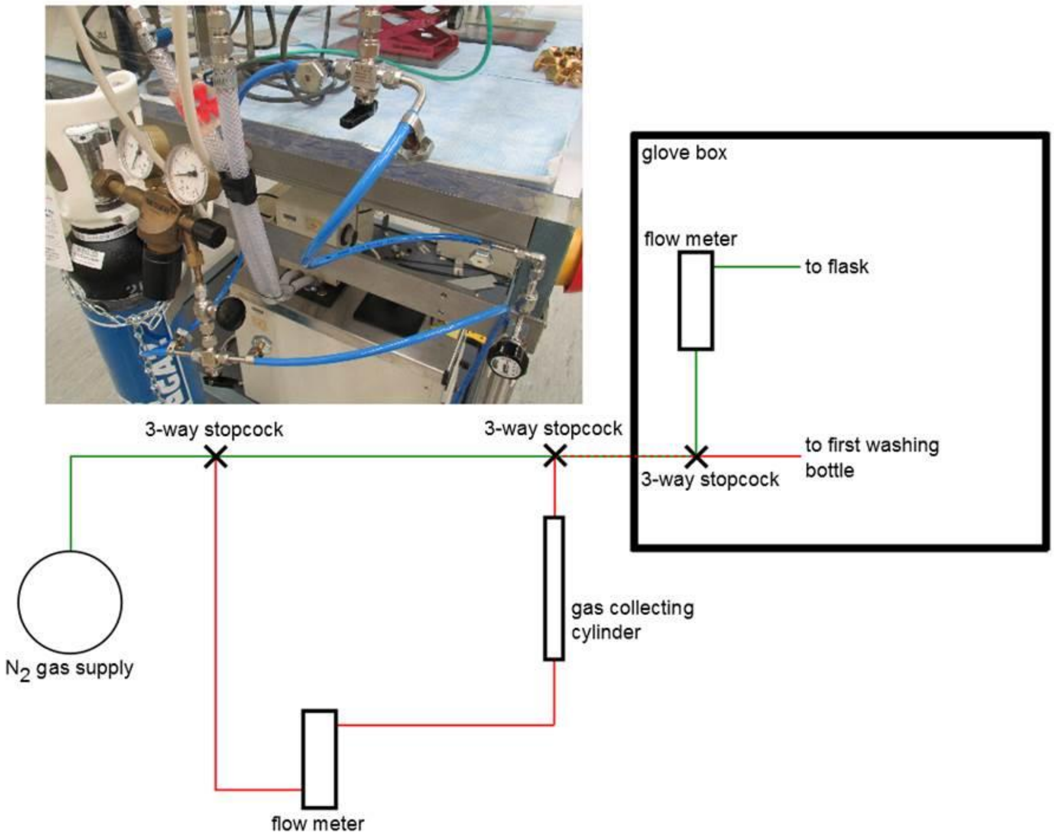

Fig. 5.85 N_2 carrier gas flow set-up for aqueous samples (green) and inclusion of the gas collecting cylinder into the system for gaseous samples (red)

5.6.2.4 Test of experimental set-up and calibration of analytical methods

Recovery tests were performed with ^{14}C-labeled sodium carbonate (Na_2CO_3, 200 kBq, Eckert & Ziegler) and sodium acetate (CH_3CO_2Na, 1.85 MBq, PerkinElmer) reference material with 100 – 1000 Bq for the inorganic and organic reference material respectively. Also different ratios of activity between sodium carbonate and acetate were investigated. The recovery tests indicate that the chemical yield of the separation method is > 88 % for both the inorganic as well as the organic ^{14}C fraction (**Tab. 5.26**).

The efficiency of the catalytic furnace was tested using a mixture of 10 % methane and 90 % argon (Air Liquide) with a yield of ~ 99 % for the conversion of CH_4 to CO_2.

Tab. 5.26 Assortment of recovery test results performed with ^{14}C labeled Na-carbonate and Na-acetate

^{14}C added		**Recovery of [Bq]**		**Recovery of [%]**	
form	**activity [Bq]**	**$^{14}C_{inorg.}$**	**$^{14}C_{org.}$**	**$^{14}C_{inorg.}$**	**$^{14}C_{org.}$**
Na_2CO_3	932.10	801.8	–	86.00	–
Na_2CO_3	983.90	855.0	–	86.90	–
Na_2CO_3	987.30	964.4	–	97.70	–
CH_3CO_2Na	1142.2	–	1086.3	–	95.1
CH_3CO_2Na	1121.8	–	1036.2	–	92.4
CH_3CO_2Na	1108.4	–	934.80	–	84.3
Na_2CO_3 + CH_3CO_2Na	955.10 + 1082.4	961.2	984.70	100.6	91.0
Na_2CO_3 + CH_3CO_2Na	71.500 + 84.000	74.70	67.500	104.5	80.4
CH_3CO_2Na	882.00	–	756.00	–	85.7
Mean ± SD				**95.1 ± 8.3**	**88.2 ± 5.6**

Acknowledgements

The KIT-INE workshop and infrastructure team in particular H. Reichert, E. Schmitt and J. Thomas are kindly acknowledged for their technical support during the project work

5.6.3 Spectroscopic investigations of Tc(IV) uptake by Fe(II) minerals: EXAFS/XANES

5.6.3.1 Introduction

Fe is one of the most important reducing agent and sorbent in Tc chemistry because of its abundance in the natural environment and repository near-field. Previous studies have shown the reduction and sorption capacity of Fe(II) minerals like magnetite (Fe_3O_4) and mackinawite (FeS) which are formed in repository relevant conditions [ZAC/HEA2007, UM/CHA2011, LLO/DEN2008]. Geraedts *et al.* [GER/BRU2002] and Maes *et al.* [MAE/GER2004] studied the system magnetite-Tc in the presence of natural and synthetic Gorleben groundwater. The authors concluded that $TcO_2 \cdot xH_2O(s)$ formed in this system, and suggested that Tc(IV) polymers or colloids were responsible for the observed increase in solubility (~10^{-6} M). Wharton *et al.* [WHA/ATK2000] studied the coprecipitation of Tc(VII) and Tc(IV) with mackinawite (FeS) and characterized the resulting solid phases by X-ray absorption spectroscopy. Tc was immobilized as a Tc(IV)S_2–like phase regardless of the initial oxidation state of Tc. Similar observations were reported by Livens *et al.* [LIV/JON2004], who investigated the interaction between Tc and mackinawite using both +VII and +IV as initial redox state of Tc. Liu *et al.* [LIU/TER2008] performed comprehensive immobilization experiments with Tc in the presence of mackinawite. The authors assessed the effect of ionic strength (≤ 1.0 M NaCl) and pH (6.1 – 9.0) on the uptake of Tc, and observed a strong pH–dependence and the increase of the uptake rate with increasing ionic strength. In contrast to Livens and co-workers, TcO_2-like instead of TcS_2-like phases were reported to form on the surface of mackinawite. Sorption experiments of Tc(VII) on nanocrystalline Fe-phases were recently performed by Kobayashi *et al.* in dilute NaCl solutions [KOB/SCH2013]. EXAFS results confirmed the predominance of Tc(IV), also indicating that Tc does not remain adsorbed at the reactive magnetite surface, but is incorporated in its structure. In this study, redox/sorption experiments of Tc were performed in 0.1 NaCl systems as a function of loading and initial Tc concentration with well-defined nanocrystalline Fe(II) minerals. After completing the wet chemistry part of the experiment at KIT-INE, EXAFS samples were prepared and sent to ROBL beamline at ESRF, where measurements were performed in collaboration with A. C. Scheinost (HZDR-ROBL).

5.6.3.2 Experimental

Magnetite (Fe_3O_4) and mackinawite (FeS) were synthesized following the protocol described elsewhere [KIR/FEL2011]. Synthesized magnetite and mackinawite phases were characterized by high energy powder XRD (D8 Advance, Bruker).

The experiments were performed in 0.1 M NaCl solutions. Heterogeneous samples with Tc sorbed in magnetite and mackinawite were equilibrated for 6 weeks. pH_c, E_h and [Tc] (after 10 kDa ultrafiltration) were determined before phase separation by centrifugation. The wet paste resulting after phase separation was placed into double confined sample holders, heat-sealed inside the Ar-glovebox and stored in a N_2 Dewar (Voyager 12, Air Liquide – DMC, France) until the collection of XAS spectra. This method has been previously proven to avoid changes in oxidation state or redox sensitive probes (e. g. Np, Pu and Tc) [KOB/SCH2013, KIR/FEL2011, GAO/DAH2011].

XAFS spectra were collected in florescence mode at the Tc *K*-edge (21044 eV) at the Rossendorf Beamline (ROBL), ESRF in Grenoble (France), in cooperation with Dr. A.

Scheinost of HZDR. The energy of the Si(111) double-crystal monochromator was calibrated using a Mo foil (edge energy 20000 eV). Samples were kept at 15 K (liquid He cryostat) during measurements to avoid changes of oxidation state and to reduce thermal disorder in the samples [KIR/FEL2011]. The EXAFS data were fitted with WinXAS [RES1998] using theoretical backscattering amplitudes and phase shifts calculated with FEFF 8.2 [ANK/BOU2002, ANK/RAV1998]. The XANES spectra were compared with a reference spectrum of $Tc(VII)O_4^-$ [SAE/SAS2012].

5.6.3.3 Results and discussion

E_h and pH_c values measured in the Fe mineral suspensions (magnetite and mackinawite) after 6 weeks of equilibration time are summarized in **Tab. 5.27**. For magnetite samples, measured E_h values are slightly below the thermodynamically calculated Tc(VII)/Tc(IV) redox borderline, whereas significantly lower E_h values prevail in the mackinawite system. Tc concentration measured in solution decreases to values below the detection limit of LSC within 6 weeks, suggesting that TcO_4^- is completely reduced to Tc(IV) and consequently removed from the aqueous phase.

5.6.3.3.1 Magnetite

Fig. 5.86a shows the XANES spectra measured at the Tc *K*-edge for Tc sorbed magnetite samples. All investigated samples show similar features and edge position. The absence of any pre-edge feature at 21050 eV confirms the absence of Tc(VII) and predominance of Tc(IV). The PCA analysis of the six XANES spectra indicates that two components are sufficient to explain all the available data. The reconstruction of all XANES spectra using these two components is also shown in **Fig. 5.86**a. Fourier Transforms and the k^3-weighted EXAFS spectra for all magnetite samples with corresponding best fit models are shown in **Fig. 5.86**b and **Fig. 5.86**c, respectively. The structural parameters resulting from the EXAFS fit are shown in **Tab. 5.28**.

Tab. 5.27 Experimental conditions and measured pH_c, E_h and $[Tc]_{final}$ of Tc sorbed by magnetite and mackinawite in 0.1 M NaCl system (after 6 weeks of equilibration time)

Fe mineral	Tc loading (ppm)	$[Tc]_0$[a]	pH_c[b]	E_h (mV)[c]	$[Tc]_{final}$
Magnetite-1	400	$2\cdot10^{-4}$	9.28	-149	$\leq 1.2\cdot10^{-9}$ [d]
Magnetite-2	600	$2\cdot10^{-4}$	9.16	-146	$\leq 1.2\cdot10^{-9}$ [d]
Magnetite-3	900	$2\cdot10^{-4}$	9.08	-139	$\leq 1.2\cdot10^{-9}$ [d]
Magnetite-4	400	$2\cdot10^{-5}$	9.12	-138	$\leq 1.2\cdot10^{-9}$ [d]
Magnetite-5	600	$2\cdot10^{-5}$	8.90	-121	$\leq 1.2\cdot10^{-9}$ [d]
Magnetite-6	900	$2\cdot10^{-5}$	8.68	-109	$\leq 1.2\cdot10^{-9}$ [d]
Mackinawite-1	400	$2\cdot10^{-4}$	9.07	-315	$\leq 1.2\cdot10^{-9}$ [d]
Mackinawite-2	600	$2\cdot10^{-4}$	9.16	-381	$\leq 1.2\cdot10^{-9}$ [d]
Mackinawite-3	900	$2\cdot10^{-4}$	8.99	-309	$\leq 1.2\cdot10^{-9}$ [d]
Mackinawite-4	400	$2\cdot10^{-5}$	9.02	-289	$\leq 1.2\cdot10^{-9}$ [d]
Mackinawite-5	600	$2\cdot10^{-5}$	8.91	-280	$\leq 1.2\cdot10^{-9}$ [d]
Mackinawite-6	900	$2\cdot10^{-5}$	8.83	-271	$\leq 1.2\cdot10^{-9}$ [d]

a: initial Tc(VII) concentration; b: ± 0.05; c: ± 50 mV; d: detection limit

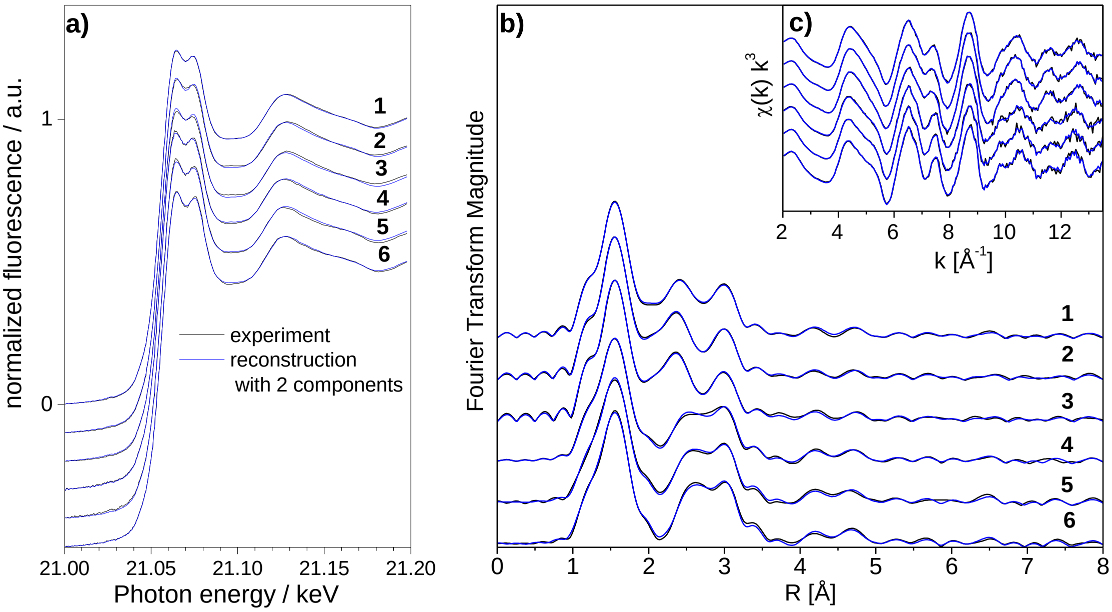

Fig. 5.86 Tc *K*-edge XAS spectra of Tc sorbed on magnetite in 0.1 M NaCl

a) experimental XANES spectra (black lines) and reconstruction with 2 components after PCA analysis (blue lines); experimental (black lines) and shell fitted (blue lines) EXAFS Fourier Transform Magnitude (b) and k^3-weighted EXAFS spectra (c)

Tab. 5.28 Structural parameters determined for Tc uptake by magnetite in 0.1 M NaCl and varying $[Tc]_0$ and loading

Sample			**Path**	**CN†**	**R(Å)**	**σ^2(Å^2)**	**ΔE_0(eV)**	**%R‡**
Fe mineral	**$[Tc]_0$**	**Upload (ppm)**						
Magnetite	$2\cdot10^{-4}$	400	Tc-O	6.2	2.03	0.0047	3.8	7.3
			Tc-Tc	2.3	2.58	0.0085		
			Tc-Fe1	3.0	3.08	0.01		
			Tc-Fe2	4.1	3.52	0.0084		
Magnetite	$2\cdot10^{-4}$	600	Tc-O	6.4	2.03	0.0046	3.7	8.1
			Tc-Tc	2.9	2.58	0.0084		
			Tc-Fe1	2.6	3.07	0.01		
			Tc-Fe2	4.3	3.52	0.0089		
Magnetite	$2\cdot10^{-4}$	900	Tc-O	6.0	2.03	0.0044	4.3	7.9
			Tc-Tc	2.2	2.58	0.0068		
			Tc-Fe1	2.9	3.09	0.01		
			Tc-Fe2	4.8	3.53	0.01		
Magnetite	$2\cdot10^{-5}$	400	Tc-O	6.0	2.03	0.0051	3.8	7.3
			Tc-Tc	1.8	2.58	0.0099		
			Tc-Fe1	3.6	3.09	0.01		
			Tc-Fe2	5.0	3.51	0.0097		
Magnetite	$2\cdot10^{-5}$	600	Tc-O	6.1	2.03	0.0049	3.6	8.5
			Tc-Tc	1.6	2.58	0.01		
			Tc-Fe1	4.0	3.09	0.01		
			Tc-Fe2	4.0	3.51	0.0075		
Magnetite	$2\cdot10^{-5}$	900	Tc-O	6.0	2.02	0.0046	3.7	7.6
			Tc-Tc	1.6	2.59	0.01		
			Tc-Fe1	4.8	3.08	0.01		
			Tc-Fe2	3.6	3.51	0.0059		

†CN(Coordination number), ‡R(Residual)

Fit errors: CN:~ 25 % ; R: 0.01 Å, σ_2: 0.002 Å^2

Magnetite samples with the same $[Tc]_0$ (either $2\cdot10^{-4}$ M or $2\cdot10^{-5}$ M) show very similar EXAFS spectra regardless of the final Tc loading. The first shell in all investigated samples corresponds to the backscattering of oxygen. The fit of this shell results in a coordination number (CN) of 6 at 2.03 ± 0.01 Å, in good agreement with the octahedral coordination environment expected for Tc(IV). In those samples with lower $[Tc]_0$ ($2\cdot10^{5}$ M, samples 4 – 6), the second and third shells can be properly fitted with Tc–Fe paths at 3.09 ± 0.01 Å and 3.52 ± 0.01 Å, corresponding to edge-sharing and corner-sharing positions in the magnetite structure. In all cases, the best fit is obtained by also considering Tc–Tc backscattering at 2.58 ± 0.01 Å. Note that in those samples with higher $[Tc]_0$ ($2\cdot10^{-4}$ M, samples 1 – 3), the coordination number of the Tc backscatterer is larger than for samples with lower $[Tc]_0$, whereas the coordination number of the second Fe shell is lower. This can be interpreted as the formation of $[TcO_2]$-dimers/polymers on the surface of magnetite in addition to the incorporation of monomeric Tc(IV) species to the magnetite structure. This hypothesis is also in line with the insights gained by PCA analysis of the XANES spectra, which indicate the predominance of two main components in all the systems evaluated.

The relatively large coordination numbers fitted for Tc–Fe1 (CN = 3 – 5) and Tc–Fe2 (CN = 3 – 4) paths hint towards the partial incorporation of Tc into the structure of magnetite. Both complete incorporation of Tc into the magnetite structure and formation of TcO_2-like dimers/polymers on the surface were reported by different authors [ZAC/HEA2007, MCB/LLO2011, KOB/SCH2013, MAE/GER2004, PER/ZAC2012]. However, none of the available studies has systematically investigated the effect of initial Tc concentration and solid to liquid ratio (or loading) as accomplished in the present work, but rather focussed on a given [Tc] and loading. Kobayashi and co-workers [KOB/SCH2013] conducted Tc uptake experiments with magnetite under analogous $[Tc]_0$ and loading ($2\cdot10^{-5}$ M and 400 ppm, respectively), but significantly lower pH values (6 – 7.5). The authors observed the complete incorporation of Tc(IV) in the structure of magnetite. The differences in the prevailing uptake mechanism observed in this work and in Kobayashi *et al.* are interpreted in connection with differences in magnetite solubility in both systems. The solubility of magnetite in the pH_c range 6 – 7.5 ($pe+pH_c = 4$, [KOB/SCH2013]) is significantly larger than at $pH_c \sim 9$ ($pe+pH_c=7$, p.w.). Higher concentrations of Fe in solution are expected to promote a greater recrystallization rate, thus facilitating the incorporation of Tc(IV) in the structure of magnetite. These observations strongly suggest that the mechanism driving the retention of Tc by magnetite strongly depends on the initial Tc concentration and pH, and to a significantly lesser extent on the loading on the surface of magnetite.

5.6.3.3.2 Mackinawite

Fig. 5.87a shows the XANES spectra of Tc *K*-edge for samples 7 to 12, corresponding to Tc sorbed on mackinawite. As in the case of Tc uptake by magnetite, all investigated mackinawite samples do not show the pre-edge feature at 21050 eV characteristic of Tc(VII), thus indicating the complete reduction of Tc(VII) to Tc(IV) within the timeframe of the experiment. The PCA analysis of the six XANES spectra also indicates that two components are sufficient to explain all the available data. The reconstruction of all

XANES spectra using these two components is also shown in **Fig. 5.87**a. Fourier Transforms and the k^3-weighted EXAFS spectra for all mackinawite samples with corresponding best fit models are shown in **Fig. 5.87**b and **Fig. 5.87**c, respectively. The structural parameters resulting from the EXAFS fit are shown in **Tab. 5.29**.

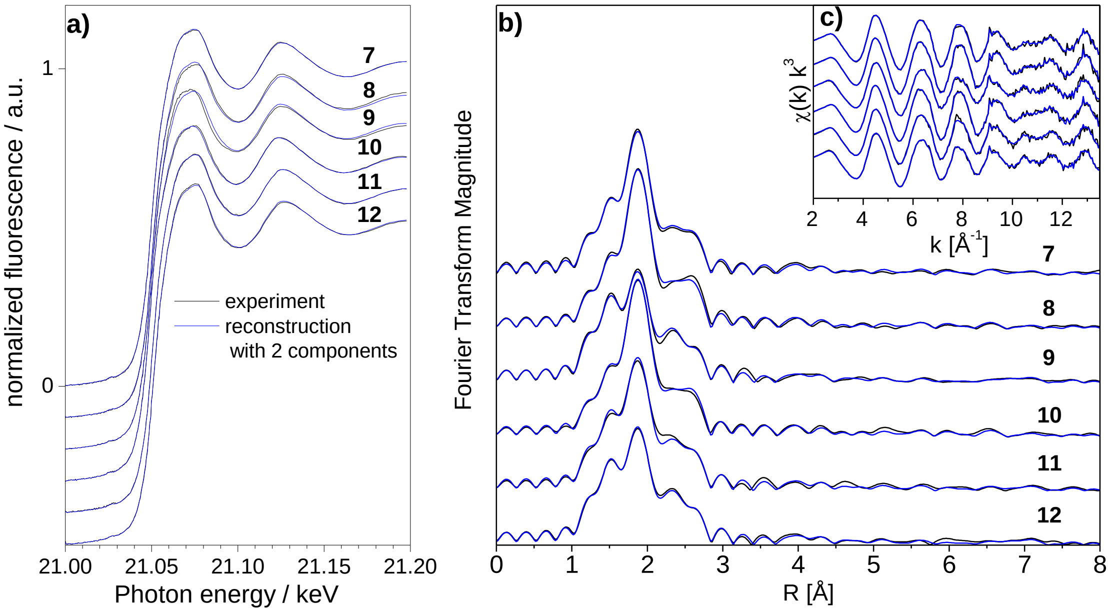

Fig. 5.87 Tc *K*-edge XAS spectra of Tc sorbed on mackinawite in 0.1 M NaCl a) experimental XANES spectra (black lines) and reconstruction with 2 components after PCA analysis (blue lines); experimental (black lines) and shell fitted (blue lines) EXAFS Fourier Transform magnitude (b) and k^3-weighted EXAFS spectra (c)

Mackinawite samples with the same Tc loading (either 400 ppm, 600 ppm or 900 ppm) show very similar EXAFS spectra regardless of the initial Tc concentration ($2 \cdot 10^{-4}$ M or $2 \cdot 10^{-5}$ M). Both O and S appear as main backscatterers in the first coordination shell of Tc at 2.01 ± 0.01 Å and 2.37 ± 0.01 Å, respectively. The distances fitted for the Tc–S ath are in good agreement with data available in the literature for Tc–sulphide compounds (2.30–2.50 Å) [WHA/ATK2000]. The number of O- and S-backscatterers in the first coordination shell is directly related with the Tc loading. Hence, greater S coordination numbers (and consequently lower O coordination numbers) are fitted for those samples with lower Tc upload, and vice versa. The outer shells are fitted with Tc–Fe and Tc–Tc paths at 2.71 ± 0.01 Å and 2.80 ± 0.01 Å, respectively. In combination with PCA analyses, these results clearly hint towards the formation of two main moieties/ species in the system mackinawite-Tc.

Tab. 5.29 Structural parameters determined for Tc uptake by mackinawite in 0.1 M NaCl and varying $[Tc]_0$ and loading

Sample			Path	CN†	R(Å)	σ^2(Å^2)	ΔE_0(eV)	%R‡
Fe mineral	**$[Tc]_0$**	**Upload (ppm)**						
Mackinawite	$2\cdot10^{-4}$	400	Tc-O	1.8	2.00	0.01	5.6	5.2
			Tc-S	4.2	2.37	0.0036		
			Tc-Fe	0.3	2.71	0.0025		
			Tc-Tc	0.5	2.80	0.0025		
Mackinawite	$2\cdot10^{-4}$	600	Tc-O	1.7	2.01	0.01	6	5.7
			Tc-S	4.3	2.37	0.0065		
			Tc-Fe	0.4	2.74	0.0032		
			Tc-Tc	0.9	2.80	0.0032		
Mackinawite	$2\cdot10^{-4}$	900	Tc-O	3.0	2.02	0.01	5.2	6.5
			Tc-S	3.0	2.37	0.0064		
			Tc-Fe	0.5	2.70	0.0024		
			Tc-Tc	0.4	2.80	0.0024		
Mackinawite	$2\cdot10^{-5}$	400	Tc-O	1.5	2.01	0.01	6	4.8
			Tc-S	4.5	2.37	0.007		
			Tc-Fe	0.4	2.70	0.0035		
			Tc-Tc	0.7	2.80	0.0035		
Mackinawite	$2\cdot10^{-5}$	600	Tc-O	2.0	2.01	0.01	5.8	5.4
			Tc-S	4.0	2.37	0.0077		
			Tc-Fe	0.6	2.71	0.0041		
			Tc-Tc	0.8	2.80	0.0041		
Mackinawite	$2\cdot10^{-5}$	900	Tc-O	2.8	2.02	0.01	5.4	5.6
			Tc-S	3.2	2.37	0.0068		
			Tc-Fe	0.6	2.71	0.0038		
			Tc-Tc	0.7	2.80	0.0038		

†CN(Coordination number), ‡R(Residual)

Fit errors: CN:~ 25 % ; R: 0.01 Å, σ^2: 0.002 Å^2

Analogous species / moieties were previously reported in the literature, based on spectroscopic evidences obtained under different experimental conditions. Kobayashi *et al.* [KOB/SCH2013] suggested the formation of a TcS_2-like phase based on their XANES data, in experiments conducted with $[Tc]_0 = 2\cdot10^{-5}$ M and 200 ppm Tc loading. With a significantly higher loading (99000 ppm) and $[Tc]_0$ ($1.5\cdot10^{-4}$ M), Liu *et al.* [LIU/TER2008] reported the immobilization of Tc by mackinawite as a TcO_2-like phase (Tc–O path at 1.99 ± 0.02 Å with CN = 6). Provided the very high loading and $[Tc]_0$, the main component is identified as $TcO_2\cdot xH_2O(s)$ by Liu and co-workers. These observations are in line with our experimental data and spectroscopic findings: i) there is a clear and systematic effect of loading on the retention of Tc by mackinawite; ii) a component with predominance of Tc-S interactions in the first shell forms in mackinawite systems with low Tc loadings; iii) TcO_2-like phase (likely surface precipitate or colloidal Tc(IV)) starts to form with increasing loading, becoming predominant at the very high loadings used by Liu and co-workers (99000 ppm). Note that the method used in [LIU/TER2008, KOB/SCH2013] and in the present work for the synthesis of mackinawite was exactly the same.

In contrast to these observations, Livens *et al.* [LIV/JON2004] reported the formation of a TcS_2-like phase (d_{Tc-S} = 2.42 ± 0.02 Å and CN = 6) in the presence of relatively high loadings (10000 ppm) of Tc on 300 mg mackinawite. A direct comparison of the data by Livens and co-workers with the present study cannot be accomplished, provided the different method used for the synthesis of mackinawite and the very limited experimental description provided by the authors, which for (among others) omits information on S:L, $[Tc]_0$ and pH.

5.6.3.4 Conclusion for Tc (IV) uptake studies in Fe-systems

The Tc reduction and uptake mechanisms by Fe (II) minerals (magnetite and mackinawite) were investigated in 0.1 M NaCl systems. The results show that Tc(VII) is reduced to Tc(IV) in contact in all investigated systems regardless of initial $[Tc]_0$ and S:L. EXAFS data shows that the mechanism of Tc(IV) retention by magnetite and mackinawite is strongly dependent on the loading, $[Tc]_0$ and pH. Hence, Tc(IV) partly incorporates into the structure of magnetite at low $[Tc]_0$ ($2 \cdot 10^{-5}$ M), but forms TcO_2-dimers/ polymers at $[Tc]_0 = 2 \cdot 10^{-4}$ M. A larger incorporated fraction is observed in those conditions favouring a higher solubility of magnetite (and thus a greater recrystallization degree), e. g. lower pH and E_h. No clear effect of loading has been observed for the uptake of Tc by magnetite. In contrast to magnetite, $[Tc]_0$ has no clear impact on the neighbouring atoms of Tc in mackinawite systems. Loading affects significantly the Tc retention mechanism in mackinawite systems: TcS_2-like phase prevails at low loadings (400 ppm), whereas higher loadings favour the predominance of TcO_2-like phases, likely surface precipitates of colloidal Tc (IV) species.

5.7 Summary

5.7.1 Aquatic chemistry, redox transformations and thermodynamics of Tc (IV)

Within VESPA, a systematic literature study on aquatic technetium chemistry was performed. A clear need for improving the state of knowledge and improving the available thermodynamic database, also considering ion-interaction processes, was identified.

Within the studies of KIT-INE, the redox chemistry of technetium was studied in aqueous systems relevant to nuclear waste disposal. Based upon a detailed and systematic investigation of Tc redox chemistry in dilute aqueous solutions to highly concentrated salt brines, the stability field of Tc(IV) (reduced Tc(IV) generally exhibiting low solubility at relevant pH conditions) was defined. The same experiments allow to draw conclusions about the kinetics affecting Tc(VII) reduction processes. By systematically investigating NaCl and $MgCl_2$ solutions from low to high ionic strength, the influence of ion-interaction processes on Tc redox transformations were assessed for the first time. The studies performed within VESPA also contribute to the validation of new and existing chemical models and thermodynamic data relevant for Tc redox chemistry. Detailed experimental information on appropriate redox chemicals for use in lab-experiments aiming at reducing Tc(IV) systems was established. The key relevance of the tetravalent oxidation state of technetium under the strongly reducing geochemical environments expected for operative deep-underground nuclear waste repository systems was highlighted.

The studies of KIT-INE within VESPA using advanced XANES and EXAFS techniques show evidence that under presence of magnetite, reduction of Tc(VII) and formation of a Tc(IV) surface complex is observed in simplified systems. Furthermore some first information was obtained that incorporation of Tc(IV) into the magnetite structure may occur. This effect was described as a potential retention mechanism in low ionic strength media. Within the extension year of VESPA, further experiments were performed using EXAFS to look deeper into this effect. The key result from the experimental studies is that both the degree and mechanism of Tc retention on iron mineral phases is depending very strongly on parameters like Tc concentration, surface loading and pH conditions. A significant part of Tc(IV) is incorporated in magnetite under conditions with low Tc concentrations, whereas precipitation processes dominate at high total Tc concentrations. The incorporation of Tc (IV) is furthermore facilitated by high magnetite concentrations and crystallization rates. These experiments performed within VESPA in simplified systems thus yield key information on Tc retention processes on relevant secondary mineral phases expected to be present in a repository.

In addition to the above mentioned experimental studies focusing on the formation and stability of Tc(IV), comprehensive experimental studies were performed to analyze solubility and speciation of amorphous Tc(IV)-oxyhydroxides phase $TcO_2.xH_2O(s)$ in aqueous solutions over a large pH range and ionic strength interval (NaCl, $MgCl_2$ und $CaCl_2$) at 25 °C. New systematic studies performed in the rad-lab facilities of KIT-INE were the basis for deriving experimentally well supported thermodynamic data (solubility products and hydrolysis constants) and ion-interaction parameters (using both SIT and Pitzer approaches). The new thermodynamic data generated within VESPA will be integrated into the German thermodynamic reference database THEREDA, following the required evaluation and quality assurance processes established within THEREDA. The thermodynamic data for Tc (IV) derived within VESPA are fundamental physic-chemical parameters. As such, they are clearly site-independent and generally applicable for the geochemical modeling of different scenarios in all host-rock formations currently discussed in Germany.

5.7.2 Influence of redox kinetics on Tc-migration in natural systems

The interaction of technetium with host-rock material was investigated with (i) granitic rock from the Äspö Hard Rock Laboratory in Sweden, and (ii) material from a potential site for a nuclear waste repository in Russia (Nizhnekansky massif (NK), Middle Siberia). The sampling of the core material from Äspö under anoxic conditions was performed in collaboration with the EC CROCK project, allowing sampling under in-situ redox conditions. Part of the Äspö diorite (ÄD) was artificially oxidized for comparison with the unoxidized in-situ material. Batch-type experiments show reduction of Tc (VII) by Fe (II) minerals and Tc(IV) retention at the mineral surface. The results also indicate a strong influence of sample handling and storage on the Tc (VII) immobilization by crystalline rock. Sorption values for ÄD are ~ 2 times higher for unoxidized material compared to oxidized samples. This can be explained by a reduction of Tc(VII) to Tc(IV)-oxyhydroxide phases by the Fe(II) present in ÄD. The reduction of Tc(VII) after adsorption on the granitic surface was identified by XPS and XANES analyses. K_d values for oxidized ÄD and NK material are very similar. The formation of a colloid phase under the adopted groundwater conditions (pH 8, *I* = 0.2 M for ÄD and pH 8, *I* = 0.005 M for NK) could not be identified. Desorption of Tc is insignificant under natural conditions, whereas artificial sample oxidation over the period of one month induces increased Tc mobility (up to ~ 95 %).

The Tc mobility under near-natural conditions was investigated in a fracture of unoxidized ÄD using column migration experiments. Injections of HTO and ^{36}Cl show long tailings because of complex fracture geometry and absence of anion exclusion under the experimental conditions. Tc migration was studied with ^{95m}Tc radiotracer in the concentration range of 10^{-11} M – 10^{-9} M. Tc transport and the respective "yield" from the column experiments is inversely proportional to transport time and indicates much faster retention kinetics compared to batch studies.

The results from the studies (using both batch experiments and migration studies) were used to evaluate Tc retention on iron oxide phases and Tc (VII) redox kinetics in natural systems. Based upon the studies performed within VESPA in natural systems, a significantly improved description of Tc retention in deep geological formations discussed as potential host rocks was achieved.

5.7.3 Structural incorporation of Selenium into mineral phases (iron sulfide, calcite)

Selenium – FeS/FeS$_2$, coprecipitation and adsorption

Under reducing conditions as they are expected in waste disposal sites over long periods of time, e. g. in clay formations, selenium is expected to be present in low oxidation states (selenide: Se$^-$, Se^{2-}). Selenide species exhibit low solubilities and are therefore strongly retained in the near-field of a waste repository. However, there is hardly any literature on selenide retention, especially not on process understanding of the retention mechanisms.

In the frame of this VESPA project, selenide retention on/in iron sulfide phases was investigated. A first step was the development and optimization of an experimental procedure for the electrochemical reduction of selenite (Se(IV)) to selenide (Se(-II)). Later, the selenide retention by coprecipitation with and by adsorption on iron sulfide were investigated. The results show solely the formation of mackinawite (FeS) upon synthesis of FeS in the presence of Se (-II). The formation of a separate Se-phase was not observed. Information on the molecular scale structure was obtained from X-ray absorption spectroscopy measurements on Se (-II) doped FeS. The results show, as expected due to similar ion sizes, the substitution of S (-II) by Se(-II) in the structure. The interaction of Se(-II) with pre-existing FeS in suspensions (adsorption experiments) was investigated as well. The FeS colloids in FeS suspensions interact strongly with dissolved Se(-II). Investigations revealed the formation of mixed phases in which Se has a very similar chemical environment as in phases formed in coprecipitation experiments. Moreover, iron selenide (FeSe), that exhibits a low solubility, was also synthesized. FeSe and FeS are isostructural and form the end-members of a $FeSe_xS_{1-x}$ solid-solution series. Formation of such phases in a waste repository will lead to an effective scavenging of selenium.

Pyrite (FeS_2) is the most stable iron (II)-sulfide phase and is abundant in natural clay formations. It may form upon FeS interaction with H_2S. Since Se (-II) can be incorporated in FeS, the reaction of this compound with H_2S will lead to Se incorporated into pyrite. Correspondingly, natural pyrite samples often contain significant amounts of selenium. This indicates that in analogy to the investigated precursor phase FeS, retention of Se in/on pyrite will be effective as well.

Selenium (IV) – calcite: the adsorption/entrapment model

The state of knowledge on selenium adsorption on/in calcite is documented in the VESPA literature survey. Especially the oxidized selenium species selenate (Se $(VI)O_4^{2-}$) and selenite (Se $(IV)O_3^{2-}$) exhibit relatively high solubilities and interact only weakly with most common mineral surfaces. Therefore, ^{79}Se has been identified as a potentially critical radionuclide with respect to the long term safety of a nuclear waste repository by many Waste-Management Organizations (e. g. ONDRAF/NIRAS (Belgium), ANDRA (France), and NAGRA (Switzerland)). Over extended periods of time it may increase the radioactivity in adjacent aquifer systems.

According to literature and the studies performed in the frame of the VESPA-project, tetravalent selenium (selenite, $Se(IV)O_3^{2-}$) may as well adsorb on the calcite surface, as be incorporated into the bulk calcite structure. It is easy to show that such processes may decrease the selenium concentration in the surroundings of a potential nuclear waste repository by orders of magnitude. Sorption and incorporation of Se $(IV)O_3^{2-}$ on/in calcite proceed via the formation of a surface-solid-solution by an ion exchange process. The Se-doped surface monolayer may be overgrown upon crystal growth at elevated supersaturation such that Se $(IV)O_3^{2-}$ gets entrapped in the crystal. In the surface monolayer, the pyramidal Se $(IV)O_3^{2-}$ ion introduces only relatively small strain in the crystal structure. Therefore, adsorption is relatively efficient (K_D = 2 ± 1 mL/g, partition coefficient (of a one monolayer thick surface-solid-solution), D = 0.02 ± 0.01). Upon fast growth the surface composition is conserved and Se is incorporated, with Se $(IV)O_3^{2-}$ substituting CO_3^{2-} structurally in the bulk crystal. Inside the bulk crystal Se $(IV)O_3^{2-}$ generates considerable strain. Therefore, the conserved Se-content corresponds to a non-equilibrium state. As a consequence of this „adsorption / entrapment“ model, [HEB/VIN2014] selenium sorption on calcite at equilibrium conditions is limited to the calcite surface monolayer. Only at elevated supersaturation (depending on the Se-concentration) selenite may be coprecipitated with calcite in significant amounts with the partition coefficient of the bulk-solid-solution, D = 0.02 ± 0.01.

5.7.4 Work performed within the extension in project year 4

The work on Tc chemistry performed in the year 4 of VESPA is presented within the part of this report focusing on aquatic chemistry, redox transformations and thermodynamics of Tc (IV). Studies on ^{14}C analytics and the preparation of Sorel phases for ^{129}I retention studies are described in separate chapters.

Analytical studies on ^{14}C speciation

A new analytical method to analyze ^{14}C speciation in aqueous and gaseous samples of experiments with highly radioactive materials has been successfully established by KIT-INE within VESPA. This is a valuable contribution to work performed by KIT-INE within the EC funded CAST project, where the ^{14}C source terms for irradiated steel and Zircaloy of a spent nuclear fuel rod segment are investigated. For the handling of the samples, which show very high concentrations of ^{60}Co and ^{137}Cs in addition to the ^{14}C to be analyzed, a specifically manufactured glove box was developed and installed in the controlled area of KIT-INE. The analytical tools and the entire apparatus for the extraction and separation of organic and inorganic ^{14}C species were tested with low ^{14}C reference samples in a fume hood. After successful operation had been established, the new apparatus was transferred into the glove box. Calibration with inorganic and organic reference samples (^{14}C doped Na_2CO_3, CH_3CO_2Na, mixtures of Na_2CO_3 und CH_3CO_2Na) was performed inside the glove box. In samples containing 10 – 1000 Bq

^{14}C, a total recovery of ≥ 90 % was reached. Different LSC-cocktails and sample vials were tested in order to optimize the precision of ^{14}C analytics via LSC (liquid-scintillation-counting).

Synthesis of a Mg-oxychloride phase as starting material for investigations on ^{129}I retention

In preparation of sorption experiments with ^{129}I, different methods for the synthesis of pure a Mg-oxychloride consisting of only one clearly defined mineral phase were employed. The synthetic Mg-oxychloride was analyzed using several complementary techniques in order to prove the required sample purity and characteristics. Mg-oxychloride samples were contacted with concentrated salt solutions and the subsequent equilibration of the Sorel phase / salt brine system monitored over several weeks. Owing to the slow pre-equilibration of the samples, it was not possible to contact the synthetic Mg-oxychloride with ^{129}I within the duration of this work package of the VESPA project. Experiments on ^{129}I retention on Mg-oxychloride are now part of the KIT-INE contribution to a future VESPA (II) project.

5.8 Contributions at conferences and workshops, and articles in peer-reviewed journals resulting from work performed by KIT-INE

KIT-INE was disseminating the work performed within VESPA by several means, thus contributing to a high international visibility of the studies. Most importantly, several peer-reviewed publications have been published or are planned for the near future. Studies have been presented either as oral or poster contributions at international conferences and workshops. The active dissemination of VESPA results by KIT-INE documented below is an important aspect of scientific quality assurance, as it established a critical discussion and validation of key findings by the international research community. Furthermore, it highlights the element and importance of training and education of young researchers (PhD and Postdoc researchers) within VESPA.

The studies of E. Yalcintas performed within Chapter 2 and Chapter 3 and the extension year will be presented in her PhD thesis to be submitted in (2015).

The studies of Y. Totskiy performed within Chapter 4.1 will be presented in his PhD thesis to be submitted in (2015).

Publications in peer-reviewed scientific journals by KIT-INE

Finck, N., Dardenne, K., Bosbach, D., Geckeis, H. (2012) „Selenide Retention by Mackinawite“, Environmental Science & Technology 46: 10004-10011.

Heberling, F., Vinograd, V.L., Polly, R., Gale, J.D., Heck, S., Rothe, J., Bosbach, D., Geckeis, H., Winkler, B. (2014) “A thermodynamic adsorption/entrapment model for selenium (IV) coprecipitation with calcite.” Geochimica et Cosmochimica Acta 134: 16-38.

Heberling, F., Eng, P., Denecke, M.A., Lutzenkirchen, J., Geckeis, H., (2014) „Electrolyte layering at the calcite(104)-water interface indicated by Rb^+- and Se(VI) K-edge resonant interface diffraction“. Physical Chemistry Chemical Physics 16: 12782-12792.

Kobayashi, T., Scheinost, A.C., Fellhauer, D., Gaona, X., Altmaier, M. (2013), „Redox behavior of Tc(VII)/Tc(IV) under various reducing conditions in 0.1 M NaCl solutions”, Radiochimica Acta 101: 323-332.

Yalcintas E., Gaona, X., Scheinost, A., Kobayashi, T., Altmaier, M. and Geckeis, H. (2014) “Redox chemistry of Tc (VII)/Tc (IV) in dilute to concentrated NaCl and $MgCl_2$ solutions.” Radiochimica Acta (DOI 10.1515/ract-2014-2272).

Publications in peer-reviewed scientific journals by KIT-INE in preparation

Totskiy, Y., Huber, F., Marsac, R., Schild, D., Schäfer, T., Kalmykov, S., Geckeis, H.: “Tc interaction with crystalline rock from Äspö (Sweden) and Nizhnekansky massif (Russia)”, Applied Geochemistry, In Preparation.

Totskiy, Y., Huber, F., Kalmykov, S., Schäfer, T., Geckeis, H.: “The influence of redox kinetics on Tc(VII) mobility in crystalline formations”, Environmental Science & Technology, In Preparation.

A second manuscript by Yalcintas *et al.* on the thermodynamic model for Tc(IV) is in preparation for publication in 2015.

The studies on ^{14}C analytics will be published within a more comprehensive once experiments within CAST project have been analyzed.

Publications in conference proceedings and reports by KIT-INE

Finck, N., Dardenne, K.: Selenide retention by mackinawite: A multi-edge XAS approach”, Mineralogical Magazine, 75 (2011) 846.

Totskiy, Y., Huber, F., Schild, D., Schäfer, T., Kalmykov, S., Geckeis, H. (2014), “Tc(VII) immobilization on granitic rocks from Äspö HRL (Sweden) and Nizhnekansky massif (Russia)” Goldschmidt 2014, Book of Abstracts, p. 2506.

Totskiy, Y., Geckeis, H., Schäfer, T. “Sorption of Tc (VII) on Äspö diorite (ÄD).” (2012) 1st Workshop Proceedings of the Collaborative Project “Crystalline Rock Retention Processes” (7th EC FP CP CROCK), KIT Scientific Report 7629, 97-106.

Totskiy, Y., Schäfer, T., Huber, F., Schild, D., Geckeis, H. Kalmykov, S., (2013) “Tc(VII) sorption on natural granitic rocks and synthetic magnetite.” Final Workshop Proceedings, 7th EC FP CP-CROCK, KIT Scientific Report, 97 – 210.

Oral contributions to International Conferences and Workshops by KIT-INE

Finck, N., Dardenne, K.: “Selenide retention by mackinawite: A multi-edge XAS approach”, Goldschmidt Conference 2011, August 14-19, Prag, Czech Republic.

Heberling, F., Eng, P., Denecke, M.A., Lützenkirchen, J., Geckeis, H.: „Rb^+ at the calcite(104)-water-interface“, Lorentz Discussion 2014, 10.03. – 14.03.2014 Leiden, Netherlands.

Heberling, F., Vinograd, V.L., Polly, R.: “A Thermodynamic Entrapment Model for the Quantitative Description of Selenite Coprecipitation with Calcite”, Goldschmidt Conference 2013, 25.08. – 30.08.2013 in Florence, Italy.

Heberling, F., Eng, P., Lützenkirchen, J., Stubbs, J.E., Schäfer, T., Geckeis, H.: “Ion-specific effects at the calcite(104) water interface“, Goldschmidt Conference 2012, 24. – 29.06.2012, in Montreal, Canada.

Herm, M., González-Robles, E., Böttle, M., N. Müller, E. Bohnert, R. Dagan, D. Papaioannou,
B. Kienzler, V. Metz1, H. Geckeis: “Quantification and speciation of C-14 from a spent nuclear fuel segment – methods and first results”, 27th International Spent Fuel Workshop, 3.-5.09.2014, Karlsruhe.

Kobayashi, T., Fellhauer, Gaona, X., D., Altmaier, M., Technetium redox and Tc(IV) solubility studies, Invited Seminar Talk, 15. Oct 2010, Loughborough University, England.

Kobayashi, T., Gaona, X., Fellhauer, D., Altmaier, M., Redox Behaviour of the Tc(VII)/Tc(IV) Couple in Diluted NaCl Solution in Various Reducing Systems. 7th International Symposium on Technetium and Rhenium – Science and Utilization, Moscow, Russia, July 4-8, 2011, book of abstracts p.26.

Kobayashi, T., Gaona, X., Fellhauer, D., Altmaier, M., Redox Behavior of the Tc (VII)/Tc (IV) Couple in Various Reducing Systems and the Solubility of Tc (IV) Hydroxide. 13th International Conference on the Chemistry and Migration Behavior of Actinides and Fission Products in the Geosphere (MIGRATION), Beijing (China), September 18 – 23, 2011.

Yalcintas, E., Gaona, X., Altmaier, M., Scheinost, A. C., Kobayashi, T., Geckeis, H., Technetium Redox Chemistry and Solubility: Applied Chemistry Relevant for Nuclear Waste Disposal., 44th IUPAC World Chemistry Congress, Istanbul (Turkey), August 11-16, 2013.

Yalcintas, E., Gaona, X., Altmaier, M., Scheinost, A. C., Kobayashi, T., Geckeis, H., Redox Chemistry, Solubility and Hydrolysis of Technetium in Dilute to Concentrated NaCl and $MgCl_2$ Solutions. 14th International Conference on the Chemistry and Migration Behavior of Actinides and Fission Products in the Geosphere, Brighton (UK), September 8-13, 2013.

Yalcintas, E., Gaona, X., Scheinost, A. C., Altmaier, M., Kobayashi, T., Geckeis, H., Aquatic chemistry and thermodynamics of Tc in dilute to concentrated saline systems, 8th International Symposium on Technetium and Rhenium: Science and Utilization, September 29th - October 3rd 2014, La Baule - Pornichet, France.

Poster contributions to International Conferences and Workshops by KIT-INE

Altmaier, M., Bischofer, B., Bosbach, D., Brendler, V., Curtius, H., Geckeis, H., Herbert, H.-J., Jordan, N.; VESPA – Verbundprojekt zur Untersuchung des Verhaltens langlebiger Spalt- und Aktivierungsprodukte im Nahfeld eines nuklearen Endlagers. GDCh Wissenschaftsforum Chemie 2011, Bremen (Germany), September 04-07, 2011.

Altmaier, M., Bischofer, B., Bosbach, D., Brendler, V., Curtius, H., Geckeis, H., Jordan, N., Munoz, A.G.; VESPA – Ein Verbundprojekt zur Untersuchung des Verhaltens langlebiger Spalt- und Aktivierungsprodukte im Nahfeld eines nuklearen Endlagers und Möglichkeiten ihrer Rückhaltung. GDCh Wissenschaftsforum Chemie 2013, Darmstadt (Germany), 1-4. September, 2013.

Finck, N., Dardenne, K., Bosbach, D., Geckeis, H.: „Selenide retention by mackinawite“, Selen2012 workshop, 08-09 Octobre 2012, KIT-IMG, Karlsruhe.

Heberling, F.: “X-ray surface diffraction investigations of calcite(104)”, Lorentz Discussion 2014, 10.03. – 14.03.2014 in Leiden, Netherlands.

Heberling, F., Heck, S., Rothe, J.: “The calcite – water interface and its interactions with selenium IV and VI” Selen workshop, 08.10. – 09.10.2012, in Karlsruhe, Germany.

Heberling, F., Heck, S., Rothe, J.: “The calcite – water interface and its interactions with selenium IV and VI”, Goldschmidt Conference 2011, 14.08. – 19.08.2011, Prag, Czech Republic.

Jordan, N.; Foerstendorf, H.; Scheinost, A. C.; Lützenkirchen, J.; Schild, D.; Weiß, S.; Heim, K.; Brendler, V.: Geological Disposal of Radioactive Waste: Underpinning Science and Technology, 18.-20.10.2011, Loughborough, England.

Kobayashi, T., Yalcintas, E., Altmaier, M., Solubility of $TcO_2(s)•xH_2O$ in dilute to concentrated NaCl, $CaCl_2$, and $BaCl_2$ solutions. ABC-Salt II workshop "Actinide Brine Chemistry in a Salt-Based Repository“, Karlsruhe (Germany), November 7-8, 2011.

Polly, R., Heberling, F., Schimmelpfennig, B., Geckeis, H.: “Quantum Chemical investigation of the sorption of selenite on the calcite (104) surface and incorporation into the bulk phase”, Migration 2013 08.09. – 13.09. 2013 in Brighton, UK

Thien, B., Heberling, F., Kulik, D.: “Modeling Non-Equilibrium Uptake of Se(IV) Upon Calcite Precipitation” Goldschmidt 2013, 25.08. – 30.08.2013, Florence, Italy.

Totskiy, Y., Geckeis, H., Schäfer, T.: “Sorption of Tc(VII) on crystalline rock material from Äspö (Sweden)”, Joint ITU-INE Research Fellow's Day, JRC-KIT, Karlsruhe, 22 June 2012, pp. 118-119.

Totskiy, Y., Stage, E., Geckeis, H., Schäfer, T., Kalmykov, S.: “Sorption of Tc(VII), Cs(I), Eu(III), U(VI) and Am(III) on crystalline rock material from Äspö (Sweden) and Nizhnekansk massif (Russia)”, Proceedings of the 7th Russian Conference on Radiochemistry “Radiochemistry-2012”, Dimitrovgrad, Russia, 15-19 October, 2012, p. 350.

Totskiy, Y., Yalcintas, E., Huber, F., Gaona, X., Schäfer, T., Altmaier, M., Kalmykov, S., Geckeis, H. A contribution from fundamental and applied technetium chemistry to the nuclear waste disposal safety case, Key Topics in Deep Geological Disposal, Cologne, Germany, 25-26 September, 2014, p. 56.

Totskiy, Y., Schäfer, T., Geckeis, H. Tc(VII) immobilization on granitoid rocks from Äspö (Sweden), 14th International Conference on the Chemistry and Migration Behaviour of Actinides and Fission Products in the Geosphere, Brighton, UK, 8-13 September, 2013.

Totskiy, Y., Huber, F., Schild, D., Schäfer, T., Kalmykov, S., Geckeis, H. Tc(VII) immobilization on granitic rocks from Äspö (Sweden) and Nizhnekansky massif (Russia), TRePro III – Workshop on Modelling of Coupled Reactive and Transport Processes, Karlsruhe, Germany, 5-7 March, 2014, p.138-139.

Yalcintas, E., Kobayashi, T., Altmaier, M., Geckeis, H., Redox behavior of Tc(VII)/Tc(IV) couple in dilute to concentrated NaCl solutions. ABC-Salt II workshop "Actinide Brine Chemistry in a Salt-Based Repository“, Karlsruhe (Germany), November 7-8, 2011.

Yalcintas, E., Kobayashi, T., Altmaier, M., Geckeis, H., Technetium redox chemistry in dilute to concentrated aqueous systems, International Conference on Nuclear and Radiochemistry (NRC-8), Como, Italy, 2012 Sep 16-21.

Yalcintas, E., Gaona, X., Kobayashi, T., Altmaier, M., Geckeis, H.,Redox chemistry and solubility of ^{99}Tc in saline NaCl and $MgCl_2$ solutions. ABC-Salt III Workshop "Actinide Brine Chemistry in a Salt-Based Repository“, Fanta Fe (USA), April 15-17, 2013.

Yalcintas, E., Gaona, X., Altmaier, M., Geckeis, H., Thermodynamic description of Tc(IV) solubility and hydrolysis in dilute to concentrated NaCl, $MgCl_2$ and $CaCl_2$ solutions, ISSP-16, 21-25 July 2014, Karlsruhe, Germany.

5.9 References (chapter 5)

[ALB/CHR1991] Albinsson, Y., Christiansensatmark, B., Engkvist, I., Johansson, W., Transport of Actinides and Tc through a Bentonite Backfill Containing Small Quantities of Iron or Copper, Radiochim. Acta, 52 (1991) 283-286.

[ALL/KIG1979] Allard, B., Kigatsi, H., Torstenfelt, B., Technetium - Reduction and Sorption in Granitic Bedrock, Radiochem. Radioanal. Letters, 37 (1979) 223-229.

[ALS1925] Alsen, N., Roentgenographische Untersuchungen der Kristallstrukturen von Magnetkies, Breithauptit, Pentlandit, Millerit und verwandten Verbindungen, Geol. Foeren. Foerhandl., 47 (1925) 19−72.

[ALT/MET2003] Altmaier, M., Metz, V., Neck, V., Müller, R., Fanghänel, T., Solid-liquid equilibria of Mg(OH)2(cr) and Mg2(OH)3Cl·4H2O(cr) in the system Mg-Na-H-OH-O-Cl-H2O at 25 °C, Geochim. Cosmochim. Acta, 67 (2003), 3595-3601.

[ALT/NEC2008] Altmaier, M., Neck, V., Fanghänel, T., Solubility of Zr(IV), Th (IV) and Pu(IV) hydrous oxides in CaCl2 solutions and the formation of ternary Ca-M(IV)-OH complexes, Radiochim. Acta, 96 (2008) 541-550.

[ANK/BOU2002] Ankudinov, A. L., Bouldin, C. E., Rehr, J. J., Sims, J., Hung, H., Parallel calculation of electron multiple scattering using Lanczos algorithms, Phys. Rev., B65 (2002) 104107.

[ANK/RAV1998] Ankudinov, L. A., Ravel, B., Rehr, J. J., Conradson, S. D., Real−space multiple−scattering calculation and interpretation of X−ray absorption near−edge structure, Phys. Rev., B58 (1998) 7565−7576.

[AST/PIN2003] Astilleros, J. M., Pina, C. M., Fernandez-Diaz, L.,Putnis, A., Metastable phenomena on calcite {10-14} surfaces growing from Sr^{2+}-Ca^{2+}-CO_3^{2-} aqueous solutions, Chem. Geol., 193 (2003) 93-107.

[AUR/FER2010] Aurelio, G., Fernandez-Martinez, A., Cuello, G. J., Roman-Ross, G., Alliot, I.,Charlet, L., Structural study of selenium(IV) substitutions in calcite, Chem. Geol., 270 (2010) 249-256.

[BAR1994] Barry, P. H., Jpcalc, a software package for calculating liquid-junction potential corrections in patch-clamp, intracellular, epithelial and bilayer measurements and for correcting junction potential measurements, J. Neurosci. Meth., 51 (1994) 107-116.

[BAS/BER1995] Baston, G.M.N., Berry, J.A., Brownsword, M., Cowper, M.M., Heath, T.G., Tweed, C.J., The sorption of uranium and technetium on bentonite, tuff and granodiorite, Mat. Res. Soc. Symp. Proc., 353 (1995) 989-996.

[BEN/FAT1998] Ben Said, K., Fattahi, M., Musikas, C., Delorme-Hiver, A., Abbe, J. C., A novel approach to the oxidation potential of the Tc(VII)/Tc(IV) couple in hydrochloric acid medium through the reduction of TcO_4^- by Fe^{2+} ion, Radiochim. Acta, 83 (1998) 195-203.

[BER1970] Berner, R. A., Sedimentary pyrite formation, Amer. J. Sci., 268 (1970) 1−23.

[BIS/HAG2009] Bischofer, B. P., Hagemann, S., Hühne, C., Schönwiese, D., Scharge, T., Influence of chloride concentrations on the signal of redox electrode and on UV-spectrophotometric determination of Fe species, in 1st Annual Workshop Proceedings 7th EC FP- Recosy CP, Barcelona, (2009).

[BLA/BAE1992] Blanchard, D. L.,Baer, D. R., The Interactions of Co, Mn and Water with Calcite Surfaces, Surf. Sci., 276 (1992) 27-39.

[BLO1994] Blochl, P. E., PROJECTOR AUGMENTED-WAVE METHOD, Phys. Rev. B, 50 (1994) 17953-17979.

[BOG/DON2010] Boggs, M. A., Dong, W., Gu, B., Wall, N. A., Complexation of Tc(IV) with acetate at varying ionic strengths, Radiochim. Acta, 98 (2010) 583–587.

[BON/FRA1979] Bondietti, E.A., Francis, C.W., Geologic Migration Potentials of Technetium-99 and Neptunium-237, Science, 203 (1979) 1337-1340.

[BOY/LAR1960] Boyd, G.E., Larson, Q.V., Motta, E.E., Isolation of Milligram Quantities of Long-Lived Technetium from Neutron Irradiated Molybdenum. J. Am. Chem. Soc., 82 (1960) 809-815.

[BRA/BAE2003] Bradbury, M.H., Baeyens, B. A., Comparison of apparent diffusion coefficients measured in compacted Kunigel V1 bentonite with those calculated from batch sorption measurements and De (HTO) Data: A Case Study for Cs (I), Ni (II), Sm (III), Am (III), Zr (IV) and Np(V), PSI Bericht Nr. 03-02, Villigen, Switzerland (2003).

[BRE/BAN2009] Brendebach, B., Banik, N. L., Marquardt, C. M., Rothe, J., Denecke, M. A., Geckeis, H., X-ray absorption spectroscopic study of trivalent and tetravalent actinides in solution at varying pH values, Radiochim. Acta, 97 (2009) 701-708.

[BRU/EMM1938] Brunauer, S., Emmett, P.H., Teller, E., Adsorption of gases in multimolecular layers, J. Am. Chem. Soc., 60 (1938), 309-319.

[BRU/MAS2013] Bruno, M., Massaro, F. R., Pastero, L., Costa, E., Rubbo, M., Prencipe, M.,Aquilano, D., New Estimates of the Free Energy of Calcite/Water Interfaces for Evaluating the Equilibrium Shape and Nucleation Mechanisms, Cryst. Growth Des., 13 (2013) 1170-1179.

[CAL/MIL2003] Calvin, S., Miller, M. M., Goswami, R., Cheng, S. F., Mulvaney, S. P., Whitman, L. J., Harris, V. G., Determination of crystallite size in a magnetic nanocomposite using extended x−ray absorption fine structure, J. Appl. Phys., 94 (2003) 778−784.

[CAN/MAE2010] De Canniere, P., Maes, A., Williams, S., Bruggeman, C., Beauwens T., Maes, N., Cowpers, M., Behavior of selenium in Boom Clay. External Report of the Belgian Nuclear Research Centre, SCK•CEN−ER−120, 2010.

[CAR/BRU1992] Carroll, S. A., Bruno, J., Petit, J. C.,Dran, J. C., Interactions of U(VI), Nd, and Th(IV) at the Calcite-Solution Interface, Radiochim. Acta, 58-9 (1992) 245-252.

[CAR/SMI1955] Cartledge, G. H., Smith, W. T., Revision of the Electrode-Potential Diagram for Technetium, J. Phys. Chem., 59 (1955) 1111-1112.

[CHE/LYM1997] Cheng, L. W., Lyman, P. F., Sturchio, N. C.,Bedzyk, M. J., X-ray standing wave investigation of the surface structure of selenite anions adsorbed on calcite, Surf. Sci., 382 (1997) L690-L695.

[CHE/UNG1967] Cherin, P., Unger, P., The crystal structure of trigonal selenium, Inorg. Chem., 6 (1967) 1589−1591.

[CHE/UNG1972] Cherin, P., Unger, P., Refinement of the crystal structure of α−monoclinic Se, Acta Cryst., B28 (1972) 313−317.

[CLA/SEG2005] Clark, S. J., Segall, M. D., Pickard, C. J., Hasnip, P. J., Probert, M. J., Refson, K.,Payne, M. C., First principles methods using CASTEP, Z. Kristall., 220 (2005) 567-570.

[COB/SMI1953] Cobble, J. W., Smith, W. T., Boyd, G. E., Thermodynamic Properties of Technetium and Thenium Compounds .2. Heats of Formation of Technetium Heptoxide and Pertechnic Acid, Potential of the Technetium(IV)-Technetium(VII) Couple, and a Potential Diagram for Technetium, J. Amer. Chem. Soc., 75 (1953) 5777-5782.

[COL/DEM1955] Cole, W.F., Demediuk, T., X-Ray, Thermal, and Dehydration Studies on Magnesium Oxychlorides, Austral. J. Chem., 8 (1955), 234-251.

[COU/CHR2008] Courdouan, A., Christl, I., Rabung, T., Wersin, P., Kretzschmar, R., Proton and trivalent metal cation binding by dissolved organic matter in the Opalinus Clay and the Callovo-Oxfordian formation. Environ. Sci. Technol., 42 (2008) 5985–5991.

[COW/ZAC1990] Cowan, C. E., Zachara, J. M.,Resch, C. T., Solution ion effects on the surface exchange of selenite on calcite, Geochim. Cosmochim. Acta, 54 (1990) 2223-2234.

[CSA/ROD2012] Csakberenyi−Malasics, D., Rodriguez−Blanco, J. D., Kovacs Kis, V., Recnik, A., Benning, L. G., Posfai, M., Structural properties and transformations of precipitated FeS. Chem. Geol., 294−295 (2012) 249−258.

[CUI/ERI1996a] Cui, D. Q., Eriksen, T. E., Reduction of pertechnetate by ferrous iron in solution: Influence of sorbed and precipitated Fe(II), Environ. Sci. Technol., 30 (1996) 2259-2262.

[CUI/ERI1996b] Cui, D. Q., Eriksen., T. E., (1996) Reduction of pertechnetate in solution by heterogeneous electron transfer from Fe(II)-containing geological material, Environ. Sci. Technol., 30 (1996) 2263-2269.

[CUI/PUR2009] Cui, D., Puranen, A., Devoy, J., Scheidegger, A., Leupin, O. X., Wersin, P., Gens, R., Spahiu, K., Reductive immobilization of 79Se by iron canister under simulated repository environment, J. Radioanal. Nucl. Chem., 282 (2009) 349−354.

[DEM/RAI2011] Demichelis, R., Raiteri, P., Gale, J. D., Quigley, D.,Gebauer, D., Stable prenucleation mineral clusters are liquid-like ionic polymers, Nat. Commun., 2 (2011) Article number 590.

[DEW/WAL1953] de Wolff, P.M., Walter-Levy, L., The crystal structure of Mg2 (OH) 3(Cl (Br)) •4H2O, Acta Crystallogr., 6 (1953), 40-44.

[DIE/NEU2011] Diener, A., Neumann, T., Synthesis and incorporation of selenide in pyrite and mackinawite, Radiochim. Acta, 2011, 99 (2011) 791−798.

[DIE/NEU2012] Diener, A., Neumann, T., Kramar, U., Schild, D., Structure of selenium incorporated in pyrite and mackinawite as determined by XAFS analyses, J. Contam. Hydrol., 133 (2012) 30−39.

[DIN/OES2012] Dinnebier, R.E., Oestreich, M., Bette, S., Freyer, D., 2Mg (OH) 2•MgCl2•2H2O and 2Mg (OH) 2•MgCl2•4H2O, two high temperature phases of the magnesia cement system, Z. Anorg. Allg. Chem., 638 (2012) 628-633.

[ELW/GER1992] Elwear, S., German, K. E. Peretrukhin, V. F., Sorption of technetium on inorganic sorbents and natural minerals, J. Radioanal. Nucl. Chem., 157 (1992) 3-14.

[ELZ/ROU2006] Elzinga, E. J., Rouff, A. A.,Reeder, R. J., The long-term fate of Cu^{2+}, Zn^{2+}, and Pb^{2+} adsorption complexes at the calcite surface: An X-ray absorption spectroscopy study, Geochim. Cosmochim. Acta, 70 (2006) 2715-2725.

[ERI/NDA1992] Eriksen, T. E., Ndalamba, P., Bruno, J., Caceci, M., The Solubility of TcO_2 . nH_2o in Neutral to Alkaline-Solutions under Constant p_{CO2}, Radiochim. Acta, 58 (1992) 67-70.

[EVA/HAL2012] Evans, N. D. M., Hallam, R., The complexation of Tc(IV) with EDTA and picolinic acid at high pH, Miner. Mag., 76 (2012) 3435–3438.

[FEI/HEL1944] Feitknecht, W., Held, F., Über die Hydroxychloride des Magnesiums, Helv. Chem. Acta, 27 (1944), 1480-1495.

[FEL2013] Fellhauer, D., Untersuchungen zur Redoxchemie und Löslichkeit von Neptunium und Plutonium, PhD Thesis, 2013, University of Heidelberg Karlsruhe, Germany.

[FEL/NEC2010] Fellhauer, D., Neck, V., Altmaier, M., Lützenkirchen, J., Fanghänel, T., Solubility of tetravalent actinides in alkaline $CaCl_2$ solutions and formation of $Ca_4[An(OH)_8]^{4+}$ complexes: A study of Np(IV) and Pu(IV) under reducing conditions and the systematic trend in the An(IV) series, Radiochim. Acta, 98 (2010) 541-548.

[FEN/KER2013] Fenter, P., Kerisit, S., Raiteri, P.,Gale, J. D., Is the Calcite-Water Interface Understood? Direct Comparisons of Molecular Dynamics Simulations with Specular X-ray Reflectivity Data, J. Phys. Chem. C, 117 (2013) 5028-5042.

[FEN/STU2012] Fenter, P.,Sturchio, N. C., Calcite (104)-water interface structure, revisited, Geochim. Cosmochim. Acta, 97 (2012) 58-69.

[FER/CHA2009] Fernández-Martínez, A., Charlet, L., Selenium environmental cycling and bioavailability: a structural chemist point of view, Rev. Environ. Sci. Biotechnol., 8 (2009) 81-110.

[FIN/DAR2012] Finck, N., Dardenne, K., Bosbach, D., Geckeis H., Selenide retention by mackinawite, Environ. Sci. Technol., 46 (2012) 10004-10011.

[FRE/ZAC2009] Fredrickson, J.K., Zachara, J.M., Plymale, A.E., Heald, S.M., McKinley, J.P., Kennedy, D.W., Liu, C., Nachimutu, P., Oxidative dissolution potential of biogenic and ablogenic TcO2 in subsurface sediments, Geochim. Cosmochim. Acta, 73 (2009) 2299-2313.

[FRE/VOI2010] Freyer, D., Voigt, W., Entwicklung eines Grundkonzeptes für langzeitstabile Streckendämme im leichtlöslichen Salzgestein (Carnallitit) für UTD/UTV; BMBF Förderkennzeichen 02C1204; Teilbericht 5: TB 5.2: "MgO-Baustoff - Untersuchungen zur Bildung von Sorelphasen". Technische Universität Bergakademie Freiberg, Freiberg, 2010, pp. 143-194.

[GAL/ROH2003] Gale, J. D.,Rohl, A. L., The General Utility Lattice Program (GULP), Mol. Simul., 29 (2003) 291-341.

[GAL/ROH2007] Gale, J. D.,Rohl, A. L., An efficient technique for the prediction of solvent-dependent morphology: The COSMIC method, Mol. Simul., 33 (2007) 1237-1246.

[GAN/STU1992] Gan, H., Stucki, J. W., Bailey, G. W., Reduction of Structural Iron in Ferruginous Smectite by Free-Radicals, Clays Clay Miner., 40 (1992) 659-665

[GAO/DAH2011] Gaona, X., Dahn, R., Tits, J., Scheinost, A. C., Wieland, E., Uptake of Np(IV) by C-S-H phases and cement paste: an EXAFS study, Environ. Sci. Technol., 45 (2011) 8765-8771.

[GAU/BLA2006] Gaucher, E. C., Blanc, P., Bardot, F., Braibant, G., Buschaert, S., Crouzet, C., Gautier, A., Girard, J. P., Jacquot, E., Lassin, A., Negrel, G., Tournassat, C., Vinsot, A., Altmann, S., Modelling the porewater chemistry of the Callovian−Oxfordian formation at a regional scale, C. R. Geoscience, 338 (2006) 917−930.

[GAU/ROB2004] Gaucher, E., Robelin, C., Matray, J.M., Negrel, G., Gros, Y., Heitz, J.F., Vinsot, A., Rebours, H., Cassabagnere, A., Bouchet, A., ANDRA underground research laboratory: Interpretation of the mineralogical and geochemical data acquired in the Callovian– Oxfordian Formation by investigative drilling. Phys. Chem. Earth, 29 (2004) 55 77.

[GER/BRU2002] Geraedts, K., Bruggeman, C., Maes, A., Van Loon, L. R., Rossberg, A., Reich, T., Evidence for the existence of Tc(IV) - humic substance species by X-ray absorption near-edge spectroscopy, Radiochim. Acta, 90 (2002) 879-884.

[GLY2000] Glynn, P. D., Solid-solution solubilities and thermodynamics: Sulfates, carbonates and halides, Reviews in Mineralogy and Geochemistry, Volume 40 (2000) 480-511.

[GRA2008] Grambow, B., Mobile fission and activation products in nuclear waste disposal, J. Contam. Hydrol., 102 (2008) 180-186.

[GRA/ROG1978] Grassi, J., Rogelet, P., Devynck, J., Tremillon, B., Radiopolarography of technetium(VII) in acidic medium, J. Electroanal. Chem., 88 (1978) 97-103.

[GRA/DEV1979] Grassi, J., Devynck, J., Tremillon, B., Electrochemical studies of technetium at a mercury-electrode, Anal. Chim. Acta, 107 (1979) 47-58.

[GRE/PUI1997] Grenthe, I., Puigdomenech, I., Modelling in aquatic chemistry, ed. OECD Nuclear Energy Agency, Paris, Elsevier, 1997.

[GUI/FAN2003] Guillaumont, R., Fanghanel, T., Neck, V., Fuger, J., Palmer, D.A., Grenthe, I., Rand, M. H., Update on the Chemical Thermodynamics of Uranium, Neptunium, Plutonium, Americium and Technetium, Chemical Thermodynamics, vol. 5, OECD Nuclear Energy Agency (NEA) (Eds), Elsevier, Amsterdam, 2003.

[HAE/KIN1933] Haegg, G., Kindstroem, A. L., Roentgenuntersuchungen am System Eisen−Selen, Z. Phys. Chem., B22 (1933) 453−464.

[HAR/MOL1984] Harvie, C.E., Møller, N., Weare, J.H., The prediction of mineral solubilities in natural waters: the Na-K-Mg-Ca-H-Cl-SO4-OH-HCO3-CO3-CO2-H2O system from zero to high concentration at 25 °C, Geochim. Cosmochim. Acta, 48 (1984) 723-751.

[HAW/FER1975] Hawthorn, F. C., Ferguson, R. B., Anhydrous sulphates. I. Refinement of the crystal structure of celestite with an appendix on the structure of thenardite, Can. Miner., 13 (1975) 181−187.

[HE/YAO2010] He, Q., Yao, K., Microbial reduction of selenium oxyanions by Anaeromyxobacter dehalogenans, Bio. Technol., 101 (2010) 3760−3764.

[HEA/ZAC2007] Heald, S.M., Zachara, J.M., Jeon, B.-H., McKinley, J.P., Kukkadapu, R., Moore, D., XAFS study of the chemical and structural states of technetium in Fe(III) oxide Co-precipitates. X-Ray Absorption Fine Structure-XAFS13: *13th International Conference. AIP Conference Proceedings*, 882 (2007) 173-17.

[HEB/BOS2014] Heberling, F., Bosbach, D., Eckhardt, J.-D., Fischer, U., Glowacky, J., Haist, M., Kramar, U., Loos, S., Müller, H. S., Neumann, T., Pust, C., Schäfer, T., Stelling, J., Ukrainczyk, M., Vinograd, V., Vučak, M.,Winkler, B., Reactivity of the calcite-water-interface, from molecular scale processes to industrial applications, Appl. Geochem., 45 (2014) 158-190.

[HEB/DEN2008] Heberling, F., Denecke, M. A.,Bosbach, D., Neptunium(V) Coprecipitation with Calcite, Environ. Sci. Technol., 42 (2008) 471-476.

[HEB/TRA2011] Heberling, F., Trainor, T. P., Lützenkirchen, J., Eng, P., Denecke, M. A.,Bosbach, D., Structure and reactivity of the calcite-water interface, J. Colloid Interf. Sci., 354 (2011) 843-857.

[HEB/VIN2014] Heberling, F., Vinograd, V. L., Gale, J. D., Heck, S., Rothe, J., Winkler, B., Bosbach, D.,Geckeis, H., A thermodynamic adsorption/entrapment model for selenium(IV) coprecipitation with calcite, Geochim. Cosmochim. Acta, 134 (2014) 16-38.

[HEC/SCH2012] Heck, S., Schäfer, T., Short Note: CP CROCK groundwater sample characterization (2012).

[HEN/KRA1928] Henderson, L. M., Kracek, F. C., Parsons, C. L., Moore, R. B., Lind, S. C., Schaefer, O. C., Niermann, J. L., Scholl, C. E., Strong, R. K., Mc Coy, H. N., Ebler, E., van Rhyn, A. J., Doerner, H. A., Hoskins, W. M.,Germann, F. E. E., Die fraktionierte Fällung von Barium- und Radiumchromaten, Fresenius J. Anal. Chem., 74 (1928) 255-259.

[HER/CRO1994] Heron, G., Crouzet, C., Bourg, A.C.M., Christensen, T.H., Speciation of Fe(II) and Fe(III) in contaminated aquifer sediments using chemical extraction techniques, Environ. Sci. Technol., 28 (1994) 1698-1705.

[HES/XIA2004] Hess, N. J., Xia, Y. X., Rai, D., Conradson, S. D., Thermodynamic model for the solubility of $TcO_2.xH_2O$(am) in the aqueous Tc(IV)-Na^+-Cl^--H^+-OH^--H_2O system, J. Solution Chem., 33 (2004) 199-226.

[HOU/KEL1984] House, C. I., Kelsall, G. H., Potential-Ph Diagrams for the Sn/H_2O-Cl System, Electrochim. Acta, 29 (1984) 1459-1464.

[HOW1977] Howard III, J. H., Geochemistry of selenium: formation of ferroselite and selenium behavior in the vicinity of oxidizing sulfide and uranium deposits, Geochim. Cosmochim. Acta, 41 (1977) 1665−1678.

[HU/ZAV2008] Hu, Q.H., Zavarin, M., Rose, T.P., Effect of reducing groundwater on the retardation of redox-sensitive radionuclides, Geochem. Trans., 9 (2008) 12.

[HUA/DEN2008] Hua, B., Deng, B., Reductive immobilization of uranium(VI) by amorphous iron sulfide, Environ. Sci. Technol., 42 (2008) 8703−8708.

[HUB/KUN2011] Huber, F., Kunze, P., Geckeis, H., Schäfer, T., Sorption reversibility kinetics in the ternary system radionuclide–bentonite colloids/nanoparticles–granite fracture filling material, Appl. Geochem., 26 (2011) 2226-2237.

[HUL1917] Hull, A. W., Crystal structure of alpha−iron, Phys. Rev., 10 (1917) 661−696.

[HUM/BER2002] Hummel, W., Berner, U., Curti, E., Pearson, F. J.,Thoenen, T., Nagra/PSI chemical thermodynamic data base 01/01, Radiochim. Acta, 90 (2002) 805-813.

[JAI/DON2009] Jaisi, D.P., Dong, H., Plymale, A.E., Fredrickson J.K., Zachara, J.M., Heald, S., Liu, C., Reduction and long-term immobilization of technetium by Fe(II) associated with clay mineral nontronite, Chem. Geol., 264 (2009) 127-138.

[JAN/NET2014] Janecek, J., Netz, R. R., Flörsheimer, M., Klenze, R., Schimmelpfennig, B.,Polly, R., Influence of hydrogen bonding on the structure of the (001) corundum-water interface. Density functional theory calculations and Monte Carlo simulations, Langmuir, 30 (2014) 2722-2728.

[KAP2003] Kaplan, D. I., Influence of surface charge of an Fe-oxide and an organic matter dominated soil on iodide and pertechnetate sorption, Radiochim. Acta 91 (2003) 173-178.

[KAP/SER1998] Kaplan, D.I., Serne, R.J., Pertechnetate exclusion from sediments, Radiochim. Acta, 81 (1998) 117-124.

[KIN/COO2009] Kinniburgh D. G. and Cooper D. M., PhreePlot: Creating graphical output with PHREEQC, (2009) available at http://www.phreeplot.org.

[KRA/HAI1988] Krause, M. O., Haire, R. G., Keski-Rahkonen, O., Peterson, J. R., Photoelectron spectrometry of the actinides from Ac to Es, J. Electron Spectrosc. Relat. Phenom. 47, 215–226.

[KRE/FUR1996] Kresse, G.,Furthmuller, J., Efficiency of ab-initio total energy calculations for metals and semiconductors using a plane-wave basis set, Comput. Mater. Sci., 6 (1996) 15-50.

[KRE/HAF1993] Kresse, G.,Hafner, J., ABINITIO MOLECULAR-DYNAMICS FOR LIQUID-METALS, Phys. Rev. B, 47 (1993) 558-561.

[KRE/HAF1994] Kresse, G.,Hafner, J., AB-INITIO MOLECULAR-DYNAMICS SIMULATION OF THE LIQUID-METAL AMORPHOUS-SEMICONDUCTOR TRANSITION IN GERMANIUM, Phys. Rev. B, 49 (1994) 14251-14269.

[KRE/JOU1999] Kresse, G.,Joubert, D., From ultrasoft pseudopotentials to the projector augmented-wave method, Phys. Rev. B, 59 (1999) 1758-1775.

[KUB1993] Kubota, M., Recovery of technetium from high-level liquid waste generated in nuclear fuel reprocessing, Radiochim. Acta, 63 (1993) 91−96.

[JOR/BUH2010] Jorg, G., Buhnemann, R., Hollas, S., Kivel, N., Kossert, K., Van Winckel, S., Gostomski, C. L. V.,Preparation of radiochemically pure Se-79 and highly precise determination of its half-life, Appl. Radiat. Isot., 68 (2010) 2339-2351.

[KAN/AOY2001] Kanesaka, I., Aoyama, S., Vibrational spectra of magnesia cement, phase 3, J. Raman Spectrosc., 32 (2001) 361-367.

[KEO/MUL2004] McKeown, D. A., Muller, I. S., Gan, H., Pegg, I. L., Stolte, W. C., Determination of sulphur environments in borosilicate waste glasses using X−ray absorption near−edge spectroscopy, J. Non−Cryst. Solids, 333 (2004) 74−84.

[KIE/BOH2014] Kienzler, B., Bohnert, E., Gonzalez-Robles, E., Herm, M., Gaona, X., Borkel, C. Speciation of C-14 in Spent Nuclear Fuel. Proceedings of 7th EC FP – FIRST-Nuclides 2nd Annual Workshop, November 5th-7th, 2013, Antwerp, Belgium, KIT Scientific Reports, Karlsruhe KIT-SR 7676 (2014).

[KIE/VEJ2003] Kienzler, B.,Vejmelka, P., Römer, J., Fanghänel, E., Jansson, M., Eriksen, T.E., Wikberg, P., Swedish-German actinide migration experiment at ÄSPÖ hard rock laboratory, J. Contam. Hydrol., 61 (2003) 219-233.

[KIE/VEJ2009] Kienzler, B., Vejmelka, P., Römer, J., Schild, D., Jansson, M., Actinide migration in fractures of granite host rock: laboratory and in situ investigations. Nucl. Technol., 165 (2009) 223-240.

[KIR/FEL2011] Kirch, R., Fellhauer, D., Altmaier, M., Neck, V., Rossberg, A., Fanghänel, T., Charlet, L., Scheinost, A. C., Oxidation state and local structure of plutonium reacted with magnetite, mackinawite, and chukanovite, Environ. Sci. Technol., 45 (2011) 7267−7274.

[KIT/INE2012] KIT-INE, Characterization of experimental material, 7th EC FP CP CROCK, Deliverable D-N° 1.2 (2012).

[KOB/SCH2013] Kobayashi, T., Scheinost, A. C., Fellhauer, D., Gaona, X., Altmaier, M., Redox behavior of Tc(VII)/Tc(IV) under various reducing conditions in 0.1 M NaCl solutions, Radiochim. Acta, 101 (2013) 323-332.

[KOP/ABU1998] Kopunec, R., Abudeab, F. N., Skraskova, S., Extraction of pertechnetate with tetraphenylphosphonium in the presence of various acids, salts and hydroxides, J. Radioanal. Nucl. Chem., 230 (1998) 51-60.

[LAU/BAE2000] Lauber, M., Baeyens, B., Bradbury, M .H., Physico-chemical characterisation and sorption measurements of Cs, Sr, Ni, Eu, Th, Sn and Se on Opalinus clay samples from Mt. Terri, PSI Bericht Nr. 00-10, Paul Scherrer Institute, Villigen, and Nagra Technical Report NTB 00-11 (2000) Nagra, Wettingen, Switzerland.

[LEN/RED1995] Lennie, A. R., Redfern, S. A. T., Schofield, P. F., Vaughan, D. J., Synthesis and Rietveld crystal structure refinement of mackinawite, tetragonal FeS, Miner. Mag., 59 (1995) 677−683.

[LIE1993] Lieser, K. H., Technetium in the nuclear fuel cycle, in medicine and in the environment, Radiochim. Acta, 63 (1993) 5–8.

[LIE/BAU1987] Lieser, K. H., Bauscher, C., Technetium in the hydrosphere and in the geosphere, Radiochim. Acta, 42 (1987) 205−213.

[LIU/TER2008] Liu, Y., Terry, J., Jurisson, S., Pertechnetate immobilization with amorphous iron sulphide, Radiochim. Acta, 96 (2008) 823−833.

[LIU/FAT2008] Liu, X., Fattahi, M., Montavon, G., Grambow, B., Selenide retention onto pyrite under reducing conditions, Radiochim. Acta, 96 (2008) 473−479.

[LIV/JON2004] Livens, F. R., Jones, M. J., Hynes, A. J., Charnock, J. M., Mosselmans, J. F. W., Hennig, C., Steele, H., Collison, D., Vaughan, D. J., Pattrick, R. A. D., Reed, W. A., Moyes, L. N., X-ray absorption spectroscopy studies of reactions of technetium, uranium and neptunium with mackinawite, J. Environ. Radioact., 74 (2004) 211-219.

[LLO/DEN2008] Llorens, I. A., Deniard, P., Gautron, E., Olicard, A., Fattahi, M., Jobic, S., Grambow, B., Structural investigation of coprecipitation of technetium-99 with iron phases, Radiochim. Acta, 96 (2008) 569-574.

[MAE/GER2004] Maes, A., Geraedts, K., Bruggeman, C., Vancluysen, J., Rossberg, A., Hennig, C., Evidence for the interaction of technetium colloids with humic substances by X-ray absorption spectroscopy, Environ. Sci. Technol., 38 (2004) 2044-2051.

[MAG/PFE2006] Magill, J., Pfennig, G., Galy, J. Chart of the Nuclides 7th edition 2006, Report EUR 22276 EN, 2006.

[MAG2007] Magnusson, A. C-14 Produced by Nuclear Power Reactors - Generation and Characterization of Gaseous, Liquid and Solid Waste. Lund Universiät, Lund, 2007.

[MAG/STE2005] Magnusson, A., Stenstroem, K. Determination of organic and inorganic C-14 on ion exchange resins - method description. Lund, 2005.

[MAG/STE2008] Magnusson, A., Stenstroem, K., Aronsson, P.O. 14C in spent ion-exchange resins and process water from nuclear reactors: A method for quantitative determination of organic and inorganic fractions, J. Radioanal. Nucl. Ch., 275 (2008) 261-273.

[MAR1991] Marcus, Y., Thermodynamics of solvation of ions, 5. Gibbs Free Energy of Hydration at 298.15 K, J. Chem. Soc.-Faraday Trans., 87 (1991) 2995-2999.

[MAR/BAN2014] Marsac, R., Banik, N. L., Diascorn, A., Kupcik, T., Lützenkirchen, J., Marquardt, C. M., Schäfer, T. , Schild, D., Rothe, J., Dardenne, K., Geckeis, H., Neptunium redox speciation at the illite surface, Geochim. Cosmochim. Acta, Submitted (2014)

[MAR/HOR2005] Marschall, P., Horseman, S., Gimmi, T., Characterisation of gas transport properties of the Opalinus Clay, a potential host rock formation for radioactive waste disposal, Oil Gas Sci. Technol., 60 (2005) 121-139.

[MAS/DEL1990] Masscheleyn, P.H., Delaune, R.D., Patrick, W. H., Transformations of selenium as affected by sediment oxidation-reduction potential and pH, Environ. Sci. Technol., 24 (1990) 91-96.

[MAS/DEL1991] Masscheleyn, P. H., Delaune, R. D., Patrick Jr., W. H., Biogeochemical behavior of selenium in anoxic soils and sediments: an equilibrium thermodynamic approach, J. Environ. Sci. Health, A26 (1991) 555−573.

[MCB/LLO2011] McBeth, J. M., Lloyd, J. R., Law, G. T. W., Livens, F. R., Burke, I. T., Morris, K., Redox interactions of technetium with iron-bearing minerals, Miner. Mag., 75 (2011) 2419-2430.

[MET/VEJ2004] Metz, V., P. Vejmelka, B. Kienzler, C.M. Marquardt, A. Seibert, T. Fanghanel, The effect of a Mg-oxychloride-brucite backfill material on the Pu behavior in MgCl2-NaCl-brines, Geochim. Cosmochim. Acta, 68 (2004) A511.

[MEY/ARN1991a] Meyer, R.E., Arnold, W.D., Case, F.I., Okelley, G.D., Solubilities of Tc(IV) Oxides, Radiochim. Acta, 55 (1991) 11-18.

[MEY/ARN1991b] Meyer, R. E., Arnold, W. D., The electrode potential of the Tc(IV)-Tc(VII) couple, Radiochim. Acta, 55 (1991) 19-22.

[MON/PAC1976] Monkhorst, H. J.,Pack, J. D., Special points for Brillouin-zone integrations, Phys. Rev. B, 13 (1976) 5188-5192.

[MON/SAR2011] Montes-Hernandez, G., Sarret, G., Hellmann, R., Menguy, N., Testemale, D., Charlet, L., Renard, F., Nanostructured calcite precipitated under hydrothermal conditions in the presence of organic and inorganic selenium, Chem. Geol., 290 (2011) 109-120.

[MOR/LUT1999] Morse, J. W., Luther, G. W., Chemical influences on trace metal-sulfide interactions in anoxic sediments, Geochim. Cosmochim. Acta, 63 (1999) 3373-3378.

[MOY/JON2002] Moyes, L. N., Jones, M. J., Reed, W. A., Livens, F. R., Charnock, J. M., Mosselmans, J. F. W., Hennig, C., Vaughan, D. J., Pattrick, R. A. D., An X-ray absorption spectroscopy study of neptunium(V) reactions with mackinawite (FeS), Environ. Sci. Technol., 36 (2002) 179−183.

[NAG2002] NAGRA, 2002. Technischer Bericht 02-03. Projekt Opalinuston - Synthese der geowissenschaftlichen Untersuchungsergebnisse, Entsorgungsnachweis für abgebrannte Brennelemente, verglaste hochaktive sowie langlebige mittelaktive Abfälle, Wettingen, Schweiz (2002).

[NEC/ALT2007] Neck, V., Altmaier, M., Fanghänel, T., Solubility of plutonium hydroxides/hydrous oxides under reducing conditions and in the presence of oxygen, C. R. Chimie, 10 (2007) 959-977.

[NEC/ALT2009] Neck, V., Altmaier, M., Fellhauer, D., Runke, J., Fanghänel, T., Collaborative Project "Redox Phenomena Controlling Systems", 1st Annual Workshop Proceeding, 2009, 65-73.

[NIE/TOF1984] Nielsen, A. E.,Toft, J. M., Electrolyte Crystal Growth Kinetics, J. Cryst. Growth, 67 (1984) 278-288.

[NIT/ROB1994] Nitsche, H., Roberts, K., Xi, R., Prussin, T., Becraft, K., Mahamid, I. A., Silber, H. B., Carpenter, S. A., Gatti, R. C., Long term plutonium solubility and speciation studies in a synthetic brine, Radiochim. Acta, 66 (1994) 3-8.

[NUT/ALL1984] Nuttall, K. L., Allen, F. S., Kinetics of the reaction between hydrogen selenide ion and oxygen, Inorg. Chim. Acta, 91 (1984) 243−246.

[OGI/SUZ1987] Ogino, T., Suzuki, T., Sawada, K., The formation and transformation mechanism of calcium-carbonate in water, Geochim. Cosmochim. Acta, 51 (1987) 2757-2767.

[OLI/NOL2005] Olin, A., Noläng, B., Osadchii, E., Öhman, L.-O., Rosen, E., Chemical Thermodynamics of Selenium, OECD Nuclear Energy Agency (NEA) (Eds), 2005.

[OMO/MUR1994] Omori, T., Muraoka, Y., Suganuma, H., Solvent-extraction mechanism of pertechnetate with tetraphenylarsonium chloride, J. Radioanal. Nucl. Chem. Art., 178 (1994) 237-243.

[OND/NIR2001] Ondraf/Niras, Technical Overview of the SAFIR 2 Report, Safety Assessment and Feasibility Interim Report 2, 2001.

[OWU/MAR1977] Owunwanne, A., Marinsky, J., Blau, M., Charge and nature of technetium species produced in reduction of pertechnetate by stannous Ion, J. Nucl. Medic., 18 (1977) 1099-1105.

[PAL/MEY1981] Palmer, D. A., Meyer, R. E., Adsorption of technetium on selected inorganic ion exchange materials and on a range of naturally occurring mineral under oxic condition, J. Inorg. Nucl. Chem., 43 (1981) 2979-2984.

[PAR/APP1999] Parkhurst, D.L., Appelo, C.A.J., User's Guide to PHREEQC (Version 2) - A computer program for speciation, batch-reaction, one-dimensional transport and invers geochemical calculations, Water-Resources Investigation Report 99-4259. U.S. Department of the Interior, U.S. Geol. Survey, Denver, Colardo, 1999.

[PEA/ARC2003] Pearson, F. J., Arcos, D., Bath, A., Boisson, J.-Y., Fernández, A. Ma., Gäbler, H.-E., Gaucher, E., Gautschi, A., Griffault, L., Hernán, P., and Waber, H. N., Mont Terri Project - Geochemistry of Water in the Opalinus Clay Formation at the Mont Terri Rock Laboratory, Report of the Federal Office for Water and Geology (FOWG) (Eds), Geology Series 5, Bern, Switzerland, pp 319 (2003).

[PER/BUR1996] Perdew, J. P., Burke, K.,Ernzerhof, M., Generalized gradient approximation made simple, Phys. Rev. Lett., 77 (1996) 3865-3868.

[PER/ZAC2008A] Peretyazhko, T., Zachara, J.M., Heald, S.M., Jeon, B.-H., Kukkadapu, R.K., Liu, C., Moore, D., Resch, C.T., Heterogeneous reduction of Tc(VII) by Fe(II) at the solid-water interface, Geochim. Cosmochim. Acta, 72 (2008) 1521-1539.

[PER/ZAC2008B] Peretyazhko, T., Zachara, J.M., Heald, S.M., Kukkadapu, R.K., Liu, C., Plymale, A.E., Resch, C.T., Reduction of Tc(VII) by Fe(II) Sorbed on Al (hydr)oxides, Environ. Sci. Technol., 42 (2008) 5499-5506.

[PER/ZAC2012] Peretyazhko, T. S., Zachara, J. M., Kukkadapu, R. K., Heald, S. M., Kutnyakov, I. V., Resch, C. T., Arey, B. W., Wang, C. M., Kovarik, L., Phillips, J. L., Moore, D. A., Pertechnetate (TcO_4^-) reduction by reactive ferrous iron forms in naturally anoxic, redox transition zone sediments from the Hanford Site, USA, Geochim. Cosmochim. Acta, 92 (2012) 48-66.

[PET/VLA2012] Petrov, V.G., Vlasova, I. E., Kuzmenkova, N.V., Petrov, V.A., Poluektov, V.V., Grivot, A., Kalmykov, S.N., Characterisation of rock samples from areas of the proposed Russian HLW and SNF repository (Nizhnekansky massive) and first sorption studies, 1st Workshop Proceedings of the Collaborative Project „Crystalline Rock Retention Processes“ (7th EC FP CP CROCK), KIT Scientific Report 7629 (2012) 37-42.

[PIC/BRO1995] Pickering, I. J., Brown Jr., G. E., Tokunaga, T. K., Quantitative speciation of selenium in soils using X−ray absorption spectroscopy, Environ. Sci. Technol., 29 (1995) 2456−2459.

[POI/FAT2006] Poineau, F., Fattahi, M., Grambow, B., Correlation between X-ray chemical shift and partial charge in Tc(IV) complexes: Determination of Tc partial charge in TcnOy(4n-2y)+, Radiochim. Acta, 94 (2006) 559-563.

[PRI2009] Prieto, M., Thermodynamics of Solid Solution - Aqueous Solution Systems, Reviews in Mineralogy and Geochemistry, 70 (2009) 47–85.

[RAI/GAL2010] Raiteri, P., Gale, J. D., Quigley, D.,Rodger, P. M., Derivation of an Accurate Force-Field for Simulating the Growth of Calcium Carbonate from Aqueous Solution: A New Model for the Calcite-Water Interface, J. Phys. Chem. C, 114 (2010) 5997-6010.

[RAR/RAN1999] Rard, J. A., Rand, M. H., Anderegg, G. and Wanner, H., Chemical thermodynamics of technetium, ed. M. C. A. Sandino and E. Östhols. Vol. 3. North-Holland, Amsterdam, Elsevier, (1999).

[RAV2000] Ravel, B. EXAFS Analysis with FEFF and FEFFIT. Part 2: Commentary. Version 0.04 (2000), electronic file available at : http://cars9.uchicago.edu/~ravel/course/notes.pdf

[RAV/NEW2005] Ravel, B., Newville, M., ATHENA, ARTEMIS, HEPHAESTUS: data analysis for X−ray absorption spectroscopy using IFEFFIT, J. Synchrotron Rad., 12 (2005) 537−541.

[REE/NUG2000] Reeder, R. J., Nugent, M., Lamble, G. M., Tait, C. D.,Morris, D. E., Uranyl incorporation into calcite and aragonite: XAFS and luminescence studies, Environ. Sci. Technol., 34 (2000) 638-644.

[REN/MON2013] Renard, F., Montes-Hernandez, G., Ruiz-Agudo, E.,Putnis, C. V., Selenium incorporation into calcite and its effect on crystal growth: An atomic force microscopy study, Chem. Geol., 340 (2013) 151-161.

[RES1998] Ressler, T., WinXAS: a program for X-ray absorption spectroscopy data analysis under MS-Windows, J. Synchrotron Rad., 5 (1998) 118-122.

[RIC2006] Rickard, D., The solubility of FeS, Geochim. Cosmochim. Acta, 70 (2006) 5779−5789.

[RIC/GRI2006] Rickard, D., Griffith, A., Oldroyd, A., Butler, I. B., Lopez−Capel, E., Manning, D. A. C., Apperley, D. C., The composition of nanoparticulate mackinawite, tetragonal iron(II) monosulfide, Chem. Geol., 235 (2006) 286−298.

[ROT/BUT2012] Rothe, J., Butorin, S., Dardenne, K., Denecke, M. A., Kienzler, B., Loble, M., Metz, V., Seibert, A., Steppert, M., Vitova, T., Walther, C., Geckeis, H., The INE-Beamline for actinide science at ANKA, Rev. Sci. Instrum., 83 (2012) 043105.

[ROU/ELZ2005] Rouff, A. A., Elzinga, E. J., Reeder, R. J.,Fisher, N. S., The influence of pH on the kinetics, reversibility and mechanisms of Pb(II) sorption at the calcite-water interface, Geochim. Cosmochim. Acta, 69 (2005) 5173-5186.

[RUS/CAS1978] Russell, C. D., Cash, A., Products of pertechnetate reduction in complexing media, J. Nuclear Medic., 19 (1978) 694-694.

[SAE/SAS2012] Saeki, M., Sasaki, Y., Nakai, A., Ohashi, A., Banerjee, D., Scheinost, A. C., Foerstendorf, H., Structural study on complex of MIDOA with $M(VII)O_4^-$ (M=Re and Tc) by ^{1}H-NMR, EXFAS and IR spectroscopy, Inorg. Chem., 51 (2012) 5814-5821.

[SAK/TAN2013] Sakuragi, T., Tanabe, H., Hirose, E., Sakashita, A., Nishimura, T. Estimation of Carbon 14 Inventory in Hull and End-Piece Wastes from Japanese Commercial Reprocessing Operation. ICEM2013, Brussels, Belgium (2013).

[SCH/BIS2010] Scharge, T., Bischofer, B. P., Hagemann, S., Schönwiese, D., Spectrophotometric and potentiometric determination of the redox potential in solutions of high ionic strength, 2nd Annual Workshop Proceeding 7th EC FP-Recosy CP, Cyprus, (2010).

[SCH/MAN1999] Schlegel, M. L., Manceau, A., Chateigner, D.,Charlet, L., Sorption of metal ions on clay minerals I. Polarized EXAFS evidence for the adsorption of Co on the edges of hectorite particles, J. Colloid Interf. Sci., 215 (1999) 140-158.

[SCH/STA2012] Schäfer, T., Stage, E., Büchner, S., Huber, F., Drake, H., Characterization of new crystalline material for investigations within CP CROCK, 1st Workshop Proceedings of the Collaborative Project „Crystalline Rock Retention Processes“ (7th EC FP CP CROCK), KIT Scientific Report 7629 (2012) 63-72.

[SCH/MAR2014] Schnurr, A., Marsac, R., Kupcik, T., Rabung, T., Lützenkirchen J., Geckeis, H. Sorption of Cm(III) and Eu(III) onto clay minerals under saline conditions: Batch adsorption, Laser-fluorescence spectroscopy and modeling. Geochim. Cosmochim. Acta, in press (2014).

[SCH/MAR2013] Schnurr, A., Marsac, R., Rabung, T., Lützenkirchen, J., Geckeis, H., Investigation of actinide and lanthanide sorption on clay minerals under saline conditions, in Migration Conference, Brighton, United Kingdom (2013).

[SHA1976] Shannon, R. D., Revised effective ionic radii and systematic studies of interatomic distances in halides and chalcogenides, Acta Cryst., A32 (1976) 751−767.

[SKB2006] The Äspö Hard Rock Laboratory, Svensk Kärnbränslehantering AB (SKB) (2006) (http://www.skb.se/upload/publications/pdf/Aspo_Laboratory.pdf).

[SHT/PUN2006] Shtukenberg, A. G., Punin, Y. O.,Azimov, P., Crystallization kinetics in binary solid solution-aqueous solution systems, Am. J. Sci., 306 (2006) 553-574.

[SLU/KAW2002] Sluiter, M. H. F.,Kawazoe, Y., Prediction of the mixing enthalpy of alloys, Europhys. Lett., 57 (2002) 526-532.

[STI/HOC1991] Stipp, S. L.,Hochella, J., Michael F., Structure and bonding environments at the calcite surface as observed with X-ray photoelectron spectroscopy (XPS) and low energy electron diffraction (LEED), Geochim. Cosmochim. Acta, 55 (1991) 1723-1736.

[TAG/UCH1999] Tagami, K., Uchida, S., Comparison of the TEVA center dot Spec resin and liquid-liquid extraction methods for the separation of technetium in soil samples, J. Radioanal. Nucl. Chem., 239 (1999) 643-648.

[TES/PAN1996] Tesoriero, A. J.,Pankow, J. F., Solid solution partitioning of Sr^{2+}, Ba^{2+}, and Cd^{2+} to calcite, Geochim. Cosmochim. Acta, 60 (1996) 1053-1063.

[TKA/SCH2009] Tkatchenko, A.,Scheffler, M., Accurate Molecular Van Der Waals Interactions from Ground-State Electron Density and Free-Atom Reference Data, Phys. Rev. Lett., 102 (2009) 073005.

[TOK/NIS1972] Tokonami, M., Nishiguchi, K., Morimoto, N., Crystal structure of a monoclinic pyrrhotite (Fe7S8), Am. Miner., 57 (1972) 1066−1080.

[UM/CHA2011] Um, W., Chang, H. S., Icenhower, J. P., Lukens, W. W., Serne, R. J., Qafoku, N. P., Westsik, J. H., Buck, E. C., Smith, S. C., Immobilization of 99-Technetium (VII) by Fe(II)-Goethite and Limited Reoxidation, Environ. Sci. Technol., 45 (2011) 4904-4913.

[UM/SER2005] Um, W., Serne, R.J., Sorption and transport behavior of radionuclides in the proposed low-level radioactive waste disposal facility at the Hanford site, Washington, Radiochim. Acta, 93 (2005) 57-63.

[UNI/STA1999] United States Environmental Protection Agency, Office of Air and Radiaion, The Kd model, methods of measurement, and application of chemical reaction codes, EPA 402-R-99-004A (1999).

[VAL/BYL2010] Valiev, M., Bylaska, E. J., Govind, N., Kowalski, K., Straatsma, T. P., Van Dam, H. J. J., Wang, D., Nieplocha, J., Apra, E., Windus, T. L.,de Jong, W., NWChem: A comprehensive and scalable open-source solution for large scale molecular simulations, Comput. Phys. Commun., 181 (2010) 1477-1489.

[VAN/SOL2003] Van Loon, L. R., Soler, J. M., Bradbury, M. H., Diffusion of HTO, 36Cl- and 125I- in Opalinus Clay samples form Mont Terri: Effect of confining pressure, J. Contam. Hydrol., 61 (2003) 73-83.

[VIC/FAT2003] Vichot, L., Fattahi, M., Musikas, C., Grambow, B., Tc(IV) chemistry in mixed chloride/sulphate acidic media. Formation of polyoxopolymetallic species, Radiochim. Acta, 91 (2003) 263-271.

[VIC/OUV2002] Vichot, L., Ouvrard, G., Montavon, G., Fattahi, M., Musikas, C., Grambow, B., XAS study of technetium(IV) polymer formation in mixed sulphate/chloride media, Radiochim. Acta, 90 (2002) 575-579.

[VIN/BRA2013] Vinograd, V. L., Brandt, F., Rozov, K., Klinkenberg, M., Refson, K., Winkler, B.,Bosbach, D., Solid-aqueous equilibrium in the BaSO4-RaSO4-H2O system: First-principles calculations and a thermodynamic assessment, Geochim. Cosmochim. Acta, 122 (2013) 398-417.

[WAN/ROM2011] Wang, J., Roman-Perez, G., Soler, J. M., Artacho, E., Fernandez-Serra, M. V., Density, structure, and dynamics of water: The effect of van der Waals interactions, J. Chem. Phys., 134 (2011) 024516.

[WAN/LIU2005] Wang, X. K.,Liu, X. P., Sorption and desorption of radioselenium on calcareous soil and its solid components studied by batch and column experiments, Appl. Radiat. Isot., 62 (2005) 1-9.

[WAN/XU2001] Wang, Y. F.,Xu, H. F., Prediction of trace metal partitioning between minerals and aqueous solutions: A linear free energy correlation approach, Geochim. Cosmochim. Acta, 65 (2001) 1529-1543.

[WAR/ALD2007] Warwick, P., Aldridge, S., Evans, N., Vines, S., The solubility of technetium(IV) at high pH, Radiochim. Acta, 95 (2007) 709-716.

[WAT2004] Watson, E. B., A conceptual model for near-surface kinetic controls on the trace-element and stable isotope composition of abiogenic calcite crystals, Geochim. Cosmochim. Acta, 68 (2004) 1473-1488.

[WHA/ATK2000] Wharton, M. J., Atkins, B., Charnock, J. M., Livens, F. R., Pattrick, R. A. D., Collison, D., An X-ray absorption spectroscopy study of the coprecipitation of Tc and Re with mackinawite (FeS), Appl. Geochem., 15 (2000) 347−354.

[WIC/MEL2010] Wicke, H., Meleshyn, A., Microhydration of the Selenite Dianion: A Theoretical Study of Structures, Hydration Energies, and Electronic Stabilities of SeO32-(H2O)(n) (n=0-6, 9) Clusters, J. Phys. Chem. A, 114 (2010) 8948-8960.

[WIE2012] Wiedemann, M., Rückhaltung von dreiwertigen Actiniden an Mg(OH)2-haltigen Feststoffen in Abhängigkeit von der Ionenstärke im System Mg2+-Na+-OH--Cl--H2O bei 25 °C, Institute for Nuclear Waste Disposal (INE), Karlsruhe Institute of Technology (KIT), Karlsruhe, 2012.

[WIL/FAR2001] Wilke, M., Farges, F., Petit, P. E., Brown Jr., G. E., Martin, F., Oxidation state and coordination of Fe in minerals: an Fe K−XANES spectroscopic study, Am. Miner., 86 (2001) 714−730.

[WIL/GIE2007] Wildner, M.,Giester, G., Crystal structures of SrSeO3 and CaSeO3 and their respective relationships with molybdomenite- and monazite-type compounds - an example for stereochemical equivalence of ESeO3 groups (E = lone electron pair) with tetrahedral TO4 groups, Neues Jahrb. Mineral.-Abh., 184 (2007) 29-37.

[WOL/CHA2005] Wolthers, M., Charlet, L., van der Linde, P., Rickard, D., van der Weijden, C. H., Surface chemistry of disordered mackinawite (FeS), Geochim. Cosmochim. Acta, 69 (2005) 3469−3481.

[WOL/GAA2003] Wolthers, M., Van der Gaast, S. J., Rickard, D., The structure of disordered mackinawite, Am. Miner., 88 (2003) 2007−2015.

[WU/COH2006] Wu, Z. G.,Cohen, R. E., More accurate generalized gradient approximation for solids, Phys. Rev. B, 73 (2006) 235116.

[XIO/DEN2010] Xiong Y., Deng H., Nemer M., Johnsen S., Experimental determination of the solubility constant for magnesium chloride hydroxide hydrate (Mg3Cl(OH)4·4H2O, phase 5) at room temperature, and its importance to nuclear waste isolation in geological repositories in salt formations, Geochim. Cosmochim. Acta, 74 (2010) 4605-4611.

[YAL/GAO2014] Yalcintas E., Gaona, X., Scheinost, A., Kobayashi, T., Altmaier, M. and Geckeis, H. (2014) “Redox chemistry of Tc(VII)/Tc(IV) in dilute to concentrated NaCl and $MgCl_2$ solutions.” Radiochim. Acta (DOI 10.1515/ract-2014-2272).

[ZAC/HEA2007] Zachara, J.M., Heald, S.M., Jeon, B.-H., Kukkadapu, R.K., Liu, C., McKinley, J.P., Dohnalkova, A.C., Moore, D.A., Reduction of pertechnetate [Tc(VII)] by aqueous Fe(II) and the nature of solid phase redox products. Geochim. Cosmochim. Acta, 71 (2007) 2137-2157.

[ZHA/TRU2008] Zhao, Y.,Truhlar, D. G., The M06 suite of density functionals for main group thermochemistry, thermochemical kinetics, noncovalent interactions, excited states, and transition elements: two new functionals and systematic testing of four M06-class functionals and 12 other functionals, Theor. Chem. Acc., 120 (2008) 215-241.

[ZHO/MUC1995] Zhong, S. J., Mucci, A., Partitioning of Rare-Earth Elements (REEs) between Calcite and Seawater Solutions at 25-Degrees-C and 1 Atm, and High Dissolved REE Concentrations, Geochim. Cosmochim. Acta, 59 (1995) 443-453

6 Solid solutions of layered double hydroxides (LDHs) ─ Synthesis, structural/thermodynamic description and their retention potential for iodide, pertechnetate and selenite

6.1 Introduction

Many countries, Germany among them, plan to dispose nuclear heat generating waste (spent fuel elements and vitrified high-level waste) in deep geological formations because this offers the largest long-term safety option. Within this context safety means that the radionuclides are isolated and no hazard doses will reach the biosphere [NOS/BEC2008]. The repository for nuclear waste includes a multi-barrier system (host rock as geological barrier and geotechnical/technical man-made barriers) but the contact of groundwater with the waste forms cannot be excluded within long-time periods (million years). Groundwater will corrode the container and the formed hydrogen will create a reducing environment. As a consequence of corrosion, radionuclides can be released by the water pathway.

Taken geological time scales into account the release of radioactivity is mostly attributed to a very mobile anionic radionuclide fraction [GRAM2008]. Of primary concern are therefore the fission and activation products (iodine-129, selenium-79, chlorine-36, carbon-14 and technetium-99), which dominate the potential long-term exposure risks from nuclear waste repositories. As soon as groundwater will come into contact with radioactive waste, these radionuclides will eventually be released as anionic species. Anionic species have a weak retention by major minerals in the repository near-field since mineral/water interfaces are under natural aqueous conditions in most cases negatively charged, hence these anionic species are highly mobile.

The key characteristics of mobile radionuclides are their very low R_d values. The R_d value reflects the distribution of a radionuclide between solid and solution phase. Even without detailed mechanistic understanding and without the association of equilibrium one may use the R_d value as an indicator for mobility. Very low R_d values cause safety analyst to assume zero retention for these radionuclides. Though, this is conservative, it might strongly overestimate the mobility and hence the risk analysis from these nuclides.

The focus of the joint project VESPA is to reduce these overestimations.

Layered double hydroxides have been the subject of intensive research because of their wide technical applications as catalysts and as anion exchangers. In the nuclear community, the interest is in LDHs as anion exchangers. Moreover, in a repository-near-field LDHs are present as corrosion products, e. g. when cementitious waste corrodes in salt solutions the so-called “Friedel`s salt” is formed [REN/KUB2009]. Friedel`s salt is an anion-exchange mineral belonging to the class of LDHs with the general formula $Ca_2Al\ (OH)_6(Cl,OH)\cdot 2H_2O$. In the octahedral layer, Ca rather than Mg is present as the divalent cation. In $MgCl_2$-$CaCl_2$ salt solution, nuclear-waste glass and basaltic-glass alteration processes occurred and the formation of LDHs was observed [ABD/CRO1994]. In many countries, spent fuel will be disposed in canisters made of iron. In contact with groundwater, iron will corrode and hydrogen will be produced, creating a reducing environment. Under these conditions, magnetite and a LDH-like compound known as ‘green rust’ (Fe(II)- and Fe(III)-containing LDHs) was identified as a corrosion product [CUI/SPA2002]. In Germany, irradiated research-reactor fuel elements with uranium silicide as the fuel will be stored in cast iron containers and, after an interim period of dry storage, direct disposal in deep geological formations is planned. Research-reactor fuel samples (UAl_x-Al- and U_3Si_2-Al-types) were leached in the presence of Fe(II) aqueous species in repository-relevant $MgCl_2$-rich salt brine. Mg-Al-layered double hydroxides and the ‘green rust’ were identified as crystalline secondary phase components [MAZ/CUR2003, CUR/KAI2010].

6.2 Objective of this study

Within the joint project VESPA the FZJ investigated the potential of LDHs as anionic radionuclide-binding material. With respect to repository conditions, these materials have to be physically and chemically stable and they have to prevent the migration of radionuclide species to the biosphere.

As radionuclide-binding materials LDHs are of interest due to their ability to retain numerous different cations and especially due to their well-known anion-exchange properties. In this study Fe-, Co- and Ni-bearing MgAl-LDHs were investigated (the metal-cations are present in the near-field and the formation of these LDH solid solutions cannot be excluded).

First, a selective synthetic pathway, followed by a detailed structural characterization of the Fe-, Co-, and Ni-bearing MgAl-LDHs, was aimed. Second, with respect to their chemical compositions the free energy of formation should be calculated from experimental data in order to estimate their aqueous solubility, also in comparison to the pure MgAl-LDH component. Third, their retention potential for the anionic radionuclide species ^{129} iodide, ^{99}pertechnetate and ^{79}selenite by ion-exchange in different groundwater compositions should be addressed. The obtained R_d values can be used in safety analysis calculations in order to reduce the overestimations, caused by the conservatism approach.

6.3 State of the art about layered double hydroxides (LDHs) and their retention potential for iodide (I-), pertechnetate (TcO_4^-) and selenite (SeO_3^{2-})

With respect to the long-term safety analysis the long-lived radionuclides ^{129}I, ^{79}Se and ^{99}Tc are of main interest. These elements are present in anionic form and very mobile. The following state of the art report summarized the knowledge on the retention of these anionic species by layered double hydroxides (LDHS). In dependence on the family of cationic clay minerals (i. e. smectite), where the uptake of cations in the interlayer is possible by ion exchange mechanism, LDHs are often named as anionic clay minerals. LDHs as anionic clays can easily exchange anions within the interlayer [CAV/TRI1991]. Due to this property the LDHs are used in different application fields (treatment of waste waters, hazardous waste deposits, medicine application (neutralization of acidity of stomach) [ULI/PAV2001].

6.3.1 Structure of LDH

LDHs are a large family of compounds represented by the general formula

$$\left[M_{1-x}^{2+}M_x^{3+}(OH)_2\right]^{x+}\cdot\left[A_{x/n}^{n-}\cdot mH_2O\right]^{x-},$$

where M^{2+} is a divalent cation (Mg^{2+}, Mn^{2+}, Fe^{2+}, Co^{2+}, Ni^{2+}, Zn^{2+}, or Ca^{2+}), M^{3+} is a trivalent cation (Al^{3+}, Cr^{3+}, Fe^{3+}, Co^{3+}, Ni^{3+}, La^{3+}) and A^{n-} is an anion (CO_3^{2-}, Cl^-, OH^-, etc.). x is a parameter, describing the divalent and trivalent ratio in the hydroxide sheet. To understand the structure of a LDH it is necessary [ALL/JEP1969] to start from the structure of brucite, $Mg(OH)_2$, in which each Mg^{2+} ion is octahedrally surrounded by six OH^- ions. These octahedra are connected to each other by edge sharing to form an infinite sheet. When some of Mg^{2+} ions are replaced by a trivalent ion whose radius is not too different (such as Fe^{3+} for pyroaurite and Al^{3+} for hydrotalcite), a charge is generated in the hydroxyl sheet. This positive charge is compensated by CO_3^{2-} or other anions, which are located in the interlayer region between the two brucite-like sheets. In the free space of this interlayer crystalline water is present too. The main features of LDHs structures and LDHs properties are determined by the nature of the brucite-like sheet, by the type of stacking of the brucite-like sheets, by the amount of water, and by the position and type of anions (**Fig. 6.1**). One of the important characteristics of LDHs are the lattice parameters c and a. The value a is affected by the trivalent metal content in the brucite-like layer and not by the nature of the interlamellar anion [CAV/TRI1991]. The c lattice parameter is determined by the interlamellar anion. There is practically no limitation in size. The number, the size, the orientation and the strength of the bonds between the anions and the hydroxyl groups of the brucite-like layers determine the thickness of the interlayer [ALL1979]. Different anions, like halogenides, oxyanions and organics can be present in the interlayer [RIV2001]. Between the brucite-layer and the interlayer electrostatic forces exist. The main stabilization of the LDH structure relies on hydrogen bonding between the hydroxyl groups and the anions and between the hydroxyl groups and water molecules.

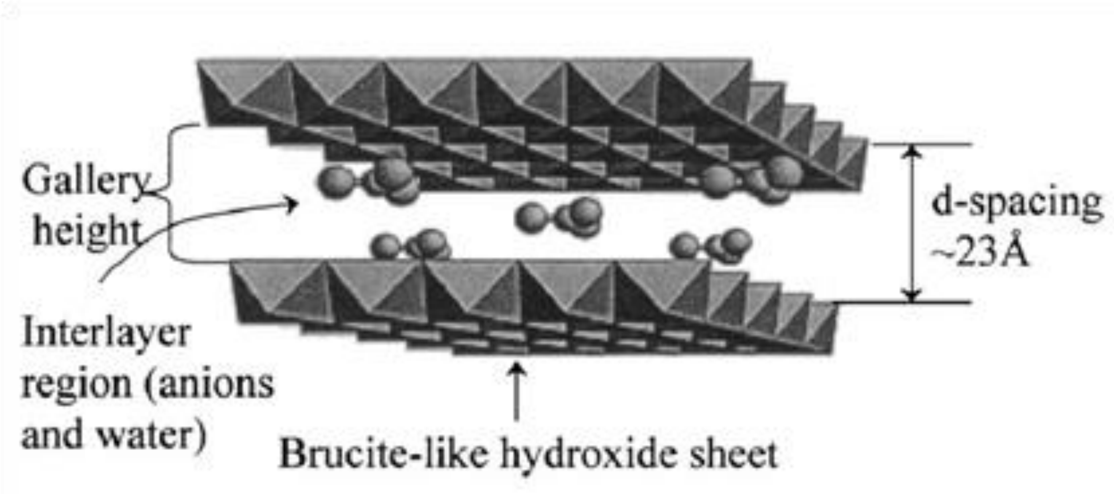

Fig. 6.1 Three-dimensional schematic representation of the LDH structure

LDHs in nature possess monovalent (hydroxide, chloride or nitrate) or divalent anion (sulphate, carbonate). LDHs with divalent anions are more stable because the higher negative charge increase the electrostatic interactions between the brucite layers and the interlayer region [FRO/MUS2007]. For the same reason the formation of LDHs with divalent anions is more favoured [WIL/NOR2004].

6.3.2 Synthesis

LDHs can be synthesised via co precipitation [HE/WEI2006], via the urea method [COS/MAR1998], via the salt-oxide process [BOE/STE1977], hydrothermal [BOE/STE1977], electrochemical [IND/KAM1994] or with the sol-gel route [LOP/BOS1996]. The co precipitation method however is the most common approach. Usually, a solution containing the metal cations in the desired ratios is dropped to an alkaline solution while the pH is hold. The steady state of the pH during synthesis is a requirement for the selectivity, crystallinity and value of the specific surface area. In order to synthesise LDHs with desired interlayer anions, the calcination method is the most powerful tool [ULI/PAV2001]. As educt a LDH with the desired metal cation composition is heated up to 500 °C and this temperature is kept for some hours. Due to the heating the layered structure will be lost and as product a mixed MgAl-oxide will be obtained. In contact with an aqueous phase containing the desired anion, the LDH structure forms back (reconstruction, the so-called memory effect) with this anion in the interlayer. As was pointed out by [ULI/PAV2001] as competing anions the hydroxyl groups are present.

6.3.3 Anion exchange, mechanistic aspects

Many investigations confirm the uptake of anionic species by LDHs from aqueous solutions by anion exchange processes [DAS/PAT2006] and [PRA/RAO2006]. Compared to the brucite like-layer, the interlayer region is less stable and this offers the possibility of exchange reactions. Discussions about mechanistic aspects of exchange reactions exist in literature. There are three main approaches: a) a two steps process [HU/DAV1994] (the LDH dissolved and re-precipitated with the desired anion in the interlayer (D-R mechanism: dissolution-re precipitation process), b) kinetic formation of the LDH according to the first rate law [KOO/HOL1977] and c) adsorption of the desired anion and then desorption of the existing anion [MIK/SAS1984]. A general agreement states, that the anion exchange process takes place in the crystal itself and that the process does not influence the structural parameters, so the structural parameters of the educts are similar to the structural parameters of the products. Chemical reactions, which in-situ lead to a new crystalline phase with identical structural orientation, are known as topotaxy [KLE/BAU1990]. It can be stated, that an anion exchange reaction does not change the structure of the brucite-layers, but there is an observable change in the lattice parameter c. The lattice parameter c depends on the nature of anion and represents the spacing of one brucite layer and one interlayer.

6.3.4 Affinity ranking of anions

According to [MIY1983], the theoretical anion exchange capacity of LDHs is 3.6 meq/g. Miyata however did show, that this theoretical value cannot be achieved in practice. The determined experimental anion exchange capacity was approximately 3 meq/g. An explanation was given by [ULI/PAV2001I]. He pointed out that in aqueous solutions the hydroxyl groups act as competing anions. Miyata investigated in detail the ranking of anions [MIY/OKA1977] and [MIY1983]. First, he synthesized LDHs with different interlayer anions (nitrate, chloride, sulphate). Then, these LDHs were treated with aqueous solutions, containing 0.1 M amounts of NaF, NaBr, KI, NaOH, Na_2CO_3, Na_2SO_4. After the reactions, he analysed the LDH obtained. The following results were obtained: a) LDHs have the highest affinity towards anions, which possess the highest charge density, b) compared to monovalent anions, the intercalation of divalent anions is preferred c) the affinity for monovalent anions is in the order: $OH^- > F^- > Cl^- > Br^- > NO_3^- > I^-$ and for divalent anions: $CO_3^{\ 2-} > SO_4^{\ 2-}$ and d) carbonate is the anion possessing the highest affinity. In fact, the most limiting factor for the exchange reaction is the presence of carbonate as the interlayer anion. For that reason, the most recent papers on anion adsorption on LDHs consider simultaneously the possibility of both processes: anion exchange on LDHs and reconstruction from calcinated LDH solids.

6.3.5 Oxyanions: Pertechnetate and selenite

Technetium-99 is formed as fission product with a fission yield of 6 %. ^{99}Tc represents a long-lived, radiotoxic element (half-live time: $2.13 \cdot 10^5$ years). Under non-reducing conditions the heptavalent oxidation state is very stable. Tc(VII) compounds are very soluble and it is assumed that the pertechnetate anion (TcO_4^-) will not be retarded by the materials of the multi-barrier system. Selenium-79 is fission product with a fission yield of 0.04 %. Selenium-79 is a long-lived, radiotoxic element (half-life time: 327000 years) and in anionic form as selenide ($(Se^2)^-$), selenite (SeO_3^{2-}) or selenate: (SeO_4^{2-}) highly mobile. Results from different investigations demonstrated that compared to uncalcined LDHs the calcined LDH compositions possess higher uptake capacities for the oxyanions selenite and pertechnetate. The calcinated compositions have higher specific surface areas [GOH/LIM2008], higher porosity but the main important feature is the very, very low carbonate content. With respect to anion uptake different adsorption mechanisms exist. Working with uncalcined LDHs the uptake of oxyanions can be explained by an ion exchange process and/or adsorption on edge sites of LDH layers or on external surfaces can occur. For the calcined material, the sorption mechanism involves the rehydration of mixed metal oxides a concurrent intercalation of oxyanions into the interlayer to reconstruct the LDHs [GOH/LIM2008].

[YOU/VAN2001] studied the adsorption of selenite Se(IV) by uncalcined MgAl-LDH and uncalcined ZnAl LDHs with chloride as interlayer anion. The adsorption process was rapid and the adsorption equilibrium time increased with the Se(IV) loading. The quasi-equilibrium for 0.063 cmol/L and 0.63 cmol/L SeO_3^{2-} was obtained within the first 30 and 60 minutes of adsorption, respectively. The adsorption isotherm for SeO_3^{2-} on both LDHs could be fitted to a simple Langmuir equation with the affinity of SeO_3^{2-} on ZnAl-LDH higher than on the MgAl-LDH. The adsorption on both LDHs was found to be a function of pH, but it should be noted that the adsorption of SeO_3^{2-} was relatively constant when the equilibrium solution pH was between 5 and 10, due to the buffering of the LDHs. For the Se(IV) adsorption on uncalcined MgAl-LDH with chloride as interlayer anion, the effect of competing anion was reported to follow the order: $HPO_4^{2-} > SO_4^{2-} > CO_3^{2-} > NO_3^-$. For example, with carbonate the adsorbed selenite could be desorbed completely from MgAl-LDH. In comparison to chloride, selenite possesses the higher affinity towards LDHs. Curtius et al. could demonstrate that the selenite uptake by ion exchange processes on uncalcined MgAl-LDH in a $MgCl_2$-rich brine (excess of chloride $1.5 \cdot 10^{13}$) existed. Results from identical investigations using water as solution (competing anions are hydroxyl groups) demonstrated, that the divalent selenite anion clearly had the higher affinity towards the LDH.

[WAN/GAO2006] found interesting results with respect to the adsorption of TcO_4^- on uncalcined LDHs. According to his results, the adsorption of TcO_4^- was correlated to the basal spacing d_{003} of the materials, which decreases with the radii of both divalent and trivalent cations. The adsorption seemed to take place at the edges sites at the LDHs, and it reached a maximum when the layer spacing was just large enough for TcO_4^- to fin in the cage space among three adjacent octahedral of metal hydroxides at the edge. Moreover, the adsorption of TcO_4^- also increased with the crystallinity of the materials. For a given choice of metal cations and interlayer anions, the best crystalline LDH phase was generally obtained with an M^{2+}/M^{3+} ratio of 3:1. The role of interlayer anion was another interesting outcome of his research. He found out, that LDH with nitrate as interlayer anion enhanced the sorption capability of TcO_4^-. This may be due to the contributions from actual interlayer anion exchanges, as well. In conclusion, the results reported by [WAN/GAO2006] indeed help to establish a general structure property relationship that will guide engineering LDH materials for removal of specific oxyanions.

A layered double hydroxide containing Fe(II) and Fe(III) is known as green-rust. This material is redox-sensitive. Interesting investigations of [SKO/CHR2009] did clearly demonstrated, that, when working with redox-sensitive layered double hydroxides, the retention of anions, here selenite, did not relay on adsorption, here a redox-reaction took place and Se(IV) is reduced to Se(0).

6.3.6 Iodide

^{129}I has a half-live time of $15.7 \cdot 10^6$ years and is produced with a fission yield of 0.72 %. Under reducing conditions iodide is stable and possesses a highly mobility, due to lack of strong interactions with the multi-barrier materials. [MIY1983] already pointed out the affinity of monovalent anions for LDHs and the following ranking was obtained: $OH^- > F^- > Cl^- > Br^- > I^-$. Clearly, iodide has the lowest position, due to the low charge density property and due to the inability to form hydrogen bonding. The ranking of these monovalent anions was confirmed by [CUR/KAT2005]. Only trace amounts of iodide were adsorbed by an uncalcined MgAl-LDH with chloride as interlayer anion. In the presence of chloride, acting as competing anion, the iodide uptake was inhibited completely. [FET/RAM1997] confirmed these results for the uncalcined MgAl-LDH. Moreover, he demonstrated the iodide uptake capability as function of uncalcined and calcined LDHs. 0.23 meq/g of iodide were adsorbed by ion exchange processes on an uncalcined MgAl-LDH, while for the calcined LDH the amounts significantly increased to 1.74 meq/g. Further on Fetter investigated the influence of interlayer anions. Nitrate as interlayer anions was the focus of interest. The MgAl-LDHs under investigation had different Al/(Mg+Al) molar ratios. [FET/RAM1997] clearly could demonstrated, that the iodide uptake increased linearly with increasing Al content. Up to 1.45 mmol/g iodide was adsorbed, when the Al/(Mg+Al) molar ratio reached 0.33. XRD data revealed the presence of iodide within the interlayer region. [KEN/LIU2010] investigated the uptake of high concentrations of iodide in the presence of high concentrations of boron on uncalcined MgAl-LDH with nitrate as interlayer anion. Boron had the higher affinity and the uptake mechanisms were suggested as ion exchange reaction and surface complexation at the external surfaces. Boron is an oxyanion, iodide not. Therefore the affinity for iodide was lower and the removal was suggested mainly by electrostatic attraction onto external sites of the LDH.

6.3.7 Conclusion

LDHs have the ability to remove anionic species from aqueous solutions. With respect to the anion uptake the following knowledge can be summarized as follows:

a) Calcined LDHs possess the highest retention capabilities due to their higher surface areas, increased porosity and their low concentration of carbonate in the interlayer region of the calcined LDHs than in the uncalcined LDHs,

b) Different mechanisms of the anion sorption exist with respect to uncalcined LDHs and calcined LDHs,

c) for the uncalcined LDHs anion exchange, adsorption on external sites and adsorption on the interlayer edges represent the anion uptake mechanisms,

d) oxyanions can adsorb on external sites (selenite, pertechnetate) and on interlayer edges (i. e. pertechnetate) by forming an oxy-complex.

e) Oxyanions can take part in anion exchange reactions and they can perform hydrogen bonding in the interlayer region. Halogenide anions (i. e. iodide) can take part in anion exchange reactions but they do not perform hydrogen bonding. From these findings it is clear that oxyanions possess higher affinities towards LDHs,

f) in general, the uptake of anions by anion exchange reactions is dominated by competition effects. Incoming anions, possessing a higher charge density as the present interlayer anion, will exchange more effective. Note, in aqueous solutions competing anions (hydroxyl groups) are always present.

The idea to establish a general structure property relationship that will guide engineering LDH materials for removal of anions was demonstrated by [WAN/GAO2006]. According to his results, the adsorption of TcO_4^- was correlated to the basal spacing d_{003} of the LDH materials. The adsorption seemed to take place at the edges sites at the LDHs, and it reached a maximum when the layer spacing was just large enough for TcO_4^- to fit in the cage space among three adjacent octahedral of metal hydroxides at the edge. A NiAl-LDH was found to be promising candidate.

Till now, the anion uptake on LDH solid solutions is not investigated. However, the composition of metal cations in the brucite-like layers can have an impact on anion uptake and this need to be clarified. The present project therefore will focus on three different LDH solid solutions and their ability to adsorb the radionuclide anionic species iodide, pertechnetate and selenite.

6.4 Layered Double Hydroxides

6.4.1 Occurrence in the environment and in the nuclear waste repository

Layered double hydroxides (LDHs) also known as anionic clay minerals or hydrotalcite-like compounds are found in nature. Hydrotalcite ($Mg_6Al_2 (OH)_{16}(CO_3) \cdot 4H_2O$) is one of the most representative minerals of the group. The layers of hydrotalcite produce a 3-layer rhombohedral structure (3*R* polytype). When the layers produce a 2-layer hexagonal structure (2*H* polytype) the mineral is known as manasseite. The most abundant minerals of the hydrotalcite and manasseite group possess carbonate as interlayer anion [FOR/COS2013].

In soils, conditions for the formations of LDH can be easily encountered. All that is required for the formation of mixed-cation hydroxide compounds is that one cation is introduced into a suitable environment in which there is a source of hydrolyzed species of the second cation. The formation of LDHs also represent a possible sorption mode for divalent metal ions when silicates or oxides are present the formation of mixed NiAl-LDHs was observed when Ni (II) sorption on pyrophyllite, kaolinite, gibbsite, and montmorillonite was investigated [SCH/LAM1997, SCH/LAM1996].

Fernández et al. [FER/CUE2010] studied concrete and compacted bentonite as components of an engineered barrier system in order to isolate high-level radioactive waste in geological disposal. Diffusion experiments with alkaline solutions and compacted bentonite columns showed that LDH occurred as alteration products. The immobilization of Co by interaction with a calcite-containing sulfate resisting Portland cement was studied by the use of (micro)-X-ray absorption spectroscopy [SCH/VES2006] and the presence of a CoAl-layered double hydroxide was observed. Portland cement is the most widely used cement type and foreseen for the construction of nuclear waste underground facilities and as matrix for the immobilization of some radioactive waste forms. The hydrated cement phases are of special interest with respect to radionuclide retention. Calcium silicate hydrates represent the main hydrate phase. In contrast, the minor hydrated cement phases bear the minerals ettringite, different Afm phases (containing chloride, carbonate and sulfate) and hydrotalcite as well. The interactions of Ni with sulfate-resisting Portland cement were studied as function of hydration time and water/cement ratio and the results indicated that a NiAl-LDH, rather than Ni-hydroxides, is the solubility-limiting phase in the Ni-doped cement system [VES/DAE2006].

Within the engineered barrier Fe is one of the most abundant materials. Metallic Fe is used as canister material for nuclear waste disposal. In contact with groundwater metallic iron will be oxidized and hydrogen gas will be formed. Under these anoxic conditions magnetite, Fe_3O_4 and a special LDH-type containing Fe (II)-Fe (III) cations and different interlayer anions (sulfate, chloride, carbonate), well known as green-rust, formed as corrosion products [CUI/SPA2002].

In view of disposal of nuclear waste glass, alteration experiments with R7T7 nuclear waste glass in $MgCl_2$-$CaCl_2$ solution were performed and the formation of LDHs as alteration products was observed [ABD/CRO1994].

Currently in Germany, irradiated research reactor fuel elements (U_3Si_2-Al-type) will be stored in cast iron containers and, after an interim period of dry storage, direct disposal in deep geological formations is planned. This fuel type and a metallic uranium spent research reactor fuel sample (UAl_x-Al) were leached in a repository relevant $MgCl_2$-rich salt-brine in the presence of Fe (II) aqueous species. MgAl-LDHs with chloride and sulfate as interlayer anions and the green rust were identified as crystalline secondary phase components [CUR/KAI2010, MAZ/CUR2003].

In conclusion, the as mentioned investigations clearly demonstrated that the formation of LDH components must be considered in nuclear waste repositories.

6.4.2 Structural aspects

Layered double hydroxides (LDHs), or the so-called ‘anionic clays,’ constitute a class of lamellar compounds containing positively charged brucite-like layers (**Fig. 6.2**) and exchangeable anions in the interlayers [MIY1975]. Besides the anions, water is also present in the interlayer spaces.

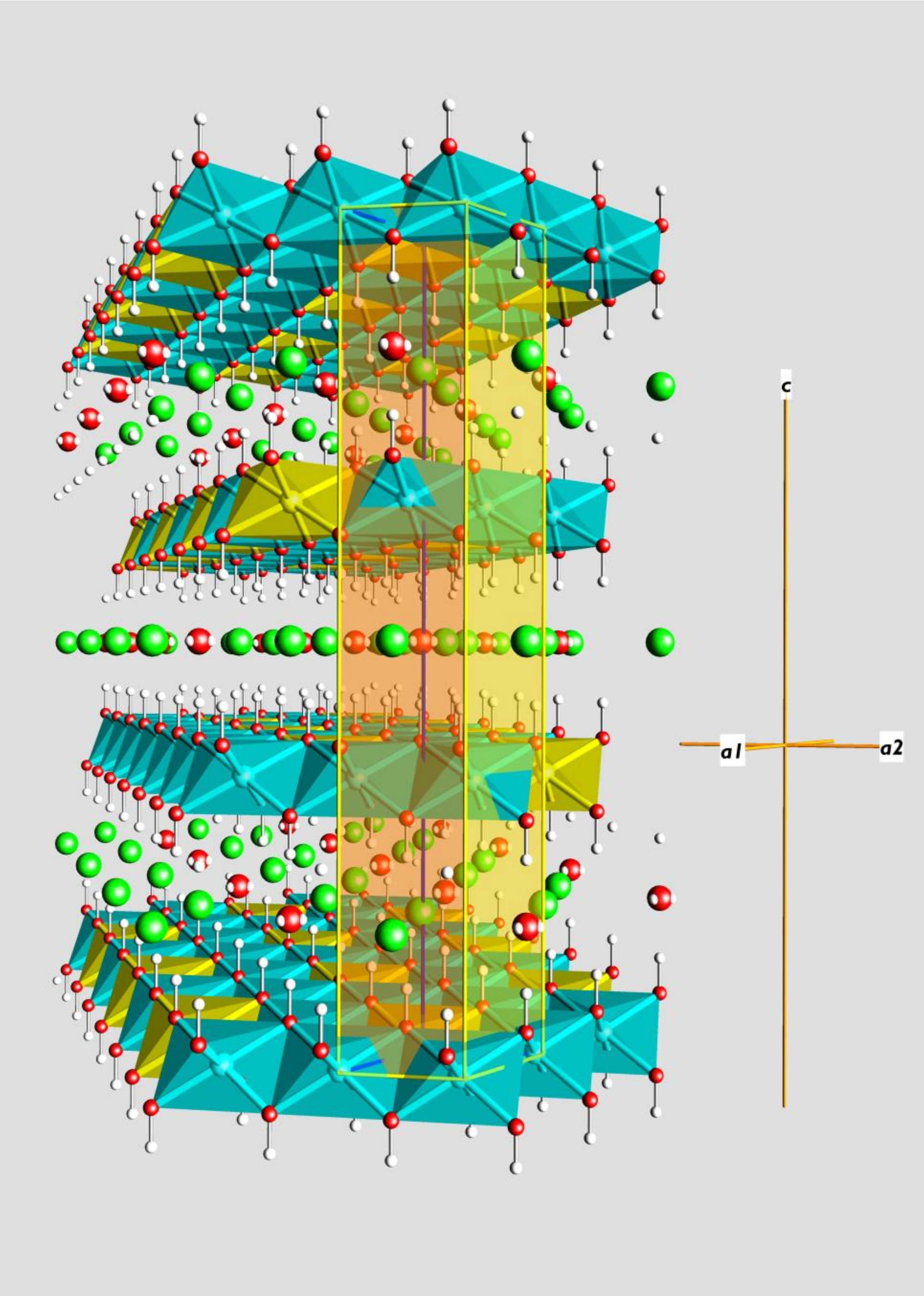

Fig. 6.2 Structure of a Mg_3Al_1-LDH compound with chloride (green spheres) and water (red-white spheres) in the interlayer

The general formula that represents this kind of material is:

$[M^{2+}_{1-x}M^{3+}_{x}]\ [A^{n-}_{x/n}\cdot m\mathrm{H_2O}]$, where M^{2+} and M^{3+} are di- and trivalent metal cations, respectively, x = ratio of $M^{3+}/(M^{2+} + M^{3+})$, and A is an interlamellar anion with charge (n^{-}), x is a parameter, describing the divalent and trivalent ratio in the hydroxide sheet. In general, the value can vary from 0.17 to 0.33 [SER/BER2000]. The x-value cannot increase much higher due to the repulsing forces of the trivalent metal cations, which create the positive charge in the brucite layer.

The structure of these compounds can be visualized as a brucite ($Mg(OH)_2$)-like octahedral layer in which part of the Mg^{2+} is replaced isomorphously with trivalent cations and the positive charge of the layer is balanced by equal negative charge from the interlayer solvated anions (e. g. CO_3^{2-}, NO_3^{-}, Cl^{-}, etc.) [CAV/TRI1991]. A large number of LDHs with variations in the M^{2+}-M^{3+} cation pair including M^{+}-M^{3+} (e. g. Li-Al) and M^{2+}–M^{4+} (e. g. Co-Ti) and their applications have been documented [TAY1984].

To understand the structure of a hydrotalcite it is necessary to start from the structure of brucite, $Mg(OH)_2$, in which each Mg^{2+} ion is octahedrally surrounded by six OH^{-} ions. These octahedra are connected to each other by edge sharing to form an infinite sheet. When some of Mg^{2+} ions are replaced by a trivalent ion whose radius is not too different (such as Fe^{3+}, Al^{3+}, Cr^{3+}), a charge is generated in the hydroxyl sheet. This positive charge is compensated by CO_3^{2-} or other anions, which are located in the interlayer region between the two brucite-like sheets (**Fig. 6.2**). In the free space of this interlayer, crystalline water is present too. The brucite-like sheets may have the stacking sequence A-B-C-A, thus having three sheets in the unit cell (rhombohedral 3R symmetry), or A-B-A-B with two sheets in the unit cell (hexagonal 2H symmetry). For example, pyroaurite and natural hydrotalcite crystallise in a rhombohedral 3R symmetry, the parameters of the unit cell are a and $c = 3c'$ (where c' is the thickness of one brucite-like sheet and one interlayer). The parameters of a unit cell for a hexagonal polytype are a and $c = 2c'$ (for example, sjogrenite and manasseite). LDHs with a rhombohedral symmetry have been found mainly in nature; the hexagonal polytype may be just the high-temperature form of the rhombohedral one.

The lattice parameter a is affected by the type of metal cation and by their amounts in the brucite-like layer and not by the nature of the interlamellar anion [CAV/TRI1991]. Within a the cation-cation distance is given, because there is only one cation in the a-direction of the unit cell [BRI/KIK1979] and because of that, the parameter a directly indicates the distance between two neighbouring cations. The c lattice parameter is determined by the interlamellar anion. There is practically no limitation in size. The num-

ber, the size, the orientation and the strength of the bonds between the anions and the hydroxyl groups of the brucite-like layers determine the thickness of the interlayer.
In conclusion, the main features of LDH structures and their properties are determined by the nature of the brucite-like sheet, by the type of stacking of the brucite-like sheets, by the amount of water, and by the position and type of anions.

6.4.3 Characterisation techniques

6.4.3.1 X-ray powder diffraction

Scattering of x-rays by crystal atoms, producing a diffraction pattern yields information about the structure (long-range order) of the crystal. Therefore, X-ray powder diffraction was used to judge the quality, especially the crystallinity of synthesised LDH samples. The X-ray powder diffraction pattern of a synthetic MgAl-LDH is presented in (**Fig. 6.3**). Due to textural effects caused by the layered structure of LDHs the intensities of patterns may vary in a wide range. The basal (00l) patterns correspond to the sum of one brucite-like layer and one interlayer. The true lattice parameter c_o is then a multiple of c which depends on the stacking sequence of the brucite like layers, the nature of the anions, and the content of trivalent cations. Therefore, (00l) patterns can be used to give detailed information about the dimension of the lattice parameter c.

On the other hand, the pattern at about 60° 2-thetha is indexed as (110) and, can be used to obtain information about the other parameter, the lattice parameter a.

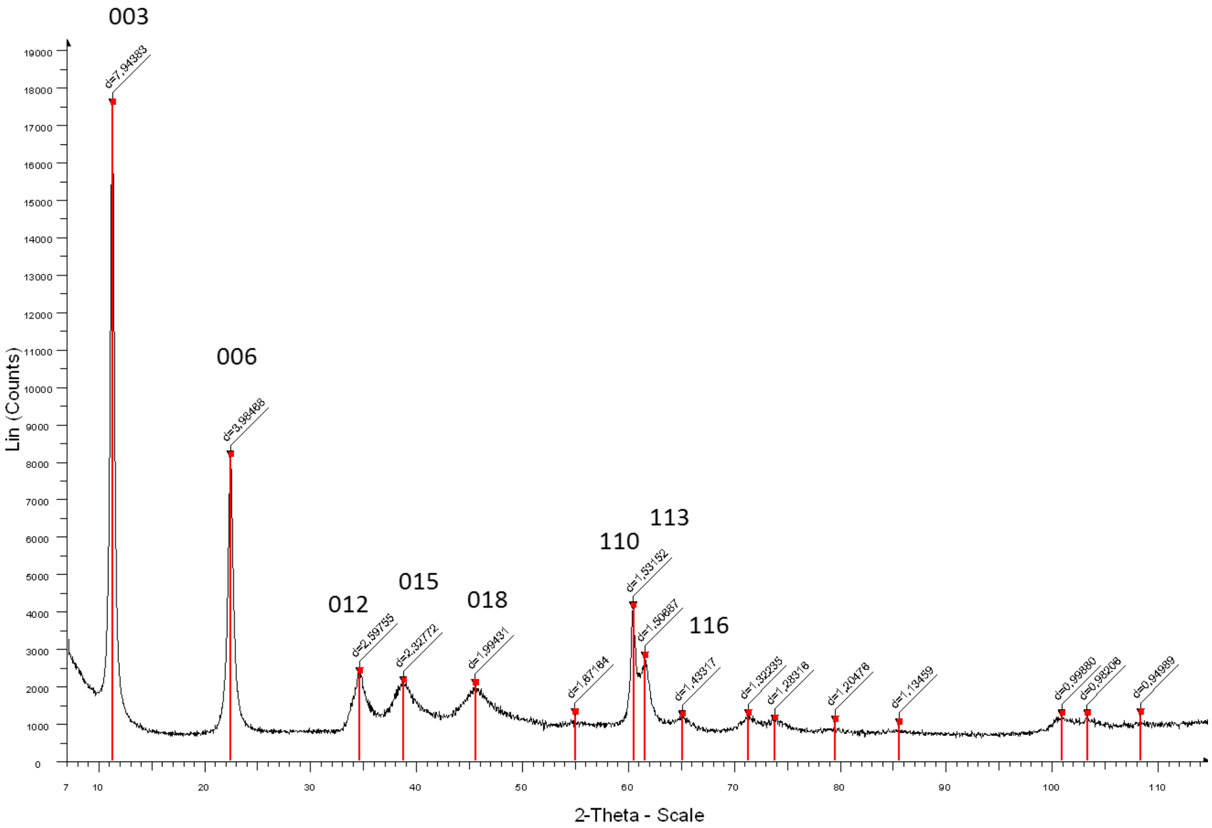

Fig. 6.3 X-ray powder diffraction pattern of a synthetic MgAl-LDH. The indices refer to a rhombohedral cell.

For all samples under investigation the obtained patterns exhibit the rhombohedral symmetry (**Fig. 6.3**). It should be noted at this point, that poor crystallinity or amorphous phases complicate the exact interpretation of the XRD pattern.

6.4.3.2 Infrared analysis

Infrared (IR) analysis is used to identify the presence of IR-active functional groups in the interlayer between the brucite-like sheets. Besides that, information about the type of bonds with the anions and about their orientations can be obtained.

There are some papers devoted to FT-IR-diagram interpretations of LDHs [CAV/TRI1991 and HER/ULI1985]. According to these authors, the absorption at 3500-3600 cm^{-1}, present in all LDHs, is attributed to the H-bonding stretching vibrations of the OH-groups in the brucite-like layers. The maximum of this band is shifted depending on the content of trivalent cations, x, in the brucite layer. For $Mg(OH)_2$ x is equal to zero and maximum of this adsorption is reached at the highest frequency of 3700 cm^{-1}.

In the 200 – 1000 cm^{-1} region there are some bands related to vibrations of the interlamellar anions and to cation-oxygen vibrations.

The main adsorption bands of anions are observed between 1000 and 1800 cm^{-1}. The most prevalent IR-active groups in LDHs are CO_3^{2-} and NO_3^-.

Carbonate has three main IR-active absorption bands: at 670 – 690 cm^{-1}, 850 – 880 cm^{-1} and 1350 – 1380 cm^{-1}. The frequency of the last band is higher if the ratio M^{2+}/M^{3+} is equal to 3 (1370 cm^{-1}) than if the ratio M^{2+}/M^{3+} is equal to 2 (1355 cm^{-1}). The band at 1625 cm^{-1} may be related to the presence of bicarbonate ions. Some other authors [FER/BAR1997] reported that this band is due to the deformation mode of water molecules. Carbonate strongly forms hydrogen bonds. At 3000 cm^{-1} the hydrogen bonds between interlayer water and carbonate are visible.

After carbonate, nitrate is the second and most frequently observed interlayer anion in HTlc-s. The infrared spectrum of LDHs with nitrate anions shows the strongest absorption at 1380 - 1390 cm^{-1} and 1425 cm^{-1} [KLO/WHA2002].

Other less frequent groups such as SO_4^{2}-, ClO_4^- can be detected by FTIR also, whereas Cl^- is IR-inactive.

In summary, the results of XRD and FTIR are useful in determining the structure and the nature of the interlayer anion.

6.4.4 Potential mineral for the retention of anions

Three main technical applications can be divided from the structural features of the LDHs; 1) anion exchange processes within the interlayer space [ULI/PAV2001], 2) cation sorption with the surface OH groups acting as proton-acceptors [LEH/ZOU1999] and c) calcined forms acting as excellent sorbents for anions [SAT/WAK1986].

LDHs are widely used in technical applications [LI/DUA2006], especially in the field of decontamination of soils, sediments and water. Due to human activities (agriculture, industry, domestic uses, etc.) the risk of contamination increases, and the chemical nature of the contaminants is widely divers. The presence of these contaminants has raised a large concern because they may affect human health, thus there is a need to develop new techniques to remove them from soil, sediments or water. One of the most widely used process to remove contaminants from water or soil is the adsorption or entrapping in an appropriate sorbent. Active carbon is still the most universal adsorbent to remove contaminants from water and soils. Clays, especially LDHs are of enormous interest nowadays. They are easily produced, their composition can vary in a wide range hence their properties can be manipulated easily, the costs are low and diverse contaminants can be hosted within the phases.

6.4.5 Long-lived fission products

Many countries intend to dispose heat generating radioactive waste in deep geological formations. Of special concern are the fission/activation products (^{14}C, ^{36}Cl, ^{79}Se, ^{129}I, ^{135}Cs and ^{99}Tc). Due to their long half-life times and their high mobility in anionic form they might reach the biosphere and contribute to the dose rate. Within the project VESPA I the investigations concentrated on the radionuclides Se, I and Tc.

^{129}I has a very long life time (half-life: 15.7 million years). In the reactor ^{129}I is produced as fission product and the fission yield is approximately 0.75 %. Under reducing conditions, expected in the final repository (European repositories) the anion iodide (I^-) is the most stable anionic form and represents therefore the species of interest.

^{79}Se is produced with a fission yield of 0.04 %. For ^{79}Se the half-life seems to be in the range between $2.8 \cdot 10^5$ and $1.1 \cdot 10^6$ years [JOE/BUH2010]. Compared to iodine the chemical behaviour of selenium is much more complicated. Selenium possesses the oxidation states (-II), (0), (+IV) and (+VI). The oxidation steps strongly depend on the reducing conditions (Eh-values) of the geochemical environment, i. e. high Eh-values (O_2 overpressure) favour high oxidation states. The oxidation states and hence the chemical behaviour of Se is as well strongly influenced by redox sensitive solid phases i. e. by redox-reactions nearly insoluble selenides can form. In the oxidation states (+IV) and (+VI) selenium is present as oxyanion selenite (SeO_3^{2-}) and selenate (SeO_4^{2-}) respectively, which are excellent complexing ligands.

^{99}Tc has a half-life of 2.1×10^5 years and the fission yield is approximately 6 %. Two oxidation states are of relevance. Tc in the oxidation state (IV) is expected under reducing conditions. In general, Tc(IV) components are hardly soluble. On the other hand, Tc can be present in the oxidation state (VII) as pertechnetate anion (TcO_4^-) and in this form it is highly mobile in an aquatic media. With respect to develop a reliable source term for the radionuclide Tc, mostly the reduction of Tc(VII) to Tc(IV) and then the solubility description of Tc(IV) components is investigated. However, considering oxic environmental conditions, the retention for the highly soluble pertechnetate anion by interaction with repository-relevant solids, is part of the source term.

6.4.6 Retention mechanism for anions

The mobility of anions can be reduced by different retention mechanisms [STU/MOR1996]. An anion (i. e. An^-) can react with a metal cation (i. e. M^+) resulting in the formation of a new compound (MAn).The reaction can be classified as **precipitation**. Note, that the precipitation can only occur, when the concentrations of the cations and anions are higher than the solubility constant of the product. Considering a LDH as solid phase the next possible retention mechanism for anionic species is the **surface adsorption**. As a clay mineral the LDH possesses surfaces, the so-called "external-surfaces", which are directly contacted to the aqueous solution. Here a reaction can take place in two directions. The first one is classified as an outer-sphere complex (physisorption) between protonated hydroxyl groups and the anions. The outer-sphere complex is characterized by weak electrostatic bonding and that the anionic hydration shell is still present. The second one is classified as an inner-sphere complex (chemisorption). Here the anion replace a hydroxyl group (divalent anionic species can replace two hydroxyl groups resulting in a bidentate complex) and chemical bonds exist. Surface adsorption as a process has to be taken into account, when the retention of anionic species under repository relevant conditions will be investigated. It should be noted that the process "surface adsorption" is pH dependent (the hydroxyl groups will be "activated" by protonation (low pH values) or "deactivated" by deprotonation (high pH values). Further on there is a limitation in existing "external surfaces" leading to saturation effects (Langmuir behaviour of the isotherms). When an element is complexed at the mineral surface first, it can precipitate in a second step by growing of layers in epitaxial direction. Then a solid solution might be able to form. The **coprecipitation** method is used often for retention of anionic species. It offers the possibility to create LDHs with the desired anionic species in the interlayer. On the other hand the composition and stoichiometry of the cations within the brucite layer can be adjusted as desired (limitations in the size of chosen cations exist) as well. In general the coprecipitation is performed, when a salt solution (containing the desired metal cations in the desired stoichiometry and the desired anion) is dropped to an aquatic phase (adjusted to a special pH value, mostly in the pH range between pH 9 and 10) and by the simultaneous addition of a base (mostly NaOH is used) in order to keep the pH constant Note the pH adjustment depends on the choice of metal cations forming the mixed hydroxides. Detail structural investigations of the resulting LDH are of high importance in order to gain information at a molecular level such as the formation of a solid solution within the cations in the brucite layer and as the formation of a solid solution within the anions in the interlayer. A solid solution is characterized by the structural incorporation of a cationic or anionic species into the structure of the mineral phase, here the LDH. Coprecipitation as well can lead to a mechanical entrapment of an element. Mechanical entrapment describes a mixture of two phases, one phase hosting the element of interest and this hosting phase determines the immobilisation of the element by its solubility. In geochemical environment, compared to surface adsorption, retention by solid solution formation possesses higher stabilities towards changes in solution composition, pH and Eh decreases/increases; hence the retention is quite effective. A special retention mechanism with respect to LDHs is the **ion exchange** process. When a LDH comes in contact to an aqueous phase which contains an anion having a higher affinity towards the LDH as the interlayer anion itself, an anion exchange reaction takes place. The uptake of the incoming anion is rapid (within minutes in the LDH systems) implicating the ion exchange mechanism [TAV/FEN2010]. Different mechanism for the anion exchange reactions are discussed in literature (two-steps process including dissolution and re-precipitation (D-R-mechanism), first order kinetic mechanism and another two steps mechanism), but to distinguish between is difficult due to the high rates [PAL/FRO2009]. Nevertheless all anion exchange reactions create only one structural change. This structural change is the variation in the interlayer distance (can be calculated from the c-parameter of the unit cell), which of course depend on the size of the incoming anion. Extensive studies by [MIY/OKA1977] and [MIY1975] demonstrated the anionic exchange properties of a number of species, establishing the ranking of affinity for intercalation. LDH shows the greatest affinity for anions of high charge density. The affinity of monovalent anions was determined to be $OH^- > F^- > Cl^- > Br^- > NO_3^- > I^-$, while the order for divalent anions was $CO_3^{2-} > SO_4^{2-}$. The carbonate anion has proven to be the preferred anion for intercalation, and once intercalated proves difficult to exchange with other anions. Care must be taken when an anion, different from carbonate, should be intercalated. Removal from carbonate from all sources is essential in exchange reactions. Besides the higher affinity (determined by the charge density) of the incoming anion the other driven force for ion exchange reaction is that the formed new LDH has a greater thermodynamic stability than the original LDH structure, reflected by a lower solubility product. This thermodynamic stability depends on the interlayer interactions of LDHs which are mediated by coulombic forces. Coulombic forces exist between the positively charged layers and the anions in the interlayer. Hydrogen bonding exists between the hydroxyl groups in the layer with the anions and with the water molecules in the interlayer as well. Especially the water molecules are connected through extensive hydrogen bonding to the hydroxyl ions of the metal hydroxides layers and interlayer anions and these bonding strongly contribute to the stability of the LDH. The quantity of the water present in the interlayer is determined by the nature of the anion. Vibrational studies did show that the LDH interlayer is highly structured. This structure strongly depends on the nature of the anion present. One can say that due to the structure in the interlayer even within the interlayer region the formation of a solid solution is possible. Results from structural and thermodynamic investigations, performed by [AIM/WIE2012] did reveal the existence of an AFm (I_2,SO_4) solid solution. LDHs however can fix most effective anionic species by another process which is known as **memory effect**. For example, a MgAl-LDH is calcined in the temperature range between 450 and 650 °C. This calcination step removes the anions and the interlayer water from the interlayer region and hydroxyl groups from the brucite layer. The result is the formation of a mixed oxide (amorphous magnesium oxide with dispersed aluminium ions as a solid solution) [FRO/MUS2006]. Re-hydrating the calcined product regenerates the LDH to its original structure, where water is absorbed to reform the hydroxyl layers, as well as being absorbed into the interlayer along with the anion in solution. It is important to note that the re-hydration of the calcined LDH form in carbonate free solution will yield a carbonate free LDH.

6.4.7 Interaction of LDHs with iodide

As already mentioned, [MIY1975] was the first, who determined the ranking of affinity for intercalation of monovalent anions as follows: $OH^- > F^- > Cl^- > Br^- > I^-$. The higher affinity of Cl^- against I^- was demonstrated as well by Curtius et al. [CUR/PAP2005]. A MgAl-LDH, with chloride as interlayer anion was contacted to an aqueous solution containing iodide. Retention of trace amounts of iodide by anion exchange was observed. In the presence of competing anions however, no retention of iodide occurred. This strong effect of competing anions towards the retention of iodide was verified by other working groups [FET/RAM1997]. On the other hand, [FET/OLG1999] showed that the retention capacity for iodide increased significantly, when the calcined LDH form was used and the results from Liang et al. [LIA/LI2007] confirm these findings. The retention mechanism of iodide on calcined LDH [MOR/ANR2012] can be described according to:

$[Mg_3AlO_4(OH)] + 4H_2O + I- \rightarrow [Mg_3Al(OH)_8] I + OH^-$.

Interesting investigations were performed by [AIM/TAV2012]. ZnAl-LDHs with iodide as interlayer anionic species were synthesized by coprecipitation. Results from structural measurements and calculations reveal that iodide is included in the interlayer, but the coordination between iodide and cations was weak, even if Al possesses a local ordering. As a consequence iodide can move easily in the interlayer and does not significantly contribute to the cohesion of the brucite layer and the interlayer. Hence, one can expect that the present LDH structure is instable because there no correlation between iodide and cation position exists. A different result was obtained by investigations using AFm-SO_4 phases (belonging to the class of LDHs as well). Via anion exchange between AFm-I_2 and AFm-SO_4 a solid solution forms and a continuous solid solution behaviour was found over a large range of iodide. Within the interlayer a local order of iodide [AIM/WIE2012] exists.

6.4.8 Interactions of LDHs with selenite

Selenite (SeO_3^{2-}) is a divalent oxyanion. [MIY1975] already demonstrated that divalent anions have a higher affinity towards LDHs, due to their higher charge density. A detailed study with respect to the interactions of LDHs with selenite was performed by [YOU/VAN2001]. Investigations were performed with a MgAl-LDH (chloride as interlayer anion). Retention of selenite by a rapid anion exchange occurred. The retention was affected by competing anions and the following ranking was determined: $HPO_4^{2-} > SO_4^{2-} > CO_3^{2-}, SeO_3^{2-} > NO_3^-$. Results from [SKO/CHR2009], working with a Fe(II)/Fe(III)-LDH, showed that the reduction to Se(0) was responsible for the retention. The Fe(II)/Fe(III)-LDH (green-rust) is a redox-sensitive LDH and selenite can easily be reduced to Se(0). It should be noted, that the selenite retention under these conditions is dominated by redox-reaction and not by sorption.

6.4.9 Interactions of LDHs with pertechnetate

As mentioned before, the radionuclide Tc is highly mobile in the chemical form as pertechnetate (TcO_4^-). Like selenite the pertechnetate anion is an oxyanion. The application of layered double hydroxides for removal of oxyanion was reviewed by [GOH/LIM2008]. The retention capacities for pertechnetate were significant using calcined LDHs. This is attributed to the higher surface area, increased porosity, fewer carbonate anions being present and the sorption mechanism involves the rehydration of mixed metal oxides and concurrent intercalation of oxyanions into the interlayer. [WAN/GAO2006] studied the sorption capability of uncalcined LDHs for pertechnetate as function of LDH composition and structure. By manipulating the LDH composition/structure, the contribution of sorption at external edges increased significantly. As a conclusion the retention capability increased because there is a contribution by interlayer anion exchange and by sorption at external edges. In future, investigations should focus on the establishment of a general structure-property relationship that will guide the engineering of LDH materials for removal of a specific oxyanion.

6.5 Experimental

6.5.1 Materials

Deionized water was boiled and stored under an argon atmosphere before use. The chemicals were of analytical grade and used without further treatment. All experiments and working steps were performed under an argon atmosphere.

6.5.1.1 Synthesis of the solid solutions $(Mg_{2.9}/Ni_{0.1})Al_1$-LDH, $(Mg_{2.9}/Fe_{0.1})Al_1$-LDH and $(Mg_{2.9}/Co_{0.1})Al_1$-LDH

The "pure" MgAl-LDH was synthesized using the coprecipitation method at controlled pH conditions as described by [WEI/TOT1996] with some modifications in relation to the purification and drying steps. A detailed description was given by [CUR/KAT2005]. The Co-, Ni-, and Fe-bearing LDHs were prepared according to the same co-precipitation method. Specifically, 250 mL of water was placed in a three-necked glass flask and a pH of 10.0 ± 0.1 was achieved using 2 M NaOH. A mixed aqueous solution containing $MgCl_2 \cdot 6H_2O$ (0.29 moles), $CoCl_2$ (0.01 moles), or $FeCl_2 \cdot 4H_2O$ (0.01 moles); or $NiCl_2 \cdot 6H_2O$ (0.01 moles) and $AlCl_3 \cdot 6H_2O$ (0.1 moles) in 250 mL of water was added over a period of 5 h while the pH was maintained at 10.0 ± 0.1 by simultaneous addition of 2 M NaOH. During the precipitation process the temperature was maintained at 70 ± 1ºC. After the addition was complete, the temperature was raised to 90 ± 1ºC and stirring was continued for 24 h. After cooling to room temperature (25 ± 1ºC), the precipitate formed was filtered and then dialyzed at 60 ± 1ºC for 72 h. For this washing step the dialysis hose was filled with the precipitated solid and then placed in a 2 L vessel containing deionized water. The water was changed three times a day until it was chloride-free (chloride measurements were performed using the cuvette test LCK 311 (Dr. Lange^{TM}). The detection limit of the used chloride test was 2.82 10^{-5} moles L^{-1}. Then the precipitate was filtered and dried in a desiccator under argon.

6.5.2 Methods

6.5.2.1 Scanning electron microscopy (SEM)

Investigation by SEM was performed using the environmental scanning electron microscope FEI Quanta 200 F (FEI, Oregon, USA). The measurements were carried out in low vacuum mode at 0.6 mbar (20 kV, spot size 4, working distance 10 mm). The counting time was 50 s and the energy setting of the energy-dispersive analysis was 20 keV. The resolution was 132.40 eV. When using this mode, sputtering of the samples with gold or carbon was unnecessary and analytical artefacts were, thus, avoided. The samples were prepared as powders on adhesive carbon tabs. The microscope is equipped with the EDX-system Genesis (EDAX).

6.5.2.2 Photometric/UV-visible analyses

The **chloride content** in the precipitates and in the corresponding supernatant liquids was determined by photometric measurement (wavelength of 300 – 600 nm, with a maximum reflection at 468 nm) (Dr. Lange photometer CADAS 100) using a test cuvette (LCK 311, Dr. Lange^{TM}). Aliquots of the liquid phases were measured, over the wavelength range mentioned above after dilution (1 to 1000) with water. Each solid (100 mg) was dissolved in 10 mL of a 2 M HNO_3 solution. Then another dilution (1 to 50) with water was performed. This solution was measured using test cuvette LCK 311 (path length = 10 mm).

The **presence of Fe (III)** in the Fe bearing LDH was determined by the formation of a Fe (III) thiocyanate-complex and the photometric measurement was performed using a Dr. Lange photometer CADAS 100 instrument. In the first step, 200 mg of the Fe-bearing LDH was dissolved in 5 mL of concentrated HNO_3 solution and then diluted with water to a volume of 20 mL. Then 50 mL of this sample solution was added to 50 mL of water. Next, 15 mL of TBP (tributylphosphate) and 15 mL of a NH_4SCN (20 wt %) solution were added. The mixture was shaken for 10 min. Finally, 5 mL of the organic phase was separated and dried with Na2SO4. After 10 min, ~2 mL of this solution was used for the measurement. The concentration of Fe (III) was calculated according to Beer Lambert law. The analytical error was in the range of ± 5 %. Pure Fe (III) Cl3 and Fe (II)Cl_2 salt solutions were used as internal standard solutions.

6.5.2.3 ICP-OES analyses

The Mg, Al, Fe, Co, Ni, and Na contents in the solid and liquid phases were determined by ICP-OES using a Perkin-Elmer ICP-OES instrument (Thermos Fisher Scientific Model 11189 (Massachusetts, USA)). The liquid samples were analysed directly without dilution steps. Each solid sample (100 mg) was dissolved in 10 mL of a 2 M HNO_3 solution. This solution was further diluted (1 to 100) with a 0.1 M HNO_3 solution and then the measurement was performed.

6.5.2.4 Thermogravimetric analyses (TGA)

The TGA measurements were carried out using a NETSCH STA 449 C Jupiter^{TM} instrument (Netsch, Selb, Germany). In the temperature range between 25 and 1000ºC the heating rate was 10 ºC/min. The measurements were carried out under nitrogen flow. Within the measurements the interlayer water contents, hydroxyl groups, and chloride anions were determined. The temperatures of removal of interlayer water, chloride, and hydroxyl groups were also determined.

6.5.2.5 FTIR analyses

The interlayer composition (anion, interlayer water) was determined by FTIR analysis using a Bruker Equinox^{TM} (Massachusetts, USA) spectrometer with the KBr pellet technique. Approximately 200 mg of KBr and ~2 mg of LDH were mixed carefully and a pressure of 10 tons was applied and held constant for 3 min to prepare each pellet. The IR spectra were recorded in the range 4000 to 400 cm^{-1}.

6.5.2.6 XRD measurements – Phase identification

The XRD measurements were carried out using a D8 Advance powder diffractometer from Bruker AXS (Karlsruhe, Germany). The structural analysis and the phase quantification were carried out using the BGMN software package [BER/FRI1998]. The program is based on the fundamental parameter approach (FPA), which considers the diffractometer geometry, i. e. physical parameters, in order to describe the device function [KLU/ALE1974]. The goniometer of the diffractometer features a θ-θ-Bragg-Brentano geometry with a radius of 250 mm. For the XRD measurements, CuKα radiation at

30 kV and 45 mA was applied. The intensity gained was registered by a 1D VAntec line detector. A nickel filter was inserted to suppress parasitic CuKβ radiation. An automatic aperture system was used to maintain a constant X-ray irradiation length on the sample of 3 mm. Primary Soller slits with a device angle of 2.376º were also applied to reduce divergence of the incident beam. The XRD measurements were carried out in continuous mode with a step size of 0.028º and with 1 s/step over the range 5 to 85º2θ. A non-certified Zincite p. a. standard of known weight (10 wt %) was added as an internal standard for goniometer alignment corrections, using DiffracPlus Eva software (by Bruker-AXS), which references the observed Zincite reflections to the entry no. 00-036-1451 of the powder diffraction file PDF-2 database of the International Centre of Diffraction Data (ICDD). The magnitude of these corrections was ~0.1 mm. Zincite was also used (by adding it to the LDH and then applying Rietveld to determine the amounts of phases) to quantify byproducts (crystalline and/or amorphous) which may have formed during the LDH syntheses. Refinement of real structure parameters of the LDH compounds using the Rietveld method was demonstrated by [UFE/KLE2008]. Practical considerations of that investigation, which refer to the sample preparation of LDH compounds and the application of Zincite as an internal standard, were followed here, e. g. for the estimation of the amorphous content.

6.5.2.7 X-ray diffraction - Rietveld refinement and quantitative phase analysis

In order to quantify the phases observed and determine their lattice parameters and the degree of disordering, the Rietveld method was applied. The arrangement of the layers in the c-direction of the LDH compounds synthesized showed no long-range ordering, i. e. the respective stacking sequences of the ordered hexagonal (ABAB) and trigonal LDH end-members (ABCABC) were randomly distributed. The analysis was carried out using the BGMN software which is able to evaluate parameters of the real structure such as the randomized stacking sequences of the layers in LDHs [UFE/KLE2008 and CUR/UFE2009]. This feature is based on a recursive approach which has been developed [TRE/NEW1991] and implemented in the DiFFaX software package. This program simulates XRD patterns of compounds which exhibit virtual stacking faults and has been applied widely in the characterization of LDH compounds [FAO/PRE2012] and [BRI/THO2008] and [PRA/KAM2007] and [RAD/KAM2007] and [THO/RAJ2004]. The stacking faults of the layers lead to anisotropic peak broadening in the XRD pattern as the long-range order perpendicular to the layers is not present. Therefore, the related hkl reflections will broaden. The model for the calculations is based on the structure given by [ARA/PUS1996]. In a projection parallel to the c axis (**Fig. 6.4**) one octahedral layer and the oxygen positions of CO_3^{2-} and H_2O are revealed. The Wyckoff positions are 3f and 3g referring to the space group P62 m (189) and could be occupied by both O_2^- and Cl^-. The cations, which occupy the Wyckoff positions 4h and 2e, have been omitted for visual reasons. Due to ordering of the Mg and Al cations the octahedra are slightly distorted. This type of LDH belongs to the $2H_1$ polytype [BOO/DRI1993]. The metal cations are six-fold octahedrally coordinated by hydroxides (transparent edge-sharing octahedra). Between chloride anions and water molecules (black and white coloured spheres) are the constituents of the interlayer. The respective colour differentiation of the spheres refers to the different atomic, i. e. Wyckoff, positions occupied by oxygen and chlorine. The transition from one octahedral layer to the next is described as a mirror operation carried out with a mirror plane being situated virtually in the interlayer. According to the nomenclature of [BOO/DRI1993] the hexagonal structure is referred to as the 2H1 polytype. The respective layer sequence has the notation AC=CA=AC. Contrary to that, the trigonal structure represents the $3R_1$ polytype and the ordering of layers exhibits the sequence AC=CB=BA=AC. The capital letter notation ''A'', ''C'', and ''B'' denotes the sites in which the hydroxyl anions of the octahedra reside. The =sign between adjacent layers indicates that the upper hydroxyl of the layer below and the lower hydroxyls of layer above form a prism and is, therefore, referred to as "p-type". If the minus sign is given, the respective hydroxyls form an octahedron. This arrangement is also referred to as "o-type". The synthesis of this study exhibits a 3:1 ratio of the (M(II)/Al(III)) cations, which is observed in $3R_1$ polytypes and the notation sequence is AC=CB=BA=AC. For this polytype the upper hydroxyls of the lower layer and the lower hydroxyls of the upper layer also form prisms. This polytype was described by [ALL/JEP1969] and by [BEL/REB1996]. The space group of this LDH is R3 m (166). The metal cations M(II) and M(III) occupy, unlike the $2H_1$ polytype, the same Wyckoff position 3a. Due to this common position of the different cations, the surrounding octahedra are not distorted, i. e. are identical considering the atomic positions, bond distances, and angles. The position of the interlayer oxygens of the CO_3^2 anion easily triggers the formation of hydrogen bonds to the adjacent hydroxyls when the arrangement of the related layers follows the p-type [RIV2001]. This site occupancy of the cations is the same as that given by [ALL/JEP1969] and [BEL/REB1996]. The layer transition of two adjacent octahedral layers for this LDH type, referred to as 3R type, is described as a 2/3 shift parallel to the a and 1/3 parallel to the b axis.

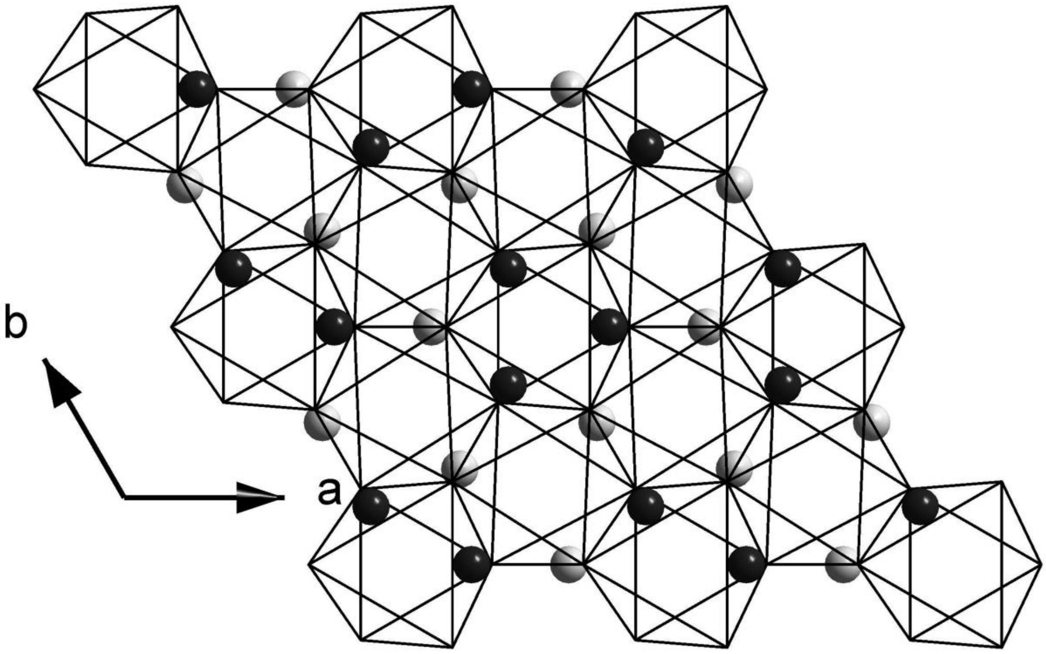

Fig. 6.4 View II c-axis on the octahedral layer of LDH (black solid lines)

Hydroxyl groups have been omitted. Black and gray spheres represent the position of water and chloride, respectively in the interlayer. The depicted structure is according to [ARA/PUS1996]

Following the notation of [BOO/DRI1993] the respective layer sequence is AC=BA=CB=AC. In order to treat structural parameters more independently for the Rietveld refinement, the symmetry of the given structures which belong to the space groups P6.2m (189) and R3 m (166) were reduced to P1 (1). As the LDH syntheses being considered do not reflect exactly the structural properties of the applied model given by [ARA/PUS1996], some further assumptions have been made for the calculation, i. e. the amount of Mg and Al and the M(II) site occupancy was a constraint on the stoichiometry listed in (**Tab. 6.1**). Chloride and carbonate occupancies were also fixed for charge-balancing reasons. The stacking vectors which characterize the layer transition sequence were also fixed to 1/3, 1/3, 1 for the $3R_1$ type and to 0, 0, 1 for the $2H_1$ type. Hydrogen was not taken into account due to its very small contribution to the scattering power of the LDH compounds. The lattice parameters, the atomic positions of the interlayer water, the chloride, and the carbonate of the pure MgAl-LDH were treated as restraints. This is also valid for the transition probability of the layers and the temperature factors which were considered to be isotropic. To account for the quality of the Rietveld refinements the ratio of R_{wp}/R_{exp} is given.

6.5.2.8 EXAFS measurements

The samples were investigated as powders pressed without diluent into 7 mm-diameter pellets. Pellet preparation and measurements were done under inert gas. Four scans were performed for the Fe and Co-bearing LDH and six scans for the Ni-doped LDH. All scans were recorded in transmission mode with an accumulation time of 2s. The accumulation time in the EXAFS range was increased by a factor square root of k, reaching its maximum at the end of the spectrum at k 16 $Å^{-1}$ with 8s counting time. The fits were performed, simultaneously on the Fourier transform (FT) of the k^2-weighted $\xi(k)$ data and on the FT of k^3-weighted $\xi(k)$ data. The Fe/Co/Ni K edge X-ray absorption fine structure (EXAFS) spectra were recorded at the INE-Beamline at ANKA. (The INE-Beamline at ANKA is located in Karlsruhe, Germany). The ANKA storage ring is operated at 2.5 GeV with a current of 180 mA.) The spectra were energy calibrated to the first inflection point in the XANES of a Fe/Co/Ni metal foil (7.112/7.709/8.333 keV, respectively) and measured simultaneously. The EXAFS signal was recorded at room temperature in transmission mode using N_2-filled ionization chambers at ambient pressure. Si<111> crystals were used in the double crystal monochromator, operating in fixed-exit mode. The parallel alignment of the crystal faces was detuned to ~70 % of the maximum beam intensity at the beginning of each scan. The incident intensity was then held constant by means of a piezo-driven feedback system to the second crystal. The EXAFS fits were performed using Artemis, a program of the IFEFFIT package [NEW2001], using phase and amplitude data calculated for a 128 atom cluster (~8 Å diameter size, centered on the individual metal cations) and based on the modified model of [BEL/REB1996] where the carbonate groups in the interlayer space were simply replaced by chloride. Among the possible occupation sites for Cl^- in the interlayer, four were represented. For Cl atoms, single-path scattering files for phase and amplitude were used. For the Ni- and Co-doped compounds, the multiple scattering paths (MS) for the first oxygen shell were taken into account in the fit. The k-range used in modeling was [4.2-14.7 $Å^{-1}$] for Ni-doped Cl-LDH, [4.2-14.2 $Å^{-1}$] for Co-doped Cl-LDH, and [3.4-11.4 $Å^{-1}$] for Fe-doped Cl-LDH. All fits were performed in the R-space simultaneously on the k_2- and k_3-weighted data.

6.5.2.9 Thermodynamic description of LDH solid solution-aqueous solution systems

Estimations of the molar Gibbs free energies, G_f at 25 ºC and 70 ºC of the LDH solids were performed in order to investigate the effect of Fe-, Ni-, and Co substitution into the Mg-Al-containing LDH on the aqueous solubility. Possible effects of oversaturation in the aqueous phases after synthesis were ignored and equilibrium between the precipitated solids and their corresponding solutions was assumed. To estimate the values of the Gibbs free energies of the solids, the following scheme was applied:

(1) the speciation of the aqueous solutions obtained from the synthesis experiments was modelled for 70 ºC using the Davies model [DAV1962] for aqueous electrolytes and Gibbs free energy minimization software GEMSelektor [KUL/WAG2013] which includes the built-in NAGRA-PSI and SUPCRT/Slop98 chemical thermodynamic databases [HUM/BER2002 and SHO/SAS1997].

(2) From the calculated chemical potentials of Mg^{2+}, Ni^{2+}, Co^{2+}, Fe^{2+}, Al^{3+}, Cl^- and OH^- species in the aqueous phase and from the measured stoichiometric compositions of the synthesized solids, the molar Gibbs free energies of formation of water-free compositions were calculated as follows:

$$Gf = \alpha \text{ x } \mu\ (Mg^{2+}) + \beta \text{ x } \mu\ (Me^{2+}) + \gamma \text{ x } \mu\ (Al^{3+}) + \delta \text{ x } \mu\ (OH^-) + \varepsilon \text{ x } \mu\ (Cl^-)$$

with $Me^{2+}= Fe^{2+}, Ni^{2+}$ or Co^{2+}. μ is the calculated chemical potential of the bracketed aqueous species, and indexes α to ε are the stoichiometric coefficients, obtained from the chemical analyses of the solids synthesized.

6.5.3 Sorption experiments

Deionised water was boiled and stored under an argon atmosphere before use. The chemicals were of analytical grade and used without further treatment. For one litre of $MgCl_2$-rich brine (brine 2), the following amounts of salts were dissolved: 937.08 g $MgCl_2$ hexahydrate, 0.126 g $MgSO_4$ heptahydrate, 1.42 g KCl, 39.68 g $CaCl_2$ dihydrate and 4.13 g NaCl. For one litre of clay pore water (Opalinus-type) the following amounts of salt were dissolved: NaCl 12.38 g, KCl 0.12 g, $MgCl_2$ hexahydrate 3.44g $CaCl_2$ dihydrate 3.79 g, $SrCl_2$ dihydrate 0.134 g Na_2SO_4 2.00 g and $NaHCO_3$ 0.05 g. The radioisotopes ^{75}Se, ^{99}Tc and ^{129}I were used. All radioactive solutions were prepared from standardised stock solutions (^{129}I: chemical form: NaI in 0.1M NaOH, carrier free, activity: 374 kBq in 5 mL, reference date: 01.08.2007. ^{99}Tc: chemical form NH_4TcO_4 in water, carrier free, activity: 3700 kBq in 5 mL, reference date: 01.03.2002 and ^{75}Se, chemical form: H_2SeO_3 in 0.1 M HCl, activity: 4.12 MBq, reference date: 01.03.2010).

6.5.3.1 Sorption investigations as function of time

All working steps were performed under an argon-atmosphere. The sorption investigations were performed according to the batch-technique. All samples were stored under an argon atmosphere in glass tubes with occasional shaking. Time-dependent sorption investigations were studied as follows: To 10 mL solution (water, 0.1 M $MgCl_2$ solution or $MgCl_2$-rich brine or Opalinus clay pore water) 100 µL of the radioisotope solution (either ^{129}I or ^{99}Tc or ^{75}Se was used) and 0.1 g LDH was added in that order (solid/solution ratio: 10 g/L). The radionuclide concentration in this mixture was $4.25 \cdot 10^{-5}$ mol/L for ^{129}I, $5.89 \cdot 10^{-7}$ mol/L for ^{99}Tc and $5.65 \cdot 10^{-12}$ mol/L for ^{75}Se. Reference samples not containing the LDH, were made for each series. These blank experiments indicated that adsorption of the radioisotopes on the glass walls was negligible. Then at different time intervals a sampling was performed. First the samples were filtered (450 nm filter). One aliquot of the filtrate was used for pH-measurement, another aliquot was diluted with 0.1 M HNO_3 (1 to 10) and the metal concentrations of Al; Ni, Co and Fe were analysed by ICP-OES. The concentrations of the radioisotopes in solution were determined radiometrically by beta-spectrometry (Liquid Scintillation Counting, LSC, Packard 2200 Tri-carb). The filtered solids were washed, dried and analysed by XRD and FT-IR.

6.5.3.2 Sorption isotherms

The sorption was studied as function of radioisotope concentration as follows: To 10 mL solution (water or 0.1 M $MgCl_2$ solution or $MgCl_2$-rich brine or Opalinus clay pore water) the radioisotope solution and then 0.1 g of Ni, Co or Fe containing LDH was added (solid/solution ratio: 10 g/L). The radionuclide concentration in this mixture was in the range between $4.29 \cdot 10^{-6}$ mol/L and $2.04 \cdot 10^{-4}$ mol/L for ^{129}I, in the range between $5.94 \cdot 10^{-8}$ to $2.97 \cdot 10^{-6}$ mol/L for ^{99}Tc and in the range between $4.40 \cdot 10^{-13}$ to $1.88\ 10^{-8}$ mol/L for ^{75}Se. The samples were stored under argon-atmosphere in glass tubes for two days with occasional shaking. Then the samples were filtered (450 nm filter). One aliquot of the filtrate was used for pH-measurement, another aliquot was diluted with 0.1 M HNO_3 (1 to 10) and the metal concentrations of Al; Ni, Co and Fe were analysed by ICP-OES. The concentrations of the radioisotopes in solution were determined radiometrically by beta-spectrometry (Liquid Scintillation Counting, LSC, Packard 2200 Tri-carb). The filtered solids were washed, dried and analysed by XRD and FT-IR.

6.5.3.3 Sorption investigations as function of pH

The effect of pH on the sorption was evaluated as follows: To 10 mL water (or clay pore water or $MgCl_2$-rich brine), 100 µL of the radioisotope solution was added, the pH was adjusted (addition of small amounts of NaOH or HCl), and then 0.1 g of Ni, Fe or Co containing Mg-Al-LDH was added. The radionuclide concentration in this mixture was $4.00 \cdot 10^{-5}$ mol/L for ^{129}I, $5.89 \cdot 10^{-7}$ mol/L for ^{99}Tc and $3.90 \cdot 10^{-12}$ mol/L for ^{75}Se. Reference samples not containing the LDH, were made for each series. These blank experiments indicated that adsorption of the radioisotopes on the glass walls was negligible. Then at different time intervals a sampling was performed. First the samples were filtered (450 nm filter). One aliquot of the filtrate was used for pH-measurement, another aliquot was diluted with 0.1 M HNO_3 (1 to 10) and the metal concentrations of Al; Ni, Co and Fe were analysed by ICP-OES. The concentrations of the radioisotopes in solution were determined radiometrically by beta-spectrometry (Liquid Scintillation Counting, LSC, Packard 2200 Tri-carb). The filtered solids were washed, dried and analysed by XRD and FT-IR.

6.6 Results and Discussion

6.6.1 (Mg/Ni)Al-Cl LDH, (Mg/Fe) Al-Cl LDH and (Mg/Co) Al-Cl-LDH solid solutions

Already in 2005 the characterization of the pure MgAl-LDH was presented [CUR/KAT2005]. In the present work the anion retention potential of solid solutions compared to the pure MgAl-LDH was the main focus of interest. Stoichiometric formulas and cationic ratios of the synthesised Fe-, Co-, and Ni-bearing LDHs are summarized in (**Tab. 6.1**). The corresponding compositions of the supernatant liquids were also analysed. The amounts of Mg, Al, Fe, Co, Ni, and Na in the solids and their concentrations in aqueous solution after synthesis were determined by ICP-OES with an analytical error of 5 % (standard solutions were used in order to determine the deviation). The EDX technique (error range of 1 – 6 %) was applied to achieve greater accuracy with respect to the stoichiometry. The chloride in aqueous solutions and in the solids was determined photometrically (analytical error of ± 5 %). For the Fe bearing LDH, the amount of Fe (III) was determined to be 5 wt. % by formation of a thiocyanate complex and this value is within the error range. Note that these measurements were performed using freshly prepared Fe-bearing LDHs. An aliquot of this solid was sent to Karlsruhe (ANKA Beamline) for EXAFS measurements. The solid was stored for 8 weeks before measurement and, during that period, oxidation of Fe (II) could not be ruled out, although the sample was stored in a glass tube under argon atmosphere. Thermogravimetric analyses produced step-wise profiles having three main temperature regions, namely 50 – 260 ºC, 260 – 500 ºC, and 500 – 650 ºC. The weight loss in the first step is related to the interlayer water. The second weight loss is due to the first step of dehydroxylation and the removal of chloride from the interlayer. Above 500 ºC, the LDHs decompose and produce a mixture of metal oxides [MIY1980]. No differences were observed in the TGA curves of the Fe-, Co-, and Ni-bearing LDHs, indicating that the temperatures required for the removal of interlayer water, dehydroxylation of the cationic layers, and removal of interlayer anions were similar regardless of cation substitution. The thermal stabilities of Fe-, Co-, and Ni-bearing LDHs are, therefore, also similar. In (**Fig. 6.5**) the thermogravimetric curve of the Ni bearing LDH is shown.

Tab. 6.1 Stoichiometric formulae and cationic ratios of the synthesized LDHs

Stoichiometric formulae	**M(II)/M(III) (ICP-OES)**	**M(II)/M(III) (EDX)**
$[Mg_3 Al_1(OH)_8]Cl_{0.88} (CO_3)_{0.060} \cdot 2.40H_2O$	3.000	2.988
$[Mg_{2.9} Fe_{0.097} Al_1(OH)_{7.954}]Cl_{1.04} \cdot 2.70H_2O$	2.997	2.883
$[Mg_{2.9} Co_{0.100} Al_{1.01}(OH)_8]Cl_{1.03} \cdot 2.25H_2O$	2.970	2.911
$[Mg_{2.9} Ni_{0.090} Al_{0.99}(OH)_{7.86}]Cl_{1.09} \cdot 2.64H_2O$	3.020	2.926

Tab. 6.2 Compositions of aqueous solutions (pH 10.00 ± 0.02) after syntheses at 25 °C and 70 °C (Mg,Al,Fe,Co Ni in µmol/kg, Na and Cl in mmol/kg and DL is the detection limit)

T [°C]	**Mg**	**Al**	**Fe**	**Ni**	**Co**	**Na**	**Cl**	**Solid**
25	70.70	1.11	DL*	DL*	DL*	90.16	117.70	MgAl-LDH
70	1.73	88.95	0.53	DL*	DL*	904	900	MgFeAl-LDH
70	34.10	1.85	DL*	DL*	1.36	903	900	MgCoAl-LDH
70	1.89	9.64	DL*	1.19	DL*	903	900	MgNiAl-LDH

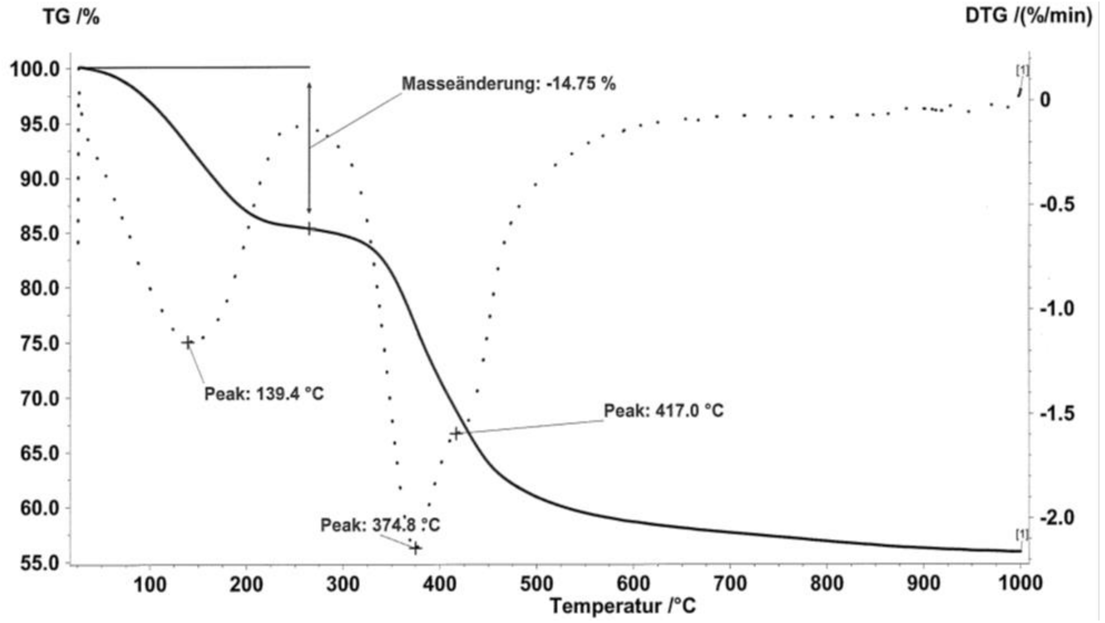

Fig. 6.5 Thermogravimetric curve of the Ni bearing MgAl-LDH

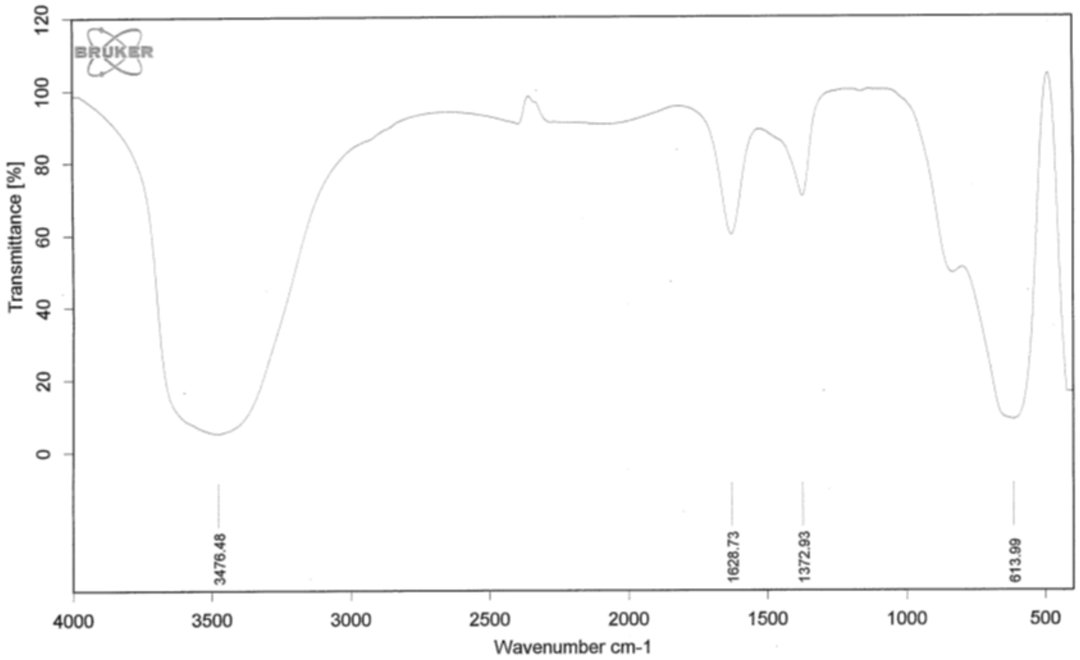

Fig. 6.6 FT-IR spectra of the Ni bearing MgAl-LDH

Fourier-transform infrared spectroscopic measurements were performed in order to gain information about the interlayer anion present within the interlayer. Strong hydroxyl stretching bands (3460 cm^{-1}) and interlayer water bending bands (1636 cm^{-1}) are observed for all LDHs. Exemplarily the spectrum for the Ni bearing MgAl-LDH is shown in **Fig. 6.6**. In the fingerprint region (1090 cm^{-1} - 550 cm^{-1}) the metal-O vibration bands were detected. All spectra showed a very weak adsorption band due to adsorbed CO_3^{2-} at 1352 cm^{-1}. The KBr pellets were produced under air and the carbonate ion had the greatest affinity for the LDHs [MIY/KUM1973].

The Scanning Electron Microscope (SEM) was used to study the morphology. The typical sand-rose structural was visible for the solid solutions (**Fig. 6.7** and **Fig. 6.8** and **Fig. 6.9**). The average crystalline size was estimated to be in the range of 0.2 µm to 0.5 µm.

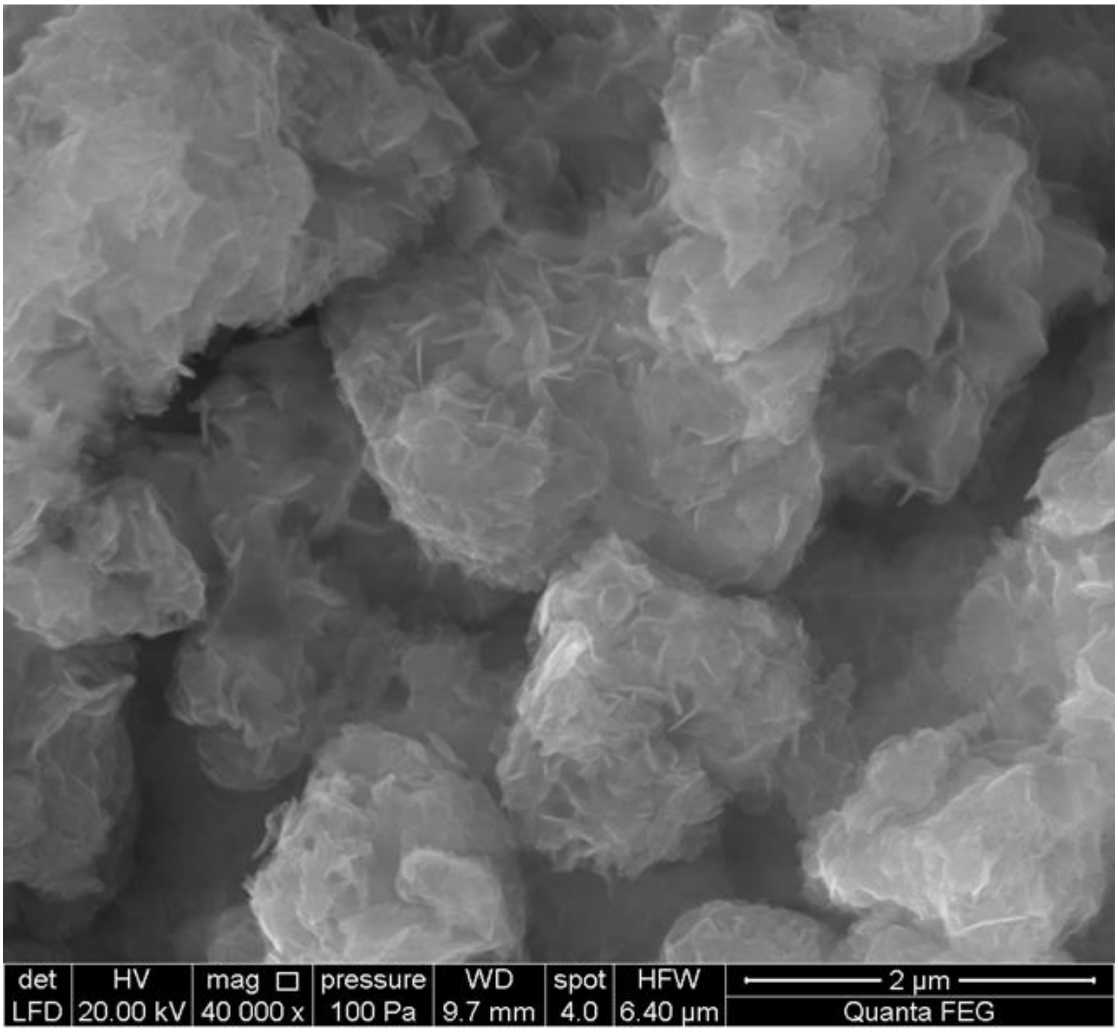

Fig. 6.7 SEM picture of the Ni bearing LDH

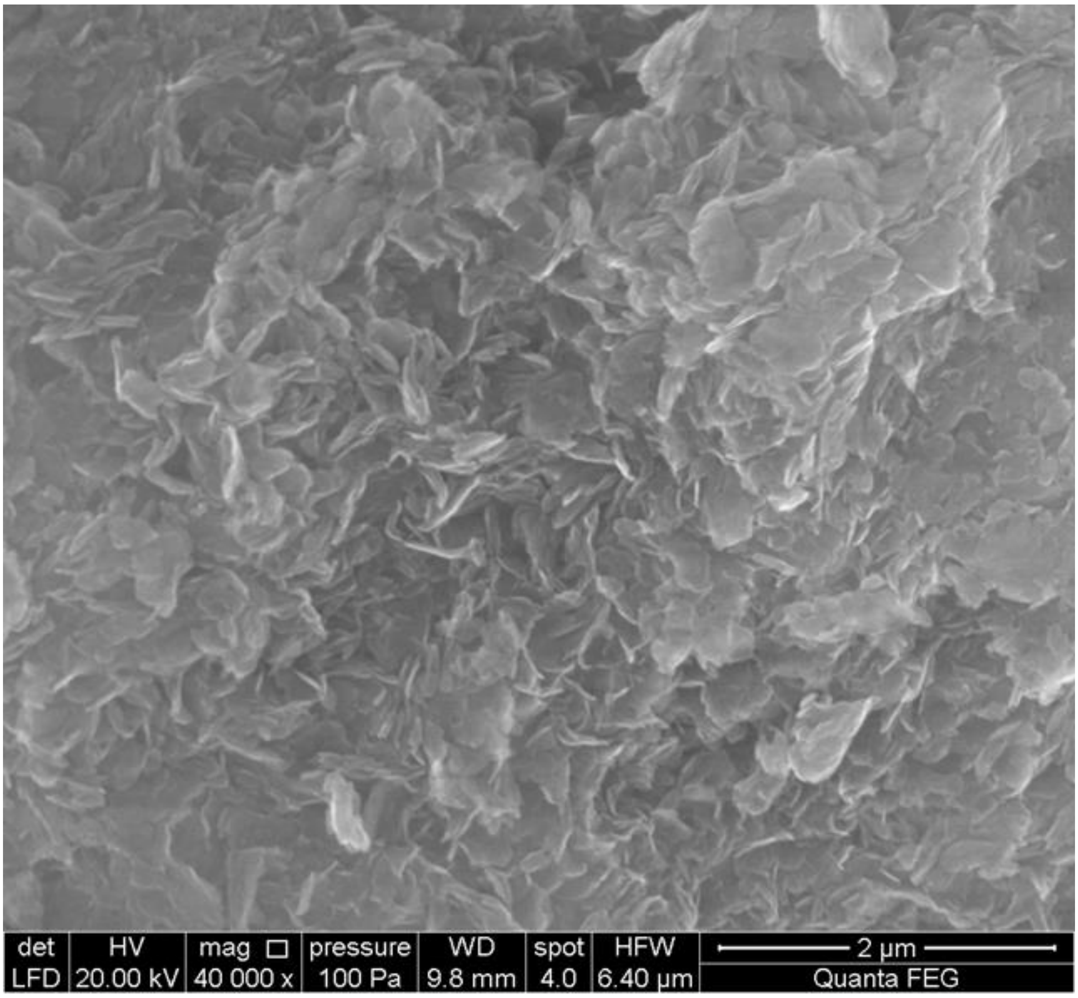

Fig. 6.8 SEM picture of the Co bearing LDH

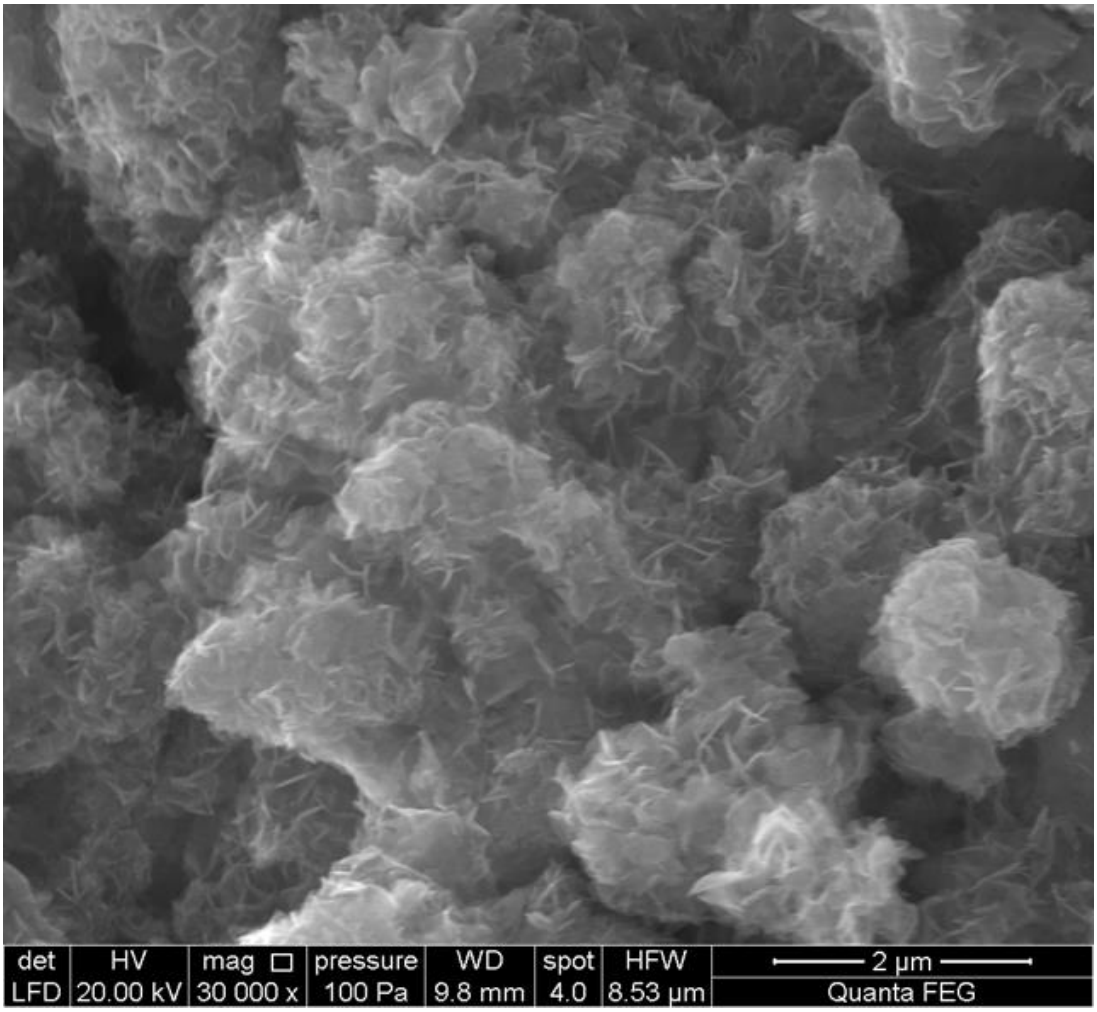

Fig. 6.9 SEM picture of the Fe bearing LDH

6.6.1.1 Estimation of the Gibbs free energies of the Ni, Co and Fe bearing LDHs

The molar Gibbs free energies of the precipitates were calculated by assuming a thermodynamic equilibrium between solids (Tab. 6.1) and corresponding mother liquor. Using the GEM-Selector [KUL/WAG2013] as described above, the compositions of liquids were modeled and the chemical potentials of the dissolved compounds calculated. The estimates demonstrated the effect of (1) intercalation of different anions (i. e. chloride and carbonate) in the interlayer space and (2) isostructural incorporation of various divalent cations (i. e. Fe^{2+}, Co^{2+}, Ni^{2+}) in the brucite-like layers, on the aqueous solubility of LDHs.

6.6.1.1.1 The effect of intercalated anion

The effect of intercalation of CO_3^{2-} and Cl^- anions in the interlayer space of the LDH has been investigated by comparing the estimated values of the formation constants. In the first step, the value of the Gibbs free energy of formation (-3619.14 kJ/mol) obtained for a pure water-free $Mg_3Al\ (OH)_8Cl_1$ LDH at 25ºC was used. Then, the reaction of formation of this composition from the aqueous species was formulated:

$$3Mg^{2+}_{(aq)} + Al^{3+}_{(aq)} + 8OH^-_{(aq)} + Cl^-_{(aq)} \leftrightarrow [Mg_3Al(OH)_8]Cl$$

The value of the Gibbs free energy of this reaction (Δ_fG) was calculated using the standard Gibbs free energies of the aqueous species $Mg^{2+}_{(aq)}$ (-453.99 kJ/mol), $Al^{3+}_{(aq)}$ (-483.71 kJ/mol), $OH^-_{(aq)}$ (-157.27 kJ/mol) and $Cl^-_{(aq)}$ (-131.29 kJ/mol) from the NAGRA-PSI database [HUM/BER2002]. Finally, the fundamental relationship Δ_fG=-RT lnK has been used in order to obtain the value of the formation constant for the LDH composition at 25 °C. The same scheme was applied to calculate the formation constant for the carbonate-bearing LDH composition $[Mg_3Al(OH)_8](CO_3^{2-})_{0.5}$ with G^0_{298} = -3746.90 [ROZ/BER2011]. The formation of the LDH was represented as:

$$3Mg^{2+}_{(aq)} + Al^{3+}_{(aq)} + 8OH^-_{(aq)} + 0.5CO_3{}^{2-}{}_{(aq)} \leftrightarrow [Mg_3Al(OH)_8]\ (CO_3^{2-})_{0.5}$$

where G^0_{298} =-527.98 kJ/mol [HUM/BER2002]. The observed difference between the formation constant of the CO_3^{2-} -bearing LDH (logK = 66.45) and the Cl^- -bearing LDH (logK = 67.29) denotes the effect of the intercalated anion, demonstrating that Cl^- containing LDHs are more soluble than carbonate-containing types. This result is in agreement with previous data [ALL/PLE2005], who performed calorimetric measurements and predicted greater solubility of chloride-containing LDHs in comparison with carbonate containing substances.

6.6.1.1.2 The effect of substituted cations

The Gibbs free energies of formation were calculated for the synthesized LDHs which include Fe (II), Co (II), and Ni(II) cations in the brucite-like layers. Note that at the present stage of this study, estimation of the formation constants for Fe (II)-, Co (II)-, and Ni (II)- containing compositions was not performed because the standard thermodynamic properties of these substances are unknown. First, no reliable database exists of the standard entropies, enthalpies, and heat capacities of these substances. Second, the calculations performed were done for the conditions during syntheses only (i. e. T = 70 ºC, P = 1 bar). The estimated Gibbs free energies of formation (**Fig. 6.10**) at 70 ºC (MgAl-Cl-LDH: -3629.65 kJ/mol; Fe-bearing LDH: -3612 ± 50 kJ/mol, Co-bearing LDH:-3604 ± 50 kJ/mol, and Ni bearing LDH:-3593 ± 50 kJ/mol) correlate strongly with the ionic radii [SHA1976] of the substituting cation in octahedral coordination (r_{Fe2+} = 0.78 Å; r_{Co2+} = 0.745 Å ; r_{Ni2+}= 0.69 Å), demonstrating that the stabilities of LDHs depend heavily on the type of substituting divalent cation. A comparison of the estimated Gibbs free energy values for Fe(II), Ni(II), and Co(II)-doped solids with mole fraction ($x_{Me}{}^{2+}$) of Fe, Co, or Ni ~ 0.1, with the Gibbs free energy of the pure CO_3^{2-} and Cl^- containing LDH end-members (**Fig. 6.10**) was performed. For this purpose the standard Gibbs free energy of a pure water free LDH (composition $Mg_3Al(OH)_8Cl_1$) was estimated at 70 ºC using the data obtained from [ROZ/BER2011] (standard molar entropy 238.46 J/(mol·K), enthalpy -4161.19 kJ/mol, and heat capacity 324.20 J/(mol·K) at 25 ºC for a CO_3^{2-} -bearing LDH with a stoichiometry of $Mg_3Al(OH)_8(CO_3)_{0.5}$). This process allows extrapolation of the data for G_f of a pure Cl^--containing LDH from 25 ºC (-3619 kJ/mol) to 70 ºC (-3629 kJ/mol) as well as for a Mg_3Al $(OH)_8(CO_3)_{0.5}$ from 25 ºC (-3746 kJ/mol) to 70 ºC (-3757 kJ/mol). The Gibbs free energies (**Fig. 6.10**) of a pure MgAl-Cl-LDH and of a pure MgAl-CO_3-LDH are smaller than the values for Fe (II)-, Ni (II)-, and Co (II)-containing LDHs. Only the addition of 0.1 stoichiometric units of Fe (II), Co (II), and Ni (II) into the LDH structure increases the Gibbs free energy value to -3612 ± 50, -3604 ± 50, and -3593 ± 50 kJ/mol, respectively, and explains the effect of the incorporation of various divalent metals into the structure on the aqueous solubility of LDHs. The effect of the incorporation of divalent metals on the aqueous solubility of LDH phases observed is in agreement with the recent literature [ALL/NAV2002]. Based on calorimetric measurements of Ni (II)- and Co (II)-containing samples [ALL/NAV2002] the calculated solubility constants increased with increased substitution of Ni(II) for Co(II) mole fractions. However, the change in solubility as Ni (II) substitutes for Co (II) exerts a relatively minor effect. The same point was confirmed in the present study. The difference between the Gibbs free energy values determined for Ni (II)- and Co (II)-containing LDH is ~11 kJ/mol, which is in the range of the estimated uncertainties. The results suggest that the difference in the solubility of Co- and Ni-containing phases will be scarcely distinguishable.

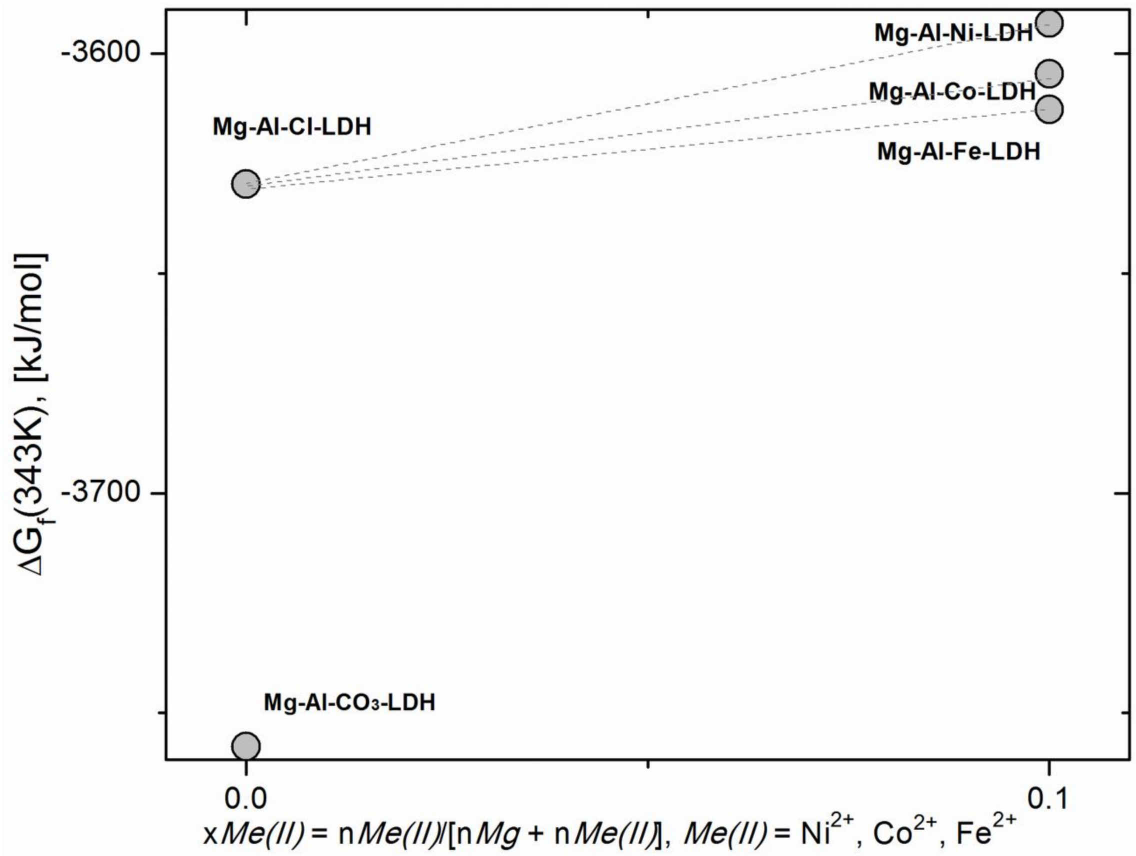

Fig. 6.10 Gibbs free energies of water-free pure MgAl-LDH and Fe(II), Co(II), and Ni(II)-containing LDHs at 70 °C as a function of mole fraction of substituted cation in octahedral coordination

In conclusion, the thermodynamic modeling using the GEMS-PSI code package was performed in order to predict the behaviour of different LDH compositions in aqueous media.

Assuming that thermodynamic equilibrium was achieved between synthesized solids and solutions, the first estimates (-3593 ± 50, -3604 ± 50, -3612 ± 50 kJ/mol) for the Gibbs free energies of formation of Ni, Co, and Ni bearing MgAl-LDHs with chloride as interlayer anion at 70ºC were obtained. The incorporation of Fe, Co, and Ni within the LDH lattice revealed no impact on the aqueous solubilities of these LDHs, in good agreement with the [ALL/NAV2002]. Moreover, the estimated Gibbs free energies correlated with the ionic radii of substituting divalent cations, a finding which is useful in the prediction of thermodynamic properties and aqueous solubilities of LDHs with variable divalent cations. The influence of the interlayer anion on the aqueous solubilities of LDHs was investigated for carbonate (Rozov et al., 2011) and chloride (present study) and carbonate-containing LDHs were shown to be significantly less soluble than analogous chloride-bearing substances.

6.6.1.2 Powder X-ray diffraction (XRD)

The XRD patterns of the samples investigated (**Fig. 6.11**) were quite similar and could be clearly identified with LDH compounds. Besides Zincite, which was added as an internal reference, no indications of other crystalline phases were observed. To explain the peak shifts due to the incorporation of Fe, Co, and Ni in the LDH structure, a displacement error correction by a Kα1/α2 stripping of the XRD patterns on basis of the Zincite PDF-2-entry 00-036-1451 (cross symbols) was carried out. The stripping helped to overcome difficulties in the determination of peak positions by peak overlapping. The XRD peaks from the synthesized LDH phases were broadened (**Fig. 6.11**) due to the statistical distribution of the layer sequences of the 2H and 3R polytypes. The hexagonal 2H type is typical of the mineral manasseite [ARA/PUS1996] and the 3R-type, of hydrotalcite [ALL/JEP1969] and [BEL/REB1996). This disordering could be observed in the distinct asymmetric peak broadening of the reflections at 39 º2θ and 46 º2θ. Yet the stacking faults do not have a strong impact on the c parameter. The interlayer distance in the c direction is not affected by this disordering and, thus, the 00l basal reflections at ~11 and 22 º2θ do not suffer from peak overlap and exhibit a full-width at half maximum (FWHM) of ~0.5 – 0.7 º2θ.

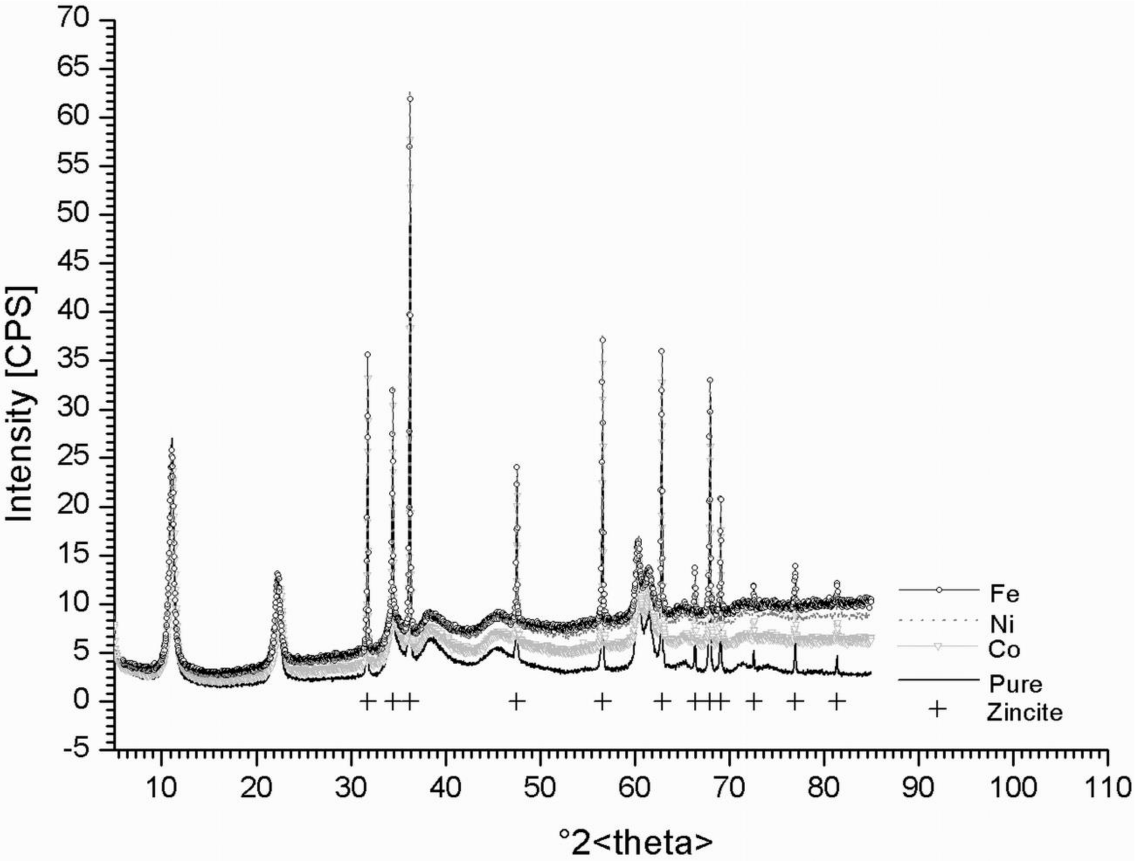

Fig. 6.11 XRD patterns of pure MgAl-LDH (solid black), Fe (dashed gray), Co (dotted light gray), and Ni (dotted dark gray) bearing LDHs

In order to assess the impact on the shift of the a and c lattice parameters due to the incorporation of the small amounts of Co (dotted light gray), Fe (dashed gray), and Ni (dotted dark gray) in the octahedral layer, the peak shift of 00l and 110 were evaluated, as, from these reflections, the lattice parameters could be derived directly (**Fig. 6.12**). The black XRD patterns refer to the pure MgAl-LDH compound. The lattice parameters obtained by the Rietveld refinement were ~0.03 Å smaller than those determined manually (**Tab. 6.3**), a difference which may be explained by the FPA which has been applied in the evaluation of the c parameter. Generally speaking, at low 2θ angles, the impact of the device function on the peak shape is greater than at higher angles [KLU/ALE1974], leading to an overestimation of the c parameter.

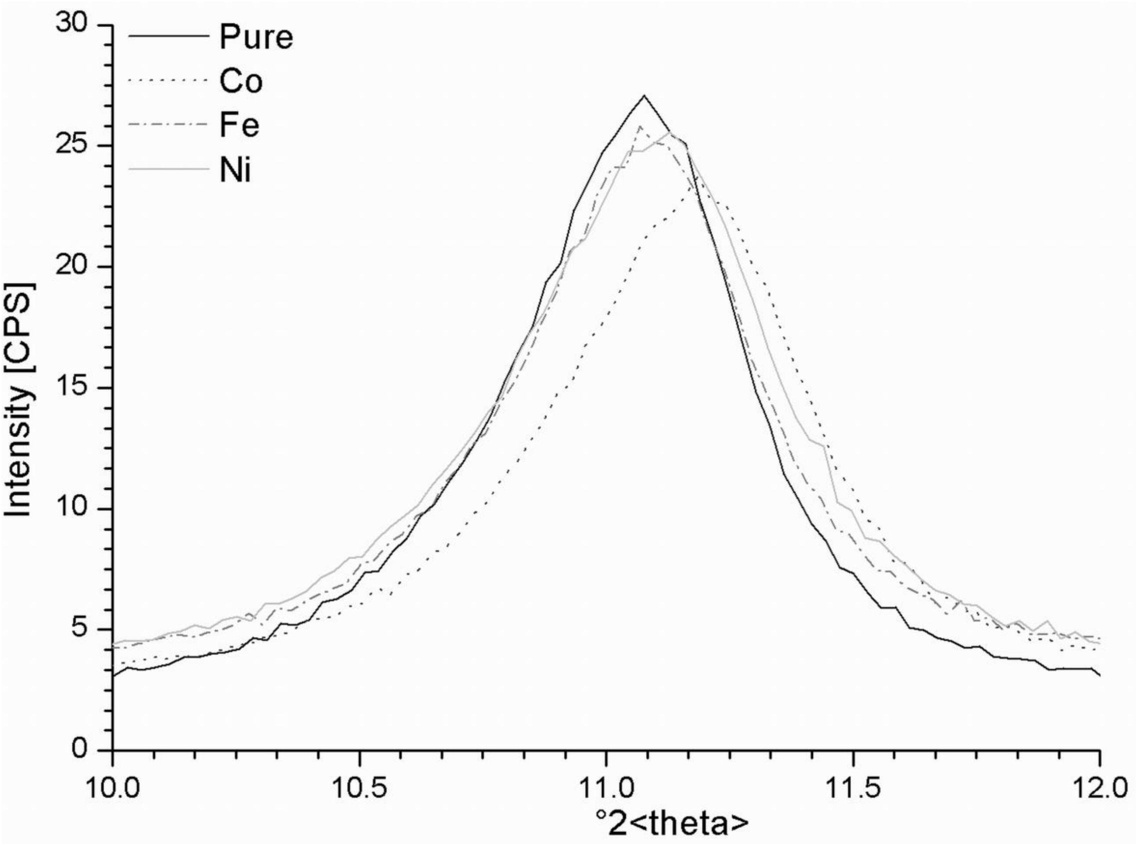

Fig. 6.12 Alteration of the LDH lattice parameter c due to the substitution of Mg (II) by Co (II) (dotted light gray), Fe (II) (dashed gray), and Ni(II) (solid light gray)

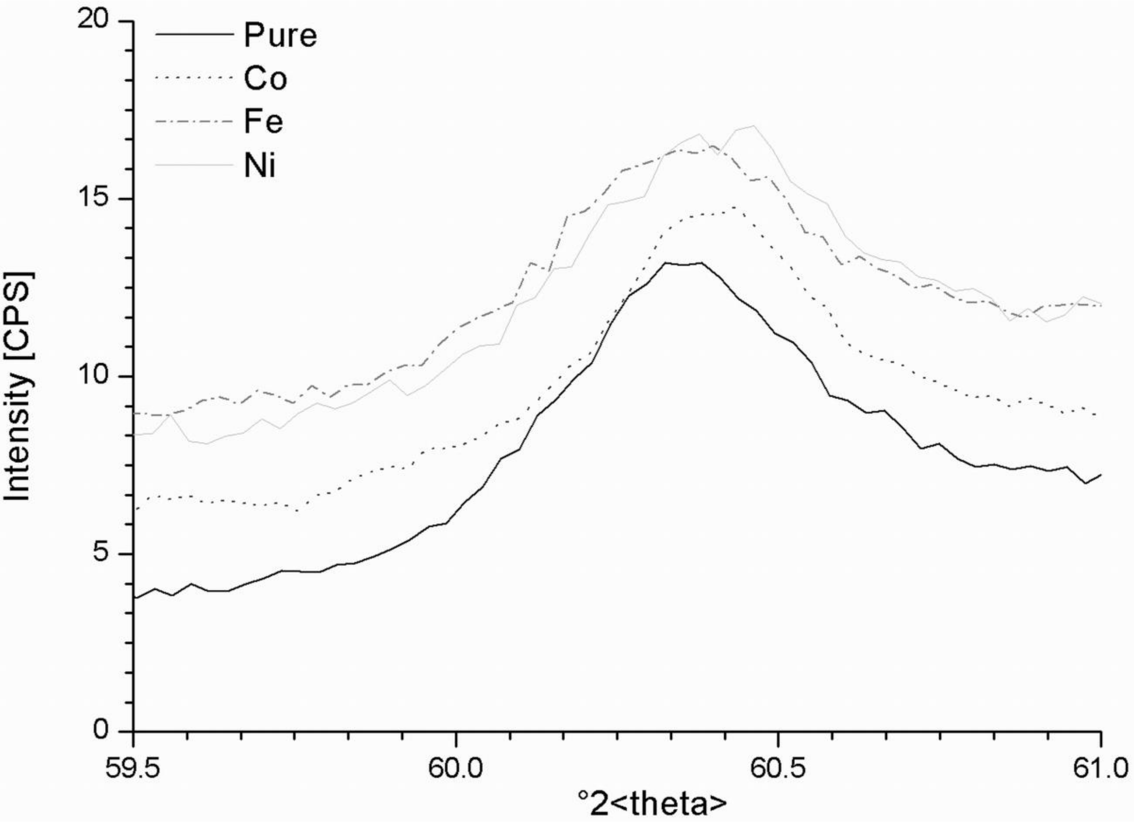

Fig. 6.13 Alteration of the LDH lattice parameter a due to the substitution of Mg (II) by Co (II) (dotted light gray), Fe (II) (dashed gray), and Ni (II) (solid light gray)

The value of the c parameter was largest in the pure MgAl-LDH, was slightly less in the Co- and Ni containing LDH, and was least in the Fe-containing LDH. Analogous decreases were also observed for the parameter a. By considering the ionic radius [SHA1976] (**Tab. 6.3**) of Fe(II), Fe(III), Co(II), Ni(II), Mg(II), and Al(III) and its effect on the lattice parameters, the observed decrease in the Fe-LDH may be explained by the relatively low radius of Fe(III). In order to estimate the Fe (II)/Fe (III) ratio, the respective occupancy density for these cations was calculated using the Rietveld method by introducing Fe (III) into the Fe (II) atomic position. The additional positive charge introduced by Fe (III) was compensated by carbonate, which was, therefore, assumed to be present due to sample alteration by the oxidation of Fe (II). The outcome of this calculation showed that Fe (III) can occupy completely the atomic position of Fe (II). The R_{wp}/R_{exp} ratio improved slightly (**Tab. 6.3**) but, considering the small admixtures of iron, no shift of any significance in the parameters a or c was observed.

Tab. 6.3 XRD analysis of the LDHs

LDH type/ r(x) [Å]	**a [Å]**	**c [Å]**	**Octahedral elongation c, [Å]**	**Rwp/ Rexp**
Fe (III) LDH rFe (III) = 0.645	3.0630 ± 0.0005	7.8949 ± 0.0019	2.1461 ± 0.0066	1.73
Ni LDH rNi(II) = 0.69	3.0636 ± 0.0006	7.9492 ± 0.0023	2.1328 ± 0.0070	1.96
MgAl LDH rMg(II= 0.72 rAl(III) = 0.535	3.0649 ± 0.0007	7.9710 ± 0.0028	2.1377 ± 0.0074	2.70
Co LDH rCo(II) = 0.745	3.0646 ± 0.0005	7.9552 ± 0.0021	2.1503 ± 0.0075	1.83
Fe (II) LDH rFe(II) = 0.78	3.0630 ± 0.0005	7.8947 ± 0.0020	2.1407 ± 0.0068	1.78

Tab. 6.4 XRD analysis of the LDHs and interlayer water analysis by TGA

LDH type/ r(x) [Å]	**Transition 3R/3R, [%]**	**Zincite weighed [%]**	**Zincite calc., [%]**	**Interlayer H_2O TGA analysis**	**Interlayer H_2O calc.**	**Density, [g/cm^3]**
Fe(III) LDH rFe(III) = 0.645	50.51 ± 0.27	10.200	9.876 ± 0.016	2.700	2.765 ± 0.016	1.979
Ni LDH rNi(II) = 0.69	49.71 ± 0.32	10.010	9.755 ± 0.014	2.640	2.617 ± 0.018	1.876
MgAl LDH rMg(II= 0.72 rAl(III) = 0.535	54.03 ± 0.41	9.990	9.579 ± 0.025	2.400	2.959 ± 0.023	1.881
Co LDH rCo(II) = 0.745	50.67 ± 0.37	10.080	9.686 ± 0.031	2.250	2.744 ± 0.021	1.903
Fe(II) LDH rFe(II) = 0.78	50.71 ± 0.29	10.200	9.927 ± 0.016	2.700	2.867 ± 0.020	1.923

These data were insufficient, however, to determine whether the sites were occupied by Fe (II) or Fe (III). The Fe concentrations used, equivalent to only 1/30 of the amount of Mg (II), were quite small. Reliable statements regarding the presence of Fe (III) due to oxidation of Fe (II) may only be made after analysing solid solutions of LDH compounds having greater Fe concentrations. During the refinement, elongation of the octahedral layer in the c direction was also computed. According to Rives (2001) this parameter, which describes the octahedral flattening perpendicular to the c axis, should become smaller as the radius of the metal cations increases. The trend of increasing ionic radii (Shannon, 1976) of Fe (III) < Ni (II) < Mg (II) and Co (II) < Fe (II) failed to yield a corresponding elongation of the octahedra in the c direction, which remained constant, thus showing a clear lack of dependency on the ionic radius. This observation may be attributed to the small concentrations of the metal cations despite their different ionic radii. Note also that this calculated parameter (hc) for the elongation exhibits a value which is generally ~ 0.1 Å larger than the reported distances [ARA/PUS1996], [BEL/REB1996], and [ALL/JEP1969]. Whether this observation could be attributed to the large amount of stacking faults (**Tab. 6.4**) or to any other cause has yet to be clarified. With respect to the stacking faults, all the LDHs investigated exhibited a transition probability of ~50 % (**Tab. 6.3**), which means that the probability of adjacent layers in the c direction being a 3R type or a 2H type is 50 %. The calculated amounts of interlayer water were in good agreement with those determined by thermogravimetric analysis. The small deviations of these values from the chemical formulae of the different LDHs (**Tab. 6.4**) could be attributed to exposure to the atmosphere during the addition of the internal standard. The amount of interlayer water could have an effect on the c parameter, i. e. the pure Mg-Al-LDH has the largest amount of interlayer water and exhibits the largest c parameter. The application of different humidities during XRD measurements could help evaluate and clarify the related impact. Generally, the calculated X-ray densities (**Tab. 6.4**) were in excellent agreement with the theoretical value of 1.87 g/cm^3. The latter calculation was based on an assumed chemical composition $[Mg_{2.25}Al_{0.75}(OH)_6]\cdot Cl\cdot 3H_2O$ of the LDH exhibiting lattice parameters of 3.05 Å and 23.85 Å for the a and c axes, respectively. A Rietveld refinement of the Ni-bearing LDH (the pure Mg-Al-LDH and the Co-, Fe-containing LDHs are not presented) was performed (**Fig. 6.14**). By simple visual inspection, the applied structural model for the LDH syntheses fits the measured XRD patterns very well. The R_{wp}/R_{exp} ratios are in the same range from 1.73 to 1.96 for the LDH synthesis doped with Fe, Ni, and Co. The equivalent ratio for the pure Mg-Al-LDH is slightly increased (**Tab. 6.3**). In order to clarify the incorporation of cations of different radius, synthesis of a solid-solution series with increased concentrations should be carried out. The structural properties of LDHs also depend on the identity and quantity of constituents in the interlayer, e. g. the water content may be altered when the samples are prepared for X-ray analysis. The possibility that carbonate was incorporated cannot be ruled out. Such alterations must, therefore, be considered as restraints, i. e. as parameters which are allowed to vary within predefined intervals in the structural model being applied for the Rietveld analysis. If the starting values and the related intervals are not well constrained, the optimization calculations within the Rietveld method could possibly end up with values which may not reflect sound structural properties. Furthermore, as the LDH samples considered suffer from distinct stacking faults, providing a suitable structure model which considers the loss of the long-range ordering of lattice constituents in crystalline samples is challenging.

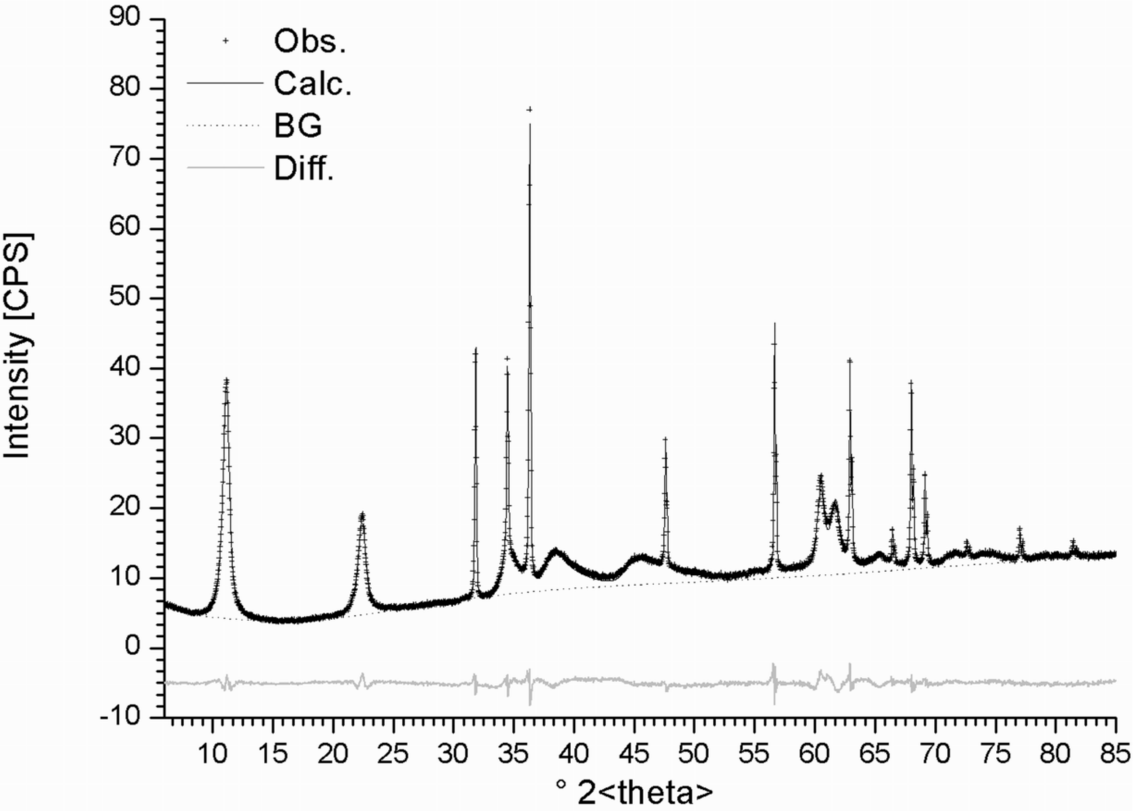

Fig. 6.14 Rietveld plot of the Ni-doped LDH with background (BG)

In conclusion, the PXRD results showed that all the samples were pure LDHs with each exhibiting distinct stacking faults (the 3R/2H-type layer stacking sequence determined was ~0.5).

6.6.1.3 EXAFS and XANES analysis

Interatomic distances and coordination numbers can be determined by EXAFS measurements. For a pure Mg-Al-LDH, taking the metal cation as the center, the interatomic distances for the nearest coordination shells are summarized in (**Tab. 6.5**). For comparison, the distances of the nearest coordination shells are given for the fougerite structure, $(Fe(OH)_2)(OH)_{0.25}(H_2O)_{0.5}$ [TRO/BOU2007], a LDH analogue compound where the Mg/Al is replaced completely by Fe with a Fe(II)/ Fe(III) ratio = 3.

Tab. 6.5 Metric parameters (R=distances, N= coordination numbers) of LDHs with a metal cation as center. Distances are given for MgAl-LDH (left) and for Fougerite (right). Cl*: five positions established among all possible positions for Cl-/CO32- in the interlayer.

Back-scatterer	N	R (Å)	Back-scatterer	N	R(Å)
O	6	2.01	O	6	2.09
Mg/Al	6	3.05	Fe	6	3.19
O	6	3.65	O	6	3.82
Cl*	1	3.79/4.18/ 4.86/5.17/6.00	Cl*	1	4.15-4.70/5.65-6.38
O	12	4.76	O	12	4.97
Mg/Al	6	5.28	Fe	6	5.53
Mg/Al	6	6.09	Fe	6	6.38
O	12	6.42	O	12	6.71

The FT magnitude taken in the range 3.2 – 13.5 $Å^{-1}$ for all samples (**Fig. 6.15**) and the EXAFS (**Fig. 6.16**) signals recorded for the Ni- and Co-bearing LDHs were very similar. The compounds seemed to have a well-organized structure as neighbour contributions can still be seen at ~6 Å (5.6 Å in the FT which has not been phase shift corrected). On the contrary, the EXAFS signal for the Fe-doped LDH and its FT differed significantly compared with the spectra of samples doped with Ni or Co. Firstly, the FT peak at ~6 Å was no longer visible, and useful information seemed to end near 3.0 Å in the FT. In addition, the O first shell FT peak was at a smaller distance than for Ni/Co; it was expected at a similar or slightly longer distance as given by the valence-bond theory: in coordination 6, Fe(II)-O is expected at 2.14 Å , Co(II)-O at 2.10 Å , and Ni(II)-O at 2.06 Å [BRO/ALT1985]. The complete predictions for oxidation states +II and +III in coordinations 4 and 6 were summarized (**Tab. 6.6**), and the fitted results obtained for the Ni-, Co-, and Fe-bearing LDHs were compiled (**Tab. 6.7**). During the fit, the overall scaling factor, S^2_0 was varied and the coordination numbers, N, were fixed to the expected values. The R factor of the fit yielded a 0 % residual disagreement between fitted and experimental data for Ni, 0.4 % for Co, and 0.1 % for Fe.

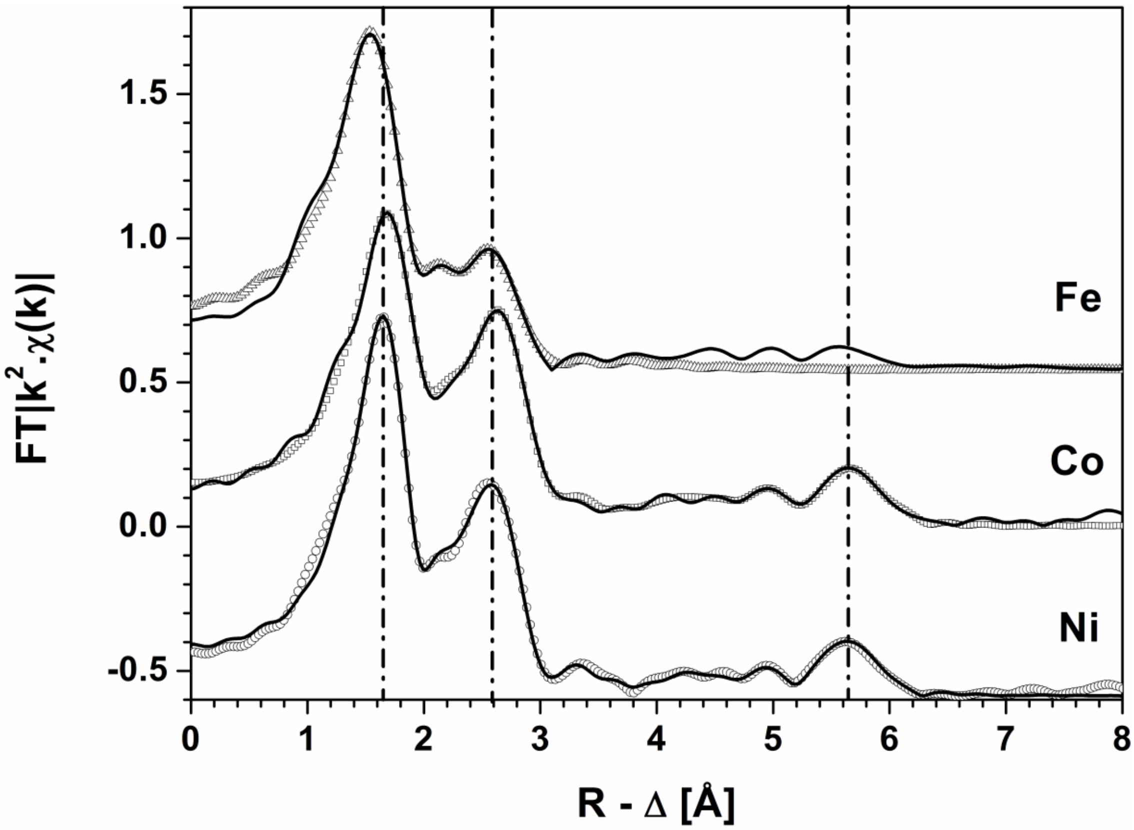

Fig. 6.15 Fourier Transform (FT) magnitude (thick solid line) and fitted result (open triangles for Fe, open squares for co, and open circles for Ni) with FT taken in the range 4.2 – 14.7 Å^{-1} for Ni (lower), 4.2 – 14.2 Å^{-1} for Co (middle), and 3.4 – 11.4 Å^{-1} for Fe (upper) as used for the fit

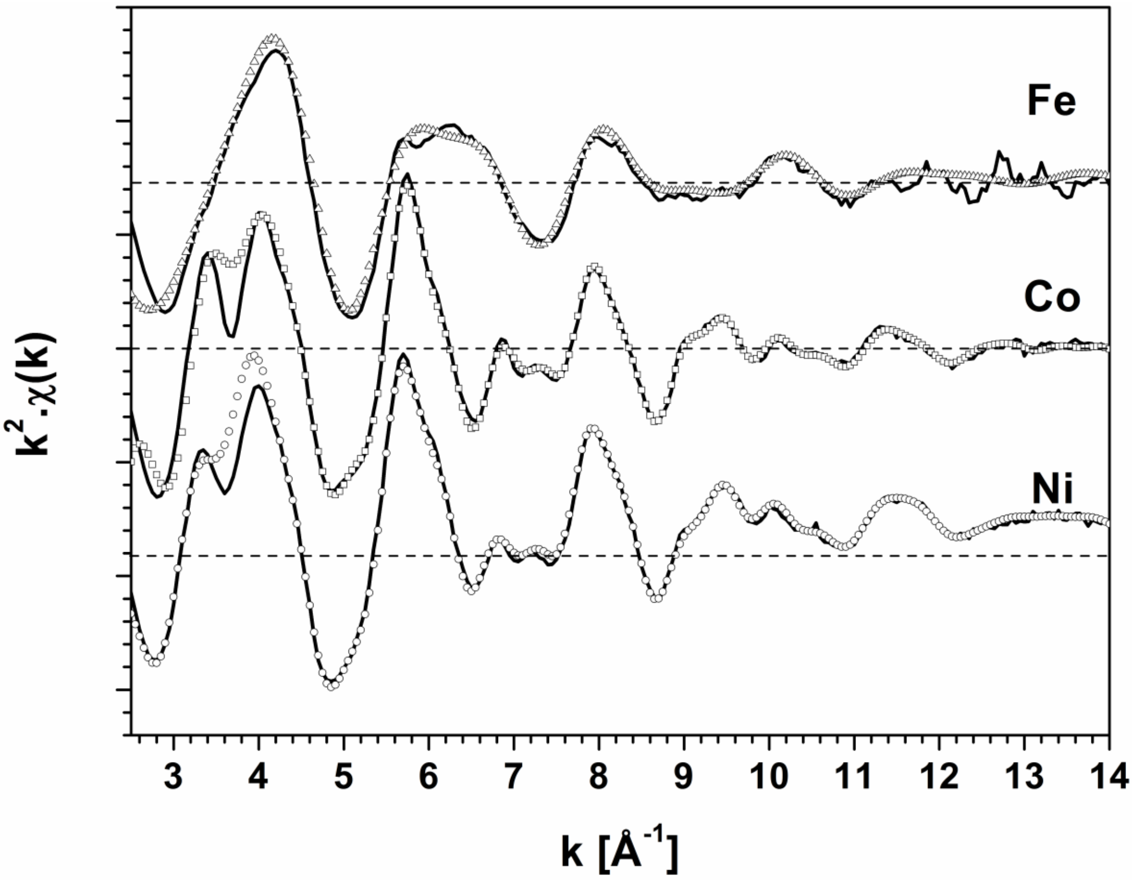

Fig. 6.16 k^2-weighted EXAFS for the samples (solid lines) and the fitted results (open triangles for Fe, open squares for Co, and open circles for Ni)

Tab. 6.6 Bond distances expected according to the bond valence theory predictions. The relationship between bond length (R) and bond valence (s) is: $s = \exp((Ro - R)/B)$ where Ro and B are bond valence parameters that depend on the two atoms forming the bond [BRO/ALT1985]. B is 0.37. CN: coordination number

Cation-O	**CN**	**R (Å)**	**R_0 (Å)**
Ni (II)	4 6	1.91 2.06	1.654
Co(II)	4 6	1.95 2.10	1.692
Fe(II)	4 6	1.99 2.14	1.734
Ni(III)	4 6	1.74 1.89	1.74
Co(III)	4 6	1.79 1.94	1.70
Fe(III)	4 6	1.87 2.01	1.759
Mg(II)	6	2.10	1.693
Al(III)	6	1.88	1.620

Tab. 6.7 Metric parameters (R=distances, N=coordination numbers, σ^2=EXAFS Debye-Waller factors, ΔE_0=relative energy shifts held as global parameters for like atoms) from least-squares fit analysis of FT data: * parameters are constrained to the same value

Sample	**Back-scatterer**	**R(Å) (±0.02 Å)**	**N fixed**	**σ^2(Å^2) ·10^{-3}**	**ΔE_0 (eV)**	**goodness of fit (%)**
Ni -doped Cl-Hydrotalcite **S_0^2 = 0.84 ± 0.03**	O	2.05	6	5.82	-1.0	0.20
	Mg/Al	3.05	6	6.84	-1.8	
	O	3.55	6	12.1	-1.0	
	O	4.78	12	20.0	-1.0	
	Ni	5.39	1	4.85	-0.0	
	Mg/Al	5.43	5	21.8	-1.9	
	Cl	5.84	1	3.25	-0.8	
	Mg/Al	6.21	6	3.83	-1.9	
	O	6.41	12	5.48	-1.0	
Co -doped Cl-Hydrotalcite **S_0^2 = 0.85 ± 0.04**	O	2.08	6	7.88	+1.7	0.40
	Mg/Al	3.08	6	6.64	+2.5	
	O	3.57	6	12.2	+1.7	
	O	4.76	12	21.8	+1.7	
	Co	5.19	1	4.60	+2.1	
	Mg/Al	5.27	5	5.80	+2.5	
	Cl	5.88	1	1.97	+2.6	
	Mg/Al	6.24	6	3.82	+2.5	
	O	6.43	12	4.78	+1.7	
Fe -doped Cl-Hydrotalcite **S_0^2 = 0.69 ± 0.05**	O	2.00	6	7.28	-1.3	0.14
	Mg/Al	3.08	5	8.28	-0.4*	
	Fe	2.94	1	9.00	-0.4*	

This similarity between the Ni and Co solids was confirmed by the structural parameters obtained. For both Ni- and Co-doped LDHs, the data were well reproduced using nine shells in the FT range [1.25 – 6.20 Å] for Ni and [1.09 – 6.20 Å] for Co (**Fig. 6.15** and **Fig. 6.16**). The first shell distance was slightly greater for Co (2.08 Å) than for Ni (2.04 Å). These distances matched well the distance predicted by the valence-bond theory for a metal cation having an oxidation state of +II in sixfold coordination. These distances were also longer than in the MgAl LDH (2.01 Å), where the distance was averaged statistically between Mg-O (2.10 Å) and Al-O (1.88 Å). This reflects the smaller mean ionic radius (0.67 Å) obtained for a statistic distribution of Mg (0.72 Å) and Al

(0.54 Å) in the undoped LDH compared to ionic radii of Ni(II) or Co(II) (≥ 0.69 Å). The first cation shell distances for Mg or Al (cannot differentiate between them) were perfectly compatible with the LDH structure for Ni (3.05 Å) and for Co (3.08 Å). The only significant difference between the Ni and Co samples was in the position of the second cation shell (5xMg/Al+1xNi or Co) which was located at the same distance as for pure LDH in the case of Co and 0.16 Å farther for Ni. For Fe-doped Cl-LDH, only three shells were needed to reproduce the data over a shorter FT range (1.13-3.15 Å) (**Fig. 6.15** and **Fig. 6.16**). A first coordination sphere with 6 oxygen atoms at 2.00 Å with a Debye-Waller factor (б^2) of 7.28 Å^2 was obtained. This bond distance was far from that expected for Fe(II) in octahedral coordination (**Tab. 6.6**) or as found for six-fold coordinated Fe(II) in the literature (2.16 Å in FeO (ICSD 82233)). Even in the case of fougerite (Fe-containing LDH), where the crystal-structure parameters account for both Fe(II) and Fe(III) (ratio 3:1) in octahedral positions, the mean value was found to be 2.09 Å (crystal-structure data by [TRO/BOU2007]). Such a short bond distance can be achieved either by Fe(II) in tetrahedral or Fe(III) in octahedral coordination. The LDH or fougerite structure does not allow for tetrahedral sites. Study by XRD of the present samples gave no evidence for the presence of other crystalline phase other than LDH. Furthermore, the Fe-K EXAFS intensity did not match the four-fold oxygen coordination. The presence of Fe(III) in the octahedra was likely as it occurred in fougerite and in the LDH at the position of trivalent cations (Al(III)). In addition, the presence of trivalent Fe, suggested by the EXAFS analysis, was confirmed by the XANES analysis (**Fig. 6.17** and **Fig. 6.18**). Most of the Fe was in oxidation state +III as the edge position matched perfectly that of Fe(III). The first derivative of the signal (**Fig. 6.18**) revealed a smaller amount of Fe(II) which was invisible in the original signal. The inset shows an enlargement of the characteristic feature for the 1s → 3d/4p transition [WIL/FAR2001] and [FIN/DAR2012] confirming that no Fe(II) was detected, and that Fe occurred as Fe(III) in the Fe-doped Cl-LDH.

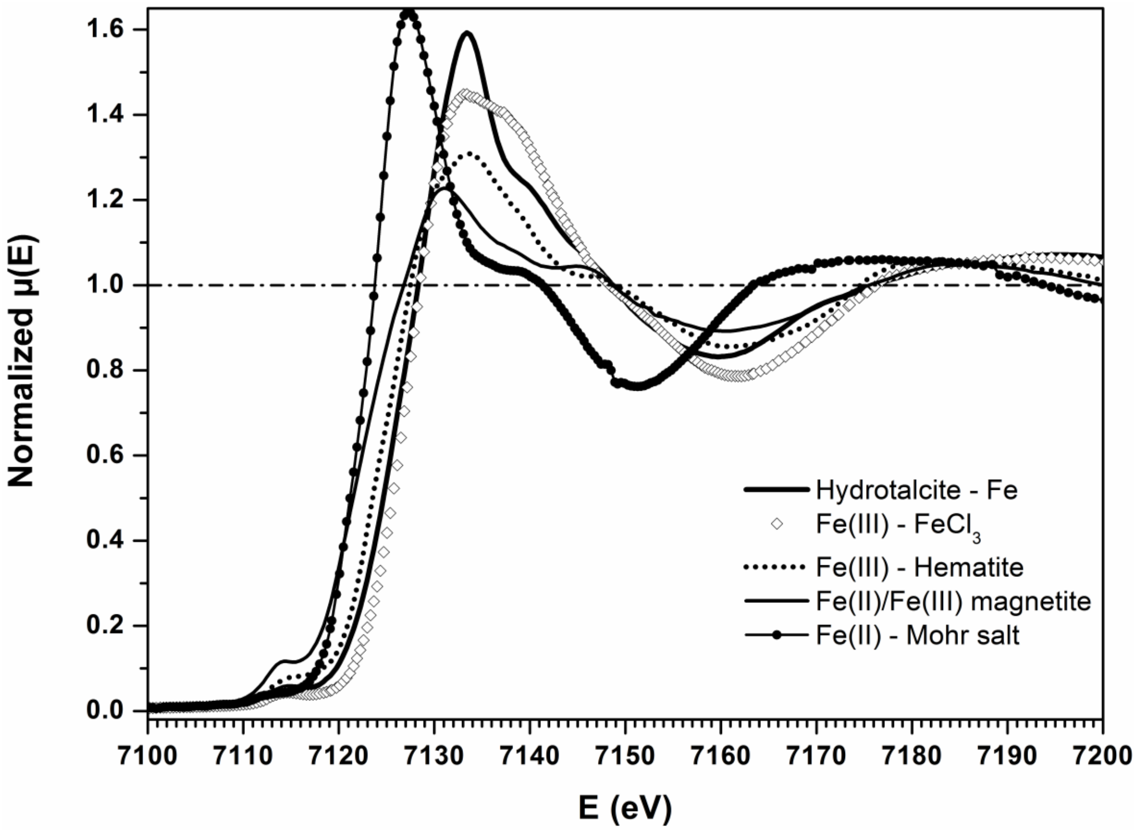

Fig. 6.17 Comparison of the normalized XANES profile for different reference samples

With respect to the first cation Mg/Al shell, the determined distance of 3.08 Å for the Fe-bearing LDH is perfectly compatible with the LDH structure. The presence of another Fe(III) located in the next direct octahedral shell forming a Fe(III)-Fe(III) pair, where the octahedra share an edge, was observed. This was not the case for Ni(II) and Co(II) cations where the next Ni/Co was further away.

In conclusion, the results of EXAFS measurements demonstrated similar structural features of Ni- and Co-bearing LDHs where Ni and Co atoms were incorporated as divalent cations in the LDH structure at octahedral crystallographic positions. The distances determined matched very well the distances predicted by the valence-bond theory for a metal cation in an oxidation state of +II in a six-fold coordination. Unexpectedly, the smallest lattice parameters were observed for the Fe-bearing LDH. The EXAFS results indicated clearly the isostructural incorporation of Fe in the octahedral layers but as Fe(III) only. For the first coordination sphere with 6 oxygen atoms, a bond distance of 2 Å was obtained. Such a short distance can only be explained by Fe(II) in tetrahedral or

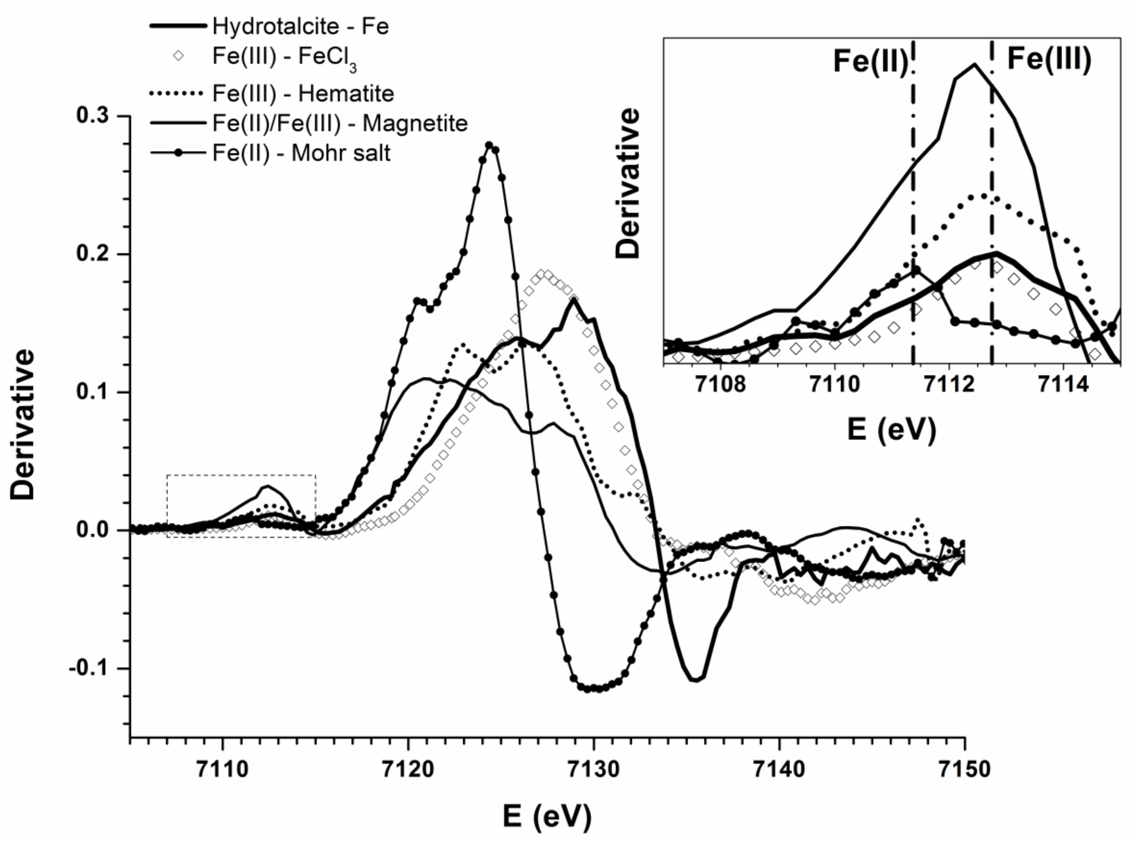

Fig. 6.18 Comparison of the first derivative of the XANES signal shown for the reference samples and the Fe bearing LDH with the characteristic feature for the 1s →3d/4p transition in the inset

by Fe(III) in octahedral coordination. With XANES measurements, the presence of Fe(III) was confirmed and no Fe(II) was detected. Nevertheless, the presence of Fe(II) in amounts up to 5 wt. % cannot be ruled out. Indeed, information about the oxidation state of iron in synthesized Mg-Al-Fe-Cl-containing LDH is contradictory. With freshly prepared Fe-bearing LDH, only Fe(II) (using the thiocyanate complex reaction) was detected.

6.6.2 Uptake of trace-level amounts of iodide, selenite and pertechnetate by Fe, Co and Ni bearing LDHs

Prior to measuring the uptake of trace-level amounts of iodide, selenite and pertechnetate by the Fe, Co, and Ni bearing LDHs the stability of these solids in the used solutions was determined. The molar ratios of the cations before and after contact with the solution were within the uncertainty of the measurement, Al was virtually undetectable in solution, and hence the LDHs were stable. In addition, after contact with the different aqueous solutions, XRD data revealed LDHs as the only crystalline component.

For the pure Mg_3Al_1-LDH (chloride as interlayer anion) with the formula $[Mg_3Al_1(OH)_8]$ $Cl_{0.88}$ $(CO_3^{2-})_{0.06}$ 2.4 H_2O, the molecular weight was calculated to 314 g/mole. For the Fe-bearing LDH $[Mg_{2.9}Fe_{0.097}Al_1(OH)_{7.95}]$ $Cl_{0.88}$ 2.7 H_2O, the molecular weight was calculated to 323.50 g/mole, for the Co-bearing LDH $[Mg_{2.9}Co_{0.1}Al_{1.01}(OH)_8]$ $Cl_{1.03}$ 2.25 H_2O, the molecular weight was calculated to 316.65 g/mole, and for the Ni-bearing LDH $[Mg_{2.9}Ni_{0.09}Al_{0.98}(OH)_{7.86}]$ $Cl_{1.09}$ 2.64 H_2O, the molecular weight was determined to 321.99 g/mole. From the molecular weights the theoretical anion exchange capacities were calculated (ignoring the carbonate in the interlayer). For monovalent anions the anion exchange capacity was 2.8 x 10^{-3} mole/g for the MgAl-LDH, 3.4 x 10^{-3} mole/g for Mg/Ni-Al-LDH, 3.33 x 10^{-3} mole/g for Mg/Co-Al-LDH, and 3.2 x 10^{-3} mole/g for Mg/Fe-Al-LDH respectively. That means that at most these values in mole/g chloride in the interlayer can be exchanged by other monovalent anions (like iodide or pertechnetate) and for divalent anions (like selenite) these values reduced by a factor of two. Note, when working in an aqueous solutions these theoretical values cannot be achieved due to hydroxide anions present in solution competing with the desired anion [MIY1980]. Considering that immobilization of iodide using hydrotalcite (hydrotalcite is a special LDH $[Mg_3Al_1(OH)_8](CO_3)_{0.5}$ 2 H_2O) with carbonate as interlayer anion) is a matter of controversy [FET/RAM1997]. The work exposed in this project studies if Ni, Co and Fe bearing MgAl-LDHs (solid solutions) with chloride as interlayer anion permit the ion exchange of chloride with iodide, or with pertechnetate or with selenite. To our knowledge investigations with LDH solid solutions were not performed yet.

6.6.2.1 Uptake as function of time and of competing anion

The temporal dependence of **iodide** uptake (initial concentration: 4.25 x 10^{-5} mole/L) in water on the different LDHs was studied according to the batch-technique. Keeping in mind the comparable characteristic data of the Fe, Co, and Ni bearing LDHs, identical anion retention potentials can be expected. The calculation of the K_d values (K_d=distribution coefficient) was performed according to the equation:

$$K_d = (Ci - Ce)/Ce \times (V/m),$$

where Ci is the initial iodide concentration in mole/L, Ce is the concentration in mole/L in equilibrium, V is the volume of the aqueous solution in mL and m is the mass of LDH in g. The uptake of iodide was rapid (**Fig. 6.19**), which is consistent with the assumption of anion exchange as reaction mechanism [TAV/FEN2010]. Approximately 60 % to 70 % of iodide was adsorbed, corresponding to an anion exchange capacity of 2.55 x 10^{-6} mole/g to 2.97 x 10^{-6} mole/g, respectively, while the equilibrium pH was determined to be pH = 7.80 ± 0.3. In comparison to the calculated log K_d value of 1.9 for the MgAl-LDH, the log K_d values for the LDH solid solutions were higher (log K_d = 2.40 for Ni, log K_d = 2.53 for Fe and log K_d = 2.28 for Co), indicating their higher anion exchange capacities.

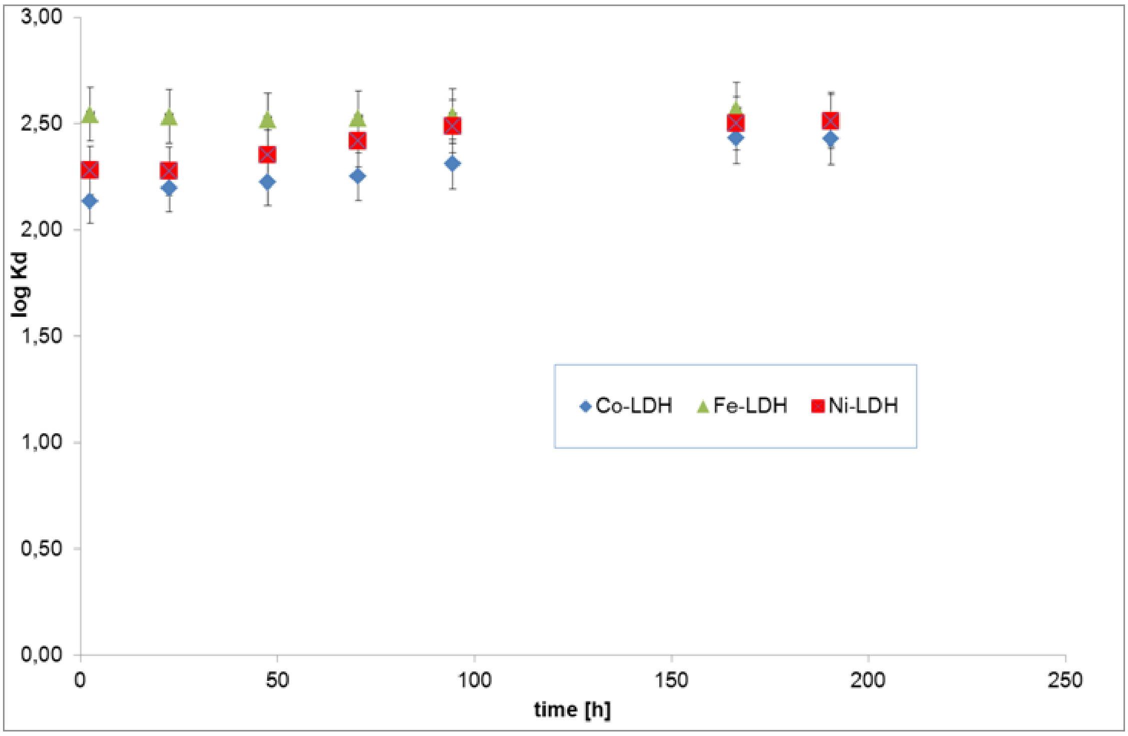

Fig. 6.19 Uptake of iodide on Co, Fe, and Ni bearing LDHs as function of time in water

The temporal dependence of **pertechnetate** uptake (initial concentration: 5.87 x 10^{-7} mole/L) in water (**Fig. 6.20**) on the different LDH solid solutions was studied under similar conditions. Again, the uptake was rapid, assuming ion-exchange processes and equilibrium was reached within 60 minutes. Approximately 50 % of pertechnetate adsorbed, corresponding to an anion exchange capacity of ~2.9 x 10^{-8} mole/g. An increase of the K_d values was observed for the solid solutions (log K_D=1.4 for MgAl-LDH, log K_d = 2.01 for Ni, log K_d = 2.21 for Fe and log K_d = 2.06 for Co). The equilibrium pH-value was pH=7.10 ± 0.2.

The uptake of **selenite** (initial concentration: 5.69 x 10^{-12} mole/L) was extremely rapid (equilibrium was reached within 30 minutes, **Fig. 6.21**) and quantitative, while the equilibrium pH was 7.10 ± 0.2.

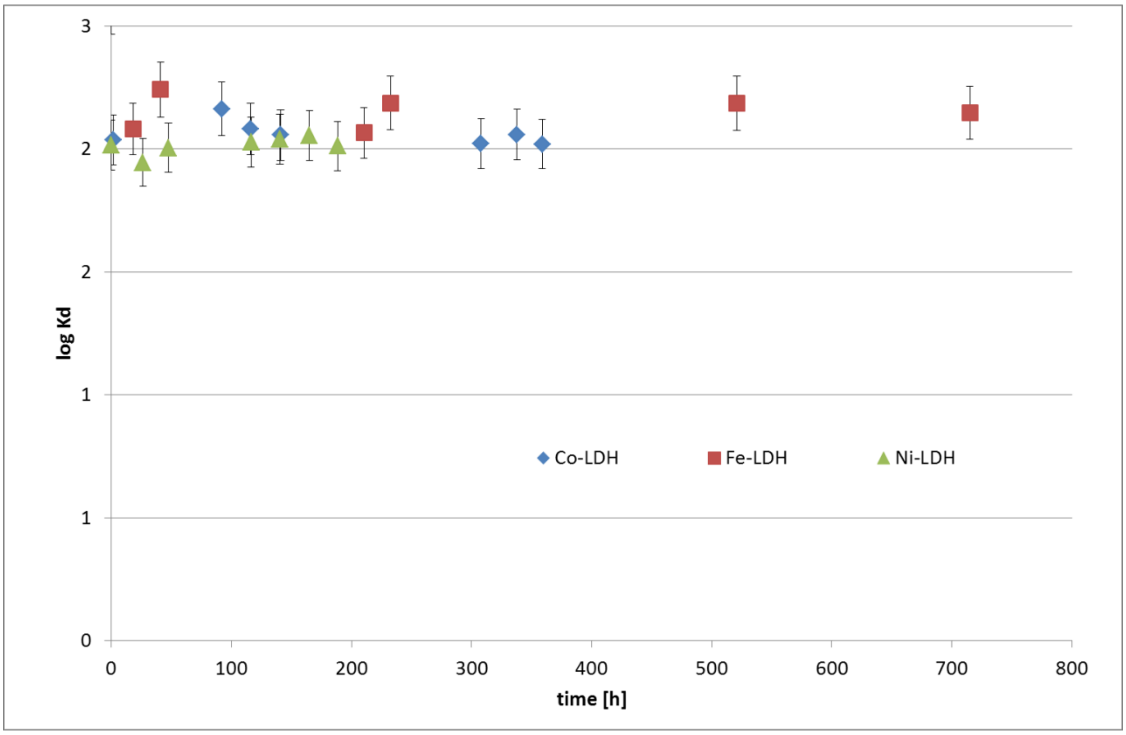

Fig. 6.20 Uptake of pertechnetate on Co, Fe, and Ni bearing LDHs as function of time in water

Compared to selenite uptake investigations on MgAl-LDH (log K_d = 4.8), again, the solid solutions possess higher K_d-values (log K_d = 6.02 for Ni, log K_d=6.38 for Fe and log K_d = 6.20 for Co), indicating their higher exchange capacities (**Fig. 6.21**).

The uptake of the iodide, pertechnetate and selenite was investigated under identical conditions in Opalinus clay pore water (Mont-Terri, Typ, A1) as well. Here, competing anions like chloride and sulphate are present and a decrease in the K_d-values was expected. It should be noted, that for the MgAl-LDH no retention of iodide and pertechnetate was observed in clay pore water, while for Fe, Co, and Ni-bearing LDHs retention was determined. The temporal uptake was rapid (ion exchange mechanism) and log K_d values of ~0.35 for iodide and ~ 0.75 for pertechnetate, respectively, were determined, while the equilibrium pH was 7.50 ± 0.2. Although low, these K_d-values may still lead to a significant decrease in the mobility of trace amounts of iodide and pertechnetate. In clay rock for example, a K_d value of about 0.1 L/kg^{-1} will slow down the migration time (break through time) for anions (diffusion coefficient about 5 x 10^{-12} m^2/s^{-1}) over a migration distance of 50 m from about 140,000 years to more than 700,000 years [ANDRA2005]. **Fig. 6.22** reveals the uptake of selenite in Opalinus clay pore water as function of time. For selenite as divalent anionic species the determined log K_d values were in the range of 2.2 to 2.5. Compared to the log K_d values for iodide and pertechnetate, these values were significant higher (a factor of 6.5 for iodide and a factor of 3 for pertechnetate was calculated). In $MgCl_2$-rich brine only the retention of selenite was observed (**Fig. 6.23**) and the calculated log K_d values were in the range of 1.6 to 1.8 while the equilibrium pH was measured to 5.50 ± 0.2 (uncorrected value). The selenite uptake clearly demonstrated that LDHs in general have the higher affinity towards anions which possess the highest charge density.

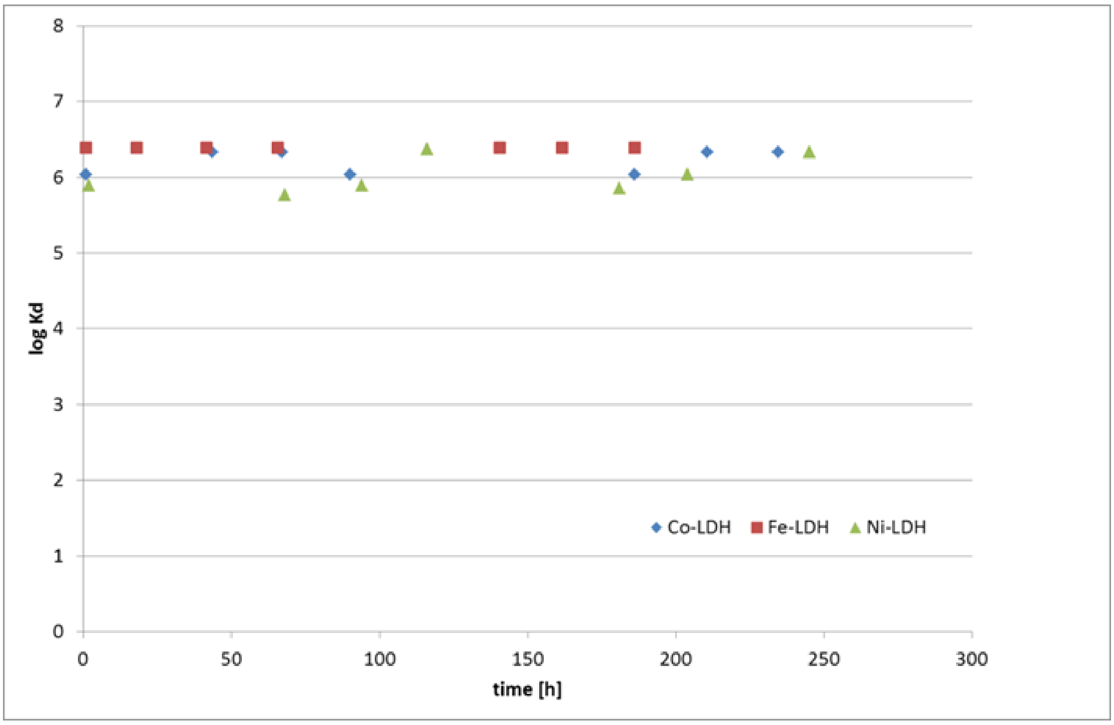

Fig. 6.21 Uptake of selenite on Co, Fe, and Ni bearing LDHs as function of time in water

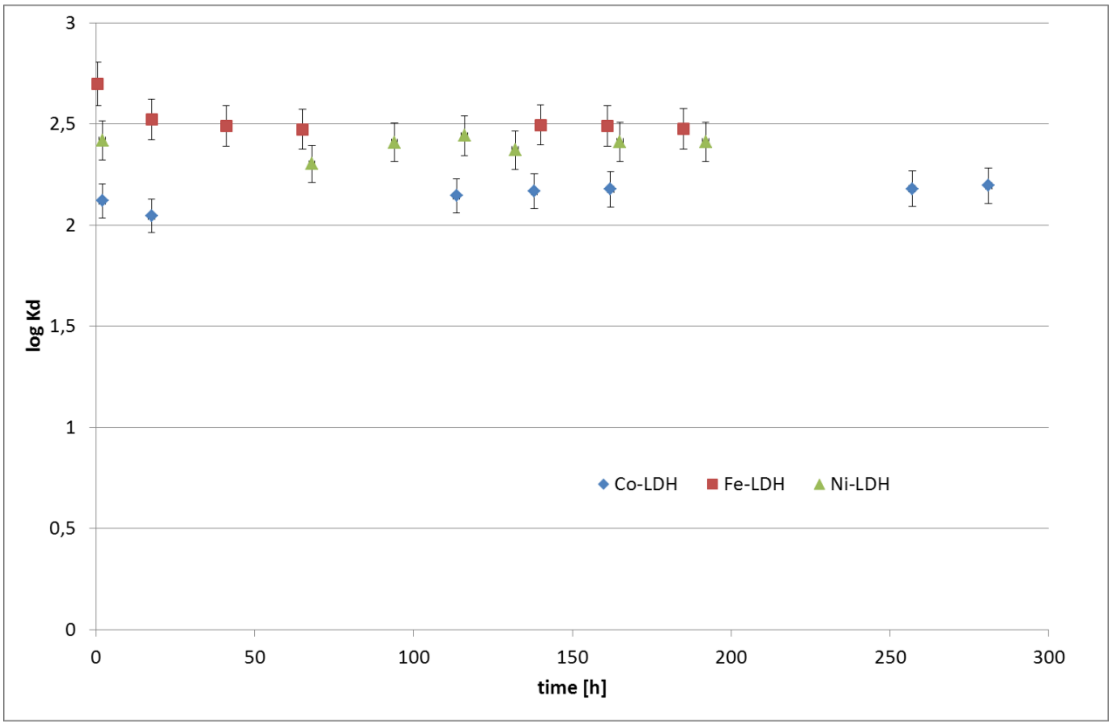

Fig. 6.22 Uptake of selenite on Co, Fe, and Ni bearing LDHs as function of time in Opalinus clay pore water

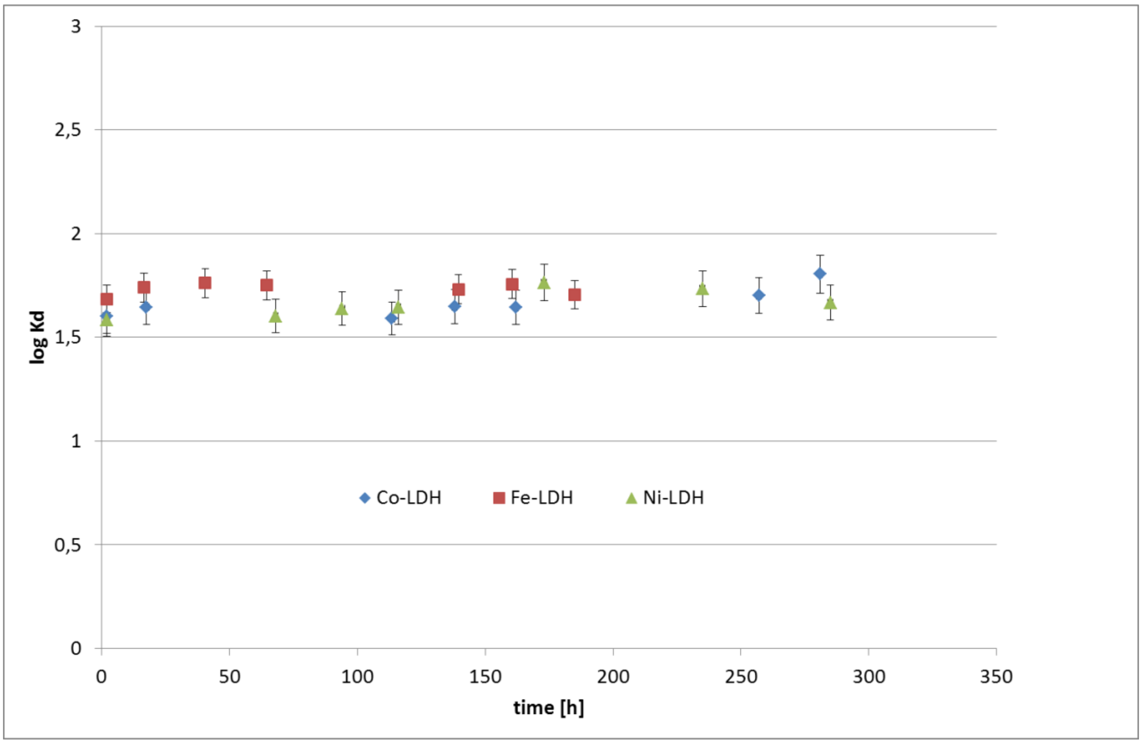

Fig. 6.23 Uptake of selenite on Co, Fe, and Ni bearing LDHs as function of time in $MgCl_2$-rich brine

The results indicated as well, that a change in the solution composition decreased the K_d values. In the sequence from water→ Opalinus clay pore water → $MgCl_2$-rich brine the amounts of competing anions (i. e. chloride) increased strongly. As was already pointed out by Das et al. [DAS/PAT2006], an equivalent molar concentration of chloride, present as competing anion, decreased the adsorption of phosphate from 100 % to 70 %. In the presented investigations, when working with the $MgCl_2$-rich brine, the molar excess of chloride was about 10^{+13} with respect to the selenite concentration. Nevertheless, an uptake for selenite (divalent anionic species) was observed, but no retention of the monovalent anionic species (iodide and selenite) was detected.

In conclusion (**Tab. 6.8**), compared to the pure MgAl-LDH (chloride is the interlayer anion), the Fe, Co, and Ni bearing MgAl-LDHs possess higher uptake capacities for the anionic species iodide, pertechnetate and selenite, indicating the influence of metal composition control on anion sorption capability. In comparison towards each other, the Fe, Co, and Ni LDH solid solutions behaved similar. The uptake was rapid indicating ion exchange processes. **In water** the higher uptake of iodide compared to pertechnetate can be explained by the size of the anions. The selectivity of monovalent anions for the ion-exchange increases with decreasing diameter of the anions. The aqueous radius of I^- is 2.20 A. The effective ionic radius of TcO_4^- is 2.40 A. The size of I^- is smaller than that of TcO_4^- and thus I^- intercalates the interlayer of LDH more easily. High amounts of competing anions, i. e. chloride, strongly influenced the retention of iodide and pertechnetate. Selenite uptake was influenced to a lower extend demonstrating that the divalent anion selenite possesses the higher affinity. From the results an anion ranking in **clay pore water** can be given as: $SeO_3^{2-} > Cl^- > TcO_4^- > I^-$.

In the scientific community exists the general consensus that the uptake of iodide by LDHs is low, supressed completely when competing anions are present. The uptake of iodide is that weak, because iodide does not participate in hydrogen bonding within the LDH structure. This hydrogen bonding is the most important strength in stabilizing and connecting the brucite-layer with the interlayer. Only a weak coordination between iodide in the interlayer and the metal cations in the hydroxide layers exist. This finding could be supported by the results obtained for the pure MgAl-LDH. The next outcome was that the uptake of iodide by calcinated LDH solids increased the K_d values some orders of magnitude [KAN/CHU1999], [FET/RAM1997]. This finding, with respect to LDH solid solutions will be investigated in future in detail.

To our knowledge the **uptake of iodide on LDH solid solutions** was never investigated before. The obtained results within this work clearly demonstrated that solid solutions can take up trace level amounts of iodide even when competing anions are present. Already molar fractions of 0.0333 for Fe, Co and Ni had this effect and in future work the uptake of iodide by a complete solid solution series will be investigated in detail.

Pertechnetate is a monovalent anion like iodide, but it is an oxyanion, hence hydrogen bonding is possible. The higher uptake of pertechnetate in comparison to iodide in the presence of competing anions (**Tab. 6.8**) (Opalinus clay pore water) might be explained by sorption dominated by the edge sites of LDHs. This mechanism of sorption at the edge sites was investigated in detail by [WAN/GAO2006]. He pointed out, that for oxyanions, the composition and hence the structure of the LDH possesses a strong impact on anion sorption capability.

For selenite (divalent anion) the highest K_d values, observed in all used solutions, were expected due to the high charge density of this anion.

Tab. 6.8 Distribution coefficients K_d (mL g^{-1}) and log Kd values of iodide, pertechnetate and selenite between aqueous phases and LDHs (initial concentrations: ^{129}I: 4.25 10^{-5} mol/L, ^{99}Tc: 5.89 10^{-7} mol/L, ^{75}Se: 5.65 10^{-12} mol/L) (V/m = 100 mL/g)

LDH	**Solution**	**$^{129}I^-$: K_d-values and (log K_d)**	**^{99}Tc: K_d-values and (log K_d)**	**^{75}Se: K_d-values and (log K_d)**
MgAl-LDH	water	79.43 (1.90)	25.12 (1.40)	630.96 (4.80)
Fe-LDH	water	338.84 (2.53)	162.181 (2.21)	1995.26 (6.38)
Co-LDH	water	190.55 (2.28)	114.81 (2.06)	1584.89 (6.20)
Ni-LDH	water	251.19 (2.40)	102.33 (2.01)	1047.13 (6.02)
MgAl-LDH	Clay water	-	-	100.00 (1.35)
Fe-LDH	Clay water	2.24 (0.35)	5.62 (0.75)	316.23 (1.80)
Co-LDH	Clay water	2.24 (0.35)	5.62 (0.75)	158.49 (1.65)
Ni-LDH	Clay water	2.24 (0.35)	5.62 (0.75)	199.52 (1.60)
MgAl-LDH	brine	-	-	22.38 (1.35)
Fe-LDH	brine	-	-	63.10 (1.80)
Co-LDH	brine	-	-	44.69 (1.65)
Ni-LDH	brine	-	-	39.81 (1.60)

6.6.2.2 Effect of pH on the uptake of anionic species

The effect of pH on the uptake of iodide, pertechnetate and selenite was studied. The adsorption of iodide, pertechnetate, and selenite in water was unaffected by pH in the pH range between 4 and 8, because of the buffer capacity of the Ni, Co, and Fe bearing LDHs (**Fig. 6.24**). The buffer capacity of these LDH solid solutions was demonstrated in Opalinus clay pore water and in $MgCl_2$-rich brine (**Fig. 6.25**) as well. Note, the pH values in the $MgCl_2$-rich brine were not corrected but according to [GRAM/MUE1990] for each pH value ~ 2 units have to be added. In general it can be stated, that due to the buffer activity of the LDHs, the initial pH values were shifted to the neutral pH area when equilibrium was reached. A difference for the different LDH solid solutions was not observed. In **Fig. 6.26** the log K_d values for the Tc uptake on the LDHs as function of pH is shown as an example. The log K_d values were stable, demonstrating that the uptake of the anionic species is unaffected by pH. This stability can be explained by the buffer capacity of the LDHs. According to [HER/PAV1996] it can be assumed that, when the initial pH value is below 4.5, the pH increased due to dissolution of the LDHs, which results in buffering of H^+ in the release of OH^- by LDHs. In pH ranges close to the neutral pH-area a protonation or deprotonation of the hydroxyl groups occur. When the initial pH was higher than 8.5 the decrease in pH was related mostly to the adsorption of OH^- directly from solution by LDHs.

X-ray diffraction of the solids, carried out to ensure that no structural changes of the Fe, Co, and Ni bearing LDHs occurred as a consequence on pH treatments, showed the most typical 003, 006 009 and 110 reflections. The lattice parameters, in particular the parameters c and a did not change.

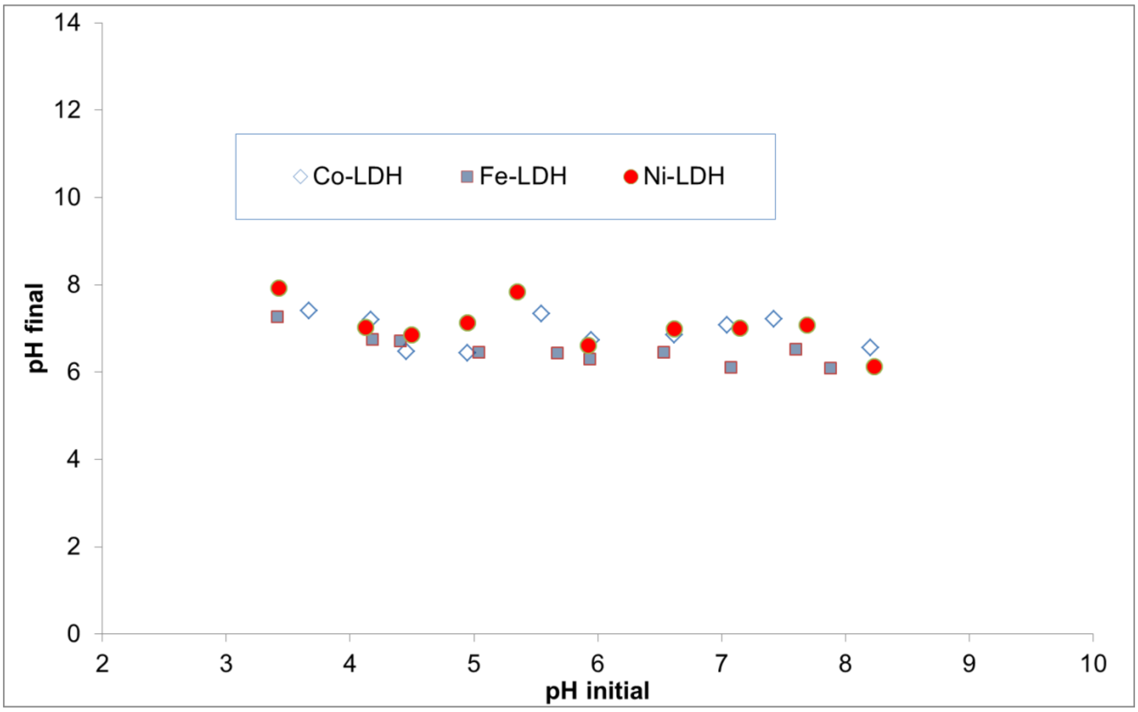

Fig. 6.24 The pH buffer capacity of Co, Ni, and Fe bearing MgAl-LDHs in water

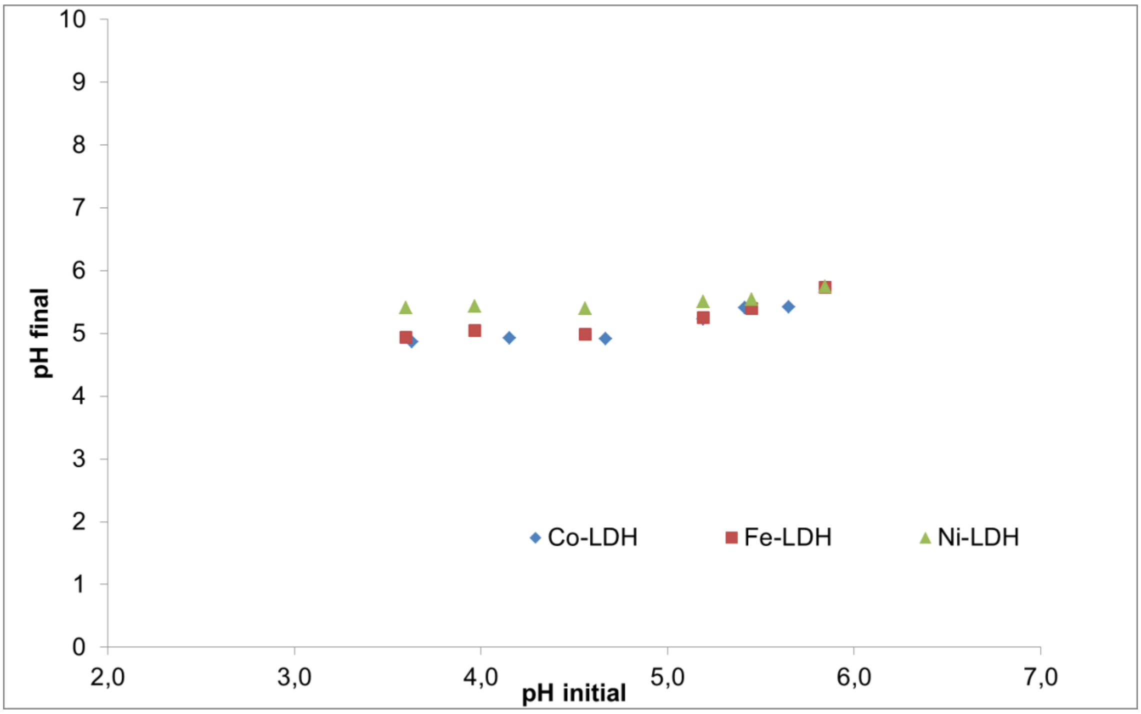

Fig. 6.25 The pH buffer capacity of Co, Ni, and Fe bearing MgAl-LDHs in $MgCl_2$-rich brine

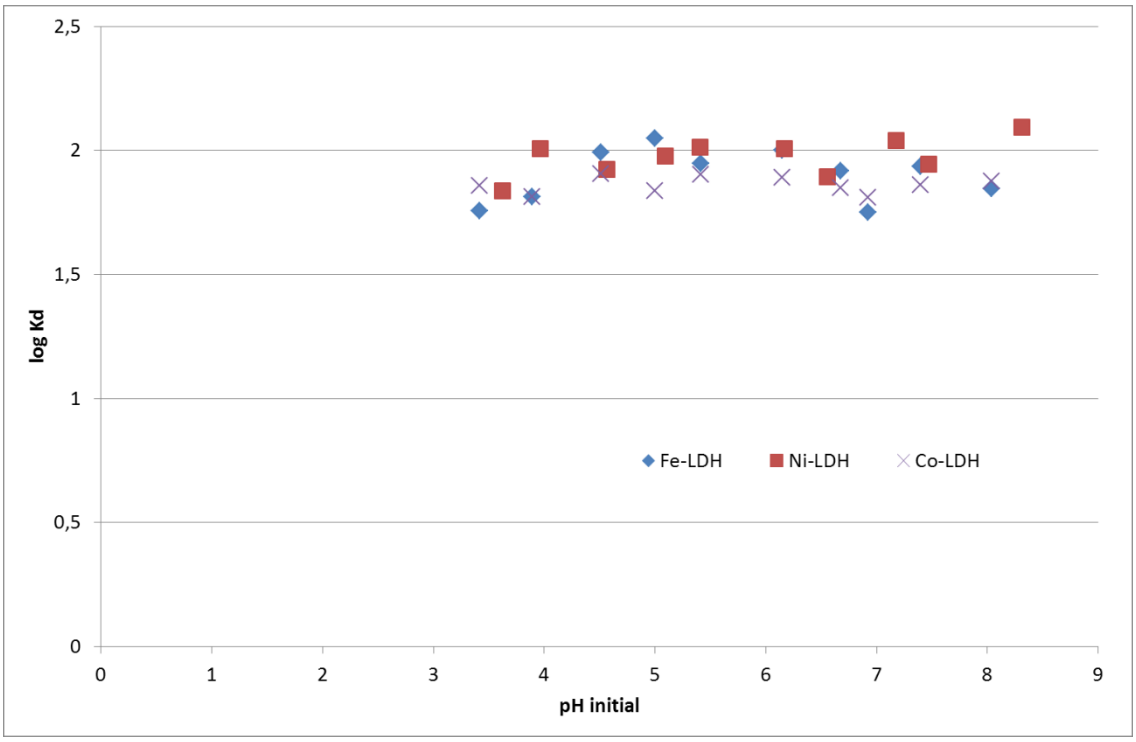

Fig. 6.26 Log K_d values for Tc uptake in water as function of the initial pH values

6.6.2.3 Isotherms and Freundlich equation

The previous described investigations were performed in order to gain first information for the uptake behaviour of anionic species (for the monovalent anions iodide and pertechnetate and for the divalent anion selenite) on the Fe, Co and Ni bearing LDHs as function of time and pH. The question about the retention mechanisms were not answered, yet. Investigations performed by [CHA/BOT1996] focused on the different retention mechanisms for monovalent and divalent anions on LDHs. The location of different adsorption sites and the competing effects between adsorbates were investigated in detail. The adsorption of divalent anions (SO_4^{2-} and CrO_4^{2-}) and of monovalent anions (Cl^-) on a LDH with carbonate as interlayer anion was very weak. In general, it was concluded, that in mixed solutions of monovalent and divalent anions, the adsorption of divalent anions was not strongly influenced by the presence of monovalent anions. On the contrary, divalent anions inhibit the adsorption of monovalent anions. This finding can be explained by the charge density of the anion. Anions possessing a high charge density have a high affinity towards the LDH because these anions stabilize the interactions between the brucite-layers and the interlayer. As a consequence, the LDH is stable and less soluble.

With respect to the adsorption mechanism, the presence of two kinds of anion retention sites on LDHs can be distinguished: (a) sites within the interlayer corresponding to the structural AEC (anion exchange capacity) of the LDH, and (b) adsorption sites on the external surface. FT-IR analysis is a useful tool to identify the type of anions. XRD analysis characterise the nature of anions as well and although identify the retention process. The retention process within the interlayer region influenced directly the basal lattice parameter c. The basal lattice parameter c describes the distance between one brucite-like layer and one interlayer and depends strongly on the nature of the anion. It must be noted, both analytical tools could not be used for the present investigations, due to the fact, that the concentrations of the anions were too low (trace-level amounts). Nevertheless, the low concentrations were chosen on purpose with respect to simulate repository-relevant conditions (high amounts of solids are expected and the concentrations of anions are low).

Which anion will be adsorbed to which extend on which sites can be approached through the study of adsorption isotherms. Generally spoken, as long as the adsorption isotherm increased steadily till the AEC (anion exchange capacity) is reached, the sites of retention are within the interlayer. When the isotherm then reaching a plateau, this discontinuity observed can be assigned to the adsorption on external edges.

In the present work, the adsorption isotherms were obtained by plotting the amount of anionic species sorbed on LDHs, Cads (mol/g]), against the anionic species in solution at equilibrium, Ce (mol/L).

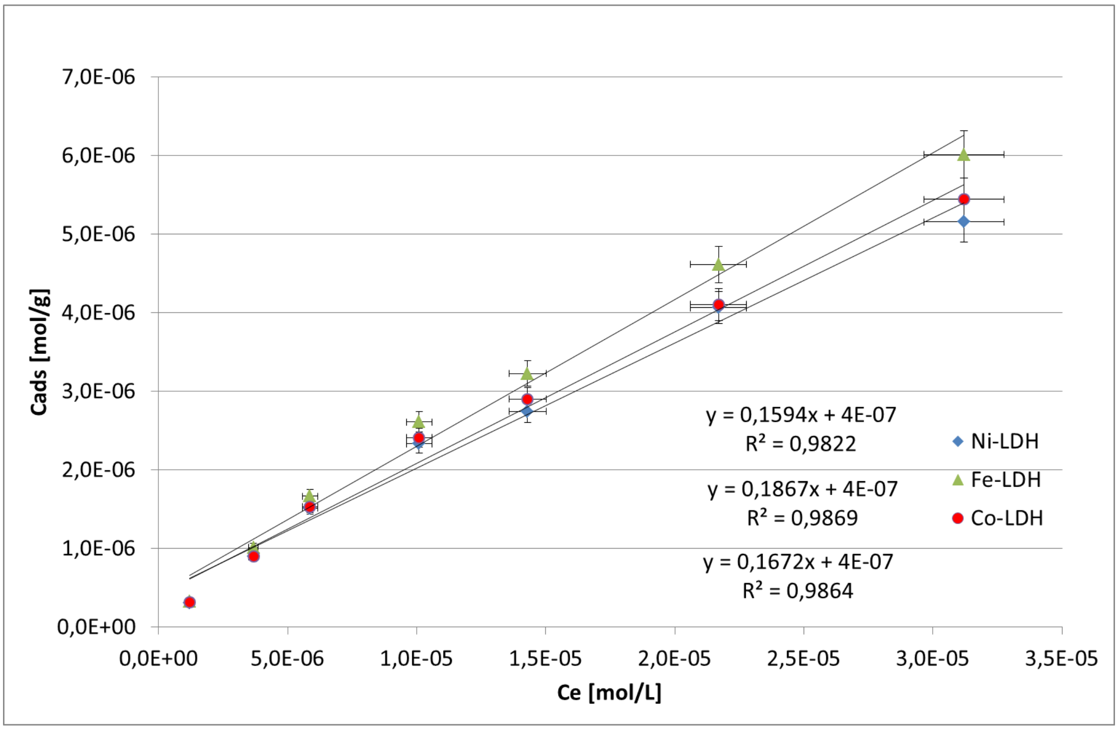

Fig. 6.27 Adsorption isotherm of iodide on Fe, Co and Ni-bearing LDHs in water

Fig. 6.27 revealed the adsorption isotherms for iodide adsorbed at pH 7.50 ± 0.2 on the LDH solid solutions in water. The isotherms were linear and the assumption was drawn that the favoured reaction were ion exchange processes. The data were fitted to the Freundlich adsorption isotherm. The Freundlich equation $x/m = K_f \cdot Ce^{1/n}$ was rearranged to the linear form: $\log(x/m) = \log K_f + 1/n (\log Ce)$ where x/m is the amount of anionic species adsorbed per unit mass of adsorbent (mol/g) and Ce is the equilibrium concentration (mol/L), K_f and 1/n are constants. While K_f gives the adsorption capacity of the adsorbent in mol/g, n is a constant related to energy and intensity of adsorption. The data (**Fig. 6.28**) showed a satisfactory fit to the Freundlich isotherm (better than the fit to the Langmuir isotherm model), particularly the adsorption of iodide on the Fe-LDH ($R^2 = 0.9834$), on the Co-LDH ($R^2 = 0.9939$) and on the Ni-LDH($R^2 = 0.9912$). Values of K_f and 1/n as calculated from the slope and intercepts were summarized in (**Tab. 6.9**). Larger K_f indicates a larger overall capacity. From the results obtained, clearly the Ni bearing LDH possessed the highest capacity for iodide uptake. The values of 1/n between 0 and 1 represent good adsorption of iodide on the Fe, Co and Ni bearing LDHs.

Tab. 6.9 Freundlich adsorption constants for adsorption of iodide on Fe,Co and Ni bearing LDHs

LDH	K_f	1/n	n	R^2
Fe-LDH	7.47	0.9246	1.0815	0.9834
Co-LDH	14.85	0.8947	1.1177	0.9939
Ni-LDH	33.67	0.8325	1.2012	0.9912

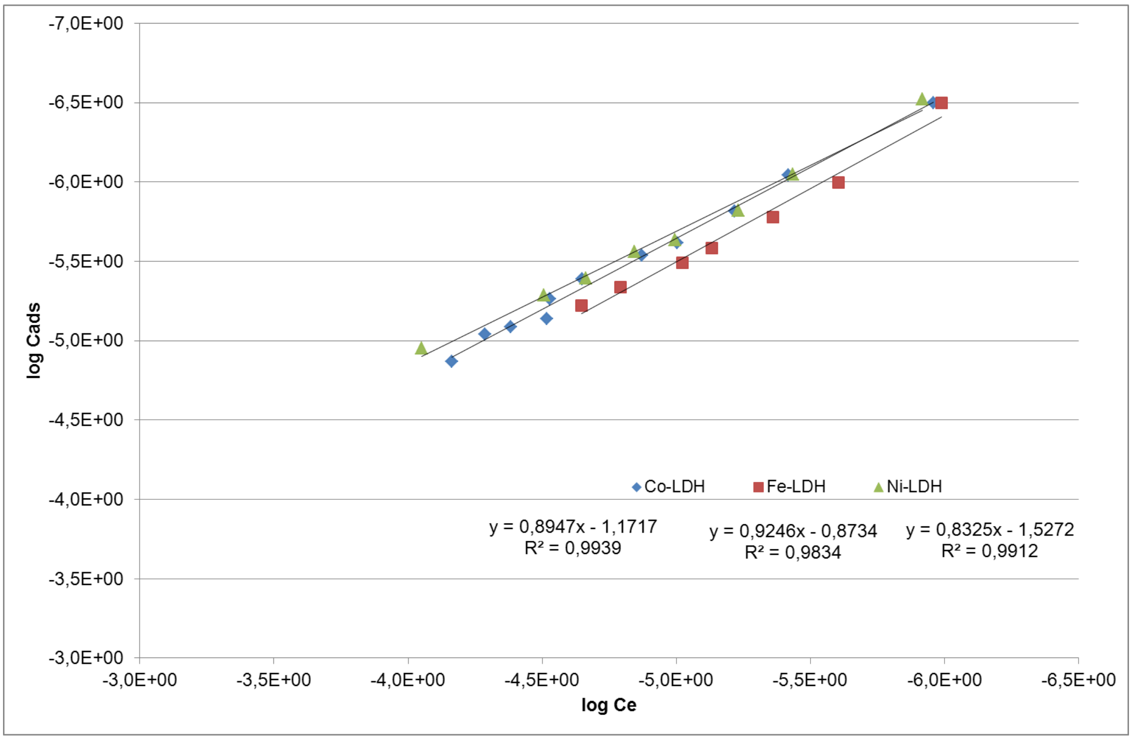

Fig. 6.28 Freundlich plots for iodide adsorption on the LDH solid solutions in water

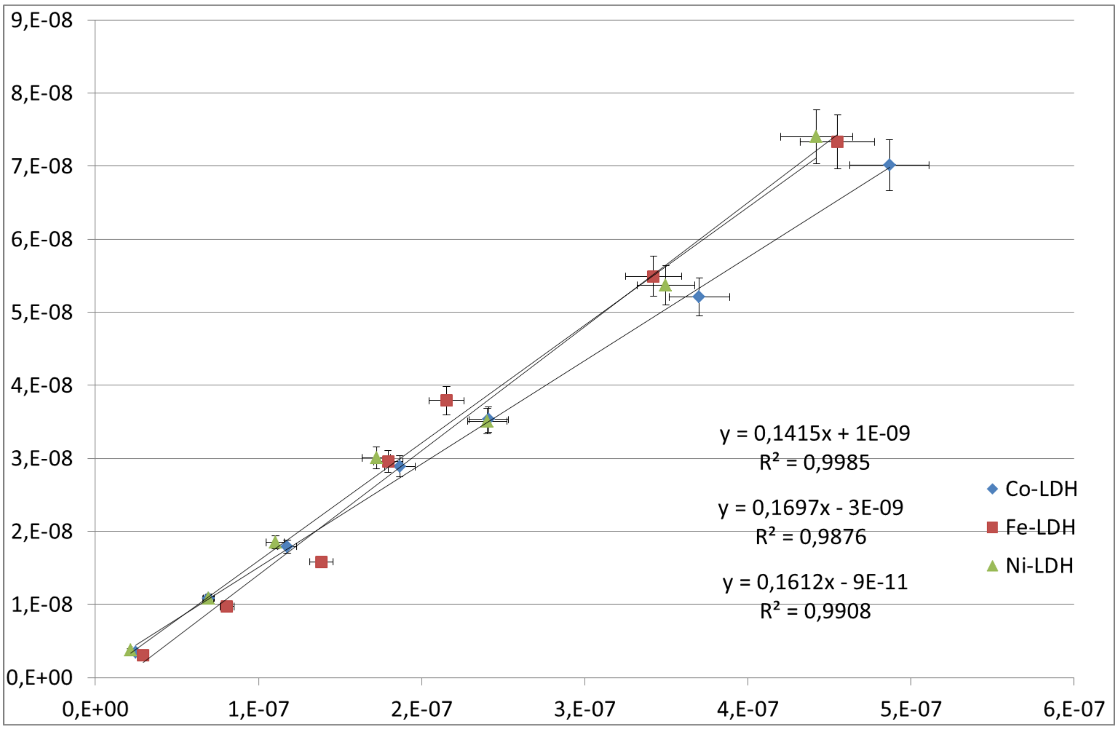

Fig. 6.29 Adsorption isotherm of pertechnetate on Fe, Co and Ni-bearing LDHs in water

The adsorption isotherms for pertechnetate were presented in **Fig. 6.29**. The similarity to the adsorption isotherms for iodide (**Fig. 6.27**) is obviously. The shapes of these isotherms are linear and according to (GIL/MAC1960) are classified as C-type. The C-type represent a constant partition of adsorbate between solution and solid, even when the concentration of the adsorbate (here pertechnetate) increased. Again the data showed a satisfactory fit to the Freundlich equation (for the Fe-LDH (R^2 = 0.9863), for the Co-LDH (R^2 = 0.9987) and for the Ni-LDH(R^2 = 0.9901)). The results are presented in (**Fig. 6.30**) and in (**Tab. 6.10**). For TcO_4^- the Co bearing LDH possessed the highest uptake capacity.

Tab. 6.10 Freundlich adsorption constants for adsorption of pertechnetate on Fe,Co and Ni bearing LDHs

LDH	**K_f**	**1/n**	**n**	**R^2**
Fe-LDH	2.15	1.1779	0.8490	0.9863
Co-LDH	9.66	0.978	1.0225	0.9987
Ni-LDH	3.72	1.029	0.9718	0.9901

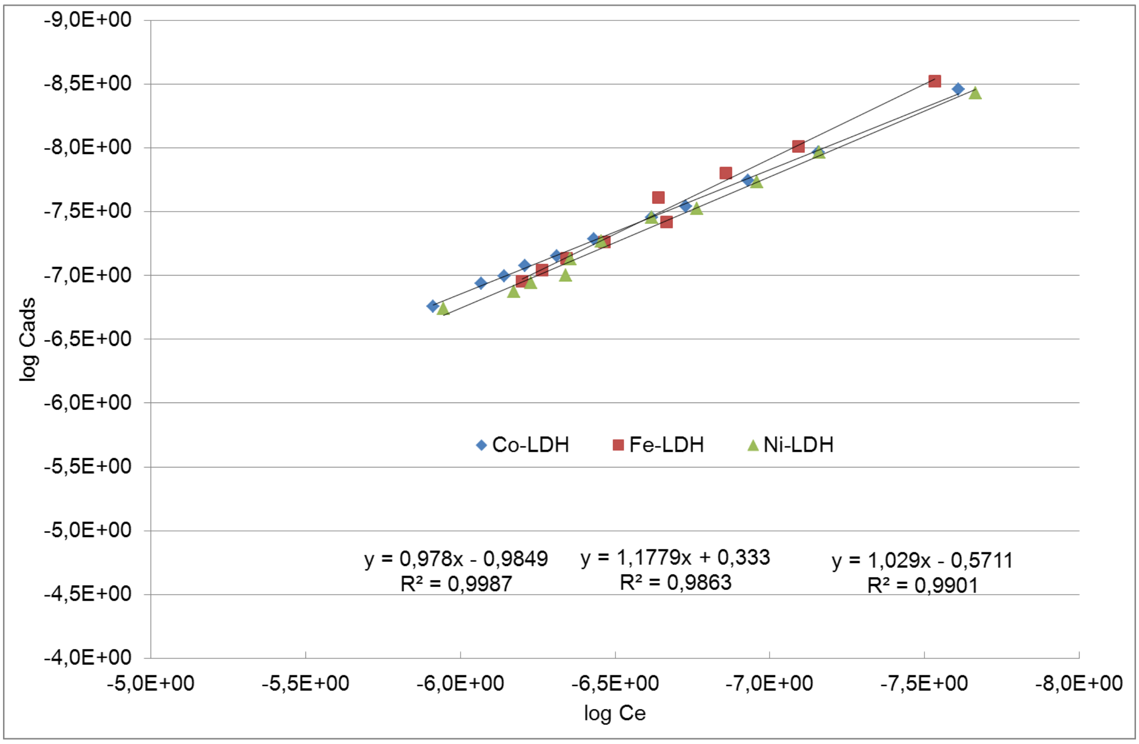

Fig. 6.30 Freundlich plots for pertechnetate adsorption on the LDH solid solutions

Selenite uptake on Fe, Co and Ni bearing LDHs was studied in water, in clay pore water (Opalinus-type) and in $MgCl_2$-rich brine. In all solutions an uptake was observed. As was pointed out by [YOU/VAN2001] selenite has a high adsorption affinity towards LDHs, especially at low concentrations. He obtained adsorption isotherms which could be clearly characterize as L-type isotherms. The L-type characterize [GIL/MAC1960] a system where the monofunctional adsorbate is strongly attracted by the adsorbent, generally by ion-ion exchange interactions that reach a saturation values represented by the plateau of the isotherm. **Fig. 6.31** reveals the adsorption isotherms of selenite on the Fe, Co and Ni LDH solid solutions in water. The Co and Ni isotherms started to reach saturation, while for the Ni-LDH no saturation occurred. First, all data were fitted according to the Langmuir equation: Ce/(x/m) = 1/bQ + Ce/Q where Ce is the equilibrium adsorption concentration in solution (mol/L), Q denotes the amount adsorbed per unit mass of adsorbent (mol/g), x/m denotes the amount adsorbed per unit mass of adsorbent at equilibrium (mol/g), b is a constant related to the affinity of the binding sites. None of the adsorption isotherms however could be fitted satisfactory to the Langmuir function. The obtained isotherms correspond more to the H-type. The H-type, according to [GIL/MAC1960], is characterized by the high affinity of the adsorbed species.

This means that even, when the concentration is increased a quantitative adsorption occurred. Exactly these characteristics matched perfectly the selenite uptake on the LDH solid solutions in water.

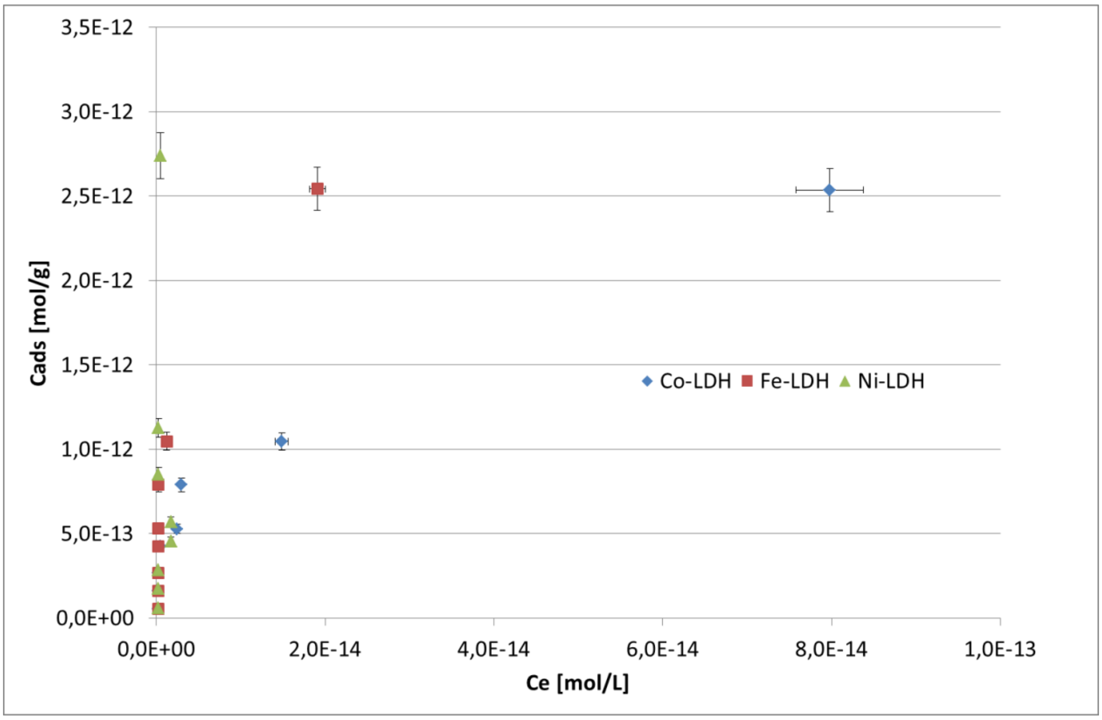

Fig. 6.31 Adsorption isotherms of selenite on Fe, Co and Ni LDH solid solutions in water at pH = 7.0 ± 0.2

Fig. 6.32 revealed the adsorption isotherms of selenite on the LDH solid solutions in clay pore water. In clay pore water competing anions (i. e. chloride (0.2998 mol/L) and sulphate (0.01408 mol/L)) are present. The presence of competing anions decreased the adsorbed amounts of selenite (ionic radius: 0.239 nm) from approximately 100 % observed in water to approximately 70 % in clay pore water. As competing anion the contribution of chloride as monovalent species is low, while the influence of sulphate (ionic radius: 0.230) as divalent species has to be taken into account. The adsorption data obtained fitted well the Freundlich equation (for the Fe-LDH: $R^2 = 0.9903$, for the Co-LDH ($R^2 = 0.9964$) and for the Ni-LDH ($R^2 = 0.9894$)). (**Fig. 6.33**) reveals the corresponding Freundlich plots and in **Tab. 6.11** the Freundlich constants are summarized. The shapes of the adsorption isotherms in clay pore water (**Fig. 6.32**) have a tendency to the S-type. The S-type implies a cooperative adsorption mechanism [BOW1978]. This implication is supported by the Freundlich 1/n constants, which represented the slopes of the Freundlich functions (**Tab. 6.11**). All values obtained are >1 suggesting a “secondary“ adsorption mechanism involving cooperative adsorption at higher concentrations. One could visualize incoming selenite species being attracted by those selenite species already held to the LDH by H-bonding.

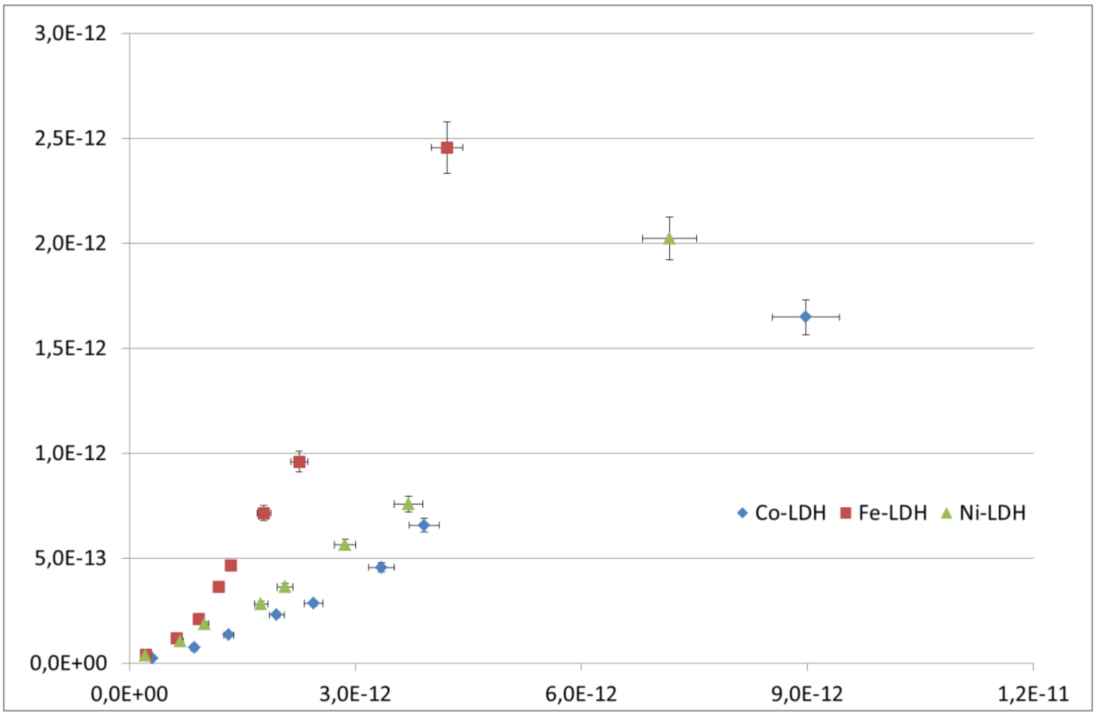

Fig. 6.32 Adsorption isotherms of selenite on Fe, Co and Ni LDH solid solutions in clay pore water at pH 7.0 ± 0.2

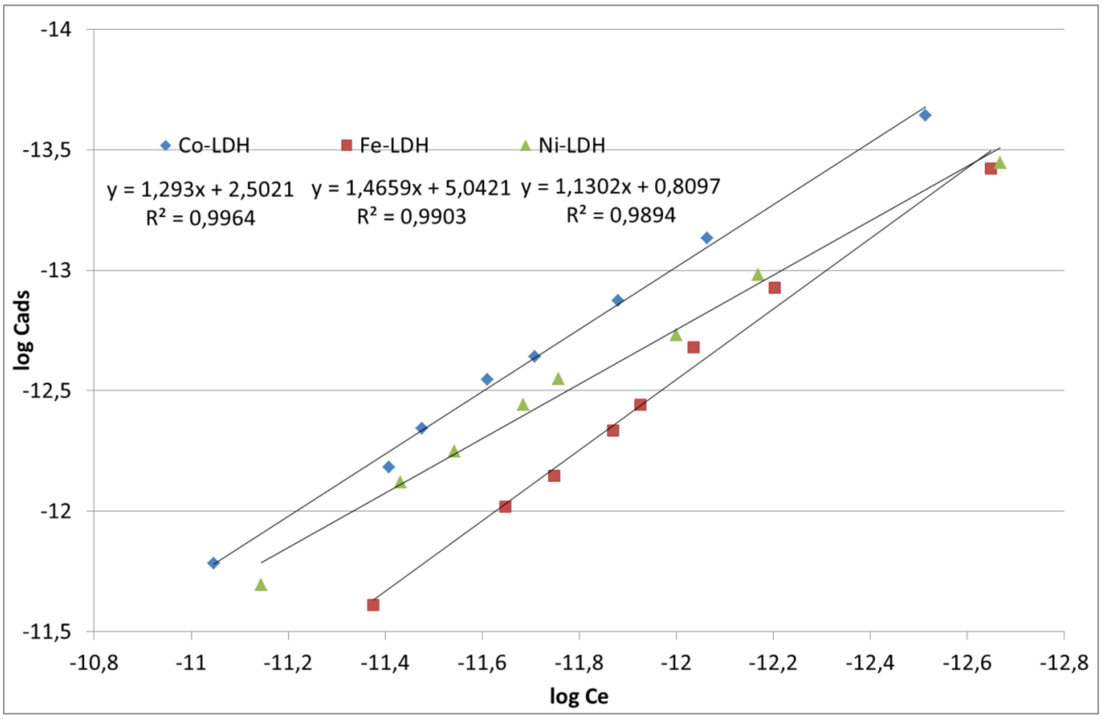

Fig. 6.33 Freundlich plots for selenite adsorption on Fe, Co and Ni bearing LDHs in clay pore water

Tab. 6.11 Freundlich adsorption constants for adsorption of selenite on Fe,Co and Ni bearing LDHs in clay pore water

LDH	**K_f**	**1/n**	**n**	**R^2**
Fe-LDH	2.15	1.293	0.7734	0.9903
Co-LDH	110179	1.466	0.6821	0.9964
Ni-LDH	6.45	1.130	0.8848	0.9894

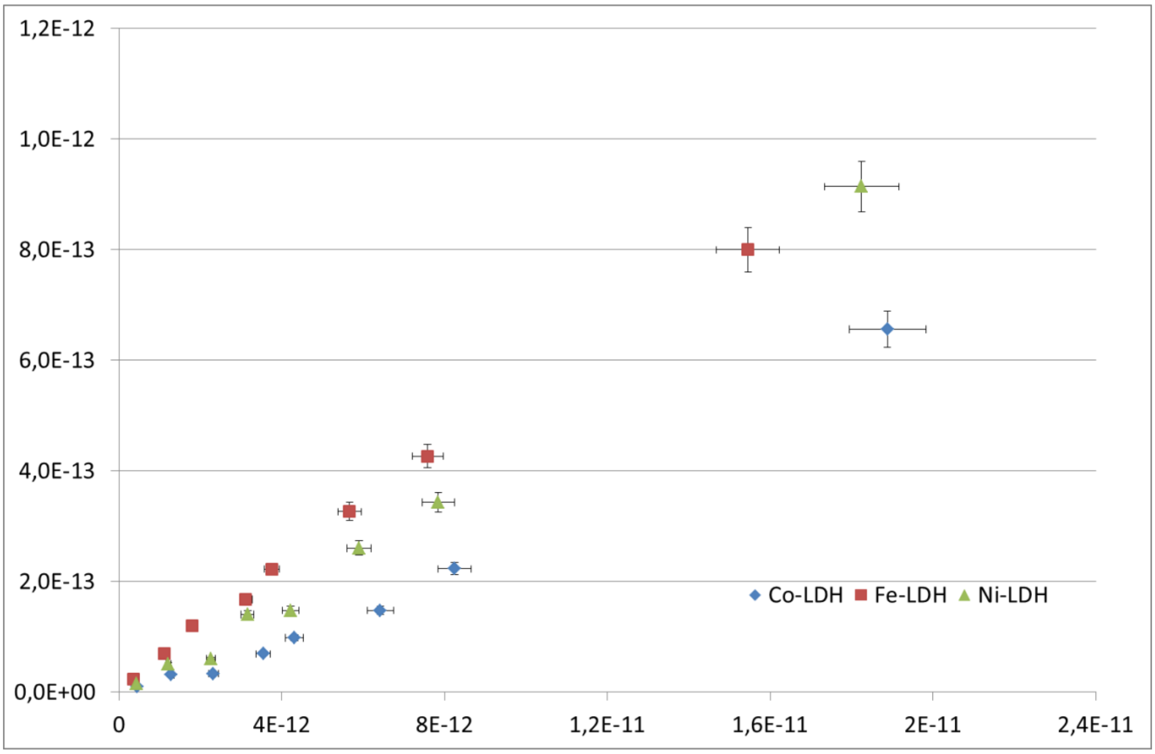

Fig. 6.34 Adsorption isotherms of selenite on Fe, Co and Ni LDH solid solutions in $MgCl_2$-rich brine at pH 4.8 ± 0.2 (not corrected)

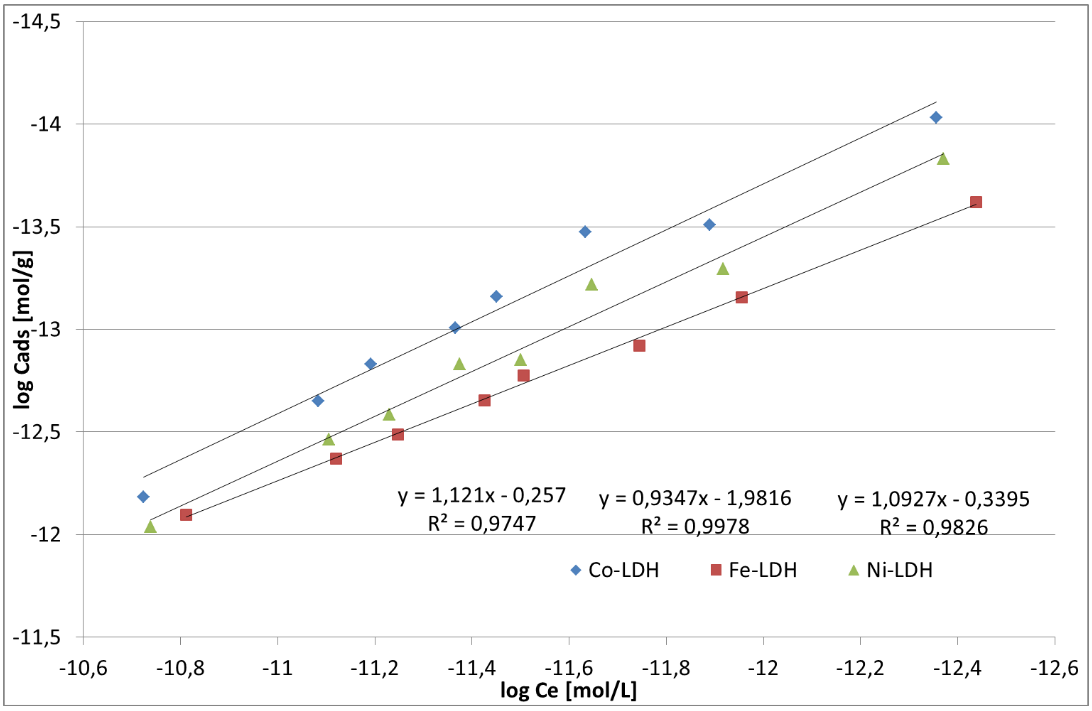

Fig. 6.35 Freundlich plots for selenite adsorption on Fe, Co and Ni bearing LDHs in $MgCl_2$-rich brine

Fig. 6.34 revealed the adsorption isotherms of selenite on the Fe, Co and Ni bearing LDHs in $MgCl_2$-rich brine. Concentrations of competing anions are enormous (9.84 mol/L of chloride and 5.11 10^{-4} mol/L sulphate). However, 40 % of adsorption was reached for the used trace level concentration range. The adsorption isotherms can be classified as C-type for the Fe bearing LDH, but the isotherm for the Co and Ni -LDH solid solutions indicate the S-type. As mentioned before the S-type indicate a secondary adsorption mechanism. The adsorption data did fit satisfactory the Freundlich equation (correlation coefficients: R^2 = 0.9747 for Co, R^2 = 0.9978 for Fe and R^2 = 0.9826 for Ni) and the plots are presented in **Fig. 6.35**. The Freundlich data is summarized in (**Tab. 6.12**). From this data set obtained, the 1/n constant for the Co and Ni bearing LDH is higher than one, confirming a cooperative adsorption mechanism.

Tab. 6.12 Freundlich adsorption constants for adsorption of selenite on Fe,Co and Ni bearing LDHs in $MgCl_2$-rich brine

LDH	**K_f**	**1/n**	**n**	**R^2**
Fe-LDH	0.01	0.9347	0.7734	0.9903
Co-LDH	0.55	1.121	0.6821	0.9964
Ni-LDH	0.46	1.0927	0.8848	0.9894

In conclusion, the adsorption isotherms for iodide, pertechnetate and selenite on the Fe, Co and Ni bearing LDHs could be classified according to (GIL/MAC1960). Constant partition of iodide and pertechnetate between solution and solid was observed (property of C-type isotherm), when the concentrations of theses adsorbates were increased.

Interesting results were obtained for selenite uptake. First, in water the high affinity of selenite (quantitative uptake) towards the Ni, Fe and Co LDH-solid solutions was confirmed by the H-type isotherms. In clay pore water the adsorbed quantity decreased (presence of sulphate as competing anion). Very interesting were the shapes of the obtained isotherms. They could be classified as S-types, which indicate cooperative adsorption mechanisms. Cooperative adsorption could be characterized by selenite species held to the LDH and attracting incoming selenite species. Consequently the uptake of selenite increased with increasing concentration. These findings were confirmed by Freundlich data. In $MgCl_2$-rich brine the adsorption isotherms were of the S-types for Co and Ni LDH solid solutions, and of the C-type for Fe bearing LDH, indicating the influence of metal composition within the hydroxide layers on the uptake mechanisms.

6.7 Conclusion

Within the joint project VESPA the FZJ investigated the potential of Fe, Co and Ni bearing LDHs as anionic radionuclide-binding material.

MgAl-LDH solid solutions (chloride as interlayer anion) with Ni, Co and Fe (~0.1 mole fraction) and (Mg+Ni)/Al, (Mg+Co)/Al, and (Mg+Fe)/Al cationic ratios close to 3:1) have been synthesized successfully by the co-precipitation method. Structural characterisation was performed by applying PXRD and EXAFS technique. The PXRD results showed that all the samples were pure LDHs with each exhibiting distinct stacking faults (the 3R/2H-type layer stacking sequence determined was ~0.5). The results of EXAFS measurements demonstrated similar structural features of Ni- and Co-bearing LDHs where Ni and Co atoms were incorporated as divalent cations in the LDH structure at octahedral crystallographic positions, whereas Fe was isostructural incorporated as trivalent species. With XANES measurements, the presence of Fe(III) was confirmed. Contradictory, in freshly prepared Fe containing LDH samples only Fe(II) was detected. The determination of the oxidation state of iron in Fe containing LDHs with storage time, remain challenging. Thermodynamic modeling using the GEMS-PSI code package was performed in order to predict the behaviour of different LDH compositions in aqueous media. Assuming that thermodynamic equilibrium was achieved between synthesized solids and solutions, the first estimates (-3593 ± 50 for Ni, -3604 ± 50 for Co, -3612 ± 50 kJ/mol) for the Gibbs free energies of at 70ºC were obtained. Due to the comparable ionic radii, the incorporation of Fe, Co, and Ni within the LDH lattice revealed no impact on the aqueous solubilities of these LDHs. This is an interesting finding, it helps to predict of thermodynamic properties and aqueous solubilities of LDHs with variable divalent cations. Further on the impact of the interlayer anion on the aqueous solubilities of LDHs was investigated for carbonate and chloride. Carbonate-containing LDHs were shown to be significantly less soluble than analogous chloride-bearing substances.

Compared to the pure MgAl-LDH (chloride is the interlayer anion), the Fe, Co, and Ni bearing MgAl-LDHs possess higher uptake capacities for the anionic species iodide, pertechnetate and selenite, indicating the influence of metal composition control on anion sorption capability. In comparison towards each other, the Fe, Co, and Ni LDH solid solutions behaved similar. Equilibrium state was reached rapidly, indicating ion exchange processes. High amounts of competing anions, i. e. chloride, influenced the retention of iodide and pertechnetate. However, even in clay pore water (Opalinus-type)

K_d values of 2.24 ml/g^{-1} for iodide and 5.62 ml/g^{-1} for pertechnetate were obtained, while no uptake by the pure MgAl-LDH was observed. Selenite uptake was influenced to a lower extend (K_d values in the range between 150 to 300 mL/g^{-1}) demonstrating that the divalent anion selenite possesses the higher affinity. From the results an anion ranking in clay pore water can be given as: $SeO_3^{2-} > Cl^- > TcO_4^- \sim I^-$. The adsorption isotherms in clay pore water were classified according to [GIL/MAC1960]. Different uptake mechanisms in clay pore water were identified. Iodide and pertechnetate showed a constant partition between solution and solid (C-shaped isotherms), while a cooperative adsorption mechanism exist for selenite (S-shaped isotherms). In $MgCl_2$-rich solution only the uptake of selenite was observed. For the Co and Ni bearing LDHs solid solution a cooperative adsorption was observed, while for the Fe bearing LDH a constant partition could be identified. This result indicates that the metal composition within the brucite-layers influences the adsorption behaviour. This finding however needs to be clarified at a molecular scale in future.

6.8 Implication for radioactive waste disposal

When disposing nuclear waste it is expected that only a few radionuclides are able to reach the biosphere and contribute to their long-term exposure risks. In this context, anionic species like ^{129}I, ^{36}Cl, ^{79}Se, ^{14}C and ^{99}Tc have to be addressed. Challenges arise in studying their retention properties. First, redox processes occur in any geochemical environment. Consequently, the redox state and hence the mobility of the anionic species change. This is a very important issue for redox sensitive species (i. e. Tc(IV) is nearly insoluble; Tc(VII) is highly mobile). Second, isotope-exchange mechanisms have to be included (i. e. in clay formations radioactive iodine might exchange with organic iodine. This exchange can reduce the mobility of iodine, because only 25 % of the natural iodine content can be mobilised by groundwater). Third, retention can be achieved via interactions with secondary phases (secondary phases forming during corrosion of waste forms, waste containers and/or other near-field materials can retain mobile radionuclide species by different mechanisms). Mostly, under natural aqueous conditions mineral/water interfaces are negatively charged and low interactions with anions exist. As a result, the mobility of anions is characterized by low R_d values. Nevertheless, in rock clay for example, even low R_d values of 0.1 ml/g^{-1} will slow down the migration time for anions (diffusion constant about 5 10^{-12} m^2/s^{-1}) over a migration distance of 50 m from about 140.000 years to more than 700.000 years [ANDRA2005].

Within this work, the retention potential of LDHs, representing secondary phases, was investigated. LDHs are of special interest due to their structure. They possess anions within their interlayers and these anions can be exchanged. The exchange reactions were studied in water and, in order to reflect repository relevant conditions, in clay pore water and $MgCl_2$-rich salt brine. The results indicate that the ion exchange reaction between LDHs and I^-, TcO^{4-} and $SeO_3{}^{2-}$ (used anionic species) offer a promising mechanism for the immobilization in the near field of a repository for radioactive waste. Owing to the determined distribution coefficients of iodide, pertechnetate and selenite by LDHs, considerable amounts are expected to be immobilized (due to the highest charge density of selenite, the largest amounts are expected) in water and in clay pore water. Clearly, as was demonstrated, the anion exchange reaction is influenced by competing anions. High amounts of chloride (present in $MgCl_2$-rich brine) decrease the retention of selenite and supress the exchange reaction with iodide and pertechnetate.

Besides the influence of competing anions the results indicate that the nature of the LDH component possesses a significant effect on anion exchange reactions. Compared to the pure MgAl-LDH compound, solid solutions (Ni, Co and Fe bearing MgAl-LDHs) showed higher retention potentials for all anionic species studied. The relationship between LDH structure/stoichiometry and retention property merits further attention.

As long as LDHs are stable in the near-field anionic species may be retained. Therefore the stability of the used LDH solid solutions was studied and the first values of their Gibbs free energies of formations were obtained. Compared to pure MgAl-LDH the used LDH solid solutions are slightly less stable; hence possess a slightly higher solubility. However, this could explain their higher anion exchange capabilities. For reliable long-term predictions, the potential stability of LDH phases (including solid solutions) in the repository near field has to be developed in detail. In future, detail investigations will include structural characterisation of the LDH solids (cation and anion positions) and characterisation of their thermodynamic parameters.

In summary, often zero retention for anionic radionuclide species is assumed and this might lead to an overestimation of the mobility and hence of the risk stemming from these nuclides. The obtained distribution constants clearly indicate that retention for iodide, selenite and pertechnetate with LDHs exist (solid solutions possess higher capabilities) and these values can be used in radionuclide transport calculations/codes.

6.9 Future work

One of the main outcomes of the present work was that LDH solid solutions, compared to a pure LDH phase, possess higher retention potentials for anionic radionuclide species like iodide, selenite and pertechnetate. In future, the relationship between LDH structure and LDH property will be the focus of interest. Is it possible to create the "best" LDH solid solution with respect to anion fixation and how stable is this compound with respect to repository near-field conditions?

A complete Mg/Ni-Al-LDH solid solution series will be synthesized. Different uptake mechanism (ion exchange, co precipitation, uptake by calcined LDH solid solutions) for iodide (^{129}Iodine is expected to be released in the non-volatile iodide (I^-) form to groundwater under the geochemical conditions expected for European disposal scenarios) will be investigated. Structural characterization of the obtained LDH phases should lead to a process understanding at molecular level. These data and thermodynamic parameters obtained from accompanying calorimetric measurements and thermodynamic calculations will result in reliable long term predictions of the stability of these LDH phases in the repository near field.

It is well known that ^{129}I has a very long-half life, its radio toxicity is not reduced during the transportation towards the biosphere and therefore ^{129}I is a major contributor to the radiological dose in safety assessment calculations. However, there are uncertainties about the inventories of ^{129}I within radioactive waste forms (i. e. in spent fuel). For a special UO_2 spent fuel type (TRISO-particles), ^{129}I quantification is aspired.

Acknowledgements

Authors thank Nicolas Finck – for providing the Fe reference data; the Synchrotron Light Source ANKA – for provision of instruments at their beam lines. Further on the authors wish to thank Dr. Kathy Dardenne for EXAFS calculations and Dr. Martina Klinkenberg for ESEM/EDX investigations.

6.10 References (chapter 6)

[ABD/CRO1994] Abdelouas, A., Crovisier, J.L., Lutze, W., Fritz, B., Mosser, A. and Muller, R., Formation of hydrotalcite-like compounds during R7T7 nuclear waste glass and basaltic glass alteration. Clays and Clay Minerals, 42 (1994) 526-533.

[ABD/CRO1994] Abdeloulas, A., Crovisier, J.L., Lutze, W., Fritz, B., Mosser, A., Müller, R. Formation of hydrotalcite-like compounds during R7T7 nuclear waste glass and basalic glass alteration, Clays and Clay Minerals 42 (1994) 526-533.

[AIM/TAV2012] Aimoz, L., Taviot-Gueho, C., Churakov, S., Chukalina, M., Dähn, R., Curti, E., Bordet, P., Vespa, M. Anion and Cation Order in Iodide-Bearing Mg/Zn-Al Layered Double Hydroxides, Journal of Physical Chemistry C, 116 (2012) 5460-5475.

[AIM/WIE2012] Aimoz, L., Wieland, E., Taviot-Guého, C., Dähn, R., Vespa, M., Churakov, S. Structural Insight into Iodide Uptake by AFm Phases (2012) Environmental Science & Technology (2012) 46 (7) 3874-3881.

[ALL/JEP1969] Allmann, R.J. and Jepsen, H.P. (1969) Die Struktur des Hydrotalkites. Neues Jahrbuch für Mineralogie Monatshefte, 544-551.

[ALL/NAV2002] Allada, R.K., Navrotsky, A., Berbeco, H.T., and Casey, W.H. Thermochemistry and aqueous solubilities of hydrotalcite-like solids. Science, 296 (2002) 721-723.

[ALL/PLE2005] Allada, R.K., Pless, J.D., Nenoff, T.M., and Navrotsky, A. Thermochemistry of hydrotalcite-like phases intercalated with CO32-, NO3-, Cl-, I-, and ReO4-. Chemistry of Materials, 17 (2005) 2455-2459.

[ALL1979] Allmann, R.(1979): Doppelschichtstrukturen mit brucitähnlichen Schichtionen [Me(II) 1-x Me (III)x (OH)2]x+. Chimia, 24 (1979) 99-108.

[ANDRA2005] Andra, Référentiel de comportement des radionucléides et des toxiques chimiqques d´un stockage dans le Callovo-Oxfordien jusqu´ a l`homme. Site de Meuse/Haute-Marne. CRP.ASTR.04.0032.

[ARA/PUS1996] Arakcheeva, A.V., Pushcharovskii, D.Y., Rastsvetaeva, R.K., Atencio, D. and Lubman, G.U., Crystal structure and comparative crystal chemistry of Al4Mg2(OH)12(CO3) 3H2O), a new mineral from the hydrotalcite-manasseite group. KRISAJ, 41 (1996) 1024-1034.

[BEL/REB1996] Bellotto, M., Rebours, B., Clause, O., Lynch, J., Bazin, D., and Elkaım, E. A reexamination of hydrotalcite crystal chemistry. The Journal of Physical Chemistry, 100 (1996) 8527-8534.

[BER/FRI1998] Bergmann, J., Friedel, P., and Kleeberg, R.. BGMN - a new fundamental parameters based Rietveld program for laboratory X-ray sources, its use in quantitative analysis and structure investigations. CPD Newsletter (1988) 5-8.

[BOE/STE1977] Boehm, H. P., Steinle, L., Vieweger C. $[Zn_2Cr(OH)_6]X\ 2H_2O$, neue Schichtverbindungen mit Anionenaustausch- und Quellvermögen. Angew. Chem., 89 (1977) 259-260.

[BOO/DRI1993] Bookin, A.S. and Drits, V.A. Polytype diversity of the hydrotalcite-like minerals - I. Possible polytypes and their diffraction features. Clays and Clay Minerals, 41 (1993) 551-557.

[BOW1978] Bowman, B.T. Effect of fulvic acid on adsorption of methyl parathion and parathion by Ca^{2+}- and Fe^{3+} montmorillonite suspensions, Soil Science of America 42 (1978) 441-446.

[BRI/KIK1979] Brindley, G.W., Kikkava, S., A crystal-chemistry study of Mg,Al and Ni,Al hydroxy-perchlorates and hydroxy-carbonates, Am. Min. 64 (1979) 836-843.

[BRI/THO2008] Britto, S., Thomas, G.S., Vishnu Kamath, P., and Kannan, S. Polymorphism and structural disorder in the carbonate containing layered double hydroxide of Li with Al. Journal of Physical Chemistry C, 112 (25) (2008) 9510-9515.

[BRO/ALT1985] Brown, I.D., Altermatt, D. Bond-valence parameters obtained from a systematic analysis of the inorganic crystal structure database. Acta Crystallographica Section B Structural Science, 41 (19985) 244-247.

[CAV/TRI1991] Cavani F., Trifiro F., Vaccari A. Hydrotalcite-type anionic clays: preparation, properties and application. Catalysis Today 11 (1991) 173-301.

[CAV/TRI1991] Cavani, F., Trifiro, F. and Vaccari, A., Hydrotalcite-type anionic clays: Preparation, properties and applications. Catalysis Today, 11 (1991) 173–301.

[CHA/BOT1996] Chalet, L., Bottero, Y.J., Yvon, J., Bouchelaghem, A. Competition between monovalent and divalent anions for calcinated and uncalcinated hydrotalcite: anion exchange and adsorption sites, Colloids and Surfaces, A: Physicochemical and Engineering Aspects, 111 (1996) 167-175.

[COS/MAR1998] Costantino, U., Marmottini, F., Nochchetti, M., Vivani,R. New synthetic routes to hydrotalcite-like coumponds-characterisation and properties of the obtained materials. Eur. J. Inorg. Chem. (1998) 1439-1446.

[COS/MAR1998]Costantino, U., Marmottini, F., Nochchetti, M., Vivani,R. New synthetic routes to hydrotalcite-like coumponds-characterisation and properties of the obtained materials. Eur. J. Inorg. Chem. (1998) 1439-1446.

[CUI/SPA2002] Cui, D. and Spahiu, K., The reduction of U(VI) on corroded iron under anoxic conditions, Radiochimica Acta, 90 (2002) 623-628.

[CUI/SPA2002] Cui, D., Spahiu, K., The reduction of U(VI) on corroded iron under anoxic conditions, Radiochim. Acta 90 (2002) 623-628.

[CUR/KAI2010] Curtius, H., Kaiser, G., Paparigas, Z., Hansen, B., Neumann, A., Klinkenberg, M., Müller, E., Brücher, H. and Bosbach, D. Wechselwirkung mobilisierter Radionuklide mit sekundären Phasen in endlagerrelevanten Formationswässern, Berichte des Forschungszentrums Jülich-4333, ISSN 0944-2952.

[CUR/KAT2005] Curtius, H. and Kattilparampil, Z. Sorption of iodine on Mg-Al-layered double hydroxide. Clay Minerals, 40 (2005) 455-461.

[CUR/PAP2005] Curtius, H., Kattilparampil, Z. Sorption of iodine on MgAl-double layered hydroxide. Clay Minerals, 40 (2005) 455-460.

[CUR/UFE2009] Curtius, H., Ufer, K., and Dardenne, K. Preparation and characterization of Zr(IV)-containing Mg-Al-Cl layered double hydroxide. Radiochimica Acta, 97 (2009) 423-428.

[DAS/PAT2006] Das, J., Patra, B.S., Baliarsingh, N., Parida, K.M. Adsorption of phosphate by layered double hydroxides in aqueous solutions, Appl. Clay. Sci. 32 (2008) 252-258.

[DAV1962] Davies, C.W. (1962) Ion Association. Pp. 41. Butterworths.

[FAO/PRE2012] Faour, A., Mousty, C., Prevot, V., Devouard, B., De Roy, A., Bordet, P., Elkaim, E., and Taviot-Gueho, C. Correlation among structure, microstructure, and electrochemical properties of NiAl-CO_3 layered double hydroxide thin films. Journal of Physical Chemistry, 116 (2012) 15646-15659.

[FER/BAR1997] Fernandez J. M., Barriga C., Ulibarri M. A., Labajos F. M., Rives V., New hydrotalcite-like compounds containing yttrium. Chemistry of Materials 9 (1997) 312–318.

[FER/CUE2010] Fernández, R., Cuevas, J., Mäder, U. K. Modeling experimental results of diffusion of alkaline solutions through a compacted bentonite barrier, Cement and Concrete Research 40 (2010) 1255-1265.

[FET/OLG1999] Fetter, G., Olguin, M.T., Bosch, P., Lara, V.H., Bulbulian, S.: 131I-sorption from aqueous solutions by nitrated hydrotalcites. J. Radioanalytical and Nuclear Chemistry, 241 (1999) 595-599.

[FET/RAM1997] Fetter, G., Ramos, E., Olguin, M.T., Bosch, P., Lopez, T., Bulbulian, S. Sorption of ^{131}Iod- by hydrotalcites. J. Radioanalytical and Nuclear Chemistry, 221 (1997) 63-66.

[FIN/DAR2012] Finck, N., Dardenne, K., Bosbach, D., Geckeis, H. Selenide retention by mackinawite. Environmental Science & Technology 46 (2012) 10004-10011.

[FOR/COS2013] Forano C., Costantino U., Prévot V., Taviot Gueho C. Layered Double Hydroxides (LDH). Chapter 14.1 In: Handbook of Clay Science - Fundamentals, (2013) 745–782.

[FRO/MUS2006] Frost, R.L, Musumeci, A.W. Nitrate absorption through hydrotalcite reformation, J. Colloid and Interface Science 302 (2006) 203-206.

[FRO/MUS2007] Frost, R. L., Musumeci, A. W., Adebajo, M. O., Martens, W. Using thermally activated hydrotalcite for the uptake of phosphate from aqueous media. Journal of Thermal Analysis and Calorimetry, 89 (2007) 95-99.

[GIL/MAC1960] Giles, G.H., MacEwan, T.H., NAKhwa, S.N., Smith, D. Studies in adsorption: Part XI. A system of classification of solution adsorption isotherms and itsuse in diadnosis of adsoption mechanism and in measurement of specific surface areas in solids. J. Chem. Soc. (19969) 3973-3993.

[GOH/LIM2008] Goh, K.-H., Lim, T.-T., Dong, Z. Application of layered double hydroxides for removal of oxyanions. A review,. Water Research, 42 (2008) 1343-1368. Wang, Y., Gao, H. (2006): Compositional and structural control on anion sorption capability of layered double hydroxides (LDHs). J. Colloid and In-terface Sci., 301, 19-26.

[GRAM/MUE1990] Grambow, B., Müller, R. Chemistry of Glass Corrosion in High Saline Brines Mat. Res. Soc. Symp. Proc. 176 (1990) 229-240.

[GRAM2008] Grambow, B. Mobile fission products in nuclear waste disposal, Journal of Contaminat Hydrology 102 (2008) 180-186.

[GRAM2008] Grambow, B., Mobile fission and activation products in nuclear waste disposal, J. Cont. Hydrology, 102 (2008) 180-186.

[HE/WEI2006] He, J., Wei, M., Li, B., Kang, Y., Evans, D.G., Duan, X. Preparation of layered double hydroxides. Struct. Bond, 119 (2006) 89-119.

[HER/PAV1996] Hermosin, M.C., Pavlovic, I., Ulibarri, M.A., Cornejo, J. Hydrotalcites as sorbent for trinitrophenol: sorption capacity and mechanism. Water Res. 30 (1996) 171-177.

[HER/ULI1985] Hernandez-Moreno M. J., Ulibarri M. A., Rendon J. L., Serna C. J., IR characteristics of hydrotalcite-like compounds. Physics and Chemistry of Minerals 12 (1985) 34-38.

[HU/DAV1994] Hu, Y., Davies, P. K. Synthesis, structures and reactions of oxides with the hexagonal MoO3 structure. Mater. Sci. Forum, 152-153 (1994) 277-280.

[HUM/BER2002] Hummel, W., Berner, U., Curti, E., Pearson, F.J., and Thoenen, T. Nagra/PSI chemical thermodynamic data base 01/01. Radiochimica Acta, 90 (2002) 805-813.

[IND/KAM1994] Indria L., Dixit, M.P., Kamath, V. Electrosynthesis of layered double hydroxides of Ni with trivalent cations. J. Power Sources, 52 (1994) 93-97.

[JOE/BUH2010] Jörg, G., Buhnemann, R., Hollas, S., Kivel, N., Kossert, K., Van Winckel, S., and Gostomski, C. L. V. (2010): Preparation of radiochemically pure Se-79 and highly precise determination of its half-life. Appl. Radiat. Isot. 68 (2010) 2339-2351.

[KAN/CHU1999] Kang, M.J., Chun, K.S., Rhee, S.W. Do, Y. Comparision of sorption behaviour of I- and TcO4- on Mg/AL layered double hydroxide, Radiochimica Acta, 85 (1999) 57-63.

[KEN/LIU2010] Kentjono, L., Liu, J.C., Chang, W.C., Irawan, C. Removal of boron and iodine from optoelectronic wastewater using MgAl(NO3) layered double hydroxide. Desalination, 262 (2010) 280-283.

[KLE/BAU1990]Kleber W., Bautsch H.-J., Bohm, J. Einführung in die Kristallographie, Verlag Technik GmbH Berlin (1990) 232-233, 17. Auflage,ISBN: 3-341-00479-3.

[KLO/WHA2002] Kloprogge J. T., Wharton D., Hickey L., Frost R. L., Infrared and Raman study of interlayer anions CO_3^{2-}, NO_3^-, SO_4^{2-} and ClO_4^- in Mg/Al hydrotalcite American Mineralogist 87 (2002) 623-629.

[KLU/ALE1974] Klug, H.P. and Alexander, L.E. (1974) X-Ray Diffraction Procedures. Wiley-Interscience, New York.

[KOO/HOL1977] Kooli M., Holgado, J., Rives, V., Sanroman, S., Ulibarri, M. A. A simple conductivity study of decavandate intercalation in hydrotalcite. Mater. Res. Bull., 32 (1077) 977-98.

[KUL/WAG2013] Kulik, D.A., Wagner, T., Dmytrieva, S.V., Kosakowski, G., Hingerl. E.F., Chudnenko, and K.V., Berner, U. GEM-Selektor geochemical modeling package, revised algorithm and GEMS3K numerical kernel for coupled simulation codes. Computational Geosciences, 17 (2013) 1-24.

[LEH/ZOU1999] Lehmann M., Zouboulis A. I., Matis K. A. Removal of metal ions from dilute aqueous solutions: a comparative study of inorganic sorbent materials. Chemosphere 39, 881-892.

[LI/DUA2006] Li, F. and Duan, X. (2006), Applications of Layered Double Hydoxides. In: Evans, D. G. and Slade, R. C. T. Layered Double Hydroxides, Springer-Verlag, Berlin, Heidelberg.

[LIA/LI2007] Liang, L. Li, L., Journal of Radioanalytical and Nuclear Chemistry 237 (2007) 211-226.

[LOP/BOS1996] Lopez, T., Bosch ,P., Ramos, E., Gomez, R., Novaro, O., Acosta, D. Figueras, F. Synthesis and characterisation of sol-gel hydrotalcites. Structure and texture. Langmuir, 12 (1996) 189-192.

[MAZ/CUR2003] Mazeina L., Curtius H., Fachinger J., Odoj R. Characterization of secondary products of uranium-aluminium material test reactor fuel element corrosion in repository-relevant brine, Journal of Nuclear Materials 323 (2003) 1-7.

[MAZ/CUR2003] Mazeina, L., Curtius, H., Fachinger, J. and Odoj, R., Characterisation of secondary products of uranium-aluminium material test reactor fuel element corrosion in repository-relevant brine, Journal of Nuclear Materials, 323 (2003) 1-7.

[MIK/SAS1984] Mikami, N., Sasaki, M., Horibe, S., Yasunaga, T. Kinetic study of ion exchange of phosphate ions for Cl- in a hydrotalcite-like compound, $Ni_{0.75} Al_{0.25} (OH)_2 Cl_{0.25}$ m H_2O, using the pressure-jump technique. J. Phys. Chem., 88 (1984) 1716-1719.

[MIY/KUM1973] Miyata, S. and Kumura, T. Synthesis of new hydrotalcite-like compounds and their physicochemical properties. Chemistry Letters (1973) 843-848.

[MIY/OKA1977] Miyata, S., Okada, A. (1977): Synthesis of hydrotalcite-like compounds and their physico-chemical properties- the systems Mg^{2+} - Al^{3+} - SO_4^{2-} - and Mg^{2+} - Al^{3+} - CrO_4^{2-} . Clays and Clay Minerals, 25 (1977) 14-18.

[MIY1975] Miyata, S., The synthesis of hydrotalcite-like compounds and their structures and physic-chemical properties, Clays and Clay Minerals, 31 (1975) 369–375.

[MIY1980] Miyata, S. Physicochemical properties of synthetic hydrotalcites in relation to composition. Clays and Clay Minerals, 28 (1980) 50-56.

[MIY1983] Miyata, S. Anion-exchange properties of hydrotalcite-like compounds. Clays and Clay Minerals, 31 (1983) 305-311.

[MIY1983] Miyata, S. Anion-exchange properties of hydrotalcite-like compounds. Clays and Clay Minerals, 31 (1983] 305-311.

[MOR/ANR2012] Morimoto, K., Anraku, S., Hoshino, J., Yoneda, T., Sato, T. Surface complexation reactions of inorganic anions on hydrotalcite-like compounds, Journal of Colloid and Interface Science 384 (2012) 99-104.

[NEW2001] Newville, M. IFEFFIT: Interactive XAFS analysis and FEFF fitting. Journal of Synchrotron Radiation, 8 (2001) 322-324.

[NOS/BEC2008] Noseck, U., Becker, D, Fahrenholz, C., Fein, E., Flügge, J., Kröhn, K.P., Mönig, J., Müller-Lyda, I., Rothfuchs, T., Rübel, A., Wolf, J., Assessment of the long-term safety of repositories, (2008), GRS-237, ISBN 978-3-939355-11-3.

[PAL/FRO2009] Palmer, S.J., Frost, R.L., Nguyen, T. Hydrotalcites and their role in co-ordination of anions in Bayer liquors: Anion binding in layered double hydroxides Coordination Chemistry Reviews 253 (2009) 250-267.

[PRA/KAM2007] Prasanna, S.V., Kamath, P.V., and Shivakumara, C. Synthesis and characterization of layered double hydroxides (LDHs) with intercalated chromate ions. Materials Research Bulletin, 42 (2007) 1028-1039.

[PRA/RAO2006] Prasanna, S. V., Rao, R. A. P., Kamath, P. V. Layered double hydroxides as potential chromate scavengers. J. Colloid Interface Sci., 304 (2006) 292-299.

[RAD/KAM2007] Radha, A.V., Kamath, P.V., and Shivakumara, C. Order and disorder among the layered double hydroxides: combined Rietveld and DIFFaX approach. Acta Crystallographica Section B: Structural Science, 63 (2007) 243-250.

[REN/KUB2009] Renaudin, G., Kubel, F., Rivera, J.P. and Francois, M., Structural phase transition and high temperature phase structure of Friedels salt, $3CaO{\cdot}Al_2O_3{\cdot}CaCl_2{\cdot}10H_2O$. Cement and Concrete Research, 29 (2009) 1937-1942.

[RIV2001] Rives, V. (2001) Layered double hydroxides: Present and future. Nova Science Publishers, New York.

[ROZ/BER2011] Rozov, K., Berner, U., Kulik, D., and Diamond, L.W. Solubility and thermodynamic properties of carbonate bearing hydrotalcite-pyroaurite solid solutions with 3:1 Mg/(Al+Fe) mole ratio. Clays and Clay Minerals, 59 (2011) 215-232.

[SAT/WAK1986] Sato T., Wakabayashi T., Shimada M. Adsorption of various anions by magnesium aluminium oxide ($Mg_{0.7}Al_{0.3}O_{1.15}$). Industrial Engineering Chemistry Research Product Research and Development 25 (1986) 89-92.

[SCH/LAM1996] Scheidegger, A.M., Lamble, G.M., Sparks, D.L. Investigation of Ni sorption on pyrophyllite: An XAFS study, Environ. Sci. Technol. 30 (1996) 548-554.

[SCH/LAM1997] Scheidegger, A.M., Lamble, G.M., Sparks, D.L. Spectroscopic evidence of the formation of mixed-cation hydroxide phases upon metal sorption on clays and aluminium oxides, Journal of Colloid and Interface Science 186 (1997) 118-128.

[SCH/VES2006] Scheidegger, A.M., Vespa, M., Grolimund, D., Wieland, E., Harfouche, M., Bonhoure, I., Dähn, R. The use of (micro)-X-ray absorption spectroscopy in cement research, Waste Management 26 (2006) 699-705.

[SER/BER2000] Serrano J., Bertin V., Bulbulian S. 2000. 99Mo sorption by thermally treated hydrotalcites, Langmuir 16 (2000) 3355-3360.

[SHA1976] Shannon, R.D. Revised effective ionic-radii and systematic studies of interatomic distances in halides and chalcogenides. Acta Crystallographica Section A, 32 (1976) 751-767.

[SHO/SAS1997] Shock, E.L., Sassani, D.C., Willis, M., and Sverjensky, D.A. Inorganic species in geologic fluids: Correlations among standard molal thermodynamic properties of aqueous ions and hydroxide complexes. Geochimica et Cosmochimica Acta, 61 (1997) 907-950.

[SKO/CHR2009]]Skobjerg, L.L., Christiansen, B. C., Nedel, S., Dideriksen, K., Stipp, S. L. S. The role of green rust in the migration of radionuclides: An overview of process that can control mobility of radioactive elements in the environment using as examples Np, Se and Cr. Radiochim. Acta., 98 (2009) 607-612.

[SKO/CHR2009] Skobjerg, L.L., Christiansen, B. C., Nedel, S., Dideriksen, K., Stipp, S. L. S. The role of green rust in the migration of radionuclides: An overview of process that can control mobility of radioactive elements in the environment using as examples Np, Se and Cr. Radiochim. Acta., 98 (2009) 607-612.

[STU/MOR1996] Stumm, W., Morgan, J. Aquatic chemistry: Chemical equilibria and rates in natural waters, Wiley-Interscience Publications, (1996) New York.

[TAV/FEN2010] Taviot-Gueho, C., Feng, Y., Faour, A., Leroux, F. Intercalation chemistry in a LDH system: anion exchange process and staging phenomenon investigated by means of time-resolved, in situ X-ray diffraction, Dalton Trans. 39 (2010) 5994-6005.

[TAY1984] Taylor, R. M., The rapid formation of crystalline double hydroxy salts and other compounds by controlled hydrolysis, Clay Minerals, 19 (1984) 591–603.

[THO/RAJ2004] Thomas G.S., Rajamathi, M., and Kamath, P.V. Diffax simulations of polytypism and disorder in hydrotalcite. Clays and Clay Minerals, 52 (2004) 693-699.

[TRE/NEW1991] Treacy, M.M.J., Newsam, J. M., and Deem, M.W. A general recursion method for calculating diffracted intensities from crystals containing planar faults. Proceedings of the Royal Society, A, 433 (1991) 499-520.

[TRO/BOU2007] Troland, F., Bourric, G., Abdelmoula, M., Refait, P. Feder, F. Fougerite, a new mineral of the pyroaurite-iowaite group: Description and crystal structure. Clays and Clay Minerals 55 (2007) 323-334.

[UFE/KLE2008] Ufer, K., Kleeberg, R., Bergmann, J., Curtius, H., and Dohrmann, R. Refining real structure parameters of disordered layer structures within the Rietveld method, Zeitschrift für Kristallographie Supplements (2008) 151-158.

[ULI/PAV2001] Ulibarri M. A., Pavlovic I., Barriga C., Hermosín M. C., Cornejo J. Adsorption of anionic species on hydrotalcite-like compounds: effect of interlayer anion and crystallinity. Applied Clay Science 18 (2001) 17-27.

[VES/DAE2006] Vespa, M., Dähn, R., Grolimund, D., Wieland, E., Scheidegger, A.M., Spectroscopic investigation of Ni speciation in hardened cement paste, Environ. Sci. Technol. 40 (2006) 2275-2282.

[WAN/GAO2006]]Wang, Y., Gao, H. Compositional and structural control on anion sorption capability of layered double hydroxides (LDHs). J. Colloid and Interface Sci., 301 (2006) 19-26.

[WEI/TOT1996] Weiss, A. and Toth, E. Untersuchungen zur Synthese, Quellungseigenschaften und Anionenaustausch von kristallchemisch modifizierten Doppelhydroxiden vom Hydrotalkit-Typ. Jahrestagung der DTTG-Freiberg (1996) 267–276.

[WIL/FAR2001] Wilke, M., Farges, F., Brown, P.E., Martin, F. Oxidation state and coordination of Fe in minerals. An Fe-XANES spectroscopic study, American Mineralogist 86 (2001) 714-730.

[WIL/NOR2004] Williams, G.R., Norquist, A. J., O'Hare, D. Time-resolved, in situ X-ray diffraction studies of staging during phosphonic acid intercalation into $[LiAl_2(OH)_6]Cl$ H_2O. Chem. Mater., 16 (2004) 975-981.

[YOU/VAN2001] You, Y., Vance, G. F., Zhao, H. Selenium adsorption on Mg-Al and Zn-Al layered double hydroxides. Applied Clay Science, 20 (2001)13-25

7 Occurrence, thermodynamic properties and migration of fission products in the near-field of a repository system

7.1 Thermodynamic properties of aqueous solutions containing iodide, selenite, selenate and caesium

7.1.1 Background and objectives

The thermodynamic properties of iodide, selenite, and selenate in solutions of the oceanic system were systematically investigated by Hagemann et al. [HAG/MOO2005]. Based on a critical evaluation of the available literature and new isopiestic und solubility investigated they derived thermodynamic models that allowed the prediction of water activities, ion activity coefficients in simple and mixed salt solutions at 25 °C. For some subsystems additional measurements were required to fill observed gaps and to complete the developed models.

For caesium no model was available so far. However, the rich number of available literature data (e. g. [CUD/FEL1942] [RAR/MIL1982] [SKR/RUM1993]) promised a good fundament. These literature data were reviewed in parallel to this project [SCH/MUN2012]. It was clear from the beginning that information on some ternary systems was not available so that additional measurements were necessary.

The ambient temperature of the host rock of a deep geological repository will likely by above 25 °C. For example, the observed temperature gradients in northern German clay formations (32 – 24 K/100m [REI/JAH2013]) would lead to temperatures at the designed disposal depth of 770 m of about 35 – 40 °C. In the first 10000 years after the placement of high level waste containers in the repository an increase of temperature will occur due to the heat generated by the radioactive decay of the radionuclides Depending on the host rock and the disposal concept temperatures may rise well above 100 °C in the environment of the container. However, these high temperatures will persist only several hundred years and moderate levels below 80 °C will occur for a much longer period [LAN/DAV2009].

Thermodynamic models derived for ion interactions and solubility constants at 25 °C cannot be applied to different temperatures if there is no sound evidence that the thermodynamic properties stay comparable. For many electrolyte solutions it is well documented that their water activities and ion activity coefficients show are temperature dependency that must be individually determined [SIL/PIT1978]. For iodide, selenite, selenate and caesium solutions such dependencies have been derived only in a few cases (Cs: [HOL/MES1983]) so that comprehensive temperature dependent models could not be developed so far.

Several data types are suitable to derive such models. They include measurements of

- water activity at elevated temperatures (e. g. isopiestic measurements)
- freezing point depression
- boiling point elevation
- heat of solution
- heat of dilution
- heat of mixing
- heat capacity

The principle theory of determining temperature dependencies of ion interaction coefficients has been described by Pitzer and coworkers in several publications [SIL/PIT1977] [SIL/PIT1978] [PIT1983] [PHU/PIT1986]. The essential equations needed to link experimental data with temperature coefficients are summarized in the following chapter.

Within this project, we have concentrated on the evaluation of literature data on the above mentioned methods and complemented them with isopiestic investigations of binary aqueous solutions. For calcium selenite and calcium selenite solubility measurements were undertaken in order to determine the solubility constants at elevated temperatures as well as the change of solubility in solutions of sodium chloride. Attempts were started to measure the activity coefficient of selenite and hydrogen selenite potentiometrically.

7.1.2 Theory: Pitzer ion interaction coefficients and their temperature dependency

7.1.2.1 The Pitzer model

The model of Pitzer [PIT1973] [PIT1991] was used to describe the influence of the solution composition on the activity of water and the ion activity coefficients. The fundamental equation for the osmotic coefficient is found below (7.1):

$$\phi - 1 = -\frac{2}{\sum_i m_i}\left[\begin{array}{l} \frac{A^{\varphi} I^{3/2}}{1+1{,}2\sqrt{I}} + \sum_c \sum_a m_c m_a B_{ca}^{\varphi} + \sum_c \sum_a m_c m_a Z C_{ca} + \\ \sum_c \sum_{c' \neq c} m_c m_{c'} \Phi_{cc'}^{\varphi} + \sum_c \sum_{c' \neq c} \sum_a m_c m_{c'} m_a \Psi_{cc'a} + \\ \sum_a \sum_{a' \neq a} m_a m_{a'} \Phi_{aa'}^{\varphi} + \sum_a \sum_{a' \neq a} \sum_c m_c m_a m_{a'} \Psi_{caa'} + \\ \sum_n \sum_c m_n m_c \lambda_{nc} + \sum_n \sum_a m_n m_s \lambda_{na} + \sum_n \sum_c \sum_a \zeta_{nca} \end{array}\right] \tag{7.1}$$

A^{φ} is the Debye-Hückel coefficient and I the ionic strength. Z is the sum of the ion molalities m_i multiplied with their absolute charge $|z_i|$:

$$Z = \sum_i |z_i| m_i \tag{7.2}$$

B and C are binary coefficients for the interaction between an anion and a cation. Ψ is a ternary coefficient for interaction between three ions (two anions and a cation or one anion and two cations). Φ is a coefficient for the interaction between ions of the same sign (two cations or two anions). λ is a coefficient for the interaction between a neutral species and an ion, ζ a coefficient for the interaction between a neutral species, anion and cation.

For the activity coefficient of cations M the following expression applies:

$$\begin{array}{l} \ln \gamma_M = z_M^2 F + \sum_a m_a B_{Ma} + \sum_a m_a Z C_{Ma} \\ \qquad \sum_{c \neq M} m_c \Phi_{Mc}^{\varphi} + \sum_{c' \neq c} \sum_a m_c m_a \Psi_{Mca} + \sum_a \sum_{a' \neq a} m_a m_{a'} \Psi_{Maa'} + \\ \qquad 2 \sum_n m_n \lambda_{nM} + \sum_n \sum_a m_n m_a \zeta_{nMa} \end{array} \tag{7.3}$$

For anions X an analog expression is valid:

$$\begin{aligned}\ln\gamma_X &= z_X^2 F + \sum_c m_c B_{cX} + \sum_c m_c Z C_{cX} \\ &\sum_{a\neq X} m_s \Phi^{\varphi}_{aX} + \sum_c \sum_{a'\neq X} m_c m_{a'} \Psi_{cXa} + \sum_c \sum_{c'\neq c} m_c m_{c'} \Psi_{cc'X} + \\ &2\sum_n m_n \lambda_{nX} + \sum_n \sum_c m_n m_c \zeta_{ncX}\end{aligned} \tag{7.4}$$

For neutral species the functions reduce to:

$$\ln\gamma_N = 2\sum_c m_c \lambda_{Nc} + 2\sum_a m_a \lambda_{Na} + \sum_c \sum_a m_c m_a \zeta_{Nca} \tag{7.5}$$

The Term F contains the following elements:

$$\begin{aligned}F &= -A^{\phi}\left[\frac{\sqrt{I}}{1+1{,}2\sqrt{I}} + \frac{2}{1{,}2}\ln\left(1+1{,}2\sqrt{I}\right)\right] + \sum_c \sum_a m_c m_a B'_{ca} + \\ &\sum_c \sum_{c'\neq c} m_c m_{c'} \Phi'_{cc'} + \sum_a \sum_{a'\neq a} m_a m_{a'} \Phi'_{aa'}\end{aligned} \tag{7.6}$$

The B terms in the preceding equations read:

$$\begin{aligned}B^{\varphi}_{MX} n\gamma_X &= \beta^{(0)}_{MX} + \beta^{(1)}_{MX} e^{-\alpha_{1,MX}\sqrt{I}} + \beta^{(2)}_{MX} e^{-\alpha_{2,MX}\sqrt{I}} \\ B_{MX} &= \beta^{(0)}_{MX} + \beta^{(1)}_{MX} g\left(\alpha_{1,MX}\sqrt{I}\right) + \beta^{(2)}_{MX} g\left(\alpha_{1,MX}\sqrt{I}\right) \\ B' &= \beta^{(0)}_{MX} + \beta^{(1)}_{MX} \frac{g'\left(\alpha_{1,MX}\sqrt{I}\right)}{I} + \beta^{(2)}_{MX} \frac{g'\left(\alpha_{1,MX}\sqrt{I}\right)}{I} \\ g(x) &= \frac{2}{x^2}\left[1-\left(1+x\right)e^{-x}\right] \\ g'(x) &= \frac{2}{x^2}\left[1-\left(1+x+\frac{x^2}{2}\right)e^{-x}\right]\end{aligned} \tag{7.7}$$

The terms Φ are formed from these expressions:

$$\begin{aligned}\Phi^{\varphi}_{ij} &= \theta_{ij} + {}^{E}\theta_{ij}(I) + I\,{}^{E}\theta'_{ij}(I) \\ \Phi_{ij} &= \theta_{ij} + {}^{E}\theta_{ij}(I) \\ \Phi'_{ij} &= {}^{E}\theta'_{ij}(I)\end{aligned} \tag{7.8}$$

The terms ${}^{E}\theta$ represent integral functions that are discussed in Pitzer (1991) in more detail. They describe unsymmetrical mixing effects between ions of different charge:

$$ {}^{E}\theta_{ij}(I) = \frac{z_i z_j}{4I}\left[J\left(x_{ij}\right) - \frac{1}{2} J\left(x_{ii}\right) - \frac{1}{2} J\left(x_{jj}\right) \right] \tag{7.9} $$

$$ {}^{E}\theta'_{ij}(I) = \frac{{}^{E}\theta_{ij}(I)}{I} \frac{z_i z_j}{8I^2}\left[x_{ij} J'\left(x_{ij}\right) - \frac{1}{2} J'\left(x_{ii}\right) - \frac{1}{2} J'\left(x_{jj}\right) \right] $$

with

$$ x_{ij} = 6 z_i z_j A_{\phi} \sqrt{I} \tag{7.10} $$

The terms J and J‘ are constructed as follows:

$$ J\left(x\right) = \frac{1}{4} - 1 + J_2 \tag{7.11} $$

$$ J'\left(x\right) = \frac{1}{4} - \frac{J_2}{x} + J_3 \tag{7.12} $$

$$ J_2 = \frac{1}{x}\int_0^{\infty} \left(1 - e^{q}\right) y^2 dy \tag{7.13} $$

$$ J_3 = \frac{1}{x}\int_0^{\infty} e^{q-y} y dy \tag{7.14} $$

$$ q = -\frac{x}{y} e^{-y} \tag{7.15} $$

Approximation functions can be used to calculate the integrals in equations (7.13) and (7.14). They have been developed by Harvie (1981) and may be found in [PIT1991] as well.

The Pitzer functions for the osmotic coefficients and the activity coefficients of aqueous species are, in principle, applicable for all temperatures. If data at different temperatures than 25 °C are evaluated, the temperature dependency of the Debye Hückel coefficient A^φ has to be taken into account. Functions to describe this relationship are taken from [MOO2011].

In the same way the variable parameters $\beta^{(0)}$, $\beta^{(1)}$, $\beta^{(2)}$,C, θ, Ψ, λ, and ζ depend on temperature. There is no general dependency that could be applied to all or most coefficients, so that their temperature function must be determined empirically for each interaction. A frequently used pattern for a parameter P contains the following terms:

$$P(T) = a_1 + a_2\left(\frac{1}{T} - \frac{1}{T_r}\right) + a_3 \cdot \ln\left(\frac{T}{T_r}\right) + a_4(T - T_r) + a_5\left(T^2 - T_r^2\right) + a_6\left(\frac{1}{T^2} - \frac{1}{T_r^2}\right) \tag{7.16}$$

This formulation with T_r=298.15 K is centered around 25 °C. At 25 °C all terms beside the first one become zero. Such an approach is especially useful, if for 25 °C parameters already exist and only the temperature dependency is of interest. The temperature coefficients a_2 to a_6 may be converted without loss to alternative Formulation that is centered around other temperatures (e. g. 0 K). For the following evaluations the first and second derivatives of the general formula (7.16) with regard to temperature formula are needed:

$$\frac{\partial P(T)}{\partial T} = -a_2\frac{1}{T^2} + a_3 \cdot \frac{1}{T} + a_4 + 2a_5T - 2a_6\frac{1}{T^3} \tag{7.17}$$

$$\frac{\partial^2 P(T)}{\partial T^2} = 2a_2\frac{1}{T^3} - a_3 \cdot \frac{1}{T^2} + 2a_5 + 6a_6\frac{1}{T^4} \tag{7.18}$$

7.1.2.2 Solution enthalpy

If a chemical substance B is dissolved in water, a solution enthalpy $\Delta_L h$ is observed (the negative amount of the measured solution heat). Is is composed of the partial molar enthalpy H_{A*} and H_{B*} of the pure solvent A (water) and solute B (salt) and two substances in the solution H_A and H_B:

$$\Delta_L h = n_A(H_A - H_{A*}) + n_B(H_B - H_{B*}) \tag{7.19}$$

An alternative formulation leads to

$$\Delta_L h = n_A H_A + n_B H_B - (n_A H_{A*} + n_B H_{B*}) = H - H_* \tag{7.20}$$

Therefore, the solution enthalpy can be expressed as the difference between the total enthalpy of the solution and the enthalpy of the pure substances H_*. $\Delta_L h$ is often written as L. The difference $H_B - H_{B*}$ is called the partial solutions enthalpy of the solute:

$$\Delta_L H_B = H_B - H_{B*} \tag{7.21}$$

On the other hand, the difference $H_A - H_{A*}$ is equal to the dilution enthalpy of water:

$$\Delta_L H_A = H_A - H_{A*} \tag{7.22}$$

If the observed solution enthalpy $\Delta_L h$ is related to the amount (mol) of the solute n_B, the integral molar solution enthalpy, the integral molar solution enthalpy is obtained:

$$\Delta_L^{in} H_B = \frac{\Delta_L h}{n_B} \tag{7.23}$$

If the amount (mol) of the solute n_B approaches zero, the integral molar solution enthalpy becomes equal to its limit value the partial molar solution enthalpy at infinite dilution:

$$\lim_{n_B \to 0} \Delta_L^{in} H_B = \Delta_L H_{B\infty} = H_{B\infty} - H_{B*} \tag{7.24}$$

At amounts n_B above zero, the observed integral molar solution enthalpy consists of two parts: the partial molar solution enthalpy at infinite dilution and the molar excess solution enthalpy that describes the non-ideal behavior of the solution.

$$\Delta_L H_B^{Ex} = H_B - H_{B\infty} \tag{7.25}$$

$$\Delta_L^{in} H_B = \frac{\Delta_L h}{n_B} = \Delta_L H_{B\infty} + \Delta_L H_B^{Ex} \tag{7.26}$$

Combination of (7.26) and (7.19) results in:

$$\Delta_L^{in} H_B = \frac{\Delta_L h}{n_B} = \frac{n_A}{n_B} \Delta_L H_A + \Delta_L H_B \tag{7.27}$$

The molar excess enthalpy is often described with the symbol ${}^{\phi}L$:

$${}^{\phi}L = \Delta_L H_B^{Ex} \tag{7.28}$$

The solution enthalpy may then be written as

$$\Delta_L h = n_B \Delta_L H_{B\infty} + \Delta_L h^{Ex} \tag{7.29}$$

After division by RT^2 the different formulations of the excess enthalpy read as follows:

$$\frac{\Delta_L h^{Ex}}{m_{H_2O} RT^2} = \frac{n_B \Delta_L H_B^{Ex}}{m_{H_2O} RT^2} = \frac{m_B \Delta_L H_B^{Ex}}{RT^2} = \frac{L}{m_{H_2O} RT^2} = \frac{m_B \, {}^{\phi}L}{RT^2} \tag{7.30}$$

For the solution enthalpy Phutela und Pitzer [PHU/PIT1986] derived the following expression that relates the temperature dependence with of the ion interaction coefficients (B^L, C^L, Ψ^L, θ^L) with the excess enthalpy:

$$\begin{aligned} \frac{\Delta_L h^{Ex}}{m_{H_2O} RT^2} = \frac{L}{m_{H_2O} RT^2} = \frac{A_L I}{RT^2} \frac{\ln\left(1 + b\sqrt{I}\right)}{b} \\ -2\sum_M \sum_X m_M m_X B_{MX}^L - \sum_M \sum_X m_M m_X Z C_{MX}^L \\ -\sum_M \sum_N m_M m_N \theta_{MN}^L - \sum_X \sum_Y m_X m_Y \theta_{XY}^L \\ -\frac{1}{2}\sum_M \sum_N \sum_X m_M m_N m_Y \psi_{MNX}^L - \frac{1}{2}\sum_M \sum_X \sum_Y m_M m_X m_Y \psi_{MXY}^L \end{aligned} \tag{7.31}$$

A slightly different but numerically equal formulation looks this way:

$$
\begin{aligned}
\Delta_L h^{Ex} = L = A_L I \frac{\ln\left(1+b\sqrt{I}\right)}{b} m_{H_2O} \\
-2RT^2 m_{H_2O}\sum_M\sum_X m_M m_X B_{MX}^L - RT^2 m_{H_2O}\sum_M\sum_X m_M m_X ZC_{MX}^L \\
-RT^2 m_{H_2O}\sum_M\sum_N m_M m_N \theta_{MN}^L - RT^2 m_{H_2O}\sum_X\sum_Y m_X m_Y \theta_{XY}^L \\
-\frac{1}{2}RT^2 m_{H_2O}\sum_M\sum_N\sum_X m_M m_N m_Y \psi_{MNX}^L \\
-\frac{1}{2}RT^2 m_{H_2O}\sum_M\sum_X\sum_Y m_M m_X m_Y \psi_{MXY}^L
\end{aligned}
\tag{7.32}
$$

The expression for the partial molar excess solution enthalpy is then:

$$
\begin{aligned}
\frac{\Delta_L h^{Ex}}{n_B} = \Delta_L H_B^{Ex} = L^{\phi} = A_L \frac{I}{m}\frac{\ln\left(1+b\sqrt{I}\right)}{b} \\
-2RT^2\sum_M\sum_X \frac{m_M m_X}{m} B_{MX}^L - RT^2\sum_M\sum_X \frac{m_M m_X}{m} ZC_{MX}^L \\
-RT^2\sum_M\sum_N \frac{m_M m_N}{m}\theta_{MN}^L - RT^2\sum_X\sum_Y \frac{m_X m_Y}{m}\theta_{XY}^L \\
-\frac{1}{2}RT^2\sum_M\sum_N\sum_X \frac{m_M m_N m_Y}{m}\psi_{MNX}^L - \frac{1}{2}RT^2\sum_M\sum_X\sum_Y \frac{m_M m_X m_Y}{m}\psi_{MXY}^L
\end{aligned}
\tag{7.33}
$$

For the observed solution enthalpy $\Delta_L h$ the following expression is valid:

$$
\begin{aligned}
\frac{\Delta_L h}{n_2} = \Delta_L H_{B\infty} + \Delta_L H_B^{Ex} = \Delta_L H_{B\infty} + {}^{\phi}L \\
= \Delta_L H_{B\infty} + \left(\nu_M + \nu_X\right)\left|z_M z_X\right| A_L \frac{\ln\left(1+b\sqrt{I}\right)}{2b} \\
-2\nu_M \nu_X RT^2\sum_M\sum_X mB_{MX}^L - 2\nu_M \nu_X \nu_M z_M RT^2\sum_M\sum_X m^2 C_{MX}^L
\end{aligned}
\tag{7.34}
$$

In the case of a simple (binary) solution consisting only of cations M and anions X equation (7.33) reduces to:

$$\frac{\Delta_L h^{Ex}}{n_B} = L^{\phi} = (\nu_M + \nu_X)|z_M z_X| A_L \frac{\ln\left(1 + b\sqrt{I}\right)}{2b} \\ - 2\nu_M \nu_X RT^2 \sum_M \sum_X m B_{MX}^L - 2\nu_M \nu_X \nu_M z_M RT^2 \sum_M \sum_X m^2 C_{MX}^L \tag{7.35}$$

where

$$\frac{m_{H_2O}}{n_B} = \frac{1}{m_B} = \frac{1}{m} \tag{7.36}$$

and

$$A_L = 4RT^2 \left(\frac{\partial A_\phi}{\partial T} \right)_P \tag{7.37}$$

The derivation of the Debye Hückel coefficient can be accomplished by using the functions summarized in [MOO2011]. In some earlier publication [SIL/PIT1978] instead of A_L the symbol A_H is used. Moreover, for A_H a deviating derivation is found:

$$A_L = A_H = 6RT^2 \left(\frac{\partial A_\phi}{\partial T} \right)_P \tag{7.38}$$

In that case the quotient in the first term of equation (7.35) contains 3b instead of 2b. The terms B^L and C^L designate the temperature dependence of the ion interaction coefficients B and C:

$$B_{MX}^L = \left(\frac{\partial B}{\partial T} \right)_{p,I} \quad mit \; \beta_{MX}^{(i)L} = \left(\frac{\partial \beta_{MX}^{(i)}}{\partial T} \right)_{p,I} \tag{7.39}$$

$$C_{MX}^L = \left(\frac{\partial C}{\partial T} \right)_{p,I} \tag{7.40}$$

Based on the general temperature function for interaction parameters (7.16) the formulation for B^L (and analogous for C^L) reads

$$B^L = \left(\frac{\partial B}{\partial T}\right)_{p,m} = -a_2 \frac{1}{T^2} + a_3 \frac{1}{T} + a_4 + 2a_5 T - 2a_6 \frac{1}{T^3} \tag{7.41}$$

For the evaluation of solution enthalpy measurements this expression is introduced into formula (7.31) or (7.33).

7.1.2.3 Dilution enthalpy

If an aqueous solution 1 of a salt is diluted to solution 2, a dilution enthalpy $\Delta_D h_B$ occurs. It is the difference of the excess solution enthalpies of the starting and the resulting solutions:

$$\Delta_D h = \Delta_D h^{Ex} = \Delta_D h_2^{Ex} - \Delta_D h_1^{Ex} = L_2 - L_1 \tag{7.42}$$

If the dilution enthalpy is related to the amount (mol) of the solute n_B the molar dilution enthalpy $\Delta_D H_B$ is obtained:

$$\Delta_D H_B = \frac{\Delta_D h}{n_B} \tag{7.43}$$

It is the difference of the molar excess solution enthalpies of the starting $\Delta_D H_{B,1}^{Ex}$ and the resulting solution $\Delta_D H_{B,2}^{Ex}$:

$$\Delta_D H_B = \Delta_D H_B^{Ex} = \Delta_D H_{B,2}^{Ex} - \Delta_D H_{B,1}^{Ex} = {}^{\phi}L_2 - {}^{\phi}L_1 \tag{7.44}$$

The molar dilution enthalpy is related to the ion interaction coefficients in the following way:

$$\begin{aligned}\Delta_D H_B = \frac{\Delta_D h}{n_B} = \Delta_S H_{B,2}^{Ex} - \Delta_S H_{B,1}^{Ex} = {}^{\phi}L_2 - {}^{\phi}L_1 = (\nu_M + \nu_X)|z_M z_X| \frac{A_L}{2b} \ln\left(\frac{1+b\sqrt{I_2}}{1+b\sqrt{I_1}}\right) \\ -2\nu_M \nu_X RT^2 \left[B_{MX}^L(I_2) m_{b,2} - B_{MX}^L(I_1) m_{b,1}\right] \\ -2\nu_M \nu_X \nu_M z_M RT^2 C_{MX}^L \left(m_{b,2}^2 - m_{b,1}^2\right)\end{aligned} \tag{7.45}$$

7.1.2.4 Heat capacity

The heat capacity of an aqueous solution c_P consists of the molar heat capacity of the solvent (water) $C_{P,A}^0$ und the solute $C_{P,B}$

$$c_P = n_A C_{P,A}^0 + n_B C_{P,B} \tag{7.46}$$

Division by the amount (mol) of the solute lead to the molar heat capacity of the solution:

$$C_P = \frac{c_P}{n_B} = \frac{n_A C_{P,A}^0 + C_{P,B}}{n_B} \tag{7.47}$$

The molar heat capacity of the solute $C_{P,B}$ depends on concentration. If the amount of the solute n_B approaches zero, the molar heat capacity of the solute at infinite dilution is obtained:

$$\lim_{n_B \to 0} C_P = C_p^0 = C_{P,B}^0 \tag{7.48}$$

In the same way as solution enthalpies heat capacities of solutions are may be divided into ideal and non-ideal fractions. The difference between the observed molar heat capacity and the molar heat capacity at infinite dilution is called the molar excess heat capacity $C_{P,B}^{Ex}$ (sometimes the symbol J is used [PIT1983]).

$$C_{P,B}^{Ex} = J = C_P - C_{P,B}^0 \tag{7.49}$$

In that case, the molar heat capacity of a solution is constituted from three parts:

$$C_P = C_{P,A}^0 + C_{P,B}^0 + C_{P,B}^{Ex} \tag{7.50}$$

The molar excess heat capacity is related to ion interaction coefficients in the following way [PIT1983]:

$$\begin{aligned} C_{P,B}^{Ex} = J = A_J I \frac{\ln\left(1+b\sqrt{I}\right)}{b} \\ -2RT^2 \sum_M \sum_X m_M m_X B_{MX}^J - RT^2 m_{H_2O} \sum_M \sum_X m_M m_X Z C_{MX}^J \\ -RT^2 \sum_M \sum_N m_M m_N \Phi_{MN}^J - RT^2 m_{H_2O} \sum_X \sum_Y m_X m_Y \Phi_{XY}^J \\ -\frac{1}{2} RT^2 \sum_M \sum_N \sum_X m_M m_N m_Y \psi_{MNX}^J \\ -\frac{1}{2} RT^2 \sum_M \sum_X \sum_Y m_M m_X m_Y \psi_{MXY}^J \end{aligned} \tag{7.51}$$

In the special case of a simple binary salt solution this expressions simplifies to

$$\begin{aligned} C_{P,B}^{Ex} = \left(\nu_M + \nu_X\right)\left|z_M z_X\right| A_J \frac{\ln\left(1+b\sqrt{I}\right)}{2b} \\ -2\nu_M \nu_X RT^2 m B_{MX}^J - 2\nu_M \nu_X RT^2 m^2 \left(\nu_M z_M\right) C_{MX}^J \end{aligned} \tag{7.52}$$

The parameters B^J and C^J are related to the interaction parameters B, B^L and C,C^L in the following way (analog expressions apply for Ψ_{MX}^J and θ_{MN}^J):

$$B_{MX}^J = \left(\frac{\partial^2 B_{MX}}{\partial T^2}\right)_{p,I} + \frac{2}{T}\left(\frac{\partial B_{MX}}{\partial T}\right)_{p,I} \tag{7.53}$$

$$C_{MX}^J = \left(\frac{\partial^2 C_{MX}}{\partial T^2}\right)_{p,I} + \frac{2}{T}\left(\frac{\partial C_{MX}}{\partial T}\right)_{p,I} \tag{7.54}$$

With regards to the general temperature function (7.16) the interaction parameters may be written as follows:

$$B_{MX}^J = \frac{a_3}{T^2} + \frac{2a_4}{T} + 6a_5 + \frac{2a_6}{T^4} \tag{7.55}$$

$$C_{MX}^J = \frac{a_3}{T^2} + \frac{2a_4}{T} + 6a_5 + \frac{2a_6}{T^4} \tag{7.56}$$

7.1.3 Experimental Methods

7.1.3.1 Isopiestic Experiments

Isopiestic measurements were performed at 25 to 90 °C. The method has been described earlier in detail [HAG/MOO2005]. As for this project, isopiestic measurements were to be conducted at higher temperatures, the experimental set up from earlier experiments at 25 °C underwent some revision. Up to 40 °C, isopiestic vessels were placed in an open water bath as shown below (**Fig. 7.1**).

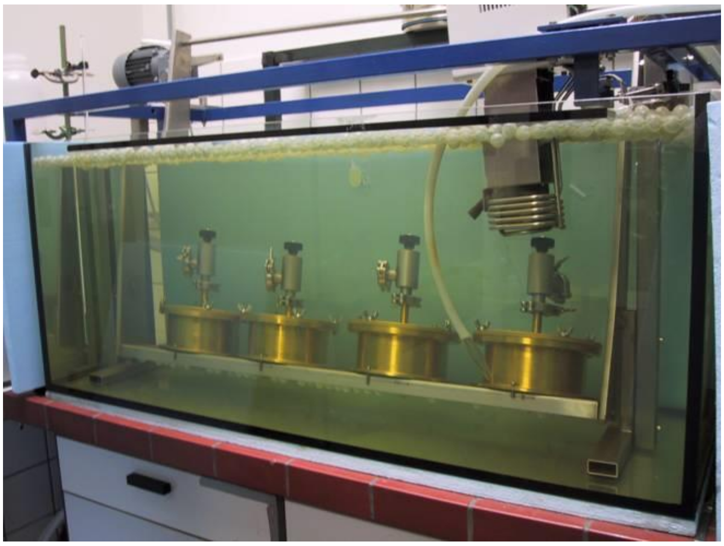

Fig. 7.1 Experimental set up for isopiestic measurements up to 40 °C

For higher temperatures the vessels were stored in ovens, whose temperature was controlled at the required temperature (60 or 90 °C). For temperatures above 40 °C the vessel itself had to be redesigned. To avoid condensation of steam in the equilibrated solutions upon cooling it had to be ensured that each cup inside the vessel be tightly closed prior to the removal from the oven (or the water bath at 40 °C, respectively). To accomplish this, a second lid was installed inside the vessel, just above the cups, which on its lower side was covered with a special rubber. Upon removal from the tempered environment, the second lid was lowered immediately using rods going through the first lid and being tightened to keep the vessels airtight.

As it was anticipated the equilibration at higher temperatures should proceed quicker than at 25 °C, the vessels were typically not rocked inside the ovens (at temperatures higher than 40 °C, **Fig. 7.2**). In some cases, a device was installed inside the ovens to exert a gentle rocking motion on the vessels (**Fig. 7.3**).

Fig. 7.2 Isopiestic vessel inside an oven

Measurements with Na_2SeO_3 and K_2SeO_3 at 60 and 90 °C were conducted with added NaOH, resp. KOH in order to prevent the formation of Hydrogen selenites. Due to the alkaline milieu the tantalum cups had to be replaced by polypropylene cups. Previous measurements have shown that at higher temperatures selenite can be reduced by the metallic surface to red selenium.

Fig. 7.3 This picture shows a motor fixed at the outside of an oven to exert a gentle rocking motion to the board on which the isopiestic vessels rest

The compositions of equilibrated solutions were determined by reweighing, taking buoyancy into account. Each cup was visually inspected for clues as to oxidation of the solution, or droplets occurring at the surface of the rubber.

Typically, the variance between the smallest and highest concentration of binary salts in parallel cups was less than 0.3 wt. - %.

Stock solutions were prepared using the chemicals and methods described in the annex. Their concentration was determined by one of the following methods:

- Weight of the dried salt and the water used for preparing the stock solution: NaCl, NaI, KI, CsCl, Cs_2SO_4
- Weight of the dry residue: $MgSeO_4$, Na_2SeO_3, Na_2SeO_4, K_2SeO_4
- ICP-OES: $CaSeO_4$, K_2SeO_3
- $CaCl_2$: density

7.1.3.2 Solubility measurements with calcium selenite and calcium selenite

Calcium selenite and calcium selenate were prepared using the methods described in the annex (B.2). Weighed amounts of the compounds (1 or 2 g) were added to sodium chloride solutions (15 or 30 g) of various concentrations in glass bottles. The closed bottles were shaken overhead at 25, 40 or 60 °C for at least four months. One bottle for each salt at each temperature served as a control experiment. Once a month a sample was taken and the selenium concentration determined using ICP-OES. After five months it became obvious that significant changes in the solution composition did not take place after one month experimental time. After that, all batches were sampled and analysed.

7.1.4 Experimental results and parameter estimation for aqueous Systems with selenite and selenate

7.1.4.1 The system Na_2SeO_3-H_2O

Pitzer Ion interaction coefficients for the system Na_2SeO_3-H2O have been determined by [HAG/MOO2012] at 25 °C. No experimental data were available that could be used to derive Pitzer coefficients at higher temperatures. In the course of this study isopiestic measurements were performed at 40, 60, and 90 °C at concentrations up to 4.9 mol/kg. Their results are summarized in chapter B.7. At concentrations of 1 mol/kg and higher the osmotic coefficients of sodium selenite solutions are decreasing with temperature (**Fig. 7.4**). Based on these data the interaction coefficients in **Tab. 7.1** were calculated. The experimental and calculated osmotic coefficients agree very well.

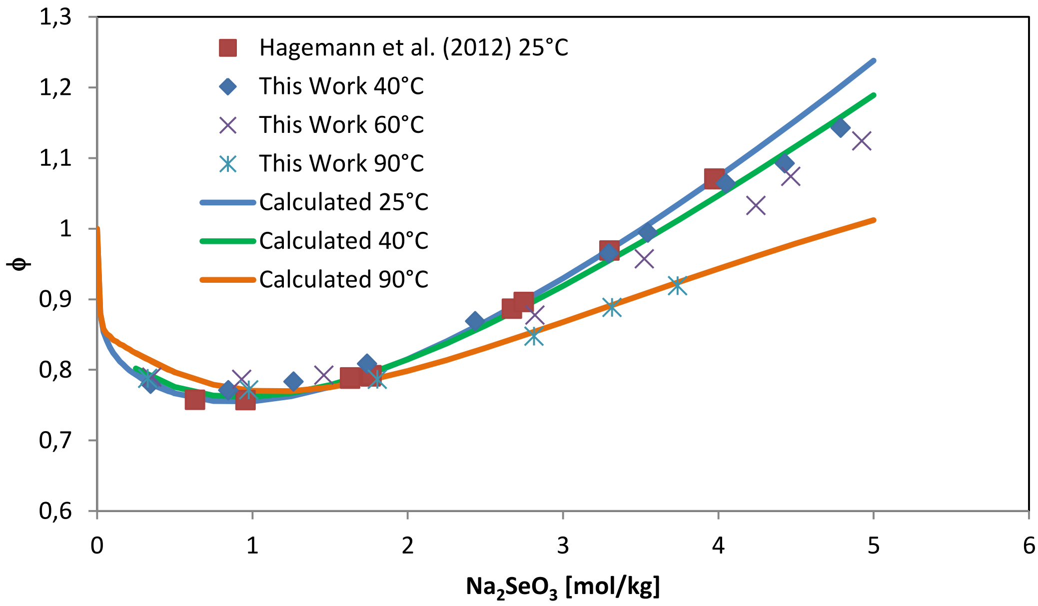

Fig. 7.4 Experimental and calculated osmotic coefficients of Na_2SeO_3 solutions

Tab. 7.1 Temperature dependent Pitzer coefficients for Na_2SeO_3

Parameter	**a_1 = p(25 °C)**	**a_4**
$\beta^{(0)}$	0.09196	0.000533821
$\beta^{(1)}$	1.60028	0.0180793
$\beta^{(2)}$		
C_γ	0.00118	-4.40167E-05
$\alpha^{(1)}$	2	0
$\alpha^{(2)}$	0	0

7.1.4.2 The system K_2SeO_3-H_2O

Pitzer Ion interaction coefficients for the system K_2SeO_3-H2O have been determined by [HAG/MOO2012] at 25 °C. Further isopiestic measurements were planned to extent the model to higher temperature. However, a comparison of the density of our stock solution with literature data showed that our solutions had a significant higher density than would be expected. A closer examination of the solution composition and concentration by using different methods (gravimetry, ICP-OES, drying at 105 and 150 °C) revealed that in the commercial product used for preparing the stock solutions (Alfa Aesar) potassium and selenium did not have the expected stoichiometric ratio (2:1). Instead, a lower value was found which lead to the conclusion that the potassium selenite must contain considerable amounts of potassium hydrogen selenite, $KHSeO_3$ or polyselenites with the general formula $K_{2+2x}Se_xO_{3+2x}\cdot yH_2O$. A number of isopiestic measurements in this study but also data from [HAG/MOO2012] on K_2SeO_3 that were based on the same product had to be disregarded. After this finding a new stock solution of K_2SeO_3 has been prepared by the procedure in the annex B.

Another problem occurred during the isopiestic equilibration at 90 °C. Some cups containing K_2SeO_3 solution turned yellow at the end of the measurements and in one case a precipitate could be identified. However this behaviour had no significant effect on the osmotic coefficient as the affected solutions are in line with other, undisturbed solutions.

A consequence of these findings was that at the end of the study no reliable data were available for 25 °C and only two data points for 40 °C. A re-investigation at both temperatures will be necessary to derive a model that can be used in the full temperature range between 25 and 90 °C.

The available data at 40, 60, and 90 °C show that the osmotic coefficients decrease slightly with temperature. However, no temperature function was needed to reflect this tendency. The osmotic coefficients, calculated using the optimized parameters in **Tab. 7.2**, agree well with the experimental data at 40 to 90 °C (**Fig. 7.5**).

Tab. 7.2 Pitzer coefficients for K_2SeO_3 solutions

Parameter	**a_1 = p(25 °C)**
$\beta^{(0)}$	0.2092
$\beta^{(1)}$	1.9927
$\beta^{(2)}$	
C_γ	-0.0030336
$\alpha^{(1)}$	2
$\alpha^{(2)}$	0

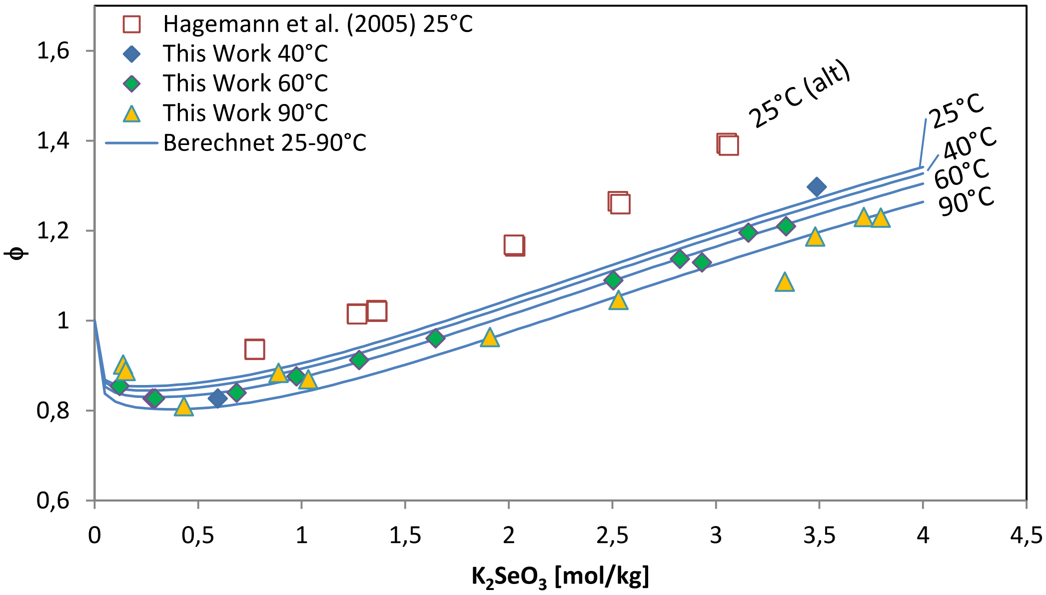

Fig. 7.5 Experimental and calculated osmotic coefficients of K_2SeO_3 solutions

7.1.4.3 The systems $CaSeO_3$-H_2O and NaCl-$CaSeO_3$-H_2O

Between 20 °C and 80 °C Calcium selenite crystallizes from a saturated solution as the monohydrate $CaSeO_3 \cdot H_2O$ [DUM/BRO1997]. Based on a critical comparison of literature data Oli et al. [OLI/NOL2005] recommended the solubility constant

$$\log K\ (298.15K) = -6.4 \pm 0.25$$

No data were available in the literature on the solubility of calcium selenite in salt solutions. The results of our measurements at 25, 40 and 60 °C are summarized in **Tab. B.37ff** (annex B) and shown in **Fig. 7.7**. They show that the up to about 2.5 mol/kg

NaCl the solubility is increasing whereas at higher concentrations a decrease is observed. With increasing temperature the solubility decreases at all concentrations.

In our first approach we assumed that the system NaCl-$CaSeO_3$-H_2O could be modelled without any additional ion interaction coefficients besides those already known:

- Na-Cl, Na-Ca, Na-Ca-Cl. (from the THEREDA database)
- Na-SeO_3 (from this study)

The solubility of $CaSeO_3 \cdot H_2O$ is very low (< 10-3 mol/kg) so that the binary interaction between Ca^{2+} and SeO_3^{2-} does not contribute to the activity coefficient of both ions. The same applies for the ternary interaction Na-Ca-SeO_3. The solubility constant was taken from the NEA report [OLI/NOL2005].

Based on these data the solubility of $CaSeO_3 \cdot H_2O$ in NaCl solutions at 25 °C was calculated. As **Fig. 7.7** shows the modelled line is considerably higher than the experimental values. Obviously the recommended solubility constant in the NEA database is too high. In the next step, the constant was derived by calculating the activity coefficients for calcium and selenite as well as the activity of water in all batches. At all temperatures the ion activity products

$$K = a_{Ca^{2+}} a_{SeO_3^{2-}} a_{H_2O} \tag{7.57}$$

varied only very weak. We found

log K (298.15 K) = -6.62 ± 0.02

log K (313.15 K) = -6.68 ± 0.02

log K (333.15 K) = -6.75 ± 0.02

The temperature dependency is weak but clearly linear (**Fig. 7.6**) and may be expressed by:

$$\log \mathrm{K}(T) = -6.61 - 0{,}00401(T - 298.15K) \tag{7.58}$$

Using this expression the calculated solubilities agree perfect with the experimental values (**Fig. 7.7** and **Fig. 7.8**).

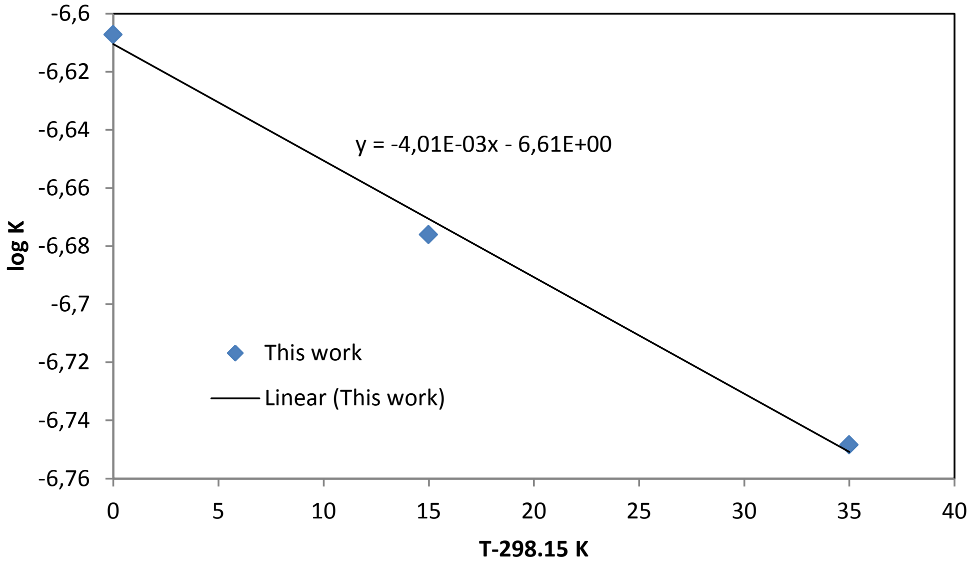

Fig. 7.6 Temperature dependence of the solubility constant for $CaSeO_3 \cdot H_2O$ between 298.15 and 333.15 K

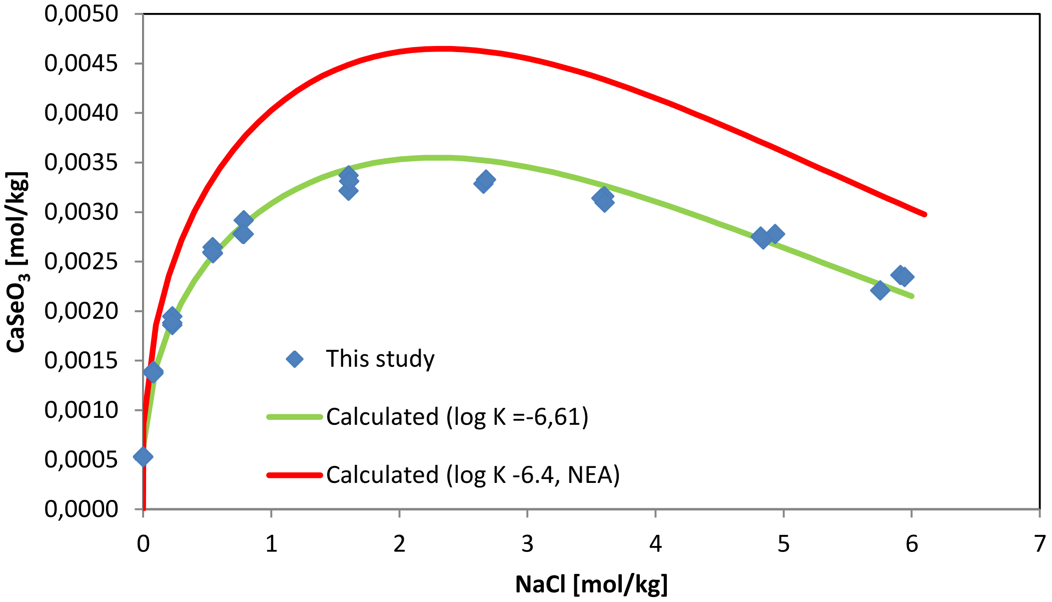

Fig. 7.7 Experimental and calculated solubility of $CaSeO_3 \cdot H_2O$ in NaCl solutions at 25° C

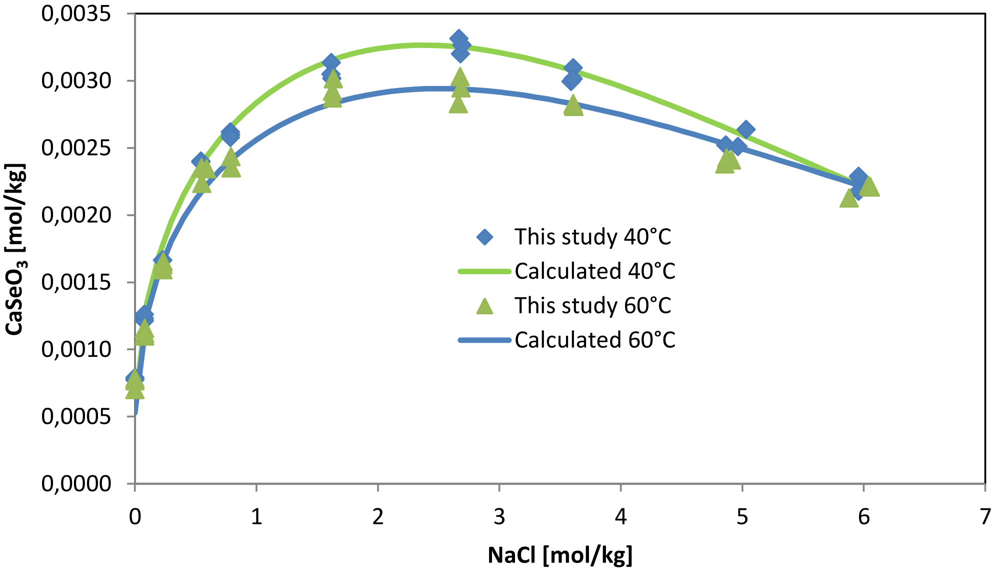

Fig. 7.8 Experimental and calculated solubility of $CaSeO_3 \cdot H_2O$ in NaCl solutions at 40° C and 60° C

7.1.4.4 The system Na_2SeO_4-H_2O

Pitzer Ion interaction coefficients for the system Na_2SeO_4-H_2O have been determined by [HAG/MOO2012] at 25 °C. No experimental data were available that could be used to derive Pitzer coefficients at higher temperatures. In the course of this study isopiestic measurements were performed at 40, 60, and 90 °C at concentrations up to 4.2 mol/kg. Their results are summarized in chapter B.7. At concentrations of 1 mol/kg and higher the osmotic coefficients of sodium selenite solutions are decreasing with temperature (**Fig. 7.9**). Based on these data the interaction coefficients in **Tab. 7.3** were calculated. The experimental and calculated osmotic coefficients fit very well.

Tab. 7.3 Temperature dependent Pitzer coefficients for Na_2SeO_4

Parameter	**a_1**	**a_4**
$\beta^{(0)}$	0.09771	-2.55183E-05
$\beta^{(1)}$	0.78265	0.0360869
C_γ	0	0
$\alpha^{(1)}$	2	

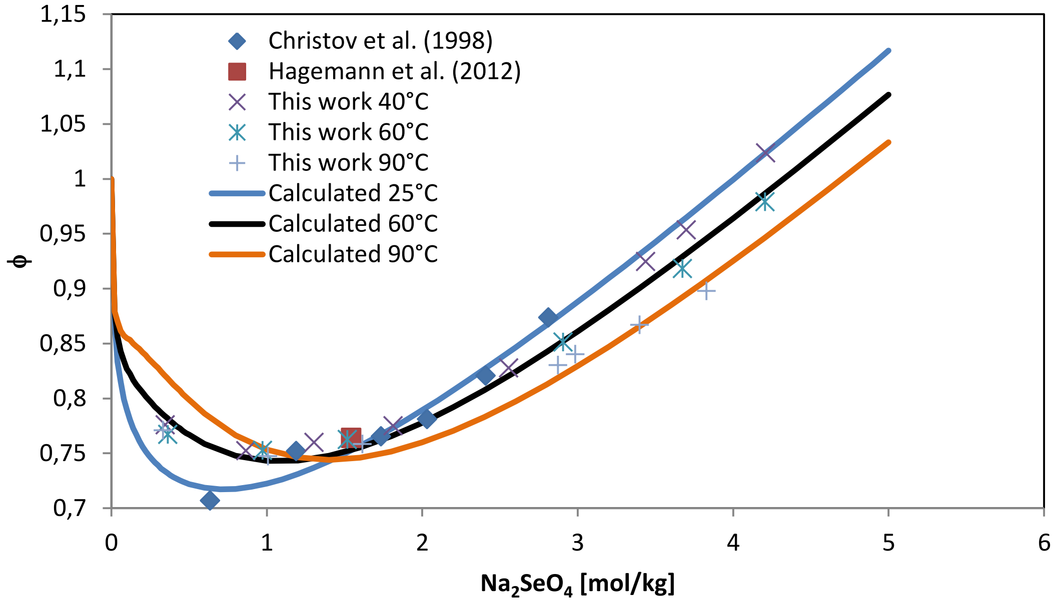

Fig. 7.9 Experimental and calculated osmotic coefficients of Na_2SeO_4 solutions

7.1.4.5 The system K_2SeO_4-H_2O

Pitzer Ion interaction coefficients for the system K_2SeO4-H_2O have been determined by [HAG/MOO2012] at 25 °C. After the completion of that report we became aware of another data source that was previously omitted when the interaction parameters were determined [OJK/CHR1999]. However, their data appear to be strongly scattered and generally too low in comparison to our data and the point from Vojtisek and Ebert [VOJ/EBE1990]. No new parameter evaluation was conducted for 25 °C.

No experimental data were available that could be used to derive Pitzer coefficients at higher temperatures. A single source reported heat of solution data, but only for a very diluted solution (0.11 mol/kg) and without possibility to extrapolate to zero ionic strength [SEL/ZUB1962].

Additional isopiestic measurements were performed at 40, 60, and 90 °C at concentrations up to 5.5 mol/kg. Their results are summarized in chapter B.7. At all concentrations the osmotic coefficients of potassium selenate solutions are decreasing with temperature (**Fig. 7.10**). Based on these data the interaction coefficients in **Tab. 7.4** were calculated. The experimental and calculated osmotic coefficients fit very well.

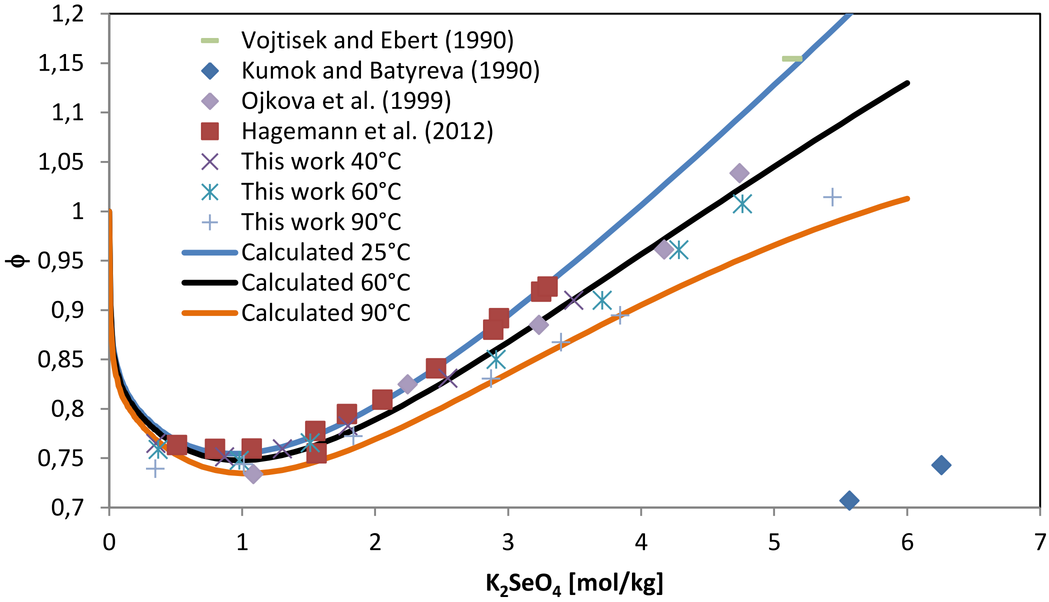

Fig. 7.10 Experimental and calculated osmotic coefficients of K_2SeO_4 solutions

Tab. 7.4 Temperature dependent Pitzer coefficients for K_2SeO_4

Parameter	a_1	a_4
$\beta^{(0)}$	0.09481	0.000403623
$\beta^{(1)}$	1.62335	0.00741599
$\beta^{(2)}$		
C_γ	0.00021	-2.99411E-05
$\alpha^{(1)}$	2	0
$\alpha^{(2)}$	0	0

7.1.4.6 The system $MgSeO_4$-H_2O

Pitzer Ion interaction coefficients for the system $MgSeO_4$-H_2O have been determined by [HAG/MOO2012] at 25 °C. No experimental data were available that could be used to derive Pitzer coefficients at higher temperatures. In the course of this study isopiestic measurements were performed at 40, 60, and 90 °C at concentrations up to 3.1 mol/kg. Their results are summarized in chapter B.7. At all concentrations the osmotic coefficients of magnesium selenite solutions are decreasing with temperature (**Fig. 7.11**). Based on these data the interaction coefficients in **Tab. 7.5** were calculated. The experimental and calculated osmotic coefficients fit very well up to 60 °C. The agreement is less satisfactory at 90 °C. Although it was possible to improve the modelling by adding four more thermal parameters (a_4 for C^γ and a_3 for $\beta^{(0)}$, $\beta^{(1)}$ and C^γ) this way was not chosen because of the limited number of experimental points and the danger of overfitting.

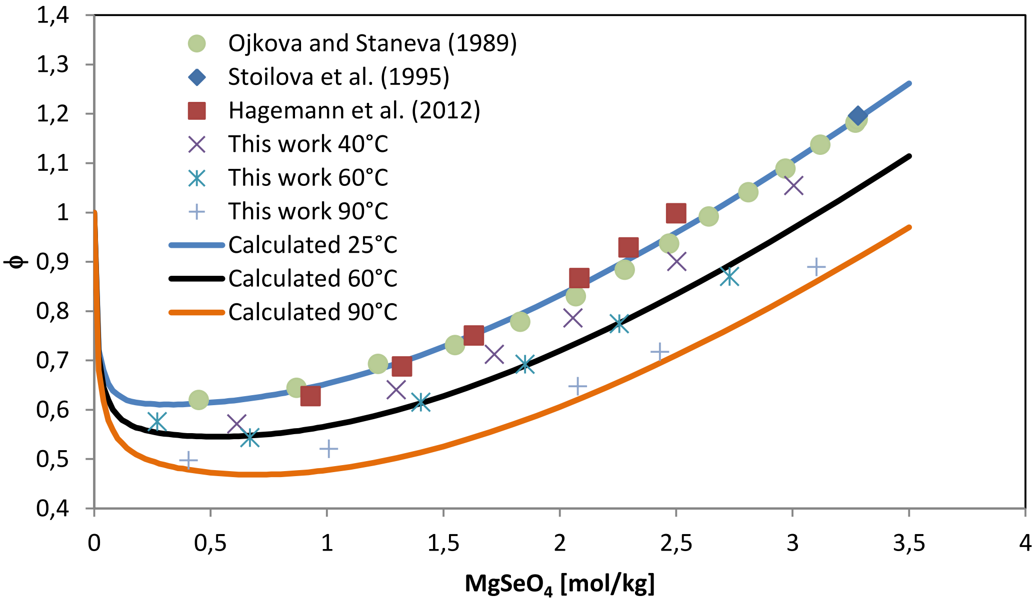

Fig. 7.11 Experimental and calculated osmotic coefficients of MgSeO4 solutions

Tab. 7.5 Temperature dependent Pitzer coefficients for $MgSeO_4$

Parameter	$\mathbf{a_1}$	$\mathbf{a_4}$
$\beta^{(0)}$	0.32761	-0.000589244
$\beta^{(1)}$	3.90403	-0.000370423
$\beta^{(2)}$		
C_γ	0.00224	0
$\alpha^{(1)}$	1.4	0
$\alpha^{(2)}$	0	0

7.1.4.7 The systems $CaSeO_4$-H_2O and NaCl-$CaSeO_4$-H_2O

So far, no experimental data were available that allowed the calculation of activity coefficients for concentrated calcium selenate solutions. The measurements of Ca2+ activity in selenate solutions by [Par/TIC1997] were limited to 0.03 m SeO_4^{2-}. Olin et al. [OLI/NOL2005] compared results from different experimental works on sulphates and concluded that the activity coefficients of calcium selenate should be similar to magnesium selenate solutions. Therefore, in this study the ion interaction coefficients found for $MgSeO_4$ were also applied to $CaSeO_4$ solutions. Within our experimental program we determined the water activity of one pure $CaSeO_4$ solution at 60 °C (**Tab. B.24**). The observed water activity (0.9944 at 0.2802 mol/kg $CaSeO_4$) is exactly the same as calculated.

Between - 2 °C and 101 °C a saturated solution of $CaSeO_4$ is in equilibrium with the dihydrate $CaSeO_4 \cdot 2H_2O$ [SEL/SNE1959]. Between 25 and 60 °C we found the following saturation concentrations in pure CaSeO4 solutions (**Tab. 7.6**). All data are a mean of three measurements, whereby the calcium and selenite concentrations were analysed independently. In all cases both concentration corresponded.

Tab. 7.6 Experimental solubility of $CaSeO_4$ at 25 to 60 °C

Temperature	$\mathbf{CaSeO_4}$ **[mol/kg]**	**log IAP**
25	0.455 ± 0.002	-2.588
40	0.36 ± 0.003	-2.794
60	0.309 ± 0.001	-2.989

The temperature dependence between 25 and 60 °C may be described by the following formula:

$$\log \mathrm{K}(T) = -2.601 - 0.0114(T - 298.15K) \qquad (7.59)$$

It must be mentioned that there is a considerable divergence between the literature data on the solubility of $CaSeO_4 \cdot 2H_2O$. Contrary to our findings, Meyer and Aulich [MEY/AUL1928] reported 0.40 mol/kg and Selivanova and Snejder [SEL/SNE1959] only 0.3557 mol/kg. The more recent investigation by Nishimura and Hata [NIS/HAT2007, NIS/HAT2009] gave 0.42 mol/kg which is closer to our results. A comparably high solubility of 0.44 mol/kg (corresponding to log K= -2.64) was found by Welton and King [WEL/KIN1939] at 30 °C, which fits very well with our linear relationship derived above. We conclude that our value of 0.455 mol/kg is reasonable.

The solubility of CaSeO4·$2H_2O$ in NaCl solutions was investigated at 25, 50 and 60 °C up to NaCl concentration of 5.8 mol/kg NaCl (**Tab. B.40ff**.). The resulting solubility curves exhibit a behaviour that is well known from the analogue system NaCl-$CaSO_4$-H_2O. The solubility initially increases until it reaches a maximum at about 1 mol/kg NaCl. At higher concentrations the solubility of calcium selenate continuously decreases.

If the system shall be modelled a couple of additional ion interaction parameters are necessary. The interaction between Na, Ca and SeO_4 could be observed in the system Na_2SeO_4-$CaSeO_4$-H_2O that was investigated by Meyer and Aulich [MEY/AUL1928]. Based on their data the ternary interaction coefficient $\Psi_{Na,Ca,SeO4}$ was determined ($\theta_{Ca,Na}$ was taken from the THEREDA database):

$$\Psi_{Na,Ca,SeO4} = -0.0489$$

The agreement between the laboratory data and the calculated solubilities is good (**Fig. 7.12**).

As Meyer and Aulich's value for the solubility of $CaSeO_4 \cdot 2H_2O$ was about 10 % lower than ours, it may be that their reported calcium concentrations in the system Na_2SeO_4-$CaSeO_4$-H_2O are systematically low as well. For the time being no better data are available and this question may only be solved by additional investigations.

In the next step the last unknown interaction parameter $\Psi_{Ca,Cl,SeO4}$ was determined by evaluating the solubility data in the system NaCl-$CaSeO_4$-H_2O at 25 °C ($\theta_{Cl,SeO4}$ was taken from [HAG/MOO2012]). It was found to be:

$$\Psi_{Ca,Cl,SeO4} = 0.1520$$

Fig. 7.12 shows that the calculated solubility of $CaSeO_4 \cdot H_2O$ agrees well with the experimental data.

It was not possible to derive temperature functions for the ternary interaction coefficient $\Psi_{Ca,Cl,SeO4}$ because the system Na_2SeO_4-$CaSeO_4$-H_2O has not been evaluated at other temperatures than 25 °C. As there are also no solubility data for the system $CaCl_2$-$CaSeO_4$-H_2O two ternary interaction parameters remain $\Psi_{Ca,Cl,SeO4}$ and $\Psi_{Na,Ca,SeO4}$ unknown at higher temperatures. It is not possible to calculate them from the solubility data in the system NaCl-$CaSeO_4$-H_2O, because they are linear dependent.

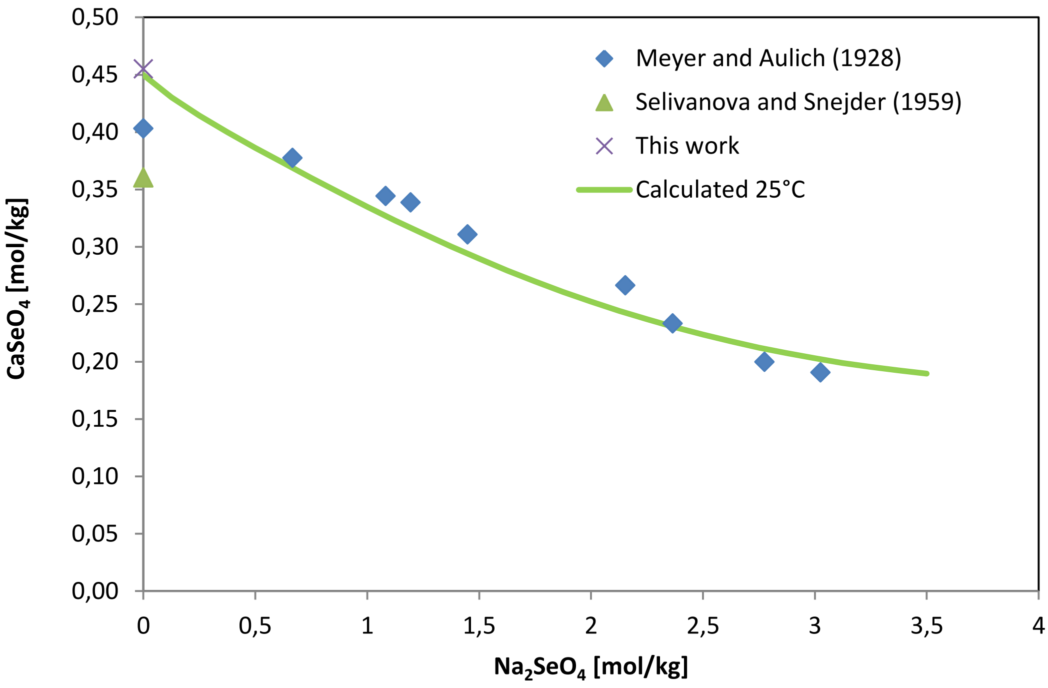

Fig. 7.12 Experimental and calculated phase equilibria in the system Na_2SeO_4-$CaSeO_4$-H_2O at 25° C

We have tested what would happen if the thermal dependence was set to zero. In this case the calculated and experimental curve agree very well up to 1.7 mol/kg, but at higher NaCl concentrations the calculated $CaSeO_4$ solubilities are too high by up to 20 % (not shown).

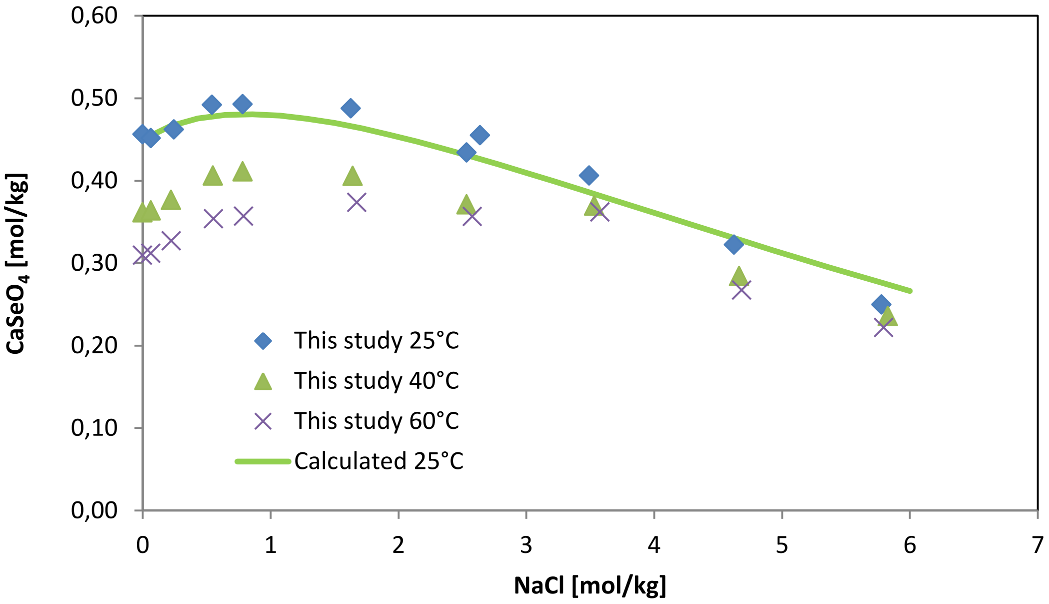

Fig. 7.13 Experimental and calculated solubility of $CaSeO_4$ in NaCl solutions

7.1.4.8 Ternary Systems

Within this study ternary systems containing selenite or selenite were not investigates experimentally. However, earlier isopiestic measurements at 25 °C [HAG/MOO2012] revealed that the systems

- $NaCl\text{-}Na_2SeO_3\text{-}H_2O$
- $Na_2SO_4\text{-}Na_2SeO_4\text{-}H_2O$
- $KCl\text{-}K_2SeO_3\text{-}H_2O$
- $K_2SO_4\text{-}K_2SeO_4\text{-}H_2O$
- $Na_2SeO_3\text{-}K_2SeO_3\text{-}H_2O$

and

- $KCl\text{-}K_2SeO_4\text{-}H_2O$
- $Na_2SO_4\text{-}Na_2SeO_4\text{-}H_2O$

followed Zdanovskij's rule [ZDA1936] and showed linear water activity lines. It may be assumed that these systems also show a linear relationship at higher temperatures. Measurements with mixed systems containing nitrates, perchlorates, chlorides and hydroxides of sodium, potassium and lithium showed that a linearity of isoactive water lines found at 25 °C always occurs at 40, 60 and 90 °C as well [HAG/SCH2015]. It would be reasonable to assume that at higher temperatures hard oxyanions like selenite and selenite would not show a principal deviation from their nearly ideal mixing properties at 25 °C. In that case it would be a good estimation that the water isoactivity curves of mixed solutions of the above mentioned systems may be represented by linear lines. Such lines could be constructed by simple arithmetic. All that is needed are the concentrations of two binary solutions that have the same water activity. The composition of a mixed solution of the two salt MX and NY is:

$$\begin{aligned} m_{MX,mix} &= z m_{MX,0} \\ m_{NY,mix} &= (1-z) m_{NY,0} \\ z &= 0..1 \end{aligned} \tag{7.60}$$

Based on such a line that may be constructed with any desired amount of points it is possible to calculated ternary interaction parameters.

In order to extent this model to solutions containing magnesium selenite it was checked whether it is possible to derive ternary interaction parameters for the system $MgCl_2$-$MgSeO_4$-H_2O purely from a constructed water isoactivity line instead from solubility data as it was done in [HAG/MOO2012]. For this purpose a line was calculated with the endpoints

m_{MgSeO4}=3.5 mol/kg

m_{MgCl2}=1.9554 mol/kg

and a water activity of 0.8529.

Two additional sets of ternary interaction parameters were calculated. In the first set, $\theta_{Cl,SeO4}$ was taken from [HAG/MOO2012] while $\Psi_{Mg,Cl,SeO4}$ was optimized based on the constructed data:

$\theta_{Cl,SeO4}$ = 0.00317 (from HAG/MOO2012)

$\Psi_{Mg,Cl,SeO4}$= 0.00129

In the second case both ternary parameters were calculated form the constructed data:

$\theta_{Cl,SeO4}$ = -0.0036

$\Psi_{Mg,Cl,SeO4}$= 0.02993

With all three sets of ternary interaction coefficients the solubility of $MgSeO_4$ in $MgCl_2$ solutions was calculated. For most parts of the diagram the calculated solubility curves are almost indistinguishable. At the highest $MgCl_2$ concentrations the difference between the measured and the calculated saturation concentration of $MgSeO_4$ is about 10 %.

Based on these consideration we set up the hypothesis that all ternary interaction parameters in ternary subsystems of the system Na,K,Mg||Cl,SO_4,SeO_4-H_2O at temperatures between 25 and 90 °C may be calculated from constructed water isoactivity lines. The validity of the hypothesis has to be proven by additional test measurements in ternary system at higher temperatures. Nevertheless, as discussed above, it seems reasonable to assume that the hypothesis is true.

For each ternary system an isoactivity line has been calculated using concentrations of binary solutions close to their solubility or close to the maximum concentration where experimental data points were available. The corners of the isoactivity lines together with they calculated water activities are listed in **Tab. B.2ff**. The following sets of interaction parameters have been derived by this method (**Tab. 7.7**).

Tab. 7.7 Temperature dependent ternary Pitzer coefficients for selenate

Parameter	**a_1 (25 °C)**	**a_4 ($T-T_R$)**
$\theta_{Cl,SeO4}$	0.00317	5.07444E-05
$\Psi_{Na,Cl,SeO4}$	0	5.72674E-05
$\Psi_{K,Cl,SeO4}$	0	9.54329E-05
$\Psi_{Mg,Cl,SeO4}$	0.00939	-0.000204945
$\theta_{SO4,SeO4}$	-0.05898	-0.00196229
$\Psi_{Na,SO4,SeO4}$	0.02598	0.000275496
$\Psi_{K,SO4,SeO4}$	0.00728	0.0021818
$\Psi_{Mg,SO4,SeO4}$	0.06050	0
$\Psi_{Na,Mg,SeO4}$	-0.01557	-3.67813E-05
$\Psi_{Na,K,SeO4}$	0.01949	-0.000326817
$\Psi_{K,Mg,SeO4}$	-0.04568	0.000521087

No attempt was made to apply the same approach to derive the temperature functions for selenite systems. As a reliable parameter set for K_2SeO_3 at 25 °C is still missing, there was no basis for make assumptions on the properties of solutions containing potassium selenite. Once more experimental data on K_2SeO_3 solutions are available, the exercise of deriving ternary interaction parameters should be continued.

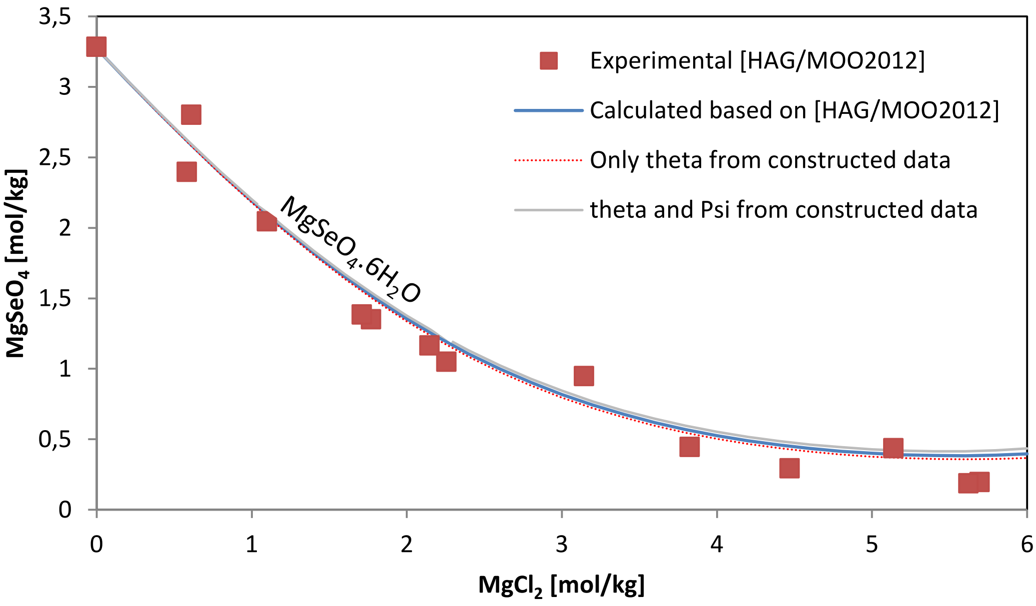

Fig. 7.14 System $MgCl_2$-$MgSO_4$-H_2O solutions at 25° C. Experimental and calculated solubility of MgSeO4·6H2O using different sets of ion interaction parameters.

7.1.4.9 Potentiometric measurements of hydrogen selenite solutions - Construction of a multi-channel measuring cell

A potentiometric multichannel cell was designed for the measurement of activity coefficients of $HSeO_3^-$ species in binary and ternary systems. The cell consists basically of several electrodes of second kind immersed in a compartment containing the bride salt as shown in **Fig. 7.15**. The compartment was closed by a cap of acrylic glass with distributed holes wherein the electrodes are inserted. The temperature of the compartment was controlled by a thermostatic bath. This type of construction aims the determination of a set of activity coefficient data in a batch experiment with different concentrations of $HSeO_3^-$ for a common salt bridge concentration and temperature. Activity coefficients are calculated from the measurement of potential between the investigated second kind electrode and an Ag/AgCl reference electrode.

The second kind electrode consists of a glass tube, on the bottom of which a pool of mercury or of an amalgam is formed. A fine glass tube submerged in the pool server to make the electrical contact by a 1 cm long Pt wire of a diameter of 0.5 mm soldered to a 10 cm long Cu wire. The corresponding slight soluble salt is dispersed on the pool surface and finally, the measuring solution is introduced. The tubes are provided with a ceramic window with separates the measuring solution from the bridge salt solution (frit). The measuring method consists in introducing the prepared electrodes in the recipient containing the bridge salt solution until reaching the frit. The system is left to equilibrate at the bath temperature. After equilibration, the measuring electrodes are slightly displaced downwards so that the frits are immersed in the bridge salt bath.

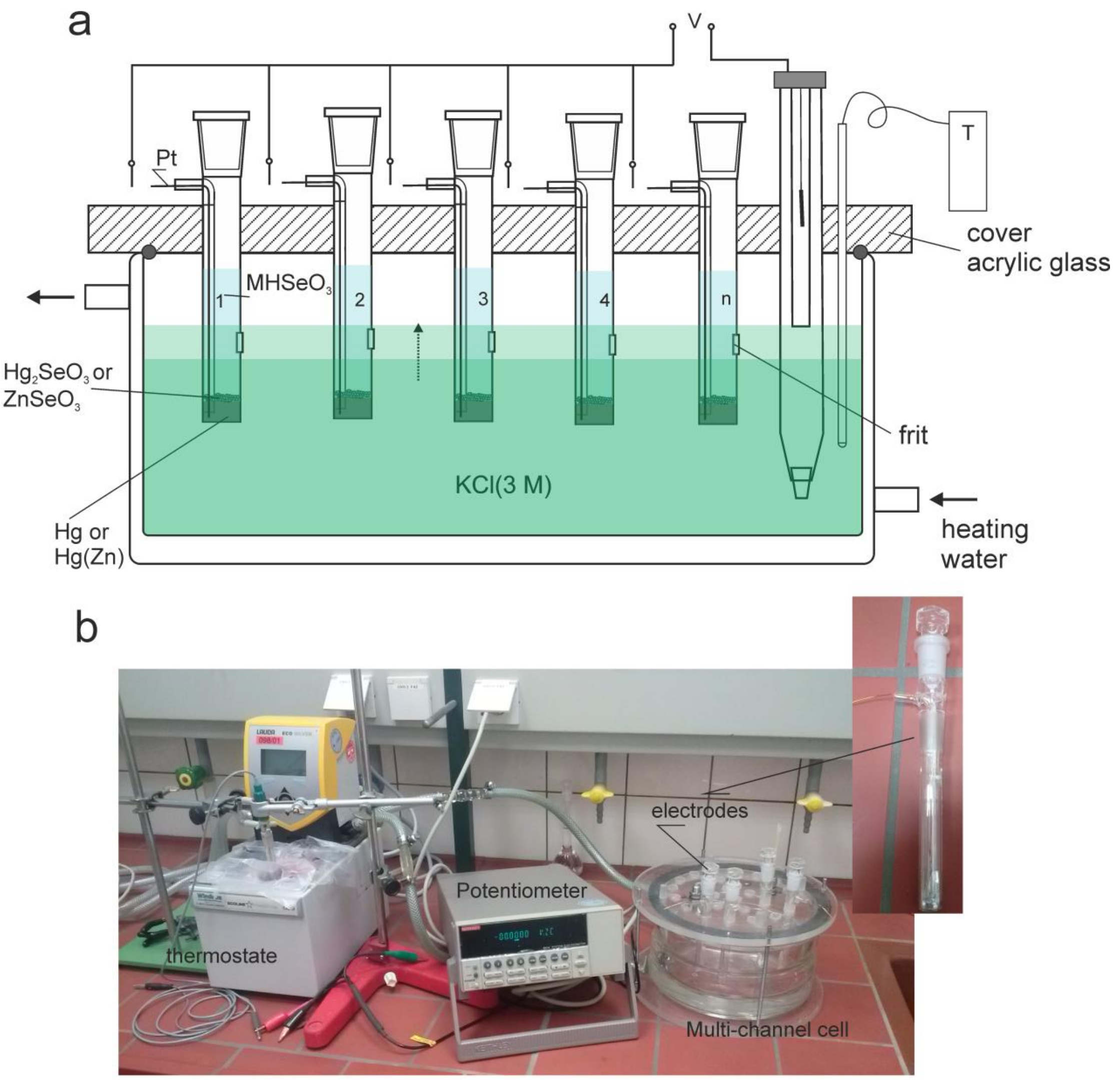

Fig. 7.15 Schematic representation of the multi-channel cell; b: picture of the measuring ensemble

Two different approaches were conceived for the measurement of activity coefficients of $HSeO_3^-$ in binary and ternary systems. For binary systems the following cell system:

$$Hg/Hg_2SeO_3(cr)/NaHSeO_3(m)//KCl(3\ mol\ l^{-1})//KCl(mol\ l^{-1})/AgCl(s)/Ag \qquad (7.61)$$

was designed. The half-cell reactions for the investigate electrode are:

$$Hg_2SeO_3 + 2e^- \rightarrow 2\ Hg^0 + SeO_3^{2-} \qquad (7.62)$$

$$SeO_3^- + H^+ \rightarrow HSeO_3^- \qquad (7.63)$$

Accordingly, the following Nernst expression results:

$$V=V^{0}-\frac{\mathrm{RT}}{2\mathrm{F}}pH-\frac{\mathrm{RT}}{2\mathrm{F}}\ln a_{\mathrm{HSeO3\text{-}}} \tag{7.64}$$

The use of 3 mol l^{-1} KCl as bridge solution ensures a minimization of the potential drop at the liquid-junction connecting the reference electrode with the measuring solution. The slight soluble salt Hg_2SeO_3 was prepared by precipitation by dropping a solution of $Hg_2(NO_3)_2$ into a solution of SeO_2. The white precipitate was decanted, vacuum filtered, washed with water and ethanol and finally dried at 40 °C for several days. The powder was characterized by X-ray diffraction as β-Hg_2SeO_3. The stability and reliability of this type of electrodes was firstly tested at 25 °C in single recipient with a similar electrode construction as schematized in **Fig. 7.16**.

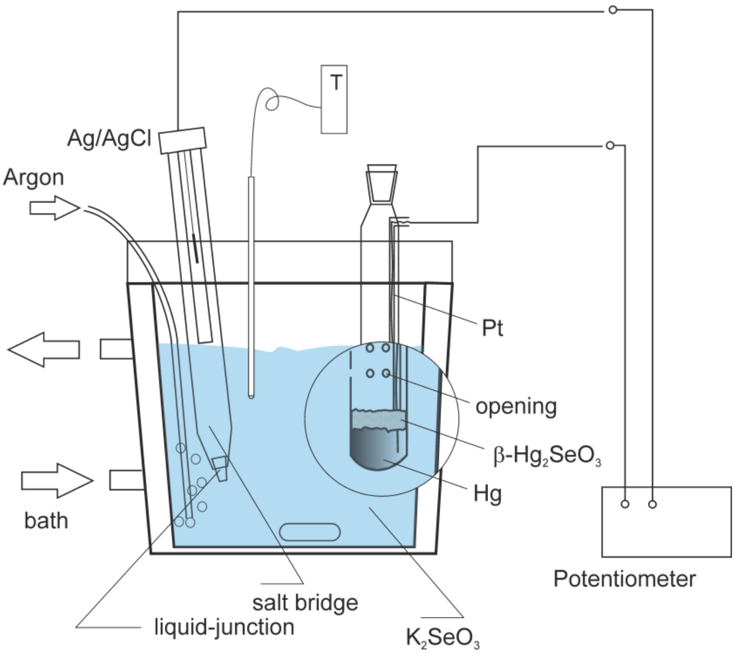

Fig. 7.16 Schematic representation of a single cell for electrode testing

For the electrode testing, solutions of K_2SeO_3 of different concentrations were used. The concentration of selenite was changed by adding weighted amounts of K_2SeO_3 into the measuring recipient. Hence, the potential difference between the test electrode and the reference electrode is given by the Nernst expression:

$$V=V_{\mathrm{Ag/AgCl}}\text{-}V^{0}_{\mathrm{Hg2SeO3/Hg}}+\frac{\mathrm{RT}}{2\mathrm{F}}\ln a_{\mathrm{SeO3\text{-}}} \tag{7.65}$$

Fig. 7.17 shows that equilibration is reached after 5 to 10 h after an increase of the selenite concentration. The recovery of the electrode in a dilute solution after being equilibrated in a two orders of magnitude more concentrated solutions, takes a time of 2 to 3 days. The electrode presents a response close to the expected Nernst relation. Hence, this test shows an adequate performance of the constructed second kind electrode and establishes a guide for the electrode equilibration times.

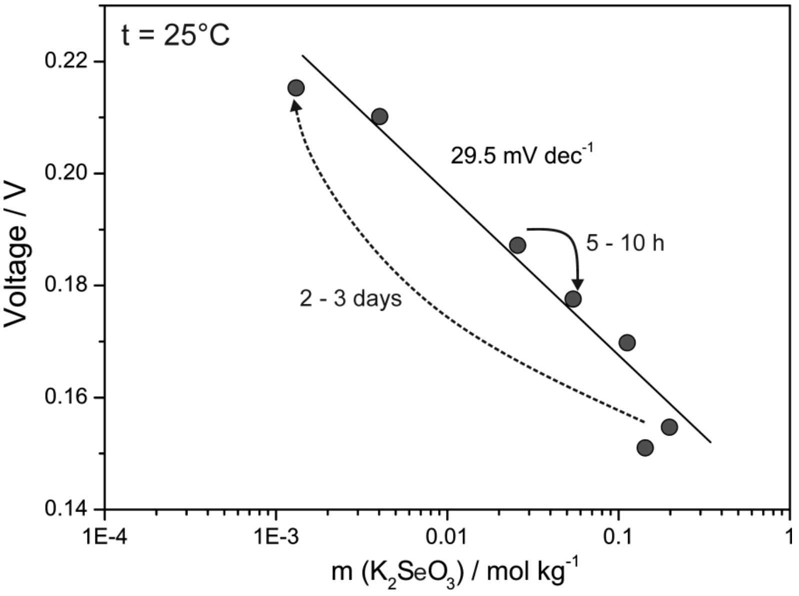

Fig. 7.17 Response of a second kind electrode $Hg/Hg_2SeO_3/K_2SeO_3(m)$

For the measurement of activity coefficients of $HSeO_3^-$ in ternary systems, the following cell arrangement is proposed:

$$Hg(Zn)/ZnSeO_3/NaHSeO_3(m_1),\ KCl(m_2)//KCl\ (m_2)/AgCl/Ag \tag{7.66}$$

For the construction of this type of second kind electrode, Zn amalgam was prepared in a glove box to avoid its oxidation. This was made by adding grains of Zn, which were previously immersed in an $HgCl_2$ solution, into a pool of mercury. Thus, a saturated liquid Zn amalgam (6.17 % Zn at 25 °C) resulted. The amalgam were mixed with powder of $ZnSeO_3$ and introduced into the electrode glass tube. $ZnSeO_3$ were added on the top of the amalgam pool and finally, the electrode tube was filled with the measuring solution $NaHSeO_3(m_1) + KCl(m_2)$. The voltage of the cell (7.66) is given by:

$$V = V_{Ag/AgCl}\,(m2) - V^0{}_{ZnSeO3/(Zn)Hg} + \frac{RT}{2F}\ln a_{SeO32-}\,(m1) \tag{7.67}$$

$$a_{HSeO3-} = a_{H+} \times \frac{a_{SeO32-}}{Ka} \qquad (7.68)$$

The term $V_{Ag/AgCl}(m_2)$ is known. $V^0_{ZnSeO3/(Zn)Hg}$ can be calculated by a regression method. Thus, the activity of $HSeO_3^-$ for determined values of m_1 and m_2 can be calculated from equations (7.67) and (7.68). This system is, however, complicated by a secondary reaction given by the reduction of $HSeO_3^-$ to Se by Zn as follows:

$$HSeO_3^- + 2\ Hg(Zn) + 5\ H^+ \rightarrow Se + 3\ H_2O + Hg + 2\ Zn^{2+} \qquad (7.69)$$

Although reaction (7.69) is thermodynamically favoured, its kinetics is very slow. In order to test this, we performed a test using the following system: $Hg(Zn)/ZnSeO_3$/0.1 m $NaHSeO_3$//1 m NaCl//3m KCl/ AgCl/Ag. It was observed that the electrode reaches a stable potential after 5 to 10 h. A perturbation of the measuring systems by the slow reduction of $HSeO_3^-$ to Se by Zn is observed after 40 h (see **Fig. 7.18**). Note, that the potential drop coincides with the appearing of small red particles attributed to elemental Se. Thus, this experiment points out a time window for the potentiometric measurement using the constructed second kind electrode.

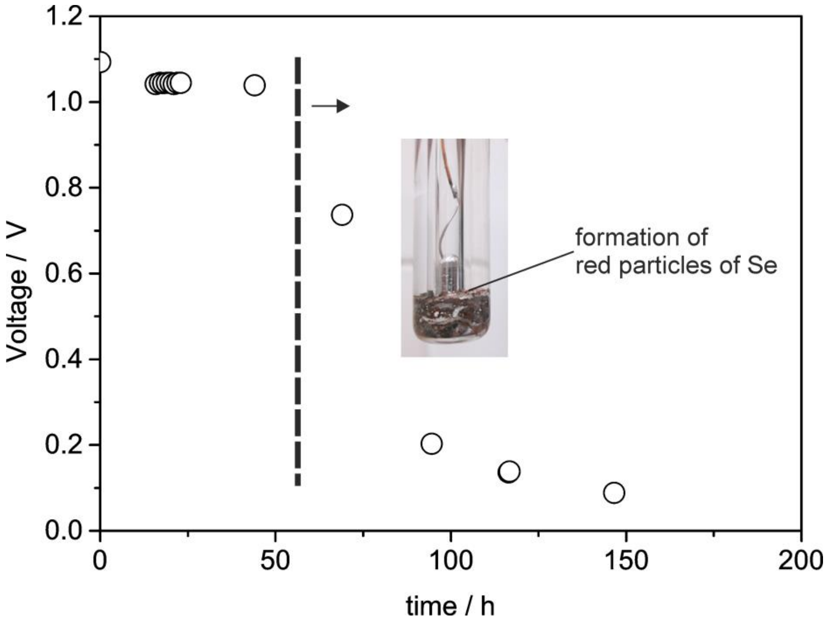

Fig. 7.18 Stability test for the electrode $Hg(Zn)/ZnSeO_3$/0.1 m $NaHSeO_3$

The appearance of a side reaction perturbing the measurement system requires a change of strategy in the measurement procedure to ensure the quality and reliability of derived thermodynamic quantities. A new strategy should include the inhibition of the side reaction, for example, by increasing slightly the pH of the solution or by changing the slight soluble salt by another not so much reactive. The carrying out of the test experiments, although instructive, was time consuming and hindered to reach the desired results in the planned timing. The development of a potentiometric method was however completed and it is ready to be activated for future projects.

7.1.5 Experimental results and parameter estimation for aqueous Systems with iodide

7.1.5.1 The system NaI-H_2O

A thorough analysis of the available literature on activity and osmotic coefficients at 25 °C was conducted by Hageman et al. [HAG/MOO2005]. At temperatures different from 25 °C vapour pressure measurements were conducted as well as investigations of the freezing point depression (**Tab. 7.8**). In addition to that we have made isopiestic measurements at 40, 60, and 90 °C (**Tab. B.18ff**.). The results of Patil et al. [PAT/OLI1994] at 75 to 95 °C were not included in the evaluation because they were neither consistent with our work nor with their own earlier measurements at lower temperatures (30 – 70 °C) [PAT/TRI1991]. The remaining measurements gave a coherent picture of the temperature dependence of the osmotic coefficient which can be expressed by the ion interaction coefficients in **Tab. 7.9**. Experimental and calculated values agree very well (**Fig. 7.19f**.).

Tab. 7.8 Previous investigations of aqueous NaI solutions at temperatures ≠ 25 °C

Source	Type of experimental data	Temperature [°C]	No. of data points	Concentration range
Rüdorff (1862) [RÜD1862]	f. p. d.	-10 - -1	4	0.2 – 2.4
Jones and Getman (1904) [JON/GET1904]	f. p. d.	-30 – 0.3	10	0.1 – 5.7
Karagunis et al. (1930) [KAR/HAW1930]	f. p. d.	-3.5 – 0.1	6	0.02 – 1
Jakli and van Hook (1972) [JAK/HOO1972]	Vap.	0 – 90	39	4 – 10
Patil et al. (1991) [PAT/TRI1991]	Vap.	30 – 70	40	1 – 8.4
Patil et al. (1994) [PAT/OLI1994]	Vap.	75 – 95	45	1.6 – 8.8

Tab. 7.9 Temperature dependent Pitzer coefficients for NaI (-30 – 90 °C, 0 – 10 m)

Parameter	a_1 =P(25 °C)*	a_4
$\beta^{(0)}$	0.12516	0.000816556
$\beta^{(1)}$	0.315256	-0.00297768
C^{γ}	0.000095	-4.7517E-05
$\alpha^{(1)}$	2	
* taken from [HAG/MOO2005].		

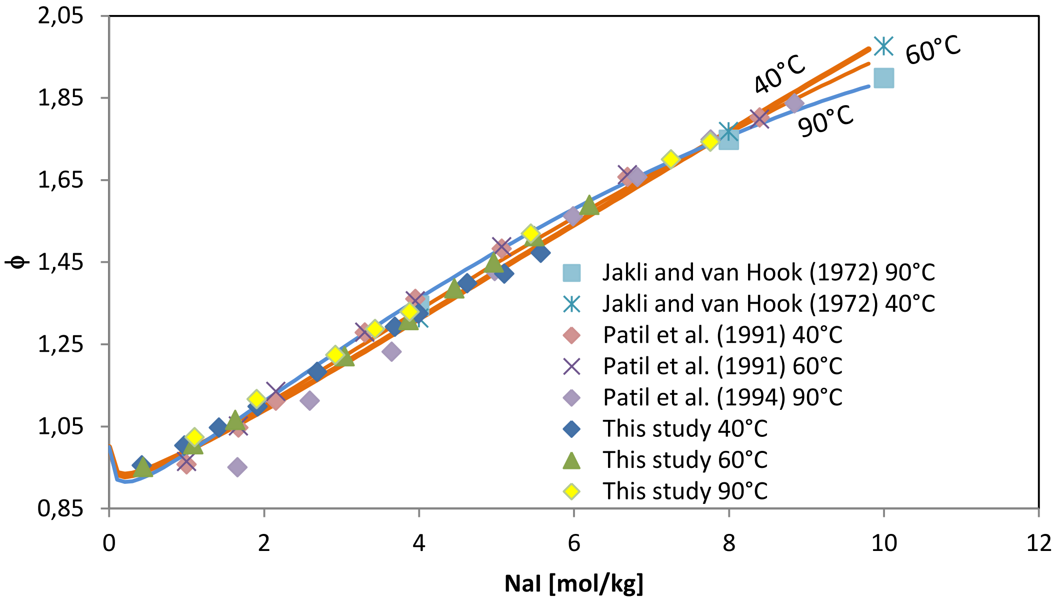

Fig. 7.19 Experimental and calculated osmotic coefficients of NaI solutions between 40 and 90° C

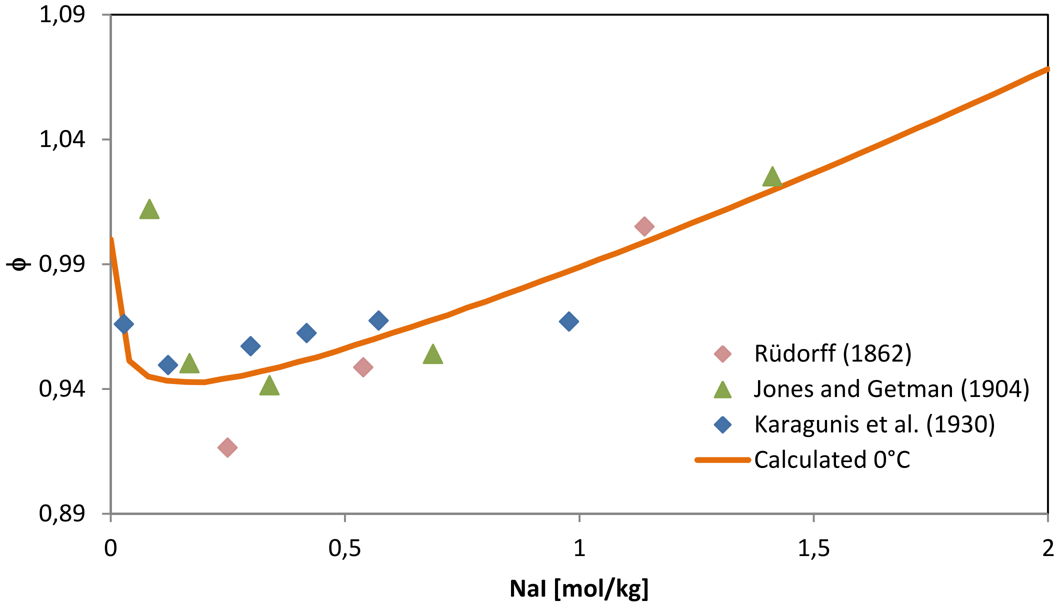

Fig. 7.20 Experimental and calculated osmotic coefficients of NaI solutions near 0° C

7.1.5.2 The system KI-H_2O

For this system few investigations of water activity of aqueous solutions at temperatures different from 25 °C were available (**Tab. 7.10**). The vapour pressure determinations of Patil et al. [PAT/TRI1991] [PAT/OLI1994] were not compatible with any other set of measurements between 25 and 90 °C and were excluded. In the same way the investigations of freezing point depressions by Rüdorff [RÜD1862], Walden and Centnerszwer [WAL/CEN1903], Sherrill [SHE1903] and Öholm [ÖHO1905] could not be taken into account because they were strongly scattered and/or did not correlate with the more precise measurements of Jones and Getman [JON/GET1904], Jabłczynski and Bałczewski [JAB/BAL1932] and Lange [LAN1936].

Tab. 7.10 Previous investigations of aqueous KI solutions at temperatures ≠ 25 °C

Source	Type of experimental data	Temperature [°C]	No. of data points	Concentration range
Rüdorff (1862) [RÜD1862]	f. p. d.	-12 – -0.8	4	0.2 – 3.5
Biltz (1902) [BIL1902]	f. p. d.	-2.8 – 0	5	0.01 – 0.8
Sherrill (1903) [SHE1903]	f. p. d.	-2 – -1	3	0.2 – 0.8
Walden and Centnerszwer (1903) [WAL/CEN1903]	f. p. d.	-1 – -0.3	4	0.1 – 0.3
Jones and Getman (1904) [JON/GET1904]	f. p. d.	-16.5 – -0.2	10	0.07 – 4.7
Öholm (1905) [ÖHO1905]	f. p. d.	-4.6 – -0.6	5	0.02 – 1.5
Jabłczynski and Bałczewski (1932) [JAB/BAŁ1932]	f. p. d.	-6.9 – -1.4	5	0.4 – 2.0
Lange (1936) [LAN1936]	f. p. d.	-0.2 – 0	20	0.04 – 0.5
Patil et al. (1991) [PAT/TRI1991]	Vap.	30 – 70	40	1 – 8.4
Patil et al. (1994) [PAT/OLI1994]	Vap.	75 – 95	45	1.6 – 8.8

Based on the remaining data sets the temperature coefficients in **Tab. 7.11** were optimized. The agreement between experimental and calculated osmotic coefficients is satisfying at all temperatures (**Fig. 7.21**).

Tab. 7.11 Temperature dependent Pitzer coefficients for KI (-16 – 90 °C, 0 – 7 m)

Parameter	**a_1^* =p(25 °C)**	**a_3**	**a_4**
$\beta^{(0)}$	0.06663	0.275748	-0.000366089
$\beta^{(1)}$	0.32206	0	0.00248184
C^{γ}	-0.001163	0	-1.34919E-05
$\alpha^{(1)}$	2		
* taken from [HAG/MOO2012].			

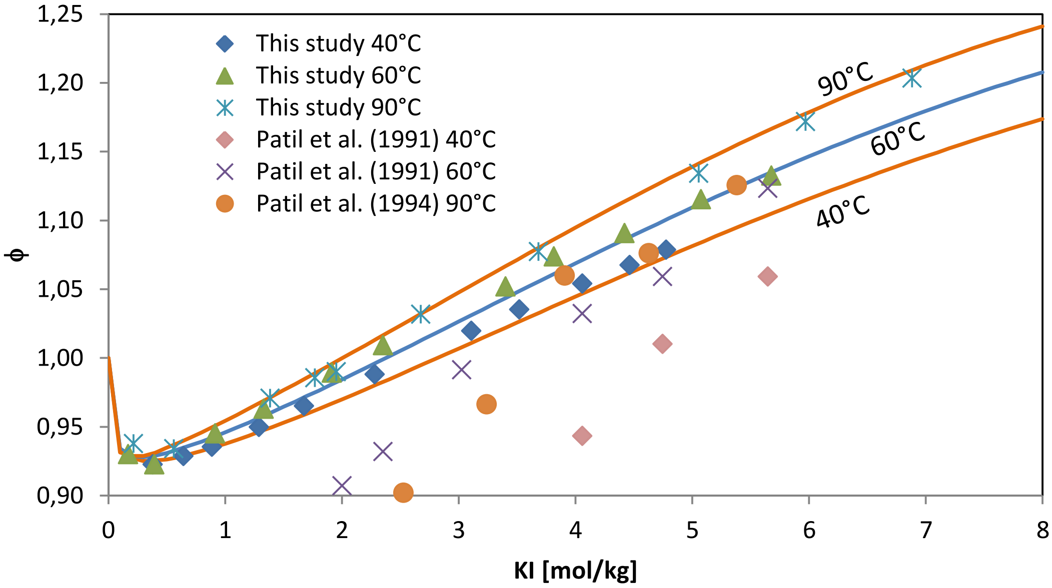

Fig. 7.21 Experimental and calculated osmotic coefficients of KI solutions between 40 and 90° C

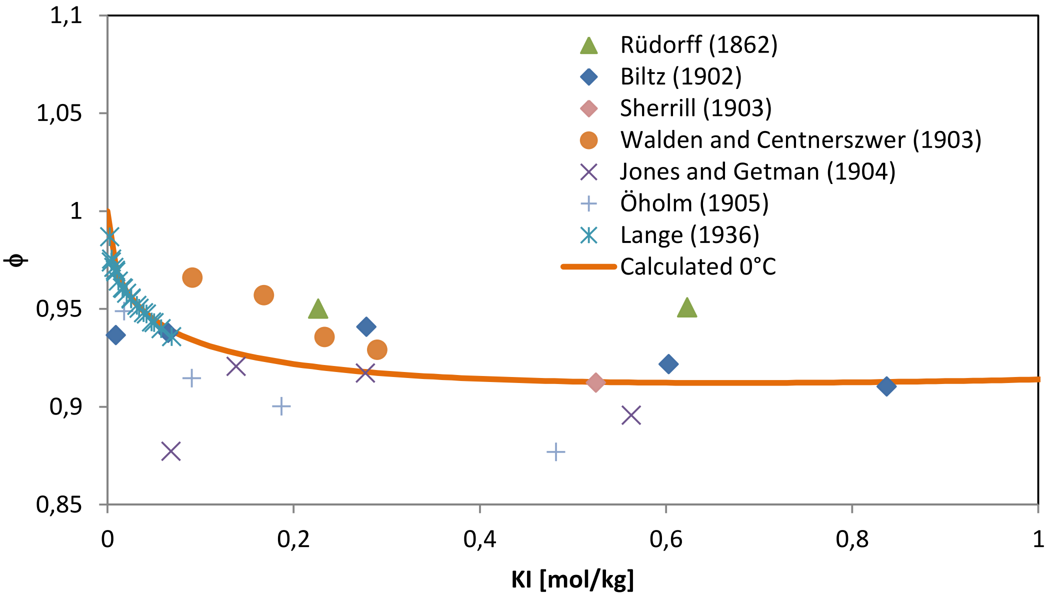

Fig. 7.22 Experimental and calculated osmotic coefficients of KI solutions near 0° C

7.1.5.3 The system MgI_2-H_2O

The water activity of MgI_2 solutions at temperatures other than 25 °C has not been investigated before. Within this study we have attempted to expand our earlier isopiestic measurements [HAG/MOO2012] to 40, 60 and 90 °C. The experiments were hampered by the tendency of concentrated MgI_2 solutions to oxidize. Smallest amounts of oxygen quickly lead to a brownish color of the solution. At the same time they become opaque, possibly by the formation of magnesium hydroxide or hydroxy iodides. This process is accelerated at higher temperatures, so that the MgI_2 solution may disintegrate within an isopiestic chamber during the experiment. Another problem was the virtual non-availability of pure MgI_2 on the market. Although it is offered by few providers delivery times were extraordinary high (up to almost a year) so that the original experimental plan could not be fulfilled. Commercial MgI_2 (the same applies for CaI_2) is water-free and immediately releases iodine vapour if water is added directly. Stock solutions of MgI_2 and CaI_2 were prepared by placing the dry salt into a desiccator together with a beaker with water. The desiccator is closed. A solution of the salt was formed slowly by absorbing water from the atmosphere. All operations are performed under oxygen free conditions in a glove-box. Because of these problems the number of experimental data is much lower than planned (**Tab. B.18ff**.). Especially at higher concentrations at 60 or

90 °C very few experimental points could be obtained. Future studies will have to look into alternative approaches to get thermodynamic data (e. g. heat of solution, heat of dilution).

Based on the new isopiestic measurements we have derived the parameters in **Tab. 7.12**. They allow a good modelling of osmotic coefficients in MgI_2 solutions between 25 and 90 °C (**Fig. 7.23**).

Tab. 7.12 Temperature dependent Pitzer coefficients for MgI_2 (25 – 90 °C, 0 – 5 m)

Parameter	**a_1 ***	**a_4**
$\beta^{(0)}$	0.4948	0.00113422
$\beta^{(1)}$	1.83094	-0.0231973
C^{γ}	0.00252846	-0.000163641
$\alpha^{(1)}$	2	

* taken from [HAG/MOO2012].

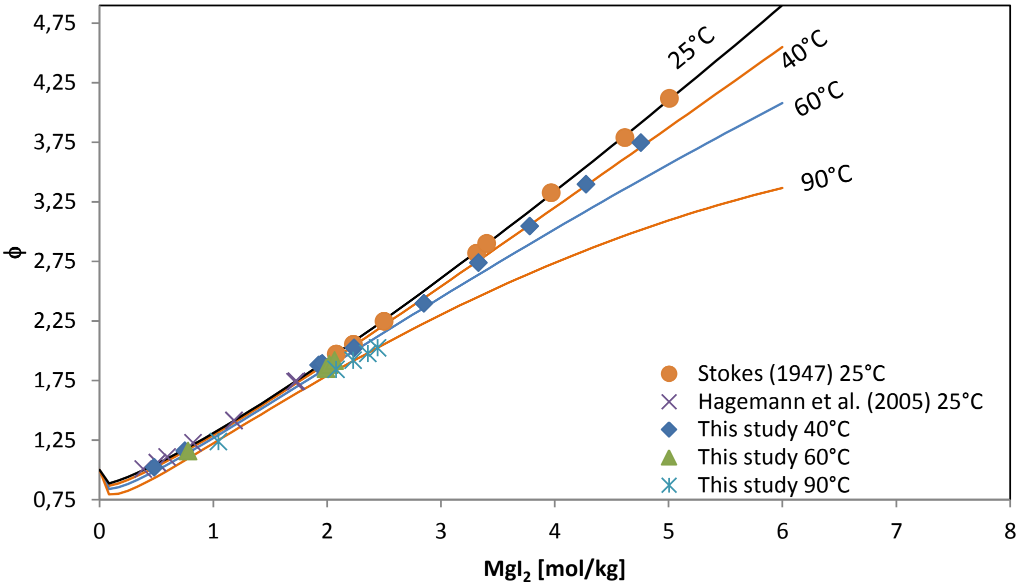

Fig. 7.23 Experimental and calculated osmotic coefficients of MgI_2 solutions between 25 and 90° C

7.1.5.4 The system CaI_2-H_2O

With CaI_2 we experienced the same problems as we did with MgI_2. The number of successful isopiestic measurements was even smaller and restricted to 40 °C (**Tab. B.18ff**.). Our data, which mostly fall into the concentration range of 2.5 to 5 mol/kg fit well to the results of Robinson at 25 °C [ROB1942] which were restricted to an upper concentration limit of 1.9 mol/kg. On the other hand, the vapour pressure measurements of Patil [PAT/TRI1991] [PAT/OLI1994] at 30 °C and higher temperatures produced systematically lower osmotic coefficients. They were excluded from the further evaluation.

Since the measurements at low concentrations by Robinson [ROB1942] at 25 °C and our measurements fit so well and show insignificant differences we decided to evaluate both sets together to produce new ion interaction coefficients that are valid from 25 to 40 °C and up to concentrations of 5 mol/kg (**Tab. 7.13**). They are almost identical of those calculated in [HAG/MOO2012] with the exception of C^γ which is now similar to that of MgI_2. Experimental and calculated osmotic coefficients agree very well (**Fig. 7.24**).

Tab. 7.13 Pitzer coefficients for CaI_2 (25 – 40 °C, 0 – 5 m)

Parameter	**a_1 = P(25 °C)***
$\beta^{(0)}$	0.422671
$\beta^{(1)}$	1.95532
C^γ	0.00136543
$\alpha^{(1)}$	2

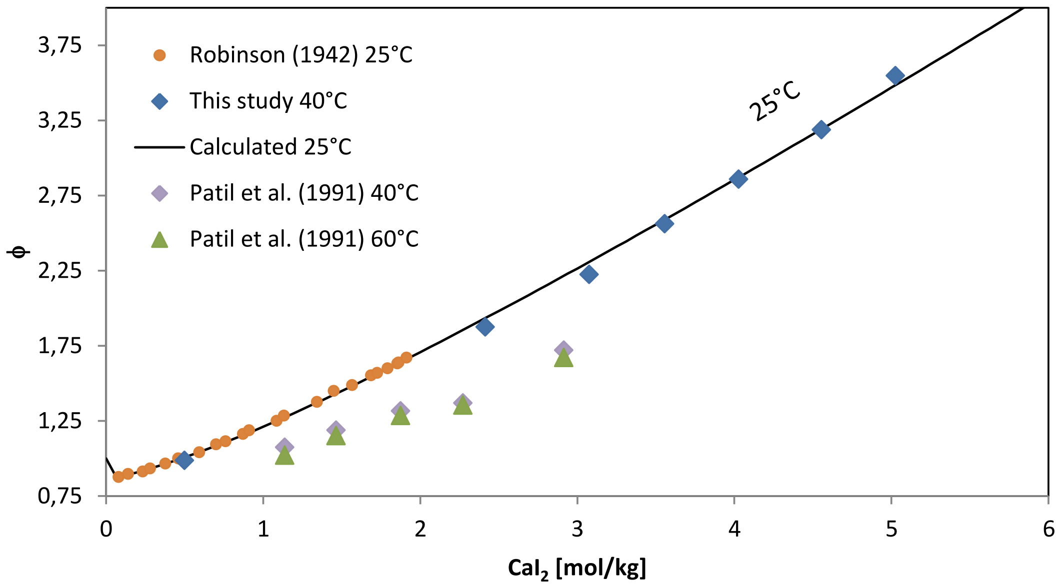

Fig. 7.24 Experimental and calculated osmotic coefficients of CaI_2 solutions at 25 – 40° C

7.1.5.5 Ternary systems

No new experimental data were produced within this study for aqueous systems containing iodide. In the section on selenate ternary ion interaction parameters were derived on the basis of the assumption that systems that obey the Zdanovskij rule at 25 °C do so at higher temperatures as well.

The previous study by Hagemann et al. [HAG/MOO2012] showed that a number of ternary iodide systems obey the Zdanovskij rule. These include

- $MgCl_2$-MgI_2-H_2O
- MgI_2-NaI-H_2O
- KI-MgI_2-H_2O

Clearly, the isoactivity lines in the system MgI_2-$MgSO_4$-H_2O were curved. All other systems were evaluated on the basis of solubility data only. However it is possible to check the validity of the Zdanovskij rule by calculating isoactivity lines using the ion interaction parameters. The following systems show linear isoactivity lines:

- $NaCl$-NaI-H_2O
- KCl-KI-H_2O
- KI-NaI-H_2O

while NaI-Na_2SO_4-H_2O and KI-K_2SO_4-H_2O do not.

For the six mentioned sulphate free ternary systems isoactivity lines were constructed for high concentration mixed solutions at 40, 60, 90 °C (**Tab. B.4)**. Each line contained 20 points. Based on these data it was possible to derive the temperature coefficients in **Tab. 7.14**. The agreement between calculated osmotic coefficients and those that result from the prediction based the Zdanovskij rule was generally excellent ($\Delta\varphi<0.004$). Only in the system $MgCl_2$-MgI_2-H_2O the deviation amounted to 0.02.

Tab. 7.14 Temperature dependent ternary Pitzer coefficients for iodide

Parameter	**a_1 (25 °C)***	**a_3 (ln T/T_R)**	**a_4 ($T-T_R$)**
$\theta_{Cl.I}$		-0.568688	0.00123899
$\Psi_{Na.Cl.I}$	-0.00400582	-	0.0000902146
$\Psi_{K.Cl.I}$	-0.00272371	-	0.0000915072
$\Psi_{Mg.Cl.I}$	-0.0113504	1.00285	-0.00280777
$\Psi_{Na.Mg.I}$	-0.0182282	0.636749	-0.00186893
$\Psi_{Na.K.I}$	-0.00366563	0.530785	-0.00155154
$\Psi_{K.Mg.I}$	-0.0160573	-1.3226	0.00384379

* from [HAG/MOO2012]

In order to check the applicability of the new parameter set to real experimental data the solubility equilibria in the systems $NaCl$-NaI-H_2O and KCl-KI-H_2O were calculated and compared with literature information (**Fig. 7.25, Fig. 7.26**). The examples show a very good agreement between predicted and experimental solubilities. The chosen approach to derive ternary interaction parameters is proven valid.

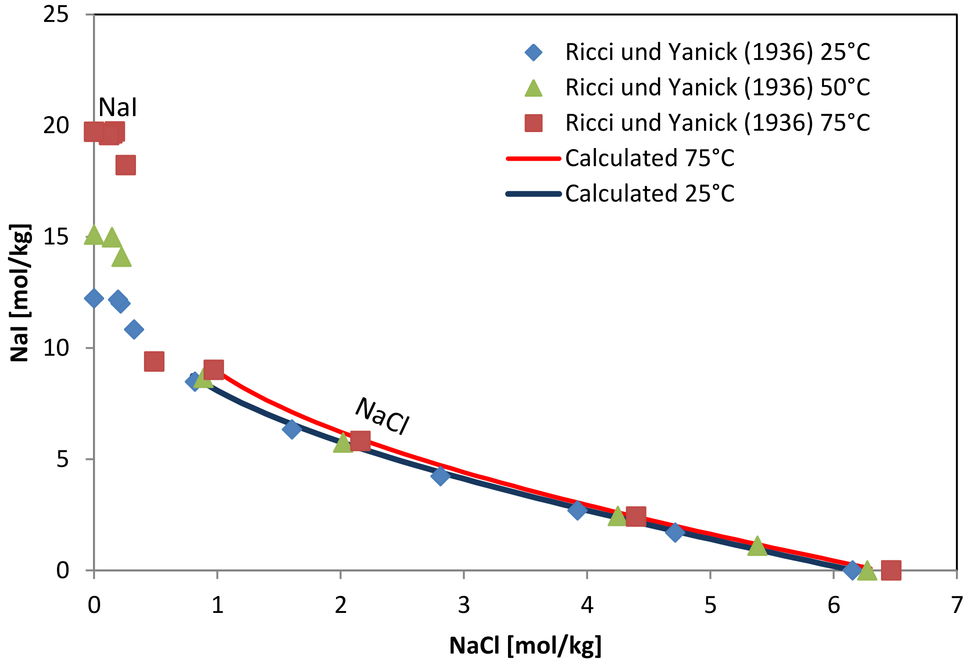

Fig. 7.25 Solubility equilibria in the system NaCl-NaI-H_2O at 25, 50, and 75 °C

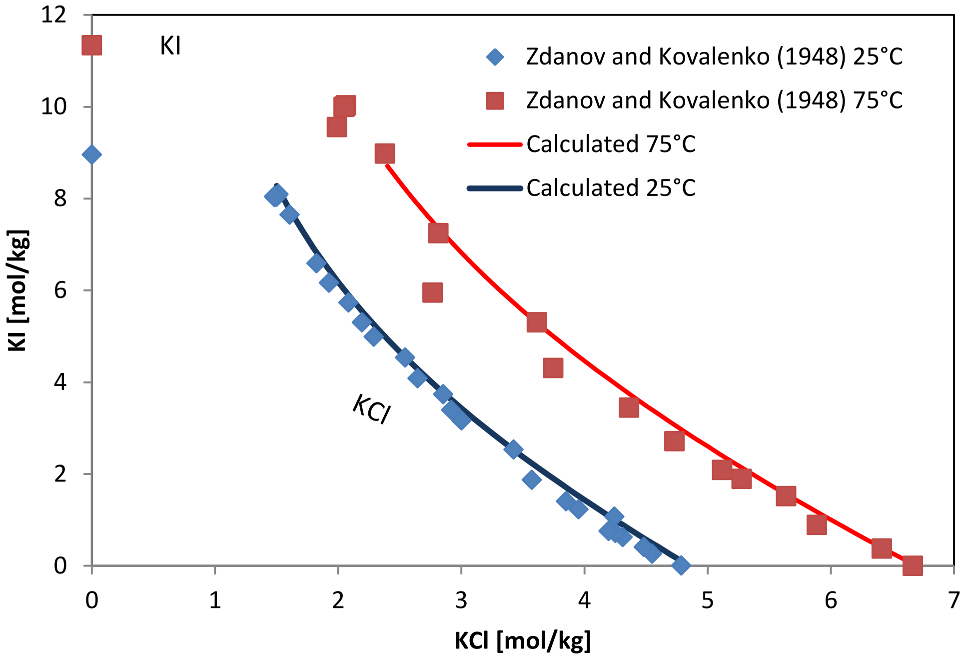

Fig. 7.26 Solubility equilibria in the system KCl-KI-H_2O at 25 and 75 °C

7.1.6 Experimental results and parameter estimation for aqueous Systems with caesium

7.1.6.1 The system CsCl-H_2O

A set of ion interaction parameters for this system has been derived earlier for 25 °C by Scharge et al. [SCH/MUN2012]. Temperature functions for interaction parameters have already been derived by Holmes and Mesmer [HOL/MES1983]. As the authors noted, there is a lack of data at elevated temperatures. Especially in the range of $25 < T < 100$ activity measurements are either missing or not very reliable. In order to fill theses gaps numerous isopiestic measurements have been made at 40, 60 and 90 °C. Further experimental data that could be used for the determination of ion interaction coefficients were available from literature source (**Tab. 7.15**). In general, only data up to 7 mol/kg were used. The aim of this study is more focussed to the modelling of saline waters containing minor concentrations of caesium. Therefore, a better modelling of solutions with lower caesium concentrations was given priority over the ability to predict the saturation concentration of caesium chloride (> 9 mol/kg).

From the sources listed below the following data sets were not included in the evaluation:

- The data from vapour pressure measurements by Patil and coworkers [PAT/TRI1991] [PAT/OLI1994] are strongly scattered and do not agree well with other data at or near the temperatures they have investigated
- The measurements of Soldano and Bien [SOL/BIE1966] at 151 °C are not compatible with the other available data in that temperature range (as already pointed out by Holmes and Mesmer [HOL/MES1983]).
- Data from Soldano and Meek [SOL/MEE1963] are internally inconsistent. Up to 2 mol/kg CsCl they are lower than other data around this this temperature
- Brendler and Voigt's data [BRE1993] [BRE/VOI1994] at 155 °C are significantly higher than the data from Holmes and Mesmer [HOL/MES1983] at 110 or 140 °C.
- Freezing point depression measurements at concentration higher than 0.5 m CsCl from Karagunis et al. [KAR/HAW1930] and Momicioli et al. [MOM/DEV1970] were not compatible with other data.

Tab. 7.15 Previous investigations of aqueous CsCl solutions at temperatures ≠ 25 °C

Source	Type of experimental data	Temperature [°C]	No. of data points	Concentration range
Karagunis et al. (1930) [KAR/HAW1930]	f. p. d.	-6 – 0	21	0.005 – 2
Soldano et al. (1959) [SOL/STO1959]	Isop.	155.5	1	1
Patterson et al. (1960) [PAT/GIL1960]	Isop.	99.6	10	1 – 5
Soldano and Patterson (1962) [SOL/PAT1962]	Isop.	121	10	0.7 – 5.8
Caramazza (1963) [CAR1963]	Pot.	35, 50	28	0.1 – 6
Soldano and Meek (1963) [SOL/MEE1963]	Isop.	140.3	9	1 – 3.5
Hellams et al. (1965) [HEL/PAT1965]	Isop.	45	10	1 – 4
Soldano and Bien (1966) [SOL/BIE1966]	Isop.	151, 165*	16	0.8 – 7.4
Mostkova et al. (1967) [MOS/KES1967]	f. p. d.	-1 – 0	27	0.001 – 0.3
Momicchioli et al. (1970) [MOM/DEV1970]	f. p. d.	-9 – 0	19	0.01 – 3
Lindsay and Liu (1971) [LIN/LIU1971]	Vap.	125(-300)	1	1
Mussini et al. (1972) [MUS/LON1972	Pot.	10 – 70	35	0.1 – 0.7
Lilley and Scott (1974) [LIL/SCO1974]	f. p. d.	-1.6 – 0	15	0.001 – 0.5
Holmes and Mesmer (1981) [HOL/MES1981]	Isop.	110 – 200 **	83	0.6 – 7.1
Sood and Krishana (1988) [SOO/KRI1988]	Diffusion	45	15	0.0001 – 0.022
Patil et al. (1991) [PAT/TRI1991]	Vap.	30 – 70	30	1.7 – 8.6
Brendler (1993)/ Brendler and Voigt (1994) [BRE1993] [BRE/VOI1994]	Isop.	155.5	9	6.7 – 9.7
Patil et al. (1994) [PAT/OLI1994]	Vap.	75 – 90	28	2 – 8

* Data at 165 °C were not used for parameter estimation because the employed model to calculate water activities for NaCl has a temperature limit of 154 °C [CLA/GLE1985]

** Only data at 110 and 140 °C were used

The following temperature parameters were optimized on the basis of experimental data (**Tab. 7.16**). Applying a temperature term to $\beta^{(2)}$ did not have any advantages. In the system CsCl-H_2O the osmotic coefficients increase with temperature until they reach a maximum at about 90 °C. At higher temperatures they decrease.

For all covered temperatures (-10 to 140 °C) the agreement between experimental and calculated osmotic coefficients is very good (**Fig. 7.27f.**).

Tab. 7.16 Temperature dependent Pitzer coefficients for CsCl (-10 – 155 °C, 0 – 7 m)

Parameter	**a_1=p(25 °C)***	**a_2**	**a_3**	**a_4**
$\beta^{(0)}$	0.03945	-1542.85	-8.13892	0.0107438
$\beta^{(1)}$	-0.000875	4324.89	24.4325	-0.0318033
$\beta^{(2)}$	0.33175			
C^{γ}	-0.000604	93.9716	0.507463	-0.000682255
$\alpha^{(1)}$	2			
$\alpha^{(2)}$	12			

* taken from [SCH/MUN2012]. In this publication C^{φ} for solutions of up to 7 m CsCl is incorrectly printed. It should read -0.00121 instead of -0.00242.

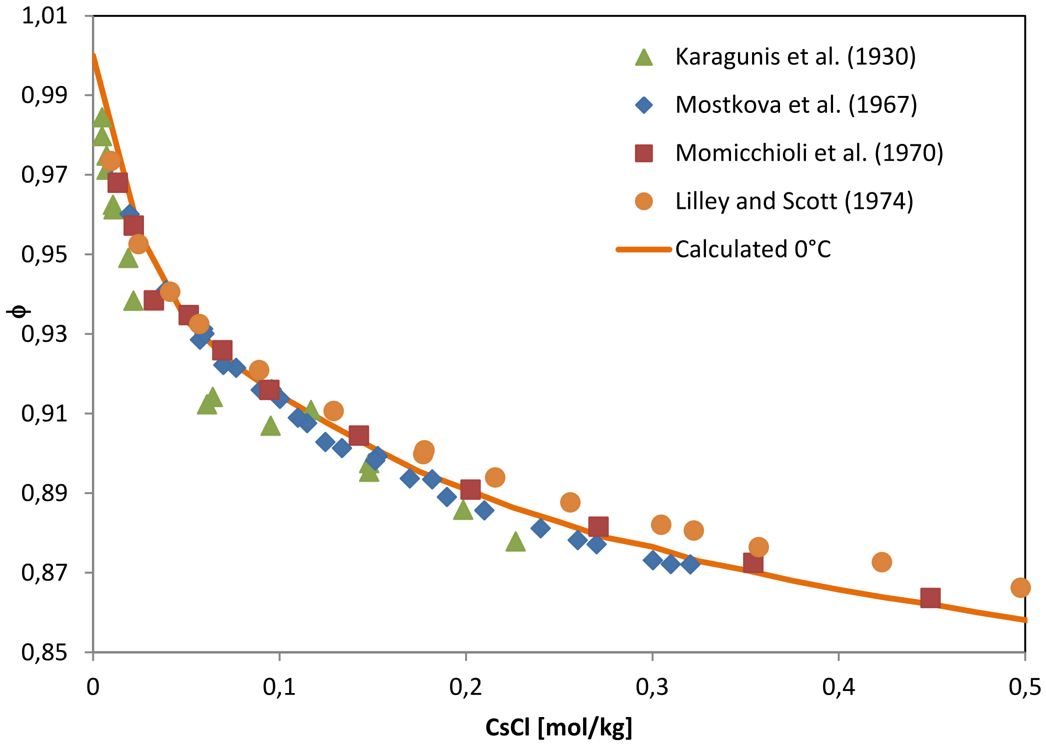

Fig. 7.27 Experimental and calculated osmotic coefficients of CsCl solutions near 0° C

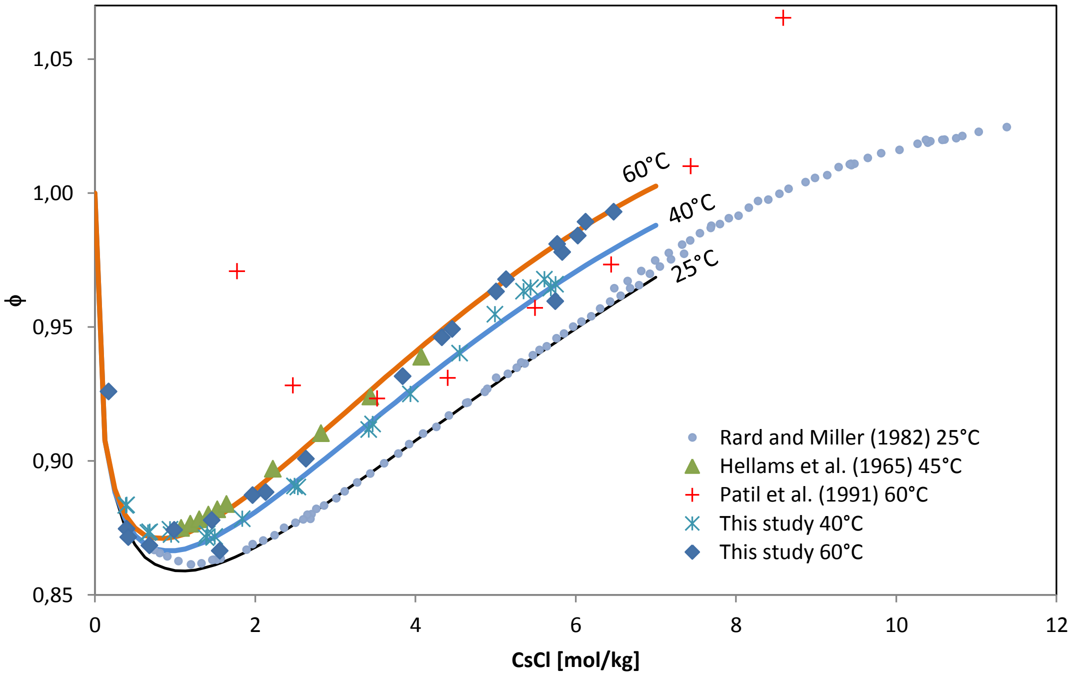

Fig. 7.28 Experimental and calculated osmotic coefficients of CsCl solutions between 25 and 60 ° C

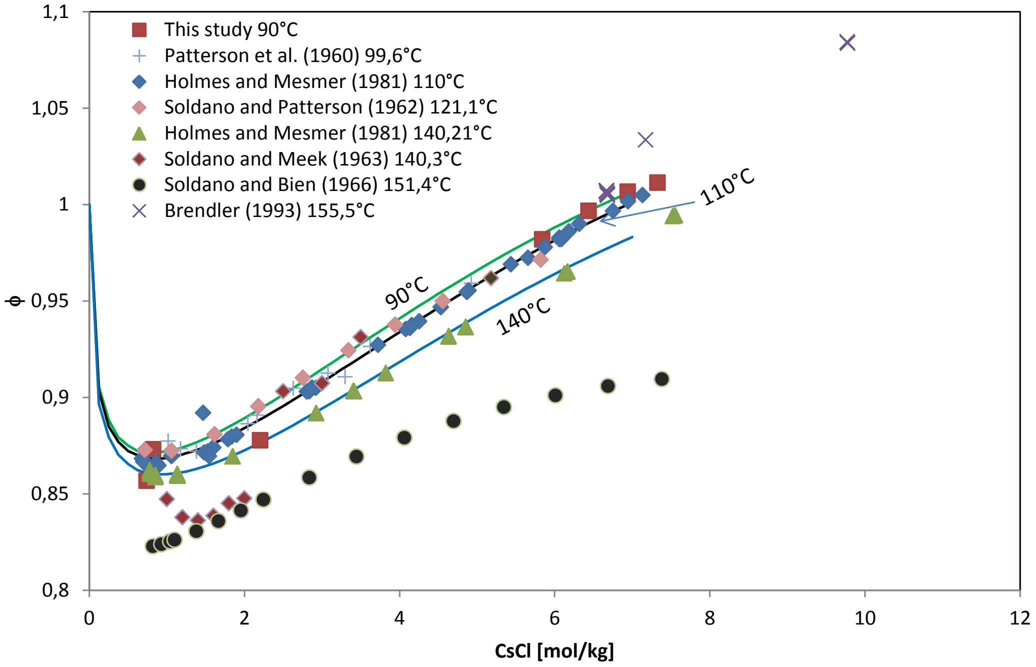

Fig. 7.29 Experimental and calculated osmotic coefficients of CsCl solutions between 90 and 155 °C

7.1.6.2 The system Cs_2SO_4-H_2O

A set of ion interaction parameters for this system has been derived earlier for 25 °C by Scharge et al. [SCH/MUN2012]. Few other experimental investigations that could be used to determine ion interaction parameters were available at other temperatures (**Tab. 7.17**). In the course of the present study a number of isopiestic measurements have been made at 40, 60 and 90 °C (**Tab. B.18**). A comparison between the data sets at different temperatures showed that the results of Palmer et al. [PAL/RAR2002] at 50 °C must be in error. On the one hand their osmotic coefficients exhibit a strong scattering, on the other hand they are significantly higher than all other data between 25 and 110 °C. The data of Palmer et al. [PAL/RAR2002] are therefore excluded from the data evaluation.

In general, the osmotic coefficients of Cs_2SO_4 solutions change very little with temperature. Especially at concentrations below 3 m Cs_2SO_4 and Temperatures between 25 and 90 °C the determined osmotic coefficients do not differ more than the experimental uncertainty. At higher concentrations the osmotic coefficients spread and become distinguishable.

Based on our own data and the information taken from the literature the parameters for the temperature function in **Tab. 7.18** have been calculated. Using these values the osmotic coefficients for Cs_2SO_4 solutions have been computed. Experimental and calculated valued agree within the margins of experimental uncertainty (**Fig. 7.30**).

Tab. 7.17 Previous investigations of aqueous Cs_2SO_4 solutions at temperatures ≠ 25 °C

Source	Type of experimental data	Temperature [°C]	No. of data points	Concentration range
Holmes and Mesmer (1986) [HOL/MES1986]	Isop.	110 – 200 *	48	0.5 – 2.5
Palmer et al. (2002) [PAL/RAR2002]	Isop.	50	41	0.1 – 3.5
* Only data at 110 and 140 °C were used				

Tab. 7.18 Temperature dependent Pitzer coefficients for Cs_2SO_4 (25 – 140 °C, 0 - 5.5 m)

Parameter	**$a_1{}^*$**	**a_3**	**a_4**
$\beta^{(0)}$	0.09849	-0.382102	0.00154658
$\beta^{(1)}$	0.53084	11.2661	-0.0217444
C_γ	-0.001061	0.0676725	-0.000215335
$\alpha^{(1)}$	2		

* taken from [SCH/MUN2012]

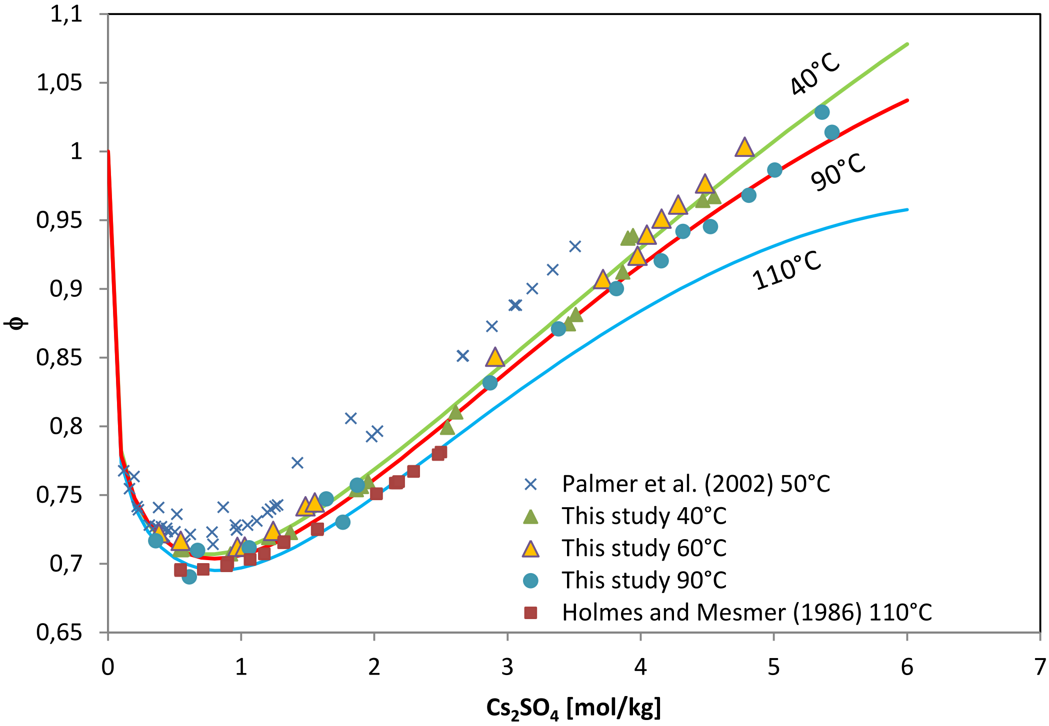

Fig. 7.30 Experimental and calculated osmotic coefficients of Cs_2SO_4 solutions

7.2 Solubility of some partly substituted hydrotalcites

7.2.1 Background and motivation

Under anaerobic conditions aluminium containing spent fuel from research reactors reacts with $MgCl_2$ rich brines as well as with Opalinus Clay water and forms hydrotalcites as a corrosion product. If carbonate is absent one of the identified phases is a chloride hydrotalcite with the general formula $Mg_{1-x}Al_x(OH)_2Cl_x \cdot yH_2O$ [MAZ/CUR2003]. The Mg/Al ratio is close to 2. However in one experiment a ratio of 3 was found. One hydrotalcite has been synthesized for further thermodynamic investigations [CUR/KAI2010]. Its formula was

$$Mg_3Al(OH)_8Cl_{0.95}(CO_3)_{0.025} \cdot 2.17H_2O$$

Although considerable efforts have been undertaken to exclude carbonate from the reaction, it was not possible to obtain a completely carbonate free substance. The solubility this compound was investigated by GRS as part of subcontract. The equilibrium constant for the reaction

$$Mg_3Al(OH)_8Cl \cdot 2.17H_2O + 8\ H^+ = 3\ Mg^{2+} + Al^{3+} + Cl^- + 10.17H_2O$$

was found to be

$$\log K = 52.0 \pm 0.5$$

at 25 °C while for a substance party substituted by Europium the following constant was found:

$$Mg_3Al_{0.898}Eu_{0.102}(OH)_8Cl \cdot 2.34H_2O + 8\ H^+ = 3\ Mg^{2+} + 0.898Al^{3+} + 0.102\ Eu^{3+} + Cl^- + 10.34H_2O$$

$$\log K_H = 66.1 \pm 0.3$$

Within the present project a similar study should determine the stability of three additional partly substituted hydrotalcites.

7.2.2 Materials and methods

FZJ provided three solid layered double hydroxide samples for thermodynamic examination. They consisted of magnesium hydrotalcite, where magnesium was partly substituted by iron, cobalt or nickel. Their formula was:

1. $Mg_{2.90}Ni_{0.09}Al_{0.99}(OH)_{7.86}Cl_{1.09}\cdot2.27H_2O$
2. $Mg_{2.92}Co_{0.10}Al_{1.015}(OH)_8Cl_{1.03}\cdot2.07H_2O$
3. $Mg_{2.90}Fe_{0.097}Al_{1.00}(OH)_{7.95}Cl_{1.04}\cdot2.46H_2O$

Samples of the three solids are depicted in Fig. 7.31. The Co and Ni containing solids were finely crystalline pure white, whereas the Fe sample showed a slight yellowish colour. The solids were delivered under a nitrogen atmosphere. Throughout the project they were stored and handled in a glove box under nitrogen in order to protect oxidation and absorption of CO_2.

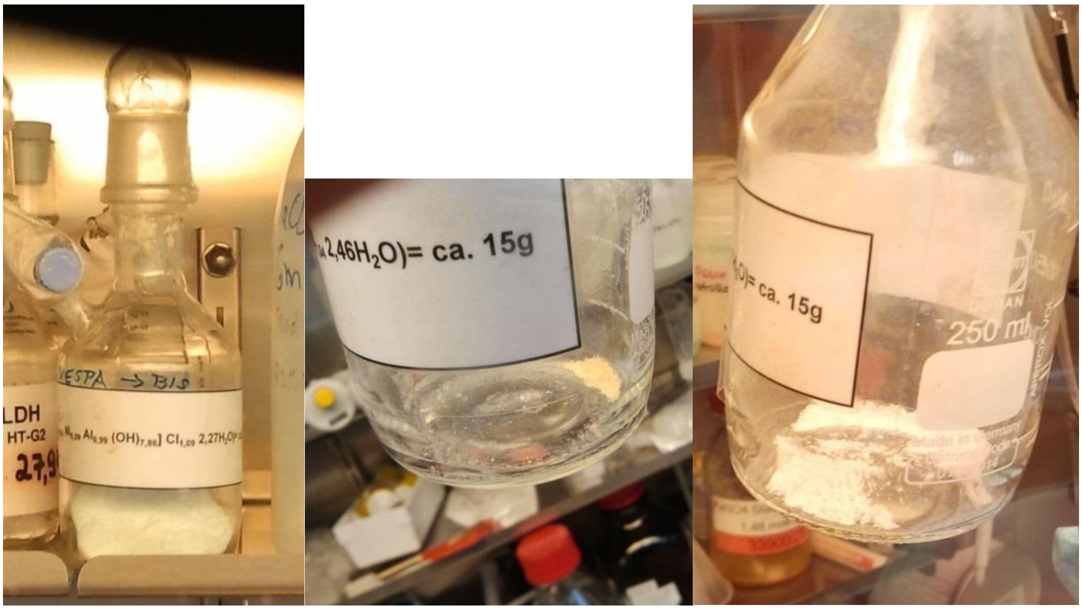

Fig. 7.31 Hydrotalcites provided by FZJ: Ni-LDH, Fe-LDH and Co-LDH.

In order to determine the solubility of the hydrotalcites 1 g of the solid sample was added to 30 ml of a deaerated aqueous solution in a screw capped LDPE bottle. All experiments were performed in four parallel batches. The following synthetic solutions were used:

1. Opalinus clay pore water (according to Pearson [PEA1999] but prepared without carbonate)
2. Mg rich brine (according to [MAZ/CUR2003a] which in turn is based on [GRA/MÜL1990])
3. 0.3 m $MgCl_2$
4. 1 m $MgCl_2$
5. 2 m $MgCl_2$

The bottles were closed and then transferred into a temperature controlled cabinet (25 ± 1 °C) and manually shaken once a week for a total duration of up to 150 days.

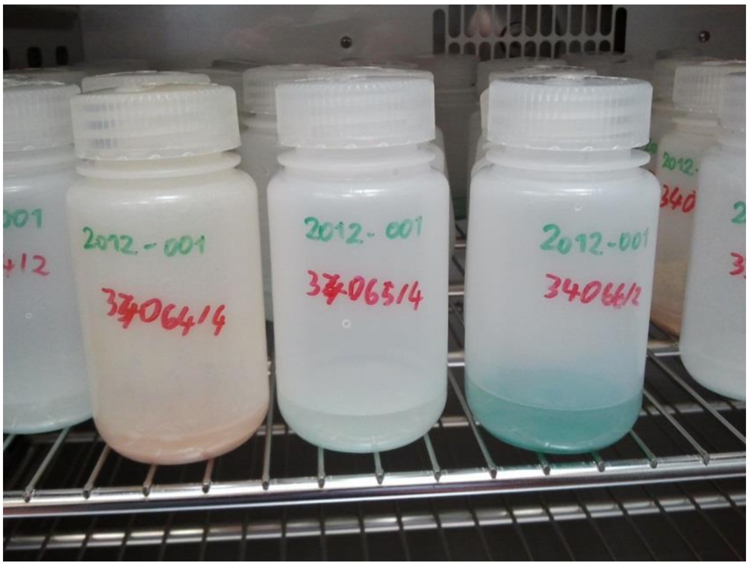

Fig. 7.32 Plastic bottles containing LDH in contact with different salt solutions

According to designed schedule samples were taken from the first (reference) of the four parallel batches. Only when the pH values were found to stable, samples were taken from the remaining three batches. Typically, equilibrium was achieved within 20 days.

The elemental concentrations in the starting solutions (**Tab. 7.19**) and the solubility experiments were determined after filtration (0.045 µm) by ICP-OES (Na, K, Mg, S), potentiometric titration (Cl), and ICP-MS (Al, Co, Ni). Iron was detected in the experiments with Fe-LDH, but could not be quantified neither by ICP-MS, voltammetry nor photometry ($< 2 \cdot 10^{-6}$ mol/l).

Tab. 7.19 Composition of starting solutions

Starting solution	Density	Na	K	Mg	Ca	Cl	SO_4
	[kg/l]	[mol/kg]					
Opalinus clay pore water	1.0113	0.247	0.00205	0.0179	0.0269	0.304	0.0144
0.3 M $MgCl_2$	1.0207	n.a.	n.a.	0.312	n.a.	0.618	n.a.
1 M $MgCl_2$	1.0728	n.a.	n.a.	1.04	n.a.	2.070	n.a.
2 M $MgCl_2$	1.1433	n.a.	n.a.	2.18	n.a.	4.269	n.a.
Mg rich brine	1.332	0.084	0.0230	5.40	0.317	11.7	< 1E-5
n.a. not analysed							

7.2.3 Interpretation of the results

The concentrations of the resulting equilibrium solutions are shown in **Tab. B.5** in the appendix. Apparent pH values were transformed into hydrogen ion concentrations (pcH) using the correction functions developed in Hagemann et al. [HAG/BIS2014]. In the case of experiments with Opalinus clay pore waters, the correction was made on the assumption that the solution composition could be represented by a pure NACl solution with a concentration equivalent to the total chloride concentration.

The key information from the measurements is summarized in **Tab. 7.20**. As a general rule the amount of dissolved cobalt or nickel is increasing with increasing ionic strength of the starting solution. Cobalt and Nickel concentrations are comparable in Opalinus clay pore water and in Mg rich brine, whereas in 0.3, 1 and 2 M $MgCl_2$ solutions the cobalt content is about two to four times higher than the nickel content in the analogue experiments with Co-LDHs. The reason for this behaviour is not clear yet. The aluminium content of the solutions is similar in all experiments ($0.8\text{-}2.2 \cdot 10^{-5}$ mol/kg). Only in the experiments with Mg rich brine it is ten times higher.

Because the iron concentrations were always below the limit of quantification ($2 \cdot 10^{-6}$ mol/kg) an interpretation of the experiments with Fe-LDHs was not possible. However, it was obvious that the pH values and the aluminium concentrations in these batches were slightly lower. It was observed that the resulting solids and the solutions in these experiments were brownish yellow. If iron were purely present as Fe^{2+} a green colour would be expected. Consequently, at least part of the iron must have been oxidized. In that case, the lower pH would be a result of the oxidation of Fe^{2+} and the complex formation of Fe^{3+} with OH^-:

$$4Fe^{2+} + O_2(aq) + 10H_2O = 4\ Fe(OH)_3(s) + 8H^+$$

The yellowish colour of the dry Fe-LDH shows that some oxidation has taken place already before the samples were received from FZJ. This conclusion is in accordance to the findings by FZJ, which found that about 5 % of the iron in freshly prepared Fe-LDH was present as Fe(III) (see **chapter 6.5.1**). It cannot be ruled out that further oxidation took place until and during the experiments.

Tab. 7.20 Key results from the LDH solubility experiments

Starting solution	pcH	Al	Co	Ni
		[mol/kg]		
Opalinus clay pore water, carbonate free	8.6	2.1E-5 Fe: 1.1E-5	2.9E-7	2.6E-7
0.3 m $MgCl_2$	8.14 Fe*: 7.76	2.2E-5 Fe: 1.2E-5	2.8E-6	0.6E-6
1 m $MgCl_2$	7.80 Fe: 7.69	1.3E-5 Fe: 1.2E-5	6.9E-6	1.5E-6
2 m $MgCl_2$	7.76 Fe:7.77	1.8E-5 Fe: 0.8E-5	4.9E-6	2.0E-6
Mg rich brine	7.7	2.6E-4	2.0E-5	1.9E-5

* experiments with Fe-LDH

The experiments in Opalinus clay pore water, that effectively is a 0.3 molal solution of alkali chlorides, were taken as a basis to calculate the solubility constant of Co- and Ni-LDHs. Due to the fact that the experiments resulted in alkaline solutions a chemical model was necessary that considered the formation of hydroxo complexes of aluminium, cobalt and nickel. So far, no Pitzer model exists that is able to predict the activity coefficients of such species in salt solutions. Instead a B dot model was chosen. An ionic strength of 0.3 is well within the margins of its applicability. We used the Yucca Mountain Project database "data0.ymp R5" which is provided together with the geochemical code EQ3/6 Version 8.0a [WOL/JOV 2007]) to calculate the aqueous chemical speciation of the elements and the activity coefficients of the species. Two changes were made with respect to this database: the polynuclear hydroxo species $Co_2(OH)_3^+$ and $Co_4(OH)_4^{4+}$ were suppressed during the calculations. Both species were found only in experiments with at 0.2 M to 1.5 M Co^{2+}. Their existence in solutions with very low Co concentration is highly questionable. At neutral pH in solution in equilibrium with solid $Co(OH)_2$ they do not play a significant role (Baes and Messmer [BAE/MES1976]). The chemical analogs $Ni_2(OH)_3^+$ and $Ni_4(OH)_4^{4+}$ are negligible at Ni concentrations below $1 \cdot 10^{-4}$ M (Gamsjäger et al. [GAM/BUG2005]).

If, on the other hand, they are allowed to occur, $Co_2(OH)_3^+$ would dominate the speciation of Co with (> 99 %). It should be noted that the analogue Ni complexes are not included in the Yucca Mountain Project database although they have, according to literature ([BAE/MES1976], [GAM/BUG2005]) a comparable stability.

Species concentrations and activity coefficients were combined with stoichiometric coefficients to produce ion activity products (IAP) for the solutions in equilibrium with Co- and Ni LDHs (**Tab. 7.21**). The results were almost identical for both LDHs:

$\log IAP(Ni\text{-}LDH) = 45.2 \pm 0.2$

$\log IAP(Co\text{-}LDH) = 45.2 \pm 0.1$

This result corresponds with the theoretical predictions made in **chapter 6.6.1.1**. For water-free LDHs was derived that the free enthalpy of formation of Ni- and Co-LDHs would be almost indistinguishable.

It may be expected that an analogue Fe-LDH that contains only Fe(II) would show a very similar ion activity product because the ionic radii of all three ions are almost identical (0.69 to 0.74 Å [LID 1991]) and the chemical behaviour in aqueous solutions is similar as well.

Earlier measurements with non-substituted chloride hydrotalcites [CUR/KAI2010] gave similar results with regards to the elemental concentrations (**Tab. B.7** and **Tab. B.8**). However, the measured pH was significantly lower (6.42 to 6.82). A slightly acidic pH is in contradiction to the principally alkaline character of chloride hydrotalcite. Its reaction with carbonate free low concentration water should lead to a slightly alkaline pH. Such a pH (8.87) was indeed found in the control batch of the experiments as well as in the experiments with the europium substituted substance. It had to be concluded that the original pH measurements were systematically in error.

In [CUR/KAI2010], the solubility constant for the pure chloride hydrotalcite was calculated using an enhanced Pitzer database based on the results of experiments in a 1 M $MgCl_2$ solution. If, on the other hand the experimental data for the solubility of chloride hydrotalcite in Opalinus clay water are used in combination with the pH observed in the control experiment and the same database (data0.ymp R5) as in the other evaluations the solubility constant would be log K = 45.5 which is in close good agreement with the values found for Ni- and Co chloride hydrotalcite (45.2 ± 0.2). In the same way the experimental results for a Eu substituted chloride hydrotalcite (**Tab. B.8**) have been re-evaluated. The calculated solubility constant is log K = 46.9 ± 0.3. All solubility constants are summarized in **Tab. 7.21**.

For experiments with Co- and Ni- hydrotalcites that started with higher concentrated solutions, reliable ion activity products could not be computed. The ionic strength of all other systems is at 1 or higher, a region where B dot models are no longer applicable. Nevertheless, some indicative calculations were performed that resulted in IAPs similar to those produced with Opalinus clay pore water.

Tab. 7.21 Ion activity products of LDHs measured in Opalinus clay pore water

LDH type	No.	Reaction	log IAP
Ni	2	$Mg_{2.90}Ni_{0.09}Al_{0.99}(OH)_{7.86}Cl_{1.09}\cdot 2.27H_2O + 7.86\ H^+ =$ $2.9\ Mg^{2+} + 0.09\ Ni^{2+} + 0.99\ Al^{3+} + 1.09\ Cl^- + 10.13\ H_2O$	45.2
Ni	3		45.4
Ni	4		45.1
Co	2	$Mg_{2.92}Co_{0.10}Al_{1.015}(OH)_8Cl_{1.03}\cdot 2.07H_2O + 8\ H^+ =$ $2.92\ Mg^{2+} + 0.1\ Co^{2+} + 1.015\ Al^{3+} + 1.03\ Cl^- + 10.07\ H_2O$	45.2
Co	3		45.2
Co	4		45.1
Eu	2	$Mg_3Al_{0.898}Eu_{0.102}(OH)_8Cl\cdot 2.34H_2O + 8\ H^+ =$ $3\ Mg^{2+} + 0.898Al^{3+} + 0.102\ Eu^{3+} + Cl^- + 10.34H_2O$	47.2
Eu	3		46.7
Eu	4		46.9
pure	2	$Mg_3Al(OH)_8Cl\cdot 2.17H_2O + 8\ H^+ =$ $3\ Mg^{2+} + Al^{3+} + Cl^- + 10.17H_2O$	45.5
pure	3		45.5
pure	4		45.5

7.3 Model for redox measurements in saline solutions

7.3.1 Relation between background concentration and the apparent redox potential

As previous measurements have shown the measured redox potential of a solution containing a constant ratio of Fe(II) and Fe(III) depends on the concentration of background salt such as NaCl, KCl or $MgCl_2$ [HAG/BIS2014]. This is partly due to the increasing complexation of Fe(III) with chloride which lead to decreasing concentrations and activities of free Fe^{3+}. But apart from that effect rising ionic strength causes an increase of the liquid junction potential between the investigated solution and the inner solution within the reference electrode (typically 3 M KCl). As a result the redox potential measured in concentrated salt solutions not only reflects the redox equilibrium of iron in solution but also a concentration dependent term. This term principally cannot be quantified without applying non-thermodynamic, arbitrary assumptions.

The situation is similar to pH measurements. The pH as a single ion activity can only be derived (and thus measured) by applying conventions that are sufficiently correct near zero ionic strength. Parts of the conventions are assumptions regarding the liquid junction potential and the value of the single ion activity coefficient of Cl^-.

In concentrated salt solutions (I > 0.1 mol/kg) these basic assumptions are clearly no longer valid. Under such conditions the pH itself loses its physical meaning and turns to be a mere construction with a weak relation to reality. However, the concentration of H^+ may be measured with an ordinary pH-electrode combination and suitable calibration. The resulting pcH is an appropriate and thermodynamically sound alternative measure.

A similar approach has been developed by [HAG/BIS2014] for the redox potential. An iron specific redox state Rx_0 of an aqueous solution has been defined that depends only on the ratio of mixed activities of Fe(II) and Fe(III) chloride in solution:

$$Rx_0 = U^0 - 0{,}059 \log \frac{a_{Fe^{2+}} a_{Cl^-}^2}{a_{Fe^{3+}} a_{Cl^-}^3} \qquad (7.70)$$

An analogue formulation has been defined for sulphate solutions:

$$Rx_0 = U^0 - \frac{0{,}059}{2}\log\frac{\left(a_{Fe^{2+}}a_{SO_4^{2-}}\right)^2}{a_{Fe^{3+}}^2 a_{SO_4^{2-}}^3} \tag{7.71}$$

The mixed activities can be calculated using suitable activity models for Fe(II) and Fe(III).

The redox state Rx_0 is related to the measured (apparent) potential Eh_{app} by a correcting term ΔRx. It represents all direct or indirect concentration effects on the measured potential, except those that influence the ion activities of Fe(II) and Fe(III):

$$Eh_{app} = Rx_0 + \Delta Rx = U^0 + \Delta Rx - 0{,}059\log\frac{a_{Fe^{2+}}a_{Cl^-}^2}{a_{Fe^{3+}}a_{Cl^-}^3} \tag{7.72}$$

For KCl solutions, the correcting term ΔRx could be expressed by the following formula

$$\Delta Rx = \text{-}32{,}12\ln\left(\frac{c_{\mathrm{KCl}}}{\mathrm{mol/kg}}\right)\mathrm{mV} - 75{,}93\,\mathrm{mV} \tag{7.73}$$

Calculated and experimentally determined values for ΔRx agree very well (**Fig. 7.33**).

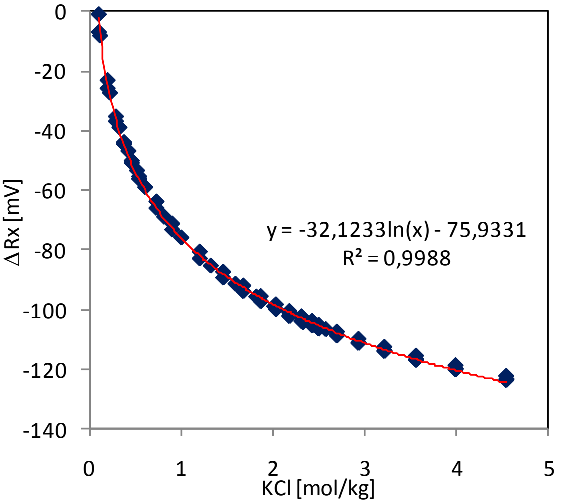

Fig. 7.33 Measured and calculated values of ΔRx in KCl solutions at 25° C

Because Fe(III) has a very low solubility in slightly acidic to alkaline solutions the measurements of ΔRx could only be performed only in strongly acidic solutions (c_{HCl}=0.01 mol/kg). A different redox pair has to be employed if the applicability of the concept is to be tested for neutral solutions as well. One such redox pair is ferricyanide/ ferrocyanide ($Fe(CN)_6^{3-}$ and $Fe(CN)_6^{4-}$) that are components of the potassium salts $K_3Fe(CN)_6$ and $K_4Fe(CN)_6$.

In order to evaluate the measurements with these to substances it was necessary to have a model that allows the calculation of ferrocyanide and ferricyanide activity coefficients in KCl solutions. Pitzer coefficients for binary solutions of potassium ferrocyanide and potassium ferricyanide were already available. As a basis to calculate ternary parameters additional solubility measurements were necessary in the systems $K_4Fe(CN)_6$-KCl-H_2O and $K_3Fe(CN)_6$-KCl-H_2O.

7.3.2 Interaction parameters in the systems KCl-$K_4Fe(CN)_6$-H_2O and KCl-$K_3Fe(CN)_6$-H_2O

Binary ion interaction parameters for $K_3Fe(CN)_6$ and $K_4Fe(CN)_4$ were derived by Pitzer and Mayorga [PIT/MAY1973] on the basis of smoothed data in Robinson and Stokes [ROB/STO1965], which in turn were based on isopiestic measurements by Robinson and Levien [ROB/LEV1946] and Robinson [ROB1937], respectively. No attempt was made in this study to compile and evaluate other experimental data in order to calculate a new set of binary parameters.

Tab. 7.22 Ion interaction coefficients for $K_3Fe(CN)_6$ and $K_4Fe(CN)_6$

Salt	**$\beta^{(0)}$**	**$\beta^{(0)}$**	**C**	**Source**
$K_4Fe(CN)_6$	0.638125	10.14375	-0.043586	[PIT/MAY1973]
$K_3Fe(CN)_6$	0.33567	4.74733	-0.01307	[PIT/MAY1973]

At 25 °C $K_3Fe(CN)_6$ is the stable phase in equilibrium with a saturated solution. Linke [LIN1965] compiled the available data on its solubility and gave 32.8 wt. - % or 1.482 mol/kg as recommended value. Using the Pitzer parameters cited above the following solubility constant could be calculated:

$$\log K (K_3Fe(CN)_6) = -1.408$$

From a saturated solution of potassium ferrocyanide(II) the hydrated salt $K_4Fe(CN)_6 \cdot 3H_2O$ crystallizes. Linke [LIN1965] reported its solubility to be at 24 wt. - % or 0.857 mol/kg. At this concentration the ion activity product equals

$$\log K\ (K_4Fe(CN)_6 \cdot 3H_2O) = -4.441$$

7.3.3 The systems $KCl\text{-}K_4Fe(CN)_6\text{-}H_2O$ and $KCl\text{-}K_3Fe(CN)_6\text{-}H_2O$

In order to derive ternary ion interaction parameters the solubility of $K_4Fe(CN)_6$ and $K_3Fe(CN)_6$ were investigated in KCl solutions at 25 °C. For each system 10 individual batches were prepared by adding $K_4Fe(CN)_6 \cdot 3H_2O$ and $K_3Fe(CN)_6$ to solutions of KCl in screw capped glass bottles. The bottles were slowly shaken overhead for at least four weeks in a temperature controlled cabinet. Samples were filtered through 0.45 µm and diluted in 1 % HNO3. The elemental composition (Fe, K) of the samples was checked by ICP-OES. The chloride content was calculated from the charge balance.

The investigation of systems with sylvite (KCl) as the solid phase is problematic because the dissolution and growth of KCl crystals is strongly inhibited by absorption of $K_4Fe(CN)_6^{4-}$ and to a lesser extent by $K_3Fe(CN)_6^{3-}$ or on their surface. Solutions may become over- or undersaturated with respect to sylvite [STE1961, STE1962]. We found indeed solution compositions with a potassium chloride concentration above the expected sylvite solubility. Such solutions were not included in the data evaluation.

The results of the measurements are shown in **Tab. B.12** and **Tab. B.13**. The solubility of $K_3Fe(CN)_6$ decreases constantly with rising KCl content. Our experimental data correspond well with the findings of Åkerlof [AKE1937], although his values are constantly a little bit lower. Both data sets were used to calculate ternary interaction coefficients:

$$\theta_{Cl-,Fe(CN)6\ 3-} = 0.4680$$

$$\Psi_{K+,Cl-,Fe(CN)6\ 3-} = -0.0919$$

The calculated solubilities of $K_3Fe(CN)_6$ and KCl (sylvite) agree well with the experimental results (**Fig. 7.34**).

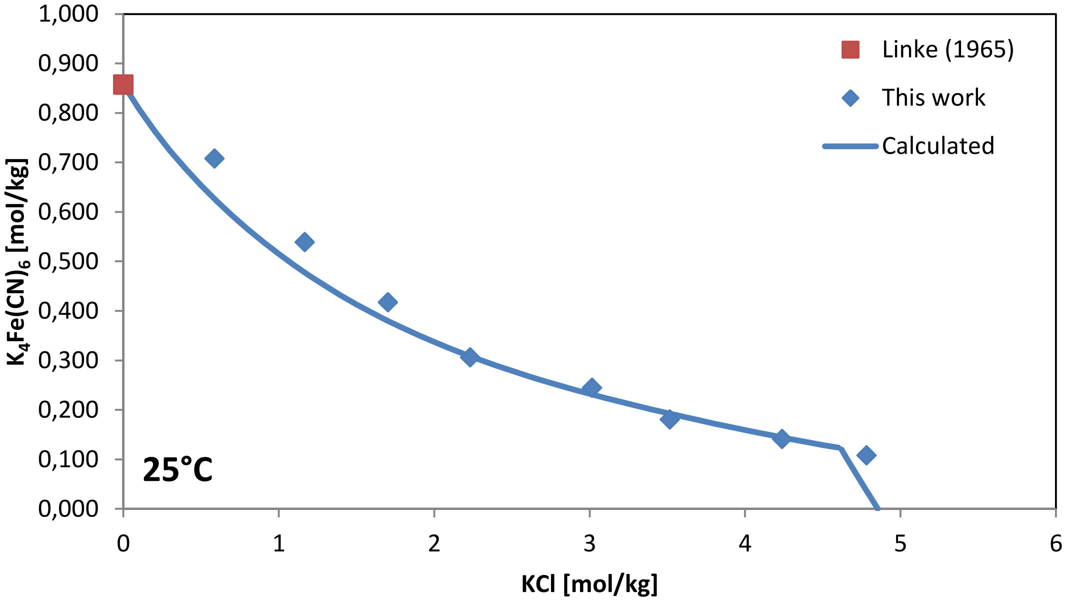

Fig. 7.34 Experimental and calculated solubilities in the system KCl-$K_4Fe(CN)_6$-H_2O at 25 °C

In a similar way the solubility of $K_4Fe(CN)_6 \cdot 3H_2O$ decreases with rising KCl content (**Fig. 7.35**). From the data the following ternary parameters could be derived:

$\theta_{Cl-,\ Fe(CN)6\ 4-}$=0.1050

$\Psi_{K+,\ Fe(CN)6\ 4-,\ Cl-}$=0.1352

Experimental and calculated solubilities correspond very well.

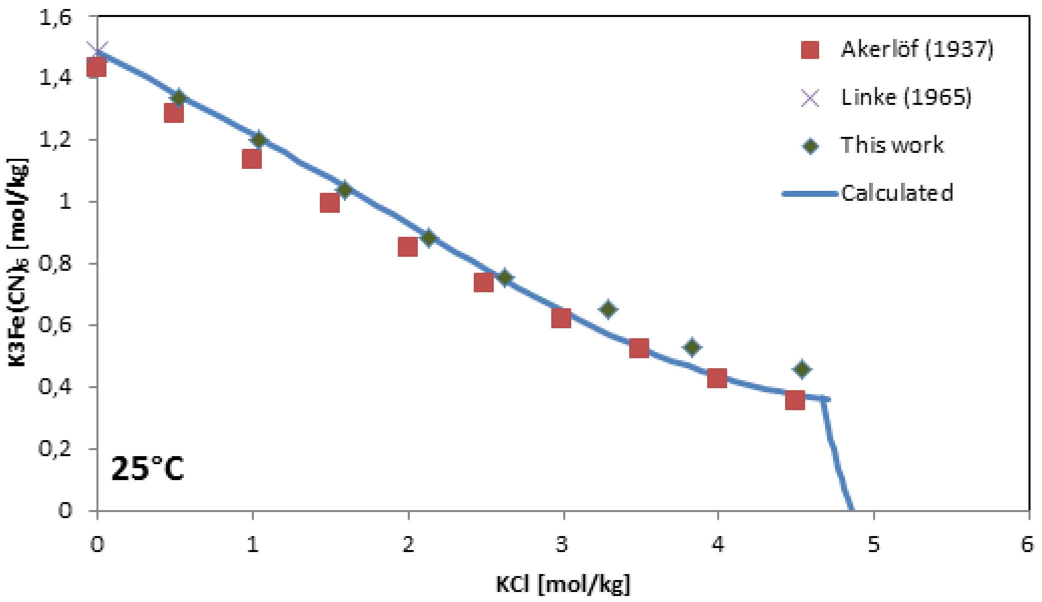

Fig. 7.35 Experimental and calculated solubilities in the system KCl-$K_3Fe(CN)_6$-H_2O at 25 °C

7.3.4 Redox measurements in mixed ferricyanide/ ferrocyanide solutions

Four stock solutions were freshly prepared before each series of titration. They contained either 0.1 or 4.5 mol/kg KCl as well as $K_4Fe(CN)_6$ and $K_3Fe(CN)_6$ in a concentration ratio of 1:1. In order to maintain a constant pH resp. H^+-concentration near 7 all solutions contained a phosphate buffer (Sigma P5244, 2.5 ml buffer solution in 250 ml stock solution). The exact values are shown in **Tab. 7.23**.

Tab. 7.23 Solubility of $K_4Fe(CN)_6$ in KCl solutions at 25 °C

No.	**KCl**	**$K_4Fe(CN)_6$**	**$K_3Fe(CN)_6$**
	[mol/kg]		
A2	0.0978	0.00473	0.00483
A3	0.0971	0.00587	0.00600
B2	4.4403	0.00537	0.00549
B3	4.4032	0.00665	0.00680

The titration experiments were conducted with a Metrohm Titrando titration system. 40 ml of the starting solutions (0.1 m KCl) were filled into a glass vessel with thermo-jacket with a constant temperature of 25 °C. The vessel was closed with a lid and flushed with argon. The apparent pH was measured with a Thermo Orion pH electrode (Ross type 8102SC) and an AgCl reference electrode (Metrohm, 6.0726.107, double junction, containing 3 mol/l KCl). For measurement of the redox potential a platinum ring electrode (Metrohm 6.0351.100) and the same reference electrode as above was employed.

The KCl concentration in vessel was increased stepwise by adding definite amounts of the higher concentrated stock solution (A2 plus B2 or A3 plus B3). The mixture was stirred for two minutes and potentials were recorded after additional two minutes.

In an additional set of experiments the concentration was decreased by starting with 4.5 m KCl and adding 0.1 m KCl. Altogether 4 titrations were conducted. The details are given in **Tab. B.14** to **Tab. B.17**.

The results of the first two series (with solutions A2 and B2) differed from the results with the other set of series (with solutions A3 and B3). While the cell potentials are equal up to KCl concentrations of about 0.5 mol/kg an increasing gap between the two sets widened until it reached 27 mV at the maximum KCl concentration (4.5 mol/kg). The reason for this behaviour could not be identified. More measurement series are necessary to bring more light into this question. The following evaluations are exemplarily in showing how the relationship between KCl concentration and cell potential could be established.

Fig. 7.36 shows the results of the first two series of measurements (after correction for the half cell potential of the reference electrode 207 mV) together with the data of Kolthoff and Tomiscek [KOL/TOM1934] which agree very well.

The observed cell potential is a combination of the two half-cell potentials (Pt-and reference electrodes) and the liquid junction potential. U_{LJ}, between the measuring solution and the KCl solution in the reference electrode

$$U = U_0(Ag \mid AgCl, 3MKCl) - U_0(Pt) - \frac{RT\ln(10)}{F}\log\frac{c_{Fe(CN)_6^{3-}}\gamma_{Fe(CN)_6^{3-}}}{c_{Fe(CN)_6^{4-}}\gamma_{Fe(CN)_6^{4-}}} + U_{LJ} \tag{7.74}$$

The half-cell potential for the platinum electrode results from the standard potential for the ferricyanide/ferrocyanide reaction (Rock [ROC1966])

$$Fe^{II}(CN)_6^{4-} = Fe^{III}(CN)_6^{3-} + e^{-} \tag{7.75}$$

$$U_0 = U_0(Pt) = -0.3704\,V \tag{7.76}$$

The half-cell potential for the single junction silver/silver chloride with 3 M KCl as an inner electrolyte is provided by the producer of the electrode (Metrohm)

$$Ag_{(s)} + Cl^{-} + e^{-} = AgCl_{(s)} \tag{7.77}$$

$$U_0 = 0.207\,V \tag{7.78}$$

The value of U_{LJ} is unknown as well as the exact value of the ratio of individual activity coefficients of the two iron cyanates. An approximation can be done by adding the activity of K^+ both in the logarithmic term and at the same time subtracting it outside (thus adding zero)

$$U = U_0(Ag\,|\,AgCl{,}3MKCl) - U_0(Pt) - \frac{RT\ln(10)}{F}\log\frac{c_{Fe(CN)_6^{3-}}\gamma_{Fe(CN)_6^{3-}}a_{K+}^3}{c_{Fe(CN)_6^{4-}}\gamma_{Fe(CN)_6^{4-}}a_{K+}^4} + \frac{RT\ln(10)}{F}\log a_{K^+} + U_{LJ} \tag{7.79}$$

The resulting expression of activity can be calculated using the Pitzer coefficients determined above, while the additional term with the activity of K^+ will be combined with the liquid junction potential to ΔRx:

$$\Delta Rx = \frac{RT\ln(10)}{F}\log a_{K^+} + U_{LJ} \tag{7.80}$$

$$U = U_0(Ag\,|\,AgCl{,}3MKCl) - U_0(Pt) - \frac{RT\ln(10)}{F}\log\frac{c_{Fe(CN)_6^{3-}}\gamma_{Fe(CN)_6^{3-}}c_{K+}^3\gamma_{K+}^3}{c_{Fe(CN)_6^{4-}}\gamma_{Fe(CN)_6^{4-}}c_{K+}^4\gamma_{K+}^4} + \Delta Rx \tag{7.81}$$

In KCl solutions ΔRx would also cover the complexation of ferro/ferricyanide with potassium [EAT/GEO1967] :

$$Fe(CN)_6^{4-} + K^+ = KFe(CN)_6^{3-} \qquad (7.82)$$

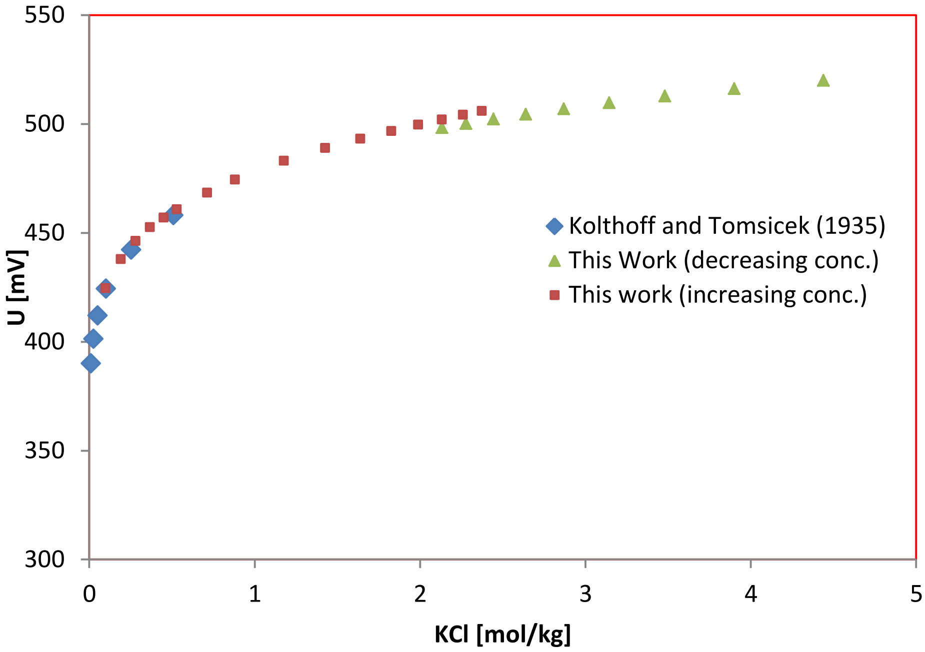

Fig. 7.36 Experimental cell potential of equimolar ferri- and ferrocyanite solutions in KCl

For each solution the expected redox potential Eh (the cell potential of a platinum electrode vs. the standard hydrogen electrode) was calculated following the Nernst equation:

$$Eh_{calc} = U_0 - \frac{RT \ln(10)}{F} \log \frac{a_{Fe(CN)_6^{3-}}}{a_{Fe(CN)_6^{4-}}} \qquad (7.83)$$

The standard cell potential U_0 can be calculated from the oxidation potential of ferrocyanide (Rock [ROC1966]):

$$U_0 = U_0(SHE) - U_0(Fe(CN)_6^{4-} / Fe(CN)_6^{3-}) - = 0 - (-0.307) = 0.307V \qquad (7.84)$$

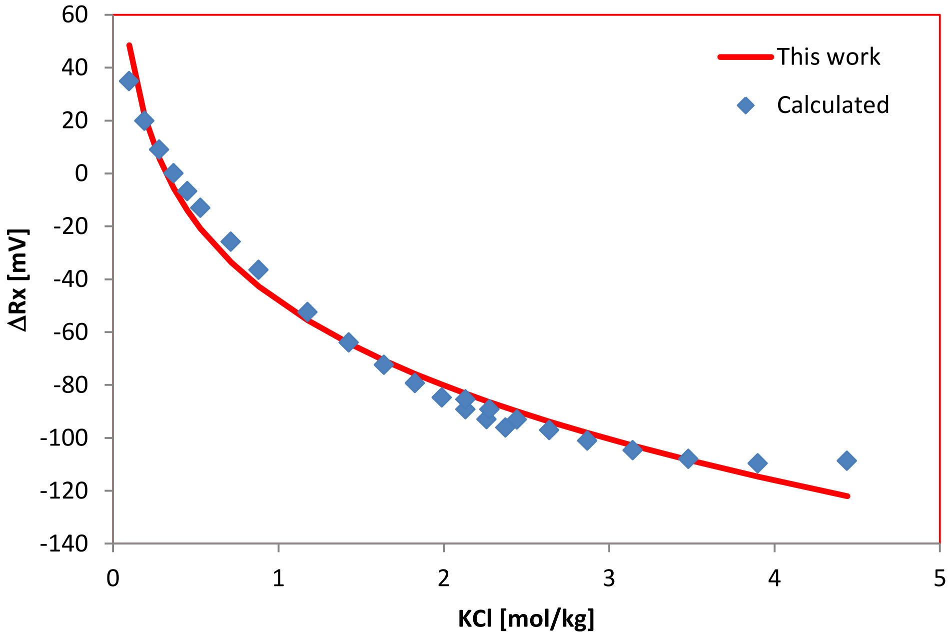

Fig. 7.37 ΔRx based on experimental values and calculated

$$\Delta Rx = -44{,}2 - 40.04 c_{KCl} - 4.0812 \ln c_{KCl} \qquad R^2 = 0.982 \tag{7.85}$$

An alternative approach would be to completely omit the calculation of activity coefficients and to include them in a ΔRx' term

$$\Delta Rx' = U_{LJ} - \frac{RT\ln(10)}{F}\log\frac{\gamma_{Fe(CN)_6^{3-}}}{\gamma_{Fe(CN)_6^{4-}}} \tag{7.86}$$

$$= \Delta Rx - \frac{RT\ln(10)}{F}\log\frac{\gamma_{Fe(CN)_6^{3-}}}{\gamma_{Fe(CN)_6^{4-}}} - \frac{RT\ln(10)}{F}\log a_{K^+}$$

$$U = U_0(Ag\,|\,AgCl, 3MKCl) - U_0(Pt) - \frac{RT\ln(10)}{F}\log\frac{c_{Fe(CN)_6^{3-}}}{c_{Fe(CN)_6^{4-}}} + \Delta Rx' \tag{7.87}$$

or

$$\Delta Rx' = U - U_0(Ag\,|\,AgCl, 3MKCl) + U_0(Pt) + \frac{RT\ln(10)}{F}\log\frac{c_{Fe(CN)_6^{3-}}}{c_{Fe(CN)_6^{4-}}} \tag{7.88}$$

ΔRx' has a similar concentration dependence values as the previously used ΔRx. Although the model is now much simpler, it is interesting to see that the regression can be done with better results.

The regression with two variables allows a much better representation (**Fig. 7.38**):

$$\Delta Rx = 104.3 - 4.216 c_{KCl} - 20.906 \ln c_{KCl} \qquad R^2 = 0.9950 \tag{7.89}$$

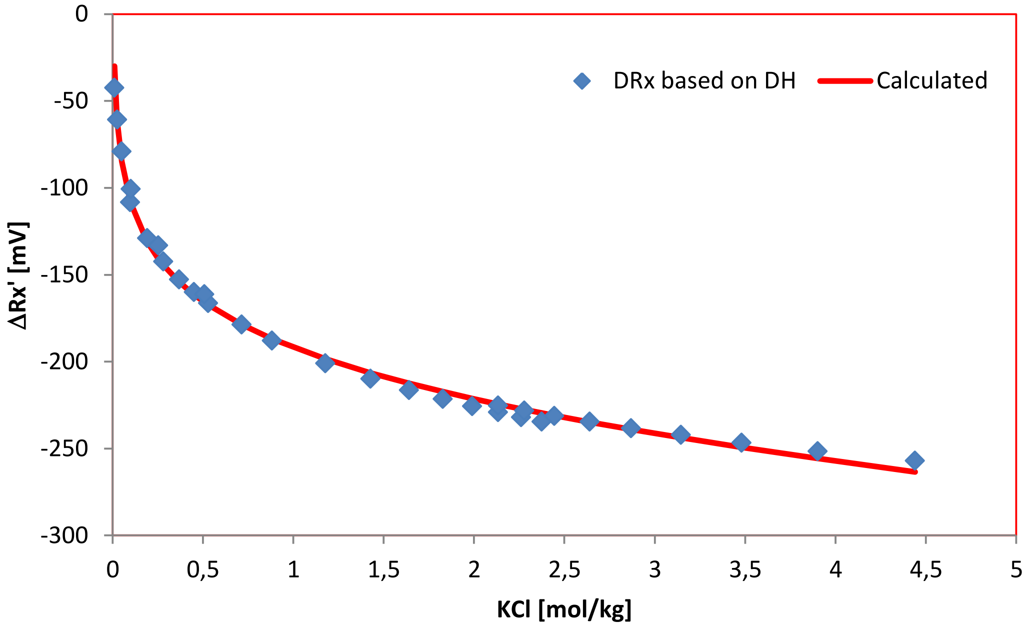

Fig. 7.38 ΔRx' calculated using concentrations only

Using one or the other equation it is possible to transform an observed redox cell potential in a KCl solution around pcH = 7 into a ratio of mixed ion ferri-/ferrocyanate activities or into a ratio of ferri-/ferrocyanate concentrations. Based on these values it is possible to calculate a generally applicable measure of the redox state of the solution, such as the logarithm of the partial oxygen pressure log f_{O2}[6], e. g. by applying the following reaction:

$$Fe(CN)_6^{4-} + 1/4O_2 + H^+ = Fe(CN)_6^{3-} + ½\ H_2O \tag{7.90}$$

The equilibrium constant for this reaction would be formulated as:

---

[6] At total pressures around 0.1 MPa the fugacity of oxygen is practically identical with the partial pressure

$$K = \frac{a_{Fe(CN)_6^{3-}} a_{H_2O}^{0.5}}{a_{Fe(CN)_6^{4-}} p_{O_2(g)}^{0.25} a_{H^+}} \tag{7.91}$$

The partial pressure of oxygen (more precisely its fugacity whose numerical value is almost the same at or below 1 bar total pressure) can be calculated from the individual redox reaction of ferri-/ferrocyanide and oxygen:

$$\text{Fe(CN)}_6^{4-} = \text{Fe(CN)}_6^{3-} + e^- \tag{7.92}$$

$$2\ H_2O = O_2 + 4H^+ \tag{7.93}$$

The standard electrode potential of the ferri-/ferrocyanide reaction is given by Rock [ROC1966]:

$$U^0 = -\frac{RT}{zF}\ln K = -0.307\,\mathrm{V} \tag{7.94}$$

It follows that the equilibrium constant for reaction (7.92) is log K = 6.26. It is combined with the equilibrium constant for reaction (7.93) (log K= -83.0908, derived from [COX/WAG1989]).

For the equilibrium constant of the reaction of ferrocyanide with oxygen (7.90) the following value results:

log K= 27.03

The partial pressure of gaseous O_2 in equilibrium with a solution containing a known concentration of ferrocyanide and ferricyanide could then be calculated by:

$$p_{O_2(g)} = \frac{c_{Fe(CN)_6^{3-}}^4 \gamma_{Fe(CN)_6^{3-}}^4 a_{H_2O}^2}{c_{Fe(CN)_6^{4-}}^4 \gamma_{Fe(CN)_6^{4-}}^4 a_{H^+}^4 K^4} \tag{7.95}$$

Finally (7.95) may be logarithmized to

$$\log p_{O_2(g)} = 4\log\frac{c_{Fe(CN)_6^{3-}}}{c_{Fe(CN)_6^{4-}}} + 4\log\frac{\gamma_{Fe(CN)_6^{3-}}}{\gamma_{Fe(CN)_6^{4-}}} + 2\log a_{H_2O} - 4\log a_{H^+} - 4\log K \tag{7.96}$$

and combined with (7.88) which allows a direct relationship between the measure log p_{O2} and the observed redox potential U:

$$\log p_{O_2(g)} = \frac{4F}{RT\ln(10)}\left(\Delta Rx' - U + U_0(Ag\,|\,AgCl, 3MKCl) - U_0(Pt)\right) \tag{7.97}$$

$$+ 4\log\frac{\gamma_{Fe(CN)_6^{3-}}}{\gamma_{Fe(CN)_6^{4-}}} + 2\log a_{H_2O} - 4\log a_{H^+} - 4\log K$$

This expression may be regrouped into

$$\log p_{O_2(g)} = -\frac{4F}{RT\ln(10)}U + f_{Rx}(medium) - 4\log c_{H^+} + c_{Rx} \tag{7.98}$$

with

$$f_{Rx}(medium) = \frac{4F}{RT\ln(10)}\Delta Rx' + 4\log\frac{\gamma_{Fe(CN)_6^{3-}}}{\gamma_{Fe(CN)_6^{4-}}} + 2\log a_{H_2O} - 4\log\gamma_{H^+} \tag{7.99}$$

$$c_{Rx} = \frac{4F}{RT\ln(10)}\left(U_0(Ag\,|\,AgCl, 3MKCl) - U_0(Pt)\right) - 4\log K \tag{7.100}$$

It is advisable to combine log p_{O2} with the hydrogen concentration to allow the comparison of solutions of different acidity:

$$\log p_{O_2(g)} + 4\log c_{H^+} = \frac{4F}{RT\ln(10)}U + f_{Rx}(medium) + c_{Rx} \tag{7.101}$$

Equations (7.98) and (7.101) allow the transformation of measured redox cell potentials into a thermodynamically meaningful measure, the oxygen partial pressure. **Fig. 7.39** shows the calculated values of log p_{O2} + 4 log c_{H+} in KCl solutions. The equations are valid even if neither ferricyanate nor ferrocyanate are present in the solution. This can be shown with the following thought experiment. If a given solution has a redox potential U_1 an infinitesimal small amount of ferricyanate or ferrocyanate are added. The concentration ratio of both species would adjust according to the ruling redox potential. In that case the redox potential U_1 also represents the redox equilibrium of ferricyanate/ferrocyanate. All parts of the variable functions f_{Rx} can be calculated without knowing the concentrations of the two iron species. They depend only on the medium ions (H^+, other cations and anions) and the temperature.

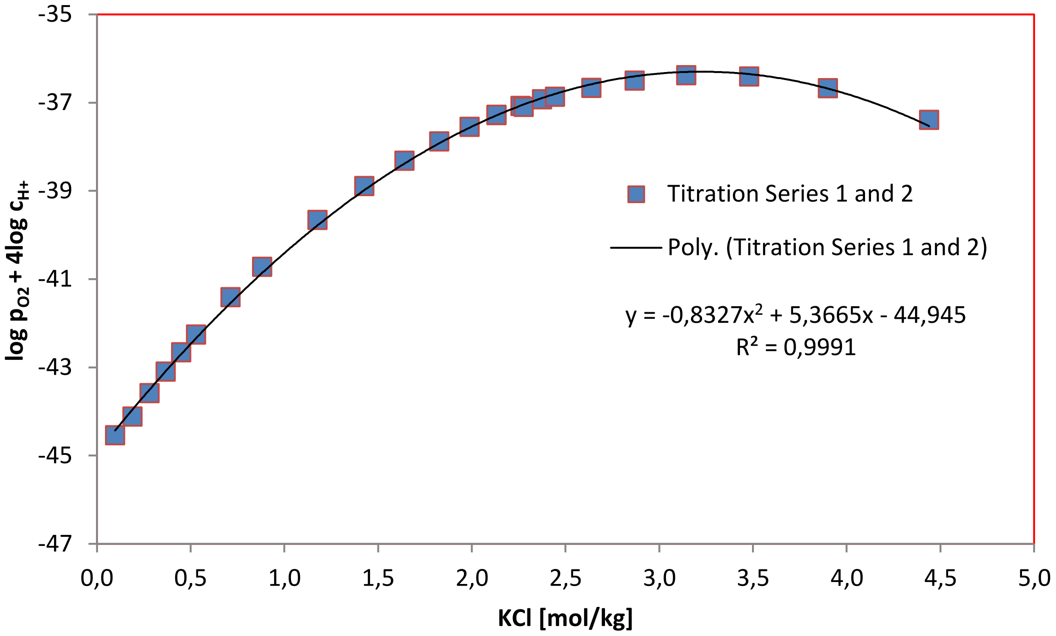

Fig. 7.39 Partial pressure of oxygen (log pO_2 + 4 log cH+) of equimolar solutions of ferricyanide/ferrocyanide in aqueous KCl

Principally the approach could be applied in all solutions where the ion activity coefficients for ferricyanate, ferrocyanate and hydrogen (H^+) can be calculated. For the time being, this is only possible in KCl solution at 25 °C. In order to make such calculations in NaCl solutions as well, further investigations are necessary to determine the activity coefficients of $Na_4Fe(CN)_6$ and $Na_3Fe(CN)_6$ in aqueous solution as well as in mixed solutions with NaCl.

7.4 Occurrence of C-14 in spent fuel

7.4.1 Introduction

^{14}C is generated mainly within the primary system of a nuclear power plant by activation of isotopes of C, N and O or as a ternary fission product. Besides a small liquid or gaseous release during operation ^{14}C has been identified as an important radionuclide in radioactive waste which has to be disposed. ^{14}C is due to the long half-life of 5730 years and its mobility of special interest in long term safety of radioactive waste disposal which requires knowledge of characteristics and occurrence of ^{14}C.

7.4.2 Methodology

The literature survey was done with „Scifinder“ (Chemical Abstracts Service). Also, freely accessible internet resources were considered such as Science-direct, Google and literature which was already available. This survey complemented and updated a literature list from an earlier study [BRA/MÜL2008]. Priority was given on literature concerning the disposal of heat-generating radioactive waste.

7.4.3 Carbon

The element carbon has three isotopes. The isotopes ^{12}C and ^{13}C are stable and the radioactive isotope ^{14}C, which generates nitrogen, ^{14}N, by β decay. Carbon occurs in elemental form and in organic and inorganic compounds. The oxidation state ranges from +IV (CO_2) to –IV (CH_4). Carbon dioxide is the most stable compound under strongly oxidizing conditions. Methane is the most stable compound under strongly reducing conditions. Organic molecules have a small area of thermodynamical stability in the predominance diagram within the area of methane and the carbon dioxide and carbonates (**Fig. 7.40**). Nevertheless, carbon has the ability to from complex molecules and a large variety of compounds. Carbon compounds are the basis of terrestrial life. The dissolved carbonate ion is the most stable compound under alkaline conditions in water.

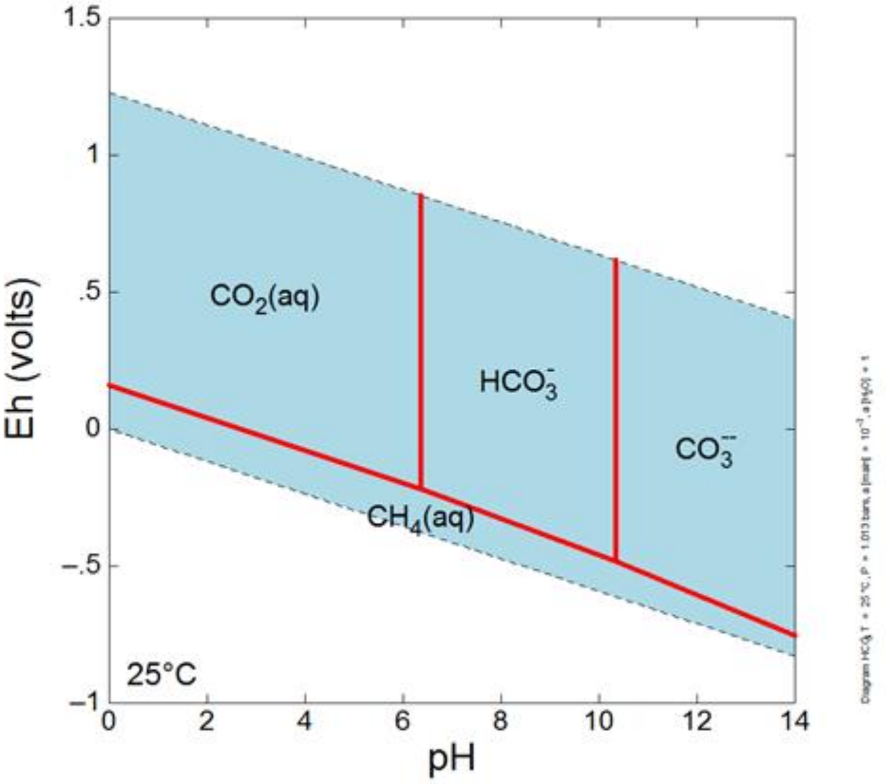

Fig. 7.40 Pourbaix-Diagram of important carbon compounds

The reactions of carbon dioxide with water have special importance. The reactions are:

1. Physical dissolution of gaseous CO_2

$$\mathrm{CO_2(g) <=> CO_2(aq)}$$

2. Chemical reaction of dissolved, gaseous CO_2 to carbonic acid, H_2CO_3

$$\mathrm{CO_2(aq) + H_2O\ <=> H_2CO_3(aq)}$$

3. The dissociation of the unstable carbonic acid under formation of H_3O^+ and H bicarbonate.

$$\mathrm{H_2CO_3(aq) + H_2O\ <=> HCO_3^-(aq) +\ H_3O^-(aq)}$$

4. The second dissociation step under formation of H_3O^+ and carbonate.

$$\mathrm{HCO_3^-(aq) + H_2O\ <=> CO_3^{--}(aq) +\ H_3O^-(aq)}$$

7.4.4 Source and production of ^{14}C

The cosmic radiation generates ^{14}C naturally via $^{14}N(n,p)^{14}C$ in the environment. The rate is nearly constant. Due to the radioactive decay and the circulation of ^{14}C in the biosphere a dynamic equilibrium (steady state) is obtained in various compartments, which leads to constant concentration of ^{14}C in the atmosphere. This is used to determine ages in archaeology.

^{14}C is generated anthropogenically in fuel, structural materials and coolant during operation of nuclear power plants [BLE1983]. The activation of ^{14}N, ^{17}O and ^{13}C to ^{14}C takes place by neutron capture. There are three main reaction mechanisms (**Tab. 7.24**). The elements N, O und C main are either main components of the materials (e. g. Air, coolant) or minor constituents (structural parts, fuel).

Tab. 7.24 Main reactions generating ^{14}C

No.	Isotope	Reaction	Cross section for neutron capture (barn)	Relative abundance of isotope in element (%)
1	^{14}N	$^{14}N(n,p)^{14}C$	1.81	99.64
2	^{13}C	$^{13}C(n,\gamma)^{14}C$	0.0009	1.103
3	^{17}O	$^{17}O(n,\alpha)^{14}C$	0.235	0.0383

The generation of ^{14}C as a ternary fission product is negligible compared to activation. The generation rate of ^{14}C as am activation product is proportional to the neutron flux, the neutron capture cross section and the abundance of the isotope, being activated. Since the relative abundance of ^{14}N in nitrogen and its cross section are high, yet trace amounts of nitrogen lead to a significant generation of ^{14}C. The generation of ^{14}C in the coolant (H_2O) and fuel (UO_2) via the reaction $^{14}N(n,p)^{14}C$ outweighs other mechanisms already, when the trace content of nitrogen is more than a few ppm. Due to smaller neutron capture cross section and the lower concentration of carbon in the coolant the absolute generation of ^{14}C from ^{13}C is by magnitudes lower than the generation of ^{14}C from ^{17}O.

The generation of ^{14}C in fuel rods is mainly caused by the oxygen content of uranium dioxide and the trace amounts of nitrogen in the components of the fuel elements (fuel, steel, zircaloy and other alloys). The estimated generation rates of operating light water reactors are given in **Tab. 7.25**.

The slightly lower generation of ^{14}C in the coolant of a boiling water reactor compared to a pressurized water reactor is caused operationally by a lower trace amount of nitrogen (**Tab. 7.25**).

The generation of ^{14}C in graphite and carbon bricks is caused by trace amounts of nitrogen and the C-13 content in carbon [NAR/SMA2010]. The total amount of ^{14}C in graphite or carbon bricks is smaller in Germany than in other countries since graphite was used only in a few reactor types.

Tab. 7.25 Generation of ^{14}C in light water reactors [YIM 2006]*

Fuel element	**Pressurized water reactor [GBq/t_{HM}]**	**Boiling water reactor [GBq/t_{HM}]**	**Main reaction**
^{17}O in UO_2	7.5	7.0	$^{17}O(n, \alpha)^{14}C$
^{14}N in UO_2[a]	29.1	28.6	$^{14}N(n, p)^{14}C$
^{14}N (Zircaloy, fuel assembly)[b]	25.6	19.1	$^{14}N(n, p)^{14}C$
Coolant			
^{17}O in H_2O	27.1	11.1	$^{17}O(n, \alpha)^{14}C$
N_2 (10–40 ppm)	5.5 – 21.6	2 – 9.5	$^{14}N(n, p)^{14}C$
Total	85.4 – 100	65 – 75	

* converted and corrected (Typo: pressurized and boiling water reactors were swapped)

[a] mean values; based on 20 ppm N_2 in fuel

[b] based on 25 ppm N_2

7.4.5 Occurrence and speciation of ^{14}C

The main components of a reactor which contain ^{14}C are the coolant as a liquid or gaseous phase and the fuel elements with the pellets, hulls and structural materials. Also graphite as a solid phase may contain ^{14}C.

7.4.5.1 Coolant

The chemical speciation of ^{14}C in the coolant is likely to be compounds which are dissolved or sorbed on fine particles. The quantitative distribution is unknown under operating conditions. The occurrence of ^{14}C onto solid corrosion products (CRUD[7]) is well known [LIN/WIL2007]. Since the chemical milieu in the primary coolant circuit of a pressurized water reactor is reducing more than 80 % of the released gaseous ^{14}C was specified as methane ($^{14}CH_4$) and some carbon oxide (^{14}CO) [BLE1983]. Other gases containing ^{14}C are ethane, propane and butane. Due to the oxidizing conditions in a BWR (boiling water reactor) about 95 % of the released gaseous ^{14}C was specified as carbon dioxide ($^{14}CO_2$) and only 5 % were dissolved as organic compounds in the coolant. The mayor part of the generated ^{14}C in the coolant was released to the atmosphere during operation. The release of ^{14}C and its detection are regulated in Germany [KTA2002].

7.4.5.2 Evaporated concentrates

Evaporated concentrates of a PWR (pressurized water reactor) contain ^{14}C as carbonates and bicarbonates. Also, oxalic acid, ethylene glycol, methanol and ethanol were detected [MIT/SAK1992].

7.4.5.3 Spent fuel / hulls

[AHN1994] and [VAN1994] assumed that the possible speciation of ^{14}C in spent fuel and. hulls, respectively, is carbide, oxycarbide or elemental carbon originating from activation of nitrogen. Such a speciation is reasonable, but neither detected experimentally or otherwise proved for spent fuel or hulls. Also [JOH/MCG2002] declares explicitly that the speciation of ^{14}C in spent fuel is unknown. In the course of this study no experimental or analytical study on the speciation of ^{14}C in spent fuel was found.

---

[7] CRUD = ...an acronym for 'Chalk River Unidentified Deposits.' ...black, highly radioactive substances found on the inside of piping and components at the Chalk River nuclear reactor ... CRUD has now become a standard industry term referring to minute, solid, corrosion products that travel into the reactor core, become highly radioactive, and then flow out of the reactor into other systems in the plant. ... CRUD can settle out in crevices or plate-out on the inside of piping in considerable quantities ... The major components of CRUD are iron, cobalt, chrome, and manganese ... CRUD is a concentrated source of radiation and represents a significant radiological risk because of its insolubility. (excerpts from: United States Federal Energy Regulatory Commission, Testimony of James K. Joosten, September 15, 1997, pg. 13-14)

Coolant, spent fuel, moderator and structural materials contain approx. 98 % of the ^{14}C generated by activation. A major part of the ^{14}C, which was generated in the coolant, is released to the atmosphere during the operation of the plant.

^{14}C generated in spent fuel and structural materials is not released and is part of the heat generating radioactive waste. There is no release during interim storage. ^{14}C is released as gas when spent fuel is reprocessed [BLE/KRO1987] which applies to some spent fuel in Germany only.

Radioactive waste

Tab. 7.26 lists a typical distribution of the remaining ^{14}C inventory on some waste components of a light water reactor (LWR) excluding the spent fuel [YIM/CAR2006] [DAM/MOO1995].

Tab. 7.26 Distribution of ^{14}C in LWR-waste [YIM/CAR2006] [DAM/MOO1995]

Waste form description	**fraction (%)**
Ion exchange resins	48.8
Irradiated hardware	24.1
Mixed active waste	13.6
Solidified liquids	4.4
Filter media	3.6
Cartridge filters	2.7
Solid non-combustibles	1.2
Incinerator ash	1.2
Air filters	0.15
Biological wastes	0.15
Total	99.9

Only a few references provided data on the ^{14}C content in spent fuel (**Tab. 7.27**). The data are based mainly on burn up calculations estimating a nitrogen impurity and neutron flux. Only [BLE1983], [BLE/KRO1987] and [STR1996] provided analytical data. [STR1996] calculated the ^{14}C content using the code ORIGEN-S (not shown). The analytical data (**Tab. 7.27**) was 6 to 15 times smaller than the calculated value. This may be caused by an overestimation of the nitrogen content. Further analytical data on ^{14}C in spent fuel from LWR was not found in the course of this study.

The data shows some scattering reflecting different estimates of the nitrogen impurity. The total generation of ^{14}C can be normalized to the electric power production (burn up) but is depending on the reactor type [YIM/CAR2006].

Tab. 7.27 ^{14}C in spent fuel

Reference	**Burn up (GWq/t_{HM})**	**^{14}C (GBq/t_{HM})**
[LIE/THO1988]	9	64*
[STR/TAI1994]	10 (Candu)	1.03 – 5.76
[DAV1977]	27.5 rsp. 33	1.1 – 55*
[BLE1983]	30	36
[BLE/KRO1987]	22.4 (BWR)	8
[BLE/KRO1987]	30 (PWR)	10.5 (up to 37)
[VAN1994]	33	22
[MAR/ESB2004]	50	21*

* converted, depending on burn up and assumed impurity of nitrogen

HM = heavy metal = spent fuel

Tab. 7.28 lists data from burn-up calculations on ^{14}C in spent fuel and hulls used as inventory in the „Vorläufigen Sicherheitsanalyse Gorleben“[PEI/MCS2011]. The range of this data is comparable to the range of data in **Tab. 7.27**. The total amount of ^{14}C in heat generating radioactive waste for disposal in Germany was estimated in the order of approx. 10^{14} Bq [PEI/MCS2011].

Tab. 7.28 ^{14}C in spent fuel and hulls [PEI/MCS2011]

Spent fuel (50-55 GWq/t_{HM})*	**^{14}C (GBq/t_{HM})**
DWR-MOX	16
DWR-UO_2	21
WWER	10 - 12
SWR-MOX	15
SWR-UO_2	22
DWR MOX hulls	6.5
DWR UO_2 hulls	16

* DWR = pressurized water reactor, SWR = boiling water reactor, WWER = water-water-energy reactor, MOX = Mixed Oxide

7.4.5.4 Graphite

Graphite was used only in a few reactor types in Germany (Thorium-Hoch-Temperatur-Reaktor, THTR; Arbeitsgemeinschaft Versuchsreaktor, AVR; Forschungsreaktor Jülich, FRJ). Depending on the type of reactor the concentration of ^{14}C varies (**Tab. 7.29**). The operation of THTR in Germany generated a total activity of approx. 5000 GBq ^{14}C in ca. 675000 spheres [KIE 2004].

Tab. 7.29 ^{14}C concentration in graphite [FAC/VON2008], [KIE/MET2004]

	THTR	**FRJ**	**AVR**
^{14}C	37 000 Bq/g	449 Bq/g	95 000 Bq/g

Research was performed on reactor graphite to minimize the waste volume, decontaminate or fixate ^{14}C and to investigate the release under conditions of a final repository by [POD2005], [FAC/VON2008], [FAC/ZHA1995], [YAN/EUN2005], [GUP2004], [DMI/KAR2003]. Presently, there is no decision on the preferred option for disposal of activated graphite. Disposal of graphite was included as an option in the preliminary safety analysis of the Gorleben site [PEI/MCS2011]. On high heating a preferential release of ^{14}C was found [POD2005] indicating a weak bonding of ^{14}C in graphite. The potential consequences of this effect for final disposal remain unclear. A use of the collected ^{14}C for medical studies may be possible due to the enrichment factor of 20 in ^{14}C concentration [VON/VUL2011].

Two research projects, CARBOWASTE (“Treatment and Disposal of Irradiated Graphite and other Carbonaceous Waste”) rsp. CARBODISP (“Disposal of irradiated Graphite”), dealing with characteristics and behavior of ^{14}C contained in graphite and coal bricks have been started in 2008 rsp. 2010 and are still being finalized [VON/VUL2011], [VUL/BAG2013]. Graphite and coal bricks represent a large share of the waste containing ^{14}C in Germany. [VUL/BAG2013] concluded on a homogeneously and heterogeneously (hotspots) distributed part of ^{14}C in graphite but also that ^{14}C is similarly bound as $^{12/13}$C. Since ^{14}N is concentrated on graphite surfaces this leads to hotspots when activated to ^{14}C. Already available covalently bound oxygen in graphite as CO-groups will lead to a release of ^{14}CO on pyrolysis. XPS measurements detected sp^3-hybridized carbon atoms indicating defects in the graphite crystal which can be caused by ^{14}C. Interestingly, an electrolysis of graphite leads to a relative enrichment of ^{14}C in the generated $^{14}CO_2$ compared to the graphite.

7.4.5.5 Other waste

Other waste from medical and chemical research or industry contains ^{14}C as non- or negligible heat generating radioactive waste for disposal. The current concept in Germany foresees its disposal in the licensed Konrad repository. The total amount of ^{14}C for disposal is limited to $4*10^{14}$ Bq. Each container has to fulfil further requirements which ensure the compliance with this limit.

7.4.6 Analysis of ^{14}C

The quantitative analysis of ^{14}C is done by radiation counter tubes, liquid scintillation, mass spectrometry, calculation of activation and the scaling factor method. An exhaustive review is given in [HOU/ROS2008].

7.4.6.1 Radiation counter tube

^{14}C decays with a half-life of 5730 years by β−decay to ^{14}N, an electron and an antineutrino (decay energy 158 keV):

$$^{14}_{6}\mathrm{C} \rightarrow {}^{14}_{7}\mathrm{N} + {}^{0}_{-1}\mathrm{e}^{-} + \bar{\nu}$$

The classical method for measurements of radio carbon is the direct detection of the electron in a counting tube. The sample is prepared as CO_2 for counting. Therefore ^{14}C has to be carbonate or has to be converted to carbonate. Due to the long half-life and the low natural abundance of ^{14}C the activity of a mol of modern carbon is only 3 decays per second. ^{14}C is called a difficult to measure (DTM) isotope. A high precision of the measurement requires a good shielding of the counting tube, the chemical separation from other radionuclides, a large sample size (up to 1 kg for modern samples) and a long measurement time.

7.4.6.2 Liquid scintillation

Liquid scintillation also uses the radioactive decay of ^{14}C for measurement. ^{14}C has to be separated from other radionuclides (β-decays) [DEC/VAN1993] . The carbon is converted to benzene via several intermediate steps using a vacuum line. An organic scintillator is added. The electrons from the decay are converted by the scintillator to light pulses, which are amplified by photomultipliers and counted.

The advantage over the counting tube is that a larger amount of carbon can be collected in the sampling chamber. This shortens measurement time and gives a better precision. The liquid scintillation is commercially available, whereas counting tubes are in-house development of laboratories.

Special technics for chemical digestion of ^{14}C containing samples such as graphite were developed by [FRE/DEG2007] using pyrolysis and mineralization by iodic acid to allow measurement ^{14}C.

7.4.6.3 Accelerator mass spectrometry

The accelerator mass spectrometry allows a direct determination of ^{14}C. The measurement of small sample sizes provides an absolute number of atoms or an isotope ratio of $^{14}C/^{12}C$ down to 10^{-15}. The sample size is approx. 1 mg and significantly smaller than required for using counting tubes or liquid scintillation. About 40000 atoms of ^{14}C in a modern sample can be detected in one hour with a precision of 0.5 %. This technique is more sophisticated and expensive. This technique is normally not used in nuclear technology but in environmental analytics for low concentrations of ^{14}C [HEL/ERL2001], [POV/ORE2000], [HOT/FIN2000], [JUL/BUR2003].

7.4.6.4 Numerical methods: Activity calculation

The generation and content of ^{14}C in spent fuel can be determined by burn-up and activity calculations to avoid tedious and costly measurements and radiation exposure [HUM2011], [MAR/ESB2004]. The main reactions of activation (**Tab. 7.24**) are implemented in the standard computer programs, e. g. ORIGEN 2.1. The further developed program ORIGEN-X implemented additional activation chains and updated neutron capture cross sections in the calculation of ^{14}C [HUM2011], (**Tab. 7.30**) leading to small improvements.

Tab. 7.30 Implemented reactions for activation in ORIGEN, ORIGEN-X

Reaction	ORIGEN	ORIGEN-X
$^{14}N(n,p)^{14}C$	Yes	Yes
$^{17}O(n,\alpha)^{14}C$	Yes (but to low)	Yes
$^{16}O(n,t)^{14}N$	No	Possible
$^{19}F(n,t)^{17}O(n,\alpha)^{14}C$	(n,t)-reaction not possible	Yes (additional chains)
		$^{19}F(n,\gamma)^{20}F \rightarrow$ beta- $\rightarrow$ $^{20}Ne(n,\alpha)^{17}O(n,\alpha)^{14}C$ $^{19}F(n,\alpha)^{16}N \rightarrow$ beta- $\rightarrow$ $^{16}O(n,\alpha)^{13}C(n,\gamma)^{14}C$
$^{20}Ne(n,\alpha)^{17}O(n,\alpha)^{14}C$	Yes	Yes

Some programs for calculation of the activation in spent fuel were compared in [KOL 2004]. According to [KOL2004] the generation of ^{14}C in spent fuel based on activation calculation with ORIGEN 2.1 was underestimated by a factor of 2 – 4 compared to other programs. A correction factor was proposed to provide a conservative upper bound for the activity. ^{14}C in reactor graphite was successfully modeled by [REM/PLU2010] when assuming 15 ± 4 ppm nitrogen.

7.4.6.5 Numerical methods: Scaling factor method

The scaling factor or correlation method is applied on difficult to measure nuclides (DTM) such as ^{14}C [LIN/WIL2007]. The method applies empirical coefficients for the ratio of easy /difficult to measure key nuclides [IAEA2009]. ^{14}C is correlated empirically to the key nuclide ^{60}Co, even though the paired radionuclides do not have much in common with respect to their production route or chemical similarity. As long as a correlation can be demonstrated to exist, the DTM nuclide can still be inferred from the concentration of the key nuclide. The scaling factor method using an insufficient data base does not give a satisfactory result for ^{14}C when not corrected for nitrogen [REM/PLU2009]. The differences between calculated and measured concentrations were rarely larger than a factor of 2.5 [ROB/HAG1992].

7.4.7 ^{14}C in final disposal

Several studies on release of ^{14}C from final disposal sites for radioactive waste and its potential radiation exposure were done [LIG/ZWA1990], [LEH/MER1994], [YIM/SIM1996], [YIM/SIM2000], [MOE/RYA2006], [MOE/RYA2007]. The described waste characteristics ranged from low, medium to highly radioactive. A number of studies have been compiled by [NIR2006].

Naturally, the conditions of a final repository determine the release behaviour of ^{14}C and different pathways for the potential radiation exposure which are important for an assessment of a site. The waste is characterized in low and medium radioactive waste (non- and negligible heat generating waste) and highly radioactive waste (heat generating waste).

7.4.7.1 Low and medium radioactive waste (non- and negligible heat generating waste)

The composition of low and medium radioactive waste is heterogeneous since it originates from sources such as different technical installations of nuclear power plants or different types of research facilities. ^{14}C can be specified as organic or inorganic. ^{14}C incorporated in organic or inorganic compounds may be released after chemical degradation as soluble or volatile compounds [BRA/MÜL2008]. It has been shown in [FRA/DON1980] that a microbial process can enhance the release of ^{14}C from low radioactive wastes.

Studies on ^{14}C in low to medium radioactive waste [LIG/ZWA1990], [LEH/MER1994], [YIM/SIM1996] und [YIM/SIM2000] assumed a release of ^{14}C as $^{14}CO_2$. [HIE/SWI2005] expected a long-term release of $^{14}CO_2$ from ion exchange resins stored in a concrete chamber. The reaction pathway is unknown. Due to the low solubility of carbonate in a chemical environment dominated by concrete and its precipitation as calcium carbonate, the potential radiation exposure was calculated to be low [KAP2005].

Assuming that ^{14}C is partially present as easy degradable organic compounds in the radioactive waste of the salt mine Asse [NIE/RES2006] expected a proportional release as methane. The long-term safety was analyzed for a given site-specific scenario. The potential radiation exposure was close to the reference limit of 0.3 mSv/a of the radiation protection ordinance.

The potential radiation exposure from ^{3}H, ^{14}C und ^{36}Cl of a surface disposal site for low radioactive waste in Maisiagala, Lithuania, exceeded the regulatory limit [GUD/NED2010]. The minor share was contributed by ^{14}C.

[NAG2008] studied the release of ^{14}C as a safety relevant nuclide from low and medium radioactive waste. For the reference case the release of ^{14}C contributed significantly to the potential radiation dose (Fig. 7.41). This is mainly caused by the fact, that an instaneous release of ^{14}C in inorganic and organic form was assumed except for ^{14}C in activated metal, which is released congruently with corrosion rate of 10^{-4} per year [SCH2008].

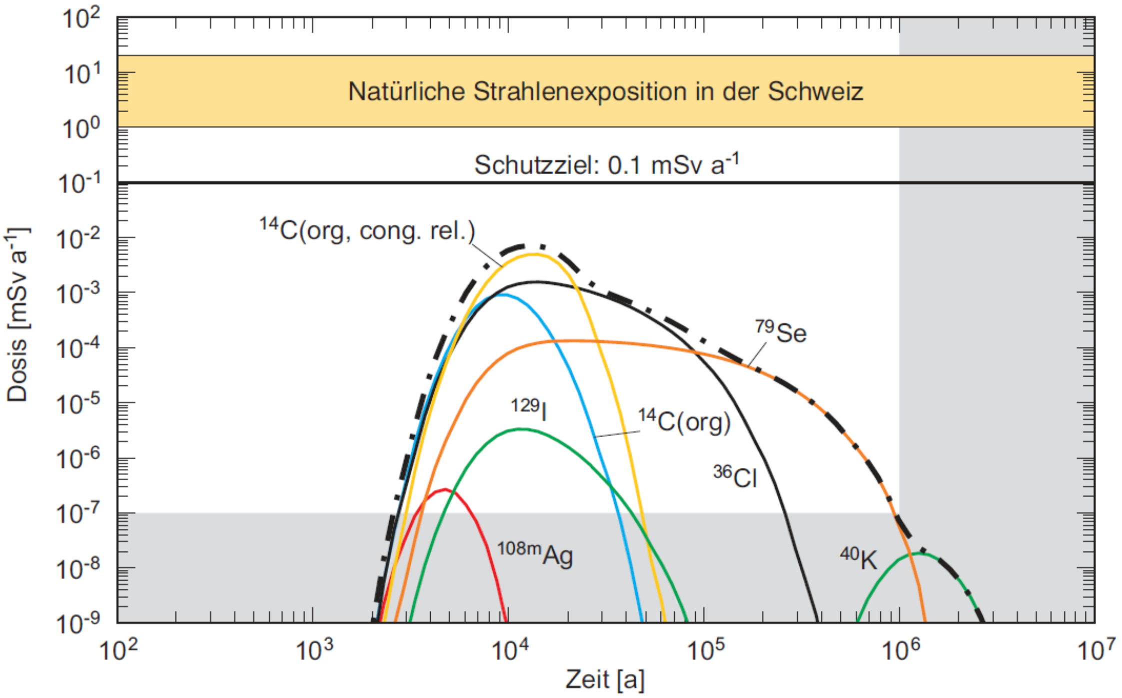

Fig. 7.41 Potential radiation exposure (dose) for disposal site of low and medium radioactive waste in Switzerland [NAG2008]

7.4.7.2 High radioactive waste (heat generating waste)

High radioactive waste for final disposal is mainly spent fuel, structural parts and vitrified waste. ^{14}C in spent fuel and structural parts is contained in fuel pellets and the metal alloys. Due to the reprocessing process vitrified waste has negligible amounts of ^{14}C [BLE/KRO1987].

[AHN 1994] assessed the release of ^{14}C from spent fuel and zircaloy and reported that 0.05 % to 7.3 % of the total ^{14}C inventory in spent fuel (LWR) is located in gaps and grain boundaries. The remaining ^{14}C was assumed in the spent fuel matrix either in elemental form or as compounds such as carbides (UC, UC_2) or oxycarbides (UC_xO_y). He concluded considering different effects such as container failure, diffusion and oxidation that ^{14}C release can be significant from spent fuel under aqueous dissolution conditions. He further concluded that the ^{14}C release from zircaloy is unlikely to be significant under dry conditions. The release of ^{14}C from structural parts (i. e. hulls / zircaloy) was also investigated in [SMI/BAL1993] and [TAB 2009]. A fraction of 10 % of the total inventory was released in the experiments of [SMI/BAL1993] with temperature and different gases. He was not able to account this for the oxide film or the metal but considered a nonuniformal distribution. [TAB 2009] confirmed a relative enrichment of ^{14}C in the oxide layer of zircaloy and detected ^{14}C as dissolved organics in leaching tests.

[STR/TAI1994] and [STR1996] investigated experimentally the release of ^{14}C from spent fuel from a CANDU reactor. The fraction of ^{14}C in the gap and grain boundaries of the total ^{14}C inventory ranged between 0.06 and 5.04 %. It was concluded based on leaching experiments on pellets that this represents the instant release fraction (IRF) with a normal distribution between 0.05 to 7.5 %. Although this release was extrapolated to take up to several hundred years, this fraction is instantaneous for long-term safety analyses.

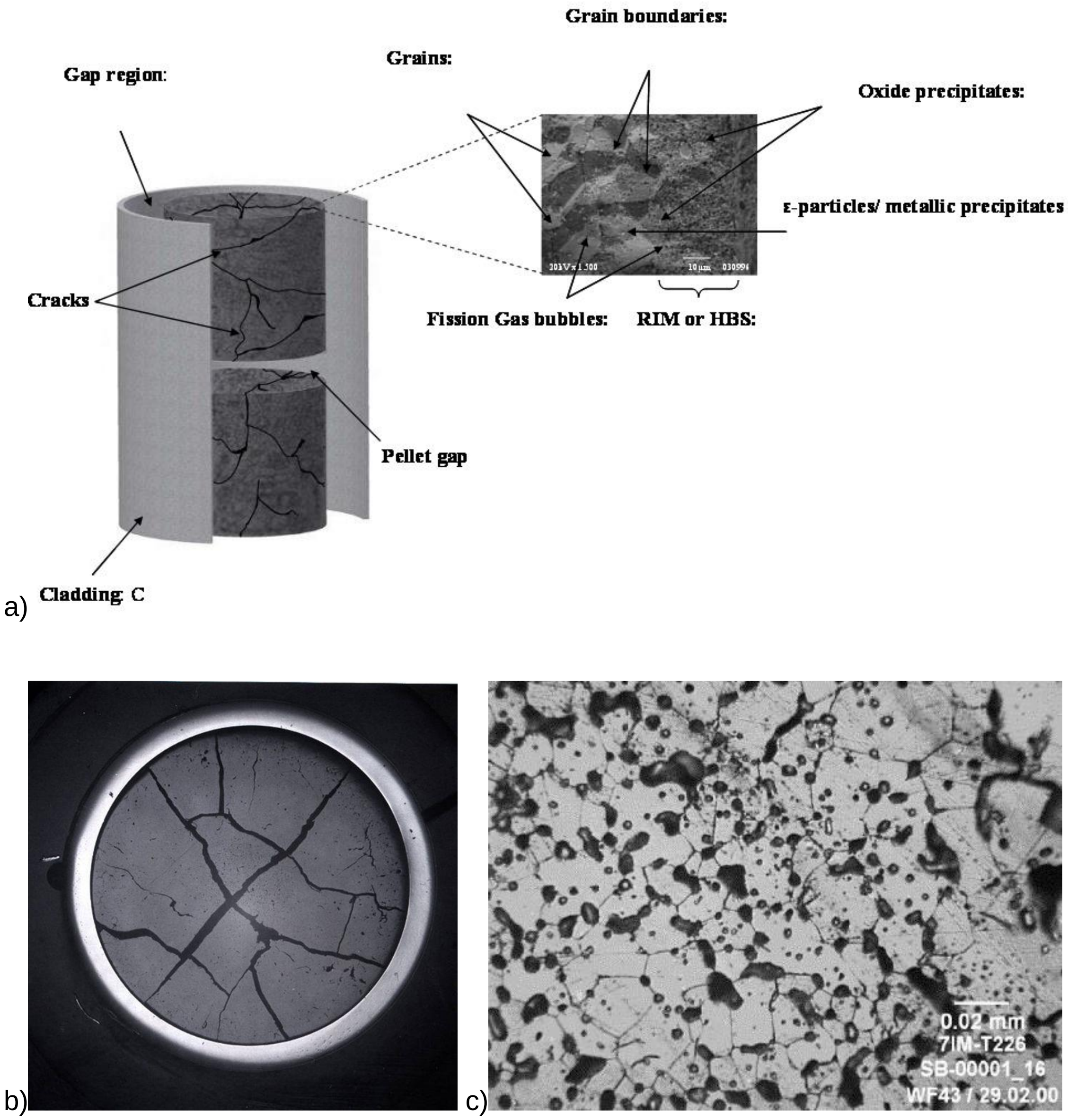

Fig. 7.42 a) rod with pellets
b) pellet with crack and gap [DEH/KLA2007],
c) etched microstructure of a pellet with visible grain boundaries [HEL/KAS2003]

The speciation of ^{14}C in the fuel is assumed to be carbides, oxycarbides or elemental carbon [AHN1994], [VAN1994]. The ^{14}C release may, therefore, be in the form of organic hydrocarbons. The leach data for ^{14}C on spent fuel are very limited. Lastly, [STR/TAI1994] reported leaching data for CANDU fuel. [STR1996] is based on [STR/TAI1994].

The recommended distribution function for the instant release fraction was suggested normal from 0.06 to 7.5 [STR1996] or triangular from 0.1 % to 10 % with a maximum at 5 % [WER/JOH2004].

[JOH/MCG2002] concluded an instant release fraction of ^{14}C by leaching. They explicitly stated that the available but scarce data on LWR spent fuel resemble those on CANDU spent fuel. Newer data were not available. The IRF of ^{14}C from spent fuel was assumed to 10 %. This agrees with [AHN1994].

Based on these results models for the instant release of ^{14}C from spent fuel are derived in [WER/JOH2004], [FER/LOV2004] and [JOH/FER2005] and propose an instant release fraction for ^{14}C. Models for the long term release are not discussed beyond 10000 years due to the half-life of ^{14}C. A congruent release of the remaining fraction with the dissolution of the spent fuel matrix is generally assumed.

The gaseous release of ^{14}C from spent fuel of a final disposal site into the biosphere is not investigated anymore in the USA [YIM/CAR2006]. The dose to the population of the world (“collective dose”) due to ^{14}C releases from the proposed Yucca Mountain repository was predicted to be large in comparison to the EPA’s limit, even though the dose per person was miniscule. However, with the changes toward the individual dose-based standards, ^{14}C release (with very small individual dose resulting from gaseous release) from spent fuel has become a non-issue. The potential radiation exposure using a “collective dose” is also not considered anymore. The release of dissolved ^{14}C results in a potential radiation exposure by ingestion which is by orders less than the potential radiation exposure by other radionuclides [YIM/CAR2006] and is therefore considered negligible. The approach in Germany is different in terms of waste amount containing ^{14}C, repository concept (“containment providing rock zone”), proof of compliance, and protection goal.

This is shown in [MOE/RYA2006] using a release rate of 10^{-5} a^{-1} for ^{14}C after 10000 years for the disposal of highly radioactive waste in Yucca Mountain. The ^{14}C-concentration in groundwater resulting from dilution is significantly below the maximum permissible limit of ^{14}C in drinking water. This is also true, when other pathways for ingestion are considered.

The ^{14}C content of a POLLUX-container for spent fuel for final disposal is approx. $8*10^{11}$ Bq [RÜB/BUH2011]. [RÜB/BUH2011] assumed conservatively that a part of this inventory can be released easily and completely on contact with water. The radioactive gases are conservatively assumed to be instantaneously released from the repository and completely dissolved in 20 000 m^3 of groundwater per year. The conversion of this concentration to a potential radiation exposure is done according to [PRO/GER2002]. As shown in **Fig. 7.43** an early release of the ^{14}C content of even one container into the biosphere could violate the permissible limit for the potential radiation exposure for these conservative assumptions. The underlying scenario does not consider a confinement providing rock zone.

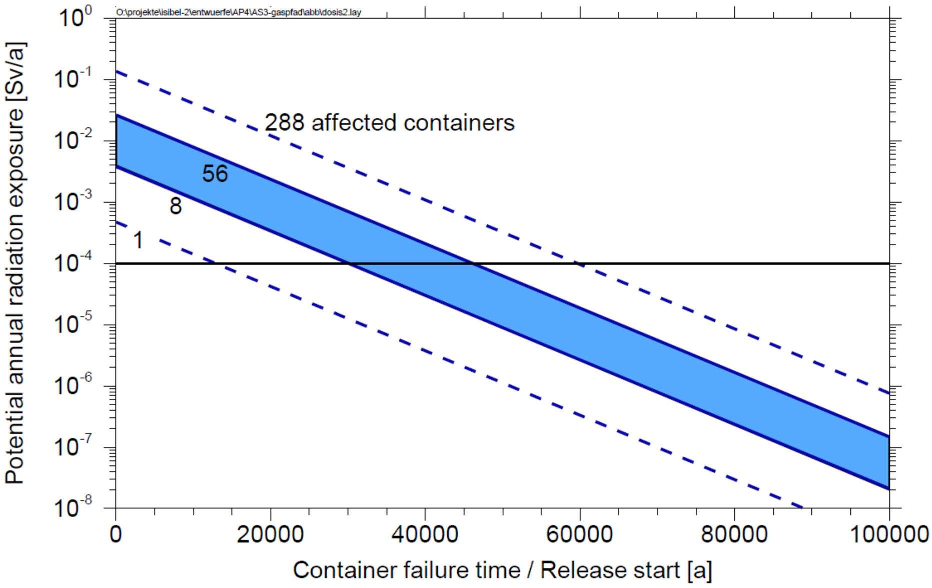

Fig. 7.43 Estimated radiation exposure from release of gaseous ^{14}C as a function of the container failure time for different numbers of simultaneously affected containers [RÜB/BUH2011]

[NAG2008] studied the release of ^{14}C as a safety relevant nuclide from high radioactive waste. For the reference case the release of ^{14}C contributed to the potential radiation dose (Fig. 7.41). This is mainly caused by the fact, that a fractional instantaneous release of ^{14}C from spent fuel after failure of the container was assumed which is distinguished between spent fuel and zircaloy metal. The remaining fraction is congruently released with dissolution of spent fuel and corrosion of the metal as organic and inorganic compounds.

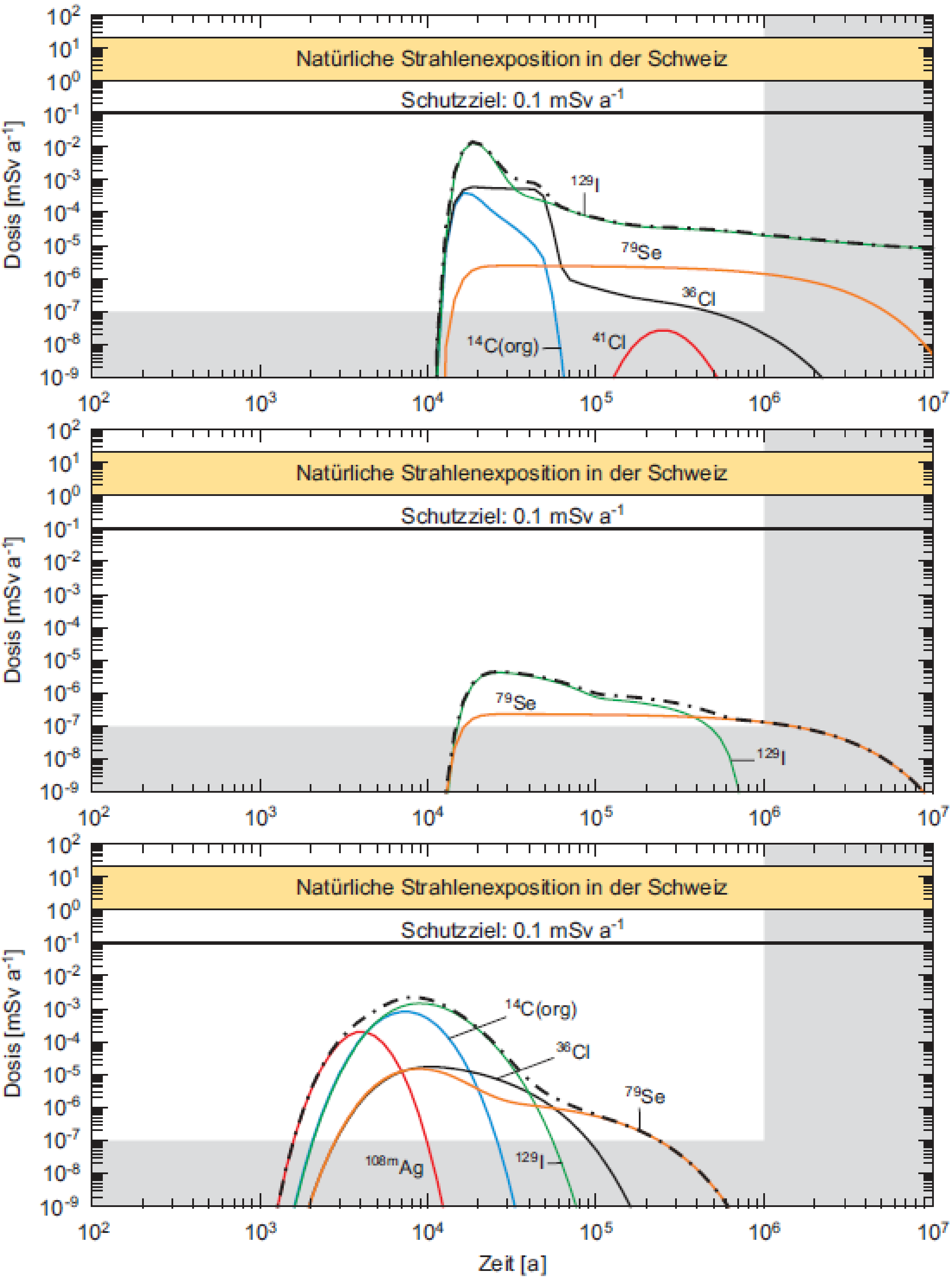

Fig. 7.44 Potential radiation exposure (dose) for disposal site high radioactive waste in Switzerland for different waste types (spent fuel, vitrified waste and medium active waste) [NAG2008]

7.4.8 Retention of ^{14}C

The main processes leading to retention of ^{14}C on a transport are [BRA/MÜL2008]:

- Sorption
- Precipitation
- Isotope exchange

The processes are difficult to separate experimentally. Usually, the retention is modeled as sorption using a specific Kd-value for the material.

[ALL/TOR1981] investigated the retention of ^{14}C on rock and concrete using experiments in flow-through columns with groundwater. A clear assignment of observed retention of ^{14}C to sorption, precipitation or isotope exchange was not possible. [SHE/TIC1998] also indicated that different processes contribute to the retention of ^{14}C and that these which are summarized as sorption. The retention of ^{14}C with calcite and carbonate bearing rock was verified, but retention on clay minerals was not confirmed.

Batch experiments using materials with cement did not retain organic compounds but inorganic compounds with ^{14}C [MAT/BAN1999]. The retention of ^{14}C was increasing with the ratio of calcium to silicon in material with cement [ASH/TAJ2002]. This supports the conclusion that the retention of inorganic compounds was mainly due to precipitation or isotope exchange.

[PLU/HUL2004] fitted by modeling Kd-values of 0.5 ± 0.1 for the soil cover of a disposal site for low-radioactive waste using $^{14}CO_2$. Kd values measured about 1 year after the injection yielded values for soil which were ranging from 0.8 to 2.4 ml/g. The factor causing the higher values could not be resolved in this study.

The exchange of the isotope ^{14}C with the stable isotopes ^{13}C and ^{12}C takes place by chemical and biological processes or in a dynamical equilibrium with different phases [TOU2002]. This is illustrated by the following:

The isotope exchange of C-14 in carbonates takes place rapidly in fluid phase by hydrogen exchange.

$$^{14}CO_3^{2-} + HCO_3^{-} \leftrightarrow CO_3^{2-} + H^{14}CO_3^{-}$$

Isotopic equilibrium between the gas phase and the fluid phase is also rapidly achieved.

$$^{14}CO_2\ (g) + HCO_3^- \leftrightarrow CO_2\ (g) + H^{14}CO_3^-$$

The isotopic equilibration of solid phase and brine may be slow, as the kinetics of dissolution and precipitation are controlled by accessible surfaces.

$$Ca^{14}CO_3\ (s) + HCO_3^- \leftrightarrow CaCO_3\ (s) + H^{14}CO_3^-$$

The isotopic equilibration of other compounds such as hydrocarbons, fatty acids, or alcohols is controlled kinetically and may be even slower.

The coupling of these reactions may lead to a retardation of transport of ^{14}C, which has not been investigated in detail for a long term safety assessment.

7.4.9 Summary and conclusions

Experimental data on the ^{14}C content in spent fuel and structural material was documented in the following references: [BLE1983], [BLE/KRO1987] and [STR/TAI1994]. All further references rely on the burn up calculations (e. g. [MAR/ESB2004]). References with experimental data on the speciation of ^{14}C in spent fuel were not found in this literature survey.

Most references were dealing with the release of ^{14}C during operation of power plants, reprocessing of spent fuel and storage of low and medium radioactive waste and related safety analyses. A large number of publications were based on experimental data from the seventies and eighties.

Only few newer experimental studies on zircaloy and graphite were available. A preferential release of ^{14}C was shown for graphite. A slight enrichment of ^{14}C in the oxide layer of zircon alloys was detected.

The literature survey confirms the low level of knowledge concerning the speciation of ^{14}C in radioactive waste in non- and low heat generating waste as well as in heat generating waste such as spent fuel.

Despite this, reaction of ^{14}C in radioactive waste to $^{14}CO_2$, $^{14}CH_4$ and lower hydrocarbon compounds is expected when disposed. Therefore, the generation of $^{14}CO_2$ and

$^{14}CH_4$ is generally assumed in a safety analysis for most radioactive wastes except for vitrified waste. During reprocessing spent fuel ^{14}C is lost as $^{14}CO_2$ to the atmosphere due to oxidation and does not occur in vitrified waste.

The potential radiation exposure by ^{14}C due to a disposal of heat generating waste has become a non-issue in USA since revision of the standards for Yucca Mountain to judge against an individual dose of 0.15 mSv per year and not a “collective dose” [EPA2005]. The currently applied models lead to an insignificant potential radiation exposure for an individual in the USA and the development of other models are no longer pursued.

Models for the potential radiation exposure from ^{14}C from disposal of spent fuel in Germany calculate that one (!) container with spent fuel elements may exceed a potential radiation exposure of 0.1 mSv per year due the gaseous release of ^{14}C [RÜB/BUH2011]. This is caused by considering conservatively current uncertainties and unknowns in the behavior of ^{14}C containing waste. This leads likely to an overestimation of the potential radiation exposure.

7.4.10 Recommendations

The uncertainties in the assessment of the potential radiation exposure by ^{14}C from a final repository for heat-generating radioactive waste can be lowered by additional research on the following topics:

- Analysis of the amount and speciation of ^{14}C in spent fuel (e. g. LWR, WWR) and hulls for different burn-ups
- Analysis of the reaction and the release of ^{14}C from spent fuel and graphite with and without the presence of humidity at varying temperatures simulating repository conditions
- Reactive transport modeling of ^{14}C containing compounds simulating repository conditions

Analytical and experimental work is extremely complex and costly due to the required radiation protection while handling spent fuel and irradiated hull materials. The currently initiated EU-projects “CAST” and “First Nuclides” do not cover this. A recent research project was started in Switzerland based on a proposal [WIE/HUM2010].

7.5 Comparative long-term safety calculations

One particular objective of the VESPA project is to improve the performance of model based long-term safety assessments for RAW repositories. Hence the execution of test calculations using newly found thermodynamic data in the context of a comprehensive repository model has been part of the project work packages. It is hereby intended – as far as possible – to demonstrate the reduction of conservatism compared to using previously overestimating or obsolete parameters due to lack of updated experimentally validated data.

7.5.1 Test case repository layouts and parameters

In order to compare test case calculation results in a meaningful manner, a set of generic repository layouts for different host rock formations has been developed. The applied scenarios have been selected in such a way to represent simplified yet prototypical layouts for two types of waste emplacements within two different host rocks. The selected scenarios are:

- salt formation – drift emplacement,
- salt formation – borehole emplacement,
- clay formation – borehole emplacement.

The inserted inventory is based on preliminary studies carried out within the frame of the German VSG research project (Preliminary Safety Assessment for the Gorleben Site) [LAR/BAL2013, PEI/MCS2011]. It mainly consists of German standard casks POLLUX-10 for drift emplacement and spent fuel canisters BSK-R for borehole emplacement.

The generic repository layout and dimensions of the test case for drift emplacement in salt formations are depicted in **Fig. 7.45**. The repository is composed of three generic elements: an emplacement drift, a connecting drift and a shaft. The drifts are supposed to be backfilled with highly compacted crushed salt, leading to a low porosity of only 2 percent, resembling long-term evolution conditions. The residual pore space is assumed to be filled with NaCl saturated brine. The shaft reaching to ground level is supposed to be sealed with concrete, effectively eliminating any brine flow and subsequently excluding advective transport of nuclides. Consequently, the only transport mechanism taken into account is diffusion.

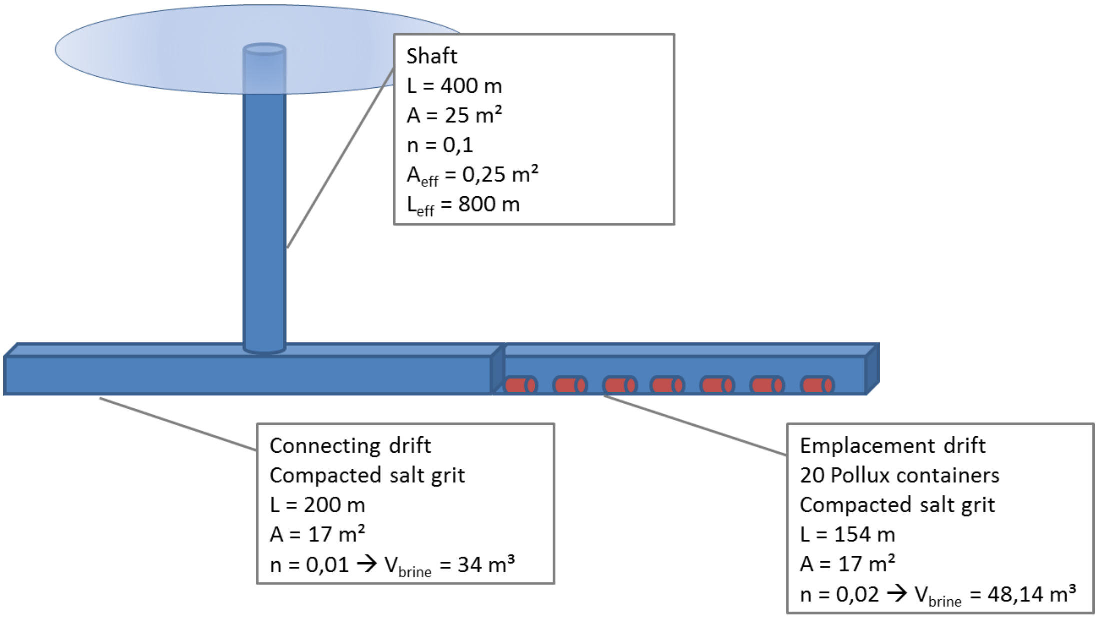

Fig. 7.45 Repository layout and dimension, salt formation – drift emplacement

For the second test case, namely borehole emplacement in salt formations, the generic repository layout is depicted in **Fig. 7.46**. Here, the 290 m long representative emplacement borehole is backfilled with non-compactable quartz sand (porosity 25 %) and connected to a short charging drift next to the connecting drift. Other parameters correspond to those of the drift emplacement scenario. Transport of released nuclides through the repository is only being enabled by diffusion.

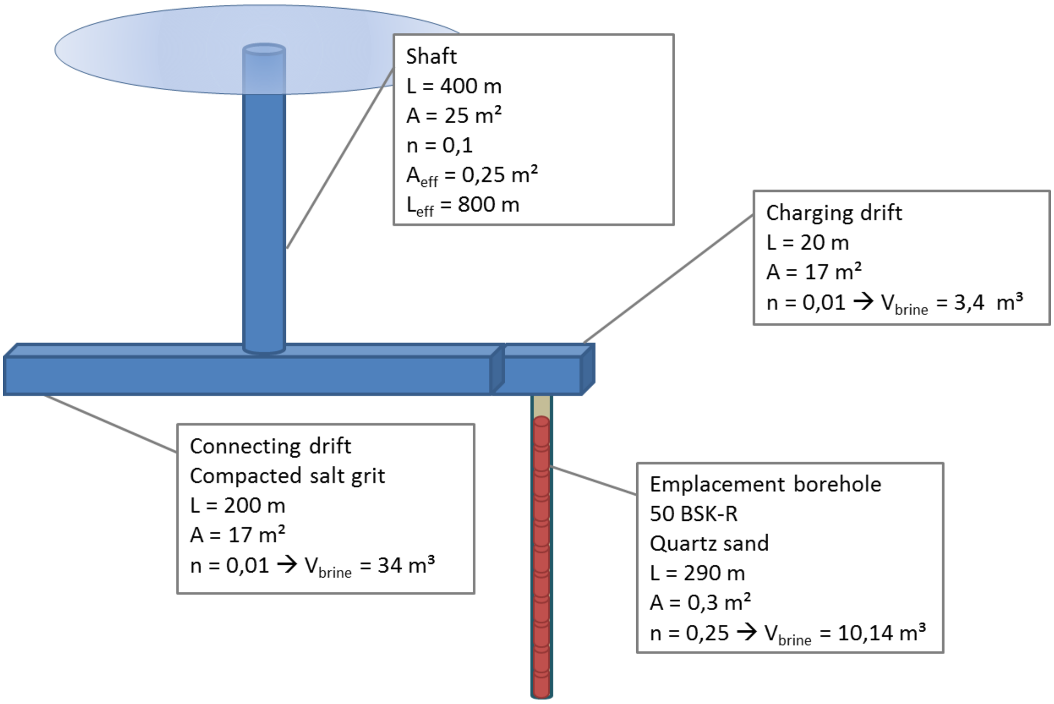

Fig. 7.46 Repository layout and dimension, salt formation – borehole emplacement

The generic repository layout for emplacement in clay formations – the third test case considered – is depicted in **Fig. 7.47**. In contrast to the salt scenarios there is no generic model reproduction of an entire repository structure but only one representative emplacement borehole containing a single canister. This approach is deemed justified since the only transport process considered in clay environments is radial diffusion through the homogenous clay barrier into the adjacent auriferous bed rock. The remaining borehole space around the canister is supposed to be backfilled with bentonite. The assumed radial distance of the clay barrier (corresponding to total diffusion length) equals 50 m.

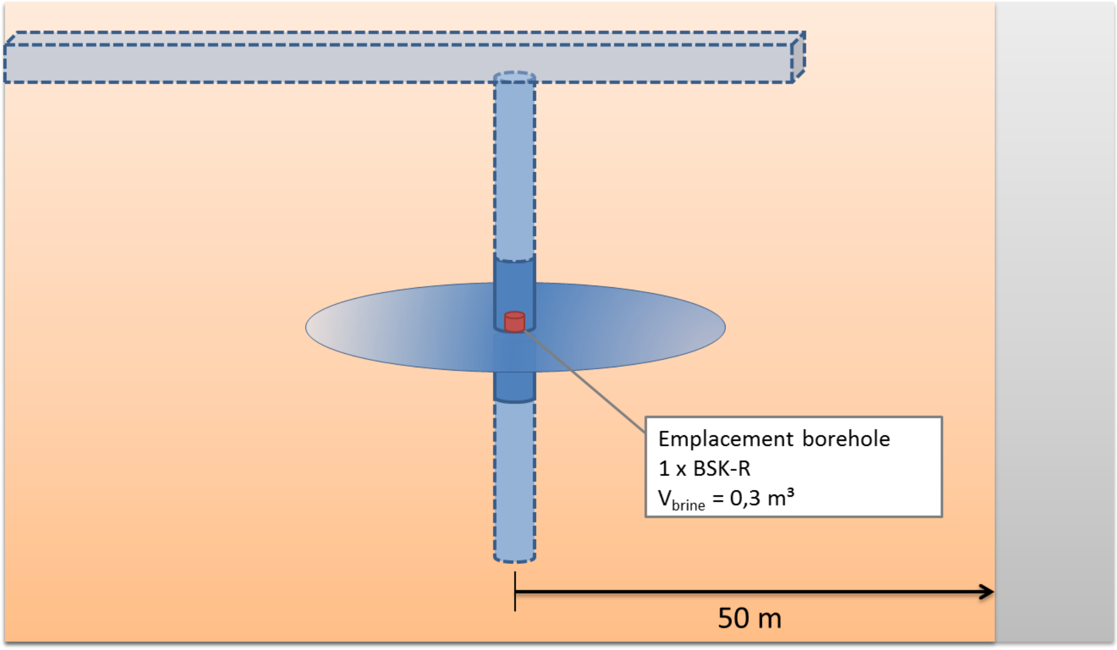

Fig. 7.47 Repository layout and dimension, clay formation

The element specific parameters for the test case calculations are given in **Tab. 7.31**, **Tab. 7.32** and **Tab. 7.33**. It includes the inventories of the considered nuclides as well as geochemical parameters for solubility limits and sorption.

Tab. 7.31 Considered Nuclides and Inventories for test calculations

Nuclide	Pollux-10	BSK-R	Half-Life
C-14	1.9E11 Bq	5.6E10 Bq	5.73E3
Se-79	1.3E10 Bq	4.0E9 Bq	1.1E6
Tc-99	4.0E12 Bq	1.2E12 Bq	2.1E5
I-129	8.3E9 Bq	2.5E9 Bq	1.57E7

Tab. 7.32 Solubility limits for test calculations

Element	Salt		Clay
	VESPA values	Previous values	VESPA values
C	-	0 … 1E-8 M	-
I	-	0	-
Se(IV)	1E-4 m	0 … 1E-8 M	5E-9 M
Tc(IV)	1E-8 m	0 … 1E-8 M	1E-8 m

Tab. 7.33 Kd-values for test calculations

Element	Salt		Clay
	VESPA values	**Previous values**	**VESPA values**
C	-	-	-
I	0	-	2.2E-3 m^3/kg
Se	1.6 m^3/kg	-	2.3 m^3/kg
Tc	0	-	5.6E-3 m^3/kg

7.5.2 Results and discussion

The calculations described above have been performed using the LOPOS and CLAYPOS program codes. The integrated safety assessment codes LOPOS (Loop structures in repositories) and CLAYPOS (Clay type repositories) have been developed by GRS to simulate one-dimensional, single-phase transport processes in the near field of nuclear waste repositories in salt and clay. A simulation in salt environment includes the calculation of the inflow of brine from the overburden, through the mine to the emplaced waste, the mobilisation of the radionuclides from the waste matrix and the transport of the radionuclides through the repository mine up to the shaft top. For clay type repositories the modelling of one dimensional (diffusive) transport of radionuclides through planar or radial oriented clay layers is possible. Retardation effects like limited solubility or sorption can be taken into account.

The LOPOS code has been used for the safety assessments in the licensing procedure for the radioactive waste repository Morsleben (ERAM) for low and intermediate-level waste [BEC/BUH09], for simulations for the ASSE mine [GRS2006] and in the preliminary safety assessment for Gorleben (VSG) [MUE/BRE12]. The LOPOS code was further used in several code comparisons and benchmark studies [BEC/BUH2002, BOE/HIR2000]. In all comparisons the LOPOS code yielded good agreement with other codes used. Additionally LOPOS was verified using analytical solutions for selected cases yielding good results [HIR/BOE1999].

The results of the preliminary test calculations of the VESPA project are shown in **Fig. 7.48** to **Fig. 7.50**. Here the activity release rate from the exit segment (top of shaft resp. boundary of geological barrier) is depicted. The solid line represents repository conditions where no retention is being applied, which means unlimited solubility of the elements and no sorption. Those conditions reflect previous states of knowledge where the absence of reliable data has led to conservative assumptions of no retention being modelled (see **Tab. 7.32** to **Tab. 7.33**).

The incorporation of some newly found data for solubility limits (dashed lines) and sorption coefficient (dotted lines) is being drawn in comparison for those nuclides, whose updated parameters have so far been obtained within VESPA: new solubility limits for selenium and technetium as well as Kd-values for iodine, selenium and technetium.

Fig. 7.48 represents the resulting activity release rates for drift emplacement in salt formations. New data for this scenario has been obtained so far for selenium (solubility, sorption) and technetium (solubility) only. The results show that the release rate of nuclides from the repository can be significantly reduced by the application of retention data. Especially for Tc-99 the release rate could be reduced by more than fife orders of magnitude. For Se-79 the reduction is somewhat lower but still significant with a combined effect of sorption on corrosion products and solubility limits of up to three orders of magnitude. Since for the remaining nuclides either no updated parameter values have been obtained or no retention could be observed, the activity outputs are unchanged.

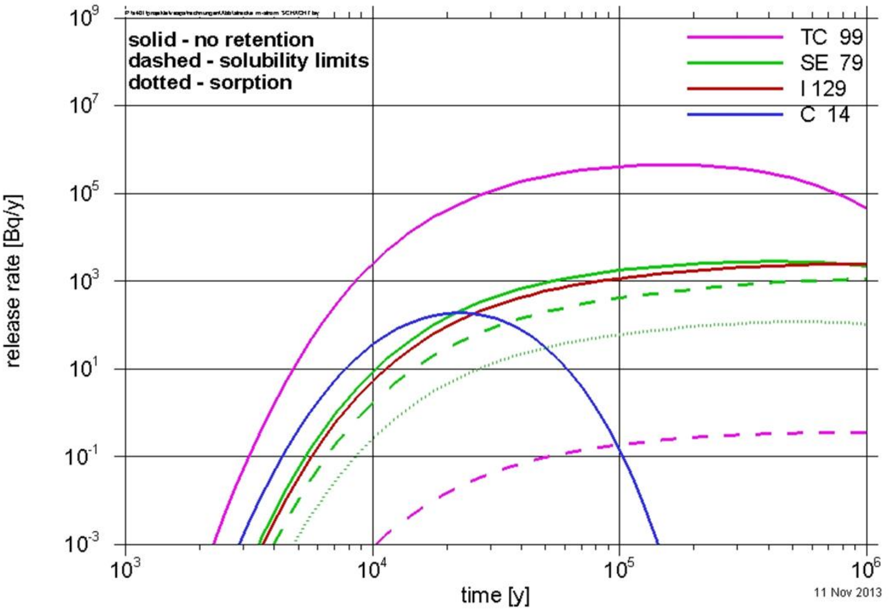

Fig. 7.48 Activity release rate over time for salt-drift-scenario

For the borehole emplacement scenario in salt rock the modelling results look similar (**Fig. 7.49**). Again, there is a strong decrease of activity release from the repository if retention is being considered. Especially the release of Tc-99 can drastically be reduced by the application of solubility limits. The effects in a borehole setting are even slightly greater than for drift emplacement due to less fluid filled pore space available. As for Se-79, the only nuclide where both solubility limits and sorption could be taken into account, the contribution of sorption on corrosion products again is greater than the sole application of limited solubility.

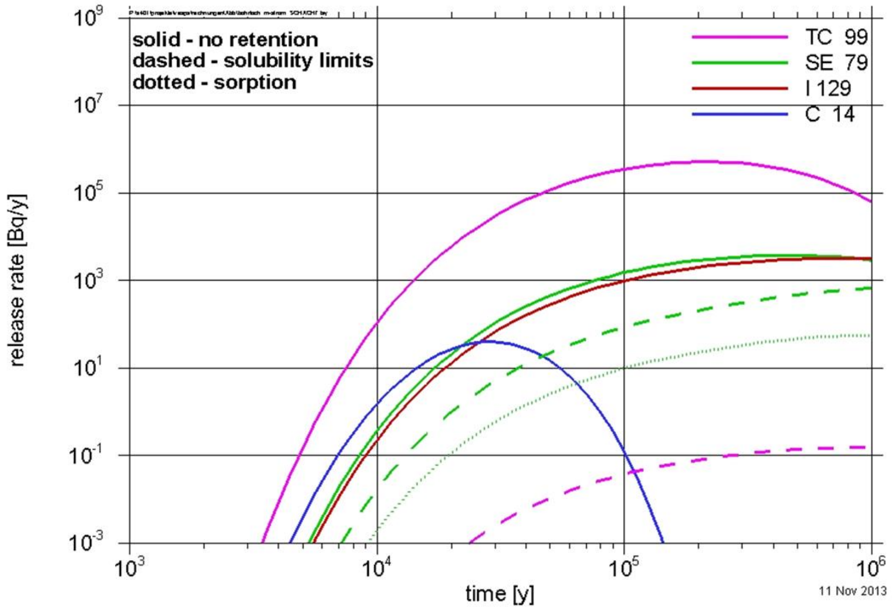

Fig. 7.49 Activity release rate over time for salt-borehole-scenario

The last scenario considered within the frame of preliminary test calculations is the clay host rock, where only borehole emplacement is being suggested. The results of that are depicted in **Fig. 7.50**. In this case, the activity release at the edge of the clay formation (50 m from centre of borehole) is being assessed. It has to be mentioned, that sorption on clay or bentonite has been assumed for all clay scenario calculation cases. In addition to nuclide release without additional retention on containment corrosion products the application of sorption as well as solubility limits are being illustrated only for Tc-99 and Se-79, since the remaining nuclides have already decayed before reaching the clay boundary.

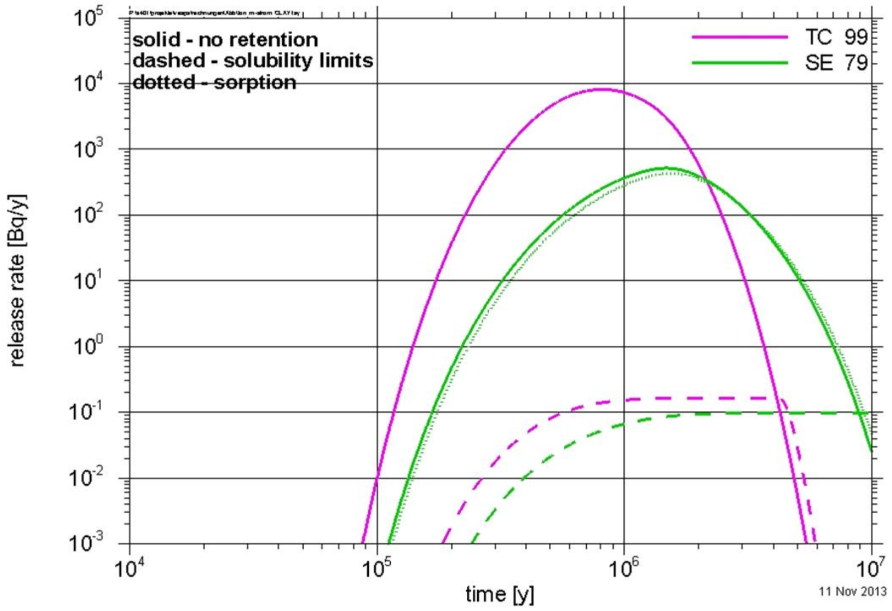

Fig. 7.50 Activity release rate over time for clay-borehole-scenario

It can be seen clearly that the effect of sorption on container corrosion products is almost negligible in contrast to the application of limited solubility. This result becomes understandable when thinking of the far higher sorption capacity of the clay material compared to container corrosion products. The relevant sorbent mass of the clay is just so much higher than the corrosion product mass that it simply has no further impact. The contribution of sorption on corrosion products to the total sorption on rock barrier material is therefore negligible.

An entirely different output gives the application of solubility limits. For the retention of Tc-99 as well as for Se-70 its effects are highly significant. The reduction of nuclide release rates amounts to almost four to five orders of magnitude. This is due to the small available pore space in container voids and bentonite backfill, effectively reducing mobilizing fluids in the vicinity of the source emplaced in a borehole in clay environment.

7.5.3 Conclusions

The calculations described above have produced the following summarized results:

The consideration of solubility limits for specified nuclides results in an effective retention within a repository in salt formations of more than 3 orders of magnitude, in clay formations of more than 4 orders of magnitude.

The consideration of sorption on iron and steel corrosion products for specified nuclides results in a retention within a repository in salt formations of more than one order of magnitude, in clay formations of negligible magnitude.

For general conclusion it may be stated, that the derivation of updated geochemical parameters for selected safety-related nuclides may have a significant effect on the long-term safety assessment of radioactive waste repositories. For repositories in salt environment the reduction of nuclide release resulting from sorption on iron and steel corrosion products as well as solubility limits are both of great relevance. For repositories in clay only the effects of limited solubility delivers significant contributions to total retention. The sorption on corrosion products is superimposed by sorption on clay material, leading to only limited added retention in clay environments.

7.6 References (chapter 7)

[AHN1994] Ahn, T.M., Long-term ^{14}C source term for a high-level waste repository. Waste Manag. (New York), 14 (1994) 393-408.

[AKE1937] Åkerlof, G., A study of the composition of the liquid phase in aqueous systems containing strong electrolytes of higher valence types as solid phases, J. Phys. Chem. 41 (1937) 1053-1076.

[ALL/TOR1981] Allard, B.; Torstenfelt, B.; Andersson, K., Sorption behavior of carbon-14 in groundwater/rock and in groundwater/concrete environments. Department of Nuclear Chemistry. Chalmers University of Technology, Göteborg, Sweden, Report PRAV-4-27 (1981) 11 pp..

[APE/KOR1998] Apelblat, A.; Korin, E., Vapor pressures of saturated aqueous solutions of ammonim iodide, potassium iodide, potassium nitrate, strontium chloride, lithium sulphate, sodium thiosulphate, magnesium nitrate, and uranyl nitrate from T = (278 to 323) K, J. Chem. Thermodyn. 30 (1998) 459-471.

[ASH/TAJ2002] Ashikawa, N.; Tajima, T.; Saito, H.; Fujiwara, A., Sorption behavior of radionuclides on calcium-leached mortar. Mater. Res. Soc. Symp. Proc. 663 (2002) 97.

[BAE/MES1976] Baes, C. F.; Mesmer, R. E., The Hydrolysis of Cations. Wiley Interscience, New York (1976).

[BEC/BUH2002] Becker, D.-A.; Buhmann, D.; Storck, R. et al., Testing of safety and performance indicators (SPIN). Final Report. European Commission EUR 19965 EN (2002).

[BEC/BUH2009] Becker, D.-A.; Buhmann, D.; Mönig, J.; Noseck, U.; Rübel, A.; Spießl, S., Endlager Morsleben, Sicherheitsanalyse für das verfüllte und verschlossene Endlager mit dem Programmpaket EMOS. Planfeststellungsverfahren zur Stillegung des Endlagers für radioaktive Abfälle Morsleben. Verfahrensunterlage P 278 (2009).

[BIL1902] Biltz, W., Zur Kenntnis der Lösungen anorganischer Salze in Wasser, Z. Phys. Chem. 40 (1902) 185-221.

[BLE1983] Bleier, A., Bildung, Verhalten und Emissionsüberwachung von radioaktivem Kohlenstoff-14 an Leichtwasserreaktoren Siemens Forsch. u. Entwickl.-Ber., 12 (6) (1983) 363-370.

[BLE/KRO1987] Bleier, A.; Kroebel, R.; Neeb, K.H.; Wiese, H.W., Kohlenstoff-14 in LWR-Brennstäben und dessen Verhalten bei Wiederaufarbeitungsprozess Jahrestagung Kerntechnik, Tagungsbericht, (1987) 417-420.

[BOE/HIR2000] Boese, B.; Hirsekorn, R.-P.; Storck, R., Vergleich der Rechenprogramme LOPOS und MARNIE. GRS-Ber. 169 (2000).

[BRA/MÜL2008] Bracke G., Müller W., Contribution to a more realistic approach in assessing the release of ^{14}C from low-level radioactive waste repositories J. Contam. Hydrol. 102 (2008) 210-216.

[BRE1993] Brendler, V., Wasseraktivitäten in den ternären Systemen $MgCl_2$-Acl-H_2O (A=Li, K, Cs) bis zu sehr hohen Salzkonzentrationen, Dissertation, Bergakademie Freiberg, (1993).

[BRE/VOI1994] Brendler, V.; Voigt, W., Isopiestic measurements at high temperatures: I. Aqueous solutions of LiCl, CsCl, and $CaCl_2$ at 155 °C, J. Solution Chem. 23 (1994) 1061-1072.

[CAR1963] Caramazza, R., The activity coefficients in concentrated aqueous solutions of strong electrolytes. I. Lithium chloride. II. Cesium chloride, Annali di Chimica, 53 (1963) 472-487.

[CHR/OJK1998] Christov C., Ojkova T., Mihov D., Thermodynamic study of ($m_1Na_2SeO_4$ + m_2NiSeO_4)(aq), where m denotes molality, at the temperature 298.15 K, J. Chem. Thermodyn., 30 (1998) 73-79.

[CLA/GLE1985] Clarke, E. C. W.; Glew, D. N. (1985): Evaluation of the thermodynamic functions for aqueous sodium chloride from equilibrium and calorimetric measurements below 154 °C, J. Phys. Chem. Ref. Data (14), 489-610.

[COX/WAG1989] Cox, J. D.; Wagman, D. D.; Medvedev, V. A., CODATA Key Values for Thermodynamics, Final report of the CODATA task group on key values for thermodynamics, Hemisphere Publishing Corporation (1989).

[CUD/FEL1942] Cudd, H. H.; Felsing, W. A., Activity coefficients of rubidium and cesium sulfates in aqueous solution at 25°, J. Am. Chem. Soc. 64 (1942) 550-551.

[CUR/KAI2010] Curtius, H.; Kaiser, A.; Paparigas, Z.; Hansen, B.; Neumann, A.; Klinkenberg, M.; Müller, E.; Brücher, H.; Bosbach, D., Wechselwirkung mobilisierter Radionuklide mit sekundären Phasen in endlagerrelevanten Formationswässern, Ber. Forschungszentrum Jülich 4333 (2010) 170 S.

[DAM/MOO1995] Dames; Moore, Waste Inventory Revision 3, North Carolina Low-Level Radioactive Waste Disposal Facility Project DM/DR-002, prepared for Chem-Nuclear Systems, Inc., (1995).

[DAV1977] Davis W., Jr., Carbon-14 production in nuclear reactors. ORNL/NUREG/TM-12, Report (1977) 38 pp.

[DEC/VAN1993] Deconinck, J. M.; Van Iseghem, P.; Boden, R.; Daniels, A.; De Regge, P.; Hurtgen, C.; Huys, D.; Klein, M.; Verrezen, F., Investigation on the determination of disposal critical nuclides in waste from PWR power plants. Task 3 - characterization of radioactive waste forms. A series of final reports (1985-89) - No. 45 Comm. Eur. Communities, [Rep.] EUR 14364 (1993) 85 pp.

[DEH/KLA2007] de Haas, G.-J. L. M.; Klaassen, F.C.; Schram, R. P. C., Disposal of nuclear waste: innovative fuels for actinide transmutation. Geochem. News 132 (2007) 7.

[DMI/KAR2003] Dmitriev, S. A.; Karlina, O. K.; Klimov, V. L.; Ojovan, M. I.; Pavlova, G. Yu.; Yurchenko, A. Yu., Minimization of carbon-14 during processing of reactor graphite waste. Internatl. Symp. Combustion Atmosph. Poll., St. Petersburg, Russian Federation, July 8-11 (2003) 537-542.

[DUM/BRO1997] Dumm, J. Q.; Brown, P. W., Phase formation in the system CaO-SeO_3-H_2O, J. Amer. Ceram. Soc. 80 (1997) 2488-2494.

[EAT/GEO1967] Eaton, W.; George, P.; Hanania, G. I. H., Thermodynamic aspects of the potassium hexacyanoferrate(III)-(II) system I. Ion association, J. Phys. Chem. 71 (1967) 2016-2021.

[EPA2005] Environmental Protection Agency (EPA) Public health an environmental radiation protection standards for Yucca Mountain, NV. 40 CFR Part 197, Federal Register, Vol. 70, No. 161, August 22, 2005.

[FAC/VON2008] Fachinger, J.; von Lensa, W.; Podruhzina, T., Decontamination of nuclear graphite. Nucl. Engin. Design 238 (2008) 3086-3091.

[FAC/ZHA1995] Fachinger, J.; Zhang Zun Xun, Brodda, B. G., Graphite corrosion and hydrogen release from HTR fuel elements in Q-brine. Proc. Internatl. Conf. Radioactive Waste Manag. Environm. Remed. 5th, Berlin, Sept. 3-7, 1995, 1 (1995) 637-640.

[FER/LOV2004] Ferry, C.; Lovera, P.; Poinssot, C.; Johnson, L., Quantitative assessment of the instant release fraction (IRF) for fission gases and volatile elements as a function of burnup and time under geological disposal conditions. Mater. Res. Soc. Symp. Proc. 807 (Scientific Basis for Nuclear Waste Management XXVII) (2004) 35-40.

[FRA/DON1980] Francis, A.J.; Dobbs, S.; Doering, R.F., Biogenesis of tritiated and carbon-14 methane from low-level radioactive waste. Nucl. Chem. Waste Manag. 1 (1980) 153-159.

[FRE/DEG2007] Frechou, C.; Degros, J.-P., Radiological inventory of irradiated graphite samples. J. Radioanal. Nucl. Chem. 273 (2007) 677-681.

[GAM/BUG2005] Gamsjäger, H.; Bugajski, J.; Gajda, T.; Lemire, R. J.; Preis, W., Chemical thermodynamics of Nickel. Elsevier, Amsterdam (2005) 645 p.

[GRA/MÜL1990] Grambow, B.; Müller, R., Chemistry of glass corrosion in high saline brines, Mat. Res. Soc. Symp. Proc. 176 (1990) 229-240.

[GRS2006] LOPOS AS6: Programmanpassungen und Verifikation für den Standort Asse. Projekt Langzeitsicherheit Asse – Transportmodellierung. Gemeinsames Projekt von NRG, Colenco und GRS. Gesellschaft für Anlagen- und Reaktorsicherheit (GRS) mbH, GRS-A-3338 (2006).

[GUD/NED2010] Gudelis, A.; Nedveckaite, T.; Prokopciuk, N.; Filistovic, V.; Remeikis, V.; Motiejunas, S., Assessment of radionuclide migration and radiological human exposure at the closed near-surface radioactive waste repository. Nukleonika 55 (2010) 251-259.

[GUP2004] Guppy, R., Long-term management of graphite arising from the nuclear industry. Nucl. Engin. 45 (2004) 121-127.

[HAG/MOO2012] Hagemann, S., Moog, H. C., Herbert, H.-J., Erich, A., Rückhaltung und thermodynamische Modellierung von Iod und Selen in hochsalinaren Lösungen, GRS-Ber. 245 (2012) 174 p.

[HAG/BIS2014] Hagemann, S.; Bischofer, B.; Scharge, T.; Schönwiese, D., Entwicklung von Methoden und Modellen zur Bestimmung des Redoxpotentials salinarer Lösungen, GRS-Ber. 260 (2014).

[HAG/SCH2015] Hagemann, S.; Schönwiese, D.; Scharge, T., Werkzeuge und Daten für die Geochemische Modellierung - Thermodynamische Daten für Schwefelspezies und Hintergrundsalze sowie Tools zur Unsicherheitsanalyse, GRS-Ber. 373 (2015).

[HAR1981] Harvie, C. E., Theoretical investigations in geochemistry and atom surface scattering, Ph. D. Thesis, University of California, San Diego (1981) 266 pp.

[HEL/ERL2001] Hellborg, R.; Erlandsson, B.; Faarinen, M.; Hakansson, H.; Hakansson, K.; Kiisk, M.; Magnusson, C.-E.; Persson, P.; Skog, G.; Stenstrom, K., Determination of ^{14}C in activated metal waste. AIP Conf. Proc. 576 (2001) 377-381.

[HEL/KAS2003] Hellwig, C.; Kasemeyer, U.; Ledergerber, G.; Lee, B.-H.;, Lee, Y.-W.; Chawla, R., Interpretation of experimental results from moderate-power in-pile testing of a Pu-Er-Zr-oxide inert matrix fuel. Ann. Nucl. Energy 30 (2003) 287-299.

[HEL/PAT1965] Hellams K. L., Patterson C. S., Prentice B. H., Taylor M. J., Osmotic properties of some aqueous solutions at 45 °C, J. Chem. Eng. Data, 10 (1965) 323-325.

[HIE/SWI2005] Hiergesell R.A., Swingle R.F., Special Analysis: Atmospheric dose resulting from the release of 14C from Reactor Moderator Deionizers in a disposal environment (U), WSRC-TR-2005-00331 Rev. 0, Westinghouse Savannah River Company, Savannah River Site, Aiken, SC 29808 (2005).

[HIR/BOE1999] Hirsekorn, R.-P.; Boese, B.; Buhmann, D., LOPOS: Programm zur Berechnung der Schadstofffreisetzung aus netzwerkartigen Grubengebäuden. GRS-Ber. 157 (1999).

[HOL/MES1981] Holmes H. F., Mesmer R. E., Isopiestic studies of aqueous solutions at elevated temperatures VI. LiCl and CsCl, J. Chem. Thermodyn., 13 (1981) 1035-1046.

[HOL/MES1983] Holmes, H. F.; Mesmer, R. E., Thermodynamic properties of aqueous solutions of the alkali metal chlorides to 250 °C, J. Phys. Chem. 87 (1983) 1242-1055.

[HOL/MES1986] Holmes H. F., Mesmer R. E., Isopiestic studies of aqueous solutions at elevated temperatures. VIII. The alkali-metal sulfates, J. Chem. Thermodyn., 18 (1986) 263-275.

[HOT/FIN2000] Hotchkis, M.; Fink, D.; Tuniz, C.; Vogt, S., Accelerator mass spectrometry analyses of environmental radionuclides: sensitivity, precision and standardization. Appl. Radiation Isotopes 53 (2000) 31-37.

[HOU/ROS2008] Hou, X.; Roos, P., Critical comparison of radiometric and mass spectrometric methods for the determination of radionuclides in environmental, biological and nuclear waste samples. Anal. Chim. Acta 608 (2008) 105-139.

[HUM2011] Hummelsheim, H., GRS mbH, München, personal communication (2011).

[IAEA2009] International Atomic Energy Agency, Determination and use of scaling factors for waste characterization in nuclear power plant. IAEA Nucl. Energy Ser. NW-T-1.18 (2009).

[JAB/BAŁ1932] Jabłczynski, K.; Bałczewski, A., Prawo równowagi dla elektrolitów mocnych: brmki i jodki potasowców, Rocz. Chem. 12 (1932) 880-887.

[JAK/HOO1972] Jakli, G.; van Hook, W. A., Osmotic coefficients of aqueous solutions of NaBr, NaI, KF, and CaCl2 between 0° and 90 °C, J. Chem. Eng. Data 17 (1972) 348-355.

[JOH/MCG2002] Johnson, L. H.; McGinnes, D. F., Partitioning of radionuclides in Swiss power reactor fuels. Nagra Technical Report, 02-07 (2002) 1-27.

[JOH/FER2005] Johnson, L.H.; Ferry, C.; Poinssot, C.; Lovera, P., Spent fuel radionuclide source-term model for assessing spent fuel performance in geological disposal. Part I: Assessment of the instant release fraction. J. Nucl. Mater. 346 (2005) 56-65.

[JOH/SCH2004] Johnson, L.H.; Schwyn, B., Proceedings of a workshop on the release and transport of ^{14}C in repository environments. Nagra Internal Report NIB 04-03 (2004).

[JON/BAS1905] Jones, H. C.; Bassett, H. P., The approximate composition of the hydrates formed by ceratin electrolytes in aqueous solutions at different concentrations, Am. Chem. J. 33 (1905) 534-586.

[JON/GET1904] Jones, A. K.; Getman, H. C., On the nature of concentrated solutions of electrolytes - hydrates in solution, Am. Chem. J. 31 (1904) 304-39.

[JUL/BUR2003] Jull, A. J. T.; Burr, G. S.; Beck, J. W.; Donahue, D. J.; Biddulph, D.; Hatheway, A. L.; Lange, T. E.; McHargue, L. R., Accelerator mass spectrometry at Arizona: geochronology of the climate record and connections with the ocean. J. Environm. Radioact. 69 (2003) 3-19.

[KAP2005] Kaplan, D., Estimate of gaseous ^{14}Carbon concentrations emanating from the intermediate-level vault disposal facility (U), Westinghouse Savannah River Company Tech. Rep. WSRC-TR-2005-00222 (2005).

[KAR/HAW1930] Karagunis, G.; Hawkinson, A.; Damköhler, G., Zur Individualität der osmotischen Koeffizienten bei Alkalihalogeniden, Z. Phys. Chem. 151 (1930) 433-466.

[KIE/MET2004] Kienzler, B.; Metz, V.; Kelm, M.; Nebelung, C.; Baraniak, L., Interaction of carbon in a repository environment. Workshop on the release and transport of ^{14}C in repository environments, Proceedings, NAGRA NIB 04-03 (2004) 25.

[KOL2004] Kolbe, E., Comparison of ORIGEN2.1 with selected computer codes Nagra Tech. Rep. 04-04 (2004).

[KOL/TOM1936] Kolthoff, I. M.; Tomiscek, W. J., The oxidation potential of the system potassium ferrocyanide-potassium ferricyanide at various ionic strengths, J. Phys. Chem. 39 (1935) 945-954.

[KTA2002] KTA 1503.1. Überwachung der Ableitung gasförmiger und an Schwebstoffen gebundener radioaktiver Stoffe, Teil 1: Überwachung der Ableitung radioaktiver Stoffe mit der Kaminfortluft bei bestimmungsgemäßem Betrieb, Fassung 6/02 (2002).

[LAN1936] Lange, J., Zur physikalischen Charaketerisierung gelöster Ionen. II. Nach Mesungen des Gefrierpunkts und der Leitfähigkiet von sehr verdünnten wässerigen Lösungen einiger Alkalihalogenide, Z. Phys. Chem. A177 (1936) 193-212.

[LAN/DAV2009] Landolt, D.; Davenport, A.; Payer, J.; Shoesmith, D., A Review of materials and corrosion issues regarding canisters for disposal of spent fuel and high-level waste in Opalinus clay, Nagra, Technical Report 09-02 (2009).

[LAR/BAL2013] Larue, J.; Baltes, B.; Fischer, H.; Frieling, G.; Kock, I.; Navarro, M.; Seher, H., Radiologische Konsequenzenanalyse. Bericht zum Arbeitspaket 10. Vorläufige Sicherheitsanalyse für den Standort Gorleben. GRS Ber. 289 (2013).

[LEH/MER1994] Lehto, Michael A.; Merrell, Gary B., Environmental release of carbon-14 gas from a hypothetical nuclear waste repository, Technology and Programs for Radioactive Waste Management and Environmental Restoration 1 (1994) 781-5.

[LID1991] Lide, D. R., Handbook of chemistry and physics. CRC Press Boca Raton (1991).

[LIE/THO1988] Liepins, L. Z.; Thomas K. W., Survey of carbon-14 literature relevant to a geologic nuclear waste repository. Radioactive Waste Management and the Nuclear Fuel Cycle, 10 (1988) 357-80.

[LIG/ZWA1990] Light, W. B.; Zwahlen, E. D.; Pigford, T. H.; Chambre, P. L.; Lee, W. W. L., Carbon-14 release and transport from a nuclear waste repository in an unsaturated medium. Lawrence Berkeley Laboratory Report LBL-28923 (1990) 36 pp.

[LIL/SCO1974] Lilley, T. H.; Scott, R. P., The osmotic coefficients of aqueous solutions of cesium chloride at the freezing temperature of the solutions, J. Chem. Thermodyn. 6 (1974) 1015-1017.

[LIN1965] Linke, W. F., Solubilities. Inorganic and metal compounds. Volume II. K-Z., from: American Chemical Society, Washington (1965).

[LIN/LIU1971] Lindsay, L. E.; Liu, C.-T., Osmotic coeffiecients of one molal alkali metal chloride solutions, J. Phys. Chem. 75 (1971) 3723-3727.

[LIN/WIL2007] Lindgren, M.; Petterson, M.; Wiborgh, M., Correlation factors for C-14, Cl-36, Ni-59, Mo-93, Tc-99, I-129 and Cs-135 in operational waste for SFR1 Svensk Kärnbränslehantering AB, SKB Rapport F-07-05 (2007).

[MAR/ESB2004] Marimbeau, P.; Esbelin, E., N and ^{14}C Content in Spent Fuel (in [JOH/SCH2004]) (2004).

[MAT/BAN1999] Matsumoto, J.; Banba, T., Sorption behavior of organic carbon-14 onto cementitious materials. Internatl. Conf. Proc. Radioact. Waste Manag. Environm. Remed. 7th, Nagoya, Japan, Sept. 26-30 (1999) 854-858.

[MAZ/CUR2003a] Mazeina, L.; Curtius, H.; Fachinger, J., Formation of hydrotalcite-like compounds during corrosion experiments on MTR-FE-Al cladding, Clay Min. 38 (2003) 35-40.

[MAZ/CUR2003b] Mazeina, L.; Curtius, H.; Fachinger, J.; Odoj, R., Characterisation of secondary products of uranium-aluminium material test reactor fuel element corrosion in repository-relevant brine, J. Nucl. Mater. 323 (2003) 1-7.

[MEY/AUL1928] Meyer, J.; Aulich, W. Zur Kenntnis der Doppelsalze der Selensäure, Z. Anorg. Chem. 172 (1928) 321-343.

[MIT/SAK1992] Mitamura, K.; Sakashita, A., Evaluation of the relationship between ^{14}C and ^{60}Co in a PWR plant Waste Management Conf., Tucson, (1992).

[MOE/RYA2006] Moeller, D. W.; Ryan, T. R.; Cherry, R. N.; Sun, L. C., Significance of ^{14}C and ^{228}Ra in terms of the proposed Yucca Mountain high-level radioactive waste repository. Health Phys. 91 (2006) 238-248.

[MOE/RYA2007] Moeller, D.W.; Ryan, T.R.; Sun, L.-S. C., Factors affecting dose estimates for long-term performance Assessments: Case-Study – Armagosa Valley.Health Phys. 92 (2007) 127- 133.

[MOO2011] Moog, H. C., Dielectric constant, vapor pressure, and density of water and the calculation of Debye-Hückel parameters A_{DH}, B_{DH}, and A^{φ} for Water. THEREDA Technical Paper (Revision 1.1 as of 2011-03-24) (2011).

[MOS/KES1967] Mostkova, R. I.; Kessler, Ju. M.; Safonova, I. V., Koefficienty aktivnosti i osmotičeskie koefficienty chloridov rubidija i cesija v vode pri temperature zamerzanija, Elektrochim. 3 (1967) 516-518.

[MUE/BRE12] Müller-Hoeppe, N.; Breustedt, M.; Wolf, J.; Czaikowski, O.; Wieczorek, K., Integrität geotechnischer Barrieren Teil 2: Vertiefte Nachweisführung. Bericht zum Arbeitspaket 9, Vorläufige Sicherheitsanalyse für den Standort Gorleben. GRS-Ber. 288 (2012).

[MUS/LON1972] Mussini T., Longhi P., Riva G., Standard potentials of the cesium amalgam electrode, and thermodynamic functions for dilute cesium almagams and for aqueous cesium chloride, J. Chem. Thermodyn., 4 (1972) 591-601.

[NAG2008] Nagra, Vorschlag geologischer Standortgebiete für das SMA- und das HAA-Lager National Genossenschaft für die Lagerung radioaktiver Abfälle, Tech. Ber. 08-05 (2008).

[NAR/SMA2010] Narkunas E.; Smaizys, A.; Poskas, P.; Kilda, P., Assessment of different mechanisms of ^{14}C production in irradiated graphite of RBMK-1500 reactors, Kerntechnik, 75 (4) (2010) 185-194.

[NIE/RES2006] Niemeyer, M.; Resele, R., Schachtanlage Asse: Freisetzung volatiler Radionuklide auf dem Gaspfad. Colenco Bericht 3331/108 (2006).

[NIR2006] NIREX, C-14: How we are adressing the issue. United Kingdom Nirex Limited, Tech. Note, Number 498808 (2006).

[NIS/HAT2007] Nishimura, T.; Hata, R., Chemistry of the Ca-Se(IV)-H2O and Ca-Se(IV)-H2O systems at 25 °C, Hydromet. 89 (2007) 346-356.

[NIS/HAT2009] Nishimura, T.; Hata, R.; Hasegawa, F., Chemistry of the M (M=Fe,Ca,Ba)-Se-H_2O systems at 25 °C, Molecules 14 (2009) 3567-3588.

[ÖHO1905] Öholm, L. W., Über die Hydrodiffuion der Elektrolyte, Z. Phys. Chem. 50 (1905) 309-349.

[PAL/RAR2002] Palmer D. A., Rard J. A., Clegg S. L., Isopiestic determination of the osmotic and activity coefficients of Rb_2SO_4(aq) and $Cs_2(SO_4)$(aq) at T = (298.15 and 323.15) K, and representation with an extended ion-interaction (Pitzer) model, J. Chem. Thermodyn., 34 (2002) 63-102.

[PAT/GIL1960] Patterson, C. S.; Gilpatrick, L. O.; Soldano, B. A., The osmotic behaviour of representative aqueous salt solutions at 100°, J. Chem. Soc. (1960) 2730-2734.

[PAT/TRI1991] Patil, K. R.; Tripathi, A. D.; Pathak, G.; Katti, S. S., Thermodynamic properties of aqueous electrolyte solutions. 2. Vapor pressure of aqueous solutions of NaBr, NaI, KCl, KBr, KI, RbCl, CsCl, CsBr, CsI, MgCl2, CaCl2, CaBr2, CaI2, SrCl2, SrBr2, SrI2, BaCl2, and BaBr2, J. Chem. Eng. Data 36 (1991) 225-230.

[PAT/OLI1994] Patil, K. R.; Olivé, F.; Coronas, A., Experimental measurements of vapor pressures of electrolyte solutions by differential static method, J. Chem. Eng. Japan 27 (1994): 680-681.

[PEA1999] Pearson, F. J., Mont Terri Project, Technical Note 99-31, January 1999, WS-A experiment: artificial waters for use in laboratory and field experiments with Opalinus clay. Status June 1998., Report (1999).

[PEI/MCS2011] Peiffer, F.; McStocker, B.; Gründler, D.; Ewig, F.; Havenith, A.; Kettler, J.; Thomauske, B., VSG: Abfallspezifikation und Mengengerüst - Basis der Laufzeitverlängerung der Kernkraftwerke (September 2010) AP 3, GRS 274 (2011).

[PHU/PIT1986] Phutela, R. C.; Pitzer, K. S. Thermodynamic of electrolyte mixtures. Enthalpy and the effect of temperature on the activity coefficient, J. Solution Chem. 15 (1986) 649-662.

[PIT1973] Pitzer, K. S. Thermodynamics of electrolytes. I. Theoretical basis and general equations, J. Phys. Chem. 77 (1973) 258-277.

[PIT1983] Pitzer, K. S., Thermodynamics of unsymmetrical electrolyte mixtures. Enthalpy and heat capacity, J. Phys. Chem. 87 (1983) 2360-2364.

[PIT1991] Pitzer, K. S., Activity coefficients in electrolyte solutions. 2nd ed., from: , CRC Press, Boca Raton (1991) 542 S..

[PIT/MAY1973] Pitzer, K. S.; Mayorga, G., Thermodynamics of electrolytes. II. Activity and osmotic coefficients for strong electrolytes with one or both ions univalent, J. Phys. Chem. 77 (1973) 2300-2308.

[PLU/HUL2004] Plummer, M.A.; Hull, L.C.; Fox, D.T., Transport of carbon-14 in a large unsaturated soil column. Vadose Zone J. 3 (2004) 109-121.

[POD2005] Podruzhina, T., Graphite as radioactive waste: Corrosion behaviour under final repository conditions and thermal treatment. Ber. Forschungsz. Jülich Juel-4166 (2005) 114 pp.

[POV/ORE2000] Povinec, P.P.; Oregioni, B.; Jull, A.J.T.; Kieser, W.E.; Zhao, X.L., AMS Measurements of ^{14}C and ^{129}I in seawater around radioactive waste dump sites. Nucl. Instrum. Meth. Phys. Res. 172 (2000) 672-678.

[PRO/GER2002] Pröhl, G., Gering, F.: Dosiskonversionsfaktoren zur Berechnung der Strahlenexposition in der Nachbetriebsphase von Endlagern nach dem Entwurf der Allgemeinen Verwaltungsvorschrift zu §47 Strahlenschutzverordnung. GSF-Forschungszentrum Umwelt und Gesundheit, Institut für Strahlenschutz: Neuherberg, (2002).

[RAR/MIL1982] Rard, J. A.; Miller, D. G., Isopiestic determination of the osmotic and activity coefficients of aqueous mixtures of sodium chloride and strontium chloride at 25 °C., J. Chem. Eng. Data 27 (1982) 342-346.

[REI/JAH2013] Reinhold, K.; Jahn, S.; Kühnlenz, T.; Ptock, L.; Sönnke, J., Endlager-standortmodell Nord (AnSichT) - Teil I: Beschreibung des geologischen Endlager-standortmodells, Bundesanstalt für Geowissenschaften und Rohstoffe, (2013).

[REM/PLU2009] Remeikis, V.; Plukis, A.; Juodis, L.; Gudelis, A.; Lukauskas, D.; Druteikiene, R.; Lujaniene, G.; Luksiene, B.; Plukiene, R.; Duskesas, G. Study of the nuclide inventory of operational radioactive waste for the RBMK-1500 reactor. Nucl. Engin. Design 239 (2009) 813-818.

[REM/PLU2010] Remeikis, V.; Plukis, A.; Plukiene, R.; Garbaras, A.; Barisevciute, R.; Gudelis, A.; Gvozdaite, R.; Duskesas, G.; Juodis, L., Method based on isotope ratio mass spectrometry for evaluation of carbon activation in the reactor graphite. Nucl. Engin. Design 240 (2010) 2697-2703.

[ROB1935] Robinson R. A., The activity coefficients of the alkali bromides and iodides in aqueous solution from vapor pressure measurements, J. Am. Chem. Soc., 57 (1935) 1161-1164.

[ROB1937] Robinson, R. A., The osmotic and activity coefficient data of some aqueous salt solutions from vapor pressure measurements, J. Am. Chem. Soc. 59 (1937) 84-90.

[ROB1942] Robinson R. A., A thermodynamic study of bivalent metal halides in aqueous solution. Part IX. The activity coefficients of some alkaline earth metal bromides and iodides, Trans. Faraday Soc., 38 (1942) 445.

[ROB/HAG1992] Robertson, D.; Haggard, D.; Thomas, C.; Wynhoff, N., Radiological characterization of neutron-activated metal wastes from nuclear power stations. J. Radioanal. Nucl. Chem. 161 (1992) 585-95.

[ROB/LEV1946] Robinson, R. A.; Levien, B. J., The vapour pressures of potassium ferricyanide and thorium nitrate solutions at 25 °C, Trans. Roy. Soc. New Zeal. 76 (1946) 295-299.

[ROB/STO1940] Robinson R. A., Stokes R. H., A thermodynamic study of bivalent metal halides in aqueous solution. Part I. The activity coefficients of magnesium halides at 25 °C, Trans. Faraday Soc., 36 (1940) 733-734.

[ROB/STO1965] Robinson, R. A.; Stokes, R. H., Electrolyte Solutions 2nd ed.revised ,Butterworths, London (1965).

[ROB/WIL1940] Robinson R. A., Wilson J. M., Part III. The Activitiy Coefficients of Potassium and Cadmium Iodide at 25 °C, Trans. Faraday Soc., (1940) 738-740.

[ROC1966] Rock, P. A., The standard oxidation potential of the ferrocyanide-ferricyanide elctrode at 25° and the entropy of ferrocyanide ion, J. Phys. Chem. 70 (1966) 576-580.

[RÜB/BUH2011] Rübel, A.; Buhmann, D.; Meleshyn, A.; Mönig, J.; Spiessl, S., Aspects on the gas generation and migration in repositories for high level waste in salt formations GRS-Bericht A-3592 (2011).

[RÜD1862] Rüdorff, F. Über das Gefrieren des Wassers aus Lösungen, Pogg. Ann. 116 (1862) 55-72.

[SCH2008] Schwyn, B., Geochemische Nahfeld-Daten für die sicherheitstechnischen Betrachtungen zum Sachplan geologische Tiefenlager, Etappe 1
Nagra Arbeitsbericht NAB 08-51 (2008).

[SCH/MUN2012] Scharge, T.; Munoz, A. G.; Moog, H. C. Activity coefficients of fission products in higly salinary solutions of Na^+, K^+, Mg^{2+}, Ca^{2+}, Cl^-, and SO_4^{2-}: Cs^+, J. Chem. Eng. Data 57 (2012) 1637-1647.

[SEL/SNE1959] Selivanova, N. M.; Šnejder, V. A., Fiziko-chimičeskie svojstva selenatov. VI. Rastvorimost selenata kal'cia v vode pri različnych temperaturach, Izv. Vysš. Učebn. Zaved. SSSR Chim. Chim Technol. 5 (1959) 651-656.

[SHE1903] Sherrill, M. S., Über die Komplexbildung und einige physikochemische Konstanten der Quecksilberhaloide, Z. Phys. Chem. 43 (1903) 705-740.

[SHE/TIC1998] Sheppard, S.C.; Ticknor, K.V.; Evenden, W.G., Sorption of inorganic ^{14}C on to calcite, montmorillonite and soil. Appl. Geochem. 13 (1998) 43-47.

[SIL/PIT1977] Silvester, L. F.; Pitzer, K. S. Thermodynamics of electrolytes. 8. High-temperature properties, including enthalpy and heat capacity, with application to sodium chloride, J. Phys. Chem. 81 (1977) 1822-1828.

[SIL/PIT1978] Silvester, L. F.; Pitzer, K. S. Thermodynamics of electrolytes. X. Enthalpy and the effect of temperature on the activity coefficients, J. Solution Chem. 7 (1978) 327-336.

[SKR/RUM1993] Skripkin, M. Yu.; Rumyantsev, A. V.; Solechnik, N. D. Thermodynamic study of Rb^+, Mg^{2+} || Cl^--H_2O and Cs^+, Mg^{2+} || Cl^--H_2O ternary systems at 25°, Russ. J. Appl. Chem. 66 (1993) 807-810.

[SMI/BAL1993] Smith, H.D.; Baldwin, D.L., An investigation of thermal release of carbon-14 from PWR Zircaloy spent fuel cladding. J. Nucl. Mater. 200 (1993) 128-37.

[SOL/BIE1966] Soldano, B. A.; Bien, P. B., Osmotic behaviour of aqueous salt solutions at elevated temperatures. Part IV, J. Chem. Soc. (1966) 1825-1827.

[SOL/MEE1963] Soldano, B. A.; Meek, M. Isopiestic vapour-pressure measurement of aqueous salt solutions at elevated temperatures. Part III, J. Chem. Soc. (1963) 4424-4426.

[SOL/PAT1962] Soldano, B. A.; Patterson, C. S. Osmotic behaviour of aqueous salt solutions at elevated temperatures. Part II, J. Chem. Soc. (1962) 937-940.

[SOL/STO1959] Soldano, B. A.; Stoughton, R. W.; Fox, R. J.; Scatchard, G. A high-temperature isopiestic unit, from: Hammer, W. J. (Edt.) (1959): The Electrochemical Society Series: The Structure of Elektrolytic Solutions. Wiley & Sons, New York, (1959) 224-235.

[SOO/KRI1988] Sood, M. L.; Krishana, P. C., Diffusion and activity coefficient of aqueous cesium chloride at 45°, J. Indian Chem. Soc. (65) (1988) 31-34.

[STE1961] Steineke, U., Lösungsbehinderung im System KCl-H_2O durch Blockierung mit einer Deckschicht komplexer Cyanide, PhD Thesis, Humboldt-Universität Berlin (1961).

[STE1962] Steinecke, U. Lösungs- und Wachstumsbehinderung im System KCl-H_2O durch Blockierung mit einer Deckschicht komplexer Cyanide, Z. Anorg. Allg. Chem. 317 (1962) 186-203.

[STO1948] Stokes R. H., Thermodynamic study of bivalent metal halides in aqueous solution. Part XVII - Revision of data for all 2:1 and 1:2 electrolytes at 25°, and discussion of results, Trans. Faraday Soc., 44 (1948) 295-307.

[STR1996] Stroes-Gascoyne, S., Measurements of instant-release source terms for ^{137}Cs, ^{90}Sr, ^{99}Tc, ^{129}I and ^{14}C in used CANDU fuels. J. Nucl. Mater. 238 (1996) 264-277.

[STR/TAI1994] Stroes-Gascoyne, S.; Tait, J.C.; Porth, R.J.; McConnell, J.L.; Lincoln, W.J., Release of 14C from the gap and grain-boundary regions of used candu fuels to aqueous solutions. Waste Manag. 14 (1994) 385-392.

[TAB2009] Tanabe H., Nishimura T., Kaneko M., Sakuragi T., Nasu Y., Asano H. Characterisation of hull waste in underground condition, in: NUCLEAR ENERGY AGENCY, ORGANISATION FOR ECONOMIC CO-OPERATION AND DEVELOPMENT, Mobile Fission and Activation Products in Nuclear Waste Disposal, Workshop Proceedings, La Baule, France, 16-19 January 2007, OECD 2009, NEA No. 6310 (2009) p. 207.

[TOU2002] Toulhoat, P., Confinement and migration of radionuclides in a nuclear waste deep repository. C. R. Physique 3 (2002) 975-986.

[VAN1994] Van Konynenburg, R.A., Behavior of carbon-14 in waste packages for spent fuel in a tuff repository. Waste Manag., 14 (1994) 363-383.

[VOJ/EBE1990] Vojtíšek P., Ebert M., The change in the standard Gibbs energy Delta G° in the formation of double selenates $K_2M(II)(SeO_4)_2 . xH_2O$ (M(II) = Mn, Co, Ni, Cu, Zn; x = 6 or 2), Collect. Czech. Chem. Commun., 55 (1990) 994-1001.

[VON/VUL2011] von Lensa, W.; Vulpius, D.; Steinmetz, H.-J.; Girke, N.; Bosbach, D.; Thomauske, B.; Banford, A.W.; Bradbury, D.; Grave, M.J.; Jones, A.N.; Grambow, B.; Petit, L; Pina, G., Treatment and Disposal of irradiated Graphite and other Carbonaceous Waste. atw – Internatl. J. Nucl. Power 56 (2011) 263-269.

[VUL/BAG2013] Vulpius, D.; Baginski, K.; Fischer, C.; Thomauske, B., Location and chemical bond of radionuclides in neutron-irradiated nuclear graphite. J. Nucl. Mater. 438 (2013) 163-177.

[WAL/CEN1903] Walden, P. J.; Centnerszwer, M., Über Verbindungen des Schwefeldioxyds mit Salzen, Z. Phys. Chem. 42 (1903) 432-468.

[WEL/KIN1939] Welton, R. C.; King, G. B., The system Calcium selenate-ammonium selenate-water at 30°, J. Am. Chem. Soc. 61 (1939) 1251-1252.

[WOL/JOV 2007] Wolery, T. J.; Jove-Colon, C. F., Qualification of thermodynamic data for geochemical modeling of mineral water interactions in dilute systems., Sandia National Laboratories, Report ANL-WIS-GS-000003 REV 01 (2007).

[WER/JOH2004] Werme, L. O.; Johnson, L. H.; Oversby, V. M.; King, F.; Spahiu, K.; Grambow, B.; Shoesmith, D. W., Spent fuel performance under repository conditions: a model for use in SR-Can. Svensk Kaernbraenslehantering Tech. Rep. TR-04-19 (2004).

[WIE/HUM2010] Wieland, E.; Hummel, W. The speciation of ^{14}C in the cementitious near field of a repository for radioactive waste. Paul-Scherrer-Institut TM 44-10-01 (2010).

[YAN/EUN2005] Yang, H.-C.; Eun, H.-C.; Lee, D.-G.; Oh, W.-Z.; Lee, K.-W., Behavior of radioactive elements during thermal treatment of nuclear graphite waste thermodynamic model analysis. J. Nucl. Sci. Technol. (42), 869-876 (2005).

[YIM/CAR2006] Yim, M.-S.; Caron, F. Life cycle and management of carbon-14 from nuclear power generation. Progr. Nucl. Energy 48 (2006) 2-36.

[YIM/SIM1996] Yim, M.-S.; Simonson, S.A.; Sullivan, T.M., Investigation of ^{14}C release in an engineered low-level waste disposal facility. Nucl. Technol. 114 (1996) 254-71.

[YIM/SIM2000] Yim, M.-S.; Simonson, S.A., Performance Assessment Models for Low Level Radioactive Waste Disposal Facilities: A Review. Progr. Nucl. Energy, 36 (2000) 1-38.

[ZDA1936] Zdanovskij, A. B., Zakonomernosti v izmenenijach svojstv smešannych rastvorov, Tr. Soljan. Lab. No. 6 (1936) 1-71

8 Summary

8.1 Chemical bonding type and release of ^{14}C in radioactive wastes

The state of knowledge concerning the speciation and release of ^{14}C in radioactive wastes was documented in a literature study conducted by GRS. It was found to be still fragmentary due to a low quantity of analytical data. This finding applies to both radioactive waste with negligible heat generation and spent fuel. In the light of insufficient information a complete conversation of the ^{14}C – inventory to CO_2, CH_4 and low molecular weight hydrocarbons is expected in the long term safety assessment.

It is assumed, that the ^{14}C-inventory is discharged in gaseous form during reprocessing of spent fuel. In the same way ^{14}C is lost when coolant is treated, where it occurs mainly as carbonate or as hydrocarbons depending on the reactor type. For spent nuclear fuels it is supposed, that ^{14}C exists as carbide (negatively charged) or as carbon (neutrally charged), depending on the prevailing chemical speciation of the mother elements oxygen and nitrogen. However, for these assumptions there is still no experimental evidence. Consequently, it is unclear, whether the release takes place primarily in the form of hydrocarbons

Consideration of uncertainties and of lack of knowledge about the behavior of different types of ^{14}C-containing wastes in a repository lead to substantially conservative assumptions in long term safety assessments. The result is a presumable overestimation of the calculated potential radiation exposure. Due to the scarce data base further investigations concerning the speciation of ^{14}C in spent fuel elements, their reactions and release processes seem to be necessary. This could lead to a reduction of uncertainties in estimated potentials radiation exposure. This objective is pursued by the EU joint research project CAST (Carbon-14 Source Term) that started in late 2013. The project intends to investigate both the chemical form and the release processes of ^{14}C in the waste types steal, zircaloy, ion exchange resin and graphite.

8.2 Analytical studies on ^{14}C speciation

A new analytical method to analyze ^{14}C speciation in aqueous and gaseous samples of experiments with highly radioactive materials has been successfully established by KIT-INE within VESPA. This is a valuable contribution to work performed by KIT-INE within the EC funded CAST project, where the ^{14}C source terms for irradiated steel and

Zircaloy of a spent nuclear fuel rod segment are investigated. For the handling of the samples, which show very high concentrations of ^{60}Co and ^{137}Cs in addition to the ^{14}C to be analyzed, a specifically manufactured glove box was developed and installed in the controlled area of KIT-INE. The analytical tools and the entire apparatus for the extraction and separation of organic and inorganic ^{14}C species were tested with low ^{14}C reference samples in a fume hood. After successful operation had been established, the new apparatus was transferred into the glove box. Calibration with inorganic and organic reference samples (^{14}C doped Na_2CO_3, CH_3CO_2Na, mixtures of Na_2CO_3 und CH_3CO_2Na) was performed inside the glove box. In samples containing 10 – 1000 Bq ^{14}C, a total recovery of ≥ 90 % was reached. Different LSC-cocktails and sample vials were tested in order to optimize the precision of ^{14}C analytics via LSC (liquid-scintillation-counting).

8.3 Chemical thermodynamics of the Fission products selenium, iodine und caesium

The aqueous speciation of selenium has a significant influence on water-rock interfacial processes. Therefore, HZDR investigated the Se speciation as a function of Se-concentration, pH, redox conditions, ionic strengths and temperature. Additionally, interactions with the metal cations Na^+, Ca^{2+} and Mg^{2+} were examined. The combination of various spectroscopies, namely NMR, FT-IR and Raman, helped to elucidate the stability ranges of different Se complexes, Se(IV) dimerization and structural parameters.

In the focus of the thermodynamical work of GRS were the chemical thermodynamics of the elements selenium (oxidation state +IV and +VI), iodine (oxidation state –I) and caesium (oxidation state +I) in the temperature range of 0° to 90 °C. For these elements, a thermodynamic temperature dependent model could be developed which allows the prediction of activity coefficients in important solutions systems.

For solution systems with caesium, selenium and iodine there were only marginal data gaps at 25 °C, so that the laboratory investigations concentrated on equilibrium characteristics at higher temperatures. Emphasis was placed on measurements of binary systems from 40° to 90 °C. A rocking device was developed for isopiestic experiments with which the equilibration adjustment at higher temperatures was accelerated.

Selenates and selenites of sodium, potassium and magnesium were investigated with isopiestic measurements at 40 – 90 °C. Solubility experiments were conducted for the less soluble analogue compounds of calcium. Potentiometric measurements on hydrogen selenite solutions were not successful for the present. The new methodology allows in principle the deduction of activity coefficients but it has to be further developed in order to eliminate chemical interferences. A polythermal model was established on the basis of laboratory experiments and additional literature data. It correctly describes the activity coefficients of selenite and selenate in binary solutions. In addition, new solubility constants for calcium selenite and calcium selenate were deducted. Especially calcium selenite could represent the solubility determining phase for selenium under slightly reducing conditions.

Solutions of sodium iodine and potassium iodine were investigated with the isopiestic method. Measurements with magnesium iodine solutions turned out to be very challenging because the preparation of the required pure stock solutions of MgI_2 needed great efforts. Moreover it decays when exposed to minimal amounts of air. These problems could be resolved in the end, but the number of measuring points gained is limited. The developed polythermal model allows the calculation of activity coefficients of iodide in the binary solutions mentioned at 25°– 90 °C. On the basis of assumptions on mixed solutions the model can be transferred to mixed solutions as well.

Investigations on caesium complemented earlier model developments which were established in previous projects. Investigations included isopiestic measurements on calcium and magnesium containing mixed systems at 25 °C as well as experiments on binary systems at 40 – 90 °C. On the basis of experimental results, the model could be completed at 25 °C. Furthermore it is now possible to predict activity coefficients of caesium in binary solutions at temperatures up to 9 °C.

On the basis of these models the solubility limit for selenium could be calculated for some solution types that may occur in repositories in salt rock or clay. If the prevailing species is selenite, solubility will be limited by the formation of calcium selenite. For selenate, for iodide and caesium no solubility limiting phases could be identified.

8.4 Aquatic chemistry, redox transformations and thermodynamics of Tc(IV)

Within VESPA, a systematic literature study on aquatic technetium chemistry was performed. A clear need for improving the state of knowledge and improving the available thermodynamic database, also considering ion-interaction processes, was identified.

As part of the studies of KIT-INE, the redox chemistry of technetium was studied in aqueous systems relevant to nuclear waste disposal. Based upon a detailed and systematic investigation of Tc redox chemistry in dilute aqueous solutions to highly concentrated salt brines, the stability field of Tc(IV) (reduced Tc(IV) generally exhibiting low solubility at relevant pH conditions) was defined. The same experiments allow to draw conclusions about the kinetics affecting Tc(VII) reduction processes. By systematically investigating NaCl and $MgCl_2$ solutions from low to high ionic strength, the influence of ion-interaction processes on Tc redox transformations were assessed for the first time. The studies performed within VESPA also contribute to the validation of new and existing chemical models and thermodynamic data relevant for Tc redox chemistry. Detailed experimental information on appropriate redox chemicals for use in lab-experiments aiming at reducing Tc(IV) systems was established. The key relevance of the tetravalent oxidation state of technetium under the strongly reducing geochemical environments expected for operative deep-underground nuclear waste repository systems was highlighted.

In addition to the above mentioned experimental studies focusing on the formation and stability of Tc(IV), comprehensive experimental studies were performed to analyze solubility and speciation of amorphous Tc(IV)-oxyhydroxide phase $TcO_2xH_2O(s)$ in aqueous solutions over a large pH range and ionic strength interval (NaCl, $MgCl_2$ und $CaCl_2$) at 25 °C. New systematic studies performed in the rad-lab facilities of KIT-INE were the basis for deriving experimentally well supported thermodynamic data (solubility products and hydrolysis constants) and ion-interaction parameters (using both SIT and Pitzer approaches). The new thermodynamic data generated within VESPA will be integrated into the German thermodynamic reference database THEREDA, following the required evaluation and quality assurance processes established within THEREDA. The thermodynamic data for Tc(IV) derived within VESPA are fundamental physic-chemical parameters. As such, they are clearly site-independent and generally applicable for the geochemical modeling of different scenarios in all host-rock formations currently discussed in Germany.

8.5 Reduction, sorption and incorporation of Tc(VII) in magnetite

The studies of KIT-INE within VESPA using advanced XANES and EXAFS techniques show evidence that under presence of magnetite, reduction of Tc(VII) and formation of a Tc(IV) surface complex is observed in simplified systems. Furthermore some first information was obtained that incorporation of Tc(IV) into the magnetite structure may occur. This effect was described as a potential retention mechanism in low ionic strength media. Within the extension year of VESPA, further experiments were performed using EXAFS to look deeper into this effect. The key result from the experimental studies is that both the degree and mechanism of Tc retention on iron mineral phases is depending very strongly on parameters like Tc concentration, surface loading and pH conditions. A significant part of Tc(IV) is incorporated in magnetite under conditions with low Tc concentrations, whereas precipitation processes dominate at high total Tc concentrations. The incorporation of Tc(IV) is furthermore facilitated by high magnetite concentrations and crystallization rates. These experiments performed within VESPA in simplified systems thus yield key information on Tc retention processes on relevant secondary mineral phases expected to be present in a repository.

8.6 Influence of redox kinetics on Tc migration in natural systems

The interaction of technetium with host-rock material was investigated with (i) granitic rock from the Äspö Hard Rock Laboratory in Sweden, (ii) material from a potential site for a nuclear waste repository in Russia (Nizhnekansky massif (NK), Siberia), and (iii) magnetite samples of varying stoichiometry. The sampling of the core material from Äspö under anoxic conditions was performed in collaboration with the EC CROCK project, allowing sampling under in-situ conditions. This is a key step to ensure largely undisturbed, near-natural geochemical conditions especially regarding redox characteristics of the samples. Part of the Äspö diorite (ÄD) was artificially oxidized for comparison with the unoxidized in-situ material to investigate and document the effect of oxidative disturbances on Tc retention processes.

Batch-type experiments show reduction of Tc(VII) by Fe(II) minerals (especially Biotite) and Tc(IV) retention on the mineral surface. Spectroscopic studies using XPS and XANES indicate only Tc(IV) present at the granite surface. Additional studies under variation of the initial Tc concentration (10^{-5} – 10^{-10} mol/L) show reduction and kinetics depending on Tc(VII) concentration, in agreement with the redox capacity of the unoxidized rock. The results from oxidized samples also indicate a strong influence of sample handling and storage on the Tc(VII) immobilization by crystalline rock. Sorption data for unoxidized ÄD after 3 months contact time and low Tc concentrations show retardation coefficients of log Kd > 2.5. Kd values for oxidized ÄD and NK materials are very comparable, but significantly lower than for unoxidized samples. The formation of a colloid phase under the adopted groundwater conditions (pH 8, I = 0.2 M for ÄD and pH 8, I = 0.005 M for NK) could not be identified. Desorption of Tc is insignificant under natural groundwater conditions, whereas oxidation of Tc induces increased mobility (~95 %).

Further studies of KIT-INE focus on Tc migration experiments in a natural fracture under anaerobic conditions, the fracture being initially characterized by µCT (Computer Tomography). Experimentally determined HTO (tritiated water) and ^{36}Cl break-through curves (BTC) under variation of the flow rate show long tailings because of complex fracture geometry. No anion exclusion effect was observed under the experimental conditions. Tc migration studies were performed with ^{95m}Tc radiotracer in the concentration range of 10^{-11} M – 10^{-9} M. The Tc retention in these experiments decreases with increasing residence time in the fracture and clearly documents the impact of kinetic effects on Tc mobility and retention. The rates for Tc surface retention and reduction kinetics (0.45 – 0.61 d^{-1}), are about one order of magnitude larger than the data generated from batch-type experiments (0.036 d^{-1}).

The results from the studies (using both batch experiments and migration studies) were used to evaluate Tc-retention on iron oxide phases and Tc(VII) redox kinetics in natural systems. The data derived for the influence of kinetic effects on Tc reduction can be used for sensitivity analyses when comparing to an equilibrium approach in transport-modelling exercises. Based upon the studies performed by KIT-INE within VESPA in near-natural systems, a significantly improved description of Tc retention in deep underground nuclear waste repositories was achieved.

8.7 Structural incorporation of selenium into mineral phases (calcite, pyrite)

The state of knowledge on selenium adsorption on/in calcite is documented in the respective literature survey performed within VESPA. Especially the oxidized selenium species selenate ($Se(VI)O_4^{2-}$) and selenite ($Se(IV)O_3^{2-}$) exhibit relatively high solubilities and interact only weakly with most common mineral surfaces. Therefore, ^{79}Se has been identified as a potentially critical radionuclide with respect to the long term safety of a nuclear waste repository by many Waste-Management Organisations (e. g. Ondraf/Niras (Belgium), Andra (France), Nagra (Switzerland)). Over extended periods of time it may increase the radioactivity in adjacent aquifer systems.

According to literature and the studies performed in the frame of the VESPA-project, tetravalent selenium (selenite, $Se(IV)O_3^{2-}$) may as well adsorb on the calcite surface, as be incorporated into the bulk calcite structure. It can be shown that such processes may decrease the selenium concentration in the surroundings of a potential nuclear waste repository by orders of magnitude. Sorption and incorporation of $Se(IV)O_3^{2-}$ on/in calcite proceed via the formation of a surface-solid-solution by an ion exchange process. The Se-doped surface monolayer may be overgrown upon crystal growth at elevated supersaturation such that $Se(IV)O_3^{2-}$ gets entrapped in the crystal. In the surface monolayer, the pyramidal $Se(IV)O_3^{2-}$ ion introduces only relatively small strain in the crystal structure. Therefore, adsorption is relatively efficient (K_D = 2 ± 1 mL/g, partition coefficient (of a one monolayer thick surface-solid-solution), D = 0.02 ± 0.01). Upon fast growth the surface composition is conserved and Se is incorporated, with $Se(IV)O_3^{2-}$ substituting CO_3^{2-} structurally in the bulk crystal. Inside the bulk crystal $Se(IV)O_3^{2-}$ generates considerable strain. Therefore, the conserved Se-content corresponds to a non-equilibrium state. As a consequence of this „adsorption / entrapment“ model,_ENREF_3, selenium sorption on calcite at equilibrium conditions is limited to the calcite surface monolayer. Only at elevated supersaturation (depending on the Se-concentration) selenite may be coprecipitated with calcite in significant amounts with the partition coefficient of the bulk-solid-solution, D = 0.02 ± 0.01.

8.8 Co-precipitation and adsorption of selenium on FeS/FeS_2

Under reducing conditions as they are expected in nuclear waste repositories over long periods of time, e. g. in clay formations, selenium is expected to be present in low oxidation states (selenide: Se_2^{2-}, Se^{2-}). Selenide species exhibit low solubilities and are therefore strongly retained in the near-field of a waste repository. However, there is hardly any literature on selenide retention, especially not on process understanding of the key retention mechanisms.

In the frame of the VESPA project, selenide retention on/in iron sulfide phases was investigated at KIT-INE. A first step was the development and optimization of an experimental procedure for the electrochemical reduction of selenite (Se(IV)) to selenide (Se(-II)). Later, the selenide retention by coprecipitation with and adsorption on iron sulfide were investigated. The results show solely the formation of mackinawite (FeS) upon synthesis of FeS in the presence of Se(-II). The formation of a separate Se-phase was not observed. For information on the molecular scale structure, Se(-II) doped FeS was investigated by X-ray absorption spectroscopy. The results show, as expected due to similar ion sizes, the substitution of S(-II) by Se(-II) in the structure. The interaction of Se(-II) with pre-existing FeS in suspensions (adsorption experiments) was investigated as well. The FeS colloids in FeS suspensions interact strongly with dissolved Se(-II). Investigations revealed the formation of mixed phases in which Se has a very similar chemical environment as in phases formed in coprecipitation experiments. Moreover, iron selenide (FeSe), that exhibits a low solubility, was also synthesized. FeSe and FeS are isostructural and form the end-members of a $FeSe_xS_{1-x}$ solid-solution series. Formation of such phases in a waste repository will lead to an effective scavenging of selenium.

Pyrite (FeS_2) is the most stable iron(II)-sulfide phase and is abundant in natural clay formations. It forms upon interaction of FeS with H_2S. Similarly to FeS, Se may as well be incorporated into pyrite. Correspondingly, natural pyrite samples often contain significant amounts of selenium. This indicates that in analogy to the investigated precursor phase FeS, retention of Se in/on pyrite will be effective as well.

8.9 Sorption of selenite and selenate onto repository-relevant mineral phases

Sorption of selenate (SeO_4^{2-}) and selenite (SeO_3^{2-}) onto repository−relevant mineral-phases has been investigated by HZDR. These minerals phases include typical iron corrosion products (hematite, maghemite), components of the geological barrier ($\delta-Al_2O_3$, kaolinite, and illite), and environmental ubiquitous model oxides (anatase, rutile).

For selected systems, the impact of temperature and ionic strengths has been determined and thermodynamic parameters relevant for databases such as THEREDA have been derived.

In general, it could be shown that the retention of selenite is much more effective than the one of selenate. For both Se-species the sorption is strongest on iron phases, whereas the sorption on clay minerals is very low. The retention of selenite and selenate is therefore supposed to be most efficient at the technical barrier of the repository. With increasing temperature the sorption of both selenate and selenite are generally reduced, whereas this impact is more pronounced for the oxides than for kaolinite. An increase in ionic strength lowers primarily the sorption of selenate.

Structural information on the sorbed complexes obtained by ATR FT-IR and EXAFS revealed the formation of inner-sphere complexes of selenite on the different mineral phases. Selenate mostly formed outer-sphere complexes. However, on the surface of the iron phases and $\delta-Al_2O_3$, outer-sphere complexes with a reduced symmetry could be identified for the first time. In summary, the spectroscopic results allowed to discriminate among two distinct types of outer-sphere complexes arising from selenate sorption on different mineral surfaces. Whereas any Se retention through outer-sphere complexes is highly reversible, a binding through inner-sphere complexes is more stable and thus can contribute to a long-term retardation.

The precipitation of a crystalline selenite phase in the presence of Ca^{2+} was investigated by means of XRD, DTA/TG measurements, and solid state NMR. From this, it can be derived that calcium ions, naturally occurring in concentrations several orders of magnitude higher than selenium, are able to precipitate Se(IV), leading to a permanent immobilization of ^{79}Se.

From sorption results quasi-thermodynamic parameters for surface complexation models have been derived (dissociation constant, surface site density, and complex formation constant). Experimentally obtained conditional distribution coefficients (K_D-values) have been evaluated by means of coupling of the codes FITEQL and UCODE. These parameters are supposed to be fed into the mineral specific sorption database RES^{3}T. They will allow the modelling of so-called “smart−K_D” values, as they are used for the joint project WEIMAR (FKZ 02 E 11072B).

8.10 Synthesis of Sorel phases as starting material for investigations on ^{129}I retention

In preparation of sorption experiments with ^{129}I, different methods for the synthesis of pure Mg-oxychloride consisting of only one clearly defined mineral phase were employed. The synthetic Mg-oxychloride was analyzed using several complementary techniques in order to prove the required sample purity and characteristics. Mg-oxychloride samples were contacted with concentrated salt solutions and the subsequent equilibration of the Sorel phase/salt brine system monitored over several weeks. Owing to the slow pre-equilibration of the samples, it was not possible to contact the synthetic Mg-oxychloride with ^{129}I within the duration of this work package of the VESPA project. Experiments on ^{129}I retention on Mg-oxychloride are now part of the KIT-INE contribution to a future VESPA (II) project.

8.11 Synthesis, characterization and long-term stability of LDH solid solutions

Retention of highly mobile radionuclides, which are present in anionic form, is of relevance with respect to the safety of radioactive waste disposal. Of interest are anionic clay minerals, the so-called layered double hydroxides (LDHs), which form as corrosion products in the near-field. For example, in the presence of cementitious materials within the near-field, the formation of the so-called Friedel-salts (general stoichiometric formula: $[Ca_2Al(OH)_6(Cl,OH)\cdot 2H_2O]$) is observed. Also, as corrosion product of steel containers, the formation of Fe(II)/Fe(III) containing LDHs (known as green rust) was observed. From corrosion experiments with research reactor fuel elements under repository-relevant conditions MgAl-LDHs with chloride and sulfate as interlayer anions and the green rust were identified as secondary phases. Due to their ability to retain anionic species, LDHs are subject of numerous scientific investigations.

Within the joint project VESPA, Jülich selected three LDH solid solutions. Their ability to retain the anionic radionuclide species, iodide, selenite and pertechnetate by anion exchange was investigated. A pure MgAl-LDH phase and three LDH solid solutions (0.0333 mol fraction of magnesium was exchanged by nickel, cobalt and iron, respectively) were tested and their retention efficiencies by anion exchange were compared. In nature, the formation of solid solutions can be observed (i. e. solid solution formation in the field of minerals (i. e. feldspar). Therefore, the formation of solid solutions under any disposal concept must be considered.

Three LDH solid solutions were synthesized without the formation of crystalline by-products. The structural incorporation (octahedral coordination) of nickel, cobalt and iron into the brucite-like layer was confirmed by XRD and EXAFS.

Within this project, thermodynamic data for the LDH solid solutions were generated in order to predict their long-term stability. The thermodynamic code GEMS (developed at the Paul Scherer Institute (PSI)) was used. The Gibbs free energies of formation were calculated by assuming equilibrium between solid and corresponding aqueous composition. From the results obtained it seems obviously that the structural incorporation of the cations (nickel, cobalt and iron, respectively) did not strongly affect the stability (solubility) of the LDH phase. The determined Gibbs free energies of formations differ within the range of 26 kJ/mol. However, the Gibbs free energies of formation differ significantly when the interlayer anion was changed. Clearly, the charge density of the anion has a strong influence on the LDH stability. For example, the MgAl-LDH with carbonate (carbonate possesses a high charge density) as interlayer anion has a higher stability (less soluble) compare to the MgAl-LDH with chloride as interlayer anion. The determined Gibbs free energies of formation had the significant difference of 127 kJ/mol.

Up to day only scare thermodynamic data for LDHs exist. In future it is planned to generate a thermodynamic data base for a complete solid solution series with different anions intercalated. This will be achieved by thermodynamic modeling (GEMS code) and calorimetric measurements. These data will be used to predict the long-term stability on a reliable level.

8.12 Determination of solubility constant of LDH solid solutions

Three synthesised LDH compounds were provided by FZJ to GRS for an experimental determination of their solubility constants. These LDH phases were partly substituted hydrotalcites in which a small amount of magnesium is substituted by cobalt, nickel, or bivalent iron. The solubility of the LDH compounds was analysed in repository relevant solutions (Opalinus clay pore water; $MgCl_2$ solutions as well as IP21 solution). After equilibration of the CO_2 and partly also O_2 sensitive solution/ solid mixture chemical analyses were performed. On the basis of experiments solubility constants could be derived for the LDH phases partly substituted with cobalt or nickel. The solubility constant is identical for both types. With this result, the theoretically derived predictions (work of FZ Jülich) were confirmed. Analogue calculations for the Fe(II) containing LDH phase were not possible because the iron concentrations in the equilibrium solutions were below the detection limit. Nevertheless, the chemical similarity of Co^{2+}, Ni^{2+} and Fe^{2+} allows the assumption that the LDH phase substituted with iron would have the same solubility constant.

8.13 Retention of anionic radionuclide species by LDH solid solutions

The retention of anionic radionuclide species by anion exchange reaction was studied in water and in order to simulate repository relevant conditions, in clay pore water and in salt brine (brine 2). The results indicate that the used LDH solid solutions possess an effective retention potential for the anionic radionuclide species (iodide, selenite and pertechnetate). Contrary to the pure MgAl-LDH phase, which only possesses a retention potential in water, the obtained distribution coefficients (K_d-values) clearly indicate, that the solid solutions can retain effectively the anionic radionuclide species in water and in clay pore water. In clay pore water the determined K_d-values were around three orders of magnitude higher for selenite ($K_d = 250$ ml/g^{-1}) and around one order of magnitude higher for iodide ($K_d = 2.24$ mL/g^{-1}) and pertechnetate ($K_d = 5.62$ mL/g^{-1}) as a K_d-value of 0.1 mL/g^{-1}. Calculations performed by ANDRA reveal that a Kd-value of 0.1 mL/g^{-1} possesses an enormous impact on migration times in clay formations. Taken a migration pathway of 50 m and a diffusion coefficient of 5 10^{-12} m^2/s^{-1} into consideration the migration time increases from 140.000 to 700.000 years.

In salt brine ($MgCl_2$-rich brine was used) the LDH solid solutions retain only selenite. Compared to chloride, only the charge density of selenite is higher, hence a LDH phase intercalating selenite is more stable and this is the driven power for this anion exchange reaction.

The results clearly indicate that the retention by anion exchange reaction is determined by the charge density of the anion and by the composition of cations within the brucite-like layer. The impact of the LDH composition/structure on the retention will be investigated in future in detail and this will contribute to a fundamental process understanding.

In conclusion, the often assumed zero retention for anionic radionuclide species must be corrected. LDH phases, especially their solid solutions can retain anionic radionuclide species effectively by anion exchange reactions and the determined distribution coefficients (K_d-values) are useful parameters in transport codes, in which the radionuclide migration in the geochemical formation can be modeled.

8.14 Methodical advancement of redox measurements at high temperatures and salinities

Potentiometric measurement of redox potential in brine solutions is impeded by the existence of a concentration dependent diffusion potential at the reference electrode that is a necessary part of the cell construction. Previous investigations showed that it is possible - at least in strongly acidic iron containing solutions – to convert the primarily gained cell potentials into activity ratios of iron(II) and iron(III) compounds. This approach opens a path to a thermodynamically defined iron specific redox state. It was checked by potentiometric investigations under pH neutral conditions in KCl solutions containing potassium ferricyanide and potassium ferrocyanide. The evaluation of these measurements required a thermodynamical model that describes the activity coefficients of potassium ferricyanide and potassium ferrocyanide in KCl solutions.

The potentiometric measurements showed that the experimental approach allows to establish a simple relationship between the activities of the ferricyanide and ferrocyanide on the one hand and the measured cell potentials on the other hand. Based on this finding it would be possible to derive an activity ratio (a redox state) from the cell potential at any given background KCl concentration. However, the numerical relationship could not be brought into agreement with the model derived from acidic mixed Fe(II)/ Fe(III) solutions. After a more detailed look into this model it must be concluded that the used activity model for Fe^{3+} may need further improvement. For near neutral solutions a slightly different, simplified approach was proposed that links the measured potential to a concentration ratio of ferricyanide and ferrocyanide.

8.15 Implementation of the research results into migration models used within long-term safety assessments

The joint project VESPA aimed at evaluating conservative assumptions regarding the radionuclides^{14}C, ^{79}Se, ^{129}I, ^{135}Cs and ^{99}Tc in long-term safety assessments. Three test cases were defined in order to demonstrate the impact of these assumptions on radionuclide migration: Drift emplacement in a salt formation – borehole emplacement in a salt formation, borehole emplacement in a clay formation. The project partners derived solubility constants and sorption coefficients on the basis of the experimental work in this project. These data were implemented within the numerical models for the radionuclide migration processes in clay (programme CLAYPOS) and salt (programme LOPOS).

The implementation of the new solubility values resulted in salt rock in a reduction of the activity release rate by three (^{79}Se) and five (^{99}Tc) orders of magnitude. In clay rock a reduction by four orders of magnitude was observed. A consideration of sorption at iron oxides phases leads to a reduction of release rates by approximately one order of magnitude. In clay rock the effect is negligible because the sorption capacity of clay is much larger. The comparative calculations show that a more detailed consideration of geochemical process may be very relevant for the long-term safety assessment because conservative assumptions regarding the mobility of radionuclides can be significantly reduced.

8.16 Conclusion

The work performed by the project partner GRS, FZJ, HZDR, and KIT-INE within VESPA highlight the key relevance of geochemistry for assessing radionuclide retention and mobilization processes in a repository for radioactive waste. Based upon detailed and systematic experimental studies, a significantly improved process understanding of the chemical behavior of long-lived fission and activation products (^{14}C, ^{79}Se, ^{99}Tc, ^{129}I, and ^{135}Cs) in repository relevant systems was achieved. Fundamental site-independent thermodynamic data and models were derived which are required for comprehensive geochemical model calculations. As a consequence of the research performed within VESPA, different repository concepts and scenarios can be analyses on a significantly improved level.

This project provided a major contribution to geochemical databases, which are mandatory for the long-term safety assessment for final repositories. Additional spectroscopic results contribute to a fundamental understanding of sorption processes of anionic species within the near field of a repository on the molecular level. The data and findings allow a more realistic setting of conservativeness; reduce the numerical uncertainty of the results of the long-term safety assessment; and increase the confidence in respective models and their results due to improved process under-standing.

List of tables

List of figures

Acronyms and Abbreviations

AAS	Atomic Absorption Spectroscopy
ACE	Affinity Capillary Electrophoresis
AMS	Accelerator Mass Spectrometry
ANDRA	Agence Nationale pour la gestion des Déchets Radioactifs
ATR FT-IR	Attenuated Total Reflection Fourier transform Infrared spectroscopy
CE	Capillary Electrophoresis
DFT	Density Functional Theory
DPSCV	Differential Pulse Cathodic Stripping Voltammetry
DTA/TG	Differential Thermal Analysis (DTA)/Thermogravimetric analysis (TG)
ETV-ICP/MS	Electro-Thermal Vaporisation-ICP/MS
EXAFS	Extended X-ray Absorption Fine Structure
HAO	Hydrous Aluminum Oxide
HAP	Hydroxylapatite
HFO	Hydrous Ferric Oxide
HG-AAS	Hydride Generation-Atomic Absorption Spectrometry
HG-AFS	Hydride Generation-Atomic Fluorescence Spectrometry
HMO	Hydrous Manganese Oxide
IC	Ionic Chromatography

ICP-OES	Inductively Coupled Plasma-Optical Emission Spectroscopy
ICP-MS	Inductively Coupled Plasma-Mass Spectrometry
LSC	Liquid Scintillation Counting
NEA-OECD	Nuclear Energy Agency-Organization for Economic Co-operation and Development
NMR	Nuclear Magnetic Resonance
OCRWM	Office of Civilian Radioactive Waste Management
ONDRAF	Organisme national des déchets radioactifs et des matières fissiles enrichies
PA	Performance Assessments
PXD-AMS	Projectile X-rays-Detection in Accelerator Mass Spectrometry
RAXR	Resonant Anomalous X-ray Reflectivity
RT	Room Temperature
TEM	Transmission Electron Microscopy
TXRF	Total Reflection X-ray Fluorescence
UV	Ultra Violet
VT-IR	Variable Temperature Infrared Spectroscopy
XANES	X-ray Absorption Near Edge Structure
XAS	X-ray Absorption Spectroscopy
XPS	X-ray Photoelectron Spectroscopy

XRD	X-ray Diffraction
XSW	X-ray Standing Wave

A Appendix A (chapter 4)

A.1 Se aqueous chemistry

Reagents and solutions

All selenium(VI) and selenium(IV) solutions were prepared by dissolving Na_2SeO_4 (Sigma Aldrich p. a.) and Na_2SeO_3 (AppliChem > 99 %), respectively, in CO_2-free Millipore de-ionized water (Alpha-Q, 18.2 MΩ cm). All solutions were prepared in a glove box under anoxic conditions (O_2 < 5 ppm). To adjust the ionic strength, dissolved NaCl (Merck powder p. a.) was used as background electrolyte. In order to avoid possible contamination of the solutions by silicate, polypropylene or polycarbonate flasks were used for all experiments. For preparation and transportation, all samples were kept in nitrogen atmosphere. For NMR spectroscopy, 10 vol- % of D_2O (Sigma-Aldrich) were added to the aqueous solutions for deuterium lock, thus concentrations being finally diluted by a factor of 10 %. Afterwards pH and concentration (by ICP-MS) were redetermined.

Se(IV) Dimerization

Samples were prepared at varying Se(IV) concentrations ranging from 1 mmol L^{-1} to 1 mol L^{-1}, with ionic strength adjustments, at pH_c 5 and 13 (see definition in Methods & Instrumentation section). Since a 1 mol L^{-1} Se(IV) solution gives an ionic strength of 3 mol L^{-1}, the samples with lower Se(IV) concentration were adjusted to $I = 3$ mol L^{-1} by addition of NaCl.

Temperature impact

For this purpose, 0.1 mol L^{-1} Se(IV) and Se(VI) aqueous solutions were prepared at ambient temperature using NaOH and HCl for pH adjustment. Se(IV) solutions were adjusted to pH values of 4 and 10, that of Se(VI) to 4 and 7.5.

Ca^{2+}/Mg^{2+} complexation

Aqueous solutions containing 10 vol.- % of D_2O were prepared with sodium selenite or sodium selenate concentrations of 0.1 mol L^{-1} under inert gas atmosphere. Appropriate amounts of $CaCl_2·2H_2O$ or $MgCl_2·6H_2O$ (both Merck p. a.) were added to yield metal concentrations of 0.05 and 0.10 mol L^{-1}. The total ionic strength in all samples was set up to 5.6 mol L^{-1} (background electrolyte: NaCl). pH_c was adjusted to 5 or 7.5 in the case of Se(IV) or Se(VI), respectively.

Methods and Instrumentation

pH adjustment

At moderate ionic strength (< 0.5 mol L^{-1}), pH measurements (pH-meter Inolab WTW series pH720) were performed using a combination glass electrode (BlueLine 16 pH from Schott Instruments) in which an Ag/AgCl reference electrode was incorporated. Combination pH electrodes (WTW SenTix® Mic) for samples at high ionic strength (3 and 5.6 mol L^{-1}) were used. Both electrodes were freshly calibrated using NIST-traceable buffer solutions (pH 1.68/pH 4.01/pH 6.87/pH 9.18 from WTW), to an accuracy of ± 0.05. The molar H^+ concentrations ($pH_c = -\log c_{H+}$) in the solutions at high ionic strength were determined as described in detail by [ALTMAIER '03; ALTMAIER '08].

NMR spectroscopy

Temperature dependence and Ca^{2+}/Mg^{2+} complexation measurements as well as dimerization experiments of pH_c 5 Se(IV) solutions were performed on a Bruker DPX 400 with a magnetic field strength of 9.4 T, corresponding to a ^{77}Se resonance frequency of 76.4 MHz, using a 10 mm broadband direct detection probe. Samples were measured in 10 mm tubes (sample) and, except for the temperature-dependent measurements, with coaxial 5 mm inner tube for deuterium lock and chemical shift referencing. Temperature dependent NMR measurements were carried out at 296, 308, 318 and 333 K with an accuracy of ± 0.1 K.

Dimerization experiments at both pHc 5 and 13 were carried out on an Agilent DD2-600 MHz NMR system, operating at 14.1 T and a ^{77}Se resonance frequency of 114.5 MHz using a 10 mm broadband direct detection probe and an 80–125 MHz quarterwave switch.

Selenium chemical shifts are reported according to 0.5 mol L^{-1} sodium selenate pH 9.6 in 10 % D_2O as a chemical shift reference, corresponding to 1031 ppm.

Solid state NMR experiments were conducted on a Bruker AVANCE 400 WB, operating at 9.4 T, using a CP/MAS probe and a 4 mm ZrO_2 rotor. The spectra are referenced externally to the solid sodium selenate signal at 1049 ppm.

FT-IR

The IR experiments were carried out with a Bruker Vertex 80/v spectrometer, equipped with a horizontal ATR diamond crystal accessory (SamplIR II, Smiths Inc., 9 reflections, angle of incidence: 45°) and a Mercury Cadmium Telluride (MCT) detector. Each IR spectrum recorded was an average over 256 scans at a spectral resolution of 4 cm^{-1} using the OPUS software for data acquisition and evaluation. For each sample, a blank solution at the same pH and ionic strength was used for the background correction. To investigate the impact of aqueous temperature (from 298 to 333 K), a thermostatic water bath (F12-MB, Julabo) for the thermal equilibration of the ATR crystal unit was used. Selenium containing solutions and their respective blanks were also thermostated. Solutions were measured as prepared.

Thermogravimetric analysis

7.52 and 9.15 mg substance were analyzed with a SSC 5200 TG/DTA 22 (Seiko Instruments) with 300 mL min^{-1} argon gas flow and a heating rate of 5 K min^{-1} up to 773 K.

XRD

Measurement was performed on a Siemens D5000 with Bragg-Brentano configuration within 2θ of 5 – 70°, 0.02° step size and 2 seconds counting, respectively. Results were analyzed using the International Centre for Diffraction Data library.

Se(IV) Dimerization

NMR spectroscopy

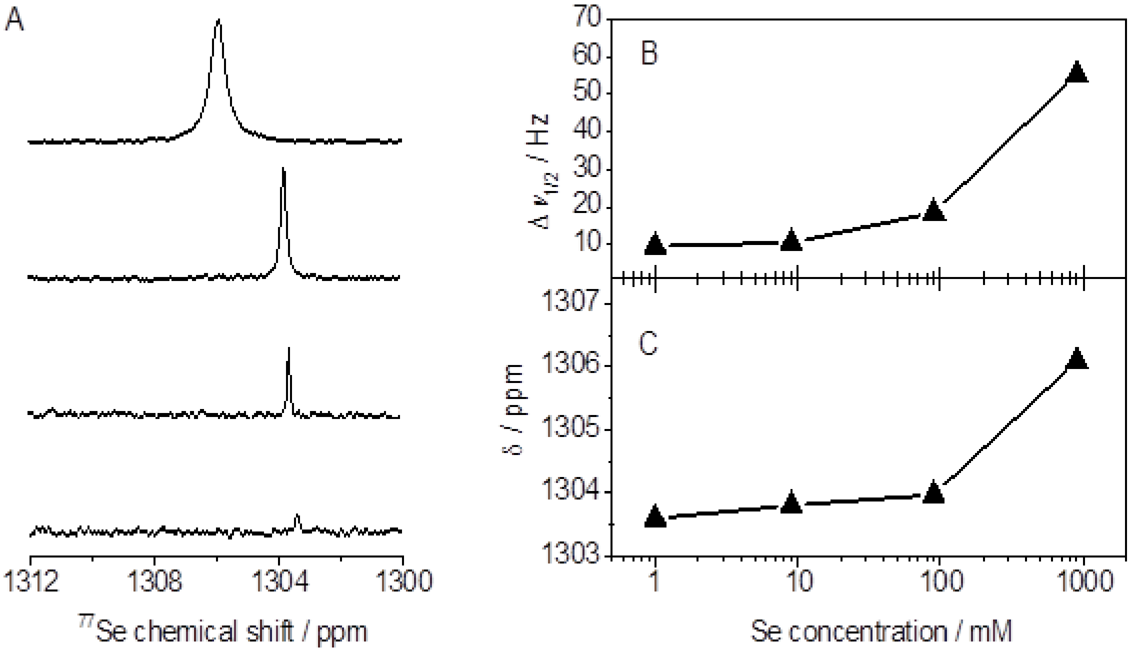

Fig. A.1 . ^{77}Se NMR spectra (recorded at B_0 = 9.4 T) of Se(IV) at pHc 5 (A) with concentrations from 1 mmol L^{-1} through 1 mol L^{-1} together with their graphical evaluation showing the dependence of selenium concentration on line width (B) and chemical shift (C).

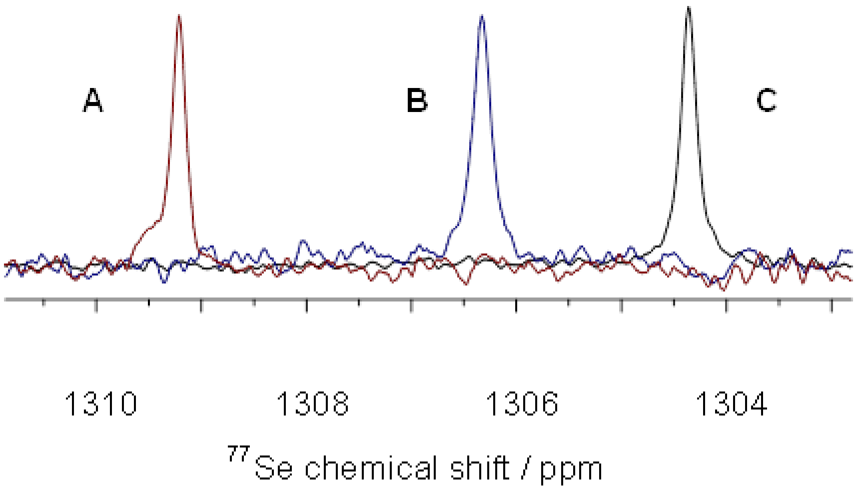

Fig. A.2 Superposition of ^{77}Se-NMR spectra of 0.1 mol L^{-1} Se(IV) samples at pH$_c$ 5 with variable ionic strengths (NaCl): (A) 5.6 mol L^{-1}, (B) 3.0 mol L^{-1}, and (C) 0.3 mol L^{-1}.

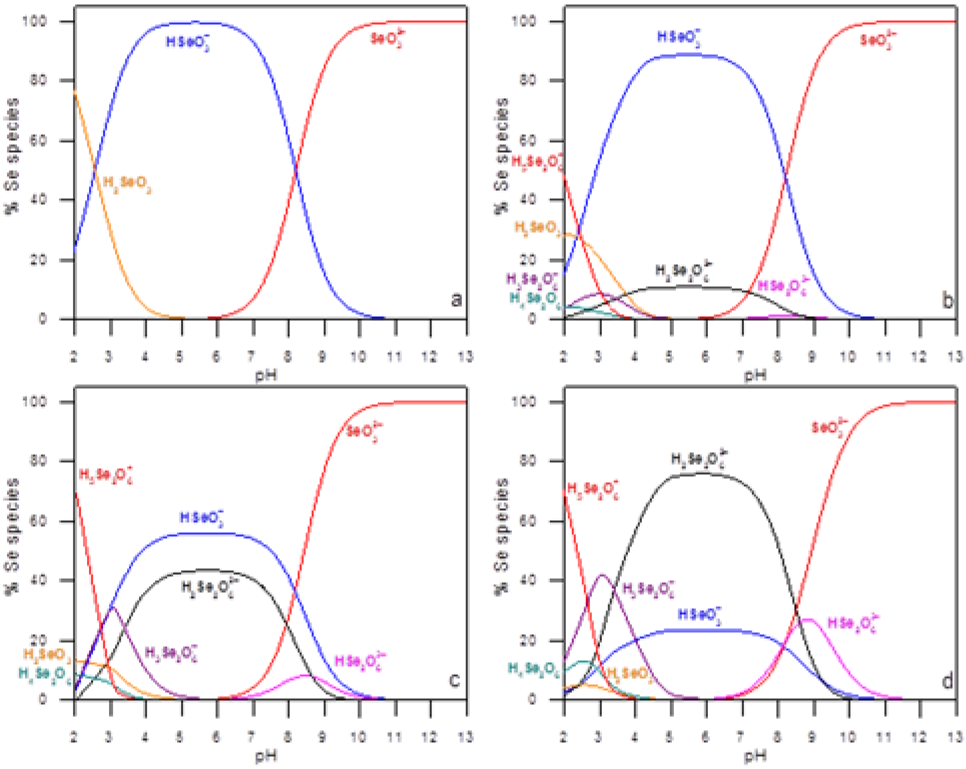

Fig. A.3 Se(IV) speciation diagrams (I = 0.3 mol L^{-1}) without considering dimerization (a) at total Se concentration of 0.1 mol L^{-1} (0.1 mol L^{-1} NaCl); considering dimerization at total Se concentrations of 1 mmol L^{-1} (0.3 mol L^{-1} NaCl) (b), of 10 mmol L^{-1} (0.3 mol L^{-1} NaCl) (c) and 0.1 mol L^{-1} (0.1 mol L^{-1} NaCl) (d).

Note that an increase of ionic strength from 0.32 – 0.57 mol L^{-1} for pH 8 – 13 (a), from 0.35 – 0.44 mol L^{-1} for pH 12.5 – 13 (b), from 0.37 – 0.46 mol L^{-1} for pH 12.5 – 13 (c) and from 0.33 – 0.58 mol L^{-1} for pH 8 – 13 (d) is predicted.

Tab. A.1 Stability constants used for speciation calculations using PHREEQC [PARKHURST '99] (with log *K* corrected to *I* = 0).

Aqueous Species	**log *K***
$H^+ + SeO_3^{2-} \rightleftharpoons HSeO_3^-$	8.60
$2H^+ + SeO_3^{2-} \rightleftharpoons H_2SeO_3$	11.33
$H^+ + 2\ SeO_3^{2-} \rightleftharpoons HSe_2O_6^{3-}$ ($\equiv H(SeO_3)_2^{3-}$)	9.55
$2\ H^+ + 2\ SeO_3^{2-} \rightleftharpoons H_2Se_2O_6^{2-}$ ($\equiv H_2(SeO_3)_2^{2-}$)	18.77
$3\ H^+ + 2\ SeO_3^{2-} \rightleftharpoons H_3Se_2O_6^-$ ($\equiv H_3(SeO_3)_2^-$)	22.57
$4\ H^+ + 2\ SeO_3^{2-} \rightleftharpoons H_4Se_2O_6$ ($\equiv H_4(SeO_3)_2$)	25.02
$5\ H^+ + 2\ SeO_3^{2-} \rightleftharpoons H_5Se_2O_6^+$ ($\equiv H_5(SeO_3)_2^+$)	27.80

log K values taken from [TORRES '10].

Impact of elevated temperature

IR spectroscopy

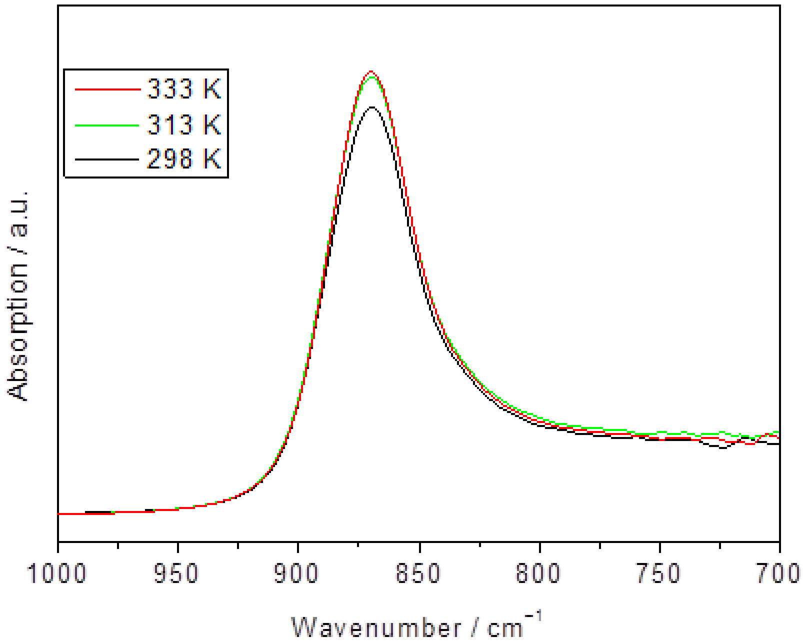

Fig. A.4 FT-IR spectra of 0.1 mol L^{-1} Se(VI) at pH 7.5 at variable temperatures.

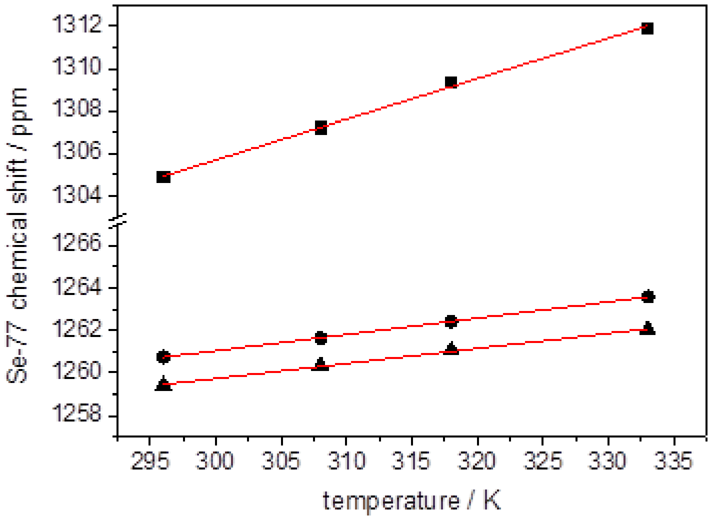

Fig. A.5 Temperature dependency of Se(IV) chemical shifts (data points) including linear fitting (lines), at pH 4 (■), pH 10 (●) and pH 13 (▲).

Tab. A.2 Temperature-induced shifts of Se(IV) obtained from linear fitting.

pH	**δT^{-1}, ppm K^{-1}**	**R²**
4	0.191 ± 0.006	0.9967
10	0.077 ± 0.001	0.9996
13	0.071 ± 0.002	0.9973

Ca^{2+}/Mg^{2+} Complexation

IR spectroscopy

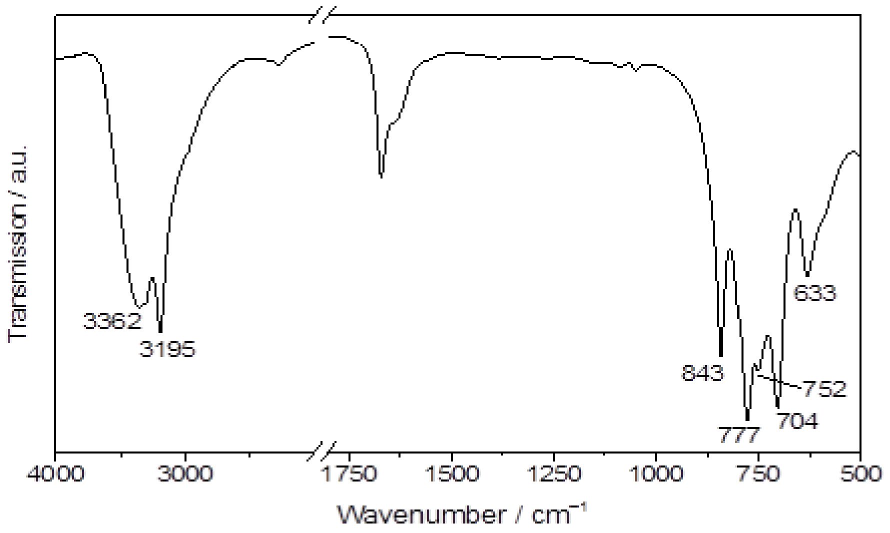

Fig. A.6 FT-IR spectrum (KBr pellet) of the Se(IV)–calcium precipitate.

DTA/TG analysis

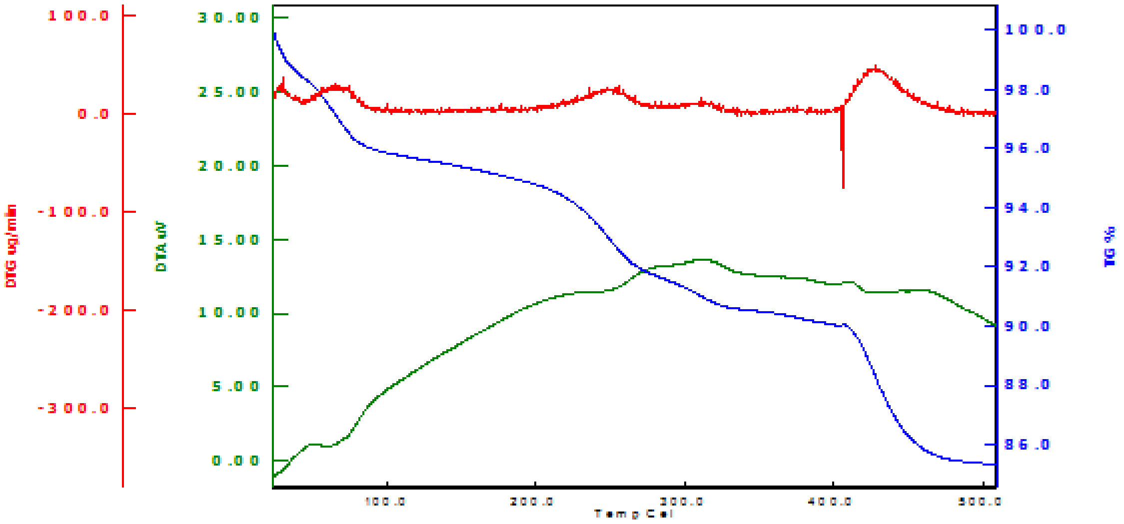

Fig. A.7 Thermogravimetric analysis of the precipitate obtained by the reaction of Se(IV) at pH_c 5 with Ca^{2+}.

XRD

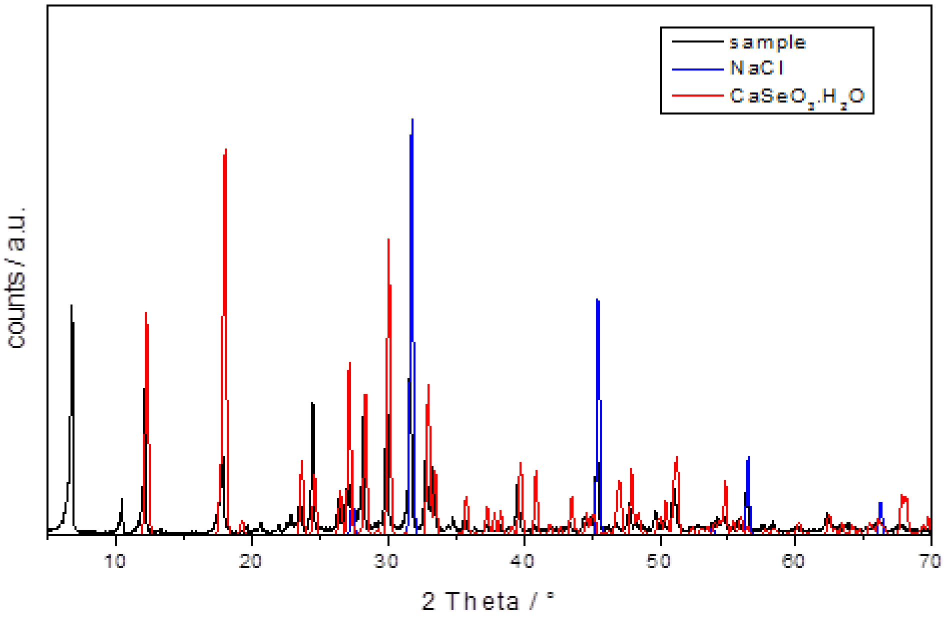

Fig. A.8 Powder diffractogram of the precipitate obtained by the reaction of Se(IV) pH_c 5 with Ca^{2+} matching the ICDD 01-077-1456 reference card.

A.2 Mineral phases characterization

Specific surface area

The specific surface area was determined by using a Multi-point Beckman Coulter surface analyzer (SA 3100) by applying the Brunauer–Emmett–Teller (BET) equation with nitrogen adsorption isotherms at 77 K.

Chemical analysis

The potential presence of impurities in studied minerals was checked by inductively coupled plasma-mass spectrometry (ICP-MS) (ELAN 9000 Perkin Elmer) after digestion with a mixture of concentrated HNO_3, HCl, HF and H_3BO_3.

For maghemite, both total iron and iron(II) concentration in our commercial powder was determined by dissolution of maghemite into concentrated HCl (30 %) and concentrated HNO_3 (65 %). The iron(II) concentration was determined by UV-VIS spectrophotometry at a wavelength λ = 511 nm by the 1,10-phenanthroline method.

X-ray Diffraction (XRD)

The samples were characterized by XRD on a D8 Bruker-AXS diffractometer using Cu Kα radiation (λ=1.5406 Å), operating in diffraction mode at 40 kV and 40 mA and equipped with a graphite secondary monochromator. Samples were step-scanned in the 2θ range of 10 – 90° in steps of 0.05° (15 s or 35 per step). Samples were loaded onto Si slide XRD holder and compressed lightly by a glass plate in order to obtain a smooth surface. The XRD pattern was compared with ICDD (International Center of Diffraction Data) for a qualitative characterization, using the EVA–Code (Bruker-AXS).

A potential mineral phase transformation up to 333 K of our commercial samples (e. g. anatase to rutile or δ-Al_2O_3 to Al(O,OH)x was checked by XRD. Anatase (7 days), hematite (2 days at pH 3.5 and 11) and δ-Al_2O_3 (7 days and pH values from 4 to 12) suspensions were shaken in a thermostatically controlled head-over-head shaker (Boekel Big SHOT III™ Hybridization Oven) under constant flow of nitrogen at 333 K. The temperature was kept constant with an accuracy of ± 1 K. A solid–liquid separation was performed by centrifugation at regulated temperature (Sigma 3-30KH centrifuge). Afterwards, the samples were freeze-dried and subsequently analyzed by XRD.

Transmission Electron Microscopy (TEM)

To study the primary particle size as well as the morphology of our commercial samples, transmission electron microscopy (TEM) investigations were performed using an image-corrected Titan 80-300 microscope (FEI) operated at an accelerating voltage of 300 kV. For sample preparation, one droplet of nanoparticles suspended in water was deposited onto a 400 mesh Cu grid coated with a carbon support film. After drying in a desiccator at room temperature and covering with an additional carbon-coated Cu grid, the specimen was placed into a double-tilt analytical holder to perform high-resolution TEM (HRTEM) analyses. All TEM measurements were done at room temperature.

Mössbauer spectroscopy

Room temperature ^{57}Fe Mössbauer spectroscopy was performed in transmission geometry using a standard spectrometer in constant acceleration mode with a ^{57}Co source in Rh matrix. All isomer shifts are given in reference to α-Fe. The transmitted γ-radiation was detected by a proportional counter. The quantitative evaluation of the Mössbauer spectra was performed with the NORMOS program based on least-squares statistics assuming Lorentzian lines [BRAND '87].

X-ray Photoelectron Spectroscopy (XPS)

Maghemite was analyzed by XPS at room temperature. XPS analysis was carried out by a XP spectrometer (PHI model 5600ci) equipped with a monochromatized Al Kα source operating at 100 W source power. The spectrometer is equipped with a hemispherical capacitor analyzer (mean diameter 279.4 mm), and the detector consists of a microchannel detector with 16 anodes.

Calibration of the binding energy scale of the spectrometer was performed using well-established binding energies of elemental lines of pure metals (monochromatic Al Kα: Cu $2p_{3/2}$ at 932.62 eV, Au $4f_{7/2}$ at 83.96 eV) [SEAH '98]. Standard deviations of binding energies of conducting and isolating samples were within ± 0.1 eV and ± 0.2 eV, respectively. Maghemite powder was deposited onto an indium foil and mounted on a stainless steel sample holder. Spectra were collected by monochromatic Al Kα X-ray excitation from an analysis area of 0.8 mm in diameter at a take-off angle of 45° (angle between sample surface and analyzer) and the pressure inside the spectrometer was about 2×10^{-7} Pa. To retrieve information about the chemical state of iron, narrow scan spectra of elemental lines were recorded at 11.75 eV pass energy of the analyzer. An electron flood gun was applied for charge compensation of the sample surface during measurement. The spectra of maghemite powder were charge referenced to the O 1s elemental line at 530.0 eV. The commonly used charge referencing to the C 1s elemental line of adventitious hydrocarbon was not applied here since the C 1s spectra was noisy at low intensity. Spectra were studied using PHI MultiPak Version 9.4 (data analysis program). Oxidation states were identified by comparison with binding energies reported in the literature.

Electrophoretic mobility

The effect of pH, temperature and selenium(VI) or selenium(IV) uptake on the zeta potential (ZP) and isoelectric point of studied minerals was evaluated using a Laser-Doppler-Electrophoresis instrument (nano-ZS, Malvern Instruments Ltd.). Solids were suspended in polypropylene tubes in the presence of NaCl as background electrolyte to get the appropriate solid-to-solution ratio. Selenium(VI) or selenium(IV) was then added into the suspensions to reach the desired concentrations and the pH was adjusted to the desired values using either HCl or NaOH. Suspensions were prepared either at room temperature or at elevated temperature in a glove box (O_2 < 5 ppm or O_2<20 ppm) under anoxic conditions and were equilibrated in a head-over-head shaker. In some cases, samples were prepared under atmospheric conditions. If that, it was previously checked that the zeta potential and isoelectric point were not significantly impacted by atmospheric CO_2. The pH of each suspension was checked daily and readjusted if necessary just before electrophoresis measurements or simply measured at the end of the equilibration period. Each sample was ultrasonicated with an ultrasonic finger (Sonopulse HD 2200, Bandelin) for 15 seconds prior to measurements. An aliquot of approximately 1 mL of the ultrasonicated suspensions was transferred into a rectangular capillary cell made of polycarbonate with gold plated copper beryllium electrodes. A voltage of 50 V was applied across them. In some cases, suspensions were transferred to the measuring cell under atmospheric conditions. If so, tests measurements evidenced no significant differences with measurements in which cells were filled inside the glovebox. After 2 min of equilibration, the electrophoretic mobility of the suspensions was measured at room temperature or elevated temperature. Between each sample, the cell was flushed using an excess of de-ionized water. The conversion of the measured velocity of the particles in the electric field to zeta potential was done using the Smoluchowski equation. Calculation of zeta potential was done with Zetasizer 6.01 software. Obtained values were averaged over at least ten measurements, allowing the calculation of statistical parameters. In the figures presented in this report, the error bars represent the standard deviation of the obtained values at a given pH, temperature and background electrolyte concentration. Detailed information for ZP measurements is given in **Tab. A.3**.

Tab. A.3 Experimental conditions for ZP measurements of minerals neat surfaces.

Solid	**Temperature (K)**	**I (NaCl) (mol L^{-1})**	**Samples prepared under N_2(g)**	**ZP cell filled under N_2(g)**
Anatase	[1]RT	0.01	Yes	Yes
	298	0.1	No	No
	333	0.1	No	No
α-Fe_2O_3	[1]RT	[2]0.1	Yes	Yes
	[1]RT	[3]0.1		
	303	[3]0.1		
	333	[3]0.1		
γ-Fe_2O_3	[1]RT	[2]0.1	Yes	pH 7.0 – 8.5
	[1]RT	[3]0.1		pH 7.0 – 8.5
[4]δ-Al_2O_3	RT	0.01	No	No
	RT	0.1	No	No
	RT	0.5	No	No
	RT	1	No	No
	333	0.1	No	No
Fe_3O_4	RT	0.1	Yes	Yes
Kaolinite	[1]RT	0.1	No	No

[1] RT: Room temperature

[2] m/v = 0.25 g L^{-1}

[3] m/v = 0.75 g L^{-1}: [4] m/v = 0.2 g L^{-1}

Solubility of minerals at room and elevated temperature

The solubility of anatase was checked from suspensions (m/v = 0.5 g L^{-1}) equilibrated during 7 days at 298 K and at 333 K. For hematite, suspensions (0.75 g L^{-1}) were equilibrated 2 days at room temperature and at 333 K. For δ-Al_2O_3 suspensions were equilibrated for 5 days at RT and 333 K. The amount of released Ti, Fe, and Al in the solution (0.1 mol L^{-1} NaCl) was determined by ICP-MS after centrifugation at the appropriate temperature.

Synthesis of magnetite

The complete synthesis was conducted under N_2-atmosphere (O_2 < 5 ppm). For the synthesis, a mixture of 3.9 g $FeCl_2$ * 4 H_2O (Merck) and 19.8 g $FeCl_3$ * 6 H_2O (Sigma Aldrich) was filled up to 50 mL with CO_2-free MilliQ water. This solution was stirred for one hour. Afterwards, 60 mL 6 mol L^{-1} NH_4OH solution was added dropwise, inducing the precipitation of magnetite. This magnetite suspension was stirred overnight. The suspension was then washed several times with 0.025 mol L^{-1} $CaCl_2$ solution and with 0.01 mol L^{-1} NaCl solution with centrifugation (6000 g, 15 min) between every washing step.

A.3 Sorption of Se(VI) and Se(IV) onto mineral phases

Batch Sorption experiments

All sorption experiments were performed in a glove box under anoxic conditions ($O_2 < 5$ or 20 ppm). For each batch sample, the mineral was suspended in 40 mL of background electrolyte in 50 mL polypropylene tubes. Aliquots of 0.1 mol L^{-1} selenium(VI) and selenium(IV) stock solution were added to obtain the target concentration. The pH of the suspensions was adjusted by the addition of either HCl or NaOH. After equilibration, samples were centrifuged and the remaining selenium concentration in the supernatant was determined by ICP-MS. The difference to the initial selenium content provided the amount of sorbed selenium. All the experiments were carried out in duplicate. Results presented in section 4 are either average of duplicate experiments or single points. Sorption of selenium(VI) and selenium(IV) onto vials was found to be negligible.

The reaction solutes were not filtered after the centrifugation. However, some measurements of the intensity of laser light scattered by particles were performed (BI-90 particle sizer (Brookhaven Instruments), laser power: 400 mW, wavelength: 514.5 nm, angle of detection: 90°). A low amount of particles was detected in the supernatants after centrifugation at 6,800 × g, but no particles were found after ultracentrifugation at 285,000 × g. Since no significant difference on the amount of sorbed selenium was observed after centrifugation and ultracentrifugation, the mineral particles left in the supernatant after centrifugation were so marginal that they did not impact sorption results in a significant way.

To avoid an activation of anatase photocatalytic properties [HANAOR '11] during selenium(VI) and selenium(IV) sorption, all tubes were wrapped in aluminum foil.

Time-dependent sorption experiments

Different mineral suspensions with the same conditions (m/v, pH and $[Se]_{initial}$) were prepared at room temperature in NaCl 0.1 mol L^{-1} (**Tab. A.4**). To determine the time needed to reach the sorption equilibrium, experiments with increasing oxide-solution contact times were carried out. The pH of the suspensions was adjusted to 4.0 throughout these experiments. pH measurements (pH-meter Inolab WTW series pH720) were performed using a combination glass electrode (BlueLine 16 pH from

Schott Instruments) in which an Ag/AgCl reference electrode was incorporated, to an accuracy of ± 0.05.

Tab. A.4 Experimental conditions for time-dependent batch experiments.

Solid	**m/v (g L^{-1})**	**$[Se^{IV}]_{initial}$ (µmol L^{-1})**	**$[Se^{VI}]_{initial}$ (µmol L^{-1})**	**[1]Centrifugation**
Anatase	0.75	50	0	2 hours @ 14,972 g
α-Fe_2O_3	0.75	0	10	1.5 hours @ 6,800 g
	0.25	50	0	
γ-Fe_2O_3	1.0	0	10	2 hours @ 6,800 × g
	0.25	50	0	

[1] Avanti J-20 XP Beckman Coulter centrifuge

Electrodes were freshly calibrated using NIST-traceable buffer solutions (pH 1.68/pH 4.01/pH 6.87/pH 9.18 from WTW), to an accuracy of ± 0.05. During pH measurements, the solutions were stirred and pH value was taken when being stable for 10 minutes.

pH- and moderate ionic strength-dependent sorption experiments

Sorption of selenium(VI) and selenium(IV) onto minerals was studied from pH 3.5 up to pH 11 at room temperature. The impact of the ionic strength was also investigated, by using a background electrolyte concentration of 0.01 mol L^{-1} and 0.1 mol L^{-1} of NaCl. pH measurements were performed identically to time-dependence sorption experiments. Detailed conditions are summarized in **Tab. A.5**.

Tab. A.5 Experimental conditions for pH and moderate ionic strength-dependent batch experiments.

Solid	**m/v ($g\ L^{-1}$)**	**$[Se^{IV}]_{initial}$ ($\mu mol\ L^{-1}$)**	**$[Se^{VI}]_{initial}$ ($\mu mol\ L^{-1}$)**	**Centrifugation**
Anatase	0.50	0	10	[1]2 hours @ 6,800 × g
	0.75	50	0	[2]2 hours @ 14,972 g
α-Fe_2O_3	0.75	0	10	[1]1.5 hours @ 6,800 g
	0.25	50	0	
γ-Fe_2O_3	1.0	0	10	[1]2 hours @ 6,800 × g
	0.25	50	0	
	1.0	0	20	[1]2 hours @ 6,800 × g
□-Al_2O_3	0.5	10	0	
Kaolinite	30	0	10	1 hour @ 6,076 × g
	30	10	0	

[1] Avanti J-20 XP Beckman Coulter centrifuge

[2] Sigma 3-30KH centrifuge

pH- and high ionic strength-dependent sorption experiments

The impact of high ionic strength at different background electrolytes (NaCl and $MgCl_2$) was studied (Tab. A.6). Combination pH electrodes (WTW SenTix® Mic) were used for samples at high ionic strength (> 0.5 mol kg^{-1}). The molar H^+ concentrations (pH_c = −log c_{H^+}) in the solutions at high ionic strength were determined as described in detail by [ALTMAIER '03; ALTMAIER '08]. Electrodes were freshly calibrated using NIST-traceable buffer solutions (pH 1.68/pH 4.01/pH 6.87/pH 9.18 from WTW), to an accuracy of ± 0.05. During pH measurements, the solutions were stirred and pH value was taken when being stable for 10 minutes.

Tab. A.6 Experimental conditions for high ionic strength-dependent batch experiments.

Solid	**m/v ($g\ L^{-1}$)**	**$[Se^{IV}]_{initial}$ ($\mu mol\ L^{-1}$)**	**$[Se^{VI}]_{initial}$ ($\mu mol\ L^{-1}$)**	**I ($mol\ L^{-1}$)**	**Centrifugation**
	0.5	10	0	0.01-1 M NaCl	[1]2 hours @ 6,800 × g
δ-Al_2O_3	1	0	20	0.01-1 M NaCl	[1]2 hours @ 6,800 × g
	1	0	20	0.01-0.5 M $MgCl_2$	[1]2 hours @ 6,800 × g

Sorption experiments at elevated temperature

The impact of pH on the sorption of Se(VI) and Se(IV) onto anatase, hematite and alumina was studied at elevated temperatures (**Tab. A.7**). The solutions were equilibrated in a thermostatically controlled head-over-head shaker (Boekel Big SHOT III™ Hybridization Oven). The pH measurements (pH-meter Inolab WTW series pH720) were performed using a combination glass electrode (BlueLine 16 pH, Schott Instruments), in which an Ag/AgCl reference electrode was incorporated, to an accuracy of ± 0.05. Electrodes were calibrated using three NIST-traceable buffer solutions (pH 1.679/1.694/1.723, pH 4.006/4.031/4.087, and pH 6.865/6.838/6.836; each value given for 298/313/333 K from WTW) at the corresponding temperatures. During pH calibration and measurements, the buffers and solutions were placed on a HLC ThermoMixer (MKR 23 BlockThermostate) and kept constant at the desired temperature, with an accuracy of ± 1K. The pH value was taken after being stable for 2 min. To minimize water evaporation, pH adjustment was performed during the equilibration and checked at the end of the sorption stage. The solid–liquid separation was performed by centrifugation at regulated temperature (Sigma 3-30KH centrifuge).

Tab. A.7 Experimental conditions for batch sorption experiments performed at different pH, ionic strength, background electrolyte media and temperature.

Solid	**[Se^{IV}]$_{initial}$ (µmol L^{-1})**	**[Se^{VI}]$_{initial}$ (µmol L^{-1})**	**I (M)**	**Temperature (K)**	**Centrifugation**
Anatase	0	10	0.1 (NaCl)	298	2hours @ 12,000 g
	0	10		313	
	0	10		333	
	10	0		303	2 hours @ 9,500 g
	10	0		318	
	10	0		333	
α-Fe$_2$O$_3$	0	10	0.1 (NaCl)	304	2 hours @ 9,500 g
	0	10		318	
	0	10		333	
	50	0		303	2 hours @ 9,500 g
	50	0		333	
□-Al$_2$O$_3$	0	100	0.1	298	2 hours @ 9,500 g
	0	100	0.1	333	2 hours @ 9,500 g
	10	0	0.1	298	2 hours @ 9,500 g
	10	0	0.1	333	2 hours @ 9,500 g

Estimation of uncertainties in batch sorption experiments

Uncertainties on the amount of sorbed Se (%) and the K$_d$ was calculated as follows:

$$\% \, Se_{ads} = \frac{Se_{initial} - Se_{solution}}{Se_{initial}} \times 100$$

$$\frac{\Delta \, \% \, Se_{ads}}{\% \, Se_{ads}} = \frac{Se_{solution} \, x \, \Delta Se_{initial} + Se_{initial} \, x \, \Delta Se_{solution}}{Se_{initial}(Se_{sorbed})}$$

$$K_d = \frac{Se_{sorbed}}{Se_{solution}} \times \frac{V}{m}$$

$$\frac{\Delta Kd}{Kd} = \frac{\Delta Se_{initial}(Se_{solution}) + (Se_{initial})\Delta Se_{solution}}{(Se_{sorbed})(Se_{solution})} + \frac{\Delta V}{V} + \frac{\Delta m}{m}$$

by using the following estimations:

$[Se]_{initial}$ = 3950 µg L^{-1} (5×10^{-5} M), $\Delta Se_{initial}$ = 200 µg L^{-1}

$[Se]_{initial}$ = 790 µg L^{-1} (10^{-5} M), $\Delta Se_{initial}$ = 40 µg L^{-1}

$[Se]_{solution}$ < 200 µg L^{-1}, $\frac{\Delta \% Se_{solution}}{\% Se_{solution}}$ = 10 %

$[Se]_{solution}$ > 200 µg L^{-1}, $\frac{\Delta \% Se_{solution}}{\% Se_{solution}}$ = 6 %

When Δ $\%Se_{ads}$ exceeded 6 % (that is the observed reproducibility of batch experiments) or was lower than 0.1 %, a correction factor was systematically applied.

Verification of the Se oxidation state in the aqueous phase

To check if the oxidation state of the aqueous selenium(VI) and selenium(IV) species were not impacted during our sorption experiments, selenium concentration was also determined using a continuous flow hydride generator (Perkin Elmer FIAS 200) attached to atomic absorption spectrometer (Perkin Elmer 4100). This HG-AAS technique involves the formation of selenium hydride (H_2Se). Hydride vapor is generated by reacting a mixture of 0.2 % (v/v) sodium borohydride solution and 3 % (v/v) HCl with the sample. A wavelength of 196.0 nm with a band pass of 0.5 nm, a lamp current of 65 % and a carrier gas flow rate of 0.15 L min^{-1} were used. HG-AAS is only able to measure the (+IV) oxidation state of selenium. Consequently, samples analyzed without chemical pretreatment and containing only selenium(IV) in the aqueous phase should give concentrations identical to those measured by ICP-MS. However, samples analyzed without chemical pretreatment and containing only selenium(VI) in the aqueous phase should give concentrations less than the detection limit of this technique (< 1 µg L^{-1}).

Impact of sorption on the pH_{IEP} of minerals

The zeta potential of selenium(VI) and selenium(IV) reacted-anatase, -hematite, -maghemite and –alumina was studied as indicated in **Tab. A.8**.

Tab. A.8 Experimental conditions for ZP measurements of Se-reacted mineral surfaces.

Solid	**$[Se^{IV}]_{initial}$ (µmol L^{-1})**	**$[Se^{VI}]_{initial}$ (µmol L^{-1})**	**I (NaCl) (mol L^{-1})**	**Samples prepared under N_2(g)**	**ZP cell filled under N_2(g)**
Anatase	0	500	0.01	Yes	Yes
	100	0	0.1		
α-Fe_2O_3	0	500	0.1	Yes	Yes
	50	0			
γ-Fe_2O_3	0	500	0.1	Yes	pH 7.0 – 8.5
	50	0			No
δ-Al_2O_3	0	1000	0.1	Yes	Yes
	500	0	0.1		

Impact of temperature

Tab. A.9 Estimated values of Δ_RG, Δ_RH, Δ_RS and R^2 (correlation coefficient of the van't Hoff plot) for the adsorption of selenium(VI) onto hematite at different pH and temperatures.

pH 4.5				
T (K)	**Δ_RG (kJ mol^{-1})**	**Δ_RH (kJ mol^{-1})**	**Δ_RS (J mol^{-1} K^{-1})**	**R^2**
304	−3.1 ± 0.1	−11.8 ± 0.2	−28.5 ± 0.7	0.999
318	−2.7 ± 0.1			
333	−2.3 ± 0.1			
pH 5.1				
T (K)	**Δ_RG (kJ mol^{-1})**	**Δ_RH (kJ mol^{-1})**	**Δ_RS (J mol^{-1} K^{-1})**	**R^2**
304	−1.4 ± 0.1	−15.7 ± 1.0	−46.9 ± 3.0	0.996
318	−0.8 ± 0.1			
333	−0.1 ± 0.1			
pH 6.1				
T (K)	**Δ_RG (kJ mol^{-1})**	**Δ_RH (kJ mol^{-1})**	**Δ_RS (J mol^{-1} K^{-1})**	**R^2**
304	1.1 ± 0.1	−50.1 ± 0.2	−168.1 ± 5.0	0.999
318	3.4 ± 0.1			
333	5.9 ± 0.1			

Tab. A.10 Estimated values of $\Delta_R G$, $\Delta_R H$, $\Delta_R S$ and R^2 (correlation coefficient of the van't Hoff plot) for the adsorption of selenium(IV) onto anatase at different pH and temperatures.

<table>
<tr><th colspan="5">pH 5.8 ± 0.1</th></tr>
<tr><th>T (K)</th><th>$\Delta_R G$ (kJ mol^{-1})</th><th>$\Delta_R H$ (kJ mol^{-1})</th><th>$\Delta_R S$ (J mol^{-1} K^{-1})</th><th>R^2</th></tr>
<tr><td>303</td><td>−12.3 ± 0.3</td><td rowspan="3">−38.5 ± 5.3</td><td rowspan="3">−86.6 ± 16.6</td><td rowspan="3">0.982</td></tr>
<tr><td>318</td><td>−11.0 ± 0.1</td></tr>
<tr><td>333</td><td>−9.7 ± 0.3</td></tr>
<tr><th colspan="5">pH 6.9 ± 0.1</th></tr>
<tr><th>T (K)</th><th>$\Delta_R G$ (kJ mol^{-1})</th><th>$\Delta_R H$ (kJ mol^{-1})</th><th>$\Delta_R S$ (J mol^{-1} K^{-1})</th><th>R^2</th></tr>
<tr><td>303</td><td>−10.0 ± 0.3</td><td rowspan="3">−45.4 ± 6.9</td><td rowspan="3">−117.1 ± 21.9</td><td rowspan="3">0.977</td></tr>
<tr><td>318</td><td>−8.2 ± 0.1</td></tr>
<tr><td>333</td><td>−6.4 ± 0.3</td></tr>
<tr><th colspan="5">pH 8.2 ± 0.1</th></tr>
<tr><th>T (K)</th><th>$\Delta_R G$ (kJ mol^{-1})</th><th>$\Delta_R H$ (kJ mol^{-1})</th><th>$\Delta_R S$ (J mol^{-1} K^{-1})</th><th>R^2</th></tr>
<tr><td>303</td><td>−6.4 ± 0.1</td><td rowspan="3">−81.5 ± 1.5</td><td rowspan="3">−247.6 ± 4.7</td><td rowspan="3">0.999</td></tr>
<tr><td>318</td><td>−2.7 ± 0.1</td></tr>
<tr><td>333</td><td>1.0 ± 0.1</td></tr>
<tr><th colspan="5">pH 8.7 ± 0.1</th></tr>
<tr><th>T (K)</th><th>$\Delta_R G$ (kJ mol^{-1})</th><th>$\Delta_R H$ (kJ mol^{-1})</th><th>$\Delta_R S$ (J mol^{-1} K^{-1})</th><th>R^2</th></tr>
<tr><td>303</td><td>−3.9 ± 0.1</td><td rowspan="3">−61.7 ± 2.1</td><td rowspan="3">−190.6 ± 6.8</td><td rowspan="3">0.999</td></tr>
<tr><td>318</td><td>−1.1 ± 0.1</td></tr>
<tr><td>333</td><td>1.8 ± 0.1</td></tr>
</table>

A.4 Spectroscopic elucidation of Se(VI) and Se(IV) sorption processes

In situ ATR FT-IR measurements

The *in situ* ATR FT-IR experiments were carried out with a Bruker Vertex 70/v or Vertex 80/v spectrometer, equipped with a horizontal ATR diamond crystal accessory (SamplIR II, Smiths Inc., 9 reflections, angle of incidence: 45°) and a Mercury Cadmium Telluride (MCT) detector. The sample compartment was purged with dry air. Each IR spectrum recorded was averaged over 256 scans at a spectral resolution of 4 cm^{-1} using the OPUS™ software for data acquisition and evaluation. To minimize interferences between the strong absorption band of H_2O below 1000 cm^{-1} and the potential SeO_4^{2-} and SeO_3^{2-} bands arising from sorption (between 900 and 700 cm^{-1}), some studies were performed in D_2O All solutions were prepared and measured in N_2 atmosphere to prevent CO_2 dissolution and fast exchanges between hydrogen and deuterium (in presence of D_2O). The pH of the selenium stock solution, measured using electrodes calibrated with aqueous buffers, was adjusted with 0.1 mol L^{-1} NaOD and DCl. pD values were then calculated from pH values using the equation $pD = pH + 0.4$ [GLASOE '60]. The determination of the selenium sorption mechanisms onto anatase, hematite, maghemite and alumina was performed comparable to earlier spectroscopic sorption studies [JORDAN '11; MÜLLER '09].

Briefly, mineral was deposited directly on the center of the diamond crystal from a 2.5 g L^{-1} suspension, dried under a gentle N_2 flow. As a first step, for equilibration of the mineral film, it was rinsed with the background electrolyte for 45 minutes. Then, the blank electrolyte solution was replaced by the selenium(VI) or selenium(IV) solution (5×10^{-4} mol L^{-1}) for 2 hours, allowing the study of sorption processes. In the last stage (flushing step), the film was rinsed again with the blank solution during 45 minutes, to study the potential desorption of selenium(VI) or selenium(IV) from the mineral film. All steps were performed under continuous flow at flow rate of 200 µL min^{-1} provided by a peristaltic pump. Sorption induced difference spectroscopy was applied similarly to former studies and enables to investigate small spectra changes studies [JORDAN '11; MÜLLER '09].

FT-IR of sorbing phases

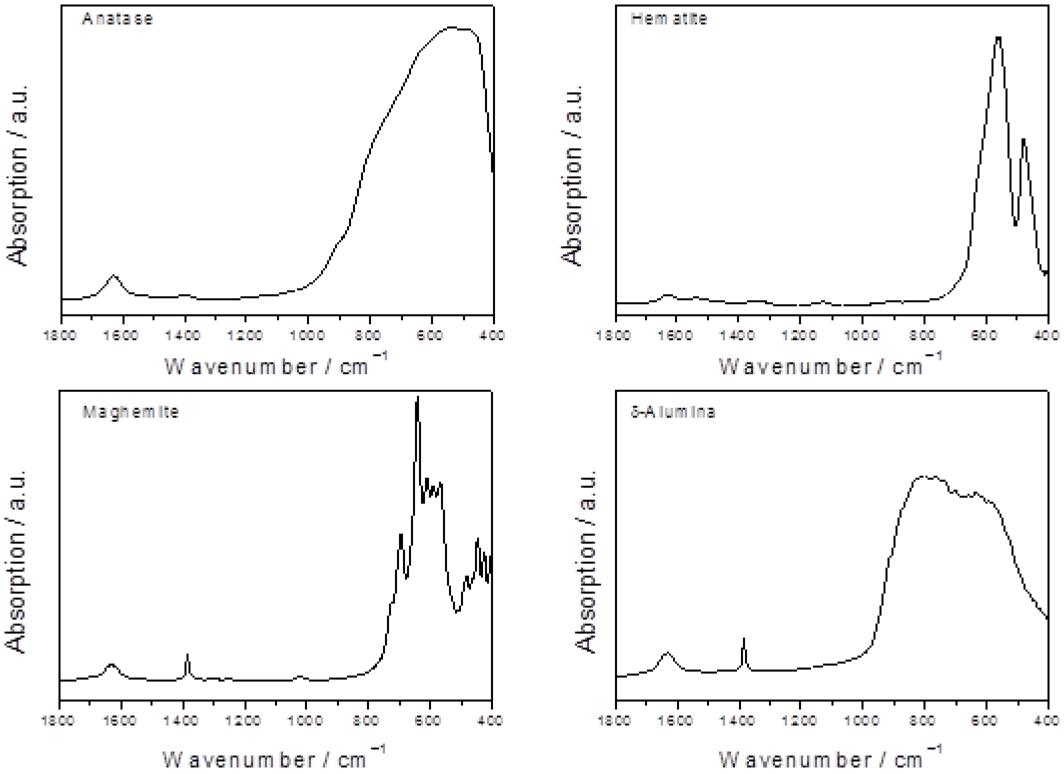

Fig. A.9 IR spectrum of anatase, hematite, maghemite and alumina measured in a KBr matrix.

Se(VI) sorption onto hematite

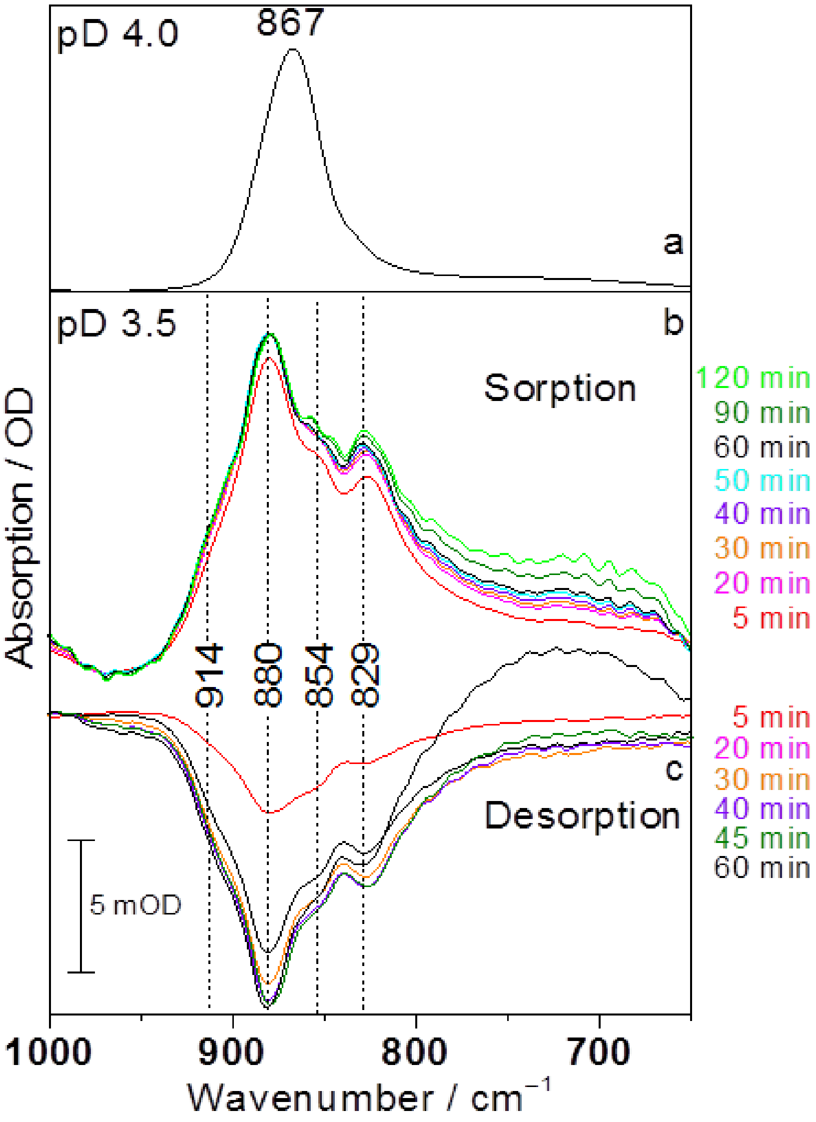

Fig. A.10 (a) IR spectrum of 0.1 mol L^{-1} selenium(VI) in aqueous solution at 0.1 mol L^{-1} NaCl in D_2O. (b) In situ IR spectra of selenium(VI) sorption complexes onto hematite ($[Se^{VI}]_{initial} = 5 \times 10^{-4}$ mol L^{-1}, D_2O, pD 3.5, 0.1 mol L^{-1} NaCl, N_2) recorded at different points of time after induced sorption. (c) In situ IR spectrum of released selenium(VI) sorption complex recorded at different points of time after subsequent flushing of the hematite phase with blank solu-tion (D_2O, pD 3.5, 0.1 mol L^{-1} NaCl, N_2).

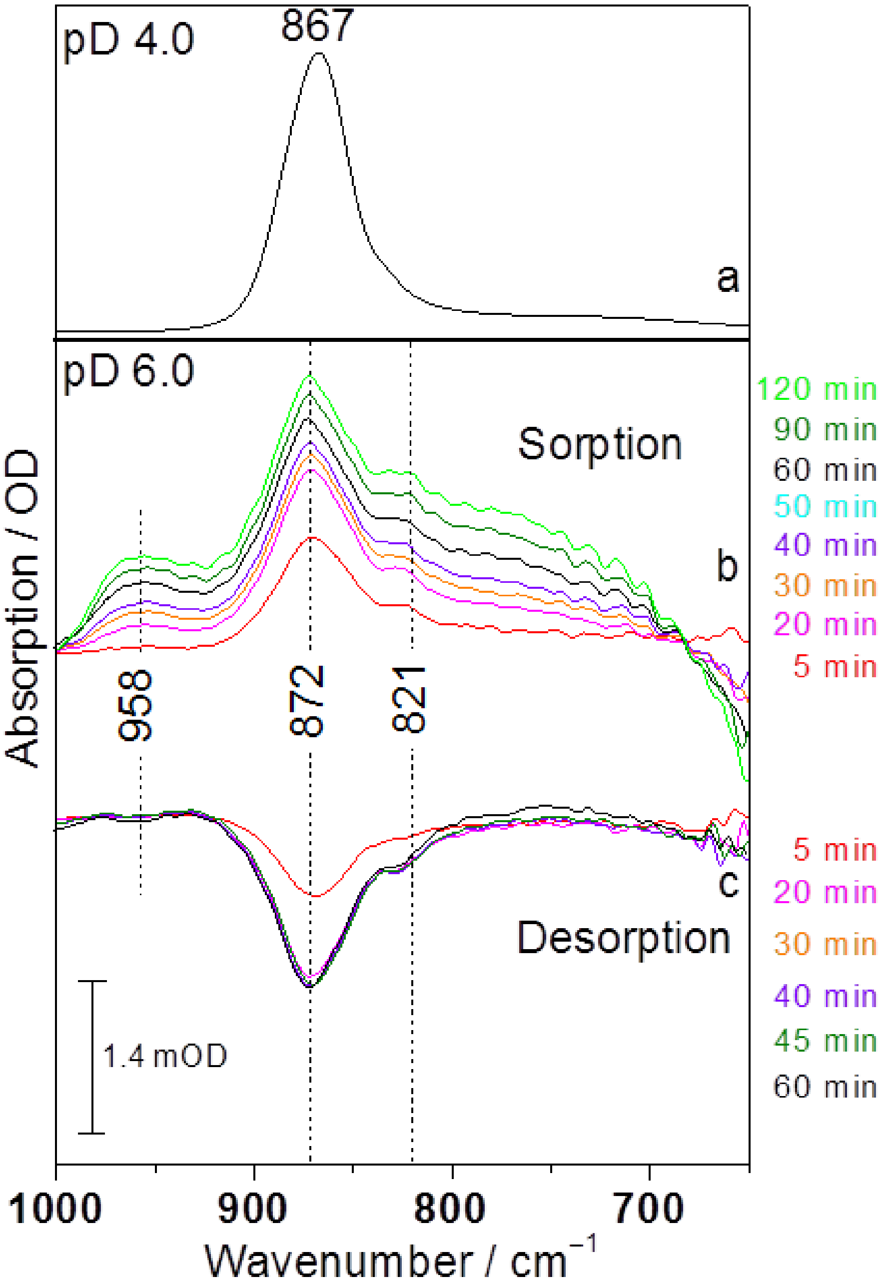

Fig. A.11 (a) IR spectrum of 0.1 M selenium(VI) in aqueous solution at 0.1 mol L^{-1} NaCl in D_2O. (b) In situ IR spectra of selenium(VI) sorption complexes onto hematite ($[Se^{VI}]_{initial} = 5 \times 10^{-4}$ mol L^{-1}, D_2O, pD 6.0, 0.1 mol L^{-1} NaCl, N_2) recorded at different points of time after induced sorption. (c) In situ IR spectrum of released selenium(VI) sorption complex recorded at different points of time after subsequent flushing of the hematite phase with blank solu-tion (D_2O, pD 6.0, 0.1 mol L^{-1} NaCl, N_2).

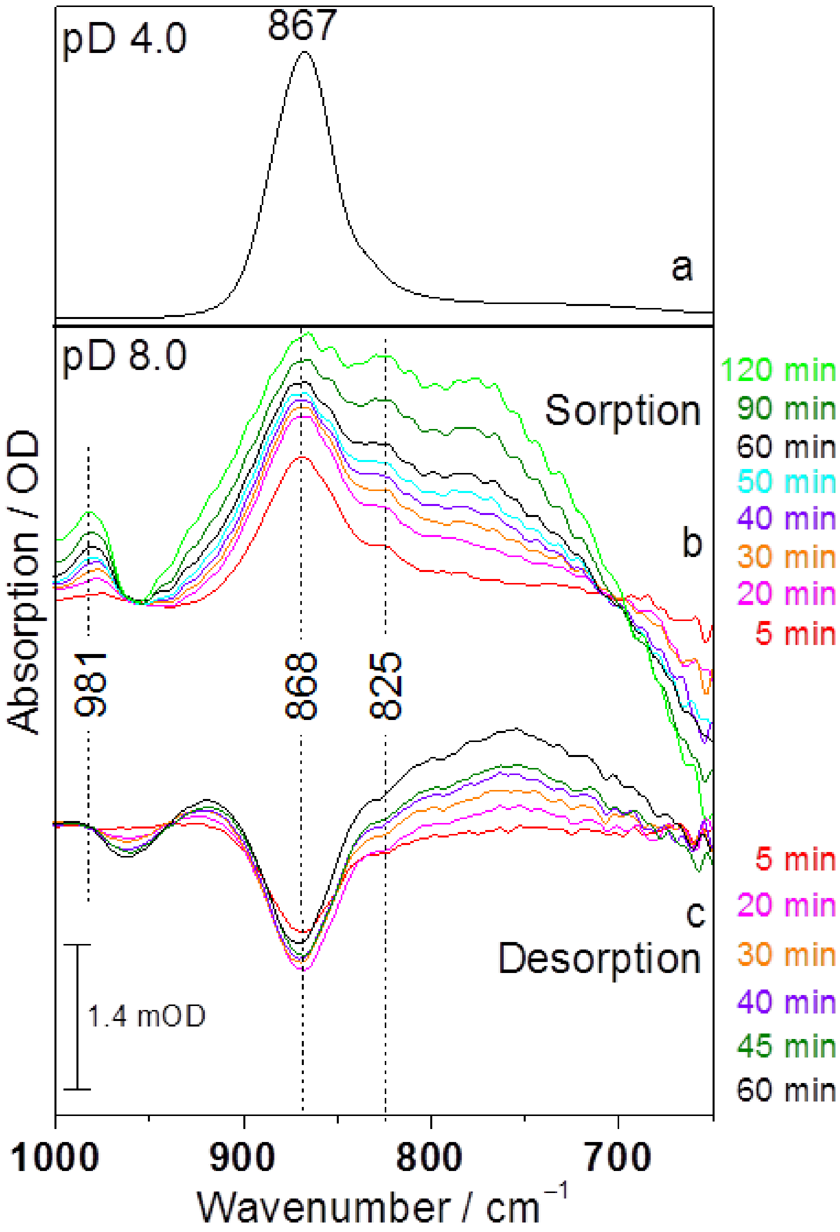

Fig. A.12 (a) IR spectrum of 0.1 M selenium(VI) in aqueous solution at 0.1 mol L^{-1} NaCl in D_2O. (b) In situ IR spectra of selenium(VI) sorption complexes onto hematite ($[Se^{VI}]_{initial} = 5 \times 10^{-4}$ mol L^{-1}, D_2O, pD 8.0, 0.1 mol L^{-1} NaCl, N_2) recorded at different points of time after induced sorption. (c) In situ IR spectrum of released selenium(VI) sorption complex recorded at different points of time after subsequent flushing of the hematite phase with blank solution (D_2O, pD 8.0, 0.1 mol L^{-1} NaCl, N_2).

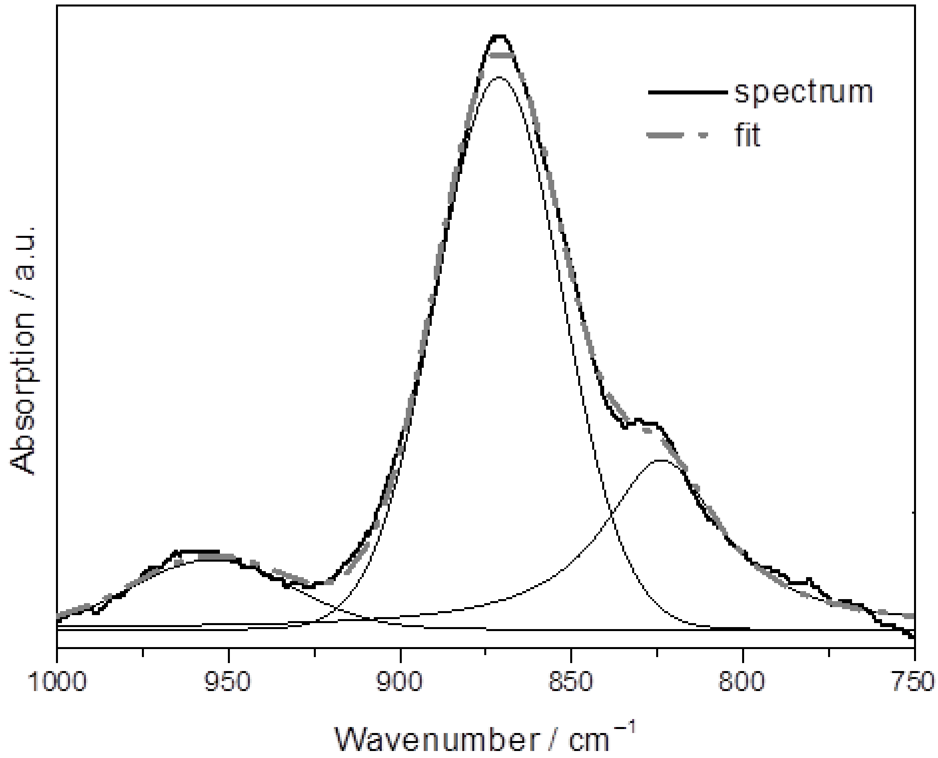

Fig. A.13 Deconvolution of the IR spectrum of selenium(VI) sorption onto hematite. ($[Se^{VI}]_{initial} = 5 \times 10^{-4}$ mol L^{-1}, D_2O, pD 6.0, 0.1 mol L^{-1} NaCl, 20 min of sorption, N_2). Dotted line indicates the overall fit.

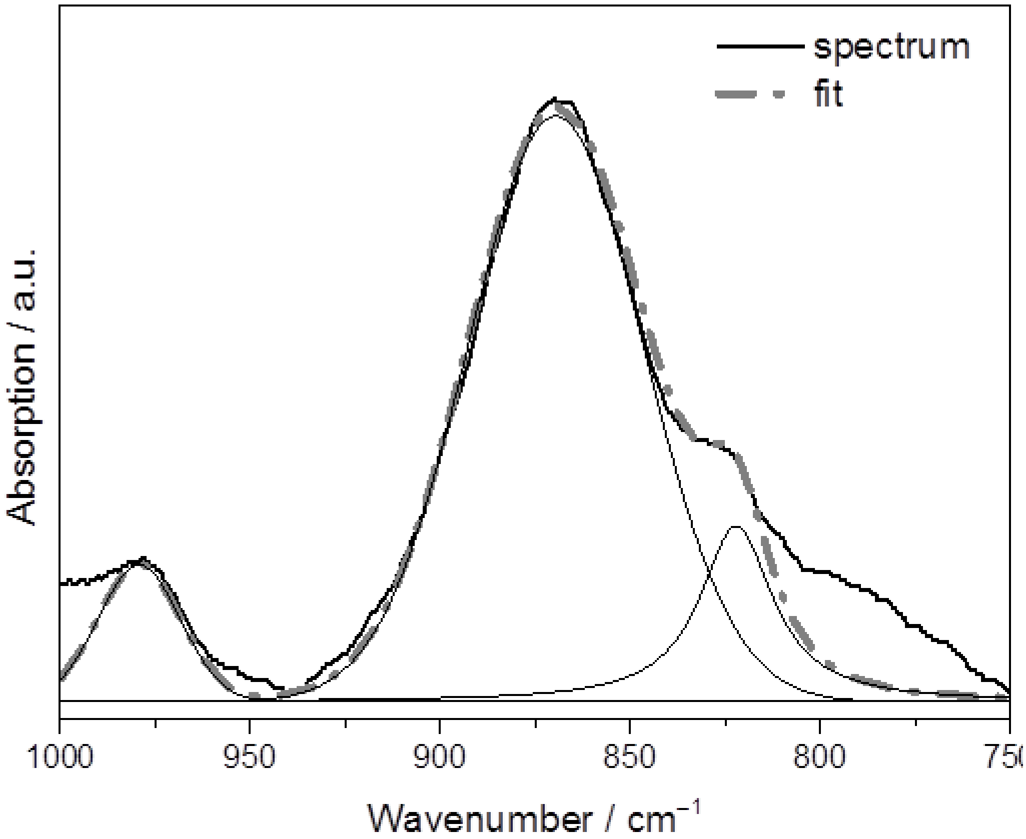

Fig. A.14 Deconvolution of the IR spectrum of selenium(VI) sorption onto hematite. ($[Se^{VI}]_{initial} = 5 \times 10^{-4}$ mol L^{-1}, D_2O, pD 8.0, 0.1 mol L^{-1} NaCl, 20 min of sorption, N_2). Dotted line indicates the overall fit.

EXAFS measurements

Selenium K-edge XANES (X-ray Absorption Near-Edge Structure) and EXAFS spectra were collected at the Rossendorf Beamline at ESRF (Grenoble, France). The energy of the X-ray beam was tuned by a Si(111) double-crystal monochromator operating in channel-cut mode. Two platinum-coated Si mirrors before and after the monochromator were used to collimate the beam into the monochromator and to reject higher harmonics. A 13-element high purity germanium detector (Canberra) together with a digital signal processing unit (XIA) was used to measure samples in fluorescence mode.

Samples with different pH values were prepared under CO_2-free conditions by reacting an appropriate mass of solid (to get sufficient solid material for XAS analysis) with selenium(IV) or selenium(VI). After shaking to reach sorption equilibrium, the samples were ultracentrifuged during 30 minutes at 187,000 × g. The wet pastes were transferred into sample holders, which were covered with Kapton tape and flash-frozen in liquid N_2. Great care was taken to exclude O_2 during sample transport and storage by keeping them in liquid N_2. At the beamline, they were rapidly (2 min) transferred to a closed-cycle He cryostat (with a large fluorescence exit window and a low vibration level (CryoVac), where they were kept at 15 K during the XAS measurements. As was confirmed by comparing repetitive short (10 min) XANES scans, the cooling prevented photon-induced redox reactions of the samples. For energy calibration, a gold foil (K-edge at 11919 eV) was chosen because of its greater inertness in comparison to Se. Data in the XANES region were collected in steps of 0.5 eV, i. e. with higher resolution than the resolution of the Si(111) crystal at the given vertical divergence (1.7 eV) and the broadening due to the core-hole life-time (2.3 eV). A comparison of single scans of the same sample showed an accuracy of better than 0.5 eV. Dead time correction of the fluorescence signal, energy calibration and the averaging of single scans were performed with the software package SixPack [WEBB '05]. Normalization, transformation from energy into k space, and subtraction of a spline background was performed with WinXAS using routine procedures [RESSLER '98]. Shell-fit of EXAFS data was performed with WinXAS using theoretical backscattering amplitudes and phase shifts calculated with FEFF 8.2 [ANKUDINOV '97]. The EXAFS data were also analyzed using the statistical software package ITFA [ROSSBERG '03] and with Morlet wavelets [FUNKE '05].

A.5 Surface Complexation Modeling of Se(VI) and Se(IV) sorption processes

Potentiometric titrations

To determine the acid–base properties of maghemite, potentiometric titrations (pH range 3 to 10) were performed in NaCl at different ionic strengths (0.1, 0.05 and 0.01 M) with a Metrohm 736 GP Titrino titrator. For each titration, a 30 g L^{-1} suspension of maghemite was inserted in a borosilicate vessel and equilibrated over night at pH ~3. A continuous argon flux (Argon N50 from Air Liquide) was streamed over the suspension to avoid dissolution of atmospheric CO_2. To ensure a homogeneous suspension, a Teflon propeller was used. After pre-equilibration, basic titration was performed by addition of 20 µL increments of 0.1 M NaOH in the suspensions. The pH electrode (Schott BlueLine 11pH) was calibrated using a three point calibration with buffer solutions (pH 4.01, 6.87 and 9.18). The allowed drift in potential between additions of the NaOH solution was set at 0.50 mV min^{-1}.

A.6 Electrochemical synthesis of Se(−II)

UV-vis spectroscopy

UV-vis measurements were performed on a TIDAS 100 (J&M Analytik) with a 5 cm pathlength cuvette. The cell was filled in the glovebox under inert conditions.

NMR spectroscopy

Solution NMR spectra were recorded on an Agilent DD2-600 MHz NMR system, operating at 14.1 T and a corresponding ^{77}Se resonance frequency of 114.4 MHz. A 10 mm dual broadband direct detection probe and a quarterwave switch for ^{77}Se was used.

B Appendix B (chapter 7)

B.1 Chemicals

Tab. B.1 Provenance and mass purity fraction of materials studied

Material	Source	Mass purity fraction	Remark
Na_2SeO_3	Sigma Aldrich	≥ 0.99999	
Na_2SeO_3	Aldrich	≥ 0.99	two times recrystallized
H_2SeO_3	Aldrich	≥ 0.99999	to prepare K_2SeO_3
$KOH \cdot H_2O$	Merck	≥ 0.99995	to prepare K_2SeO_3
$Na_2SeO_4 \cdot 10H_2O$	Aldrich	≥ 0.99999	
K_2SeO_4	Alfa Aesar	≥ 0.995	
H_2SeO_4 40 %	Aldrich	≥ 0.9995	to prepare MgSeO4 and $CaSeO_4$
$4MgCO_3 \cdot Mg(OH)_2 \cdot 5H_2O$	Merck		to prepare $MgSeO_4$
$CaCO_3$	Merck		
NaI	Merck	≥ 0.9999	
KI	Merck	≥ 0.99995	
MgI_2	Alfa Aesar	≥ 0.9996	
CaI_2	Alfa Aesar	≥ 0.99999	
CsCl	AppliChem	≥ 0.999	
Cs_2SO_4	Alfa Aesar	≥ 0.99997	
$MgCl_2 \cdot 6H_2O$	Merck	≥ 0.99	
$MgSO_4 \cdot 7H_2O$	Sigma Aldrich	≥ 0.995	
$CaCl_2 \cdot 4H_2O$	Merck		reference solution and to prepare $CaSeO_3$
NaCl	Merck	≥ 0.9999	
KCl	Merck	≥ 0.99999	
$K_3[Fe(CN)_6]$	Sigma Aldrich	≥ 0.99	
$K_4[Fe(CN)_6] \cdot 3H_2O$	Sigma Aldrich	≥ 0.99	
Phosphate buffer solution pH 7.5 0.1M	Sigma		

B.2 Preparation of reagents for isopiestic and solubility measurements

K_2SeO_3 solution

1. A solution of selenious acid is prepared by dissolving H_2SeO_3 in water. Its concentration is determined by ICP-OES using a standard addition procedure
2. A solution of KOH is prepared by adding KOH pellets to water in a plastic bottle. The KOH content is determined by means of an acid-base titration
3. The solution of K_2SeO_3 is prepared by mixing the H_2SeO_3 and KOH solutions in a stoichiometric ratio. The pH is test by using pH test strips
4. A rotary evaporator is employed to increase the concentration of K_2SeO_3

$CaSeO_3$

Calcium selenite has been prepared by adding a solution of $CaCl_2$ to a solution of K_2SeO_3 (prepared by the procedure written in the section above). The precipitate is washed with water until a test with silver nitrate gave no precipitation.

$CaSeO_4$

1. 16 ml of a 40 % solution of selenic acid (H_2SeO4) are added to 200 ml water and heated to 80 °C

2. 4.6 g $CaCO_3$ are added in small amounts under stirring. A surplus of a not dissolvable solid should be visible that ensures that the acid has been completely consumed. The resulting pH should be neutral to slightly alkaline (7 – 8)

3. The solution is filtered through a folded filter and left standing over night

4. The pH is tested again (pH test strip) and the solution filtered for another time

5. The solvent is removed almost until dryness by means of a surface evaporator

6. The crystals are dissolved in a minimal amount of water in order to produce a near saturated solution

7. The solution is filtered through a membrane filter (0.45 to 2 µm). The resulting pH should be at 7.5 (pH test strip)

8. The filtered solution is placed in a desiccator above a molecular sieve

9. The crystals are further dried on filter paper an placed in a desiccator again

10. The resulting crystals are weighed and placed in a desiccator again. This procedure is repeated until the weight is constant between two measurements.

11. The determination of the Ca and Se content is made by ICP-OES

12. X-ray diffraction is used to confirm the identity of the synthesized compound (calcium selenite dihydrate)

$MgSeO_4$

1. 100 ml selenic acid (H2SeO4, 40 %) are filled in a beaker

2. 40 g magnesium hydroxide carbonate (4 $MgCO_3 \cdot Mg(OH)_2 \cdot 5\ H_2O$ are added in small portions under constant stirring. The addition must be done slowly because a strong foaming occurs

3. Let the solution stand until the gas formation is concluded. There must be a surplus of a not dissolved solid. This is a sign that the selenic acid has been completely consumed. The pH must be neutral to slightly alkaline (pH test stripes)

4. The solution is filtered through a folded filter and left standing overnight

5. The solvent is removed by a surface evaporator until the remaining solid is almost dry

6. The crystals are removed and dissolved in a minimum quantity of water

7. The almost saturated solution is filtered through a membrane filter (0.45 to 2 µm). The pH of the filtered solution should be near 7.5 (pH test stripes)

8. The filtered solution is placed in a desiccator above a molecular sieve

9. The crystals are further dried on filter paper an placed in a desiccator again

10. The resulting crystals are weighed and placed in a desiccator again. This procedure is repeated until the weight is constant between two measurements

11. The determination of the Mg and Se content is made by ICP-OES

B.3 Calculated isoactivity lines

Tab. B.2 Calculated water isoactivity lines for the systems (Na,Mg,K)-Cl-SeO$_4$-H$_2$O at 40° -90 °C

Temp.	Salt 1	Salt 1 concentration	Salt 2	Salt 2 concentration	Water activity
[°C]		[mol/kg]		[mol/kg]	[]
40	$MgCl_2$	2	$MgSeO_4$	3.6082	0.8515
40	NaCl	5.6	Na2SeO$_4$	4.4607	0.7786
40	KCl	5	K_2SeO_4	3.5676	0.8340
60	$MgCl_2$	2	$MgSeO_4$	3.6788	0.8564
60	NaCl	5.6	Na_2SeO_4	4.5096	0.7798
60	KCl	5	K_2SeO_4	3.6536	0.8330
90	$MgCl_2$	2	$MgSeO_4$	3.8180	0.8639
90	NaCl	5.6	Na_2SeO_4	4.5723	0.7837
90	KCl	5	K_2SeO_4	3.7841	0.8335

Tab. B.3 Calculated water isoactivity lines for the systems (Na,Mg,K)-SO$_4$-SeO$_4$-H$_2$O at 40°-90 °C

Temp.	Salt 1	Salt 1 concentration	Salt 2	Salt 2 concentration	Water activity
[°C]		[mol/kg]		[mol/kg]	[]
40	$MgSO_4$	2.8	MgSeO4	2.4961	0.9217
40	Na_2SO_4	2	Na2SeO4	1.6948	0.9325
40	K_2SO_4	0.7	K2SeO4	0.6265	0.9746
60	$MgSO_4$	2.8	MgSeO4	2.4906	0.9281
60	Na_2SO_4	2	Na2SeO4	1.7313	0.9312
60	K_2SO_4	0.7	K2SeO4	0.6314	0.9745
90	$MgSO_4$	2.8	MgSeO4	2.5128	0.9375
90	Na_2SO_4	2	Na2SeO4	1.7375	0.9320
90	K_2SO_4	0.7	K2SeO4	0.6317	0.9749

Tab. B.4 Calculated water isoactivity lines for the systems containing iodide at 40°-90°C

Temp.	Salt 1	Salt 1 concentration	Salt 2	Salt 2 concentration	Water activity
[°C]		[mol/kg]		[mol/kg]	[]
40	$MgCl_2$	5.05103	MgI_2	4.3524	0.44532442
40	KI	4.5000	MgI_2	1.8012	0.8416412
40	MgI_2	2.5000	NaI	5.5664	0.74133559
60	$MgCl_2$	5.05103	MgI_2	4.3818	0.46519122
60	KI	4.5000	MgI_2	1.8499	0.83808267
60	MgI_2	2.5000	NaI	5.4079	0.74750656
90	$MgCl_2$	5.05103	MgI_2	4.4675	0.49469375
90	KI	4.5000	MgI_2	1.9191	0.83429166
90	MgI_2	2.5000	NaI	5.1615	0.75751368
40	NaCl	5.05103	NaI	4.4427	0.80390325
40	KI	4.5000	NaI	3.7309	0.8416412
40	KCl	4.5000	KI	4.2385	0.85137365
60	NaCl	5.05103	NaI	4.3837	0.80441113
60	KI	4.5000	NaI	3.7555	0.83808267
60	KCl	4.5000	KI	4.1799	0.85035618
90	NaCl	5.05103	NaI	4.2645	0.80734068
90	KI	4.5000	NaI	3.7686	0.83429166
90	KCl	4.5000	KI	4.0845	0.85070817

B.4 Solubility of LDH phases

Tab. B.5 Final composition of Opalinus pore solutions in contact with chloride hydrotalcite partly substituted by Co, Ni or Fe

LDH type	No.	Density	pH (app.)	pcH	Na	K	Mg	Ca	Cl	SO_4	Al	Co/Ni/Fe	log K
		[kg/l]			[mol/kg]								
Ni	2	1.0114	8.82	8.95	0.254	0.00225	0.0179	0.0280	0.329	0.0107	2.33E-05	2.64E-07	45.2
Ni	3	1.0118	8.82	8.73	0.274	0.00235	0.0198	0.0301	0.360	0.0114	2.68E-05	2.63E-07	45.4
Ni	4	1.0114	8.8	8.73	0.250	0.00223	0.0180	0.0268	0.325	0.0104	2.29E-05	2.46E-07	45.1
Co	2	1.0114	8.72	8.71	0.257	0.00241	0.0175	0.0284	0.338	0.0120	1.95E-05	3.08E-07	45.2
Co	3	1.0114	8.73	9.01	0.259	0.00239	0.0172	0.0288	0.335	0.0120	1.83E-05	3.18E-07	45.2
Co	4	1.0114	8.71	8.63	0.271	0.00241	0.0185	0.0296	0.350	0.0124	1.47E-05	2.39E-07	45.1
Fe	2	1.0114	8.69	8.64	0.248	0.00211	0.0175	0.0270	0.322	0.0096	9.07E-06	<2E-6	-
Fe	3	1.0113	8.62	8.62	0.250	0.00213	0.0172	0.0266	0.323	0.0095	1.19E-05	<2E-6	-
Fe	4	1.0113	8.45	8.73	0.244	0.00213	0.0172	0.0275	0.321	0.0097	1.30E-05	<2E-6	-

Tab. B.6 Final composition of Mg rich brine in contact with chloride hydrotalcite partly substituted by Co, Ni or Fe

LDH type	No.	Density	pH (app.)	pcH	Na	K	Mg	Ca	Cl	SO_4	Al	Co/Ni/Fe
		[kg/l]			[mol/kg]							
Ni	2	1.3339	4.85	7.62	0.0781	0.0233	5.73	0.280	10.01	<2E-5	2.55E-04	1.88E-05
Ni	3	1.3341	4.51	7.73	0.0785	0.0231	5.84	0.284	10.15	<2E-5	2.30E-04	1.29E-05
Ni	4	1.3338	4.55	7.73	0.0758	0.0228	5.70	0.284	10.02	<2E-5	2.56E-04	2.39E-05
Co	2	1.3341	4.94	7.65	0.0775	0.0233	5.82	0.283	10.07	<2E-5	1.99E-04	2.01E-05
Co	3	1.3342	4.49	7.78	0.0779	0.0232	5.84	0.282	10.06	<2E-5	1.99E-04	1.99E-05
Co	4	1.3341	4.6	7.73	0.0769	0.0228	5.76	0.284	10.02	<2E-5	1.88E-04	1.98E-05

Tab. B.7 Final composition of Opalinus pore solutions in contact with chloride hydrotalcite (data not previously published)

LDH type	No.	Density	pH	pcH	Na	K	Mg	Ca	Cl	SO_4	Al	log K	log K
		[kg/l]			[mol/kg]							based on documented pH	based on pH=8.86
pure	2	1.01078	6.82	6.73	0.233	0.00124	0.0163	0.0241	0.298	0.0135	3.19E-05	36.7	45.5
pure	3	1.01082	6.52	6.43	0.237	0.00135	0.0164	0.0245	0.300	0.0139	3.12E-05	35.1	45.5
pure	4	1.01075	6.42	6.33	0.236	0.00128	0.0162	0.0238	0.297	0.0134	3.14E-05	34.5	45.5

Tab. B.8 Final composition of Opalinus pore solutions in contact with chloride hydrotalcite partly substituted with Eu^{3+} (data not previously published)

LDH type	No.	Density	pH	pcH	Na	K	Mg	Ca	Cl	SO_4	Al	Eu	log K
		[kg/l]			[mol/kg]								
Eu	2	1.01115	8.82	8.72	0.240	0.00176	0.0170	0.0229	0.299	0.0136	3.45E-05	2.49E-06	47.2
Eu	3	1.01093	8.77	8.67	0.239	0.00153	0.0169	0.0228	0.298	0.0136	1.77E-05	7.96E-09	46.7
Eu	4	1.01156	8.79	8.70	0.239	0.00160	0.0168	0.0231	0.297	0.0139	2.23E-05	1.46E-08	46.9

Tab. B.9 Final composition of 0.3 M $MgCl_2$ solutions in contact with chloride hydrotalcite partly substituted by Co, Ni or Fe

LDH type	**No.**	**Density**	**pH (app.)**	**pcH**	**Mg**	**Cl***	**Al**	**Co/Ni/Fe**
		[kg/l]			**[mol/kg]**			
Ni	2	1.0209	8.14	8.11	0.314	0.627	2.39E-05	6.22E-07
Ni	3	1.021	8.14	8.12	0.325	0.650	2.09E-05	5.74E-07
Ni	4	1.021	8.15	8.12	0.307	0.614	2.29E-05	5.62E-07
Co	2	1.0205	8.20	8.17	0.306	0.612	2.09E-05	2.50E-06
Co	3	1.0209	8.15	8.12	0.308	0.617	1.97E-05	2.92E-06
Co	4	1.0209	8.22	8.19	0.312	0.623	2.16E-05	2.95E-06
Fe	2	1.0209	7.76	7.74	0.317	0.633	1.10E-05	<2E-6
Fe	3	1.0209	7.8	7.78	0.322	0.644	1.56E-05	<2E-6
Fe	4	1.0209	7.78	7.76	0.317	0.633	1.08E-05	<2E-6

Tab. B.10 Final composition of 1 M $MgCl_2$ solutions in contact with chloride hydrotalcite partly substituted by Co, Ni or Fe

LDH type	**No.**	**Density**	**pH (app.)**	**pcH**	**Mg**	**Cl***	**Al**	**Co/Ni/Fe**
		[kg/l]			**[mol/kg]**			
Ni	2	1.0763	7.44	7.80	1.08	2.16	9.66E-06	1.45E-06
Ni	3	1.0766	7.49	7.84	1.06	2.13	1.04E-05	1.40E-06
Ni	4	1.0769	7.46	7.83	1.09	2.18	1.88E-05	1.54E-06
Co	2	1.0737	7.44	7.80	1.08	2.17	1.17E-05	6.59E-06
Co	3	1.0747	7.39	7.76	1.09	2.18	1.36E-05	6.77E-06
Co	4	1.0738	7.39	7.80	1.17	2.35	1.07E-05	7.28E-06
Fe	2	1.0748	7.31	7.68	1.09	2.17	1.02E-05	<2E-6
Fe	3	1.0752	7.33	7.70	1.09	2.18	1.75E-05	<2E-6
Fe	4	1.0746	7.33	7.70	1.09	2.19	8.64E-06	<2E-6

Tab. B.11 Final composition of 2 M $MgCl_2$ solutions in contact with chloride hydrotalcite partly substituted by Co, Ni or Fe

LDH type	**No.**	**Density**	**pH (app.)**	**pcH**	**Mg**	**Cl***	**Al**	**Co/Ni/Fe**
		[kg/l]			**[mol/kg]**			
Ni		1.1485	6.96	8.00	2.32	4.65	1.73E-05	1.57E-06
Ni	2	1.1454	6.77	7.79	2.29	4.57	2.34E-05	1.97E-06
Ni	3	1.1444	6.7	7.71	2.28	4.55	1.63E-05	1.90E-06
Ni	4	1.1441	6.8	7.79	2.24	4.48	1.68E-05	2.08E-06
Co	2	1.1484	7.14	8.17	2.31	4.62	2.10E-05	2.41E-06
Co	3	1.1457	6.7	7.73	2.31	4.62	1.61E-05	4.91E-06
Fe	2	1.1485	6.93	7.97	2.32	4.64	1.02E-05	<2E-6
Fe	3	1.1452	6.7	7.70	2.25	4.50	7.64E-06	<2E-6
Fe	4	1.1450	6.84	7.87	2.30	4.59	8.77E-06	<2E-6
Fe		1.1440	6.68	7.68	2.24	4.48	7.91E-06	<2E-6

B.5 Solubility of $K_4Fe(CN)_6$ and $K_3Fe(CN)_6$ in KCl

Tab. B.12 Solubility of $K_3Fe(CN)_6$ in KCl solutions at 25 °C

No.	Density	KCl	$K_3Fe(CN)_6$
	[kg/l]	[mol/kg]	
1	1.1848	0.517	1.339
2	1.1848	1.042	1.200
3	1.1841	1.586	1.038
4	1.1846	2.135	0.886
5	1.1859	2.621	0.757
6	1.1884	3.288	0.654
7	1.1925	3.825	0.530
8	1.1977	4.540	0.459

Tab. B.13 Solubility of $K_4Fe(CN)_6$ in KCl solutions at 25 °C

No.	Density	KCl	$K_4Fe(CN)_6$
	[kg/l]	[mol/kg]	
1	1.1848	0.588	0.708
2	1.1848	1.168	0.539
3	1.1841	1.703	0.417
4	1.1846	2.232	0.306
5	1.1859	3.016	0.244
6	1.1884	3.516	0.180
7	1.1925	4.239	0.141
8	1.1977	4.783	0.108

B.6 Titration experiments

Tab. B.14 Titration experiment 1: Increasing KCl concentration (using stock solutions A2 and B2)

Step	**KCl**	**$K_3Fe(CN)_6$**	**$K_4Fe(CN)_6$**	**pH_{app}**	**Eh_{app}**
	[mol/kg]				**[mV]**
0	0.0978	0.00481	0.00492	7.379	217.5
1	0.1914	0.00486	0.00497	7.271	230.8
2	0.2812	0.00490	0.00501	7.215	239.2
3	0.3672	0.00495	0.00506	7.175	245.6
4	0.4497	0.00499	0.00510	7.145	249.9
5	0.5289	0.00503	0.00514	7.121	253.8
6	0.7139	0.00512	0.00524	7.074	261.4
7	0.8822	0.00521	0.00533	7.040	267.4
8	1.1769	0.00536	0.00548	6.993	276.0
9	1.4266	0.00549	0.00561	6.961	281.9
10	1.6407	0.00560	0.00572	6.937	286.2
11	1.8265	0.00569	0.00582	6.920	289.7
12	1.9891	0.00577	0.00590	6.906	292.6
13	2.1327	0.00585	0.00598	6.895	295.0
14	2.2604	0.00591	0.00604	6.886	297.1
15	2.3747	0.00597	0.00610	6.878	299.0

Tab. B.15 Titration experiment 2: decreasing concentration of KCl (using stock solutions A2 and B2)

Step	**KCl**	**$K_3Fe(CN)_6$**	**$K_4Fe(CN)_6$**	**pH_{app}**	**Eh_{app}**
	[mol/kg]				**[mV]**
0	4.4403	0.00702	0.00718	6.779	313.0
1	3.9011	0.00675	0.00690	6.796	309.2
2	3.4811	0.00653	0.00668	6.810	305.8
3	3.1446	0.00636	0.00650	6.823	302.7
4	2.8690	0.00622	0.00636	6.831	300.0
5	2.6391	0.00611	0.00624	6.844	297.5
6	2.4444	0.00601	0.00614	6.858	295.3
7	2.2775	0.00592	0.00605	6.869	293.2
8	2.1327	0.00585	0.00598	6.891	291.3

Tab. B.16 Titration experiment 3: increasing concentration of KCl (using stock solutions A3 and B3)

Step	KCl	$K_3Fe(CN)_6$	$K_4Fe(CN)_6$	pH_{app}	Eh_{app}
	[mol/kg]				[mV]
0	0.0971	0.00598	0.00611	7.397	218.4
1	0.1901	0.00604	0.00617	7.286	231.0
2	0.2791	0.00609	0.00623	7.230	238.7
3	0.3645	0.00615	0.00628	7.190	244.2
4	0.4464	0.00620	0.00634	7.160	248.4
5	0.5251	0.00625	0.00639	7.137	251.8
6	0.7087	0.00637	0.00651	7.090	258.3
7	0.8756	0.00647	0.00661	7.056	263.0
8	1.1681	0.00666	0.00680	7.010	269.5
9	1.4158	0.00681	0.00696	6.979	273.7
10	1.6282	0.00695	0.00710	6.957	276.7
11	1.8125	0.00706	0.00722	6.940	278.8
12	1.9738	0.00717	0.00732	6.928	280.5
13	2.1162	0.00726	0.00742	6.917	281.8
14	2.2428	0.00734	0.00750	6.908	282.8
15	2.3561	0.00741	0.00757	6.900	283.7

Tab. B.17 Titration experiment 4: decreasing concentration of KCl (using stock solutions A3 and B3)

Step	KCl	$K_3Fe(CN)_6$	$K_4Fe(CN)_6$	pH_{app}	Eh_{app}
	[mol/kg]				[mV]
0	4.403	0.00870	0.00889	6.830	286.1
1	3.869	0.00836	0.00855	6.846	285.6
2	3.453	0.00810	0.00828	6.859	284.7
3	3.119	0.00789	0.00806	6.868	283.6
4	2.846	0.00772	0.00789	6.875	282.5
5	2.618	0.00757	0.00774	6.886	281.3
6	2.425	0.00745	0.00762	6.897	280.2
7	2.260	0.00735	0.00751	6.905	279.0
8	2.116	0.00726	0.00742	6.917	277.9

B.7 Isopiestic Measurements

Tab. B.18 Isopiestically determined water activities of binary solutions at 40 °C - I

Ves sel	CsCl	Cs_2SO_4	NaI	KI	MgI_2	Reference	aW
	[mol/kg]						
1-2	0.6630	0.5431	0.6206	0.6245		0.6243	0.9794
1-3		0.5526	0.6307	0.6349		0.6345	0.9790
1-4	0.6850	0.5613	0.6405	0.6443		0.6447	0.9787
4-2	5.6113				1.9270	4.6381	0.8223
4-3	5.6889	3.9043	4.2574	5.0445	1.9436	4.6758	0.8206
4-4	5.7483	3.9427	4.2992	5.0999	1.9573	4.7191	0.8187
7-2	1.4944	1.2078	1.3107	1.3704	0.7497	1.3578	0.9541
Reference		NaCl					

Tab. B.19 Isopiestically determined water activities of binary solutions at 40 °C - II

Vessel	NaI	Na_2SeO_3	K_2SeO_4			Reference	aW
	[mol/kg]						
10-1	5.5765	4.7876				3.1026	0.7440
10-2	5.6820	4.7987				3.1206	0.7419
11-1	5.1061	4.4278	4.7805			2.8785	0.7699
11-2	5.2749	4.4189	4.8513			2.8819	0.7696
Reference		$CaCl_2$					

Tab. B.20 Isopiestically determined water activities of binary solutions at 40 °C - III

Vessel	**Cs_2SO_4**	**NaI**	**Na_2SeO_3**	**K_2SeO_4**	**Na_2SeO_4**	**Reference**	**aW**
	[mol/kg]						
12-1	4.4677	4.6247	4.0502	4.3420	4.2093	5.3048	0.7923
12-2	4.5518	4.7465	4.0361	4.3878	4.2200	5.3927	0.7882
13-1	3.8659	3.9971	3.5468	3.7743	3.6997	4.5444	0.8264
14-1	3.4588	3.5845	3.1604	3.3652	3.3379	4.0237	0.8492
14-2	3.5127	3.6259	3.2435	3.4302	3.3851	4.0995	0.8459
15-1	2.5502	2.6254	2.3678	2.4810	2.5130	2.9068	0.8957
15-2	2.6119	2.6870	2.4361	2.5474	2.5574	3.0006	0.8919
16-1	1.8646	1.9203	1.7385	1.7962	1.8134	2.1054	0.9268
16-2	1.9040	1.9585	1.7740	1.8418	1.8534	2.1510	0.9251
16-3	1.9543	2.0122	1.8191	1.8874	1.9031	2.2099	0.9229
17-1	1.3711	1.4210	1.2649	1.3046	1.3043	1.5342	0.9479
18-1	0.9221	0.9754	0.8456	0.8679	0.8666	1.0363	0.9654
19-1	0.3775	0.4246	0.3461	0.3531	0.3480	0.4390	0.9855
Reference		NaCl					

Tab. B.21 Isopiestically determined water activities of binary solutions at 40 °C - IV

Vessel	**CsCl**	**KI**	**$MgSeO_4$**			**Reference**	**aW**
	[mol/kg]						
20-1	5.3487	4.7769				4.4512	0.8306
20-2	5.4381	4.8508				4.5145	0.8278
21-1	4.9928	4.4649				4.1854	0.8422
22-1	4.5510	4.0596				3.8385	0.8571
23-1	3.9392	3.5194				3.3662	0.8770
24-1	3.4181	3.0648	2.9769			2.9540	0.8938
24-2	3.4679	3.1073	3.0061			2.9958	0.8921
25-1	2.4912	2.2514	2.4813			2.2027	0.9232
25-2	2.5318	2.2813	2.5036			2.2335	0.9220
26-1	1.8403	1.6752	2.0565			1.6573	0.9434
27-1	1.3869	1.2766	1.7053			1.2658	0.9574
27-2	1.4034	1.2897	1.7196			1.2819	0.9568
28-1	0.9383	0.8769	1.2843			0.8759	0.9709
28-2	0.9524	0.8883	1.2976			0.8867	0.9705
29-1	0.3870	0.3695	0.5964			0.3709	0.9878
29-2	0.3959	0.3792	0.6125			0.3795	0.9875
Reference		NaCl					

Tab. B.22 Isopiestically determined water activities of binary solutions at 40 °C - V

Vessel	**MgI_2**	**CaI_2**	**K_2SeO_3**	**KOH in K_2SeO_3**		**Reference**	**aW**
	[mol/kg]						
30-1	4.7579	5.0246				6.3428	0.3818
31-1	4.2761	4.5556				5.5198	0.4563
32-1	3.7802	4.0279				4.7888	0.5370
33-1	3.3290	3.5572				4.1824	0.6112
34-1	2.8523	3.0757				3.5409	0.6912
35-1	2.2384	2.4148	3.4885	0.000193		2.7628	0.7830
39-1	0.4821	0.4994	0.5948	0.000162		0.5407	0.9738
Reference		$CaCl_2$					

Tab. B.23 Isopiestically determined water activities of binary solutions at 60 °C - I

Vessel	**CsCl**	**Cs_2SO_4**	**NaI**	**KI**	**MgI_2**	**Reference**	**aW**
	[mol/kg]						
2-4	0.6796	0.5492	0.6345	0.6403		0.6364	0.9790
5-1	5.7453	3.9783	4.2420	4.9748	1.9902	4.7017	0.8198
5-2	5.8324	4.0482	4.3569	5.1091	2.0187	4.8296	0.8142
5-4	6.0271	4.1585	4.4889	5.2820	2.0657	4.9806	0.8076
8-2	1.5571	1.2431	1.3430	1.4144	0.7783	1.3997	0.9525
Reference		NaCl					

Tab. B.24 Isopiestically determined water activities of binary solutions at 60 °C - II

Vessel	**CsCl**	**KI**	**K_2SeO_3**	**KOH in K_2SeO_3**	**$MgSeO_4$**	**$CaSeO_4$**	**Reference**	**aW**
	[mol/kg]							
40-1	6.1224	5.3722	3.3388	0.000217			5.0632	0.8039
40-2	6.4757	5.6776					5.3059	0.7932
41-1	5.7702	5.0750	3.1573	0.000257			4.8007	0.8155
42-1	5.0051	4.4199	2.8270	0.000305			4.2246	0.8405
42-2	5.1330	4.5283	2.9331	0.000317			4.3272	0.8361
43-1	4.3287	3.8136	2.5058	0.000284			3.7004	0.8628
43-2	4.4587	3.9276					3.8013	0.8586
44-1	3.8408	3.4015					3.3093	0.8790
45-1	2.6355	2.3524	1.6473	0.000251	2.7299		2.3305	0.9180
46-1	1.9693	1.7796	1.2775	0.000245	2.2568		1.7735	0.9390
46-2	2.1323	1.9147			2.3673		1.9076	0.9340
47-1	1.4588	1.3298	0.9749	0.000235	1.8511		1.3336	0.9549
48-1	0.9881	0.9140	0.6861	0.000220	1.4041		0.9195	0.9694
48-2		0.9658			1.4437		0.9668	0.9677
49-1	0.3978	0.3765	0.2806	0.000200	0.6377		0.3781	0.9875
49-2	0.4175	0.3944	0.2934	0.000210	0.6698		0.3953	0.9870
49B-2	0.1692	0.1684	0.1222	0.000195	0.2720	0.2802	0.1697	0.9944
Reference		NaCl						

Tab. B.25 Isopiestically determined water activities of binary solutions at 60 °C - III

Vessel	**NaI**	**Reference**	**aW**
	[mol/kg]		
50-1	6.2018	3.5455	0.7012
51-1	5.4921	3.1984	0.7414
Reference		$CaCl_2$	

Tab. B.26 Isopiestically determined water activities of binary solutions at 60 °C - IV

Vessel	Cs_2SO_4	NaI	Na_2SeO_3	NaOH in Na_2SeO_3	K_2SeO_4	Na_2SeO_4	Reference	aW
	[mol/kg]							
52-1	4.7834	4.9686	4.4681	0.000123	4.7630		5.7906	0.7716
53-1	4.1451		3.9355	0.000226		4.3328	5.2026	0.7978
53-2	4.4863	4.6451	4.2420	0.000244	4.4503	4.4191	5.3957	0.7892
53-3	4.2834	4.4588			4.2845	4.2047	5.1406	0.8005
54-2	3.7195	3.8681	3.5247	0.000230	3.7075	3.6737	4.3914	0.8333
55-2	2.9101	3.0428	2.8203	0.000223	2.9109	2.9071	3.4119	0.8748
57-1	1.4867	1.5683	1.4058	0.000177	1.4470	1.4584	1.6875	0.9421
57-2	1.5551	1.6298	1.4611	0.000184	1.5117	1.5181	1.7633	0.9394
58-1	0.9736	1.0447			0.9233		1.0966	0.9632
58-2	1.0287	1.0928	0.9320	0.000170	0.9799	0.9735	1.1558	0.9612
59-2	0.3867	0.4406	0.3536	0.000131	0.3680	0.3640	0.4543	0.9850
Reference		NaCl						

Tab. B.27 Isopiestically determined water activities of binary solutions at 90 °C - I

Vessel	CsCl	Cs_2SO_4	NaI	KI	MgI_2	Reference	aW
	[mol/kg]						
3-2	0.7393	0.6118	0.6867	0.6855		0.6859	0.9774
3-4	0.8226	0.6747	0.7600	0.7630		0.7746	0.9745
6-1	5.8405	4.1537	4.3782	5.0564	2.0781	4.9238	0.8133
6-2	6.4370	4.5248	4.7767	5.5641	2.2297	5.3894	0.7936
6-3	6.9414	4.8123	5.1012	6.0067	2.3599	5.7717	0.7774
6-4	7.3267	5.0072	5.3307	6.3194	2.4451	6.0488	0.7657
9-2	2.2027	1.7655	1.8562	1.9527	1.0455	1.9538	0.9327
Reference		NaCl					

Tab. B.28 Isopiestically determined water activities of binary solutions at 90 °C - II

Ves-sel	KI	K_2SeO_3	KOH in K_2SeO_3	$MgSeO_4$		Refer-ence	aW
	[mol/kg]						
61-1	6.8828					6.6128	0.7420
62-1	5.9336	3.7145	0.000137			5.6826	0.7812
63-1	5.0716	3.3332	0.000238			4.7115	0.8223
63-2	5.4162	3.4809	0.000249			5.2404	0.7999
63-3	5.9711	3.7960	0.000271			5.7782	0.7771
64-1	3.6836	2.5299	0.000185			3.6402	0.8668
65-1	2.6749	1.9101	0.000196			2.6737	0.9054
66-1	1.7700			2.4308		1.7808	0.9391
67-1		0.8890	0.000166	1.8692		1.2407	0.9584
67-2	1.3859	1.0321	0.000193	2.0775		1.4038	0.9527
68-1	0.5620	0.4322	0.000155	1.0088		0.5711	0.9813
68-2				1.1282		0.6319	0.9792
69-1	0.1972	0.1385	0.000125	0.3587		0.2048	0.9933
69-2	0.2151	0.1515	0.000137			0.2204	0.9928
Reference		NaCl					

Tab. B.29 Isopiestically determined water activities of binary solutions at 90 °C - III

Ves-sel	NaI					Refer-ence	aW
	[mol/kg]						
70-1	7.7637					4.5338	0.6143
71-1	7.2539					4.2725	0.6414
Reference		$CaCl_2$					

Tab. B.30 Isopiestically determined water activities of binary solutions at 90 °C - IV

Ves sel	Cs_2SO_4	NaI	Na_2SeO_3	NaOH in Na_2SeO_3	K_2SeO_4	Na_2SeO_4	Refer-ence	aW
		[mol/kg]						
72-1	5.4369	5.4849	5.2707	0.000097	5.4817		6.6039	0.7423
73-1	4.3172	4.4061	4.2533	0.000181	4.3516		5.1747	0.8027
73-2	5.3625	5.4475			5.4318		6.6073	0.7422
74-1	3.8183	3.8822	3.7388	0.000232	3.8423	3.8281	4.5160	0.8305
75-1	2.8688	2.9248	2.8141	0.000214	2.8723	2.8730	3.3378	0.8790
75-2	3.3837	3.4357	3.3167	0.000252	3.3971	3.3981	3.9802	0.8528
77-1	1.6405	1.6651	1.5847	0.000188	1.5987	1.6165	1.8676	0.9359
77-2	1.8735	1.9073	1.8041	0.000217	1.8366	1.7341	2.1283	0.9262
78-1	1.0602	1.1062	0.9777	0.000181	1.0139	1.0092	1.1943	0.9601
79-1	0.3585	0.4190	0.3262	0.000148	0.3475	0.3332	0.4211	0.9862
Reference		NaCl						

Tab. B.31 Isoactive solutions in the system $CaCl_2$-CsCl-H_2O at 25 °C I

T [°C]	Vessel 1		Vessel 2		Vessel 3	
step	$CaCl_2$	CsCl	$CaCl_2$	CsCl	$CaCl_2$	CsCl
	[mol/kg]					
1	0.0765	3.8604	0.1129	4.5044	0.0829	2.7262
2	0.1822	3.8287	0.2392	4.2949	0.1670	2.5940
3	0.2865	3.6445	0.3647	4.0872	0.2547	2.4525
4	0.2810	3.5863	0.4984	3.8549	0.3412	2.3096
5	0.3769	3.2624	0.5011	3.8500	0.3430	2.3100
6	0.4692	3.0986	0.6338	3.6128	0.4306	2.1586
7	0.5940	2.9106	0.7743	3.3450	0.5274	1.9904
8	0.6925	2.7236	0.9092	3.0771	0.6178	1.8258
9	0.6935	2.6820	1.0504	2.7829	0.7186	1.6315
10	0.8388	2.5615	1.0538	2.7755	0.7111	1.6450
11	0.9624	2.3180	1.1897	2.4757	0.8003	1.4676
12	1.0875	2.0696	1.3182	2.1754	0.8896	1.2870
13	1.1974	1.7867	1.4457	1.8607	0.9776	1.1006
14	1.1754	1.7450	1.5706	1.5337	1.0638	0.9096
15	1.3090	1.4815	1.5719	1.5308	1.0633	0.9111
16	1.4334	1.2035	1.6846	1.2169	1.1449	0.7211
17	1.5170	0.8885	1.7910	0.9048	1.2246	0.5345
18	1.6247	0.5925	1.8917	0.5930	1.2988	0.3507
19	1.7456	0.2912	1.9846	0.2907	1.3690	0.1725
20	0	4.1940	0	4.6931	0	2.8597
21	0	4.1923	0	4.6883	0	2.8599
22	0	4.1275	2.0698	0	1.4343	0
23	0	4.1282	2.0700	0	1.4336	0
Reference solution	**NaCl**		**NaCl**		**NaCl**	
Conc [mol/kg]	1.89901		3.90153		2.49153	
a_W	0.87126		0.85545		0.91284	

Tab. B.32 Isoactive solutions in the system $CaCl_2$-CsCl-H_2O at 25 °C II

No.	Vessel 1W		Vessel 4	
	$CaCl_2$	CsCl	$CaCl_2$	CsCl
	[mol/kg]			
1	0.0765	6.9930		0.9275
2	0.1822	6.7037		0.8771
3	0.2865	6.4134		0.8254
4	0.2810	6.4114		0.7646
5	0.3769	6.0785		0.7682
6	0.1665	5.7157	0.0338	0.7111
7	0.3342	5.3247	0.0683	0.6611
8	0.5004	4.9035	0.1039	0.5971
9	0.5026	4.8919	0.1428	0.5393
10	0.6845	4.4614	0.1412	0.5404
11	0.8744	3.9711	0.1776	0.4805
12	1.0662	3.4892	0.2158	0.4228
13	1.2616	2.9811	0.2506	0.3604
14	1.2663	2.9873	0.2869	0.3013
15	1.4549	2.4677	0.2863	0.3029
16	1.6557	1.9482	0.3230	0.2409
17	1.8374	1.4459	0.3588	0.1810
18	2.0166	0.9484	0.3965	0.1176
19	2.0139	0.4577	0.4314	0.0599
20	2.1877	7.2821	0.4305	0.9783
21	2.3395	7.2813	0.4664	0.9779
22	2.4776	7.2776	0.5008	0.0000
23	2.6026	7.2840	0.5368	0.0000
Reference solution	**CaCl2**		**NaCl**	
Conc [mol/kg]	2.81737		0.90516	
a_W	0.77217		0.97001	

Tab. B.33 Isoactive solutions in the system $MgSO_4$-Cs_2SO_4-H_2O at 25 °C I

No.	**Vessel 5**		**Vessel 6**		**Vessel 7**	
	$MgSO_4$	**Cs_2SO_4**	**$MgSO_4$**	**Cs_2SO_4**	**$MgSO_4$**	**Cs_2SO_4**
	[mol/kg]					
1	0.1464	1.7264	0.1247	1.3083	0.0938	0.8829
2	0.3100	1.6999	0.2597	1.2847	0.2011	0.8604
3	0.4863	1.6657	0.4301	1.2488	0.3107	0.8331
4	0.6826	1.6183	0.5710	1.2124	0.4276	0.7991
5	0.6820	1.6180	0.5729	1.2134	0.4274	0.7996
6	0.8909	1.5527	0.7385	1.1612	0.5495	0.7595
7	1.1064	1.4735	0.9152	1.0951	0.6781	0.7116
8	1.3190	1.3735	1.0896	1.0168	0.7976	0.6592
9	1.5334	1.2493	1.2630	0.9238	0.9229	0.5967
10	1.5393	1.2469	1.2586	0.9249	0.9258	0.5954
11	1.7253	1.1141	1.4144	0.8249	1.0383	0.5304
12	1.8985	0.9655	1.5665	0.7077	1.1458	0.4594
13	2.0488	0.8087	1.6822	0.6005	1.2385	0.3896
14	2.1728	0.6583	1.7880	0.4873	1.3288	0.3124
15	2.1713	0.6581	1.7896	0.4858	1.3268	0.3151
16	2.2715	0.5076	1.8776	0.3756	1.3949	0.2497
17	2.3538	0.3644	1.9494	0.2719	1.4580	0.1821
18	2.4178	0.2348	2.0071	0.1766	1.5175	0.1132
19	2.4669	0.1150	2.0568	0.0837	1.5614	0.0549
20	0.0000	1.7463	0.0000	1.3278	0.0000	0.9031
21	0.0000	1.7460	0.0000	1.3270	0.0000	0.9037
22	2.5094	0.0000	2.0983	0.0000	1.6018	0.0000
23	2.5094	0.0000	2.0984	0.0000	1.6019	0.0000
Reference solution	**NaCl**		**NaCl**		**NaCl**	
Conc [mol/kg]	1.97051		1.48562		1.01293	
a_W	0.93246		0.94996		0.96635	

Tab. B.34 Isoactive solutions in the system $MgSO_4$-Cs_2SO_4-H_2O at 25 °C II

No.	**Vessel 8**	
	$MgSO_4$	**Cs_2SO_4**
	[mol/kg]	
1	0.0559	0.4576
2	0.1150	0.4390
3	0.1793	0.4174
4	0.2435	0.3941
5	0.2430	0.3947
6	0.3077	0.3702
7	0.3756	0.3436
8	0.4430	0.3131
9	0.5079	0.2833
10	0.5078	0.2832
11	0.5704	0.2529
12	0.6325	0.2190
13	0.6873	0.1873
14	0.7447	0.1524
15	0.7397	0.1557
16	0.7963	0.1197
17	0.8349	0.0920
18	0.8794	0.0590
19	0.9186	0.0302
20	0.0000	0.4752
21	0.0000	0.4753
22	0.9552	0.0000
23	0.9552	0.0000
Reference solution	**NaCl**	
Conc [mol/kg]	0.54559	
a_W	0.98202	

Tab. B.35 Isoactive solutions in the system $MgCl_2$-CsCl-H_2O at 25 °C I

No.	**Vessel 9**		**Vessel 10**		**Vessel 11**	
	$MgCl_2$	**CsCl**	**$MgCl_2$**	**CsCl**	**$MgCl_2$**	**CsCl**
	[mol/kg]					
1	0.1396	6.2658	0.1137	4.5074	0.0773	2.7567
2	0.2926	5.9779	0.2275	4.3017	0.1587	2.6213
3	0.4439	5.6804	0.3574	4.0630	0.2491	2.4631
4	0.6056	5.3565	0.4751	3.8362	0.3357	2.3078
5	0.5990	5.3676	0.4781	3.8301	0.3343	2.3125
6	0.7574	5.0431	0.6055	3.5828	0.4224	2.1477
7	0.9230	4.6721	0.7300	3.3199	0.5123	1.9798
8	1.0912	4.2834	0.8623	3.0336	0.5949	1.8143
9	1.2538	3.8859	0.9895	2.7460	0.6845	1.6349
10	1.2545	3.8788	0.9888	2.7487	0.6827	1.6363
11	1.4152	3.4689	1.1119	2.4558	0.7715	1.4528
12	1.5714	3.0370	1.2402	2.1360	0.8551	1.2724
13	1.7266	2.5799	1.3572	1.8294	0.9374	1.0885
14	1.8686	2.1372	1.4729	1.5118	1.0191	0.8962
15	1.8678	2.1400	1.4716	1.5123	1.0192	0.8975
16	2.0007	1.6914	1.6379	1.0259	1.0940	0.7175
17	2.1250	1.2489	1.6810	0.8905	1.1694	0.5291
18	2.2390	0.8275	1.7767	0.5864	1.2387	0.3509
19	2.3436	0.4013	1.8658	0.2892	1.3080	0.1687
20	0.0000	6.5223	0.0000	4.7110	0.0000	2.8894
21	0.0000	6.5243	0.0000	4.7109	0.0000	2.8872
22	2.4390	0.0000	1.9495	0.0000	1.3693	0.0000
23	2.4390	0.0000	1.9495	0.0000	1.3691	0.0000
Reference solution	**NaCl**		**NaCl**		**NaCl**	
Conc [mol/kg]	5.19925		3.91322		2.51115	
a_W	0.79767		0.85495		0.91208	

Tab. B.36 Isoactive solutions in the system $MgCl_2$-CsCl-H_2O at 25 °C II

No.	**Vessel 12**	
	$MgCl_2$	**CsCl**
	[mol/kg]	
1	0.0323	0.9395
2	0.0698	0.8819
3	0.1055	0.8268
4	0.1443	0.7666
5	0.1400	0.7734
6	0.1779	0.7131
7	0.2147	0.6548
9	0.2895	0.5318
10	0.2863	0.5373
11	0.3222	0.4760
12	0.3601	0.4131
13	0.3942	0.3542
14	0.4261	0.2980
15	0.4274	0.2955
16	0.4611	0.2362
17	0.4926	0.1792
18	0.5263	0.1179
19	0.5581	0.0599
20	0.0000	0.9887
21	0.0000	0.9892
22	0.5900	0.0000
23	0.5901	0.0000
Reference solution	**NaCl**	
Conc [mol/kg]	0.91543	
a_W	0.96966	

B.8 Solubility of $CaSeO_3$ and $CaSeO_4$ in NaCl solutions

Tab. B.37 Solubility of $CaSeO_3$ in NaCl solutions at 25 °C

Batch No.	Density	NaCl	CaSeO3
	[kg/l]	[mol/kg]	
1/1	0.998116	0	0.000529
1/2	0.998116	0	0.000522
1/3	0.998116	0	0.000521
2/1	1.000563	0.0794	0.00139
2/2	1.000563	0.0805	0.00138
2/3	1.000563	0.0793	0.00137
3/1	1.006710	0.2287	0.00186
3/2	1.006710	0.2270	0.00194
3/3	1.006710	0.2285	0.00188
4/1	1.018974	0.5456	0.00258
4/2	1.018974	0.5437	0.00264
4/3	1.018974	0.5415	0.00259
5/1	1.028306	0.7857	0.00291
5/2	1.028306	0.7750	0.00278
5/3	1.028306	0.7866	0.00277
6/1	1.059604	1.6047	0.00337
6/2	1.059604	1.6046	0.00321
6/3	1.059604	1.6086	0.00331
7/1	1.094169	2.6567	0.00328
7/2	1.094169	2.6775	0.00332
7/3	1.094169	2.6579	
9/1	1.124672	3.6007	0.00316
9/2	1.124672	3.5786	0.00314
9/3	1.124672	3.6023	0.00309
10/1	1.158800	4.9347	0.00277
10/2	1.158800	4.8416	0.00272
10/3	1.158800	4.8231	0.00275
11/1	1.194052	5.9133	0.00236
11/2	1.194052	5.9463	0.00234
11/3	1.194052	5.7559	0.00220

Tab. B.38 Solubility of $CaSeO_3$ in NaCl solutions at 40 °C

Batch No.	Density	NaCl	$CaSeO_3$
	[kg/l]	[mol/kg]	
1/1	0.992577	0	
1/2	0.992577	0	0.000773
1/3	0.992577	0	0.000789
2/1	0.995604	0.0779	0.00123
2/2	0.995604	0.0777	0.00121
2/3	0.995604	0.0779	0.00126
3/1	1.001646	0.227	0.00166
3/2	1.001646	0.229	0.00166
3/3	1.001646	0.229	
4/1	1.013665	0.573	
4/2	1.013665	0.544	0.00240
4/3	1.013665	0.543	0.00239
5/1	1.022846	0.787	0.00262
5/2	1.022846	0.789	0.00260
5/3	1.022846	0.787	0.00258
6/1	1.053517	1.623	0.00302
6/2	1.053517	1.615	0.00313
6/3	1.053517	1.613	0.00305
7/1	1.087720	2.680	0.00320
7/2	1.087720	2.668	0.00331
7/3	1.087720	2.694	0.00327
9/1	1.117692	3.608	0.00310
9/2	1.117692	3.591	0.00300
9/3	1.117692	3.608	0.00301
10/1	1.151060	4.965	0.00251
10/2	1.151060	4.865	0.00252
10/3	1.151060	5.033	0.00264
11/1	1.186333	6.012	0.00222
11/2	1.186333	5.958	0.00218
11/3	1.186333	5.958	0.00229

Tab. B.39 Solubility of $CaSeO_3$ in NaCl solutions at 60 °C

Batch No.	Density	NaCl	$CaSeO_3$
	[kg/l]	[mol/kg]	
1/1	0.983480	0	0.000767
1/2	0.983480	0	0.000784
1/3	0.983480	0	0.000702
2/1	0.986444	0.0799	0.00110
2/2	0.986444	0.0792	0.00116
2/3	0.986444	0.0801	0.00112
3/1	0.992497	0.232	0.00165
3/2	0.992497	0.230	0.00159
3/3	0.992497	0.230	0.00163
4/1	1.004293	0.591	0.00234
4/2	1.004293	0.548	0.00235
4/3	1.004293	0.550	0.00224
5/1	1.013408	0.793	0.00235
5/2	1.013408	0.793	0.00235
5/3	1.013408	0.791	0.00244
6/1	1.043491	1.634	0.00301
6/2	1.043491	1.628	0.00287
6/3	1.043491	1.628	0.00292
7/1	1.077149	2.664	0.00283
7/2	1.077149	2.677	0.00303
7/3	1.077149	2.684	0.00295
9/1	1.107056	3.613	0.00281
9/2	1.107056	3.609	0.00283
9/3	1.107056	3.609	0.00282
10/1	1.140091	4.911	0.00241
10/2	1.140091	4.858	0.00238
10/3	1.140091	4.873	0.00242
11/1	1.175229	5.880	0.00213
11/2	1.175229	6.041	0.00222
11/3	1.175229	6.055	0.00221

Tab. B.40 Solubility of $CaSeO_4$ in NaCl solutions at 25 °C

Batch No.	Density	NaCl	$CaSeO_4$
	[kg/l]	[mol/kg]	
1/1	1.071866	0	0.458
1/2	1.071866	0	0.457
1/3	1.071866	0	0.453
2/1	1.074479	0.0696	0.470
2/2	1.074479	0.0645	0.442
2/3	1.074479	0.0636	0.442
3/1	1.082200	0.230	0.460
3/2	1.082200	0.227	0.460
3/3	1.082200	0.278	0.465
4/1	1.096297	0.542	0.490
4/2	1.096297	0.543	0.487
4/3	1.096297	0.546	0.497
5/1	1.103792	0.789	0.499
5/2	1.103792	0.777	0.490
5/3	1.103792	0.782	0.488
6/1	1.128505	1.634	0.493
6/2	1.128505	1.636	0.485
6/3	1.128505	1.618	0.485
7/1	1.155750	2.542	0.439
7/2	1.155750	2.539	0.421
7/3	1.155750	2.527	0.440
8/1	1.155748	2.648	0.458
8/2	1.155748	2.631	0.451
9/1	1.173579	3.495	0.413
9/2	1.173579	3.490	0.409
9/3	1.173579	3.495	0.395
10/1	1.199270	4.634	0.325
10/2	1.199270	4.624	0.322
10/3	1.199270	4.623	0.319
11/1	1.224410	5.815	0.252
11/2	1.224410	5.805	0.249
11/3	1.224410	5.720	0.248

Tab. B.41 Solubility of $CaSeO_4$ in NaCl solutions at 40 °C

Batch No.	Density	NaCl	$CaSeO_4$
	[kg/l]	[mol/kg]	
1/1	1.052996	0	0.364
1/2	1.052996	0	0.358
1/3	1.052996		
2/1	1.056552	0.0662	0.374
2/2	1.056552	0.0632	0.353
2/3	1.056552	0.0685	0.355
3/1	1.064299	0.222	0.375
3/2	1.064299	0.223	0.379
3/3	1.064299	0.225	0.374
4/1	1.078120	0.550	0.407
4/2	1.078120	0.558	0.411
4/3	1.078120	0.544	0.401
5/1	1.087177	0.782	0.409
5/2	1.087177	0.788	0.411
5/3	1.087177	0.780	0.412
6/1	1.112752	1.657	0.412
6/2	1.112752	1.648	0.413
6/3	1.112752	1.628	0.398
7/1	1.136240	2.537	0.372
7/2	1.136240	2.529	0.370
7/3	1.136240	2.535	0.369
9/1	1.162269	3.542	0.378
9/2	1.162269	3.526	0.372
9/3	1.162269	3.530	0.361
10/1	1.187658	4.672	0.285
10/2	1.187658	4.671	0.283
10/3	1.187658	4.655	0.283
11/1	1.214503	5.799	0.232
11/2	1.214503	5.825	0.233
11/3	1.214503	5.864	0.238

Tab. B.42 Solubility of $CaSeO_4$ in NaCl solutions at 60 °C

Batch No.	**Density**	**NaCl**	**$CaSeO_4$**
	[kg/l]	**[mol/kg]**	
1/1	1.034691	0	0.322
1/2	1.034691	0	0.321
1/3	1.034691	0	0.323
2/1	1.038319	0.0613	0.323
2/2	1.038319	0.0640	0.321
2/3	1.038319	0.0692	0.324
3/1	1.045984	0.229	0.333
3/2	1.045984	0.223	0.334
3/3	1.045984	0.223	0.334
4/1	1.059946	0.557	0.353
4/2	1.059946	0.554	0.349
4/3	1.059946	0.552	0.348
5/1	1.069599	0.790	0.356
5/2	1.069599	0.785	0.356
5/3	1.069599	0.795	0.359
6/1	1.097702	1.665	0.341
6/2	1.097702	1.687	0.347
6/3	1.097702	1.679	0.350
7/1	1.122230	2.579	0.313
7/2	1.122230	2.602	0.316
7/3	1.122230	2.562	0.309
9/1	1.147813	3.594	0.283
9/2	1.147813	3.566	0.283
9/3	1.147813	3.575	0.283
10/1	1.174154	4.681	0.224
10/2	1.174154	4.701	0.224
10/3	1.174154	4.677	0.223
11/1	1.201603	5.829	0.182
11/2	1.201603	5.772	0.183
11/3	1.201603	5.791	0.183

**Gesellschaft für Anlagen-
und Reaktorsicherheit
(GRS) gGmbH**

Schwertnergasse 1
50667 Köln
Telefon +49 221 2068-0
Telefax +49 221 2068-888

Forschungszentrum
Boltzmannstraße 14
85748 Garching b. München
Telefon +49 89 32004-0
Telefax +49 89 32004-300

Kurfürstendamm 200
10719 Berlin
Telefon +49 30 88589-0
Telefax +49 30 88589-111

Theodor-Heuss-Straße 4
38122 Braunschweig
Telefon +49 531 8012-0
Telefax +49 531 8012-200

www.grs.de

**Forschungszentrum Jülich GmbH
Institut für Energie- und Klimaforschung**
Wilhelm-Johnen-Straße
52428 Jülich

**Helmholtz-Zentrum Dresden-Rossendorf e. V.
Institut für Ressourcenökologie**
Bautzner Landstraße 400
01326 Dresden

**Karlsruher Institut für Technologie
Institut für Nukleare Entsorgung**
Hermann-von-Helmholtz-Platz 1
76344 Eggenstein-Leopoldshafen

ISBN 978-3-944161-55-6